

4th INTERNATIONAL ENGINEERING SYMPOSIUM – IES2015

**100th Anniversary Memorial Hall &
Faculty of Engineering (Building No.2)
Kumamoto University**

March 4-6, 2015



Conveners
Shuichi TORII
Professor, Department of Mechanical System Engineering
Kumamoto University, Japan
&
Katta VENKATARAMANA
Professor, Department of Civil Engineering
NITK, Surathkal, India

Organized by
Graduate School of Science & Technology
Kumamoto University, Japan

In association with
National Institute of Technology Karnataka, India

PROCEEDINGS OF
**4th INTERNATIONAL ENGINEERING
SYMPOSIUM – IES2015**

Venue

100th Anniversary Memorial Hall & Faculty of Engineering (Building No.2)
Kumamoto University

Date

March 4-6, 2015

Conveners

Shuichi TORII

Professor, Department of Mechanical System Engineering
Kumamoto University, Japan

&

Katta VENKATARAMANA

Professor, Department of Civil Engineering
NITK, Surathkal, India

Organized by

**Graduate School of Science & Technology
Kumamoto University
Kumamoto City, Japan**

In association with

**National Institute of Technology Karnataka
Surathkal, Mangalore, India**

PREFACE

The 1st International Engineering Symposium (IES 2011), 2nd International Engineering Symposium (IES 2012) and the 3rd International Engineering Symposium (IES 2013) were organized very successfully at Kumamoto University with more than 100 participants from India, Japan, Indonesia, Thailand, Taiwan, Vietnam and other countries. With the objective of continuing the interaction initiated between the researchers during these symposia, the 4th International Engineering Symposium (IES 2015) has been organized in the month of March, 2015 on similar lines. This symposium provides a common platform for bringing together researchers from participating institutions for expanding academic collaboration. It is expected that the emerging technologies and scientific advancements in these themes will be disseminated during the Symposium. Presentations will also feature new and innovative technologies in the relevant fields.

As part of this symposium, the researchers and the students from abroad have been invited to visit Kumamoto University and get exposed to its educational and research activities. The event focuses on the current R&D of the participating institutions on topics of mutual interest, with a special emphasis on "Science & Technology". The emerging technology and scientific advancements are discussed during the symposium. Presentations feature new and innovative technologies in the relevant fields.

This proceedings volume contains the technical papers presented at the symposium. The topics include a wide spectrum of themes covering major disciplines of science and engineering. The effort put in by the faculty, the staff and the students of Kumamoto University in organizing this event are greatly appreciated.

We sincerely hope that you will find the contents of this proceedings volume useful and productive. We look forward to more intense academic collaborations and research interactions in the coming days, to achieve the common goal of technological advancement for global peace and prosperity.

Shuichi Torii
Katta Venkataramana
Conveners

4th International Engineering Symposium - IES 2015

March 4-6, 2015, Kumamoto University, Japan

IES2015 Program Schedule

March 4, 2015 (Wednesday)		March 5, 2015 (Thursday)	
10:00 – 10:30	Registration	9:30 – 11:00	Technical Sessions <i>(M1, C1, C4)</i>
10:30 – 11:00	<i>Opening Address & Introduction of GSST</i>	11:00 – 11:30	Tea Break
11:00 – 11:20	Keynote Lecture (K1)	11:30 – 13:00	Technical Sessions <i>(M2, C2, C5, E1)</i>
11:20 – 11:50	Tea Break	13:00 – 14:00	Lunch
11:50 – 12:30	Keynote Lectures (K2)	14:00 – 15:30	Technical Sessions <i>(M3, C3, C6, S1)</i>
12:30 – 14:00	Lunch	15:30 – 16:00	Tea Break
14:00 – 17:00	Campus Tour & Laboratory Visits	16:00 – 17:15	Technical Sessions <i>(M4, C7)</i>
17:00 – 17:30	Free Time	17:00 – 17:30	Free time
17:30 – 19:00	Welcome Reception	17:30 – 19:00	Symposium Dinner

March 6, 2015 (Friday)

Lunch & Dinner Venue - FORICO Cafeteria

9:00 – 18:00	Field visits
--------------	---------------------

Notations:

- K** Keynote Lectures
 - M** Technical Sessions (Mechanical Engineering & Related Fields)
 - C** Technical Sessions (Civil Engineering & Related Fields)
 - E** Technical Sessions (Electrical, Electronics, Computer Engineering & Related Fields)
 - S** Technical Sessions (Chemistry, Chemical Engineering, Environment & Related Fields)

Contents

Keynote Lectures

- K1-1 Strengthening and rehabilitation of a century old heritage church (Chapel)
R. Jagadish and H Sharada Bai
- K2-1 Design of a novel PVDF-based piezoelectric energy harvester with beating mechanisms - *Hsin-Han Huang and Kuo-Shen Chen*
- K2-2 Investigating texture properties in four different guava species
B.-H. Wu, S. Topaiboul and N.-S. Liou

Mechanical Engineering & Related Fields

- M1-1 Design of a six-degree-of-freedom active vibration isolation system using sky-hook damper concept - *Yun-Hui Liu, Hung-En Hsieh*
- M1-2 A wiimote 3D localization scheme without channel constraints
Ting-Hao Li and Kuo-Shen Chen
- M1-3 Damping analysis of laminated composite tapered beam using higher order finite element method - *P. Jeyaraj and R. Vasudevan*
- M1-4 Multiagent system inspired distributed control of manipulator
Soumya S and K R Guruprasad
- M1-5 Graphene integrated waveguide for mass sensing
Sagar H P, D.Roy Mahapatra, G M Hegde and Rizwanur Rahaman
- M1-6 MEMS based different enhanced diffuser/nozzle micropumps
Roopa R, Navin Karanth P and S M Kulkarni
- M1-7 Effect of exhaust gas recirculation rate on a single cylinder four stroke CRDI engine using CFD modeling - *Venkatesh T Lamani, Ajay Kumar Yadav and G N Kumar*
- M1-8 Development of a novel vibration absorber utilizing smart elastomer for damping of torsional vibration- *Subhasankar Dwibedi and K V Gangadharan*
- M2-1 Spectroscopic ellipsometry analysis of strained ZnO:Al films using various optical models - *Wen-Yeong Huang, Yang-Hsien Lee, Sin-Bo Wang, Sin-Wei Wu, Chih-kai Hsu and Keh-moh Lin*
- M2-2 Spectroscopic ellipsometry studies on optical properties of InGaZnO thin films deposited by RF Sputtering method CAE tools
Keh-moh Lin, Yong-Ruei Cheng, Sin-Wei Wu, Sin-Bo Wang
- M2-3 Implementation of Automatic Colorization Algorithm of Electroluminescent Images for Detecting Defects on Si-based Solar Cells
Keh-moh Lin, Yong-Ruei Cheng, Sin-Wei Wu, Sin-Bo Wang

4th International Engineering Symposium - IES 2015

March 4-6, 2015, Kumamoto University, Japan

- M2-4 Wettability and bond strength of Sn-0.7Cu lead-free solder alloy reflowed on copper substrate - *Mrunail Sona and K Narayan Prabhu*
- M2-5 Experiments on multi-robotic search
Jeane Marina D'Souza and K R Guruprasad
- M2-6 Coverage by mobile robots
Ranjitha T D and K R Guruprasad
- M2-7 Adoptive control system for CNC machine
Rashmi L Malghan, Karthik Rao, Arun Shettigar, Srikantha S Rao and R J D'Souza
- M2-8 Application of Geospatial Software in mapping the biomass resources based on its availability and location - *Ranipet Hafeez Basha, Raju Aedula and Shuichi Torii*
- M3-1 Constitutive model for elastic and viscoelastic properties of Thai rice
Niwat Moonpa, Nai-Shang Liou and Subongkot Topaiboul
- M3-2 Preliminary study of the effect of mill gap of 2-milling rollers on reducing sugar of milled Thai rice malt in beer brewing process
A. Inpramoon, M. Wongkaew and S. Topaiboul
- M3-3 Investigating mechanical properties of sapwood and heartwood of rain tree in Thailand - *C.-C Guo, N. Phantkankam, N. Moonpa and N.-S. Liou*
- M3-4 A review on machining process of glass materials
Pravin Pawar, Raj Ballav and Amaresh Kumar
- M3-5 Stress and elastic properties evolutions of thin films under thermal treatment
Tsu-Huei Yang, Yin-Geng Tsai and Kuo-Shen Chen
- M3-6 Mechanical behaviour of HDPE syntactic foam composite
B R Bharath Kumar and Mrityunjay Doddamani
- M3-7 Parametric optimization in hot turning of Inconel 718 alloy using Taguchi method
Venkatesh Ganta and D Chakradhar
- M3-8 Hot corrosion-erosion behaviour of HVOF sprayed NiCrFeSiB coatings on boiler tube steels – *M R Ramesh, S Prakash, S K Nath and Mrityunjay Doddamani*
- M3-9 Purification of biogas by treating combined absorption and adsorption chemical method - *Muhammad Rashed Al Mamun and Shuichi Torii*
- M4-1 A new method for predicting stability lobe diagram in high speed ball end milling
Mithilesh K Dikshit, A B Puri and A Maity
- M4-2 Effect of cutting conditions on tool performance in CBN hard turning of HCWCI
Ravi A M, S M Murigendrappa and P G Mukunda

4th International Engineering Symposium - IES 2015

March 4-6, 2015, Kumamoto University, Japan

- M4-3 Effect of geometry on heat transfer in microchannels for microsystem cooling
Udhav Ulhas Gawandalkar, Girish Anant Kini and Arun M
- M4-4 Hybrid Monte Carlo approach to estimate heat flux in steady state fin problem
K Srinivasa Sagar and N Gnanasekaran
- M4-5 Study to improve the heat efficiency of heat exchanger with 0.5vol% Al2O3 nanofluid
Fukuoka Yukiko and Torii Shuichi
- M4-6 Generation of water-in-diesel emulsion fuel stabilized by two kinds of surfactants
Keisuke Goto and Shuichi Torii
- M4-7 An innovative renewable energy application for algae and its combination with other materials - *An-Peng Chen and Shuichi Torii*

Civil Engineering & Related Fields

- C1-1 Parametric study on rotation and plastic hinge formation in RC beams
Prabhakara R, Nambiyanna. B, Atul Gopinath and Nakul R
- C1-2 Analysis of torsional behaviour of reinforced normal, medium and HSC beams
Prakash M R, Sadanand Patil and Prabhakara R
- C1-3 Investigation on in-plane shear strength using push-off specimens with different clamping reinforcement
Harish Kumar N R, Snehal K, Nagaraj K P and Prabhakara R
- C1-4 Potential use of recycled coarse aggregates in concrete
Subhash C Yaragal, Vivek V B, M Padmini, M Jacob, J Niveditha and Anil Kumar Pillai
- C1-5 Structural optimization using perfect nodal position search method
Premanand Shenoy, K S Babu Narayan and Katta Venkataramana
- C1-6 Effect of nodal placement for a beam using meshfree method
Bhavana Patel S S, K S Babu Narayan and Katta Venkataramana
- C1-7 Numerical studies of a tunnel excavation and its effect on stress distributions around the tunnel in underground Bangalore metro project
Ishaan Rajankar, T G Sitharam
- C1-8 A comprehensive study to evaluate the performance of road transport undertakings in Karnataka using data envelopment analysis
T.G. Sitharam, Siddeshwar N. Hebbal, Devaraj Hanumappa and Raviraj.H.Mulangi
- C2-1 Effect of heat stress on smelter workers
Rajeev A and Manjunath G
- C2-2 Soil-structure interaction effects on multi-storey buildings considering site specific ground response
Chinmayi H K and Jayalekshmi B R

4th International Engineering Symposium - IES 2015

March 4-6, 2015, Kumamoto University, Japan

- C2-3 Transient analysis of multi storey shear wall buildings in soft soil
Jayalekshmi B R and Chinmayi H K
- C2-4 Studies on response of beams under dynamic loading
Neha Madhulika and Manasa Bhat K I
- C2-5 Applications of shape memory alloy devices in vibration control of structures
Vajreshwari Umachagi, Manasa Bhat K I and Katta Venkataramana
- C2-6 Earthquake response of masonry infill panels
Catherin Jeselia M, Jayalekshmi B R and Katta Venkataramana
- C2-7 Rheology and strength behaviour of self compacting concrete with ternary cementitious materials
H Sharada Bai, Bharathi Ganesh and Vijaya Kumar Madapur
- C2-8 Bond strength assessment of self compacting concrete containing pond ash and manufactured sand as fine aggregates
Bharathi Ganesh, H Sharada Bai, R Nagendra, Harisha C and Krishna L
- C3-1 Mitigation of delayed ettringite formation in concrete structures
Amde M Made and Richard A Livingston
- C3-2 Failure analysis of RMHS silo – A case study
Sheggoju Ramyasri, Aishwarya M Bansode and Arun T Udupa
- C3-3 Durability of concrete in coastal areas (severe zone)
Girish Kumar, Abhishek Salkar, Anand Bhattad, Katt Venkataramana and Rajendra Prabhu
- C3-4 Embodied energy in cost effective rural housing
G C Gayathri and G C Priyanka
- C3-5 Life cycle energy analysis of a traditional building in India : A case study
G C Priyanka and G C Gayathri
- C3-6 Composite corrosion protection system in rehabilitation of steel structures in corrosive environment – A case study
Raghuvir Salkar, Ishita Manjrekar, and Abhishek Salkar
- C3-7 Experimental studies on the performance of blended cement mortars at elevated temperatures
Subhash C. Yaragal, R Pavan Kumar, Prathipati Vivek, Sujeet Kumar Ranjan, and Anil Hegde
- C4-1 Engineering properties of laterites and utilization of lateritic powder and quarry dust in building blocks - *P Shubhanand Rao and Sitharam Nayak*
- C4-2 Stabilization of lithomargic clay using quarry dust and cement
Betsy Maria Lukas and Sitharam Nayak

4th International Engineering Symposium - IES 2015

March 4-6, 2015, Kumamoto University, Japan

- C4-3 Effects of ground vibration due to the passage of trains in underground tunnels- a numerical modelling approach - *Sarika K and V R Sastry*
- C4-4 Effect of aggregate gradation and bitumen content on workability of HMA mixtures *Abhijit B S and Suresha S N*
- C4-5 Review of vetiver grass properties for its application in stabilisation of slopes and erosion control - *Nivedita Prabhu N and T G Sitharam*
- C4-6 Reliability analysis of slope stability using RSM method *S Subhashree, L G Sathosh and G L Shivakumar Babu*
- C4-7 Assessment of dynamic properties of municipal solid waste sites using multichannel analysis of surface waves - *B P Naveen, T G Sitharam and P V Shivapullaiah*
- C5-1 Ground water quality - hurdles and remedies at solid waste processing site in Mysore city, India - *C Nanjunda Swamy and Lokeshwari M*
- C5-2 Assessing change-outcome and impact evaluation of Dabaspet-Sompura area by REIA - *Ramya R, Rajesh Gopinath, Akash Sirsikar, Amar, Balaji Biradar and Jai Prakash Reddy*
- C5-3 Groundwater flow and mass transport modelling – A case study *B V Sai Charitha, M J Nandan and V V S Gurunandha Rao*
- C5-4 Prediction of air temperature by conjunctive method *Karthika B S and Pares Chandra Deka*
- C5-5 Analysis of spatial and temporal trend in rainfall of Mangalore region using Mann-Kendall Test - *Aparna P and B M Dodamani*
- C5-6 The influence of policy decisions on the wetlands of Bangalore *Fathima Samana S and K S Anantha Krishna*
- C5-7 Analysis of morphometry and flow pattern of Chalakudy river basin, Kerala with GIS tools - *Nigee K, K Subrahmanyam, Aparna P, Shimna P and Drissia T K*
- C5-8 Application and test of the SWAT model in the upper Cauvery river basin, Karnataka, India - *Kumar Raju B C and Lakshman Nandagiri*
- C6-1 Study on the utilization of unconventional materials as a substitution material for fine aggregates in concrete - *B M Sunil, Madhura and Balasubramanya M*
- C6-2 Use of recycled coarse aggregates as an alternative in construction industry – a review - *Suman Saha, C Rajasekaran and T Vinayak Pai*
- C6-3 Studies on fly ash mixed concrete in aggressive environment *G Vijayakumar, C Rajasekaran and Muralidhara*
- C6-4 Improvement of fly ash concrete strength by bacterial mineral precipitation *M Suresh Babu, M Jyothi, C Rajasekaran and K V Arun Raj*

4th International Engineering Symposium - IES 2015

March 4-6, 2015, Kumamoto University, Japan

- C6-5 An experimental study on the hardened property of concrete by partial replacement of cement with sugarcane bagasse ash
K Vinay, Y M Vijayakumar, C Rajasekaran and Gokulraj
- C6-6 Critical analysis on ranking of delay factors with reference to the Indian construction industry – *C Rajasekaran, Hashim Yousuf and Gregory D'Silva*
- C6-7 Procurement system integrated with building information modelling (BIM)
C Rajasekaran, A Girish Baburao and B Madhukar
- C6-8 Lime fly-ash soil bricks
Anvin Sebastian, S Latheswary, C Rajasekaran and Shankaranarayan Kotian
- C7-1 Heavy metal contamination of soils
B M Sunil and Vijaya Vishnu Mayya
- C7-2 Hazardous waste management
B M Sunil and Ranganath Aithal P
- C7-3 Study on unlined rock caverns for storage of crude oil and stability analysis using numerical methods
B M Sunil, Deepthi K Achar and Anil S D'Souza
- C7-4 Water quality modelling using GIS
Devatha C P and Bharat J
- C7-5 Ground water treatment methodologies - Review
Devatha C P and Suresh A V, Proprietor
- C8-1 Strutural and vibroacoustic Analysis of Aircraft fuselage section with passive noise reducing materials : A material performance study
Balakrishnan B, Divyadev C M, Raja S and Katta Venkataramana
- C8-2 Integrity evaluation of bored cast-in-situ piles – a non destructive approach
Rao Katapadi Anirudh and Rao Arun Prabha Katapadi Sripathi
- C8-3 Potential application of experimental prediction equation in estimating the corrosion of RC structures
Akshatha Shetty, Katta Venkataramana, Babu Narayan K. S. and Srinath Shetty
- C8-4 Crystal heated comfort jacket
Saudamini Rao Katpadi, Arun Prabha K S and Vishnuprasad P V
- C8-5 Analysis of floating offshore wind turbine
Jobil Varghese, Freeda Christy and Katta Venkataramana
- C8-6 An overview of meshfree methods and its advancements
Bhavana Patel S.S, K.S. Babu Narayan and Katta Venkataramana
- C8-7 Pyroclastic flow deposit called shirasu as aluminosilicate source in geopolymers
Dhruva Narayana Katpady, Koji Takewaka and Toshinobu Yamaguchi

4th International Engineering Symposium - IES 2015

March 4-6, 2015, Kumamoto University, Japan

- C8-8 MeshFree method for beam convergence
Bhavana Patel S.S, K.S. Babu Narayan and Katta Venkataramana
- C8-9 Influence of geometric parameters on the in-plane response of masonry walls – analytical studies
Ashwin Thammaiah K, Raghunath S and Aswath M U

Electrical, Electronics, Computer Engineering & Related Fields

- E1-1 Real-time pedestrian detection and tracking
Anmol J Bhattad, Sharukh S Shaikh, Sumam David S., K. P. Anoop and Venkat R Peddigari
- E1-2 Analysis of emerging workflow scheduling algorithms in cloud
S Raghavan and K Chandrasekaran
- E1-3 Meta-classifier based approach to software change classification: towards better performance
Sreecharan Sankaranarayanan, Vidyashankar B Lakshman, Swapna Bhattacharya and K Chandrasekaran
- E1-4 Cluster based routing in NDN
Arun Nandewal and K Chandrasekaran
- E1-5 Transport layer protocols for network based gaming
Aditya Hendre, Gaurav Choudhary, Yash Kedia and B R Chandavarkar
- E1-6 Clique-clique domination number of a graph
R.S.Bhat, Smitha Holla, Sayinath Udupa N and Surekha R Bhat
- E1-7 Phase Balancing Techniques
Swapna M and Udaykumar R Y

Chemistry, Chemical Engineering, Environment & Related Fields

- S1-1 Enzymatically Derived Chitosan Hydrogels: Preparation and Application
Ritu Raval, Stephan Kolkenbrock and Bruno Moerschbacher
- S1-2 Bioprocess development of Chitin Deacetylase production from recombinant E. coli pLysS cells
Keyur Raval, Ritu Raval, Nitasha Chinaan, Stephan Kolkenbrock and Bruno Moerschbacher
- S1-3 Design, synthesis and characterization of colorimetric receptors for fluoride ion detection in competitive media - *Vijil A T V, Madhuprasad and Darshak R. Trivedi*
- S1-4 Study on the improved VBO model applied to NBR and on the deterioration of NBR
Fumiko Kawashima, Yuma Otsuka, Atsushi Ota, Yasutaka Miyazaki, Kazuhito Fujiwara And Hidehiro Hata

4th International Engineering Symposium - IES 2015

March 4-6, 2015, Kumamoto University, Japan

- S1-5 Decolorisation of synthetic and textile wastewater by fenton process
Kumara Guru B N and M K Krishna

- S1-6 Synthesis of site-specifically PEGylated Uricase conjugates with improved pharmaceutical properties for the treatment of hyperuricemia
Pooja Nanda and P E Jagadeesh Babu

- S1-7 Treatment of methoxyaniline containing solution using anaerobic- aerobic sequential batch reactor
Basavaraju Manu and Dangmei A P

- S1-8 Study of microbial fuel cell operated on sludge from waste water treatment plant - a case study - *Rahul Gautam, Arunabh Choudhury, S.K. Deepak, Patel Jay Mahendra, Arun Kumar Thalla*

KEYNOTE LECTURES

Strengthening and Rehabilitation of a Century Old Heritage Church (Chapel)

R. Jagadish and H Sharada Bai
Bangalore University, Bangalore, India

The church (Chapel) located in the campus of Good Shepherd Convent, Residency Road, Bangalore was constructed during 1904. The Convent (Guest House) attached to the Chapel was constructed during 1914. The convent consists of about 90 guest rooms, a dining hall (120 capacity) and an auditorium of 250 capacity. The sisters coming from all over the world used to stay in this convent whenever a conference was held in the auditorium. The entire complex was self content with a chapel for prayers, auditorium for conducting world conferences and the convent for the stay of the participants.

During the last few years the chapel and the convent was not being used due to its dilapidated condition. It was thought by the Management (Sisters) that it should be brought down and a new structure should be constructed. But it could not be done since it was declared as a Heritage Structure and the Government Authorities would not permit to demolish the building. At this stage, the authors were invited by the management to inspect the building and advise appropriately whether it could be rehabilitated and put into service conditions or abandon the building.

A detailed physical inspection was carried out during 2013 by us to assess the existing condition of the building. During inspection it was noticed that the building comprises of ground floor plus two upper floors with traditional sloped roof with wooden / rafters and Mangalore tiles and the chapel with high head room with curved roof finished with weatherproof tiles. The roof was profusely leaking, rafters were either broken or deflected. Floors made of madras arch terrace had deflected considerably and was vibrating while walking on it giving a feeling that it may collapse any time. Most of the masonry arches had cracked at the ridges giving a feeling of instability. All the windows and doors had deteriorated with broken window panes. On the whole the building was in a very bad shape due to aging and as it was existing the building was unstable.

After detailed discussions with the management, a feasible strengthening scheme was finalized. All the arches strengthened by providing sufficient reinforcement at the soffit of the arch and across the vertical cracks above the ridge and finished with micro concrete. The floors were strengthened by providing additional reinforcement as per design and finished with self compacting concrete. Existing plaster of all the walls were removed and replaced with 1:4 cement mortar. Entire deteriorated sloped roof was removed and a new composite roof with steel rectangular box section rafters with Indalium sheets and covered with Mangalore tiles. It was taken as a challenge and the building was strengthened and rehabilitated to the required service condition.

A similar procedure was adopted in strengthening and rehabilitating the deteriorated chapel and care was taken to see that the original Gothic Architecture is maintained even after completing the work. The present presentation gives the details of the strengthening scheme, execution of strengthening scheme successfully and Rehabilitation to the required service conditions.

DESIGN OF A NOVEL PVDF-BASED PIEZOELECTRIC ENERGY HARVESTER WITH BEATING MECHANISMS

Hsin-Han Huang¹ and Kuo-Shen Chen²

- ¹ Graduate Student, Department of Mechanical System, National Cheng-Kung University, Taiwan. email: spiwol@gmail.com
² Professor, Department of Mechanical Engineering, National Cheng-Kung University, Taiwan. email:kschen@mail.ncku.edu.tw
-

ABSTRACT: A new energy scavenging concept is proposed and demonstrated to convert environmental vibrations into electricity by using polymer piezoelectric materials in collaborating with a beating mechanism. By creating high frequency impact force via the low frequency vibration motion, it is possible to excite device natural frequency with environmental vibrations and to operate the entire system at the natural frequency. This work presents the concept, designing piezoelectric harvester systems with flexible PVDF elements, exploring their vibration characteristics, and energy accumulating strategies by using a capacitor with a full-bridged rectifier. By experimental characterization, the overall efficiency of the design is much greater than that from the design without the beating mechanism. It indicates that the efficiency is significantly improved and the proposed method could potentially improve the future design paradigm for piezoelectric energy harvesters significantly.

Keywords: Energy harvester, Piezoelectricity, Impedance matching, Cantilevers, Impact

INTRODUCTION

In these days, sensor networking becomes important in various applications [1]. All those applications require electric power for powering sensors, performing acquisitions, and providing data transfers. However, due to massive numbers of sensors and wide spatial distribution, it is not practical to power the entire systems using central power hub or individual batteries. Furthermore, the refresh rates of these condition monitoring are usually low. This implies that it might be feasible to power these sensor nodes using environmental power with proper energy scavengers. Hence, except for limit researches (e.g., [2]), the role of energy harvesters is to serve as a key component for supporting wireless sensor network, not as a major source of clean energy.

One major source of environmental power is the vibration of structures from natural driven forces. How to extract electricity

from this usually being wasted source has been studied by numerous researchers in the past decade [1-3]. Recently, with the advance in MEMS technology, various micro vibration energy harvesters have been proposed and realized [4,5]. For achieving maximum power generation efficiency, the devices are usually operated near resonance. However, MEMS devices have a much higher natural frequency and this implies that these devices are actually operated at a quasi-static state when subjecting to environmental vibrations. The situation could be further deteriorated for further scaling down. Therefore, how to operate energy harvesters near the excitation frequency is a key issue. Finally, if one can increase the operating frequency from the environmental vibration level to device natural frequency level, the improvement in power density would be significant.

For a larger energy harvester, it is possible to match the frequencies by proper

structural design. However, the size could be significantly enlarged for MEMS and this fails to follow the tendency of MEMS field. Meanwhile, for environmental vibrations induced by car operations [6], the frequency is velocity dependent and a fixed natural frequency design may not be able to handle this situation.

Here we propose an impact-based mechanism approach. As shown in Fig. 1, the environmental vibration is used to excite the beating mechanism. The mechanism is then interacting with a carrier structure where the energy harvesters are located, this near impact interaction excites the structure vibration of the structure and the mounted energy harvester. By careful design, it is possible to match both frequencies. That is, it serves as a media to convert the environmental excitations ($\sim 0(1-10)$ Hz) to high frequency harvester natural frequency ($\sim 0(100-1\text{kHz})$). This design is independent from the environmental vibration frequency since it only represents the excitation input and the matching condition is guaranteed.

This work is limited in demonstrating the feasibility of the concept. However, in real services, the structural longevity due to such loadings is a concern and a stress analysis should also be performed.

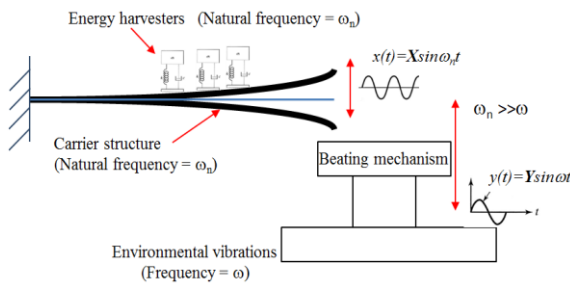


Fig. 1 Schematic plot for illustrating the proposed concept

BASIC CONCEPT

A piezoelectric vibration energy harvester is schematically shown in Fig. 2. It consists of an elastic structure, a piezoelectric element mounted on it (in together, called as a piezoelectric vibrator),

a diode-based rectified circuit, and an energy storage component. The induced charges are then passing through the bridge rectifier and flow into either the load or stored in the capacitor or battery. To achieve the power harvesting, the generated voltage should exceed the threshold of full-bridge rectifiers, which is approximately 1.4V.

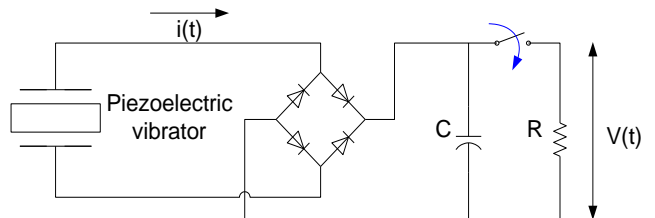


Fig. 2 Basic structure of piezoelectric energy harvester

The dynamic modeling of the harvesters can be referred to many previous works[7] and is not introduced here. For achieving optimal conversion, the systems are usually operated at resonance state and this is difficult for direct excitation. However, if the environmental vibration is for inducing impact vibrations of the structure carrying energy harvesters, it is possible to results in a resonance criterion by carefully design the carrier.

SYSTEM SETUP

As shown in Fig. 3, a polyvinylidene difluoride (PVDF) - based structure, LDT0 element (Meas-Spec. Corp., Hampton, VA, USA), is used as for energy harvesting. It contains a thin PVDF sheet bonded by two layers of Mylar polymer with an equivalent capacitance of 570pF and a coupling coefficient around 0.1 and a Young's modulus ~ 3 GPa [8]. Notice that in comparison with other PZT materials, its conversion efficiency is poor and is not an ideal material for harvesting. The reason is solely on its availability and its compliant nature. Yet, once the concept is validated, it is possible to use other materials to achieve the same design goal with more sophisticated analyses for ensuring reliability considerations.

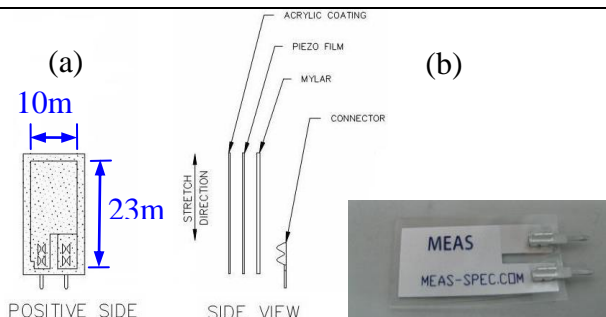


Fig. 3 The LDT0 PVDF element.

(a)dimension and (b)a picture

Three systems are setup. The first system, shown in Fig. 4, is a regular cantilever with a LDT0 and is excited by a shaker for serving as the standard for evaluating the performances of the proposed designs. The second system, shown in Fig. 5, contains 8 LDT0s attached on a fixed support. A shaker is used to cause impact. These LDT0 are connected to full bridge rectifiers and the generated electricity is either consumed by a resistive load or stored in a capacitor. Finally, as shown in Fig. 6, the third system consists of two LDT0s and is actuated by a motor for proving the feasibility in real applications.

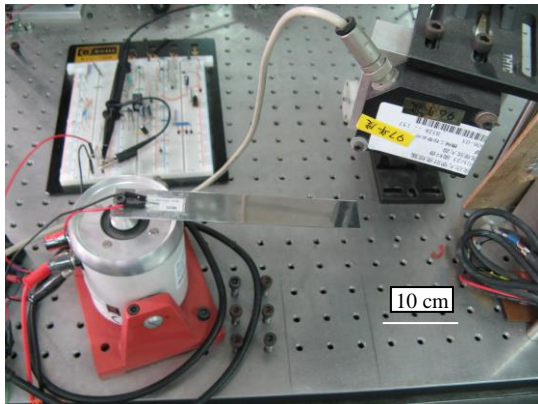


Fig. 4 The first system: a LDT0 element attached cantilever

For all of these designs, their vibration characteristics are examined for defining the optimal operating frequency. The powers delivered to resistive loadings are then investigated for determining the optimal loading. Finally, the capacitor charging histories are also studied for evaluating the harvesting performance.

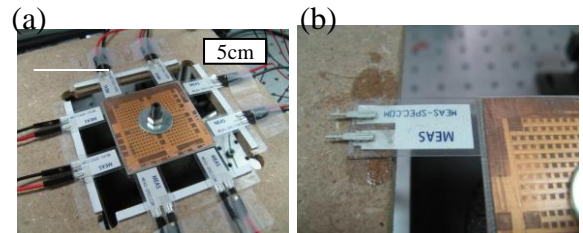


Fig. 5 The 2nd and the proposed system: (a)(b) the system and (c) the equivalent circuit model.

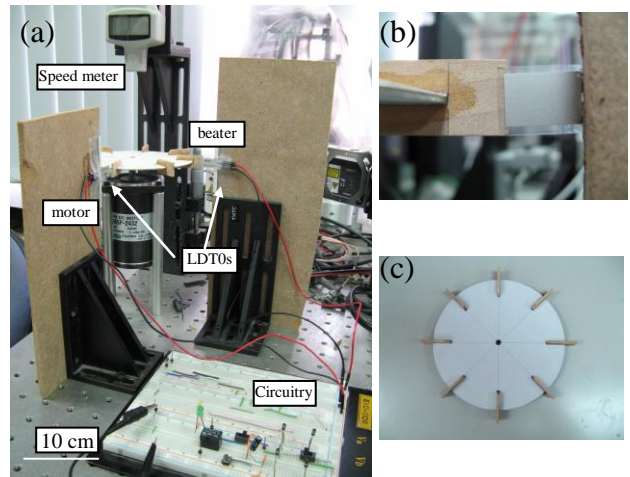


Fig. 6 The third system: a rotation type beating design aimed for demonstrating future applications. (a) the system, (b)a closer view, and (c) the beater.

EXPERIMENTAL RESULTS

For the first system, the natural frequency of the beam is 25 Hz. By operating at the frequency with different resistive loads, it is possible to determine the optimal loading impedance. As shown in Fig. 7a, it can be seen that the optimal power delivery occurs with a loading of 10 MΩ, which is close to the impedance of the LDT0 (~ 11.2 MΩ by using a pure capacitance estimation) and the result essentially agrees with the impedance matching criterion. Meanwhile, the charging curves

of the system with two capacitors ($10\mu F$ and $22\mu F$) are also shown in Fig. 7b. It can be seen that for a 20-minute charging period, the capacitor can only be charged to near $1.7V$ and this represents a stored electric energies of 32 and $16\mu J$, respectively. These results serve as the standards for evaluating the performance improvement of our proposed designs in the second and the third systems.

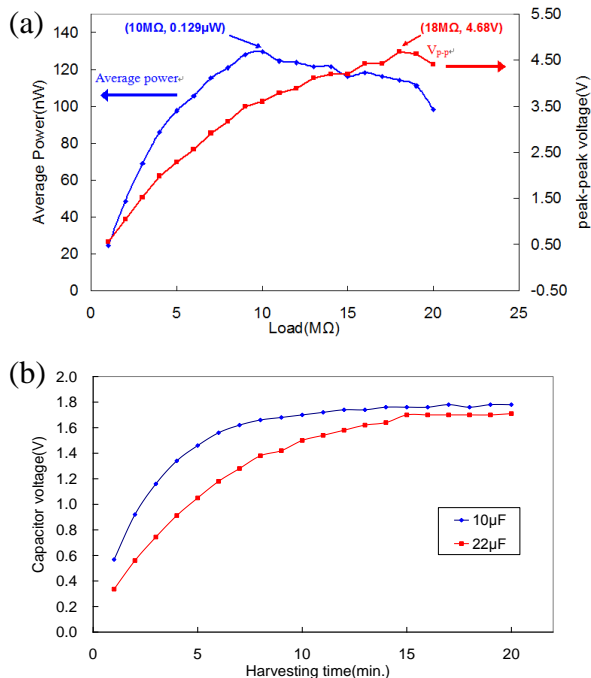


Fig. 7 The performance of the first system.
 (a) the effect of the external resistive loading and (b) the charging history.

Meanwhile, several concerns can also be drawn from the above test results. In short, the optimal loading impedance ($10M\Omega$) is much larger than that of typical loadings. The maximum power delivered ($0.13\mu W$) is too small. And the peak voltage generated during charging ($1.8V$) is not high enough even with a long charging period. These concerns should be further improved by subsequent designs.

For the second system, the vibration under beating action is firstly characterized and shown in Fig. 8 subjected to a single impact. Here, a pulse command is chosen for maximizing the impact efficiency. By spectrum analysis, the natural frequency

of the system is 212 Hz. It can be seen that it is able to generate electric signal up to a level of $20V$ (peak to peak) and it also shows that a low frequency environmental excitation can induce a high frequency vibration on the harvester by incorporating a beater and to improve the power harvesting efficiency.

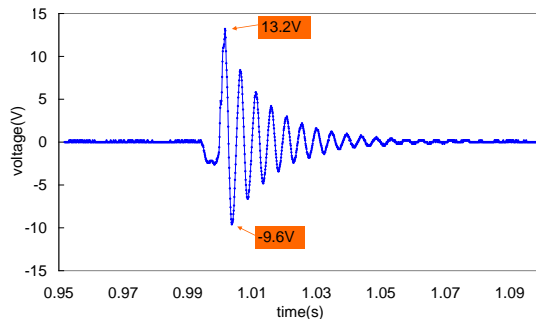


Fig. 8 Voltage generated by a LDT0 subjected to a single impact

Meanwhile, the relationship between the powers delivering with different resistive loading is shown in Fig. 9. It indicates that the optimal power delivery occurs at an external loading around $1M\Omega$ and the peak power delivery is increased to $1.36\mu W$. Finally, as shown in Fig. 10a, it can be seen that after 20 minutes, the capacitors have been charged to $7V$ and $6.5V$ by 1 Hz beating actions. In comparison with the results reported in the first system, the capacitor can be charged to a higher voltage and this represents an increase in stored energy. For further increasing in beating frequency up to 6 Hz, as shown in Fig. 10b, the corresponding charged voltage is then improved to 13 and 11 volts for the $10\mu F$ and $22\mu F$ capacitors and the electric energies stored are 245 , 465 , 845 , and $1331\mu J$, respectively. By comparing the performance of the first system, the improvement is significant.

The results demonstrate the feasibility of enhancing power generation efficiency by introducing a beater. It is now ready to use multiple LDT0 elements for further enhancing the power scavenges. With more LDT0s used for power generation, more power can be delivered into the charged capacitor. With the concept being proved, it is possible to design the third

system for demonstrating its applicability in high speed rotating motions.

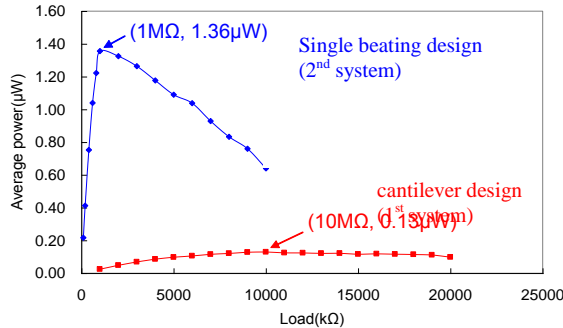


Fig. 9 The effect of external loading on the power delivered for the second system.

Finally, the third system consists of two LDT0s and a rotating beater driven for further increasing beating frequency by a factor of 8 for mimicking some possible energy application scenarios, for example, extracting energy from rotating machines such as bicycles. Furthermore, it is also possible to design a mechanism to convert environmental vibration to yield fast rotating motions. By utilizing much higher beating rates, it is expected that one can extract more energies from environments.

For the rotating system, the charging history of the system with a $22\mu\text{F}$ under different rotating speeds is characterized and the results are shown in Fig. 11. It only requires 1 minute for charging the capacitor up to 10V (i.e., stored energy to $\sim 1000 \mu\text{J}$). In comparison with the second system, the power generation rate is further improved due to increase in actuation rate.

A brief comparison on the energy harvesting rate for the three systems are shown in Fig. 12, it can be seen that our proposed beating approach can effectively increase the power generation rate over the traditional cantilever beam design. By using a much faster beating rate (i.e., the third system), the energy harvesting rate can be further improved to a practical level and should be able to fit into certain applications with high rotating speeds.

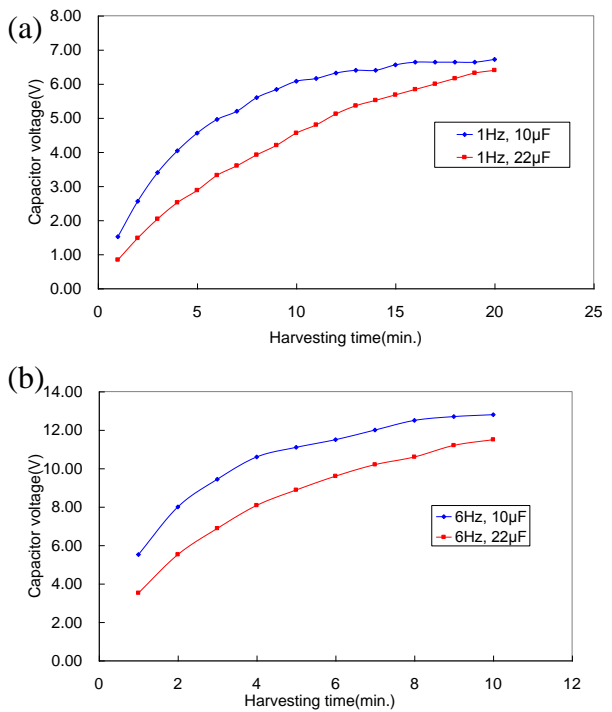


Fig. 10 Charging histories of the second system with (a) 1 Hz and (b) 6 Hz beating.

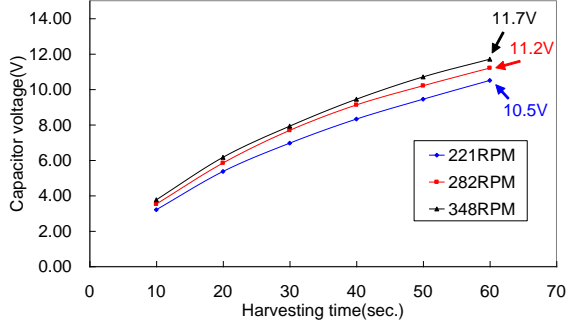


Fig. 11 The charging history of the third system using two LDT0 elements with a $22\mu\text{F}$ capacitor at different rotating speeds.

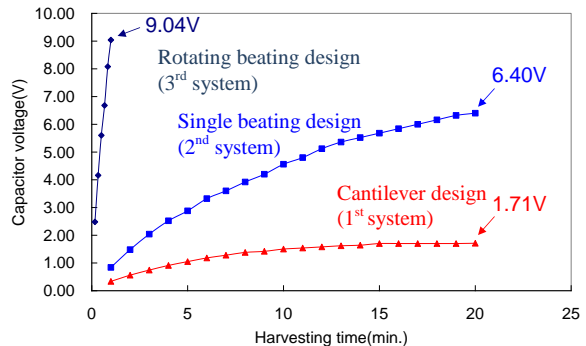


Fig. 12. Comparison on energy harvesting capability of the three systems (with single LDT0 and a $22\mu\text{F}$ capacitor)

4th International Engineering Symposium - IES 2015

March 4-6, 2015, Kumamoto University, Japan

CONCLUSION

DISCUSSION

Matching the natural frequency of energy harvesters and the environmental vibration frequencies is usually desired in harvester operations. However, these two groups usually have big difference and the harvesting efficiency is usually low. By using the proposed approach, it is possible to excite structural resonance by low frequency environmental vibration. By careful structural design, it could possible to achieve resonance condition on energy harvesters. Furthermore, as the operating frequency being increased, the impedance of these harvesters can be reduced to a more reasonable level and the chance to achieve optimal power delivery would be increase. Finally, as the working frequency increases, the power density of energy harvester is also improved and the amount of energy scavenged rises for the same period of harvesting time.

It should be emphasized here that without a suitable design analysis, the proposed approach could bring serious structural reliability concern. Although the impact motion could enhance power generation, possible high stress concentrations could also happen and this threaten the device longevity. Since PVDF is a ductile polymer, no fracture needs to be concerned. However, by replacing the LDT0 by more efficient PZT5H materials, the system could possibly fail due to high impact stress acting on this brittle material. Therefore, although PVDF is less efficient, it is still chosen due to its compliant nature for enhancing structural reliability. In the future, it is possible to use more efficient materials and incorporated sophisticated design for realistic applications.

Finally, the third system has demonstrated the possibility in increasing power harvesting efficiency in fast moving systems. By this concept, possible designs utilizing rotational motion of machinery (such as car axle motion) could be used for energy scavenge in the future.

A new beating type piezoelectric energy harvester is proposed and fabricated to convert environmental vibrations into electricity for demonstrating the feasibility of the proposed concept. A prototype by using PVDF-based LDT0 is designed and tested to verify this concept. The experimental results indicate that the proposed design can significantly improve the energy harvesting efficiency. In the future, with sophisticated structural design, the proposed concept can be applied in various vibration harvesting applications for supporting sensor network applications.

Acknowledgments

This work is supported by Ministry of Science and Technology (MOST) of Taiwan under NSC-100- 2628-E-006-020-MY3.

References

- [1] Park, G. et al (2008), Energy Harvesting for Structural Health Monitoring Sensor Networks, *J. Infrastruct. Syst.* Vol. 14, pp. 64-79.
- [2] Hagood, N. et al (2000), Microhydraulic transducer technology for actuation and power generation, *Proceedings of SPIE*, Vol. 3985, pp. 680-688.
- [3] Roundy, S. et al (2005), Improving power output for vibration-based energy scavengers, *IEEE Pervasive Computing.*, Vol. 4, pp. 28-36.
- [4] Jeon, Y. B. et al (2003), MEMS power generator with transverse mode thin film PZT, *Sensors and Actuators A: Physical*, Vol. 122, pp. 16-22.
- [5] Meninger, S. et al (2001), Vibration-to-electric energy conversion, *IEEE Trans. on Very Large Scale Integration (VLSI) Systems*, Vol. 9, pp. 64-76.
- [6] Wang, Y. J. et al (2010), Design of a frequency-adjusting device for harvesting energy from a rotating wheel, *Sensors and Actuators A*, Vol. 159, pp. 196-203.
- [7] Kim, H. et al (2006), Modeling of piezoelectric energy harvesting using cymbal transducers, *Japanese Journal of Applied Physics*, Vol. 45, pp. 5836-5840.
- [8] Ramsay, M. J. and Clark, W. (2001), Piezoelectric energy harvesting for bio MEMS applications, *Proc. SPIE*, Vol. 4332, pp. 429-438, 2001.

Investigating Texture Properties in Four Different Guava Species

B.-H. Wu¹, S. Topaiboul² and N.-S. Liou¹

1 Department of Mechanical Engineering, Southern Taiwan University of Science and Technology, No. 1, Nan-Tai Street, Yongkang Dist., Tainan 710, Taiwan. e-mail : nliou@stust.edu.tw

2 Division of Food Process Engineering, College of Integrated Science and Technology, Rajamangala University of Technology Lanna, 98 Moo 8 T.Papong Doi Saked, Chiang Mai, 50220 Thailand. e-mail : subongkoj@gmail.com

ABSTRACT: From market point of view, fruit with adequate texture would have the better chance to be accepted by consumers. Crispness, the favoured texture property of fruit, is the gustatory sensation of brittleness in the mouth, such that the fruit crushes immediately upon mastication. In this study, texture profile analysis was used to investigate the crispness of guava (*Psidium guajava*) of 4 different guava species two species in Thailand and two species in Taiwan). Specimens of 4 different species of guava were subjected to double-bite tests. The relations between crispness and texture properties such as hardness, fracturability, cohesiveness, springiness measured from texture property analysis were investigated. Furthermore, the relation between crispness and the more objective mechanical properties such as elastic modulus, compression strength and fracture toughness of guava was also studied.

Keywords: texture properties, crispness, food sensory, texture analysis

INTRODUCTION

Guava (*Psidium guajava*) is a tropical fruit that is rich in high profile nutrient such as vitamin C, vitamin A, lycopene and soluble dietary fibre. Beside the health benefits of the fruit, people tend to love the sharp and sweet taste of guava as well as its unique texture. To define how a fruit texture is like, one may explain it as soft or hard, tough or brittle, fluffy or firm. For guava, crispness may be a sensory property used to explain it in a more subtle way. Generally, crispness is defined as the gustatory sensation of brittleness, hardness, dryness and pleasantly firmness in the mouth [Merriam Webster]. However, chewing or crushing crisp fruit, one can expect such feelings but dryness. To describe the crispness of fruit, it is always difficult and subjective to just ask people to explain. Hence, unbiased objective test methods to grade this sensory property of different fruits are more favourable.

Many test methods have been used to investigate the texture profile of fruits such as ultrasound and acoustic emission (Zdunek A. and Bednarczyk J. (2006)), fracture tests (Vincent JFV, 2004), tensile tests (Herrero A.M. et.al (2008)) and impact tests (Lien, C-C. and Ting, C-H. (2014)), in order to represent the sensory properties by the measurable texture properties. Among all methods, texture profile analysis (TPA) provides a useful way to investigate many texture parameters of fruit in one test (Bourne M.C. (1994), Abbot J.A (1992)). The TPA method provides 2-cycle compression (double-bite) on food specimens at a certain speed and length to gain some mechanical properties of food that can be interpreted as hardness, fracturability, cohesiveness, springiness, chewiness, gumminess and resilience. To distinguish guava's crispness by its texture properties, this study applied the double-bite test of

4th International Engineering Symposium - IES 2015

March 4-6, 2015, Kumamoto University, Japan

TPA method on 4 different species of guava. The relations of the crispness and texture properties were investigated.

MATERIAL AND METHOD

Four different Guava species were used in this study are two white meat guavas (ThaiW-P and ThaiW-K) from Thailand and one white meat (TaiwanW) and one red meat (TaiwanR) guavas from Taiwan as shown in Fig.1. They were selected due to their most popularity in the two marketplaces. Before the test, well mature guavas were purchased from local markets and stored at the room temperature to avoid temperature effect. Then all the tests were conducted within two days. Specimens were prepared by cutting the fresh guavas into 10x10x10 mm³ pieces. For large guava, ThaiW-P and ThaiE-K, the specimens were taken from the top, middle and bottom parts of the fruit while for small guava, TaiwanW and TaiwanR, the specimens were taken from the middle part only. These cubic specimens were prepared by slices cut perpendicular to the long axis of the fruit as shown in Fig.2. Right after that, the cubic samples were put into the analyser.

In order to access guava texture properties, a set of preliminary double-bite TPA tests or 2-cycle compression, was performed to estimate suitable compression speed and distance at rupture. The preliminary results suggested no sign of fracture in some guava until the press went to 50% of the specimen height (5 mm). At that point, the specimens were crushed. Since a measurement of how food recovers from deformation was also observed as springiness, so, it was decided that the 2-cycle compression test would be done at the compression speed of 0.2 mm/s to the distance of 3 mm. The tests of Thai white guavas were done using CT3 Texture Analyser while Taiwan red and white guavas were tested on Instron 5685 tensile test machine. Fig.3 shows the TPA test with both machine.

From the force-time curve obtained from double-bite TPA test, the texture parameters including hardness, fracturability, cohesiveness, springiness,

gumminess chewiness and resilience were calculated. Elastic modulus could also be obtained from the relationship between compressive stress and compressive strain.

RESULTS AND DISCUSSION

The force-time curves of 4 guava species are shown in Fig.4 and 5 while the comparison of TPA parameters are shown in Fig.6. Oral sensory tests were performed on all guava species prior to the mechanical tests by six researchers in order to inspect their crispness. They suggested that ThaiW-P and TaiwanW were harder and crispier than ThaiW-K and TaiwanR. All guavas were firm and not so brittle. Among all, ThaiW-K was the softest.

In Fig.4, two peak forces that can be noticed from the force-time profile are the results of two compressions. The first peak force at the first compression represents the hardness of the fruit. As can be seen in Fig.4, there is no sharp drop in force detected from any guava species before the first peak force detected. In this case, hardness and fracturability were reported at the same point. At the second compression, the force required to compress the specimen to 3 mm. is less than the first due to food deformation. The results agree with the sensory test and can tell that TaiwanW meat is the hardest and crispier while ThaiW-K meat is the softest.

Fig. 5 shows stress-strain curves of 4 guava species deducted from the first compression. It can be noticed that the elastic modulus is not constant. This is similar to the properties of another biomaterial found in Moonpa, et al. (2014). The elastic modulus increases as an increase of strain until a certain point the modulus starts to decrease. Furthermore, the elastic modulus is changed with time. This behaviour is called viscoelastic behaviour and it can be found in rubber-like material (Moonpa (2003), Sungparn (2007)). At small strain percentage, it seems that the stiffness of guavas from the same origin are almost identical. Taiwan guavas have more stiffness than

4th International Engineering Symposium - IES 2015

March 4-6, 2015, Kumamoto University, Japan

Thai's. At high strain percentage, the stiffness only depends on species. At this point, rate of the change in modulus of elasticity may be used to consider crispness. The less of the change, the less crispness of the food. From the curve, ThaiW-K and Taiwan-R are less crisp than the other 2 guavas.

To further compare the crispness of guava, all texture properties obtained from the double-bite TPA test are shown in Fig.6. Hardness and fracturability are shown again in this bar chart for better comparison. Other properties should have been focused here are cohesiveness, springiness, gumminess, chewiness and resilience. Cohesiveness indicates the strength of internal bonds making up the body of the food. Energy required to chew a solid food and disintegrate a semi-solid food before swallowing are indicated by chewiness and gumminess respectively. These 3 properties can be looked up all together. The other 2 properties, springiness and resilience represent how food recovered from deformation and will be considered together. However, the springiness focuses on the height of food that bounces back after the first compression until the second compression while the resilience focuses on recovery work done in the first bite only.

Cohesiveness and hardness tell how hard we first bite our food and break it into small pieces or they can represent firmness. It is more difficult to bite TaiwanW and ThaiW-P than the rest. The resilience of both guavas are similar while the springiness of TaiwanW is higher than ThaiW-P. Since the chewiness of TaiwanW is less than ThaiW-P, it is easier to chew the former even though it has higher springiness. This also points to TaiwanW that it is crispier than ThaiW-P. The authors suggest crispness may relate to springiness as well as hardness and fracturability. However, the compressions level performed in this study was only 30%. Higher degree of compression should be done to verify the assumption.

Considering the different texture properties of the large guava species like

ThaiW-P and ThaiW-K, TPA results are shown in Fig.7. The top part of guava was observed to be the hardest or crispier while the bottom was opposite. This suggests that one shall experience the difference in texture and sensory from a larger guava more than a smaller fruit.

CONCLUSIONS

From the study, it can be concluded as the followings

- TPA tests on four guava species from Thailand and Taiwan had been conducted. The results showed different texture properties related to different sensory feelings.
- The texture parameters including hardness, fracturability, cohesiveness, springiness, gumminess, chewiness and resilience of four guava were reported as well as their elastic modulus.
- Crispiness may relate to springiness as well as hardness and fracturability. Higher degree of compression should be done to verify the assumption.
- The texture properties of a fruit is not consistent throughout the whole fruit body. Difference sensory feelings can be noticed especially in a larger fruit.

ACKNOWLEDGEMENTS

The authors would like to thank the Department of Mechanical Engineering, Southern Taiwan University of Science and Technology, Taiwan and the Department of Food Process Engineering, Rajamangala University of Technology Lanna, Thailand for providing the test facility and financial support throughout this study.

REFERENCES

- [1] Abbot J.A., Affeldt H.A., Liljedahl L.A. (1992). Firmness measurement of stored 'Delicious' apples by sensory methods, Magness-Taylor, and Sonic transmission, Journal of the American Society for Horticultural Science. 119, no. 3, pp. 510-515.
- [2] Bourne M.C. (1994). Food Texture and Viscosity, Academic, New York.
- [3] Herrero A.M., de la Hoz L., Ordonez J.A., Herranz B. de Avila M.D.R., Cambero M.I. (2008). Tensile properties of cooked meat sausages and their correlation with texture profile analysis (TPA) parameters and physio-chemical characteristics, Meat Science. Vol.80, no.3, pp.690-696.

4th International Engineering Symposium - IES 2015

March 4-6, 2015, Kumamoto University, Japan

- [4] Lien C-C, Ting C-H. (2014). Assessing guava maturity by statistical analysis of dropped fruit impact responses, Postharvest Biology and Technology, Vol.95, pp.20-27.
- [5] Moonpa, N., Liou, N. S., and Topaiboul, S., (2014), Effect of Amylose Ratio on the Elastic and Viscoelastic Properties of Thai Rice, The 6th International Conference on Science, Technology and Innovation for Sustainable Well-Being (STISWB VI), 28-30 August 2014, Apsara Angkor Resort & Conference, Siem Reap, Kingdom of Cambodia.
- [6] Moonpa, N., (2003), Dynamics Properties of Carbon Back Filled Rubber at Difference Temperatures, Ph.D. thesis, King Mongkut's Institute of Technology North Bangkok.
- [7] Sungparn, J., (2007), Analysis of Viscohyperelastic Properties of Vulcanized Rubber at Various Temperatures, Master thesis, King Mongkut's Institute of Technology North Bangkok.
- [8] Vincent J.F.V. (2004). Application of fracture mechanics to the texture of food, Engineering Failure Analysis, Vol. 11, no.5, pp.695-704.
- [9] Zdunek A. and Bednarczyk J. (2006). Effect of mannitol treatment on ultrasound emission during texture profile analysis of potato and apple tissue. Journal of Texture Studies, Vol.37, no.3, pp. 339-359.

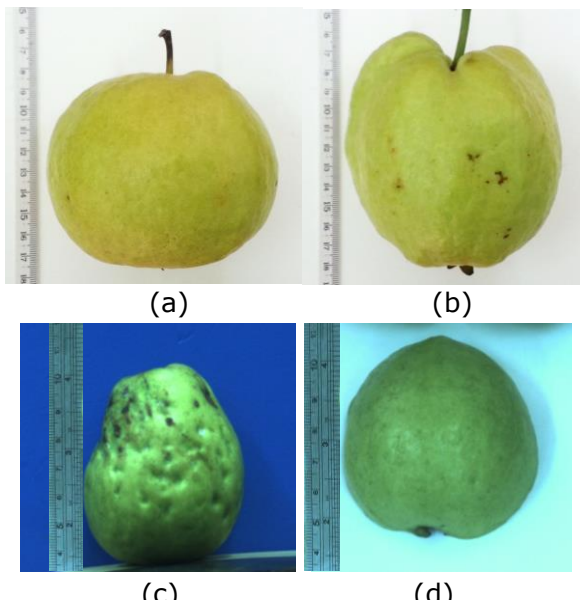


Fig.1 Four guava species
(a) ThaiW-P, (b) ThaiW-K,
(c) TaiwanR, (d) TaiwanW

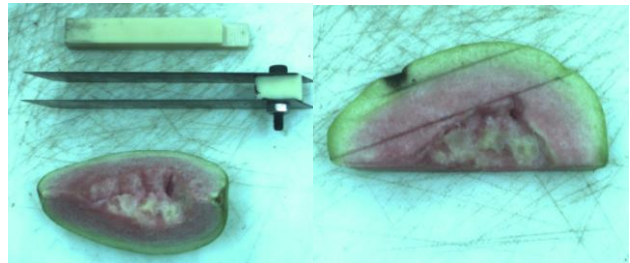


Fig.2 Preparation of test specimen



Fig.3 TPA test with (a) CT3 Texture analyser and (b) Instron 5865

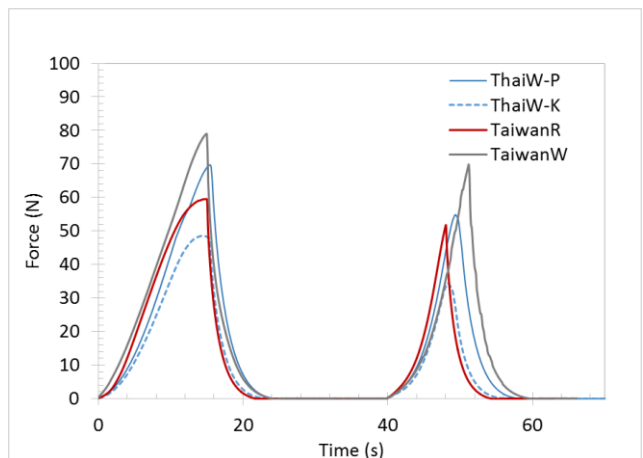


Fig.4 Typical TPA test results of middle section of 4 guava species

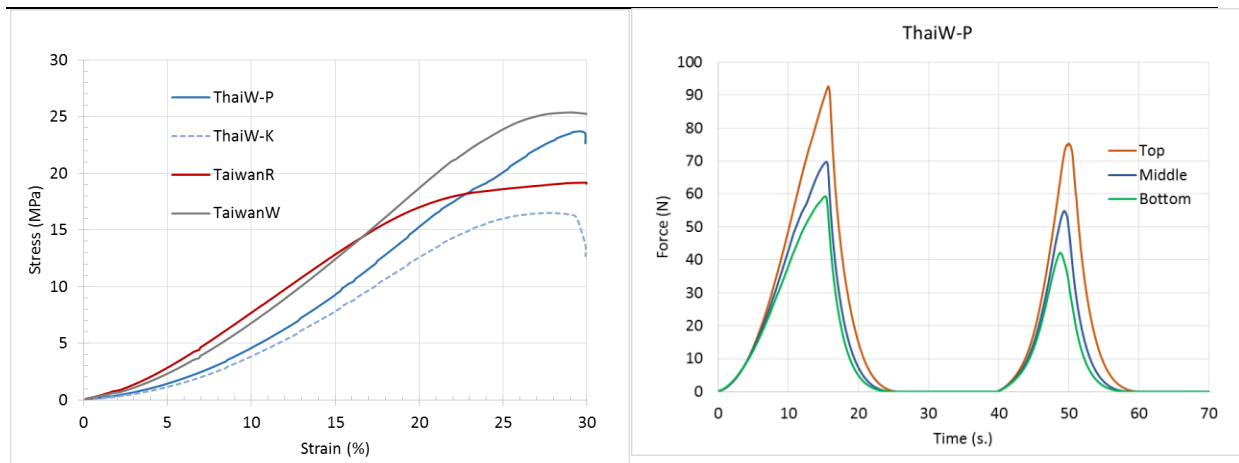


Fig.5 Stress-strain curve of middle section of 4 guava species

(a)

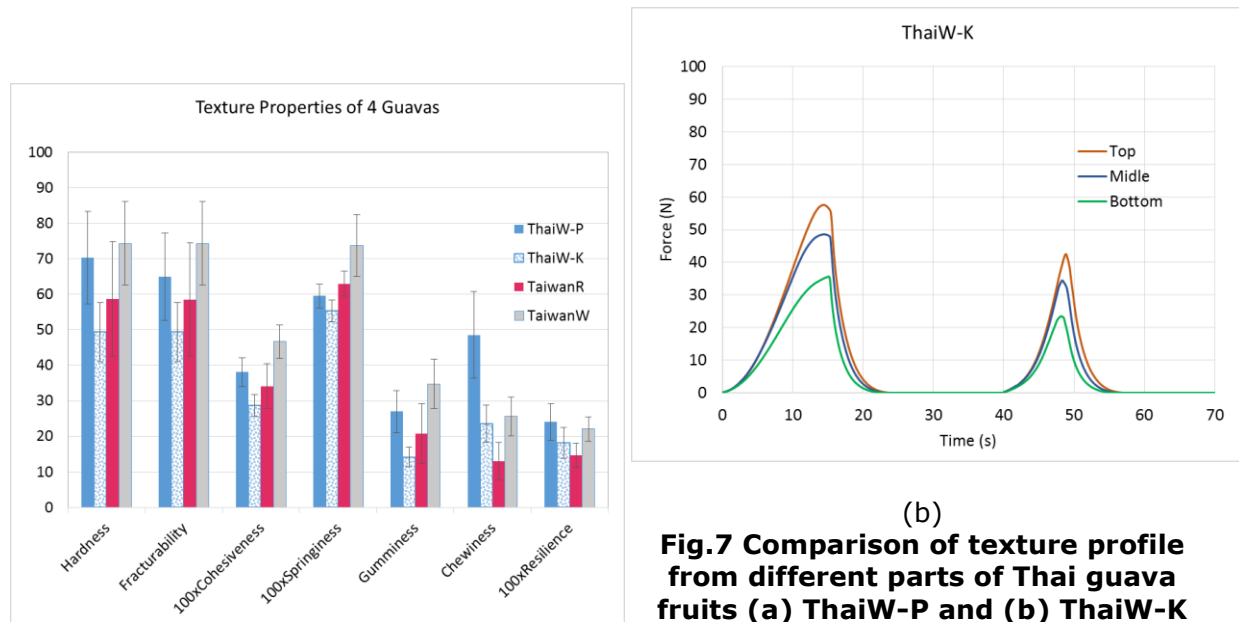


Fig.6 TPA parameters of 4 guava species at the middle section

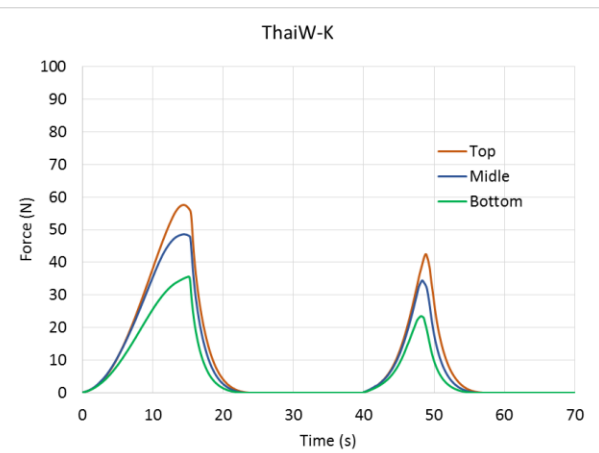


Fig.7 Comparison of texture profile from different parts of Thai guava fruits (a) ThaiW-P and (b) ThaiW-K

4th International Engineering Symposium - IES 2015

March 4-6, 2015, Kumamoto University, Japan

**MECHANICAL ENGINEERING
&
RELATED FIELDS**

Design of a six-degree-of-freedom active vibration isolation system using sky-hook damper concept

Yun-Hui Liu¹, Hung-En Hsieh²

1 Profesor, Department of Mechanical Engineering, Southern Taiwan University of Science and Technology, Tainan, Taiwan, R.O.C. e-mail: yhliu@mail.stust.edu.tw

2 Graduate student, Department of Mechanical Engineering, Southern Taiwan University of Science and Technology, Tainan, Taiwan, R.O.C. email: ma210206@stust.edu.tw

ABSTRACT: A six-degree-of-freedom active vibration isolation system (AVIS) is designed by using the sky-hook damper concept in order to reduce transmission at resonance frequency. The mechanisms of this AVIS include eight accelerometers to acquire vibration signal and eight voice coil actuators to produce anti-vibration force. Both of accelerometer and voice coil actuator are specially designed to suit to micro-vibration control for highly sensitive measurement equipment, e.g. atomic force microscopes, suffering from building vibration. The AVIS is controlled considering the phase error in the input signal due to the phase response of integrator and an adaptive filter is used to compensate the phase error in this paper. The results show that the proposed method significantly reduces transmissibility at resonance without the penalty of increased transmissibility at higher frequencies. The robustness of this AVIS is also verified in this paper.

Keywords: *six-degree-of-freedom, active vibration isolation, sky-hook damper, adaptive filter, accelerometer, voice coil actuator*

INTRODUCTION

The isolation of vibration-sensitive equipment from floor vibration is usually carried out using elastomeric isolators [1-3]. However, there is a trade-off between low and high frequency isolation performances depending on the damping of this resilient isolator [1]. Traditional passive isolators can efficiently isolate high frequency vibration, but it has a critical defect with a low frequency resonance, which is a frequency where passive isolators amplify vibrations instead of isolating them. If we choose a high damping ratio, we gain superior good resonant frequency control but poor frequency isolation. However, as we decrease the damping ratio, we begin to trade off the resonance control for high frequency isolation.

To solve the trade-off problem, active isolation solutions such as skyhook

damping [4] was appeared, which are usually based on elastic mounts and controllable actuators. Detailed theorem and application about active vibration control can be found in reference [5]. For the active vibration control at micron or nanometer scale displacement ranges, the piezoelectric actuators are often chosen to get good positioning accuracy and external perturbation control due to both their high accuracy and stiffness [6-9]. In the other hand, because PZT actuator is excessively stiffer than spring, the isolation performance of a spring-supported platform is reduced when actuators and springs are arranged in parallel. Therefore, application of the electromagnetic actuator [10-11] instead of PZT actuator in active vibration isolation has been the popular research topic in the recent years.

Inertial actuators which do not need to react off a base structure was used in active vibration isolation systems [10], so

4th International Engineering Symposium - IES 2015

March 4-6, 2015, Kumamoto University, Japan

they can be used as modules that can be directly installed on a vibrating structure. It has been shown that in order to implement stable skyhook damping with an inertial actuator, the natural frequency of the actuator must be below the first resonance frequency of the structure under control and the actuator resonance should be well damped. The active isolation of a system containing a distributed parameter isolator using absolute velocity feedback control with four electromagnetic actuators was presented in 2012 [11]. They investigate and compare two techniques to stabilize the system which have the instability due to the isolator resonances and flexibility of the base. The first involves the addition of mass on the base structure, and the second involves an electronic lead compensator.

According to sky-hook damper concept, an active vibration isolation system that applies feedback control of absolute vibration velocity to reduce the transmission of base excitations to a precision instrument is proposed in this paper. This system is simple and straightforward to implement, but getting correct absolute velocity is crucial to influence the performance of vibration isolation. In practice, the absolute vibration velocity signal is acquired from an accelerometer and being processed through an integrator. The phase response of integrator at low frequency such as 2~6 Hz deviate from the 90 degree which is the exact phase difference between the vibration velocity and acceleration, and the phase error of absolute vibration velocity signal will appear. Therefore, an adaptive filter is used to compensate the phase error in this paper. The theoretical equation which governs the system vertical vibration is established and the theoretical transmissibility is obtained in following section. Compared with the passive system, the theoretical transmission of the active isolation system at resonance frequency nearby can be reduced below the value of 1, and the isolation at high frequencies is not influenced by this active control.

Active Vibration Isolation using Sky-Hook Damper Concept

The absolute vibration velocity signal acquired from an accelerometer and processed through an integrator is input to the controller as a feedback signal, and the controller output signal drives the voice coil actuator to produce a sky-hook damper force. The single-degree-of-freedom mechanism of this system is shown as Fig. 1.

The voice coil actuator is installed in parallel with four steel-spring isolators, which are placed between a rigid upper platform of mass m and a rigid base foundation as a passive weight support mechanism. The four passive isolators are considered to have a total stiffness k , and both mass and the damping constant are neglected. Usually, such a system features six-degree-of-freedom rigid-body motions of the upper platform but, for the sake of convenience, the heave mode of the upper platform is the only motion considered in the theoretical derivation. The active control theory of vibration along another two horizontal axes is the same. Environmental vibration displacement on the foundation is z_0 , and vibration displacement on the upper platform is z_1 . The active control for suppressing the resonant oscillation of the passive vibration isolator is achieved by electromagnetic force f induced by the voice coil carrying electric current through a magnetic field. The theoretical equation which governs the system vibration can be written in following form.

$$m\ddot{z}_1 + k(z_1 - z_0) = f \quad (1)$$

where electromagnetic force f is

$$f = C_{amp} \times C_{voice} \times V \quad (2)$$

in which C_{amp} is the response function of the power amplifier, C_{voice} is the response function of the voice coil actuator. When active control is carried out, the voltage signal V from the controller output must first pass through a power amplifier in order to provide enough electric current for the voice coil. Following the concept of sky-hook damping, the actuator force is proportional to the absolute velocity of the

upper platform. Therefore, the voltage signal V is also proportional to this absolute velocity as following equation if both of C_{amp} and C_{voice} are linear response.

$$V = K_p \times (\dot{z}_1 \times S) \quad (3)$$

Where K_p is the proportional coefficient of controller and S is the sensitivity of sensor that includes accelerometer and integrator. After combining the above three equations and C_{amp} , C_{voice} , S are merged as a parameter C^* , the final governing equation can be obtained as follows.

$$m\ddot{z}_1 + k(z_1 - z_0) = C^* \times K_p \times \dot{z}_1 \quad (4)$$

The excitation (building vibration at the floor) is considered as

$$z_0 = a_0 e^{i\omega t} \quad (5)$$

with a_0 as the excitation amplitude and ω as the circular excitation frequency. The system response is given by

$$z_1 = a_1 e^{i\omega t} \quad (6)$$

Substituting (5) and (6) into (4), the transmissibility can be obtained as

$$\frac{a_1}{a_0} = \frac{k}{(k - m\omega^2) + i\omega K_p C^*} \quad (7)$$

Numerical Simulations

Numerical simulations were conducted to verify the aforementioned theoretical model as applied to an active vibration isolation system. The upper platform has mass $m = 55$ kg. Four passive isolators have a total stiffness $k=13600$ N/m and parameters $C_{amp}=1$, $C_{voice}=0.18$ N/V, $S=393.7$ V·s/m. These parameters are substituted into equation (7), and transmissibility of the active vibration system is obtained as different values of K_p . As shown in Fig. 2, when K_p exceeds 16, the theoretical transmission of the active isolation system at resonance frequency can be reduced below 1, and the isolation at high frequencies is not influenced by this active control.

Adaptive Algorithm

The numerical simulation results indicate that the control strategy employing the absolute velocity feedback control to activate the actuator with an appropriate gain of K_p can suppress the resonance of the passive isolation system at natural frequency. In practice, the absolute vibration velocity signal is acquired from an accelerometer and processed through an electric integrator, but the phase response of the integrator at low frequencies (e.g., 2~5 Hz) deviate from 90 degrees, which is the exact phase difference between the vibration velocity and acceleration. In this paper, an adaptive algorithm is designed to filter the feedback signal after integration to compensate for the phase error.

An adaptive algorithm consists of two parts: a digital filter which processes the expected output signals, an algorithm to adjust the weighting coefficients of the digital filter. One of two digital filters are usually applied to AVC, i.e., the finite impulse response filter (FIR filter) or the infinite impulse response filter (IIR filter). In this study, FIR filter is used as the system controller. Suppose a linear discrete-time FIR filter with length L , a series of weight coefficients, $w_l(n)$, $l=0, 1, \dots, L-1$, and a series of reference inputs $\{x(n) \ x(n-1) \ \dots \ x(n-L+1)\}$ are considered, where n is the time index, and the output signal is calculated as

$$y(n) = \sum_{l=0}^{L-1} w_l(n) x(n-l) = W^T(n) X(n) \quad (8)$$

where n is the time index, $X(n)$ is the reference input vector defined as

$$X(n) = [x(n) \ x(n-1) \ \dots \ x(n-L+1)]^T \quad (9)$$

and $W(n)$ is the weight vector defined as

$$W(n) = [w_0(n) \ w_1(n) \ \dots \ w_{L-1}(n)]^T \quad (10)$$

where the superscript T denotes transpose. The reference input $X(n)$ which is the velocity signal from the electric integrator has the phase error relative to exact velocity. The filter is used to modify the phase error, and get the exact velocity signal $y(n)$. Then, LMS (Least Mean Square)

4th International Engineering Symposium - IES 2015

March 4-6, 2015, Kumamoto University, Japan

algorithm is adopted to renew the weight coefficients in this study as

$$W(n+1) = W(n) + \mu X(n) e(n) \quad (11)$$

where μ is a convergence factor that controls stability and the rate of convergence, and $e(n)$ is the residual vibration signal defined as

$$e(n) = d(n) - y(n) \quad (12)$$

where $d(n)$ is the exact velocity signal that is generated from theoretical calculation. The adaptive filter which weight coefficients $W(n)$ is obtained by off-line experiment is put after integrator to compensate the phase error. As shown in Fig. 3, this adaptive processing method is proposed to adjust the phase error.

Experimental Investigation

In addition to the numerical simulations, experiments are carried out to investigate the proposed active vibration isolation system. Configuration of a six-degree-of-freedom active vibration isolation system is built in the experiments, as shown in Fig. 4 and Fig. 5. A steel plate supported by four springs as a general passive isolator is located on the granite platform. Four modules which each combine accelerometer with voice coil actuator are put on four corners beside spring of the plate, and other modules are put on the side of the plate.

In the experimental work, an FFT Analyzer (B&K pulse system 3560) is used to measure the response of the steel plate. The velocity signal which is measured using accelerometer we designed and electric integrator is fed back to the controller to implement adaptive proportional control. Because the vibration level is very low, the velocity signal must be amplified by analogue circuit before it transmits to controller. Furthermore, there are many kinds of noise and high frequency signal in measured signal, so it is necessary to use a low pass filter to purify the measured signal. In addition, the power of control signal from the controller must be amplified, because the voice coil actuator needs enough input power to produce electromagnetic force. Please note that the velocity signal on the

plate and the granite platform are measured using accelerometer Wilcoxon Research 731A in the measurement of the transmissibility and transient response.

The control performance of the active vibration isolation system was investigated by transient response and transmissibility experiments. The experimental results show that the proposed method can quickly reduce the resonance translation vibration while active control is activated, as shown in Fig. 6. It is observed that more than 98% of the vibration energy at resonant frequency can be cancelled by the proposed method, and the response time needed to effectively control vibration at the resonance frequency is less than 0.3 second. The rotation vibration is also reduced when active control is activated, as shown in Fig. 7.

Another, the experimental results show that the proposed method can significantly reduce transmissibility from 24 dB to 0 dB at resonance without the penalty of increased transmissibility at higher frequencies shown as Fig.8.

CONCLUSIONS

A six-degree-of-freedom active vibration isolation by adaptive proportional control has been investigated both theoretically and experimentally. Absolute velocity feedback control is implemented experimentally to active vibration control incorporated with a passive vibration isolator to suppress the resonant oscillation of natural frequency. In practice, conventional passive isolators suffer from an inherent trade-off between poor high-frequency isolation and amplification of vibration at the fundamental mounted resonance frequency. In this paper, the best isolation performance is achieved by using an active system in combination with passive isolators, where the fundamental resonance can be actively controlled without reducing the high-frequency performance. The theoretical analysis shows that the effect of active control is similar to a sky-hook damper to suppress its resonant oscillation. The experiment results show that 98% of the vibration energy at resonant frequency can be cancelled by the proposed method in this

4th International Engineering Symposium - IES 2015

March 4-6, 2015, Kumamoto University, Japan

paper. Control performance demonstrates application of adaptive proportional controller on active control of vibration isolator can effectively reduce the resonant vibration of passive isolators.

Acknowledgements

This work is supported by National Science Council of Taiwan with contract no. MOST 102-2622-E-218 -001 -CC2, and MOST 103-2221-E-218 -022.

References

- [1] S. S. Rao (1984), Mechanical Vibrations. Massachusetts: Addison-Wesley
- [2] D. J. Mead (1999), Passive Vibration Control. Chichester: Wiley.
- [3] C. E. Crede, J. E. Ruzicka (2002), Theory of vibration isolation, in: C. M. Harris, A. G. Piersol, Shock and Vibration Handbook. NewYork: McGraw-Hill.
- [4] D. Karnopp (1995), "Active and semi-active vibration isolation," American Society of Mechanical Engineers, Journal of Mechanical Designs, vol. 117, pp. 177-185.
- [5] A. Preumont (2011), Vibration Control of Active Structures: An Introduction, Third Edition, Kluwer Academic Publishers, Netherlands.
- [6] M. K. Kwak, S. Heo (2007), "Active Vibration Control of smart grid structure by multiinput and multioutput positive position feedback controller," Journal of Sound and Vibration, vol. 304, pp. 230-245.
- [7] A. Rashid, C. M. Niculescu (2006), "Active Vibration Control in palletized workholding system for milling," International Journal of Machine Tools & Manufacture, vol. 46, pp. 1626-1636.
- [8] J.M. Rodriguez-Fortun, J. Orus, J. Alfonso, and J.A. Castellanos (2010), "Nonlinear active vibration control using piezoelectric actuators," American Control Conference, Baltimore, MD, June 30-July 2, 2010, pp. 744-749
- [9] Y. Yun and Y. Li (2012), "Modeling and Control Analysis of a 3-PUPU Dual Compliant Parallel Manipulator for Micro Positioning and Active Vibration Isolation," Journal of Dynamic Systems, Measurement, and Control, vol. 134, Issue 2, 021001, March 2012.
- [10] L. Benassi, S.J. Elliott, P. Gardonio (2004), "Active vibration isolation using an inertial actuator with local force feedback control," Journal of Sound and Vibration, vol. 276, pp. 157-179.
- [11] B. Yan, M.J. Brennan, S.J. Elliott, N.S. Ferguson (2010), "Active vibration isolation of a system with a distributed parameter isolator using absolute velocity feedback control," Journal of Sound and Vibration, vol. 329, pp. 1601-1614.

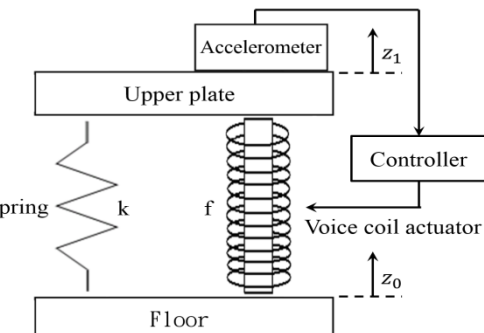


Fig.1 The mechanism of system

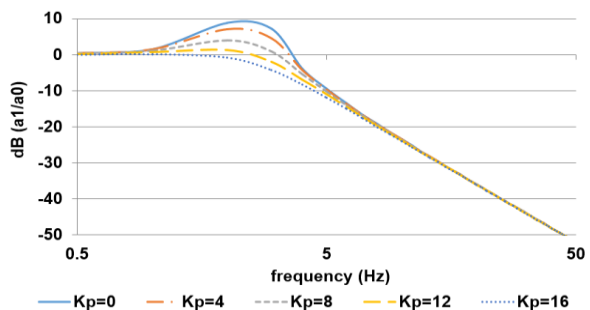


Fig.2 Theoretical transmission of active vibration isolation system for different value of K_p

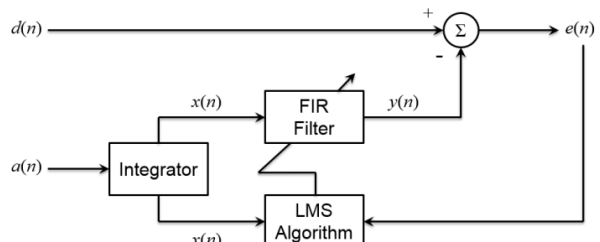


Fig.3 Flowchart of adaptive processing method, $a(n)$ is the acceleration signal

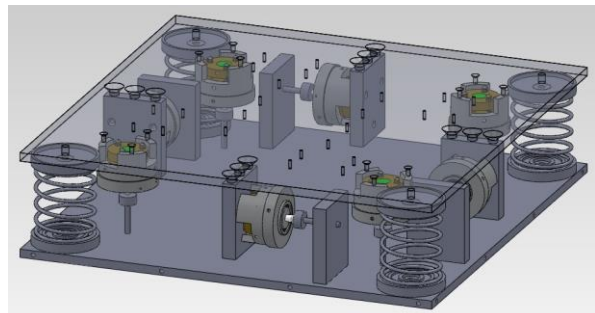


Fig.4 Configuration of the isolation system

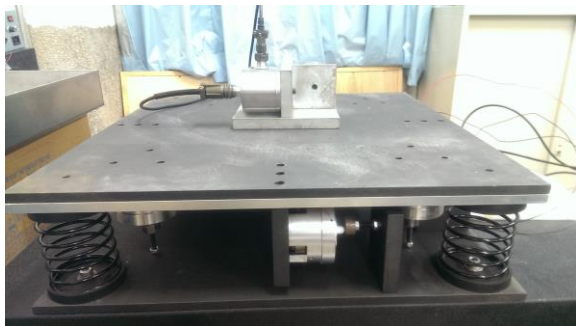


Fig.5 Photo of experimental configuration

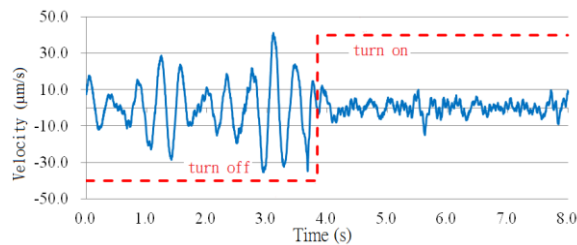


Fig.6 Time history of vibration velocity on payload in horizontal direction

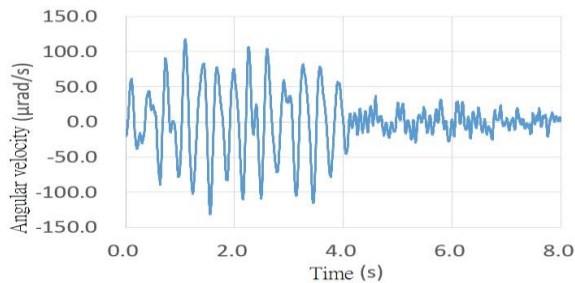


Fig.7 Time history of vibration angular velocity on payload in horizontal direction

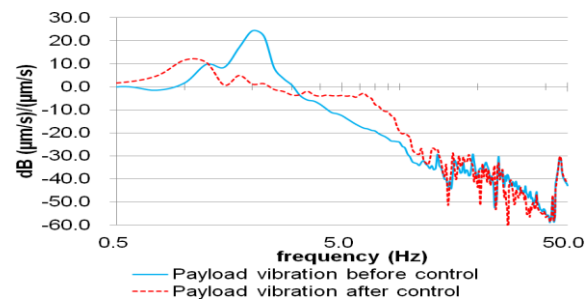


Fig.8 Experimental transmission of passive and active isolation systems in vertical direction

A Wiimote 3D Localization Scheme without Channel Constraints

Ting-Hao Li¹ and Kuo-Shen Chen²

¹ Graduate Student, Department of Mechanical Engineering, National Cheng-Kung University, Tainan, Taiwan, 701, R.O.C. e-mail: blackstone0711@hotmail.com

² Professor, Department of Mechanical Engineering, National Cheng-Kung University, Tainan, Taiwan, 701, R.O.C. email: kschen@mail.ncku.edu.tw

ABSTRACT: In this work, a novel 3D Wiimote localization scheme with no channel constraints has been proposed for smart living or computer animation applications. This scheme utilizes two Nintendo Wiimotes and simple trigonometry for performing stereo range finding and an Arduino-based IR LED switching for breaking the constraint on maximum available channels commonly existed in Bluetooth-based devices. That is, by controlling the switching of IR LED units to be turned on/off sequentially, the equivalent available channels can be extended with a trade off in system bandwidth. As a result, this Wiimote-based 3D localization system can detect more IR LEDs than the number of original channels and each IR LED can be identified correctly even if it passes through a shelter, which could cause temporary vanishing of the IR LEDs. A testing system is also setup for evaluating the performance on the 3D localization and IR LED switching control. The preliminary results indicate that the position of IR LEDs can be accurately detected and the system can identify IR LEDs without channel constraints. This novel 3D localization system is expected to have a great potential on indoor smart living related applications such as mobile robots monitoring or human motion capture for animations.

Keywords: Wiimote, 3D localization, Arduino-based IR LED control

Introduction

Position sensing plays a critical role in indoor mobile robot navigation applications. With accurate positioning information, navigation, feedback control, coordinated motion, and task planning can be realized. Typical localization techniques, such as inertial navigations [1], ultrasonics [2], vision [3], and RFID [4], have been used. However, due to the integrated consideration in terms of cost, resolution, and signal reliability, a flawless positioning technique has not yet been achieved.

IR localization is another possible choice. In particular, IR-LED based Wiimotes have been proposed for many other applications beyond its original TV game design [5]. Due to simple relationship between the displayed pixel and the sensing distance, it

has been used as an alternative choice for indoor localization sensors.

In our previous studies, Chen et al utilized Wiimotes to develop an accurate 2D localization system for indoor environment [5]. Fu and Chen proposed a Wiimote 2D localization system with a controllable IR LED array [6]. By the controlled input of the IR LED array, it is possible to extend the sensing area to cover the entire living space and the target can be identified correctly even if it passes through a shelter.

Recently, 3D indoor localization becomes important for robot control and for computer animation applications. In this work, based on our previous experiences in Wiimote 2D localization, the 3D Wiimote localization technique is proposed and validated. The system utilizes two parallel

Wiimotes and simple trigonometry for performing stereo range finding. However, Wiimote has the constraint on the number of detectable IR LEDs. It significantly restricts the usage of Wiimote 3D localization system. Therefore, similar to the concept of controllable IR LED arrays proposed earlier [6], this work develops a novel IR LED switching technique to extend the detectable IR LEDs from four to virtually no limit. By such an effort, the proposed 3D localization scheme could be cost effective and with reasonable accuracy and bandwidth and should be useful in indoor living related applications such as mobile robots monitoring or human motion capture for animations.

Wiimote 3D Localization System

Wiimote is the primary controller for Nintendo's Wii Remote shown in Fig. 1 originally designed for TV games. It contains Bluetooth wireless communication and a built-in high pixel CMOS image sensor, which is called "Wiimote camera" in this paper. Wiimote camera is able to detect up to four IR LEDs with visual angles of approximately 45° (X) and 35° (Y) to form a sensing zone with a resolution of 1024×768 pixels. It also has great tracking ability with the sampling rate of 100 Hz. In addition, Wiimote can identify the different IR LEDs by the entering sequence of these IR LEDs into the sensing zone of Wiimote.

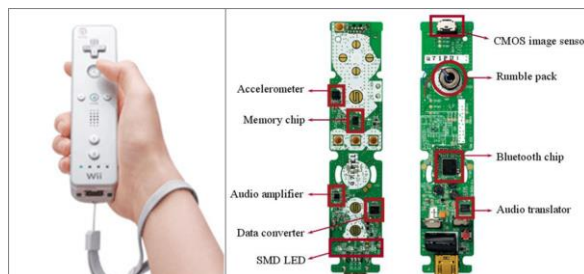


Fig. 1 The Nintendo Wiimote and its circuit board

Fig. 2 shows the schematic concept of the Wiimote 3D localization system. When the IR LED is in the overlapped zone of the sensing zone of two Wiimotes, both Wiimotes detect the pixel coordinate of the IR LED and then transmit the information to PC through the built-in Bluetooth wireless communication to calculate the

3D position of the IR LED by simple trigonometry and the known parameters.

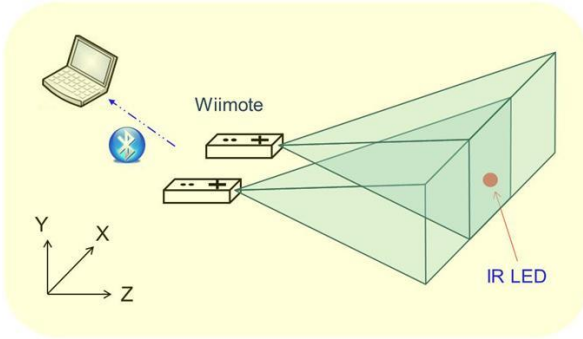


Fig. 2 Schematic plot of Wiimote 3D localization

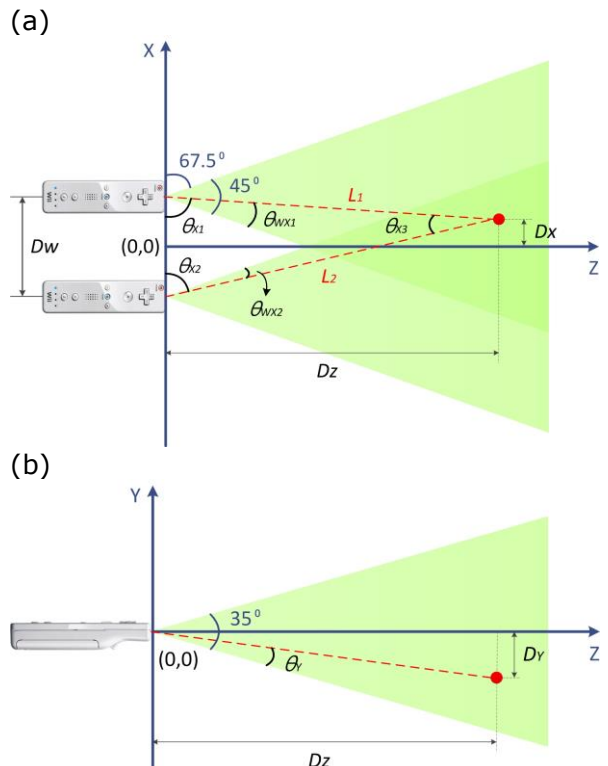


Fig. 3 The coordinated relationship between Wiimotes and IR LED (a) top view (b) side view

As shown in Fig. 3(a), the goal is to find the position of the IR LED (i.e., D_x , D_y , and D_z) from the readout of these Wiimotes. Here, we define the central position of the front end of two Wiimotes for the origin of coordinate. The distance between the two Wiimotes (D_w) also needs to be determined in advance. A $D_w = 10$ cm is chosen for the subsequent development.

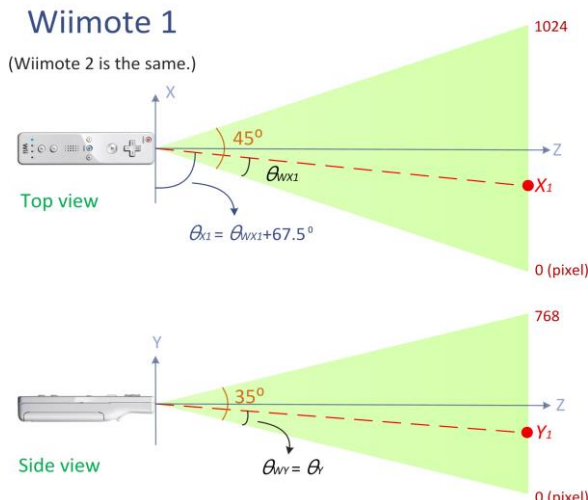


Fig. 4 Geometric relationship between pixel coordinate and visual angles

From Fig. 3(a), it can be seen that these two Wiimotes and the IR LED form a triangle. We can calculate the three side lengths and the angles of this triangle, so that the horizontal position (D_x), vertical position (D_y), as well as the distance between Wiimotes and the IR LED (D_z), can be determined. By referring to Fig. 3,

$$D_x = \frac{D_w}{2} - (L_1 \times \cos \theta_{x1}), \quad (1)$$

$$D_y = D_z \times \tan(\theta_y - 17.5^\circ), \quad (2)$$

$$D_z = L_1 \times \sin \theta_{x1}, \quad (3)$$

where

$$L_1 = \frac{D_w \times \sin \theta_{x2}}{\sin(180^\circ - \theta_{x1} - \theta_{x2})}. \quad (4)$$

As shown in Fig. 4, based on the detected pixel coordinate (X, Y) of the IR LED and the geometric setting, it is possible to calculate the visual angles θ_{wx1} , θ_{wx2} , and θ_{wy} from the law of Sine:

$$\frac{X_1}{\sin \theta_{wx1}} = \frac{1024 - X_1}{\sin(45^\circ - \theta_{wx1})} \quad (5)$$

$$\frac{X_2}{\sin(45^\circ - \theta_{wx2})} = \frac{1024 - X_2}{\sin \theta_{wx2}} \quad (6)$$

$$\frac{Y_1}{\sin \theta_{wy}} = \frac{768 - Y_1}{\sin(35^\circ - \theta_{wy})} \quad (7)$$

where (X_1, Y_1) and (X_2, Y_2) are the pixel coordinates detected by the two Wiimotes respectively. By referring to Fig. 4,

$$\theta_{x1} = \theta_{wx1} + 67.5^\circ \quad (8)$$

$$\theta_{x2} = \theta_{wx2} + 67.5^\circ \quad (9)$$

$$\theta_y = \theta_{wy} \quad (10)$$

Thus, θ_{x1} , θ_{x2} , and θ_y can be calculated from Eq.5 to Eq.10 and substituted into Eq.1 to Eq.4 to determine the position of the IR LED (i.e., D_x , D_y , and D_z).

IR LED Switching Technique

Since Wiimote can only detect up to four IR LEDs at one time, this represents a significant limitation on applications. Therefore, we develop IR LED switching technique to extend the number of the detectable IR LEDs.

Fig. 5 shows the schematic concept of the IR LED switching technique. We utilize Arduino controller for rapidly switching the IR LED units. With sufficient switching speed, the system will behave as many IR LEDs being simultaneously detected by the Wiimote. Ideally, there are 4 IRLEDs per unit for optimizing the switching efficiency. Once the Wiimote detects the current IR LED unit and transmit the information through Bluetooth, the next unit will be switched on by Arduino.

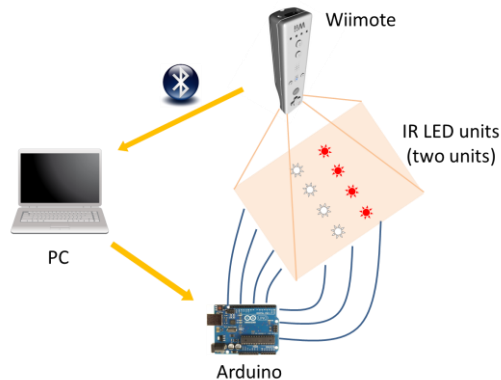
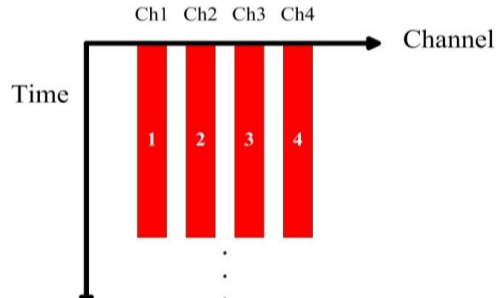


Fig. 5 IR LED switching scheme

Fig. 6(a) shows the original condition of the Bluetooth channel data occupation during Wiimote localization. Each channel can only detect one IR LED at one time and therefore, four IRLEDs in total for a single Wiimote. On the other hand, Fig. 6(b) shows the condition of switching two IR LED units. By carefully controlling the switching sequence, each channel can detect two IR LEDs and there are 8 IR LEDs can be detected in this particular case. Similarly, if we use three IR LED

units, it can detect twelve IR LEDs at most. Therefore, we can even extend the number to virtually no limit with a trade off on the equivalent bandwidth.

(a)



(b)

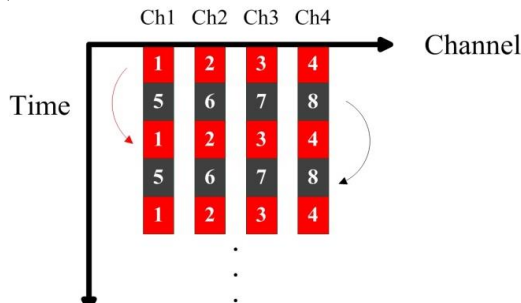


Fig. 6 Schematic plot of IR LED switching
(a) no switching and (b) switch two IR LED units

Meanwhile, for IR LEDs in the same IR LED unit, how to keep the same channel alignments in each sampling is also a problem. If we switch on these four IR LEDs simultaneously, we cannot identify the entering sequence of these IR LEDs into the sensing zone of Wiimote and the channel sequence cannot be controlled. To keep the desired sequence, we also control the switches of these IR LEDs in the same unit and make them switch sequentially. Therefore, these IR LEDs will sequentially enter the sensing zone and the channels will be aligned correctly in each sampling.

In addition, sequentially switching on the IR LEDs also avoids the misalignment when the IR LEDs pass through a shelter, which cause temporary vanishing of the IR LEDs. In general condition, if the IR LEDs pass through a shelter and are detected once again, the entering sequence may not be the same to the origin and the channels will be misaligned. On the contrary, this technique can reset the

misaligned channels to the original alignment because of the sequential switch in each sampling.

System Integration

In the previous two sections, we develop the Wiimote 3D localization system and IR LED switching technique for 3D positioning and breaking the channel constraint, respectively. Therefore, we will integrate these two techniques to make the Wiimote 3D localization system detect more than four IR LEDs for further applications.

With the same concept as IR LED switching technique, we utilize two Wiimotes to monitor the IR LED units. Once both Wiimotes detect the current unit and process the information to calculate 3D position, the next unit will be switched on by Arduino. With sufficient switching speed, the system will behave as many IR LEDs being simultaneously detected by both Wiimotes and thus the 3D positions of IR LEDs can be determined.

Experiments

I. Wiimote 3D localization

Experimental setup for evaluating the performance of Wiimote 3D localization is shown in Fig. 7. Two Wiimotes are placed on a precision rotary stage to monitor the motion of the IR LED, which is mounted on a two-axis linear servo motor. The linear motor is programmed to perform 2D motions with various paths and speeds.

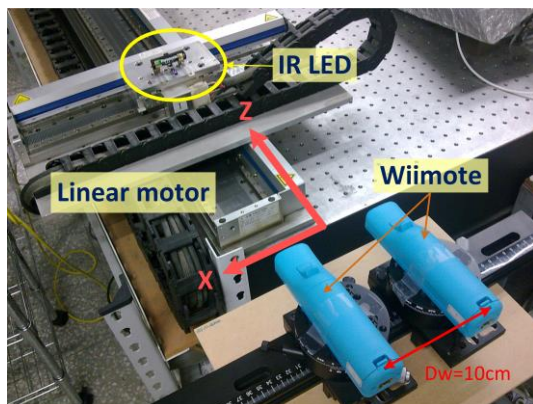


Fig. 7 The experimental setup for Wiimote 3D localization

By controlling the linear motor using various motion patterns such as line, saw-tooth, circle, and rectangular loops, it is

possible to compare the paths localized by Wiimote vs. their actual moving paths. Fig. 8 shows the typical results with travel speeds of 10cm/s and 20cm/s.

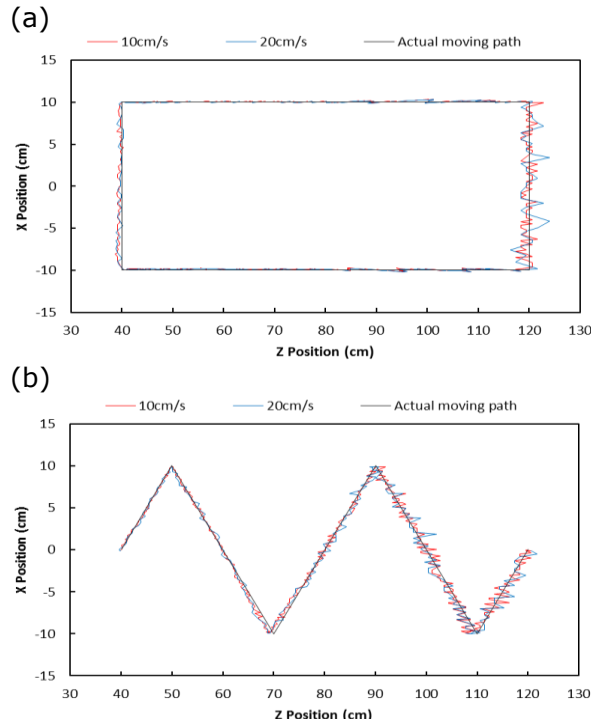


Fig. 8 Localization experimental results (a) a rectangular loop and (b) saw tooth path

The maximum position errors in X and Z directions are 0.37cm and ± 4 cm, respectively. They correspond to 3.7% and 3.3% of the nominal distance. Observe that there are no obvious differences with various travel speeds in 10cm/s and 20cm/s. That is, Wiimote 3D localization system has an excellent ability in tracking. However, it is also found that the positioning errors in Z direction become larger as the sensing distance farther increases. We believe this is due to the larger pixel for a larger Z and this worsens the positioning resolution.

II. IR LED switching technique

Experimental setup for evaluating the performance of IR LED switching is shown in Fig. 9. We utilize two Wiimotes to detect the switch of two IR LED units and to find the relationship between switching rate and data integrity. Ideally, the switching frequency should be identical to the sampling frequency of the Wiimote. However, we cannot control the sampling

of the Wiimote to synchronize with that of IR LED units switching because the sampling is determined by the Wiimote itself. Thus, we need to reduce the switching frequency to confirm the data integrity. It is therefore important to find the maximum switching rate to confirm all the IR LEDs can be detected correctly.

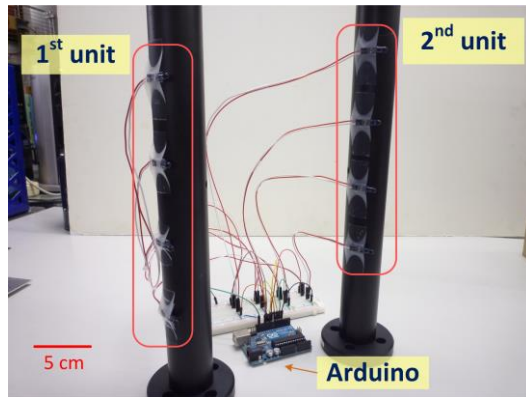


Fig. 9 The experimental setup for IR LED switching

By controlling the switching frequency, it is possible to compare the actual positions of two IR LED units vs. the positions localized by Wiimotes to calculate the data integrity. Fig. 10 shows the relationship between switching frequency and data integrity. It is found that approximately 22Hz is the maximum switching frequency which is sufficient to confirm all the IR LEDs can be detected correctly.

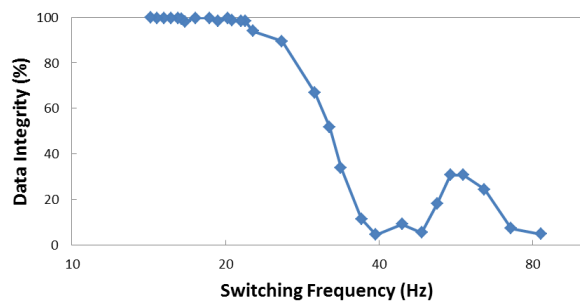


Fig. 10 The relationship between switching frequency and data integrity

Therefore, based on the switching frequency and the number of units, we can determine the sampling frequency of each unit. For two units, the sampling frequency of each unit is the half of the switching frequency (i.e., 11Hz). For three units, the sampling frequency becomes one-third of the switching frequency.

III. Wiimote 3D localization with two units

From the experimental results of IR LED switching, we use the switching frequency of 22Hz for controlling the switch. In addition, with a trade-off between the number of the IR LED units and the sampling rate, we choose two units for the experiment and thus the sampling frequency of each unit is 11Hz.

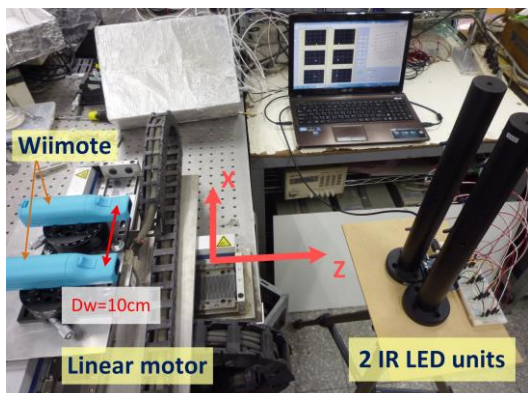


Fig. 11 The experimental setup for Wiimote 3D localization with two units

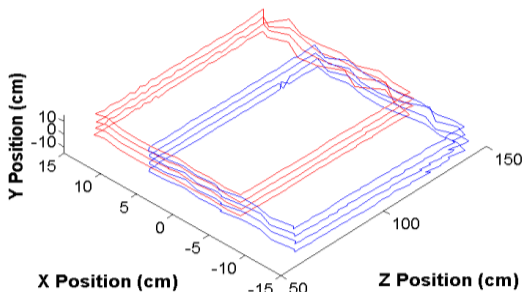


Fig. 12 Localization experimental results with two IR LED units

Experimental setup of Wiimote 3D localization with two IR LED units is shown in Fig. 11. For evaluating the performance of this integrated system, two Wiimotes are mounted on the two-axis linear motor to monitor the motion relative to these two stationary units. Similarly, the linear motor is programmed to perform the same motions as the previous experiment for 3D localization. Fig. 12 shows the typical results with travel speed of 20cm/s and indicates that the relative trajectory of these two units can be monitored excellently. Thus, with this integrated system, further applications such as

mobile robots monitoring or human motion capture for animations can be realized.

Conclusion

A novel 3D Wiimote localization scheme with virtually no channel constraints is proposed for smart living or computer animation applications. We develop the Wiimote 3D localization system and IR LED switching technique for 3D positioning and breaking the channel constraints, respectively. By integrating the 3D localization system with IR LED switching, it is possible to detect the 3D position of many IR LEDs more than original channel constraints. A testing system is also setup for evaluating the performance on the 3D localization and IR LED switching. The preliminary results indicate that the position of IR LEDs can be accurately detected and the system can identify IR LEDs without channel constraints. This simple while effective 3D localization system is expected to have a great potential on indoor smart living related applications such as robots monitoring or motion capture for animations.

Acknowledgements

This work is supported by Ministry of Science and Technology (MOST) of Taiwan (NSC101-2221-E-006-032-MY3.)

References

- [1] Wu, Q P and Han, F T (2011), New Optimal Approach to Space-stable Inertial Navigation System, 10th International Conference on Electronic Measurement and Instruments, pp. 296-299.
- [2] Priyantha, N B et al (2001), The Cricket Compass for Context-aware Mobile Applications, 7th ACM Conf. on Mobile Computing and Networking, Rome, Italy.
- [3] Gao, F et al (2014), An Active Target Localization with Monocular Vision, IEEE International Conference on Control and Automation, Taichung, Taiwan, pp. 1381-1386.
- [4] Chen, X et al (2013), Adaptive Accurate Indoor-Localization Using Passive RFID, IEEE International Conference on Parallel and Distributed Systems, Seoul, South Korea, pp. 249-256.
- [5] Chen, P W et al (2010), IR Indoor Localization and Wireless Transmission for Motion Control in Smart Building Applications Based on Wiimote Technology, in Proceedings of SICE Annual Conference, pp. 1781-1785.
- [6] Fu, Y T and Chen, K S (2013), A Novel Indoor Localization Scheme by Integrating Wiimote Sensing and A Controllable IR-LED Array, Mechatronics 2013: Recent Technological and Scientific Advances, pp. 567-574.

Damping Analysis of Laminated Composite Tapered Beam using Higher Order Finite Element Method

P. Jeyaraj¹ and R. Vasudevan²

1 Department of Mechanical Engineering, NITK Surathkal, Mangalore, Karnataka, India 575025. e-mail: jeyaraj@nitk.ac.in

2 School of Mechanical and Building Sciences, VIT University, Vellore, Tamilnadu 632014, India. email: vasudevan.r@vit.ac.in

ABSTRACT: Tapered laminated composite beam has been used as a structural member in several engineering applications. Termination of laminate plies to form the tapered beams results in resin pockets in the laminated beams. The location and amount of resin is depending on the nature of ply termination. It is important to analyze damping behaviour of the laminated beams with different types of ply termination. Different parameter studies are carried out to analyze the influence of type of taper, taper angle, structural boundary condition and lamination orientation on damping behaviour of the laminated taper beam. It is found that natural frequencies increases significantly with taper angle while there is no significant variation in damping with increase in taper angle for a particular type of taper. Modal damping of Model A is less than that of the other Models such as Model B, C and D. It is also found that structural boundary conditions influence on modal damping is not significant.

Keywords: Tapered Beam, Laminated Composite, Ply drop-off, Finite Element Method

INTRODUCTION

Due to high strength-to-weight and stiffness-to-weight ratios associated with composite materials they are being used to make structural components in mechanical, automotive and aerospace industries. Tapered structures are preferred wherever the stiffness of the structure needs to be varied along the length of the structure. Helicopter blades, turbine blades and robot arms are some of the examples for tapered structures. Such laminated tapered structures are made by terminating the plies along the length of the beam. Composite structures have more inherent damping than conventional metallic structures due to the fiber matrix interaction associated with them.

Several researchers investigated free vibration and damping analysis of uniform laminated composite beams. Abaracar and Cunniff (1972) investigated vibration analysis of cantilever beam made of fiber reinforced material. Teoh and Huang (1977) analyzed vibration of beams made

of fiber reinforced material theoretically. Chen and Yang (1985) formulated an efficient solution procedure for an anisotropic symmetrically laminated beam finite element for static and dynamic analysis. Chandrashekara *et al.* (1990) presented exact solutions for the free vibration of symmetrically laminated composite beams including first-order shear deformation and rotary inertia.

Gibson and Plunket (1977) and Gibson and Wilson (1979) reviewed the extensive initial research work carried out on the damping analysis of fiber composite material. Sun *et al.* (1987) predicted material damping of laminated polymer matrix composites analytically. Crane and Gillespie (1992) developed analytical model for prediction of the damping loss factor of composite materials. Berthelot and Sefrani (2004) carried out damping analysis of unidirectional glass and Kevlar fiber composites experimentally. Abderrahim *et al.* (2008) presented damping analysis of unidirectional fiber composites using finite element analysis

4th International Engineering Symposium - IES 2015

March 4-6, 2015, Kumamoto University, Japan

and compared the results with experimental values.

Limited research work has been carried out on free vibration behavior of tapered laminated composite beams. Rao and Ganesan (1997) analyzed response of tapered composite beams under harmonic excitation using higher-order shear deformation theory. Farghalay and Gadelrab (1995) investigated free vibration behavior of stepped composite beam based on the Timoshenko beam theory. Gupta and Rao (1978) and Cleghorn and Tabarrok (1997) analyzed free vibration behavior of linearly-tapered beams using finite element method. He et al. (2000) carried out a complete review of different tapered models of tapered composite beam. Recently Ganesan and Zabihollah (2007) carried out undamped vibration response of different types of tapered models using higher order finite elements. They presented the differential equation of motion and the higher order element for different kinds of taper configurations.

From literature survey it is revealed that detailed study on damping behavior of laminated tapered composite beams with ply drop off has not been carried out. Depending on the ply termination in each of the tapered model the interaction between the fiber and the resin pocket will be varying which will result in different level of damping in different taper configuration. It is important to investigate influence of different taper configuration, structural boundary conditions and lamination schemes on damping behavior of laminated taper beams. In the present work, a detailed investigation on damping behavior of laminated tapered composite beams using finite elements.

METHODOLOGY USED

Higher-order tapered composite finite element developed by Ganesan and Zabihollah (2007) has been used to carry out different parameter studies presented in the present work. The reader is referred to Ganesan and Zabihollah (2007) for detailed information on the formulation of the elements. Damping associated with each mode, modal damping ratio, has

been obtained based on modal strain energy approach. All the elastic properties associated with the composite material considered in the present work are assumed as complex. The structural stiffness matrix $[K]$ is complex and can be decomposed as

$$[K] = [K_R] + [K_I] \quad (1)$$

Where $[K_R]$ and $[K_I]$ are the real and imaginary parts of the structure stiffness matrix, respectively. The natural frequencies are evaluated by solving the eigenvalue problem

$$([K_R] - \omega^2 k [M]) \{\phi_k\} = 0 \quad (2)$$

where $[M]$ is the structural stiffness matrix, ω_k is the circular natural frequency and ϕ_k is the corresponding mode shape. Modal loss factor of a particular mode can be obtained using

$$\eta_k = \frac{\{\phi_k\}^T [K_I] \{\phi_k\}}{\{\phi_k\}^T [K_R] \{\phi_k\}} \quad (3)$$

RESULT AND DISCUSSION

Laminated tapered composite beam made up of four different models as shown in Fig. 1, analyzed by Ganesan and Zabihollah (2007) is considered for detailed investigation of damping behaviour of tapered composite beam with ply drop off. The thick section of the different models made of 36 plies while thin section is made of 12 plies resulting in 24 drop-off plies. The stacking sequence of layers at the thick section is $[0/90]_{9s}$ while at the thin section is $[0/90]_{3s}$. It is assumed that the laminates are made of Glass-Epoxy composite material having material properties as $E_1=37.78(1+0.0014j)\text{GPa}$; $E_2=10.9(1+0.0008j)\text{GPa}$; $G_{12}=G_{13}=4.91(1+0.011j)\text{GPa}$; $\nu_{12}=0.3$; $\rho=1870\text{kg/m}^3$. The material properties of the epoxy resin are: $E=3.93\text{GPa}$; $G=1.034\text{GPa}$; $\nu=0.37$. Here the notations have the usual meaning.

4th International Engineering Symposium - IES 2015

March 4-6, 2015, Kumamoto University, Japan

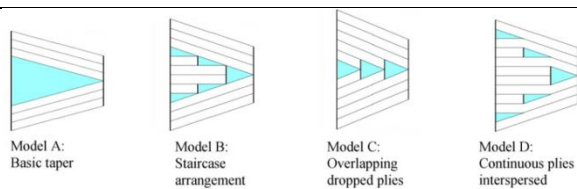


Fig.1 Four different taper models

Influence of Taper angle and Taper Model

Taper angle (α) has been varied from 1° to 4° and corresponding variation in natural frequencies and modal damping values are analyzed for different boundary condition and different taper models. Table 1 shows variation of natural frequencies of first four lowest frequency modes of different taper models with clamped-free (CF) boundary condition.

Table 1 Natural Frequencies (10^3 rad/sec) CF beam

Model	Mode	Taper angle (deg.)			
		1	2	3	4
A	1	3	10	22	39
	2	13	45	93	148
	3	37	114	215	328
	4	73	197	355	529
B	1	3	11	23	40
	2	13	45	94	154
	3	37	116	224	348
	4	80	209	376	563
C	1	3	11	24	41
	2	13	46	96	156
	3	37	117	227	351
	4	81	211	379	566
D	1	3	12	26	44
	2	15	51	104	169
	3	40	126	242	371
	4	84	221	396	589

From Table 1, it is clear that natural frequencies are increasing with taper angle irrespective of the taper model and beam with taper model D has better natural frequency value compared to other types of taper models. Similar trend has been observed for other boundary conditions such as clamped-clamped (CC) and simply supported-simply supported (SS) boundary conditions also. Table 2 shows variation of modal damping of first four

lowest frequency modes of different taper models with clamped-free (CF) boundary condition.

Table 2 Modal damping (x10) of CF beam

Model	Mode	Taper angle (deg.)			
		1	2	3	4
A	1	0.046	0.047	0.047	0.048
	2	0.047	0.048	0.048	0.048
	3	0.049	0.051	0.051	0.051
	4	0.057	0.055	0.053	0.051
B	1	0.055	0.055	0.055	0.055
	2	0.055	0.056	0.056	0.056
	3	0.057	0.058	0.058	0.058
	4	0.060	0.060	0.059	0.059
C	1	0.055	0.055	0.055	0.055
	2	0.055	0.056	0.056	0.056
	3	0.057	0.059	0.058	0.058
	4	0.060	0.061	0.060	0.059
D	1	0.055	0.055	0.055	0.055
	2	0.056	0.057	0.057	0.057
	3	0.059	0.060	0.060	0.059
	4	0.063	0.063	0.061	0.060

There is no significant variation in modal damping value with increase in taper angle for the CF boundary condition as seen in Table 2. Modal damping value of the CF beam with model A differs is low compared to other types of models as shown in Table 2 for the CF beam.

Table 3 Modal damping (x10) of SS beam

Model	Mode	Taper angle (deg.)			
		1	2	3	4
A	1	0.047	0.047	0.047	0.047
	2	0.049	0.049	0.048	0.048
	3	0.057	0.055	0.053	0.051
	4	0.058	0.059	0.057	0.055
B	1	0.055	0.055	0.055	0.055
	2	0.056	0.057	0.056	0.056
	3	0.061	0.060	0.059	0.058
	4	0.061	0.061	0.061	0.060
C	1	0.055	0.055	0.055	0.055
	2	0.056	0.057	0.057	0.056
	3	0.061	0.061	0.059	0.058
	4	0.061	0.062	0.061	0.060
D	1	0.055	0.056	0.055	0.055
	2	0.057	0.058	0.057	0.057
	3	0.064	0.063	0.061	0.060
	4	0.065	0.065	0.064	0.063

Table 3 and Table 4 show variation of modal damping of first four lowest frequency modes of different taper models with simply supported (SS) and clamped-clamped (CC) beams respectively. Influence of taper model on modal damping of the SS and CC beams is similar to the CF beam. From Table 2 to Table 4, it is clear that basic taper, Model A, exhibits relatively less damping due to less modal damping compared to other taper models. It indicates less interaction between the fiber and matrix associated with Model A taper. Resin pocket is sandwiched between the laminates in Model A which results in less fiber-matrix interaction in turn less modal damping. However presence of resin pockets at different location in other models results in significantly higher fiber-matrix interaction in turn results in better modal damping.

Table 4 Modal damping (x10) of CC beam

Model	Mode	Taper angle (deg.)			
		1	2	3	4
A	1	0.047	0.047	0.047	0.047
	2	0.047	0.048	0.047	0.047
	3	0.050	0.051	0.050	0.049
	4	0.050	0.052	0.051	0.050
B	1	0.055	0.055	0.055	0.055
	2	0.055	0.055	0.055	0.055
	3	0.056	0.057	0.057	0.056
	4	0.056	0.057	0.057	0.057
C	1	0.055	0.055	0.055	0.055
	2	0.055	0.056	0.056	0.055
	3	0.057	0.057	0.057	0.057
	4	0.056	0.058	0.058	0.057
D	1	0.055	0.055	0.055	0.055
	2	0.056	0.056	0.056	0.056
	3	0.058	0.059	0.058	0.057
	4	0.057	0.059	0.059	0.059

Influence of taper angle and structural boundary conditions on modal damping is not significant as seen in Table 2 to Table 4. This indicates that same kind of fiber-matrix interaction exists irrespective of taper angle and structural boundary conditions.

Influence of Lamination Scheme

Three different laminate schemes (i) L1: [0/90]_{9s} at the thick section and [0/90]_{3s} at thin section (ii) L2: [±45]_{9s} at thick section and [±45]_{3s} at thin section, (iii) L3: [0₄/±45₇]_s at thick section and [0₄/±45]_s at thin section are considered to analyze influence of lamination scheme on damping behaviour of the tapered beam. Table 5, Table 6 and Table 7 shows influence of lamination scheme on modal damping of CC, CF and SS respectively for different taper models with a taper angle of 2 deg. From Table 5, it is clear that influence of lamination scheme on the modal damping of the CC beam is not significant. Some variation in modal damping of higher mode (4th mode) has been observed but the variation is not significant.

Table 5 Influence of lamination scheme on Modal damping (x10) of CC beam

Model	Mode	L1	L2	L3
A	1	0.047	0.047	0.047
	2	0.048	0.047	0.048
	3	0.051	0.049	0.052
	4	0.052	0.050	0.053
B	1	0.055	0.055	0.055
	2	0.055	0.055	0.056
	3	0.057	0.056	0.058
	4	0.057	0.056	0.059
C	1	0.055	0.055	0.055
	2	0.056	0.055	0.056
	3	0.057	0.056	0.059
	4	0.058	0.056	0.059
D	1	0.055	0.055	0.055
	2	0.056	0.055	0.056
	3	0.059	0.056	0.058
	4	0.059	0.056	0.058

Influence of lamination scheme on modal damping of the CF and SS beams is similar to the CC beam as seen in Table 6. However lamination scheme L2 exhibits less modal damping value compared to other lamination schemes for most of the modes. This can be clearly observed for higher modes.

From the free vibration studies carried out on laminated taper beam with same four different taper models Ganesan and

4th International Engineering Symposium - IES 2015

March 4-6, 2015, Kumamoto University, Japan

Zabihollah (2007) concluded that the tapered beam having Model D as the section results in higher natural frequencies compared to other taper models due to more number of plies with taper angle of zero during their ply drop-off.

Table 6 Influence of lamination scheme on Modal damping (x10) of CF beam

Model	Mode	L1	L2	L3
A	1	0.047	0.046	0.047
	2	0.048	0.047	0.049
	3	0.051	0.049	0.054
	4	0.055	0.052	0.057
B	1	0.055	0.055	0.055
	2	0.056	0.055	0.057
	3	0.058	0.056	0.060
	4	0.060	0.057	0.063
C	1	0.055	0.055	0.055
	2	0.056	0.055	0.057
	3	0.059	0.056	0.060
	4	0.061	0.057	0.063
D	1	0.055	0.055	0.055
	2	0.057	0.055	0.056
	3	0.060	0.056	0.059
	4	0.063	0.057	0.061

Table 7 Influence of lamination scheme on Modal damping (x10) of SS beam

Model	Mode	L1	L2	L3
A	1	0.047	0.046	0.047
	2	0.049	0.048	0.050
	3	0.055	0.052	0.057
	4	0.059	0.054	0.062
B	1	0.055	0.055	0.056
	2	0.057	0.055	0.058
	3	0.060	0.057	0.063
	4	0.061	0.057	0.065
C	1	0.055	0.055	0.056
	2	0.057	0.055	0.058
	3	0.061	0.057	0.063
	4	0.062	0.058	0.065
D	1	0.056	0.055	0.055
	2	0.058	0.055	0.057
	3	0.063	0.057	0.061
	4	0.065	0.057	0.063

From the detailed study carried out on modal damping of the laminated taper

beam it is observed that Model A has less damping value compared to the other taper models. Even though the resin pockets are formed at different locations for the taper models B, C and D the amount of resin is same. Due to this reason the modal damping values are not significantly varying for taper models B, C and D.

CONCLUSIONS

Laminated taper polymer composite beam with four different taper models has been investigated for modal damping using higher order finite element method. It is observed that:

- Beams with taper model D gives better natural frequencies compared to other models.
- Tapered beams with Model A taper configuration gives less modal damping due to the formation of resin pocket at the same location.
- There is no significant variation in modal damping of the tapered beams with Model B, C and D due to same amount of resin pocket in all the models.
- Tapered beams with Model B, C and D gives better modal damping than tapered beams with Model A due to better fiber-matrix interaction.
- Influence of the lamination scheme on modal damping is not significant however lamination scheme L2 gives less modal damping than other schemes for most of the cases.

REFERENCES

- [1] Abarcar R B, and Cunniff P F (1972), The vibration of cantilevered beam of fiber reinforced material, Journal of Composite Materials, Vol. 6, pp. 504-516.
- [2] Abderrahim, E M, Mustapha, A, Youssef S and Berthelot, J M (2008), Damping analysis of orthotropic composite materials and laminates, Composites Part B, Vol. 39, pp. 1069-1076.
- [3] Berthelot, J M, and Sefrani Y, (2004) Damping analysis of unidirectional glass and Kevlar fibre composites, Composite Science and Technology, Vol. 64, 1261-1278.
- [4] Chandrashekara, K, Krishnamurthy K, and Roy, S, (1990), Free vibration of composite beams including rotary inertia and shear deformation, Composite Structures, Vol. 14, pp. 269-279.
- [5] Chen A T, and Yang T Y, (1985), Static and dynamic formulation of a symmetrically laminated

4th International Engineering Symposium - IES 2015

March 4-6, 2015, Kumamoto University, Japan

- beam finite element for a microcomputer, *Journal of Composite Material*, Vol. 19, pp.459-475.
- [6] Cleghorn, W L and Tabarrok, B, (1997) Finite element formulation of a tapered Timoshenko beam for free vibration analysis, *Journal of Sound and Vibration*, Vol. 152, pp. 461-470.
- [7] Crane, R M, and Gillespie, J W, (1992) Analytical model for prediction of the damping loss factor of composite materials, *Polymer Composites*, Vol. 13, pp. 448-453.
- [8] Farghaly, S H, and Gadelrab, R M, (1995) Free vibration of a tapered composite Timoshenko cantilevered beam, *Journal of Sound and Vibration*, Vol. 187, pp.886-896.
- [9] Ganesan, R and Zabihollah, A (2007) Vibration analysis of tapered composite beams using a higher order finite element. Part I: Formulation, *Composite Structures*, Vol. 77, pp. 306-318.
- [10] Ganesan, R and Zabihollah, A (2007) Vibration analysis of tapered composite beams using a higher order finite element. Part II: Parametric Study, *Composite Structures*, Vol. 77, pp. 319-330.
- [11] Gibson R F, and Plunkett R A, (1977), Dynamic stiffness and damping of fiber reinforced composite materials, *Shock and Vibration Digest*, Vol. 9, pp. 9-17.
- [12] Gibson R F, and Wilson D G, (1979), Dynamic properties of fiber reinforced composite materials, *Shock and Vibration Digest*, Vol. 11, pp. 3-11.
- [13] Gupta, R S and Rao, S S, (1978), Finite element eigenvalue analysis of tapered and twisted Timoshenko beams, *Journal of Sound and Vibration*, Vol. 56, pp.2643-2657.
- [14] He, K, Hoa, S V and Rao, S S, (200) The study of tapered laminated composite structures: a review, *Composites Science and Technology*, Vol. 60, 2643-2657.
- [15] Rao, R S, and Ganesan N, (1997), Dynamic response of non-uniform composite beams, *Journal of Sound and Vibration*, Vol. 200, 563-577.
- [16] Sun, C T, Wu, J K, and Gibson R F, (1987), Prediction of material damping of laminated polymer matrix composites, *Journal of Materials Science*, Vol. 22, pp. 1006-1012.
- [17] Teoh, L S, and Huang C C (1977), The vibration of beams of fiber reinforced material, *Journal of Sound and Vibration*, Vol. 51, pp. 467-473.

Multiagent system inspired distributed control of manipulator

Soumya S and K R Guruprasad

*Department of Mechanical Engineering, NITK Surathkal, India
Email: soumya5.subbu@gmail.com*

In this research work, it is planned to mathematically model the robot manipulator and investigate the advantage of the multiagent controller over the centralized controller. Execution of the task involves the interaction between adjacent links. This paradigm is applied to a manipulator control problem without the use of inverse kinematics. An Estimated manipulators Jacobian matrix can be used to design the decentralized controller. The proposed manipulator control system has multiple functional agents and each agent individually attempts to contribute in a positive way towards improving the degree of achievement of the given task. Enormous computational cost and the potential difficulty to adapt to a dynamically challenging environment of model based controller are inevitable. The computational advantage in terms of time and performance will be studied. Moreover, the developed control logic will be experimentally validated to prove the simulation result.

Keywords: manipulator control, Jacobian, model based control

Graphene integrated waveguide for mass sensing

Sagar HP¹, D. Roy Mahapatra², G.M. Hegde² and Rizwanur Rahaman¹

¹*Department of Metallurgical and Materials Engineering, NITK Surathkal, India*
Email: sagarhp2589@gmail.com

²*Indian Institute of Science, Bangalore, India*

Owing to its exceptional mechanical & electrical properties, graphene is an ideal material for NEMS devices. With added advantage of its unique optical characteristics like high absorption we can use this novel membrane for mass detection by evanescently integrating it with a nano sized silicon waveguides. Graphene is used for mass sensing using electrical output, graphene is also integrated on waveguides for rainbow trapping and photo detection, but mass sensing using graphene integrated on wave guides is yet to be realized. In this work, we are trying to use the graphene for mass sensing by correlating the transmission peak shift of the silicon waveguide to the added mass by linear fit.

MEMS based different enhanced diffuser/nozzle micropumps

Roopa R, Navin Karanth P and S M Kulkarni

Department of Mechanical Engineering, NITK Surathkal, India

Email: roopa.hassan89@gmail.com

Different micropumps have been proposed in recent years based on the actuation principle, diaphragm type, operating parameters, geometry, fabrication techniques and valves. Micropumps are used in the field of medical, biomedical applications such as injection of glucose for diabetes patients, insulin injection, blood transportation, for chemical and biological analysis and automobile applications. Performance of micropump can be improved by different methods like diaphragm design, valves, and multiple chambers.

Microvalves controls fluid flow in a micropumps, so valves play an import role in micropump performance. This paper reports overview of the MEMS based valves in micropumps which will provide detailed ideas about the valves of micropumps. Conventional diffuser/nozzle micropumps suffer from low efficiency so in this paper different enhanced diffuser/nozzle designed is simulated. The enhanced structures will improve the micropump performance. The maximum flow rate can be achieved by using the enhanced structures in micropumps.

Since the microfluids field has been growing rapidly, this paper only deals with the different types of valves used in the micropumps. Research and developments on micropumps has been done and less importance is given to the valves of micropumps. In this paper, we present a new enhanced diffuser/nozzle design for micropumps. Simulation of different enhances diffuser/nozzle structures have been performed and compared with conventional diffuser/nozzle using CFD.

Keywords: MEMS, micropump, diffuser/nozzle

EFFECT OF EXHAUST GAS RECIRCULATION RATE ON A SINGLE CYLINDER FOUR STROKE CRDI ENGINE USING CFD MODELING

Venkatesh T. Lamani , Ajay Kumar Yadav and G. N. Kumar

*Department of Mechanical Engineering, NITK, Surathkal, Mangalore 575025, India.
email: venkateshtlnitk@yahoo.com*

ABSTRACT: Exhaust Gas Recirculation (EGR) is one of the effective method to decrease NOx emission from Internal Combustion Engines. The CFD simulation of Common Rail Direct Injection (CRDI) diesel engine has been carried out to study the effect of Exhaust Gas Recirculation rate on spray characteristics and in cylinder process at constant speed. Results are validated with the published experimental results for in cylinder pressure and heat release rate and found a good agreement. The simulation is carried out for diesel as a fuel. The simulation results shows that increase in EGR rate affects the ignition delay, in-cylinder temperature and pressure, and spray characteristics such as liquid kinetic energy, penetration bore and sauter mean diameter.

Keywords: *CFD, Combustion, Exhaust gas recirculation, Common rail direct injection, Sauter mean diameter (SMD), Ignition delay*

INTRODUCTION

Diesel engines operate at high compression ratio and lean fuel mixture resulting in high thermal efficiency. The wide applications of diesel engine in on-road vehicles, power generation and marine applications are mainly focused by emission standards because of related emissions from diesel engine such as nitrogen oxides and particulates. The engine development and after treatment are way to meet the emission standards. The EGR is effective among the after treatment technology. Furthermore, oil-based fuel availability might become a problem due to limited reserves (Knecht, W., 2008). Shi, L (2006), investigated the effects of internal and cooled external exhaust gas recirculation (EGR) on the combustion and emission performance of diesel fuel homogeneous charge compression ignition (HCCI). To achieve the homogeneous mixture and to minimize NOx and smoke emissions fuel is injected before the top dead center (TC) of an exhaust stroke. Experimental study has been carried out to study the influence of

EGR on performance and emissions in a 3-cylinders, air cooled direct injection diesel engine. They observed the reductions in NOx and exhaust gas temperature, and increase in emission of particulate matter (PM), HC, and CO with usage of EGR (Hussain, J et al. (2012), Agarwal, D et al., 2011).

Agarwal, D et al. (2011), studied the effect of EGR on performance, emissions, soot deposits, and wear of engine parts especially piston rings, are investigated by two cylinder, air cooled, constant speed direct injection diesel engine, which is typically used in agricultural farm machinery. The engine was operated for 96 hours in normal running conditions and the deposits on engine parts were assessed. Higher carbon deposits of engine parts and higher wear of piston rings were observed for engine with EGR (Agarwal, D et al. (2011)).

Li, T (2009), studied the combustion and exhaust emissions characteristics of a CRDI engine with high rates of cooled EGR by addition of ethyl tert-butyl ether (ETBE) in diesel fuel. Smoke emission is suppressed by increasing the ETBE fraction

4th International Engineering Symposium - IES 2015

March 4-6, 2015, Kumamoto University, Japan

and increasing the EGR rate Li, T (2009). The effect of water-in-diesel emulsion (WDE) experimentally investigated by Maiboom, A (2011), on automotive high speed direct injection diesel engine. The experiment is conducted for two injection pressure and four injection strategies (with and without pilot injection). WDE in parallel with EGR (with various EGR rates) an effective way for NOx and PM emission reduction (Maiboom, A et al., 2011). The effect of EGR and fuel evaporation on charge cooling was investigated by Zhang, Z (2014), Charge cooling effect was found on addition of EGR and alcohol. The anti-knock ability mainly depends on the octane number and charge cooling effect of fuels, as well as EGR. (Zhang, Z et al., 2014). Park et al., (2014), investigated the effects of the high pressure and low pressure EGR proportion on engine operation. They observed that intake manifold temperature decreased gradually as the LP EGR portion increased. A higher LP EGR portion showed a lower fuel consumption level than the HP EGR. Nitrogen oxide (NOx) emissions were also decreased Park et al., (2014). Zheng, Z et al., (2014), studied the CFD simulation on the effects of reformed exhaust gas recirculation (REGR) on combustion and emissions of dimethyl ether (DME) by HCCI combustion. The results show that REGR combining EGR and DME reformed gases (DRG) improves combustion. REGR can delay ignition time by both EGR and DRG, and makes main combustion closer to top dead center (TDC) (Zheng, Z et al., 2014). Voicu, A I (2012), conducted experimental study to the premixed charge compression ignition operation. In this technique part fuel injected in catalytic reformer fitted into the exhaust gas recirculation (EGR) system. The produced gas mixture is fed back to the engine as reformed EGR (REGR). REGR resulted in a higher premixed combustion rate and reduction of the diffusion combustion phase. The potential of the technique in terms of achieving reduction of smoke and NOx emissions and improved fuel economy (Voicu, A. I. et al., 2012).

NUMERICAL MODEL

CFD code and calculating meshes

Engine geometry and meshing are generated in AVL FIRE Engine simulation environment tool FIRE manual (2011). A six hole orifice nozzle is located centrally on the top of the piston, hence 60° sector is chosen for the computational simulation. In the simulation high pressure cycle is considered for simulation. The simulation starts at inlet valve close and ends at exhaust valve open position respectively. Mesh cells at TDC and BDC are 15000 and 95780 respectively.

The Spray Model

Aerodynamic force causes surface instabilities in the combustion chamber as fuel is injected resulting primary and secondary atomization. The atomization of the droplets is studied employing standard WAVE model by Liu, A B et al., (1993). The blob injection method is used for drop parcels injection which assumes nozzle exit diameter as the diameter of drop parcels. Dukowicz model (Dukowicz, J K (1979) is employed for treating the droplet parcels and evaporation of droplets. Wall jet model is selected for spray wall interaction.

Combustion Model

Combustion process is studied by three zone extended coherent flame model (ECFM-3Z) based on flame surface density approach. With ECFM features ECFM-3Z takes care of diffusion flame and mixing process. In this model, each computational cell is divided into three mixing zones i.e., pure fuel zone, air plus EGR zone and mixed zone. $k-\zeta-f$ model is used to treat the turbulent effect. (FIRE manual (2011)). Correlation 1 is used to compute ignition delay in diesel combustion. When the delay time is reached, the mixed fuel is oxidized with a chemical characteristic time.

$$\tau_d = 4.804 \times 10^{-8} \left(\frac{N_{O_2}^{u,M}}{N_{O_2}} \right)^{-0.53} \left(\frac{N_{F_u}^{u,M}}{N_{F_u}} \right)^{0.05} (\bar{\rho}^u)^{0.13} e^{\frac{5914}{T^u}} \quad (1)$$

Where, molar concentrations are given in mole/m³, the temperature in K, the density $\bar{\rho}^u$ in kg/m³.

4th International Engineering Symposium - IES 2015

March 4-6, 2015, Kumamoto University, Japan

THE POLLUTANT MODELS

The NOx model

Combustion in the diesel engine produces different nitrogen based emissions. Among the different nitrogen oxides nitrogen monoxide contributes major portion of emissions. Hence nitrogen monoxide is modelled in the present study. The equation 2 is used to solve the transport phenomenon to so solve formation of nitrogen monoxide.

$$\frac{\partial(\bar{\rho}\bar{Y}_{NO})}{\partial t} + \frac{\partial(\bar{u}_i \bar{\rho}\bar{Y}_{NO})}{\partial x_i} = \frac{\partial}{\partial x_i} \left(\bar{\rho} D_t \frac{\partial \bar{Y}_{NO}}{\partial x_i} \right) + \bar{S}_{NO} \quad (2)$$

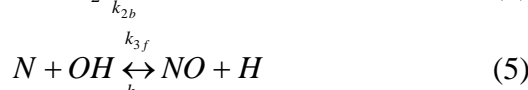
Where, $\bar{\rho}$, \bar{Y}_{NO} , \bar{u}_i , x_i , D_t and \bar{S}_{NO} are Reynolds averaged fuel density, the mean mass fraction of NO, density-weighted average, velocity and Cartesian coordinates, diffusion coefficient, and mean nitric oxide source respectively(Kuo et al., 1986).

The terms in the above equation (2) represents unsteady state, change due to convection and change due to diffusion of NO respectively. The term \bar{S}_{NO} represents NO pollutant formation in the equation.

Thermal NO Mechanism

In the combustion of clean fuels with air NO is formed mainly by the Zeldovich Mechanism. This mechanism consists of three principal reactions as follows

Zeldovich et al. (1947) described that using a set of three reactions (Eqs. 3 to 5). The nitrogen reacts with the atomized oxygen O created due to the high combustion temperature, as shown in Eq. (3). Nitrogen oxide and unstable nitrogen products of the initial reaction which is further oxidized, are shown in Eq. (4). The term O₂ represents the oxygen molecule. The additional reaction is added for fuel rich conditions, which considers the high concentration of OH radicals as shown in Eq. (5).



By using the Arrhenius law reaction rate coefficients k_{1f}, k_{1b}, k_{2f}, k_{2b}, k_{3f} and k_{3b} are modelled by Kuo et al., (1986). Subscripts f and b represent the forward and backward reaction respectively.

Prompt NO Mechanism

Prompt NO mechanism formation occurs at early stage of fuel rich regions of the flames. The reaction initiated by rapid reactions of the hydrocarbon radicals due to fuel fragmentation in the presence of nitrogen.

The expression for the prompt NO formation rate (Vujanovi, C. M. et al. 2009) is shown in Eq. (6), where f is the correction factor, A_p is pre-exponential factor and b is the order of reaction for the molecular oxygen:

$$\frac{dc_{NO,prompt}}{dt} = f A_p c_{O_2}^b c_{N_2} c_{fuel} \exp\left(-\frac{E_a}{RT}\right) \quad (6)$$

Soot model

The carbonaceous particles are formed by diesel fuel at high temperature and under fuel-rich conditions are called soot. A various models for the soot calculation are proposed in the literature such as the Keneddy/Hiroyasu/Magnusen, Hiroyasu/Nagle Strickland-Constable, Lund Flame let, Kinetic and Residence time models. (FIRE manual, 2011).

VALIDATION CASE STUDY

The simulation is validated from the literature Mobasher, R. et al., (2012). Engine specification, Injection fuel specification, and comparison of experimental and simulation data are presented in Table1, Table 2 and figure 2 respectively.

The details of boundary conditions and initial values are presented in Table 3.

RESULT AND DISCUSSIONS

The figure 3 shows the comparison of in-cylinder pressure traces at various EGR rates (5%, 10%, 15% and 20%). With increase in the EGR rate fuel charge heat capacity increases as the result of this there is reduction in the O₂ availability and hence incomplete combustion occurs. Finally as EGR rate increases, in- cylinder pressure decreases.

Fig. 4 represents the temperature versus crank angle for different EGR rates. The cylinder temperature is one of the core features for controlling the auto-ignition process. EGR in the cylinder contains gases like water vapor and CO₂. By absorbing heat from cylinder these gases, increase the specific heat capacity of the EGR composition. This composition acts like as a thermal sink and reduces the cylinder temperature. If more EGR is introduced in the cylinder ignition delay increases, because of less oxygen availability during the combustion.

Fig. 5 indicates the HRR versus crank angle for different EGR rates. Auto ignition is the main process which controls the combustion in the diesel engine depends on HRR and EGR rate. Due to shortage of oxygen at high EGR rate ignition delay increases and combustion shifts towards post flame reason.

Fig. 6 represents the sauter mean diameter versus crank angle. Results show that at the beginning of the injection the sauter mean diameter is larger for small duration of time. This may be attributed to less drag of air in the cylinder at lower pressure. As the cylinder approaches to TDC, part of injected droplets get evaporated and remaining particles experience larger drag force, and hence sauter mean diameter reduces. The average sauter mean diameter is approximately 25 μm.

The key parameter to nitrogen oxide formation is local temperature and concentration of oxygen in higher flame temperature zone. Fig. 7 shows the well-established advantage of EGR in decreasing NOx emissions from diesel engine. The use of EGR leads to less oxygen interaction with fuel available in the chamber results in decreased flame temperature. Hence NOx emission in exhaust with increase in EGR shows a decreasing trend.

Fig. 8 represents soot formation versus crank angle for different EGR rates. Formation of soot in combustion chamber occurs at high equivalence ratio and medium temperature conditions. Soot is produced in high fuel-rich reason and medium temperature zone. In post flame combustion soot emission increases

obviously with an increase in EGR rate. EGR resulted in a decrease in oxygen concentration and rise in the number of anoxic zones in the cylinder leading to a comparatively partial combustion and the high soot formation.

CONCLUSIONS

The following conclusions are deduced from this study:

- The peak value of in-cylinder mean temperature decreases as EGR rate increases from 5 to 20%.
- NOx emission level decreases with increase in EGR rate.
- The soot in the exhaust increases marginally in post flame combustion.

With above simulation results it can be concluded that the use of EGR is most effective way to reduce exhaust emissions.

ACKNOWLEDGMENTS

The authors would like to acknowledge AVL-AST, Graz, Austria for granted use of AVL-FIRE under the University partnership program.

REFERENCES

- [1] Agarwal, D et al. (2011), Effect of Exhaust Gas Recirculation (EGR) on performance, emissions, deposits and durability of a constant speed compression ignition engine. Applied Energy, Vol. 88, No.8, pp. 2900-2907.
- [2] Dukowicz, J K (1979), "Quasi-steady droplet phase change in the presence of convection". Los Alamos Scientific Lab., NM (USA).
- [3] FIRE v2011 Manuals, 2011. Graz, Austria, AVL LIST GmbH.
- [4] Hussain, J et al. (2012), Effect of exhaust gas recirculation (EGR) on performance and emission characteristics of a three cylinder direct injection compression ignition engine. Alexandria Engineering Journal, Vol. 51, No.4, pp.241-247.
- [5] Hanson, R K (1984), Survey of rate constants in H/N/O system. In: Gardiner Jr., W.C. (Ed.), Combust. Chem. Springer, New York, pp. 361-421.
- [6] Knecht, W. (2008), Diesel engine development in view of reduced emission standards. Energy, Vol. 33, No.2, pp.264-271.
- [7] Kuo (1986), Principles of combustion, 1986.
- [8] Li, T (2009), Effects of ethyl tert-butyl ether Addition to diesel fuel on characteristics of combustion and exhaust emissions of diesel engines. Fuel, Vol. 88, No.10, pp. 2017- 2024.
- [9] Liu, A B (1993), Modeling the Effects of Drop Drag and Breakup on Fuel Sprays. SAE Paper 930072.
- [10] Maiboom, A (2011), NOx and PM emissions reduction on an automotive HSDI Diesel engine with

4th International Engineering Symposium - IES 2015

March 4-6, 2015, Kumamoto University, Japan

- water-in-diesel emulsion and EGR: An experimental study. Fuel, Vol. 90, No.11, pp. 3179-3192.
- [11] Mobasher, R(2012), Analysis the effect of advanced injection strategies on engine performance and pollutant emissions in a heavy duty DI-diesel engine by CFD modeling, International Journal of Heat and Fluid Flow, Vol. 33, No.1, pp.59-69.
- [12] Park, (2014), "Experimental study on the effects of high/low pressure EGR proportion in a passenger car diesel engine." Applied Energy, Vol. 133, pp. 308-316.
- [13] Petranović, Z (2014), Towards a More Sustainable Transport Sector by Numerically Simulating Fuel Spray and Pollutant Formation in Diesel Engines. Journal of Cleaner Production.
- [14] Shi, L (2006), Study of low emission homogeneous charge compression ignition (HCCI) engine using combined internal and external exhaust gas recirculation (EGR), Energy, Vol. 31, No.14, pp. 2665-2676.
- [15] Voicu, A. I (2012), A Numerical Simulation of the Influence of Injection Characteristics on Performance and Emissions of A tractor Diesel Engine. UPB Sci Bull, Series D: Mech Eng, Vol. 74, No.3, pp. 43-54.
- [16] Vujanović M (2009), Validation of reduced mechanisms for nitrogen chemistry in numerical simulation of a turbulent non-premixed flame. React. Kinetics Catal. Lett, Vol. 96, No.1, pp. 125-138.
- [17] Zhang, Z (2014), Combustion and particle number emissions of a direct injection spark ignition engine operating on ethanol/gasoline and n-butanol/gasoline blends with exhaust gas recirculation. Fuel, Vol. 130, No.130, pp. 177-188.
- [18] Zheng, Z (2014), Numerical study of effects of reformed exhaust gas recirculation (REGR) on dimethyl ether HCCI combustion. International Journal of Hydrogen Energy, Vol. 39, No.15, pp. 8106-8117.

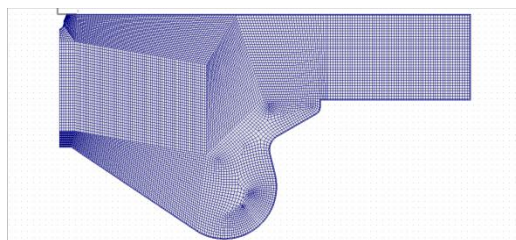


Fig. 1 Three dimensional computational domain at TDC position

IVO/IVC	-32° ATDC / -147° ATDC
EVO/EVC	134° ATDC/29° ATDC
Engine speed	1600 rpm
IMAP	184 kPa
IMAT	310 K

Table 2 Injector fuel system specifications

Parameters	Values
Injector type	Common Rail
Injection Pressure	Variable (up to 1200 MPa)
Number of nozzle holes	6
Nozzle hole diameter	0.26 mm
Start of Injection	-9 °ATDC
Fuel Injected	1622g/cycle
Injection duration	21.5° C

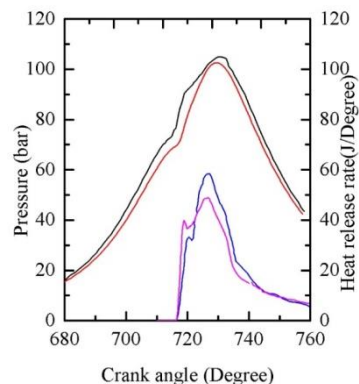


Fig. 2 In-cylinder pressure versus crank angle experimental and simulation

Table 1 Engine specifications

Parameters	Values
Bore × stroke	13.719 cm × 16.51 cm
Compression ratio	15.1:1
Connecting rod length	26.162 cm
Displacement	2.44 litre

Table 3 Calculation domain boundaries

Parameters	Boundary conditions	Initial value
Piston	Moving mesh	Temperature 550 K
Axis	Periodic inlet/outlet	Periodic
Cylinder head	Wall	Temperature 550 K
Compensation volume	Wall	Thermal / Adiabatic boundary
Liner	Wall	Temperature 425 K

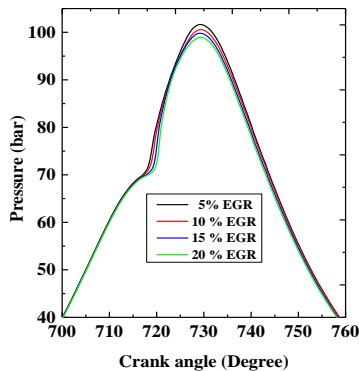


Fig. 3 In-cylinder pressure versus crank angle for various EGR rate

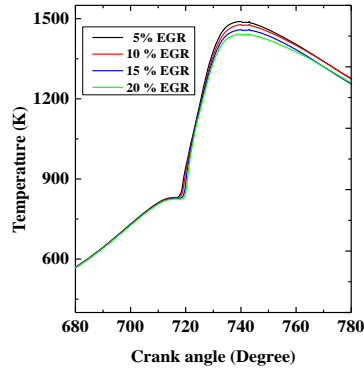


Fig. 4 Effects of EGR rate on the in cylinder temperature

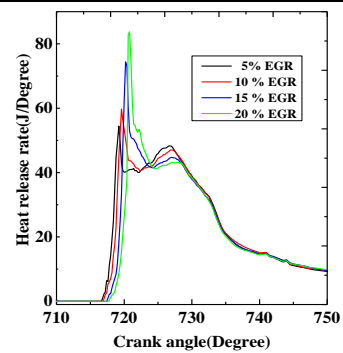


Fig. 5 Effects of EGR rate on the heat release rate

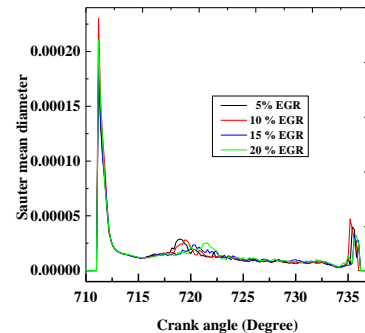


Fig. 6 Effects of EGR rate on the sauter mean diameter

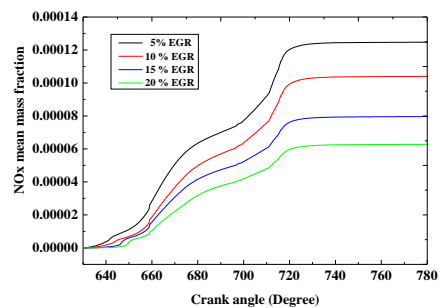


Fig. 7 Effects of EGR rate on NOx formation

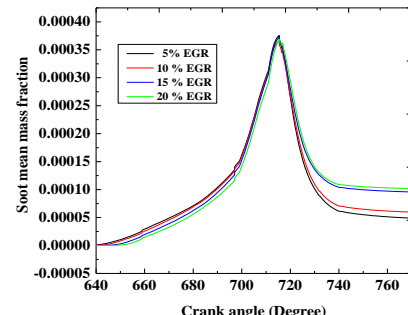


Fig. 8 Effect of EGR rate on Soot formation

Development of a novel vibration absorber utilizing smart elastomer for damping of torsional vibration

Subhasankar Dwibedi and K V Gangadharan

Department of Mechanical Engineering, NITK Surathkal, India

Email: shubha261@gmail.com

In rotating machinery and power transmission systems, torsional vibration is often a matter of concern as it can lead to catastrophic effects if not controlled. The focus of this study is to design and develop a vibration absorber utilizing smart elastomer for damping of torsional vibration. The smart elastomer used to develop the vibration absorber consists of silicone rubber and carbonyl iron particle (CIP) of average diameter 5 μm . 25% by volume CIP is added to the elastomer matrix. The system natural frequencies and damping value were calculated theoretically. With the derived values, a magnetorheological elastomer-based noble vibration absorber is designed and manufactured. A test setup was fabricated to simulate the vehicle power train system. Experimental testing is to be conducted to validate the design and to determine the degree of agreement between the theoretical and experimental data. The frequency range in which the vibration absorber can work effectively has to be identified by conducting experiment on the developed setup. Numerical simulation of the proposed design has been carried out and it was observed that the excitation frequencies are shifted away from the system natural frequencies. Thus, the powertrain's steady-state vibration can be significantly reduced. This developed coupler utilizing magnetorheological elastomer will be a promising new device for vibration reduction of vehicle powertrains and other rotating machineries.

Spectroscopic Ellipsometry Analysis of Strained ZnO:Al Films Using Various Optical Models

**Wen-Yeong Huang, Yang-Hsien Lee, Sin-Bo Wang, Sin-Wei Wu, Chih-kai Hsu,
Keh-moh Lin***

Department of Mechanical Engineering, Southern Taiwan University of Science and Technology, No. 1, Nan-Tai Street, Yungkang Dist., Tainan City 710, Taiwan R.O.C.

*e-mail:kemo@mail.stust.edu.tw

Abstract: Spectroscopic ellipsometry (SE) technique is applied to characterize the state of residual stress in the interface region between the ZnO:Al (AZO) films and the substrates. The thermal stress is mainly caused by different thermal expansion coefficients of substrate materials and AZO films. Especially for the films on flexible substrates, it affects the film quality significantly. Different construction methods with optical models such as Cauchy, Lorentz, Simple-Grade, and Surface models were used to estimate the film thickness, refractive index, and extinction coefficient of the AZO films. The fitting results reveal that the optical constant of the substrate affects the fitting results obviously when the AZO film is very thin (< 50 nm). The refractive index of the AZO films in the interface region will change when the stress state change in this region. XRD stress analysis confirms this observation.

Keywords: Residual stress; ellipsometry; transparent conductive oxide;

Introduction

Transparent conductive oxides (TCOs) thin films have become an essential material for transparent electrodes of opto-electrical products, such as smart phones, touch panels, LCD, and solar cells [1]. Especially, with the coming of the plastic electronic devices, the TCOs films are also deposited on flexible substrates. The difference of thermal expansion coefficients of the TCOs films and the underlying substrate cause serious thermal stress which will affect the optical properties and performance of the TCOs films [2]. Spectroscopic ellipsometry (SE) technology is widely used to measure film thicknesses and optical constants due to its high precision and sensibility [3].

In our earlier studies, we found that the refractive index of the AZO films varied when the residual stress of the films was released. This allowed us to obtain the information on the residual stress state of the films. Although the MSE value was low, the fitting and measured curves matched well with each other. However, there are still some problems to be improved. For

example, when the AZO films are quite thin, the curves of the film thickness and sputtering time weren't reasonable. At the same time, the refractive index of the AZO film was also too low. Therefore, in this study, we use different construction methods of optical models to extract the surface roughness, thickness, and refractive index of the AZO films more precisely. The fitting results will be compared with the XRD measurements and will be used to verify the strain evolution related to the change of film thickness.

Preparation and characterization

In this experiment, a 3-inch AZO (ZnO with 2 wt.% Al₂O₃) target was used in the RF sputtering process to obtain different thicknesses of AZO films on glass (Eagle® 2000). The distance between the target and the glass substrate was 5 cm; the substrate temperature was set at room temperature. The flow rate of Ar gas was set at 40 sccm. The working pressure was set at 8 mtorr. The power for sputtering was set at 80 W; the deposition time was

4th International Engineering Symposium - IES 2015

March 4-6, 2015, Kumamoto University, Japan

between 200 ~ 600 sec. After the characterization steps, the AZO films were post-heated in vacuum (~1.0 mtorr) for 600°C/1 h.

The thickness and refractive index of the AZO films were estimated by using a variable angle spectroscopic ellipsometry (M-2000U, Woollam). All data analysis was carried out by using WVASE32® software. The transmittance was measured by a UV-Vis-NIR spectrophotometer (V-670, Jasco).

Result and discussion

Optical constant

A precise optical constant of the glass substrate is very important for improving the accuracy of the fitting results of the AZO films. Therefore, we estimate the refractive index of the glass substrate in the transparency region (set extinction coefficient $k = 0$). Then, this refractive index is used in our optical models instead of using the refractive index value from the WVASE32® software. It is well-known that the transmittance T_A at the air/glass interface (set $n_{air} = 1$) is given as follows:

$$T_A = \frac{4n_g}{(1+n_g)^2} \quad (1)$$

where n_g is the refractive index of the glass. If the glass is optical thick, the interference effect from the front and rear sides can be neglected. Thus, the total transmittance of the glass is derived as:

$$T = \frac{1}{\frac{1}{T_A} + \frac{1}{T_B} - 1} \quad (2)$$

By this way, one can obtain n_g as a function of the transmittance of the glass:

$$n_g = \frac{1 + \sqrt{1 - T^2}}{T} \quad (3)$$

Fig. 1 depicts the calculated refractive index n_g of the Corning glass (Eagle® 2000).

Spectroscopic ellipsometry analysis

In order to reduce the measured errors, all SE measurements are carried out with three incident angles (65°, 70° and 75°). The measurements are performed in the wavelength range 400 ~ 1000 nm, with incremental steps of 5 nm. The lower wavelength of 400 nm is chosen to avoid

spectral overlap with the absorption of the AZO films in the UV region. A least squares fitting method is performed and a mean squared error (MSE) is used to evaluate the quality of the fitting processes.

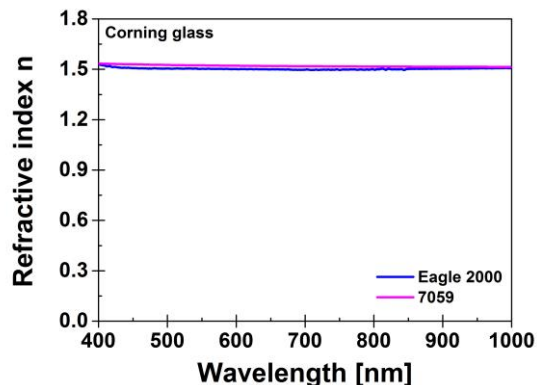


Fig. 1: the calculated refractive index n_g of the Corning glass (Eagle® 2000), set extinction coefficient $k = 0$.

SE optical modeling

In this study, two construction methods for optical modelling are used to estimate the films' properties. In the first modelling process, it is assumed that the AZO films are fully transparent in this wavelength range. So only the Cauchy model is needed for the fitting processes. The Cauchy model describes the dispersion of film refractive index as a slowly varying function of wavelength with an exponential absorption tail. It is used to roughly estimate film thickness and optical constants. In Addition, a Simple-grade model and a surface roughness model are adopted to reflect the physical properties of the films. The dielectric constant of the surface layer ϵ_{surf} consists of 50 vol% voids ϵ_{void} and 50 vol% of underlying layer ϵ_{Cauchy} , an effective medium approximation (EMA) obtained by utilizing Bruggeman, which is often used to model effective complex permittivity of a two-phase composite [4]. In the second modelling process, the Lorentz model replaces the Cauchy model, which is a classic harmonic oscillator and is derived in optics texts usually. It has also long absorption tails like the Cauchy model and can, thus, cause unwanted absorption in transparent regions. However, it works well for where absorption exists over all wavelengths [4].



Fig. 2: structures of the two optical models.

Results based on Cauchy model

One of the fitting results of the AZO films based on the Cauchy model is given in Fig. 3. The generated data agree well with the experimental data. The MSE of all fitting results are smaller than 3.1. Although it is higher than that of our early experiment [5], but the variation of the total film thickness d_t to the deposition time is more physically reasonable (Fig. 4). As described in [5], d_t consists of film thickness d_{Cauchy} and surface roughness thickness $0.5 d_{rough}$ which is the thickness of the surface roughness in the SE model. Due to graded characters of the sputtered AZO films, the Simple-grade model effectively allows us to obtain better fitting results. Finally, the average values of the refractive index are calculated over the visible region as a function of the deposition time (Fig. 5). Different to our early experiment, the average refractive index slightly increases with the increasing deposition time.

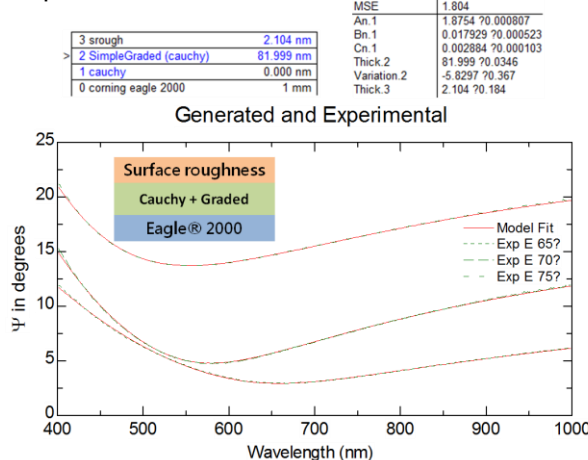


Fig. 3: one of fitting results, Cauchy model

Figure 6 give the ratio of roughness thickness d_{rough} to film thickness d_{Cauchy} ($R_d = d_{rough}/d_{Cauchy}$) as a function of deposition time. Both curves demonstrate a sharp bend between 200 and 300 sec in Fig. 6, which are also observed in the XRD stress

analysis [5]. Fig. 7 depicts the variation of the refractive index of the AZO films at top and bottom positions. There is an obvious gradient of the refractive index within the AZO films. At the beginning, the film is very thin. The thermal stress affects the optical properties so that the refractive index at top area is larger than that at the bottom area. After the stress is released, the profile of the refractive index reverses to normal state. Therefore, the value at bottom is larger than that at top.

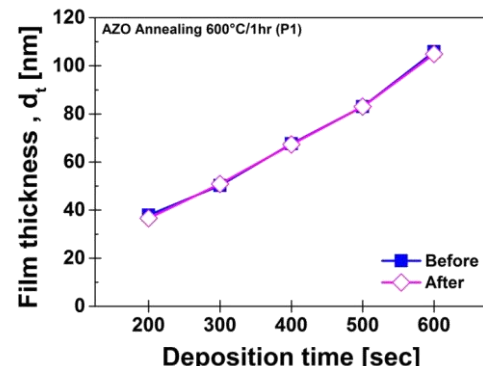


Fig. 4: Total thickness of the AZO films, Cauchy model

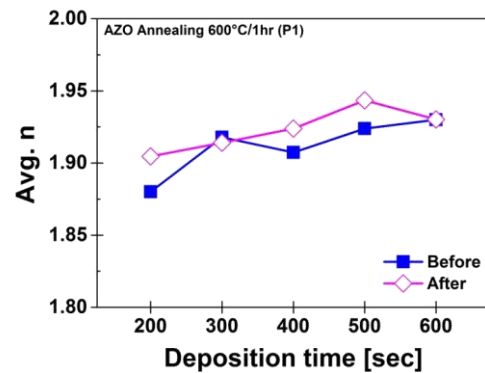


Fig. 5: Variation of average refractive index of the AZO films, Cauchy model

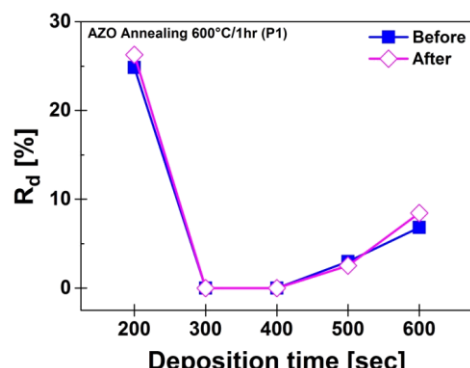


Fig. 6: Variation of the ratio of roughness thickness d_{rough} to film thickness d_{Cauchy} , Cauchy model

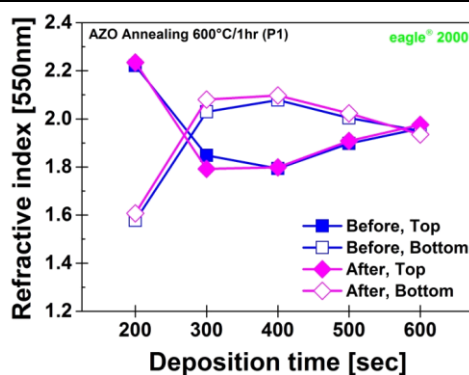


Fig. 7: Refractive index of the AZO films at top and bottom position, Cauchy model

Results based on Lorentz model

Although the MSE and the fitting quality of the Lorentz model are worse than the Cauchy model, the average refractive index in the visible region as well as the total film thickness are similar to that of the Cauchy model. More important, the variation behaviour of the refractive index of the AZO films at top and bottom positions predicted by the Lorentz model agrees well with the results of the Cauchy model (Fig. 8). That means, the refractive index is strongly influenced by the thermal stress. Moreover, the fitting result becomes apparently worse when the film thickness increases. Thus, a more precise optical model including multi-absorption centres is needed in order to describe the optical properties of the AZO films accurately.

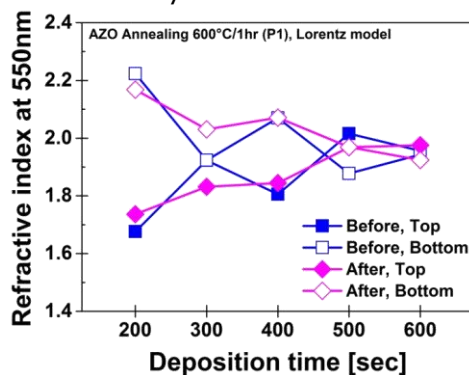


Fig. 8: Refractive index of the AZO films at top and bottom position, Lorentz model

Conclusions

In this study, we show that a precise optical constant of the glass substrate is important for achieving accurate optical properties of the AZO films. At the same time, different dispersion models of the

AZO films were applied to SE fitting processes and led to similar results, i.e. the thermal stress has strong impact on the film's optical properties, especially when the film is very thin. This fact enables us to construct an in-line inspection system by using SE technique.

Acknowledgements

The authors gratefully acknowledge the financial support provided by the Ministry of Science and Technology of Republic of China under contact number NSC 102-2221-E-218-039.

REFERENCES

- [1] K. Nomura, H. Ohta, K. Ueda, T. Kamiya, M. Hirano, H. Hosono, *Science* Vol. 300 (2003), p. 1269.
- [2] Y. Leterrier, *Prog. Mater. Sci.* Vol. 48 (2003), p. 1.
- [3] Á. Németh, Cs. Major, M. Fried, Z. Lábadi, I. Bársóny, *Thin Solid Films* Vol. 516 (2008), p. 7016.
- [4] J.A. Woollam: *Guide to Using WVASE32®* (2003).
- [5] K. Lin, C.-T. Hsieh, W.-Y. Huang, Y.-H. Lee, C.-k. Hsu, proceeding of the 7th International Conference on Advanced Materials Development and Performance, July 17-20, 2014, Busan, Korea.

Spectroscopic Ellipsometry Studies on Optical Properties of InGaZnO Thin Films Deposited by RF Sputtering Method

**Yang-Hsien Lee, Wen-Yeong Huang, Liang-yan Li, Sin-Wei Wu, Sin-Bo Wang,
Keh-moh Lin***

Department of Mechanical Engineering, Southern Taiwan University of Science and Technology, No. 1, Nan-Tai Street, Yungkang Dist., Tainan City 710, Taiwan R.O.C.

*e-mail:kemo@mail.stust.edu.tw

Abstract: InGaZnO (IGZO) film is one of the important materials for multicomponent transparent conductive oxide films at the moment. However, a lot about its optical properties and compositions still need to be clarified. In this study, IGZO thin films of different composition ratios are fabricated by RF sputtering method. Spectroscopic ellipsometry (SE) technique with different optical models is applied to characterize the optical properties of IGZO thin films. Experimental results show that the composition ratio of the IGZO films affects their optical properties considerably, which can be detected by the SE technique.

Keywords: *IGZO; ellipsometry; multicomponent oxide;*

Introduction

Taking the advantage of the different physical and chemical properties of binary and ternary oxides, multicomponents oxide (MCO) thin films are composed of binary or ternary oxides to obtain a new form of oxide thin films. Thus, one can overcome the physical and chemical properties shortcomings of usual MCO films by choosing oxide films of apposite composition ratios [1-3]. In this study, we will first prepare InGaZnO (IGZO) thin films of different composition ratios deposited by RF sputtering method. Then, SE will be applied to analyze the influences of gallium concentration on their optical properties. UV-Vis-NIR spectrophotometer will be used to investigate the change of transmittance and energy band gaps along with the change of the composition ratios so as to understand the relation between the optical properties and the composition ratios of IGZO films.

Preparation and characterization

In this experiment, 3-inch IGZO (In:Ga:Zn=1:1:1 and 2:1:2, noted as G1 & G2, respectively) targets are used in the RF sputtering process to obtain different

thicknesses of IGZO films on quartz glass. The distance between the target and the glass substrate is 5 cm; the substrate temperature was set at room temperature. The flow rate of Ar gas is set at 40 sccm. The working pressure was set at 8 mtorr. The power for sputtering was set at 60, 70 and 80 W; the deposition time was set at 5, 10, 15 and 20 min.

The thickness and optical constant of the IGZO films are estimated by using a variable angle spectroscopic ellipsometry (M-2000U, Woollam). All data analysis was carried out using WVASE32® software [4]. Their transmittance and band gaps are measured by a UV-Vis-NIR spectrophotometer (V-670, Jasco).

Result and discussion

Spectroscopic ellipsometry analysis

In order to reduce the measured errors, all SE measurements are carried out with three incident angles (65°, 70° and 75°). The measurements are performed in the wavelength range 245 ~ 1000 nm, with incremental steps of 5 nm. A least squares fitting method is performed and a mean squared error (MSE) is used to evaluate the quality of the fitting.

SE optical modeling

In this study, a two-step process is used to estimate the films' properties. In the first step, it is assumed that the IGZO films are fully transparent in the wavelength range 400 ~ 1000 nm. So only the Cauchy model is needed for the fitting processes. Then, a Simple-grade model and a surface roughness model are applied to improve the precision of the fitting results. In the second step, an Oscillator model is used to replace the Cauchy model, which allows us to extend the fitting wavelength range down to 245 nm. By this way, one can investigate the absorption behaviour of the IGZO films.

Results based on Cauchy model

One of the fitting results of the AZO films based on the Cauchy model is given in Fig. 1. All generated data agree well with the experimental data. The MSE of all fitting results are smaller than 2.5. As mentioned in our another report [5], the sputtered TCO films have obvious graded character and roughness. Therefore, the Simple-grade and surface roughness models have to be considered in our optical model.

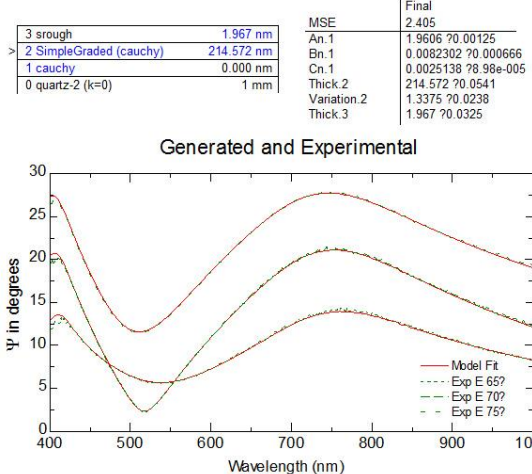


Fig. 1: one of the fitting results, Cauchy model

The total thickness of the IGZO films is plotted in Fig. 2. The composition ratio has no influence on the film thickness. The film growth rate depends mainly on the sputtering power and the deposition time. Moreover, the average value of the refractive index versus deposition time over the visible region is given in Fig. 3. The average refractive index slightly

increases from 5 min to 10 min, then remains at the same level. The reduction of Ga amount enables the film refractive index to increase slightly.

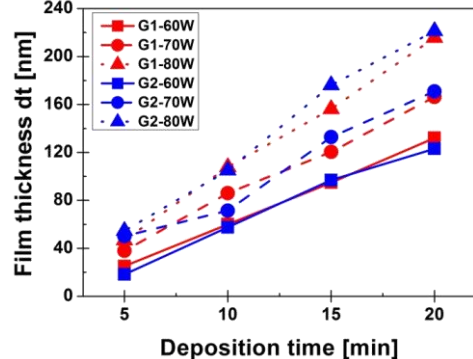


Fig. 2: Total thickness of the IGZO films, Cauchy model

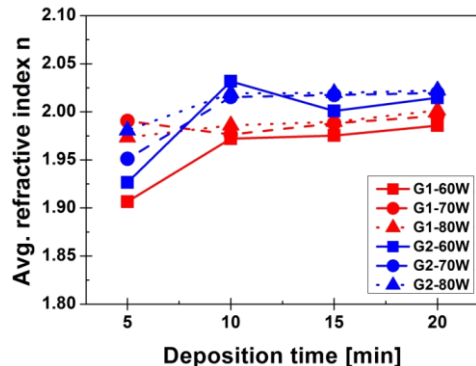


Fig. 3: Average refractive index of the IGZO films, Cauchy model

Fig. 4 gives the roughness thickness d_{rough} of the IGZO films as a function of deposition time. These curves reveal a boost before 50 nm firstly. Then, a sharp reduction occurs between 50 ~ 100 nm. Finally, the thickness of the roughness remains unchanged. This behaviour is independent on the sputtering power and the composition ratio of the IGZO films.

Fig. 5 depicts the variation of the refractive index of the IGZO films at top and bottom positions. Similar to our earlier study [6], there is an obvious gradient of the refractive index within the IGZO films. There is still a reverse of the refractive index gradient. However, the thermal stress affects the optical properties in different manner, i.e. the refractive index at the top area is larger than that at the bottom area after the stress is released. Before the stress is released, the value at bottom is larger than that at top as the films are very thin.

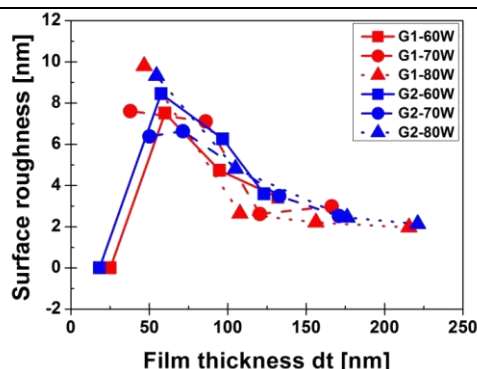


Fig. 4: Variation of thickness of surface roughness of the IGZO films, Cauchy model

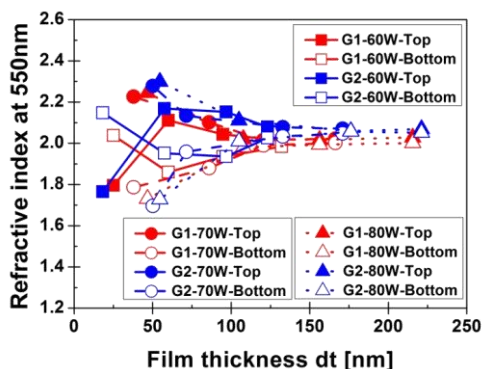


Fig. 5: Refractive index of the IGZO films at top and bottom position, Cauchy model

Results based on Oscillator model

In order to investigate the absorption behaviours of the IGZO films, we apply an Oscillator model to approach the optical properties of the IGZO films. This model essentially includes Cauchy model, point-by-point approximation, Lorentz model and Gauss model [4]. The point-by-point approximation is applied to obtain an initial value of the optical constant of the films, which does not ensure the Kramers-Kronig consistency. Furthermore, the Lorentz and Gauss models are used to recover the Kramers-Kronig consistency. Although the MSE and the fitting quality of the Oscillator model are worse than the Cauchy model, we can obtain the absorption behaviour of the IGZO in the UV region. Fig. 6 shows that the absorption peaks k shift to high energy with increasing Ga concentration. The sputtering power has no obvious influence on the position of the absorption peaks.

Conclusions

In this study, IGZO films of different composition ratios have been prepared by

RF sputtering method. SE technique with different optical models is used to obtain the optical properties of IGZO thin films. SE analysis shows that the composition ratio of the IGZO films affects the position of absorption peaks considerably

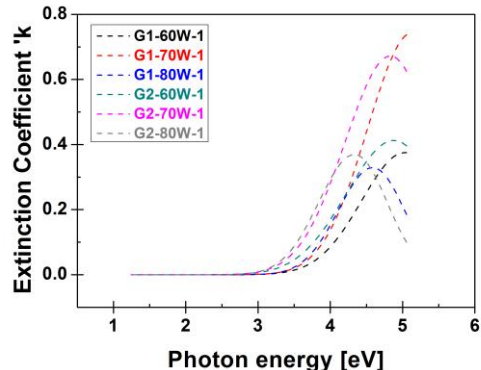


Fig. 5: Extinction coefficient of the IGZO films, Oscillator model

Acknowledgements

The authors gratefully acknowledge the financial support provided by the Ministry of Science and Technology of Republic of China under contact number MOST 103-2221-E-218-032.

REFERENCES

- [1] C. Li, Y. Bando, M. Nakamura, M. Onoda, N. Kimizuka, J. Solid State Chem. 139 (1998) 347 – 355.
- [2] J.M. Phillips, R.J. Cava, G.A. Thomas, S. A. Carter, J. Kwo, T. Siegrist, J.J. Krajewski, J.H. Marshall, W.F. Peck, Jr., D.H. Rapkine, Appl. Phys. Lett. 67 (1995) 2246.Y. Leterrier, Prog. Mater. Sci. Vol. 48 (2003), p. 1.
- [3] K.J. Chen, F.Y. Hung, S.J. Chang, Z.S. Hu, Appl. Surf. Sci. 255 (2009) 6308 – 6312.
- [4] J.A. Woollam: Guide to Using WVASE32® (2003).
- [5] W.-Y. Huang, Y.-H. Lee, S.-B. Wang, S.-W. Wu, C.-k. Hsu, K. Lin, 4th International Engineering Symposium - IES 2015 March 4-6, 2015, Kumamoto University, Japan.
- [6] K. Lin, C.-T. Hsieh, W.-Y. Huang, Y.-H. Lee, C.-k. Hsu, proceeding of the 7th International Conference on Advanced Materials Development and Performance, July 17-20, 2014, Busan, Korea.

Implementation of Automatic Colorization Algorithm of Electroluminescent Images for Detecting Defects on Si-based Solar Cells

Keh-moh Lin¹, Yong-Ruei Cheng¹, Sin-Wei Wu¹, Sin-Bo Wang¹

¹ Department of Mechanical Engineering, Southern Taiwan University of Science and Technology, No. 1, Nan-Tai Street, Yungkang Dist., Tainan City 710, Taiwan R.O.C.
e-mail:kemo@mail.stust.edu.tw

Abstract: Electroluminescence (EL) technology has been successfully applied to sc-Si solar cell inspection. However, because of the high defects density in mc-Si, applying EL technology to filtering solar cells shows inefficiency. Therefore establishing an evaluation process to speed up inspection speed and enhance accuracy is quite important. In this study, we developed an image processing program to colorize EL images. The results showed that the automatic colorization by using blocks algorithm did improve the readability. In the future we will focus on the optimization of this program, including shortening the processing time.

Keywords: automatic colorization, electroluminescence, mc-Si solar cell

Introduction

In recent years, photovoltaic (PV) industry has put more focus on reducing manufacturing costs and increasing cell efficiency. As of now, crystalline silicon solar cells are mostly made up of multi crystalline silicon (mc-Si), for their manufacturing cost is about 20 to 30 percent lower. It is expected that in 2014, mc-Si solar cells will make up 60 percent of the market [1]. Although its market share is predicted to decline in the future, this decline is slight. It is estimated that 50 percent of the market will still rely on mc-Si solar cells for the next 10 years. The demand for high-efficient mc-Si solar cells has increased rapidly [1]. But due to the problem of high defect density, such cells suffer from low efficiency. Thus, the PV industry must figure out how to measure and correct these defects in order to produce high-efficient cells.

In recent years, fluorescent technique has developed quickly, such as the electroluminescence EL technique, which has been applied to monocrystalline silicon (sc-Si) solar cells for efficiently detecting over-soldering, floating solders, and cracks. Although EL technique has been successfully applied to detecting over-

soldering and cracks of sc-Si solar cells, it could not be applied to inspecting mc-Si solar cells due to their high defect density. Figure 1 is an EL image in which different defects can be observed. The EL images of a mc-Si cell and a sc-Si cell in figure 2 show that the defect in the mc-Si cell is difficult to identify. Thus, if we can use the EL technique to inspect mc-Si solar cells and to efficiently detect the location of defects, we could enhance the cells reliability and also increase the lifetime of modules.

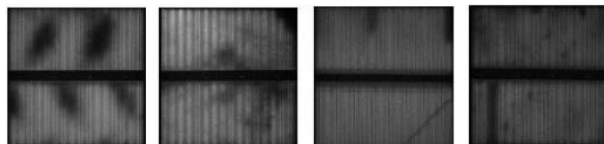


Fig. 1: EL image showing defects, from left to right: Procedure contaminant, soldering defects, cracks, and over soldering [2].

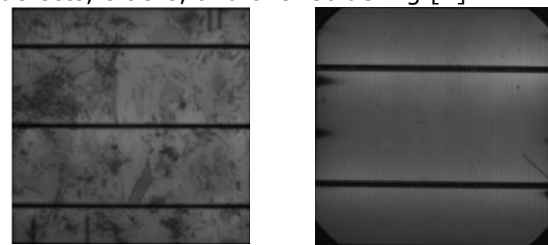


Fig. 2: Comparison of EL image of a mc-Si cell and a sc-Si cell.

EL detection cells

During the cell manufacturing process, defects of the material itself, contamination, or cracks will all affect the cell efficiency. Even though human eyes can spot damages or ruptures on the surface, the high defects density hidden inside the cell cannot be seen by naked eyes. When a solar cell is electrified with a forward bias ($35\text{mA}/\text{cm}^2$), the electrons and electron holes will be combined, releasing near-infrared (NIR) lights, whose intensity will change proportionally to the forward voltage. The intensity of the NIR lights is also affected by the defect's distribution over the cell. When the defects density is high, the greyscale value is naturally low (dark); when the defects intensity is low or there is no defect, the greyscale value is relatively high (bright). By this way, we can determine the quality of the solar cell.

In this study, the Si-CCD detector of the EL machine we used can detect up to 1200 nm of NIR lights. With an 850nm filter we can detect the NIR excitation light of the mc-Si solar cell. A further GaAs-CCD detector is used to detect up to 1800 nm of NIR lights. With a 1600 nm filter we can detect the NIR excitation light of the dislocations of a ms-Si solar cell. The EL inspection system is showed in Figure 3.

Experiments

This study is divided into several steps: Manufacturing samples, taking EL images, conducting aging experiment, and image processing.

Samples preparation

In this study, 6-inch mc-Si solar cells were first soldered with SnPb40 ribbon by using a hot-air soldering machine. Then, the soldered cells were laminated by an industrial laminator in order to ensure the encapsulation quality.

Thermal cycle experiments

In order to understand the impact of the aging process on the EL images, a 200 TC experiment according to standard IEC 61215 were carried out on the samples. In Fig. 4, the flowchart of the aging process is given: the temperatures were between -40°C to 85°C. There were 200 cycles. EL

images of the samples were taken after every 25 TC with different current intensities. The greyscale values of the EL images taken with different current intensities were compared with each other. As a result, the impact of the aging process on the cell performance and the defect distribution could be investigated.

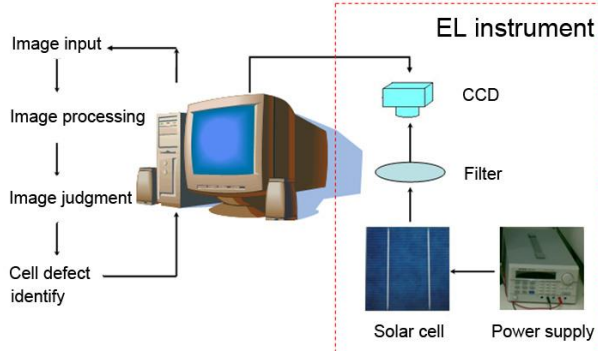


Fig. 3: Functional schematic diagram of the EL system [2].

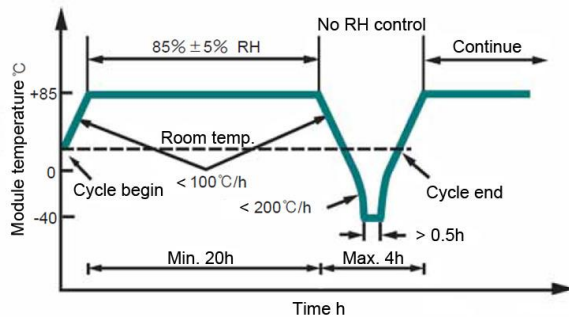


Fig. 4: Temperature profile according to IEC 61215 [3]

Image Processing

In early experiments, we used several methods to colorize the EL images: (1) colorizing specific greyscale levels; (2) transforming the EL images to 4-, 16- or 64-color images; (3) using a semi-automatic colorization algorithm. The first two methods could roughly distinguish between high and low efficient areas. However, specific defects such as cracks could not be identified by these methods. The semi-automatic colorization method could increase the interpretation accuracy of the EL images. But there were still some drawbacks, such as the need for manual scribble, subjective color choices, and slow processing speed etc. In order to improve these problems, we intend to use the blocks algorithm for colorization [4]. By

this way, the colorization time can be shortened. Moreover, by selecting suitable colors, we can construct an analysis program for EL inspection, in which different areas of efficiencies will be set at different colors so that one can easily find out the damage regions in mc-Si cells. Fig. 5 shows the flowchart of the blocks algorithm for colorization.

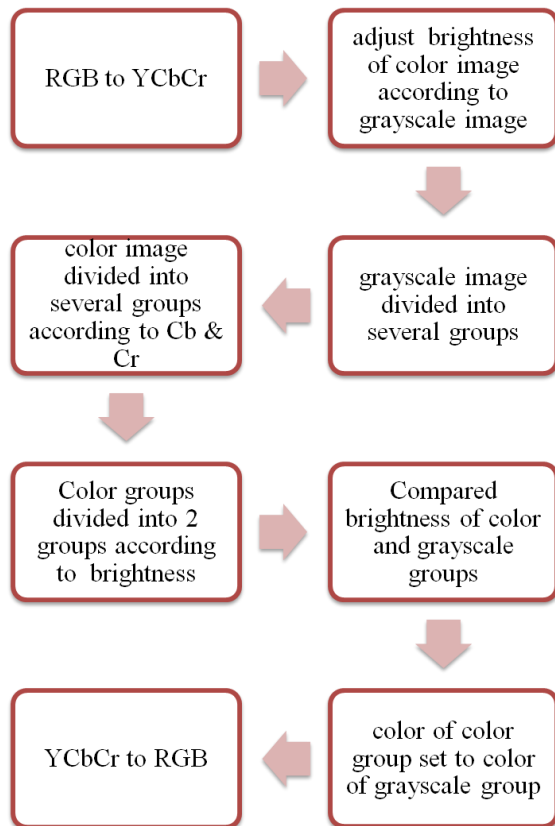


Fig. 5: flowchart of the blocks algorithm for colorization.

Results and discussion

In this study, we performed two experiments, EL images with Si/GaAs cameras and Colorization of EL images, in order to understand the characteristics of defect distribution in mc-Si solar cells.

EL image with GaAs detector

In addition to the usual EL images with Si camera, we used a GaAs camera to take EL images of defect structures. The GaAs camera has a detective spectrum up to 1800 nm. Fig. 6 shows the EL images taken by the Si and GaAs cameras. Top left is a conventional EL image, top right is an image taken by the GaAs camera. Because of the limited pixel number, the

resolution of the GaAs camera is worse than that of the Si camera. The image at bottom is taken by the GaAs camera with 1500 nm filter. The white points indicate the positions of dislocations with an emission wavelength around 1600 nm [5]. However, it is difficult to obtain more information of defect structures due to the low resolution of the GaAs camera.

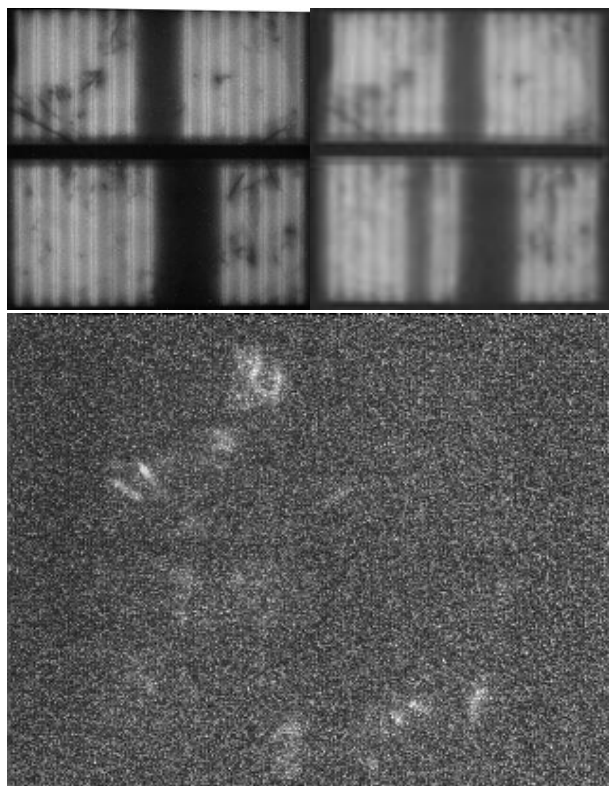


Fig. 6: EL image taken by Si and GaAs cameras.

Colorization of EL images

In the second experiment, we implemented a colorization program based on the blocks algorithm to improve the accuracy of interpretation of the EL images. Some of the results are given in Fig. 7. The pictures in the left column are original greyscale images; the pictures in the middle column are the referent color images; the pictures in the right column are the colorized images. In general, the colorization quality is good. The color distribution of the sky and the forest in the right column is correct and natural. However, there are some mistakes. The intensity variation of the sky at the top right image is not smooth enough while the color distribution of the sky at middle right image is not correct. That is

attributed to the blocks algorithm in which only the brightness of the color and greyscale groups will be compared with each other. The neighbour textures of these groups are not considered. On the other hand, the pictures at the bottom row show that this colorization program is good enough for the colorization of an inspection image. Moreover, in Fig. 8 one can see that the cracks in an ms-Si cell can be colorized with deep blue color. By this way, we could use this information for further automatic inspection system.

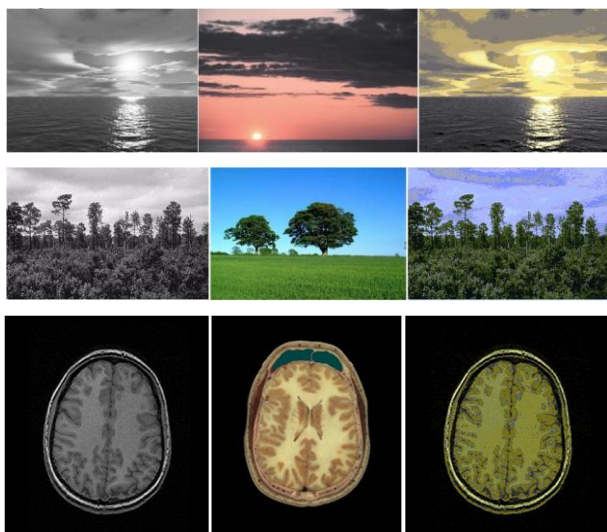


Fig. 7: some of the results by using the block algorithm.

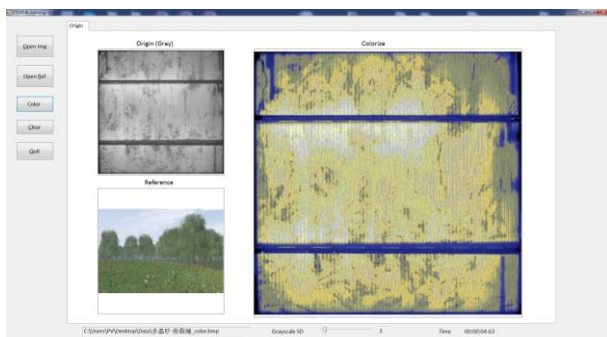


Fig. 8: one of the colorized EL image of an ms-Si solar cell.

Conclusions

In this study, EL and image technologies were used to understand the characters of defect structures and to improve the readability of the EL images. The results of the experiments can be concluded as follows:

(1) The comparison of the EL images which were taken by the Si and GaAs

cameras separately indicate that the dislocation positions can be identified. But the resolution of the GaAs camera is worse than that of the Si camera. Thus, if one would like to obtain more information about the defect structures of ms-Si cells, the resolution of the GaAs camera has to be enhanced considerably.

(2) The automatic colorization program based on the blocks algorithm successfully increased the readability the EL images of ms-Si cells. Although there are still some drawbacks, this colorization program is good enough for the colorization of an EL image of an ms-Si cell. In the future we will focus on automatic inspection and improvement of colorization quality by using the texture synthesis methods.

Acknowledgements

The authors gratefully acknowledge the financial support provided by the Ministry of Science and Technology of Republic of China under contact number MOST 103-2622-E-218-002-CC3.

REFERENCES

- [1] International Technology Roadmap for Photovoltaic (ITRPV) 2014 Results.
- [2] Li-wei Chen, Efficiency decay behavior and interfacial characteristics of solders in PV modules, master thesis, department of Mechanical engineering, southern taiwan university of science and technology (2011).
- [3] YI-wen Kuo, Efficiency decay behavior and interfacial characteristics of solders in PV modules, master thesis, department of mechanical engineering, Southern Taiwan University of Science and Technology (2012).
- [4] T. Welsh, M. Ashikhmin, K. Mueller, Transferring Color to Greyscale Images, Proceedings of SIGGRAPH (2002).
- [5] E. Sveinbjörnsson, J. Weber, Room-temperature electroluminescence from dislocations in silicon, Thin Solid Films 294 (1997) 201.

Wettability and bond strength of Sn-0.7Cu lead-free solder alloy reflowed on copper substrate

Mrunali Sona and K Narayan Prabhu

Department of Mechanical Engineering, NITK Surathkal, India

Email: soumya5.subbu@gmail.com

The use of lead bearing solders in electronic devices is banned due to the toxicity and environmental risks associated with lead. In the present study, the effect of reflow time on the wetting behaviour, interfacial reactions and the formation of intermetallic compounds (IMCs) during solidification of Sn-0.7Cu solder alloy on Cu substrate is studied. Experiments were carried out at various reflow times of 10, 100, 300 and 500s. The reflow temperature was maintained at 270°C. Contact angle measurements were performed using FTA 200 dynamic contact angle analyzer. The solder alloy showed enhanced wettability on the substrate at higher reflow time. The thickness of IMC layer formed during the reflow time of 10s was 0.93µm and the thickness increased to 1.62µm, 2.28µm, 3.25µm during 100s, 300s and 500s of reflow time respectively. The joint shear test was performed to assess the integrity of Sn-0.7Cu solder solidified on Cu substrate surfaces. The bond strength was maximum between reflow times of 100 and 300s and the strength found to be lower when the reflow time was 500s.

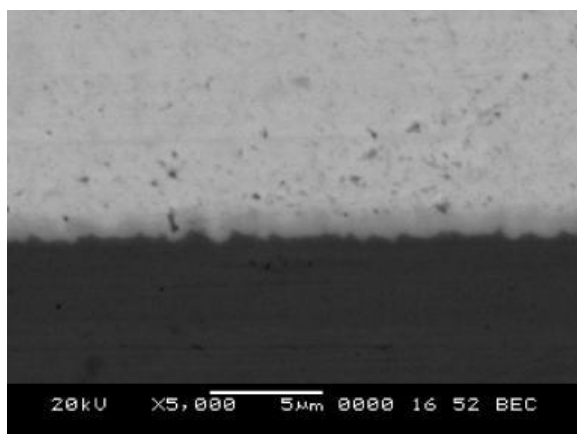


Fig. 1(a)

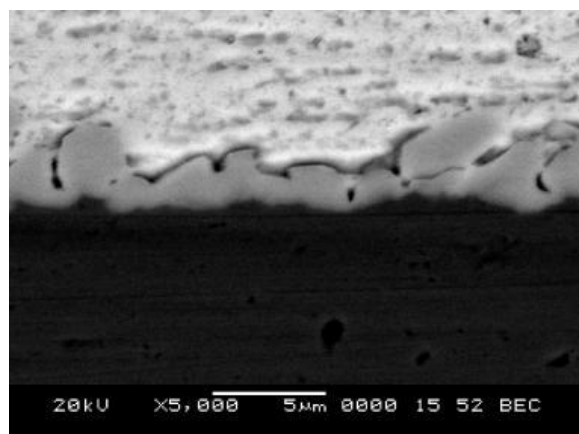


Fig.1(b)

Fig.1: SEM micrographs of Sn-0.7Cu/Cu interface
(Figs. (a) and (b) correspond to reflow times of 10s and 300s respectively.)

Keywords: Lead-free solders, IMC, bond strength

Experiments on multi-robotic search

Jeane Marina D'Souza and K R Guruprasad

Department of Mechanical Engineering, NITK Surathkal, India

Email: jeanemdsilva@gmail.com

Research on multi-agent or multi-robot systems has become prevalent over the last few years. For search and rescue operations by autonomous robotic agents equipped with remote sensing instrumentation offer numerous opportunities in disaster related situations. The objective of coverage control is to disperse robots over an environment to do environmental monitoring and surveillance. Robotic agents deployed over an affected area could act as eyes in the sky for quick information gathering about potential victims, accessible roads, etc. Good information gathering, assessment, compilation, and recording will improve response efforts. Key areas of research problem addressed include autonomous missions, localization, multi-vehicle coordination and image processing. The lack of information about the search space is modelled as an uncertainty density distribution over the search space. Keeping in mind the real world scenarios of search and rescue during a catastrophe an experimental evaluation of the search strategy is to be carried out in the laboratory environment. The distributed control law moves the agents under a few realistic constraints on the control input such as constant speed, limit on maximum speed, and also sensor range limits.

In this paper, we present experiments for autonomous mobile robots ensuring complete search and coverage. Centroidal Voronoi configuration coverage is considered for co-ordination among multi-robots. The multi-robotic experiments for search and coverage are verified by simulating and also for validation on ground/air robot and using ROS (Robotic operating system).

Keywords: Area coverage, search, multi-robotic experiments, Robotic operating system

Coverage by mobile robots

Ranjitha T D and K R Guruprasad

*Department of Mechanical Engineering, NITK Surathkal, India
Email: ranjithatd.26@gmail.com*

Area coverage is an important task for mobile robots in many real-world applications such as autonomous floor cleaning, lawn moving, land mine detection etc. One important aspect in area coverage of mobile robots is to cope up with irregular workspace thereby covering even the minute spaces without retracing the path. Coverage path planning refers to the task of determining a path that passes over all points of an area of interest while avoiding the obstacles. Previous investigation on the single robot coverage showed that most of the control strategies focused mainly on time complexity, and failed to cover the regions which were partially occupied by the obstacles.

Most of the coverage methods were based on approximate cell decomposition. In this paper, we propose a coverage algorithm for an autonomous mobile robot ensuring complete coverage (covering partially occupied cells) without unnecessary overlap. Spanning tree coverage is taken as a basic idea for the proposed algorithm. The developed algorithm is verified by simulating in the MATLAB and is validated on ground robot using ROS.

Keywords: Spanning tree coverage(STC), MATLAB, Robotic operating system(ROS)

Adaptive control system for CNC machine

Rashmi L Malghan, Arun Shettigar, Srikantha S Rao and R J D'Souza

Department of Mechanical Engineering, NITK Surathkal, India

Email: rashmi.malghan@gmail.com

Karthik Rao

Department of Mechantronics,

Manipal Institute of Technology, Manipal University, Manipal, India

The proposed Adaptive controller is meant to minimise machining time during rough machining of raw uneven work pieces, where profile or contour of job varies from piece to piece and hence cannot be programmed precisely. The concept is based on principle of 'Adaptive Control', where a process parameter controls one or more of control parameters to achieve desired output/result. In the case of power monitored adaptive controller, the system measures the cutting force or cutting power (Process parameter) by measuring spindle power during machining and controls feed rate (Control parameter). By this technique the power utilization of the spindle power is improved and machining time reduced increasing production.

Keywords: adaptive controller, process parameters, spindle power

Application of Geospatial Software in mapping the biomass resources based on its availability and location

Ranipet Hafeez BASHA¹, Raju Aedla² and Shuichi TORII¹

1 Graduate School of Science and Technology, Kumamoto University, Kurokami, 2-39-1, Kumamoto 860-8555, Japan. Email: 139d9214@st.kumamoto-u.ac.jp

2 Department of Civil Engineering, Malla Reddy Engineering College, Doolapally Road Maisammaguda, Secunderabad 500043, India. Email: rajuaedla.nitk@gmail.com

Abstract: Geospatial technology can ensure optimum biomass resource sites for efficient renewable power generation. This software can help users to organise the geographic data and facilitate the selection of necessary data for a specific application. It has a feature to add layers of information to a basemap of real world locations hence creating a thematic map with geographical information system. This enables proper biomass characterization and determination of chemical composition of samples before and after pre-treatment. In this study a geospatial model was prepared which can map the various biomass resources based on its availability and location. The results obtained were recorded and stored in a database management system, which can be retrieved by other simulation software.

Keywords: Geospatial techniques, biomass, remote sensing, geographical information system, global positioning system

1. Introduction:

1.1 Background:

The biomass fuel is emphasized as an alternative to the conventional fossil fuels like coal and natural gas, even though the energy produced is considerably low. This is because of the easy availability of biomass from various natural sources, benefit of waste management and reduction of global warming.

In order to tap the potential of biomass energy sources, there is a need to assess the availability of resources spatially as well as temporally. Geographic Information Systems (GIS) along with Remote Sensing (RS) helps in mapping on spatial and temporal scales of the resources and are well appropriate for identifying of these potential zones. It is possible to identify and assess the biomass resources by developing accurate model through database containing information about land cover, land use, regional cartography, administrative boundaries, populated areas, road network, a digital terrain model, lithological map, climatic data, industry, and a civil census.

Biomass resources generally assessed using direct and indirect relationship methods. In a direct relationship methods, the relationship between spectral response and biomass using multiple regression analysis (Drake et al., 2003), k-nearest neighbor (Means et al, 2000) and neural networks (Naesset, 2002) were used for assessment of biomass. In indirect relationships, attributes data estimated from the remotely sensed data, such as Leaf Area Index (LAI), structure (crown closure and height) or shadow fraction were used in equations to estimate biomass.

A variety of remotely sensed data were used for biomass mapping including coarse spatial resolution data such as Spot-Vegetation and AVHRR (Neuenschwander, 2009) and MODIS (Hill et al., 2013). To linkage of ground measurements to coarse spatial resolution remotely sensed data (e.g., MODIS, AVHRR, IRS-WIFS), studies have integrated multi-scale imagery into biomass assessment methodology and also incorporated moderate spatial resolution

4th International Engineering Symposium - IES 2015

March 4-6, 2015, Kumamoto University, Japan

imagery (e.g., Landsat, ASTER) as an intermediary data between the field data and coarser imagery (Means et al, 2000). Landsat TM and ETM+ data were the most widely used data of remotely sensed imagery for biomass estimation (Stilla and Jutzi, 2009; Wagner et al., 2006; Pirotti et al., 2013) and moderate spatial resolution imagery like ASTER and Hyperion data were also used for biomass estimation. Likewise, high spatial resolution data such as QuickBird and IKONOS have been used for biomass estimation. GIS-based modelling using ancillary data, such as climate normal, precipitation data, topography, and vegetation zones is another approach to biomass estimation and geostatistical approaches (i.e., kriging) are to generate spatially explicit maps for above-ground biomass (AGB) from field areas. More frequently, GIS is used as the mechanism for integrating multiple data sources for biomass estimation (e.g., forest inventory and remotely sensed data). With this background, there is a lot of scope to prepare geospatial model for map various biomass resources locations using several spectral and temporal satellite images.

1.2 Problem Description:

In order to conserve sustainable development of energy resources, it is essential to develop accurate and complete geospatial model for identification and continuous assessment of biomass resources. Monitoring and development of database management system for large and inaccessible locations is complex through conventional methods, because of huge man power, cost effective and time consuming by these methods. The advanced Geospatial techniques such as Remote Sensing, Geographical Information System (GIS) and Global Positioning System (GPS) are overcoming the drawbacks of conventional methods and provide accurate database. By integrating, the generated database can be efficiently analyzed using these tools to develop models for proper assessment of biomass resources. Remotely sensed satellite imagery such as aerial and satellite imagery, provide an efficient and reliable monitoring of biomass resources over

time. The temporal imagery of satellite imagery helps in continuous assessment of biomass resources.

1.3 Hypothesis:

Based on the demand and importance of biomass resources, it is necessary to identify and assess the biomass resources to replace non-renewable resources. In view of this, the present study is developing the geospatial model for identification and assessment of biomass resources using geospatial techniques. The study is going to prepare the database management system to record and store information of various earth surface layers and chemical composition of samples. The study is going to adopt geospatial software (GS), which was innovated and developed by National Laboratory of Renewable Energy (NLRE) and it is a powerful tool for evaluation and assessment of biomass sources. Geospatial Toolkit (GST) is the mapping software, developed by the National Renewable Energy Laboratory (NREL) and it supports in planning, project development, and help researchers for identify a region which is good potential for renewable energy projects (biomass, wind energy, solar, etc.). This software provides data on renewable energy sources about information of geography, population, border and transportation infrastructure etc.

The remote sensing satellite images provide various spectral and temporal information of the study area and it will be highly helpful in continuous assessment and planning of database for biomass resources. Geographical information system aids in preparation of database for various sample locations for better and efficient assessment of biomass resources.

By considering remotely sensed satellite images, GIS, GPS and geospatial toolkit, the present study is going to develop the model, which can provide the database of various biomass resources for better identification and accurate assessment of biomass resources.

4th International Engineering Symposium - IES 2015

March 4-6, Kumamoto University, Japan

1.4 Significance:

The developed geospatial model for biomass resources using remote sensing, GIS, GPS and geospatial tool kit really helps the researchers to store the data of various samples, which can be used for analysis of biomass locations. This model also benefits researchers for better identification of biomass locations using various spectral and temporal remotely sensing satellite data sets. Researchers can manage the database of biomass locations for further identification, analysis and assessment of biomass locations using this model. This model extremely helps the researchers for continuous assessment of biomass resources with regular intervals within short time. This model definitely becomes a major tool for identification and assessment of biomass resources.

1.5 Scope of the study:

Based on the advantages of geospatial techniques, it is widely used in identification and assessment of biomass resources. The appropriate model for identification, monitoring and assessment of biomass resources using geospatial techniques is possible to improve the accuracy in identification and assessment of biomass locations. It is also potential to get the information of isolated biomass regions from the satellite images and this model helps in storing more information of biomass locations in the database. The present study provides the scope to develop geospatial model for identification and assessment of biomass resources using geospatial techniques.

2. Methods:

The processing of satellite images using geospatial techniques consists of pre-processing, processing and post-processing. In pre-processing, satellite images were geometrically radiometrically corrected. In processing stage, satellite images were enhanced for better quality and classified or information extracted using classification techniques such as supervised classification and unsupervised classification. In post-processing stage, classified images were used for change detection analysis and accuracy assessment.

In general, the geospatial techniques were empirical because they depend on the image characteristics of data and application. After pre-processing and enhancement stages, the remotely sensed data were subjected to quantitative analysis to assign individual pixels to specific ground cover types or classes. The class identified the type of ground cover (for example, water, vegetation, soils, etc.). The pixels were identified based on their numerical properties or attributes. This phase can be performed by analyzing the properties of individual pixel (per pixel) or group of pixels (region). In latter, the image was firstly segmented into a set of regions that can be described by a set of attributes (area, perimeter, texture, color, statistical information). These sets of attributes were used to characterize and identify each object in the image. This operation of recognizing objects in the image was called image classification and it results in thematic maps as output.

After classification, it is necessary to evaluate its accuracy by comparing the classes on the thematic map with the areas of known identity on the ground (reference map). A reference map was created using information acquired by the user in the field work. Indexes to measure the classification accuracy such as Kappa (Landis and Koch, 1977) were often used. The index values ranges from 0 to 1, and values greater than 0.6 indicates a good overall result. Post-processing was an optional processing step. Figure 1 shows the fundamental steps in image processing.

The present study develop the Geospatial model to improve accuracy of identification and assessment of biomass resources using satellite images by preparing various thematic maps such as, Land use and land cover map, forest map, crop map, waterbody and soil map etc. Other thematic maps like, boundary map, slope map were prepared from toposheets. Population map and filed data were used as reference data for analysis of all thematic maps using overlay analysis or spatial analysis tool, which existed in GIS

4th International Engineering Symposium - IES 2015

March 4-6, 2015, Kumamoto University, Japan

software. The data base model was developed in GIS software, based on the information of earth surface layers and samples of chemical composition of biomass location and it will be helpful for further analysis and continuous assessment of biomass locations. After the analysis of data, the final map was generated, which gives the locations of biomass presented in the study area.

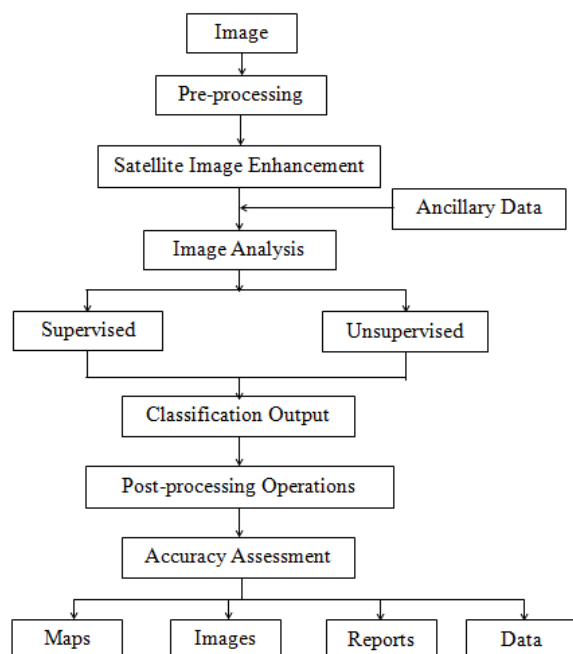


Fig.1 Steps in Remote Sensing

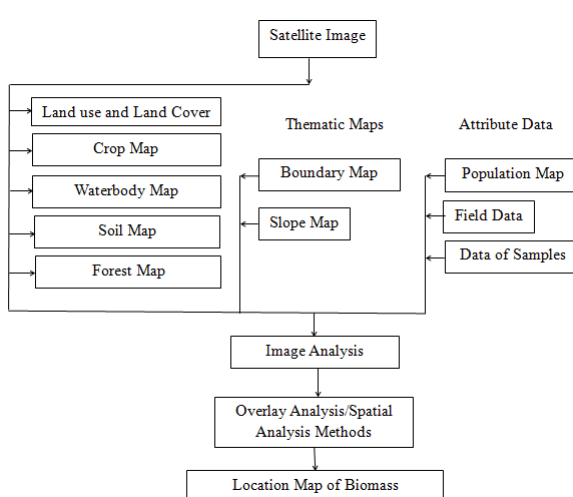


Fig.2 Steps in Identifying Biomass Resources

Base map of the study area is prepared using toposheets and for identification of biomass locations various spatial and temporal satellite images are considered. In order to develop the geospatial model using geospatial tool kit, ERDAS Imagine and GIS software's for identification of biomass resources using satellite images. The present study needs Geospatial software (GS), Earth Resources Data Analysis System (ERDAS) Imagine 9.2, remote sensing software, ArcGIS 10.1, GIS software.

3. Expected Results:

In the present study, the geospatial techniques such as remote sensing, geographical information system and global positioning system are improving the accuracy in identification and assessment of biomass resources.

The various spatial and temporal satellite images will increase the precision of information extraction from satellite images. The developed geospatial model helps the researchers for easy and better identification and assessment of biomass locations. The developed database management system also benefits the researchers for continuous monitoring and assessment of biomass locations. The developed geospatial model and database management system can be useful for identification and assessment of biomass regions for universal users.

4. Conclusion:

The developed geospatial model is more precise in identification and assessment of biomass resources and continuous monitoring of identified biomass regions using developed database model. The prepared database management system highly helpful in monitoring and analysis of biomass resources in short time. The remote sensing techniques provide data of isolated regions for better identification of biomass resources. The various spectral and temporal satellite images improve the accuracy in identification biomass resources. Geospatial Toolkit (GST) is efficient mapping software for planning, project development, and assessment of biomass resources, which help researchers for identifying a region which is more potential of biomass energy resources.

4th International Engineering Symposium - IES 2015

March 4-6, 2015, Kumamoto University, Japan

References:

- [1] R. Schowengerdt, A Remote Sensing Models and Methods for Image Processing, London: Academic Press, 1997, pp. 521.
- [2] R. C. Gonzalez and P. Wintz, Digital Image Processing, 2nd edition, Ed., Massachusetts: Addison-Wesley Publishing Co., Reading, 1987.
- [3] R. C. Gonzalez and R. E. Woods, Digital Image Processing, vol. 2nd ed., Prentice Hall, 2002.
- [4] R. C. Gonzalez and R. E. Woods, in Digital Image Processing, 3rd ed., Uppaer Saddle River, NJ, USA, Prentice-Hall, Inc., 2006.
- [5] R. C. Gonzalez, R. E. Woods, "Digital Image Processing," 2nd edition Reading, MA. Addison-Wesley, 1992, pp.85-103.
- [6] Lillesand, M. T., Kiefer, R. W., and Chipman, J. W., (2004). Remote Sensing and Image Interpretation, John Wiley and Sons, Newyork, 1-48.
- [7] Lillesand, M.T. and Kiefer, R. W. (1994). Remote Sensing and Image Interpretation, John Wiley and Sons, Newyork, 1-48.
- [8] Cuong Tien Nguyen, Luong Hoang Pham, Tu Huy Nguyen, Linh Tuan Le, Tho Dinh Son Van, (2014). Evaluation a potential of biomass for combination biomass gasification - electric generation in Vietnam using Geospatial Software, International Journal of Renewable Energy and Environmental Engineering., Vol. 02, No. 02, April 2014.
- [9] Survey of Biomass Resource Assessments and Assessment Capabilities in APEC Economies, Energy Working Group, November 2008. NREL/TP-6A2-43710.
- [10]Drake, J.B.; Knox, R.G.; Dubayah, R.O.; Clark, D.B.; Condit, R.; Blair, J.B.; Hofton, M. Above-ground biomass estimation in closed canopy neotropical forests using lidar remote sensing: Factors. *Glob. Ecol. Biogeogr.* 2003, 12, 147–159.
- [11]Means, J.E.; Acker, S.A.; Fitt, B.J.; Renslow, M.; Emerson, L.; Hendrix, C.J. Predicting forest stand characteristics with airborne scanning lidar. *Photogramm. Eng. Remote Sens.* 2000, 66, 1367–1371.
- [12]Naesset, E. Predicting forest stand characteristics with airborne scanning laser using a practical two-stage procedure and field data. *Remote Sens. Environ.* 2002, 80, 88–99.
- [13]Neuenschwander, A.L. Landcover classification of small-footprint, full-waveform lidar data. *J. Appl. Remote Sens.* 2009, 3, 033544.
- [14]Hill, T.C.; Williams, M.; Bloom, A.A.; Mitchard, E.T.A.; Ryan, C.M. Are inventory based and remotely sensed above-ground biomass estimates consistent? *PLoS One* 2013, 8, e74170
- [15]Still, U.; Jutzi, B. Waveform analysis for small-footprint pulsed laser systems. In *Topographic Laser Ranging and Scanning: Principles and Processing*; Shan, J., Toth, C.K., Eds.; CRC Press: Boca Raton, FL, USA, 2009; pp. 215–234.
- [16]Wagner, W.; Ullrich, A.; Ducic, V.; Melzer, T.; Studnicka, N. Gaussian decomposition and calibration of a novel small-footprint full-waveform digitising airborne laser scanner. *ISPRS J. Photogramm. Remote Sens.* 2006, 60, 100–112.
- [17]Pirotti, F.; Guarneri, A.; Vettore, A. Vegetation filtering of waveform terrestrial laser scanner data for DTM production. *Appl. Geomat.* 2013, 5, 311–322.
- [18]Basha R. H., Torii S., "Design of a computer model with enhanced feature of predicting optimum composition for biomass simulation using J2SE 5.0 program" *International Journal of Earth Sciences and Engineering*, ISSN 0974-5904, Vol. 7, No. 4, August 2014, pp 1619-1622
- [19]Basha R. H., Torii S., "A numerical study on thermal performance of Biomass and its impact due to moisture for direct combustion based electricity generation" *International Journal of Energy Engineering*, ISSN 2225-6563, Vol. 4, No. 3, August 2014, pp 159-163
- [20]Basha R. H., Torii S., "Use of Information Technology and Numerical methods to increase the thermal performance of Biomass based renewable fuel" *International Journal of Renewable Energy and Environmental Engineering*, ISSN 2348-0157, Vol. 2, No. 2, April 2014, pp 105-108
- [21]Basha R. H., Torii S., "Design of a computer model for simulation of combustion parameters of biomass using J2SE 5.0 program" *International Journal of Earth Sciences and Engineering*, ISSN 0974-5904, Vol. 7, No. 1, April 2014, pp 179-183
- [22]Chen A. P., Basha R. H., Torii S., "Classification of biomass based on its role in combustion for sustainable and renewable source of energy using proximate and ultimate analysis" *International Journal of Earth Sciences and Engineering*, ISSN 0974-5904, Vol. 7, No. 1, April 2014, pp 143-149
- [23]Basha R. H., Torii S., "Composition analysis of biomass utilization in combustion to increase the thermal performance by using computer methods" *Bioinfo Renewable and Sustainable Energy*, ISSN 2249-1694, Vol. 3, No. 1, December 2013, pp 29-32

Constitutive Model for Elastic and Viscoelastic Properties of Thai Rice

Niwat Moonpa¹, Nai-Shang Liou² and Subongkoj Topaiboul³

- 1 *Division of Agricultural and Biological Engineering, Faculty of Engineering, Rajamangala University of Technology Lanna, 128 Hauy kaew Road, Changpuak, Muang, Chiangmai, 50300 Thailand. e-mail : nmp@rmutl.ac.th*
 - 2 *Department of Mechanical Engineering, Southern Taiwan University of Science and Technology, No. 1, Nan-Tai Street, Yongkang Dist., Tainan 710, Taiwan. e-mail : nliou@stust.edu.tw*
 - 3 *Division of Food Process Engineering, College of Integrated Science and Technology, Rajamangala University of Technology Lanna, 98 Moo 8 T.Papong Doi Saked, Chiang Mai, 50220 Thailand. e-mail : subongkoj@gmail.com*
-

ABSTRACT: Using a computer aid design and engineering analysis to optimise the design of rice milling machinery requires the understanding of rice mechanical behaviour. The constitutive model, which represents the relationship of stress and strain for both time dependent and time-independent properties such as elastic and viscoelastic behaviour are necessary in the Material function part of the simulation programme. This paper proposes elastic and viscoelastic models of 3-different-Amylose-ratio rice species from Thailand. This resulted in individual model constant for each rice related to their Amylose ratio. A software package, ABAQUS, was used to find necessary parameters for the mathematical model of the rice. It could be concluded that the models was able to predict the mechanical properties of the rice grain under compressive stress and was useful for further study for the designing of rice mill.

Keywords: *Constitutive model, Thai Rice, Elastic model, Viscoelastic model, Amylose ratio.*

INTRODUCTION

When processing rice, mostly it involves many mechanical processes applying on rice grains, for example peeling husk and polishing rice grain of milling process and crushing and grinding for making rice flour. Under forces and stresses, like other materials, the rice grain is usually deformed. Sometimes too much load and stress occurring can alter the quality of final rice products. The rice grains that have uniform shape and size without breakage as well as there is no discolouration resulted from excessive heat generated during processing are more preferable. It is then necessary to know the rice grain mechanical behaviour under forces, which leads to simulation models that can be useful for the design of rice milling machinery eventually. However,

with the asymmetrical shape of rice grain and complicate loads during processing, there are no direct simulation results can be acquired. This study seeks approximation results using calculation software that requires constitutive model of material in terms of stress-strain relationship. Similar works have been done on other engineering materials such as polymers and composites. While many of them have been published broadly, there are a few related to rice grain modelling. As far as the authors concern, some of the previous related studies are Le, et al. (2013) and Moonpa., et al (2014) which only focused on mechanical properties of rice at different load setting. To explain the rice mechanical behaviour by mathematical model, hyperviscoelastic and linear viscoelastic of rubber materials under loads

4th International Engineering Symposium - IES 2015

March 4-6, 2015, Kumamoto University, Japan

as described by Moonpa (2003) and Sungparn (2007) are considered since their mechanical behaviour results are resemble.

METHOD

Three rice varieties including Chainat-1, Jasmine and RD-10 had been selected from their popularity among Thais and different amylose ratio ranged from high to low. Table 1 shows the different in their amylose percentage. In the previous work done by the authors (Moonpa, et al. (2014)), the rice grains were pressed at 0.5-mm displacement and held for 600 seconds as shown by the test profile in Fig.1. Then the relationship of compressive stress and time and compressive stress and strain can be obtained as seen in Fig.2-4. The constitutive model of rice grain can be derived from this pre-strain test results. To analyse, it can be started with the Hooke's law of linear elastic properties as in Eq.1

Linear elastic properties model

$$\sigma = E_o \varepsilon \quad (1)$$

Since the compressive stress results was reduced with time when applying constant strain, it could be concluded that this rice's property was time dependent or called viscoelastic behaviour. This behaviour can be represented as spring stiffness E that is connected in series with dashpot η as in Maxwell model. While applying pre-strain, the behaviour can be redrawn by the Standard liner solid model (Zener model) as seen in Fig.5. However, since the stress was not linear with time, the Generalized Maxwell model (Fig.6) was applied as represented by Eq.2.

Stress relaxation modulus

$$\frac{\sigma(t)}{\varepsilon_o} = E_o + \sum_{i=1}^n E_i \exp\left(-\frac{t}{\tau_i}\right) \quad (2)$$

The parameters need to be found for Eq.2 are elastic modulus of elasticity of pre-strain loading, E_0 , modulus of elasticity of stress relaxation, E_i , and relaxation

time, τ_i . These parameters were found by Prony series spectrum in Eq.3-4. Relation of prony series and modulus

$$g(t) = \frac{G(t)}{G_o} = \frac{E(t)}{E_o} \quad (3)$$

$$g(t) = 1 - \sum_{i=1}^N g_i \left(1 - \exp\left(-\frac{t}{\tau_i}\right) \right) \quad (4)$$

Parameter g_i and τ_i were increased until the simulation curve was fit with the experiment results so that different viscoelastic model can be obtained for different rice varieties.

RESULT AND DISCUSSION

From the previous work done by the authors (Moonpa, et al. (2014)), it suggested rice had viscoelastic behaviour with the modulus of elasticity rice, E_0 , that could be calculated right away. These results are shown in Table 2. Using ABAQUS, a software package, the parameters of prony series spectrum are listed as in Table 3 while Fig.7 shows the fitting curves of this calculation. It can be seen that the Generalized Maxwell model can be used to represent the viscoelastic behaviour of the selected rice grains. When considering what amylose ratio affects to the rice mechanical properties, it also affects the viscoelastic model. Among all 3 rice types, the least amylose ratio rice like RD-10 has the least compressive strength and tends to reduce with time the most. The nonlinear stress relaxation character of RD-10 then yields the maximum numbers of model elements as well as the maximum value of required prony series terms in the constitutive model in Eq.2. In the opposite way, Chainat-1, the most amylose ratio and the highest compressive strength, yields the minimum numbers of model element and minimum prony series term values. As expected, Jasmine rice, with its amylose ratio ranged in between those two, yields both the numbers of model element and the prony series term value in between the two rice.

4th International Engineering Symposium - IES 2015

March 4-6, 2015, Kumamoto University, Japan

The Generalized Maxwell model can be perfectly used to represent the mechanical properties of rice grain. This mathematical model can be further applied to study stress and strain of the rice under different desired boundary conditions using FEM software. Hence, this is very useful for the design of specific machine in rice milling process. This will be developed by the authors in the next step.

CONCLUSIONS

From the study, it can be concluded as the followings

- The mechanical properties of 3 popular Thai rice varieties which had been previously studied were used as the raw data to derive a mathematical model for the design of rice milling machinery.
- Due to its viscoelastic behaviour, a Generalized Maxwell model with a set of elastic modulus, stress relaxation and Prony series relation equations were applied. All necessary values for the mathematical model were calculated and the results showed good fitting with the experiment data.
- When giving the suitable boundary constraints, these results can be used in rice milling machine design using FEM software. This will be further studied.

ACKNOWLEDGEMENTS

The authors would like to thank the department of Mechanical Engineering, Southern Taiwan University of Science and Technology, Taiwan for providing the facility for mechanical test study. Specially thanks Mr.Utid Supira, R&D Department, Mould Mate Co.Ltd., Thailand, for the help on software work and the Rajamangala University of Technology Lanna who provided financial support to carry out this research.

REFERENCES

- [1] Le, V. C., Topaiboul, S., Bangphan, S., Moonpa, N. and Liou, N. S. (2013). The Effect of Amylose Ratio on the Mechanical Properties of Rice Grain, Paper Presented in the 3rd International Engineering Symposium IES-2013, Kumamoto, Japan.
- [2] McCrum, N. G. and C. P. Buckley. Principles of Polymer Engineering. UK : Oxford University Press, 1988.

[3] Moonpa, N., Liou, N. S., and Topaiboul, S., (2014), Effect of Amylose Ratio on the Elastic and Viscoelastic Properties of Thai Rice, The 6th International Conference on Science, Technology and Innovation for Sustainable Well-Being (STISWB VI), 28-30 August 2014, Apsara Angkor Resort & Conference, Siem Reap, Kingdom of Cambodia.

[4] Moonpa, N., (2003), Dynamics Properties of Carbon Back Filled Rubber at Different Temperatures, Ph.D. thesis, King Mongkut's Institute of Technology North Bangkok.

[5] Sungparn, J., (2007), Analysis of Viscohyperelastic Properties of Vulcanized Rubber at Various Temperatures, Master thesis, King Mongkut's Institute of Technology North Bangkok.

Ramp-hold test profile

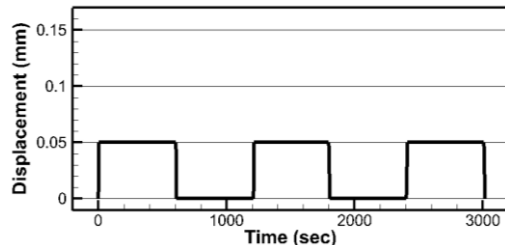


Fig.1 The ramp hold testing profile

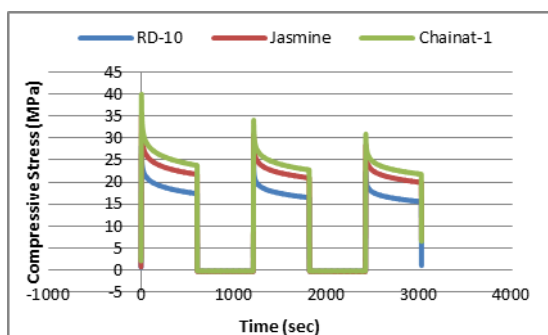


Fig.2 Ramp-hold test results

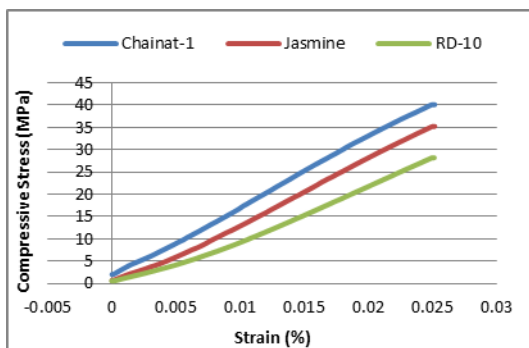


Fig. 3 Stress-strain relation testing results

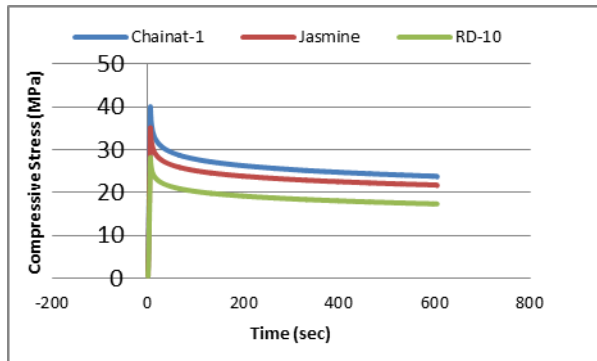


Fig.4 Stress relaxation testing result

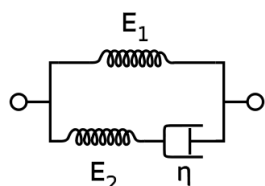


Fig.5 Standard linear solid (Zener) model

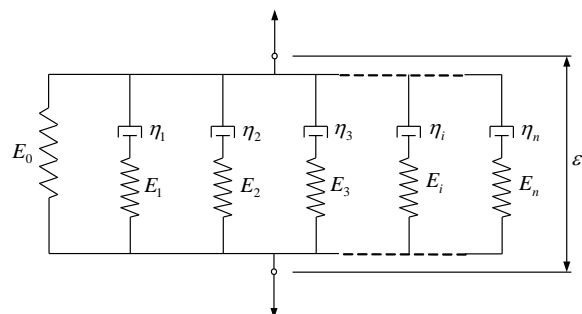


Fig.6 Generalized Maxwell model

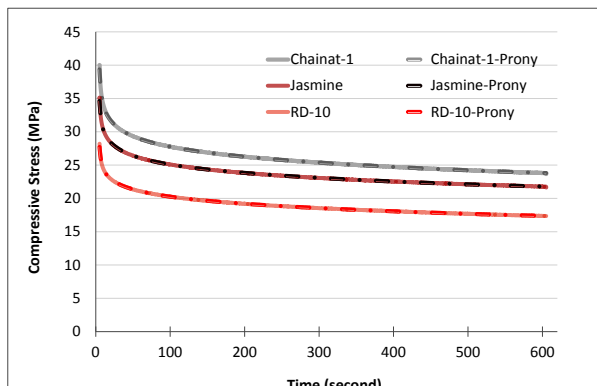


Fig.7 Compare the results of mathematical model and previous experiments

Table 1 Three types of rice for whole grain compression tests*

No	Type	Amylose percentage*
1	RD-10	0-2
2	Jasmine	13-18
3	Chainat-1	27-30

*Bureau of Rice Research and Development of Thailand www.ricethailand.go.th)

Table 2 The modulus of elasticity E_0 of Thai rice

RD-10	Jasmine	Chainat-1
1.12 GPa	1.40 GPa	1.60 GPa

Table 3 The parameters of prony series spectrum

Element	RD-10		Jasmine		Chainat-1	
	g_i	τ_i	g_i	τ_i	g_i	τ_i
1	0.0010	0.0139	0.0010	0.0139	2.5790	0.4706
2	0.0050	0.0012	0.0050	0.0012	12.587	0.0612
3	0.0500	0.0030	0.0500	0.0030	46.411	0.0508
4	0.1000	0.0653	2.4833	0.4564	255.54	0.0515
5	2.2677	0.4489	11.819	0.0514	979.94	0.0585
6	10.945	0.0484	42.581	0.0523		
7	42.926	0.0456	257.59	0.0508		
8	266.66	0.0480	994.76	0.0529		
9	1010.7	0.0521				

Preliminary Study of the Effect of Mill Gap of 2-Milling Rollers on Reducing Sugar of Milled Thai Rice Malt in Beer Brewing Process

A. Inpramoon, M. Wongkaew and S. Topaiboul

Division of Food Process Engineering, College of Integrated Science and Technology, Rajamangala University of Technology Lanna, 98 Moo 8 T.Papong Doi Saked, Chiang Mai, 50220 Thailand. email: aeengineer@gmail.com

ABSTRACT: In order to optimize the design of rice crusher for malt production in beer brewing process, it is important to understand the parameters of roller mill related to the obtained wort quality, which can be represented by the amount of reducing sugar or maltose. Mill gap of 2-roller mill type was the main parameters for this preliminary study. An adjustable 2-roller mill had been specially built for the study. Following the procedure of making malt for rice beer, *Kaw Kum Doi Saked*, a local Thai rice from Doi Saked area had been used as raw material and then was crushed at various mill gaps ranged from 0.6-1.4 mm. The results suggested that the obtained malt crushing size and wort appearance were different depending on the gap settings. The maximum maltose concentration was obtained from the gap size of 0.6-0.8 mm and reduced with larger gap size. Wort from finer gap required less time for starch hydrolysis so the amount of maltose was highest at the mash time of 90 minutes for 0.6, 0.8, 1.0, 1.2-mm gap size and more than 120 minutes for 1.4-mm gap size. Furthermore the smaller gap size increase friction and hence power required to drive the rollers. This results can be useful for conducting a 2-roller mill design requirements dedicated for the rice beer brewing in the next step.

Keywords: *roller mill, reducing sugar, Thai rice malt, maltose*

1. INTRODUCTION

Beer is the most popular beverage in the world. Start from grain, there are several steps in beer brewing process, which include malting, milling, mashing, lautering, boiling and fermenting. After malting, the starch in grains, usually barley or wheat, is converted to sugars. Then yeast is added to change those sugars into alcohol, carbon dioxide and other components. The properties of grain play an important role on beer final taste. Other raw materials called beer adjunct may be added to give either more subtle characters and distinguish tastes or to reduce cost of production.

Mashing process primarily utilizes the action of two enzymes (α - and β -amylase) naturally presenting in the malt to carry out the conversion of malt starch into sugars of different molecular weights. α -amylase is primarily responsible for digesting starch into lower molecular weight fermentable sugars, whereas the action of β -amylase produces maltose, (Tse et al., 2003).

Milling is an important process in brewing to reduce size of raw materials down by crushing. This is to provide more surface area that can enhance the activity of internal microorganisms and hence producing more sugar. Generally, malt grains are crushed by 2-roller mill. Mill gap and mill speed were reported to affect the husk and starch damage. Maltose

concentration was always higher for the smaller gap size throughout the mashing process (Mousia et al., 2004) while the roll speed did not seem to have a noticeable effect (Warpala and Pandiella, 2000).

Kaw Kum Doi Saked, a purple long grain rice, harvested from local area, are rich of antioxidants and higher nutrition than other Thai rice. It is intended to put this rice as an adjunct on beer to add more useful substance and create a signature product. The key success factor is the amount of maltose from the rice grain as a result of malt crushing and mashing process. To find the potential of utilizing *Kaw Kum Doi Saked* as a beer adjunct and at the same time, study an effect of mill gap on reducing sugar focusing on maltose in the wort of this rice type, in this research, a 2-roller mill prototype was built for grain crushing and the mashing process was performed afterwards. The difference of roller gaps was varied and amount of reducing sugar were then compared.

2. Materials and method

2.1 Thai rice malt preparation

Kaw Kum Doi Saked, Thai rice grains obtained from Doi Saked, Chiang Mai, Thailand was put on germination process by steeping in water for 3 days until see some roots came out of the grain. The rice was then dried at 50°C for 24 hours to reduce moisture and increase its color. This is called malting. All rice malt was kept in the freezer at -20°C until needed for further methods.

2.2 Milling conditions

The rice malt was crushed under various mill gaps ranged from 0.6-1.4 mm. (0.6, 0.8, 1.0, 1.2 and 1.4 mm.) Fig. 1 show 2-roller mill used to crush the rice and Fig. 2 shows the grit and husk after crushing at 0.8-mm roller gap.

2.3 Wort production

Wort was produced by two different mashing temperatures controlled using a hot water bath. Applying modified decoction mashing method, dried rice malt sample of 250 g was mixed with 1,000 ml distilled water at 55°C and left for 1 hour

in the water bath at the same temperature. Later, the mixture was heated up to 70°C and left at that point for another hour. At these steps of temperature adjustment, enzymes in the rice grain were supposed to convert rice starch into several sugars including maltose.

2.4 Wort analyses

A Spectrophotometer (Fig.2) was used to measure the amount of reducing sugar from starch hydrolysis in the wort at 540 nm wave length. Every 10 minutes, 3 samples of 10-ml wort were collected and centrifuged to remove excessive starch residue. The 0.5 ml of supernatant was taken for mixing with 0.5 ml of 3, 5-dinitrosalicylic acid solution in the 16 ml test tube. The development of color was conducted by boiling the reaction tube for 5 min. Finally all solutions were put in the spectrophotometer. Averaged from 3 samples, the concentrations of reducing sugar were calculated referring on standard curve of maltose concentration in order to get the maltose amount. Fig.4 shows wort samples obtained from various mill gaps.

3. Results and discussion

During mashing process, 10 ml of wort was collected every 10 minutes to measure the reducing sugar until the mashing time reached 120 minutes. The wort samples taken from different setting of mill gaps and times are shown in Fig.4. It can be seen that the colour of the wort got darker with longer mashing time as well as the smaller mill gap. This shows a sign of more antioxidant in the grain can be washed off when increasing mashing time. All samples were then analysed in the spectrophotometer. The results of maltose converted from reducing sugar (g/l) of different roller mill gaps from the start to 120 minutes are shown in Fig. 5.

From Fig.5, the results suggest that, similar to the wort colour changes, the maltose increases with mashing time and gap size reduction. At the roller gap size of 0.6-1.2 mm, the maximum maltose can be obtained at 90 minutes then starts to decrease while at the largest gap size of

1.4 mm, the sugar keeps increasing over the 120-minute mashing time. This means the internal enzymes are still working on the starch-sugar conversion as a result of less surface area of grain. To receive similar amount of sugar, the mashing of grain from 1.4-mm gap requires more time to complete and this may not be feasible in terms of production.

The maximum maltose concentrations detected from different gap distances are reported in Table 1. Agreed with the previous study (Usansa, 2008), the smaller the gap distance is, the higher the amount of maltose is detected. As a consequence of smaller grit size and increasing malt grit surface area, 0.6-mm gap size provides the maximum maltose of 17.61 g/l while the larger size of 0.8-mm gap provides less but merely the same amount. With smaller gap setting for crushing the grain, it was noticed that it was more difficult to crush the rice malt due to more friction in the system. So, one should realize that more torque and power are required for driving rollers. Choosing larger gab with an acceptance level of maltose concentration should be reconsidered together with the rollers and machine configuration for the machine optimization.

4. CONCLUSIONS

The effect of 2-roller milling gap size on maltose concentration during mashing process had been analysed. As a sign of higher antioxidant concentration, colour of wort got darker and maltose amount were increased with mashing time and mill gap reduction. The maltose concentration was maximum at the mill gap of 0.6 and 0.8 mm. However, the results of maltose from 1.0 and 1.2-mm mill gap were also acceptable when concerning on less power required to drive the crushing rollers. At 1.4-mm mill gap, the starch-maltose conversion took longer time than the others and did not finish within 120 minutes. This setting was considered not feasible for production.

5. ACKNOWLEDGEMENTS

The authors would like to thank Rajamangala University of Technology Lanna for all the facilities and supports to carry out this research.

6. REFERENCES

- [1] Tse K.L., Boswell C.D., Nienow A.W. and Fryer P.J. (2003), Assessment of the effects of agitation on mashing for beer production in a small scale vessel, Trans IChemE, Vol 81, Part C.
- [2] Mousia Z., Balkin R.C., Pandiella S.S., Webb C. (2004), The effect of milling parameters on starch hydrolysis of milled malt in the brewing process, Process Biochemistry, Vol. 39, pp. 2213-2219.
- [3] Warpala I.W.S. and Pandiella S.S. (2000), Grist fractionation and starch modification during the milling of malt, Trans IChemE, Vol 78, Part
- [4] Usansa C.U. (2008), Beer Production from Thai Rice, Suranaree University of Technology, Nakhonratchasima, Thailand.



Fig. 1 The 2-roller mill built for the study



Fig. 2 Rice malt after crushing at 0.8-mm mill gap



Fig. 3 Spectrophotometer



Fig. 4 Wort samples

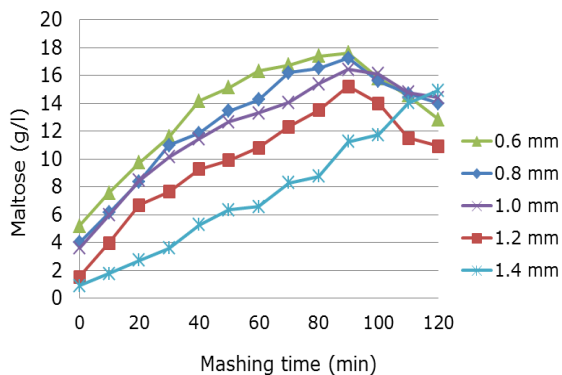


Fig. 5 Effect of gaps distance and mashing time on starch hydrolysis

Table 1 Effect of gap distance on the maximum maltose amount.

Gaps distance (mm.)	Maximum maltose amount (g/l)
0.6	17.61
0.8	17.23
1.0	16.41
1.2	15.20
1.4	14.93

Investigating Mechanical Properties of Sapwood and Heartwood of Millettia Leucantha Kurz in Thailand

C.-C Guo¹, N. Phantkankam², N. Moonpa² and N.-S. Liou^{1*}

1 Department of Mechanical Engineering, Southern Taiwan University of Science and Technology, No. 1, Nan-Tai Street, Yongkang Dist., Tainan 710, Taiwan.
nliou@stust.edu.tw

2 Division of Agricultural and Biological Engineering, Faculty of Engineering, Rajamangala University of Technology Lanna, 128 Hauy kaew Road, Changpuak, Muang, Chiangmai, 50300 Thailand.

ABSTRACT: The necessity to assess the mechanical properties of wood species by using small clear wood specimens is always there. In this study, the mechanical properties of heartwood and sapwood of Millettia Leucantha Kurz were investigated. The wood log used to assess wood properties is selected in north of Thailand and the samples for mechanical tests were prepared from heartwood and sapwood. Small clear wood samples were prepared by using CNC milling machine. Compression and three point bending tests were performed on wood samples of sapwood and heartwood cut in directions tangential, longitudinal and radial to grain. The results showed that there are differences between mechanical properties such as elastic moduli under bending and compression of heartwood and sapwood in different directions.

Keywords: Wood Mechanics, Experimental Mechanics, Elastic Modulus of Wood

INTRODUCTION

The necessity to assess the mechanical properties of wood species by using small clear wood specimens is always there[1]. Sapwood is the outer light-colored portion of a tree trunk through which the water passes from the roots to the leaves, and heartwood is the central core of the trunk. Some woods have little difference in the color of the heartwood and the sapwood; however, some woods have very different colors of the heartwood and the sapwood [2]. Furthermore, the decay resistance of heartwood and sapwood could be very different[3]. Taking Millettia leucantha Kurz as an example, compared with the color of sapwood, the heartwood has very dark color (Fig. 1). In the United States, Many tests showed no effect upon the mechanical properties of the wood due to its change

from sapwood into heartwood has been found in most species. However, in some species the heartwood has been found to be considerably stronger in certain strength properties than the sapwood [2, 4, 5]. In this study, the physical and mechanical properties of heartwood and sapwood of Millettia Leucantha Kurz were investigated.

MATERIAL AND METHOD

The Millettia Leucantha Kurz log used to assess wood properties is selected in north of Thailand and the samples for mechanical tests were prepared from heartwood and sapwood. Small clear wood samples were prepared by using CNC milling machine (Fig. 2). Compression and three point bending tests were performed on wood samples of sapwood and heartwood specimens in three mutually perpendicular directions (longitudinal, radial and

4th International Engineering Symposium - IES 2015

March 4-6, 2015, Kumamoto University, Japan

tangential directions). The specimens used for compression tests and three point bending tests are shown in Fig. 3. The tests were performed by using Instron tensile test machine. The test configurations are shown in Fig. 4. The length, width and height of specimens are 40mm, 10mm and 10mm respectively. The ramp-hold compression tests were conducted to investigate the time dependent mechanical properties of aforementioned wood specimens cut in three different directions under compression. The displacement rate used for the compression test is 0.2mm/sec and the specimens were held at 2mm nominal compression displacement for 600 sec (Fig. 4a). The ramp-hold three point bending tests were used to measure the time dependent mechanical behaviours of aforementioned wood specimens under bending load. The wood beam specimens were supported and loaded using 12 mm diameter aluminium cylindrical rollers. The distance between two support rollers is 30mm (Fig. 4b). The loading displacement rate used in this study is 0.1 mm/s, and the mid-point deflections of beam specimen were hold at 2mm for 600 second respectively.

RESULT AND DISCUSSION

The ramping parts of force-displacement curves of sapwood and heartwood in three directions under compression tests are shown in Fig. 5. and Fig. 6. Respectively; and the ramping parts of force-displacement curves of sapwood and heartwood in three directions under three point bending tests are shown in Fig. 7. and Fig. 8. respectively. The elastic moduli of sapwood and heartwood in three directions under compression and 3 point bending tests are shown in Table 1 and 2 respectively. It can be seen, from the compression moduli of sapwood and heartwood in three directions that the elastic moduli of sapwood are higher than those of heartwood. However, the bending stiffnesses of heartwood in the three directions are higher than those of sapwood. Due to the amount of longitudinal specimens is small; the deviation of elastic modulus and bending stiffness in longitudinal direction could be large. Besides, the experimental force-time curves under compression and three point bending tests show relaxation

behaviour thus heartwood and sapwood are time dependent materials. In order to better describe the mechanical properties of heartwood and sapwood, time dependent constitutive model such as viscoelastic model can be used.

CONCLUSIONS

The results showed that there are differences between mechanical properties such as elastic moduli and bending stiffness of heartwood and sapwood of Millettia Leucantha Kurz. This study also showed that the mechanical behavior of Millettia Leucantha Kurz wood is time-dependent. Developing more realistic constitutive models of Millettia Leucantha Kurz wood can be used in the study of wood biomechanics.

ACKNOWLEDGEMENTS

This research was partially supported by NSC 101-2221-E-218 -026 -MY3 from the R.O.C government and the Department of Food Process Engineering, Rajamangala University of Technology Lanna, Thailand.

REFERENCES

1. ASTM, *Standard Test Methods for Small Clear Specimens of Timber*, 2000.
2. U.S. Forest Service Research Note FPL-0147, 1936, Forest Products Laboratory, U.S. Department of Agriculture: Madison, WIS, USA.
3. Anagnos, S.E. and W.B. Smith, *Comparative decay of heartwood and sapwood of red maple*. Wood and Fiber Science, 1997. **29**(2): p. 189-194.
4. Ayobi, E., M. Kiaei, and R. Bakhshi, *Heartwood and Sapwood Properties of Quercus castaneaefolia in the Iranian Forests*. Middle-East Journal of Scientific Research, 2011. **8**(3): p. 669-673.
5. Merela, M. and K. Cufar, *Mechanical properties of sapwood versus heartwood, in three different oak species*. Drvna Industrija, 2013. **64**(4): p. 323-334.



Figure 1: The section of Millettia Leucantha Kurz Wood used to make specimens.

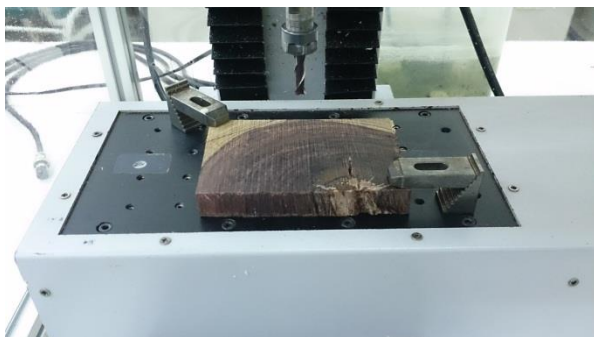


Figure 2: Specimens preparation by using CNC machining.



Figure 3: Specimens used for compression tests and three point bending tests.

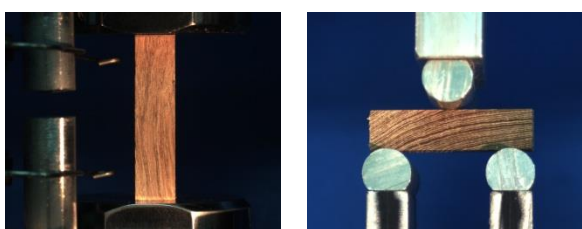
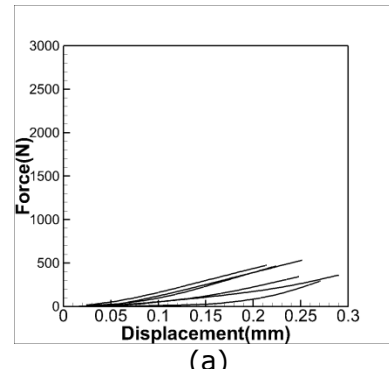
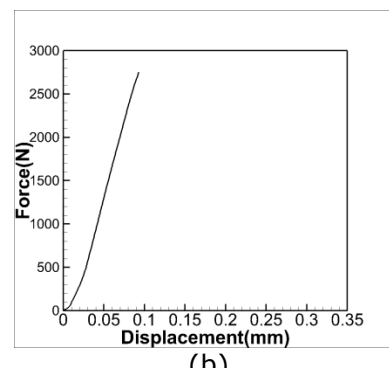


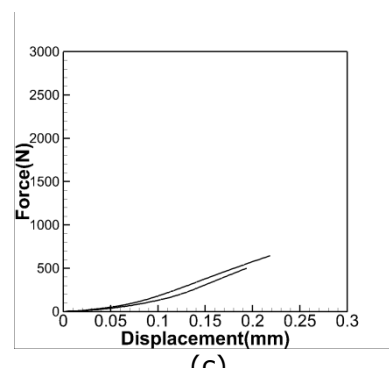
Figure 4: Test configurations for compression test and 3 point bending test.



(a)

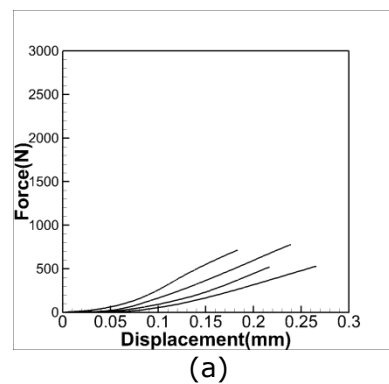


(b)



(c)

Figure 5: Force-displacement curves of sapwood specimens under compression tests. (a) Tangential, (b) Longitudinal and (c) Radial to grain.



(a)

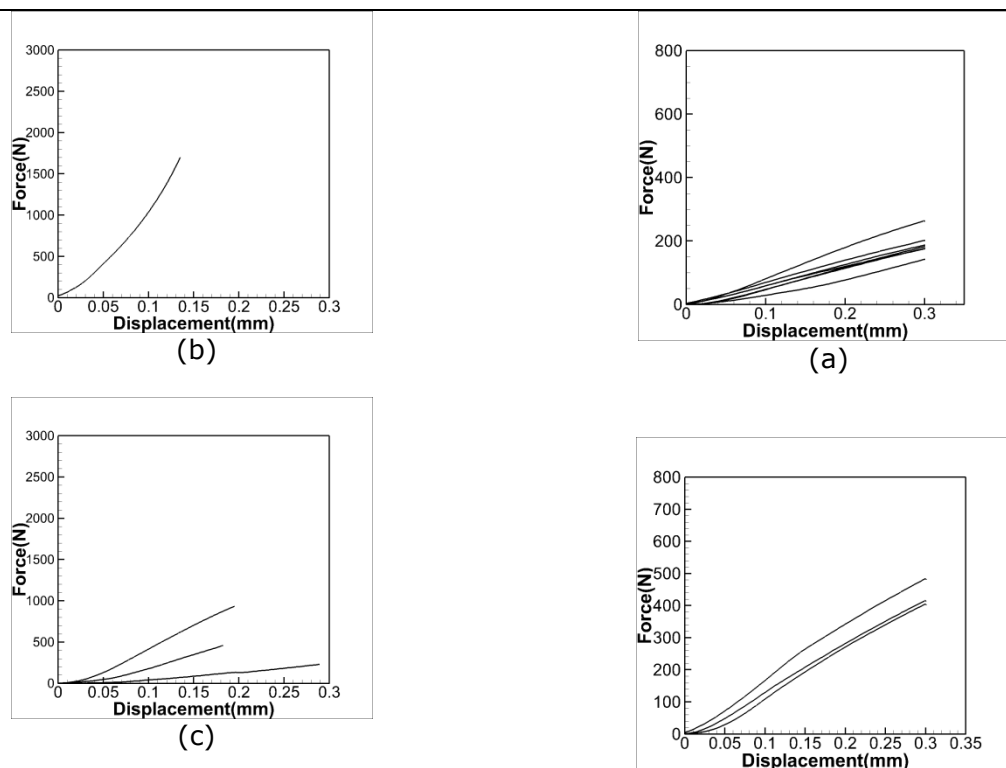


Figure 6: Force-displacement curves of heartwood specimens under compression tests. (a) Tangential, (b) Longitudinal and (c) Radial to grain.

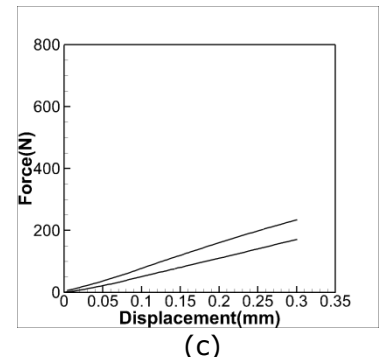


Figure 7: Force-deflection curves of sapwood specimens under three point bending tests. (a) Tangential, (b) Longitudinal and (c) Radial to grain.

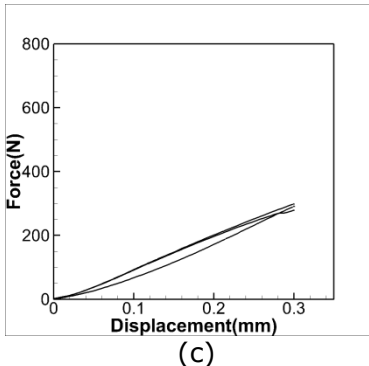
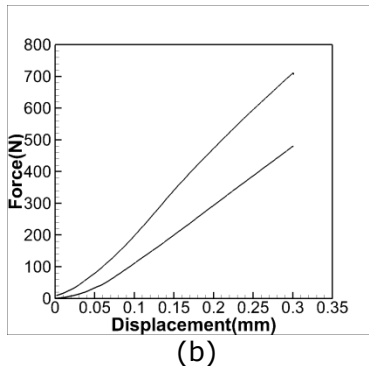
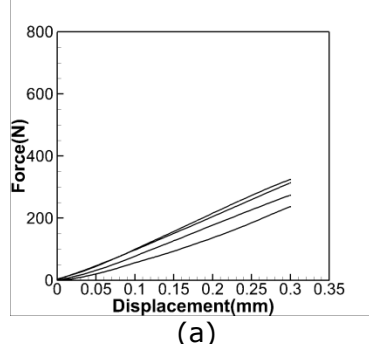


Table 1: Elastic moduli of sapwood and heartwood in three directions under compression tests

	Tangential (Mpa)	Longitudinal (Mpa)	Radinal (Mpa)
Sapwood	5591±1570	14539	15696±33
Heartwood	1152±470	5997	1315±894

Table 2: Elastic moduli of sapwood and heartwood in three directions under three point bending tests

	Tangential (Mpa)	Longitudinal (Mpa)	Radinal (Mpa)
Sapwood	451±82	1039±64	480±109
Heartwood	678±74	1452±350	689±12

Figure 8: Force-deflection curves of heartwood specimens under three point bending tests. (a) Tangential, (b) Longitudinal and (c) Radial to grain.

A REVIEW ON MACHINING PROCESS OF GLASS MATERIALS

Pravin Pawar¹, Raj Ballav² and Amaresh Kumar³

¹ Department of Manufacturing Engineering, National Institute of Technology, Jamshedpur, Jharkhand 83101 India. Email : pravin.1900@gmail.com

² Department of Manufacturing Engineering, National Institute of Technology, Jamshedpur, Jharkhand 83101 India. Email : rballav.prod@nitjsr.ac.in

³ Department of Manufacturing Engineering, National Institute of Technology, Jamshedpur, Jharkhand 83101 India. Email : akumar.prod@nitjsr.ac.in

ABSTRACT: This paper provides an intensive literature review to enhance machining process on brittle materials glass taken into consideration. The paper starts with the classification of current & past manufacturing processes based on the processes being used for machining of glass material. The major part of this paper reviews existing machining processes used machined to glass material reported over the past two decades, Finally this paper attempts to identify output results with respective their machining process.

1. INTRODUCTION

Glasses used as key structural material for optical, bio and chemical devices due to their excellent & superior properties such as high strength, hardness thermal resistance, corrosion resistance, wear resistance, relatively light weight high chemical and heat resistance, high electrical isolation, low optical absorption, amorphous solid material, large optical transmission range and biocompatibility [6][9][12][34][38][35]. However, such materials are generally difficult-to-machine due to the properties of extreme hardness, brittleness[27][6][9][19]. Glass also has the distinction of being transparent and having low electrical as well as thermal conductivity. It is increasingly being used in micro fabricated devices like solid oxide fuel cells, pumps, optics, electronics part, biomedical diagnostics, thermodynamics fluidics reactors, micro-electromechanical systems(MEMS)[24][25][33][37][14][19]

measured with different machine parameter of water pressure, abrasive flow rate, traverse speed and standoff distance. Particle swarm optimization is used to for optimization parameters [1].The Surface roughness and kerf taper ratio aspect were studied of machining of glass/epoxy composite laminate Material & also produce a better quality of cuts for that Taguchi's design tool used for experiments and analysis of variance[2].The taper of cut slot increases with increase in standoff distance. Garnet abrasives produce a larger taper of cut followed by Al₂O₃ and SiC. The taper of the cut also increases with increase in work feed rate. The average width of cut produced by SiC is higher in this case[15].Micro machining and fluid polishing of glass using stagnation produced under the jet nozzle by using this technique crack-free machining of micro grooves & polishing of micro channels was done[21]

2. CLASSIFICATION OF MACHINING PROCESS

2.1 Abrasive Water Jet Machining (AWJM)

The Authors investigated on machining of borosilicate glass by AWJM. Depth of cut is

2.2 Micro Abrasive Air Jet Machining (MAJM)

Predictive mathematical models for the erosion rates in micro-hole drilling and micro-channel cutting on glasses with an abrasive air jet are developed. This model

4th International Engineering Symposium - IES 2015

March 4-6, 2015, Kumamoto University, Japan

prediction provides better experimental results[10] The Authors conducted Machining of glass by abrasive jet machining while the glass is cooled to a low temperature by using a liquid Nitrogen. Due to this technique Material removal rate of glass was increased [22].The experimented results shows that micro-grooving on glass, Results obtaining that combination of the fine-tuning of the masking process & MAJM. This is applicable for micro-machining of semiconductors, electronic devices & LCD[27].The author optimized machining parameters such as Standoff distance, Pressures and different Nozzle Diameters by using Taguchi Method & this method compared to Analysis of Variance(ANOVA) The output results found out MRR & KERF[30].In this paper discusses abrasive-jet machining of glass by using silicon carbide or aluminium oxide abrasives were mixed with air & directed at high velocity onto the glass and because of that optimum MRR was found to be 10mg/min[32] The Author has been produced Analytical models for prediction of the shape, sidewall slope, and depth of abrasive jet micro-machined planar areas. In that developing two techniques (i) machining micro-channels adjacent to the planned planar area, and (ii) Target oscillation with an obliquely. This technique used for machining of flat planar areas at a single elevation [11]

2.3.Abrasive Slurry Jet Micro Machining(ASJM)

The authors studied the effect of dilute polymer solutions on the width, shape, and centreline roughness of micro-channels machined using new developed abrasive slurry-jet micro-machining (ASJM) apparatus. The results found out little amount of polymer can affect decrease the width of machined micro- channels[17] They found surface evolution model to predict the profiles of micro-channel sand

holes machined in borosilicate glass for ASJM System. By using this model accurately predicted the profiles of micro-channels with a maximum error of 7% for aspect ratios (depth/ width) of up to 5 [26]

2.4. Ultrasonic Machining (USM)

The author investigated surface formation mechanisms involved in rotary ultrasonic machining (RUM) of a glass BK7 process. A novel theoretical model developed for RUM process was connected by ultrasonic effects, such as the low dynamic fracture toughness of the material, cyclical variation in the effective work angle of the abrasive, and the larger abrasive inertia force. It reduces cutting force of the diamond tool without affecting surface quality of work-piece[8].The researcher develops new method of micro ultrasonic machining it achieves micro holes as small as 5μm in diameter in quartz glass and silicon. The high tool wears problem reduced by using a sintered diamond tool [9].The author studied the influence of rotation of the work-piece in addition to an ultrasonically oscillated tool was effective on MRR & Surface Roughness, Also this technique is superior to conventional ultrasonic machining [16]. In this aluminium oxide or silicon carbide or boron carbide was mixed with water and feeds to a tool oscillating at frequencies between 15 & 20 kc/s and finding out material removal rate [32].The author produced hybrid process of micro electrical-discharge machining (MEDM) and micro ultrasonic vibration machining (MUSM) is proposed for making precise micro-holes with high aspect ratios in borosilicate glass type. In the roundness investigations, the machining tool rotation speed had a close relationship to the degree of micro-hole roundness. Using this Micro-holes with a roundness value of about 2μm could be obtained[33] The Authors Experimented results show that the machining speed decreases with an increase in the static load beyond a certain level also find out the debris accumulation was proposed as the main reason leading to low machining efficiency & particle size was the dominant element influencing the surface [36] The

authors demonstrate a process in which USM added a low concentration hydrofluoric acid solution with alumina slurry(CUSM). The output results compare with conventional methods it shows that material removal rate increase to 200% & also the surface roughness was improved [6].

2.5. Electro Chemical Discharge Machining (ECDM)

The Author developed thermal model for the calculation of material removal rate (MRR). The temperature distribution within zone of influence of single spark is obtained by using finite element method (FEM). The developed FEM based thermal model was found to be in the similarity of accuracy with the experimental results [3] In this author obtained micro-structures less than 100µm in size, such as Ø60µm micro-holes, a 10µm thin wall, and a 3D micro-structure were fabricated in glass material by using micro ECDM process[5]. In this work experimented was done on electrochemical spark abrasive drilling (ECSAD) process by using abrasive cutting tools and find out output result such as material removal and increased machined depth, Also abrasive cutting tool is compared with conventional cutting tool [13]. The author obtained in this research the high aspect ratio micro tools fabricated in-house used in deep micro-hole drilling on glass using low electrolyte concentration. An aspect ratio of 11 has been achieved & surface features less than 100µm were developed on glass for that purpose the tungsten carbide micro-tool produced by using pulse electrochemical micromachining (PECMM). The surface roughness was found to be in the range of 250–350 nm. [14]. In this study, wire electrochemical discharge machining (WECDM) was applied to processing quartz glass with electrolyte supplied with titrated flow. The investigated droplet titration approach to machining of quartz glass required less cost and pollution free [18]. In this researcher studied longitudinal oscillation applied to the cathode electrode during the electrochemical discharge micro drilling of glass and the effects of electrolyte flushing alteration in both discharge and hydrodynamic regimes of

the process has been found out. In this experimentation longitudinal waveform including square and sinusoidal were applied to the tool. The experimented results show that improvement in material removal rate (MRR) using square waveform and a small amount of improvement in the sinusoidal waveform. [28]

2.6. Laser Machining-

This article examines ultrafast laser machining of tapered micro channel trenches in both hard soda-lime and borosilicate glasses. The author developed a model for channel width and depth as a function of processing parameters and threshold fluence calculated channel sizes from the model are in good similar match's experimental results [7]. The authors got from this research a focused laser beam integrated with a CAD-based scanning motion may be used effectively to generate complex and highly precise micro features on glass substrate [19] In this research short pulse solid-state lasers with pulse duration in the nanosecond to femtosecond range were used to process different types of glass materials. The cause of the pulse duration and other process parameters on the machined features was analyzed & their thermal effects and nonlinear processes. Edge quality, circularity, aspect ratio, formation of the redeposit material and machining rate were investigated with about the process variables such as focusing optics, laser power, wavelength and repetition rate[25].The 400 W pulsed Nd-YAG laser used machined to a glass-matrix composite optimising the laser pulse waveform parameters with respect to both material removal rate/efficiency and material damage [31].The researchers carried out methods, including focused ion beam, Femto-second laser, KrF eximer laser and dicing techniques, were used for preparing glassy carbon micro-molds and results were in terms of the process rate, quality of machined surface, quality of microstructures on machined surface area and the shape of machined structure [35] The author conducts machining of microgrooves on fused silica substrates

4th International Engineering Symposium - IES 2015

March 4-6, 2015, Kumamoto University, Japan

using a p-polarised femtosecond laser beam was developed with groove profile and surface morphology. Micro-channels with width and spacing of 20mm were generated with no micro-cracks. The beam polarisation had been affected machining results [38]

2.7. Acoustic Energy Micromachining (AE)

The author obtained AE energy in micro grinding is sensitive to changes in the mechanism of material removal & also material removal more AE energy in a plastic flow dominated process than in a fracture-dominated process [4]

2.8. Nano Abrasion Machining (NAM)

The new method of Nano-abrasion machining is carried out for optical finishing of brittle materials. The experiments suggest that the material removal rate and surface roughness are suitable for optical finishing. The flatness is improved from 151 to 29 nm of optical glass of BK7 taking as a material [12]

2.9. Ultra precision Machining-

This paper presents a specific cutting-energy based model to predict the ductile-brittle transition point in ultra-precision machining of brittle materials. The energy produced in brittle and ductile modes of machining is modeled as a function of work-material intrinsic properties, tool geometry and process parameters. The developed model is validated by single-edge cutting tests on single-crystal silicon and BK7 glass [24]. The author found the different material removal mechanisms involved in the machining of brittle materials & due to reason of Free abrasive machined surfaces of materials indicate that the material removal occurs due to micro indentations by the abrasive particles, which cause lateral cracking [29]

2.10 Vibration-Assisted Machining (VAM)

In this paper authors developed the specific cutting energy based model is with VAM by taking vibration parameters in

addition to the work-material intrinsic properties, tool geometry and machining parameters for that single crystal silicon taking as work-piece and single crystal diamond used as tool Material [37]

2.11 Atmospheric Pressure Plasma Jet (APPJ)

This paper shows the development of an APPJ chemical machining process for defect free and high efficiency machining of Zerodur. In this chemical machining mechanism for multi-phase multi-composite materials is identified. The chemical property of the plasma jet is investigated via the atom emission spectrum analysis method and the experimental results of Zerodur material removal function and surface roughness variation with different processing parameters are investigated [34]

2.12 Powder Blasting Technique (PBT)

The author developed glass plates of the Zeus panel, a new type of flat and slim display, are developed. Particularly the fabrication of the holes in the very thin selection plates is obtained. In Powder blasting a nozzle in which abrasive particles are accelerated to velocities in the range of 100 to 200 m/s by applying pressurized air, moves relative to the glass substrate. [20]

2.13 Micro Milling

In this paper find out ductile mode machining of glass by micro milling process, Fracture-free slots have been cut in soda-lime glass work-piece by micro-end milling. Experimental results have investigated that fracture-free slots can be machined in glass by micro milling process within controlled set of cutting conditions. The feed per edge and the axial depth of the cut was getting as the critical factors for the ductile-brittle transition in micro cutting of glass by milling process [23]

3. RESULTS & OBSERVATIONS

The Bar Chart Shows that numbers of paper published with respect to their Machining process. The Pie Chart shows that percentage of research conducted in different machining process on glass material & its output results

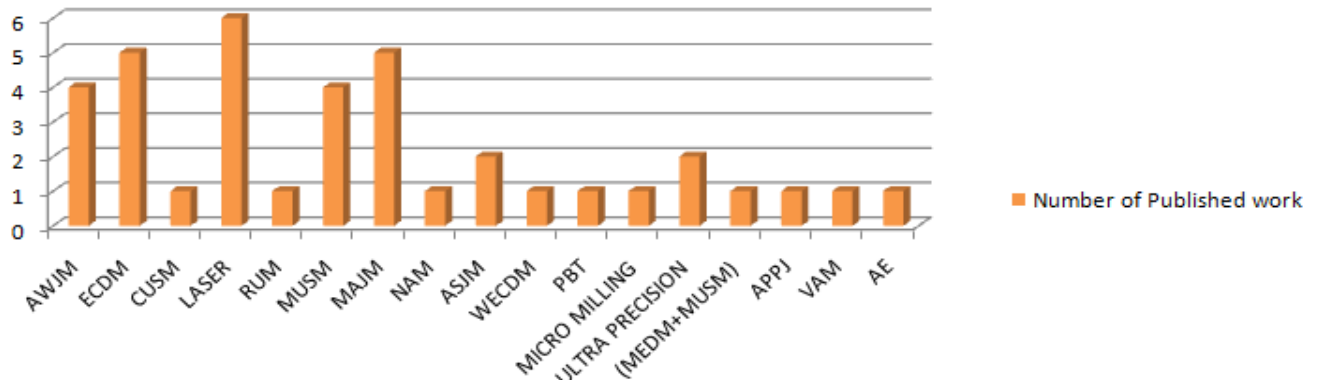


Fig 1 Distribution of the collected research papers for machining on Glass Material.

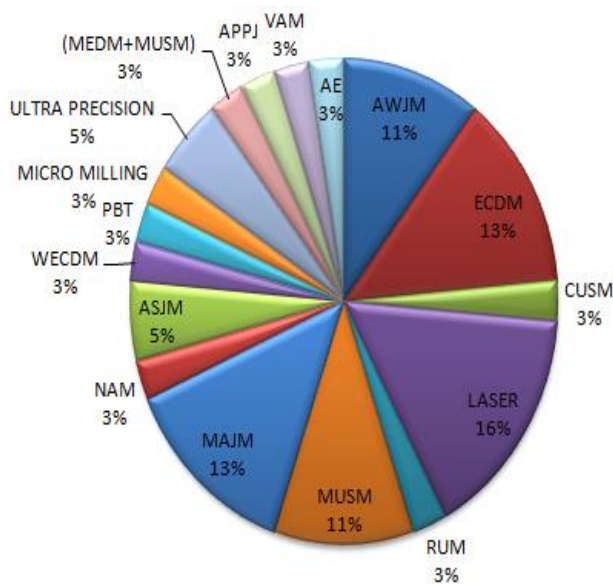


Fig.2.Percentage of Research conducted in different machining process on glass

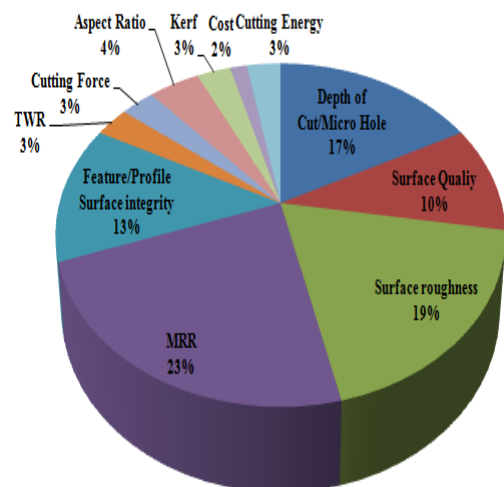


Fig.3. Percentage of research focused on different types of results on Glass

4.CONCLUSION

- 1.The review shows that most of machining process is used machined to glass material by Laser,USM,ECDM,AWJM, MAJM process.
2. The researchers found out mostly MRR, Ra, Surface quality,Features or profile surface quality and Depth of cut/micro hole are output results.
- 3.This review shows that development of machining process on glass material from past to present state.

ACKNOWLEDGEMENTS

The author gratefully acknowledge the help provide to guiding this research paper by Dr. Raj Ballav & Dr. Amresh Kumar Department of Manufacturing Engineering, National Institute of Technology, Jamshedpur.

4th International Engineering Symposium - IES 2015

March 4-6, 2015, Kumamoto University, Japan

REFERENCES

- [1] Aich Ushasta Abrasive Water Jet Cutting of Borosilicate Glass Procedia Materials Science 6 (2014) 775 – 785
- [2] Azmir .A. A study of abrasive water jet machining process on glass/epoxy composite laminate Journal of Materials Processing Technology 209 (2009) 6168–6173
- [3] Bhondwe K.L. et al Finite element prediction of material removal rate due to electro-chemical spark machining International Journal of Machine Tools & Manufacture 46 (2006) 1699–1706
- [4] Bifano T.G. et al Acoustic emission as an indicator of material removal regime in glass micro machining precision Engineering oct 1992 vol 14 no 4 pp 219–228
- [5] Cao Xuan Doan et al Micro-structuring of glass with features less than 100um by electrochemical discharge machining Precision Engineering 33 (2009) 459–465
- [6] Choi J.P. et al Chemical-assisted ultrasonic machining of glass Journal of Materials Processing Technology 191 (2007) 153–156
- [7] Darvishi Samira Ultrafast laser machining of tapered micro channels in glass and PDMS Optics and Lasers in Engineering 50 (2012) 210–214
- [8] Dongxi Lv et al Influences of vibration on surface formation in rotary ultrasonic machining of glass BK7 Precision Engineering 37 (2013) 839– 848
- [9] Egashira Kai et al Micro ultrasonic machining by the Application of work-piece Vibration Annals of the CIRP Vol.48/1/1999 pp 131-134
- [10] Fan J.M. et al Modelling the erosion rate in micro abrasive air jet machining of glasses Wear 266 (2009) 968–974
- [11] Ghobeity A. et al Abrasive jet micro-machining of planar areas and transitional slopes in glass using target oscillation Journal of Materials Processing Technology 209 (2009) 5123–5132
- [12] Horiuchi Osamu Nano-abrasion machining of brittle materials and its application to corrective figuring Precision Engineering 31 (2007) 47–54
- [13] Jain V.K. et al On the machining of alumina and glass International Journal of Machine Tools & Manufacture 42 (2002) 1269–1276
- [14] Jui Sumit K. High aspect ratio micromachining of glass by electrochemical discharge machining (ECDM) Journal of Manufacturing Processes 15 (2013) 460–466
- [15] Khan A.A. et al Performance of different abrasive materials during abrasive water jet machining of glass Journal of Materials Processing Technology 191 (2007) 404–407
- [16] Komaraiah M. Et al Investigation of surface roughness & Accuracy in ultrasonic machining Precision Engineering April 1988 vol 10 no 2 pp 59-65
- [17] Kowsari K. Et al The effects of dilute polymer solution elasticity and viscosity on abrasive slurry jet micro-machining of glass Wear 309(2014)112–119
- [18] Kuo Kuan-Yuan et al Wire electrochemical discharge machining (WECDM) of quartz glass with titrated electrolyte flow International Journal of Machine Tools & Manufacture 72(2013)50–57
- [19] Li Chengde et al Ultra-fine surface machining of glass using Laser-produced charged particles Applied Surface Science 219 (2003) 264–270
- [20] Lighthart H.J. Glass and glass machining in zeus panels Philips J. Res. 50 (1996) 475–499
- [21] Matsumura T. Abrasive water jet machining of glass with stagnation effect CIRP Annals - Manufacturing Technology 60 (2011) 355–358
- [22] Muju M.K. et al Abrasive jet machining of glass at low temperature Journal of Mechanical Working Technology 17 (1988) 325–332
- [23] Muhammad Arif et al Ultraprecision ductile mode machining of glass by micromilling process Journal of Manufacturing Processes 13 (2011) 50–59
- [24] Muhammad Arif A predictive model of the critical undeformed chip thickness for ductile-brittle transition in nano-machining of brittle materials International Journal of Machine Tools & Manufacture 64 (2013) 114–122
- [25] Nikumb S. Precision glass machining, drilling and profile cutting by short pulse lasers Thin Solid Films 477 (2005) 216– 221
- [26] Nouraei H. Surface evolution models for abrasive slurry jet micro-machining of channels and holes in glass Wear 309(2014)65–73
- [27] Park Dong-Sam et al Micro-grooving of glass using micro-abrasive jet machining Journal of Materials Processing Technology 146 (2004) 234–240
- [28] Razfar Mohammad Reza Study of the effects of tool longitudinal oscillation on the machining speed of electrochemical discharge drilling of glass Precision Engineering (2014)
- [29] Sreejith P.S. et al Material removal mechanisms in precision machining of new materials International Journal of Machine Tools & Manufacture 41 (2001) 1831–1843
- [30] Srikanth D.V. Metal Removal and Kerf Analysis in Abrasive jet drilling of Glass Sheets Procedia Materials Science 6 (2014) 1303 – 1311
- [31] Tuersley Ian P. . et al Nd-YAG laser machining of SiC fibre/ borosilicate glass composites. Part I. Optimisation of laser pulse parameters Composites Part A 29A (1998) 947–954
- [32] Venkatesh V.C. Machining of Glass By impact Processes Journal of Mechanical Working Technology 8 (1983)247-260
- [33] Yan B.H. Study of precision micro-holes in borosilicate glass using micro EDM combined with micro ultrasonic vibration machining International Journal of Machine Tools & Manufacture 42 (2002) 1105–1112
- [34] Yao Y.X. et al chemical machining of Zerodur material with atmospheric pressure plasma jet CIRP Annals - Manufacturing Technology 59 (2010) 337–340
- [35] Youn S.W. et al Microstructuring of glassy carbon mold for glass embossing – Comparison of focused ion beam, nano/femtosecond-pulsed laser and mechanical machining Microelectronic Engineering 83 (2006) 2482–2492
- [36] Yu Z. et al Influence of Debris Accumulation on Material Removal and Surface Roughness in Micro Ultrasonic Machining of Silicon Annals of the CIRP Vol. 55/1/2006
- [37] Zhang Xinquan et al A model to predict the critical undeformed chip thickness in vibration-assisted machining of brittle materials International Journal of Machine Tools & Manufacture 69(2013)57–66
- [38] Zheng H.Y. et al Polarisation-independence of femtosecond laser machining of fused silica Applied Surface Science 236 (2004) 114–119

Stress and Elastic Properties Evolutions of Thin Films under Thermal Treatment

Tzu-Huei Yang ¹, Yin-Geng Tsai ² and Kuo-Shen Chen ³

- ¹ Graduate Student, Department of Mechanical Engineering National Cheng-Kung University Tainan, Taiwan, R.O.C. e-mail: thy1919@gmail.com
² Graduate Student, Department of Mechanical Engineering National Cheng-Kung University Tainan, Taiwan, R.O.C. e-mail: aaron24205@hotmail.com
³ Professor, Department of Mechanical Engineering National Cheng-Kung University Tainan, Taiwan, R.O.C. email: kschen@mail.ncku.edu.tw

ABSTRACT: Metallic and dielectric films are important functional and structural materials in interconnect systems for integrated circuit applications. In particular, stress state of films influence the device reliability significantly and it also strongly depends on the deposition histories and post-deposition thermal treatments. This makes it is extremely difficult for performing analytical stress generation model for subsequent device reliability evaluations. In this paper, a phenomenological model is proposed for simulating the stress and elastic properties evolutions of metal films, Al and Cu, and dielectric films, Si₃N₄ and SiO₂, after rapid thermal annealing for guiding the device longevity evaluation. In parallel, essential experiments on characterizing the stress states and elastic properties of those films are performed. The simulation and experimental results agree with each other relative well.

Keywords: thin film, thermal cycling, residual stress, nanoindentation

INTRODUCTION

Physical vapor deposited (PVD) metallic films and Plasma-enhanced chemical vapor deposited (PECVD) dielectric films have been widely used in modern IC devices and MEMS. The device reliability is mainly controlled by the residual stress, which is resulted from many sources, such as thermal mismatch, microstructure defects. This issue has been investigated intensively by in our previous works [1-3]. In summary, the stress states of the films during deposition and after post-deposition thermal annealing are process-dependent. Therefore without a careful stress evaluation, it is challenging to perform the subsequent structural integrity evaluation. In this paper, the mechanical issues of dielectric and metallic films were both characterized. For the dielectric films, this paper proposed an effective intrinsic stress model for modeling the temperature and time dependent stress evolution by

simultaneously considering the diffused void-generation and subsequent void shrinkage effect. The results were then combined with material viscoelasticity and a multi-layer structure model for evaluating the stress existed in each layer during thermal processing.

For metallic films, the effect of rapid thermal annealing on the residual stress and modulus of aluminum and copper films were investigated. Essential indentation testing was also performed for characterizing the stress and stiffness variations after thermal processing. By this effort, it should be possible to provide more precise information for optimizing thermal annealing for improving structural longevity of IC and MEMS devices.

Overall investigation plan

The stress of PECVD films has been observed to be sensitive to the subsequent thermal treatment [1]. As shown in Fig.1,

it can be seen that the residual stress increases significantly once the RTA temperature over 400°C. The residual stress generation at mid-temperatures is due to microstructure evolution with impurity diffusion [1] and it is hard to perform a physical-based modeling. Here, we propose a model by using a time and temperature dependent thermal expansion coefficient to represent the effect of microstructure evolution. An experimental plan is also conducted to systematically characterizing the residual stress, modulus, hardness and fracture behavior of films for evaluating the structural integrity.

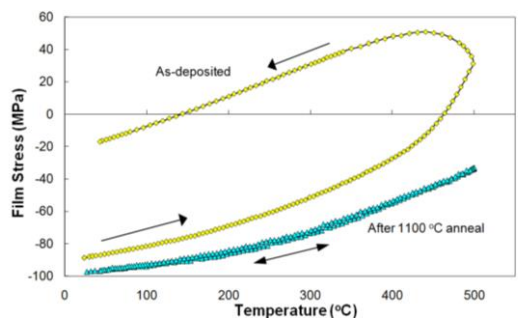


Fig.1 Stress of PECVD oxide subjected to temperature cycling [1]

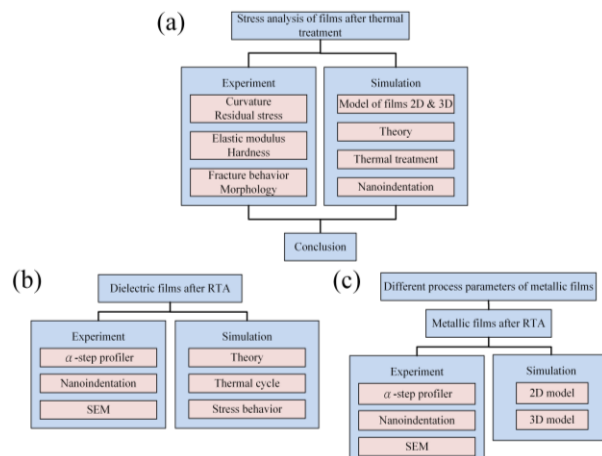


Fig.2 (a) overall plan, (b) dielectric, and (c) metallic films characterization flow

The schematic flow of the entire research is shown in Fig.2 (a). On the other hand, Fig.2 (b) and 2(c) are the schematic flows for dielectric films and metallic films investigation, respectively. Mechanical characterization was performed after different RTA. After finishing with different process parameters and RTA temperature, residual stress, modulus, and morphology characterization were figured out by instruments and 2D and 3D FE models

were performed to investigate the profile and effects of tip curvature by simulation.

Experiment plan

All films were deposited on 4" silicon wafers. For the dielectric films, PECVD nitrides and oxides were deposited by a Samco/PD-220NA system. For the metallic films, PVD aluminium and copper were deposited by an ULVAC EBX-6D and an Ion Tech Microvac 450CB system, respectively. The deposition thickness was 600 nm for Al film and 500 nm for copper. There were four types of specimens for dielectric films schematically shown in Fig.3 for evaluating the multi-layered deposition effect. On the other hand, metallic films were designed to be single layer with thickness ranged from 300–700 nm. After deposition, the samples were then experienced a rapid thermal annealing (RTA) with the same annealing period. For single layer, residual stress measurements were performed by using KLA-Tencore FLX 2320 curvature measurement system and the data were converted via Stoney's formula [4] to evaluate the influence of RTA. In addition, nanoindentation by using MTS XP was also performed to characterize the elastic modulus, hardness using Oliver's model [5], and for qualitatively observing the fracture behaviour. The model proposed by Marshall and Lawn [6] was used to characterize the fracture toughness.

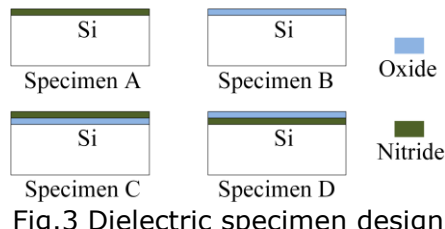


Fig.3 Dielectric specimen design

Experimental results

I. Dielectric film

The residual stress varying with RTA temperature are shown in Fig.4 and it can be seen that the stress of multi-layered films (i.e., C and D) reduces in comparison with nitride-only (i.e., A) due to the presence of oxide. Meanwhile, it can also be observed that oxide film experiences an earlier relaxation as RTA temperature over 400°C. The modulus characterization results shown in Fig.5 indicated that the modulus of the composite films (i.e., C and

D) were significantly depends on the deposition sequence.

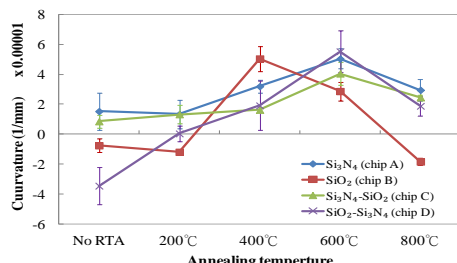


Fig.4 Residual stress of dielectric films after RTA

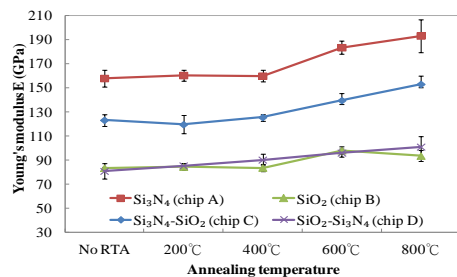


Fig.5 Young's modulus of dielectric films after RTA

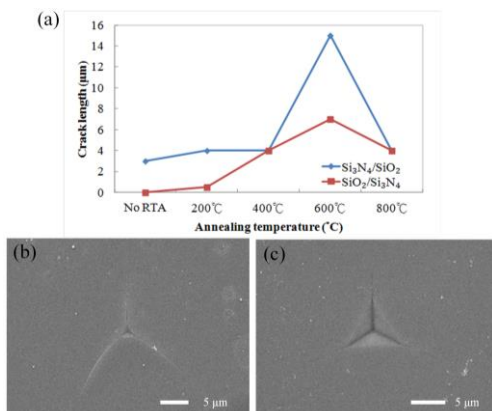


Fig.6 (a) Indentation crack length at different RTA temperatures, (b) specimen C and (c) D after 600°C RTA

For specimen C, the result was influenced by the presents of softer oxide film underneath (i.e., substrate effect). On the other hand, for specimen D, the presence of nitride did not influence the measured results of the top layer oxide. Furthermore, the indentation test also revealed the significant difference in fracture behaviour. The results are shown in Fig.6. It can be seen that specimen C generates very long crack after 600°C RTA during indentation test and its equivalent fracture toughness becomes very low. On the other hand, specimen D shows the results with no special crack growth. This

implies that the RTA processing could induce significant change in fracture behaviour. Finally, correlation between the stress of individual layer and the equivalent stress converted by measured curvature was calculated. It was found that the stress of nitride layer was much larger than the corresponding equivalent value and this implies that without proper stress measurement and analysis procedure, the structural integrity could be a concern for multi-layered films.

II. Metallic film

Residual stresses of metallic films after RTA are shown in Fig.7. When RTA temperature increases, residual stresses of both metallic films also increase. It might be attributed to the effect of grain growth and coalescence, as well as defect elimination in microstructure. All of these mechanisms contribute tensile stresses. After RTA with temperatures exceed 400°C (for Al) and 200°C (for Cu), the residual stresses of both Al and Cu films decreased possibly due to stress relaxation. As shown in Fig.8 , it is interesting to observed that the surface morphology of Al films also changes with RTA temperature and this microstructural changes could generate additional stress variations.

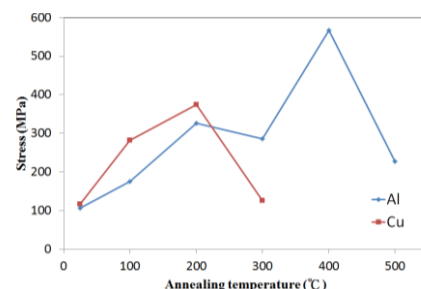


Fig.7 Residual stress of metallic films after RTA

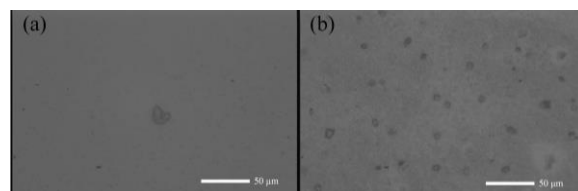


Fig.8 Morphology of Al film after different RTA (a)100°C and (b)400°C

Fig.9 shows the nanoindentation elastic modulus of metallic films after RTA. The moduli of Al and Cu films are higher than 100 and 120 GPa. This is much higher

4th International Engineering Symposium - IES 2015

March 4-6, 2015, Kumamoto University, Japan

than the reported buck values. We believe that this is due to both the substrate effect and the effect of round tip. A more comprehensive study on the round tip is shown in the subsequent section. In short, after considering both issues, we believe that the indentation tested modulus can be close to the bulk value. Nevertheless, the major issue to be addressed here is the effect of RTA temperature. From Fig. 10, it can be seen that at 400°C (for Al) and 300°C (for Cu), the elastic moduli of films are in minimum and this is coincident with the maximum residual stress temperature. From indentation theory, the tensile stress will reduce the apparent elastic modulus. Finally, the SEM micrographs of Al films with no RTA and different indentation depth of Al film are shown in Fig.10. It can be seen that as the indentation depth increases, the pile up of aluminium becomes more severe, which indicate considerable plastic deformation occurs during indentation.

Simulations

I. Dielectric film

The simulation flow is shown in Fig.11. Considering a multi-layered film-substrate system, the stress of each layer can be determined using force balance, moment equilibrium and the constitutive law of beam structures. Furthermore, mismatched strains exist between layers. Here we follow the derivation of DeVoe and Pisano [7] on multi-layered piezoelectric structure by replacing the mismatch strain to a temperature dependent mismatch strain causing from both thermal and intrinsic stresses. This mismatched strain also varies with time by considering the stress relaxation effect. The concept is simple and straightforward and is presented in below but the mathematics is a little bit messy and cannot be clearly stated here due to size limitation. As a result, readers are encouraged to refer [2] for the technical detail.

From [1], the intrinsic stresses of PECVD films are due to void shrinkage in order to minimizing its total free energy. However, these micro voids are generated due to the breaking of hydrogen bonds and diffusion out of hydrogen gases. Both of the

shrinkage and diffusion are temperature and time dependent and this implies that intrinsic stress also depends on both factors and this agrees with the observation. As a result, it needs to take both hydrogen diffusion dynamics and void shrinkage mechanics into account for a proper intrinsic stress generation dynamics. That is, diffusion process provides vacancy for shrinking and stress generation.

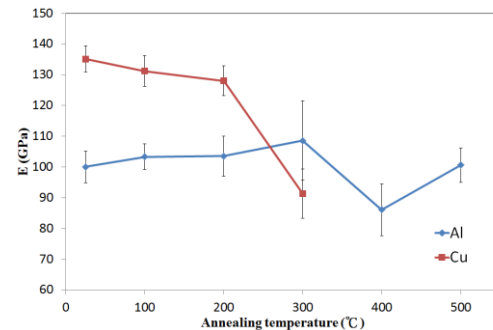


Fig.9 Young's modulus of metallic films after RTA

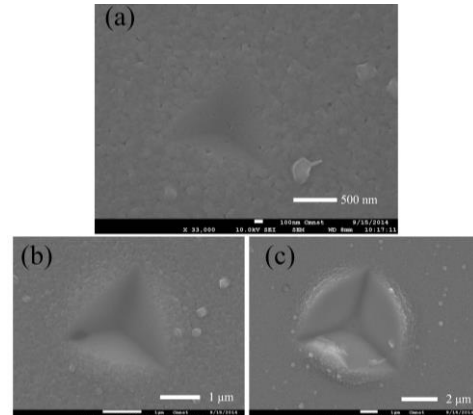


Fig.10 SEM image of Al film with no RTA after nanoindentation depth (a)120 nm, (b)300 nm and (c)800 nm

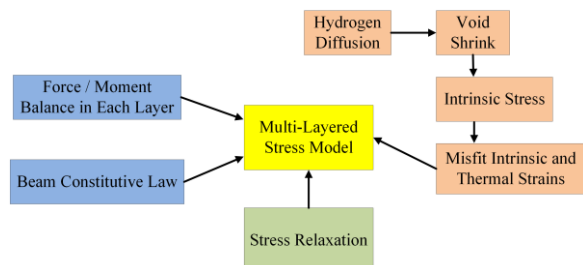


Fig.11 Flowchart on film stress simulation

In this work, we use a simplified Gaussian diffusion model to deal with the diffusion and consequently, qualitatively expressing the dependency on both temperature and time in intrinsic stress generation. Detail

parameters are determined by comparing with experimental data using curve fitting. Once the intrinsic stress is obtained, we implemented it as an equivalent hysteresis thermal stress by treating it as a time and temperature dependent CTE for performing finite element simulation in ABAQUS with the help of a FORTRAN subroutine for modeling the equivalent CTE. On the other hand, the stress relaxation behavior is simply modelled by using a Maxwell model in the form of Prony series [8] for finite element analysis.

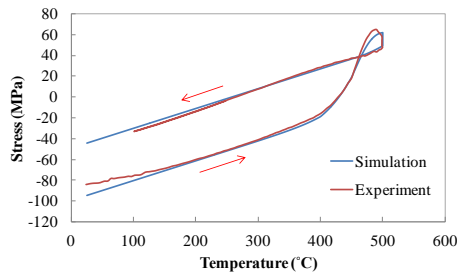


Fig.12 The simulation result of PECVD oxides during RTA

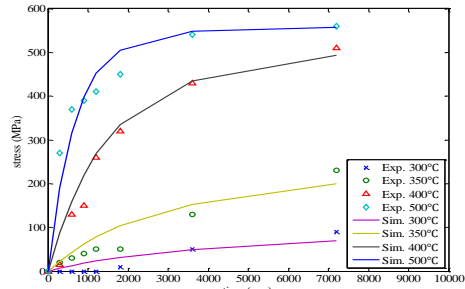


Fig.13 The finite element model for analyzing silicon nitride stress

Fig.12 shows the stress history after a complete thermal cycling between room temperature and 500°C. It can be seen that the simulation agree with experimental results [1]. The stress evolution data of PECVD silicon nitride of [3] are also employed here for the purpose of validation. The data has already shown in Fig.13. It can be seen that simulation results essentially catch the major characteristics of the experimental data. However, for data with lower temperature deposition and at earlier stage of thermal cycling, the discrepancy between data and simulation is more severe, which indicate that the real evolution dynamics is actually more complicate than the assumed model. However, the agreement in global

behaviour suggested that this model could model the applicability of proposed model. After validating the intrinsic model with the reported oxide thermal cycling data, it is able to calculate the stress of each film in these specimens. For example, as shown in Fig.14, it can be seen that the stress of each layer varies significantly with their equivalent value via Stoney equation [4]. The results demonstrate the applicability of the proposed method and can also explain why the film cracking significantly of specimen C as shown in Fig.6 (b) due to much high stress of nitride layer.

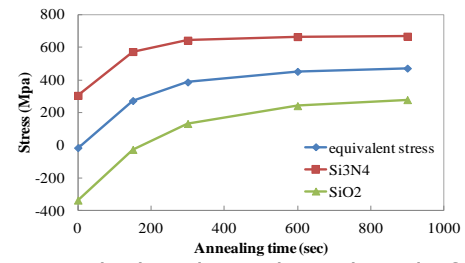


Fig.14 Calculated nitride and oxide film stress of specimen D and equivalent stress using Stoney equation

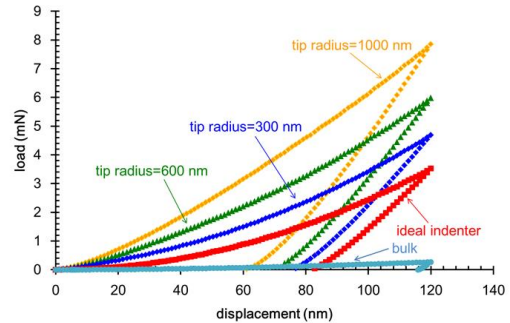


Fig.15 The indentation of simulation with different tip curvature

II. Metallic film

As mentioned in above, the reported moduli of metallic films were much higher than expected and part of this result was attributed to the tip curvature and the effect was discussed. The FEM simulation results are shown in Fig.15. The tip radius was from 0 (ideal) to 1000 nm for thin film structure and an ideal bulk Al case was used for the purpose of comparison. It can be seen that as tip radius increases, the contact area also increases and the indenter becomes more difficult to penetrate the film, and a higher load must be applied. Therefore, as shown in Table I, the modulus was overestimated if one using the Oliver and Pharr's model [5].

4th International Engineering Symposium - IES 2015

March 4-6, 2015, Kumamoto University, Japan

Meanwhile, the ideal bulk structure shows a consistent result. Therefore, in this work, the value of modulus of metallic film must be modified by additional modeling work.

Table I Summary of indenter tip roundness simulation results for Al film
(thickness: 600 nm, penetration: 120 nm)

	bulk	Radius of tip (nm)			
		0 (ideal)	300	600	1000
E (GPa)	110	174	207	247	296
H (GPa)	0.8	15.5	22.4	31	44.7

DISCUSSIONS

Both dielectric and metallic films are key materials for IC and MEMS. From mechanical perspective, the major focus between them is that dielectrics are brittle and metals are ductile. Therefore, the interested behaviours are different. That is, fracture and delamination are the major concerns for dielectric films. On the other hand, for metallic films, the plastic deformation and hillock formation are the issues to be observed. In devices manufacturing process, residual stress of deposited films strongly depends on the process during deposition and annealing.

For dielectric films, simulation and experimental studies have been performed for this issue. Alternatively, various nitride and oxide films were fabricated and tested for evaluating residual stress, elastic modulus, and fracture behaviours. The simulation and experimental results indicated that the true film stress could be much higher than their corresponding effective stress in multi-layer films and thus impact their structural integrity.

For metallic films, as RTA temperature increases, the tensile stress of films becomes higher. The minimum value of Young's modulus happens at the same RTA temperature with the maximum tensile stress. This is key information should be aware in process design. Meanwhile, there is no delamination observed of aluminium films after RTA. This suggests that the adhesion between Al film and Si wafer is sufficient. The study results indicate that

strong stress relaxations all occur at 400°C for Al film and 200°C for Cu film. This is also important information for designing fabrication process. In the future, the multi-layer of dielectric and metallic films can be studied.

CONCLUSIONS

Investigations on characterizing the stress states and elastic properties of both dielectric and metallic films with different RTA temperatures have been performed. From these studies, the stress or fracture behaviours are easy and clear to be explained. Besides, an efficient simulation model was built for evaluating the stress evolution for dielectric films. Based on void shrinkage, diffusion, and stress realization, a finite element model was proposed to predict their residual stress behaviour. In parallel, simulations for metallic films verified the experimental results. All of these results would be invaluable for guiding the device longevity evaluation.

ACKNOWLEDGEMENTS

This work is supported by Ministry of Science and Technology (MOST) of Taiwan (NSC-101-2221-E-006-032-MY3).

REFERENCES

- [1] Chen, K S et al. (2003) Intrinsic stress generation and relaxation of plasma-enhanced chemical vapor deposited oxide during deposition and subsequent thermal cycling, *Thin Solid Films*, Vol.434, pp.190-202.
- [2] Tsai, Y G (2013), Analysis, simulation, and experimental studies on stress behavior of PECVD multi-layer structures after thermal cycling, Master Thesis, Department of Mechanical Engineering, National Cheng-Kung University, Taiwan.
- [3] Yang, Y et al. (2008), Effect of heat treatment on internal stresses in PECVD SiNxHy thin films, IEEE conference on Optoelectronic and Microelectronic Materials and Devices, Sydney,Australia, pp. 181-184.
- [4] Stoney, G G (1909), The tension of thin metallic films deposited by electrolysis, *Proc. Royal Society*, Vol. 82, pp. 172.
- [5] Oliver, W C and Pharr, G M (1992), An Improved Technique for Determining Hardness and Elastic Modulus Using Load and Displacement Sensing Indentation Experiments, *Journal of Materials Research*, Vol. 7, pp. 1564-1583.
- [6] Marshall, D B, and Lawn, B R (1986), Indentation of brittle materials, microindentation techniques in materials science and engineering, *ASTM STP 889*, pp. 26-46, 1986.
- [7] DeVoe, D L, and Pisano, A P (1997), Modeling and Optimal Design of Piezoelectric Cantilever Microactuators, *Journal of MEMS*, Vol. 6, NO.3.
- [8] Ferry, J D (1980), *Viscoelastic Properties of Polymers* 3rd ed., New York: Wiley.

Mechanical Behavior of HDPE Syntactic Foam Composite

B. R. Bharath Kumar¹ and Mrityunjay Doddamani²

- ¹ Research Scholar, Department of Mechanical Engineering, National Institute of Technology Karnataka, Surathkal, Mangalore 575025, India. email: bharathranga@gmail.com
- ² Assistant Professor, Department of Mechanical Engineering, National Institute of Technology Karnataka, Surathkal, Mangalore 575025, India. email:mrd_phd@rediffmail.com
-

ABSTRACT: Hollow particle filled polymer matrix composites, called syntactic foams, are investigated for flexural response. Four compositions of these foams are characterised to assess the effect of weight fraction of hollow inclusions (cenospheres). In the present work, cenospheres are varied by 20, 40 and 60% (by weight) in HDPE matrix. Composite samples are prepared by Injection molding route with temperature and pressure combination of 160°C and 30 kg/cm² respectively. The results show that the flexural modulus of reinforced foams is significantly higher than that of neat HDPE. Nevertheless, the flexural strength of the composites is lower than that of the neat HDPE. It is found that the flexural strength decreases as the inclusion weight fraction increases. Tractable formulas are used for computing the flexural modulus and strength from the mechanical and geometrical properties of the constituents.

Keywords: syntactic, flexural, cenosphere, HDPE

INTRODUCTION

The growth of lightweight composite materials is continuously increasing with regard to demand for superior mechanical properties. Several attempts are made to improve mechanical properties for commonly used materials like polymers (Deepthi M V et al (2014)). These polymers when reinforced with fillers (fiber, particle, flakes etc.) exhibit interesting characteristics. Composite properties are relatively uniform when filler in the form of particles are embedded in the matrix.

Syntactic foams are made by embedding hollow microspheres in the matrix, called microballoons (Kishore et al (2005)). Composites with hollow particles being of lower density have the advantage of higher weight savings, higher fracture strain under compression (Rahul Maharsia et al (2006)). Syntactic foams used in marine and aerospace structural applications need higher compression and

flexural properties (Nikhil Gupta et al (2002)).

Cenospheres are a naturally occurring byproduct of the combustion process of coal-fired power plants, and they suffer most of the similar properties as manufactured hollow-sphere products (Deepthi M V et al (2014)). These are low density hollow microspheres for which efforts are being continuously pursued to manufacture value added products (Tiwari V et al (2004), Aixiang Z et al (2005), Shukla S et al (2001), Shukla S et al (2002), Dou Z Y et al (2007)).

The present study deals with the characterization of Cenosphere/HDPE composites, to investigate strength and modulus under flexural loading condition. Correlation is established between different parameters of modulus and strength as a function of filler content. During the test samples did not show distinct failure.

4th International Engineering Symposium - IES 2015

March 4-6, 2015, Kumamoto University, Japan

MATERIALS and METHODS

High Density PolyEthylene (HD50MA180) was procured from Reliance Polymers, Mumbai, India having true particle density of 950 kg/m³. Cenospheres was purchased from Cenospheres India Pvt. Ltd. Kolkata, India having true particle density of 800 kg/m³. HDPE/Cenospheres composites are manufactured by Injection molding technique. Cenospheres are mixed in HDPE in 0-60% by weight in the increments of 20%.

HDPE and Cenosphere were mixed in the predetermined weight %. Total mass is added in the hopper Injection molding machine (WINDSOR SP 80, Single screw type). Temperature of 160°C and 30 kg/cm² pressure is maintained in the machine for casting the composite samples as per ASTM D 790-10 standards. Five replicates of each configuration (0, 20, 40 and 60%) are prepared and average values are presented for results interpretation .

Neat resin samples are too prepared and examined under the same conditions. Neat resin density measured from these samples was used in the rule of mixture for the computation of the theoretical density of syntactic foams. Density for fabricated specimens is experimentally estimated (ASTM standard D792 – 13) and are presented in Table 1.

EXPERIMENTAL WORK

Flexural tests are conducted as per ASTM D 790-10 standard using a universal testing machine (Zwick Roell, Z2020) equipped with a load cell of 20 kN. The machine was programmed to apply a load at the rate of 1.5 mm/min with span length of 56 mm. and sample dimension of 127 mm x 12.7 mm x 3.2 mm (length, breadth and thickness).

Figure 1 depicts the test in progress. The Flexural modulus and strength of samples are estimated from the stress-deflection data. The typical stress-deflection curve for the neat HDPE and with 60 % cenosphere by weight are presented in Figures 2 and Figure 3 respectively.

RESULTS and DISCUSSION

Density of the prepared syntactic foam composites is seen to be decreasing with filler content except for 60%. Drop in density signifies weight saving in the system (Table 1). Increased density above 40% filler content is attributed towards particle breakage as seen from the micrograph (Figure 4).

Figures 2 and 3 show stress-deflection curves obtained from the flexural testing of Cenosphere/HDPE syntactic foam composites, respectively. These figures show marginally less variability in the trend confirming suitability of the existing manufacturing methodology for the system under study. Behavior of all the samples is seen to be dominated by ductile regime. Large amount of straining could be seen profoundly leading to non failure of all samples until the maximum limit of 5% strain.

The load-displacement data is used in calculating the flexural modulus and strength presented in Table 2. The table also contains standard deviation values. It can be observed from the data that in the flexural modulus and strength; increases and decreases respectively with increase in filler content. Substantial rise in modulus is observed by addition of 20% reinforcement (55%) as compared to neat HDPE. Thereafter it consolidates (Figure 5). Rise in modulus is attributed to higher modulus Cenosphere particles. Flexural strength dropped in the range of 6-18%. Poor interfacial adhesion might be the reason for such drop (Figure 6).

CONCLUSION

Flexural tests are carried out on four types of syntactic foams having the same matrix material and varying cenosphere weight fraction. Modulus and strength of syntactic foams can be tailored by selecting cenospheres of correct weight fraction. It is concluded that with a decrease in density flexural modulus increases while strength decrease.

The following conclusions are drawn based on this study.

4th International Engineering Symposium - IES 2015

March 4-6, 2015, Kumamoto University, Japan

- Incorporation of cenospheres made the composite system lighter (weight saving) by 4%.
- In comparison with neat HDPE, rise in flexural modulus is in the range of 55 - 76%.
- Flexural strength decreased in the range of 6 - 18% as compared to neat HDPE.
- There is no specific fracture point of syntactic foams tested under flexural loading conditions.

REFERENCE

- [1] Deepthi M V et al (2014), High density polyethylene and silane treated silicon nitride nanocomposites using high-density polyethylene functionalized with maleate ester: Mechanical, tribological and thermal properties, Materials and Design, Vol. 56, pp. 685–95.
- [2] Kishore et al (2005), Short Beam Three Point Bend Tests in Syntactic Foams. Part I: Microscopic Characterization of the Failure Zones, Journal of Applied Polymer Science, Vol. 98, No. 2, pp. 673–9
- [3] Rahul Maharsia et al (2006), Investigation of flexural strength properties of rubber and nanoclay reinforced hybrid syntactic foams, Materials Science and Engineering A, Vol. 417, No. 1–2, pp. 249–58.
- [4] Nikhil Gupta et al (2002), Response of Syntactic Foam Core Sandwich Structured Composites to Three-Point Bending, Journal of Sandwich Structures and Materials, Vol. 4, No. 3, pp. 249–72.
- [5] Tiwari V et al (2004), Acoustic properties of cenosphere reinforced cement and asphalt concrete, Applied Acoustics, Vol. 65, No. 3, pp. 263–275.
- [6] Aixiang Z et al (2005), Electroless Ni-Co-P coating of cenospheres using $[\text{Ag}(\text{NH}_3)_2]^+$ activator, Materials Letters, Vol. 59, No. 4, pp. 524–8.
- [7] Shukla S et al (2001), Study of mechanism of electroless copper coating of flyash cenospheres particles, Applied Surface Science, Vol. 181, No. 1–2, pp. 35–50.
- [8] Shukla S et al (2002) Electroless copper coating of cenospheres using silver nitrate activator, Materials Letters, Vol. 57, No. 1, pp. 151–6.
- [9] Dou Z Y et al (2007), High strain rate compression of cenosphere-pure aluminum syntactic foams, Scripta Materialia, Vol. 57, No. 10, pp. 945–8.

Table 1 Average Density and standard deviation

% Cenosphere by weight	Average density (g/cm^3)	Standard deviation
0	1.0553	0.0014
20	1.0278	0.0034
40	1.0218	0.0007
60	1.0035	0.0009

Table 2 Average Flexural Modulus and Strength

% Filler	Modulus (MPa)	Std. Dev.	Strength (MPa)	Std. Dev.
0	713.78	44.03	22.61	0.62
20	1108.14	36.39	21.13	0.55
40	1192.5	38.74	19.54	0.42
60	1253.69	40.85	19.17	0.21



Fig. 1 Test in-progress

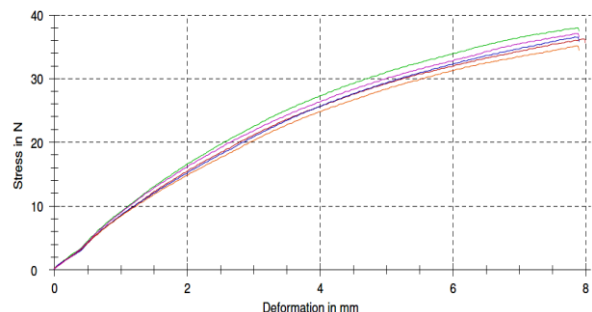


Fig. 2 Stress-Deflection curves for neat HDPE

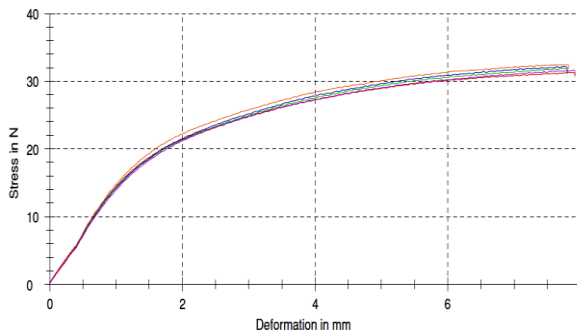


Fig. 3 Stress-Deflection curves for HDPE with 60% cenosphere.

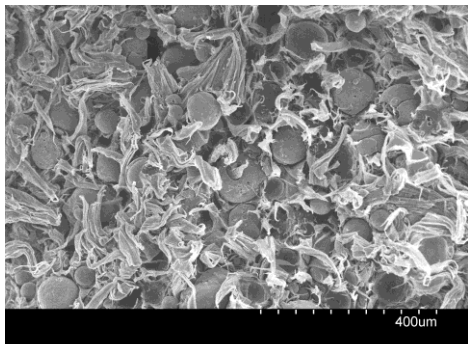


Fig. 4 Micrograph of as cast sample of 60% filler in HDPE matrix.

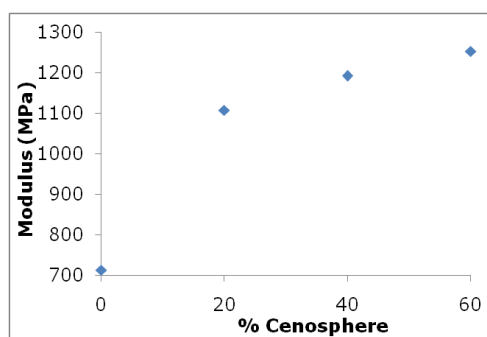


Fig. 5 Modulus as function of filler content

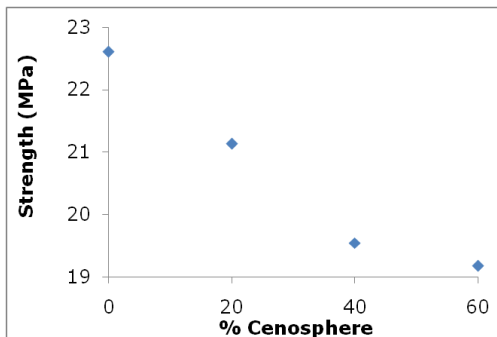


Fig. 6 Strength as function of filler content

Parametric Optimization in Hot Turning of Inconel 718 alloy using Taguchi Method

Venkatesh Ganta¹ and D. Chakradhar²

1 Dept. of Mechanical Engg., National Institute of Technology Karnataka, Surathkal, Mangalore 575025, India. email:venkatesh.8056@gmail.com

2 Dept. of Mechanical Engg., National Institute of Technology Karnataka, Surathkal, Mangalore 575025, India. email:chakradhar.d@nitk.edu.in

ABSTRACT: This paper investigates the effect and parametric optimization of machining parameters on material removal rate and surface roughness in a hot turning operation by using Taguchi method. The process parameters considered are cutting speed, feed rate, depth of cut and workpiece temperature. An orthogonal array, the signal-to-noise ratio (S/N), and the analysis of variance (ANOVA) were employed to the study of performance characteristics in the hot turning of nickel based Inconel 718 super alloy using TiAIN PVD coated carbide insert cutting tools. Through this study not only the optimal machining parameter were obtained, but also the main process parameters that affect the machining performance in hot turning were found.

Keywords: Hot Machining, Surface Roughness, Metal Removal Rate, Taguchi Method.

INTRODUCTION

Nickel based Superalloys, have high strengths at elevated temperatures, strong resistance to chemical degradation and superior wear resistance under severe temperature and pressure conditions (Ezugwu et al., 2005). Among these alloys Inconel 718 has been widely used due to its exceptional thermal resistance and the ability to retain its mechanical properties at elevated temperatures over 700°C which make them attractive toward various applications, such as in aerospace and gas turbine applications, cryogenic storage tanks, nuclear fuel element spacers, pump body components, downhole shafts, wellhead parts. However, these desirable material properties make them extremely difficult to machine at room temperature using conventional methods.

The main aim of machining is to produce the parts most economically. An unsuitable decision causes expensive production cost and decreases the machining quality (Ozler and Tosun 2002). The materials having mechanical

properties like high strength and hardness, good corrosive resistance, weldability, low distortion, which are frequently used in aerospace and nuclear industries, are generally difficult to cut materials. Conventional machining of these materials have problems like low speeds, feeds, poor surface finish, high tool wear, less tool life, low production, in another aspect unconventional machining is often employed for machining of these materials. But, the unconventional machining of these materials involves a high capital cost and offers a low material removal rate (MRR). To overcome these problems hot machining is one of the most potential techniques developed to machine difficult to cut materials.

In hot machining a part or whole workpiece is heated before or during machining (Lei et al., 2001). Heating of the material makes high hardness of the material become soft, resulting in improved machinability, high production rate, low power consumption. From all these advantages hot machining is extremely used full to machine hard to cut materials like ceramics (Ozler et al.,

4th International Engineering Symposium - IES 2015

March 4-6, 2015, Kumamoto University, Japan

2001). Many researchers have used different heating techniques like laser heating, plasma heating, induction heating, electrical heating and they were proved that these heating techniques are expensive. Several researchers reported that there is an improvement in both surface finish and tool life in hot machining (Akasawa et al., 1987, Uehara et al 1986., Hinds et al 1980, Raghuram et al., 1979, Chen et al., 1973, Pal et al., 1969). In hot machining it was observed that the cutting mechanism of the ceramics changes from brittle fracture type to plastic deformation type (Uehara et al., 1986). Thandri et al. (2010) they conducted experiments in both conventional and hot machining and they observed that hot machining was effective in bringing down the cutting forces, surface roughness and flank wear by about 34%. Tosun et al. (2004) heated high manganese steel with liquid petroleum gas flame and showed that cutting speed and feed rate were the dominant variables on multiple cutting performance characteristics like tool life and surface roughness. The cooling method of the cutting tool is very effective for reducing the tool wear in the hot machining process (Akasawa et al., 1987). In plasma hot machining cutting forces is decreasing by machining high hardness materials (Kitagawa et al., 1990). Hot machining is mainly used in turning. Some researchers used it for shaping and milling also (Pal et al., 1971).

Table 1 Chemical composition of Inconel 718

Element	Composition
Cr	19.0
Ni	52.5
Mo	3.0
Nb	5.1
Ti	0.91
Al	0.5
Fe	18.5
C	0.08
Cu	0.15

Table 2 Parameters and their levels

Cutting parameters	Levels			Units
	I	II	III	
Speed (A)	31	77	120	m/min
Feed (B)	0.05	0.1	0.15	mm/rev
DOC (C)	0.4	0.6	0.8	mm
Temp (D)	200	400	600	°C

Table 3 Experimental results of hot machining

A	B	C	D	Ra	S/N Ratio	MRR	S/N Ratio
31	0.05	0.4	200	0.52	5.67	5.24	14.38
31	0.1	0.6	400	0.59	4.58	9	19.08
31	0.15	0.8	600	0.81	1.83	18.42	25.3
77	0.05	0.6	600	0.63	4.01	13.08	22.33
77	0.1	0.8	200	0.65	3.74	16.6	24.4
77	0.15	0.4	400	0.7	3.09	21.84	26.78
120	0.05	0.8	400	0.36	8.87	19.8	25.93
120	0.1	0.4	600	0.29	8.4	28.08	28.96
120	0.15	0.6	200	0.55	5.19	34.38	30.72

Based on the literature review, research work carried on hot machining on difficult to cut materials is to improve the machinability such as cutting forces, surface roughness and tool wear. After an extensive research and survey of existing heating techniques (Kitagawa et al., 1990; Uehara et al., 1983) it has been concluded that the oxy-acetylene heating set-up will be in expensive compared to others techniques.

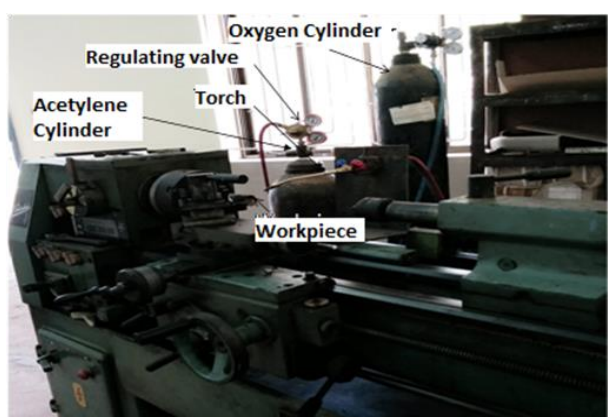


Fig.1. Experimental setup

Experimental setup

An Inconel 718 rod of 32 mm diameter was used for experiments. The chemical composition of Inconel 718 with hardness 40 HRC is shown in Table 1. TiAlN coated carbide insert is specified as SNMP 120408 is used as a cutting tool. The input parameter ranges were decided on the basis of machine capability and pilot experiments. The selected ranges of input parameters are shown in Table 2. In this paper L₉ orthogonal array is employed to analyze experimental results of machining obtained from 9 experiments for hot machining individually varying four parameters speed, feed rate, depth of cut, and workpiece temperature. For conducting experiments, an oxy acetylene heating setup was used to heat the work piece material. Oxy acetylene heating is one of the best choices for hot machining it requires low cost equipment the heat transfer to the workpiece is very low, although the gross heat available and the energy transfer density will be low and metallurgical damage of the workpiece is low (Larine and Martynow., 1966). The flame was generated through the nozzle of torch. A special attachment was used to move the torch mounted on carriage to provide a flexible movement of heat source while machining. During all the experiments, the distance between the torch and workpiece is 25 mm. Flow rates for acetylene and oxygen were adjusted by pressure regulator and kept constant to get a neutral flame, which was used throughout the machining.

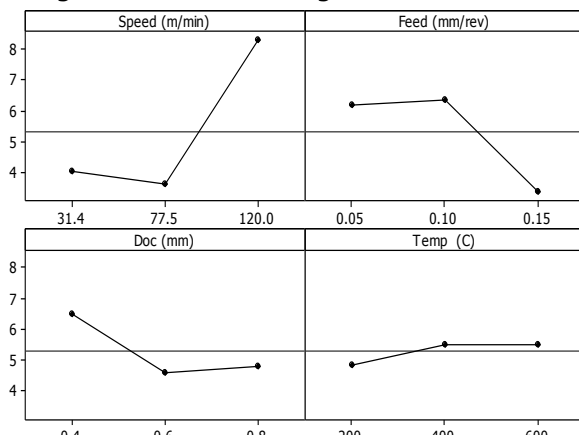


Fig. 2. Main effect plot of S/N ratios of Surface Roughness

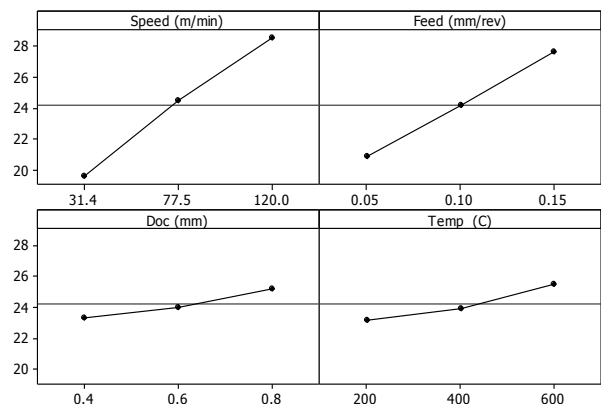


Fig. 3. S/N graph for MRR

Table 4. S/N response table for surface roughness

Parameter	Mean S/N ratio		
	Level 1	Level 2	Level 3
Speed	4.031	3.618	7.490
Feed	6.189	5.576	3.374
DOC	5.727	4.596	4.815
Temp	4.871	5.518	4.749

Table 5. S/N Response table for MRR

Parameter	Mean S/N ratio		
	Level 1	Level 2	Level 3
Speed	19.59	24.51	28.54
Feed	20.88	24.15	27.61
DOC	23.38	24.05	25.21
Temp	23.17	23.93	25.54

Table 6. ANOVA for Surface Roughness

Source	DF	SS	MS	F	%
Speed	2	120.5	60.3	8.67	59.59
Feed	2	67.8	33.9	4.87	16.76
DOC	2	5.2	2.6	0.37	2.57
Temp	2	8.7	4.4	0.63	4.3
Total	8	202.2			

Table 7. ANOVA for Metal Removal

Rate

Source	DF	SS	MS	F	%
Speed	2	39.8	19.92	5.32	62.06
Feed	2	16.8	8.43	2.26	26.28
DOC	2	6.5	3.29	0.87	10.25
Temp	2	0.9	0.4	0.10	1.40
Total	8	64.1			

DESIGN OF EXPERIMENTS

Taguchi method is a powerful tool for the design of high quality systems. It provides a simple, efficient and systematic approach to optimize design for performance, quality and cost. To study effect of four process parameters like speed, feed, depth of cut, workpiece temperature on two important output parameters surface roughness, MRR. Based on the degree of freedom of process parameters, L9 orthogonal array is selected. Accordingly, 9 experiments were carried out to study the effect of machining input parameters on output parameters. In all tests surface roughness was measured by Mitutuyo surface tester and metal removal rate is calculated by the ratio of weight loss of the workpiece to the time. The specimen was weighed before and after machining by using digital weighing scale. The time was measured using a digital stopwatch. Parameter design study involves control and noise factors.

ANALYSIS OF S/N RATIO

The surface roughness of the hot machined parts has been considered as smaller the better, whereas the metal removal rate, is considered as higher the better. These considerations have been taken for good quality characteristics of interest.

For the present study S/N ratio for metal removal rate is calculated using the formula.

$$\eta = -10 \log \frac{1}{n} \sum (1/y_i^2) \quad (1)$$

S/N ratio for surface roughness of the machined parts is calculated using the formula

$$\eta = -10 \log \frac{1}{n} \sum (y_i^2) \quad (2)$$

The experimental results and S/N ratios calculated according to Taguchi's "The smaller the better" and "larger the best" quality characteristics were given in Table 3.

RESULTS AND DISCUSSION

The quality of machined surface formed in hot turning is evaluated in terms of average surface roughness (Ra) and metal removal rate MRR. S/N ratios of the surface roughness and MRR which will be used to determine the optimal levels of each variable, were calculated according to the Eq. (1) & (2) are shown in Table 3. Figure 2 and Figure 3 illustrates the graphs of S/N ratios for surface roughness and material removal rate respectively. The optimal process parameters to minimize the surface roughness are A₃ B₁ C₁ and D₂ are shown in Table 4. The optimum process parameters to maximize the material removal rate are A₃ B₃ C₃ D₃ are shown in Table 5. Minimum surface roughness 0.29 μm was obtained at 120 m/min cutting speed, 0.1 mm/rev feed rate, 0.4 depth of cut and 600°C temperature are shown in Table 4. Maximum metal removal rate 34.38 gm/min was obtained at 120 m/min cutting speed, 0.05 mm/rev feed rate, 0.8 depth of cut and 400°C temperature are shown in Table 5.

ANALYSIS OF VARIENCE

The purpose of ANOVA analysis is to find the effect of design parameters on quality characteristics (Yang and Tarng., 1998). The results of ANOVA which was done to determine the significant level of variable on the surface roughness obtained during the hot turning of Inconel 718 is given in Table 6. The ANOVA is analyzed at significance level of α=0.05, i.e. for the 95% confidence level. Table 6 shows the percentage contribution of process parameters on the surface roughness. The most significant parameter effecting the surface roughness is the cutting speed 62.06%. The other variables that have effect on Ra are feed rate 26.68%, depth of cut 10.25% and workpiece temperature 1.40%. Table 7 shows ANOVA that determines the significant level of parameters on the MRR. The most efficient parameter on the MRR is cutting speed 59.59%, feed rate 16.76%,

4th International Engineering Symposium - IES 2015

March 4-6, 2015, Kumamoto University, Japan

workpiece temperature 4.30% and depth of cut 2.57%.

CONCLUSIONS

This paper has discussed an application of the Taguchi method for optimizing the cutting parameters in hot machining of Inconel 718 alloy.

- From the investigation, minimum surface roughness 0.29 μm was obtained at 120 m/min cutting speed, 0.1 mm/rev feed rate, 0.4 mm depth of cut and 600°C temperature.
- The maximum metal removal rate 34.38 gm/min was obtained at 120 m/min cutting speed, 0.05 mm/rev feed rate, 0.8 mm depth of cut and 400°C temperature.
- Cutting speed is the most significant parameter that effects the surface roughness.
- Cutting speed and feed rate are the most significant parameters that effects the material removal rate.

REFERENCES

- [1] Antony J (2003) Design of experiments for engineers and scientists. ISBN: 0750647094. Elsevier, New York
- [2] Ezugwe E.O, J. Bonny, Finish machining of nickel-base Inconel 718 alloy with coated carbide tool under conventional and high-pressure coolant supplies, *Tribology Transactions* 48 (2005) 76–81.
- [3] Pal D. K., Basu S. K. (1971), Hot machining of austenitic manganese steel by shaping, *International Journal of Machine Tool Design Research*, Vol. 11, pp. 45–61.
- [4] Madhavulu G, Basheer Ahmed, (1994), Hot Machining Process for improved Metal Removal Rates in turning operation, *Journal of Material Process Technology*, Vol. 44, pp. 199–206.
- [5] Hsiao YF, Tarng YS, Huang WJ. (2010), Optimization of plasma arc welding parameters by using the Taguchi method with the grey relational analysis. *Journal of Material Manufacturing Process* Vol. 23(1) pp. 51–58
- [6] Lopez de Lacalle, L.N., Sanchez, J.A., Lamikiz, A.Celaya.(2004), Plasma assisted milling of heat-resistant super alloys, *Journal of Manufacturing Science & Engineering*, Vol. 126, pp.274–285.
- [7] Maitya,K.P, Swain P., (2008), An experimental investigation of hot-machining to predict tool life, *Journal of materials processing technology* Vol. 198, pp. 344–349.
- [8] Uehara Kunio, Hideo Takeshita.(1986) .Cutting Ceramics with a Technique of Hot Machining.*Annal CIRP*, Vol. 32, pp. 55–58.
- [9] Ozler,L., Inan,A C. Ozel. (2001), Theoretical and experimental determination of tool life in hot machining of austenitic manganese steel, *International Journal of Machine Tools & Manufacture* Vol. 41, pp.163–172
- [10] Ragunath N, Pandey PM.(2007), Improving accuracy through shrinkage modeling by using Taguchi method in selective laser sintering. *International Journal of Machine Tools Manufuring* Vol. 47, pp. 985–995
- [11] Lei,Y.C. Shin, F.P. Incropera (2001), Experimental investigation of thermo-mechanical characteristics in laser assisted machining of silicon nitride ceramics, *Journal of Manufacturing Science & Engineering*, Vol. 123, pp.639–646.
- [12] Thandra S.K. and Choudhury S.K..(2010), Effect of cutting parameters on cutting force, surface finish and tool wear in hot machining, *International Journal of Machining and Machinability of Materials*, Vol. 7, Nos. ¾.
- [13] Kitagawa,T., Maekawa K. (1990), Plasma Hot Machining for new Engineering materials. *Wear*, Vol. 139, pp.251–26
- [14] Kitagawa T .and Maekawa K .(1988), Plasma hot machining for high hardness metals, *Bulletin of Japan Society of Precision Engineering*, Vol. 22, pp.145–151.
- [15] Chen, N.N.S, Lo K.C., 1974. Factors affecting tool life in hot machining of alloy steels, *International Journal of Machine Tool Design Research*, Vol. 14, pp.161–173.
- [16] Tosun Nihat, Latif Ozler. (2002), A study of tool life in hot machining using artificial neural networks and regression analysis method, *Journal of Materials Processing Technology* Vol. 124, pp. 99–104.
- [17] Tosun N. and Ozler L. (2004), Optimization for hot turning operations with multiple performance characteristic, *International Journal of Advanced Manufacturing Technology* Vol. 23, pp. 777–782.
- [18] Patel Pulak KM,Pandy M, VenkateswaraRao P.,(2010),Optimisation of process parameters for multi-performance characteristics in EDMof Al₂O₃ ceramic composite, *International Journal of Advanced Manufacturing Technology* Vol. 47, pp. 1137–1147
- [19]Raghuram V, M.K. Muju.(1979), Improving tool life by magnetization in hot machining, *International Journal of Machine Tool Design Research*, Vol. 20, pp.87–96.
- [20]Yang W.H., Tarng, Y.S. (1998), Design optimization of cutting parameters for turning operations based on the Taguchi method, *Journal of Material. Process.Technology*. Vol. 84, pp. 122–129.

Hot Corrosion-Erosion Behaviour of HVOF Sprayed NiCrFeSiB Coatings on Boiler Tube Steels

M.R. Ramesh^{1*}, S. Prakash², S.K. Nath², Mrityunjay Doddamani¹

1 National Institute of Technology Karnataka, Surathkal-575 025, India

2 Indian Institute of Technology Roorkee, Roorkee-247 667, India

Email: rameshmr@nitk.edu.in

ABSTRACT: Fireside corrosion and erosion of structural materials at elevated temperature in complex multicomponent gas environments that include particulates are potential problems in many fossil energy systems, especially those using coal as feedstock. Combating these problems involves a number of approaches, one of which is the use of protective coatings. High-Velocity-Oxy-Fuel thermal spraying with oxygen and liquid petroleum gas as the fuel gas has been used to deposit NiCrFeSiB alloy coatings on boiler tube steels. The coatings and alloy samples were exposed to actual service conditions of the coal fired boiler for 1000 hours. The extent of erosion-corrosion has been monitored by measuring the thickness loss and weight change of the samples after exposure. NiCrFeSiB coatings showed superior hot corrosion resistance in the coal fired boiler due to the protective oxides formed on the surface, mainly consist of SiO₂ and Cr₂O₃.

Keywords: HVOF thermal spray process, Erosion, Hot corrosion, NiCrFeSiB coating, Boiler tube steel, Characterization

INTRODUCTION

Superheaters are a series of tubes placed within the flue gas path of the boiler, whose purpose is to heat the boiler steam beyond saturated conditions. The supersaturated steam is then delivered to a turbine for electric power generation in thermal power plants, to run plant and machineries in a process and manufacturing industry.

Fire side corrosion and erosion of metallic structural materials at elevated temperature in complex multicomponent gas environments that include particulates are potential problems in many fossil energy systems, especially those using coal as a feedstock (Natesan 1993). The fly ash which is the combustion product of pulverized coal in a thermal power station at high temperature is likely to form deposits on the boiler tubes in its path. The buildup of ash deposits in the convective pass may also be detrimental from a corrosion aspect. However, when passing through the latter stages of the boiler where the temperatures are

substantially lower, the fly ash displays rebound as opposed to captive behavior. This causes localized erosive wear that can lead to unscheduled and costly boiler tube failures (Suckling and Allen 1995).

The corrosion steps start with the formation of Na₂O and K₂O in the flame, and the reaction with SO₃ to form sodium or potassium sulfate (Na₂SO₄ or K₂SO₄) in the ash deposit. Iron oxide, alkali sulfate and sulfur trioxide, react to form the trisulfates on the cooler tube surface. These alkali-iron trisulphates are molten at the operating temperature of the boiler due to their low melting temperature and can flux the scale or react with metallic iron resulting in the formation of massive amount of FeS in the corroded areas (Srivastava et al. 1997 and Weulersse-Mouturat et al. 2004). Fly ash erosion accelerates tube wastage by direct material removal and by removal of fireside oxide which increases the fireside oxidation rate. The free oxygen content in power plant boiler atmosphere is sufficient to account for a combined erosion-

4th International Engineering Symposium - IES 2015

March 4-6, 2015, Kumamoto University, Japan

corrosion process, consisting of an oxidizing gas at elevated temperature carrying erosive fly ashes which impact against metallic surfaces.

Combating erosion-corrosion problems involves a number of approaches, one of which is the use of protective coatings. In the present study the high velocity oxy fuel process belongs to thermal spray technology has been used to deposit self-fluxing alloy on boiler tube materials. The hot corrosion-erosion behaviour of coatings are studied in actual service conditions of the boiler.

EXPERIMENTAL PROCEDURE

Substrate Materials

Low carbon steel ASTM-SA210 grade A1 (GrA1) and chrome moly steel ASTM-SA213-T11 and ASTM-SA213-T22, which are used as material for water wall, super heater and reheater tubes in some coal fired thermal power plants in northern part of India has been used as a substrate in the study.

Deposition of the Coatings

HVOF spraying has been carried out using a HIPOJET 2100 equipment (M/S Metallizing Equipment Co. Pvt. Ltd. (MEC), Jodhpur, India), which uses the supersonic jet generated by the combustion of liquid petroleum gas and oxygen mixture. A commercially available NiCrFeSiB powder (MEC-1260A) of nominal composition Ni-14.5Cr-4.3Fe-4.3Si-3B- 0.6C (wt. %) was used in the study. Parameters used during HVOF spraying are Oxygen flow rate-250 l/min, LPG Fuel flow rate-60 l/min, Air-flow rate-700 l/min, Spray distance-200 mm and Powder feed rate-28 g/min. The samples of dimensions 20mm × 15mm × 5mm were coated on all the sides.

Erosion-Corrosion Studies

The coatings and alloy samples were exposed to actual service conditions of the coal fired boiler for 1000 hours. The samples were tested in super heater region of boiler of Guru Gobind Singh Super Thermal Plant, Ropar, India. The flue gas temperature in this region is about $778 \pm 20^\circ\text{C}$ and volumetric flow of flue gas was around $250 \text{ m}^3/\text{s}$. The samples were exposed to combustion

gases for 10 cycles each of 100 hours duration and followed by one hour cooling at ambient conditions. After the end of each cycle thickness change and weight change of the samples were measured subsequently.

RESULTS

Coatings Characterisation

NiCrFeSiB powder particles have spherical morphology and the particle size distribution of the powder found to be $-45 + 15\mu\text{m}$. The average value of coating thickness was found to be $295 \mu\text{m}$. The porosity measured along the cross-sectional area of the coatings is found to be less than 0.5%. The lower value of porosity obtained for the HVOF sprayed coatings may be related to higher kinetic energies of powder particles and to the melting behavior exhibited by the particles.

The microstructure of NiCrFeSiB coatings (Fig.1a) has a dense and isotropic structure. The chemical composition profile (Fig.1b) indicates homogeneous elemental concentration throughout the thickness of the coating which indicates complete melting of the coating powder. The X-ray diffraction (Fig.2) patterns for the coatings exhibit almost similar peaks as compared to that of the powder indicating no change in their phase composition after spraying. The powder and coating have a nickel-rich FCC structure as a principal phase. The presence of CrSi and CrB phases indicate the melting of powder during spraying to the extent of dissolution of the borides and silicides in the liquid phase. The dissolution of B and Si makes the crystallization process impossible. Evidently, a very broad peak accompanied by reduction in peak intensity at 2θ of about 44.5° can be observed for the as-sprayed coating in comparison to the XRD pattern for the initial powder. This difference reveals the formation of amorphous matrix.

Thermo gravimetric studies and Thickness Monitoring

The scale developed on the substrate steel is fragile, showed intense spalling resulted in a weight loss throughout the exposure to the boiler environment for 1000 hours.

4th International Engineering Symposium - IES 2015

March 4-6, Kumamoto University, Japan

Weight gain square curve (Fig.3) shows considerable deviations from the parabolic rate law. The fluctuation in the weight change data as observed from the plot might be due to fly ash erosion and suspected spalling of formed oxide scale accompanied with falling off and regeneration of the ash deposits on the surface of the exposed sample. Coated T11 steel showed a maximum weight gain followed by coated T22 and GrA1 steels. The parabolic rate constant K_p for NiCrFeSiB coated GrA1, T11 and T22 steels are found to be 0.01×10^{-10} , 0.027×10^{-10} and $0.018 \times 10^{-10} \text{ g}^2 \text{ cm}^{-4} \text{ s}^{-1}$ respectively.

Erosion-corrosion in terms of thickness loss from the surface of exposed samples is represented in bar chart (Fig.4). Degradation rate at the end of 1000 hours of study for NiCrFeSiB coated GrA1, T11 and T22 steels are found to be 6.2, 8.62 and 7.24 mpy respectively which are very small.

X-ray Diffraction Analysis

The main phases identified on the surface of exposed NiCrFeSiB coated steels (Fig.5) were Ni, NiO, Cr₂O₃, and Fe₃O₄ along with mixed oxide spinals NiCr₂O₄, and Ni₂SiO₄. XRD result also shows the presence of Al₂O₃ and FeS phases indicates the fly ash deposits on the surface of exposed coated steels.

EPMA Analysis

Elemental X-ray mapping for the NiCrFeSiB coated T11 steel after exposure to superheater zone of coal fired boiler is shown in Fig.6. By combining the maps for O, Si and Cr, it is revealed that, thin oxide layer of SiO₂ and Cr₂O₃ formed on the surface of corroded coating. Presence of SiO₂ in the surface scale might be formed from the oxidation of coating element and partly due to formation of condensed phases from boiler environment (Fly ash deposit). A thin streaks of Ni co-exists with O, confirm the presence of NiO. The presence of patches of Na and S on the surface provides the evidence of interaction of ash with the oxide scale. The arrow mark shown on the Fe map indicates the outward diffusion of Fe from the substrate in to the coating. The absence of oxygen and other corrosive species beneath the uppermost oxide scale

indicates protective behavior of the NiCrFeSiB coating in the given environment.

DISCUSSION

The problem of erosion of superheater and reheater tubing caused by fly ash cannot be ignored. Even though, fly ash consisted of very small particles, high velocity gas streams wear away or erode the leading tube (French 1983). The NiCrFeSiB coated GrA1, T11 and T22 boiler steels show better erosion-corrosion resistance and thickness loss was about 1/13, 1/4, 1/4 respectively that of uncoated steels. Degradation rate for coated GrA1, T11 and T22 steels, expressed in mils per year are 6.2, 8.62, and 7.24 mpy respectively. The weight change of the coated samples during 1000 hours of exposure (Fig.3) found to follow nearly parabolic behavior and hence the oxide scale formed on the surface act as barrier to the diffusion of oxidizing and corrosive species. Further EPMA (Fig.6) analysis along the cross-section confirm the absence of O, Na and S, beneath the uppermost oxide scale indicating protective behavior of the NiCrFeSiB coatings in the given environment. Although, 1000 hours of exposure to boiler environment is relatively short duration to extrapolate the obtained result to predict the coating performance in long term of service, the erosion corrosion behavior of NiCrFeSiB coating is promising in comparison to substrate steels used in the present study. XRD and EPMA analysis shows that the thin and continuous oxide scale mainly composed of protective oxides of SiO₂, Cr₂O₃ and NiO. Although, XRD analysis on the surface showed no peaks corresponding to Si-related oxide phases, EPMA results supports the existence of SiO₂ in the oxide scale. The silica is obviously amorphous, might be formed from oxidation of coating element and partly from the condensed deposits of boiler environment on the surface of exposed sample. Presence of mixed spinel oxides of NiCr₂O₄, and Ni₂SiO₄ has been revealed by X-ray diffraction on surface. Wu et al, (2006) and Kerr (1975) have reported spinels Ni₂SiO₄ have similar

4th International Engineering Symposium - IES 2015

March 4-6, 2015, Kumamoto University, Japan

crystallographic and thermodynamic properties as NiCr_2O_4 , can hinder the ion diffusion effectively during oxidation and decrease the oxidation rate.

Presence of Fe and Ni along the coating-substrate interface as indicated in EPMA analysis along the cross section has shown the interdiffusion of Fe from substrate into coating and Ni from coating into substrate.

CONCLUSIONS

- HVOF thermal spraying with oxygen and liquid petroleum gas as the fuel gas has been successfully used to deposit NiCrFeSiB alloy coatings having dense and layered structure with porosity less than 0.5%. Coating has retained the phase of the powder, having nickel-rich FCC structure as a matrix phase.
- The erosion corrosion behavior of the NiCrFeSiB coating is promising in comparison to substrate steels in the coal fired boiler. All the uncoated steels suffered a weight loss. Lower thickness loss from the surface has been observed and the degradation rate is minimum.
- The protective oxides formed on the surface mainly consist of SiO_2 , Cr_2O_3 and NiO . Low porosity content (<0.5%) and rapid growth of protective oxides during the initial cycles lead to enhanced hot corrosion resistance of these coatings.
- The coatings got oxidized only at the uppermost surface to form thin protective oxide scale and rest of the coatings remain unoxidised.

REFERENCES

- [1] French, David N (1983), Metallurgical Failures in Fossil Fired Boilers, A Wiley-Interscience Publication, Singapore
- [2] Kerr, T W, (1975), Hot corrosion and oxidation studies of pure nickel and Ni-Cr, Ni-Si and Ni-Cr-Si alloys at 1000 °C. In: Rep. AD-A024, U.S. Department of Commerce, pp. 708.
- [3] Natesan, K, (1993), Applications of coatings in coal-fired energy systems, Surface and Coatings Technology, Vol. 56, pp. 185-197.
- [4] Srivastava, S C and Godiwala K M, (1997), Fuel ash corrosion of boiler and superheater tubes, Journal of Materials Science, Vol. 32, pp. 835-849.
- [5] Suckling M and Allen C, (1995), The design of an apparatus to test wear of boiler tubes, Wear, Vol. 186-187, pp. 266-272.
- [6] Weulersse-Mouturat K, Moulin, G, Billard,P and Pierotti,G, (2004), High Temperature Corrosion of Superheater Tubes in Waste Incinerators and Coal-

Fired Plants, Mater.Sci. Forum, Vol. 461-464, pp. 973-980

[7] Wu,Y N, Wang, Q M, Ke, P L, Sun, C, Gong, J, Wang, F H, and Wen, L S, (2006), Evaluation of arc ion plated NiCoCrAlYSiB coatings after oxidation at 900-1100°C, Surface and Coatings Technology, Vol. 200, pp. 2857-2863.

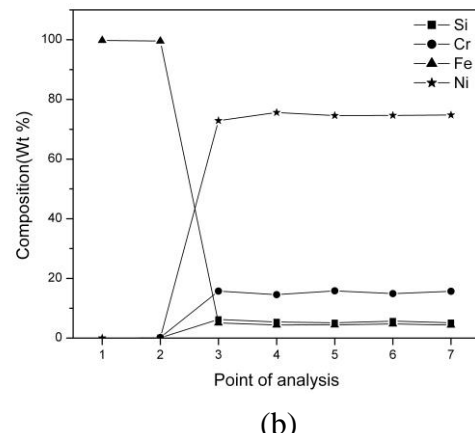
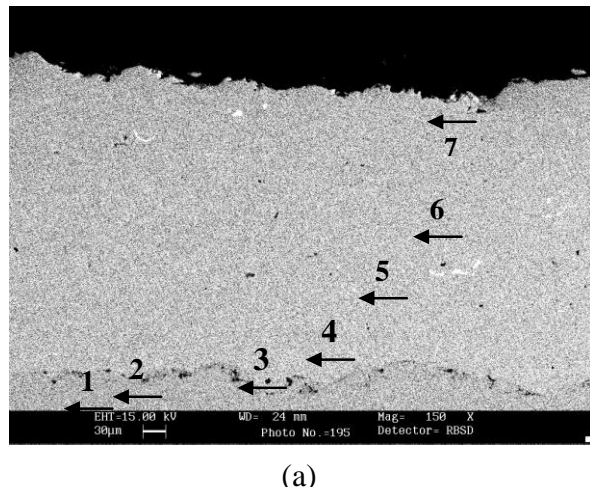


Fig. 1 (a) BSEI across the cross-section of the as-sprayed coatings (b) EDAX point analysis (wt %)

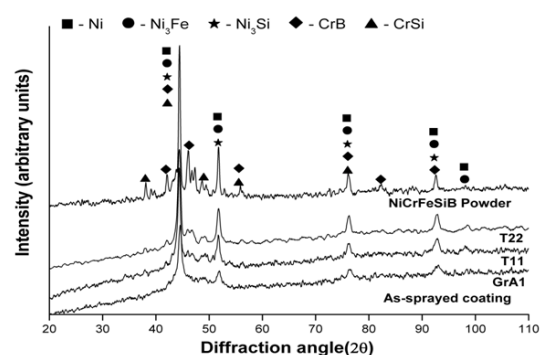


Fig. 2 X-ray diffraction patterns for powder and as-sprayed coating

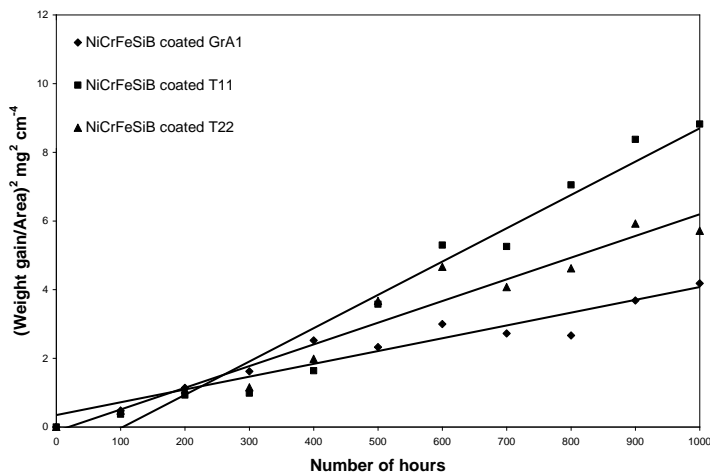


Fig.3 (Weight change/area) 2 plot for NiCrFeSiB coated steels

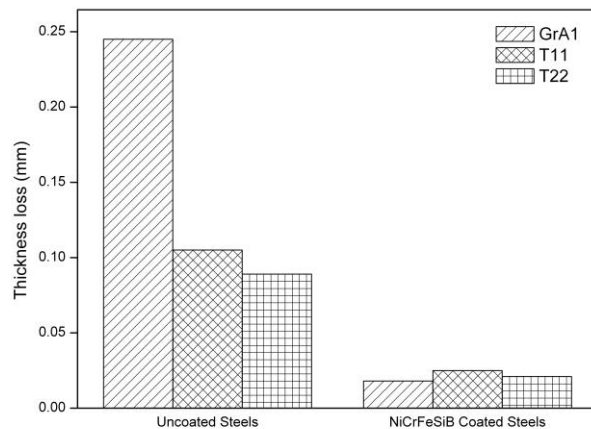


Fig.4 Bar chart indicating the thickness lost after 1000 hours of exposure to super heater zone of coal fired boiler

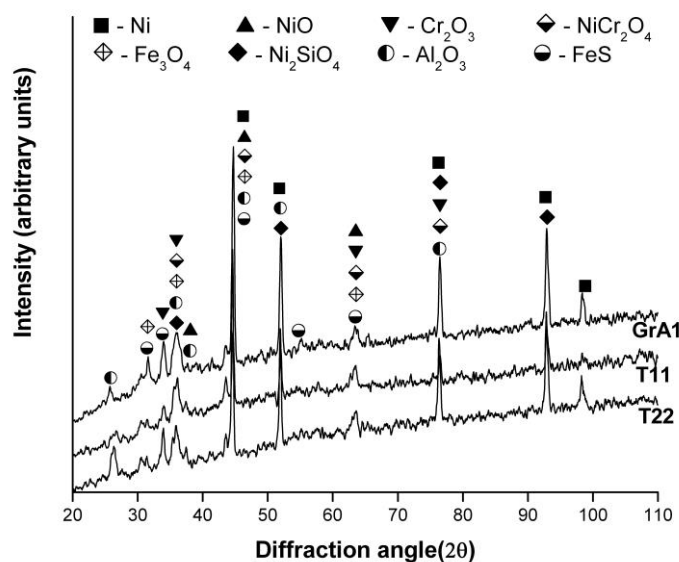


Fig.5 X-ray diffraction patterns for coated steels after 1000 hours of exposure

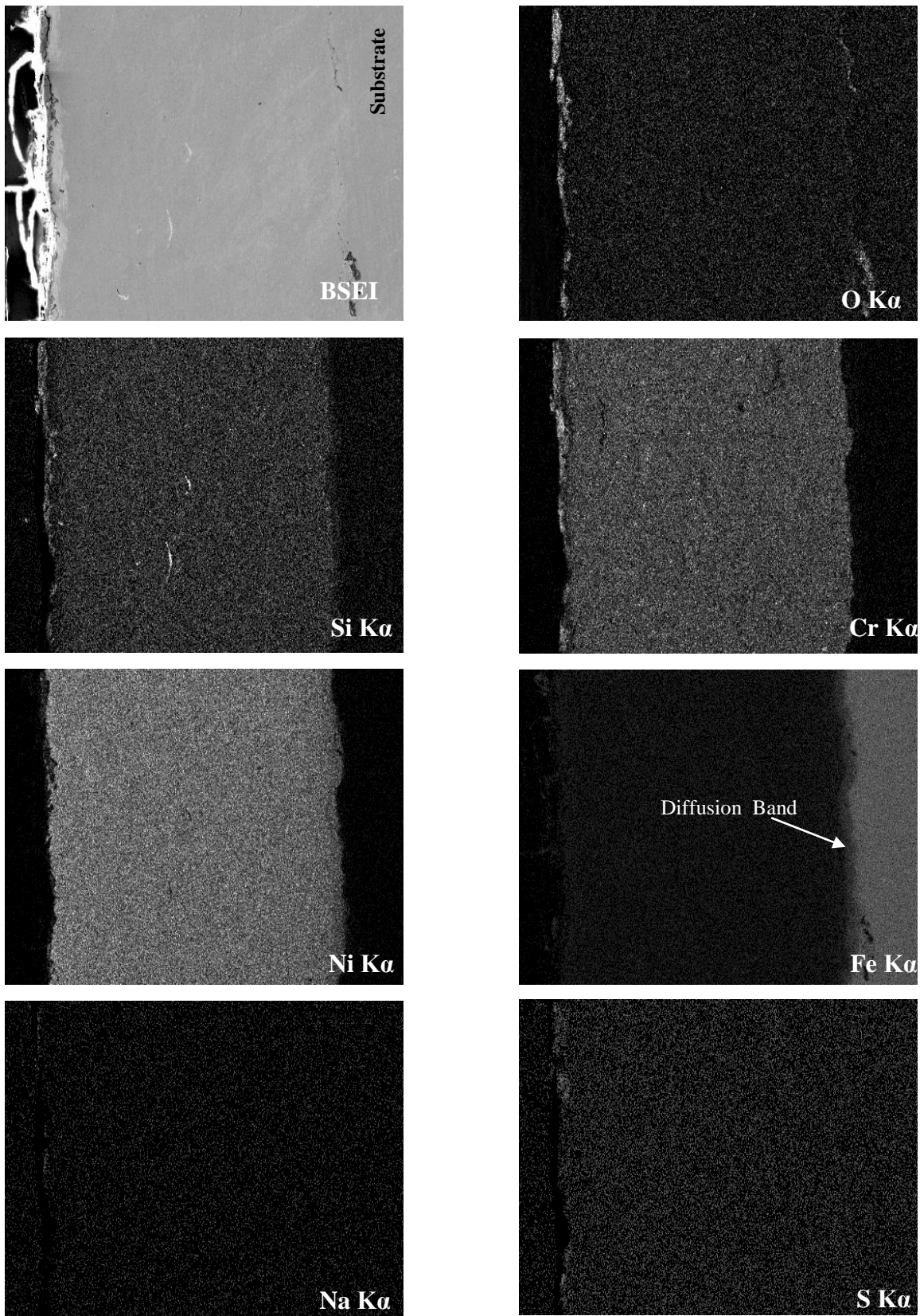


Fig.6 Elemental X-ray mapping along the cross-section of the NiCrFeSiB coated T11 steels exposed to superheater zone of coal fired boiler for 1000 hours

Purification of Biogas by Treating Combined Absorption and Adsorption Chemical Method

Muhammad Rashed Al Mamun and Shuichi Torii

*Department of Advanced Mechanical System Engineering,
Graduate School of Science and Technology,
Kumamoto University, 2-39-1 Kurokami, Kumamoto, 860-8555 Japan
E-mail: rashedshahi@gmail.com; torii@mech.kumamoto-u.ac.jp*

ABSTRACT: This study was undertaken with the aim of evaluating biogas generated from organic wastes in lab scale and purification process for the biogas in order to be used later as biofuel for internal combustion engines. This process was achieved in combined adsorption and absorption chemical way. The results show that the average inlet H₂S concentration was 365 ppm and 384 ppm for T1 and T2 which was reduced to 14 ppm and 29 ppm with the derived activated carbon and zero-valent iron (Fe⁰) adsorbent nanomaterial respectively. The average 34% concentration of CO₂ in the raw biogas was reduced to below 3% and 5% in T1 and T2, respectively. The maximum 97% H₂O concentration removal efficiency was realized in T1 by treating silica gel. This study represents a 42% improvement in the CH₄ content from the initial average value of 67% to above 95% for both tests. Thus, given the successful contaminants elimination, the combined chemical process is a feasible system for biogas purification.

Keywords: Anaerobic digestion, Biogas, Adsorption, Absorption, Purification, Methane

INTRODUCTION

Due to strategic of energy crisis and environmental reasons, currently, there is an increasing interest in biofuels as alternative energy source. The Kyoto Protocol has explicitly defined methane as one of the six key greenhouse gases where the global warming potential of methane is 25 times higher than that of carbon dioxide (United Nations, 1998). In this regards, anaerobic digestion of solid biomass is capable of producing enrich methane contain biogas and reducing the global warming effects caused by the biodegradable wastes. Biogas is a combustible gas generated by micro-organisms in the absence of air known as anaerobic metabolism at digestion plant for organic wastes, both mesophilic (30 °C) and thermophilic (65 °C) (Al Mamun and Torii, 2015). It is a medium-energy content fuel (~22 MJ/kg) (Horikawa et al.,

2004). It can be produced natural fertilizer in farms after 25-45 days of residence time. Due to its gaseous nature and the impossibility of producing it intensively, it is not attractive for large scale power generation. However, recently, a new approach for power generation has been emerging. The biogas generated in the plants can be used as fuel for internal combustion engines becomes a very attractive alternative for power generation because of its very low cost, high benefit cost ratio and very high positive impact on the environment.

Biogas is made up mainly of methane (CH₄, 40-75%) and carbon dioxide (CO₂, 15-60%). It also contains trace amounts of other components such as water (H₂O, 5-10%), hydrogen sulfide (H₂S, 0.005-2%), siloxanes (0-0.02%), halogenated hydrocarbons (VOC, < 0.6%), ammonia (NH₃, <1%), oxygen (O₂, 0-1%), carbon

4th International Engineering Symposium - IES 2015

March 4-6, 2015, Kumamoto University, Japan

monoxide (CO, <0.6%) and nitrogen (N₂, 0-2%), its composition varies depending on the type of biomass and production methods (Wellinger and Lindberg, 2005, Wheless and Pierce, 2004, Hagen et al., 2001, Persson and Wellinger, 2006, Krich et al., 2005). The biogas calorific power is proportional to the CH₄ concentration. Therefore, biogas to be used as fuel for internal combustion engines, it has been recommended a CH₄ concentration greater than 90% (Harasimowicz et al., 2007). However, CO₂ has a typical concentration of ~40%. This high CO₂ concentration reduces the engine power output proportionally to its concentration, limiting the use of biogas such as in power plants and in internal combustion engines (Marchaim, 1992). The high content of H₂S causes corrosion in the metallic parts at the interior of the engine. The H₂S is an inorganic acid that attacks the surface of metals when they replaced in direct contact. Sulfur stress cracking (SSC) is the most common corrosive mechanism that appears when the metal makes contact with H₂S. Sulfides of iron and atomic hydrogen are formed in this process. This mechanism starts to take place when the H₂S concentration is higher than 50 ppm (Gosh, 2007). The admission valves, bronze gears and the exhaust system are also attacked by the presence of H₂S. The degree of deterioration of the engines varies considerably. Results obtained experimentally on this regard is contradictory (Marchaim, 1992). It has been found that H₂S in biogas diminishes the life time of the engine by 10 to 15% (Horikawa et al., 2004). Finally, time between oil changes is reduced since lubricant oils contain H₂S and corrosion inhibitors to protect the engine. It increases the maintenance cost of the engine. Water also the leading corrosion causing agent in compressors, gas storage tanks and engines due to reaction with H₂S, NH₃ and CO₂ to form acids, accumulation in pipes and condensation and/or freezing due to high pressure (Ryckebosch et al., 2011). But these entire problems are possible to prevent only after removing CO₂ H₂S and water vapour from crude biogas.

Various methods for biogas cleaning and purifying are used and comprise the removal of carbon dioxide, the drying of the gas, the removal of trace substances such as hydrogen sulphide, oxygen, ammonia, nitrogen or siloxanes (Ryckebosch et al., 2011). But, several drawbacks also have of these methods include selectivity of chemicals used, high energy requirement for regeneration, stability of the method, waste liquids impact on environmental, large size equipment and high corrosion rate. Herein, we report the removal of CO₂, H₂S and H₂O by treating nanotechnology because of providing high surface areas of nanomaterials, developing a nanoscale adsorbent with high adsorption capacity becomes promising for hydrogen sulfide removal (Li et al., 2007, Yan et al., 2010).

We used calcium oxide (CaO), zero valent iron (Fe⁰), Activated carbon, silica gel and Sodium sulfate (Na₂SO₄) for the removal of CO₂, H₂S and H₂O. The aim of the study is to optimize purification process in terms of low energy consumption and high efficiency giving high methane content in the purified gas. We propose that, the results of the experimental work are used in the design of biogas treatment system especially in the farm sectors.

MATERIALS AND METHODS

A. Anaerobic metabolism unit

A piece of equipment which can turn biodegradable waste into usable fuel energy in absence of oxygen is known as bio-digester. A laboratory scale batch digester made of 200 L polypropylene tank (used as a reactor) with an air tight rubber gasket was used for biogas production.

B. Preparation of feedstocks

Four organic wastes namely: cafeteria waste (CW), vegetable waste (VW) and fruit waste (FW) was collected from Kumamoto university, Kokai vegetable market, Kumamoto, Japan. And cow manure (CM) was collected from dairy farm, Fukuoka, Japan. Then all substrates were crushed into small pieces of 2 mm sizes with mechanical blender except (CM). The blended sample was mixed with

equal proportion CW: VW: FW: CM (1:1:1:1) and diluted with tap water in a ratio of 1:1. The prepared feedstock was fed by a volume of 160 L in the biogas digester.

C. Purification materials

For the laboratory study, all chemicals were reagent grade or above and used without further purification. The purification materials were used divided into two categories namely: test 1 (T1) (calcium oxide (CaO), activated carbon and silica gel) and test 2 (T2) (calcium oxide (CaO), Zero-valent iron (Fe^0) and sodium sulfate (Na_2SO_4)) were used to evaluate the removal efficiency of CO_2 , H_2S , and H_2O from the gas stream respectively. All purification reagents were derived from Kanto Chemical Co., Ltd, JAPAN. Calcium Oxide (CaO), Sodium sulfate and silica gel was crushed manually into powder form to increase the internal surface area.

D. Experimental procedure

The experiments have been carried out in laboratory scale set-up schematically as shown in Fig. 1. The set-up consists of three sections: a metabolism section to generate the desired biogas, a contaminants removal section to purify the biogas and an analysis section. During the study the experiment was operated batch wise with respect to absorption and adsorption phase. The first section (1) is digester as previously described. The second (2) section are raw gas collection chamber, purification and raw biogas sampling section. And the third (3) section is the purified biogas sampling bag. The purification unit consists of three glass flasks (2 L). The first flask contains CaO solution was varied from 1-10 g per liter of water for test 1 and 2, respectively. The raw gas collection flask and first purification flask was interconnected by 5 mm diameter 0.4 m long hose pipe. Under batch mode conditions, the raw biogas is introduced by 5 mm diameter 0.3 m long glass tubing at 0.3 mm above from the bottom of the absorber flask as small bubbles through the CaO solution to remove CO_2 , in both tests.

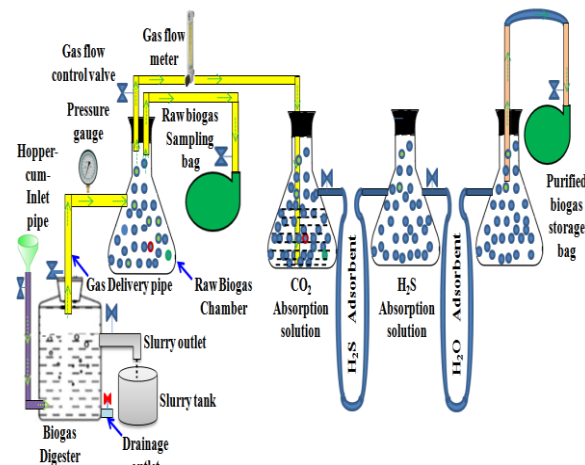


Fig.1. Schematic of experimental apparatus for purification of methane in biogas.

For test1, the first, second and third removal flask was interconnected by 5 mm diameter and 1 m long U-shaped hose pipe respectively. Removal of H_2S hose pipe was filled with activated carbon and zero-valent iron for test 1 and 2, respectively. The contaminate biogas enters the H_2S removal unit after passing the CO_2 capture trap by hose pipe column through the activated carbon and zero-valent iron to remove H_2S for test 1 and 2, respectively.

Similarly, the removal of H_2O the U-shaped adsorption hose pipe column was filled with a freshly prepared powder form of silica gel and sodium sulfate for test 1 and 2, respectively. The biogas enters the moisture eliminate column after passing the H_2S removal unit to ensure that the biogas was dry in both tests. As silica gel, and Na_2SO_4 ; activated carbon and zero-valent iron materials have significant water and H_2S adsorbing capability. Therefore, biogas flows through these adsorbents from the one end to the other end of the hose. In this regard, both ends of the hose pipe column were attached by cotton to increases adsorbing capacity. Finally, purified methane rich biogas comes out on the top of the flask with CO_2 , H_2S , and H_2O being stripped off. Then the purified gas is accumulated in a 50 L aluminium gas sampling bag for analyzing gas compositions. Biogas samples were collected before and after it flowed through these substances and CH_4 enriched as well

as the removal efficiency was investigated as the percentage of CO₂, H₂S, and H₂O removed from the biogas of each samples. The design consideration was that there was to be no energy requirements for the system operation.

E. Sampling and analyses

Gas composition was analyzed off line by gas chromatography (GC-8AIT / C159 R8A SHIMADZU Corporation, JAPAN) and Testo-350 portable gas analyzer (Testo AG., Germany). The gas chromatograph (GC) was fitted with a Porapak N 80/100, 274.32 cm, 1/8 mesh 250×250×145 mm column, a molecular sieve (Mole sieve 5 A 60/80, 182.88 cm, 1/8), maximum temperature 399 °C, temperature stability ±0.1°C a stainless-steel column and a thermal conductivity detector. Detector type was TCD made by Tungsten rhenium filament. Maximum temperature and sensitivity of the detector was 400 °C and 7000 (mV/mL/mg) respectively. Argon (Ar) was used as the carrier gas at a flow rate of 30 mL/min. The column temperature was 60 °C and the injector/detector temperatures was 80 °C and current 60 (mA). Methane, CO₂, H₂S, and H₂O content of raw biogas and purified biogas were analyzed and compared. The rate of gas flow, pressure, pH, water content were measured using gas flow meter, pressure gauge, digital pH meter (HM-25R), and moisture meter (MOC63u), respectively.

RESULTS AND DISCUSSION

A. Absorption of CO₂

In this study CaO solution was used as chemical solvent to for optimizing the energy content of biogas derived. The untreated biogas was introduced through the CaO solution in the first flask where it activated for the removal of CO₂ in both tests. The calcium oxide (slaked lime) solution to promote the chemical reactions as shown in equations 1 and 2:

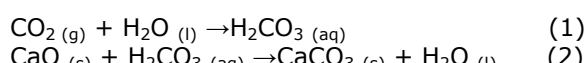


Fig. 2 shows the input and output CO₂-concentration of biogas of all experiments

was varied after treating with CaO solution. This base solvent guaranteed CO₂ reaction in the gas stream intensively through an acid-base neutralization reaction decreasing the CO₂ gas. The CO₂-concentration of biogas decreased gradually 22% and 27% to 2.6% and 4.8% at 1 to 10 g of CaO in T1 and T2, respectively. We observed that the T1 of CO₂-concentration decreased significantly higher than T2. The exact reason is that in test 1 (T1) some quantity of CO₂ absorbed and reversibly bound on surface of activated carbon before come out from the reactor column. However, it can be seen that the concentration of CO₂ concentration reduced sharply in all experiment up to 6 g of CaO and the reducing trends decreased gradually and almost remained stable at 7 to 10 g.

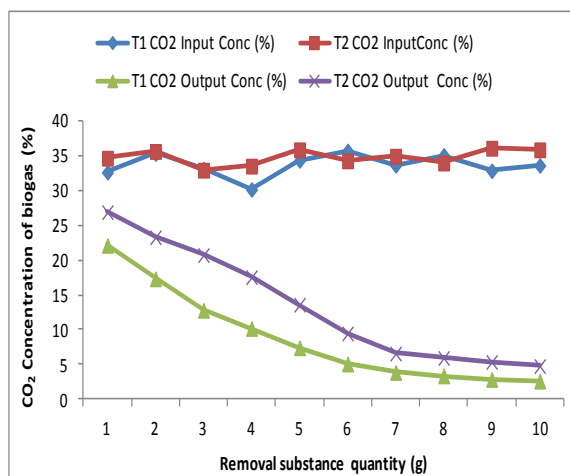


Fig. 2. Input and output CO₂-concentration of biogas for test 1 (T1) and Test 2 (T2).

B. Adsorption of H₂S

To evaluate the removal performance of H₂S from biogas using the adsorption process with activated carbon and Fe⁰ for T1 and T2 respectively. The removal H₂S concentration of the tests was modulated by activated carbon and Fe⁰. The activated carbon and Fe⁰ was chosen because of these materials are represents a nanotechnology material providing high surface areas, promising for H₂S removal (Li et al., 2007, Yan et al., 2010).The experimental data are presented in Fig. 3. The results showed that at 10 g, the H₂S-concntration was less than 50 ppm with

respect to quantity and the initial concentration of H₂S in the gas for both tests. This is well below the maximum concentration of H₂S acceptable for running in internal combustion engines (Wellinger and Linberg, 2000). The average sulfide concentration was passed approximately 365 ppm and 385 ppm in T1 and T2, respectively. Approximately 357 ppm and 355 ppm of sulfide concentration was removed at 10 g in T1 and T2, come to 14 ppm and 29 ppm, respectively. The sulfide removal concentration decreased as mass of removal substances increased. To see a substantial remained almost stable in H₂S concentration, between the quantities 8 to 10 g for both tests. The comparative results showed that the reduction capability higher in T1 process than T1. It may have activated carbon is a extremely porous form of carbon and thus it have a very large surface area available for adsorption (Horikawa et al., 2004).

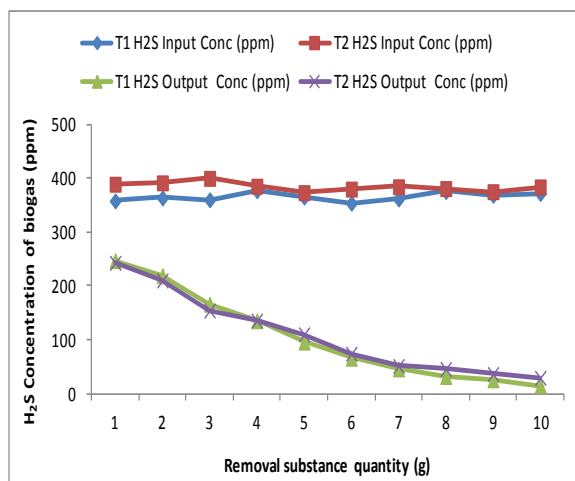


Fig. 3. Input and output H₂S-concentration of biogas for test 1 (T1) and Test 2 (T2).

C. Adsorption of water vapour (H₂O)

The removal of water vapor (moisture) from biogas reduces corrosion that results when the H₂S and CO₂ has not been removed from the biogas because the H₂S and CO₂ and water vapor react to form sulfuric acid (H₂SO₄) and carbonic acid (H₂CO₃), which can result in severe risk factor in equipment that comes into contact with the biogas. The adsorption process was carried out at different mass

of adsorbent substances in the range from 1 to 10 g. Fig. 4 represents the change in H₂O-concentration in raw and purified biogas for the all experimental tests. During the operation the concentration of H₂O of the gas was monitored entering and leaving the reactor column. When the mass of silica gel 1 g the removal media was capable of decreasing the H₂O-concentration in the gas with approximately 1.9% for test T1. As silica started taking up moisture, they turned blue to pink gradually. When the silica gel quantity of the removing reactor increased until 10 g, the degree of removal increased considerably. The H₂O-concentration in the gas at the end of the experiment the purified biogas contained 0.03% for test T1. The results show that the removal of H₂O-concentration almost remained stable at 8 to 10 g of silica gel. The silica gel was reactivated after saturation by heating it in an oven at 150 °C for 3 hours to remove the adsorbed H₂O.

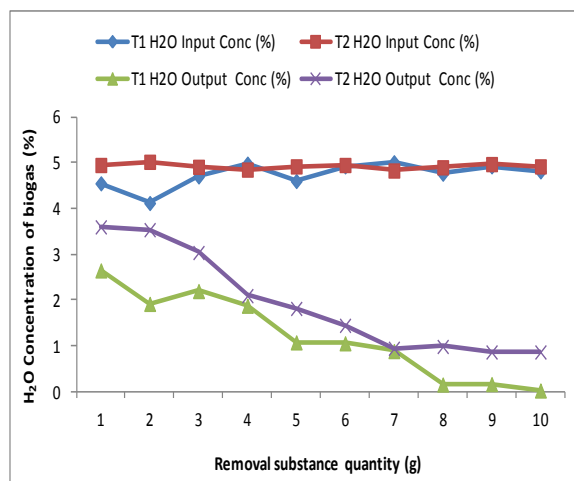


Fig.4. Input and output H₂O-concentration of biogas for test 1 (T1) and Test 2 (T2).

Similarly, also the adsorption of H₂O from biogas in Na₂SO₄ substance on lab scale reactor plant was monitored as shown in Fig. 4. From this figure it can be seen that when the Na₂SO₄ quantity in the removal column is significantly high (10 g), the Na₂SO₄ substance is capable of decreasing the H₂O concentration in the gas with approximately 4.05% from 4.9% in test T2. The concentration of H₂O in the biogas stream leaving the adsorption column was

approximately 0.8% at 10 g of Na_2SO_4 . The results showed that the T2 removal capability significantly lower than T1. The exact reason is that in T1 the activated carbon also adsorbed some water molecules before entering moisture trapped column of silica gel. We also investigated that the H_2O concentration remained almost stable at 7 to 10 g of Na_2SO_4 and then the experiment was stopped.

D. Removal efficiency of the study results

The contaminants of biogas removal efficiency for T1 and T2 increased during the experimental period as shown in Fig. 5. The results showed that the most efficient performance in T1 was investigated to compare with T2. The operation of the system in T1 was observed better results than T2 with respect to CO_2 removal efficiency although same material used. A possible reason for this was that in T1 was contained activated carbon which extremely porous and thus to have a very large surface area for adsorption of H_2S simultaneously CO_2 .

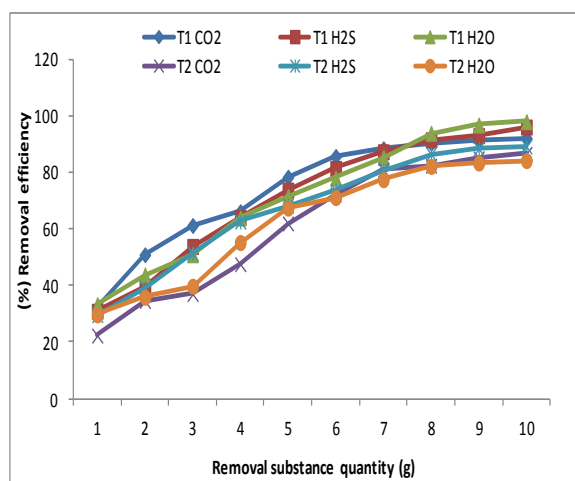


Fig. 5. Removal efficiency of CO_2 , H_2S , and H_2O from biogas under the treatments of test 1 (T1) and Test 2

However, the T1 and T2 are able to achieve removal efficiency of $\text{H}_2\text{S} > 96\%$, and 89% at 10 g respectively. Regarding this conditions the removal efficiency of $\text{CO}_2 > 92\%$, and 86% and $\text{H}_2\text{O} > 98\%$, and 84% at 10 g, respectively. It can be seen that the elimination performance

significantly lower in T2 than T1 regarding H_2O elimination due to hard granular form of Na_2SO_4 .

E. Methane concentration of purified biogas

Fig. 6 shows that the comparison CH_4 -concentration enrichment trend from raw gas to purified gas is depicted for tests 1 and 2. The result shows that the relative concentration of CH_4 upgraded with proportional to the increasing concentration of chemical substances in both tests. In this study investigated that between 1 to 10 g there was a steady increase in CH_4 -concentration. The average input CH_4 -concentration was 68%. The concentration of CH_4 increased at treated biogas is 76% and 97% at 1 g and 10 g in test 1. The enriched CH_4 -concentration is the permitted of standard gas grid level. While in test 2, CH_4 -concentration was increased 71% to 95% at 1 g and 10 g. The highest percentage of methane 97% was possible to avail by using 10 g of test 1 due to CO_2 and H_2S is removed by activated carbon.

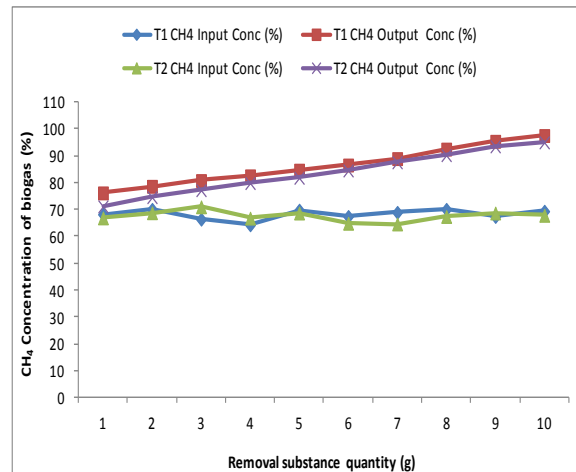


Fig. 6. Biogas CH_4 Input and output concentration for test 1 (T1) and Test 2 (T2).

This chemical method is fascinating as it eliminates the pollutant H_2S . The Fe° and activated carbon removes H_2S by simple adsorption through its mesoporous surface. The water vapour is removed by physical adsorption only. The experimental results revealed that CH_4 is possible to enrich above 95% using the combined

4th International Engineering Symposium - IES 2015

March 4-6, 2015, Kumamoto University, Japan

chemical and physical removal process for CO₂, H₂S and H₂O. For sake of comparison, the best methane concentration in the feed biogas was achieved in T1 regarding of CH₄/CO₂/H₂S/H₂O mixtures. Finally, we concluded in this study the optimum purification can be possible at 10 g of removal substances.

CONCLUSIONS

The study results show that in anaerobic digestion of cafeteria, vegetable and food wastes, and combined adsorption and absorption purification process can be used to produce a biogas with a higher concentration of CH₄. We applied nanotechnology for removal of H₂S and H₂O. The results showed that the CaO solutions capable to reduce CO₂ concentration below 3% and 4% in the biogas mixture, with a corresponding 10 g of CaO, can be achieved by T1 and T2, respectively. The H₂S concentration was reduced to 96%, and 89% for treating the raw biogas with 10 g of Fe⁰, and activated carbon for T1 and T2, respectively. The maximum H₂O removal efficiency was obtained 97% in T1, due to large surface area. The removal efficiency was found to be mass dependent. The CH₄ concentration improved above 95% in comparison to the initial 67% concentration in the raw biogas this representing an increase in efficiency of up to 42%. Although the purification process will add some operational costs to the system, it is still highly recommended for preventing corrosion and increasing energy levels of biogas.

ACKNOWLEDGEMENT

This research was conducted at Kumamoto University, Kumamoto, Japan with funding support from Graduate school of science and technology (GSST). We thank our biomass group lab mates for helping with the measurements.

REFERENCES

- [1] Al Mamun, M. R. and Torii, S. (2015), Removal of hydrogen sulfide (h₂s) from biogas using zero-valent iron. J. clean energy technology, vol. 3(6), pp. 428-432.
- [2] Gosh, D. P. (2007), Wet H₂S cracking problem in oil refinery processes - Material selection and operation control issues, The 2007 Tri-Service Corrosion Conference, Denver, Colorado, USA.
- [3] Hagen, M., Polman, E., Jensen, J., Myken, A., Jönsson, O., Dahl, A. (2001), Adding gas from biomass to the gas grid. 144. Malmö, Sweden: Swedish Gas Center; pp. Report SCG 118.
- [4] Harasimowicz, M., Orluk, P., Zakrzewska-Trznadel, G., Chmielewski, A. (2007), Application of polyimide membranes for biogas purification and enrichment. Journal of Hazardous Materials, Vol. 144(3), pp. 698-702, ISSN 0304-3894.
- [5] Horikawa, M.S., Rossi, M.L., Gimenes, M.L., Costa, C.M.M., da Silva, M.G.C. (2004), Chemical absorption of H₂S for biogas purification, Brazilian journal of chemical engineering, Vol. 21(3), pp. 415-422.
- [6] Krich, K., Augenstein, A., Batmale, J., Benemann, J., Rutledge, B., Salour, D. (2005), Upgrading dairy biogas to biomethane and other fuels. In: Andrews, K., Editor. Biomethane from dairy waste -A sourcebook for the production and use of renewable natural gas in California. California: Clear Concepts;pp. 47-69.
- [7] Li, X. Q., Brown, D. G., Zhang, W. X. (2007), Stabilization of biosolids with nanoscale zero-valent iron (nZVI). Journal of Nanoparticle Research, vol. 9(2), pp. 233-243.
- [8] Marchaim, U. (1992), Biogas processes for sustainable development, FAO, ISBN 92-5-103126-6, Rome, Italy.
- [9] Persson, M., Wellinger, A. (2006), Biogas upgrading to vehicle fuel standards and grid injection. IEA Bioenergy [Report].
- [10] Ryckebosch, E., Drouillon, M.H., Vervaeren, H. (2011), Techniques for transformation of biogas to biomethane. Biomass Bioenergy, 35, pp.1633-45.
- [11] United Nations, (1998), Kyoto Protocol to the United Nations Framework Convention on Climate Change, United Nations, New York, NY, USA.
- [12] Wellinger, A., Linberg, A. (2000), Biogas upgrading and utilization. IEA Bioenergy Task 24. Paris, France: International Energy Association.
- [13] Wellinger, A., Lindberg, A. (2005), Biogas upgrading and utilisation. [Internet] IEA Bioenergy Task 24: Energy from biological conversion of organic waste, [cited January 2011]. Available from: http://www.biogasmax.eu/media/biogas_upgrading_and_utilisation_018031200_1011_24042007.pdf.
- [14] Wheless, E., Pierce, J. (2004), Siloxanes in landfill and digester gas update. [Internet] Whittier (Canada) and Long Beach (California): Los Angeles County Sanitation Districts and SCS Energy, [cited January 2011]. Available from: http://www.scsengineers.com/Papers/Pierce_2004Siloxanes_Update_Paper.pdf.
- [15] Yan, W. L., Herzing, A. A., Kiely, C. J., Zhang, W. (2010), Nanoscale zero-valent iron (nZVI): aspects of the core-shell structure and reactions with inorganic species in water. Journal of Contaminant Hydrology, vol. 118(3-4), pp. 96-104.

A NEW METHOD FOR PREDICTING STABILITY LOBE DIAGRAM IN HIGH SPEED BALL END MILLING

Mithilesh K. Dikshit ¹, A. B. Puri ², A Maity³

- 1 Department of Mechanical Engineering, NIT Durgapur, WB-713209 India, e-mail Id: dixit.mithilesh@gmail.com
2 Department of Mechanical Engineering, NIT Durgapur, WB-713209 India, e-mail Id: abpuri2000@yahoo.co.in
3 Advance Design & Optimization, CSIR-CMERI, Durgapur, WB-713209 India, e-mail Id: maity@cmeri.res.in
-

ABSTRACT: Machine tool chatter is a self-excited vibration due to interaction of the structural and process dynamics in a machining process. In this paper, chatter stability of single degree of freedom is investigated in a high speed ball end milling process with zero order approximation. A mathematical model for stability model has been developed and process parameters like damping coefficients, damping ratio, natural frequency and stiffness constants are determined by a comparatively new method using inverse calculation. In this approach, the experimental values of chatter frequency obtained at different depth of cut and spindle speed have been used to find the above model parameters. The chatter prediction using stability lobe diagram is validated through experiments.

Keywords: chatter, high speed milling, stability lobe, surface roughness

INTRODUCTION

The quality of finished products highly influenced by machine tool vibration and chatter occurred during machining process. Rapid production of products can be achieved by reducing the machining time. Increase in cutting speed leads to decrease in the machining time but can provoke machine tool vibration and chatter. Chatter can cause premature tool failure, tool breakage and poor surface finish. Ball end milling process is an interrupted milling process in which chip thickness varies as the cutting progresses. Variation in chip thickness is the main reason for variations in cutting forces which brings regenerative effect and causes chatter. Machine tool chatter is a self-excited vibration due to interaction of the structural and process dynamics in a machining process which can deteriorate the machined surface and affects the

productivity. Regeneration in metal cutting was firstly studied by Tulsty et al. (1962) and Tobias (1965) and they developed a stability lobe diagram to predict the stability and instability region. They conclude that regeneration causes instability in turning and milling process. In milling process, it was found that regenerative phenomena arises at a certain combination of spindle speed and axial depth of cut. Stability lobe diagram (SLD) act as a boundary between stable and unstable cut and helps in identifying the chatter and non-chatter region as a function of axial depth of cut and spindle speed. SLD were predicted as a function of axial depth of cut and spindle speed using analytical approaches by many researchers previously Altintas and Budak, Insperger and Stepan, Gradisek et al. (1995, 2002, 2004, 2005). Therefore, chatter prediction attracts the attention of various researchers previously. Altintas and Budak

4th International Engineering Symposium - IES 2015

March 4-6, 2015, Kumamoto University, Japan

(1995) presented an analytical method for predicting stability lobes using regeneration in chip thickness and dynamic modelling of milling process. An analytical model in time domain was developed and critical depth of cut and spindle speed was evaluated as a function of dynamic time varying cutting coefficients. Altintas et al. (2008) studied chatter stability by employing frequency and semi-discrete time domain method using zero order and multi frequency solution and observed that semi-discretization method can predict stability lobes at any speed and its accuracy depends on the sampling interval. Li and Liu (2008) studied the time domain chatter model and dynamic regeneration effect using the instantaneous undeformed chip thickness for end milling and employed numerical methods to obtained stability lobe diagram. They concluded that higher machining efficiency can be obtained by using the combination of spindle speed and axial depth of cut obtained by simulated result in rough milling. In finishing process, superior surface finish can be obtained beyond the resonant frequency. Ahmadi and Ismail (2008) predicted upper and lower bound of stability curve in plunge turning using the non-linear process damping. In high-speed milling, the cutting speed should be 10 times higher than conventional milling. For the last couple of decades the application of high speed ball end milling is proved to be very efficient metal removal and free form generation techniques in industries like automotive and aerospace as well as thin-walled component manufacturing to strive for better part quality as well as low cost and high efficiency production in order to compete on a global scale, Kovacic M. et al. (2004). Investigation of dynamic behaviour of milling process was performed by many researchers some of them was stated above and several modelling and analysis techniques were developed. In most of the literatures, the stability lobes were developed by considering the initial modal parameters obtained from the static, non-destructive hammer testing. In the present research the modal parameters like natural frequency and damping ratio of the

machine tool structure were directly from the cutting experiments during high speed ball end milling. Through hammer excitation it is difficult to get very high harmonic components of frequency response function (FRF). In this new approach there is no need to measure the transfer function before conducting the cutting tests and chatter prediction becomes more feasible.

STABILITY LOBES IDENTIFICATION

Structural vibrations arises due to the engagement of machine tool and workpiece material. Due to the exponential increase of dynamic displacement and chip thickness regenerative occurs in machine tool structures which causes self-excited vibration of chatter, Solic et al. (2004). This type of chatter is also termed as regenerative chatter. Axial and radial engagement of the cutting edge on the ball end milling cutter with the workpiece causing variation in chip thickness. There is a tool relative displacement due to the cutting forces in the ball end milling process which induces fluctuating dynamic forces and its effect can be described by a closed feedback loop as shown in the Fig. 1. Chatter arises due to the regeneration of chip thickness due to the regenerative dynamic ball end milling process and there is a phase shift between the present dynamic displacement and previous one and can be given by the time delay factor as shown in the Fig. 2.

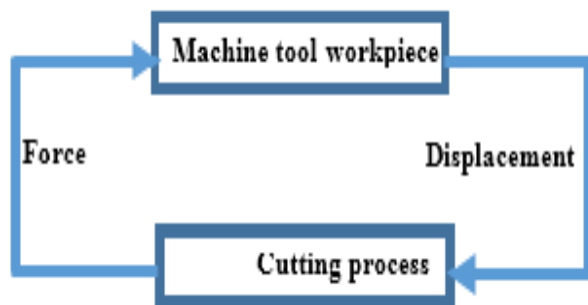


Figure 1. A closed feedback loop of cutting process and structural dynamics.

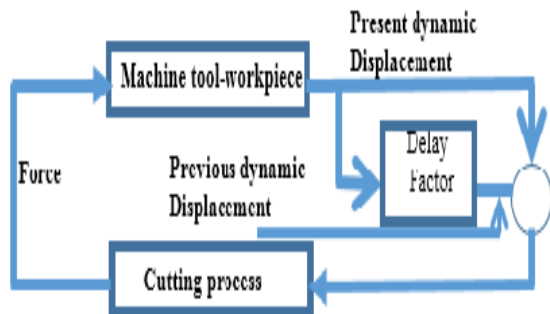


Figure 2. A schematic presentation of regenerative process

The stability of the cutting process can be given by the characteristic equation of the closed-loop which determines whether chatter occurs or not. The settings of cutting parameters include the depth of cut (or chip width) and spindle speed. The overhang of the tool is also crucial for the process stability. A schematic single degree of freedom mechanical system for ball end milling process is shown in the Fig. 3. The tool is assumed to be flexible in x-direction only in comparison to the rigid workpiece.

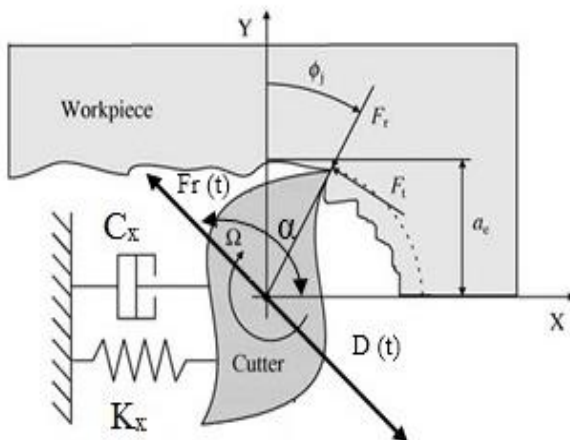


Fig. 3. Schematic single degree of freedom regenerative mechanical model for ball end milling process.

An equivalent spring-damping mass model for a viscously damped single degree of freedom system of the Fig. 3. is shown in Fig. 4. Where, M, C, K are are mass, damping coefficient, stiffness constant

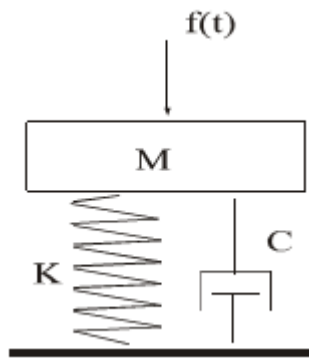


Fig. 4. A spring-mass-damper model for a single degree of freedom system

respectively. The governing equation of the system can be given by:

$$M \ddot{X}(t) + C \dot{X}(t) + K X(t) = f_x(t) \quad (1)$$

Where M is the modal mass of the tool, \ddot{X}, \dot{X}, X are acceleration, velocity and displacement vector in x- direction. $f_x(t)$ is the force in x-direction. On dividing the Eq. (1) by M on both sides, Eq. (1) can be written as:

$$\ddot{X}(t) + 2\xi\omega_n \dot{X}(t) + \omega_n^2 X(t) = \frac{f_x(t)}{M} \quad (2)$$

Where ω_n , and ξ are natural frequency and damping ratio respectively. In terms of Laplace variable S, transfer function can be written as:

$$H(S) = \frac{1}{MS^2 + CS + k} \quad (3)$$

The frequency response function (FRF) as the function of stiffness constant, damping ratio and natural frequency can be given as:

$$H(j\omega) = \frac{\omega_n^2}{(\omega_n^2 - \omega^2 + 2\xi\omega_n\omega)K} \quad (4)$$

In the mode direction the dynamic displacement D(t) at the tool tip should be collinear with the total dynamic force in x-direction as shown in the Fig. 3. Total

dynamic displacement as the function of dynamic force in x-direction and transfer function can be given by:

$$D(t) = h(D)F_r(t) \quad (5)$$

CUTTING FORCE MODELING FOR BALL END MILLING

A semi-mechanistic force model is adopted to predict the dynamic cutting force in ball end milling and it is assumed that the average cutting force from the experiments are the input factors to derive the specific cutting force coefficient. The ball end milling cutter is discretized into finite number of discs along the z-axis. The geometry of the cutter is shown in the Fig. 5.

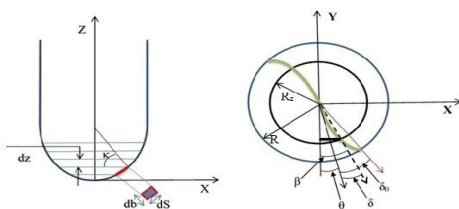


Fig. 5. (a) Front view of discretized cutter, (b) top view and position

The position of the i_{th} element on the j_{th} cutting edge with elevation z can be given by:

$$\phi_{ji}(z) = \Omega + (j-1)\phi_p - \delta_i(z) \quad (6)$$

Where ' Ω ' is the spindle rotation angle, ϕ_p is the pitch angle defined by $\phi_p = 2\pi/N$ and $\delta_i(z)$ is radial lag angle. Cutting force for the ball end milling can be expressed as:

$$\bar{F}_r(x) = \frac{1}{\phi_p} \int_{\phi_{st}}^{\phi_{ex}} \int_{z_1}^{z_2} dF_r(\phi, z) d\phi \quad (7)$$

Where ϕ_{st} and ϕ_{ex} are the start and exit radial immersion angles, respectively. The axial integration limits for each cutting tooth can be determined from cutter-workpiece engagement area. In a slot milling $\phi_{st} = 0$ and $\phi_{ex} = \pi$. Dynamic force $F_r(t)$ for ball end milling process in Eq. (5) at the position a from the X-axis in the mode direction can be given by:

$$F_r(t) = [T] * a_p [A_{ij}] * (e^{-TD} - 1) \begin{bmatrix} x(t) \\ 0 \end{bmatrix} \quad (8)$$

Where $[T] = \begin{bmatrix} \cos(180^\circ - \alpha) & \cos(\alpha - 90^\circ) \end{bmatrix}$

and $[A_{ij}] = \begin{bmatrix} a_{11}(t) & a_{12}(t) \\ a_{21}(t) & a_{22}(t) \end{bmatrix}$. $[A_{ij}]$ is the directional coefficients matrix which varies with time. The components of the matrix is given by:

$$a_{11}(t) = \frac{1}{2} \sum \left[-g_{ji} \left[K_t \sin(2\phi_{ji}) + K_r (1 - \cos(2\phi_{ji})) \right] \right]$$

$$a_{12}(t) = \frac{1}{2} \sum \left[-g_{ji} \left[K_t + K_r \cos(2\phi_{ji}) + K_r \sin(2\phi_{ji}) \right] \right]$$

$$a_{21}(t) = \frac{1}{2} \sum \left[g_{ji} \left[K_t - K_r \cos(2\phi_{ji}) - K_r \sin(2\phi_{ji}) \right] \right]$$

$$a_{22}(t) = \frac{1}{2} \sum \left[g_{ji} \left[K_t \sin(2\phi_{ji}) - K_r (1 + \cos(2\phi_{ji})) \right] \right]$$

Since, it was assumed that the tool is flexible in x-direction only, therefore, displacement in y-direction is assumed to be zero for a single degree of freedom system in ball end milling process. Displacement $x(t)$ in x-direction as the function of total displacement can be given by:

$$\begin{bmatrix} x(t) \\ 0 \end{bmatrix} = \begin{bmatrix} \cos(\alpha) \\ \sin(\alpha) \end{bmatrix} * D(t) \quad (9)$$

From Eq. (8) and (9) characteristic equation for single degree of freedom in terms of Laplace variable, natural frequency, axial depth of cut, damping ratio and tooth passing time period T can be written as:

$$1 - \frac{\omega_n}{s^2 + 2\xi\omega_n s + \omega_n^2} a_p C_p (1 - e^{-ST}) = 0 \quad (10)$$

Substituting $S = j \times \omega_c$ in Eq. (10), equation for natural frequency can be given as:

$$\omega_n^2 = \omega_c^2 + 2\xi\omega_n\omega_c \tan\left(\frac{T\omega_c}{2}\right) \quad (11)$$

Phase shift for two successive tooth engagements and tooth time period can be given by Eq. (12) and (13) as:

$$T\omega_c = \left(2\pi - 2 \tan^{-1} \left(\frac{\omega_n^2 - \omega_c^2}{2\xi\omega_n\omega_c} \right) \right) + 2k\pi; \quad k = 0, 1, 2 \quad (12)$$

$$T = \left(\frac{2(k+1)\pi}{\omega_c} - \frac{2}{\omega_c} \tan^{-1} \left(\frac{\omega_n^2 - \omega_c^2}{2\xi\omega_n\omega_c} \right) \right); \quad k = 0, 1, \quad (13)$$

Critical depth of cut and spindle speed for machine tool stability and chatter can be given from the above developed analytical equations as:

$$N = \frac{1}{nT} = \frac{\omega_c}{n \left(2(k+1)\pi - 2 \tan^{-1} \left(\frac{\omega_n^2 - \omega_c^2}{2\xi\omega_n\omega_c} \right) \right)}$$

$$a_p = \frac{\omega_n^2 - \omega_c^2 + 4\xi^2\omega_n^2\omega_c^2}{2C_p\omega_n^2(\omega_n^2 - \omega_c^2)} \quad (14)$$

Stability lobe diagram can be generated by mapping the axial depth of cut and spindle speed from the Eq. (14).

RESULTS AND DISCUSSIONS

As mentioned in the introduction section, in most of the literatures modal parameters for generating stability lobes, like natural frequency, damping ratio and stiffness constant were identified from the hammer impact test keeping the cutting tool in static position with the tool holder. In the present study, modal parameters were directly identified from the cutting tests. In this new method chatter frequency is identified directly from the cutting test using the VIBXpert. Sandvik Coromant pulra ball end milling cutter of diameter 10 mm and helix angle 30° is used in the slot milling of aluminium alloy Al2014-T6. All the cutting tests were performed on 3-axis vertical CNC high

speed milling centre Mikron VCP-10. Each cutting tests were repeated 10 times and stable cutting zone were identified from the force signal recorded by 3-component piezoelectric dynamometer. Frequency of maximum amplitude at two different axial depth of cut 0.6 mm and 1.4 mm is identified. At the rotational speed of 5026 and 4586 RPM frequency of maximum amplitude were 4750 Hz and 5250 Hz respectively. Tooth engagement time period for successive cutting were 0.010 sec and 0.0123 sec respectively. Chatter frequency and tooth engagement time period at two different axial depth of cut (0.6 and 1.4 mm) were used in Eq. (11). Natural frequency and damping ratio were obtained through the mathematical manipulation. The obtained natural frequency was 5250 Hz and damping ratio was 0. Zero damping ratio indicates that at low depth of cut there is no damping in the machine tool structure. Obtained natural frequency and damping ratio were introduced in the MATLAB program and stability lobe diagram was generated as shown in the Fig. 6. From the Figure 6. It can be seen that at the critical depth of cut 1.4 mm chatter can exist at the rotational speed of 5000, 7000 and 10000 rpm. Analytical prediction was validated with experimentation at rotational speed of 6880 RPM, feed per tooth 0.07 and depth of cut 1.4 mm and it was found that no chatter was predicted as shown in the Figure 7. The maximum amplitude and frequency was recorded as (1.17 m/S²) and 5100 Hz.

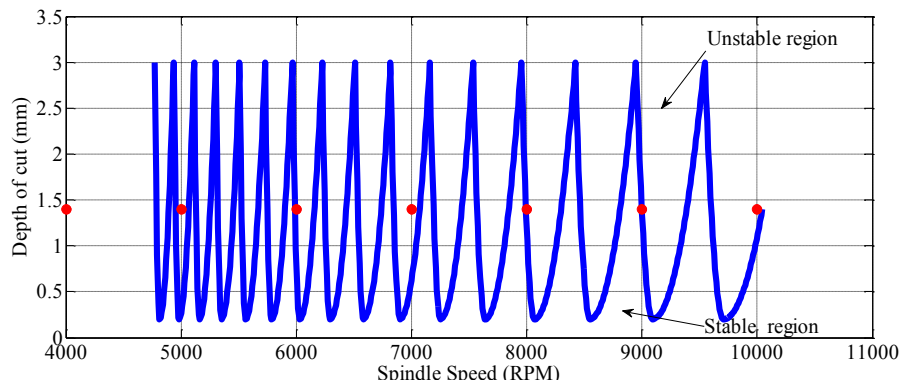


Fig. 6. Analytically predicted stability lobe diagram and stability region at different rotational speed.

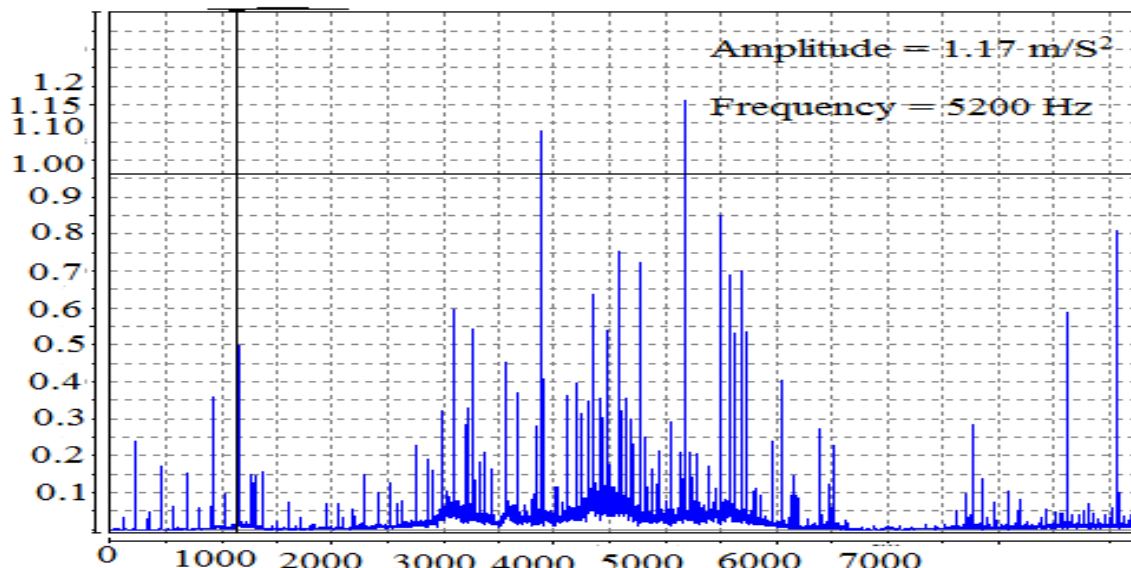


Fig. 7. Experimental observation of amplitude Vs. frequency at $f_z = 0.07$ mm/tooth, $N = 6880$ RPM, $ap = 1.4$ mm and $ae = 0.3$ mm.

CONCLUSIONS

In this paper stability lobe diagram for single degree of freedom has been developed in high speed ball end milling. Critical depth of cut has been found for a specific spindle speed using chatter frequency directly from experiments. A new method was employed for determining modal parameters like natural frequency and damping ratio. The adopted method was found to be fast and accurate for predicting modal parameters. A complicated and static impact hammer test is not necessary as the modal parameters were directly decided from the real time experimental values. The predicted stable and unstable region are in good agreement with the experimental results. Chatter free cutting is predicted for smaller depth of cut below 5000 RPM. Even at high RPM milling process is chatter free as when compared with experimental and analytical results. Future work can be done by extending the current research work for multi-degree of freedom system considering the phase shift.

REFERENCES

- [1] J. Gradišek, M. Kalveram, T. Insperger, K. Weinert, G. Ste'pa'n, E. Govekar, (2005), On stability prediction for milling, International Journal of Machine Tools and Manufacture 45 (7-8), 769-781.
- [2] J. Tlusty, M. Polacek, (1963), The stability of machine tools against self-excited vibrations in machining, International Research in Production Engineering, 465-474.
- [3] K. Ahmadi, F. Ismail, (2011), Analytical stability lobes including nonlinear process damping effect on machining chatter, International Journal of Machine Tools and Manufacture 51, 296-308.
- [4] Kovacic M. Brezocnik, M. and M. Ficko. (2004) Prediction of surface roughness with genetic programming. Journal of Materials Processing Technology, 157:28-36.
- [5] Li Zhongqun, Liu Qiang, (2008), Solution and analysis of chatter stability for end milling in the time domain, Chinese Journal of Aeronautics 21, 169-178.
- [6] S.A. Tobias, W. Fishwick, (1958), Theory of regenerative machine tool chatter, The Engineer.
- [7] T. Insperger, G. Ste'pa'n, (2002), Semi-discretization method for delayed systems, International Journal for Numerical Methods in Engineering 55 (5), 503-518.
- [8] T. Insperger, G. Ste'pa'n, (2004), Updated semi-discretization method for periodic delay-differential equations with discrete delay, International Journal for Numerical Methods in Engineering 61 (1), 117-141.
- [9] Y. Altintas, E. Budak, (1995), Analytical prediction of stability lobes in milling, CIRP Annals-Manufacturing Technology.
- [10] Y. Altintas, G. Stepan, D. Merdol, Z. Dombovar, (2008), Chatter stability of milling in frequency and discrete time domain, CIRP Journal of Manufacturing Science and Technology, 1, 35-44.

Effect of cutting conditions on tool performance in CBN hard turning of HCWCI

Ravi A.M¹, S.M.Murigendrappa², P.G.Mukunda³^{1, 2} Department of Mechanical Engineering, National Institute of Technology Karnataka, Surathkal, Mangalore 575025, India³ Department of Metallurgical & Materials Engineering, Indian Institute of Technology, Kharagpur, 721302, India**Abstract**

In recent times, the use of cubic boron nitride (CBN) cutting tools is common in hard part machining process. Their performance is of at most importance in hard turning to minimize the product cost. In this work, the experimental and analytical studies have been carried out to investigate the influence of the cutting parameters on tool performance in hard turning of high-chrome white cast iron (HCWCI). Tests have been performed for different cutting conditions chosen in accordance with the Taguchi procedures. To investigate the statistical significance among cutting parameters considered in the study, analysis of variance (ANOVA) techniques have been used. It is observed from the study that cutting speed plays a dominant role in determining the tool performance in the form of tool life followed by feed rate and depth of cut, and overall tendencies agree with predictions from the artificial neural networks (ANN) model. The proposed methodology in evaluating the tool performance can help to optimize the hard turning process and, eventually, help hard turning to be a viable technology.

Keywords: Hard Turning, CBN, Flank and Crater Wear, ANOVA, ANN.

1. Introduction

Chromium based alloys such as high- chrome white cast iron are extensively used in mining and process industries, especially in slurry handling, because of their excellent mechanical and chemical, and temperature resistant properties. To improve the machinability characteristics of the hard materials (viz. Tool steel, manganese steel, Inconel 718, AISI 4340, high chrome Iron/Steels) without material property deterioration is a tough job in the present scenario. Many conventional procedures are followed by using high cost CBN, PCBN and diamond cutting tools. Generally, evaluation of these are done by measuring the process responses like machining forces, material removal rate, tool temperatures and tool wear. Among these, influences of tool wear is more important in the machining process, Nilrudra et al (2011), Lin et al 1998, Kaith et al. (1998). In this paper, the performances of the CBN tools are evaluated at different cutting conditions to cut hard-to-machine HCWCI.

Nomenclature

ANOVA	Analysis of variance
BHN	Brinnell hardness number
CBN	Cubic boron nitride tool
DF	Degrees-of-freedom
DOE	Design of experiments
<i>d</i>	Depth of cut (mm)
<i>f</i>	Feed rate (mm/rev)
F	Statistical characteristics
HRC	Rockwell Hardness
<i>K_b</i>	Crater wear (μm)
MS	Mean of squares
MSE	Mean square error
P	Contribution (%)
<i>S</i>	Cutting speed (m/min)
SS	Sum of squares
S/N ratios	Signal- to- noise ratio
<i>V_b</i>	Flank wear (μm)

The favourable properties of this iron makes it an automatic for use in many process industries but is hampered by lack of optimized cutting conditions needed in to enhance its wider usage in engineering applications.

Many researchers reveal the suitability of CBN in hard turning and discusses its wear mechanisms. As per

their study, there are six wear mechanisms, either of which or of combinations of any of these involved in cutting tool wear. The wear may be any of these types; Abrasion, adhesion, attrition, fatigue, dissolution/diffusion, and tribo-chemical type, in which abrasion, adhesion, and diffusion are dominating in hard part machining, Thamizhmanii and Hasan (2008), Yong et al. (2005), Poulachon et al. (2004). The factors influencing on these are cutting conditions, tool-work material, binder phase, chemical stability and tool geometry.

Liu et al. (2002) conducted experiments on carbon steels using CBN, PCBN, coated carbides, and analyzed the different wear mechanism for each tool-work combination. Thamizhmanii et al. (2008) studied the wear mechanisms of CBN and PCBN tools during machining of hard steels, and observed that abrasion and diffusion mechanisms are the main cause for flank and crater wear. Similarly, tool wear is a serious issue in machining of HCWCI due to the presence of hard eutectic carbides bonded in the austenite matrix, Masood et al. (2011). In the beginning, Industries adopted conventional procedures to cut these metals using high-hard CBN/PCBN cutting tools. Interestingly, there are quite a few literature [e.g. Masood et al (2011), Armitage et al. (2003) reported on the machinability characteristics of this metal. Masood et al. (2011) conducted experiments on HCWCI using CBN with the aid of local heat remarked that flank and crater wear are prominent during the machining process, and remarkable improvement of tool life at higher shear zone temperatures. In their experiments on HCWCI, Ravi et al. (2014) investigated the abilities of multilayer hard-coated carbide inserts (TiC/TiCN/Al₂O₃) at different cutting conditions. As per their reports, the types of wear generated on the tool were flank and crater type. Extending their work, Ravi et al. (2014) analyzed the machinability characteristics with the aid of Oxy-LPG flame as preheat and CBN inserts as cutting tools. They observed the minimum tool wear (both flank and crater wear) formation at

higher cutting speeds and preheat temperatures in comparison with lower ones.

To optimize the machining process many researchers used statistical tools viz. Taguchi, ANOVA and ANN. Tsao, (2008) implemented Taguchi, ANOVA and ANN techniques to carry out experiments on step drilling of composite material and determines the optimum results of the process.

This paper reports the performances of CBN tool at different cutting conditions. Taguchi's L₉ - Orthogonal array was used to carry out the experiments. Analysis has been made using ANOVA, and derived results are verified with ANN model.

2. Work material and cutting tools

The work material chosen for this experiment was sand blasted air quenched HCWCI alloy in the form of round bars of 65mm diameter. Its chemical compositions are; 2.5%C, 0.7%Si, 0.66%Mn, 0.068%S, 0.7%P, 0.5%Cu, 19%Cr, and iron. The important properties of HCWCI (As-cast type) are; density of 7.7mm/cm³, 1260°C of melting point, 13W/mK thermal conductivity and hardness of 522BHN. The cutting tool selected for the experimental work was CBN inserts (Mitsubishi make) having -6° normal rake angle, -6° back rake angle, and 6° clearance angle, Mitsubishi Materials catalogue (C005N) (2011-2012).

3. Experimental work

The classical experimental design looks cumbersome when numbers of process parameters are numerous. To solve this problem, Taguchi L₉ standard orthogonal array was used, which brought the entire parameter space into a small number of experiments, Suresh et al. (2012), Nilrudra et al. (2011). The cutting parameters selected for the experimental work are; cutting speed of 55, 88 and 132m/min, depth of cut of 0.1, 0.2, and 0.3mm, and feed rate of 0.096, 0.124 and 0.179mm/rev. A piezoelectric lathe tool dynamometer (Kistler model 9712B500) was used to measure 3-dimensional cutting forces. Flank and crater wear are measured (As per the ISO standards) after every 342mm length of turning operation using scanning electron microscope

(SEM). Table 1 shows the results of the experiments at different cutting conditions.

4. Results and discussion

In this discussion, the process parameters are analyzed using Minitab-16 statistical software. The significance of the control factors on the process responses are analyzed using ANOVA,

Table 1 – Taguchi's L₉ Orthogonal array, cutting parameters and process responses (Flank and crater wear).

S,m/min	d,mm	f, mm/rev	V _b ,μm	K _b ,μm
55	0.1	0.096	79	53
55	0.2	0.124	108	57
55	0.3	0.179	63	38
88	0.1	0.124	77	61
88	0.2	0.179	101	91
88	0.3	0.096	95	83
136	0.1	0.179	70	69
136	0.2	0.096	107	66
136	0.3	0.124	89	61

Table 2 – Analysis of variance (ANOVA) table for the flank wear.

Factors	DF	Seq SS	Adj SS	F	%P
S	1	352.43	309.83	5.0656	9.72
d	1	400.17	453.56	7.4155	11.31
f	1	492.34	1085.61	17.7494	14.38
S*d	1	557.95	1673.51	27.6315	16.57
S*f	1	3.83	952.41	15.5725	-1.91
d*f	1	579.82	1128.55	18.4515	17.30
S ²	1	549.85	549.85	8.9900	16.30
Error	1	61.16	61.16		
Total	8	2997.56			

4.1 Effect of cutting parameters on the flank wear, V_b

The ANOVA table (Table 2) depicts the percentage contribution of control factors on the flank wear, in which, cutting speed, depth of cut and feed rate have more influence followed by the interaction terms S*d and d*f, and quadratic term S². This notices the involvement of all the cutting parameters in the formation of flank wear. However, the interaction term S*f appears to be insignificant due to low value. Figure 1 shows the SEM images of the flank and crater wear of CBN when turning HCWCI at 88m/min cutting speed and 0.3mm depth of cut for about ten minutes duration. The wear of the tool seems to be strongly linked to the strong work hardening tendency of austenite matrix and its abrasive action,

and its optimum values are identified by constructing main effect plots. In ANOVA analysis, the cutting parameters (cutting speed, depth of cut and feed rate) are considered as control factors, and flank and crater wear as process responses. The results derived are confirmed using the results of ANN model.

Zhi et al. (2008). Figure 1a illustrates the deep, multiple scratches/scores on the land (flank) of the tool and its uniformity over a localized area. The wear accelerated with the increased cutting temperature. The reason for this is the softening cutting edge encounters the hard matrix/particle in the workpiece. The experimental observation reveals that flank wear decreases as the cutting speed or feed rate increases, and is shown in Figs. 2a and b. At higher cutting speeds, the amount of heat generated at the tool-work interface softens the workpiece due to which less resistance to shear the metal. On the other hand, at 88 m/min of cutting speed flank wear increases due to insufficient heat generation at the shear zone, Suresh et al. (2012), Gaithonde et al. (2009). To determine the optimum value for the flank wear, plotted S/N

ratio with the mean values of the flank wear. The flank wear is optimum for the

cutting parameters; $S=55\text{m/min}$, $d=0.1\text{mm}$, and $f=0.179\text{mm/rev}$.

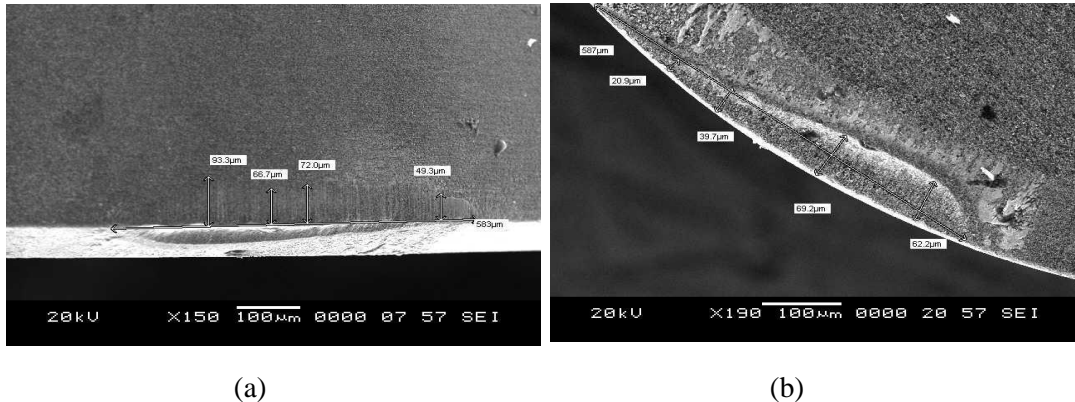


Fig. 1- SEM images of flank and crater wear of CBN at 132m/min cutting speed and 0.1 mm depth of cut.

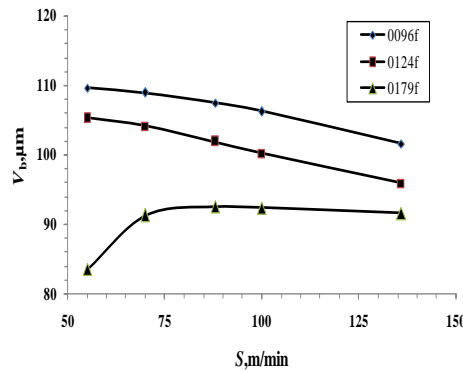


Fig. 2a- Comparison of flank wear vs. cutting speed at 0.3 mm depth of cut.

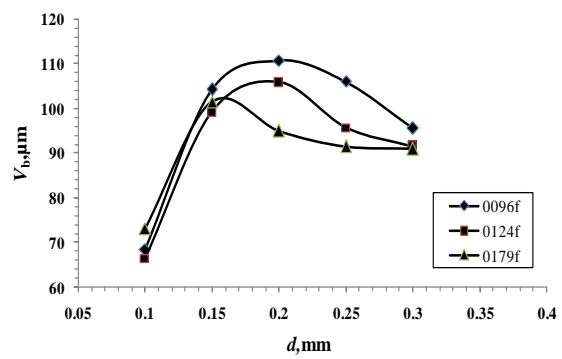


Fig.2b- Comparisons of flank wear vs. depth of cut at a 88 m/min of cutting speed.

Table 3 – Analysis of variance (ANOVA) table for the crater wear.

Control factors	DF	Seq SS	Adj SS	F	%P
S	1	1258.81	46.360	0.7195	33.64
d	1	728.20	1.210	0.0188	18.69
f	1	57.50	100.946	1.5666	-0.20
$S*d$	1	872.29	695.787	10.7980	22.75
$S*f$	1	1.35	64.268	0.9974	-1.78
$d*f$	1	500.01	91.621	1.4219	12.27
S^2	1	68.28	68.276	1.0596	0.11
Error	1	64.44	64.440		
Total	8	3550.88			

4.2 Effect of cutting parameters on the crater wear, K_b : Table 3 depicts the ANOVA for the crater wear, in which the cutting speed has significant contribution (33.64%) on the crater wear followed by the depth of cut (18.69%), and interactions of $S*d$ (22.75%) and $d*f$ (12.27%). However, the interaction term $S*f$ appears to be insignificant. Figure 1b shows the formation of crater wear at 88m/min cutting speed and 0.3mm depth of cut.

It is observed from the experiments that, at higher cutting speeds, continuous ribbon type saw-tooth chips were formed, Yong et al. (2005), Liu et al. (2002). This was due to plastic deformation and fracture at the shear zone forms a segmented structure before it leaves the tool, Thamizhmanii and Hasan (2008), Lin et al. (1995). The chips constitute high hard carbides when flows on the rake face generates grove and is known as crater. The size of the

grove increases with the increase of cutting speed and feed rate as well, Gaithonde et al. (2009). Figures 3a and b shows the comparative study of formation of crater wear at 0.1mm and 0.2mm depth of cut, in each case crater

wear increases as the cutting speed increases. From the main effect plots, the crater wear is optimum for the cutting parameters; S=55m/min, d=0.3mm, and f=0.179mm/rev.

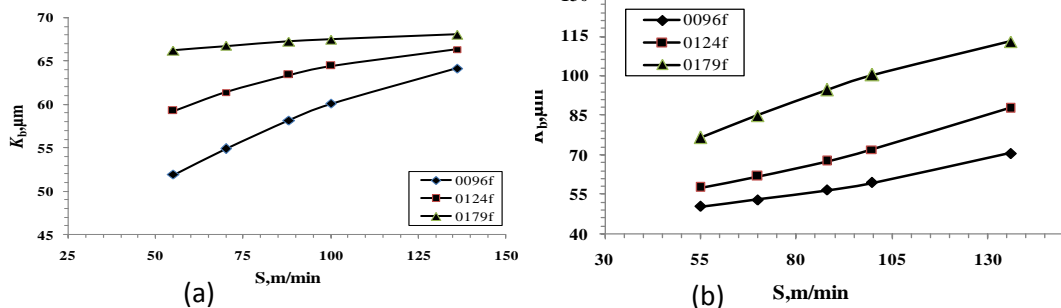


Fig. 3- Comparison of crater wear vs. cutting speed at deptn or cut of (a) 0.1mm, and (b) 0.2mm.

Table 4 - Cutting conditions set for confirmation test and comparison of results of flank and crater wears.

Sl. No.	S, m/min	d, mm	f, mm/rev	V _{b-Exp} , µm	V _{b-ANN} , µm	% of error	K _{b-Exp} , µm	K _{b-ANN} , µm	% of error
1	60	0.15	0.179	102	100	2	63	62	2
2	70	0.1	0.096	76	76	0	65	63	3
3	75	0.3	0.096	110	108	2	61	62	-2
4	80	0.1	0.124	91	90	1	63	64	-2
5	100	0.15	0.096	104	103	1	53	54	-2
6	100	0.15	0.179	108	108	0	72	71	1
7	130	0.3	0.096	93	93	0	72	70	3
8	140	0.1	0.124	67	68	-2	76	75	1

Note : Exp -Experimental method, ANN- Artificial neural network method.

4.3. Analysis using artificial neural networks:

In this research work, MATLAB software (version 2008a) was used to develop the ANN model. The model has 3-5-2 network topology to predict flank and crater wear. It consists of three layers. The first layer is known as the input layer consists of three neurons S , d , and f . The second layer is the hidden layer networks with input data and output data. The third layer is the output layer having two neurons (V_b and K_b). The models was trained by setting the network properties, and are; Network- feed forward, back propagation, Training function-TRAINLM, Adoption learning function- LEARNGDM, Performance function-MSE, Transfer

4.4 Confirmation test analysis: To validate the neural network model, eight experimental trials were conducted considering the same inputs that are not similar to those in the plan of the experiment (Table 4). The tool wear

function- LOGSIG and Target goal error- 1.00E-04. ANN model was developed based on the available experimental data. The properties of the ANN model were set to train the model with 750 iterations. After trial and error method, the momentum constant value, number of neurons and the learning rate were set to 09, 5 and 0001 respectively. The training was found with a small error at 53 training iterations. This indicates that the network is well trained with three inputs and meets the target responses. After the establishment of the model, the performance characteristics predict with more accuracy, (Srinivas et. al. (2012), Tsao, (2008)).

predicted by the ANN model has least deviation from the experimental results, and is being confirmed that the trained ANN model has demonstrated good interpolation capability and can be used as an efficient predictive tool to

4th International Engineering Symposium - IES 2015

March 4-6, 2015, Kumamoto University, Japan

determine the performance of the CBN tool.

5. Conclusion: In this study, Taguchi techniques are used to carry out the experimental work, and the tool performance (tool wear) is investigated experimentally as well as arrived using analytical method. ANOVA analysis identifies the significance of cutting parameters on the tool wear. The experimental observations reveals that, flank wear decreases at higher cutting speed and depth of cut, on the other hand, crater wear increases as the cutting speed and feed rate increases. The results predicted by the ANN model have close values to the experimental results. The optimized cutting condition enhances the machinability characteristics of HCWCI, and ANN method found to be more accurate predictive tool to measure the process responses.

References:

- [1] Armitage K, Masood S, Brandt M, (2003), Laser assisted machining of wear resistant white cast irons. Proceedings of the 9th Int. Conference on Manufacturing Excellence, Melbourne, p13-15.
- [2] Gaithonde V N, Karnik S R, Figueira I, Davim I P, (2009), Machinability investigation in hard turning of AISI D2 cold work tool steel with conventional and wiper ceramic inserts, International Journal of Refractory Material and Hard Material, 27: p754-763.
- [3] Kainth G S, Dey B K, (1998), Experimental investigation in to tool life and temperature during hot machining of EN-24 steels. Bulletin Cercle Etudesdes Me'taux 14(11) p22.1-22.7.
- [4] Lin Z C, Chen D Y (1995) A study of cutting with a CBN tool, Int. J. of Mater Process Technol, 49, p149-164.
- [5] Liu Z Q, Ai X, Zhang H, Wang Z T, Wan Y, (2002), Wear pattern and mechanisms of cutting tools in high speed face milling, Int.J.of Mater. Proc. Technol., 129, p222-226.
- [6] Mantegomery D C, (2000).Design and Analysis of Experiments, 7th Edition. Wiley India Edition. India.
- [7] Masood S H, Armitage K, Brandt M, (2011), An experimental study of laser-assisted machining of hard-to-wear white cast iron. Int. J. of Mach. Tools and Manuf. 51, p450-456.
- [8] Mitsubishi Materials catalogue (C005N) (2011-2012) Mitsubishi Materials Corporation, India.
- [9] Nilrudra Mandal, B. Doloi, B. Mondal, Reeta Das, (2011), Optimization of flank wear using Zirconia Toughened Alumina (ZTA) cutting tool: Taguchi method and Regression analysis, Measurements 44 p2149-2155.
- [10] Poulachon G, Bandopadhyaya B P, Jawahir I S, Pheulpin S, Seguin E, (2004), Wear behavior of CBN tools while turning various hardened steels. Int.J. of WEAR, 256, p302-310.
- [11] Ravi AM, Murigendrappa SM, Mukunda PG, (2014), 'Machinability Investigations on High Chrome White Cast Iron Using Multi Coated Hard Carbide Tools', Springer- Trans Indian Inst Met, DOI 10.1007/s12666-013-0369-0
- [12] Ravi AM, Murigendrappa SM, Mukunda PG, (2014), Experimental Investigations, on TEM of High Chrome White Cast Iron and to study its Machinability characteristics Using Taguchi and ANN, Springer- Int.J.Adv. Manuf. Tech., DOI 10.1007/s00170-014-5752-4
- [13] Suresh R, Basavarajappa S, Samuel G L, (2012), Some studies on hard turning of AISI 4340 steel using multilayer coated carbide tool, International J. of Measur, 45: p1872-1884.
- [14] Srinivas C G, Devadasan S R, Sivaram N M, Karthi S, (2012), Resource optimization through neural network for handling supply chain constraints, International Journal of Logistics Economics and Globalization, 4: p5-9.
- [15] Thamizhmanii S, Hasan S, Measurement of surface roughness and flank wear on hard martensitic stainless steel by CBN and PCBN cutting tools, J. of Achievements in Mat. and Manuf. Engg., 31(2), (2008), p415-421..
- [16] Tsao C C, (2008), Prediction of thrust force drill in drilling composite material by Taguchi method and radial basis function network, Int. J.of Adv Manuf Technol, 36: p11-18.
- [17] Yong Huang, Dawsonb Ty G, (2005), ' Tool crater wear depth modelling in CBN hard turning, 'Wear 258 p1455-1461.
- [18] Zhi X, Xing J, Gao Y, Fu H, Xiao J P B, (2008), Effect of heat treatment on microstructure and mechanical properties of a Ti-rearing hypereutectic white cast iron, International Journal Material Science Engineering-A, 487 : p171-179.

Effect of geometry on heat transfer in microchannels for microsystem cooling

Udhav Ulhas Gawandalkar, Girish Anant Kini and Arun M

Department of Mechanical Engineering, NITK Surathkal, India

Email: udhavgawandalkar@gmail.com

Fluid flow at micro scale is being studied extensively in recent years. Understanding the heat transfer characteristics and fluid flow at these scales has relevance to electronics cooling, micro heat exchangers, MEMS devices amongst others. In this investigation, three dimensional models of micro-channels with different geometrical cross-sections have been numerically simulated using the CFD software tool FLUENT. Both the H2 (constant heat flux) and T (constant wall temperature) boundary conditions are simulated. The numerical data obtained from this work provides better understanding and insight into the heat transfer mechanisms in micro-channels and co-relations with hydraulic diameter.

Keywords- *Microchannels, Cooling, Numerical simulation, Heat transfer coefficient, H2 and T boundary condition*

Hybrid Monte Carlo approach to estimate heat flux in steady state fin problem

K Srinivasa Sagar and N Gnanasekaran

*Department of Mechanical Engineering, NITK Surathkal, India
Email: ksrinivasasagar@gmail.com*

Natural convection heat transfer and fluid flow is an important phenomenon in daily life and engineering applications such as building heating and cooling applications, renewable energy sources, cooling of electronic equipments, heat exchangers and computer cooling technologies. Natural convection fin heat transfer is essential to design a heat transfer equipment to enhance heat transfer for various applications. Placing the fin increases the surface area, thereby increasing the heat transfer. The present study investigates the temperature, flow and the velocity profile emerging due to natural convection to estimate heat flux.

The fin contains two aluminum base plates of size 120x120x10mm and a steel plate which is sandwiched between two aluminum plates of dimension 120x60x10 mm. The present work can be solved as two dimensional conjugate heat transfer problem. Geometry is created using ANSYS 14.5. Grid independence studies are done in order to fix the proper grid for the study considered. Heat flux at base is specified as input and temperature distribution from the fin is obtained. This can be posed as an inverse problem where in heat flux can be considered as unknown. For the obtained temperature distribution, the aim is to estimate heat flux. In order to estimate the heat flux, heat transfer coefficient information is essential which depends on the flow. Buoyancy is the driving factor for natural convection flow, where in Navier Stokes equation is solved to obtain flow information. This study is carried out to estimate different heat flux from various temperature distributions and in order to reduce the computational cost, a neural network is trained between various heat flux and temperature distribution data. Now this trained neural network acts as a fast forward model for estimating the heat flux. Hybrid Monte Carlo algorithm is used as an inverse model to estimate heat flux in the steady state fin problem.

Study to Improve the Heat Efficiency of Heat Exchanger with 0.5vol% Al₂O₃ Nanofluid

Fukuoka Yukiko¹ and Torii Shuichi²

¹ Department of Mechanical System Engineering, Kumamoto University, Kurokami, 2-39-1, Kumamoto 860-8555, Japan. e-mail:142d8555@st.kumamoto-u.ac.jp

² Department of Mechanical System Engineering, Kumamoto University, Kurokami, 2-39-1, Kumamoto 860-8555, Japan. e-mail:torii@mech.kumamoto-u.ac.jp

Abstract: Thermal management is a key factor for proper operation of electronic components used in various ways. Recently, a new way to enhance thermal conductivity of working fluid is to suspend small diameter particles in a fluid which is called nanofluid. The nanofluid is found to possess long time stability and large efficient thermal conductivity. This is because the suspended ultrafine particles cause a substantial enhancement of the thermal conductivity of mixture and improve its capability of energy change. The motivation of this study is to improve heat transfer capability uses 0.5 vol% Al₂O₃-water nanofluid as the working fluid of heat exchanger and try to change the nozzle of heat exchange unit. The most effective nozzle was the one which has the most number of holes. Future work is to elucidate the reason with using numerical simulation.

Keywords: nanoparticles, thermal efficiency, heat exchanger

Introduction

Water or oil is well known as an operation medium is used for various industrial fields. In the field of energy, a lot of people have been tried to increase the efficiency of heat transfer. Thermal management is a key factor for proper operation of electronic components used in computers and data centers, in microwave weapons in defense industry, radio transmitters, gas turbine blades and in another numerous technologies. A new way to enhance thermal conductivity of working fluid is to suspend small diameter particles in a fluid. First, solid metal material's thermal conductivity is higher than any fluid is generally well known. For example, thermal conductivity of copper at room temperature is about 700 times greater compared with water, and about 3,000 times greater compared with oil. And also the thermal conductivity of the oxide substance such as Al₂O₃ which has smaller then copper is much larger than that of water. Table 1 shows thermal conductivity of some materials. That is,

the fluid that contains the particles are expected to show a much higher thermal conductivity as compared with the conventional single-phase flow.

The water, which has an excellent stability has oxide preeminent dispersion characteristics, such as oil and alumina in the working fluid, such as ethylene glycol (Al₂O₃) and copper oxide (CuO) has become clear. Fluid contains nanoparticles is called nanofluid. The nanofluid is found to possess long time stability and large efficient thermal conductivity [1]. Heat transfer performance for the nanofluid is superior to that of the original pure fluid. This is because the suspended ultrafine particles cause a substantial enhancement of the thermal conductivity of the mixture and improve its capability of energy change. Among numerous studies, Xuan and Li [2] measured convective heat transfer coefficient of Cu/water nanofluid of 0.3% in volume fraction to 2.0% at constant heat flux, and reported a substantial heat transfer enhancement.

Nanoparticles and Nanofluid

4th International Engineering Symposium - IES 2015

March 4-6, 2015, Kumamoto University, Japan

Nanoparticles are nano sized particles which have average diameter in 10~100nm. There are various types of them. In this study, Al₂O₃ is used as nanoparticles. Fig.1 shows the nanoparticles and Table 1 shows the properties of Al₂O₃ nanoparticles. Al₂O₃ is relatively easy to obtain and has outstanding stability for physical and also chemical. In my study, Al₂O₃ was used as nanoparticles and distilled water was used as suspension. The test fluid which is 0.5vol% Al₂O₃ nanofluid was produced by ultrasonic wave stirrer the following procedure.

- (1) Pour the accurate amount of distilled water and nanoparticles into the container which was well washed and dried.
- (2) Wind up the entrance unit with tape to airtight situation when close a cover
- (3) After close the cover, spread over with tape around entrance unit
- (4) Sink containers 4 hours in ultrasonic wave stirrer

Experimental apparatus

Fig.2 shows a picture of my experiment apparatus. This is a heat exchanger made by my senior. In the central part, there is a heat exchange unit. Heat exchange unit has jet nozzle and heater block. Heater block is heated by three 6.5 mm diameter 45 mm long cartridge heaters that were inserted into holes drilled into the bottom of the heater block. The power to the cartridge heaters was adjusted to the desired level by a variable transformer. The current and voltage supply to the heaters were monitored by HIOKI 3334 AC/DC power tester. The combined maximum power rating of the cartridge heaters was 300W which was sufficient to provide a high enough heat flux along the block to the surface that accurate determination of the centreline temperature distribution and surface temperature could be measured. In left part, there are two pumps and a thermostat to control and keep the temperature of fluid. Two different magnetically driven pump is used to circulate working fluid in the system. Pump-1 is used to force the working fluid to the nozzle while a less capacity pump (pump-2) is utilized to drain the working

fluid after impingement due to keeping impinging jets under the free surface condition. And in the right part, there is a data logger and computer to observe the temperature of heat block through thermocouple. All thermocouple readings within the block were monitored by a KEYENCE NR-500 digital data logger and temperature results were stored in a laptop PC. Heater surface that is exposed to impingement is 31.5mm in diameter. To prevent lateral heat losses, heater block is inserted in a 150mm diameter 35mm height Teflon insulation block that wrapped heater block outer periphery tightly. Fig.3 shows the construction of mentioned above.

Experimentation

This time, the test fluids are pure water and 0.5vol% Al₂O₃ nanofluid. For the heat exchange part, there is a nozzle jet plate. Illustrations and diameters each of them are shown in Fig.4 the number of holes are 9, 17 and 25 jets respectively. Jet plates are manufactured from aluminum and its thickness is 2mm. It is mounted to a brass, cylindrical plenum chamber that has 32mm inner and 80mm outer diameter. The Fluid entering to jet orifice plate holes does not have enough distance to develop prior discharging toward impinging surface so it can be assumed that jets issuing from nozzles has uniform velocity profile at the nozzle tip. In order to adjust nozzle to impingement plate distance long enough bolts are also mounted to the orifice plate with adjustment nuts. From my apparatus, flow rate, temperature of heat block and electric power can get and I can calculate Nusselt number and Reynolds number with them. These numbers can make an evaluation of heat transfer. The evaluation was consist of Nusselt number and Reynolds number and also investigate the difference between pure water and 0.5vol% Al₂O₃ nanofluid for each kind of nozzle jet plate.

Nusselt number and Reynolds number

Average Nusselt number is defined as;

$$Nu = \frac{hL_c}{k_f} \quad (1)$$

4th International Engineering Symposium - IES 2015

March 4-6, Kumamoto University, Japan

Since there is one impingement surface size considered in experiments, characteristic length L_c is taken half of the impingement surface diameter, $L_c=15.75$ mm. Nusselt number based on nozzle diameter also can be evaluated from equation (1) above, as;

$$Nu_L = 0.0952 \times Nu$$

(2)

0.0952 is the coefficient divided nozzle jet diameter to half heater length as, $1.5/15.75 = 0.0952$.

Heat transfer characteristics of a jet array impingement in terms of jet velocity can be examined by a dimensionless number, called Reynolds number. The jet Reynolds number in this study was determined from the average jet velocity calculated from the measured water flow rate. The jet velocity and thus the jet Reynolds number can then be calculated using the equations below.

$$Re = \frac{V_n d_n}{v_{film}}$$

(3)

$$V_n = \frac{4V}{N\pi d_n^2}$$

(4)

Results and discussion

Fig.5 to Fig.7 shows Reynolds number dependency of average Nusselt number for pure water and 0.5vol% Al₂O₃ nanofluid and each kind of nozzle jet plate respectively. From Fig.5, uses the nozzle jet plate which has 9 holes, the maximum Nusselt number is about 500. There are no big deference between pure water and 0.5 vol% Al₂O₃ nanofluid. From Fig.6, uses the nozzle jet plate which has 17 holes, the maximum Nusselt number is about 600, it is bigger than Fig.5. This is the result which difference is smallest between pure water and 0.5 vol% Al₂O₃ nanofluid. From Fig.7, uses the nozzle jet plate which has 25 holes, the maximum Nusselt number is about 700, it is the highest number for each plate. It might mean this is the best result what I get. At the beginning there is some difference, but the difference became smaller when Re

increases. Such a result has consistently been observed for water and the 0.5vol% Al₂O₃ nanofluid and for each of the nozzle jet plate the number of holes; N= 9, 17 and 25. With regard to the nanofluid effects on average Nusselt number relative to that of pure water, the results have surprisingly revealed that the use of nanofluid does not necessary provide a higher value of average Nusselt number.

Conclusion

The following conclusions are deduced from this study:

- Increasing Reynolds Number cause heat transfer augmentation
- From these result, 0.5 vol% Al₂O₃ Nanofluid does not provide heat transfer enhancement!
- Better heat transfer performance is obtained when the holes of nozzle is increased.

Future works

Now I am studying numerical simulation in the laboratory. Since aforementioned, this time my study didn't get good result for nanofluid so I would like to elucidate the reason why there are no difference between Al₂O₃ nanofluid and pure water with using numerical simulation.

Reference

- [1] Khanafer, K., Vafai, K. and Lightstone, M., International Journal of Heat and Mass Transfer, 46 (2003) 3639-3653.
- [2] Xuan, Y. and Li, Q., Journal of Heat Transfer, 125 (2003) 151-155.

Table 1 thermal conductivity of some kind of materials

Solids	Thermal Conductivity of the Particle (W/mK)	Liquids	Thermal Conductivity of the Fluid (W/mK)
Silver	425	Water	0.613
Copper	395	Ethylen Glycol	0.253
Aluminum	237	Engine Oil	0.145
Brass	120	Alcohol	0.115
Titania (TiO ₂)	11.7		
Alumina(Al ₂ O ₃)	39		
Carbon Nanotubes	3200-3500		



Fig.1 Al₂O₃ nanoparticles

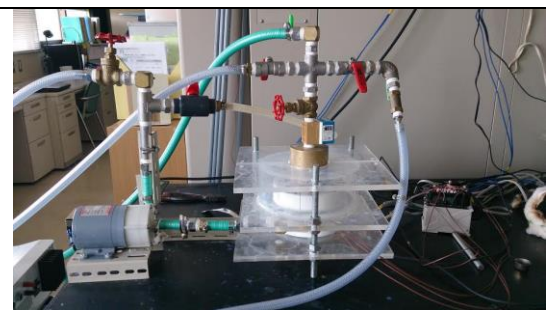


Fig.2 experimental apparatus

Table.1 The properties of Al ₂ O ₃ nanoparticles		
Physical properties	Color	White
	Particle shape	Sphere
	Smell	None
Molecular weight	101.96	
pH	6.5	
Average particle diameter [nm]	31	
Melting point [°C]	2054	
Boiling point [°C]	3000	
Density [g/cm ³]	3.53	
Specific particle surface area [m ² /g]	50.7	

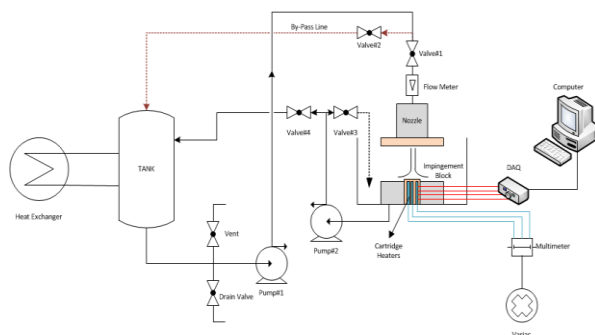


Fig.3 the construction of machine

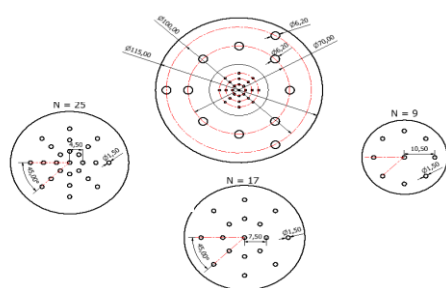


Fig.4 nozzle jet plate

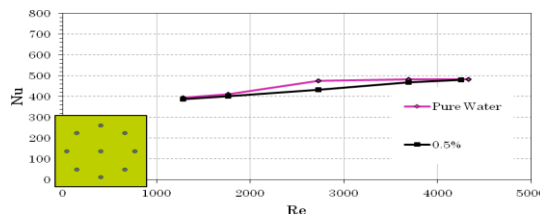


Fig.5 Average Nusselt Number for Various Reynolds Number
(N=9)

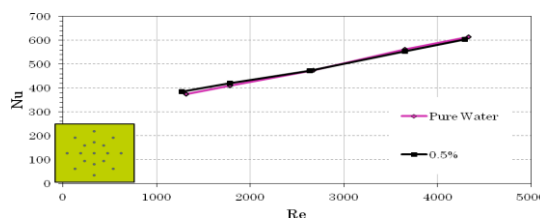


Fig.6 Average Nusselt Number for Various Reynolds Number
(N=17)

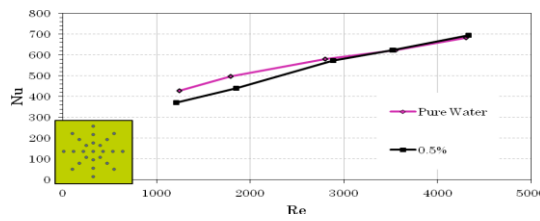


Fig.7 Average Nusselt Number for Various Reynolds Number
(N=25)

Generation of water-in-diesel emulsion fuel stabilized by two kinds of surfactants

Keisuke Goto 1, and Shuichi Torii 2

1 Graduate School of Science and Technology, Kumamoto University, Kurokami, 2-39-1, Kumamoto 860-8555, Japan. e-mail:135d8518@st.kumamoto-u.ac.jp

2 Graduate School of Science and Technology, Kumamoto University, Kurokami, 2-39-1, Kumamoto 860-8555, Japan. e-mail: torii@mech.kumamoto-u.ac.jp

Abstract: Emulsion fuel has been considered as one of the solutions to save the fossil fuel and suppress the environmental pollutions. But the separation between oil and water has been a big issue. In this research, combination of two surfactants, Sorbitan sesquioleate and Polyoxyethylene (20) sorbitan monopropionate, is applied to stabilize emulsion fuel. Samples are composed of 19%-water, 4.7%-Surfactants and 76.2%-diesel fuel. HLB number is changed to 6, 8, and 10. Then samples are emulsified by rotary homogenizer at around 45 °C. Samples are evaluated by visual observation, heating value measurement and particle size distribution. Results show that sample of HLB=6 shows the highest water concentration, and average particle size is around 704 nm. The sample also shows good stability.

Keywords: Emulsion fuel, Surfactants, HLB

Introduction

The exhaust gas of diesel engine especially from motor vehicles and other heat engines generally includes nitrogen oxides (NO_x) and particle matter (PM), which is harmful for both human body and natural environment. It is necessary to reduce these emissions and improve the fuel consumption.

Emulsion fuel has been considered as one of the solutions to save the fossil fuel and suppress these pollutions. The fuel is composed of diesel fuel, water and a small amount of surfactants. Reduction of NO_x and PM is due to the micro explosion caused by early evaporation of water droplet which covered by oil film [1][2]. There many reports that emission of NO_x and PM in exhaust can be reduced by using emulsion fuel. For example, it is reported that up to 30% reduction of NO_x and 60% reduction of PM can be achieved by the use of up to 15%-water emulsion fuel [3]. Besides, it has been reported that fuel consumption is often reduced by using emulsion fuel [3].

However, most of these researches are mainly focused on combustion, and there

is less research about emulsification conditions or stability of generated emulsion fuel. The stability of emulsion is also considered to be very important. Generically, emulsion is unstable in thermodynamic terms and will eventually separate [3]. Therefore, it is needed to keep stable emulsion for as long as possible.

In this study, we try to stabilize the emulsion fuel by the use of mixture of 2 kinds of surfactants.

Surfactants

Choice of surfactants is one of the important factors for generating stable emulsion. Non-ionic surfactants, which are often used for emulsion fuel, have HLB (Hydrophile Lipophile Balance) number. The number runs from 0 to 20. A surfactant its HLB closes to 0 means that it dissolves well in oil. On the contrary, a surfactant its HLB close to 20 means that it dissolves well in water.

In case of generating emulsion fuel, which needs water-in-oil emulsions, it has been considered that HLB from 4~6 is suitable. On the other hand, some

4th International Engineering Symposium - IES 2015

March 4-6, 2015, Kumamoto University, Japan

researchers have reported that the mixture of two surfactants, one is hydrophilic and another is lipophilic, often give a better emulsification result than a single use [3]. In the previous research, the most often used combination of surfactants is Sorbitan monooleate (HLB=4.3) and Polyoxyethylene (20) sorbitan monopropionate (HLB=15.0). In this research, Polyoxyethylene (20) Sorbitan monopropionate is used for hydrophilic surfactant as well, but Sorbitan sesquioleate (HLB=3.7) is used for lipophilic surfactant. As far as we know, there is no report of using this combination of surfactants. Properties of these used two surfactants are shown in Table 1. The formula of calculating HLB value of mixed 2 kinds of surfactants is shown below.

$$HLB_{A,B} = (H_A * X + H_B * Y) / (X + Y) \quad \dots\dots[4]$$

Here, H_A is HLB value of surfactant A, and H_B is HLB value of surfactant B. X and Y means amount of quantity of surfactant A and B, respectively.

Experimental method

Details of samples are shown Table 2. Sample is composed of 76.2% of diesel fuel, 19.0% of pure water, and 4.7 % of surfactant. This time, 3 kinds of sample are prepared by changing the HLB from 6 to 10.

These two surfactants and diesel fuel are blended and stirred using magnetic stirrer until the surfactants are dissolved entirely. Here, temperature is controlled around 45 °C. After the surfactants are dissolved, water is added into the liquid slowly. After the addition of water, the liquid begin to get cloud.

Homogenization of the compound liquid is done by the use of rotary homogenizer (Model;AHG-160A, shaft;HT1018, AS ONE Company, Japan). Photograph is shown in Fig.1. Number of rotations is 15,000 rpm, and it's continued for 3 minutes.

Evaluation of emulsion is done by visual observation, water content measurement, and particle size measurement.

In the Visual observation, samples are fixed in the motionless environment and

are observed the separation between diesel and water.

The water content is calculated by the use of heating value of sample. The small amount emulsion is picked up from intermediate layer of sample. The emulsion is completely burned by the use of calorimeter (CA-4AJ, Shimadzu Corporation, Japan). In this calorimeter, high calorific value is measured. Which means the heating value of sample (J/g) would be decreased linearly along with the addition of water. Using this mechanism, by comparing emulsion sample with neat diesel fuel, water content of emulsion is finally calculated.

The particle size distribution of emulsion sample is determined by the use of dynamic light scattering equipment (Zetasizer Nano ZS, Malvern Instruments Ltd, UK).

Results and Discussion

Fig.1 shows the results of visual observation. It is a little difficult to recognize, but the sample of HLB=8 is separated at lower layer of bottle. The rest of two samples look like uniformly white and cloud.

Fig.2 shows the results of heating value measurement, and calculated water content is shown in Fig.3. From these figure, it becomes clear that the sample of HLB=6 has the best stability of the three kinds of HLB. On the other hand, sample of HLB=6 shows the lowest stability.

Fig.4 and Table 3 show the particle size distribution of the three emulsion sample. Sample of HLB=8 shows the smallest particle size, while sample of HLB=6 shows the biggest particle size. It is considered that unstable emulsion couldn't keep relatively bigger water particle inside, and these particles become deposited.

Conclusions

The following conclusions are deduced from this study:

- Samples are prepared with different HLB value (6, 8, and 10), and the sample of HLB=6 shows the best stability, and water particle diameter is around 700 nm.

4th International Engineering Symposium - IES 2015

March 4-6, 2015, Kumamoto University, Japan

- The unstable emulsion couldn't keep relatively bigger water particle inside, which eventually deposited.
- The combination of Sorbitan monopropionate and Polyoxyethylene (20) sorbitan monopropionate is useful for generating water-in-diesel emulsion.

References

- [1] Kadota, T. and Yamasaki, H. (2002), Recent advances in the combustion of water fuel emulsion, Progress in Energy and Combustion Science, 28(5), pp.385–404.
 [2] W.M. Yang, et al (2013), Impact of emulsion fuel with nano-organic additives on the performance of diesel engine, Applied Energy, 112, pp.1206–1212
 [3] Lif A and Holmberg K (2006), Water-in-diesel emulsions and related systems, Advances in Colloid and Interface Science, 123–126, pp. 231–239
 [4] Horiuchi T (2010), Basic Theory of Emulsification, J.Soc.Cosmet.Chem.Jpn., 44(1), pp.2-22

Table 1 Properties of used surfactants

Material	HLB	Source
Sorbitan sesquioleate	3.7	Kao Co. Japan
Polyoxyethylene (20) sorbitan monopropionate	15.0	Kao Co. Japan

Table 2 Experimental conditions

HLB values	Diesel (wt.%)	Water (wt.%)	Surfactant (wt.%)
6.0	76.2	19.0	4.7
8.0	76.2	19.0	4.7
10.0	76.2	19.0	4.7



Fig.1 Emulsion sample: 17 days later.

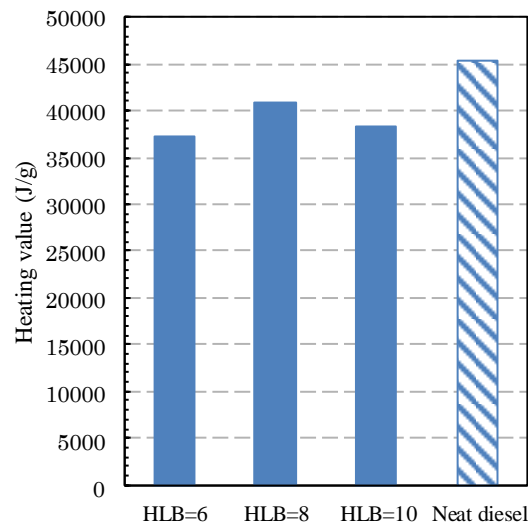


Fig.2 Heating value of emulsion fuel and neat diesel fuel: 16 days later.

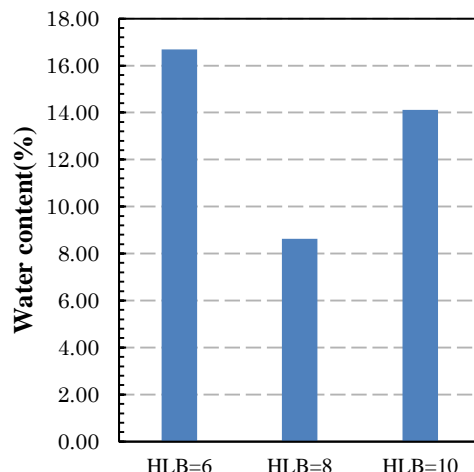


Fig.3 Water content of emulsion fuel: 16 days later.

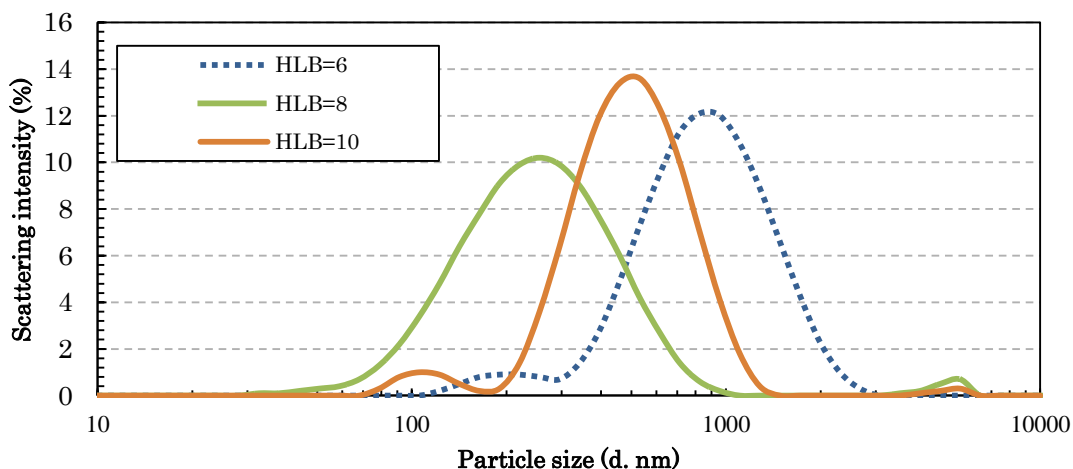


Fig.4 Particle size distribution of emulsion sample: 3 days later

Table 3 Average of particle size and PDI: 3 days later.

Sample	particle size (d.nm)	PDI
HLB=6	704.5	0.253
HLB=8	219.6	0.255
HLB=10	433.9	0.218

An Innovative Renewable Energy Application for Algae and its Combination with other Materials

An-Peng Chen¹ and Torii Shuichi²

¹ Graduated School of Science and Technology, Kumamoto University, Kurokami, 2-39-1, Kumamoto 860-8555, Japan. e-mail:abc_10@kumamoto-u.ac.jp

² Department of Mechanical System Engineering, Kumamoto University, Kurokami, 2-39-1, Kumamoto 860-8555, Japan. e-mail:abc_10@kumamoto-u.ac.jp

Abstract: Biomass is a composition of various types of waste materials that can be utilized as useful form of energy. However this new kind of energy hasn't met its full potential in production of energy especially electricity generation due to its lower performance in terms of thermal efficiency. Algae and microalgae has been treated as the source of bio-fuel and some algae also used in fermentation for bio-gas and other phase of energy. In this paper we selected the two type of freshwater microalgae "Chlorella Vulgaris" & "Spirulina" and macro algae (*Laminariaceae* & *Undaria pinnatifida*) as the main materials and we combined with vege-oil in different combination, which analysed calorific values (heat of combustion).

We found combination ratio for the analysed caloric values similar as fossil fuel (coal), and compared with the other biomass materials for its potential use in combustion system. The results in this paper will be used as a reference material for microalgae multi-oriental energy application and biomass composition proximate and ultimate research development in the future.

Keywords: Biomass Energy, Macroalgae, Renewable Energy,

Introduction

Global warning and climate change are very serious environmental topics in this decade. Reducing the emission of CO₂ and finding alternative energy source become an important issue now. Since 19th century industrial evolution, the usage of fossil fuel is increasing rapidly. However the fossil fuel is limited and the CO₂ emission is also related to the climate change and global warming, the studies and research lead to focus on sustainable development, and renewable energy plays an important role in 21st century. Renewable energy is the energy from nature resource, such as wind, sunlight, tides, OTECs, and biomass matters i.e. Lau. L.C et al.(2012). Biomass energy has been wildly used in decades, especially in some developing countries i.e. Dincer (2000). Biomass is a combination of different types materials, includes woods, agricultural waste, animal grease, and aquatic plant waste (Table1.) and these materials provide up to 33.7

MJ/Kg energy in the combustion system. Biomass becomes an important role in renewable energy.

Table.1 List of biomass and its energy.

Biomass Type	MJ/Kg
Forest Wood	18.80
Wood Waste	19.45
Seeds	20.01
Composite Waste	25.36
Husk	21.8
Oils Type	33.7

(i.e. Chen. A.P et al. (2014))

The 1st generation biofuel, which is made for soybean, corn or food crop etc., is linked to food crisis in the early 21st century. The 2nd generation is using biomass waste materials, is not able to compare to fossil fuel. The focus shifted to 3rd generation of biofuel, which the main source is different from the other two generations i.e. Sims. R et al.(2008) .

4th International Engineering Symposium - IES 2015

March 4-6, Kumamoto University, Japan

Algae play an important role in East Asia food culture. For example, in Japan, Taiwan, Korea and China, people eat algae everyday. The algae application into energy related field began in 1978, U.S government found the Aquatic Species Program (ASP) in Hawaii, just after the oil crisis and the mid-east war. Japanese government also held the projects using algae for CO₂ fixation and utilization in 1990 to 1996. However, these projects failed to apply in large-scale aquaculture, and make the economic balance in the same. These projects had been stopped in late 90s, but these programs still provided some crucial results and some of them such as lipid production strains; aquatic culture system and principles for photo-bioreactor design are still the main focus research projects today in many countries. When time entered 21st century, the studies about renewable raised rapidly. Microalgae are the most promising non-food source of biofuels. Seeking the new energy source and potential material has become the trend in this century. Microalgae as the third generation biomass fuel has the great potential become the solution (Fig 1) i.e. Wijffels R.H. and Barbosa M.J (2010).

In recent studies, the using algae likes other main objective to biomass energy is about to overcome low performance and increase the efficiency. In purpose of improving the efficiency effectively, those algae needed to be treated or pretreated before used in energy system or transform into other energy phase. However, the algal biodiesel production has shown that lipid extraction and harvesting procedures could jeopardize the environment and cost energy waste. Some studies use the fermentation, which is anaerobic reaction with a biological process in which sugars such as glucose, fructose, and sucrose are converted into cellular energy and thereby produce ethanol and carbon dioxide as metabolic waste products. Anaerobic digestion is a spontaneous process mediated by micro-organisms converting biomass into biogas i.e. Ras. M et al.(2011). In this study, we try to analysis the algae biomass and combination with vege-oil as solid fuel for their calorific values. These data will be used as the foundation database for future using with the biomass boiler development, and it will provide the basic information as an alternative biomass material for combustion boiler system.

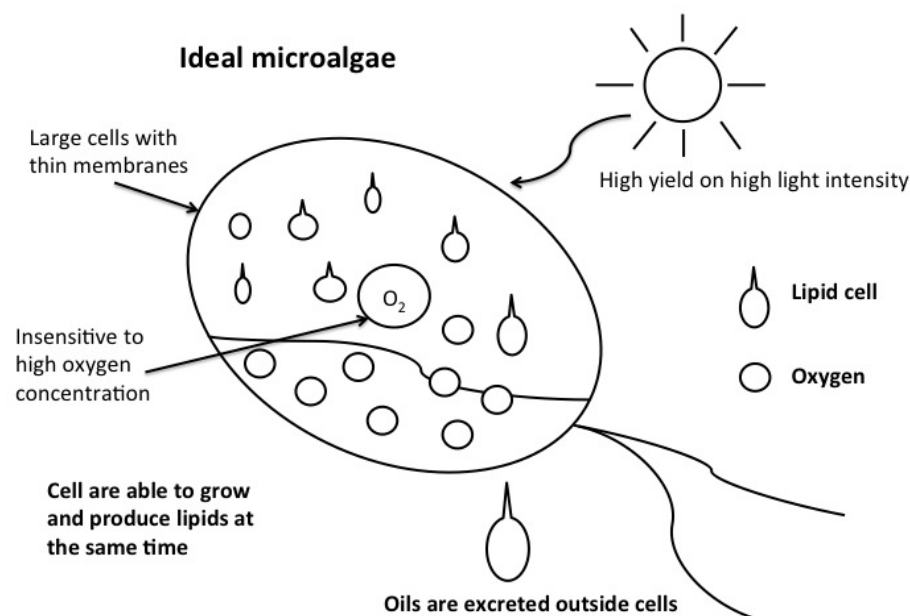


Fig 1.: The ideal photosynthetic cell factory for production of biofuel

Materials and Method

In this study, we analysed four different species algae and one kind of Vege-oil. The two species of microalgae powder (*Chlorella V.* and *Spirulina*) are from Taiwan Chlorella Manufacturing Company, and these microalgae powder uses wildly in food, nutrient supplements, cosmetic, medicine and fishery aquaculture. Two kinds of macro-algae includes *Laminariaceae* and *Undaria pinnatifida*., they are from local supermarket in Kumamoto City.

The calorific value analysis method covers the determination of the gross calorific value of a prepared analysis sample of solid forms of biomass by the bomb calorimeter method. The calorific value, or heat of combustion, is a measure of the energy available from the microalgae. Calorific value is determined in this method by burning a weighed analysis sample in an oxygen bomb calorimeter under controlled conditions.

The macro algae samples had been grinded by food mixer and all sample are dried before bomb detection. (Fig 2)

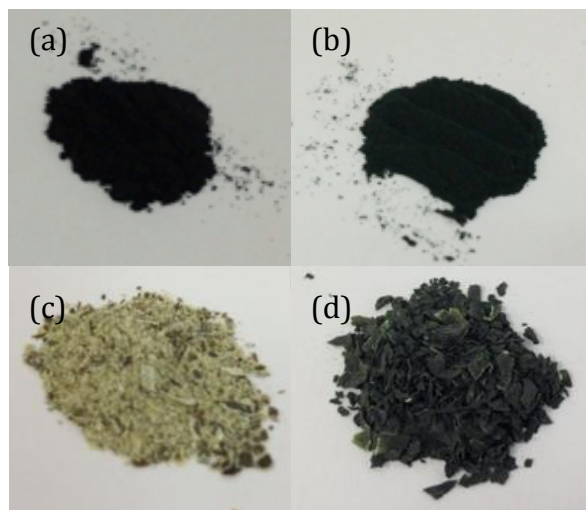


Fig 2 Algae Samples

- (a) *Chlorella*
- (b) *Spirulina*
- (c) *Laminariaceae*
- (d) *Undaria pinnatifida*

Results and Discussions

In calorific values analysis, we test four species of algae, Vege-oil and fossil fuel (coal) samples. As the results show in Table 2., the *Chlorella* and *Spirulina* calorific value are both are near or over 5000 KC/KG and the other two species of macro algae are much lower, calorific value only near 2,500 Kcal/KG. However, none of them is higher than fossil fuel (6548 Kcal/KG), these kinds of algae need to mix other biomass materials to increase the calorific value, which might be able to compete with the fossil fuel.

Table 2 Calorific value from algae species and fossil fuel

	KJ/KG	Kcal/KG
Algae		
<i>Chlorella V.</i>	21174.5	5057.4
<i>Spirulina</i>	20866.3	4983.8
<i>Laminariaceae</i>	11665.5	2786.3
<i>Undaria P.</i>	9759.0	2330.9
Fossil Fuel		
Coal	28665.7	6846.7

We used the data from algae and simulated calorific value with combination with Vege-oil (9567.8 Kcal/KG), and we selected several combinations that calorific vale similar to fossil fuel (coal). We found that the using ratio for Vege-oil is over 40% and with macro algae is up to 60%.

Table 3 Calorific value from algae combination with Vege-Oil

Vege Oil (%)	Algae (%)	Simulate (Kcal/KG)	Test (Kcal/KG)
40	60 (a)	6861.6	6729.8
40	60 (b)	6817.4	6593.9
60	40 (c)	6855.2	6683.0
60	40 (d)	6673.0	6548.3

- (a) *Chlorella*
- (b) *Spirulina*
- (c) *Laminariaceae*
- (d) *Undaria pinnatifida*

4th International Engineering Symposium - IES 2015

March 4-6, 2015, Kumamoto University, Japan

Conclusions

We analyzed algae sample and combination with Vege-oil, and the following conclusions are deduced from this study:

- Calorific value from microalgae is almost twice higher than macro-algae.
- Even using the *Chlorella V.*, the specie with highest calorific value 5057.4 Kcal/KG, the calorific value is still lower the fossil fuel.
- Combinations with algae and Vege-oil, the calorific values are similar to fossil fuel, and Vege-oil must content over 40%~60%.

In Taiwan, and some other Southern Asian countries have the euphotic effects in the lakes, ponds or dams. Algae not only damage the ecosystem in the aquatic area and also become a waste treatment issue. In this study, we analyzed calorific value from algae and the combination with Vege-oil. Algae can provide high energy, but still need to combine with other materials for higher calorific value as fossil fuel. Algae and biomass energy related technologies still have a huge space for improvement and microalgae related researches would be even better optimized in the near future.

References

- [1] Chen, A P et al (2014), Classification of biomass based on its role of combustion for sustainable and renewable source of energy using proximate and ultimate analysis, IJEE JOURNAL, Vol. 07, No. 01, pp.136-142.
- [2] Dincer, I (2000), Renewable energy and sustainable development: a crucial review, RSER RSER JOURNAL, Vol. 04, No. 02, pp.157-175.
- [3] Lau, L C et al (2012), Global warming mitigation and renewable energy policy development from the Kyoto Protocol to the Copenhagen Accord—A comment, RSER JOURNAL, Vol. 16, No. 07, pp.5280-5284.
- [4] Sims, R et al (2008), From 1st to 2nd generation biofuel technologies, an overview of current industry and R&D activities, IEA Report
- [5] Wijffels R H and Barbosa, M J (2010) An outlook on microalgal biofuels, Science JOURNAL. Vol. 379, No. 5993. pp. 796-799.

4th International Engineering Symposium - IES 2015

March 4-6, 2015, Kumamoto University, Japan

**CIVIL ENGINEERING
&
RELATED FIELDS**

PARAMETRIC STUDY ON ROTATION AND PLASTIC HINGE FORMATION IN RC BEAMS

Prabhakara R¹, Nambiyanna. B², Atul Gopinath³ and Nakul R⁴

- 1 Civil Engg. Dept., M S Ramaiah Institute of Technology, Bangalore, India, e-mail: r.prabhakara@gmail.com
- 2 Civil Engg. Dept., M S Ramaiah Institute of Technology, Bangalore, India, e-mail: nambiyanna1@gmail.com
- 3 Civil Engg. Dept., M S Ramaiah Institute of Technology, Bangalore, India, e-mail: atulcgopinath@gmail.com
- 4 Civil Engg. Dept, University of Delaware, USA, e-mail: nakul@udel.edu

Abstract: Plastic Hinge is an inelastic rotation of a joint of a structural member under the constant moment. The formation of plastic hinge in RC structural member is slightly different than that of steel. It has been observed from the literature that plastic hinge in RC structural member is influenced by several parameters and makes it to be a complicated phenomenon. Parametric analysis was carried out by collecting more than hundred data from the available literature. Graphs were plotted to demonstrate the variation of plastic hinge length (l_p) to the influencing parameters such as cross sectional dimensions of the beams, grade of the concrete, tension reinforcement, and span to depth ratio. The plastic hinge length was calculated based on existing analytical models given by researchers. The analytical methods are becoming popular in design of RC structures. These analytical models are very useful and provide more knowledge on the behaviour of RC structures. In this study, existing analytical models are evaluated based on the different variables. The plastic hinge length was determined by nonlinear regression analysis. It was found from the analysis that both existing plastic hinge models and proposed Nonlinear Regression analysis model yielded results that are almost comparable.

Keywords: Beams, Nonlinear Regression Analysis, Parametric Study, Rotation Capacity, Plastic Hinge length.

I. INTRODUCTION

In RC structures as the applied load is increased, the hinges starts forming in succession at locations where the hinge moment capacity is reached, with further increase in the applied load, these hinges continue to rotate until the last hinge forms converting the structure into a mechanism and further resulting in failure. The multi-storey framed structures are designed to achieve by proportioning the beams and columns so that majority of the plastic hinges formed in the beams not in the columns. In case the plastic hinge formed in columns earlier than beams then structure will collapse without giving any warning. For this reason plastic hinge is an important parameter to be understood in RC structures.

There are two different types of plastic hinges may formed in RC structures, such

as reversing plastic hinges and unidirectional plastic hinges. The reversing plastic hinge is sustaining both positive and negative inelastic rotation in the same region and unidirectional plastic hinge sustain both in different regions of the beam element during earthquake [26]. The studies performed to indicate that determine the plastic hinge length and various parameters that affect the plastic hinge length. The plastic hinge length l_p of RC beams depends on a number of parameters such as, cross sectional dimensions, yielding and ultimate curvatures, material characteristics, tension and compression reinforcement ratios, support conditions and the magnitude and type of loading [1].

The main objective of this study is to propose a soft computing method based algorithm that can estimate the length of a plastic hinge by using experimental studies

conducted for the RC beams [3]-[8]. For this study, numbers of RC beams test results have been collected from the literature. The numbers of parameters that can affect the plastic hinge length such as, cross sectional dimensions, yielding and ultimate curvatures, material characteristics, tension and compression reinforcement ratios, support conditions and the magnitude and type of loading etc. In this study, when determining the length of plastic hinge, using the experimental test results, the Regression Analysis have been carried out to find out the length of plastic hinge and compared with each other [2].

II. PLASTIC HINGE LENGTH

It is generally agreed that the inelastic rotations are concentrated over a length called "plastic hinge length" where $M_y < M < M_u$. Plastic hinge length is dependent on the shape of the bending moment diagram at the ultimate stage, and is also affected by the distance between points of contra flexure, and distance between support, reinforcement ratio, the compressive strength of concrete and depth of section [1]. The equivalent plastic hinge length can be calculated based on integration of the curvature distribution for typical members.

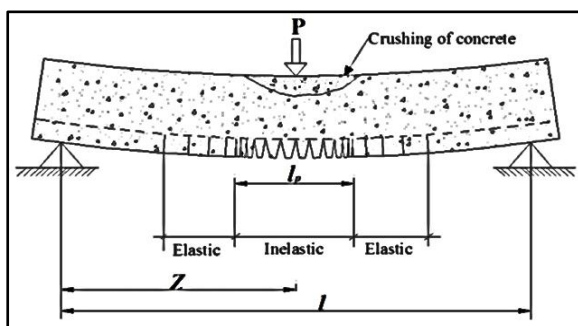


Fig.1 Plastic hinge length

The length of plastic hinge l_p of RC members depends on a number of parameters, cross sectional dimensions, yielding and ultimate curvatures, material characteristics, tension and compression reinforcement ratios. These parameters also affect the section ductility of the member and shape of moment-curvature curve. Therefore, the relationship between the cross-section ductility and the plastic

joint length must be accurately determined. According to the proposed various formulas, some important parameters that are more effective on the plastic hinge length ' l_p ' have been used [2].

TABLE.1 Existing Length of Plastic Hinge (l_p) Models [7]

Researcher Reference	Plastic Hinge Length Expression (l_p)
Baker (1956)	$k(z / d)^{1/4} d$
Sawyer (1964)	$0.25d + 0.075z$
Corley (1966)	$0.5d + 0.2 \sqrt{d} (z / d)$
Mattock (1967)	$0.5d + 0.05z$
Priestley and Park (1987)	$0.08z + 6d_b$
Paulay and Priestley(1992)	$0.08z + 0.022d_b$
Sheikh and Khoury (1993)	$1.0h$
Coleman and Spacone (2001)	$G_c^c/[0.6f'_c(\epsilon_{20^-} - \epsilon_c + 0.8 f'_c/E_c)]$
Panagiotakos and Fardis (2001)	$0.18z + 0.021db$

The researchers proposed formulas gives a constant l_p regardless of the important parameters given above. For instance, Sawyer, Corley and Mattock consider only length and depth of the section shown in TABLE.1. Priestley & Park expressions the l_p depends on length and diameter of reinforcement of the beam.

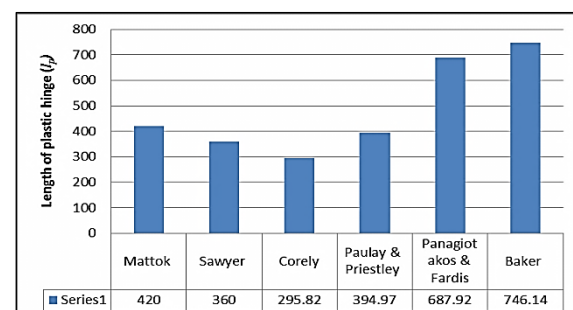


Fig. 2 Variation of plastic hinge length (l_p)

Keeping the same parameters such as $l=6000$, $b=300$, $d=540$, $f'_c=30.9$, $Z=3000$ $l/d=11.11$, $\sqrt{d}=23.23\text{mm}$ the plastic hinge

length was obtained using the above equations and they were plotted as shown in **Fig 2**. It was observed a large variation in the plastic hinge length which encouraged us to study on the parameters effect and regression analysis.

III. PARAMETRIC STUDY

In this study, the central point loading configuration and different equivalent length of beams were selected from literature [3] - [8]. The range of the parameters such as characteristics strength of concrete and steel, width and depth of beams, tension and compression steel percentages and all other essential parameters that affecting the beam behaviour under central point loadings as shown in **TABLE 2**.

TABLE. 2 Range of parameters used

Parameters	Parameters Range
$f'c$ (MPa)	20-129.1
f_y (MPa)	250-678
L (mm)	1000-12000
b (mm)	50-500
d (mm)	90-950
z (mm)	500-6000
ρ (%)	0.13-6.45
ρ' (%)	0-4.84
I/d	4.17-21.82

IV. DETERMINATION OF PLASTIC HINGE LENGTH

In this study, length of the plastic hinge l_p was determined based on different parameters obtained from the previous studies. The beam plastic rotation (θ_p) was calculated from equation (1) [11].

$$\theta_p = \frac{0.004}{(x_u/d)} \dots \dots \dots (1)$$

The plastic hinge length l_p was calculated based on Equation (2) [1] by using the plastic rotation value (θ_p) from Equation(1) curvature at yielding moment (φ_y), and the curvature at ultimate moment (φ_u), plastic hinge length values were analytically calculated.

$$l_p = \frac{\theta_p}{\varphi_u - \varphi_y} = \frac{\theta_p}{\varphi_p} \dots \dots \dots (2)$$

Using the above equations plastic hinge length was calculated. Illustrative graphs have been plotted to observe the variation of l_p over the above listed parameters as shown in **FIG 3 – FIG 8**

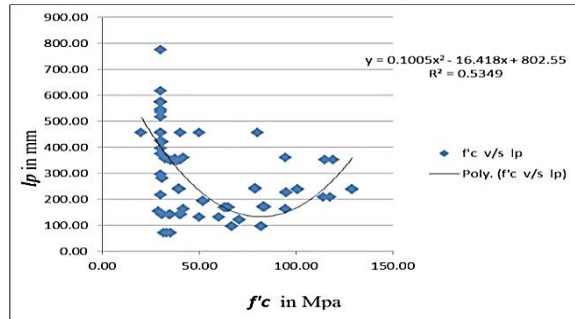


Fig. 3: Plastic hinge length l_p Vs $f'c$.

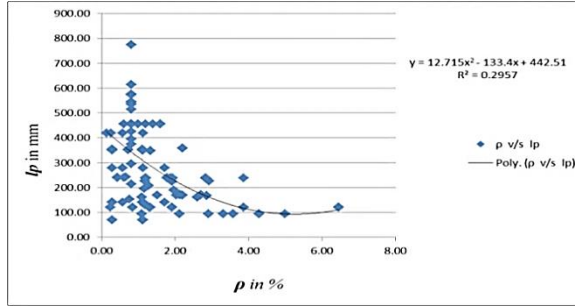


Fig. 4: Plastic hinge length l_p Vs ρ in %

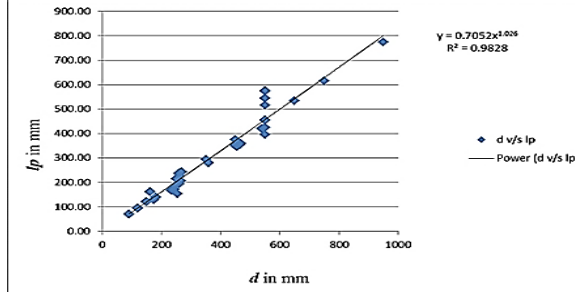


Fig. 5: Plastic hinge length l_p Vs d in mm

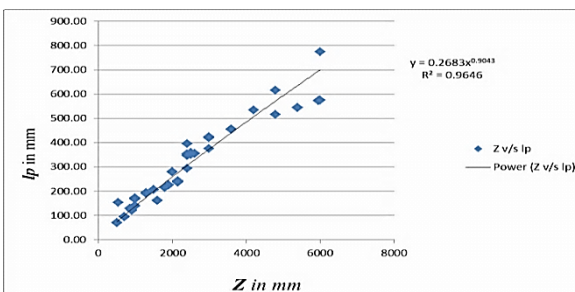


Fig. 6: Plastic hinge length l_p Vs z in mm

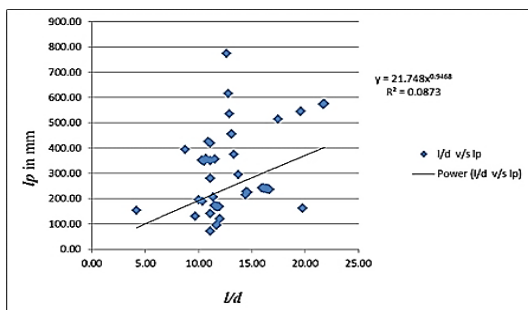


Fig. 7: Plastic hinge length I_p Vs I/d ratio

It has been observed from **Fig 2 – Fig 7**, the length of plastic hinge has not shown much variation with grade of concrete however reduction in I_p was observed with increase in reinforcement ratio and further it was observed that I_p increased with increase in depth, span to depth ratio, Z and Z/d ratio.

V. NONLINEAR REGRESSION ANALYSIS

Nonlinear Regression analysis is a method of mathematical modelling. In this study, cross sectional dimensions, material characteristics, yielding and ultimate deflections, tension and compression reinforcement ratios were observed and parameters that effects on plastic hinge length is analysed by using the Nonlinear Regression Analysis. The variables correlation matrix is given in **TABLE 3**.

TABLE 3 Variables Correlation Matrix.

	I_p	b	d	f'_c	z	p	I/d	\sqrt{d}
I_p	1.000	0.802	0.986	-0.549	0.974	-0.504	0.291	0.980
b	0.802	1.000	0.785	-0.358	0.789	-0.284	0.385	0.769
d	0.986	0.785	1.000	-0.566	0.923	-0.510	0.145	0.994
f'_c	-0.549	-0.358	-0.566	1.000	-0.501	0.471	0.105	-0.544
z	0.974	0.789	0.923	-0.501	1.000	-0.472	0.475	0.917
p	-0.504	-0.284	-0.510	0.471	-0.472	1.000	-0.074	-0.524
I/d	0.291	0.385	0.145	0.105	0.475	-0.074	1.000	0.158
\sqrt{d}	0.980	0.769	0.994	-0.544	0.917	-0.524	0.158	1.000

The analysed values in **TABLE 3** the effective depth of the section was found the largest correlation variable in analysis. This value is considered to be positively correlated with Length of Plastic Hinge dependent of variables in **TABLE 3**.

TABLE 4 Nonlinear Regression Analysis results

	Coefficients	Standard Error	t Stat	P-value
Constant	0.370	0.009521	-43.6971	1.28E-92
b (mm)	0.00896	0.004097	2.18688	0.030159
d (mm)	0.667466	0.013165	50.69865	1.6E-102
f'_c(mpa)	-0.0016	0.002688	-0.59403	0.553306
z (mm)	0.326426	0.0142	22.9876	2.57E-53
p (%)	-0.00207	0.00164	-1.26063	0.209221
I/d (mm)	0.059266	0.015058	3.935793	0.000122

In **TABLE 4**, the results are shown in the nonlinear regression analysis. With respect to those results, we have formulated our Regression equation for plastic hinge length (I_p) as follows.

$$I_p = 0.37 * b^{0.00896} * d^{0.667} * f'_c^{-0.0016} * z^{0.3264} * p^{-0.00207} * I/d^{0.059266} \dots \dots \dots (3)$$

The plastic hinge length **Equation (3)** is determined by regression analysis and comparison between Regression I_{preg} and exiting models I_p (I_p is calculated by using existing models are tabulated in **TABLE. 1**) is shown **Fig. 8.**

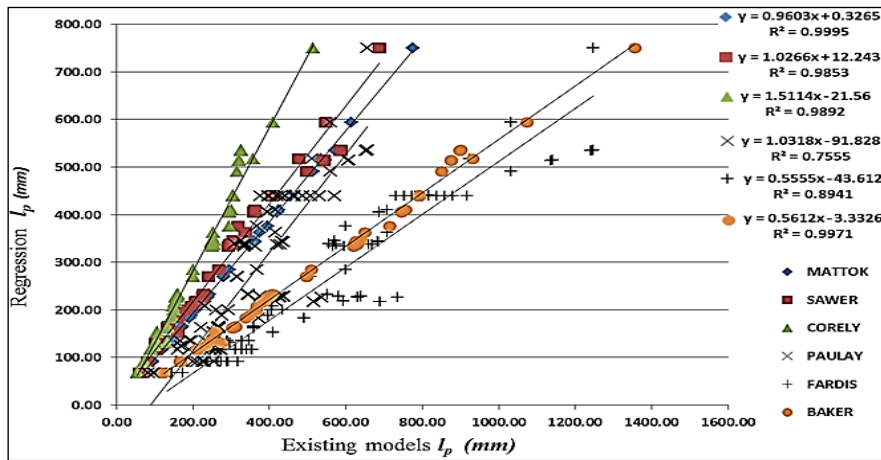


Fig.9: Comparison between Regression I_{preg} and Existing models I_p

It has been observed from **Fig.9** the comparison between regression plastic hinge length I_{preg} v/s existing models I_p trend lines shows that the proposed model is well predicted with Mattock, Sawyer, Corely and Baker's models and R^2 values are almost equal to unity

VI. CONCLUSIONS

Based on the parametric study and proposed Nonlinear Regression analysis the following conclusions have been drawn.

The plastic hinge length results obtained by using plastic rotation and curvatures at ultimate and yield load (vide EQ 1- 2)

Total of 173 data from available literature were collected and systematically tabulated to obtain the plastic hinge length

Demonstrative graphs have been plotted to show the variation of influencing parameters. It was observed from **Fig. 3-**

Fig. 8, the length of plastic hinge has not shown much variation with grade of concrete however reduction in I_p was observed with increase in reinforcement ratio.

Further it was observed that I_p increased with increase in depth, span to depth ratio, Z and Z/d ratio.

Analytical expressions given in literature assumed that only the cross-sectional dimensions were under the bending effect

of beam. They were not considered the effect of other parameters.

The plastic hinge length obtained by expressions given by the authors gave different results and the variation was very large.

Nonlinear regression analysis was carried out for 173 data by considering all the influencing parameters

The variable correlation matrix shows that (**TABLE.3**), the depth of beam (d) is more influencing parameter on I_p and other parameters have shown less effect.

It has been observed that analytical plastic hinge expression and proposed Nonlinear Regression expression yielded results that are comparable.

Based on comparison between I_p calculated by existing model and $I_{p, reg}$ calculated by nonlinear regression model the results shows that, the nonlinear regression Plastic hinge model ($I_{p, reg}$) is general and can be used all types of beams concrete Beams.

NOTATIONS

d =effective depth of beam, mm
 l = effective length of the beam, mm
 l_p = plastic hinge length, mm
 $l_{p\ reg}$ = pl hinge length by regression mm
 Z = distance from critical section to point of contra flexure, mm
 f'_c =designed cylinder compressive strength in MPa
 f_y =specified yield strength of the reinforcement, MPa
 ρ = tension reinforcement in %
 θ_p =plastic rotation, (rad)
 ϕ_y =curvature at yield moment, (rad/mm)
 ϕ_u =curvature at ultimate moment, (rad/mm)
 ϕ_p =curvature at plastic moment, (rad/mm)
 Δ_y = deflection at yield, mm
 Δ_u = deflection at ultimate, mm

VII. REFERENCES

1. Ali Kheyroddin and Hosein Naderpour "Plastic Hinge Rotation Capacity of Reinforced Concrete Beams", International Journal of Civil Engg. Vol. 5, No. 1, March 2007.
2. M. Alpaslan, M. H. Arslan, and M. K. Körez, "Use of Regression Analysis in Determining the Length of Plastic Hinge in Reinforced Concrete Columns," no. 4, pp. 62-67, 2014.
3. Bigaj A., Walraven J. (1993). Size effect on rotational capacity of plastic hinges in reinforced concrete beams. CEB Bulletin d'Information No. 218, Ductility - Reinforcement, pp. 7-23
4. Bosco C, Debernardi P.(1993). Influence of some basic parameters on plastic rotation of reinforced concrete elements. CEB Bulletin d'Information No.218, Ductility Reinforcement, pp. 25-44
5. S. M. R. Lopes and L. E. A. Bernardo, "Plastic rotation capacity of high-strength concrete beams," vol. 36, no. February, pp. 22-31, 2003.
6. Hakan Fransson (1997)"Rotation Capacity of Reinforced High Strength Concrete Beams" TRITA-BKN. Bulletin 32 1997 ISSN 1103-4270 ISRN KTH/BKN/B-32—SE, Licentiate Thesis.
7. X. Zhao, Y.-F. Wu, A. Y. Leung, and H. F. Lam, "Plastic Hinge Length in Reinforced Concrete Flexural Members," Procedia Eng., vol. 14, pp. 1266-1274, Jan. 2011.
8. Man-Young Ko, Sang-Woo Kim, and Jin-Koo Kim, "Experimental Study on the Plastic Rotation Capacity of Reinforced High Strength Concrete Beams," Journal of Architectural Institute of Korea.
9. An L., Cederwall K. (1995). Rotational Capacity of Concrete Beams. Summary of Re-evaluation of Test Results. Betongbyggnad, Chalmers Tekniska Högskola, Report 95:
10. Alberto Carpinteri, Mauro Corrado, Giuseppe Mancini, and Marco Paggi, "A Numerical approach to modelling Size Effects on the flexural ductility of RC beams," Material and structures. Pp.1353 – 1367, Dec. 2008.
11. Alberto Carpinteri, Mauro Corrado, Giuseppe Mancini, and Marco Paggi, "Size -Scale Effects on Plastic Rotation Capacity of Reinforced Concrete Beams," ACI Structural Journal. pp. 887-896, Dec. 2009.
12. A. L. Gamino and T. N. Bittencourt, "Numerical evaluation of plastic rotation capacity in R C beams."
13. Mattock, A.H. (1964). "Rotational Capacity of Hinging Regions in Reinforced Concrete Beams", Proceedings of the International Symposium on Flexural Mechanics of Reinforced Concrete, Miami, Florida, ACI SP-12, pp. 143-181.
14. Sawyer H.A. (1964), "Design of Concrete Frames for Two Failure States", Proc. of the International Symposium on the Flexural Mechanics of Reinforced Concrete. ASCE-ACI, Miami, pp.405-431.
15. Park, R., Priestley, M.J. and Gill, W.D., Ductility of Square Confined Concrete Columns, Journal of the Structural Division, ASCE, Vol.108, No. ST4, pp. 929- 950, 1982.
16. Paulay, T. and Priestley, M.J.N., Seismic Design of Reinforced Concrete and Masonry Buildings, John Wiley and Sons, New York (1992).
17. Panagiotakos TB, Fardis MN. 2001. Deformations of reinforced concrete members at yielding and ultimate. ACI Structural Journal. 98:135-148.
18. Bae, S. and Bayrak,"Plastic hinge length of reinforced concrete columns", ACI Structural Journal, 105(3), pp. 290-300 (2008).
19. Stefano, M. De et al., 2001. "Effects of randomness in steel mechanical properties on rotational capacity of RC beams", 34(March), pp.92-99.
20. Ali, M.S.M., Oehlers, D.J. & Griffith, M.C., 2009. "Simulation of Plastic Hinges in FRP-Plated RC Beams., 12(6), pp.617-625.
21. Haskett, M. et al., 2009. Yield Penetration Hinge Rotation in Reinforced Concrete Beams.(February), pp.130-138.
22. M S Mohamed Ali, Ph.D., D J Oehlers, M Haskett, and M C Griffith. "Discrete Rotation in RC Beams" 138 (11): 1317-1325. 2013.
23. Naaman, A. E., Harajli, M. H. and Wight, J. K., 'Analysis of ductility in partially prestressed concrete flexural members', PCI Journal 31 (3) (1986) 64-87.
24. A. Mortezaei and H. R. Ronagh, "Sharif University of Technology Plastic hinge length of FRP strengthened reinforced concrete columns subjected to both far-fault and near-fault ground motions," Sci. Iran., vol. 19, no. 6, pp. 1365-1378, 2012.
25. P. Mendis, "Plastic hinge lengths of normal and high-strength concrete in flexure," vol. 4, no. 4, p. 2001, 2001.
26. Megget,L.M. and Fenwick, R.C. (1989) " The Seismic Behaviour of reinforced concrete Portal Frame sustaining Gravity Loads" Bulletin of NZ National Society for Earthquake Engineering. Vol.26 No.1, pp28-41
27. Richard C, Fenwick et al., 1996 " Load deflection characteristics of Plastic hinges in ductile concrete Beams" the university of Auckland Private Bag 92019, Auckland, New Zealand.

"Analysis of Torsional Behaviour of Reinforced Normal, Medium and HSC Beams"

Prakash M R¹, Sadanand Patil² and Prabhakara R³

-
1. Dept of Civil Engg, Acharya Institute of Technology, Soladevanahalli, Bangalore.
 2. Dept of Civil Engg, Gogte Institute of Technology, Belgaum.
 3. Dept of Civil Engg, M S Ramaiah Institute of Technology, Bangalore.
-

ABSTRACT: To understand the behaviour of beams in torsion an experimental investigation was carried out on Normal, Medium and High Strength Concrete beams, Nine NSC, Nine MSC and Nine HSC beams with constant width, depth, effective span, varying longitudinal and transverse reinforcement ratio was studied under standard testing conditions. The parameters studied in this investigation are ductility behaviour, cracking torsional strength, ultimate torsional strength, failure pattern, longitudinal and transverse reinforcement, torque-rotation behaviour and torsional stiffness. The results obtained from the experimental investigations were compared with the different codal provisions and also the equations given by researchers. Also a parametric analysis was carried out for different models, theories and codal equations for 102 data collected from 8 investigations. Relevant conclusions were listed.

Keywords: Torsion, parametric, ultimate, transverse, models.

INTRODUCTION:

Many structural elements in building and bridge construction are subjected to significant torsional moments that affect the design. Reinforced concrete members in a structure may be subjected to axial forces, shear forces, bending moments, torsion, or a combination of these effects. For most design situations, bending moments and shear forces are considered primary effect, whereas torsion is regarded secondary. Torsion often appears with bending, shear as in the spandrel beam or in curved girders, beams in eccentrically loaded frames of multi-deck bridges and box girder bridges are example of such elements. Torsion becomes a primary effect, where beams are curved in plan. These structures are often required to resist torsion and should be designed or at least be checked for torsion. The analysis and design of torsion are getting more important for structural engineers. The mechanism of torsional

failure is as yet not clearly understood and all formulas developed for the calculation of the torsional strength of the reinforced concrete beams are either wholly or partly empirical. This is due to the lack of rationality in our approach to the problem of torsion. The behaviour of members under the effect of torsion is still a subject of extensive research. Investigations was carried out on total of Twenty seven beams, Nine NSC, Nine MSC & Nine HSC beams were tested to understand the Torsional behavior with variation in longitudinal & transverse reinforcement. To observe the influence of longitudinal steel, 3 beams in each category, were cast and tested with longitudinal reinforcement 2%, 3% and 4 % & transverse reinforcement of 8 mm diameter at the spacing of 1D, 1.5D, 2D. The span to depth ratio was maintained constant with a value of 8. The breadth & depth of the beam was also kept constant with 100mm.

The theories and codes used in the analysis are Skew bending theory, Space truss Analogy, ACI , British standards, Australian code, Euro code, Canadian standards and Indian Standards. The equations are as specified below.

$$T_{\text{ap}} = \frac{x^2 y}{3} (0.85 f_r), \quad T_{\text{uk}} = \frac{2 A_b d_1 (0.87 f_y)}{s_y}, \quad T_{\text{ur}} = \frac{\sqrt{f_c}}{3} \left(\frac{A_{\text{ap}}^2}{p_{\text{ap}}} \right), \quad T_{\text{uw}} = \frac{0.8 x_p y_1 A_{\text{ap}} (0.87 f_y)}{s}$$

$$T_{\text{uw}} = \frac{2 A_{\text{ap}} A_{\text{uw}} f_{\text{yw}}}{s} \cot \theta_t, \quad T_{\text{ul}} = \frac{2 A_k A_{\text{uw}} f_{\text{yw}}}{s} \cot \theta_t, \quad T_{\text{u2}} = \frac{2 A_{\text{ap}} f_y}{u_k} \tan \theta_t$$

The beams cast were tested in specially fabricated equipment shown in **FIG.1**, applying constant load increments as per standards using loading frame at MSRIT laboratory.



FIGURE 1- LOADING ARRANGEMENT

The details of the specimens are tabulated in **TABLE-2**. The first letter indicates the mix, the second number indicates the percentage of longitudinal reinforcement, and the third indicates the spacing of stirrups. The effective length of the specimen was 800mm. The total span

provided was 1200mm, 200mm bearing on each side. To avoid the failure of the specimen at the support section, the support was provided with higher amount of reinforcement than the test region. The beams were cast as per standards and tested using 500 tonnes loading frame under standard conditions. The results obtained were tabulated and analyzed by using different codes and theories.

Prior to obtaining the final mix proportions for different grades of concrete, numerous trial mixes were done having right consistency and workability. The results of these final proportions for M40, M80, M100 concrete is given in the **TABLE-1**.

MIX PROPORTION

TABLE - 1. MIX PROPORTION

Mix	Cement (kg)	Water (lit)	W/B	FA (kg)	CA (kg)	SP (%)
M-40	450	202.5	0.44	656.65	984.97	-
M-80	636	150	0.36	744	1050	2
M-100	750	150	0.20	470	1050	3

The beams tested shows the failure at centre of the beam as shown in **FIG.2** with the inclination of cracks from 40° to 50° and the width of crack varied from 0.3 mm to 7 mm, the single crack leading to several cracks without any further increase in load.



FIGURE 2 – CRACKING PATTERN OF SPECIMEN

TORSIONAL MOMENT Vs TWIST CURVES FOR REINFORCED NSC BEAMS

To know the behaviour of NSC reinforced beams, the parameters like the concrete strength, ductility and influence of longitudinal and transverse steel the variations of twist with respect to torsional moment were plotted. A typical torsional moment v/s twist curve of all NSC beams is drawn to see their behaviour with variation of longitudinal steel and transverse steel on the torsional moment carrying capacity is as shown in **FIG.3.**

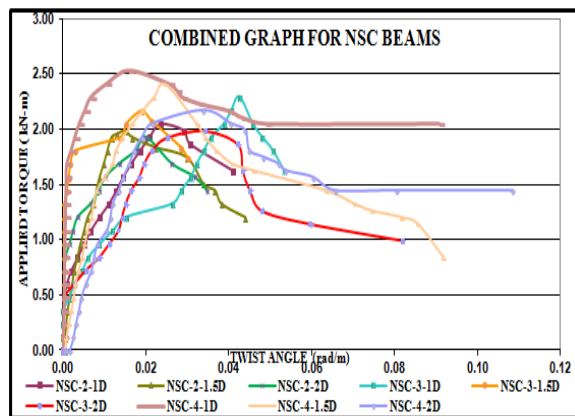


FIGURE 3- TORSIONAL MOMENT v/s TWIST CURVE FOR ALL NSC BEAMS.

From the graphs it was observed that, the torsional moment v/s twist curves are linear up to cracking and after that the non-linear behaviour of curves takes place. At this stage the concrete fails to take the torsional moment. After cracking, the twist of beam rapidly increased with yielding of the reinforcement and decreasing the torsional moment carrying capacity. Up to certain level the moment carrying capacity got reduced. It is observed that as the spacing of stirrups increases the torsional moment carrying capacity decreases. The longitudinal reinforcement ratio is less effective when considered to the torsional moment.

The results obtained were compared with the earlier tested beams of MSC and HSC beams

COMPARISON OF TORSIONAL STRENGTH OF EXPERIMENTAL DATA

The details of the specimens are tabulated in **TABLE 2**. Analysis of torsional behavior is also important in understanding the influence of parameters such as concrete strength, aspect ratio, influence of longitudinal and transverse reinforcement. The torsional behavior of reinforced beams is slightly different than that of the plain beams, where the redistribution of the stresses takes place in the cracked section of concrete beams. With the further deformation of concrete beams the stresses in the longitudinal and transverse steel increases. A fully cracked concrete beam resembles like a truss carrying the external load.

**TABLE 2 - RATIO OF EXPERIMENTAL
TO THEORETICAL TORSIONAL
MOMENT STRENGTH**

BEAM	T _u (exp)/T _u (theory)								
	Skew bending theory	Space truss analogy	IS-456	AS 3600	BS 8110	ACI	Euro1	Euro2	CSA
NSC/2/1.0D	1.83	0.69	0.66	1.05	0.71	0.57	0.57	0.64	0.68
NSC/2/1.5D	1.88	1.00	0.96	1.52	1.03	0.84	0.84	0.62	0.99
NSC/2/2.0D	1.87	1.29	1.24	1.97	1.33	1.08	1.08	0.60	1.28
NSC/3/1.0D	2.04	0.77	0.74	1.17	0.79	0.64	0.64	0.47	0.76
NSC/3/1.5D	2.06	1.09	1.05	1.66	1.12	0.91	0.91	0.45	1.08
NSC/3/2.0D	1.96	1.33	1.28	2.03	1.37	1.11	1.11	0.41	1.32
NSC/4/1.0D	2.17	0.85	0.81	1.29	0.87	0.71	0.71	0.39	0.84
NSC/4/1.5D	2.11	1.15	1.11	1.75	1.18	0.96	0.96	0.36	1.14
NSC/4/2.0D	2.08	1.46	1.40	2.22	1.49	1.22	1.22	0.34	1.44
MEAN	2.00	1.07	1.03	1.63	1.10	0.89	0.89	0.47	1.06
SD	0.12	0.27	0.26	0.41	0.27	0.22	0.22	0.12	0.26
CV	0.06	0.25	0.25	0.25	0.25	0.25	0.25	0.24	0.25
MSC/2/1.0D	1.91	1.62	0.87	2.46	1.66	1.35	1.35	0.84	1.60
MSC/2/1.5D	1.80	2.21	1.19	3.37	2.27	1.85	1.85	0.77	2.19
MSC/2/2.0D	1.74	2.80	1.51	4.27	2.88	2.34	2.34	0.73	2.77
MSC/3/1.0D	2.08	1.80	0.97	2.74	1.84	1.50	1.50	0.62	1.78
MSC/3/1.5D	2.07	2.59	1.40	3.94	2.66	2.16	2.16	0.60	2.56
MSC/3/2.0D	1.98	3.24	1.75	4.92	3.32	2.70	2.70	0.56	3.20
MSC/4/1.0D	2.17	1.91	1.03	2.90	1.96	1.59	1.59	0.50	1.88
MSC/4/1.5D	1.96	2.48	1.34	3.78	2.55	2.07	2.07	0.43	2.45
MSC/4/2.0D	1.88	3.09	1.67	4.71	3.17	2.58	2.58	0.40	3.06
MEAN	1.95	2.42	2.24	3.68	2.48	2.02	2.02	0.61	2.39
SD	0.14	0.57	0.69	0.82	0.59	0.48	0.48	0.15	0.57
CV	0.07	0.24	0.31	0.22	0.24	0.24	0.24	0.25	0.24
HSC/2/1.0D	2.19	2.05	1.11	3.12	2.10	1.71	1.71	1.07	2.03
HSC/2/1.5D	2.30	3.13	1.69	4.76	3.21	2.61	2.61	1.09	3.09
HSC/2/2.0D	2.29	4.10	2.21	6.24	4.21	3.42	3.42	1.07	4.05
HSC/3/1.0D	1.81	1.73	0.93	2.63	1.77	1.44	1.44	0.60	1.71
HSC/3/1.5D	2.11	2.91	1.57	4.43	2.99	2.43	2.43	0.67	2.88
HSC/3/2.0D	2.42	4.37	2.64	6.50	4.56	3.68	3.68	0.73	4.40
HSC/4/1.0D	2.16	2.09	1.13	3.17	2.14	1.74	1.74	0.54	2.06
HSC/4/1.5D	2.48	3.45	1.86	5.25	3.54	2.88	2.88	0.60	3.41
HSC/4/2.0D	2.57	4.68	2.52	7.12	4.80	3.90	3.90	0.61	4.62
MEAN	2.26	3.17	2.24	4.80	3.26	2.65	2.65	0.77	3.14
SD	0.22	1.08	0.69	1.61	1.11	0.90	0.90	0.23	1.07
CV	0.10	0.34	0.31	0.34	0.34	0.34	0.34	0.30	0.34

It can be observed for the NSC beams that mean values of the torsional strength ratios for all standards are greater than one except for ACI and European codes. This indicates that, except for ACI European Codes, all other standards have predicted the torsional capacities conservatively. The average of torque ratios show that Indian standard and CSA are more successful in predicting the ultimate torques comparing other standards for NSC beams. The values submitted in the thesis for the MSC and HSC, the EURO code predicts better results, with mean of 0.61 and 0.77, SD = 0.15 and 0.23 and CV = 0.25 and 0.3 respectively. All the codes underestimate the experimental values.

Parametric analysis carried out of the data collected from research papers published on the above topic from 1995 to 2008. 102 data from 8 investigations were tabulated with the available parameters, is specified in **TABLE 3**. It has been found that, from the theories analyzed, Euro code-II predicts better results with the mean of 0.62, SD = 0.21 and CV = 0.34.

TABLE 3 - DETAILS OF LITERATURE DATA

SL No.	RESEARCHERS	B (mm)	D (mm)	l/d	ρ_t (%)	p_t (%)	f'_c (MPa)	NO OF DATA
1	Rasmussen, Baker 1995	160	241	12.45	4	1.83	36.3-109.8	12
2	Ashour, Samman, Radain 1999	100	370	1.02-5.48	0.85	0.75	53.97-93.93	20
3	Koutchoukali, Belarbi 2001	203	255	15.53	0.1-0.15	1.2-1.7	39.93	10
4	I-K Fang, J-K Shiao 2004	350	464	6.68	0.6-2.0	0.6-2.0	33.5-78.38	16
5	H-J Chiu, J-K Shiao, W-T Young, I-Kuang Fang 2007	250-420	370-650	4.77-8.38	0.51-0.91	0.17-0.77	35-78	13
6	M. Ameli, H R Ronagh 2007	127-254	118.3-346	5.02-16.91	0.74-3.31	0.71-2.27	20-42.4	11
7	Adam Csikos, Istvan Hegedus 2007	130	117.3	17.05	0.74-1.48	0.74-1.34	20	12
8	Mehmet Huseyin, Ercan Ortekin and Selim Pulu	150	250-300	1.67-2	1.2-2.2	0.66-0.91	66	08
							TOTAL	102

CONCLUSIONS

The increase in longitudinal reinforcement ratio was less effective for NSC beams compared to the torsional moment carrying capacity in MSC and HSC beams.

It was observed that as the compressive strength of concrete increases the torsional strength of beams also increases.

The beams designed with the same amount of reinforcement, the torsional strength of NSC beams is less compared with MSC and HSC beams.

The angle of twist for NSC beams was greater when compared MSC and HSC beams.

It has been observed that the torsional shear stress increases with increase in the compressive strength of concrete.

It has been found that as the percentage of longitudinal reinforcement increases, the ultimate torsional shear stress of all the beams increases in the case of both experimental and literature data.

As the spacing of transverse reinforcement increases in case of experimental and literature data, the torsional stress increases for all the reinforced beams.

The Torsional stress increases as the total reinforcement increases for the experimental as well as the literature data.

For the experimental values of **NSC** reinforced beams Space Truss Analogy and I S method predicts better results, with **mean = 1.07, SD = 0.27, CV = 0.25** and for I S method **mean = 1.03, SD = 0.26, CV = 0.25** respectively.

For the experimental values of **MSC** reinforced beams, EURO CODE II predicts better results, with **mean = 0.61, SD = 0.15, CV = 0.25**.

For the experimental values of **HSC** reinforced beams, EURO CODE II predicts better results, with **mean = 0.77, SD = 0.23, CV = 0.3**.

NOTATIONS

x = smaller dimensions of the rectangular cross section. y = larger dimensions of the rectangular cross section. T_{cr} = Torsional cracking moment, kN-m. f'_c = designed cylinder compressive strength, MPa. f_r = modulus of rupture of the concrete, MPa

4th International Engineering Symposium - IES 2015

March 4-6, 2015, Kumamoto University, Japan

f_y = specified yield strength of the reinforcement, Mpa. A_{cp} = area enclosed by outside perimeter of concrete cross section mm². A_l =longitudinal reinforcement area mm². A_{sv} = total cross-sectional area of the stirrup legs within a distance s_v , mm². P_{cp} = outside perimeter of the concrete cross section, mm. b = breadth of beam, mm. s_v = spacing of the stirrups along the length of the member, mm.

ACKNOWLEDGEMENTS: We sincerely thank our management, Principal, HOD of MSRIT and VTU Belgaum for their support in completion of this project.

REFERENCES

1. I-KUANG FANG and JYH-KUN SHIAU, "Torsional behavior of NSC and HSC concrete beams", ACI Structural Journal, Vol.101, No.3 May-June 2004 pp. 304-313.
2. SAMIR A ASHOUR, TAMIM, A SAMMAN AND TALAL A RADIAN, "Torsional behavior of reinforced high strength concrete deep beams", ACI Structural Journal, Vol.96, No.6 November- December1999, pp. 1049-1058.
3. RASMUSSEN L J and BAKER G, "Torsion in Reinforced Normal and High - Strength Concrete Beams". Part 2: Theory and Design, ACI Structural Journal, Vol.92, No.2, March-April 1995, pp. 149-156.
4. M AMELI and H R RONAGH, "Treatment of torsion of reinforced concrete beams in current structural standards", Division of Civil Engineering, School of Engineering, University of Queensland, QLD, 4072, Australia, Asian Journal of Civil Engineering (Building and Housing), Vol.8, No.5, 2007, pp. 507-519
5. METIN HUSEM, ERTEKIN OZTEKIN, SELIM PUL, "A calculation method of cracking moment for the high strength concrete beams under pure torsion", Sadhana Vol. 36, Part 1, Volume 36, Issue 1, February 2011, pp. 1-15.
6. NASAR-EDDINE KOUTCHOUKALI and ABDELDJELIL BELARBI, "Torsion of high strength reinforced concrete beams and minimum reinforcement requirement", ACI Structural Journal, Vol.98, No.4 July-August 2001, pp. 462-468.
7. HAO-JAN CHIU, I-KUANG, WEN-TANG YOUNG, JYH-KUN SHIAU, "Behavior of reinforced concrete beams with minimum torsional reinforcement", Science Direct Journal of Engineering structures, Vol.29 2007, pp 2193-2205.
8. ADAM CSEKOS and ISTVAN HEGEDUS, "Torsion of Reinforced concrete Beams", 2nd Int. PhD Symposium in Civil Engineering, 2007, Budapest.

Investigation on In-Plane Shear Strength Using Push-Off Specimens with Different Clamping Reinforcement

Harish Kumar N R¹, Snehal K², Nagaraj K P³ and Prabhakara R⁴

Department of Civil Engineering

M S Ramaiah Institute of Technology, Bangalore, India

Abstract: Computation of In-Plane shear strength is gaining importance in structural design of precast reinforced concrete elements like ledger beam bearing and connectivity issues in between various pre-cast elements. Generally Pre-cast elements fail catastrophically in direct shear due to brittleness of concrete. This paper exemplifies the investigation carried out to study the in-plane shear behavior of Normal Strength Concrete (NSC), High Strength Concrete (HSC) and Self Compacting Concrete (SCC) by conducting a recently developed simple test method called push-off test, using push off specimen. The types of concrete used are M30-NSC; M30-SCC and M70-HSC. Specimen size of 150×150×260mm with shear plane area of (150 x 80)12000mm² was provided, notches of 5mm thick and 130mm length were cut 80mm apart and perpendicular to the loading axis on the specimen. The specimen size was chosen from the available literature and clamping reinforcement was introduced across the shear plane. The ultimate shear stress was computed to demonstrate the change in behavior between clamped and plain concrete specimens. The clamping reinforcement is varied with one, two and three bars of 8mm, 10mm and 12mm diameters in each type of concrete. The ultimate shear stress obtained from the experiments was compared with that of codal provisions and other researchers' formulae. Non-linear regression analysis was performed for better estimation of shear stress values.

Keywords: Shear, Push-off test, shear plane, clamp reinforcement.

1. INTRODUCTION

Progress in concrete technology has resulted in different types of concrete such as High strength concrete (HSC), self-compacting concrete (SCC), Geo-polymer concrete (GPC), Fiber reinforced concrete (FRC) etc. Their mechanical and engineering properties such as compressive strength, flexural strength, and modulus of elasticity, fracture energy, shear and torsional strengths are very important as they influence the structural behavior of concrete. Many investigations are available on flexure, however investigation on shear and torsion are limited. Advances in the structural design made the designers to use the complicated structural forms which are subjected to shear and torsion. For introduction of ductility or toughness parameter in relevant structural design,

knowledge of shear failure is essential [7, 12]. Push-off test is one of the simplest techniques to study the mechanism of shear transfer in concrete members (shear stress-displacement behavior) [1, 2, 4, 6, 17]. Push-off specimen has been quite popular for estimation of In-plane shear strength of material. In-plane shear strength computation is gaining importance in the design of precast elements like shear keys, web flange stress transfer, brackets in columns, corbel and ledger beams.

Shear strength of specimens depends both on concrete and reinforcement contribution and also aggregate interlock or crack shear friction [1, 7, 13]. Addition of clamping reinforcement improves the tensile and ductile behavior of a structural element increasing its load carrying

capacity. In case of HSC initially upon loading, the shear reinforcement take only a small portion of the shear force; most of the shear force is taken by the concrete itself [3,5]. It is assumed that the total shear is resisted by concrete until the formation of diagonal cracks, while in NSC and SCC shear reinforcement takes major portion of load than concrete [7, 8].

It was found from the literature that, pre-existing crack along shear plane will reduce the ultimate shear transfer strength and also increase the slip [11]. Change in strength, size and spacing of reinforcement affects shear transfer mechanism [14]. Plain concrete-(PC) shows sudden brittle failure, Fiber concrete-(FC) shows discrete closely packed cracks less brittle, while reinforced concrete-(RC) and Fiber reinforced concrete-(FRC) have ductile failure [9,10]. In the present experimental investigations, the clamping reinforcement is varied with one, two and three bars of 8mm, 10mm and 12mm dia bars in type of concrete.

II SCOPE OF INVESTIGATION

- To compare shear stress values through push off specimens with varying clamping reinforcement against the plain push off specimen.
- Evaluation of codal provisions for ultimate shear stress obtained from experiments.
- Non linear regression analysis of test results for better estimation of shear stress.

III. MATERIALS AND MIX PROPORTION

Materials used:

Cement: 43 grade OPC as per IS 8112-1989 [NSC and SCC] and 53 grade OPC as per IS 12269 [HSC] of Specific gravity 3.15. **Fly Ash:** Class F confirming to IS 3812-2003, with specific gravity 2.15.

Coarse Aggregates: 20mm downsize-(NSC) with Specific gravity 2.65, and

12.5mm down size-(SCC and HSC) of specific gravity 2.62 conforming to IS 383-1970. **Fine Aggregates:** River sand, Zone II conforming to IS 383-1970, with fineness modulus of 3.02, Specific gravity of 2.63. **Super plasticizers:** Naphthalene based polymer (Conplast SP 430) complying with IS: 9103:1999 and BS 5057 part 3 for HSC. Glenium B233 Modified poly-carboxylic ether for SCC.

Viscosity Modifying Agent: Glenium Stream 2 is used in SCC. **Steel:** Fe 415 HYSD steel bars conforming to IS 1786.

Water: Potable water free from injurious salts as per IS 456:2000.

Mix Proportion: Mix design adopted in present study is as follows, **NSC** (M30)-IS 10262:2009, **SCC** (M30)-NAN-SU Method (Chinese) and in case of HSC (M70) Mix design procedure given by Prabhakara et. Al [16] was used. Constituents used for NSC (30), SCC (M30) and HSC (M70) for different aggregate size is tabulated below in Table1.

Table1: Mix proportion of NSC, SCC and HSC

Type of concrete	NSC	SCC	HSC
Aggregate Size (mm)	20	12.5	12.5
Cement (kg/m ³)	358.58	214.29	630
Fly Ash (kg/m ³)	-	330	-
Coarse aggregate (kg/m ³)	1131.82	681.1	1000
Fine aggregate (kg/m ³)	687.58	849.2	616
SP(GeleniumB233) (kg/m ³)	-	7.08	-
VMA (kg/m ³)	-	0.979	-
SP(Conplast) (lit/m ³)	-	-	12.86
Water (lit/m ³)	197.32	174.2	140
w/b ratio	0.55	0.32	0.22

IV EXPERIMENTAL INVESTIGATION

The size of test specimen was chosen from literature available. Two notches of 75mm length and 5mm width were cut at 80mm apart and perpendicular to loading axis on the specimen. Geometry of the push-off specimen used in present study is shown in the Fig1.

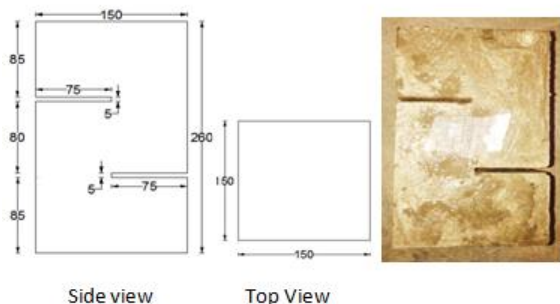


Fig1 Geometry of Push off specimen

Clamping reinforcement, Fe 415 steel bar of 140mm length with 5mm of clear cover on both ends was provided. The bars were positioned by tying with binding wires at the ends. Specimen Reinforcement details is given in Table2. The compressive strength for each type of concrete is found by casting standard cubes.

Table 2 Reinforcement details

No. of Bar and size of Bar	Percentage of steel (p)%	Shear plane area(A)	Vertical Spacing provided
#1-8mm bar	0.42	80×150	36mm
#2-8mm bar	0.83	80×150	22mm
#3-8mm bar	1.25	80×150	14mm
#1-10mm bar	0.65	80×150	35mm
#2-10mm bar	1.3	80×150	20mm
#3-10mm bar	1.95	80×150	13mm
#1-12mm bar	0.94	80×150	34mm
#2-12mm bar	1.9	80×150	19mm
#3-12mm bar	2.8	80×150	11mm

Specimens were tested for ultimate shear stress after 28 days of curing. All the push-off specimens were tested using compressive testing machine. Loading arrangement on the specimen is as shown in Fig 2. 20mm thick plate with 30mm wide was used to apply the line load on the specimen. Initial cracking load, ultimate load and crack widths were observed and recorded.

V RESULTS AND DISCUSSIONS

The companion cubes were also tested for compressive strength for NSC, SCC and HSC by casting the push-off specimens and test results are tabulated in Table 3.



Fig2 Specimens during the test and after the test [failed specimens]

It was observed from Table 3, that the 28 days compressive strength of NSC, SCC was greater than the target strength.

Table 3: Compressive Strength of NSC, SCC and HSC

Specimen	Cube Size (mm ³)	Cube compressive strength f_{ck} (MPa)	
		7days	28day
M30NSC	150×150	20.80	47.60
M30SCC	150×150	16.60	48.68
M70HSC	100×100	61.15	73.80

Fig 3 shows a typical failure patterns observed in plain and reinforced concrete push-off specimens during the tests. The cracks were observed along the shear plane in plain push-off specimens, initiating from one of the notch tip and propagating towards the other notch tip; however few specimens were failed producing cracks deviating from notch tip. In NSC and SCC inclined and irregular crack pattern was noticed, while in HSC smooth vertical crack was observed.



Fig 3: Failure patterns of clamped NSC, SCC and HSC

Ultimate shear stress of SCC (M30) was observed to be less compared to NSC

(M30). Clamping reinforced push-off specimen along shear plane was seen to carry more shear load compared to plain concrete push-off specimen and cracks were examined to be deviated from the notch face (Fig 3). The crack widths observed were less in reinforced specimens compared to specimens without shear reinforcement. Push-off specimens with clamping reinforcement were found to fail in ductile manner while plain push-off concrete specimens showed brittle failure. Test results for plain and reinforced push-off specimens obtained from present experimental study are given in Table 4.

It is clearly observed from the Table 4, that reinforced push-off specimens showed higher shear carrying capacity compared to the specimens without clamping reinforcements. It is also noticed that with increase in the area of reinforcement the shear strength has increased with reduction in crack width.

Demonstrative graph was plotted to show the variation of shear stress over percentage of reinforcement as shown in Figure 4. The graph clearly describes that, in all types of concrete the shear carrying capacity of reinforced concrete is more as compared to plain concrete. From the graph fig 4, it was observed that coefficient of correlation R (R^2) value found to be 0.805 for NSC; 0.958 for SCC and 0.966 for HSC. It is also found that as the percentage of steel increases shear strength tends to increase.

Steel reinforcement provided in the shear plane resists the shear crack and the cracks deviate from the notch. The occurrences of cracks were also delayed in the Push-off concrete specimens provided with clamping reinforcement.

An attempt has been made to bring about a comparative study between the experimental data and various available Codal expressions (Eq1 to Eq4). The expressions which have been found from

regression analysis also brought into consideration.

Table 4: results of plain and RC-push-off specimens

Specimen	$\rho\%$	A_{st} (mm ²)	f_{ck} (MPa)	V_u (kN)	W_{cr} (mm)	τ_u (MPa)
NSC/0	0	-	42.85	73.09	73.32	2.63 6.11
NSC/0.42	0.42	50.4	42.85	92.46	93.6	2.3 7.83
NSC/0.83	0.83	99.6	42.85	92.96	94.89	1.89 7.9
NSC/1.25	1.25	150	42.85	97.95	99.45	1.67 8.28
NSC/0.65	0.65	78	42.85	94.4	96.05	1.9 8
NSC/1.3	1.3	156	42.85	100.47	102.8	2.03 8.57
NSC/1.95	1.95	234	42.85	101.62	106.47	1.85 8.87
NSC/0.94	0.94	112.8	42.85	97.8	98.04	1.8 8.17
NSC/1.95	1.9	228	42.85	103.9	105.47	1.68 8.79
NSC/2.8	2.8	336	0.42	111.21	112.93	1.55 9.41
SCC/0	0	-	52.4	66.44	66.96	1.96 5.58
SCC/0.42	0.42	50.4	52.4	67.96	68.48	2.28 5.7
SCC/0.83	0.83	99.6	52.4	70.77	71.52	2.02 5.96
SCC/1.25	1.25	150	52.4	73.57	74.72	1.86 6.22
SCC/0.65	0.65	78	52.4	70.1	71.2	1.93 5.9
SCC/1.3	1.3	156	52.4	74.51	75.39	1.68 6.28
SCC/1.95	1.95	234	52.4	73.37	76.67	1.46 6.39
SCC/0.94	0.94	112.8	52.4	72.27	73.76	1.44 6.14
SCC/1.95	1.9	228	52.4	75.91	77.3	1.52 6.44
SCC/2.8	2.8	336	52.4	80.3	81.1	1.48 6.76
HSC/0	0	-	73.8	102.36	102.6	1.11 8.55
HSC/0.42	0.42	50.4	73.8	101.32	103.96	2.1 8.66
HSC/0.83	0.83	99.6	73.8	102.02	107.23	1.8 8.93
HSC/1.25	1.25	150	73.8	107.92	112.6	1.5 9.38
HSC/0.65	0.65	78	73.8	104.13	106.64	1.28 8.88
HSC/1.3	1.3	156	73.8	108.12	111.4	1.3 9.28
HSC/1.95	1.95	234	73.8	115.3	116.81	1.28 9.73
HSC/0.94	0.94	112.8	73.8	102.5	107.1	1.33 8.92
HSC/1.95	1.9	228	73.8	114.6	116.4	1.12 9.71
HSC/2.8	2.8	336	73.8	113.85	120.46	1.2 10.1

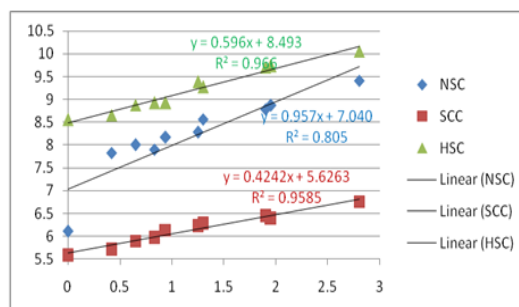


Fig 4: Plot of shear stress v/s percentage of shear reinforcement

According to ACI 318-02(1999):

$$V_u = (0.8A_{sf} + K_1 A_c) \quad \dots \text{Eq-1}$$

Where, $K_1 = 400 \text{ Psi} = 2.76 \text{ MPa}$

According to IS 456: 2000 [15]:

$$V_u = \tau_c b d + 0.87 f_y A_{st} \quad \dots \text{Eq-2}$$

Where, $\tau_{cmax} = 2.2 \text{ N/mm}^2 (\text{M30})$;

$\tau_{cmax} = 2.5 \text{ N/mm}^2 (\geq \text{M40})$

According to EURO Code 2 (EN2):

$$V_{Rd,s} = (A_{sv}/S) 0.78 d f_y k \cot \theta \quad \dots \text{Eq-3}$$

Where, $\cot\Theta=1$;

$$k = (1.6 - d) = 1.6 - 0.15 = 1.45$$

According to Predicted Equation (Regression Analysis):

$$\tau_u = 2.898(\gamma f'_c)^{0.577} \rho^{0.088} \quad \dots \text{Eq-4}$$

Using the equations 1 to 4 the ultimate shear was calculated theoretically for the tested specimens, The ratio of EXP/CAL was obtained and further Mean, SD and CV were calculated and shown in Table 5.

From the Table5, it is understood that for reinforced Push-off specimens Euro code EN2 adequately predicted with experimental results with mean value of 0.89 and correlation variation of 0.03. Whereas for predicted equation obtained from regression analysis also showed good comparison with a mean value of 0.91 and with least coefficient of variation of 0.15.

Table5: Experimental/Calculated Ultimate Shear Stress of Plain & Reinforced Push-off Specimen.

Sl.No	specimen	EXP/CAL			
		ACI	IS	EN2	Pre. Eq
1	NSC/0	0.87	1.02	1.04	1.0
2	NSC/0.42	1.88	2.10	0.96	1.05
3	NSC/0.83	1.44	1.52	0.95	1.00
4	NSC/1.25	1.21	1.23	0.87	1.01
5	NSC/0.65	1.63	1.76	0.89	1.03
6	NSC/1.3	1.22	1.24	0.87	1.04
7	NSC/1.95	0.97	0.96	0.89	1.04
8	NSC/0.94	1.40	1.46	0.89	1.02
9	NSC/1.95	0.97	0.97	0.88	1.03
10	NSC/2.8	0.79	0.76	0.92	1.07
11	SCC/0	0.87	0.99	1.04	1.0
12	SCC/0.42	1.38	1.54	0.90	0.72
13	SCC/0.83	1.09	1.15	0.89	0.71
14	SCC/1.25	0.91	0.93	0.90	0.72
15	SCC/0.65	1.21	1.30	0.84	0.72
16	SCC/1.3	0.89	0.91	0.87	0.72
17	SCC/1.95	0.70	0.69	0.85	0.71
18	SCC/0.94	1.05	1.10	0.84	0.72
19	SCC/1.95	0.71	0.71	0.85	0.71
20	SCC/2.8	0.56	0.55	0.86	0.73
21	HSC/0	0.87	0.9	1.04	0.98
22	HSC/0.42	2.09	2.33	0.89	0.99
23	HSC/0.83	1.63	1.72	0.91	0.97
24	HSC/1.25	1.36	1.40	0.94	0.98
25	HSC/0.65	1.81	1.95	0.90	0.98
26	HSC/1.3	1.32	1.35	0.92	0.97
27	HSC/1.95	1.06	1.05	0.90	0.98
28	HSC/0.94	1.52	1.60	0.89	0.95
29	HSC/1.95	1.08	1.07	0.89	0.98
30	HSC/2.8	0.84	0.82	0.87	0.98
	MEAN	1.21	1.27	0.89	0.91
	SD	0.38	0.44	0.03	0.14
	CV	0.31	0.35	0.03	0.15

Figure 5, gives a combined comparison of calculated and experimental shear stress

values for reinforced concrete Push-off specimens. It is clear from the graph that Euro Code EN2 predicts the best compared to all the Equations with experimental shear stress values for reinforced specimens, COR value obtained was 0.968. However regression Equation predicts well for NSC and HSC Reinforced specimens compared SCC.

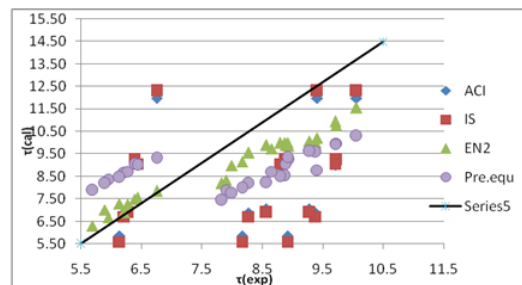


Fig 5 Combined graph of shear stress values obtained for different codes and predicted equation

V CONCLUSIONS

The specimens of NSC, SCC and HSC were tested with different percentage of shear reinforcement using push-off concrete specimen and following observations and conclusions are drawn. Trial mixing plays an important role for arriving at final mix proportion. Workability of concrete is also an important criteria to be considered.

It was observed on testing that in plain concrete push-off specimens first crack initiates at one end of the notch face and propagated towards the other notch tip however few were failed with cracks deviating from the notch tip. Since fines are more in SCC the shear carrying capacity compared over NSC was observed less. It was observed that presence of shear reinforcement across the shear plane area resists crack in the vicinity of shear plane; Hence cracks were found to deviate from notch sides.

Reinforced push-off specimens were observed to fail in ductile manner while Plain push-off specimen failed in brittle manner. It is observed that change in size and spacing of reinforcement affects the shear transfer strength and it was found,

as the reinforcement ratio across the shear plane increased the shear stress increased. Initial cracks were delayed with the increase in reinforcement ratio.

The shear capacity was estimated using the ultimate load equations suggested by ACI 318, IS 456 and Euro Code EN2 and compared with the experimental values. It was observed from Table 5 that for reinforced concrete push-off specimen by Euro code EN2 was best prediction compared to others with least error of 3%. From the combined graph shown in Figure 5, it is clear that EN2 code shear stress values showed best graph with R^2 value equal to 0.968.

ACKNOWLEDGEMENT

We acknowledge the support of Management of MSRIT, Principal, HOD, Faculty and staff of Civil Dept. In particular we express our deep sense of gratitude to Hiranyiah, chief engineer Bhagirata constructions for extending his help throughout the investigations.

REFERENCES

- [1] A. Khanlou , G.A. MacRae , A. N. Scott , S. J. Hicks and G. C. Clifto "Shear performance of steel fiber-reinforced concrete" Steel Innovations Conference 2013 Christchurch, New Zealand, pp 21-22 .
- [2] Alan H Mattock , Neil M Hawkins "Shear transfer in reinforced concrete-recent research" PCI Journal/March-April 1972.
- [3].Amer Bin Yusuff "Behavior of high strength reinforced concrete beam with metkaolin under static loading" M Tech Thesis, Dept of Civil Engineering, University Technology Malaysia, April 2005.
- [4]. American Concrete Institute "Building Code Requirements for Structural Concrete and Commentary" ACI 318-02,1999.
- [5]BCA Academy"Design guide of HSC to Singapore standards cp 65", BC, 2, 2008
- [6].Benny Joseph, George Mathew "Interface shear strength of fly ash based geo polymer concrete" Annals of faculty engineering Hunedoara, International journal of engineering, Tome X1(year 2013).
- [7]. Birkeland P W and H W Birkeland "Connections in Precast Concrete Construction" , ACI Journal, Proceedings, Vol. 63, No. 3, pp. 345-368.,1966
- [8].Bureau of Indian Standards "Design Aid to Reinforced Concrete to IS 456:1978" SP 16, 1980.
- [9].Chitra G.B "Investigation on long term deflection of high strength concrete beams" MTech Thesis, Department of civil Engineering, V.T.U, Belgaum 2005.
- [10]Constantinescu H. et. Al"Study of shear behaviour of high performance concrete using push-off tests" Jaes_1(14)_2_2011, pp.77-82 .
- [11]Dr.Maha M.S Ridha, Nagam T.Hamad, Dr.Kaiss F. Sarsam "Predicting the strength of fiber reinforced high performance concrete based on push-off tests" Eng & Tech Journal,Vol.30, No.12, 2012.
- [12] en.m.wikipedia.org/wiki/Regression - analysis.
- [13].Hofbeck, Ibrahim, and Mattock, 1969."shear transfer in reinforced concrete" ACI Journal, Proceedings, V. 66, No. 2, pp. 119-128.
- [14]Husain M.Husain, Moayad M.Kasim, Esam M. Aziz,"Experimental study in direct shear strength of fiber reinforced concrete" Received: 18/9/2006, Accepted: 9/11/2008.
- [15]. IS 456:2000 "Plain and Reinforced concrete-code of practice (fourth revision)" Bureau of Indian standards ,New Delhi.
- [16] R.Prabhakara, Nadar Nissar Shaik et al "In-plane shear strength of Normal, High strength and Self Compacting concrete using push off specimen" International conference on advances in architecture and civil engineering, paper ID SAM, Vol. 1, 21st-23rd June 2012
- [17] Walraven J. C.; Frenay, J.; and Pruijssers, A. (1987) "Influence of Concrete Strength and Load History on the Shear Friction Capacity of Concrete Members", PCI Journal, Vol. 32, No. 1, pp. 66-84.

Potential Use of Recycled Coarse Aggregates in Concrete

Subhash C. Yaragal, Vivek V B, M Padmini, M Jacob and J Niveditha

*Department of Civil Engineering, National Institute of Technology Karnataka,
Surathkal - 575025, India. e-mail:subhashyaragal@yahoo.com*

Anil Kumar Pillai

*Technical Services, The Ramco Cements Ltd, Mylapore, Chennai - 600004, India.
e-mail:akp@ramcocements.co.in*

ABSTRACT: Concrete continues to be the most consumed construction material in the world, only next to water. This fact is due to its appealing properties of high compressive strength and the property of mould-ability to any conceivable shape. Due to rapid increase in construction activities, it is important to assess the amount of construction and demolition waste being generated and analyse the practices needed to handle this waste from the point of waste management and disposal and also with regard to waste utilization in concrete from the sustainability aspects. Construction and Demolition (C&D) waste constitutes a major portion of total solid waste production in the world, and most of it is used in landfills. Research by concrete engineers has clearly suggested the possibility of appropriately treating and reusing such waste as aggregate once again in concrete, especially in applications such as bed concrete and in road beds for pavement i.e. where works are of less importance as regards to the strength. The use of such waste as recycled aggregate in concrete can be useful for both environmental and economic aspects in the construction industry. This study reports some interesting results of the utilization of recycled coarse aggregates in concrete from construction and demolished waste.

Keywords: Demolished concrete, Recycled aggregate, Compressive strength

INTRODUCTION

Due to high demand for construction activities in recent years in India and all over the world, the natural aggregates resources are remarkably waning day by day. On the other hand, millions of tonnes of C&D residues are generated. Natural resources are dwindling day by day due to their extensive use to cope with the increasing demand of Civil Engineering Projects. Therefore, the use of C&D waste as an alternative aggregates for new concrete production gains importance to preserve natural resources and reducing the need for disposal, (S Manzi et al. 2013). The amount of construction and demolition waste has increased enormously over the last decade in the entire world, (Sami W. Tabsh et al 2009). Disposal of construction and demolition waste has also emerged as a problem in

India. Therefore, recycling of waste concrete is beneficial and necessary for the environmental preservation and effective utilization of natural resources, (Ashraf M. Wagih et al. 2013). The use of recycled coarse aggregate obtained from construction and demolition waste in new concrete is a solution for effective waste utilization, (M. Chakradhara Rao et al.2011).

The management of construction and demolition waste is a major concern due to increased quantity of demolition rubble, shortage of dumping sites, increase in cost of disposal and transportation and above all the concern about environment degradation. Although a substantial portion of construction materials could be substituted by re-processed construction waste material, these options are not

4th International Engineering Symposium - IES 2015

March 4-6, Kumamoto University, Japan

exercised in developing countries due to lack of knowledge and insufficient regulatory frameworks resulting in waste getting piled up causing disposal problems, (R.V.Silva et al. 2014). The increasing problems associated with construction and demolition waste, have led to a rethinking in developed countries and many of these countries have started viewing this waste as a resource and presently have fulfilled a part of their demand for raw material, (Shi-Cong Kou et al. 2012).

Many developed countries have been recycling C&D waste and using it for construction works. In Scotland about 63% of the C&D waste was recycled in 2000. The Government there is working out specifications and code of practice for recycling of C&D waste. U.K uses 49-52% of the C&D wastes and Australia reuses 54% of the wastes generated. Belgium has a higher recycling rate (87%) and uses majority of C&D for recycling purposes. Japan is one of the pioneer countries that recycle C&D waste. 85 million tonnes of C&D waste was generated in 2000, of which 95% of concrete was crushed and reused, (Akash Rao et al. 2007).

Using recycled concrete aggregates, will require checking the quality of the aggregates, since they are collected from different sources, grades of concrete and age, (A.K.Padmini et al. 2009). Concrete workability is more influenced by the shape, texture and grain size distribution of the recycled aggregates than by their total amount, (S. Manzi et al. 2013). The compressive strength primarily depends upon adhered mortar, water absorption, Los Angeles abrasion, size of aggregates, strength of parent concrete, age of curing and ratio of replacement, interfacial transition zone, moisture state, impurities present and controlled environmental condition (Isabel Martínez-Lage et al. 2012). Absorption of RCA is one of the major contributing factors in the strength of concrete, (K C Panda and P K Bal 2013). This study reports some important changes in properties such as compression strength and absorption of recycled aggregate concrete.

MATERIALS

Ordinary Portland Cement (OPC) 43 grade was used and its properties are tabulated in Table 1. Coarse aggregate was crushed stone with a maximum size of 20 mm. Locally available natural river sand conforming to zone III (IS 383-1970 grading requirements) was used as fine aggregate. Physical properties of fine and coarse aggregates are presented in Tables 2 and 3 respectively. Potable quality water is used. Recycled aggregates were obtained from demolished concrete made in the laboratory with maximum size of 20 mm.

Table 4 shows the properties of recycled coarse aggregates and Table 5 gives mix proportions for OPC based concrete. The sieve analysis results of natural and recycled aggregates are shown in Table 6.

Sources and processing of RCA

In order to obtain correct assessment of strength of RCA based concrete, it was thought necessary to produce construction and demolished waste from same quarry virgin coarse aggregates. To achieve C & D waste, about 30 Nos. of 150 mm concrete cubes were cast and cured for a period of 28 days. Later all these were compressed to failure, to produce C & D waste.

A common procedure adopted to recover the coarse aggregates from C & D wastes is as follows. The C & D waste, was fragmented manually further, and then 10 Kg of C & D waste was placed in Los Angeles aggregates testing machine with constant charge and the apparatus was run for 5 minutes.

Later this processed material is removed, and sieve analysis was carried out. After sieve analysis, the obtained RCA, was agitated and washed in a water tank to remove surface crushed rock fines (dust) and sun dried before their being used as RCA to cast specimen.

EXPERIMENTAL METHODOLOGY

The obtained aggregates are mixed in proportions of 0% (no RCA), 20%, 40%, 60%, 80% and 100% (all RCA) by weight of the total natural coarse aggregates in concrete. So for each mix 3 Nos. of 150 mm cubes concrete cubes as stipulated by the code were cast. 18 Nos. of 150 mm cubes were cast and 28 days water cured before testing them for compressive strengths. Experiments were aimed for achieving workable slump between 50-75mm without using super plasticizers. Standard slump cone apparatus is used for measuring the value of slump. During the slump tests it was found that the workability of fresh concrete made with 100% replacement of RCA had slump value close to zero mm. With increase in percentage of RCA in concrete the workability was getting lower and lower. This was mainly due to the high absorption rate (2.69%) of the RCA as compared to the fresh coarse aggregate (0.2%). Adding water to compensate for this absorption was not a good option as exact amount could not be ascertained. So it was decided to soak the RCA for 24 hours before use, so that it does not absorb water during the process of mixing (M. Etxeberria et al. 2007), this method of soaking helped to attain moderate workability of concrete without use of plasticizers. The test matrix for compression test is shown in Table 7.

The concrete samples with RCA are tested for 28 day strengths and compared with the results of the strengths of concrete made with virgin natural aggregates.

RESULTS AND DISCUSSION**Compressive strength**

Table 8 presents the results of the compressive strength tests for OPC based concrete specimen. It can be noticed that the compressive strength of the cubes goes on decreasing as the percentage of the RCA replacement gets increased from 42.1 MPa for the control mix to 30.8 MPa in the fully RCA replaced cubes. The drop

in strength with increase in RCA proportion is attributed to the bond strength becoming weaker and weaker with RCA increase.

From Table 8, it is observed that there is a decrease in strength from 7% to 27%, when 20% of virgin aggregates is replaced by RCA, to the case when 100% of virgin aggregates is replaced by RCA. These findings are in agreement with other investigators. S.C.Kou et al. (2012) reports a fall in the compressive strength. Sami W. Tabsh and Akmal S. Abdelfatah (2009) have reported that the decrease in strength is by about 10-25%. Sumaiya Binte Huda and M. Shahria Alam (2014) have got a decrease in 15-20% when aggregates were replaced. Figure 1 shows the normalized compressive strength variation, with increase in RCA. These findings are similar to the results of Wai Hoe Kwan et. al (2012). Shi-Cong Kou and Chi-Sun Poon (2013) have also reported a decline in their compressive strength. K.K.Sagoe-Crentsil et al (2001) have similar results with recycled aggregates replaced concrete. According to the studies by Isabel Martínez-Lage et al. (2012) the estimated loss for concrete with 100% recycled aggregate was 23%, with values ranging from 20% to 31%.

There is a reduction from normalized strength factor of 1.00 to 0.73, when the natural aggregate was completely replaced with recycled aggregate. Hisham Qasrawi (2014) has also reported a reduction in concrete strength when replaced with RCA. K C Panda and P K Bal (2013) have reported that compressive strength, flexural strength and split tensile strength of concrete decreases with increase in the amount of RCA.

Figure 2 shows the best fit line, showing the drop in strength of concrete with increase in percentage of RCA. The proposed equation can be used to predict the normalized strength of concrete as a function of RCA, with maximum error in prediction of less than 2.5%.

$$\text{Normalized strength} = 0.9848 - [0.0026 \times \text{RCA}(\%)] \dots (1)$$

4th International Engineering Symposium - IES 2015

March 4-6, 2015, Kumamoto University, Japan

Water absorption test

Water absorption was used to determine the amount of water absorbed under specified conditions that indicates the degree of porosity of a material. The results of the water absorption tests are as shown in Table 9. The results indicate that the water absorption was higher in all the cases when there is a replacement by recycled aggregate. The percentage of absorption varied from 4.22% to 5.23%. It is clear that the concrete with RCA has more absorption rate than that of the control mix. This is mainly due to the high absorption of the recycled aggregate compared to the natural aggregate (Isabel Martínez-Lage et al 2012). The residual mortar attached to recycled concrete particles serves as a potential conduit for moisture transport. Figure 3 shows water absorption in a graphical form. Hence we can say that the RAC has more porosity when compared to the normal concrete. Though this may not have a direct relation with the durability of the concrete, it is affecting the strength of the concrete.

K.K.Sagoe-Crentsil et al (2001) have got absorption rates ranging between 5-7%. The absorption rate of this investigation ranges between 4-6%.

CONCLUSIONS

(1) RCA exhibits similar behaviour like fresh aggregate in concrete; therefore, RCA could be incorporated into many concrete structures. However, RCA that has an unknown origin should be tested to ensure that the RCA was not from a structure that was suffering from alkali-silica reaction, alkali-aggregate reaction, sulphate attack, or some other harmful reaction. Such RCA could affect adversely the strength and durability of the concrete and may be harmful.

(2) A maximum reduction of about 27% was noticed in compressive strength when the entire coarse natural aggregate was replaced with RCA. Moreover, environmental benefits may be able to compensate for the negative effect of loss in strength to some extent due to the use

of recycled coarse aggregate in concrete leading us to sustainable development.

(3) Absorption for RCA concrete was more than that for control mix. This may affect the durability of the concrete.

(4) As the degree of processing gets higher the RA tends to be more similar to NA. Hence RA after processing shows better results than unprocessed RA.

REFERENCES

- [1] A.K.Padmini, K.Ramamurthy, M.S.Mathews (2009), Influence of parent concrete on the properties of recycled aggregate concrete. Construction and Building Materials, 23, 829-836.
- [2] Akash Rao, Kumar N. Jha, Sudhir Misra, (2007), Use of aggregate from recycled construction and demolition waste in concrete, Resources Conservation and Recycling, 50, 71-81.
- [3] Ashraf M. Wagih , Hossam Z. El-Karmoty , Magda Ebid , Samir H. Okba (2013), Recycled construction and demolition concrete waste as aggregate for structural concrete, HBRC Journal , 9, 193-200.
- [4] Hisham Qasrawi (2014), The use of steel slag aggregate to enhance the mechanical properties of recycled aggregate concrete and retain the environment, Construction and Building Materials, 54, 298–304.
- [5] Isabel Martínez-Lage , Fernando Martínez-Abella, Cristina Vázquez-Herrero, Juan Luis Pérez-Ordóñez (2012), Properties of plain concrete made with mixed recycled coarse aggregate , Construction and Building Materials ,37 ,171-176.
- [6] K C Panda, P K Bal (2013), Properties of self-compacting concrete using recycled coarse aggregate, Procedia Engineering, 51, 159 – 164.
- [7] K.K.Sagoe-Crentsil, T.Brown, A.H.Taylor (2001), Performance of concrete made with commercially produced coarse recycled concrete aggregate, Cement and Concrete Research, 31 , 707-712.
- [8] M. Chakradhara Rao , S.K. Bhattacharyya , S.V. Barai (2011), Behaviour of recycled aggregate concrete under drop weight impact load, Construction and Building Materials, 25 ,69-80.
- [9] M. Etxeberria , E. Vázquez, A. Marí, M. Barra (2007), Influence of amount of recycled coarse aggregates and production process on properties of recycled aggregate concrete, Cement and Concrete Research, 37, 735-742.
- [10] R.V. Silva, J. de Brito, R.K. Dhir (2014), Properties and composition of recycled aggregates from construction and demolition waste suitable for concrete production, Construction and building materials, 65, 201-217
- [11] S. Manzi , C. Mazzotti, M.C. Bignozzi (2013), Short and long-term behavior of structural concrete with recycled concrete aggregate, Cement & Concrete Composites , 37 , 312-318
- [12] S.C. Kou, C.S. Poon (2012), Enhancing the durability properties of concrete prepared with coarse recycled aggregate, Construction and Building Materials, 35, 69-76.

4th International Engineering Symposium - IES 2015

March 4-6, 2015, Kumamoto University, Japan

[13] Sami W. Tabsh ,Akmal S. Abdelfatah (2009), Influence of recycled aggregate concreteon strength properties of concrete, Construction and Building Materials ,23, 1163-1167.

[14] Shi-Cong Kou, Chi-Sun Poon (2013), Long-term mechanical and durability properties of recycled aggregate concrete prepared with the incorporation of fly ash, Cement & Concrete Composites, 37, 12-19.

[15] Shi-Cong Kou, Chi-Sun Poon, Hui-Wen Wan (2012), Properties of concrete prepared with low-grade recycled aggregates, Construction and Building Materials, 36, 881-889.

[16] Sumaiya Binte Huda, M. Shahria Alam (2014), Mechanical behavior of three generations of 100% repeated recycled coarse aggregate, Construction and Building Materials, 65, 574-582.

[17] Wai Hoe Kwan , Mahyuddin Ramli, Kenn Jhun Kam, Mohd Zailan Suliman (2012), Influence of the amount of recycled coarse aggregate in concrete design and durability properties, Construction and Building Materials, 26, 565-573.

Table 1 Physical properties of Ordinary Portland Cement

No.	Property	Result obtained		Requirements as per IS code	
1	Specific gravity	3.12		--	
2	Normal consistency	29%		--	
3	Setting times, minutes	Initial 65 Final 270		Not less than 30 Not more than 600	
4	Fineness, m ² /Kg	330		Not less than 300	
5	Soundness, mm	2.50		Not more than 10 mm	
6	Comp. strength, Mpa	3d 34	7d 51	28d 61	3d 22
					7d 33
					28d 43

Table 2 Properties of fine aggregates

Property	Result	
Specific gravity	2.62	
Bulk density	Loose: 1463 Kg/m ³	Compact: 1661 Kg/m ³
Moisture content	Nil	

Table 3 Properties of coarse aggregates

Property	Result
Specific gravity	2.73
Bulk density	Loose: 1360 kg/m ³ Compact: 1527 kg/m ³
Moisture content	Nil

Table 4 Properties of recycled coarse aggregates

Sl. No.	Property	Results
1	Specific gravity	2.59
2	Water absorption	2.69%
3	Fineness modulus	6.96

Table 5 Composition of various mixes for OPC blended concrete

Mix	RCA (%)	C (kg)	FA (kg)	CA (kg)	RCA (kg)	W (kg)
Mix 1	0	400	600	1200	-	200
Mix 2	20	400	600	960	240	200
Mix 3	40	400	600	720	480	200
Mix 4	60	400	600	480	720	200
Mix 5	80	400	600	240	960	200
Mix 6	100	400	600	0	1200	200

(RCA-Recycled Coarse Aggregate, C-Cement, FA-Fine Aggregates, CA-Coarse Aggregates, W- Water)

Table 6 Sieve analysis results of natural and recycled coarse aggregates

Sieve size (mm)	% Finer	
	NCA	RCA
20	100	100
16	68.5	71.5
12.5	32.1	27.7
10	0.7	0.5

(NCA-Natural Coarse Aggregates, RCA-Recycled Coarse Aggregates)

4th International Engineering Symposium - IES 2015
March 4-6, Kumamoto University, Japan

Table 7 Test matrix for compression on 150 mm cubes

RCA (%)	No. of cubes
0	3
20	3
40	3
60	3
80	3
100	3
Total	18

Table 8 Compressive strength of cubes for OPC based concrete specimen

RCA (%)	Comp. Strength (N/mm ²)	Average Comp. Strength (N/mm ²)	Relative Comp. Strength	Average Relative Comp. Strength
Control 0	40.44	42.1	0.96	1.00
	43.11		1.02	
	42.67		1.01	
20	39.11	39.3	0.93	0.93
	40.89		0.97	
	37.78		0.90	
40	37.78	37.5	0.90	0.89
	37.33		0.89	
	37.33		0.89	
60	34.22	34.4	0.81	0.81
	34.22		0.81	
	34.67		0.82	
80	33.77	33.5	0.80	0.79
	34.67		0.82	
	32.00		0.76	
100	30.22	30.8	0.72	0.73
	31.11		0.74	
	31.11		0.74	

Table 9 Water absorption results for OPC based concrete

RCA (%)	Dry weight (kg)	Wet weight (kg)	Absorption (%)
0	8.232	8.579	4.22
20	8.080	8.470	4.83
40	7.844	8.256	5.23
60	8.093	8.485	4.84
80	7.956	8.371	5.22
100	7.963	8.36	4.99

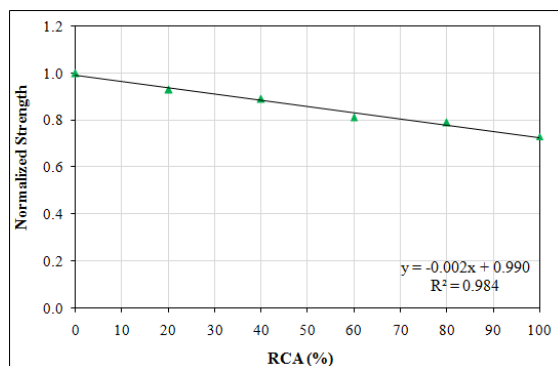


Fig. 1 Compressive strength variation of OPC based concrete with RCA (Mean data)

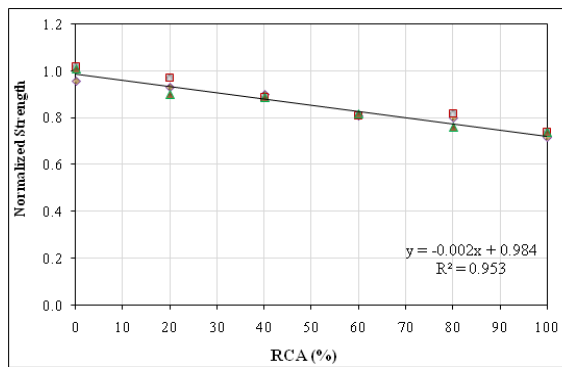


Fig. 2 Compressive strength variation of OPC based concrete with RCA (Full data)

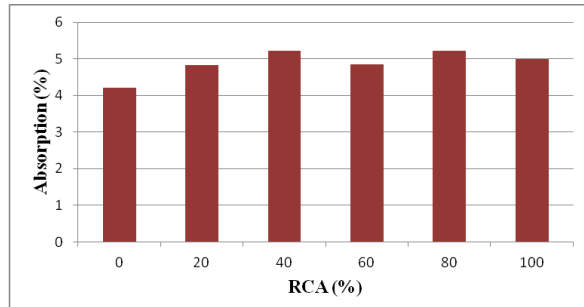


Fig. 3 Variation of percentage of absorption for OPC, with RCA

Structural Optimization Using Perfect Nodal Position Search Method

Premanand Shenoy , K S Babu Narayan and Katta Venkataramana

*Department of Civil Engineering, National Institute of Technology Karnataka,
Surathkal India. email: pshenoy_cv11p03@nitk.edu.in*

ABSTRACT: A novel iterative for the evolution of optimum design of trusses is presented. This method does the analysis, design, generates the optimum topology and arrives at minimum sizes of members, subjected to given stress and movement constraints. Efficiency of a member is determined at every level of iteration, end nodes are moved to improve the efficiency of the member. A forceful refinement of length of each member and hence the movement of end nodes leads to a refined geometry of the truss . Three parameters are identified corresponding to member properties determining the extent of modification of length and repositioning of nodes.

Keywords: Structural Optimization, Topology, Sizing, Shape, Trusses, Iterative Process, nodal position

INTRODUCTION

Two dimensional trusses are basic and commonly used form of construction. Evolutionary ideas in optimizing the size of members, shape and topology lead to preservation of precious material.

In the analysis of a structure by the Standard Direct Stiffness Matrix Method, a Global Stiffness Matrix is assembled from individual element stiffness matrices. Support conditions are imposed by manipulation of corresponding elements in global stiffness matrix. With the force vector on the right hand side, simultaneous equations are solved to get displacements at nodes and forces in members. Stresses in the material are determined to check the adequacy of cross sectional areas provided for all members.

Sizing is mainly governed by the permissible stresses in the material under different conditions. The tensile stress limit could be a factor of the yield stress. But the slenderness ratio and Young's modulus play a critical role in compressive stress limit. An ideal situation is the one for which the material

strength gets fully exploited for all the members, simultaneously.

Shape Optimization involves finding out a shape of a truss which gives minimum weight.

Trying to find out the perfect shape of truss, some members may turn out to be totally inefficient, with the cross sectional areas demanded by size optimization reducing to minimum. Judicious removal of such members from the configuration of the truss, give rise to the best topology.

EVOLUTION OF PERFECT NODAL POSITION SEARCH METHOD

Motivation to develop the proposed Perfect Nodal Position Search Method (**PNPSM**) comes from the necessity of an algorithm that uses the basic principles of structural mechanics effectively, efficiently and intelligently to reduce material consumption in trusses in a systematic and sequential manner. Though sizing optimization is member based, **PNPSM** uses nodes as points of attraction in shape and topology optimization.

4th International Engineering Symposium - IES 2015

March 4-6, 2015, Kumamoto University, Japan

The proposed method uses the Direct Stiffness Matrix Method for the analysis of the truss, with the initial values of member properties like \mathbf{A} (Cross sectional area) and \mathbf{E} (Young's Modulus of the material) and \mathbf{l} (Length of the member) are taken as inputs for the determination of element stiffness.

Solution is obtained for forces and the axial stresses . The ratio of actual stress to the permissible stress in the material at a cross section of a member is called utility ratio of that member, \mathbf{U} . If $\mathbf{U} > 1$, the member is unsafe.

At a typical node, let us assume that there are ' m ' number of members connected to it. Let the cross sectional areas be $\mathbf{A}_1, \mathbf{A}_2, \mathbf{A}_3, \dots, \mathbf{A}_m$ and lengths be $\mathbf{l}_1, \mathbf{l}_2, \mathbf{l}_3, \dots, \mathbf{l}_m$.

Performing the analysis and getting a safe design, need not lead to an optimum design. Let us assume the utility ratios of the members be $\mathbf{U}_1, \mathbf{U}_2, \mathbf{U}_3, \dots, \mathbf{U}_m$, all of them being less than unity for a safe design. Utility ratios of members is the guiding premise for the formulation of Perfect Nodal Position Search Method (**PNPSM**) that lead to optimum design through a sequential achievement of the following criteria

Criterion-1: Sizing optimization is achieved by forcing change in cross sectional areas of members to reach values that give utility ratios close to unity.

Achieving this condition for all the members, necessitates search for strategic node location, which has prompted the criterion given below.

Criterion-2 : If a node can be moved to a new position such that all the members connected to it reach the utility ratios very close to unity simultaneously, then that position is deemed to be the perfect position for the node.

Criterion-3 : In the search process, If a member area demanded is negligible (Cross sectional area) the indication is that such members are ineffective and

the truss can perform without that member in question, as a part of the current configuration.

Criterion-4: If all the members at a node are ineffective, then the truss can survive without that node, indicating it can be collapsed to any node .

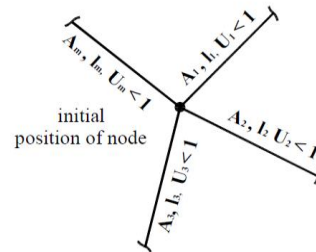


Fig. 1. Initial Position of Node

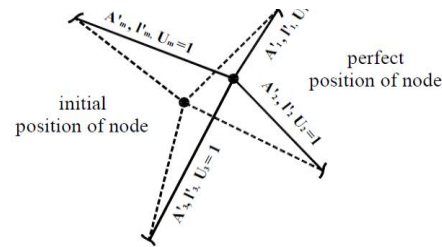


Fig. 2. Perfect position of Node

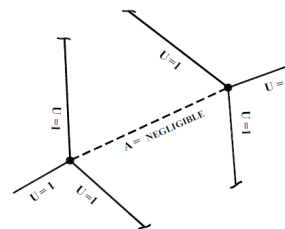


Fig. 3. Criterion for Removal of a Member

MOVEMENT OF NODES

The multi objective optimization of trusses with same material can now be viewed as finding out the perfect nodal

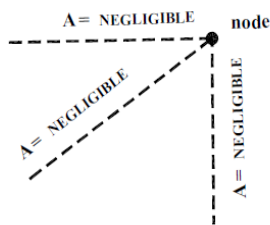


Fig. 4. Criterion for Removal of a Node

positions such that all the members of the truss, subjected to given set of constraints

- a) have non negligible cross sectional areas
 - b) have utility ratios equal to unity (ideal situation)
 - c) have a set of lengths such that total weight of the truss W , is minimum
- Where

$$W = \text{Unit wt} \times \text{Sum of } (A_i \times l_i) \quad \text{--- Eq. 1}$$

$i = 1 \text{ to } m$, where A_i is cross sectional area and l_i is the length of the i th member.

Movement of node changes the lengths of members connected to the node. The reverse is also true. The change in lengths of members connected to a node, moves the node.

To achieve the minimum, the problem is approached from three angles.

- i. Reduce the length, if cross sectional area is to remain the same
- ii. Reduce the cross sectional areas if the lengths is to remain the same.
- iii. Increase the effectiveness

With these in mind, the lengths of members connected at a node are changed based on their relative qualification.

Factor for weight consideration (C_1)

$$C_{1i} = w_i / \text{sum of } (w_i) \quad \text{--- Eq. 2}$$

$i = 1 \text{ to } m$, where w_i is the weight of the i th member

Factor for area consideration (C_2)

$$C_{2i} = A_i / \text{sum of } (A_i) \quad \text{--- Eq. 3}$$

$i = 1 \text{ to } m$, where A_i is sectional area of the i th member

Factor for inefficiency (C_3)

$$C_{3i} = 1 - U_i \quad \text{--- Eq. 4}$$

where U_i is utility ratio of the i th member

Total forced change in length of i th member , dl in the direction of member

$$dl_i = MF \cdot C_{1i} C_{2i} C_{3i} l_i \quad \text{--- Eq. 5}$$

where **MF** is the maximum percentage modification desired per iteration

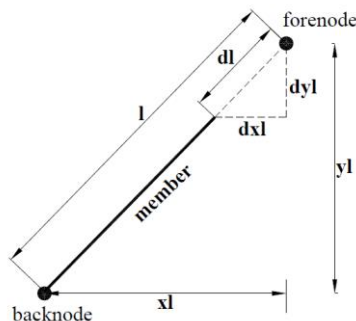


Fig. 5. Forced Change in Length of a member

When the member length changes by dl , the node will be moved with respect to its original position by dxl in the global **X** axis and dyi in the Global **Y** axis.

$$X_{\text{new}} = X_{\text{old}} + \text{sum of } (dxl) \quad \text{--- Eq. 6}$$

$$Y_{\text{new}} = Y_{\text{old}} + \text{sum of } (dyi) \quad \text{--- Eq. 7}$$

If all the members at a joint are efficient, the node is not moved. This ensures the convergence of the solution for optimization. On the other hand, the node will be forced to move relatively when every member is subjected to a forced change in length, every time checking the node position for a possible set of movement restrictions specified in the problem.

ITERATIVE PROCEDURE

The PNPSM is an iterative procedure with distinct loops for sizing and shape optimization. Topology optimization is achieved during the course of shape optimization.

After every loop for solution for stresses, member lengths are modified as per **Eq. 5** to effect change in nodal positions and the whole procedure is repeated to get another set of stabilized utility ratios. This is named as the combined shape optimization loop. The procedure is repeated till we get a stabilized set of utility ratios of all effective members equal to unity.

While iterative loop in progress, some of the members of the truss are identified ineffective and Young's modulus values of such members are considered negligible for the consecutive loop. Fig.9 shows the flowchart for the implementation of the PNPSM.

NUMERICAL EXAMPLE

The 15 bar truss problem, shown in Fig.6, solved by many researchers [6] has been treated as benchmark to check the efficiency of the PNPSM algorithm. The optimum design is to be achieved with the properties and movement restrictions stated in Table 1.

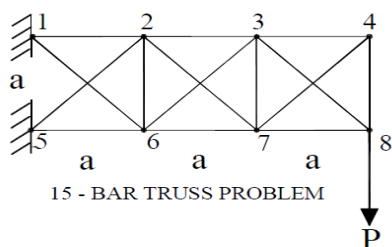


Fig. 6. Benchmark Problem

$$\begin{aligned}
 P &= 10 \text{ kips} \quad (44.48 \text{ kN}) \\
 a &= 120 \text{ in} \quad (3048 \text{ mm}) \\
 \text{density} &= 0.1 \text{ lb/cu.in} \quad (2768 \text{ kg/Cu.m}) \\
 e &= 10000 \text{ ksi} \quad (68947.6 \text{ N/Sq.mm}) \\
 \text{limit} &= 25 \text{ ksi} \quad (172.0 \text{ N/Sq.mm})
 \end{aligned}$$

Table 1. Constraints for Nodal Movements

JOINT No.	CO-ORDINATES		Permissible Freedom			
	X	Y	Min X	Max X	Min Y	Max Y
1	0	120	0	0	120	120
2	120	120	100	140	100	140
3	240	120	220	260	100	140
4	360	120	360	360	50	90
5	0	0	0	0	0	0
6	120	0	100	140	-20	20
7	240	0	220	260	-20	20
8	360	0	360	360	20	60

Additional Conditions : $X_6 = X_2$, $X_7 = X_3$, $X_8 = X_4 = 360$

RESULTS AND DISCUSSION

The optimum topology evolved is shown in Fig. 7. Table 2 shows the set of Length, Area and Utility ratio for every member at the instance of optimum design. PNPSM clearly identifies member numbers 3,7,8,9 and 15 as ineffective.

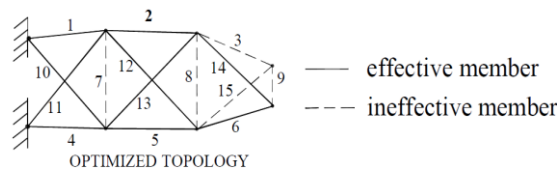


Fig 7. Configuration for Minimum Weight - Topology

Table 3 shows the sizing and layout variables obtained by PNPSM in comparison with the results given in references. Fig. 8 shows the weight reduction of the truss corresponding to iterations performed with a typical Modification Factor 5%

A study has been conducted to know the effect of Modification Factor (MF) in PNPSM on the convergence to the optimum design of the 15-Bar Truss. Fig. 9 shows the individual convergences for various Modification Factors. It is seen that the value of Modification Factor up to 15% has no much effect on the convergence to the optimum design in terms of the shape, topology, sizing and finally, the weight. Fig.10 shows the effect of Modification Factor on the

4th International Engineering Symposium - IES 2015

March 4-6, 2015, Kumamoto University, Japan

Convergence to minimum weight. Fig. 11 shows the flow chart for PNPSM.

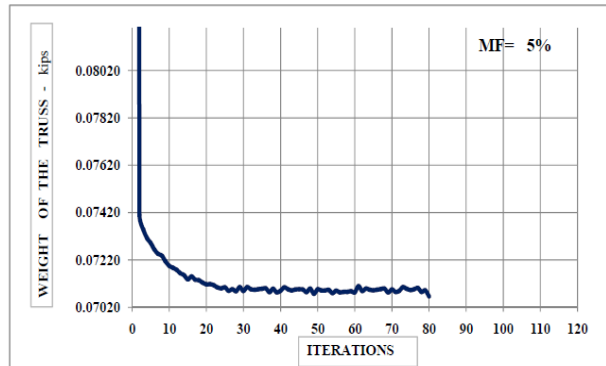


Fig 8. Typical Graph Showing Weight Reduction of Truss

Table 2. Final Sectional Areas and Utility Ratios

RESULTS WITH REDUCTION FACTOR = 5 %				
15 - MEMBER TRUSS - OPTIMUM DESIGN				
	AREA	STRESS	Allow. Stress	RATIO
Memb	Sq. in	ksi	ksi	
1	0.8671	25.00	25.00	1.00
2	0.7321	25.00	25.00	1.00
3	0.0000	0.00	25.00	0.00
4	1.1332	-25.00	25.00	1.00
5	0.4670	-25.00	25.00	1.00
6	0.4050	-25.00	25.00	1.00
7	0.0000	0.00	25.00	0.00
8	0.0000	0.00	25.00	0.00
9	0.0000	0.00	25.00	0.00
10	0.4700	25.00	25.00	1.00
11	0.0951	-25.00	25.00	1.00
12	0.0960	25.00	25.00	1.00
13	0.4710	-25.00	25.00	1.00
14	0.5200	25.00	25.00	1.00
15	0.0000	0.00	25.00	0.00

CONCLUSIONS

Perfect Nodal Position Search Method is appealing, as convergence is faster and the optimum shape, topology and member sizing is accomplished simultaneously. Suitable modifications to element stiffness matrix, extends its usage potential to 3D trusses too.

Table 3. Comparison of Results for Benchmark Problem.

MEMB	MEMB AREAS - COMPARISON OF RESULTS					
	EARLIER WORKS [6]					Present Work
	Gholiz a-deh	Tang et	Hwan g and He	Raha- mi	Kulkar- ni	
Sizing variables (in.²)						
A1	0.95	1.08	0.95	1.08	0.95	0.87
A2	0.54	0.54	1.08	0.54	0.54	0.73
A3	0.27	0.29	0.44	0.29	0.11	0.00
A4	1.08	0.95	1.17	0.95	0.95	1.13
A5	0.54	0.95	1.49	0.54	0.54	0.47
A6	0.17	0.22	0.03	0.14	0.35	0.41
A7	0.11	0.11	0.27	0.11	0.11	0.00
A8	0.11	0.11	0.35	0.11	0.11	0.00
A9	0.44	0.29	0.22	0.54	0.11	0.00
A10	0.44	0.22	0.44	0.44	0.44	0.47
A11	0.35	0.44	0.35	0.54	0.44	0.10
A12	0.22	0.44	0.22	0.27	0.17	0.10
A13	0.22	0.11	0.27	0.22	0.17	0.47
A14	0.17	0.22	0.44	0.14	0.35	0.52
A15	0.27	0.35	0.22	0.29	0.11	0.00
Wt (lbs)	73.93	79.82	104.57	76.69	72.52	70.66

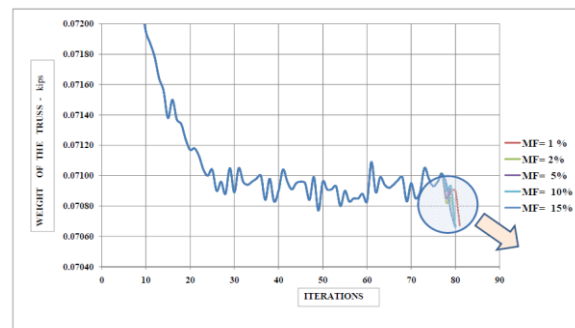


Fig 9. Effect of Modification Factor on The Optimum Design

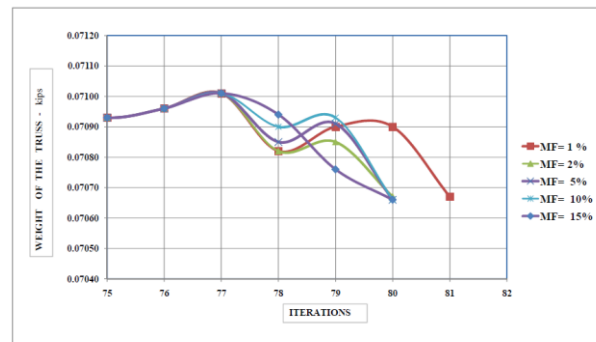


Fig 10. Effect of Modification Factor on Convergence to minimum weight

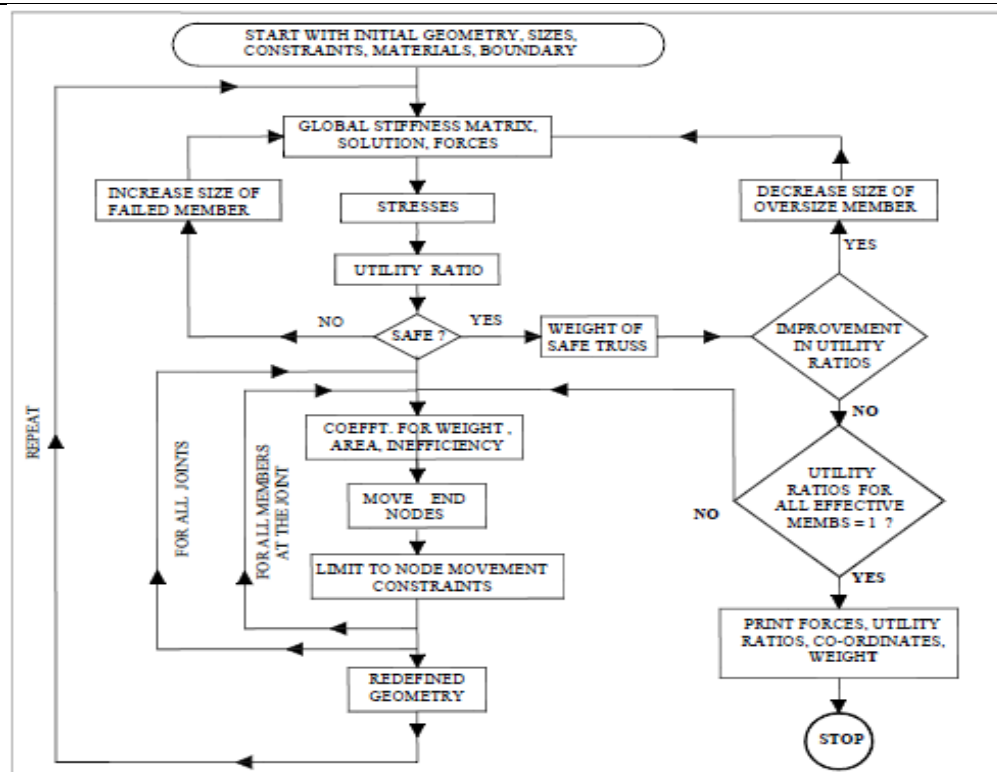


Fig. 11. Flowchart for the Perfect Nodal Position Search Method

REFERENCES

- [1] Chun-Yin Wu · Ko-Ying Tseng (2010) Topology Optimization Of Structures Using Modified Binary Differential Evolution, *Journal of Structural Multidisciplinary Optimization*, Springer-Verlag , s00158-010-0523-9 2010
- [2] Farzin A , Farrokh A, Daryoush N (2013) Optimal design of truss structures via an augmented genetic algorithm, *Turkish Journal of Engineering & Environmental Sciences*, (2013) 37: 56 – 68
- [3] Gholizadeh and H. Barati (2012) A Comparative Study Of Three Meta heuristics For Optimum Design Of Trusses, *International Journal Of Optimization In Civil Engineering* 2012; 3:423-441
- [4] Hadi E, Pouya Salehi, Ghodssian A (2010). Imperialistic Competitive Algorithm for Truss Structures with Discrete Variables, 2nd International Conference on Engineering Optimization, Sept 6-9, 2010, Libson, Portugal.
- [5] Hwang S-F, He R-S(2006) .A hybrid real-parameter genetic algorithm for function optimization." *Journal of Engineering Optimization* ' Volume 38, Issue 7, 2006
- [6] Jayant Kulkarni A, Kazemzadeh Azad (2012) .Structural Optimization Using A Mutation-Based Genetic Algorithm, *International Journal Of Optimization In Civil Engineering* 2012; 2(1):81-101
- [7] Kalatjari V., P. Mansoorian (2011) Sizing and Topology Optimization of Trusses by Development of Algebraic Force Method and Parallel Genetic Algorithm , 6th National Congress on Civil Engineering, April 26-27, 2011, Semnan University, Semnan, Iran
- [8] Novapart, Sujin. (2013) Simultaneous Topology, Shape and Optimization of Plane Trusses Adaptive Ground Finite Elements Using MOEAs, *Mathematical Problems in Engineering*, Hindawi Publishing Corporation, Article ID 838102 Vol. 2013 Jan 2013
- [9] Pavel Tomsic , JoDe Duhovnik (2014), Simultaneous Topology and Size Optimization of 2D and 3D Trusses Using Evolutionary Structural Optimization with regard to Commonly Used Topologies *Advances in Mechanical Engineering* Hindawi Publishing Corporation, Article ID 864807, Volume 2014
- [10] Rahami H, Kaveh A, Gholipour Y (2008) .Sizing, geometry and topology optimization of trusses via force method and genetic algorithm. *Engineering Structures*, Elsevier 2008; 30(9):2360,69.

Effect of Nodal Placement for a Beam Using MeshFree Method

Bhavana Patel S.S., K.S. Babu Narayan and Katta Venkataramana

Department of Civil Engineering, National Institute of Technology Karnataka, Surathkal, Mangalore 575025, India. email: bhavana8patel@gmail.com

ABSTRACT: Mathematical modeling and simulation of physical systems has greatly advanced in last five decades because of the increased demand for innovative structures. MeshFree is one of the mathematical modeling techniques, which has gained its importance in modeling high stress gradients region and crack growth. This paper is an attempt to model beam structure using Element Free Galerkin (EFG) scheme, which is one of the MeshFree methods. Shape function is constructed using Moving Least Square (MLS) and the displacements and stresses are computed for uniform and non-uniform nodal distribution. In CASE 1, nodes are distributed equally on the beam and in the CASE 2 placement of nodes are varied by ten percent. The results obtained by EFG method are compared with the traditional Finite Element Method (FEM), it can be observed that the nodal placement do not affect the displacements and stresses obtained using EFG method.

Keywords: MeshFree, moving least squares, nodal distribution, element free Galerkin

INTRODUCTION

Finite Element Method (FEM) is one of the very well developed numerical techniques used for solving most of the engineering problems. The main disadvantage of FEM is that, modeling and simulation of crack propagation requires re-meshing (Robert et al., 2001). This becomes a major concern due to lack of accuracy obtained from distorted elements. Simulation of crack growth, breakage of material can't be modelled, as FEM is based on continuum mechanics in which it is difficult to introduce damage within the element.

To overcome the drawback of FEM, MeshFree method is introduced as discussed in Daxini and Prajapati (2014). MeshFree is the method of arriving at the algebraic equations without predefined nodal connectivity (Liu,2009). Element Free Galerkin (EFG) (Belytschko et al.,1994) method is one of the MeshFree methods which has gained popularity because of its similarity to that of FEM, and the major difference arises in the construction of shape function. The Moving

Least Square (MLS) technique is adopted for the shape function construction in EFG method.

In this paper, the effect of placement of nodes on a beam (Someshwar, 2013) using FEM and EFG method has been illustrated. If nodes are present in the region of importance, the accuracy is more in case of FEM. Whereas MeshFree method can accurately interpolate the results irrespective of the placement of nodes for simple beam structure. From the results it can be concluded that FEM is very sensitive to the nodal placement when compared to that of EFG method.

FORMULATIONS

MLS (Kushawaha, 2012) technique has been adopted to carry out interpolation of the field variables. Shape function can be constructed as shown in Eq. 1

$$u^h(x) = \sum_I^N N_I(x)d \quad \dots (1)$$

where, $N_I(x) = \sum_j^m p_j(x)(A^{-1}(x)B(x))_{jl} = p^T A^{-1} B_l$

$N(x)$ is the matrix of MLS shape function

corresponding to n nodes in the support domain, $N(x) = [N_1(x), N_2(x), \dots, N_n(x)]$.

$$A(x) = \sum_i^n W_i(x) p^T(x_i) p(x_i)$$

$$B(x) = [B_1, B_2, \dots, B_n]$$

$$B_i = W_i(x) p(x_i)$$

$$d = \{u_1, u_2, \dots, u_n\}^T$$

d is the vector that collects the discrete nodal parameters of the field variables for all the nodes in the support domain.

In the above equations p is a polynomial basis of order m and for one dimension it can be written as,

$$p^T(x) = \{p_0(x), p_1(x), \dots, p_m(x)\} = \{1, x, x^2, x^3, \dots, x^m\}$$

and W is weighting function, which decides the weightage of each node present in the domain. Exponential weight function is used in the present paper as the first and second order differential of the exponential weight function and follows continuity in the field variable interpolation.

$$W(x - x_i) = W(d) = \begin{cases} e^{-(d/\alpha)^2} & \text{for } d \leq 1 \\ 0 & \text{for } d > 1 \end{cases}$$

where, α is constant and taken as 0.3;

$$d = \frac{|x - x_i|}{d_w} \text{ and } x \text{ is any point in the domain, } x_i \text{ is the node of interest and } d_w \text{ is the smoothing length.}$$

Based on the material used, forces and moments can be computed as in Eq. 2,

$$\begin{bmatrix} N_x \\ M_x \\ Q_x \end{bmatrix} = [MAT] \begin{bmatrix} \varepsilon_{xx}^0 \\ \kappa_x \\ \gamma_{xy} \end{bmatrix} = \begin{bmatrix} EA & 0 & 0 \\ 0 & EI & 0 \\ 0 & 0 & GA \end{bmatrix} \begin{bmatrix} \varepsilon_{xx}^0 \\ \kappa_x \\ \gamma_{xy} \end{bmatrix} \dots (2)$$

where,

E is the Young's modulus of a material, I is area moment of interia and A is the cross-sectional area.

N_x is force, M_x is moment, Q_x is shear force.

ε_{xx}^0 is normal strain, κ_x is the curvature strain and γ_{xy} is the shear strain.

The strains and displacements are related using the constructed shape function as given in Eq. 3, where B_i is the strain-displacement matrix,

$$\begin{bmatrix} \varepsilon_{xx}^0 \\ k_x \\ v_{xy} \end{bmatrix} = \sum_{i=1}^n B_i \begin{bmatrix} u_i \\ v_i \\ \theta_{zi} \end{bmatrix} = \sum_{i=1}^n \begin{bmatrix} \frac{\partial N_i}{\partial x} & 0 & 0 \\ 0 & 0 & \frac{\partial N_i}{\partial x} \\ 0 & \frac{\partial N_i}{\partial x} & N_i \end{bmatrix} \begin{bmatrix} u_i \\ v_i \\ \theta_{zi} \end{bmatrix} \dots (3)$$

and, u_i , v_i and θ_{zi} are the displacements.

By the stationary minimum potential energy principle, the stiffness K can be derived as,

$$K = \int_{-1}^1 B^T [Mat] B |J| d\xi \dots (4)$$

where, $J = \sum_{i=1}^n \frac{\partial N_i}{\partial x} X_i$ and X_i are the coordinates of the nodes in the domain.

Eq. 4 is numerically integrated by applying Gaussian quadrature, which is represented in terms of Gauss points and weights as,

$$K = \sum_{i=1}^{N_g} w_i B^T(\xi_i) [Mat] B(\xi_i) J(\xi_i) \dots (5)$$

where, N_g is the number of Gauss points

RESULTS AND DISCUSSIONS

A steel cantilever beam of length 1000 mm, cross-sectional area $100 \times 100 \text{ mm}^2$ and point load (P) of 1000N as shown in Fig. 1 is considered to verify the effect of nodal position in FEM and MeshFree method.

Five nodes are placed along the length of the beam at different nodal positions named as X1, X2, X3, X4 and X5. Nodes X2 and X4 are moved away from the node X3. The percentage variations of the displaced nodes are detailed in Table 1.

Fig.2 shows the displacement plots for FEM and EFG method with the variation of the nodal placement. It can be observed that the displacements obtained by EFG method remains same irrespective of the change in nodal positions. Whereas in case of FEM as the percentage of nodal variation increases, the displacement values are also moving away from the actual result. It can also be seen that EFG method exactly coincides with the exact solution with five nodes but FEM even in case of 0 percent variation the results have not converged to the exact solution.

4th International Engineering Symposium - IES 2015

March 4-6, 2015, Kumamoto University, Japan

Further increase in nodes will lead the FEM solution to converge to the exact solution.

Similar observation can be made in case of stress plot shown in Fig.3. In case of FEM, when the nodes move closer to each other at the high stress region, the estimated stress moved closer to the exact solution. EFG method converges to the exact solution irrespective of its nodal position.

CONCLUSIONS

MeshFree Method is the solution to overcome the drawbacks of FEM. The present study shows that, FEM is much dependent on the location of the nodes present on the beam. Whereas EFG method is independent of the nodal position while computing displacements and stresses. It is also observed that the convergence of displacements and stresses are good in case of EFG method in spite of lesser number of nodes. This is basically because of shape function construction using MLS technique, which results in better interpolation. MeshFree methods are well suited for the fracture mechanics

problems in which FEM has difficulty to solve.

ACKNOWLEDGEMENTS

The authors are grateful to Technical Education Quality Improvement Programme (TEQIP) for funding this study.

REFERENCES

- [1] Belytschko T. et al. (1994), Element-free Galerkin method, International Journal For Numerical Methods In Engineering, 37, 229-256.
- [2] Daxini S. D. and Prajapati J.M. (2014), A Review on Recent Contribution of MeshFree Methods to Structures and Fracture Mechanics Application, The Scientific World Journal, Article ID 247172.
- [3] Kushawaha J. S. (2012), MeshFree shape function from moving least square, e-Journal of Science and technology, 29-41
- [4] Robert D.C et al. (2001), Concepts and Application of Finite Element Analysis, Fourth edition, John Wiley and sons, INC.
- [5] Liu G.R. (2009), MeshFree Methods Moving beyond the Finite Element Method, Second edition, CRC press, Taylor and Francis group, New York.
- [6] Someshwar S. P. et al. (2013), Introduction of MeshFree methods and implementation of EFG methods to beam problem, International Journal on Theoretical and Applied Research in Mechanical Engineering, 2, 2319 – 3182.

Table 1: Nodal locations of non-uniform nodal distribution

% Variation	Nodal locations in mm				
	X1	X2	X3	X4	X5
0	0	250	500	750	1000
20	0	200	500	800	1000
40	0	150	500	850	1000
60	0	100	500	900	1000
80	0	50	500	950	1000



Figure 1 – Cantilever Beam

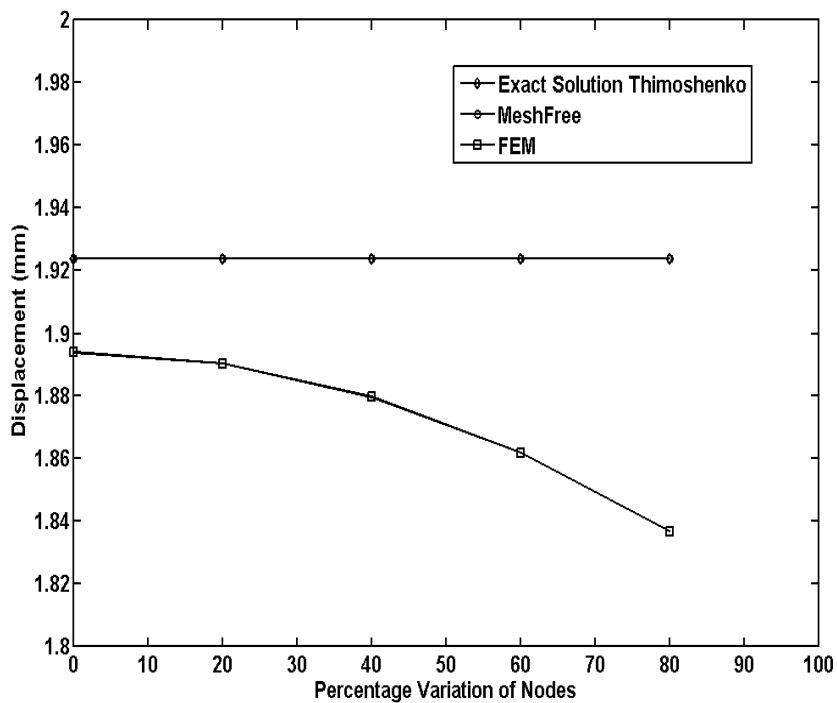


Figure 2 – Displacement plot for uniform and non-uniform nodal distribution

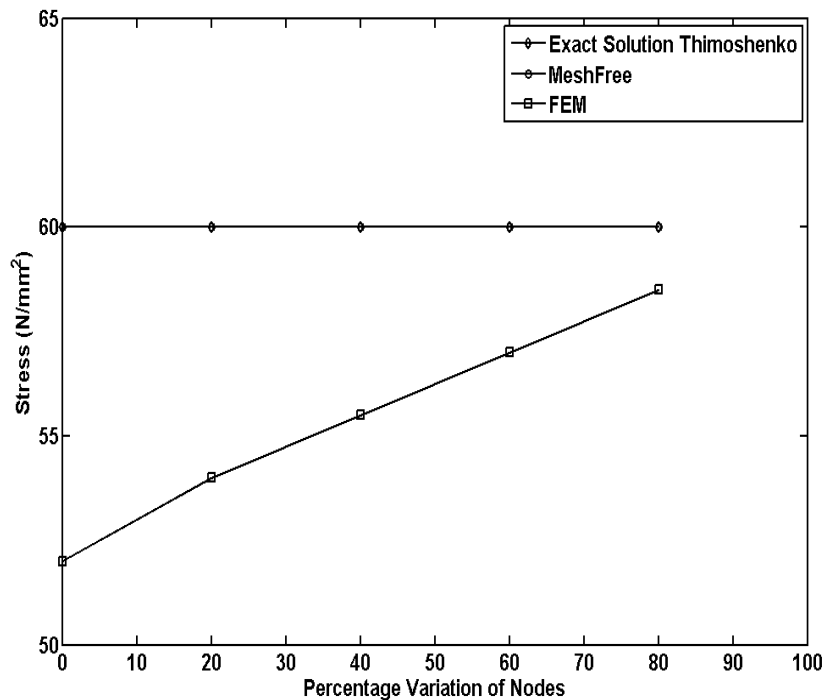


Figure 3 – Stress plot for uniform and non-uniform nodal distribution

Numerical Studies of A Tunnel Excavation and Its Effect on Stress Distributions around the Tunnel in Underground Bangalore Metro Project

Ishaan Rajankar¹ and T.G. Sitharam²

¹ National Institute of Technology Karnataka, Surathkal, India, 575025, Email: ishaanrajankar@gmail.com

² Department of Civil Engineering, Indian Institute of Science, Bangalore, India, 560012, E-mail: sitharam@civil.iisc.ernet.in

ABSTRACT: 'Namma Metro' or Bangalore Metro is a metro system which runs in the city of Bangalore situated in Karnataka, in the busy central districts to provide a sustainable public transport. Due to the presence of Gneisses and Granites which is a part of the Peninsular Granitic complex geology, the Tunnel Boring Machine is finding difficulties in proceeding in the Bangalore Metro Project. After analyzing the bore log report, a two dimensional, linearly elastic model and Elasto – plastic model is created using a finite element method software package, ABAQUS/CAE and the results have been compared with the tangential and radial stress distribution obtained using the Kirsch's Solution and Bray's Solution. In order to validate the accuracy of results derived from ABAQUS, and to determine its coherence with existing work, example problems were considered with Elastic and Elasto-plastic analysis. Several cases have been reviewed and summarized. This paper also includes an analysis to check the effect of the redistribution of stresses by varying the Lateral Earth Pressure ratio and to compare the stress distribution around the tunnel at different stages of construction which includes Boring, Lining, Grouting and insertion of Dowels. Further, results are presented to understand the difference in stresses in the presence and absence of Dowels present around the tunnel excavation.

Keywords: Underground Bangalore Metro Tunnel; ABAQUS/CAE; Elastic Model; Elasto-plastic Model; Lateral Earth Pressure Ratio; Stress Distribution at different Stages of Construction; Stresses in Dowels

INTRODUCTION

Tunnels are the vital elements for everyday life of people, especially those living in heavily crowded urban areas. Tunnels are built to move people or materials in a precise route where the movement without a tunnel is impossible or it is impractical or inadequate. The salient features of the Bangalore Metro are given as follows:-The total length of the Bangalore metro line is 42.3 kms, which is divided into two corridors. The first one runs along the east – west corridor extending up to 18.1 kms and the other running along the north-south corridor is 24.2 kms long. The total length of underground section is about 8.7 km. The focus of this study is confined to the

underground section with a twin tunnel for a length of 4.8 kms along the east-west section. Tunnels are bored using slurry TBM with an inner diameter of 5.6 m which is reinforced with a concrete lining of thickness 280 mm. The depth of the tunnel from the ground level is approximately 15 to 18.3m below the surface of the ground, the twin tunnel centres are 15.04 m apart from each other. The Tunnel Boring Machine (TBM) is successfully used to carry out the excavation process for the completion of the underground work in Bangalore using Helen and Margarita, two drilling machines, with a capacity of 11m per day. An Overburden of 10-12m is present above the TBM which has a diameter of 6.44m.

4th International Engineering Symposium - IES 2015

March 4-6, 2015, Kumamoto University, Japan

In this study, the comparison of Tangential and Radial stresses in an Elastic and Elasto-plastic medium has been validated with the Kirsch's Solution and Bray's Solution. In this paper, the Analyses by varying the in-situ stress ratio (Lateral Earth Pressure ratio) as 0.3, 0.5, 0.6 to see how it affects the redistribution of stresses is being conducted in the Elasto-plastic condition. Also, the stress analysis around the tunnel at different stages of construction from the TBM boring, Lining, Grouting and the dowels surrounding the tunnel followed by an analysis to compare the impact stresses of dowels present around the tunnel has also been conducted. For this purpose, a finite element method software package, ABAQUS/CAE, has been utilized. ABAQUS is software used for Finite Element Analysis and Computer Aided Engineering. The analysis in the software is conducted in three stages which are pre-processing, simulation, and post processing. All the analysis for modelling the whole tunnel construction has been carried out by using this program.

The Bangalore metro comprises of twin tunnels. But, for the analysis, we restrict it to a single tunnel stress analysis.

The Bangalore Metro Project uses three types of tunneling methods which includes – NATM (New Austrian Tunneling Method), cut and Cover Method and TBM. We would be restricting the study to the TBM Method.

Literature review plays a very important role in the basic analyses before undertaking an experiment.

LITERATURE STUDY

Geo-technical study

From the Standard Penetration Test Value(SPT) N number which is defined as the Standard Penetration Test Resistance we would be able to calculate the Young's Modulus, the internal friction angle, Bearing Capacity factors, unit weight of soil, and would know the complete soil profile to the required depth.

After locating and analyzing the Bore-log Reports of the Bangalore Metro at the current location of the TBM we would be

able to analyze the stresses which are created at the particular location listed in Table 1(Joseph E Bowles, 1997) and Table 2(USACE Settlement Analysis).

Equations used for the analytical solution of stresses

Kirsch's (Kirsch, 1898) Solution -

The below equation from Brady and Brown, 2005, describes the elastic stresses around a circular hole i.e. the Radial and Tangential stresses.

$$\sigma_{rr} = \frac{p}{2} \left[(1+k) \left(1 - \frac{a^2}{r^2}\right) - (1-k) \left(1 - 4 \frac{a^2}{r^2} + \frac{3a^4}{r^4}\right) \cos 2\theta \right]$$

$$\sigma_{\theta\theta} = \frac{p}{2} \left[(1+k) \left(1 + \frac{a^2}{r^2}\right) + (1-k) \left(1 + \frac{3a^4}{r^4}\right) \cos 2\theta \right]$$

p = Top Load (Pa)

k = Constant – Lateral Earth Pressure

a = Radius of the Tunnel (m)

r = Distance from the radius of the tunnel (m)

(1)

Bray's (John Bray, 1967) Solution -

$$m_1 = \frac{2 \cdot \sin(\phi)}{(1 - \sin(\phi))}$$

$$m_2 = \frac{c \cdot \cos(\phi)}{\sin(\phi)}$$

$$m_3 = \frac{m_2}{r_o^{m_1}}$$

$$m_4 = \frac{m_3 \cdot (1 + \sin(\phi))}{(1 - \sin(\phi))}$$

Plastic zone stresses are given by –

$$\sigma_r = m_3 \cdot r^{(m_1 - m_2)}$$

$$\sigma_\theta = m_4 \cdot r^{(m_1 - m_2)}$$

σ_r = Radial Stress

σ_θ = Tangential Stress

Radius of the Plastic Zone –

$$r_p = r_o \left[\frac{(p + c \cdot \cot(\phi))}{c \cdot \cot(\phi)} \right]^{\frac{(1 - \sin(\phi))}{2 \cdot \sin(\phi)}}$$

ϕ = Internal Friction angle

c = cohesion (Pa)

r_o = Radius of tunnel (m)

p = Vertical Load (pa)

(2)

Using the above formulae from Stanley Jose and Vivek S.S, 2014 the results of the FEM to the analytical solutions are compared with each other.

ANALYSIS

Stress analysis around the Tunnel constructed in the Bangalore Metro Project, was analyzed using the Finite Element Method software ABAQUS in a two dimensional, plain strain, elastic and

4th International Engineering Symposium - IES 2015

March 4-6, 2015, Kumamoto University, Japan

Elasto-Plastic domain. The analysis was performed to calculate the Radial, Tangential stresses which are produced at different locations and the stress distribution around the tunnel at different stages of construction. This is followed by the extraction of the stresses along the dowels and comparing the solution it in its absence.

Properties of soil profile, lining, shotcrete, dowels

Circular excavation in an infinite soil profile: The following is the analysis of the Bore-log Report of Bore-68 having $N = 49$ at the upper half of the tunnel and $N = 48$ at the lower half for N-S Profile of the Bangalore metro Project. A circular tunnel is modelled within the infinite soil profile having a diameter of 6.42 m which is the diameter of the tunnel in the Bangalore metro.

It has the following Young's modulus (Pa), Poisson's Ratio, Density, Cohesion and Internal Friction angle which is shown in Table 3.

Construction of lining within the tunnel: A 0.28m lining is been constructed inside the tunnel made of 53G cement of M200 having cement: sand: ingredient stone ratio of 1:1.5:3.4. The lining has the following parameters which are listed in Table 4. Introduction of Shotcrete along with cement and water as a Grouting material around the circular excavation: A thickness of 3m Shotcrete layer is being created around the tunnel. The following parameters of Shotcrete were used in the analysis provided in Table 5.

8 Rock Bolts have been placed around the tunnel made of mild steel having a length of 6m and a diameter of 0.1m at a spacing of 3m each between the bolts.

Following are the parameters of the Rock Bolt listed in Table 6.

Modelling

There are 4 different stages for the construction of the complete model and analysis is being conducted in two steps, for the excavation of the tunnel in a two dimensional infinite soil so as to compare the changes of stress around the tunnel after each development. The model consists of a 60x60m soil profile which is taken to be an infinite plate medium when

compared to the diameter of the tunnel which is equal to 9.34 times of the diameter.

There are two loads which are applied on the model in compression, the upper load and the side load. The weight of the vertical stress can be estimated with the weight of the overburden, but the horizontal load is estimated with suitable lateral earth pressure ratio. Isotropic Load Condition and varying the lateral earth pressure ratio (k) by 0.3, 0.5, and 0.6 respectively. The boundary conditions is applied so as to restrict the movement of the soil profile in the x and y direction respectively.

A tie constraint has been added between the lining, Shotcreting and the soil to keep it intact, which helps in the interaction of the two materials. The Dowels have been tied to the Lining for the interaction between the two materials. The initial In-situ stress is applied first to the model and then the elements present inside are been removed to show the process of excavation.

*At the current location of the construction where the details were being collected Dowels are not being used to stable surrounding weathered rock around the tunnel. It may be used depending on the ground conditions. As an academic exercise, the analysis of the Dowels has been carried out.

Validation of ABAQUS for Elastic and Elasto-plastic analysis

After Modelling and the specific parameters have been fed into the ABAQUS software, the Post Processing step which is the collection of the data and the analysis along with the comparison with analytical solution could be completed.

The radial and tangential stress graph obtained from ABAQUS and Kirsch, Bray's Solutions are compared as shown. The superimposition of the graphs validates this Elastic and Elasto-plastic analysis in ABAQUS as shown in Figure 1 and Figure 2. The green line denotes the Tangential Stress and the red line Radial Stress. Figure 3 and Figure 4 shows the S11 stresses in Isotropic Condition's and

4th International Engineering Symposium - IES 2015

March 4-6, 2015, Kumamoto University, Japan

Figure 5 shows the variation of the In-Situ Stress Distribution in Elasto-Plastic conditions.

Analysis of the stress distribution at different stages of tunnel construction

Figure 6, Figure 7 and Figure 8 shows the S11 stress, to compare the stress distribution in lining, shotcreting and the insertion of dowels during the excavation and construction of the tunnel. The Analysis is being performed in an Elasto-Plastic Medium with lateral earth pressure equal to 1.

Analysis of the extraction of stresses along the dowels and comparing it in its absence

Plots shown in Figure 9 and Figure 10 denote the comparison of Stress distribution in the presence and absence of Dowels with lateral earth pressure equal to 1.

CONCLUSION AND DISCUSSION

- In the plane Strain Model of the Elastic and Elasto-Plastic Medium of the Tunnel Excavation it is seen that when comparing between the FEM Solution with the Kirsch's Solution and the Bray's solution, the two graphs have very similar Radial Vs Tangential Stress plots which match very well.
- When varying the Lateral Earth Pressure Ratio (k) applied in Elasto-plastic medium, it is seen that it does not have much influence on the Plastic Zone but the peak stress increases from $k = 0.3$ to $k = 0.5$ and decreases from $k = 0.6$ to 1 .
 $k = 0.3 - (439294) \text{ Pa}$
 $k = 0.5 - (440711) \text{ Pa}$
 $k = 0.6 - (434304) \text{ Pa}$
 $k = 1 - (383838) \text{ Pa}$
- From comparing the stress distribution at different stages of tunnel excavation, it is seen that the stresses at the point of opening increases when the lining, grouting and the attachment of the Dowels.

Stress without lining = $1.345 \times 10^4 \text{ Pa}$

Stress with lining = $1.914 \times 10^5 \text{ Pa}$

Stress with grouting = $3.007 \times 10^5 \text{ Pa}$

Stress with Bolt = $6.925 \times 10^5 \text{ Pa}$.

- The stress on the lining also increases during the stage of shotcreting and the attachment of the dowels.
- After the comparison it is analyzed that the stresses along the dowel is 553991 Pa when compared to 218003 Pa when the dowel is not inserted.

The linear Elastic and Elasto-plastic model has been used, thus giving results which are deviating from the realistic model. The Soil profiling in the model is of uniformity throughout which is deviating from the realistic model consisting of various different soil profile at varied depths and is constructed in the centre of the profile. The grouting around the rock bolts is not simulated throughout the length. Grouting simulated is not a mixture of Cement, Bentonite and water.

REFERENCES

- [1] Joseph E Bowles, (1997), Foundation Analysis and Design, Fifth Edition, the McGraw-Hill Companies, Inc, New York
- [2] B.H.G.Brady and E.T.Brown, (2005), Rock Mechanics for underground mining, Third Edition, Kluwer Academic Publishers – New York/Boston/Dordrecht/London/Moscow, pp 174
- [3] Kirsch, 1898, the theory of elasticity and the needs of the strength of materials. Journal of the Association of German Engineers, 42, 797-807
- [4] Stanley Jose. A & Prof.Vivek.S.S, Static Analysis of Tunnels in Urban Areas for Metro Construction, International Journal of Engineering Research & Technology (IJERT), Vol. 3 Issue 5, May -2014
- [5] U.S. Army Corps of Engineers. 30 September 1990, Settlement Analysis, Washington DC

Table 1 Empirical values of density, of granular soils based on the standard penetration number, (Joseph E Bowles, 1997)

SPT Penetration, N-Value (blows/foot)	Density(lb/ft ³)
0-4	70-100
4-10	90-115
10-30	110-130
30-50	110-140
>50	130-150

4th International Engineering Symposium - IES 2015

March 4-6, 2015, Kumamoto University, Japan

Table 2 Empirical values of Young's Modulus against soil profile (USACE, Settlement Analysis)

Soil	E(tsf)
very soft clay	250 - 2000
soft clay	1000 - 2000
medium clay	250 - 1000
stiff clay, silty clay	100 - 250
sandy clay	1000 - 2000
clay shale	250 - 2000
loose sand	500 - 1000
dense sand	200 - 500
dense sand and gravel	50 - 200
silty sand	5 - 50

Table 3 Soil Properties

Young's Modulus (Pa)	60000000
Poisson's Ratio	0.33
Unit Weight(Kg/m^3)	2100
Cohesion(Pa)	40000
Internal Friction Angle (phi)	34

Table 4 Lining Properties

Young's Modulus (Pa)	5000000000
Poisson's Ratio	0.15
Density (Kg/m^3)	2400

Table 5 Shotcreting properties

Young's Modulus (Pa)	220000000
Poisson's Ratio	0.3
Density (Kg/m^3)	2750

Table 6 Dowels Properties

Young's Modulus (Pa)	200000000
Poisson's Ratio	0.3
Density (Kg/m^3)	7845

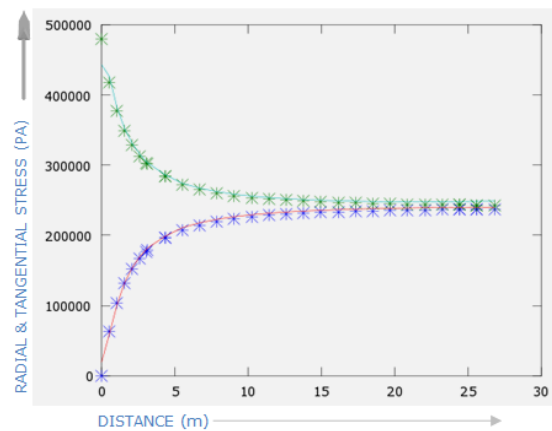
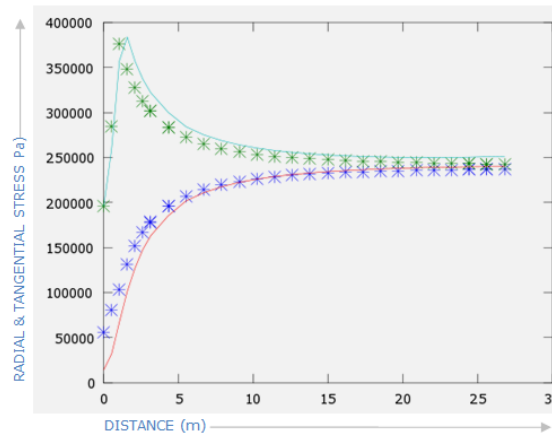


Fig.1 Comparison of FEM and Kirsch's Solution, Kirsch's Solution - (*)



**Fig.2 Comparison of the FEM and Bray's Solution
Bray's Solution - (*)**

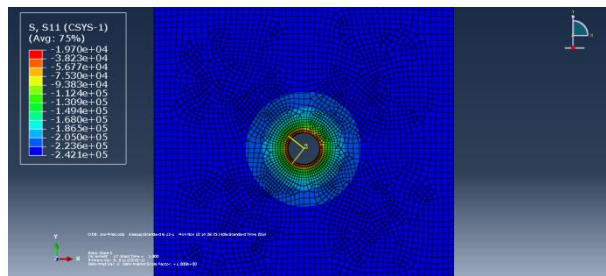


Fig.3 Stress distribution of S11-Elastic Model

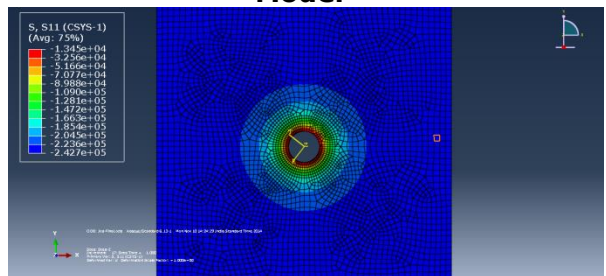


Fig.4 Stress distribution of S11-Elasto Plastic Model

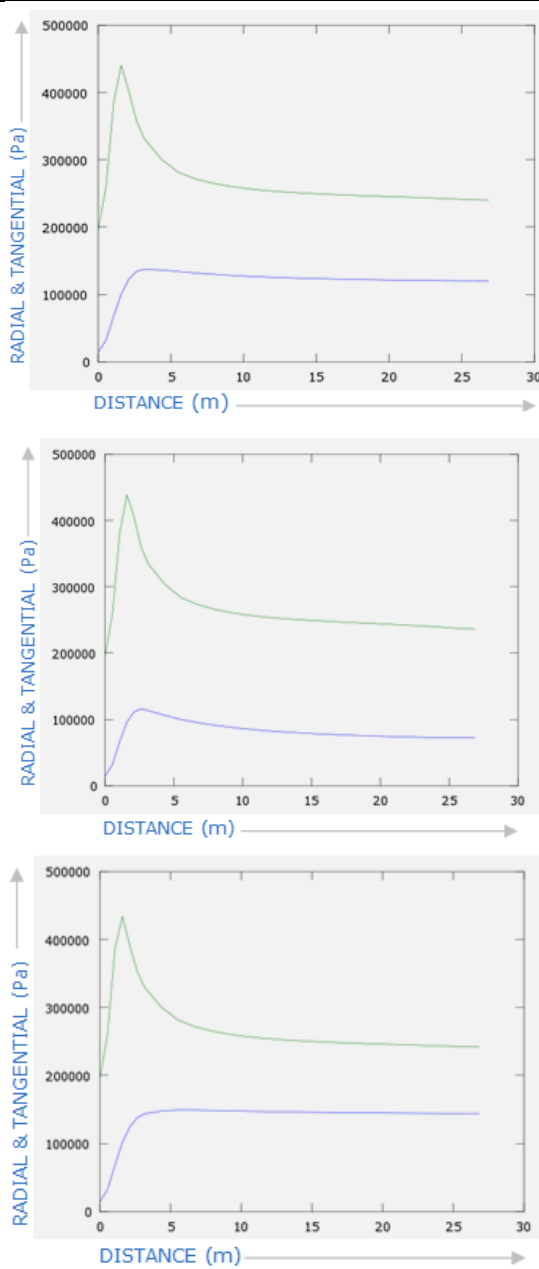


Fig.5 Plot for Variation of In-Situ Stress Loads ($k=0.5, 0.3, 0.6$)

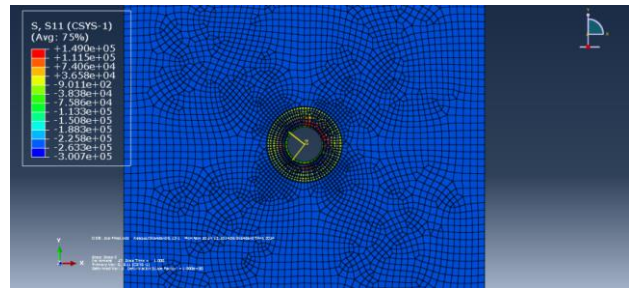


Fig.7 Stress distribution of S11 after Introduction of Shotcrete material around the circular excavation (3m Thickness)

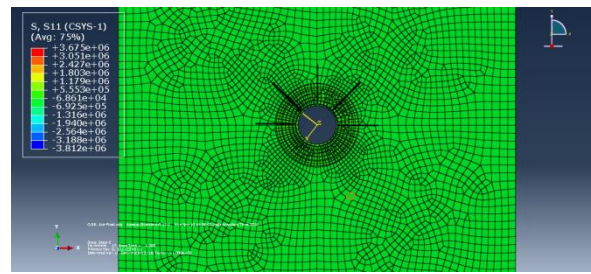


Fig.8 Stress distribution of S11 after introduction of Dowels 6m long

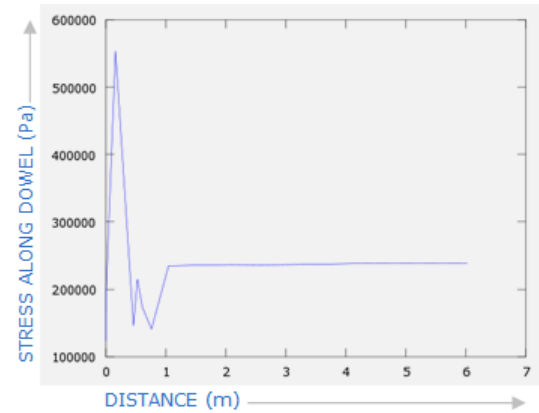


Fig.9 Extraction of stresses In dowel lying horizontal

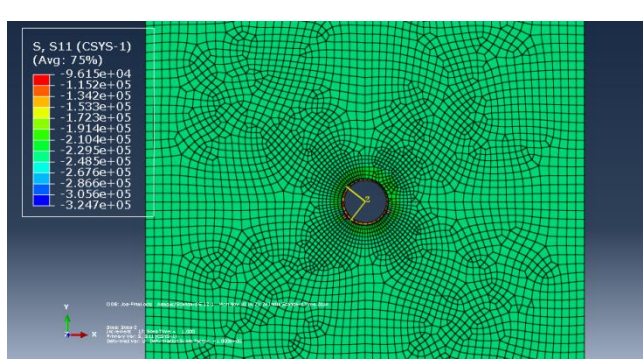


Fig.6 Stress distribution of S11 after the introduction of a lining 0.28m in thickness

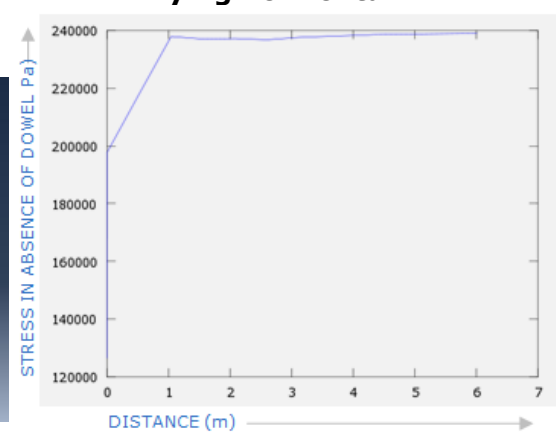


Fig.10 Extraction of stresses in the absence of the Dowels

A COMPREHENSIVE STUDY TO EVALUATE THE PERFORMANCE OF ROAD TRANSPORT UNDERTAKINGS IN KARNATAKA USING DATA ENVELOPMENT ANALYSIS

**T.G. Sitharam, Siddeshwar N. Hebbal, Devaraj Hanumappa
and Raviraj.H.Mulangi**

*Department of Civil Engineering, Indian Institute of Science, Bangalore-560012, India
Email: devaraj@cistup.iisc.ernet.in*

ABSTRACT

In this paper we have carried out a comprehensive case study to evaluate the performance of different State Road Transport Undertakings considering Karnataka as case study at divisional level. These State Road Transport Undertakings provide intercity bus services and rural bus service in the state of Karnataka and neighbouring states. Data Envelopment Analysis is used to evaluate the performance of different divisions in three State Road Transport Undertakings of Karnataka. The results are compared and the inefficiencies in the divisions are evaluated in terms of slack and surplus variables. Suitable recommendations are also made to the corporations in order to achieve the maximum efficiency.

Key words: Data Envelopment Analysis, Efficiency, Performance, State Road Transport Undertakings

1. INTRODUCTION

A large number of commuters are using bus services as their mode of travel in Karnataka. SRTU's in Karnataka cater 70 percent of the travel needs of the commuters for intercity transport. Since bus transport provides services with less initial cost and also provides door to door facilities, bus transport system has become major service provider for intercity transport in Karnataka.

The Karnataka State Road Transport Corporation was established in August, 1961 under the provisions of Road Transport Corporation Act 1950 with the objective of providing "adequate, efficient, economic and properly coordinated road transport services". In Karnataka three corporations provide intercity bus services. Karnataka State Road Transport Corporation (KSRTC) provides service in the southern part, North West Karnataka Road Transport Corporation (NWKRTC) in the North West part and North East Karnataka Road Transport Corporation

(NEKRTC) in the North East part of Karnataka. The salient features of all the three corporations in Karnataka state are given in the Table 1.

Good planning of transport is essential to make smooth traffic flow and ease the burden on the service provider. In recent years the cost of operation has reached its peak due to the increase in fuel price and staff cost. It is essential to evaluate the public transport system due to the severe operating conditions in which they operate. The main objective of this paper is to analyse the performance of three State Road Transport Undertakings in Karnataka. The performance is measured in terms of technical efficiency using output oriented DEA approach.

2. BACKGROUND

In the literature review we come across both the quantitative and qualitative techniques to measure the performance of the SRTU's. Qualitative

analysis measures the performance by measuring the customer satisfaction with respect to the service provided. Friman and Fellesson (2008) Conducted a transnational comparison of customer's public transport perceived service satisfaction in six cities of Europe with respect frequency of service, overall satisfaction, availability of seat and travel time.

Benchmarking analysis and Data Envelopment Analysis (DEA) are the commonly used quantitative techniques in performance measurement. Researchers such as Lema and Price, (1995), Alter (1976), Nissam and Penman, (2001), Feng and Wang (2001), Badami and Haider (2007) etc. have used different financial ratios to measure the performance by converting the benefits into monetary values.

DEA is the widely used method for the performance evaluation of public transit system when multiple parameters are involved. Therefore in this paper we are using DEA for the performance evaluation of SRTU's in Karnataka. Some of the commonly used indicators for the performance measurement are given in Table 2.

3. METHODOLOGY

The DEA constant return to scale (CRS) model is initially proposed by Charnes et.al, (1978). DEA evaluates the relative technical efficiency of a group of decision-making units (DMUs: where DMU is defined as one or more individuals involved in making decision who share the same objectives and risks) by simultaneously evaluating multiple inputs and outputs common to each DMU's; thus each DMU is assigned an efficiency score (Charnes et al. 1995). Efficiency of DMU is defined as the ratio of weighted output to the weighted input.

Thus if we consider n homogeneous Units ($j=1,2,\dots,n$), for each of which we use the same inputs (x_1, x_2, \dots, x_m) to obtain the same outputs (y_1, y_2, \dots, y_s), the efficiency of DMU's is calculated by solving the following linear programming problem:

$$(LP_0) \quad \text{max output} = \sum_{r=1}^s u_r y_{rj}$$

subjected to,

$$\sum_{r=1}^s u_r y_{rj} - \sum_{i=1}^m v_i x_{ij} \leq 0 ; j=1,2,\dots,n \quad (1)$$

$$\sum_{i=1}^m v_i x_{io} = 1;$$

$$u_r, v_i \geq 0;$$

To calculate the inefficiency in the inefficient DMU's the following dual variant of the model with the slack and surplus variable in the constraints is typically used and is given by;

$$(DLP_0) \quad \text{Min } h_0 = \theta_o - \sum_{i=1}^m s_i^- + \sum_{r=1}^s s_r^+$$

$$\text{subjected to } s_i^- = \theta_o x_{io} - \sum_{j=1}^n \lambda_j x_{ij}, \quad i=1,\dots,m$$

$$s_r^+ = \sum_{j=1}^n \lambda_j y_{rj} - y_{r0}, \quad r=1,\dots,s \quad (2).$$

$$\lambda_j, s_r^+, s_i^- \geq 0, \quad j=1,\dots,n, \dots$$

In the optimal solution of model (DLP₀)

1. If $h_0 = 1$ and $s_r^+ = s_i^- = 0$, the DMU is called DEA efficient.
2. If $h_0 < 1$ and $s_r^+ \neq 0, s_i^- \neq 0$, the DMU is called DEA inefficient.

Input slack variable (s_i^-) is defined as idle resources still remaining in stock at any point in time during the production process, similarly the output surplus variable (s_r^+) is the excess produced. The names slack and surplus serve merely to indicate the direction of the difference.

4. DATA USED FOR THE STUDY

The study is based on the data, which are collected from the Divisional Statistical Department of KSRTC, NWKRTC and NEKRTC. The collected data are duly edited and classified for the analysis. 28 divisions were analysed in this study from three SRTU's.

The yearly average data of seven years from 2004-05 to 2010-11 was collected for the following parameters.

1. *Fleet Utilization (O):* It measures the extent to which vehicles are used. Computed as the ratio of sum total kilometres operated by all the vehicles on a given day to the total number of vehicles on road that day.
2. *Vehicle Utilization (O):* It is defined as the ratio of total number of vehicles on road to the total number of vehicles held by the company.
3. *Staff per schedule (O):* it is the ratio of the number of staff members assigned to the depot to the number of schedules operated by the depot.
4. *Breakdown rate (O):* Breakdowns per 10000 vehicle Kilometres
5. *Accident rate (O):* Accidents per 100000 vehicle Kilometres.
6. *Staff productivity (O):* It is defined as the ratio of the total number of kilometres operated by all the vehicles assigned to the depot to the total number of staff assigned to the depot.
7. *Fuel Efficiency (O):* In terms of Kilometre per litre of fuel consumption.
8. *Earnings per kilometre (EPKM) (O):* It is defined as the total revenue generated per passenger kilometre.
9. *Profitability (O):* It is the ratio of earnings per kilometer to the cost per kilometer.
10. *Total revenue (O).*
11. *Total Number of vehicles (I).*
12. *Total Number of employees (I).*
13. *Total Fuel consumed (I).*
14. *Total Number of schedules (I).*
15. *Total Effective Kilometers (I).*

5. ANALYSIS AND DISCUSSION

The efficiencies of the KSRTC divisions are given in the Figure 1 which shows Bangalore Central, Tumkur and Mandya divisions are performing at 100 percent efficiency throughout the study period. Mysore Rural division is performing with an average efficiency of 93 percent which is the least among all the divisions. The efficiency values of all the other divisions lie between 94 percent and 99 percent.

Figure 2 shows the efficiency values of divisions of NEKRTC, it is observed that all the divisions are performing with an average efficiency of 100 percent. Similarly the efficiency values of NWKRTC are calculated and given in Figure 3, where all the divisions are performing at an average efficiency of 99 percent except Belgaum which is performing with an average efficiency of 98 percent.

Note: The broken line in the figure represents the in established division at that time.

The efficiency values obtained by DEA are the relative values. But all the SRTU's in Karnataka are operated by Government of Karnataka (GoK) under the same Transport Secretariat, so it is essential to know the relative efficiency among all the SRTU's, in order to get the relative efficiency of the divisions among all the SRTU's. DEA is applied on the data with all the divisions of KSRTC, NEKRTC and NWKRTC as DMU's together and the obtained results are as given in Figure 1.

When each SRTU is analysed separately all the divisions of KSRTC are performing with an average efficiency of more than 93 percent whereas NEKRTC and NWKRTC are performing with nearly 100 percent efficiency. But, the trend in the efficiency values change completely when all the divisions three SRTU's were analysed simultaneously (Figure 1). The efficiency value of the DMU's (divisions) varies between 1.00(maximum) and 0.75 (minimum for Kolar in 2004-05). The observed efficiency values parts into three groups, (1) Divisions of KSRTC which has the average efficiency value of 0.95, and efficiency values varies between 0.75 and 1.00, (2) Divisions of NEKRTC which has the average efficiency value of 0.97, and efficiency varies between 0.80 and 1.00, (3) Divisions of NWKRTC which has the average efficiency value of 0.84 and efficiency varies between 0.88 and 1.00

Bangalore central, Yadgiri and Koppal division have shown 100 percent efficiency in all the observed years. The other divisions which belong to KSRTC and NEKRTC are showing better efficiency values of more than 85 percent in all the

observed years when compared to the divisions of NWKRTC, which are having lesser efficiency values lying between 0.76 and 0.98.

None of the divisions of NWKRTC is 100 percent efficient. Figure 5 shows the improvement potential for the inefficient divisions for the year 2007-08 is expressed as percentage reduction in input or percentage increase in output from the current levels (calculated using DLP₀). The negative values in the Figure 5 indicates the input surplus which is remaining unused, similarly the positive values shows the output slack associated with each of the DMU's. The amount of slack associated with the inefficient DMU's ranges up to 40 percent similarly the output slack variable ranges up to 60 percent of the original values respectively. As discussed earlier Bangalore Urban (DMU no. 1) in KSRTC is one such DMU which is efficient among all the DMU's in all the years (In 2007-08 Mandya Chikmagalur and Mandya are also efficient). This DMU has no slack and surplus variable associated with it. Similarly Koppal and Yadgiri in NEKRTC does not have slack and surplus variable associated with it (In 2007-08 Raichur is also efficient). (All DMU's from 15 to 21 (which are under NWKRTC) having large amount of input surplus associated with it, these divisions have significant potential improvements in terms staff productivity, breakdown rate, earning per kilometer, staff per schedule, vehicle utilisation, number of vehicle and total number of employees. Similar kind of analysis is conducted for the divisions of KSRTC and NEKRTC for all the years, which showed the potential improvement in profitability, staff productivity, number of schedules, number of vehicle and total number of employees for the inefficient divisions.

6. CONCLUSIONS

Divisions of KSRTC and NEKRTC are operating with a better average efficiency than the divisions of NWKRTC. The main reason is that both the SRTU's are utilizing their allocated resources optimally (KSRTC is performing better in terms revenue

generation, earnings per kilometer, vehicle utilization and staff productivity. Similarly NEKRTC is performing better in fuel efficiency, staff ratio and staff productivity). There is a significant potential to improve the inefficiency in the operations NWKRTC divisions in terms of number of staff per schedule, number of vehicle and total number of employees, vehicle utilisation and earning per kilometer. The SRTU's should aim at optimising the above resources to reach the maximum efficiency from the available resources.

Acknowledgement

The authors thank the managements of the KSRTC, NEKRTC and NWKRTC for their willingness to share the microscopic data of their respective SRTU's with us and their diligence in maintaining such a high quality data set. We also acknowledge the work of Mr. Deepak (DTO, KSRTC) who played important roles in collecting the data and for useful comments. Also thanks to Center for infrastructure, Sustainable Transportation and Urban Planning (CiSTUP) and Human Settlement Management Institute (HSMI) for the financial support through research projects awarded to the first author for carrying out this work.

List of References:

1. Alter C.H. (1976), Evaluation of public transit services: the level-of-service concept. *Transportation Research Record*, issue number 606, pp.37- 40.
2. Charnes, A., W.W. Cooper and E. Rhodes (1978), Measuring the efficiency of decision making units, *European Journal of Operational Research*, Vol 2, pp. 429-444.
3. Charnes, A., W.W. Cooper, A.Y. Lewin, and L.M. Seiford, (1995) "Data Envelopment Analysis: Theory, Methodology and Application", Kluwer Academic Publishers, Massachusetts USA.
4. Cheng-min Feng and Rong-tsu Wang (2001), Considering the financial ratios on the performance evaluation of highway bus industry, *Transport reviews*, Vol. 21, No. 4, pp.449-467.
5. D Nissim and S H Penman. (2001), Ratio analysis and equity valuation: From research to practice. *Review of Accounting Studies*.

6. Friman M and Fellesson M (2009), Service Supply and Customer Satisfaction in Public Transportation: The Quality Paradox. *Journal of Public Transportation*, Vol. 12, No. 4, pp. 57-69
7. M Garcia Sanchez.(2009), Technical and Scale Efficiency in Spanish Urban Transport: Estimating with Data Envelopment Analysis. *Advances in Operations Research*.
8. James Odeck. (2006), Congestion, ownership, region of operation, and scale: Their impact on bus operator performance in Norway. *Socio Economic Planning Sciences*, Vol.40, No.1. pp: 52-69.
9. Lema, N. and A. Price (1995), Benchmarking: performance improvement towards competitive advantage, *Journal of Management in Engineering*, Vol-11, no 1, pp. 28-37.
10. Levaggi, R (1994), Parametric and nonparametric approaches to efficiency: the case of urban transit in Italy, *Study- Economics*, Vol. 49 No. 53, pp. 67-88.
11. Madhav G Badami and Murtaza Haider. (2007), An analysis of public bus transit performance in Indian cities. *Transportation Research Part A: Policy and Practice*, Vol. 41. No.10, pp: 961-981.
12. Matthew G Karlaftis. (2004) A DEA approach for evaluating the efficiency and effectiveness of urban transit systems. *European Journal of Operational Research*, Vol.152, No.2. pp: 354-364.
13. Nolan, J.F (1996), Determinants of productive efficiency in urban transit. *Logistics and Transportation Review*, Vol 32, No.3, pp. 319-342.
14. Pina, V., Torres, T.L (2001), Analysis of the efficiency of local government services delivery. An application to urban public transport. *Transportation. Research. Part .A* Vol 35, No.10, pp. 929-944
15. Ramanathan, R (1999), Using Data Envelopment Analysis for assessing the productivity of the State Transport Undertakings, *Indian Journal of Transport Management*, Vol 23 No.5, pp. 301-12.
16. S. Agrawal, S.P. Yadav, and S.P Singh. (2006) A data envelopment based efficiency assessment of public transit sector of Uttar Pradesh State in India. *Indian Journal of Transport Management*, Vol.30, No.1. pp: 5-30.
17. Sunil Kumar. (2011), State road transport undertakings in India: technical efficiency and its determinants. *Benchmarking: An International Journal*, Vol.18, No.5. pp: 616-643.
18. Viton, P.A. (1998), Changes in multi-mode bus transit efficiency, 1998-1992. *Transportation* Vol-25, pp. 1-21.
19. W.G. Waters and Michael W. Tretheway. (1998) Comparing the total factor productivity and price performance: Concepts and applications to Canadian railways. *Journal of Transport Economics and Policy*, Vol. 33, pp: 209-220.

Table 1: SRTU's of Karnataka at a glance

	KSRTC	NWKRTC	NEKRTC
Depots	73	48	45
Divisions	13	7	8
Bus stations	142	128	120
Vehicles	7864	4711	4206
Effective Kms per day (in Lakhs)	25.79	14.5	9.78
Schedules	7366	4126	3736
Average passengers travelled per day (in lakhs)	25.7	21	10
Number of Staff	36758	21750	18714

Table 2: Some commonly used input and output measures in DEA of urban transit Systems

Input Variables	
Number of employees	[10,13,15,18,12,16,8,17]
Fuel consumption	[10,13,18,15,12,8,17]
Distance travelled	[10,18]
Average speed	[10,13,15,12,16,8,17,7]
Cost per unit distance	[10,18]
Driving hours	[14]
Driving hours	[8]

Output Variables	
Distance travelled	[10,18]
Vehicles kilometer	[13,7,19]
Passenger count	[18,12,7]
Passenger kilometers	[15,8,17]
Fleet size per unit distance per employee	[14]
Accident rate	[14]
Revenue per passenger per unit distance	[16,17]
Revenue per day	[17]

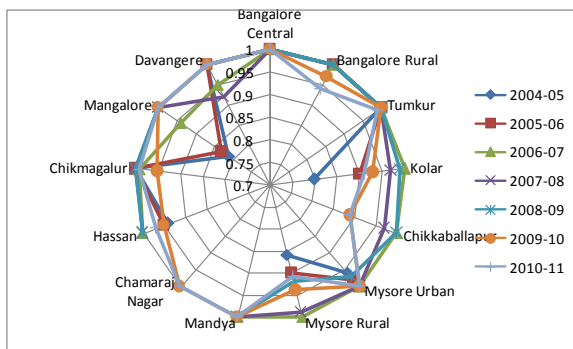


Figure 1: Efficiency values of the Divisions of KSRTC

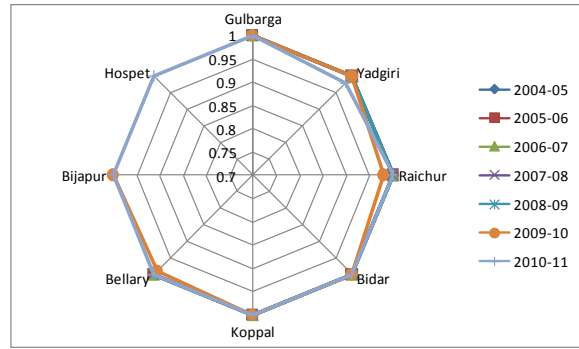


Figure 2: Efficiency values of the Divisions of NEKRTC

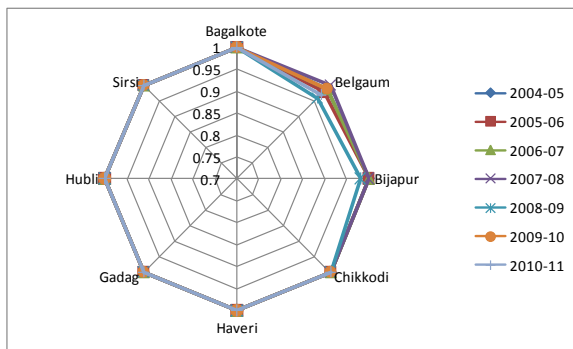


Figure 3: Efficiency values of the Divisions of NWKRTC

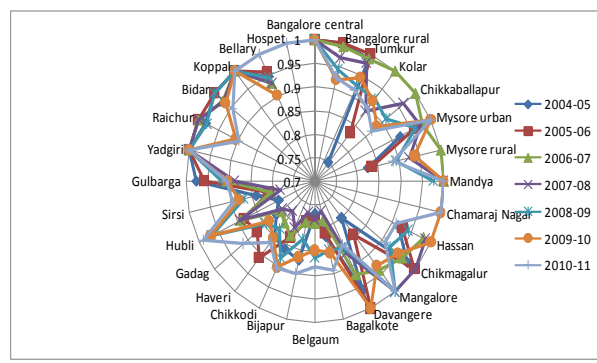


Figure 4: Efficiency score of the 28 divisions of SRTU's in Karnataka

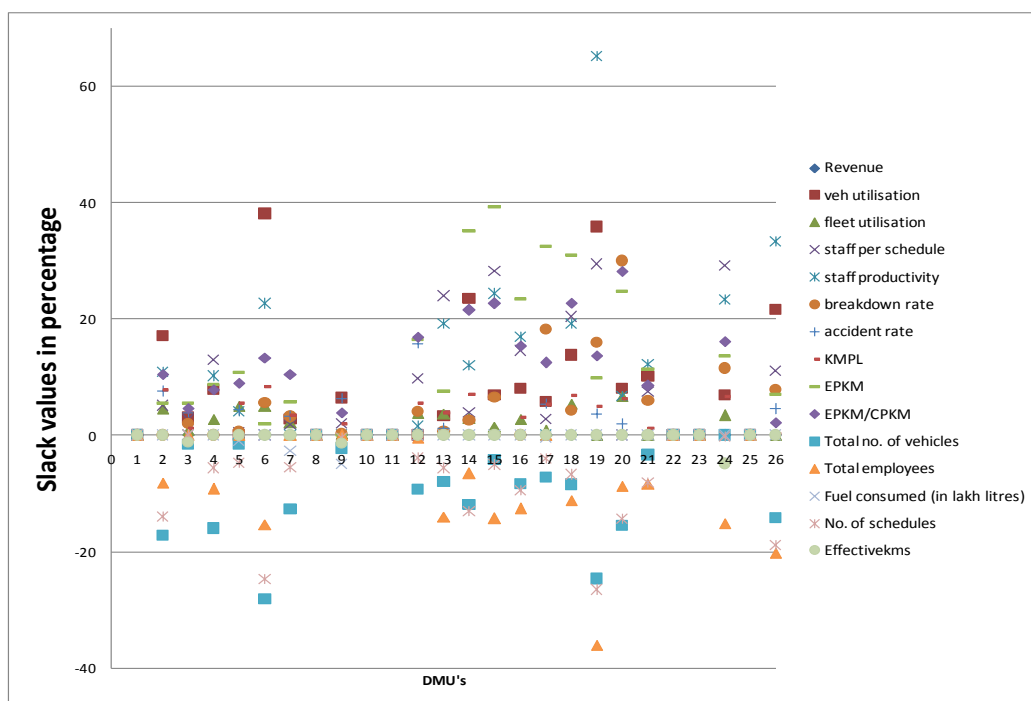


Figure 5: Slack and surplus values for the inefficient DMU's

Effect of Heat Stress on Smelter Workers

Rajeev A¹ and Manjunath G²

- 1 Department of Community Medicine, Pushpagiri Institute of Medical Sciences and Research Centre, Tiruvalla, Kerala 689101, India. e-mail:rajeevtka@gmail.com
2 Sohar Aluminium Company, Sohar 560065, Sultanate of Oman.
email: gtmnath@yahoo.com

ABSTRACT: An experimental investigation on various physiological parameters of workers of an aluminium smelter in the Middle East who are engaged in strenuous routine work at extremely unfavourable environmental conditions was carried out. The results revealed the positive correlation between various rational and empirical indices of heat stress. The physiological parameters showed strain levels which required constant monitoring to prevent episodes of heat illness. A Heat Stress Prevention and Mitigation Guidance Manual has been made based on the findings.

Keywords: Heat stress, TWL, WBGT, PHS, Heart Rate, Core temperature, Urine specific gravity

INTRODUCTION

Industrial processes have undergone tremendous improvement in the last few decades. Production has multiplied by leaps and bounds. In spite of this, developing countries typically are not spending enough money on safety and health concerns in occupations. Operations involving high air temperatures, radiant heat sources, high humidity, direct physical contact with hot objects or strenuous physical activities have a high potential for causing heat stress in employees engaged in primary metal, ceramic, food processing and electrical power as well as unorganised construction industries. Even in the developed world, problems such as heat stress remain one of the most frequent complaints among industrial workers. [Meyer J P, Rapp R, 2004]

The present work was aimed at using sophisticated measuring instruments to assess the physiological strain and correlating the same with the heat stress measurements/indices which are suitable for the local environmental conditions. Present study representing an ongoing collaborative international research in one of the harshest climates has pointed out the need to conduct proper investigations

into the occurrence of potential heat stress events in hot humid conditions prevalent in middle-east region of the world.

METHODS AND MATERIALS

In an aluminium smelter in this backdrop, environmental conditions were measured using Calor TWL equipment. The measurements included the dry bulb air temperature, humidity, globe temperature and air velocity at voluntarily chosen intervals during the last one and a half years.

The following indices were calculated and interpreted accordingly. (a) TWL (Thermal Work Limit) (b) WBGT (Wet Bulb Globe Temperature index) (c) PHS (Predicted Heat Strain index). These indices are based on calculations of thermal balance rooted in physical relationships between the parameters and try to predict the heat storage in human body in a given set of conditions. Each index is unique in its own way and tries to measure the input accordingly. They do correlate to some extent with each other. However, the work limits for each of these vary from each other and adds to confusion among occupational physicians.

TWL

4th International Engineering Symposium - IES 2015

March 4-6, 2015, Kumamoto University, Japan

This is defined as the limiting (or maximum) sustainable metabolic rate (M) that well-hydrated, acclimatized individuals can maintain in a specific thermal environment, within a safe deep body core temperature ($< 38.2^{\circ}\text{C}$) and sweat rate ($< 1.2 \text{ kg}$). [Brake (2002)]

$$M - W = C + R + E + B + S_{sk} + S_c$$

where W is rate of mechanical work, C is rate of heat loss from skin due to convection, R is radiation, E is evaporation, B is heat loss from respiration, S_{sk} is heat storage in skin, and S_c is heat storage in deep core.

The algorithm works out the optimal sweating rate (E_{sk}) for allowable maximum sustainable work output for a given set of conditions where the heat transfer from core to skin (H) equals heat flow from skin to environment (E_{sk}). Metabolic heat production (M) equals heat flow from core to skin (H) + heat flow via respiration (B).

$$H = E_{sk}; \quad M = H + B$$

The thermal work limit for a person in this environment is then given by $\text{TWL}=M$. The advantage of this index is in directing the work manager to restrict the workloads above the calculated for a given set of environmental variables.

WBGT index

The easiest and widely used WBGT index is given below. [Bernard and Cross (1997)].

$$\text{WBGT} = 0.7T_w + 0.2T_g + 0.1T_d$$

where T_w is the natural wet bulb temperature, T_g is the globe temperature and T_d dry bulb temperature.

The advantage of this measurement is to judge the work-rest cycles for a given environment.

PHS

From the base measurements of environmental conditions it is able to calculate the ideal working conditions of the human beings. ISO 7933 as laid down by Malchaire *et al.* derives these based on

the general formula given below. [Malchaire, 2006]

$$M - W = C_{res} + E_{res} + K + C + R + E + S$$

This equation gives the difference between the metabolic rate actually carried out by the person (M) and the effective mechanical power (W) which is equal to the heat produced by the human body in getting the work done. This excess energy is dissipated by the heat sink mechanism of the body such as respiration (Convective (C_{res}) & Evaporative (E_{res}))), direct skin cooling by conduction/convection/radiation (K,C,R), sweating and evaporation (E); the remaining being stored in the body (S) which results in the increase in the core temperature. The required evaporative heat flow is then calculated as,

$$E_{req} = M - W - (C_{res} + E_{res} + C + R + dSeq)$$

where, $dSeq$ is the body heat storage rate for increase of core temperature.

Since body can only function in a range of healthy internal temperature, this overheating can have adverse effects. The required sweat rate can be estimated from standard equations for heat equilibrium. However, there is a maximum limit to which body can sweat and can overcome heating due to excessive work or heat stress. The maximum sweat rate Sw_{max} can be estimated as,

$$Sw_{max} = (M - 32).Adu$$

where Adu is the body surface area.

If the average rectal temperature predicted reaches 38°C then there is a chance of one person in 10000 shifts touching 39.2°C and causing undesirable outcomes. Excel spreadsheet solution by Malchaire *et al.* was used to calculate the time for the rectal temperature to reach 38°C or the dehydration levels to reach 7.5% of body weight for an average subject.

These set of environmental measures essentially were determined in ideal conditions and under sustained work levels in experimental situations. Many a time

4th International Engineering Symposium - IES 2015

March 4-6, Kumamoto University, Japan

these indices do not consider the various individual parameters of the workers though the PHS algorithm allows us to factor in the personal characteristics into consideration.

However, the aluminium industry in the study setting is peculiar in that the work cannot be stopped at any point in time for fear of freezing out of the plant which would shut down the entire operation. Secondly the industry itself is hydrophobic so much so any intervention; human or engineering; involving water has to be carried out outside the perimeter of actual working environment. This requires a lot of employee motivation and managerial commitment to pull off.

In addition, all the above indices are not suitable for thermal conditions beyond which these have been tested in experimental settings. Environmental conditions in Oman and other Arabian Gulf countries are some of the harshest in the world. Primary Aluminum smelting is an energy intensive industry requiring enormous amounts of energy. Workers engaged in physically strenuous manual tasks in hot environments can be easily fatigued and be at risk of heat stress induced illnesses.

In this setting, we were forced to monitor the physiological parameters of the working individuals because the indices were only guides which could be applied in moderate thermal conditions. Standards have not been applied to middle-east countries where the temperatures cross to extremely high values coupled with the high temperature work conditions of smelters.

On the given day of measurements, one or two workers in a shift would be selected purely on volunteer basis from one of the following operational areas. 1) Cast House (due to high temperatures from metal melting and casting furnaces), 2) Carbon plant (due to radiation from anode baking furnaces) and 3) Reduction (due to temperature in the pot cells: about 950 °C). Consent was taken from the employees for the physiological

measurements. They would be given basic awareness regarding the procedures in particular and heat stress prevention in general.

Heat strain was measured using a heart-rate (HR) monitoring chest strap to record heart rate continuously, which was a surrogate for physical strain resulting from activity and heat. Heart rate data were transmitted to a remote recorder (Polar watch®) worn by worker (Fig. 1). Hydration status was assessed from urine specific gravity measured at the start and end of the shift, and mid shift. Tympanic temperatures and blood pressure were also measured at these times. In addition the workers swallowed the HQNC electronic pills which can measure the intestinal temperatures for a continuous period and the data retrieved by a remote unit and plotted in conjunction with the polar heart rate recorder.

The points of interest were the average heart rate (HR) and the peak core temperature (T_{re}) measured by the pill during the period/tasks which would indicate the amount of excess work being delivered by the worker in spite of the excessively stressful conditions. The work output and work rest cycles etc. were correlated with the predictions derived from TWL /WBGT/ PHS.

RESULTS

The table 1 shows the harsh conditions as per TWL in which works got done and the corresponding anthropometric values of workers in those settings. There was almost an intuitive re-distribution of fitter individuals to the withdrawal zones and there is strict monitoring and regulation of work in those areas.

The existing conditions of work were quite strenuous. A substantial number of environmental measurements went into the harshest category of withdrawal zone as per TWL as well as the individual parameters as shown in table 2.

Table 3 shows the correlations derived between the three best environmental indices of heat stress and we could see

4th International Engineering Symposium - IES 2015

March 4-6, 2015, Kumamoto University, Japan

fairly good correlations between all of them. The TWL were proportionately lower as the WBGT and PHS increase.

Table 4 shows the work-rest cycles to be followed in the various categories of heat stress zones as per the American WBGT standards. The disparate regions are amplified by the Fig. 4 as well.

Physiological monitoring

The American index, WBGT, appreciably is the toughest standard to maintain in terms of guidelines as shown in tables 5 and 6. [Rowlinson S, Jia Y A, 2013]

Since a management call was difficult in terms of regulating work based on any single index, the physiological monitoring was deemed inevitable because of the nature of the work and continuity of the process of smelting. The physiological parameters were monitored as per suggestions of international bodies which recommended such procedures when the WBGT crossed tolerable limits.

The mean heart rates were kept below 110 beats per minute (BPM) in most places. The kilocalories consumed in various tasks were estimated by integrating the minute to minute heart rate by the Polar® software. The Watt-hour equivalents were calculated to observe the metabolic rate of each worker.

The urine specific gravity was seen to improve through the work shift (table 7). The core temperature monitoring using the HQNC electronic pills directly measured the heat strain in high risk areas and the highest core temperature measured averaged less than the permissible maximum of 38°C as shown in table 8. The employee awareness had resulted in intelligent self-pacing which regulated the core temperature effectively. (Fig.3)

DISCUSSION

A robust and aggressive program to prevent and mitigate heat stress at Sohar Aluminium had made a major and significant difference to the employees and contractors and helped in reducing the incidence of heat illnesses. (Table 9)

Results of monitoring were analyzed daily, weekly and monthly and were shared with relevant management staff. Medical Team analyzed the environmental parameters under guidance of the authors and created 'Heat Stress Risk Map' for the whole organization as well as major work areas and this had helped each area manager to plan work activities prudently during summer months. (Fig. 4)

CONCLUSIONS

Present study demonstrated that the climate and working temperatures of an aluminum smelter could have effects on the productivity of the employees.

Effect of heat stress on the physiological parameters of body were correlated with the best environmental indices available such as WBGT, TWL and PHS so much so the standards could be laid down for fixing the work conditions.

Medical Team developed a comprehensive Heat Stress Prevention and Mitigation Guidance Manual that has been incorporated as a system manual for the said company.

ACKNOWLEDGEMENTS

We thank the management, the medical staff and the workers of the aluminium smelter who co-operated with us in every way possible. We also thank our referees who helped us with resources given below.

REFERENCES

- [1] Brake, D J (2002), The Deep Body Core Temperatures, Physical Fatigue, Fluid Status of Thermally Stressed Workers and the Development of Thermal Work Limit as an Index of Heat Stress, School of Public Health, Curtin University of Technology.
- [2] Bernard, T E and Cross RC (1997), Case Study Heat stress management: Case study in an aluminum smelter, International Journal of Industrial Ergonomics. Vol. 23, pp. 609-620.
- [3] Malchaire, J B M (2006), Occupational Heat Stress Assessment by the Predicted Heat Strain Model, Industrial Health, Vol. 44, pp. 380-387.
- [4] Meyer, J P and Rapp, R (2004), Survey of heat stress in industry, Ergonomics, Vol. 38, No. 1, pp. 36 - 46.
- [5] Rowlinson, S and Jia, Y A (2013), Application of the Predicted Heat Strain Model in Development of Localized, Threshold-based Heat Stress Management Guidelines for the Construction Industry. Ann. Occup. Hyg., Vol. 58, No. 3, pp. 326-339.

4th International Engineering Symposium - IES 2015

March 4-6, 2015, Kumamoto University, Japan

Table 1: Demographics of subjects

Area/Zone as per TWL limits	Age (Yrs)	Weight (Kg)	BMI (Kg/m ²)
Unrestricted (4)	30	56.6	22.1
Acclimatization (13)	32.1	66.2	23.6
Buffer (8)	28.6	68.7	24.7
Withdrawal (23)	27.9	63.5	23.8

Table 6: Work suggested in existing conditions as per observed WBGT

Area/Zone as per TWL limits (N)	WBGT Work	WBGT Rest
Unrestricted (4)	40 to 58	2 to 20
Acclimatization (13)	35 to 60	0 to 25
Buffer (8)	32 to 59	1 to 28
Withdrawal (23)	28 to 42	18 to 32

Table 2: Environmental conditions

Area/Zone as per TWL limits	DB °C	RH %	Urine Specific Gravity
Unrestricted (4)	31.5	71.7	1017
Acclimatization (13)	31.6	70.9	1024
Buffer (8)	35.6	60.4	1014
Withdrawal (23)	31.5	81.5	1017

Table 3: Pearson Correlations

	PHS	TWL
WBGT	.790**	-.871**
PHS		-.646**

**. Correlation is significant at the 0.01 level (2-tailed)

Table 4: Suggested Work-Rest Cycles in minutes

WBGT °C	Easy	Moderate	Heavy	% Work done		
					Unrestricted	Acclimatization
26.7-	NL	50/10	30/30	75 to 100		
29.3						
29.4-	NL	40/20	30/30	50-75		
31.0						
31.1-	NL	30/30	20/40	25-50		
32.1						
=> 32.2	50/10	20/40	10/50	0-25		

Table 5: WBGT versus TWL

Area/Zone as per TWL limits (N)	WBGT °C	WBGT Range
Unrestricted (4)	28.95	27.7 to 29.7
Acclimatization (13)	29.41	24.7 to 32.6
Buffer (8)	32.78	31.1 to 33.7
Withdrawal (23)	34.86	32.1 to 38.8

Table 7: Physiological monitoring

Area/Zone as per TWL limits (N)	Mean HR (BPM)	Max HR (BPM)	Urine Specific Gravity
Unrestricted (4)	95.7	190	1019
Acclimatization (13)	85.9	187.8	1012
Buffer (8)	95.5	191.4	1029
Withdrawal (23)	91.1	192	1014

Table 8: Core temperature as per corresponding work levels.

Area/Zone as per TWL limits	Calories utilized per minute	Core temperature Max °C	Time to Max Core Temperature
Unrestricted (4)	4.99	37.7	2:36:15
Acclimatization (13)	3.82	37.7	2:30:00
Buffer (8)	4.91	37.5	2:23:20
Withdrawal (23)	4.35	37.8	2:58:05

Table 9: PHS limits to endpoints as per observed climatic conditions

Area/Zone as per TWL limits (N)	Time to 7% Dehydr	Time to 38 °C Core
Unrestricted (4)	220 to 400	25* to NL
Acclimatization (13)	190 to 410	24 to 345
Buffer (8)	190 to 390	46 to 392
Withdrawal (23)	150 to 280	13 to 56

* Heavy work; NL – no limit



Fig.1 Heart Rate (HR) Monitor

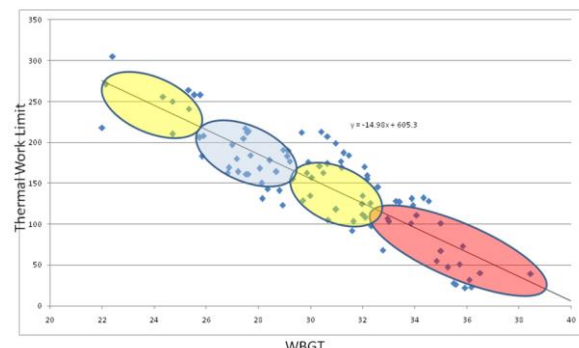


Fig.2 Correlation of WBGT with TWL

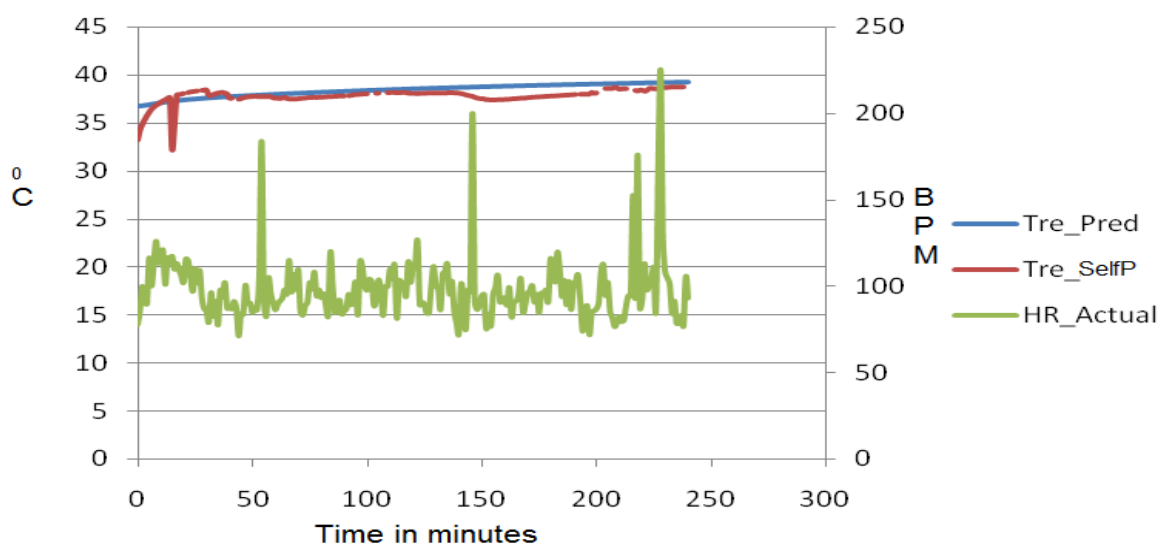


Fig.3 Self Pacing Controls Rectal Temperature (Tre)

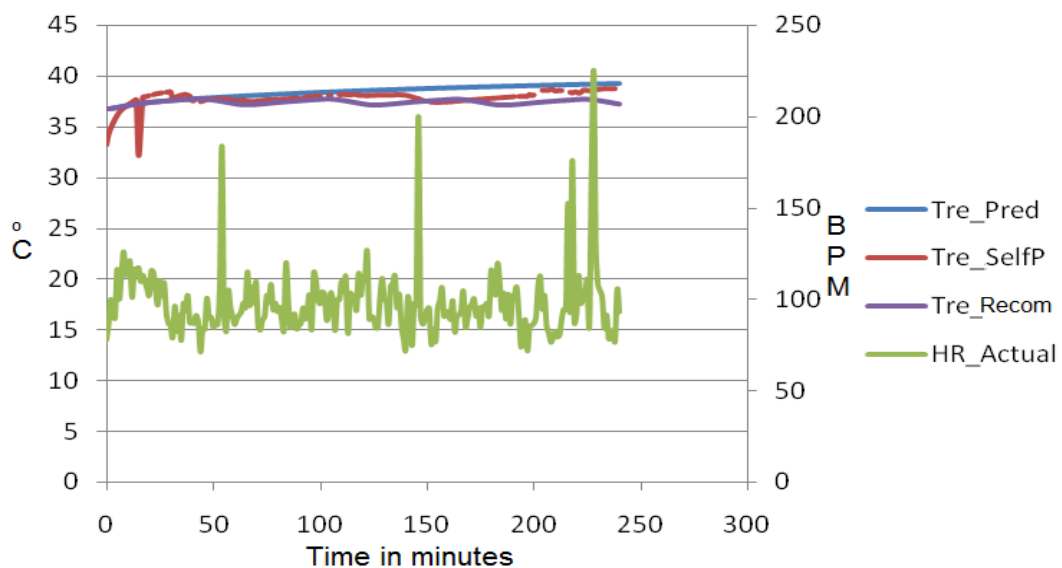


Fig.4 Effect of Work Rest Cycles on Rectal Temperature (Tre)

Soil-structure interaction effects on multi-storey buildings considering site specific ground response

Chinmayi H.K. and Jayalekshmi B.R.

Department of Civil Engineering, National Institute of Technology Karnataka, Surathkal, Mangalore 575025, India. email:chinmayi.moorthy@gmail.com

ABSTRACT: Ground motion during earthquake is affected not only by its source characteristic but also by its source-to-site path properties and local site conditions. Local soil conditions have major influence on amplitude and response spectral characteristics which results in variations of surface ground motions at different places. Present study determines the amplification of earthquake motion at the ground surface based on borehole data of the site using one dimensional equivalent linear ground response analysis. Finite element soil-structure interaction analysis of multi-storey buildings at this site is also performed to determine the effect of supporting soil in varying the base shear. For this, ground motion with the highest peak ground acceleration generated from the ground response analysis is used. Study shows significant amplification in surface motion due to geotechnical characteristic of site as compared to rock level motion. The base shear obtained from SSI analysis is considerably low when compared with conventional analysis.

Keywords: *soil-structure interaction, ground response analysis, base shear, natural period, amplification ratio, roof deflection.*

INTRODUCTION

During earthquakes, ground responses are fundamentally influenced by the local soil conditions. The topography and nature of depositional soils are the principal components that influence local modifications to the underlying motion. Estimation of site-specific dynamic response of a layered soil deposit is referred to as a site-specific response analysis. The time histories generated from ground response analysis can be employed right away to represent the ground surface motions.

Studies on ground response analysis for seismic design in Fraser river delta, British Columbia was carried out by [1] to determine the significant amplification in the earthquake motions for four sites for periods longer than 0.2 second. Similar site amplification study and seismic hazard analysis for Coimbatore region was carried out by [2]. Site specific ground motion simulation and seismic response analysis

for microzonation of Kolkata to generate site specific ground motion and local site effects for Kolkata Metropolitan District area was carried out by [3]. The analysis was carried out using synthetic ground motion for determination of rock level time history followed by ground response using SHAKE2000. [4] carried out a case study on ground response analysis of a site in Ahmedabad city during the Bhuj earthquake showing varying degree of damage in multi-storey buildings in close proximity of Sabarmati river area in Ahmedabad due to amplification of ground motion. Study also stated the engineering importance of site-specific ground response analysis, difficulties faced in conducting a complete ground response analysis and steps to be followed in conducting a meaningful site amplification study.

Buildings are usually analysed assuming the base to be fixed. However in reality, supporting soil influence plays a major role on response of structure. Natural ability of

4th International Engineering Symposium - IES 2015

March 4-6, 2015, Kumamoto University, Japan

soil to deform permits the movement of substructure to some extent affecting the response of structure. Lessons learned from past earthquakes show the significance of regarding soil-structure interaction in seismic analysis of structures. When earthquake acts on a structural system, structural displacement and soil displacement are dependent on each other. This dependency in response between the soil and structure is termed as soil-structure interaction (SSI).

In seismic design of buildings, effects of soil flexibility are generally ignored. Studies carried by [5] and [6] have expressed the potential severities of overlooking the effects of the SSI. Flexibility of soil causes lengthening of lateral natural periods due to overall decrease in lateral stiffness leading in considerable variation of seismic responses which was reported by [7] and [8]. Similar studies on low-rise buildings expressing the implication of lengthening of natural period in seismic behavior of structure bearing fundamental lateral period in short period region of the design response spectrum was carried out by [9]. A seismic soil-structure interaction study on massive concrete structures supported over raft foundation using ANSYS and LS DYNA software to determine the stress resultants in raft and normal and shear stresses developed at interface between the foundation rock and the raft was carried out by [10].

In present study, an attempt has been made to generate site specific ground motion using ground response analysis. Ground response analysis has been done using SHAKE2000 for determination of ground level time history. 20 nos. of bore holes of depth varying between 7- 15m below ground level were considered. Due to unavailability of recorded strong ground motion data in study area, Elcentro earthquake motion was used by scaling down to maximum acceleration of 0.1g. Further, the synthetic ground motion generated from ground response analysis using SHAKE programme having the highest peak ground acceleration (PGA) was used in soil-structure interaction analysis of multi storey building. Finite

element method was utilized in evaluating the seismic responses of structure.

GROUND RESPONSE ANALYSIS:

Ground response analysis was carried out for the geological study area covering the latitude 12°87'N and longitude 74°88'E. Study area is located in Mangalore city at NITK campus. The location of the site is as shown in Fig. 1.

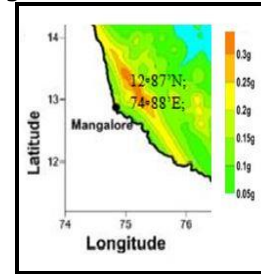


Fig.1: Spatial variation of mean PHA (g) values at bedrock of Mangalore city

Borehole data of study area was used in ground response analysis. Typical borehole log of the site showing the peak ground acceleration is as shown in Fig.2. SHAKE2000, ground response analysis program was used for the one dimensional equivalent linear ground response analysis utilizing subsurface profile information such as SPT value, ground water level, unit weight etc. as the input.

Depth(m)	Soil strata	SPT	Soil description
2.0		12	
4.5		24	Sandy silt
6.0	Rebound		Weathered rock
7.0	Rebound		Rock

Borehole18

Fig. 2: Typical soil profile

The essential input demands for the program are acceleration time history at bedrock, shear wave velocity, shear modulus reduction curve and damping curves of soil layers. Shear wave velocity (V_s) in the study was estimated using SPT (N) values obtained from geotechnical investigation by adopting the empirical equation stated by [11].

$$V_s = 61N^{0.5} \quad (1)$$

Where,

V_s is the shear wave velocity

4th International Engineering Symposium - IES 2015

March 4-6, 2015, Kumamoto University, Japan

N is the standard penetration test value of soil.

Shear modulus reduction curve and damping curve of the soil layer was assumed as the upper bound curve of [12]. Due to unavailability of strong motion data in study area, Elcentro earthquake motion was chosen as input motion at bed rock. Input motion was scaled down to maximum acceleration of 0.1g based on the study of seismicity and seismic hazard for Karnataka State by [13]. The acceleration time history of input motion is shown in Fig. 3.

Acceleration time history and peak acceleration value at the ground level of borehole 18 shows the highest acceleration in the one dimensional equivalent linear ground response analysis and is shown in Fig. 4.

From Fig. 4 it is observed that maximum acceleration at borehole 18 is greater than the maximum acceleration of input motion showing an amplification in the wave due to soil layer hence bringing out the influence of local site condition. The maximum acceleration of 0.184g is observed at borehole location 18.

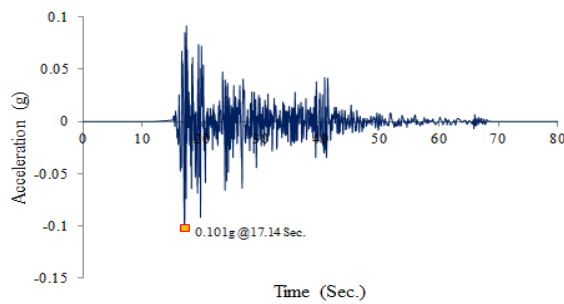


Fig. 3. Typical input acceleration time history used in SHAKE2000

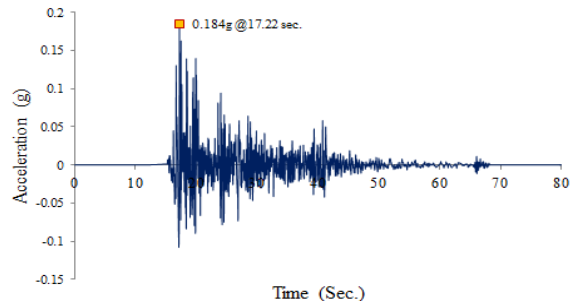


Fig.4. Acceleration time history plots of Borehole 18

Response spectra of ground acceleration time history for input motion at bed rock level and output motion at surface of various representative borehole locations

5, 10, 12, 18 and 19 obtained for 5% damping and represented as BH5, BH10, BH12, BH18 and BH19 are shown in Fig. 5. Acceleration response spectra of input motion are represented by dashed line. From Fig 5, it is observed that the first peak in spectral acceleration of input ground motion corresponds to 0.55 sec. However, with the influence of local site condition the first peak in spectral acceleration of output motion at surface corresponds to 0.14sec, 0.26sec, 0.55sec, 0.10sec and 0.08sec respectively at borehole location 5, 10, 12, 18 and 19.

Ground motions are generally amplified as waves travel through the soil column depending on the soil type, soil thickness and soil stiffness. The variation in maximum accelerations with depth is as shown in Fig 6. From figure 6, it is noted that there is considerable modification in acceleration values from 0.101g to 0.158g, 0.154g, 0.150g, 0.184g and 0.159g respectively at borehole locations 5, 10, 12, 18 and 19.

Amplification between surface motion and the base motion at varying frequency are as shown in Fig. 7. Amplification ratios of 9.0, 8.3, 7.6, 10.6 and 9.1 is observed at frequencies 8.2 Hz, 3.8 Hz, 1.6 Hz, 9.4 Hz and 10.9Hz respectively at borehole location 5, 10, 12, 18 and 19. Maximum amplification is observed in borehole location 18 as the average shear velocity of top layers of soil is very less compared to other borehole locations. Soft soil amplifies low-frequency (long period) motion.

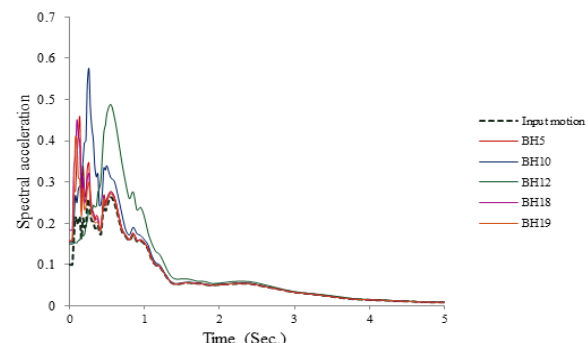


Fig.5: Response spectra of the ground acceleration time history

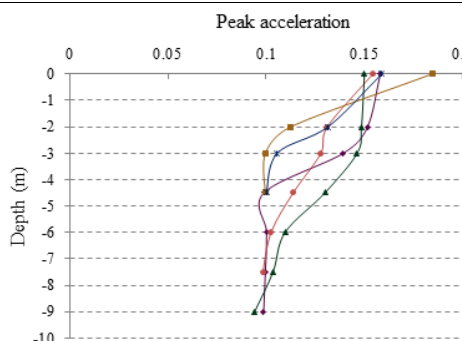


Fig.6: PGA variation with depth

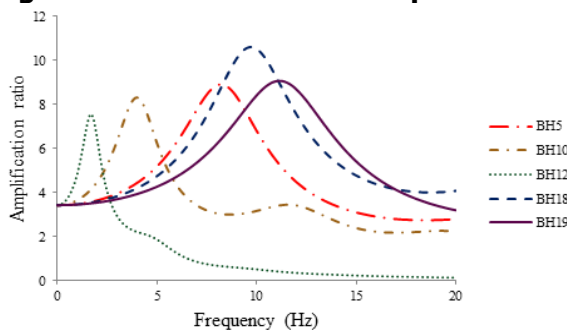


Fig.7: Amplification ratio between surface and base motion

SOIL-STRUCTURE INTERACTION

Analyses of structures are normally carried out by assuming the base of the structure to be fixed. During earthquakes, structural displacements and ground displacements are independent of each other. Response of soil influencing the motion of the structure and vice versa is termed as soil-structure interaction. Analysis of superstructure and substructure by neglecting the flexibility of soil leads in deceptive estimation of structural response. It is, hence essential to carry out the analysis considering soil, substructure and superstructure, as a single compatible unit.

Present study, considers ordinary moment resisting frames of 4, 8, 12, and 16 storeys by neglecting the effect of infill. Building frames are of 3 bays equal length in each direction. The storey height and length of each bay are chosen as 3m and 4 m respectively. The dimensions of building components were arrived on the basis of structural design adopting the respective Indian standard codes for design of reinforced concrete structures IS 456:2000[14]. Dimensions of building components are as shown in Table 1.

Table 1: Dimensions of components of building.

Storey	Columns (m)	
	Up to 3 storey	Above 3 storey
4	0.32 X 0.32	0.32 X 0.32
8	0.40 X 0.40	0.35 X 0.35
12	0.50 X 0.50	0.40 X 0.40
16	0.60 X 0.60	0.50 X 0.50
Raft slab:	0.3m	
Roof and floor slab:	0.15m	
Beams :	0.23X0.23m	

FINITE ELEMENT ANALYSIS

The commercially available finite element software LS DYNA is used in the finite element modeling and analyses.

(a) Structural Idealization

Belytschko-Schwer resultant beam element having three translational and three rotational degrees of freedom at each node are used in idealization of building frames. The roof slab, floor slabs and foundation slab are modelled using four-node shell element Belytschko-Tsay having bending and membrane capabilities. Belytschko-Tsay shell element possesses six degrees of freedom at each node.

(b) Soil Idealization

3D soil stratum is modelled with eight-node fully integrated S/R solid having three translational degrees of freedom at each node. The node compatibility problem occurring between soil and structure due to varying degrees of freedom occurring between shell and solid element is overcome by a tied surface to surface contact. The width of the soil medium is taken as 1.5 times the least width of the raft foundation. The influence on the settlement beyond it is considered to be negligible as per the studies of [15] and [16]. The boundary elements at the bottom were restricted from translations. While, the lateral vertical soil boundaries were modelled with non-reflecting boundaries. Finite element model of idealized soil-structure system of typical 16 storey building on raft foundation is shown in Fig. 8.

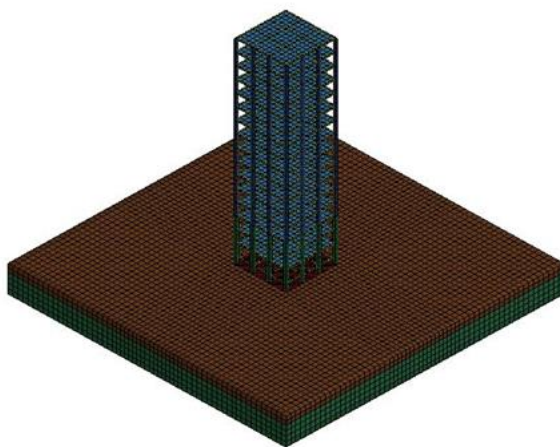


Fig. 8 Idealized soil-foundation-structure model of 16-storey building.

In the present study, Eigen value analysis is carried out to determine the fundamental natural period 'T' of 3D finite element model of soil-foundation-structure. Further, the time history analysis was carried out on the model using acceleration time history having maximum PGA of 0.184g to determine the seismic response such as base shear and roof deflection in buildings.

Lateral natural period

Fundamental natural period plays an important role in the seismic response of structure. The value of natural period obtained from the free vibration analysis of 3D finite element models with and without incorporation of the soil flexibility is as shown in Fig.9. From figure 9 it is apparent that value of natural period obtained from model with incorporation of soil stiffness are higher than conventional fixed base condition. Natural period increases with increase in number of stories

Seismic base shear

Maximum anticipated lateral force probable to occur at the base of a structure due to seismic ground motion is referred to as base shear. It reflects the seismic lateral vulnerability of the structure and is considered as one of the principal inputs in seismic design of structures. The seismic base shear of building with and without incorporating soil flexibility is as shown in Fig.10. The values of base shear obtained from conventional fixed base condition are higher than the values obtained by considering soil flexibility making the seismic design more

conservative and uneconomical. Representative time history plot of base shear is shown in Fig.11. The absolute maximum base shear of building is obtained at different times for building with and without incorporating soil flexibility.

Roof deflection

Roof deflection of buildings with and without incorporation of soil flexibility is as shown in Fig.12. Divergence of the tip of the building with reference to the base of the structure is referred to as roof deflection. From figure 12, it is observed that values of roof deflection in buildings incorporating the effect of soil are higher than the fixed base condition.

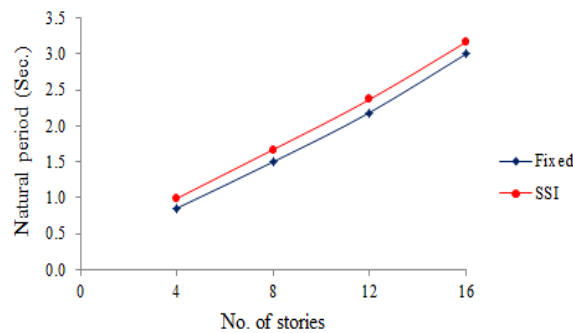


Fig. 9: Lateral natural period of buildings.

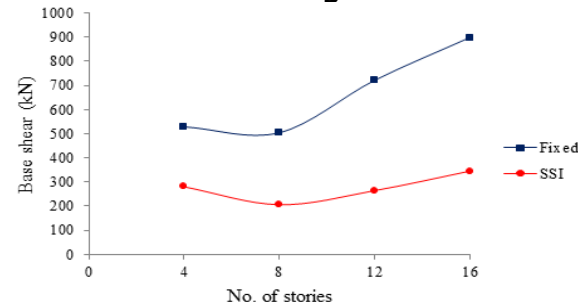


Fig. 10: Base shear of buildings.

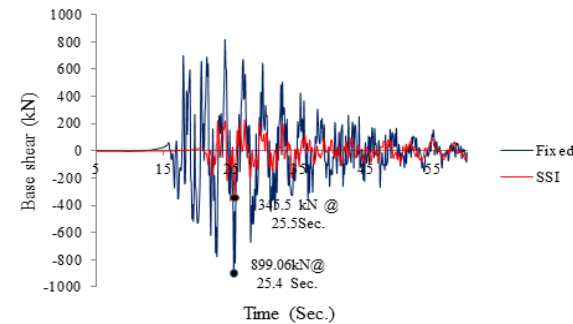


Fig. 11: Time history of base shear in 16 storey building.

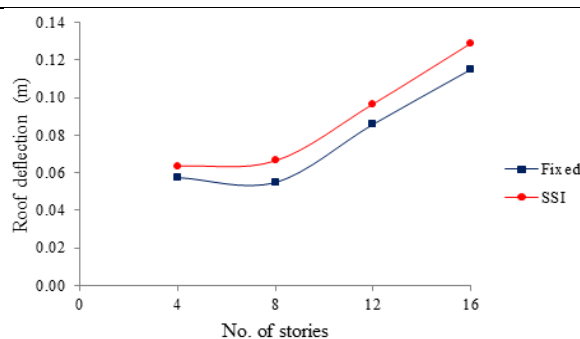


Fig. 12: Roof deflection of buildings.

CONCLUSIONS

Present study carry out a ground response analysis to determine the local soil effect followed by soil-structure interaction analysis of multi-storey reinforced concrete buildings to determine the seismic response of building with consideration of effect of soil flexibility. Following major conclusions were drawn from the study.

- Soil layers significantly amplify the input motion. Peak ground acceleration was amplified by 50 to 84% at the specific site.
- Amplification ratio between surface motion and the base motion were observed to be of 9.0, 8.3, 7.6, 10.6 and 9.1 at frequencies 8.2 Hz, 3.8 Hz, 1.6 Hz, 9.4 Hz and 10.9Hz. Maximum amplification is observed at locations where the top layer consists of soil with very low shear wave velocity.
- Soft soil amplifies low-frequency motion.
- Incorporation of soil flexibility increases the roof deflection and decreases the value of base shear.

REFERENCES

- [1] Uthayakumar, U.M. and Naesgaard, E. (2004), "Ground response analysis for seismic design in Fraser river delta, British Columbia", 13th World Conference on Earthquake Engineering Vancouver, B.C., Canada. Paper No. 2104.
- [2] Chandrasekaran, S.S., Bharadwaja, G. S., Bharathi, P. and Dutt, H. H. (2012), "Seismic Ground Response Analysis for a Site in Coimbatore", ISET Golden Jubilee Symposium, IIT Roorkee, Roorkee. Paper No. A005.
- [3] Roy, N. and Sahu, R.B. (2012), "Site specific ground motion simulation and seismic response analysis for microzonation of Kolkata", Geomechanics and Engineering, Vol. 4(1), pp 1-18.
- [4] Raju, L. G., Ramana, G. V., Rao, C. H. and Sitharam, T. G. (2004), "Site specific ground response analysis", Current science, Vol. 87(10), pp 1354-1362.
- [5] Mylonakis, G., Nikolaou, A. and Gazetas, G. (1997), "Soil-pile-bridge seismic interaction: kinematic and inertial effects. Part I: soft soil", Earthquake Engineering and Structural Dynamics, Vol. 26, pp 337-359.
- [6] Roy, R. and Dutta, S.C. (2001), "Differential settlement among isolated footings of building frames: the problem, its estimation and possible measures", International Journal of Applied Mechanics and Engineering, Vol. 6, pp 165-186.
- [7] Bielak, J. (1975), "Dynamic behaviour of structures with embedded foundations", International Journal of Earthquake Engineering and Structural Dynamics, Vol. 3, pp 259-274.
- [8] Stewart, J.P., Fenves, G.L. and Seed, R.B. (1999), "Seismic soil-structure interaction in buildings I: analytical method", Journal of Geotechnical and Geoenvironmental Engineering, ASCE, Vol.125, pp 26-37.
- [9] Bhattacharya, K. and Dutta, S.C. (2004), "Assessing lateral period of building frames incorporating soil-flexibility", Journal of Sound and Vibration, Vol. 269, pp 795-821.
- [10] Rajasankar, J., Iyer, N. and Swamy, B. (2007), "SSI analysis of a massive concrete structure based on a novel convolution/deconvolution technique", Sadhana, Vol. 32(3), pp 215-234.
- [11] Seed H.B., Idriss I.M. (1981), "Evaluation of liquefaction potential sand deposits based on observation of performance in previous earthquakes. ASCE National Convention, Missouri, pp 81-544.
- [12] Seed, H.B., Wong, R.T., Idriss, I.M. and Tokimatsu, K. (1986), "Soil moduli and damping factors for dynamic analyses of cohesionless soils", Journal of Geotechnical Engineering, Vol. 112(11), pp 1016- 1032.
- [13] Sitharam, T. G., James, N., Vipin, K. S. and Raj, K. G. (2011), "A study on seismicity and seismic hazard for Karnataka State", J. Earth Syst. Sci., Vol. 121(2), pp. 475-490.
- [14] IS: 456-2000 Indian standard code of practice for plain and reinforced concrete. Bureau of Indian Standards, New Delhi, India.
- [15] Maharaj, D.K., Amruthavalli, A. and Nishamathi, K. (2004), "Finite Element Analysis for Frame Foundation Soil Interaction", Electronic Journal of Geotechnical Engineering.ege.
- [16] Thangaraj, D. and Ilamparuthi, K. (2010), "Parametric Study on the Performance of Raft Foundation with Interaction of Frame", Electronic Journal of Geotechnical Engineering, 15, 861-878.

Transient analysis of multi storey shear wall buildings in soft soil

Jayalekshmi B.R. and Chinmayi H.K.

Department of Civil Engineering, National Institute of Technology Karnataka, Surathkal, Mangalore 575025, India. email:br.jaya@gmail.com

ABSTRACT: Generally conventional design practice neglects the effect of supporting soil in the analysis of structures considering it to be beneficial. However, from studies it is evident that effect of soil is not always beneficial. Present study focuses on soil-structure interaction analysis of multi storey concrete shear wall buildings resting on soft soil. Shear walls of various geometric shapes are considered to determine the effects of shapes in varying the seismic response of structure and the advantages of various shapes over regular rectangular shape shear wall in attracting the least earthquake forces. It is observed that the base shear obtained by conventional fixed base analysis is very conservative. L shape shear wall attracts the least earthquake forces in buildings while considering soil-structure interaction.

Keywords: Soil-structure interaction, Shear wall, Transient analysis, Base shear, Roof deflection, Perfectly matched layer.

INTRODUCTION

In seismic design of structures it is essential to design the structure considering the various detrimental effects of earthquake. One of the chief concerns in this respect is the effect of interaction between the structure and soil underneath. Effects of soil-structure interaction (SSI) are usually neglected considering the stiffness of the soil to be large. However, to find accurate structural seismic responses the interaction effects need to be accounted especially if the structure is supported on a soft soil deposit. The possible severities of omitting the effects of SSI in the analysis of structures are highlighted in the studies carried by [1] and [2]. Flexibility of soil varies the seismic responses of structures. Lengthening of lateral natural period due to overall decrease in lateral stiffness by the effect of soil flexibility is reported by [3] and [4]. The impact of dynamic soil-structure interaction on structural responses of building is studied by [5] and [6]. Impact of base flexibility on responses of torsionally coupled system using lateral components of El Centro (1940)

earthquake records was assessed by [7]. Interaction analysis of space frame-shear wall-soil system was carried out by [8] to investigate foundation forces under seismic loading.

Present study focuses on three-dimensional dynamic SSI analysis of multi storied RC buildings with shear wall of varying shapes over raft foundation subjected to Elcentro ground motion with peak ground acceleration scaled down to 0.1g in time domain. Finite element method is employed for the evaluation of seismic responses of structure.

SOIL-STRUCTURE INTERACTION ANALYSIS

During earthquake, displacements of structure and ground are dependent of each other. This dependency in which response of soil influences the motion of structure and vice versa is termed as soil-structure interaction. Conventional design practice of fixed base assumption for structures implies high stiffness of elastic soil media which constrain the motion of foundation. Wherein reality certain amount of soil-structure interaction always exist

4th International Engineering Symposium - IES 2015

March 4-6, 2015, Kumamoto University, Japan

during earthquake and the interaction is predominant in structures found on soft soil. Present study considers multi-storey reinforced concrete framed buildings of 4, 8, 12 and 16 stories with shear wall of varying shapes resting over raft foundation on soft soil.

STRUCTURAL AND GEOTECHNICAL MODEL CHARACTERISTICS

(a) Structural Characteristics

Multi-storey reinforced concrete framed buildings of 4, 8, 12 and 16 stories with and without shear wall resting on raft foundation is considered. Symmetric buildings with 3 bays equal in length along each direction are considered. The effect of infills is not considered. Shear walls of various shapes are placed symmetrically in both directions of exterior frames to study the effect of varying shapes of shear wall. Considering the building to be for residential use, storey height is chosen as 3m and length of each bay of frames as 4m. Reckoning on the building height, thickness of rectangular shape shear wall is varied from 150-250 mm and thickness of other shear wall shapes are deviated consequently such that the total mass of the structure remain same as rectangular shear wall buildings. Dimensions of building elements are arrived at by complying the respective Indian standard codes IS 456:2000[9] and IS13920:1993[10]. Details of different geometric parameters of building components are as given in Table 1. For the design of structural elements M20 grade concrete and Fe 415 grade steel are selected. Schematic representation of idealized distinctive 3 bay x 3 bay frame plan of with various shapes of shear walls are shown in Fig. 1.

(b) Geotechnical Characteristics

Soil is an unbounded domain. Present study treats soil as a homogenous, isotropic and elastic half space medium. The properties of soil are chosen on the basis of shear wave velocity of soil. Soft soil bearing shear wave velocities in the

range of 185 to 365 m/sec are considered. The properties of soil are as shown in Table 2. In analysing soil-structure interaction problems, both the structure and soil are required to be brought in the computational domain. Soil domain is practically infinite when compared to structure. Hence to represent the infinite soil domain in an efficient manner present study adopts perfectly matched layer (PML) [11]. PML layer form a cuboid box around the bounded domain of soil to simulate unboundedness of the soil domain at the boundary. The nodes on outer boundary of PML are fully constrained.

FINITE ELEMENT MODELING

Commercial finite element software LS DYNA is adopted in finite element modeling and analyses of structures. Building frames are modelled using Belytschko-Schwer resultant beam elements possessing three translational and three rotational degrees of freedom at each node. Slabs at various storey levels, shear wall and raft are modelled using four-node Belytschko-Tsay shell element having both bending and membrane capabilities. Belytschko-Tsay element possesses six degrees of freedom at each node. To model the three dimensional soil stratum, fully integrated S/R solid having three translational degrees of freedom at each node is employed. Node compatibility problem occurs at interface due to varying degrees of freedom at nodal points, which is overcome by INTERFACE_SSI card. INTERFACE_SSI card creates a tied-contact interface between the soil and the structure. A three dimensional finite element model of idealized soil-foundation-structure system with PML are as shown in Fig. 2.

Table 1 Geometric properties of building components

Storey	Columns (m)			Shear wall thickness (m)		
	Up to 3 story	Above 3 story	Rectangular	Cylindrical	Trough	L section
4	0.32 X 0.32	0.32 X 0.32	0.15	0.11	0.13	0.13
8	0.40 X 0.40	0.35 X 0.35	0.20	0.15	0.17	0.17
12	0.50 X 0.50	0.40 X 0.40	0.20	0.15	0.17	0.17
16	0.60 X 0.60	0.50 X 0.50	0.25	0.19	0.20	0.21
Raft foundation slab:	0.3m					
Roof and floor slab:	0.15m					
Beams :	0.23X0.23m					

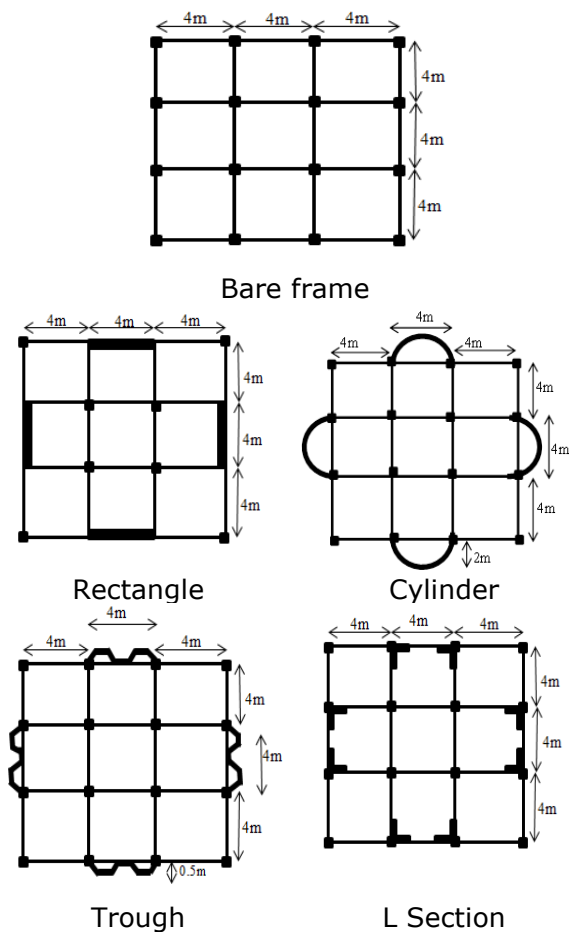


Fig. 1 Plan of bare frame and frame with various shapes of shear wall

Table 2 Details of soil parameters

Soil description	Shear wave velocity (Vs) (m/sec)	Poisson ratio (μ)	Unit weight (ρ) (kN/m ³)	Young's modulus (E _s) (kN/m ²)
Se(upper bound)	365	0.35	18	6.60E+5
Se(lower bound)	185	0.4	16	1.56E+5

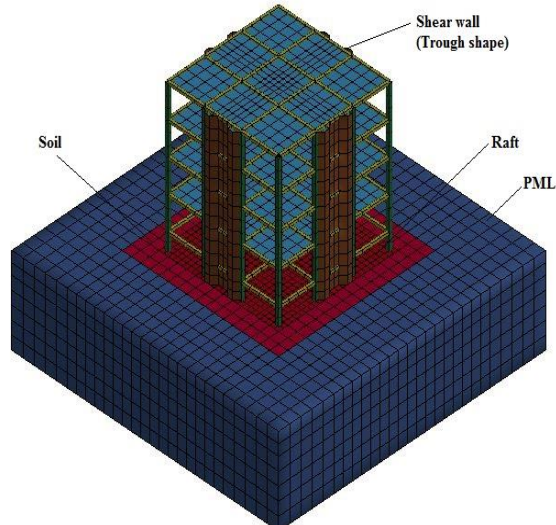


Fig.2: 3D Finite element structure-foundation-soil model

4th International Engineering Symposium - IES 2015

March 4-6, 2015, Kumamoto University, Japan

METHODOLOGY

The three-dimensional finite element model generated using finite element software LS DYNA is utilized for the Eigen value analysis to determine the fundamental natural period of the building which forms the important component in finding the anticipated seismic loads coming on structures. Further, the time history analysis is carried out using Elcentro ground motion scaled down to 0.1g to determine the responses in building due to the effect of soil flexibility and varying shear wall shapes using free field ground motions generated from ProSHAKE, a deconvolution analysis software. Acceleration time histories are employed at the interface in the global X direction of the integrated SSI system. Damping ratio equivalent to 5% of critical damping is chosen for both the structures and soil. The free field ground motions corresponding to soil types and input Elcentro ground motion scaled down to 0.1g are as shown in Fig. 3.

RESULTS AND DISCUSSIONS

Three-dimensional SSI studies were conducted using finite element software LS DYNA to determine the effects of SSI on shear wall buildings with four different shear wall shapes resting on soft soil possessing shear wave velocity in the range of 365 m/sec to 185 m/sec. The variation in responses of buildings are expressed in terms of base shear variation, roof deflection, absolute shear force and absolute bending moments of columns for flexible base which are further compared with conventional rigid base.

(a) Lateral natural period

Fundamental natural period possess an important role in varying the seismic response of structures. Values of lateral natural period found from the free vibration analysis of integrated SSI system are as plotted in Fig. 4. From Fig. 4 it is observed that value of natural period obtained in shear wall buildings are lower than bare frame buildings due to the additional stiffness by inclusion of shear wall. Among the shear wall configurations considered, buildings with L shape shear wall shows the highest value of natural period. The value of natural period increases with increase in flexibility of soil. It falls in the range of 0.251-2.044sec. for shear wall buildings with conventional fixed base and 0.321-2.284 sec. with effect of soil. However, for bare frame buildings the value of natural period is in the range of 0.852-3.0sec. for conventional fixed base and 0.990-3.224 sec. with effect of soil. Percentage increase in natural period of L shape shear wall building with respect to regularly employed rectangle shape shear wall building is observed to be in the range of 52.4-5.13. Highest percentage increase of 52.4 is observed in 4 storey building over soil type Se upper and lowest percentage increase of 5.13 in 16 storey building over soil type Se lower.

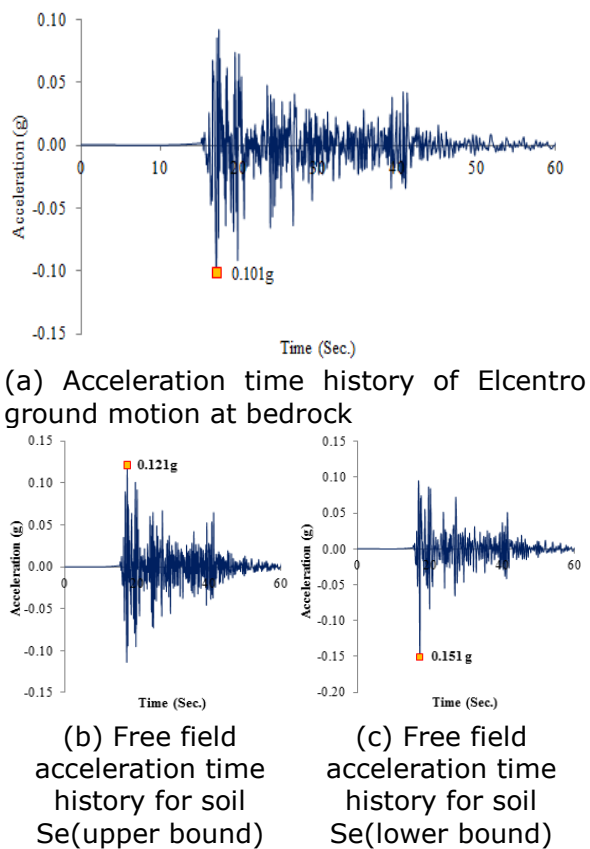


Fig. 3 Acceleration time history

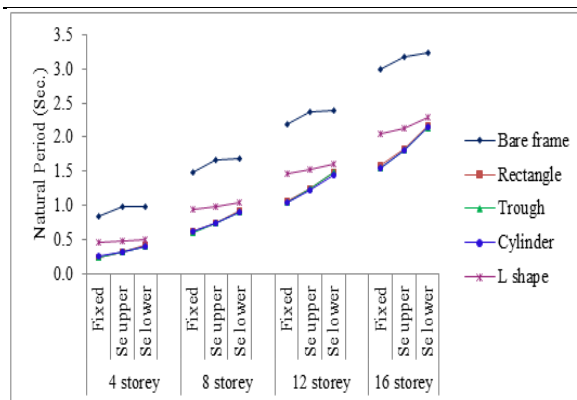


Fig. 4: Lateral natural period of building

(b) Base shear

Seismic base shear is one of the main inputs required for seismic design of structures. It defines the seismic vulnerability of structures. Variations in value of seismic base shear in terms of total seismic weight (W) of the structure are as expressed in Fig. 5. From Fig. 5 it is observed that values of seismic base shear obtained by conventional fixed base condition are higher than the values obtained by consideration of SSI. Base shear values are observed to decrease with increase in flexibility of soil in shear wall buildings of all shapes, except for L shape shear wall configuration where the value increases with increase in flexibility of soil similar to bare frame buildings. In general with consideration of effect of SSI, L shape shear buildings shows the least value of base shear when compared to the other shear wall configurations considered. Wherein, trough shape shear wall shows the least value of base shear in conventional fixed base condition. The value of base shear varies in the range of $0.0077W$ to $0.0887W$ in shear wall buildings resting on soft soil with shear wave velocity in the range of 185m/sec. to 365 m/sec. However, for the conventional fixed base condition it varies in the range of $0.0369W$ to $0.1740W$, where W is the seismic weight of the structure.

(c) Roof deflection

Deflection of roof of the building with reference to base of the structure is referred to as roof deflection. Roof deflection values of buildings with varying shear wall shapes over raft foundation are

as shown in Fig. 6. From Fig. 6, it is observed that roof deflection values increases with increase in flexibility of soil. In general for the buildings resting over soil, cylindrical shape shear wall shows the lowest value of roof deflections for buildings upto 12 stories. Above which the L shape shear wall configuration shows the least roof deflection. The lowest and highest values of roof deflection are observed to be 0.033m and 0.118m in 4 storey cylindrical shape shear wall building and 16 storey bare frame buildings respectively.

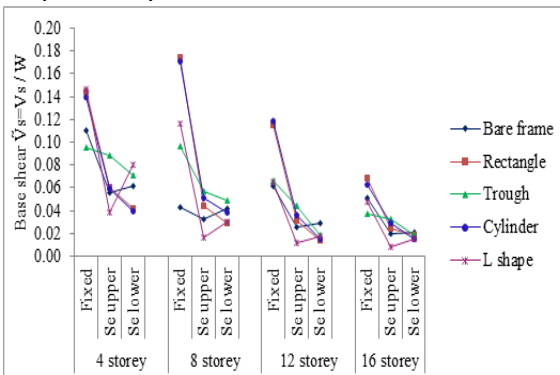


Fig. 5: Seismic base shear of building

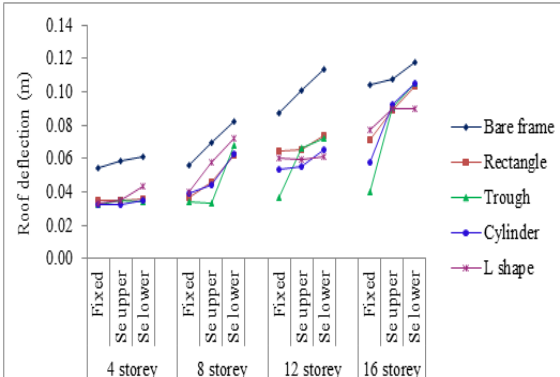


Fig. 6: Roof deflection of buildings

(d) Absolute shear force and absolute bending moment in columns

Absolute shear force and bending moment values of ground floor column due to the effect of soil and varying shapes of shear wall with respect to bare frame building are as shown in the Figs. 7 and 8. It is observed that absolute shear force and absolute bending moment values of shear wall buildings are greatly reduced by the inclusion of shear wall in framed buildings. The reduction in shear force and bending moment is highest in conventional fixed base condition which decreases with

increase in flexibility of soil. The highest and lowest reduction in shear force and bending moment with the effect of soil flexibility are observed in rectangle and L shape shear wall buildings respectively. The reduction in shear force is observed to be in the range of 17.45% to 84.38% and bending moment in the range of 9.78% to 81.50% in buildings with the inclusion of soil flexibility.

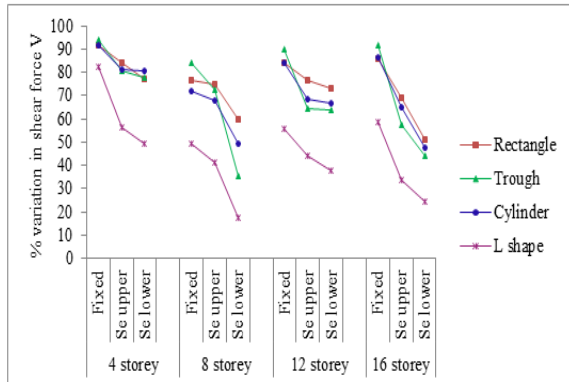


Fig.7: Shear force in ground floor column of buildings

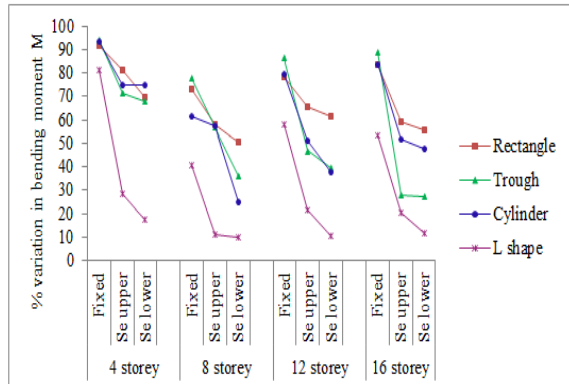


Fig.8: Bending moment in ground floor column of buildings

CONCLUSIONS

The following general conclusions are drawn from the present study

- Natural period of building increases with increase in flexibility of supporting soil. Buildings with L shape shear wall shows the highest value of natural period among the shear wall configurations considered.
- Seismic base shear obtained by conventional fixed base condition are higher than the values obtained by consideration of SSI. The least value of base shear is observed in L shape shear wall buildings with consideration of effect of SSI.

- Cylindrical shape shear wall buildings show the least value of roof deflection with the consideration of effect of SSI.

REFERENCES

- [1]Mylonakis, G., Nikolaou, A. and Gazetas, G. (1997), "Soil-pile-bridge seismic interaction: kinematic and inertial effects. Part I: soft soil", Earthquake Engineering and Structural Dynamics, Vol. 26, pp 337-359.
- [2]Roy, R. and Dutta, S.C. (2001), "Differential settlement among isolated footings of building frames: the problem, its estimation and possible measures", International Journal of Applied Mechanics and Engineering, Vol. 6, pp 165-186.
- [3]Bielak, J. (1975), "Dynamic behaviour of structures with embedded foundations", International Journal of Earthquake Engineering and Structural Dynamics, Vol. 3, pp 259-274.
- [4]Stewart, J.P., Fenves, G.L. and Seed, R.B. (1999), "Seismic soil-structure interaction in buildings I: analytical method", Journal of Geotechnical and Geoenvironmental Engineering, ASCE, Vol.125, pp 26-37.
- [5]Saad, G., Saddik, F. and Najjar, S. (2012),"Impact of soil-structure interaction on the seismic design of reinforced concrete buildings with underground stories," Proceedings of the 15th World Conference on Earthquake Engineering, Lisbon, Portugal.
- [6]Tabatabaeifar, S. H. R., Fatahia, B. and Samalib, B. (2013),"Lateral seismic response of building frames considering dynamic soil-structure interaction effects," Structural Engineering and Mechanics, vol. 45, no.3, pp.311-321.
- [7]Shakib, H. and Fuladgar, A. (2004),"Dynamic soil-structure interaction effects on the seismic response of asymmetric buildings," Soil Dynamics and Earthquake Engineering, vol. 24, no.5, pp. 379-388.
- [8]Jain, D. K. and Hora, M. S. (2014), "Interaction analysis of space frame-shear wall-soil system to investigate foundation forces under seismic loading," ARPN Journal of Engineering and Applied Sciences, vol. 9, no. 8, pp. 1267- 1281.
- [9]IS: 456-2000, "Indian standard code of practice for plain and reinforced concrete," Bureau of Indian Standards, New Delhi, India.
- [10]IS: 13920-1993, "Ductile detailing of reinforced concrete structures subjected to seismic forces -code of practice," Bureau of Indian Standards, New Delhi, India.
- [11]Basu, U. and Chopra, A. K. (2003), "Perfectly matched layers for time-harmonic elastodynamics of unbounded domains: theory and finite-element implementation," Computer Methods in Applied Mechanics and Engineering, vol. 192, pp.1337-1375.

STUDIES ON RESPONSE OF BEAMS UNDER DYNAMIC LOADING

Neha Madhulika and Manasa Bhat K I

*Undergraduate Students, Department of Civil Engineering,
National Institute of Technology Karnataka, Surathkal, India, 575 025,
E-mail: madhulikaneha@gmail.com*

ABSTRACT: There are two types of loading that a beam can be subjected to - static and dynamic. Static loading deals with load which is gradually applied and remains in place for longer duration of time. Dynamic loading deals with load that is time dependent and in which the magnitude, direction and position of mass changes quickly with respect to time. The increase in the effect of a dynamic load is given by the Dynamic Modification Factor. In this paper we study the response of a beam when subjected to static and dynamic loading and compare their responses. We concentrate on the occurrence of resonance when natural frequency coincides with the driving frequency of the system. Analysis of the shape of curve obtained for response to dynamic loading using Dynamic Modification Factor has been done.

Keywords: Dynamic Modification factor, Resonance, Dynamic Response, Static Response, Anti-resonance

INTRODUCTION

Static analysis deals with load which is gradually applied and remains in place for longer duration of time. Static responses are independent of time.

Structural response refers to the behaviour of a structure associated with a particular loading. The response of a system to a given loading (static or dynamic) depends on the system characteristics, as reflected in differential equations of motion. If the response increases proportionally to the excitation, then the system is said to be linear; otherwise it is non-linear.

Dynamic analysis deals with loads which are time dependent and in which magnitude, direction and position of mass changes quickly with respect to time. Dynamic loads include people, wind, waves, traffic, earthquakes, and blasts. Any structure can be subjected to dynamic loading. Dynamic analysis can be used to find dynamic displacements, time history,

and modal analysis. A dynamic analysis is also related to the inertia forces developed by a structure when it is excited by means of dynamic loads applied suddenly. A dynamic load can have a significantly larger effect than a static load of the same magnitude due to the structure's inability to respond quickly to the loading (by deflecting).

Vibrations occur when a system is subjected to restoring forces that make it swing back and forth about an equilibrium position. In a lightly damped system when the forcing frequency nears the natural frequency the amplitude of the vibration can get extremely high. This phenomenon is called resonance.

BEAM SPECIFICATIONS

For a beam subjected to uniformly distributed load, as shown in Figure1, the beam specifications are assumed as follows:

- Modulus of elasticity of steel, $E=200$ GPa

4th International Engineering Symposium - IES 2015

March 4-6, 2015, Kumamoto University, Japan

- Sectional modulus, $I=498*10^{-5}$ m⁴
- Length of the beam, $L=5$ m
- Mass element representing the inertial characteristics of a structure, $m=2.806$ kN/m
- Static load, $q=14.02$ kN
- Natural frequency, $\omega=n^2*\pi^2*(EI/(m*L^4))^{0.5}$
- Spring element k representing elastic restoring force and potential energy storage
- Damping constant c representing frictional characteristics and energy dissipation of the structure

STATIC RESPONSE

The beam is subjected to a uniformly distributed static load of q kN as specified above. The response of the beam is measured in terms of deflection, shear force and bending moment at various positions along the beam. The study is mainly done for mid-span, quarter span and at $L/\sqrt{2}$ positions.

The details of the responses of the beam study are given in Table 1, at the end.

DYNAMIC RESPONSE

Damping refers to the presence of frictional forces in a structure which converts the mechanical energy of a system into other forms of energy.

If damping is completely absent in an ideal system, a structure once excited will oscillate ceaselessly. Various damping methods, including viscous damping, visco-elastic damping, and tuned-mass dampers have been tested to reduce the steady state vibration of structures.

The increase in the effect of a dynamic load is given by the Dynamic Modification Factor which is the ratio of dynamic response to static response.

The beam is assumed to be a Euler-Bernoulli beam. It is subjected to a dynamic loading of $f(x,t)$. In this case, the loading is assumed to be $q\cos\lambda t$.

This can be represented mathematically by the following differential equation:

$$(EI y'')'' + m\ddot{y} + c\dot{y} = f(x,t) \quad \text{---(1)}$$

where c is dashpot constant and $C/m=2\eta\omega_n$

The beam is assumed to be at rest initially. It is assumed that there is no initial displacement in the beam. The initial conditions are:
 $y(x,0)=y_0(x)=0$
 $\dot{y}(x,0)=\ddot{y}_0(x)=0$

As one of the supports is hinged and the other is roller support, the displacement and bending moments at the ends are zero. Boundary conditions:

$$y(0,t)=0, y(L,t)=0 \\ \ddot{y}(0,t)=0, \ddot{y}(L,t)=0$$

To solve the differential equation, separation of variable method is used.

To obtain $y(x,t)$ in equation (1), we take
 $y(x,t)=\sum a_n(t) \varphi_n(x) \quad \text{---(2)}$

To get $a_n(t)$, we solve
 $\ddot{a}_n + 2\eta\omega_n\dot{a}_n + \omega_n^2 a_n = p_n(t) \quad \text{---(3)}$
 where
 $p_n(t)=qL/n\pi(1-\cos n\pi)\cos\lambda t(2/mL)^{0.5}$

Solving equation (3) for a_n , we obtain
 $a_n=e^{(-ct)}(A\cos(ft)+B\sin(ft))+ a\cos(\lambda t) + b\sin(\lambda t)$
 where,
 $c=\eta\omega$,
 $f=(\omega^2-\eta^2\omega^2)^{0.5}$,
 $a=qL(1-\cos(n\pi)(\omega^2-\lambda^2))/(n\pi(\omega^2-\lambda^2)^2+4\eta^2\omega^2\lambda^2)$,
 $b=2\eta\omega\lambda qL(1-\cos(n\pi))/(n\pi(\omega^2-\lambda^2)^2+4\eta^2\omega^2\lambda^2))$,
 $A=-a$,
 $B=-(b\lambda + ac)/f$

Also, in equation (2), $\varphi_n(x)$ is:
 $\varphi_n(x)=(2/mL)^{0.5} \sin(n\pi x/L)$

The complementary solution, represents the transient response of the system which damps out exponentially. The transient response is the vibrations caused by the initial application of the load.

The particular solution represents the steady-state harmonic response of the system due to the applied load. This response accounts for any resonance between the driving frequency and the system.

4th International Engineering Symposium - IES 2015

March 4-6, 2015, Kumamoto University, Japan

The dynamic response of the beam in terms of variation of deflection, shear force and bending moment with respect to time is obtained. Figure2, Figure3 and Figure4 shown at the end depict the dynamic response variance of beam with respect to time at different sections of the beam. With increase in damping constant the response decreases due to higher loss of energy in the system.

FREQUENCY RESPONSE PLOTS

Resonance is the phenomenon that occurs when the applied driving frequency on the system coincides with one of its natural frequencies.

It can be seen that for low values of damping (which is generally the case in most structures) very high dynamic modification factors occur.

Driving frequency ω is represented by $\omega = n^2 * \pi^2 * (EI/(m*L^4))^{0.5}$.

Frequency response plots of beams depict the ratio of dynamic response to static response with varying time. The variation of dynamic modification factor for deflection and shear force at quarter span with change in driving frequency is represented by Figure6 and Figure7 respectively. The variation of dynamic modification factor for deflection (for three various damping constants, for a single peak) with change in driving frequency is represented by Figure8.

Resonance is depicted by points where there is a peak. The dips depict minima. The downward peak shows anti-resonance. With increase in damping constant, the response decreases.

CONCLUSIONS

When the beam is subjected to harmonic dynamic loading, the response observed varies sinusoidal with time.

With increasing eta values the response observed decreases at region of resonance.

Initially, for lesser values of driving frequency the dynamic response is greater than static response. Hence, while designing greater care should be given to lower driving frequencies.

In the response plot, the point where minimum response occurs is anti-resonance.

Anti-resonance occurs due to negative interference between natural frequency and dynamic frequency.

The frequency response plot has a parabolic (convex) dip in its shape where the lowest point of the dip represents minima.

The shape of the curve is different for BM, SF, displacement, and etc. due to change in $\phi_n(x)$.

$$y(x,t) = a_n(t) * \phi_n(x)$$
$$\phi_n(x) = (2/mL)^{0.5} \sin(n\pi x/L)$$

APPLICATIONS

The dynamic responses of a beam subjected to a moving load or mass have been of importance in the design of railway tracks, bridges and machining processes. The importance of this problem find uses in many applications in the field of transportation, Bridges, guide ways, overhead cranes, cableways, rails, roadways, runways, tunnels and pipelines. Beam type structures are widely used in many branches of civil, mechanical and aerospace engineering.

ACKNOWLEDGEMENTS

This research was carried out as part of summer internship at IISc Bangalore under the guidance of Prof. C.S. Manohar and we are extremely grateful for his guidance and constant support. We are also thankful to our Professor Katta Venkataramana for encouraging us to prepare this paper.

REFERENCES

- [1] Fundamentals of Mechanical Vibration – S. Graham Kelly
- [2] Fundamentals of Vibrations- L. Meirovitch
- [3] Introduction to Statics and dynamics –Rudra Pratap
- [4] Structural dynamics – Mario Paz and W. Leigh
- [5] Vibration of a structure induced by fluid flow- R.D. Blevins

Table 1: Static response of beam subjected to uniformly distributed static loading

	Deflection(mm)	Bending Moment (kNm)	Shear Force (kN)
Mid-span	$(5/384EI)qL^4 = 0.115$	$qL^2/8 = 43.8$	0
Quarter-span	$8.138 \times 10^{-3} * qL^4/EI = 0.0716$	$3qL^2/32 = 32.85$	$qL/4 = 1.75 \times 10^4$
At $L/\sqrt{2}$	$0.01042 * qL^4/EI = 0.0916$	$0.10355 qL^2 = 36.28$	$0.207qL = 1.4506 \times 10^4$

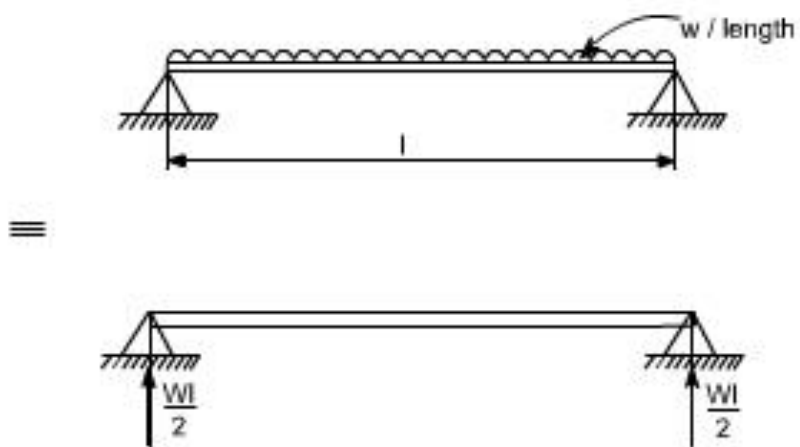


Figure 1: Beam subjected to uniformly distributed load

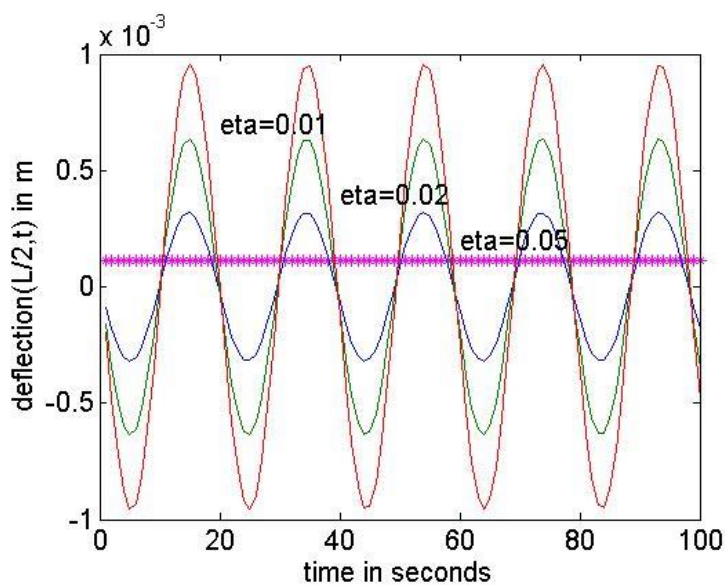


Figure 2: Dynamic deflection response of the beam at mid-span

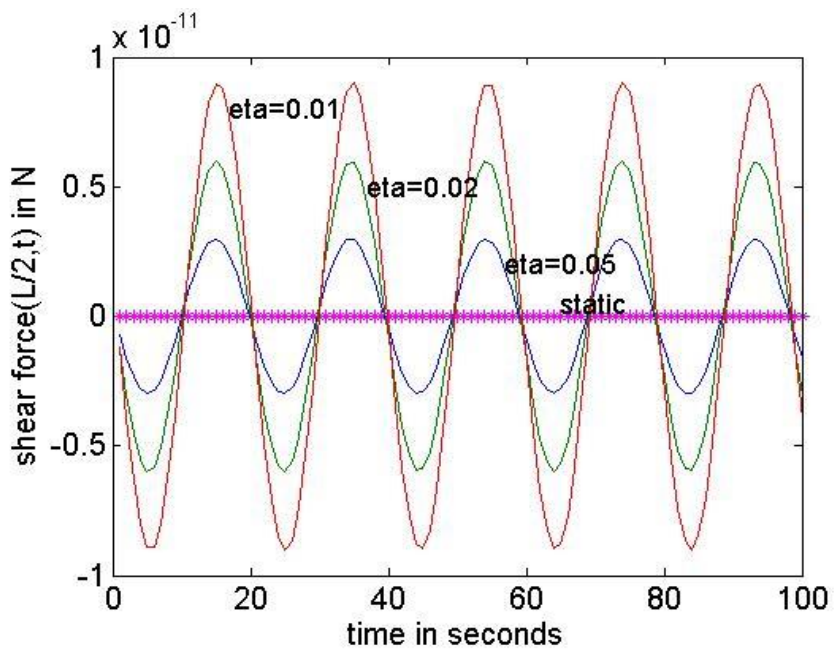


Figure 3: Dynamic shear force response of the beam at mid-span

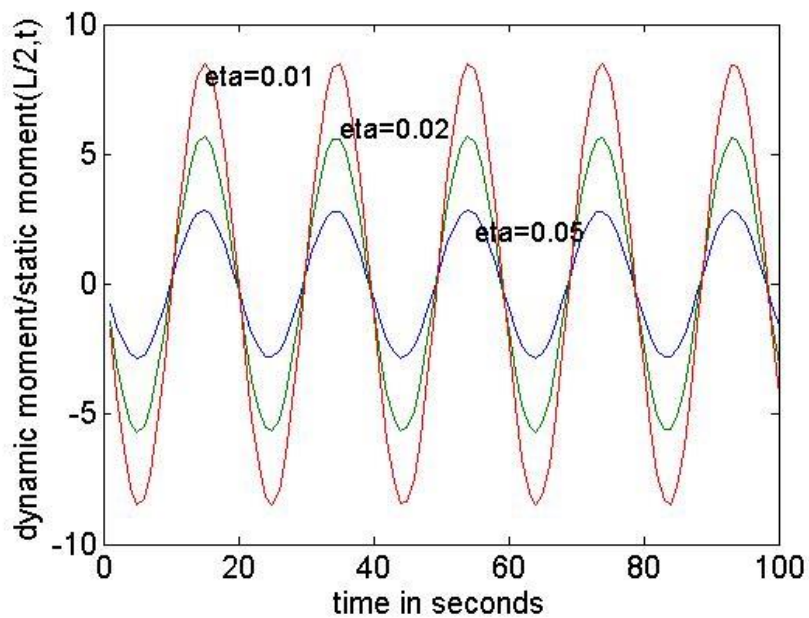


Figure 4: Dynamic bending moment response of the beam at mid-span

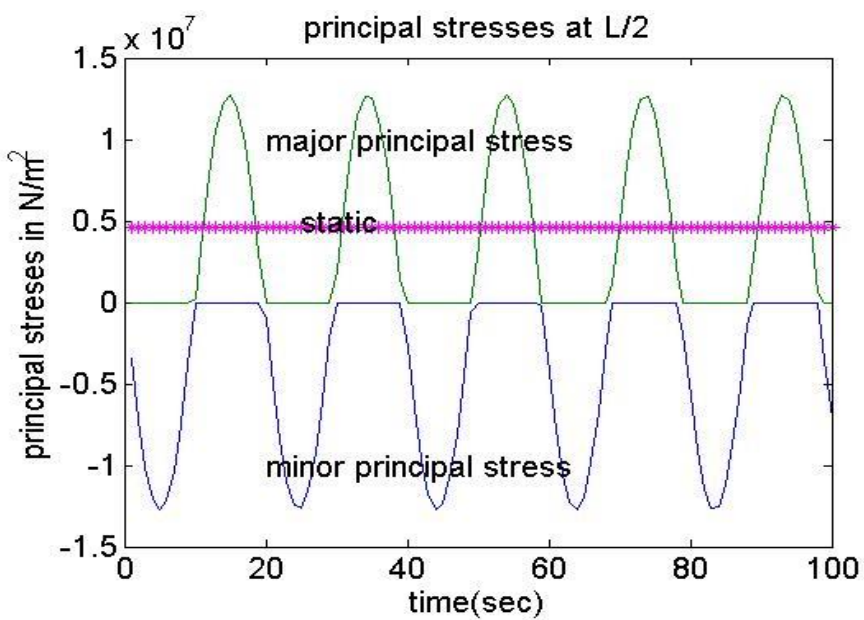


Figure 5: Dynamic principal stress response of the beam at mid-span

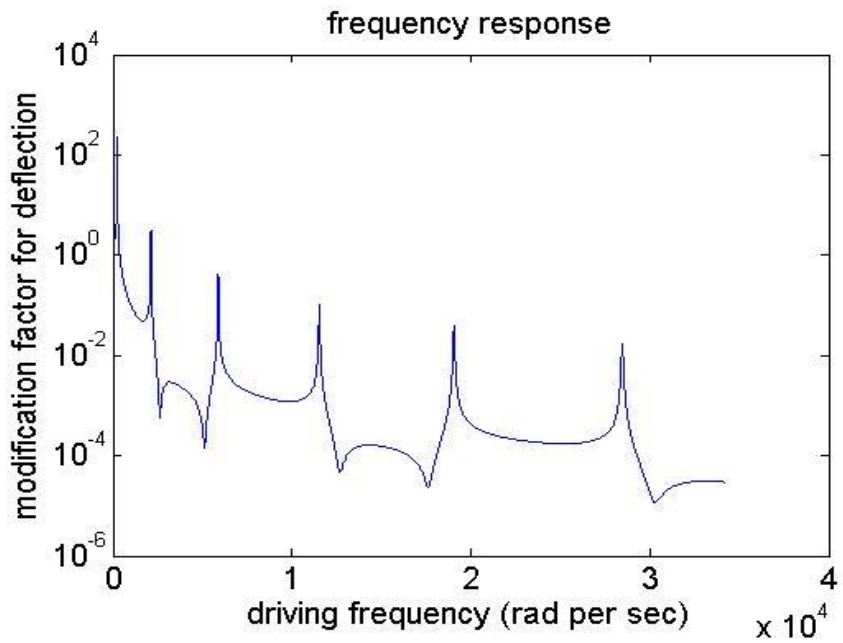


Figure 6: Frequency response plot of the beam for deflection at quarter-span for damping constant equal to 0.05

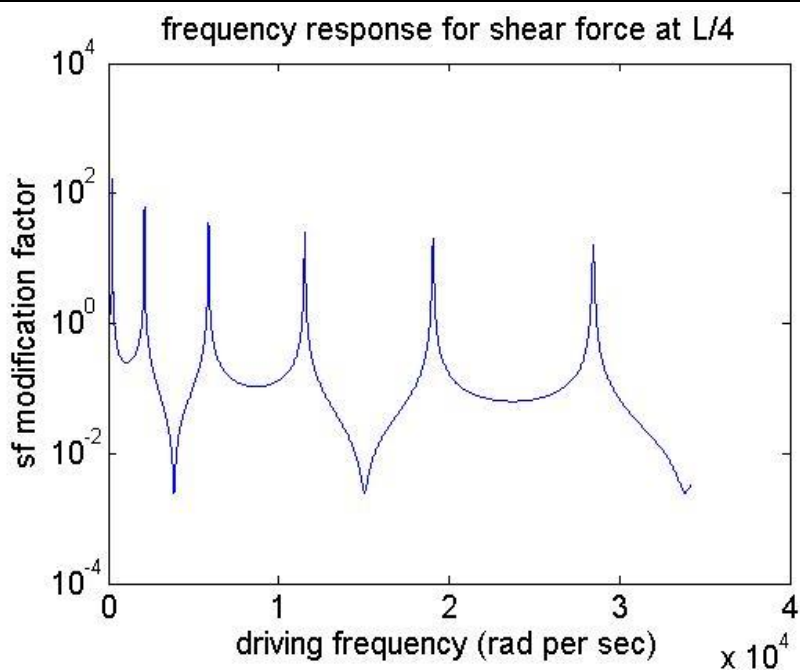


Figure 7: Frequency response plot of the beam for shear force at mid-span for damping constant of 0.05

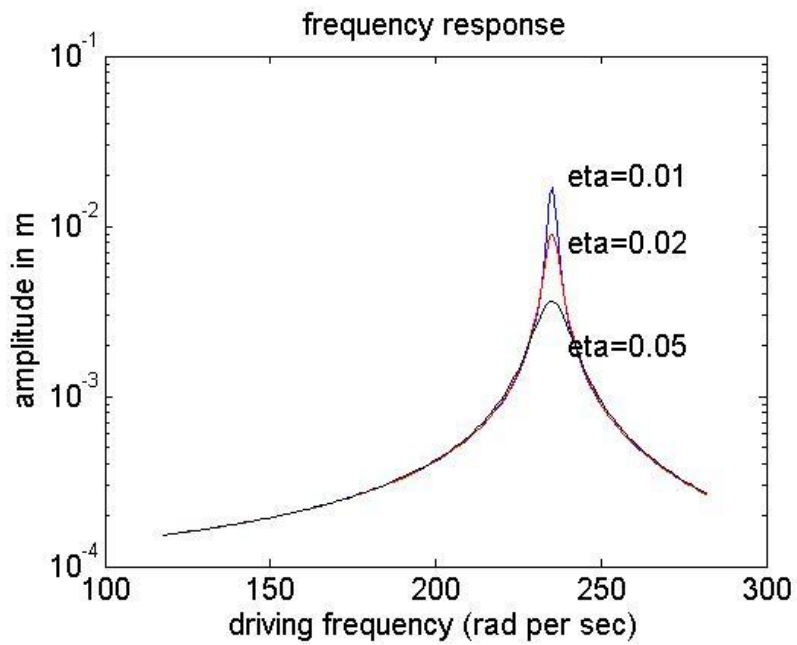


Figure 8: Frequency response plot of the beam for bending moment at quarter-span for varying values for damping constant

APPLICATIONS OF SHAPE MEMORY ALLOY DEVICES IN VIBRATION CONTROL OF STRUCTURES

Vajreshwari Umachagi, Manasa Bhat K I and Katta Venkataramana

Department of Civil Engineering, National Institute of Technology Karnataka, Surathkal, Mangalore 575025, India, e-mail: molu1694@gmail.com

ABSTRACT: Shape memory alloys (SMAs) are a class of novel materials that exhibit several unique properties such as shape memory alloy effect, hysteretic damping, good cyclic fatigue resistance and excellent corrosion resistance. These unique properties of SMAs attract them in numerous applications in areas like medical devices, scientific field, aerospace and industrial purposes. Currently, analytical and experimental investigations of SMAs in seismic design and retrofit of structures and bridges have been conducted. This paper focuses on an overview of uses of SMAs for vibration control of structures, and general characteristics of SMAs and their properties are included. Further, the mechanism of SMA based devices equipped in buildings and bridges are also discussed.

Keywords: SMAs, hysteretic damping, vibration control, SMA effect, superelasticity

Introduction

Earthquakes are unpredictable natural events that can cause tremendous damages, loss to human life and structures by Housner et al. (1997). Thus, in recent years much attention has been paid for the design (Soong and Spencer 2002) and development of seismic control devices to control the response of the structures during earthquake and wind motion (Spencer and Nagarajaiah 2003). Earlier, so many researchers developed analytical and experimental methods for the design of seismic control devices. According, to this during seismic event the inelastic response of building can be reduced using energy dissipation devices. Generally, structural control systems are divided into three groups, passive, active and semi-active control systems. Nowadays several types of passive energy dissipation devices are used and implemented. Passive devices do not require any external power supply and they reduce damages to structures by dissipating the input energy of the excitation in the form of heat and the original structures withstand with less severe actions. Fluid viscous damper,

rubber based devices, steel yielding devices like friction damper, metallic damper etc. are the some of the passive control devices. These devices have some complexity in maintenance and durability like strength of rubber and operation of fluid viscous damper after severe earthquake is very difficult. So, other method to overcome this problem is use of passive energy based shape memory alloy device by Dolce et al. (2000).

Shape memory alloys are innovative smart materials. Recently, the use SMAs become more popular in seismic application due to its re-centering property, high damping capacity and corrosion resistance. In the most of the literature SMA devices are considered as passive control systems (Dolce et al. (2000) and Aiken et al.(1993)). SMAs (usually called as NiTi alloys) have capable of undergoing large deformation strain up to 8% without any residual strain during dissipation of significant amount of energy.

The first shape memory transformation and the metallographic phenomena and resistivity changes are observed in aurum cadmium alloy (AuCd) proposed by Chang and Read (1932), but the shape memory

4th International Engineering Symposium - IES 2015

March 4-6, 2015, Kumamoto University, Japan

effect was discovered in the nickel-titanium (the material was named Nitinol). Graesser and Cozzarelli (1991) developed one dimensional stress-induced micromechanical phase transition NiTi shape memory alloy model to achieve large hysteretic deformation in SMAs due to the hysteresis behavior, which is associated with phase transformation. In dynamic applications on structures, the SMAs show a greater potential for use as a passive damping device. Since then, many types of shape memory alloys have been discovered. Among the various alloys, like copper and ferric and ferrous alloys, Nitinol possesses superior thermo mechanical and thermo-electrical properties. and it is most commonly used SMA alloy. Generally, these materials get deformed at lower temperature, and regain their original shape by heating to some higher temperature before going to the deformation. The most important properties showed by the SMA are the shape memory and super elastic effects. These unique properties were the result of reversible phase transformations of SMAs. The frequently used elements in NiTi alloys are iron and chromium (to lower the transformation temperature), and copper (to decrease the hysteresis and lower the deformation stress of the martensite). Because common contaminants such as oxygen and carbon can also shift the transformation temperature and degrade the mechanical properties, it is also desirable to minimize the amount of these elements.

Further, SMAs are efficient passive vibration suppression devices comprising hysteretic dampers with unique characteristic of Young's modulus, temperature relations, shape memory effects, and high damping capacity make them to use as devices for seismic resistant design and retrofit.

This paper describe the review of SMA properties related to the civil engineering applications. The paper divided into the basic Ni-Ti SMA properties, hysteretic modelling of Ni-Ti SMAs, stress-strain-temperature curve of Ni-Ti SMA, hysteretic modelling of Ni-Ti SMAs and application of SMA in structural control systems,

limitations of SMAs and cost of shape memory alloys.

Basics of NiTi alloys

SMAs have a unique behavior of phase transformation. Austenites with high symmetry and martensite have lower symmetry. These are the two important crystallographic phases of SMA. Austenite phase is stable at higher temperatures and lower stresses; while Martensite is stable at lower temperatures and higher stresses. There are two effects of SMAs one with superelasticity and Shape memory alloy effect. Fig.1 by Mortazavi et al. (2013) shows SMA behaviour a) superelasticity in austenite phase b) shape memory effect in martensite phase. In, superelasticity effect the ambient temperature is above Austenite finish temperature, the specimen is in Austenite phase and the large strain induced by stress can be completely recovered by removal of stress. If it is in Martensite phase the temperature is below Martensite finish temperature, and a large residual strain will remain on the specimen after unloading which is also recoverable by means of heating above Austenite finish temperature it is known as shape memory alloy effect (Mortazavi et al. 2013). The mechanical properties of Ni-Ti SMAs are summarized in Table 1.

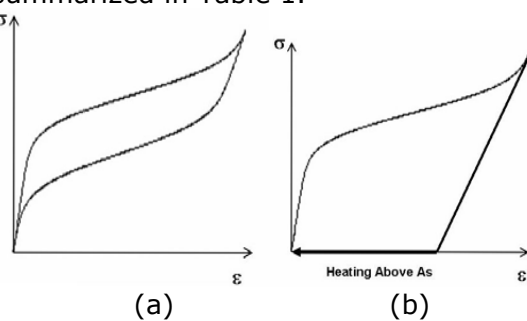


Fig.1 a) superelasticity in austenite phase b) shape memory effect in martensite phase

Stress-Strain-temperature curve of Ni-Ti SMA

From the practical point of view, (Piedboeuf et al. 1998) a more interesting part of SMAs is two other types of energy dissipation mechanisms. The intrinsic damping of the austenite is low but if the applied stress is high enough, martensite can be stress induced and this phase

transformation will lead to high energy dissipation. The intrinsic damping of the martensitic phase is quite high due to the reorientation of the martensite twin variants under stress. Some applications of martensitic alloys as dampers have been considered. Fig.2 by Piedboeuf et al. (1998) shows the stress-strain curve of an austenitic shape memory alloy. When transformation level reaches the stress σ_{Ms} , at this level austenite phase transferred at constant stress level and the martensite phase will be induced. Later, after the release of stress level, the martensite unloads elastically down to stress level σ_{Ms} , again it come back to austenite state once again at constant stress level. After completion of this transformation stage, it reaches austenite phase at elastic unloading case. This is known as superelastic effect, even if the behavior is nonlinear there is no permanent deformation. During this transformation cycle it gives rise good damping capacities of these alloys due to surface hysteresis is equal to energy dissipation. At higher temperature, the martensite is stress induced, the transformation stresses will increase linearly and curve shifts upwards as shown in Fig.2 by Piedboeuf et al. (1998).

Hysteretic Modelling of Ni-Ti SMAs

The new modified constitutive model of Wilde is extended constitutive model for SMA initially developed by Graesser and Cozzarelli (1991) for modelling of the Ni-Ti SMA device (Fig.3) and this model includes the hardening behaviour of SMA materials i.e. phase transformation from austenite to martensite phase is completed (DesRoches et al (2004) and Graesser and Cozzarelli, 1991). This model describes the one-dimensional stress-strain relationship of super-elastic SMA wires.

APPLICATION OF SMA IN STRUCTURAL CONTROL SYSTEMS

The specific characteristics of SMAs led to several applications in civil engineering. The use of SMAs in newly built structures and retrofitted structures are in the form of bracing systems, restrainers and bolted connections.

Table 1 Mechanical Properties of Nitinol

Property	Austenite	Martensite
Density(g/cm ³)	6.45	6.45
Recoverable Elongation (%)	Up to 8	Up to 8
Young's Modulus(GPa)	30-83	21-41
Yield Strength (MPa)	195-690	70-140
Ultimate Tensile strength(MPa)	895-1900	895-1900
Elongation Failure (%)	5-50 (typically 25)	5-50 (typically 25)
Poisson's ratio	0.33	0.33
Transformation temperature (°C)	-200-110 °C	-200-110 °C

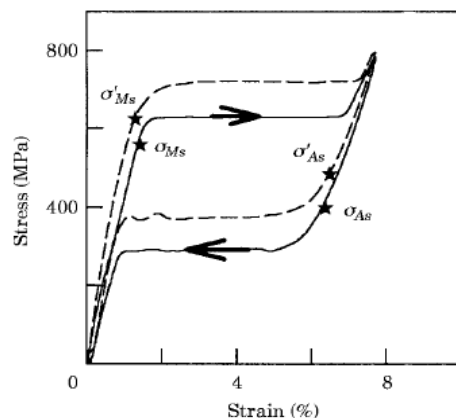


Fig.2 Superelastic stress-strain curve of an austenite SMA. The dashed curve of SMA at a higher temperature.

SMA wire as Retainers

The damages to building and bridges because of earthquake motion become more in recent years due to excessive lateral displacement. This indicates that the better methods to provide to control the structures from damages and reduce the damage effect from the seismic load. Wilde et al. (2000) investigated the SMA bar for elevated highway bridges as isolation system as shown in Fig.4. Superelastic SMA rebars are used as reinforcement in the plastic hinge area of columns will deform when subjected to earthquake but, it will not retain significant amount of its original shape after

deformation (Wang 2004). It was observed that the use of SMA restrainers in RC columns were provide more effective replacement in limiting hinge displacement then the normal steel reinforcement.

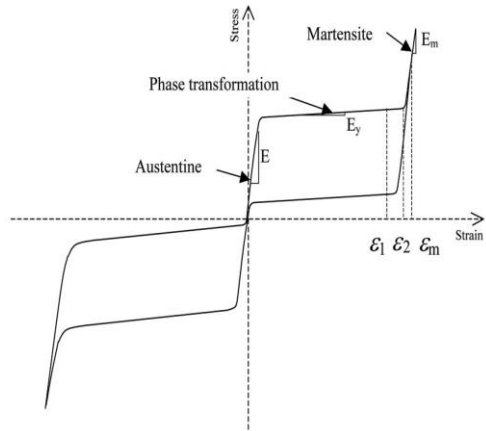


Fig.3 Stress-strain relation of the extended hysteretic model of Ni-Ti shape memory alloy.

Russell et al. (2010) have developed shape memory alloy (SMA) restrainers cable to determine their effectiveness in limiting hinge opening and it was tested on a four-span, one-quarter scale concrete slab bridge. The experimental results show that the SMA cables reduce the as-built hinge openings by 52% and reduce the column drifts by 47%. The innovated passive control based SMA device was designed by Alaa and Bassem (2009) and implemented in cable stayed bridge model. The device was attached to the bridge at the deck tower and deck pier for the seismic control of the structure. Details of the 3D cable stayed bridge have a centre span of 670.5 m with side spans of 292.6 m; two A-shaped central towers supporting the bridge had a height of 170.8 m and a width at the foundation level equal to 36m. The comparative study shows that by introduction of SMA damper in bridge there was a large reduction of displacement compared to the response of reference bridge.

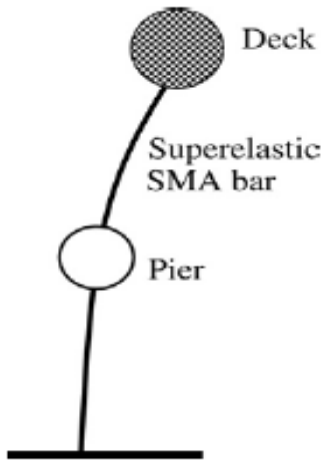


Fig.4 SMA bar for elevated highway bridges as isolation system(Song, G et al.,2006)

SMA as bracing systems:

SMA diagonal bracing wires in a one storey prototype building model subjected to harmonic base excitation was studied by Salichs et al. (2001) Because of hysteresis characteristics and additional damping properties of SMA bars reduced the displacement of building compare with the steel bracing systems. At lower level of damages, they can be easily replaceable after the earthquake. DesRoches and Delemont (2002) proposed for seismic retrofit of bridges using SMA restrainers. Han et al. (2003) investigated a SMA wire based damper in a steel frame of 2m height to determine the vibration reduction of the frame as shown in Fig.5. The experimental and numerical results illustrate that the proposed SMA damper effectively reduces the structural response of buildings.

SMA based devices and isolators

Clark et al. (1995) investigated the analytical and experimental based devices using SMA wires. The SMA device consists of 0.508mm thick superelastic, 210 loops of wire wrapped around two cylindrical supports. The SMA device is tested in plane cyclic loading, with initial prestressed at strain rate is 2.75%. Test results showed that with little reduction in yield stress with good hysteresis behaviour. The tested device was fitted in six storeys, two bays by two bay steel

frames and observed that reduction in displacement and acceleration responses of the frame.

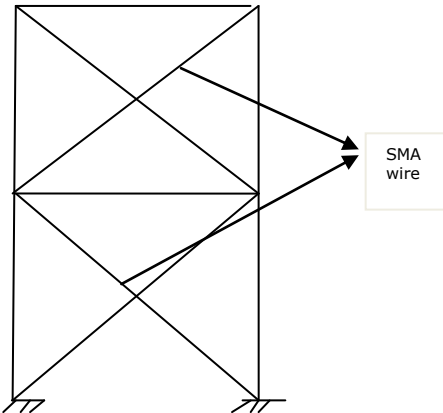


Fig.5 Schematic representation of SMA bracing system in building frame

Billah et al. (2010) have analytically investigated the behavior of SMA wire as a base isolator in the highway bridge under various ground excitations. Results show that SMA base isolators reduce the maximum displacement between base and superstructure. Dolce et al. (2000) proposed the SMA wire device for passive control of structures as shown in Fig.6 by (Song, G et al.,2006). Several experiments were conducted to understand the properties and characteristics of SMAs such as durability, fatigue resistance under large strain cycles and reliability. Osman and Stefan (2010) studied the seismic performance of a sliding-type base isolation system with the effect of temperature. A multi-span continuous bridge was modelled with a steel-Teflon sliding bearings and a SMA device. The results show that in all temperature considered in the study with a sliding-type isolation system, a SMA re-centering device can effectively reduce the seismic response of bridge. Torra et al. (2012) studied the essential properties of NiTi alloys such as damping, creep effect and fracture level for the modelling of SMA device. The new proposed device was situated in the cable stayed bridge and observed that the subsequently frequency reduction verses time.

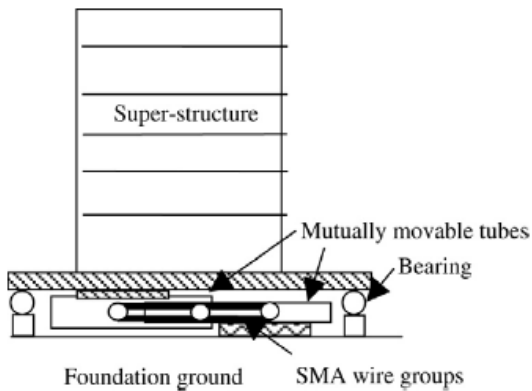


Fig.6 Schematic representation of SMA elements in building(Song, G et al.,2006)

SMA in Beam Column Joint:

Justin et al. (2004) investigated the effectiveness of SMAs for connecting steel beam-column. There are two connections, consists of four large diameter NiTi SMA bars of size 381 mm long with a diameter of 35 mm in the 229 mm central gage length and the ends of the bars are of size 44 mm diameter with a 12-pitch threading connecting the beam flange to the column flange. The second connection was same as first but beam was replaced with a lighter sections. Both connections were tested using, (SEAOC-ATC-CUREE) SAC loading protocol. Results show that energy dissipation from these connections was very high after being subjected to cycles up to 4% drift level.

LIMITATIONS OF USING SMAs

Cost of SMAs

SMAs have significant utilization in civil engineering structures. Implementation of SMA based devices; cost of the material is a primary issue. Because of size of civil engineering structures are large, associated forces are also large and requires a good amount of materials, which is another problem to use of costly SMAs in civil engineering applications. Process of getting a high strength of NiTi alloys into particular shaped form is also a difficult task (Frick et al. 2004). Therefore, getting the desired size and machining have a considerable effect on the cost of SMAs. From last few decades there is huge reduction in cost of Ni-Ti alloys, from more

4th International Engineering Symposium - IES 2015

March 4-6, 2015, Kumamoto University, Japan

than US\$1000/kg to below US\$150/kg. But the price of SMA is considerably higher than the other construction materials. Thus, it is essential to development of low cost SMAs for large scale civil engineering buildings.

Conclusions

This paper describes a review of basic properties of Ni-Ti shape memory alloys and their applications in civil engineering. The SMA elements in the form of retainers, devices, bracing system and beam column bolted connections were used. Both austenite and martensite SMAs during loading and unloading condition shows strong hysteretic effects in their stress strain curves. These properties used for development of passive control based SMA devices and implemented in control of structures from the earthquake. The effectiveness of SMAs elements also demonstrated in this paper.

Acknowledgements

The present research has been funded by Bhabha Atomic Research Centre, (BARC) Mumbai.

References

- [1]Aiken, I D et al (1993), Testing of Passive Energy Dissipation Systems, *Earthquake Spectra*, Vol.9, No.3, pp. 335 - 369.
- [2] Alaa, M S and Bassem, O A (2009), Application of shape memory alloy dampers in the seismic control of cable-stayed bridges, *Engineering Structures*, Vol.31, pp. 607-616.
- [3] Billah, A H et al (2010), Seismic performance of a multi-span bridge fitted with superelastic SMA based isolator, *IABSE-JSCE Joint Conference on Advances in Bridge Engineering-II*.
- [4] Chang, L C and Read, T A (1932), Shape memory alloys, *Trans. AIME*.
- [5] Clark, P et al (1995), Experimental and analytical studies of shape memory alloy dampers for structural control. In: *Proceedings of passive damping*.
- [6] DesRoches, R and Delemont, M (2002), Seismic retrofit of simply supported bridges using shape-memory-alloys. *Engineering Structures*, Vol. 24, pp.325–332.
- [7] DesRoches, R (2004), Cyclic properties of superelastic shape-memory-alloy wires and bars. *Journal of Structural Engineering, ASCE*, Vol.130, pp.38–46.
- [8] Dolce, M et al (2000), Implementation and testing of passive control devices based on shape memory alloys. *Earthquake Eng. Struct. Dyn.*, Vol.29, No.7, pp.945–968.
- [9] Frick, C P et al (2004) Multi scale structure and properties of cast and deformation processed polycrystalline NiTi shape-memory alloys, *Vol.35*, No.7, pp.2013-2025
- [10] Graesser, E J and Cozzarelli F A (1991), Shape-memory alloys as new materials for aseismic isolation. *J. Eng. Mech.*, Vol.117, No.11, pp.2590–2608.
- [11] Han, Y L (2003), Structural vibration control by shape memory alloy damper, *Earthquake Engng Struct Dyn*, Vol. 32, pp.483–494.
- [12] Housner, G W et al (1997), Structural control: Past, present and future. *J. Eng. Mech.*, Vol.123, No. 9, pp. 897–971.
- [13] Justin, O et al (2004), Steel Beam-Column Connections Using Shape Memory Alloys, *Journal of Structural Engineering*, Vol.130, No.5, pp.732–740.
- [14] Mortazavi, S M R et al (2013), Seismic Control of Steel Structures with Shape Memory Alloys, *International Journal of Automation and Control Engineering* Vol. 2, No.1.
- [15] Osman, E O and Stefan, H (2010), Evaluation of the performance of a sliding-type base isolation system with a NiTi shape memory alloy device considering temperature effects, *Engineering Structures*, Vol. 32, pp.238–249.
- [16] Piedboeuf, M C et al (1998), Damping behaviour of shape memory alloys: strain amplitude, frequency and temperature effects , *Journal of Sound and Vibration*, Vol.214, No.5, pp. 774-890.
- [17] Salichs, J et al (2001), Vibration suppression of structures using passive shape-memory-alloy energy dissipation devices. *Journal of Intelligent Material Systems and Structures*, Vol.12, pp. 671–680.
- [18] Spencer, B F and Nagarajaiah, S (2003), State of the art of structural control. *J. Struct. Eng.*, Vol.129, No.7, pp.845–856.
- [19] Song, G et al (2006), Applications of Shape Memory Alloys in Civil Structures. *Engineering Structures*, Vol.28, No. 9, pp.1266-1274.
- [20] Soong, T T and Spencer, B F (2002), Supplemental energy dissipation: state-of-the-art and state-of-the-practice. *Eng. Struct.*, Vol.24, pp. 243–359.
- [21] Torra, V et al (2013), Built in dampers for stayed cables in bridges via SMA. The SMARTeR-ESF project: A mesoscopic and macroscopic experimental analysis with numerical simulations *Engineering Structures* Vol.49 pp.43–57
- [22] Russell, E et al (2010), Experimental response modification of a four-span bridge retrofit with shape memory alloys, *Struct. Control Health Monit.* , Vol.17, pp.694–708.
- [23] Wang, H (2004), A study of RC columns with shape-memory-alloy and engineered cementitious composites. *M.Sc. thesis*, University of Nevada, Reno, Nev.
- [24] Wilde, K et al (2000), Base isolation system with shape-memory-alloy device for elevated highway bridges. *Engineering Structures*, Vol.22, pp.222–229.

Earthquake Response of Masonry Infill Panels

Catherin Jeselia M, Jayalekshmi B R and Katta Venkataramana

Department of Civil Engineering, National Institute of Technology Karnataka, Surathkal, Mangalore 575025, India, e-mail: jeni.0719@gmail.com

ABSTRACT: Shaking table tests are used extensively in seismic research, as they provide the ways to excite structures. The structures (model or prototype) are subjected to conditions which are representative of true earthquake ground motions. In this study, shake table tests are carried out for RC frames with and without brick masonry infills for 3 different aspect ratios 0.7, 1.0 & 1.3. The similar structure was modelled using FE (ANSYS) software and their dynamic characteristics variation is studied both experimentally and analytically. It is found that aspect ratio plays a significant role in the behaviour of masonry infills.

Keywords: Masonry Infills, Shake table test, Modeling, ANSYS

INTRODUCTION

Masonry Infills are the most significant construction all over the world. But they are easily prone to natural hazards like earthquakes, cyclones, tsunami etc., even though modern materials, construction practices and techniques are available. Owing to great usage of masonry buildings all over the world, it is necessary to study its dynamic characteristics, when subjected to these hazards i.e., under the action of dynamic loads. Many researches have been carried out in the past few decades, to understand the behavior of brick masonry, when subjected to complex loading conditions, but the information is still scarce. In order to supplement the existing studies, there is a need to improve and enhance the performance of complex masonry structures and its response to the real time situations. In the present study, shake table tests are carried out for RC frames with (BF-Bare Frame) and without (IF-Infilled Frame) brick masonry infill, and its response to the calibrated earthquake input. The resonance frequency and damping values

were calculated for various aspect ratios (AR) of the RC frame structure.

MODELING OF MASONRY

Masonry is a composite material and there are 2 mechanical approaches for the analysis of masonry structures, i.e., Micro modeling and Macro modeling depending on the level of accuracy and simplicity. Micro-modeling is a complex method of analysis and it is always done by using finite element method (FEM). Malick and Severn [1] were the first ones to use this FEM approach. Later, different FEM modeling approaches were followed by various researchers [2], [3], and [4]. Later, Laurencio [5] proposed different approaches for modeling masonry such as detailed micro-modeling, simplified micro-modeling and macro modeling which are shown in Fig.1, 2 & 3 respectively.

Detailed micro-modeling

In this, brick units and mortar in the joints are represented by continuum elements whereas, the unit-mortar interface is represented by discontinuous elements.

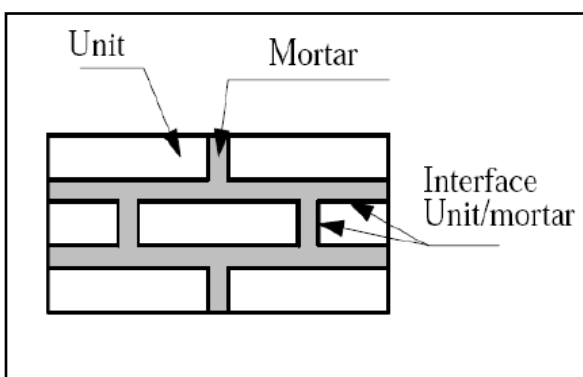


Fig.1: Detailed micro-modeling of masonry
Simplified micro-modeling

The brick units are represented by continuum elements whereas, the behavior of the mortar joints and unit-mortar interface is lumped in discontinuous elements.

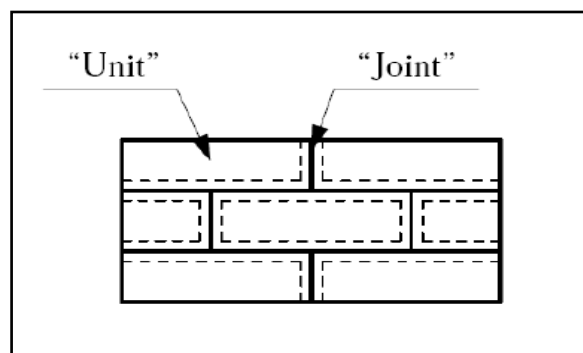


Fig.2: Simplified micro-modeling of masonry

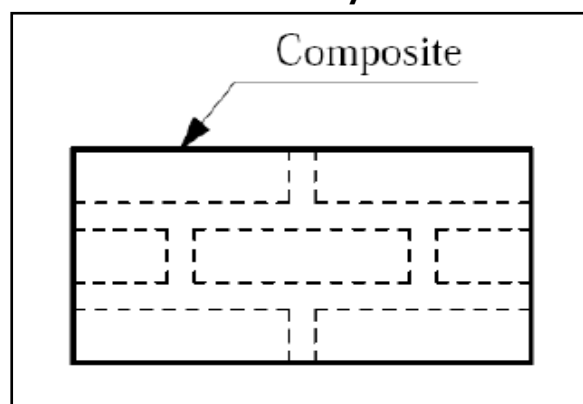


Fig.3: Macro-modeling of masonry

Macro-modeling

The brick units, mortar and unit-mortar interface are smeared out in the continuum.

The third approach does not make a distinction between individual units and joints but treats masonry as a homogeneous anisotropic continuum.

In the present work, detailed micro-modelling is used for representing brick masonry using finite element software ANSYS.

EXPERIMENTAL SETUP

SHAKE TABLE TESTS

Among several experimental techniques which are used to test the response of structures, shaking table tests are the most direct and accurate way to detect the seismic performance of the structures. This test is used for shaking structural models or prototypes with a wide range of simulated ground motions, including reproductions of recorded earthquakes time-histories. Accelerometers are fixed to the structures, in order to obtain the response when excited with calibrated earthquake input or during a dynamic loading. Shake tables typically consist of a rectangular platform that is driven in up to six degrees of freedom (DOF) by servo-hydraulic or other types of actuators. Test specimens are fixed to the platform and shaken, often adding load to the point of failure. By using the data obtained from transducers and accelerometers, it is possible to interpret the dynamic behaviours of the specimen.

A one bay one storey bare RC frame and brick masonry infilled RC frame with various aspect ratios (AR) 0.7, 1.0 & 1.3 was taken as prototype. The structure was fixed to the tri-axial shake table and excited as per test parameters. The geometrical properties of both Bare Frame and Infilled Frame are shown in table 1.

Table 1: Geometrical Properties of RC frame

Aspect Ratio (AR)	Length (mm)	Breadth (mm)
0.7	2170	1450
1.0	2170	2400
1.3	2170	2890

4th International Engineering Symposium - IES 2015

March 4-6, 2015, Kumamoto University, Japan

The brick infill walls were comprised of 2nd class bricks with sizes 75mm x 115mm x 230mm. An isolated footing with 600 mm x 600 mm cross-section and depth 200 mm is provided for each column.

In order to obtain the effect of masonry infill panels on the stiffness of the structure, sine sweep tests were conducted on the structure with and without infill panels. Fundamental frequency is one of the most important parameter which needs to be estimated correctly for better prediction of forces. Infill panels contribute significantly towards the stiffness of the structure and the natural frequency of RC structures is largely dependent on whether it has masonry infill panels or not [6]. Moreover, the natural frequency and mode shapes will enable us to visualize the after effects of natural hazards.

In order to evaluate the damping values and identify the natural frequencies, the accelerometer responses were analysed using Data Analysis Package (DAP) software. The first peak of the graph obtained is the fundamental frequency or resonance frequency and the damping values are calculated using Half-Power Band width method.

$$\text{Damping} \approx \frac{(\omega_2 - \omega_1)}{2 \times \omega} \quad (1)$$

The frequency and damping values that are obtained for both bare frame (BF) and infilled frame (IF) for various aspect ratios when excited using tri-axial shake table tests are shown in Table 2 and 3.

Table 2: Resonance Frequency & Damping values of Bare Frame

AR	Axis	Accelera	Resonance	Dampi
		-tion	Frequency	ng
		m/s ²	Hz	%
0.7	X	1.0	28	5.14
	Y	0.5	7.5	11.2
1.0	X	1.0	24	14.9
	Y	0.5	2	16.7
1.3	X	1.0	16	29.2
	Y	0.5	1	60

Table 3: Resonance Frequency & Damping values of Infilled Frame

AR	Axis	Acceler	Resonance	Dampi
		-ation	Frequency	ng
		m/s ²	Hz	%
0.7	X	1.0	38.5	13.3
	Y	0.5	4	23.3
1.0	X	1.0	17	6.46
	Y	0.5	4	20.6
1.3	X	1.0	10	7.57
	Y	0.5	2 & 20.5	23.7

FINITE ELEMENT ANALYSIS

The commercially available finite element software ANSYS is used in the modeling and analysis of RC frames. The detailed micro modeling is employed, in which all the components including concrete, steel reinforcement and brick masonry infill materials are modelled as distinct elements. And the mutual interactions are simulated using proper constraints and contact properties. In the ANSYS model, SOLID65 is used to model the reinforced concrete beam and column members.

ELEMENTS USED FOR MODELING

SOLID65

The element SOLID65 is a solid element with 8 nodes and has 3 degrees of freedom at each node (UX, UY, and UZ). The concrete is capable of cracking (in three orthogonal directions), crushing, plastic deformation and creep.

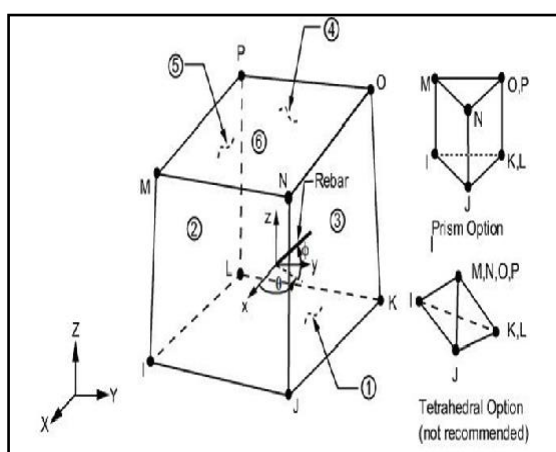


Fig.4: Geometry of element SOLID65 (ANSYS 13)

4th International Engineering Symposium - IES 2015

March 4-6, 2015, Kumamoto University, Japan

The most important aspect of this element is the treatment of non-linear material properties.

CONTA174

CONTA174 is used to represent contact and sliding between 3-D "target" surfaces (TARGE170) and a deformable surface, defined by this element.

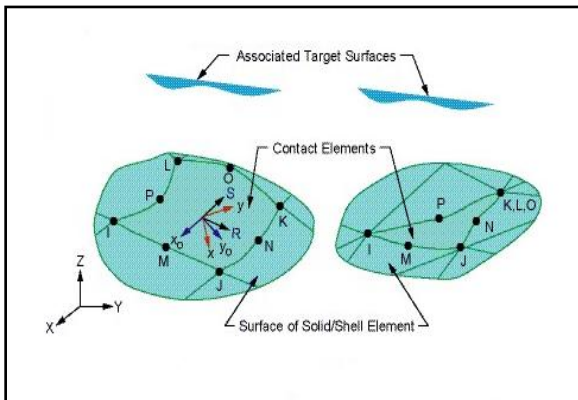


Fig.5: Geometry of element CONTA174 (ANSYS 13)

The element is defined by eight nodes I, J, K, L, M, N, O, P. It can degenerate to a six node element depending on the shape of the underlying solid or shell elements. Non-linear, Large deflection, Isotropic or Orthotropic friction and De-bonding are the special features of this element.

TARGE170

TARGE170 is used to represent various 3-D "target" surfaces for the associated contact (CONTA173 & CONTA174) elements.

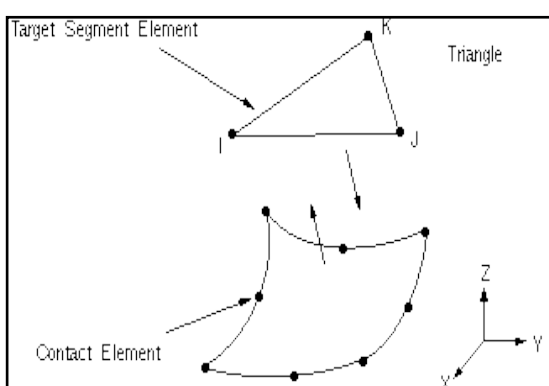


Fig.6: Geometry of element TARGE170

This target surface is discretized by a set of target segment elements and is paired with its associated contact surface via a shared real constant set. The following

material properties are given to each material as shown in Table 4.

Table 4: Material Properties of the material used in ANSYS

Material	Young's Modulus (E)	Poisson's Ratio (u)	Density (ρ)
	N/mm ²	no unit	KN/m ³
Brick	5000	0.2	21
Mortar	2000	0.15	21.6
Concrete	30000	0.2	24
Steel	200000	0.3	78.5

Modeling of reinforcement in concrete can be done either as discrete or as smeared as shown by various researchers [7], [8], and [9]. If the rebars are provided discretely by providing spar elements (Link8) attached to the nodes of SOLID65, then it is called discrete modeling. Smeared modeling is the one in which the rebars are smeared within the SOLID65 element and are defined by using real constants. The real constant set consists of the volume ratio (ratio of steel to concrete), orientation angle θ , ϕ etc as defined by the user. In the present work, RC is modelled using smeared modeling. The real constant set used for the models are shown in the table 4.

Table 5: Real constants SET 1 for concrete used in SOLID65

Particulars	Real Constants		
	Rebar 1	Rebar 2	Rebar 3
Angle θ	90°	0°	90°
Angle ϕ	0°	90°	0°
Aspect Ratio	Volume Ratio		
0.7	0.3104	0.0383	0.0039
1.0	0.3104	0.0038	0.0039
1.3	0.3104	0.0369	0.0039

MESHING

In this FE model, mapped meshing was done for brick and concrete materials and free meshing was done for mortar materials, since the element size is very less i.e., 10 mm.

4th International Engineering Symposium - IES 2015

March 4-6, 2015, Kumamoto University, Japan

LOADING & BOUNDARY CONDITIONS

The foundation or base of the RC frame for both BF & IF model is assumed to be fixed. So, all the nodes on the base are restrained for all degrees of freedom (DOF). The BF and IF model of the structure in ANSYS software is shown below in Fig.7 & 8.

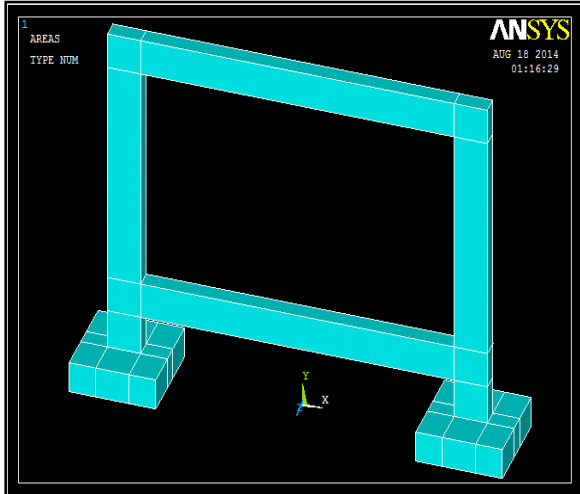


Fig.7: Bare Frame Model in ANSYS for Aspect Ratio 0.7

For Infilled frame, contact pairs are formed between the target (TARGET 170) and contact elements (CONTA 174).

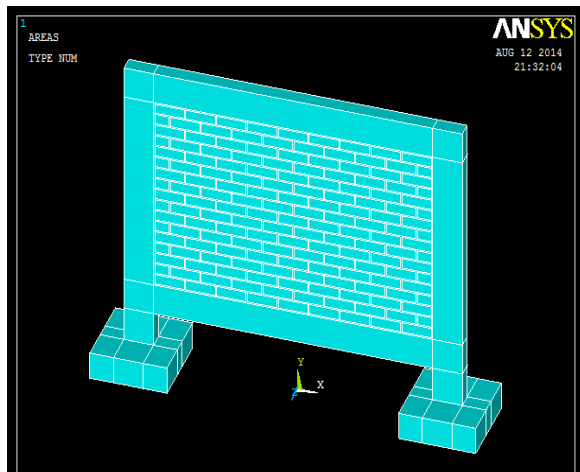


Fig.8: Infilled Frame Model in ANSYS for Aspect Ratio 0.7

At first a separate contact pair was formed between the outer layer of the RC frame and the inner layer of the brick masonry infill. The second contact pair was formed between the horizontal beds of brick as target element and horizontal beds of

mortar as contact element. The contact elements are provided so that when the load acts, there will be interaction between the frame and the infill.

Modal analysis was performed on the BF and IF models. From the analysis, the dynamic properties (natural frequencies and mode shapes) of the structure can be determined. In the present study, Block Lanczos Eigen solver is used for solution. This is an efficient algorithm which is suitable for modal analysis of large models. The dynamic properties obtained from the analysis, provide insight into the possible causes for vibration problems and therefore they can be used as a basis for quality assurance in the design analysis.

The resonance frequency values that are obtained from the shake table tests are imported in the model as frequency range in ANSYS, and the modal analysis were carried out. The first 3 mode shape frequencies of both BF and IF models are listed below in table 6.

Table 6: First 3 mode shape frequencies of BF and IF models

Aspect Ratio (AR)	Frequency (Hz)	
	Bare Frame	Infill Frame
0.7	28.105	38.532
	28.245	38.55
	28.428	38.569
1.0	24.237	17.004
	24.267	17.024
	24.337	17.059
1.3	16.063	10.009
	16.091	10.113
	16.241	10.023

CONCLUSIONS

The following conclusions are deduced from the shake table tests:

- The resonance frequencies of the IF are around 1.5 times as that of BF.
- As the AR increases, the resonance frequency decreases for both BF & IF, increasing the percentage of damping simultaneously.

4th International Engineering Symposium - IES 2015

March 4-6, 2015, Kumamoto University, Japan

- It is found that aspect ratio plays an important role in the behaviour of masonry infills.
- The frequency values are higher, even for lesser acceleration of input in Y-axis (out-of-plane), when compared to X – axis (in-plane).
- The need for damping increases in the out-of-plane direction.
- When the frequencies of BF, when compared with IF, it has increased from 28 Hz to 38.5 Hz (AR 0.7), in X-axis and has reduced from 7.5 Hz to 4 Hz in Y-axis respectively, due to the additional mass in the IF.

The following conclusions are deduced from the analytical modeling,

- Detailed micro-modeling provides better insight to the real time application of the masonry.
- The frame- infill interaction needs to be taken into account when the lateral loads are being applied to the structure.
- When the experimental results are compared with analytical results the values are almost similar due to the detailed modeling of masonry.

[6] Akanshu Sharma, Reddy G.R and Vaze K. K (2012), "Shake table tests on a non-seismically detailed RC frame structure", Structural Engineering and Mechanics, Vol. 41(1), pp.1-24

[7] Yunus Dere, Fatma Tuba Dede., (2011), "Nonlinear finite element analysis of an R/C Frame under lateral loading", Association for Scientific Research, 16, 947-958.

[8] Patil S.S., Manekari S.S., (2008), "Analysis of Reinforced Beam-Column Joint subjected to Monononic Loading", International Journal of Engineering and Innovative Technology (IJEIT), Vol.2 (10), ISSN 2277-3754.

[9] Antonio F. Barbosa and Gabriel O. Ribeiro (1998), "Analysis of reinforced concrete structures using ANSYS Non-linear concrete model", Federal University of Minas Gerais.

REFERENCES

- [1] Mallick, D.V. and Severn, R.T.,(1967), "The Behavior of Infilled Frames under Static Loading", Proceedings of ICE, 39(113), pp. 639-656.
- [2] Dhanasekar, M and Page, A.W., (1986), "Influence of brick masonry infill properties on the behaviour of infilled frames", Proceedings of ICE, Part 2, pp. 593-605.
- [3] Ali, S. Sk. and Page, A.W., (1988), "Finite Element Model for masonry subjected to concentrated loads", The Journal of Structural Engineering, 114(8), pp.1761-1784.
- [4] Asteris, P.G. (2008), "Finite Element Micro-Modeling of Infilled Frames", Electronic Journal of Structural Engineering, Vol.8, pp.1-11.
- [5] Lourenco, P.B., Rots, J. G., Johan B., (1995), "2 approaches for the analysis of masonry structures: micro and macro-modeling", Heron Journal, Vol.40 (4), ISSN 0046-7316.

Rheology and strength behaviour of selfcompacting concrete with ternary cementitious materials

H Sharada Bai Bharathi Ganesh , Vijaya Kumar Madapur

1. Faculty of Engg – CIVIL, UVCE, Bangalore University, Bangalore – 560056, Karnataka, India, E Mail - sharadaj29@yahoo.com
2. Dept. of Civil Engineering, Global Academy of Technology, Bangalore - 560098, Karnataka, India, Email - bharathi.gan@gmail.com
3. Nagesh Consultants, Bangalore, Karnataka, India, Email -vijaymdr@gmail.com

ABSTRACT: Use of Binary and Ternary (Tertiary) cementitious materials are generally believed to enhance the performance of concrete. However, such studies on Self Compacting Concrete (SCC) are limited. The present investigation deals with the assessment of behaviour in terms of rheology and compressive strength of M40 grade Triple Blend Self Compacting Concrete (TBSCC) in which cementitious material is constituted by cement, fly ash and GGBS in three different proportions of 50:30:20 %, 33.33:33.33:33.33 % and 25:25:50%. The fresh properties and the compressive strength of TBSCC mixes are assessed and compared with Conventional SCC (CSCC) consisting of Cement and fly ash as cementitious materials in proportion of 70:30 % for curing periods of 7, 28 and 56days.

The results showed better rheological properties of TBSCC mixes in terms of Slump flow test, V-funnel test, J-ring test and L-box tests assessed as per EFFNARC specifications. The investigation also showed that SCC with Triple Blends of cement, fly ash and GGBS as cementitious materials exhibit comparable or slightly higher compressive strengths than the CSCC in spite of considerable reduction in amount of cement in total cementitious content, effectively utilizing the industrial by-products.

Keywords: Supplementary Cementitious Materials, Triple blend SCC, Industrial by-product, GGBS, Rheology and Strength

INTRODUCTION

Supplementary cementitious materials can be used for improved concrete performance in its fresh and hardened state. Concrete mixtures with high cement content increase the heat generation and are susceptible to cracking which can be controlled to a certain degree by using supplementary cementitious materials such as fly ash, slag and silica fumes. Triple Blend is the blend of Ordinary Portland Cement – OPC, Pulverized Fuel Ash - PFA, and Ground-Granulated Blast-Furnace Slag - GGBS[Sharada Bai 2013]. These materials enable the concrete industry to use a huge quantity of materials that would otherwise be land filled as waste reducing the consumption of Portland cement per unit volume of concrete.

The aim of the present investigation is to

study the effect of the use of Fly ash and GGBS together with cement as parts of total cementitious content in different combinations on fresh and hardened properties of Self Compacting Concrete (SCC). This study is taken up as the literatures on the studies on Self Compacting concrete in which both Fly Ash as well as GGBS along with cement form the total cementitious content are scanty.

Materials Used

Cementitious materials – Cement, Flyash and GGBS are used as cementitious materials in different proportions.

Cement

In the present work, Ordinary Portland Cement of 43 grade conforming to IS 12269:1987 was used. The OPC with Physical properties such as specific gravity of 3.14, fineness of 7.446% and

4th International Engineering Symposium - IES 2015

March 4-6, Kumamoto University, Japan

Soundness by Le-chattelier's apparatus of 1mm showed that the properties are within the codal specified range of values as per IS 8112-1989.

Fly ash

Fly ash was collected from Bellary Thermal Power Station (BTPS), Karnataka. The physical and chemical properties of this Fly ash got tested by a standard Laboratory as per IS: 1727 - 1967 (Reaffirmed 2004) are specific gravity of 2.10, specific surface of $410.0 \text{ m}^2/\text{kg}$ by Blaine's Air-Permeability method, as fineness, lime reactivity of 4.6 N/m^2 and residue on 45 microns sieve of 18.4%. Chemical contents were 57.65% of Silica, 26.90% of Alumina, CaO of 2.32% and loss of ignition of 1.0%. Physical and Chemical properties of Fly Ash show that properties are within the codal specified range of values.

Ground Granulated Blast Furnace Slag (GGBS)

GGBS from Bellary JINDAL steel plant, Karnataka was also used as part of cementitious content in SCC. The physical and chemical properties determined are within the codal specified range of values as per IS 12089-1987 (reaffirmed 2008). They are Specific gravity - 2.9, fineness - 3.9%, insoluble residue - 3.58%, manganese oxide of 0.35%, Magnesium Oxide of 9.97% and sulphide sulphur of .71%.

Aggregates

The details of Fine Aggregate (FA) and Coarse Aggregate (CA) used are as follows

Natural river Sand

Locally available clean river sand obtained from Kaveri river bed near Kanakapura Taluk conforming to specification IS: 383-1970 (zone-II) was used. The physical properties and Sieve Analysis results of Natural River Sand are given in Table 1.

Coarse Aggregate

The granite metal jelly of 12.5mm passing (60%) and 10mm passing (40%) obtained from stone crusher near Bidadi was used as Coarse Aggregate. The sieve analysis of coarse aggregates conforms to well graded aggregates as per the specification of IS 383: 1970 and specific gravity of Coarse

Aggregate is 2.739. The properties of FA and CA are presented in table 1.

Water and Chemical Admixture

Potable water available in the laboratory satisfying the codal requirements [IS 456-2000] was used for mixing SCC. Commercially available Poly-Carboxylic Ether (PCE) based Super plasticizers was used to get required workability of concrete without increasing water demand.

Mix Proportions

SCC with cementitious content of $440\text{kg}/\text{m}^3$ (\approx M40 grade) was considered for the study and design mix was obtained using Absolute Volume method.

For **Triple Blend SCC**, four types of mix proportions were considered by varying the proportions of the three cementitious contents Cement, Fly Ash and GGBS by weight. In the **Mix-1 (Conventional SCC-CSCC)** the cementitious materials used were Cement and Fly Ash only in 70:30 ratio i.e. 30% of cement was replaced by Fly Ash. In the **Mix 2 (Triple Blend SCC - TBSCC-1)** the cementitious contents used were 30% Fly Ash and 20% GGBS as replacement to Cement. In the **Mix 3 (TBSCC-2)** 33.33% Fly Ash and 33.33% GGBS were used as replacement to Cement Content. Finally, in **Mix 4 (TBSCC-3)** cement was replaced by 25% Fly Ash and 50%GGBS. The design mix details are as presented in the table 2 and table 3.

Test Conducted and Results Obtained

The fresh properties of different SCC were assessed as per EFNARC 2005 and compressive strength as per IS516-1959 (reaffirmed in 1999). The test results of SCC in its fresh state and hardened state are presented.

Results of rheology of mixes measured using tests on Slump flow, J-ring, V-funnel and L-box are tabulated in Tables 4. The results of Compressive strength of Triple Blend SCC are tabulated in Tables 5 followed by the discussion on test results in comparison with Conventional SCC of M40 grade for different curing periods.

Rheology of TRSCC and NSCC Mixes

As per EFNARC, the **slump flow** and **slump flow time (T50)** ranging from

4th International Engineering Symposium - IES 2015

March 4-6, Kumamoto University, Japan

650-800 mm and 2 to 5 seconds respectively are considered adequate for a SCC. It can be seen that the slump flow obtained in the above test is in the range of 660-690mm. The slump flow obtained for Mix-4(TBSCC-3) is maximum i.e., 685.3 mm due to increased replacement level of cement with GGBS (Table 4). If the concrete has higher slump flow value it means the SCC is good in workability. Similarly for **time T50** sec i.e., time to flow 500mm diameter from the above test is in the range of 3-5sec. The time T50 required for mix 4 is minimum i.e., 3.6sec while the T50 time for mix 2 & 3 are 5.3 and 4.56sec. Hence the time required to flow 500mm diameter is decreased with the higher replacement level of GGBS.

As per EFNARC, **J-Ring** values (difference in height) ranging from 0-10 mm is considered adequate for SCC. It can be seen that the J-Ring values obtained in the above test are in the range of 3-5mm. The J-Ring value obtained for Mix-4 is minimum i.e., 3.8mm among TBSCC mixes due to higher replacement level of cement with GGBS (Table4). Test results of this investigation indicate that all the above SCC mixes meet the requirements of allowable limit for J-ring test (EFNARC, 2005).

V-Funnel Test - It can be seen that both V-funnel time and V-T5 time of all the above SCC mixes meet the requirements of allowable limit for V- funnel test (EFNARC, 2005). The V-funnel time obtained for mix 4 is minimum i.e., 7sec while for mix 2 & 3 is 8.8 and 8.4sec as compared to Conventional SCC (Mix 1) due to higher replacement level of cement with GGBS (Table 4).

L-Box Test From the above results it can be seen that the ratio of heights at beginning & end of flow for the above test is in the range of 0.83-0.96 which meet the requirements of allowable limit 0.8-1.0 for L-Box test (EFNARC, 2005). The ratio obtained for Mix-4(TBSCC-3) is 0.83 while the flow for Mix-2 & 3 is 0.96 & 0.92 (Table 4). If the ratio is less, it means that the concrete can easily pass through congested reinforcement.

From results of all the above fresh state tests (Slump flow test, V-funnel test, J-ring test and L-box test), it can be seen

that the TBSCC-3 (Mix 4) showed better workability as compared to other Triple Blend SCC mixes and Conventional SCC due to higher GGBS content present in it.

Compressive Strength of TRSCC and NSCC Mixes

The test results of compressive strength of M40 grade TBSCC are compared with Conventional SCC -NSCC for three curing periods of 7, 28 and 56days (table 5). Compressive Strength Ratio CSR-1 is the ratio of compressive strength of TBSCC concrete with respect to Conventional SCC at a particular age as presented in Figure4.

From the results of the tests, it can be seen that at any curing period all TBSCC gradually show higher strength than CSCC. For any particular curing period, increase in the percentage of GGBS, gradually increases the compressive strength in SCC up to 50% replacement of GGBS (Maximum considered in the present study). Therefore from Table 5 and figure 3 it can be seen that compressive strength is higher for mix 4 (TBSCC3) when compared to mix 2 & mix 3. This may be due to GGBS being finer than Fly Ash when mixed with cement & water forms a fine paste, which fills majority of the pores and reduces voids there by resulting in dense concrete.

From the earlier investigations (Donald Burden E, 2006) it was proved that the compressive strength decreased with an increase in the percentage of Fly Ash content in SCC. Even though the higher percentage of Fly Ash decreased the compressive strength, the ternary use of FA with GGBS for partial replacement of Cement, is found to mostly improve the compressive strength of the SCC. So that Mix-3 (TBSCC-2) and Mix-4 (TBSCC-3) show higher compressive strength values than those of the Conventional SCC especially at 56 days (Figure 5). The SCC containing 50% GGBS and 25% Fly Ash shows approximately 20% higher compressive strength than the Conventional SCC at 56 days curing (TBSCC-3). In a similar way, 33.33% GGBS and 33.33% Fly Ash shows approximately 12% higher compressive strength than the Conventional SCC at 56

4th International Engineering Symposium - IES 2015

March 4-6, Kumamoto University, Japan

days curing (TBSCC-2). Depending mainly on the replacement level, the concretes with Triple Blends exhibit comparable or slightly higher compressive strengths than the Conventional SCC in spite of the reduced cement in total cementitious content.

The 7days and 56 days strength of Conventional SCC i.e. CSCC is about 69% and 110% of the 28 days Strength respectively. The 7days and 56 days strength of Triple Blend SCC i.e. TBSCC-3, is about 80% and 121% of the 28 days Strength respectively (Table 5).

Using Fly Ash and GGBS in concrete is more sensitive to curing condition than Conventional SCC. Due to lower hydration rate of Fly ash and GGBS, curing time should be prolonged than CSCC. The hydration of GGBS requires Ca(OH)₂ from Portland cement hydration, and it will not start until the hydration of OPC has taken place. Therefore SCC containing Fly Ash and GGBS usually exhibit longer setting times and lower early strength and show higher later strength, and denser microstructure than NSCC. However, in the present investigation both 7 days and 56 days strength gaining of all TBSCC was higher than that of CSCC and higher content of GGBS than Fly Ash seem to increase the strength at both 7 days and 56 days.

Similarly the rheological test results indicate that the presence of Fly Ash is necessary to achieve and/or to improve SCC attributes in SCC with GGBS[Sharada 2011]. So it was recognized that concrete would gain strength with the secondary hydration of pozzolanic materials (Fly Ash and GGBS) even after 28 days.

Hence Mix-3 (TBSCC-2) and Mix-4 (TBSCC-3) show higher compressive strength values than those of the Conventional SCC especially at 56 days (Table 5.5). The SCC containing 50% GGBS and 25% Fly Ash shows approximately 20% higher compressive strength than the Conventional SCC at 56 days curing (TBSCC-3). In a similar way, 33.33% GGBS and 33.33% Fly Ash shows approximately 12% higher compressive strength than the Conventional SCC at 56 days curing (TBSCC-2).

Conclusions

From the discussions on the results, the following conclusions may be drawn.

1. All the triple blend and Conventional and Conventional SCC mixes meet the requirements of allowable limits for fresh state properties namely Slump test, Slump flow time-funnel test-Ring values and L-Box values as per the EFNARC-2005.
2. From the results of fresh state properties of TBSCC mixes, it can be seen that the TBSCC-3 (Mix-4) showed the better workability as compared to the TBSCC and Conventional SCC due to higher GGBS content present in it.
3. For any particular curing period, increase in the percentages of GGBS, gradually increases the compressive strength in SCC up to 50% replacement of cement by GGBS.
4. The 7 days and 56 days strength TBSCC-3 (Mix-4) is about 80% and 121% of the 28 days strength respectively, and about 9.6% and 20% higher compressive strength than CSCC.

Triple blend SCC with fly ash and GGBS is a viable offer and with in the scope of the test the best proportion of cementitious contents (cement, fly ash and GGBS) by weight seems to be to be 25:25:50.

4. References

- [1] Sharada Bai , H, Bharathi Ganesh Kowshika V.R. . "Workability Retention of Triple Blend Self Compacting Concrete" Proceedings of UKIERI Concrete Congress, Innovations in Concrete Construction, 5 - 8 March2013,
- [2] Donald Burden, "The Durability of Concrete Containing High Levels of Fly Ash", Research and Development Information, PCA R&D Serial No. 2989, Janaury 2006
- [3] EFNARC 2005 - European SCC Guidelines (2005), Specifications and Guidelines for self Compacting Concrete.
- [4] IS: 456-2000, "Code of practice for plain and reinforced cement concrete".
- [5] IS: 10262- 2009, Indian standards, "Recommended Guidelines for Concrete Mix Design"

4th International Engineering Symposium - IES 2015

March 4-6, Kumamoto University, Japan

- [6]IS:516-1959 Indian Standard Methods of Test for Strength of concrete. Bureau of Indian Standards, New Delhi.
- [7] IS: 12269-1987, Indian Standard "Specifications for 53 Grade Ordinary Portland Cement".
- [8] IS: 383 - 1970, Indian Standard "Specifications for Coarse and Fine Aggregates From Natural Sources for Concrete".

[9]Sharada Bai H, Bharathi Ganesh, Nagendra R, "Effective utilisation of pond ash for sustainable construction – need of the hour", International Journal of Earth Sciences and Engineering ,Volume 04, No 06 SPL, pp 151-154,October 2011.

Tables & Figures

Table 1 Physical Properties of Fine Aggregate and Coarse Aggregate

Sl. no	Physical properties	FA		CA	
		Specific gravity	2.617	Fineness modulus	2.739
1	Loose Bulk density(kg/m ³)	2.85	1372	6.29	1437
2	Rodded Bulk density(kg/m ³)	1573	1550		
3	Moisture content	2.0%	2.5%		
4	Water Absorption	0.8%	2.5%		
5	Zone	II	Well graded		
6					

Table 2- Mix proportions of M40 grade Triple blend SCC and Conventional SCC

Sl. No	Concrete Type	Designation of the Mix	cement		Fly ash		GGBS		Kg/m ³
			%	Kg/m ³	%	Kg/m ³	%	Kg/m ³	
1	NSCC	CSCC	70	308	30	132.0	-	-	440.0
2	TBSCC	TBSCC-1	50	220.0	30	132.0	20	88	440.0
3		TBSCC-2	33.33	146.52	33.33	146.52	33.33	146.52	440.0
4		TBSCC-3	25	110.0	25	110.0	50	220	440.0

Table 3 – Design Mix in proportions for Triple blend SCC and Conventional SCC

Designation of the Mix	Total Cementitious content	Fine Aggregate	Coarse Aggregate	Water	SP Dosage
CSCC	1.00	2.21	1.49	0.46	1.0
TBSCC-1	1.00	2.29	1.53	0.46	1.1
TBSCC-2	1.00	2.29	1.53	0.46	1.2
TBSCC-3	1.00	2.29	1.53	0.46	1.2

Table 4 Rheology of Mixes of CSCC and TBSCC

Mix No.	Designation	Slump flow		Difference in height- J ring (mm)	V-funnel Time Sec	V-funnel Time-T5 Sec	L-box Blocking ratio
		Flow (mm)	T50 (sec)				
1	CSCC	661.0	4.2	3	8.4	12.1	0.90
2	TBSCC-1	645.6	5.3	4.75	8.8	12.3	0.96
3	TBSCC-2	671.0	4.56	4.7	8.42	12.0	0.92
4	TBSCC-3	685.3	3.6	3.8	7.0	11.01	0.83
Specifications as per EFNARC 2005		650-800	2-5	0-10	6-12	9-15	0.8-1.0

Table 5 Compressive Strength of M40 PRSCC and NSCC Mixes

Mix No.	Designation	Cement	Fly Ash	GGBS	Compressive strength (N/mm ²)		
		%	%	%	7 days	28 days	56 days
1	CSCC	70	30	-	25.62	36.88	40.88
2	TBSCC-1	50	30	20	26.22	32.44	41.185
3	TBSCC-2	33.3	33.33	33.33	29.03	37.480	45.777
4	TBSCC-3	25	25	50	32.50	40.44	49.03



Figure 1 Rheology of TBSCC and NSCC Mixes

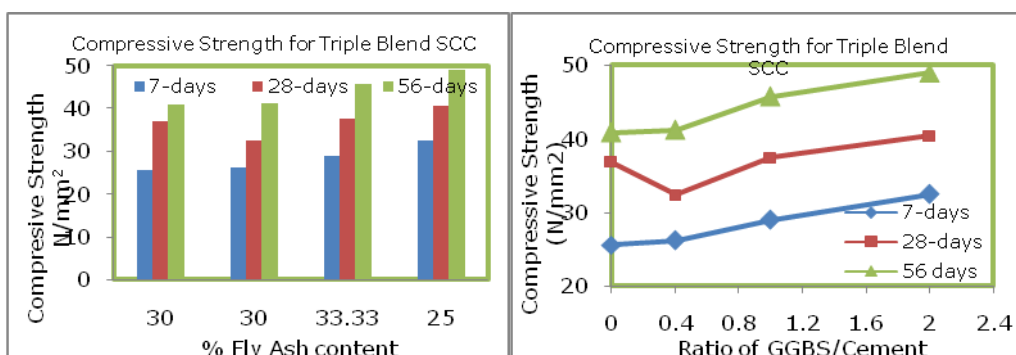


Figure 2 - Compressive Strength of M40 TBSCC Mixes- Effect of Fly ash content

Figure 3 - Compressive Strength of M40 TB SCC Effect of ratio of GGBS/Cement contents

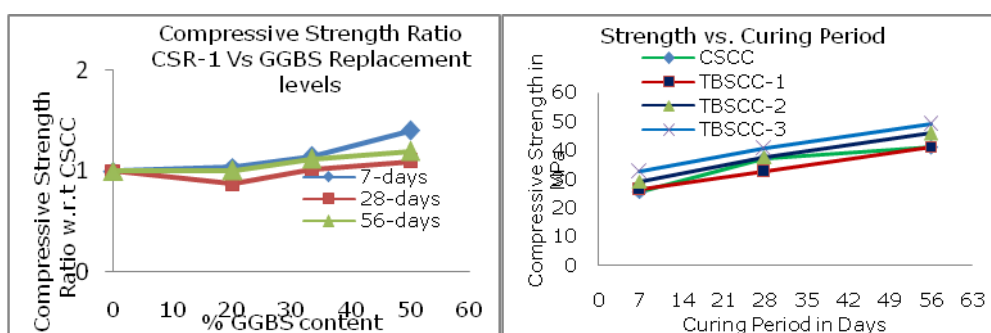


Figure 4 - Compressive Strength Ratio CSR-1 Vs % GGBS Content

Figure 5 Compressive Strength of M40 Triple Blend SCC w.r.t Different Curing Periods

Bond Strength Assessment of Self Compacting Concrete Containing Pond Ash and Manufactured Sand as Fine Aggregates

Bharathi Ganesh, H Sharada Bai, R Nagendra, Harisha C and Krishna L

1. Faculty of Engg – CIVIL, UVCE, Bangalore University, Bangalore – 560056, Karnataka, India, E mail - sharadaj29@yahoo.com
2. Dept. of Civil Engineering, Global Academy of Technology, Bangalore - 560098, Karnataka, India, Email – bharathi.gan@gmail.com
3. Civil-Aid Technoclinic Pvt. Ltd, Bangalore, Karnataka, India rnagendraramaswamy@yahoo.com, nr.ctpl@gmail.com
4. Practicing Engineer, Bangalore. E Mail-harish.555.hsc@gmail.com
5. V S Consultants, Bangalore, Karnataka, India, Email-kris_gowda007@yahoo.com

ABSTRACT: This paper deals with evaluation of bond strength of Self Compacting Concrete (SCC) mixes with cementitious content of 400 kg/m³ in which Manufactured Sand (M sand) is replaced by pond ash – a Thermal Power Plant waste at an optimum replacement range of 0, 10, 20 and 30 Replacement Levels (RL) by weight. The Pond Ash Replaced SCC (PRSCC) cube specimens of 150mm sides, reinforced with 20mm dia. TMT bars are tested as per IS 2770 (Part I) – 1967.

The results showed that the bond stress of PRSCC mixes measured at different slips and at failure are slightly less than that of Normal SCC (NSCC) mixes with variation of 4, 17 and 18% at 10, 20 and 30% RLs respectively in comparison with NSCC mixes i.e., at 0% correspond to the reduction in rheology and compressive strength of PRSCC mixes.

The failure behaviour of both PRSCC and NSCC specimens are associated with brittle mechanism, governed by a mixed splitting-pull out behaviour, involving formation of two or more radial splitting cracks around the bar showing that the PRSCC up to 20% replacement level performs almost similar to NSCC.

Keywords: Alternative Materials, Fine Aggregate, Bond Strength, Replacement levels

INTRODUCTION

Performance of reinforced concrete is based on an effective bond between concrete and the reinforcing bars. The concrete bond strength should be sufficient to prevent bond failure. The effectiveness of bond depends on the position of the embedded bars, its diameter, type, grade and the quality of concrete, the materials used for concrete and an adequate concrete cover. In order to properly transfer bond stresses between steel and concrete, it is necessary to avoid poor quality of materials, bleeding and segregation of the concrete during placing, compacting it etc., Pond Ash, a waste product of Thermal Power Plants, is one such material, that can be adopted as a suitable material as Fine aggregate in concrete/SCC, replacing Natural Sand/M sand partially or fully[Bharathi Ganesh

2012]. Hence this paper is aimed at evaluating bond strength of Self Compacting Concrete – SCC containing pond ash - a Thermal Power Plant Waste as fine aggregate, replaced for M-Sand at different percentage of replacement levels. It is possible however, to produce an SCC without adding any extra fine material [Goodier C I 2003] and replacing cement with other industrial by-products which reduce cost without compromising in its quality.

Literature Review

Though many studies on use of pond ash in sintered applications, structural fills, geotechnical applications, clay-fly ash bricks (burnt type), agricultural applications etc., are available worldwide, research work related to application of pond ash as a constituent material of

4th International Engineering Symposium - IES 2015

March 4-6, Kumamoto University, Japan

mortar and concretes is not considerable. SCC is in great demand in the industry. Successful utilisation of pond ash as fine aggregate in SCC can enhance the use of huge amount of pond ash in not only onsite constructions but also in the precast industry[Bharathi Ganesh 2011]. This motivates investigation on the use of pond ash as fine aggregate in SCC. Study on bond strength is essentially to evaluate the feasibility of using pond ash in RSCC - Reinforced SCC.

Materials and Their Characterisation

The tests on various properties of the materials used for SCC mixes carried out as per the relevant codes of practice are as follows.

Ordinary Portland Cement - OPC 53 grade with specific gravity of 3.15 and all other properties conforming to IS 12269-1987 was used for SCC. Pulverized fuel ash obtained from RTPS conforming to specification - IS 3812, Part (1 & 2) - 2003 and testing requirements conforming to IS1727 - 1967, with specific gravity 2.2 and fineness (specific surface by Blaine's air-permeability method) of 328 m²/kg, were used as fines which contribute to the powder content of SCC.

Clean potable water available in the laboratory satisfying the requirement as per IS 456-2000 was used for preparation of SCC. PC based admixture - Superplasticizer was used in required dosage to get the rheology of SCC mixes. Coarse Aggregates (CA) of size 20 and 12.5 mm passing conforming to specification IS 383:1970 and also to testing requirements as per IS 2386 Part I were used for SCC mixes (table 1).

The pond ash samples from ash pond II, RTPS was found suitable [Bharathi ganesh 2013]as fine aggregate (FA), was used replacing manufactured sand partially in SCC. Pond ash is coarser in particle size having fineness of 178.0 m²/kg as specific surface by Blain's Air permeability method. The physical properties of aggregates are presented in table 1.

The chemical contents of pond ash are almost in line with that of fly ash with 93.70 % (>70) of (SiO₂ + Al₂O₃ + Fe₂O₃), 60.08% (\geq 35) of SiO₂ and Loss of Ignition

of 2.60MPa (\leq 5) when tested and compared as per the requirements of IS 3812 -2003 for fly ash.

Mix Design

SCC mix is designed using absolute volume method for 400kg/M³ of cementitious content-CC (70%Cement+30%Fly ash) to get a design mix of C:FA:CA=1:2.42:1.98 with w/c = 0.45. The M sand content of FA is replaced with pond ash from 0-50% to evaluate rheology and compressive strength. The bond strength was evaluated at an optimum replacement range of 0-30%.

Rheological Behaviour of Pond Ash Replaced SCC - PRSCC

The main characteristics of SCC are the properties in the fresh state tested for its filling ability, passing ability and segregation resistance to be tested as per EFNARC 2005. The comprehensive results of various tests on rheology namely, slump flow test, T 50 time, J ring test , V funnel test and L box test, carried out to study the behaviour of PRSCC mixes in fresh state, in comparison with that of NSCC mixes are presented in table 2 along with their specifications as per EFNARC 2005.

Inferences on Rheological Properties of SCC Mixes

From the results of tests on rheology of PRSCC mixes in comparison with NSCC mix and also with the specifications as per EFNARC 2005 presented in table 2, the following observations are made.

1. Results of various tests on rheology of PRSCC mixes are comparable with that of NSCC mixes at different replacement levels of M sand by pond ash. The results are with in the specified range of values as per EFNARC 2005(table 2).
- 2.The PRSCC mixes were slightly harsh and became more viscous as the replacement level of M - sand by pond ash increased[Sharada Bai 2013]. There was slight reduction in the cohesiveness of the mixes at higher percentages of replacement levels. This may be due to the presence of irregularly shaped and lumped particles of pond ash, relatively coarser having vesicular texture which

might have reduced the flow rate of SCC due to inter particle friction, making it slightly viscous.

Properties of Hardened PRSCC Mixes - Compressive Strength

The compressive strength of PRSCC mixes upto RL of 50 % in increments of 10%, at cementitious content of 400 kg/m³ and NSCC mixes at the same cementitious content are evaluated for cubes of 150 mm sides as per the standard procedure of IS 516- 1959 (reaffirmed1999). The specimens cast and cured in water were tested under a constant loading rate of 140 kg/sq cm/min until the specimen fails and failure load was recorded. The results of compressive strength test of PRSCC mixes upto RL of 50 % and that of NSCC mix at cementitious content of 400kg/m³ at 28 days curing period are presented in table 3 along with ratio CR₁ where CR₁ is the relative strength of PRSCC mixes at different RLs at curing period of 28 days in terms NSCC mixes (fig.2).

Inferences on Compressive Strength of PRSCC and NSCC Mixes

1. The compressive strength of PRSCC mixes at different RLs is found to be less than that of NSCC mixes and decreases as RL increases (table 3, fig.1). The reduction of only 8% is found at RL of 30%.
2. For RL of pond ash higher than 30%, the compressive strength in comparison to NSCC, reduces at a higher rate, being min at RL of 50%. The strength reduction of PRSCC mixes at 50% RL is 26% of that of NSCC (fig.2).
3. The compressive strength decreases with increase in RL of pond ash. The strength of PRSCC mixes up to RL of 30% are comparable with that of NSCC, with the maximum reduction amounts only to 9% at 20% replacement level. This behaviour corresponds to the rheological properties of PRSCC mixes upto 30% RL1. Hence 0% - 30% can be said to be the optimum replacement range of pond ash to replace M-Sand at CC 400kg/m³ with a reduction of < 10% in strength, which can be addressed during trial mix of SCC. Further, bond strength is evaluated for PRSCC mixes upto 30% replacement levels.

Properties of Hardened PRSCC Mixes - Bond Strength

The bond test (pull out test) is conducted as per IS 2770 (Part I) – 1967. The cube specimens of 150mm sides were prepared using standard procedure with a helix of 6 mm diameter plain mild steel bar at 25 mm pitch. 20mm dia. TMT bars were (figure 3a, b). The specimens were cured for 28 days. The test specimen were loaded axially at rate of loading not greater than 2.250 kg/mm(fig.4a, b). The slip at the loaded and unloaded ends were measured carefully using the Demec gauge at a regular intervals corresponding to 0.1 kN increment of loading and also at slips of 0.025 mm, 0.25 mm until, either the yield point of the reinforcing bars has been reached, or enclosing concrete has failed (the type of failure is noted), or a minimum slippage of 2.5 mm has occurred at the loaded end. The load for each type of failure i.e., a) at a slip of 0.025 mm at the free end, b) at a slip of 0.25 mm at the free end and c) at failure was recorded.

The average bond stress is the value obtained for each specimen by dividing the applied load at the slip specified, by the surface area of the embedded length of the bar ($f_{bond} = P/nld$) and then taking the average value for the group of each type of bar in the test series.

The results of the bond test conducted on PRSCC mixes for RLs of 0, 10, 20 and 30% of M sand by pond ash for CC of 400 kg/m³, presented in table3.

Inferences - Bond Strength Behaviour of PRSCC Mixes

From the results of bond test i.e., bond stress corresponding to different slips and also at failure of bond of PRSCC specimens up to RLs of 30% and comparing those with that of NSCC specimens, the following observations are made.

The values of bond stress at failure of PRSCC mixes are slightly less than that of NSCC mixes with variation of 4.0, 17.0 and 20% at RL of M sand by pond ash of 10, 20 and 30% respectively for CC of 400 kg/m³.

Reduction in the failure bond stress of PRSCC mixes at different RLs correspond

4th International Engineering Symposium - IES 2015

March 4-6, Kumamoto University, Japan

-
- to the reduction in compressive strength of PRSCC mixes.
3. The values of bond stress of pond ash replaced SCC mixes with RL upto 10% are comparable with normal SCC mixes with very less variation in the values at .025mm slip, 0.25mm slip and also at failure load. However, variation is upto 20% at RL of 30% of M sand by pond ash in SCC.
4. It is observed during the test that, the failure behaviour of both PRSCC and NSCC specimens is associated with brittle mechanism, governed by a mixed splitting-pull out behaviour, involving the nearly simultaneous formation of two or more radial splitting cracks around the bar and the development of the crushing of the concrete.
Hence pond ash replaced SCC up to 20% replacement level performs similar to normal SCC.
- ### Conclusions
- From the discussions on the test results, the following conclusions can be made.
Pond ash is found to be suitable as FA in concrete (Ranganath R V1999] and SCC.
1. Results of various tests on rheology, compressive strength of PRSCC mixes are comparable with that of NSCC mixes at different replacement levels of M sand by pond ash satisfying the requirement of rheology as per EFNARC 2005.
 2. The PRSCC mixes were slightly harsh and became more viscous as the replacement level of M - sand by pond ash increased.
 3. The compressive strength of PRSCC mixes at different RLs is found to be less than that of NSCC mixes and decreases as RL increases. The reduction of 8% is found at RL of 30%, and 26% at 50% RL in comparison with NSCC mix. Hence 0% - 30% can be said to be the optimum replacement range of pond ash to replace M-Sand at CC 400kg/m³ with a reduction of < 10% in strength, which can be addressed during trial mix of SCC.
 4. The values of bond stress of pond ash replaced SCC mixes with RL upto 10% are comparable with normal SCC mixes and variation is upto 20% at RL of 30% of M sand by pond ash in SCC.
 5. The failure behaviour of both PRSCC and NSCC specimens are associated with brittle mechanism, governed by a mixed splitting-pull out behaviour, involving formation of two or more radial splitting cracks around the bar showing that the PRSCC up to 10% replacement level performs almost similar to NSCC.

Acknowledgement

Authors are highly grateful to Dr. C S Viswanatha, Chairman Civil-Aid Technoclinic Private Limited (CTPL), Bangalore for supporting in respect of characterization of samples and also for conducting various tests in its NABL accredited laboratory, encouraging research activities.

References

- [1]Bharathi Ganesh, R, Nagendra, H. Sharada Bai, Shivaram Bagade, " Pond Ash: An Alternative Material as Fine Aggregate in Concrete for Sustainable Construction."International Journal Advanced Materials Research Vols. 306-307 (2011) pp 1071- 1075, 2011/Aug/16 at www.scientific.net (IJAMR2011)
- [2] Bharathi Ganesh, H. Sharada Bai, R, Nagendra, "Characterisation of Pond Ash as Fine Aggregate in Concrete", conference Proceedings International Conference on "Advances in Architecture and Civil Engineering - AARCV 2012" MSRIT, Bangalore , pp 119 – 128
- [3] Bharathi Ganesh, Krishna K L, R Nagendra, Sharada Bai, "Strength Assessment of SCC with Pond Ash as partial Replacement to Fine Aggregate " Proceedings of National Conference on New Horizon in Civil Engineering -2013, MIT, Manipal, Udupi, 13th-14th Apr 2013, pp 59-65.(NHCE 2013)
- [4]Goodier C I Development of self-compacting concrete, Proceedings of the Institution of Civil Engineers, Structures & Buildings 156, November 2003, Issue SB4, Pages 405-414.
- [5]IS12269-1987 (Reaff.2008)
"Specification for 53 grade OPC."
- [6]IS 2770-part I-1967 - Bond Resistance of Reinforcing Bars With Concrete.
- [7] IS 2386 Part II - Method of Test for Aggregates for Concrete
- [8] IS 456 - 2000 "Plain and reinforced concrete - code of practice" .

4th International Engineering Symposium - IES 2015

March 4-6, Kumamoto University, Japan

- | | |
|---|---|
| [9] IS 516 -1959 re aff 1999 - Test For Compressive Strength of Concrete. | [12] Sharada Bai H, Bharathi Ganesh, Dr. R. Nagendra, Dr. Krishna K L, Harisha C to Rheology of SCC with Pond Ash as Partial Replacement to Fine aggregate, Proceedings of "International Conference on Innovations in Concrete for Meeting Infrastructure Challenges, ICI -IWC 2013, Hyderabad , September – 2013. |
| [10] IS 383 - 1970 - Specifications for Coarse And Fine Aggregates From Natural Sources For Concrete. | |
| [11]Ranganath R V, Bhattacharjee B and Krishnamoorthy S, (1999), "Proportioning of Aggregate Mixes for Optimal Workability with Pond Ash as Fine Aggregate in Concrete", The Indian Concrete Journal, pp 441 – 449. | |

Table 1 Physical Properties of Aggregates

SI.No	Test Conducted	Coarse Aggregate		Fine Aggregate	
		20 mm	12.5 mm	M- sand	Pond Ash
1	Specific Gravity	2.72	2.70	2.69	2.02
2	Loose Bulk Density kg/m ³	1385.6	1408.01	1720.7	916.66
3	Rodded Bulk Density kg/m ³	1536.94	1543.1	1900	1042.5
4	Particles finer than 150µm			9.3%*	19.4%
5	Moisture Content	-	-	3.7%	
6	Water Absorption: Slump Cone Method Frying Pan Method	0.3	0.3	4.2%	10% 20.6%
7	Zone	Single Graded	Single Graded	Zone II	Nearly Zone IV

*For Manufactured sand, the requirement of cumulative percentage passing through 150 microns is [0-20]% as per IS 383-1970 (Reaff.2007) Max 3% for natural river sand .

Table 2 Rheological Properties of SCC mixes - 400 kg/m³

Sl. No	Name of the test	Replacement levels in % of M Sand by Pond Ash Cementitious Content - 400 kg/m ³			Specification as per EFNARC 2005
		0	10	20	
1	Slump Flow (mm)	690.00	690.00	695.00	600 - 800
2	T _{50cm} (Sec)	5.97	5.44	4.30	2 - 5
3	J Ring - Dia. mm	650.00	650.00	670.00	
4	J Ring - T50Sec.	6.43	5.74	6.89	0 - 10
	V-funnel (Sec)	7.85	7.85	6.02	8 - 10
5	L-box (h2/h1) mm	6.20/7.10	6.80/7.80	6.50/7.50	
	(Blocking Ratio)	0.87	0.87	0.87	0.8 – 1.0

Table 3 – Compressive Strength of PRSCC and NSCC mixes

Specimen Designation	Compressive Strength in MPa		CR ₁	
	RL in %	28days	28days	
4NS10/0	0	32.87	1.00	
4PRS9/1	10	30.98	0.94	
4PRS8/2	20	30.07	0.91	
4PRS7/3	30	30.20	0.92	
4PRS6/4	40	26.89	0.82	
4PRS5/5	50	24.89	0.76	

4th International Engineering Symposium - IES 2015
March 4-6, 2015, Kumamoto University, Japan

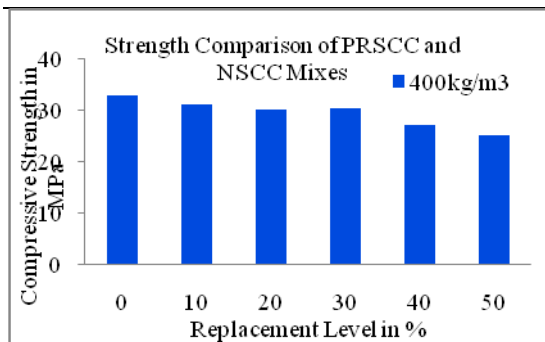


Figure 1 Cube Compressive Strength at 28 day of PRSCC and NSCC Mixes

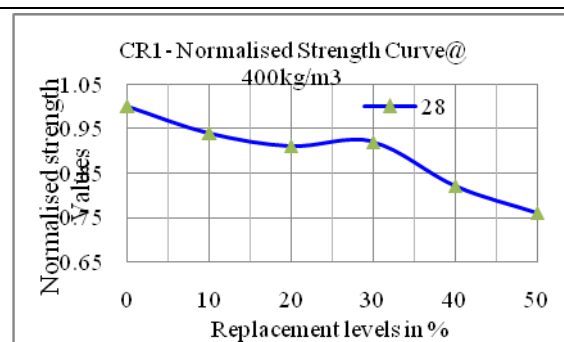


Figure 2 CR₁ Relative Strength of PRSCC Mixes at 28 day in terms of that of NSCC Mixes at Different Replacement Levels



Fig.3 (a) Cube Specimens Ready to Cast Reinforced with 6mm Dia. Helix (b) Close up



Figure 4(a) Fresh Concrete Bond Test Specimens and (b)Test Under Progress

Table 4 Bond Strength of PRSCC and NSCC mixes

Sl. no	Designation of specimen	Replacement Level in %	Bond stress in MPa at		
			0.025mm slip	0.25mm slip	failure
1	4NS10/0	0	5.4	8.5	10.1
2	4PRS9/1	10	4.9	9.4	9.6
3	4PRS8/2	20	5.3	7.4	8.3
4	4PRS7/3	30	4.6	7.0	8.0

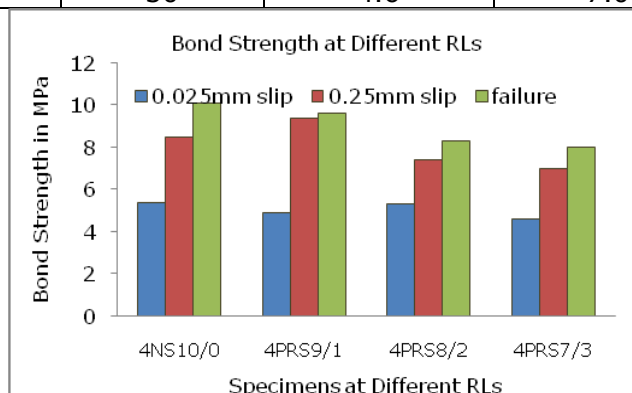


Figure 5 Bond Strength of PRSCC and NSCC mixes at Different slips.

Mitigation of Delayed Ettringite Formation in Concrete Structures

Amde M. Amde¹ and **Richard A. Livingston³**

1 Professor, Department of Civil and Environmental Engineering, University of Maryland, College Park, MD 20742, USA; amde@umd.edu

2 Adjunct Professor, Department of Material Science and Engineering, University of Maryland, College Park, MD 20742, USA; rliving1@umd.edu

ABSTRACT: The effects on delayed ettringite formation (DEF) of partially replacing the Portland cement by different amounts of Class F fly ash or using mix water conditioners (MWC) are discussed. Recent studies have shown that DEF may be associated with deterioration problems in concrete. Partially replacing the Portland cement with Class F fly ash decreased the expansion, with specimens showing larger reductions as the percentage of fly ash increased. The SEM results correlated with the observed expansions. The effect of using MWC was found to be similar to using 10% fly ash with respect to expansion but not with respect to compressive strength. Whether the growth of DEF in existing concrete can be mitigated was also investigated using water repellents and crystal growth inhibitors. Three of the four products showed positive results.

Keywords: crystal growth inhibitors, ettringite, delayed ettringite formation, fly ash, mix water conditioner, concrete durability

INTRODUCTION

The results presented in this paper are part of an ongoing comprehensive study on DEF that is being conducted at the University of Maryland, Amde et al (2005, 2005, 2004, 2004), Livingston and Amde (2000). The DEF problem first gained attention in Germany in the 1980's when DEF caused precast railroad ties to fail prematurely, Thomas (2001). Based on extensive analysis of available literature Day concluded that there appears to be a potential for secondary ettringite formation problem in North America given the current cement production and construction methods, Day (1992). The effects of expansion due to alkali silica reaction (ASR) and delayed ettringite formation (DEF) are well documented in laboratory experiments. DEF causes distributed micro cracking, loss of compressive strength, and reduced service life, Tepponen and Eriksson (1987), Shayan and Quick (1994), Heinz and Ludwig (1986, 1987, 1989).

To understand DEF, some discussion of the hydration process is required and of particular interest to this study is the hydration of aluminates, which is fundamental to the proper setting of concrete. Due to the rapid hydration of the aluminates ($3\text{CaO}\cdot\text{Al}_2\text{O}_3$), the cement paste would immediately harden not allowing the formation of the C-S-H gel. In order to form C-S-H gel, gypsum is added to the cement prior to the hydration process to retard the rapid hydration of aluminates. Retardation occurs because ettringite, $(3\text{CaO}\cdot\text{Al}_2\text{O}_3\cdot 3(\text{CaSO}_4\cdot 2\text{H}_2\text{O}) + 26\text{H}_2\text{O} \rightarrow 3\text{CaO}\cdot\text{Al}_2\text{O}_3\cdot 3(\text{CaSO}_4\cdot 32\text{H}_2\text{O})$, forms a coating around the $3\text{CaO}\cdot\text{Al}_2\text{O}_3$ particle, Collepardi (1978). The chemical reaction for the formation of ettringite in this stage is as follows:



As ettringite grows, the cement is still plastic and thus it can accommodate the expansive stresses. This initial formation of ettringite during the setting process is

4th International Engineering Symposium - IES 2015

March 4-6, 2015, Kumamoto University, Japan

sometimes called primary ettringite formation to distinguish it from delayed ettringite formation. Primary ettringite does not cause damage to the concrete, and after a period of days to weeks, the primary ettringite seems to disappear although what happens to its chemical constituents remains unclear. Some researchers think that the C-S-H gel of the concrete takes up the calcium aluminum and sulfate ions. Others believe that the ettringite transforms into another calcium aluminum sulfate phase called monosulfate. In a recent study, Stark et al. (2003) dispute the hydration model that results in monosulfate. Using Environmental Scanning Electron Microscope with Field Emission Gun (ESEM-FEG) they found that ettringite does not become unstable and does not gradually convert to monosulfate or tetracalciumsulfoaluminatehydrate. They conclude that both ettringite and tetracalciumsulfoaluminatehydrate are the final products of hydration of ordinary Portland cement.

The deleterious effects of DEF occur after the concrete has hardened when ettringite, for some reason, reforms and expands. The mechanism of expansion is not fully understood, but it is believed, that during the formation of the crystal, either the absorption of water into the crystal or the crystal growth causes the concrete to be stressed particularly at the aggregate/paste interface. Once the stress exceeds the interface tensile strength, a micro crack forms along the aggregate/paste interface, and if this process is extensive, micro cracking will lead to deterioration of the concrete matrix and reduction of the concrete strength.

Diagnosis of DEF in the field is made difficult because there is no nondestructive test for the presence of ettringite itself. Map cracking is a visible symptom of micro cracking, but it has been thought to occur only in the presence of ASR. Some have gone so far as rule out DEF in favor of ASR when map cracking is observed. If the association between ASR and map cracking is not unique, then the possibility of misdiagnosis exists.

DEF itself can only be confirmed by finding ettringite crystals in the concrete,

which utilizes a process that requires destructive sampling. State DOT's generally do not core concrete structures on a routine basis. Consequently, DEF has usually been found in samples from the field that have been taken from damaged structures in the course of forensic investigations. This is inherently a biased sampling method, and moreover since the investigation is done in the context of litigation, the interpretation of the results typically involves disputes among expert witnesses.

Despite the large amount of attention that has been paid to DEF in the literature and in technical meetings, there is very little actual data from the field that would make it possible to resolve the various controversies. Lawrence et al. (1999) document Texas Department of Transportation's (TxDOT) experience with DEF and premature concrete deterioration, and they indicate in several cases that DEF caused micro cracking leading to premature deterioration. In particular, 50 box beam bridge girders had to be rejected because they developed DEF while still in the precast plant yard. Gress (1997) studied the possible cases of DEF in pavements, mainly in Iowa. Many countries, including USA, South Africa, Egypt, United Kingdom, Germany and Scandinavia have reported deterioration of concrete structures where the main cause of distress has been identified as DEF. A recent study found different morphologies of ettringite in Maryland bridges, Amde et al. (2004).

OBJECTIVES

The objectives include studying the effect of adding different amounts of Class F fly ash, as a partial replacement of Portland cement, and the effect of adding mix water conditioner on the formation of DEF and its associated expansion. The objectives also included investigating whether the growth of DEF in existing concrete can be mitigated with commercial products such as water repellents and crystal growth inhibitors.

EXPERIMENTAL PROGRAM

In this series of the study, five batches of concrete specimens were prepared

4th International Engineering Symposium - IES 2015

March 4-6, 2015, Kumamoto University, Japan

according to the modified test method described below. All mixing materials and proportions were the same. Portland cement type III and Laurel sand were used. The first four batches differed only in the amount of Class F fly ash added to the mix as a partial replacement of cement, which were 0%, 10%, 20%, 30%. MWC was added to the last batch. One percent of potassium carbonate was added to all mixes to increase the alkali level, which also favors DEF. All the prisms and cylinders were water - cured. The prisms were subjected to the Duggan heat cycle described below one week after casting and subsequently immersed in water for the test duration. Cylinders from each set were prepared for compressive strength testing, which was measured at 28 days and 6 months.

The concrete prisms were monitored and the length changes of the prisms were measured during the test duration. All the samples showed expansion after the Duggan heat cycle. Concrete prisms made of a high percentage of fly ash showed the lowest expansion. The expansion results at 21 days were compared to threshold value of 0.05% expansion that was suggested by Duggan as a pass/fail criterion.

Scanning electron microscopy (SEM) and X-ray diffraction were used to detect ettringite at different intervals. Prior to SEM examinations, samples from the expanded prisms were coated with a thin film of carbon, which does not contain interfering X-ray fluorescence responses. The SEM was equipped with energy dispersive analysis X-ray (EDAX) to evaluate the elemental chemical composition of the samples. X-ray computed tomography (CT) was used as well to reveal the internal cracks.

Materials

Portland cement Type III, which is commonly used to produce high early strength concrete, was used in all specimens. This type of cement was chosen because it is suspected of being particularly susceptible to DEF. In comparison to other cement types, Type III cement has a higher sulfate content, which would favor the crystallization of ettringite Taylor (1994). All the cement

came from the same batch and was blended in a drum mixer.

Laurel sand, a highly reactive fine aggregate, and dolomite limestone, a non-reactive coarse aggregate with a maximum diameter of one inch, were used in all specimens. Potassium carbonate was added directly to the mix water at the rate of 1 % of the weight of cement, and water/cement ratio was maintained at 0.5. All specimens were water cured for one week after casting, subjected to the Duggan heat cycle and then stored in water.

Sample Preparation

The specimens used in this research differ from the core samples that are recommended for use in the Duggan test. Duggan suggested the use of cores 25 mm in diameter and 50 mm in length with parallel and smooth ends. The use of cores allows for sampling from a general source of concrete that may be of interest including existing structures. However, when laboratory specimens are used, this method of obtaining test samples is unduly arduous. Therefore, under this research program, a modified Duggan Sample Preparation method, proposed by UMD/FHWA, was used Amde et al. (2004). The modified sampling technique uses prisms (75 mm x 75 mm x 275 mm) cast from concrete mixed in a laboratory instead of the cores Duggan suggested. The prisms are made with end steel inserts for linear length change measurements following ASTM C192-88 and ASTM C1293.

The Duggan test heating cycle is an eight-day heating regimen with prescribed intervals of heating and cooling at specific temperatures and duration. The heating temperature is eighty-two degrees Celsius and the cooling temperature is twenty-one degrees Celsius. The first two cycles are identical and include one day of heating followed by one day of cooling. The samples are cooled in a limewater bath. The third and final cycle involves three days of heating followed by a day of cooling.

DISCUSSION OF RESULTS

Fly Ash

4th International Engineering Symposium - IES 2015

March 4-6, 2015, Kumamoto University, Japan

The effect of partially replacing the Portland cement by different amounts of fly ash is shown in Figure 1. Clearly, the control batch exhibited the highest expansion compared to those containing fly ash. Further, the expansion increased steadily as time proceeded. Partially replacing the Portland cement by Class F fly ash decreased the expansion. The expansion decreased as the replacement percentage increased. SEM results correlate with the expansion results. The control samples exhibited the highest amount of ettringite formation. Samples containing 30% fly ash demonstrated the lowest amount of ettringite formation. Samples, which contained 20% fly ash showed a much lower expansion and a slight decrease in the compressive strength when compared to the control specimens. This study show that 20% is close to optimal and also results in only small reduction in the compressive strength.

Ouyang and Lane (1999) reported that the replacement of cement with 15% Class C fly ash increased the expansion. Class F fly ash has been effective in reducing expansive reaction resulting from alkali-silica reaction. Cement alkalis react with fly ash that contains silica instead of reacting with silica aggregate. Azzam (2002) reported that studies showed that fly ash of high fineness, high silica content, low calcium oxide, high Fe₂O₃ and highly amorphous silica is the most effective pozzolan for reducing expansion due to sulfate attack.

Since Class F fly ash contains a low-calcium level, it may not be as reactive as Class C fly ash, which contains a higher level of calcium. Therefore, the compressive strength was low at 28 days and decreased as the amount of fly ash increased. However, at six months, the compressive strength was higher and slightly increased as the fly ash content increased. Figure 1 shows that as the fly ash level increased, the expansion greatly decreased. The effect on expansion as the fly ash % increased from 20 to 30 was not as significant. The reduction in the compressive strength was 4.3% and 9.9% at 28 days and six months, respectively, as the fly ash amount increased from 20%

to 30%. Figure 2 shows SEM micrograph and EDAX results of a control specimen (0% fly ash and no MWC) at six months; and Figure 3 shows SEM micrograph and EDAX results for a specimen with 30% fly ash at 28 days.

Mix Water Conditioner

Concrete prisms that contained MWC exhibited the same expansion level as those, which contained 10% fly ash. However, cylinders containing MWC showed the highest compressive strength. There was no distinguishable difference in the re-formation of ettringite in these samples and those of other sets. At the first stage of ettringite formation, calcium hydroxide and calcium silicate hydrate were found in the weakest areas. Then, at the intermediates stages, ettringite needles and balls emerged form calcium hydroxide and the calcium silicate hydrate changed to ettringite gel, which underwent a physical transition into needles. Figure 4 shows SEM results of a fracture sample made with Laurel sand and containing MWC, showing ettringite nests in the transition phase to needles in a transition zone, at six months. At the advanced stage, both calcium hydroxide and calcium silicate hydrate disappeared completely and only ettringite could be detected.

Mitigation of DEF in Existing Concrete

A study was also conducted to determine if the growth of delayed ettringite formation (DEF) in existing concrete can be mitigated with commercial products. Externally applied water repellents and crystal growth inhibitors were tested. The research required casting laboratory specimens for expansion and weight measurements, for strength testing, and for scanning electron microscope (SEM) investigations. The testing consisted of four products: ChimneySaver, Radcon Formula #7, Dequest 2060S, and Noveon Good-Rite K752. These products were chosen based on the criteria that they be easy to apply, safe to use, and safe for the environment. ChimneySaver and Radcon Formula #7 are water repellents, and Dequest 2060S and Noveon Good-Rite K752 are crystal growth inhibitors. Because the two types of products are fundamentally different, cross

4th International Engineering Symposium - IES 2015

March 4-6, 2015, Kumamoto University, Japan

combinations of a crystal growth inhibitor and water repellents were also tested. Three of the four products, ChimneySaver, Dequest 2060S, and Good-Rite K752, reduced concrete expansion and weight change when compared to the control set. The study indicates that ettringite may have to be identified and mitigated early to prevent deleterious effects.

CONCLUSIONS

Class F fly ash and mix water conditioners had positive effects on controlling DEF. The study found that the optimum amount of fly ash is close to 20% as partial cement replacement for type III Portland cement. The mix water conditioner results were equivalent to those obtained for 10% fly ash.

The study also conducted laboratory tests to determine if the growth of delayed ettringite formation (DEF) in existing concrete can be mitigated with commercial products. Externally applied water repellents and crystal growth inhibitors were tested. The testing consisted of four products: ChimneySaver, Radcon Formula #7, Dequest 2060S, and Noveon Good-Rite K752. These products were chosen based on the criteria that they be easy to apply, safe to use, and safe for the environment. ChimneySaver and Radcon Formula #7 are water repellents, and Dequest 2060S and Noveon Good-Rite K752 are crystal growth inhibitors. Three of the four products, ChimneySaver, Dequest 2060S, and Good-Rite K752, reduced concrete expansion and weight change when compared to the control set. The study also indicated that ettringite may have to be identified and mitigated early to prevent deleterious effects.

ACKNOWLEDGEMENTS

The project gratefully acknowledges financial support from the National Science Foundation and the Maryland State Highway Administration.

REFERENCES

- [1] Amde, A M et al. (2005), Correlation between Map Cracking and Delayed Ettringite Formation in Field Specimens, The Eleventh International Conference on Fracture, Turin, Italy.
- [2] Amde, A M et al. (2005), Investigation Of Maryland Bridges for DEF and ASR, Journal of Structural Engineering, Vol. 32, No.1, pp. 33-36.
- [3] Amde, A M et al. (2004), Pilot Field Survey of Maryland Bridges for DEF Damage, Maryland SHA, Report No. MD-04-SP107B4U, Maryland.
- [4] Livingston, R A and Amde, A M (2000), Nondestructive Test Field Survey for Assessing the Extent of Ettringite-Related Damage in Concrete Bridges, 10th International Symposium on the Nondestructive of Materials, Karuizawa, Japan.
- [5] Amde, A M et al. (2004), Influence of Fine Aggregate Lithology on Delayed Ettringite Formation in High Early Strength Concrete, Maryland SHA Report No. MD- 04-SP107B4U, Maryland.
- [6] Thomas, M (2001), Delayed Ettringite Formation in Concrete: Recent Developments and Future Directions, Materials Science of Concrete VI, S. Mindess and J. Skalny, Eds., The American Ceramic Society, Westerville, OH, pp. 435-481.
- [7] Day, R L (1992), The Effect of Secondary Ettringite Formation on the Durability of Concrete: A Literature Analysis, Portland Cement Association.
- [8] Tepponen, P, and Eriksson, B E (1987), Damages in Concrete Railway Sleepers in Finland, Concrete Research, pp. 199-209.
- [9] Shayan, A, and Quick, G W (1994), Alkali Aggregate Reaction in Concrete Railway Sleeps From Finland, Proceedings 16th International Conference on Cement Microscopy, Richmond, VA., pp. 64-79.
- [10] Heinz, D, and Ludwig, U (1986), Mechanism of Subsequent Ettringite Formation in Mortars and Concretes after Heat Treatment, Proceedings, 8th International Congress on Chemistry of Cement, Rio de Janeiro, Brazil, Vol. 5, pp. 189-194.
- [11] Heinz, D, and Ludwig, U (1987), Mechanism of Secondary Ettringite Formation in Mortars and Concretes Subjected to Heat Treatment, Concrete Durability, SP-100, Vol. 2, American Concrete Institute, Detroit, MI. pp. 2059-2071.
- [12] Heinz, D, and Ludwig, U (1989), Delayed Ettringite Formation in Heat Treated Mortars and Concretes, Concrete Precast Plant & Technology, Vol. 11, pp. 56-61.
- [13] Collepardi, M, et al. (1978), Tricalcium Aluminate Hydration in the Presence of Lime, Gypsum or Sodium Sulfate, Cement Concrete Research.
- [14] Stark, J et al. (2003), New Approaches to Cement Hydration in Early Hardening Stage, Proc. of the 11th Int. Congress on the Chemistry of Cement (ICCC), Cement's Contribution to the Development in the 21st Century, Durban, South Africa, pp. 261-277.
- [15] Lawrence, B L et al. (1999), Evaluation and Mitigating Measures for Premature Concrete Distress in Texas DOT Concrete Elements, Cement, Concrete, Aggregates, pp. 73-81.
- [16] Gress, D (1997), Early Distress in Concrete Pavements, FHWA-SA-97-045, Washington, DC.
- [17] Taylor H F W (1994), Delayed Ettringite Formation, Advances in Cement and Concrete, New Hampshire, ASCE, pp. 121-131.
- [18] Ouyang C and Lane O J (1999), Effect of infilling of Air Voids by Ettringite on Resistance of Concretes to Freezing and Thawing, American concrete Institute, SP-177-16, pp. 249-261.
- [19] Azzam A (2002), Delayed Ettringite Formation, PhD Dissertation, University of Maryland College Park.

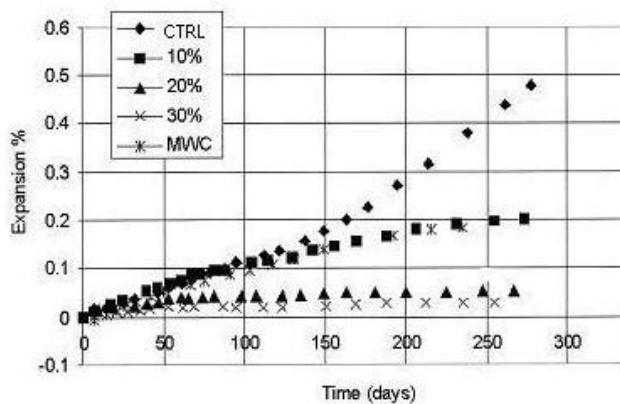


Fig.1 Expansion of water-Cured concrete prisms made with Laurel Sand and containing MWC or different amounts of Class F Fly Ash

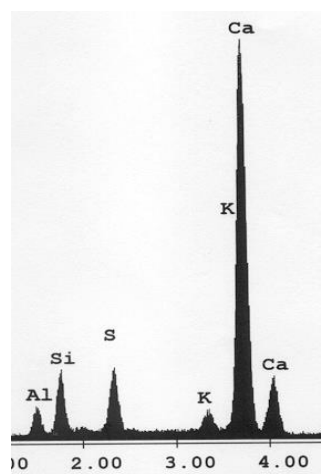
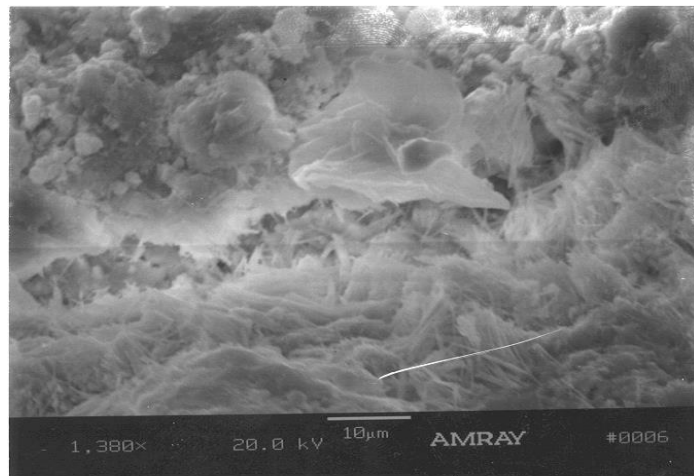
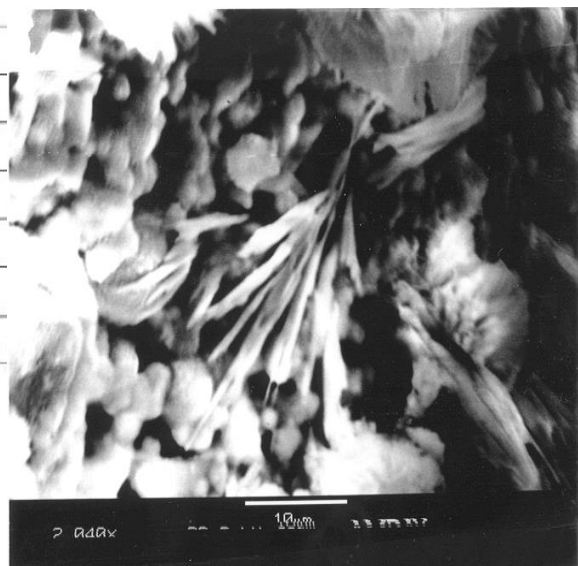


Fig.2 SEM and EDAX of fracture sample, Laurel sand, 0% fly ash at 6 months, a crack filled with ettringite

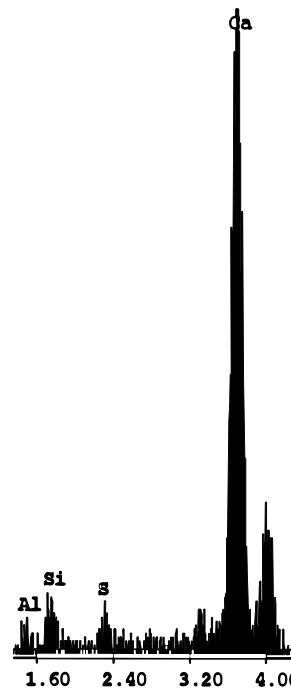


Fig.3 SEM of fracture sample made of Laurel Sand (30% fly ash) showing mainly calcium hydroxide, few ettringite clusters and EDAX element composition, at Age of 28 days

FAILURE ANALYSIS OF RMHS SILO – A CASE STUDY

Sheggoju Ramyasri¹, Aishwarya M Bansode² and Arun T Udupa³

- 1 Department of Civil Engineering, National Institute Of Technology, Karnataka, Surathkal, Mangalore-575025, India. email: ramyasheggoju@gmail.com
- 2 Department of Civil Engineering, National Institute Of Technology, Karnataka, Surathkal, Mangalore-575025, India. email: aishu.gappu1@gmail.com
- 3 Deputy General Manager, Civil and Engineering Services, JSW Steel Limited, Karnataka, India- 583275 email: arun.udupa@jsw.in

ABSTRACT: Recent failures of storage bins, silos and other structures highlight the need to increase awareness of hazards associated with these structures. Careful examination and prompt correction of hazards are essential to maintain them. This paper is a case study of the failure of a storage silo in an industry in India, used for Raw Material Handling i.e., Iron Ore in this case. The failure occurred majorly due to increase in density of the raw material due to various reasons which resulted in over loading of the silo, and inappropriate methods of installation of the silo led to difficulties in welding the conical part of the silo with the cylindrical portion. Finite element analysis of the silo is done to calculate stresses at different points of the silo and the welded joint to predict its structural performance during the failure. And also other factors like non-functioning sensors etc., led to collapse of the silo punching its conical part through the slab underneath to a depth 7m below. It was later restored to its position by welding it from the inside and providing rib plates to increase the weld area and strengthen the weld and also other safety measures like checking for corrosion, cracks etc. were taken.

Keywords: silos, impact load, weld failure.

INTRODUCTION

Silos fail with a frequency which is much higher than almost any other industrial equipment. Sometimes the failure only involves distortion or deformation which, while unsightly, does not pose a safety or operational hazard. In other cases, failure involves complete collapse of the structure with accompanying loss of use and even loss of life. The cost of a silo failure is never small. It includes immediate cost of lost production and repairs, people in the vicinity are exposed to significant danger etc., Carson, J.W. (2000).

The paper is about the analysis of failure of a Raw Material Handling Silo (RMHS), mainly aiming at investigating the possible causes of the accident and also lists the measures taken after the failure.

DESCRIPTION OF STRUCTURAL DESIGN

DESIGN PARAMETERS

1. The basic wind speed for the structural design is 33m/s.
2. The Soil Bearing Capacity is 20.0kPa.
3. The live load of the platform is 6kN/m².

MATERIALS ADOPTED AND REQUIREMENTS

1. Foundation concrete M30, Foundation cushion course M10, Beam, Slab and Column M35.
2. The steel bars used are Mild Steel Fe250 and High Strength Deformed Steel Fe415.
3. Welding rod adopted is Mild Steel Fe250, according to IS 813 – 1961.

4th International Engineering Symposium - IES 2015

March 4-6, 2015, Kumamoto University, Japan

-
- 4. Concrete cover
 - a. Column 35mm
 - b. Foundation 40mm
 - c. Beam 25mm
 - d. Slab 15mm.

DIMENSIONS OF THE SILO

- The silo in the present case consists of:
- a. Hollow cylindrical portion of diameter 8000mm and height 4836mm.
 - b. Hollow conical portion of height 1788mm, pour in diameter of 8000mm and pour out diameter of 1200mm.

The cylindrical and conical portions were joined by a tight strong weld of the fillet type with an angle of 45° welded with a weld rod of 6mm diameter to a weld in length of 10mm.

A 12mm thick mild steel plate was used to make the hollow silo. The cylindrical portion of the silo rests on a load bearing beam of 2.1m depth and the columns were connected by tie beams of 0.5m depth.

The model of the storage silo is shown in fig.1

INSTALLATION

The silo was installed in parts, i.e., the different parts of the silo were brought to the site and then welded together. The cylindrical portion was first installed and so placed that 554mm of its total height is in contact with the load bearing beams. Then the conical portion was erected and welded in position from the outside.

FAILURE ANALYSIS

VISUAL INSPECTION

The site of the accident was visited and the following observations could be made. The failure occurred during the discharge of the raw material from the storage silo. The complete conical part of the silo got detached from the cylindrical portion due to the failure of the weld joining them and because of sudden impact from the silo, the concrete slab underneath it completely failed [see fig. 2(b)]. Fortunately, there was no loss of life when the accident occurred.

STUDY

To study the causes of the failure, the load in the silo was considered in two cases and the stresses developed on the weld were found using finite element analysis.

Case 1: the silo was considered to be filled till the brim.

- 1. Total load was taken to be 900 tons on the inside part of the silo [see fig.3(a)]
- 2. Stress on the weld is 24N/mm² which is in safe limit. [fig.3(b)]

Case 2: the silo was considered to be filled only till the conical portion

- 1. Total load was taken to be 900 tons (worst case possible) [see fig.4(a)]
- 2. Stress on the weld is 51N/mm² which is still in safe limits. [see fig.4(b)]

Hence the steel structure was found to be safe for the particular load conditions.

EARLIER PRECAUTIONS TAKEN TO AVOID FAILURE

The weld portion was not secure earlier due to incorrect methods employed in welding the joint, between the cylindrical and the conical portion. Hence to avoid any further failure steel channels connected to the tie members were provided to support the conical part of the silo.

CAUSES

After the analysis has been done, the following causes of the failure have been identified.

- 1. The density of the ore stored in the silo is supposed to be 2.2g/cc, but because of weather conditions there was an increase in the moisture content of the ore and its density had increased by 1.3g/cc. Due to which certain amount of the ore got stuck to the walls of the lower part of the conical portion, increasing the load on the weld.
- 2. The overload detecting sensors weren't functioning properly and hence failed to indicate the over load.
- 3. The steel channels provided transferred the load of the conical part to the tie beams which were not designed to take such an amount of load [see fig. 5(b)].

4th International Engineering Symposium - IES 2015

March 4-6, 2015, Kumamoto University, Japan

4. A weld of 12mm thick was provided even though 6mm was safe. But since the installation was done in parts, the cylindrical portion was so placed that there was no enough space between the cylindrical part and the load bearing beams (see fig.1) to properly carry out continuous welding with the conical part, this led to improper welding at the points of contact of the beams and the cylindrical part i.e, the welding was safe as per the design but not on site.
5. The concrete slabs under the silo were not designed to take such a huge amount of impact load.

When the weld failure was identified the decision of unloading the ore from the silo was taken. While unloading, due to the ore that got stuck to the walls of the conical portion of the silo the material failed to exit the mouth of the conical section, hence increasing the stress on the already strained weld, leading to the collapse of the conical part of the silo and punching it through the slab under it to a depth of 7m, which led to the failure of the entire structure.

SOLUTIONS

1. After the failure, the silo was emptied and erected back to its position.
2. But this time, the welding was carried out from the inside of the silo and rib plates were provided throughout to increase the weld area so as to strengthen the weld.
3. Thick liner plates made of high manganese (Mn) steel [acc. to IS2062:2011] were provided to avoid wear and tear.
4. The sensors were changed.
5. The slab, beams, columns were reconstructed. And other safety measures were taken.

CONCLUSIONS

Silos that are designed, built, operated, and maintained properly, will provide long life. The design, construction, operation

and maintenance of silos are not being described in any national legislation or industrial standard. Therefore, it is the responsibility of the designer to establish related written procedures to ensure its safe use. Essentially, the design should comply with relevant international and local code of practice, incorporate complete understanding of materials stored and include all possible loading combinations, DOSH (2013).

- Whenever possible, silos should be designed for center fill and center withdrawal. If eccentric fill or withdrawal is contemplated, structural check should be performed first to make sure that the silo can withstand the non-uniform loading conditions, Carson, J.W. (2000).
- In the construction phase, the problems due to poor workmanship and faulty construction practices like using wrong materials, unauthorized changes in design etc., should be avoided.
- Frequent inspections of the general conditions during loading, storing and discharging should be one to identify problems related to bulk material flow and load distribution.
- The silo should be inspected to detect any spills of the stored material from distorted walls or thinning of walls due to corrosion or abrasion and loose or missing bolts. Also, signs of distress like cracks in the walls or tilting of the walls should be checked for and expert help should be summoned immediately if there is any problem, Carson, J.W. (2000).
- Frequency of these inspections should depend on the usage of the silo.

It is the joint responsibility of the designer, builder, and owner that construction is of an acceptable standard, and fulfils the intent of the design. It is then the responsibility of the owner to properly maintain the structural and mechanical components and to ensure that any intended alteration in usage, discharge geometry or hardware, liner material, or any other specified parameter, is preceded by a design review with strengthening applied as required.

REFERENCES

- [1] Carson, J. W.: Silo Failures: Case Histories and Lessons Learned, presented at the Third Israeli Conference for Conveying and Handling of Particulate Solids, Dead Sea Israel, May 2000
- [2] Preventing Silo Failures. 2013. Department of Occupational Safety and Health (DOSH) Malaysia. Website: <http://www.dosh.gov.my>

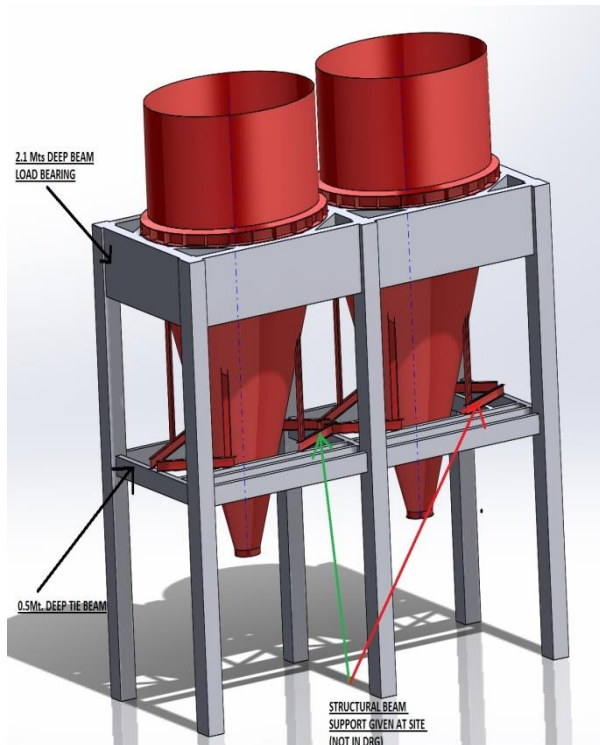


Fig.1 Model of the storage silo



Fig.2 (a): Silo before failure



Fig. 2(b): Silo after failure.

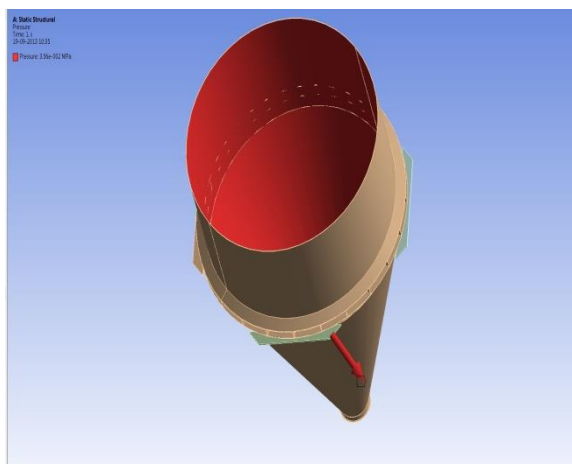


Fig. 3(a): 900T load on inside of silo [marked in red]

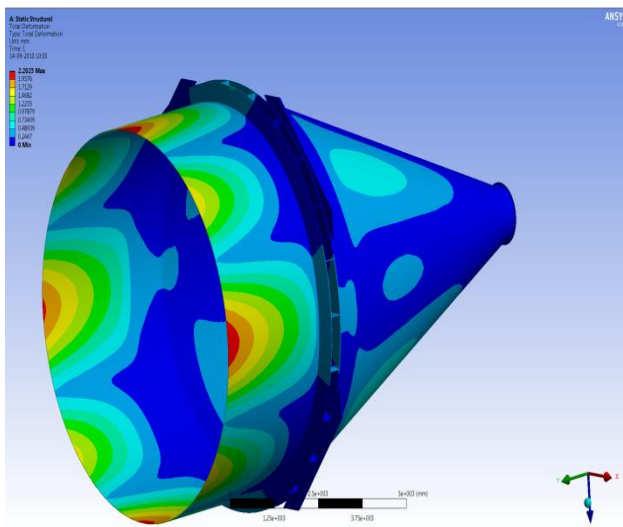


Fig. 3(b): FEM model showing stress on weld as 21N/mm^2 (within safe limit)

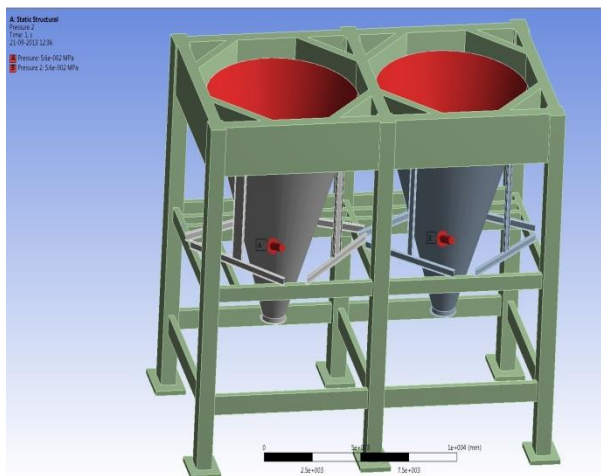


Fig. 5(a): After weld failure load transferred to tie beam through site supported steel channel

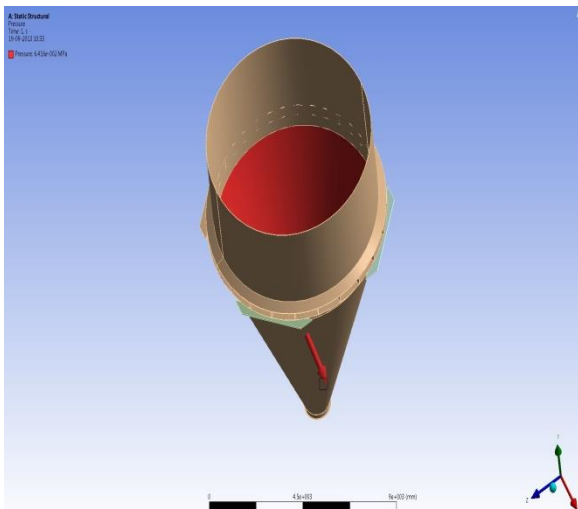


Fig. 4(a): 900T load only on the conical part of the silo.

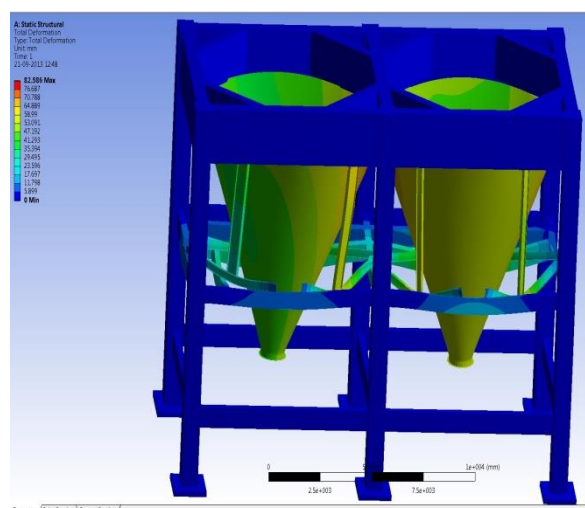


Fig. 5(b): Failure of tie beam as it is not designed to take such an amount of load.

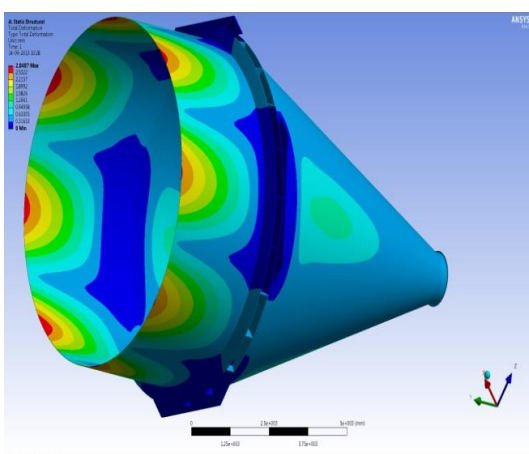


Fig. 4(b): FEM model showing stress on the weld to be 51N/mm^2 which is in safe limits.

DURABILITY OF CONCRETE IN COASTAL AREAS (SEVERE ZONE)

**Girish Kumar, Abhishek Salkar, Abhishek Master, Anand Bhattad,
Katta Venkataramana and K Rajendra Prabhu**

*Department of Civil Engineering, National Institute of Technology Karnataka,
Surathkal, Mangalore 575025, India. e-mail:girish.karuti@gmail.com*

ABSTRACT: The Indian code of practice for plain and reinforced concrete (IS 456:2000) specifies that the minimum compressive strength of concrete in Reinforced Cement Concrete works, to achieve desired durability, shall be minimum of 30 MPa in coastal areas. However, durability is a measure of permeability of concrete, rather than its strength. Higher strength does mean denser concrete, and thus, strength is indirectly related to durability. On the other hand, the same level of permeability of concrete can be achieved in concrete mixes of compressive strength 30 MPa and 25 MPa, depending upon the micro structure of concrete. In the present research, an exploratory study is conducted to delink durability and strength of concrete. Concrete specimens (specimens in the form of cubes and slabs) of compressive strength 30 MPa and 25 MPa blended with 70% content of Ground Granulated Blast Furnace Slag were tested using newly introduced "Permit Ion Permeability Test Apparatus". Chloride ion permeability values for 28th day, 56th day and 90th day were determined experimentally. The results obtained were inconclusive and this study needs further investigation using other blends before generalization. If this research succeeds to delink durability from strength, consequently leading to substantial savings in consumption of cement, the specifications in IS 456:2000 regarding durability requirements can be reconsidered. It is expected that the present research will provide significant contributions by reducing carbon foot prints due to lesser consumption of cement.

Keywords: Durability of Concrete, Compressive Strength, PERMIT ion-permeability, Ground Granulated Blast Furnace Slag (GGBS), Chloride ion.

1. INTRODUCTION

India has a long coastal belt that stretches for about 7500 km with approximate use of millions of tonnes of concrete per day along this belt. Concrete used in the structures built in this area is susceptible to high levels of moisture and chloride ions, which is one of the prime deteriorating factor for concrete's durability. The durability of concrete is defined as its ability to resist weathering action, chemical attack, abrasion, or any other process of deterioration. According to IS 456:2000, a 'durable' concrete is one that performs satisfactorily in the working environment during its anticipated exposure conditions during service. The materials and mix

proportions specified and used should be such as to maintain its integrity and, if applicable, to protect embedded metal from corrosion. When designing a concrete mix or designing a concrete structure, the exposure conditions are to be assessed in the beginning with good judgement. Presently, the use of concrete has been extended to more hostile environments, having already used up all favourable sites. Even the good materials such as aggregate, sand are having shortage of supply. Even though cement production is modernised now, sometimes, the second grade raw materials such as limestone containing excess of chloride is being used for economical reasons. Earlier,

specifications of Portland cement permitted a maximum chloride content of 0.05 per cent. Recently, maximum permissible chloride content in cement has been increased to 0.1 per cent. This high permissible chloride content in cement demands much stricter durability considerations in other aspects of concrete making practices to keep the total chloride content in concrete within the permissible limits. In other words, considerations for durability of modern concrete constructions assume much more importance, than hitherto practised. IS 456:2000 specifies that the minimum grade of concrete to achieve the desired durability in coastal areas shall be M30. This paper explores the possibility of achieving the desired durability with the help of concrete of a lower grade, blended with Ground Granulated Blast Furnace Slag (GGBS). This would also lead to substantial savings in the consumption of cement and make the design more economical.

2. OBJECTIVES

1. To study the effect of addition of mineral admixtures (GGBS) on durability of concrete.
2. To delink strength from durability by showing that a high strength concrete need not be necessarily a more durable concrete.
3. To minimize the consumption of cement and thus reducing carbon footprints in atmosphere.

3. METHODOLOGY

Three standard cubes (15cm x 15cm x 15cm) and two slabs (40cm x 40cm x 5cm) were casted for each M30 and blended M25 grade of concrete respectively. The de-moulding was done after twenty four hours of casting. The specimens were kept under curing for 28 and 56 days. The cubes were tested for 28 days compressive strength. The slabs of M30 and blended M25 grade of concrete were tested for knowing the permeability of concrete using Permit Ion-Permeability apparatus (a Non-Destructive Test). The PERMIT test was further conducted on slabs to check the permeability of concrete after 56 days. All the ingredients of the concrete mix design were tested and their properties were determined. Once the constituents

satisfied the required specifications, they were used for preparing concrete mixes. The mix design for both the blended concrete (70%GGBS) and the Ordinary Portland Cement (OPC) concrete is shown in Table 1 and 2 respectively. The required amounts were determined in order to cast 3 concrete cubes and 3 concrete slabs. The amounts of the constituents which were determined for blended concrete are given in Table 1. In coarse aggregates, weights of 12.5 mm and 20 mm sizes were 42.77 kg and 14.27 kg respectively in the ratio of 1:3 by weight. Similarly, the required amounts of constituents for OPC concrete were determined in order to cast 3 concrete cubes and 3 concrete slabs. The calculated amounts are given in Table 2. In coarse aggregates, weights of 12.5 mm and 20 mm sizes were 37.31 kg and 12.44 kg respectively in the ratio of 1:3 by weight.

4. EXPERIMENTAL PROCEDURE

The experimental apparatus adopted to determine the permeability of the casted specimens in this study is Permit Ion-permeability Test. The Permit ion-permeability test unlike any other permeability test is a Non Destructive Test (NDT). It measures the rate at which the ions are passing through the specimen and thereby providing a diffusion ion migration coefficient, a permeability coefficient, which is indirectly indicative of durability of concrete. The working principle behind this test is that the ions in the inner catholyte chamber are forced to migrate to the outer anolyte chamber due to a potential gradient acting as the driving force. A schematic representation of the movement of ions is shown in Fig 1.

The amount of ions reaching the outer cell (anolyte chamber) is monitored indirectly by the change in conductivity of the anolyte using the conductivity probes. When the conductivity readings indicate the establishment of a steady state of flow of ions into the anolyte chamber, the slope of the steady state conductivity is determined. Using the slope of the steady state conductivity curve in the Nernst-Plank equation we obtain the diffusion migration co-efficient. In this work the experiment was conducted in accordance

with the specifications as directed by the Permit test manual. The diffusion migration co-efficient is given by the equation below

$$D_{mig-in-situ} = - \left(\frac{dc}{dt} \frac{T}{E} \right) \left(\frac{R}{zCF} \right) \left(\frac{L}{A} V \right) \quad (1)$$

$D_{mig-in-situ}$ = Diffusion migration coefficient, m^2/s

$\frac{dc}{dt}$ = rate of change in concentration of anolyte, $\text{mol}/\text{m}^3\text{s}^1$

T= absolute temperature (average during steady state), K

R= universal gas constant (8.31 J/K-mol)

z= valency of the ions (chloride ion=-1)

C= concentration of ion source solution ($0.55 \times 10^3 \text{ mol/m}^3$)

F= Faraday's constant ($9.65 \times 10^4 \text{ C/mol}$)

E= electrical potential applied between the anode and the cathode, (60 V)

V= volume of the anolyte ($6.5 \times 10^{-4} \text{ m}^3$)

$\frac{L}{A}$ =ratio of the flow length to the exposed area (3.74 m^{-1})

5. OBSERVATIONS

The graphs for variation of conductivity of ions, conductivity rate and current against time are plotted for specimens cured for 28 days and 56 days. The slope of the steady state conductivity region is used to obtain the diffusion migration coefficient of ions through a particular specimen. The diffusion migration coefficient is an indirect measure of durability of concrete. Higher the diffusion coefficient higher is the permeability and hence lower is the durability and vice-versa. Fig 2, Fig3, Fig 4 show the variation of conductivity of ions, conductivity rate and current with time respectively for plain cement concrete of compressive strength 30MPa after 28 days.

Fig 5, Fig 6 and Fig 7 show the variation of conductivity of ions, conductivity rate and current with time respectively for blended concrete mix (70% GGBS) of compressive strength of 25MPa after 28 days.

Fig 8, Fig 9 and Fig 10 show the variation of conductivity of ions, conductivity rate and current with time respectively for

plain cement concrete of compressive strength 30 MPa after 56 days.

Fig 11, Fig 12 and Fig 13 show the variation of conductivity of ions, conductivity rate and current with time respectively for blended cement concrete mix (70% GGBS) of compressive strength 25 MPa after 56 days.

6. RESULTS AND DISCUSSIONS

The diffusion migration coefficients are obtained from equation 1 by using the slope of steady state conductivity curve of the specimens each of OPC and blended concrete mix (70%GGBS) at 28 days and 56 days. The parameters used in determining the diffusion coefficients are taken as provided in the permit ion-permeability test manual. Table 3 and 4 shows the migration coefficients and peak currents of the two mixes after 28 and 56 days.

- The diffusion migration coefficient for plain cement concrete of 30 MPa after 28 days was found to be $3.5 \times 10^{-12} \text{ m}^2/\text{s}$ and the peak current was found to be 330 mA.
- The diffusion migration coefficient for blended concrete mix (70% GGBS) of 25 MPa after 28 days was found to be $1.3 \times 10^{-12} \text{ m}^2/\text{s}$. The peak current was found to be 100 mA.
- The diffusion migration coefficient of OPC is almost thrice as that of the diffusion migration coefficient of blended concrete mix (70% GGBS). Indirectly meaning that the permeability of blended concrete mix is much less than the OPC mix.
- The diffusion migration coefficient of chloride ions for OPC of 30 MPa, after 56 days was found to be $4.4 \times 10^{-12} \text{ m}^2/\text{s}$ and the peak current was found to be 360 mA.
- The diffusion migration coefficient of chloride ions for blended concrete mix of 25 MPa, after 56 days was found to be $1.7 \times 10^{-12} \text{ m}^2/\text{s}$ and the peak current was found to be 210 mA.
- The diffusion migration coefficient of OPC is almost thrice as that of the blended concrete mix (70% GGBS) for measurements done after 56 days.

7. CONCLUSIONS AND FUTURE

SCOPE OF STUDY

Durability of concrete in coastal areas is addressed in this paper and the following conclusions are drawn from the study.

- The migration coefficients of the M30 PCC mix were higher after 28 and 56 days.
- Owing to higher migration coefficients, M30 OPC mix was found to have higher permeability and hence lesser durability than the blended concrete (70% GGBS).
- Durability is not directly related to strength. It rather depends on the micro structure of concrete.
- This study needs further investigation using other blends before generalization. Similar tests using reinforced cement concrete also need to be conducted to incorporate actual site conditions.
- Positive results for other concrete mixes and different admixtures may lead to substantial savings in the consumption of cement.

8. REFERENCES

- [1] Adil K Al-Tamimi et al. "Guidelines for Concrete Durability Testing in the UAE".
- [2] C Mc.McNally and P Semour, "Durability Aspects of Mixer Addition Blends of GGBS"
- [3] Indian Standard Plain and Reinforced Concrete-Code of Practice (4th Revision), IS 456: 2000.
- [4] Indian Standard- Concrete Mix Proportioning Guidelines (1st Revision), IS 10262:2009
- [5] P Kumar Mehta and Paulo J M Monteiro, "Concrete Micro structure properties and materials", Tata McGraw-Hill Edition.
- [6] Shahim Z Bosunia, J R Choudhary, "Durability of Concrete of Coastal Areas in Bangladesh", Journal of Civil Engineering, the Institution of Engineers, Bangladesh (2001)

Table 1: Mix Design for Blended Concrete (70% GGBS)

Sl. No	Materials	Weight (kg)	Ratio
1	Cement	7.50	0.30
2	Water	10.23	0.41
3	Fine Aggregates	38.90	1.56
4	Coarse Aggregates	57.04	2.28
5	GGBS	17.50	0.70

Table 2: Mix Design for OPC Concrete

Sl. No	Materials	Weight (kg)	Ratio
1	Cement	18.10	1.00
2	Water	8.71	0.48
3	Fine Aggregates	26.30	1.45
4	Coarse Aggregates	49.75	2.75

Table 3: Migration coefficients of each mix at 28th day and 56th day

No. of Days	D_{mig} (m ² /s)	
	OPC Concrete mix	Blended Concrete (70% GGBS) mix
28	3.5×10^{-12}	1.3×10^{-12}
56	4.4×10^{-12}	1.7×10^{-12}

Table 4: Peak Current in anolyte solution at 28th and 56th day

No. of Days	Peak Current (mA)	
	OPC Concrete mix	Blended Concrete (70% GGBS) mix
28	330	100
56	360	210

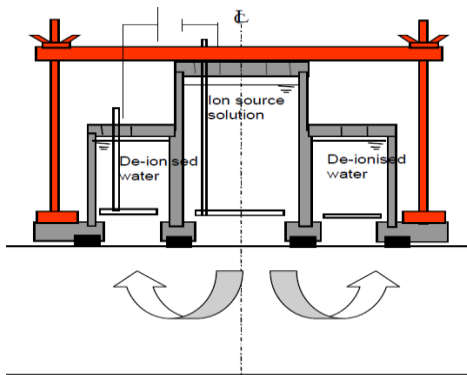


Fig 1: A Schematic representation of movement of ions

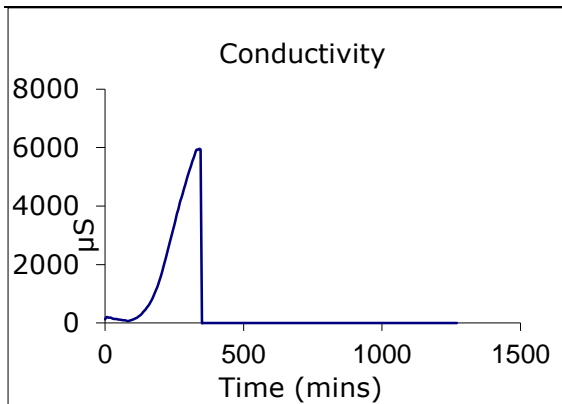


Fig 2: Conductivity v/s Time

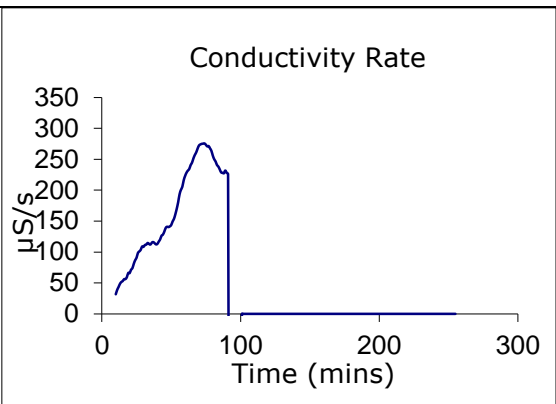


Fig 6: Conductivity rate v/s Time

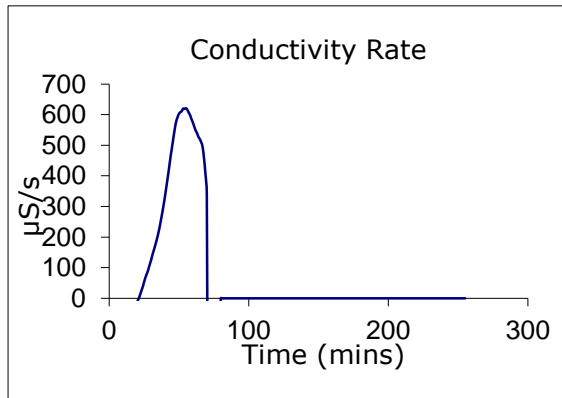


Fig 3: Conductivity rate v/s Time

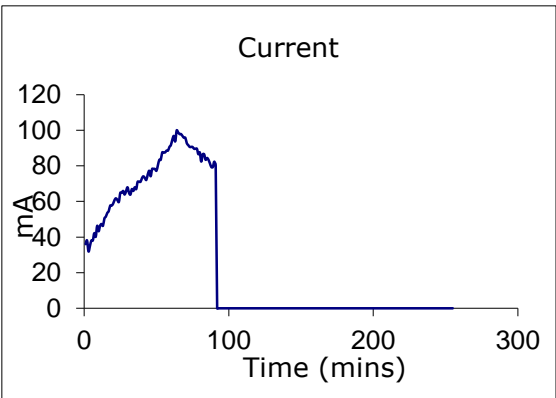


Fig 7: Current v/s Time

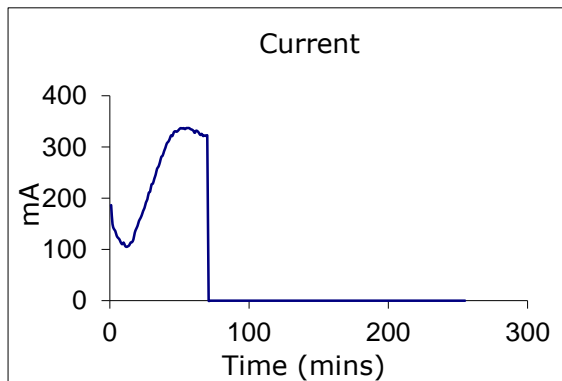


Fig 4: Current v/s Time

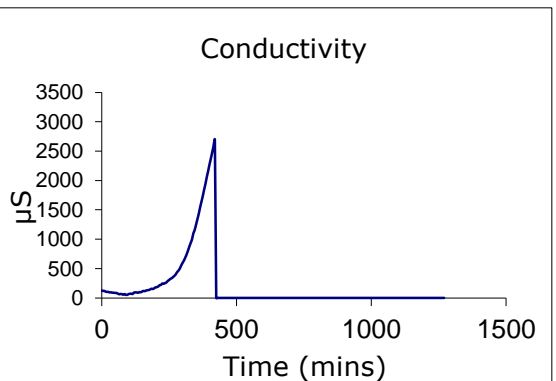


Fig 8: Conductivity v/s Time

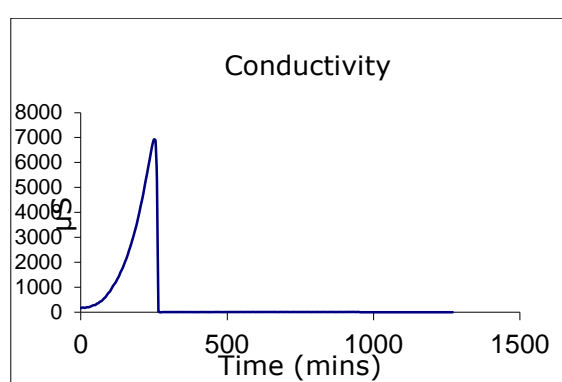


Fig 5: Conductivity v/s Time

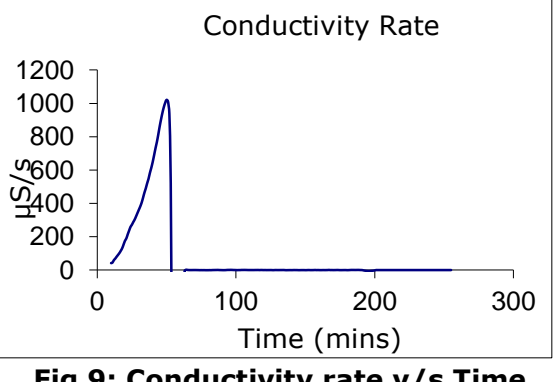


Fig 9: Conductivity rate v/s Time

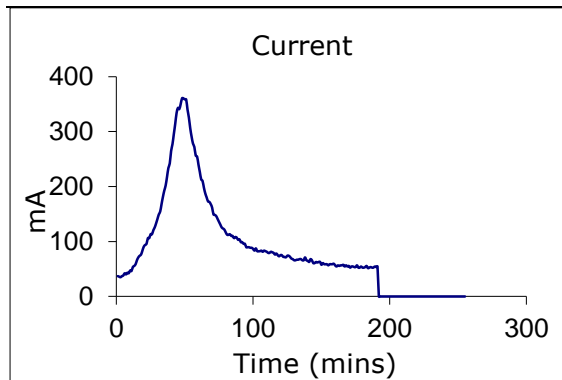


Fig 10: Current v/s Time

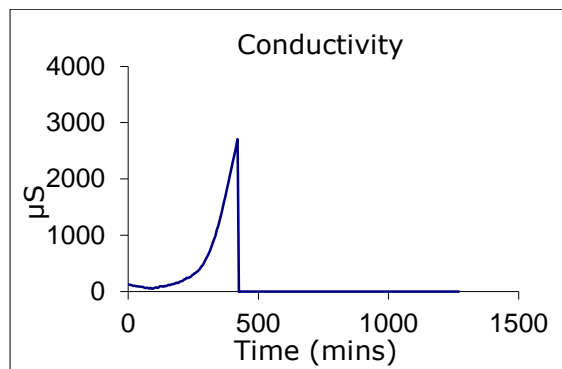


Fig 11: Conductivity v/s Time

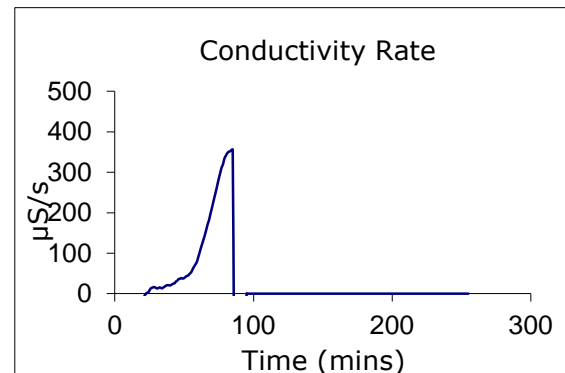


Fig 12: Conductivity rate v/s Time

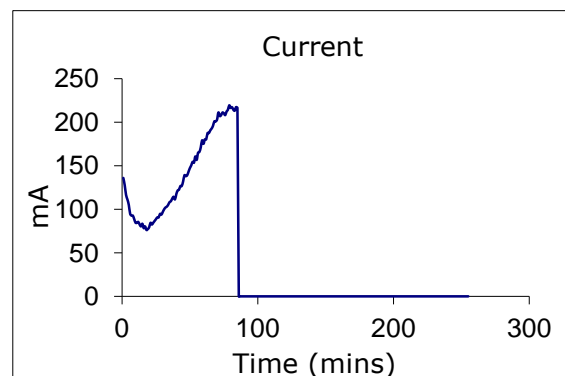


Fig 13: Current v/s Time

EMBODIED ENERGY IN COST EFFECTIVE RURAL HOUSING

G.C.Gayathri¹ and G C Priyanka²

1 Department of Civil Engineering, Anna University, Chennai 600025, India.
e-mail:gayathrichandramohan7@gmail.com

2 Department of Environmental Engineering, Erode Senguntha Engineering College, Anna University, Erode, India. e-mail:priyankacivilstud@gmail.com

ABSTRACT: Building construction is one of the major fast growing and major consuming section. The rate of growing population in under developing countries requires affordable shelter. The alarming cost escalation of various building elements need to be planned and designed in a systematic way of construction. The depletion of natural resources forced to search for alternative cost effective and energy efficient building elements such as Bricks, Cement, Steel, Aluminium, Plastic products, Paints, Stone are the commonly used materials for construction. These materials are energy intensive and are trapezoid larger dissevers before used for construction. This paper discussed the issues and problems related to rural housing and the choice of building technology, block size and their embodied energy utilized during the construction. An attempt has been made towards the assessment by the embodied energy in various types of housing with alternate building elements in wall and roofs. For the purpose of study three types of basic building blocks and three types of walling and roofing elements with different types of mortar and materials have been combined for obtaining the embodied energy values for the building blocks.

Keywords: Embodied energy values, Walling elements, Roofing elements, Embodied energy rates (EER)

INTRODUCTION

Housing is one of basic requirements for human survival. **The rural housing stock in India is expected to see a rise of 42-44 million by 2025 according to a report by the National Council of Applied Economic Research.**^[1]

Construction Week highlights the reasons for the growth. An analysis of the housing scene in the rural areas suggests continued poor quality of the rural housing stock in the country, though considerable improvements in quality have been indicated over the period. Also, while there has been continuous growth in the rural housing stock, its pace has been lower than urban housing. The rural areas

in India are characterized by small and highly dispersed habitations, apart from a poor village or community level infrastructure.^[2] In the context of housing, factors such as availability of land, skilled labour and building materials are critical. About 40% have their houses on agricultural land and an equal proportion on non-agricultural land. About 10% of houses are on Panchayat/government land. The houses on Panchayat land belong to the poor. Nearly one-fifth of the households felt that acquiring land is not easy. In case of building materials, most households were satisfied, save for the fact that materials are usually sourced from outside the

4th International Engineering Symposium - IES 2015

March 4-6, Kumamoto University, Japan

village.^[3] It is the availability of skilled labour that seems to pose a problem. However the assessment of the embodied energy in buildings is still in its nascent stage in India and requires serious research.

NEED FOR ENERGY EFFICIENT BUILDINGS

The International Energy Report (IER) 1987 points out "Investment in energy conservation at a margin provides a better return than investment in energy supply" (Trilok Singh, 1999). The concept of green buildings is still at an emerging stage in India. The concept of sustainable buildings and use of environmentally friendly construction materials like stones, timber, thatch, mud etc have been practiced since ancient times. But the perception of people about strong and durable buildings have changed with the advent and lavish use of the present modern materials like steel, cement, aluminium , glass etc. A large amount of fuel energy gets consumed in producing such materials. These materials being industrial products further need to be transported to large distances before getting consumed in the buildings thus making them energy intensive. An estimate of the energy consumed in buildings using different permutations of materials and techniques will facilitate their appropriate selection and reduce the embodied energy consumption.

METHODOLOGY

The embodied energy of the building materials have been tabulated as per Building Materials Promotion Council (BMTPC) data. The quantity of building block elements and sub data were computed as per the procedure applied for quantity estimation. The material requirements for each element and their corresponding embodied energy value are obtained and tabulated.

EMBODIED ENERGY

The values of embodied energy of building materials are the estimates of energy

consumed in the manufacture / extraction of a few building materials chosen from various sources (Gartner and Smith, 1976. K.S. Jagadesh).

- (1) Cement: The dry process, wet process and semi dry process are the methods used for the manufacturing of cement. Among the three, dry process method was adopted by the much cement manufacturing industry. The embodied energy value is 5.85 MJ/kg.
- (2) Steel: The steel manufacturing industry use iron ore lumps, sinters and pellets, coke and fluxes such as limestone and dolomite for various process such as melting, refining, casting and rolling. It requires high energy. The embodied energy for steel was estimated as 42 MJ/kg.
- (3) Bricks: The production of bricks includes, soil preparation, moulding, drying and firing. The firing process required more energy depending upon the weather condition and nature of coal or fire wood calorie values. It was estimated that embodied energy values will be 3.00 MJ/ unit.
- (4) Lime: The limestone is used for the manufacture of lime. The firing process is involved. The embodied energy is more due to melting process.
- (5) Fly Ash & Sand: Fly ash is the by-product of burnt coal from thermal power plants. The embodied energy for the fly ash and sand is taken as zero.

CHOICE OF BUILDING TECHNOLOGIES

Most of rural housing was constructed with locally available building resource like bricks, mud fly ash, bamboo and thatches. These materials have minimum impact on environment. The locally available resources reduce significant transport cost

4th International Engineering Symposium - IES 2015

March 4-6, Kumamoto University, Japan

and energy asserted with construction site. However the use of cement and steel in the construction industry will increase the cost and embodied energy. It has been estimated that 22% of green house gas emission is contributed by the construction sector in India. Energy conservation, minimize the use of high energy materials, concern for environment, adoption of environment friendly technologies, minimize the transportation and maximize the local resources and recycling of building waste and use of renewable energy sources will help us to promote sustainable development.

SOIL BASED TECHNOLOGIES

Stabilized Mud Blocks: The stabilized mud block is a solid block compacted using a machine with a mixture of soil, sand, soil stabilizer and water. It is compacted after curing it is suitable for wall construction. The change of stabilizer depends upon the quality of soils used for compaction. The fly ash, cement, lime, rice husk ash, corn cob ash, granulated GGBS force slag and steel slag is recommended. The quarry dust can also be used for manufacturing of SMB. These are durable and free from maintenance and 230x230x90 mm size blocks are 2.5 to 2.8 times bigger in volume when compared to locally available conventional burnt clay blocks. The strength of the blocks depends upon the composition of materials and percentage of stabilizer and compaction.

RAMMED EARTH WALL

The rammed earth wall is a solid wall constructed with a mixture of soil, sand and stabilizer and water. Compaction of the wall by hammer helps to dense the soil mat and thereby improving the compressive strength and decrease the porosity. A uniform rise of wall in to curing shows better results.

PRECAST JOIST AND PANEL ROOFING SYSTEM

The roofing system consists of precast or cast-in-situ ribs/beams at a fixed spacing covered with panels. The roof shall be finished by thin layer of concrete with weathering tiles. In this technique, saving in volume of materials and cost

effectiveness is achieved. The filler slab roofs are the solid reinforced concrete slab with partial replacement of concrete in the tensile zone by filler. These filler materials are cheaper and lighter. The brick panel, filler slab and hollow panels are the roofing system which increases the thermal comfort and cost of the unit comparatively low.

EMBODIED ENERGY IN MASONRY WALLS FOR 1M³

The masonry walls considered for calculations are brick masonry, hollow block masonry, rat trap bond wall using bricks and stabilised mud block. The calculated values are tabulated in Table 2. The obtained data values are interpreted with the rural housing. If the building is constructed with brick and cement mortar 1:6, the energy contribution for the wall of 1 m³ is about **2085 MJ** and plastering of wall of 1m² is **0.0819 MJ**. The data that reveals for the construction of a house for low income group, the total quantity of walling is equal to 10 m³. A reaction of **50%** is observed in this case of the brick wall replaced with stabilized mud block or rat trap bond wall or hollow block were **592.88 MJ, 1080 MJ and 840 MJ** respectively. Among the three alternate walling systems, the SMB walling system has the embodied energy value **72% lesser**. This technique is cost effective and environment friendly.

EMBODIED ENERGY COMPUTATION FOR ROOFS

Various building materials are required for casting a roof of 1 Sq. m. In this study the funicular shell, brick panel roofs, Ferro cement channels and RC joists are compared with the reinforced cement concrete roof. For this purpose of study, plan area of 1 Sq. f is taken. Table 3 gives the computed energy values for different roofs.

RESULTS AND DISCUSSION

The following are the conclusions from the studies

1. The use of building elements for masonry construction reduces the energy consumptions up to **50%** as

4th International Engineering Symposium - IES 2015

March 4-6, Kumamoto University, Japan

- compared with the conventional brick work construction.
2. The reinforced cement concrete is an energy intrinsic technology with embodied values of **8430.45 MJ**. The funicular shell roof, brick panel system have energy intrinsic **540.03 MJ** and **177.49 MJ** respectively.
 3. The RC joist beam has low embodied energy among the various alternatives considered.
 4. The building materials like cement, steel, bricks and glass are the major contribution to the total energy of reinforced concrete buildings.
 5. With the calculated values, the most energy efficient and cost effective choice for a rural housing would be the stabilized mud block for walling and RC joist for roofing.

CONCLUSION

There is no single solution to assure sustained green architecture, but that designers should be aware of the factors to be evaluated when materials and components are specified. The production of sustainable building involves resolving many conflicting issues and requirements. Each design decision has environmental implications. Buildings are the aggregation of multitude of components made from a wide range of different materials. There is no universal agreement of how to calculate embodied energy and there are no universally acknowledged parameters for defining sustainable materials, products or building systems. Environmental energy is one of the methods of assessing the environmental impact of a building. However the environmental implication of material selection extends beyond the embodied energy of the materials.

ACKNOWLEDGMENTS

The authors would like to express their gratitude to Dr K Chinna Raju,, Dr A Balu and Dr K Nagamani for their valuable guidance and support. They would also like to thank their parents for helping me to complete this project.

REFERENCES

- [1] A.Debnath et al., (1995), Comparative Assessment of energy requirements for Different types of residential building in India, Energy and Buildings, Vol.23, No.2, pp. 141-146
- [2] B N Dutta (1976), Estimation and costing in civil engineering, S Dutta and company, Lucknow, pp.471-489
- [3] Ministry of Power, Government of India, 2012, Power sector at a glance All India.
- [4] M.Rai (1984), Energy Conservation in production of building materials, Energy and habitat, Wiley Eastern Ltd, New Delhi, pp.63-65
- [5] Tata Energy and Resources Institute (TERI) (2004), Sustainable Building Design Manual, Vol.2, New Delhi.

Table 1: Embodied energy values for building materials

TYPE OF MATERIAL	UNIT	EMBODIED ENERGY VALUE PER UNIT (MJ)
Burnt bricks	190x90x90 mm	3.00
Hollow concrete block	400x200x200 mm	12.30
Mud block	230x190x100	2.60
Cement	Kg	5.85
Sand	m ³	-
Aggregates	m ³	20.5
Steel	Kg	42

Table 2: Embodied Energy in Masonry walls for 1m³

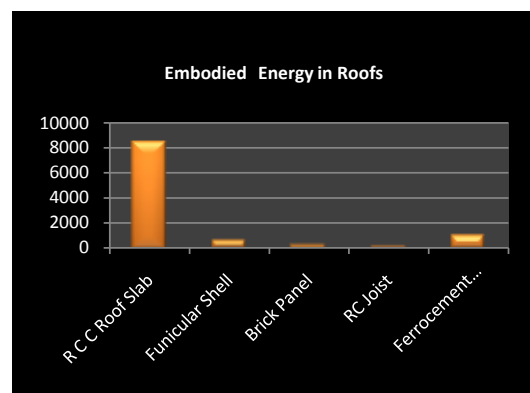
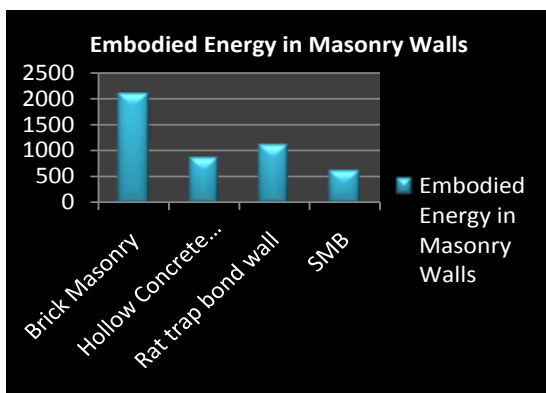
S.No	Types of masonry adopted	Consumption of materials for masonry	Energy contribution of each material in (MJ)	Total energy consumed by masonry for entire building (MJ)
1.	Brick masonry	Bricks	1500	2085
		Cement	585	
		Sand	-	
2.	Hollow concrete block masonry	Hollow blocks	738	840
		Cement	102.08	
		Sand	-	
3.	Rat trap bond wall	Bricks	1080	1080.17
		Cement	0.1755	
		Sand	-	
4.	Stabilised Mud Block	Mud block	228	592.88

Table 3: Embodied energy in roof area for 1m²

S.No	Types of roof adopted	Consumption of materials for roof	Energy contribution of each material (MJ)	Total energy consumed for entire roof (MJ)	Energy saving in %
1.	R.C.C roof slab 120mm thick	Cement (kg)	4212	8430.45	
		Sand (m ³)	-		
		Aggregates (m ³)	18.45		
		Steel (kg)	4200		

4th International Engineering Symposium - IES 2015
March 4-6, 2015, Kumamoto University, Japan

2.	Funicular shell including joist	Cement (kg)	336.96	540.03	93.5%
		Sand (m ³)	-		
		Aggregates (m ³)	1.476		
		Steel (kg)	201.6		
3.	Brick Panel including joist	Brick	90	177.49	97%
		Cement(kg)	45.85		
		Sand(m ³)	-		
		Aggregate(m ³)	0.45		
		Steel(kg)	41.19		
4.	RC joist for running metre	Cement(kg)	63.18	126.46	98.5%
		Sand(m ³)	-		
		Aggregate(kg)	0.277		
		Steel(kg)	63		
5.	Ferro cement channel	Cement(kg)	884.52	947.52	89%
		Sand(m ³)	-		
		Steel(kg)	63		



LIFE CYCLE ENERGY ANALYSIS OF A TRADITIONAL BUILDING IN INDIA: A CASE STUDY

G C Priyanka¹ and G C Gayathri²

1 Department of Environmental Engineering, Erode Sengunthar Engineering College, Anna University, Erode, India. e-mail:priyankacivilstud@gmail.com

2 Department of Civil Engineering, Anna University, Chennai 600025, India. e-mail:gayathrichandramohan7@gmail.com

ABSTRACT: Some of the major environmental concerns of our time are the depletion of the ozone layer, the wastage of limited resources such as oil, gas and minerals, the loss of forested areas, toxic chemical manufacture and emissions, the destruction of natural habitats and pollution of land, water and air. The environmental crisis has made us focus our attention on the impact buildings will have on the environment. Hence we need to be aware of the possibilities of saving energy by designing buildings according to vernacular architecture, which normally involves informal building of structures through traditional building methods by local builders and locally available materials. This paper discusses the significance of material selection and construction system with respect to its energy incurred throughout its life cycle (Raw material acquisition, product manufacture & transportation, construction, operation and maintenance, renovation and demolition). It is all mainly related to the multi-faceted nature of environmental sustainable design.

Keywords: Vernacular Architecture, Traditional Buildings, Life Cycle Energy Analysis

INTRODUCTION

The architecture of India is rooted in its history, culture and religion. Throughout India, buildings are constructed by traditional methods and without architects. Whether creating family houses or village temples, grain stores or fine mansions, the Indian builder works according to the ancient and sometimes religious practice with whatever materials are to hand, to suit local conditions and extremes of climate. The builders of these structures are unschooled in formal architectural design and their work reflects the rich diversity of culture. Usually a large number of buildings are built for residential, commercial and industrial purposes. World-wide buildings consume 30 – 40% amount of primary energy in their construction, operation and maintenance and held responsible for emitting 40% of global warming. In India, 24% of primary energy and 30% of electrical energy is consumed in buildings. Indeed, the

designers of these traditional buildings were often concerned with saving energy, fuel costs historically being higher than they are now, we should understand that older buildings have important lessons to teach, with regard both to the design of new buildings and the repair of existing ones.

The aim of the paper is to demonstrate and discuss the use of LCEA in the context of traditional buildings and to stimulate the awareness upon the society that the old traditions in art and building architecture and to bring them in the main stream of National construction and to create traditional construction concept extracting the essence from ancient text and interpret it to suit modern constructions.

TYPICAL OUTLINE OF THE TRADITIONAL BUILDING

For simplicity and clarity, Life cycle energy analysis is demonstrated for a traditional residential building. The building analysed

4th International Engineering Symposium - IES 2015

March 4-6, Kumamoto University, Japan

is built before 300 years and is situated in Tamilnadu, India. It is designed according to the climatic conditions and with the number of energy saving techniques.

LIFE CYCLE ENERGY

The life-cycle energy use for the building derived by the summation of three main components: initial and recurring embodied energy and operating energy. Demolition energy is insignificant.

i) EMBODIED ENERGY OF STRUCTURAL SYSTEM

The embodied energy of a building is the energy used to acquire raw materials and manufacture, transport and install building products in the initial construction of a building. Table 1 summarizes the results of studies on the initial embodied energy of the traditional building. The initial embodied energy for the studies building is about MJ.

ii) RECURRING EMBODIED ENERGY

Life cycle energy analysis must account for the changes in embodied energy associated with building up-keep and improvements. It is useful to distinguish regular repainting, recarpenting, replacement of systems, lamps etc. and major periodic refurbishment due to changes in tenancy.

Maintenance and replacement occur periodically over the life of a building. It can be divided in to two categories:

- Maintenance incurred during a completed life cycle of a material or component. For a product which completes its lifecycle, the number of maintenance (repair) cycles required is the product life/repair interval corrected for the possibility of forgone repairs near the end of the product life.
- Maintenance incurred during the incomplete lifecycle of a product due to the expiration of the building. For the last replacement of a product, the number of repair cycles will depend on the years remaining before the life of the building expires rather than the product life.

Replacement refers to the total replacement (100%). The number of times a component is replaced is given by the building life or product life corrected for

the possibility that if the replacement occurs near the end of the building life, non-essentials and replacements would be avoided. For this particular type traditional building, the recurring embodied energy is very less and hence it is neglected.

iii) DEMOLITION ENERGY

Energy used to demolish buildings and transport and disposal of waste material is referred to as demolition energy. Current demolition practice involves intense application of energy and haulage to landfill. In any case, the energy required to demolish the building is generally considered to be very small compared to the rest of the life cycle energy. Therefore the demolition energy is neglected. Furthermore, embodied energy savings from recycling or reusing demolished materials should be attributed to the next user, not to the demolished building.

iv) OPERATING ENERGY

Operating energy comprises the energy used for space heating and cooling, hot water heating, lighting, refrigeration, cooking and appliance and equipment operation. Space heating and cooling is often simulated using computer programs such as CHENATH, TRANSYS, TEMPAL and DOE 2. The energy used to heat, cool, ventilate and light buildings represent over 50% of India's national energy use, with approximately 20% used in residential buildings and the remainder in commercial buildings. Operating energy varies considerably with the building use patterns, climate and season and the efficiency of the building and its system. The building is partially occupied during day time between 8.00 a.m to 6.00 p.m and is fully occupied during night time and fully operated during week end i.e. Saturday, Sunday and other public holidays. Thus calculated annual operating energy demand of the building for its operation is then converted to primary energy using primary energy conversion factor. A primary energy conversion factor of 3.4 is adapted for electricity from National Grid. Annual operating energy of the building is assumed to be constant throughout its life span.

4th International Engineering Symposium - IES 2015

March 4-6, Kumamoto University, Japan

Table 2 summarizes the operating energy associated with the building and chart 2 gives the summary of annual operating energy.

v) LIFE CYCLE ENERGY

The main benefit of LCEA is that the embodied energy costs of products, design modifications and strategies used to optimize operational energy can be evaluated. Life cycle energy was calculated using the equation:

$$\text{LCE} = \text{EE}_i + (\text{EE}_{\text{rec}} + \text{OE}) \times \text{building lifetime}$$

where:

LCE = the life-cycle energy;

EE_i = the initial embodied energy of building;

EE_{rec} = the annual recurrent embodied energy (for example, in maintenance); and

OE = the annual operational energy (including space conditioning and other domestic energy uses).

SIGNIFICANCE OF OPERATING ENERGY

The energy used to operate the building is by far the largest component of life cycle energy use for a common residential building. For this typical building, the energy to heat, cool, light and provide ventilation is considerably less because of its sustainable design. The **annual operating energy** was found to be **24393 MJ**. The space provided at the centre supplies the building with natural ventilation and lighting thereby reducing the operating energy costs. Also the fuel used for cooking is obtained from small scale biogas plant with the biomass as cow dung slurry. Though the efficiency of the biogas plant depends upon the quantity of biomass fed in to it, the building manages to get the fuel for cooking throughout the year. Operating energy can be reduced by utilizing the biogas, which can be converted to electrical energy by proper transferring devices. Moreover, if the building operating energy was reduced by 75% representing a performance which will likely be common place early in the 21st century, operating energy would fall to

approximately 5.5% life cycle energy use for India respectively.

SIGNIFICANCE OF RECURRING EMBODIED ENERGY

At the current energy standards, the embodied energy for replacement and repair is very insignificant. The recurring energy is very less when compared with the initial embodied energy particularly for this building, the reason being the use of natural materials such as jiggery, agle marmelos, chebulic myrobalan which generally made the building to sustain for longer years. The use of teak wood which is prone to termite attacks needs to be repaired and taken care of at frequent intervals for a general building. But the use of herbal slurry such as neem prevents the material from such attacks. It also increases the life of the material. Now a days, in almost all residential buildings, the recurring embodied energy is found to be equal as that of initial embodied energy at its end-period. The addition of herbal slurries in the construction of the building not only increases the life time but also reduces the recurring energy of the building.

SIGNIFICANCE OF EMBODIED ENERGY

Though a net zero operational energy building is now achieved, a zero life cycle energy is likely to be more difficult. This is due to the fact that the embodied energy cannot be achieved to zero. The energy involved in processing the materials and its transportation will certainly increase the initial embodied energy. We cannot completely attain a zero initial embodied energy, but it can be minimized by suitable construction techniques. By adopting the traditional building materials and techniques, the embodied energy can be drastically reduced. Another alternative solution is utilizing the locally available materials for construction, which will reduce the transportation and fuel costs. By doing so, vernacular architecture can save up to 25% of the overall cost.

SENSITIVITY ANALYSIS

Life cycle energy of the building is also evaluated for different life spans of the building to assess its impact on LCE

demand of the building. The demand is decreasing with increase in life span of the building. The embodied energy which decreases in increase in the life span of the building causes LCE of the building to come down.

CONCLUSION

Arising the way they are designed and constructed, traditional buildings respond to changes in temperature in very particular ways. Properly understood, the way traditional buildings behave can be exploited to make them more comfortable and more energy efficient, while saving money on heating bills. Good architectural conservation is environmentally, sustainable as a nation we should be conserving historic buildings not only for their cultural value but also because it makes environmental sense.

ACKNOWLEDGEMENTS

I would take this opportunity to thank my guide Mr Sampathkumar and Erode Sengunthar Engineering College for providing me resources and extending a great support. I am very much grateful to my father Mr.V.G.Chandramohan for his suggestions to complete this paper.

REFERENCES

- [1] B.Thomas, A Jonsson and A.M.Tillman, (1996), LCA of building framed structures, Technical Environment and planning report, Goteborg.
- [2] Development Alternatives (1995), Energy Directory of building materials, BMTPC, New Delhi.
- [3] K.Adalberth (1999), Energy use in four Multi-family houses during their life cycle, International Journal of Low energy and sustainable buildings, Vol.1, pp. 1-20.
- [4] T.N.Gupta (1998), Building Materials in India, BMTPC, Wordsmithy, New Delhi
- [5] T.Ramesh, R.Prakash and K.K.Shukla, (2012), Life Cycle approach in Evaluating energy performance of residential buildings in Indian Context, Energy and Buildings, Vol.54, pp.259-265

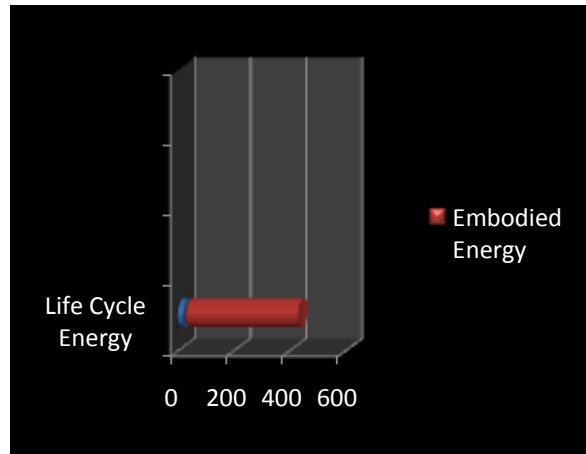


Chart 1 : Life Cycle Energy

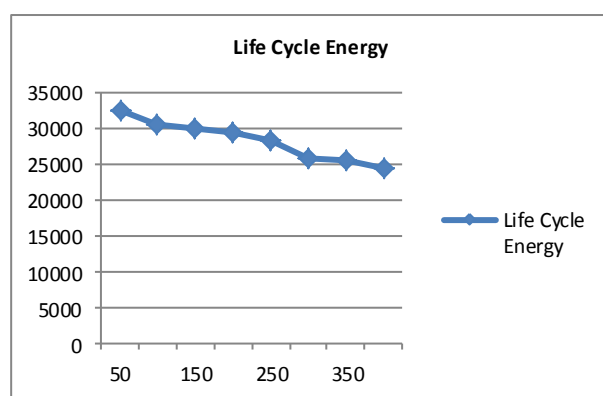
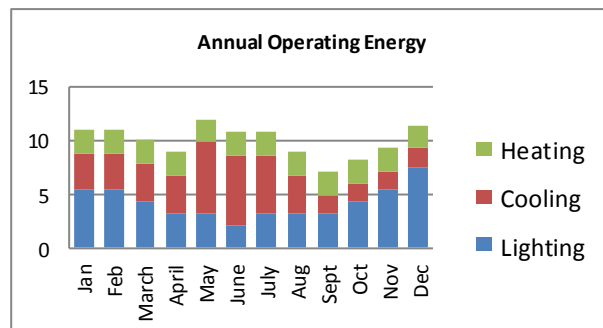


Chart 2 And Chart 3: Annual Operating Energy Summary & Sensitivity Analysis

4th International Engineering Symposium - IES 2015
March 4-6, 2015, Kumamoto University, Japan

Table 1: Initial Embodied Energy of the Building

MATERIAL	UNIT	QUANTITY	ENERGY INTENSITY (MJ/UNIT)	EMBODIED ENERGY (MJ)
Aegle Marmelos	M ³	0.14	-	-
Brick	M ³	105	3	315
Chebulic Myrobalan	M ³	0.14	-	-
Cow dung slurry	M ³	2	-	-
Egg	M ³	2	-	-
Jaggery	M ³	0.11	-	-
Lime slurry	M ³	5.10	7.12	36.31
Mud Slurry	M ³	4.2	-	-
Stone	M ³	10.26	1.00	10.26
Tiles	M ²	15	1.47	22.05
Teak	M ³	5.5	2.12	11.66
Wood	M ³	21.5	0.751	16.146
Total				411.43 MJ

Table 2 : Operating Energy of the Building

Type of Appliances	Units	No. Of Appliances	No of hours Used/day	Load	Energy (MJ)
Lamp	60 watts	5	7	300 watts	7.56
Ceiling Fan	60 watts	4	7	240 watts	6.048
Table Fan	40 watts	1	2	40 watts	0.288
TV	150 watts	1	5	150 watts	2.7
Heater	1500 watts	1	15 minutes	1500 watts	2.16
Radio	50 watts	1	5	50 watts	0.9
Total					19.656

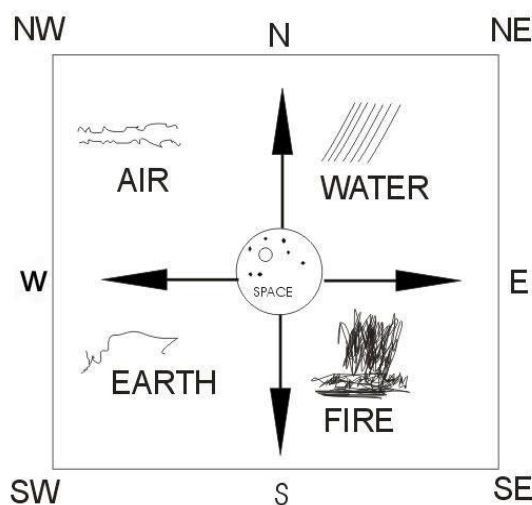


Fig.1 Typical outline of the traditional building

Composite Corrosion Protection System In Rehabilitation Of Steel Structures In Corrosive Environment - A Case Study

Raghuvir Salkar¹, Ishita Manjrekar², and Abhishek Salkar³

1. *Kuvelkar Salkar Associates, Consulting Engineer, A2, Ramakant bldg., 18 June Road, Panaji 403001, India. (Corresponding Author) Email : salkar@ksa-india.com*
 2. *Sunanda Speciality Coatings Pvt. Ltd., Senior Associate, Satyadham, Road No. 2, Sion (E), Mumbai 400022, India. Email : ism@sunandaglobal.com*
 3. *National Institute of Technology Karnataka, Surathkal, Mangalore 575025, India. Email : salkarabhishhek@gmail.com*
-

ABSTRACT: India loses USD 33 billion every year due to corrosion of infrastructure, industrial equipment and other vital installations, according to last estimates from Corrosion Management Committee of Confederation of Indian Industry. This paper addresses corrosion management and prevention using Galvanic Systems, through a case study of a structural steel bridge in Goa, a coastal and corrosive zone of West India. The bridge was found to be in advanced stage of corrosion damage merely one year after its construction, and was treated with a composite treatment of galvanic corrosion protection using custom designed sacrificial anodes, and systematic protective coating system of acyclic, polyisocyanate reticulant based polyurethane. The performance against atmospheric corrosion of this system was observed through of periodic visual observations and physical measurements since early 2012; electrochemical readings were taken at the end of 30 months of treatment. It is seen that the composite system exhibits satisfactory protective behaviour, and may be considered for treatment of similar structures in corrosive environments.

Keywords: galvanic anodes, corrosion protection, coatings, half cell potential, bridges

INTRODUCTION

Corrosion of steel has been established as the predominant factor causing widespread premature deterioration of marine construction worldwide leading to the failure of the structures.

The use of steel in bridges goes back over 100 years. Modern bridges currently have a design life requirement of 120 years, and the performance of the protective system is a critical factor. Furthermore, reductions in the number of repainting cycles have become significant in the evaluation of whole life costs.

As a result, the repair costs nowadays constitute a major part of the current spending on existing infrastructure. Quality control, maintenance and planning for the restoration of these structures need non-destructive inspections and monitoring techniques that detect the corrosion at an early stage. Corrosion loss consumes considerable portion of the budget of the country by way of either restoration measures or reconstruction. There have been a large number of investigations on the problems of corrosion of steel. Properly monitoring the structures for corrosion performance and taking suitable measures at the appropriate time could effect a lot of saving.

4th International Engineering Symposium - IES 2015

March 4-6, 2015, Kumamoto University, Japan

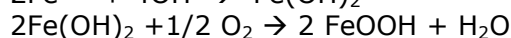
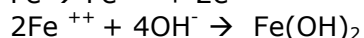
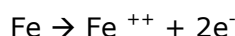
Moreover, the repair operation themselves are quite complex and require special treatments, and in most instances the life expectancy of the repair is limited. In such conditions, the corrosion protection methodology is not addressed properly. This paper explains in detail about the usage of sacrificial anodes, which postpones the corrosion to a maximum and a case study on the marine structures rehabilitated using the sacrificial anodes at highly corrosive environmental zone Goa, India.

CORROSION

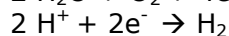
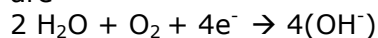
Corrosion mechanism

All metals except gold and platinum are thermodynamically unstable under normal atmospheric conditions and will eventually revert to their oxides (or other compounds). Therefore the information of importance to the engineer who would use the metal is not whether the metal will corrode but how fast the corrosion will occur.

The corrosion of steel is an electrochemical process that involves the transfer of charge (electrons) from one species to another. For steel, the anodic half cell reaction involves the oxidation or dissolution of iron:



The most likely cathodic half cell reactions are



Which of these anodic and cathodic reactions will actually occur in any specific case depends on the availability of oxygen and on the pH of the environment in the vicinity of the steel.

Corrosion is commonly caused by either the presence of sufficient concentrations of chloride ions or an otherwise acidic environment. The most common cause of initiation of corrosion of steel is the presence of chloride ions. The source of

chlorides may be contaminants, marine environments, industrial brine or de-icing salts. The actual detailed mechanism of breakdown is not known because of the difficulties in examining the process on an atomic scale. However, the net result is that chloride induced active corrosion, once started proceeds auto catalytically, that is, in a self feeding manner. The chloride and ferrous ions react to form a soluble complex that diffuses away from the anodic site. When the complex reaches a region of high pH it breaks down, precipitating an insoluble iron hydroxide and liberating the chloride to remove more iron from the steel member. Moreover, because of the region of local breakdown on the passive film becomes anodic, more chloride ions are attracted to that area of the steel than the surrounding cathodic areas so the local concentration of chloride ions increases.

The initial precipitated hydroxide has a low state of oxidation and tends to react further with oxygen to form higher oxides.

Cost of Corrosion

The observed bridge corrosion damage can be broken down into three distinct phases: the corrosion initiation phase, the corrosion propagation phase, and the replacement phase.

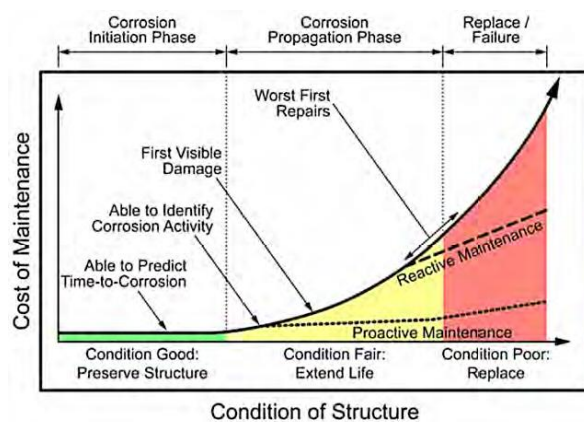


Fig1: Typical Bridge Condition as a Function of Time

Corrosion Initiation Phase

Early in a bridge's life corrosion-related damage is usually not a factor. The length of this initiation phase can be extended by selection of corrosion-resistant materials,

4th International Engineering Symposium - IES 2015

March 4-6, 2015, Kumamoto University, Japan

upgrading the quality of the materials, and by construction detailing.

Corrosion Propagation Phase

Once corrosion initiates, it takes time before the process creates damage that is visually obvious. Measurement of corrosion potential can identify corrosion before the rust is actually visually noticed. During this initial corrosion propagation phase is when maintenance repairs typically occur.

Replace / Failure Phase

At the far right of Figure 1, the condition of the bridge has degraded to poor, and the restoration costs may become prohibitive, and instead the structure must be replaced even if it is not functionally obsolete. This phase also is one where there is an increasing risk of failure.

TYPICAL METHODS USED TO PROTECT STEEL STRUCTURES AND WHY THEY FAIL

Structural Steel infrastructure has been typically protected with coatings. Over the last 10 years coating technologies have significantly matured and are contributing significantly to increasing the service life of structural steel bridges.

But as with all coatings, the most important pre-requisite for a coating to provide protection to steel is proper surface preparation of the steel surface before the application of the steel. Typically sand blasting or grit blasting is carried out to rid the steel of existing corrosion as per standard specification. Various methods and grades of cleanliness are presented in ISO 8501-1: 2001, (BS 7079, Part A1 1989). This standard essentially refers to the surface appearance of the steel after abrasive blast cleaning, and gives descriptions with pictorial references of the grades of cleanliness.

However, while the good intent of this specification is appreciated at job sites it is often noticed, that the actual application of coating takes place a few hours or sometimes days after the blasting is done. And in the case of newly blasted steel, the

exposed surface is so raw and reactive that a layer of rust or corrosion product is seen to form on the surface within a few hours of blasting. This phenomenon is known as "flash rusting" of steel. Flash rusting is most common in humid, marine environments. And the best coatings applied on a well treated surface on which a layer of flash rust has formed, compromises the life of the coating and therefore the service life of the bridge.

Consequently it is important to stabilize the freshly blasted steel with a rust inhibitor or a surface passivator immediately after blasting is complete. Numerous case studies around the world point to the importance of this step as critical in designing a surface protection methodology for structural steel.

USE OF GALVANIC ANODES TO INCREASE SERVICE LIFE

Galvanic anodes are galvanic devices designed to neutralize or slow down new corrosion cells, which would otherwise develop in the structure, thereby extending the service life. These discrete units are designed to be attached to the structure. Based upon many of the same principles used for protecting pipelines and ships from corrosion, these anodes are "sacrificial" in nature. The anodes take advantage of the natural galvanic differences which exist between different metals.

The heart of the devices is a metallic anode composed of a proprietary zinc based alloy, which is cast around a pair of steel tie wires. This unit is encased within a cementitious shell. The device is shaped like a disc.

As the anode corrodes, it releases a supply of electrons. This electrical current travels through the tie wires, into the surrounding steel to reduce new corrosion activity on the steel. The output from the anode will vary according to a number of variables including resistivity of the steel, moisture content, temperature, and quantity of steel. In the same way that climatic

4th International Engineering Symposium - IES 2015

March 4-6, 2015, Kumamoto University, Japan

variations will affect the degree of corrosion in an unprotected structure, the environment into which the anode is installed will have a large influence on its current output. In humid and/or warm climates the anodes tend to corrode more aggressively than in cool and/or dry regions. There, fluctuations in the current output of the anode will vary with changes in the corrosion activity of the steel.

The more severe the situation, the more aggressive the corrosion will be if anodes are not installed. By installing galvanic anodes on the bridge, the anodes provide galvanic protection, thereby reducing the tendency for the steel in the adjacent area to corrode.

Galvanic anodes used for galvanic protection are typically constructed using aluminum, magnesium or zinc. There are several reasons for the usage of zinc alloys namely.

- Zinc has high corrosion efficiency i.e., higher percentages of electrons are discharged from the zinc as it corrodes. These electrons are available to protect the steel.
- As zinc corrodes, it has a relatively low rate of expansion compared to other metals, including steel. This makes zinc anodes particularly suitable for application where the anodes are embedded into concrete structures.

CASE STUDY – CORROSION IN NEW STRUCTURAL STEEL BRIDGE IN MARINE ENVIRONMENT, USAON, GOA, INDIA

DESCRIPTION OF STRUCTURE AND PROBLEM OF PREMATURE CORROSION

Bridge in the case study is a four lane bridge over river Mhadei in Goa (India), and has 4 spans with a total length of 180 meters, and maximum span of 62.4 meters. The bridge has a steel superstructure, and a composite deck of steel beams and reinforced concrete slab. Piers are of reinforced concrete, and rest on bored cast-in-situ RC piles. All

structural steel that was used in bridge construction was sand blasted to Sa2 standard, and then its surface treated with one coat of zinc rich epoxy primer of 50 micron DFT and two coats of coal tar epoxy paint of total 100 micron DFT. Figure 2 shows a photograph of the bridge from the downstream side of the river.



Figure 2 : Bridge Elevation

The bridge was opened to traffic on 25th February, 2009, after it successfully passed prescribed load test. Figure 3 shows load test in progress.



Figure 3 : Load Test in Progress

It was agreed that the bridge would be visually inspected every six months for a period of 3 years from the date of its opening. During the second inspection carried out in February, 2010, signs of corrosion were noted in the bridge trusses. Figure 4 shows some of the corroded areas. This was alarming since the bridge structure was just one year old and was well treated with suitable paints.



Figure 4(a) : Corrosion at a Joint



Figure 4(b) : Corrosion in a Member



Figure 4(c) : Corrosion in a Member



Figure 4(d) : Corrosion in a Member

DESCRIPTION OF PROTECTION SYSTEM

The protection system recommended included the following steps:

1. Sand Blasting was carried out to remove all the deposits of existing corrosion product from the surface of the bridge. Sand and machines of proper specification and grading were brought from Mumbai, about 600 Km away from the job site to ensure proper surface treatment.
2. Within an hour of blasting the freshly blasted steel surface was treated with rust passivating and stabilizing chemicals so as to prevent the build up of flash rust. The coating is spray or brush applied to the surface. The chemical reacts with corrosion products to convert them to a stable passivating nanofilm on the surface of the steel and return the steel back to its original greyish white colour and special surface acting chemicals help in promoting the adhesion of consequent coatings to the steel surface.
3. Next the sacrificial anodes were installed on the entire structure at the rate of 1 anode per 2 square meters of area. Electrical connectivity between the structure and the anodes was established.
4. As a special measure, to further enhance the service life of the structure, a composite corrosion protection system of galvanic anodes followed by a multilayered long chain, high build, epoxy primer was applied.
5. The final two coats of the composite anode plus protective coating system were done using a two component, acyclic, polyisocyanate reticulant based polyurethane coating for its notable UV resistance, ability to adhere to the

4th International Engineering Symposium - IES 2015

March 4-6, 2015, Kumamoto University, Japan

substrate and high efficiency of corrosion protection.

Figures 5 and 6 show photographs of the bridge after it received the above treatment.



Figure 5 : Anodes on Bridge Truss



Figure 6 : General View after Treatment

The structure's performance was then periodically monitored every six months through visual observations of the treated surfaces, and also physically through dimensional measurements of various members using micrometer screw gage. Also, corrosion state of the bridge was evaluated at the end of 30 months of treatment, using an electrochemical method viz. Half cell potential of the structure.

HALF-CELL ELECTRICAL POTENTIAL METHOD

Half-cell potential measurements involve measuring the potential of the steel structure relative to a reference half cell placed on the surface of the steel. The half-cell is usually a copper/copper sulphate or silver/silver chloride cell. The risk of corrosion of the steel in the immediate region of the test may be related empirically to the measured potential difference. The case study presented in this paper, the half cell used to measure corrosion potential used was copper/copper sulphate.

The half cell testing apparatus consists of the following:

The cell consists of a rigid tube or container composed of dielectric material that is non-reactive with copper or copper sulphate, a porous wooden or plastic plug that remains wet by capillary action, and a copper rod that is immersed within the tube in a saturated solution of copper sulphate. The solution is prepared using reagent grade copper sulphate dissolved to saturation in distilled or de-ionized water. The rigid tube should have an inside diameter of not less than 25 mm; the diameter of the porous tube should not be less than 13 mm; the diameter of the immersed copper rod should not be less than 6mm and its length should be at least 50 mm. Present criteria based on half cell reaction of $Cu \rightarrow Cu^{++} + 2e^-$ indicate that the potential of the saturated copper-copper sulphate half cell as referenced to the hydrogen electrode is -0.316 V at 22.2°C.

An electrical junction device is used to provide a low electrical resistance liquid bridge between the surface of the steel and the half-cell. It consists of a sponge or several sponges pre-wetted with a low electrical resistance contact solution. The sponge can be folded around and attached to the tip of the half-cell so that it provides electrical continuity between the porous plug and the concrete member.

4th International Engineering Symposium - IES 2015

March 4-6, 2015, Kumamoto University, Japan

The battery operated voltmeter with $\pm 3\%$ end of scale accuracy at the voltage ranges in use. The divisions on the scale used should be such that a potential of 0.02 V or less can be read without interpolation.

The electrical lead wire should be such that its electrical resistance for the length used does not disturb the electrical circuit by more than 0.0001 V. This has been accomplished by using no more than a total of 150 m and the wire should be suitably coated with direct burial type of insulation.

The structure is connected to one terminal of the voltmeter through the half cell. The other terminal of the voltmeter is connected to ground / earth or water. Under some circumstances the steel surface has to be pre-wetted with a wetting agent. The electrical half cell potentials are recorded to the nearest 0.01 volts (V).

The reference guidelines for predicting probability of corrosion or in other words the performance of the corrosion protection system are as below:

Table 1 : Correlation Corrosion Potential of Steel in Soil and Corrosion

Measured Potential Difference	Probability of Corrosion
More negative than - 600 mV	High probability of corrosion
Between -400 mV and -600 mV	Uncertainty of corrosion
More positive than - 400 mV	No probability of corrosion

VISUAL OBSERVATIONS, PHYSICAL MEASUREMENTS, ELECTROCHEMICAL READINGS

As mentioned earlier in the paper, treatment was carried out in March, 2012, and first inspection was carried out 6 months later in September, 2012. Subsequent inspections were carried out every 6 months. During each of these inspections, visual observations were made to note signs of corrosion, if any,

and physical measurements of thickness of various members were carried out using a vernier calliper. None of the visual inspections including the last one carried out in September, 2014 revealed any signs of corrosion in the bridge. Practically, there was no change in thickness of truss members over the 30 month period from March, 2012 to September, 2014; thickness was measured at 243 number of locations evenly spread over 3 trusses of the bridge. Random voltage readings using Half Cell Potentiometer were taken at 113 points on each of the three bridge trusses. The average reading for upstream, central and downstream trusses were -537, -258 and -567 mV, respectively, and the respective standard deviation were 0.126, 0.172 and 0.208. Voltage reading was also taken on a "witness specimen" which was kept at the bridge site since March, 2012. This specimen was a bare steel specimen, without any protective treatment or coating. Voltage reading on this specimen which was in rusted condition was noted as -113 mV. The above voltage readings on the bridge and the witness specimen do not reflect the actual corrosion free condition of the bridge, and therefore, the voltage readings cannot be treated as reliable.

CONCLUSIONS

The following conclusions are deduced from this study:

- Voltage readings taken using half cell potentiometer were found to be unreliable in the present case.
- Visual observations and physical measurements of thickness of various bridge members taken every 6 months over the last 30 months, suggest that the treatment has worked well in providing corrosion resistance to the bridge.
- The treatment described in this paper may be considered for treatment of similar structures in corrosive atmosphere.

ACKNOWLEDGEMENTS

The authors would like to express their thanks for Mr. G. Mishra of Kuvelkar Salkar

4th International Engineering Symposium - IES 2015

March 4-6, 2015, Kumamoto University, Japan

Associates, Goa, for his help in monitoring
of this bridge.

REFERENCES

- [1] Corbett, W.D., "The Future of Bridge Coating: A National Qualification System for Structural Steel Coatings," *Journal of Protective Coatings and Linings* (January 2004).
- [2] Corrosion Control Plan for Bridges – A NACE International White Paper, November 2012 Corrosion Management Committee of Confederation of Indian Industry – Press Release.
- [3] Foley, R.T., "Complex Ions and Corrosion," *Journal of the Electrochemical Society*, V, 122, No. 11, 1975, pp 1993 – 1549.
- [4] Kline, E.S., "Steel Bridges: Corrosion Protection for 100 Years," *Journal of Protective Coatings and Linings* (May 2008).
- [5] Lee, S.K., "Current State of Bridge Deterioration in the U.S. – Part 1," *Materials Performance* 51, 1 (2012).
- [6] Romanoff, M., "Underground Corrosion", National Bureau of Standards Circular 579, 1957, Reprinted by NACE, 1989.

Experimental Studies on the Performance of Blended Cement Mortars at Elevated Temperatures

Subhash C. Yaragal ¹, R Pavan Kumar ¹, Prathipati Vivek ¹, Sujeeet Kumar Ranjan ¹, and Anil Hegde ²

1 Department of Civil Engineering, National Institute of Technology Karnataka, Surathkal - 575025, India. e-mail:subhashyaragal@yahoo.com

2 Vimal Anil Civil & Structural Engineers, Sterling Chambers, Kalakunj Road, Kodialbail, Mangalore - 575 003, India.

ABSTRACT: An experimental study was carried out to understand the performance of blended cement mortar subjected to elevated temperature. After the specimen were subjected to elevated temperature, its residual compressive strength was studied. Ordinary Portland Cement (OPC) along with Fly Ash and Ground Granulated Blast Furnace Slag (GGBS) were used as blended cement that was used in this investigation. Cement was partially replaced with different percentages of fly ash and GGBS by weight. Four different mixture compositions of mortar specimen (30 each type) were cast . OPC mortar was prepared as reference mortar. All mortar compositions had Binder : Sand ratio of 1:3. The blend compositions include Ternary blend of OPC, Fly Ash and GGBS, Binary blend of OPC and GGBS. The investigation was planned in two phases. In the first phase, the compressive strength of mortar specimen of all the four different compositions at ambient temperature was investigated. In the second phase, the specimen were exposed to elevated temperatures of 200°C, 400°C, 500°C and 600°C in an electrical furnace for one hour retention time after which the residual compressive strength was obtained. The residual compressive strength as a percentage of original compressive strength at different temperatures for the above blend compositions were investigated. The observations showed that the compressive strength of OPC attains maximum in 28 days while other blended mortar attain strength in around 2 months. Following this, the effect of elevated temperature on normal and blended mortar was studied. Mortar spalls at around 500°C. Mortar blended with fly ash showed better results.

Keywords: Mortar, Blended cement, Fly ash, GGBS, Compressive strength

INTRODUCTION

Cement mortar in various blended forms is widely used in different parts of Civil engineering structures. Blended mortar in right composition can give additional and superior properties compared to normal cement mortar. These properties are useful in improving the performance of RCC structure as a whole. During its life time, every structure is exposed to external agents which can affect its serviceability. One among them is fire where the structure has to sustain high temperature. The risk of being exposed to

high temperatures is high. Thus, better understanding of the behaviour of high-strength mortar at high temperatures gains importance for predicting the mortar residual properties. Concrete structures are subjected to high temperatures (reactor, vessels, thermal shock, fire, coal gasification vessels, some industrial applications etc.) The mechanical properties such as strength, modulus of elasticity and volume stability of concrete and mortar are significantly reduced during these exposures. This may result in undesirable structural failures. Therefore, the properties of concrete

4th International Engineering Symposium - IES 2015

March 4-6, Kumamoto University, Japan

retained after a fire are of importance for determining the load carrying capacity and for reinstating fire-damaged constructions. The cement mortar forms the outer most coat of the concrete structure, which prevents the temperature rise in the inner concrete core and reinforcement. As steel reinforcement is more susceptible to the effect of elevated temperatures than concrete, it is necessary to provide enough cover for the steel reinforcement. The mortar should have good heat insulating properties. Several blends of cement mortar with materials of good heat insulating properties can be used. Fire endurance of such material blends have been investigated in this study.

When exposed to high temperatures, the chemical composition and physical structure of the cement mortar change considerably. The dehydration such as the release of chemically bound water from the Calcium Silicate Hydrate (CSH) becomes significant above about 110°C. The dehydration of the hydrated calcium silicate and the thermal expansion of the aggregate increase internal stresses and from 300°C micro cracks are induced through the material. Calcium hydroxide [Ca(OH)₂], which is one of the most important compounds in cement paste, dissociates at around 530°C resulting in the shrinkage. Fire is generally extinguished by water and CaO turns into [Ca(OH)₂] causing cracking and crumbling of concrete. Therefore, the effects of high temperatures are generally visible in the form of surface cracking and spalling. Some changes in colour may also occur during the exposure. The alterations produced by high temperatures are more evident when the temperature surpasses 500°C. Most changes experienced at this temperature level are considered irreversible. CSH gel, which is the strength giving compound of cement paste, decomposes further above 600°C. At 800°C, mortar is usually crumbled. As a result, severe micro-structural changes are induced and cement mortar loses its strength and durability. Cement mortar is a composite material produced from cement, sand and water. Therefore, the type and properties of aggregate also play

an important role on the properties of concrete exposed to elevated temperatures. So, in this work, a study on the response of both normal and blended cement mortar to different temperatures by varying the proportion and type of blending material is made.

M. Shariq, J. Prasad and A.K. Ahuja (2008) have studied the effect of curing procedure on the compressive strength development of cement mortar and concrete incorporating ground granulated blast furnace slag. The compressive strength development of cement mortar incorporating 20, 40, and 60% replacement of GGBS for different types of sand and strength development of concrete with 20, 40 and 60% replacement of GGBS on two grades of concrete was investigated. The compressive strength of cement mortar and concrete were obtained at the ages of 3, 7, 28, 56, 90, 150 and 180 days. Test results showed that incorporation of 20% and 40% GGBS is highly significant to increase the compressive strength of mortar after 28 days and 150 days respectively. The magnitude of compressive strength of mortar for standard sand is higher than that of the magnitude of river sand. Incorporating 60% GGBS replacement is showing lower strength at all ages and water-cement ratio for both types of sand. The compressive strength of OPC concrete shows higher strength as compared to GGBS based concrete for all percent replacement and at all ages. Incorporating 40% GGBS, is highly significant to increase the compressive strength of concrete after 56 days than the 20% and 60% replacement. Among GGBS based concrete 40% replacement is found to be optimum.

Md. Moinul Islam, Md. Saiful Islam, Md. Aftabur and Amrita Das (2011) have studied the effects of GGBS on strength development of mortar and the optimum use of slag in mortar. Cement was partially replaced with seven percentages (10%, 20%, 30%, 40%, 50%, 60% and 70%) of slag by weight. OPC mortar was also prepared as reference mortar. A total

4th International Engineering Symposium - IES 2015

March 4-6, Kumamoto University, Japan

of 400 cubes and briquet mortar specimen were cast and compressive as well as tensile strength of the mortar specimen were determined at curing age of 3, 7, 14, 28, 60, 90 and 180 days. Test results show that strength increases with the increase of slag up to an optimum value, beyond which, the strength values start decreasing with further addition of slag. Among the seven slag mortars, the optimum amount of cement replacement is about 40%, which provides 19% higher compressive strength and 25% higher tensile strength as compared to OPC mortar.

Md. Moinul Islam and Md. Saiful Islam (2010), have reported the results of an experimental investigation carried out to study the effects of fly ash on strength development of mortar and the optimum use of fly ash in mortar. Cement was partially replaced with six percentages (10%, 20%, 30%, 40%, 50%, and 60%) of class F fly ash by weight. Ordinary Portland Cement (OPC) mortar was also prepared as reference mortar. Compressive as well as tensile strengths of the mortar specimen were determined at 3, 7, 14, 28, 60 and 90 days. Test results show that strength increases with the increase of fly ash up to an optimum value, beyond which, strength values start decreasing with further addition of fly ash. Among the six fly ash mortars, the optimum amount of cement replacement in mortar is about 40% which provides 14% higher compressive strength and 8% higher tensile strength as compared to OPC mortar.

Monal D Rao, Subhash C. Yaragal, Kiran Sara Chacko, Nivedita G and K S Babu Narayan (2012) made an investigation to compare the compressive strength of cement based concretes containing silica fume and fly ash at elevated temperatures and when suddenly quenched in water. Four concretes of different mixtures with varying amounts of fly ash and silica fume were exposed to elevated temperatures of 150°C, 300°C, 450°C, 600°C and 750°C for a retention period of one hour. The residual strengths of these specimen were determined by axial compressive strength

tests after cooling by sudden quenching in water. Strength and weight losses have been compared with the initial values.

Omer Arioz (2007) has presented the effects of elevated temperatures on the physical and mechanical properties of various concrete mixtures prepared by OPC, crushed limestone and river gravel. Test samples were subjected to elevated temperatures ranging from 200 to 1200°C. After exposure, weight losses were determined and then compressive strength test was conducted. Test results indicated that weight of the specimen significantly reduced with an increase in temperature. This reduction was very sharp beyond 800°C. The effects of water/cement ratio and type of aggregate on losses in weight were not found to be significant. The results also revealed that the relative strength of concrete was more pronounced for concrete mixtures produced by river gravel aggregate. The results of the physical and mechanical tests were also compared with those obtained from differential thermal analysis, and colour image analysis.

This work reports the performance of different cement mortar compositions (normal and blended) at elevated temperatures.

MATERIALS

Ordinary Portland Cement (OPC) 43 grade was used and its properties are tabulated in Table 1. Chemical compositions of OPC are tabulated in Table 2.

Ground Granulated Blast Furnace Slag (GGBS)

The GGBS was procured from M/s. Jindal Steel works, Hospet, Karnataka State (JSW). Tests were conducted to find the physical properties of GGBS and the results are tabulated in Table 3. The chemical properties are shown in Table 4.

Fly ash

Along with GGBS was also used as blending material. It is whitish in color.

Water

4th International Engineering Symposium - IES 2015

March 4-6, 2015, Kumamoto University, Japan

Water used for both mixing and curing was free from injurious and deleterious materials. In the present investigation potable tap water was used.

Sand

Indian Standard Sand (Ennore sand) confirming to IS 650 was used. The sand is a quartz. It was free from silt and whitish in color. All the sand was passing through 2mm sieve and retained on 90 μ IS sieve. Particle size distribution is presented in Table 5.

Cement mortar mixes

In the present study, a total of 4 mixes consisting of different blend proportions of binder were made. The binder : cement ratio was maintained as 1:3 throughout. Water was taken as per cement blending consistency. All mixes were prepared at room temperature.

Mix 1 - 100%OPC

Mix 2 - 50%OPC & 50%GGBS

Mix 3 - 70%OPC & 30%Fly ash

Mix 4 - 60%OPC, 25%GGBS &15%Fly ash

All test cubes 50 mm² in area were cast and water cured for 28 days.

Heating furnace

The specimen cast were subjected to elevated temperatures with the help of an electric heating furnace. The capacity of the furnace is such that 12 specimen could be placed. The maximum temperature level that the furnace can operate at is 1500 $^{\circ}$ C. The heating and cooling regime of the furnace is linearly varying with time. The heating rate at all temperatures was maintained at 5 $^{\circ}$ C/min. Heat is assumed to be maintained uniformly from all the directions.

EXPERIMENTAL METHODOLOGY

The cured specimen were removed from water and their compressive strength at room temperature was obtained. After that the specimen were tested for their response to temperature. The specimen were dried, weighed and placed in furnace. The orientation in the furnace was maintained such that all the cubes were

exposed to heat properly. Then the cubes were subjected to elevated temperature of 2000 $^{\circ}$ C, 400 $^{\circ}$ C, 600 $^{\circ}$ C, 800 $^{\circ}$ C for 1 hour retention time. Then the cubes were removed and weighed. The residual compressive strength and weight loss of specimen at different temperatures were obtained. The surface deterioration was also studied.

RESULTS AND DISCUSSION

Compressive strength variation at ambient conditions

Table 6 presents the results of compressive strengths of mortars of different compositions at room temperature. Figure 1 presents the consolidated results graphically.

Binder composition	Strength in (MPa) for different curing periods (days)					
	7	28	42	56	70	84
100% OPC	260	41.3	43.3	44.0	44.0	44.0
70%OPC+ 30%Fly ash	18.7	27.3	36.6	42.0	42.6	43.3
50%OPC+ 50% GGBS	25.3	34.0	38.7	40.0	42.0	42.6
60%OPC+ 15%Flyash+ 25%GGBS	26.0	41.3	43.0	46.0	46.6	46.6

From Table 6 and Fig. 1, the following findings are noted. Mix 1 achieves nearly 98% of its compressive strength in 28 days. There is no significant increase at the 84 days age. Mix 4 achieves nearly the full strength in 28 days. Blended Mixes 2 and 3 achieves full strength in at least 56 days. Results indicate that Mix 1 and Mix 4, are alright if 28 days strength is considered. However for Mixes 2 and 3, 56 days strength is to be ascertained.

Compressive strength variation at elevated temperatures

Table 7 and Fig. 2 presents variation of compressive strength of cubes of various compositions at elevated temperatures. The following observations are drawn, up to 400 $^{\circ}$ C Mix 1 and Mix 4, do not experience so much strength loss, as compared to mix 2 and Mix 3. At 600 $^{\circ}$ C except Mix 1, all other mixes experienced

4th International Engineering Symposium - IES 2015

March 4-6, 2015, Kumamoto University, Japan

explosive blasting. At 500°C, Mix 1 and 2 showed strength loss but no explosive blasting was encountered, but Mixes 3 and 4 suffered explosive blasting.

CONCLUSIONS

(1) At room temperature, the rate of strength gain was found more for OPC mortar compared to blended cement mortar. OPC attained maximum strength at around a month while other blend compositions took three months to attain the similar strength. But the blend compositions provide the later strength. Hence, for blended cements, to obtain early strength (before 3 months) it is recommended to keep blending limit less than 50%.

(2) All the mortar compositions could not resist the temperature beyond 500°C unlike blended concrete. The residual compressive strength increases up to 200°C, due to autoclaving effect. Most of the specimen failed by explosive blast beyond 500°C. Unlike concrete, mortar is more uniform in all directions. This could be one of the reasons for the explosive blast due to which specimen fails suddenly in all directions.

(3) Weight loss at 200°C was observed to be 2 to 3% of the actual weight and it was found to be 6-7% beyond 400°C.

REFERENCES

- [1] Md. Moinul Islam, Md. Saiful Islam, Md. Aftabur Rahman and Amrita Das, (2011), Strength behaviour of moratr using slag as partial replacement of cement, MIST Journal: Galaxy (Dhaka), Vol. 3.
- [2] Md. Moinul Islam and Md. Saiful Islam, (2010), Strength behaviour of mortar using fly ash as partial replacment of cement, Vol. 1(3), pp. 98-106.
- [3] Monal S Rao, Subhash C. Yaragal, Kiran Sara Chacko, Nivedita G and K S Babu Narayan, (2012), Studies on elevated temperatures and quenching effects on blended concretes, International Journal of Applied Engineering and Technology, Vol. 2 (2) April – June, pp. 31-38.
- [4] Omer Arioz, (2007), Effect of elevated temperature on properties of concrete, Fire Safety Journal, Vol. 42, pp. 516-522.
- [5] Shariq, M., Prasad, J., and Ahuja, A.K. (2008), "Strength development of cement mortar and concrete incorporating GGBS", Asian Journal of Civil Engineering (Building and Housing), 9(1), pp. 61-74.

Table 1 Physical properties of

Ordinary Portland Cement

N o . .	Property	Result obtained			Requirements as per IS code		
1	Specific gravity	3.15			--		
2	Normal consistency	32%			--		
3	Setting times, minutes	Initial 65 Final 225			Not less than 30 Not more than 600		
4	Fineness, m ² /Kg	330			Not less than 300		
5	Soundness, mm	2.50			Not more than 10 mm		
6	Comp. strength, Mpa	3d 30	7d 42	28d 51	3d 22	7d 33	28d 43

Table 2 Chemical composition of OPC

Constituents	Percentage
SiO ₂	20.1
Al ₂ O ₃	3.9
CaO	Nil
Fe ₂ O ₃	2.5
MgO	3.1
SO ₃	2.3
Na ₂ O ₃	0.2
K ₂ O	0.4

Table 3 Physical properties of GGBS

Properties	Result obtained
Color	White
Specific gravity	2.9
Fineness	370 m ² /kg

Table 4 Chemical composition of GGBS

Constituents	Percentage
SiO ₂	33.87
Al ₂ O ₃	10.65
CaO	37.71
MnO	0.65
MgO	9.17
SO ₃	2.97
Na ₂ O ₃	0.70
K ₂ O	0.95
TiO ₂	1.39

Table 5 Particle size distribution

Type	Size	Percent
Grade 1	<2mm, >1mm	33.3
Grade 2	<1mm, >500μ	33.3
Grade 3	<500μ, >90μ	33.3

Table 5 Compressive strengths at room temperatures

Binder composition	Compressive strength (MPa) for different curing periods (days)					
	7	28	42	56	70	84
100% OPC	26.0	41.3	43.3	44.0	44.0	44.0
70%OPC+ 30%Fly ash	18.7	27.3	36.6	42.0	42.6	43.3
50%OPC+ 50% GGBS	25.3	34.0	38.7	40.0	42.0	42.6
60%OPC+ 15%Flyash+ 25%GGBS	26.0	41.3	43.0	46.0	46.6	46.6

Table 6 Compressive strength at elevated temperatures

Binder composition	Compressive strength (MPa) at elevated temperatures			
	200°C	400°C	500°C	600°C
100% OPC	48.0	45.0	38.0	24.0
70%OPC+ 30%Fly ash	45.3	40.0	33.0	#
50%OPC+ 50% GGBS	41.0	34.0	#	#
60%OPC+ 15%Flyash+ 25%GGBS	48.0	46.0	#	#

- Cubes suffered explosive blast

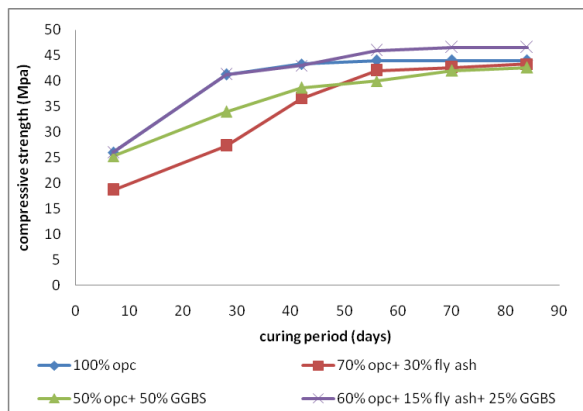


Fig. 1 Compressive strength variation for different compositions at room temperatures

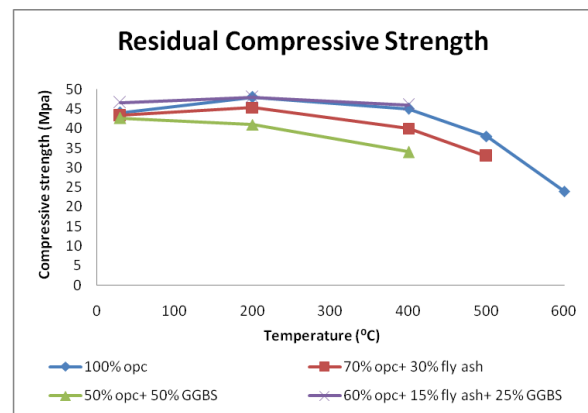


Fig. 2 Compressive strength variation for different compositions at elevated temperatures

Engineering Properties of Laterites and Utilization of Lateritic powder and Quarry Dust in Building Blocks

P.Shubhananda Rao ¹, Sitaram Nayak ²

1 Proprietor, Rao Builders, Mangalore, India. email:raobuilders@yahoo.com

2 Department of Civil Engineering, National Institute of Technology Karnataka, Surathkal, Mangalore 575025, India. email:snayak65@yahoo.co.in

ABSTRACT: Laterites are the products of intensive and long lasting tropical rock weathering which is intensified by high rainfall and elevated temperatures. In this work, an attempt is made to collect laterites from various locations of southwest India and its compressive strength, water absorption and chemical characteristics are established by laboratory testing. Protodyakonov tests are conducted on laterites and a correlation is developed between compressive strength and Protodyakonov strength index which can be directly used for quick assessment of compressive strength of lateritic rocks. Typical study is also carried out on utilization of lateritic powder and quarry dust in the manufacture of building blocks.

Keywords: Laterites, Compressive strength, Protodyakonov test, quarry dust, building blocks

INTRODUCTION

Laterite is well known as a building material for more than 1000 years. Laterites are the products of intensive and long lasting tropical rock weathering which is intensified by high rainfall and elevated temperatures. Laterite is a residual ferruginous rock, commonly found in tropical regions and has close gentle association with bauxite. It is highly weathered material rich in secondary oxides of iron, aluminium or both. It is either hard or capable of hardening on exposure to moisture and drying. Laterites are formed from the leaching of parent sedimentary rocks (Sandstones, lime stones,) metamorphic rocks (genesis, migmatites), igneous rocks (granite, basalt) and mineralized proto-ores; which leaves the more insoluble ions, predominantly iron and aluminium. Laterite was being used in the form of powder, odd shaped blocks and regular cut blocks.

Laterites from western coastal region of India has been utilized for the construction

of historic monuments like forts, palaces, temples, churches and residential buildings (Fig. 1 - Fig. 6).



Fig.1 Laterite regular block for building

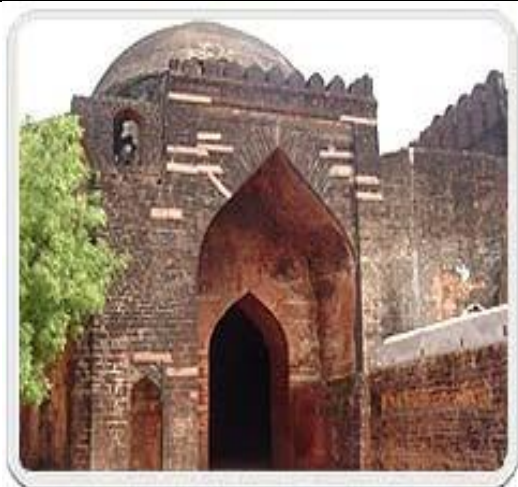


Fig. 2 Bidar Fort, Karnataka

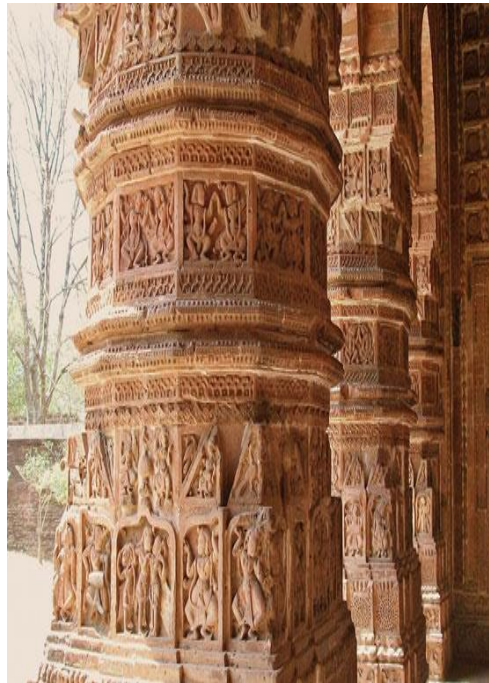


Fig. 5 Kalchand temple pillar made of Laterite



Fig. 3 Laterite sculpture of Orissa



Fig. 4 Church constructed with Laterite masonry infill



**Fig. 6 Art made of laterite stone in Bengal
Laterite masonry infill**

4th International Engineering Symposium - IES 2015

March 4-6, Kumamoto University, Japan

STAGES OF LATERIZATION

The first stage (Decomposition) is characterized by physio-chemical break down of primary minerals and the release of constituent elements (SiO_2 , Al_2O_3 , Fe_2O_3 , CaO , MgO , $\text{K}_2\text{ONa}_2\text{O}$ etc.,) which appear in simple ionic forms. Second stage (Laterization) involves leaching, under appropriate drainage conditions, of combined silica and bases and relative accumulation or enrichment from outside sources of oxides and hydroxides of sesquioxides (mainly Al_2O_3 , Fe_2O_3 , TiO_2). The soil conditions under which the various elements are rendered soluble and removed through leaching or combination with other substances appear to depend mainly on the P^{H} of the ground water and the drainage conditions. Under conditions of intense and prolonged physiochemical weathering, however, clay minerals are destroyed and silica is leached. The remainder will merely consist of aluminium oxides such as gibbsite or hydrous iron oxides such as limonite or goethite derived from iron; this is the process of Laterization. Third stage (Dehydration and desiccation) involves partial or complete dehydration (sometimes involving hardening) of the sesquioxides rich materials and secondary materials. The dehydration of colloidal hydrated iron oxides involves loss of water, and the concentration and crystallization of the amorphous iron colloids into dense crystalline iron minerals in the sequence; limonite, goethite and haematite with haematite to haematite.

LITERATURE REVIEW

Protodyakonov(1962) evolved a simple method for estimating 'f' (strength index), known as crushing method (also called pounding method). This test attempts to evolve spot method of estimating the hardness coefficient 'f', the value thus obtained is used to correlate a crude approximation of the compressive strength.

Gidigasu(1974) has attempted to assemble available information useful for the identification and evaluation of all grades of lateritic materials for engineering

purposes. From a study of literature it is concluded that the genesis and degree of decomposition, laterization or dehydration of laterite materials give them diverse genetic, morphological, chemical and mineralogical characteristics. Each of these exists considerable influence upon their geotechnical characteristics and engineering behavior.

Sunil et al(2005) The compressive strength of the laterite reduces as the P^{H} is maintained at lower values say 5. Alkalinity decreases, sulphate content and hardness reduces. The iron content also decreases which means decrease in the cementation properties i.e destruction of aggregate structure. The decrease in iron content cause reduction in the compressive strength. P^{H} value has strong influence on the chemical and engineering properties of laterite.

Srikantaiah (1993) in his exclusive work on Dakshina Kannada laterites defines the laterite in D.K as a residual product, resulting from the sin-sites weathering of the parent rock, granite gneiss under the intense condition of tropical climate, high temperature and rainfall. The laterite at the top is hardened due to exposure to air, and strength decreases when we go deeper.

Kasturba et al(2006) study revealed that high strength laterite was abundant in heavier minerals like haematite and goethite and was marked by dense and continuous crystalline matrix, whereas low strength laterites were abundant in clay minerals (mainly Kaolinite) and showed a scattered distribution of iron minerals. High water absorption capacity of the material is attributed to the abundance of clay in the material matrix.

LABORTORY TESTING OF LATERITE STONES

Laterite stones are collected from various location and are tested in the laboratory. Average compressive strength and water absorption values are provided in Table 1.

Various chemical tests are conducted and some of the important test results are provided in Table 2.

4th International Engineering Symposium - IES 2015

March 4-6, Kumamoto University, Japan

Table 1 Compressive strength and water absorption of Laterite stones

S.I. N o	Place of quarry	Compre ssive strength N/mm ²	Water absorption %
1	NITPO, Kerala	2.2	7.95
2	Ratnagiri, Maharastra	4.5	27.5
3	Sampege	9.48	8.21
4	Yekkar	2.30	8.7
5	Mudipu Mangalore	2.95	2.35
6	Permanki	1.72	5.93
7	Parari, Vamanjoor	1.16	3.68

Table 2 Chemical properties of latetite stones

Location	pH	Al ₂ O ₃	Fe ₂ O ₃	Silica %
NITPO, Kerala	7.7	7.8	22.2	30.4
Ratnagiri ,	10.5	9.7	25.9	32.5
Maharast ra				
Sampege	8.6	15.1	22.9	39.0
Yekkar	9.5	15.4	16.6	50.0
Mudipu Mangalor e	7.9	9.8	19.2	37.0
Permanki	5.4	10.7	14.3	25.0
Parari, Vamanjo or	5.5	9.3	10.7	43.0

PROTODYAKONOV STRENGTH INDEX OF LATERITES

The Protodyakonov strength scale finds wide use in Russia, Poland and other East European countries. This scale assigns a series of numbers for laterites in ascending order of strength. The evaluation of this hardness was suggested by Prof. M. M. Protodyakonov (Sr), in 1907 A.D. Later Dr. M. M. Protodyakonov (Jr) (1962) attempted to evolve simpler methods and proposed a simple and on the spot method of estimating the same hardness

coefficient 'f' (according to the definition of Prof. M. M. Protodyakonov). The value thus obtained is used for approximation of the compressive strength.

This method was originally developed for determining the strength of coal and later extended to rocks also. Here samples in the form of lumps are taken from Insitu laterites. Each sample is broken up with a hammer and 5 test specimens consisting of fragments of 20 to 40 mm in size and of each 10 to 20 cm³ are picked. Each test specimen is placed in a cylinder of 76 mm internal diameter and is pounded with a 2.4 kg drop mass falling through a distance of 0.6 m. The number of impacts 'n' to which these test specimens are subjected is 5 to 15 depending upon the strength of the laterites. After pounding all the five specimens, the test material is sieved on a 500 micron screen. Fines which pass through 500 micron screen are poured into the tube of a volumometer of 23 mm diameter and height of the column of dust 'l' in mm in the volumometer is recorded.

The strength coefficient 'f' is given by the following equation.

$$f=20n/l \quad (1)$$

Table 3 Protodykonov strength index

Sl. No	Place of Quarry	$f=Volumetricreading$	$f=20nl$
1	Kerala	46	4.34
2	Ratnagiri	36	5.55
3	Sampige	31	6.45
4	Yekkari	48	4.16
5	Mudipu	33	4.75
6	Permanki	50	4.0
7	Vamanjoor	54	3.7

The empirical relation is established between compressive strength of laterite stones and Protodyakonov strength index and is given below.

$$Y=2.858X-9.915 \quad (2)$$

where Y=Compressive strength(N/mm²)
X= Protodyakonov strength index

4th International Engineering Symposium - IES 2015

March 4-6, Kumamoto University, Japan

This equation can be directly used for quick assessment of compressive strength of laterite rocks by conducting Simple Protodyakonov test at site.

UTILIZATION OF LATERITIC POWDER IN BUILDING BLOCKS

Laterite stones from NITPO, Kerala, which has not passed the IS code standard i.e 3.5 N/mm² are selected to cast for laterite quarry dust cement blocks. Six combinations of lateritic powder, quarry dust and cement are used in the manufacture of blocks and are tested for chemical characteristics and compressive strength. Some of the important results are tabulated in Table 4 and Table 5.

Table 4 Chemical constituents of Laterite quarry dust cement blocks

Combinations			P ^H Value	Silica %	Fe ₂ O ₃ %	Al ₂ O ₃ %
L	Q	C				
40	60	5	10.9	31	7.2	13
50	50	5	11	30	8	15
60	40	5	11.3	32	9.8	10.3
40	60	7	11.2	29	6.9	11.4
50	50	7	11.7	28	6.2	9.7
60	40	7	12	30	6.4	9.9

(L: Lateritic Powder, Q:Quarry dust, C:Cement)

Table 5 Compressive strength of Laterite quarry dust cement blocks

Combinations			Compressive strength @ 7 days N/mm ²	Compressive strength @ 15 days N/mm ²
L	Q	C		
40	60	5	2.29	3.15
50	50	5	2.15	2.58
60	40	5	2.39	2.9
40	60	7	2.38	3.1
50	50	7	2.26	3
60	40	7	2.28	3.14

(L: Lateritic Powder, Q:Quarry dust, C:Cement)

CONCLUSIONS

From the studies carried out on laterites and also on laterite powder, quarry dust and cement blocks, the following conclusions are drawn:

- It is conclusive and evident from the tabulated results that the compressive strength of laterite stones varies widely from 1.16 N/mm² to 9.48 N/mm² with respect to the geographical location of laterite quarry, and its chemical composition.
- The Protodyakonov test to get the quick assessment of the compressive strength of the laterite is useful. The established equation from this work, derives the compressive strength of the laterite stones directly from Protodyakonov strength index.
- Block casted with appropriate mixture of laterite, quarry dust and cement yielded increased compressive strength by about 30%. Laterite stones of Kerala with their compressive strength of around 2.2 N/mm² will yield blocks having compressive strength of 3.0 N/mm², in close proximity to the IS code

4th International Engineering Symposium - IES 2015

March 4-6, Kumamoto University, Japan

specifications and recommendations for building construction.

• P^H value increases with increase of quantity of cement in the block.

REFERENCES

- [1] Gidigasu M.D.(1976), Laterite soil engineering Pedogenesis and Engineering principles, Elsevier Scientific publishing company, Amsterdam Oxford Newyork.
- [2] Kasturba A. K, Santhanam M, Achyuthan H (2006), "Investigation of laterite stones for building purpose from Malabar region, Kerala, SW India Part 3: Chemical analysis and microstructure studies, Construction and building materials.
- [3] Protodyakonov M.M. (1962), Mechanical properties and drillability of Rocks, Proceeding. 5th Symposium on Rock Mechanics Article, Russia.
- [4] Srikantaiah H R (1993), "Laterites and Lateritic soils of Dakshina Kannada district", Seminar proceedings on Geotechnical problems in construction in the lateritic formation, 27th November 1993 organized by Indian Geotechnical Society, Surathkal chapter, K.R.E.C, Surathkal, India.
- [5] Sunil B.M., Sitaram Nayak, S. S. Shri Hari (2006), "Effect of P^H on the geotechnical properties of laterite" Journal of Engineering Geology, UK, Elsevier, VOL. 85, pp. 197-203.

Stabilization of Lithomargic Clay using Quarry Dust and Cement

Betsy Maria Lukas and Sitharam Nayak

*Department of Civil Engineering, NITK Surathkal, India
Email: bethmlukas44@gmail.com*

This paper contains a series of laboratory tests conducted on lithomargic clay (shedi soils), which is found over parts of south west India, to evaluate its uses in foundation and pavement construction. The following test such as index properties, compaction characteristics and unconfined compressive strength are conducted to assess its suitability, the tests are conducted on the soil sample alone and by mixing it with the chosen materials in different proportions. Quarry dust of proportions ranging from 10% to 50% by weight is taken and mixed with soil and results are compared and analysed. The cement proportions range from 2,4,6,8 and 10%. These results are also recorded for various tests. The optimum of the two percentage is found and a mixture of lithomargic clay with these optimums are prepared and a final sample is analyzed. The results obtained are studied and final optimum required percentages are suggested.

Keywords: manipulator control, Jacobian, model based control

Effects of ground vibration due to the passage of trains in underground tunnels- a numerical modelling approach

Sarika K and V R Sastry

NITK Surathkal, India
Email: sharikakvr@gmail.com

The metro, that is a boon to the busy congested cities, could also become annoying and damaging if not properly planned. The vibrations generated during and after the construction could affect the building and monuments nearby, causing loss or damage to properties. Present work is an attempt to study the effect of vibration on different strata of soil due to the passage of metro trains in underground tunnels. The variation of peak particle velocity due to the presence of different soil types like clayey silt, silty sand and hard rock is studied. The work is carried out numerically using the finite element package PLAXIS Professional V8.0. To validate the numerical prediction of vibration due to the movement of underground trains ten different stations are selected. The majority of the tunnel passes through the very old towns, housing mostly buildings over 100 years old. Thus it is important to study the effects of vibration in these areas.

Effect of Aggregate Gradation and Bitumen Content on Workability of HMA Mixtures

Abhijith B.S¹ and Suresha S.N²

1 Department of Civil Engineering, National Institute of Technology Karnataka, Surathkal, Mangalore 575025, India. email:abi123bs@gmail.com

2 Department of Civil Engineering, National Institute of Technology Karnataka, Surathkal, Mangalore 575025, India. email:sureshasn@nitk.ac.in

ABSTRACT: The workability of Hot Mix Asphalt (HMA) mixtures can be defined as the ease with which the mixtures can be placed, handled and compacted. Workability is considered to be very important since it is directly related to the compactibility of the mixture in field. At a given temperature, the workability is a function of the compositional properties of a mix such as aggregate gradation and the bitumen content. The study focused on evaluating the compaction characteristics of asphalt mixes with aggregate structure designed using the Bailey method of aggregate gradation evaluation. Two fine graded mixtures with different aggregate gradation and the binder content varying from 5 to 6.5 percent were compacted to 225 number of gyrations using Superpave Gyratory Compactor (SGC). The locking point and the compaction indices (Compaction Densification Index and Traffic Densification Index) were determined from the data obtained using SGC. The results were statistically analyzed with ANOVA (Analysis Of Variance) using Minitab 16-trial version and it was observed that the change in gradation and bitumen content significantly affects the workability of the HMA mixture. This study as a whole concludes that optimization of the bitumen content and better selection of aggregate structure could provide a better workable HMA mixes.

Keywords: Workability, Aggregate gradation, Bitumen content

INTRODUCTION

Hot Mix Asphalt (HMA) mixtures are most widely adopted in the construction of flexible pavements. It comprises of aggregates and binder heated to sufficiently high temperature. The movement of HMA mixture through construction equipment to the roadway, handwork of HMA and compactibility on the roadway requires a better workable mixture and also satisfactory workability is important to obtain the desired smoothness and density within a compacted pavement (Gudimetla et al. 2003). Workability is defined as "the property which allows the production, handling, placing, and compaction of a mix with minimum application of energy (Delrio-Prat et al. 2011). Compactibility of HMA mixture is a function of workability. Many researchers have focussed on evaluating the workability in terms of compactibility of HMA mixtures.

Compaction of HMA mixture to the desired level is of major concern since it provides stiffness and good resistance to moisture damage by reducing the mix air voids, providing aggregate interlock and reducing the HMA to desired thickness (Dessouky et al. 2013). Compaction reduces the mix air voids and enables the mix to occupy smaller space thereby increasing the unit weight or density of the mass which has a direct influence on the performance of HMA mixtures (Roberts et al. 1996). The compaction level affects the workability and finishability of asphalt mixtures (Lee et al. 2007). The mechanical properties and response of the mixture in pavement are strongly dependent on the compaction degree achieved (Perez-Jimenez et al. 2014). Insufficient compaction leads to premature permanent deformation, excessive aging and moisture damage of asphalt mixtures (Kassem et al. 2012). Achieving the desired density is generally

4th International Engineering Symposium - IES 2015

March 4-6, 2015, Kumamoto University, Japan

related to better durability and performance (Ali et al. 2014).

The workability of HMA also depends on the composition of the mixture such as binder grade, amount of binder, aggregate type, aggregate gradation etc. (Gudimetla et al. 2003). The stiffness, workability, fatigue resistance, resistance to moisture damage is significantly affected by change in gradation (Roberts et al. 1996). Workability is influenced by the nature of binder, aggregate shape and gradation (Freddy 2007). Aggregate grading is an essential property to be considered since it can be related to many aspects such as compactibility, durability and resistance to permanent deformation (Andrea et al. 2012). The aggregate gradation has a significant effect on the compactibility of asphalt mixtures and the grade and amount of binder content also influences the compaction process i.e. stiff asphalt mixture would be produced at lower asphalt content and usually requires more compaction effort than a mixture with high asphalt content (Kassem et al. 2014).

The primary objective of the present study is to find the effect of aggregate gradation and amount of Binder Content (BC) on the workability of asphalt mixtures. Here, the aggregate gradation is designed using Bailey method of aggregate gradation evaluation and the effect of two fine graded mixtures which vary in terms of their Bailey ratios were studied. The BC was taken as percentage by weight of total mixture. The bitumen of grade VG-10 was used. The workability of the asphalt mixtures was measured using densification curves obtained from Superpave Gyratory Compactor (SGC). The results were statistically analysed using a tool Analysis of Variance (ANOVA).

LITERATURE REVIEW

Several research have been conducted over the years to study the workability characteristics of asphalt mixtures. The prototype device was used by some of the authors to analyse the workability of asphalt mixtures which simulates the field condition (Gudimetla et al. 2003; Freddy 2007; Ali et al. 2014). The workability was analysed in terms of measuring torque

required for mixing i.e. the reciprocal of resistance moment produced by the mix against the rotation of the blade as the mixture workability. The main observations that could be drawn from Gudimetla et al. (2003) was the change in binder content had no direct influence on workability and as the filler content increased workability decreased. However, in the same paper it was also reported that with the same binder type and aggregate source the change in workability with change in gradation is likely to occur. In another research conducted by Freddy 2007, it was reported that increase in gravel content diminished the workability and the reason could be either the aggregate size or the gradation shape.

The workability in terms of compactibility of asphalt mixtures could be effectively analysed using the data from the Superpave Gyratory Compactor (SGC). The densification curves obtained from SGC were used to analyse the compactibility of asphalt mixtures. In 1999, Mallick (see ref. Louay and Khalid 2007) found the gyratory ratio to differentiate the stable and unstable mixes. Before that earlier in 1998, analysis have been performed by Bahia and co-researchers (see ref. Louay and Khalid 2007) using Compaction Energy Index (CEI) and Traffic Densification Index (TDI) through which the modifications were made by Louay and Khalid (2007) and also another concept called locking point was defined. The experimental studies conducted by them concluded that the compactibility is a function of particle size distribution. In another research conducted by Dessouky et al. (2013) modified compaction indices were introduced which link the lab compaction to field workability and long term performance to rutting. Their findings indicated that compactibility depends on various parameters such as aggregate shape, aggregate gradation, bitumen grade and amount etc. and therefore importance has to be given to evaluate the effect of these parameters on the workability of the asphalt mixtures. Gao et al. (2013) used two energy indices i.e primary compactibility and secondary compactibility energy indices and

4th International Engineering Symposium - IES 2015

March 4-6, 2015, Kumamoto University, Japan

compactibility factor to evaluate the compactibility of the asphalt mixtures and the sensitivity of these indices to change in aggregate gradation, compaction temperature etc. were identified. An attempt has also been made by Kassem et al. (2012) to evaluate the workability of asphalt mixtures in which two statistical mixed models were used to predict slope and intercept based on parameters that describe shape characteristics, aggregate gradation, BC and binder viscosity at compaction temperature using SGC.

The Bailey method was provided by Robert Bailey which is an analytical tool used to blend fine aggregate and coarse aggregate to get a rut-resistant mix (Vavrik et al. 2002). The packing characteristics of the coarse and fine portion of the final blend obtained is well explained using Coarse aggregate (CA), Fine Aggregate Coarser (FA_c) and Fine Aggregate Finer (FA_f) ratios respectively in this method. According to the principles of Bailey method, CA ratio higher than that of the suggested value will be difficult to compact; FA_c ratio below the limit indicates that the gradation is not uniform and these mixtures is generally said to be gap graded which indicates instability and may lead to compaction problems. Some of the researchers (Louay and Khalid 2007; Andrea et al. 2012) have adopted the Bailey method for gradation evaluation in their study and an attempt have been made by them to relate Bailey ratios with the compactibility of the asphalt mixtures. Danny (2007) reported in his study that the Bailey method evaluates the aggregate gradation and their effect on volumetrics, compactibiliy etc. and also it would provide a reasonable indication of field compactibility problems. Bailey method maintains appropriate workability and durability (Andrea et al. 2012).

Here in the present research the effect of aggregate gradation and BC individually and the interaction effect of the both on mixture workability is determined using the densification indices (see Fig. 1) obtained from SGC. In the Fig.1 CDI corresponds to area under curve from N=1 to N=locking point, TDI is the area under curve from N at locking point to N at 98 % Theoretical maximum density (G_{mm}) and

Locking point is the No. of Gyration after which the rate of change in height is equal to or less than 0.05 mm for three consecutive gyrations. High CDI values indicate the mixes that are difficult to compact. High TDI value indicate better mixture stability

PRESENT STUDY

The crushed Granite aggregates available from the local quarry conforming to IS: 383 1970 was used in the present investigation. The viscosity grade bitumen VG-10 obtained from Mangalore Refinery and Petrochemical Limited (MRPL) conforming to IS 73: 2006 was used. Fly-ash meeting the requirements as per IS 3812: 1981 was used as filler. Two typical fine graded gradations of 19 mm NMPS was designed using Bailey method of aggregate gradation. Gradation-1 and Gradation-2 as shown in Fig. 2 were obtained by considering the lower limit and upper limit of the Bailey recommended ratios for asphalt mixtures (Vavrik et al. 2002)

Further, the asphalt mixtures were designed using Superpave Method of mix design according to ASTM D 6925. The asphalt mixtures were compacted to 225 number of gyrations. The influence of the known Bailey ratios in terms of aggregate gradation and BC on the workability of the asphalt mixtures were studied considering 50 design number of gyrations (Traffic level <0.3 Equivalent single axle loads). A total of 24 specimens were produced at the same compaction and mixing temperature by varying the BC from 5 percent to 6.5 percent in interval of 0.5 percent. The data obtained from the densification curves were used to determine the workability of the asphalt mixtures in terms of CDI and TDI.

RESULTS, ANALYSIS AND DISCUSSION

The treatment factors considered in the study was the BC and gradation type and the response factor evaluated were CDI and TDI. The data was statistically analyzed using MINITAB (release 16- trial version). The CDI and TDI were calculated based on the SGC densification curves obtained.

The compaction indices of 24 samples were determined. The mean values for three replicates are reported. The mean value of CDI varied from 438.86 to 639.67 and also it could be seen that as the BC increased the difficulty level of compaction increased for both the mixes. Gradation-2 was found to be requiring more compaction energy than Gradation-1 which could be due to higher CA ratio in gradation-2. The mean values of TDI varied from 352.57 to 458.74 and also it was observed that the TDI of both the mixtures increased till around optimum binder content and decreased thereafter.

The gradation type was found to be the significant factor which is affecting the compactibility of the asphalt mixtures, whereas stability of the mixtures were influenced mostly by the BC. However, the locking point which varied in the range of 45-62 No. of gyrations was not found to be sensitive with the change in gradation type or BC.

The effect of two different gradations and four different BC were also obtained using the mean values for the CDI and TDI as shown in fig. 3.

Further, the influence of the treatment factors (BC and gradation type) on the compactibility of the asphalt mixtures was determined. The response factors include

the CDI and TDI of the mixture. The data was generated using the data size of 24 numbers which corresponds to two different gradations and four varying BC. The statistical analysis tool ANOVA was used to investigate the effect of individual treatment factor as well as the combined effect of the treatment factor on the response properties. Table 1 shows the test results of ANOVA which includes Degree of Freedom (DF), Sum of Squares (SS), Mean Square (MS), Fisher distribution statistics (F), p value and results of null hypothesis. The prime source of variation could be obtained using the MS value. The gradation type was considered to be the main source of variation for the results of CDI and BC was found responsible for the variation in TDI. The null-hypothesis was tested at a confidence level of 95 percent. The null-hypothesis was that the mean of the response variables do not vary with the variation in the treatment factors. Here, the null-hypothesis proved to be wrong indicating that the means of the response variable vary significantly with the variation in BC and gradation type. However, when the interaction (BC*gradation type) effect was studied, the variation in the means of the TDI were not found significant

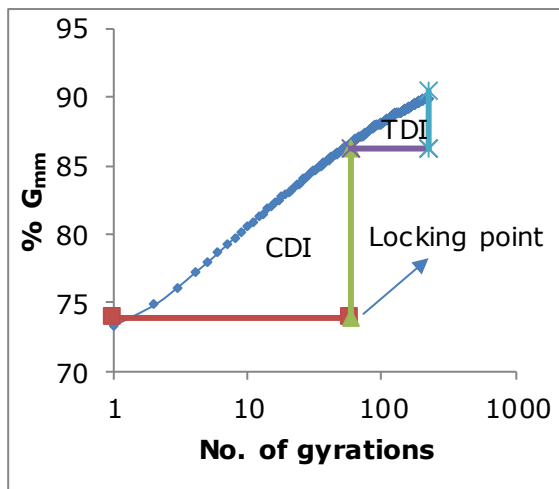


Fig.1 SGC curve showing densification indices adopted in the present research

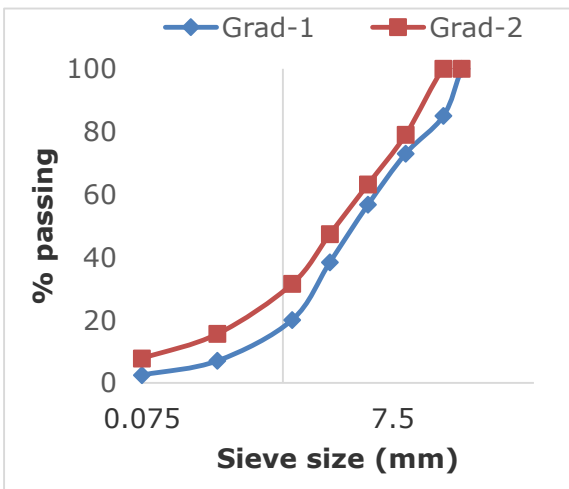


Fig.2 Gradation curves of 19 mm NMPS

Table 1 ANOVA test results

Source	DF	SS		MS		F		P	
		CDI	TDI	CDI	TDI	CDI	TDI	CDI	TDI
BC	3	30412	19488.40	10137.20	6496.13	10.61	13.01	0.000	0.000
Grad-type	1	86277	3243.50	86276.80	3243.54	90.26	6.50	0.000	0.021
Interaction	3	11770	4424.80	3923.30	1474.94	4.10	2.95	0.024	0.064
Error	16	15294	7987.10	955.90	499.19				
Total	23	143752	35143.90						

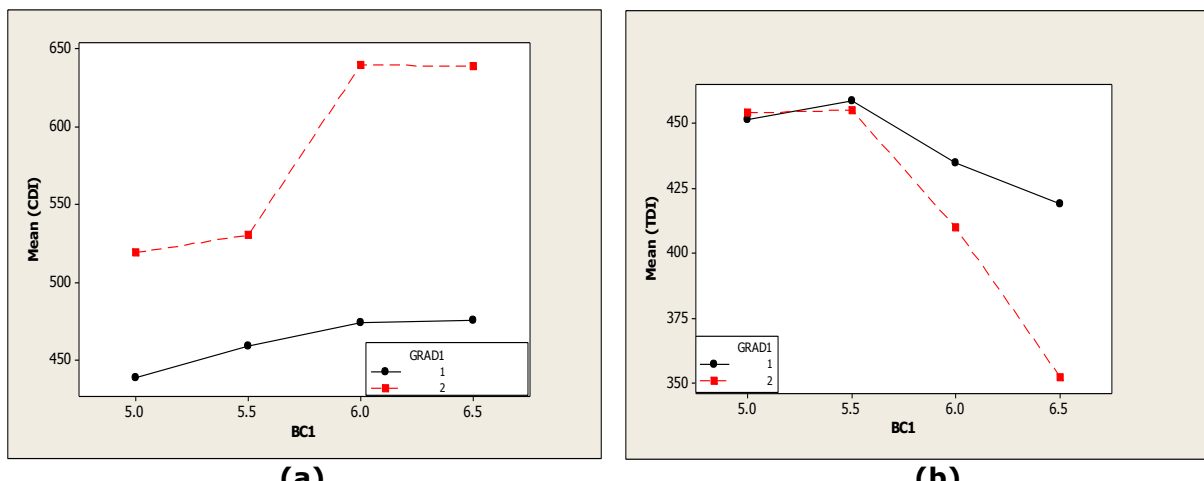


Fig .3 Effect of gradation type and binder content on mean values of (a) CDI (b) TDI

Conclusions and Recommendation

The compaction characteristics of two fine graded asphalt mixtures with aggregate structures designed using Bailey method of aggregate gradation were evaluated using the data from the SGC densification curves. The findings of this study are summarized as follows

- Among the two parameters aggregate gradation and BC, aggregate gradation is the major factor which influences the compactibility of asphalt mixtures.
- The CA ratio, which is a function of aggregate blend seemed to correlate with CDI of the mixtures. Higher CA ratio as in gradation-2 was found more difficult to compact as when compared to the compactibility of gradation-1.
- The LP was found to be less sensitive to the change in

gradation considered in the study.

- BC seemed to have major influence on the TDI of the asphalt mixtures considered in the study. As the BC increased, the TDI of the mixture increased till around optimum binder content and decreased thereafter.
- The gradation type considered here significantly contributed to the change in CDI having highest variation in MS value of 86276.80 and BC was considered to be the major cause for the changes in TDI having a highest variation in MS value of 6496.13.
- The Interaction effect (BC and gradation type) was found to be statistically significant in the case of CDI. No such significance was addressed in the case of TDI.

4th International Engineering Symposium - IES 2015

March 4-6, 2015, Kumamoto University, Japan

However, the study limits only to two fine graded gradations. Therefore, in order to draw more proper conclusion it is recommended to consider more number of data which corresponds to variation in gradation type.

References

1. Ali, A., Abbas, A., Nazzal, M., Alhasan, A., Roy, A. & Powers, D., 2014. Workability evaluation of foamed warm-mix asphalt. *Journal of Materials in Civil Engineering, ASCE*, Volume 26.
2. Andrea, G., Gilda, F., Emiliano, P. & Francesco, C., 2012. *An application to the European practice of the Bailey method for HMA aggregate grading design*. .. Social and Behavioral Sciences.
3. ASTM D6925-09, 2009. *Standard test method for preparation and determination of the relative density of hot mix asphalt (HMA) specimens by means of the superpave gyratory compactor*. West Conshohocken, PA, US: Annual Book of ASTM Standards volume information.
4. Bahia, H. U., Friemel, T., Peterson, P. & Russell, J., 1998. Optimization of constructibility and resistance to traffic: A new design approach for HMA using the superpave gyratory compactor. *Journal of the Association of Asphalt Paving Technologists*, Volume 67, pp. 189-232.
5. Danny, G., 2007. Analysis of Oklahoma mix designs for the national center for asphalt technology test track using the Bailey method. In: *Transportation Research Circular-E-C124*. Washington, DC: Transportation Research Board, pp. 33-44.
6. DelRio-Prat, M., Vega-Zamanillo, A., Castro-Fresno, D. & Calzada-Perez, M. A., 2011. Energy consumption during compaction with a gyratory intensive compactor tester, estimation models. *Construction and Building Materials*, Volume 25, pp. 979-986.
7. Dessouky, S., Pothuganti, A., Walubita, L. F. & Rand, D., 2013. Laboratory evaluation of the workability and compactibility of asphaltic materials prior to road construction. *Journal of Materials in Civil Engineering, ASCE*, Volume 25, pp. 810-818.
8. Freddy, S.-L. J., 2007. Gradation chart for asphalt mixes: Development. *Journal of Materials in Civil Engineering, ASCE*, Volume 19, pp. 185-197.
9. Gao, L., Ni, F., Charmot, S. & Luo, H., 2013. Influence on compaction of cold recycled mixes with emulsions using the superpave gyratory compaction. *Journal of Materials in Civil Engineering, ASCE*, Volume 26.
10. Gudimetla, J. M., Cooley, L. A. & Brown, E. R., 2003. *Workability of hot mix asphalt*. Auburn: NCAT.
11. IS : 3812-1981, 1999. *Specification for fly ash for use as pozzolana and admixture*. New Delhi: Bureau of Indian Standards.
12. IS : 383-1970, 2002. *Specification for coarse and fine aggregates from natural sources for concrete*. New Delhi: Bureau of Indian Standards.
13. IS 73 : 2006, 2011. *Paving Bitumen-specification*. New Delhi: Bureau of Indian Standards.
14. Kassem, E., Masad, E., Awed, A. & Little, D., 2012. *Laboratory evaluation of friction loss and compactibility of asphalt mixtures*. Texas: Texas Transportation Institute.
15. Lee, S.-J., Amirkhanian, S. N., Putman, B. J. & Kim, K. W., 2007. Laboratory study of the effects of compaction on the volumetric and rutting properties of CRM asphalt mixtures. *Journal of Materials in Civil Engineering, ASCE*, Volume 19, pp. 1079-1089.
16. Louay, M. N. & Khalid, S. A., 2007. A look at the Bailey method and locking point concept in superpave mixture design. In: *Transportation Research Circular-E-C124*. Washington, DC: Transportation Research Board, pp. 12-32.
17. Mallick, R. B., 1999. Use of superpave gyratory compactor to characterize hot-mix asphalt. In: *Transportation Research Record-1681*. Washington, DC: Transportation Research Board, pp. 86-96.
18. Perez-Jimenez, F., Martinez, A. H., Miro, R. & Hernandez-Barrera, D., 2014. Effect of compaction temperature and procedure on the design of asphalt mixtures using Marshall and gyratory compactors. *Construction and Building Materials*, Volume 65, pp. 264-269.
19. Roberts, F. L. et al., 1996. *Hot mix asphalt materials, mixture design and construction*. Lanham, Maryland: National Asphalt Pavement Association Research and Education Foundation.
20. Vavrik, W. R. et al., 2002. Bailey method for gradation selection in HMA mixture design. In: *Transportation Research Circular-EC044*. Washington, DC: Transportation Research Board.

REVIEW OF VETIVER GRASS PROPERTIES FOR ITS APPLICATION IN STABILISATION OF SLOPES AND EROSION CONTROL

N. N. Prabhu¹ and T. G. Sitharam²

¹*National Institute of Technology Karnataka, Surathkal, India, 575025,
Email: nivedita.prabhu5@gmail.com*

²*Department of Civil Engineering, Indian Institute of Science, Bangalore, India, 560012,
E-mail: sitharam@civil.iisc.ernet.in*

ABSTRACT: Vetiver grass is a tropical clump grass of the Poaceae family from India having a biological name "Chrysopogon zizanioides". In western and northern India, it is called as "Khus". In India, it grows naturally in highlands to lowlands in various soil and water conditions. Vetiver grows in a dense clump and grows fast through tillering and can grow easily up to 1.5m deep into the soil.

This paper reviews the use of vetiver grass as an eco-friendly tool to control soil erosion and slope stability in geotechnical applications. This is also being used in paddy fields for water retention, for making perfumes & insecticides and has medicinal value. Vetiver grass is now used for a wide range of purposes in civil engineering as pozzalonic material (vetiver root ash), fibre boards, slope stability, river bed reclamation, mine dump stabilisation etc. We review the special features of the Vetiver grass system, which makes it a useful tool in slope stabilisation and erosion control. We present the case studies where these roots of vetiver grass functions similar to soil nail in creating temporary retaining systems. This paper is an attempt to analyse the slope supported by vetiver grass system using slide software and the increase in Factor of Safety of slope reinforced with Vetiver roots has been demonstrated. The paper finally concludes that vetiver grass systems are very effective in controlling the shallow slips in any slope stability problems and also acts as an excellent tool to control soil erosion.

Keywords: *Vetiver systems, slope stability, erosion control*

1. INTRODUCTION

In a subtropical country like India with topography consisting of hilly terrains, ghats and mountainous areas and heavy rainfall due to the south-west monsoons slope stability and soil erosion control is a major concern to avoid disasters like landslides, floods, flash floods, rock fall, debris flow etc. The construction of retaining walls, shotcreting, soil nailing are expensive and have environmental impacts. An alternative eco-friendly, cost effective solution to this problem is the use of the Vetiver grass. Apart from its use in medicine, soil fertility, cosmetics, perfumes and aroma therapy, it can be used in civil engineering problems of slope stability and erosion control. The vetiver shoots grow up to a maximum height of 1.5m above the ground surface within 2-3 months and forms a

dense hedgerow. The uniqueness of this grass lies in its roots which grow

vertically up to a depth of 2-4 metres within a year of planting it. The vetiver grass has a vigorous and massive root network which can even penetrate 5cm thick layer of asphalt concrete. Hengchaovanich (1998). The roots grow rapidly within a year and therefore are much better compared to trees which usually take 2-3 years to act effectively for slope stabilisation purpose. The roots of the plant reinforce the soil by forming a composite material of roots with high tensile strength and adhesion and the soil being low tensile strength matrix. The vetiver roots increase the tensile and shear strength of the soil. The root network act similar to soil nails, vetiver is also called as "living nail". Hengchaovanich (1998). Also the use

of vetiver in comparison with hard engineering measures like concrete or masonry works is more eco-friendly, aesthetically appealing and cost effective. Since the promotion of vetiver for soil and water conservation by World Bank in 1980 many countries like China, Thailand, Zimbabwe, Bangladesh, Nepal have used it for various purposes like embankment stabilisation, stabilise floods and canals, saline land remediation etc. A lot of research on the tensile strength, shear strength, hydraulic characteristics have been carried out to design a relevant method to use this plant effectively for the purpose of stabilisation of slope and erosion control.

This paper reviews the various properties of the vetiver grass that makes it an effective tool in slope stability and erosion control problems. It also presents the cases where vetiver systems have been used to counter shallow slip failures. A simple slope is analysed to study the increase in Factor of Safety when vetiver root reinforcements are used.

2. LITERATURE REVIEW

It is found that Vetiver grass when planted closely (10cm apart) across slope forms a dense hedgerow that decreases the flow velocity, hydraulic forces of surface water and spreads the water evenly across the length of the hedge barrier. Grimshaw (1994). In Golden Congkou Section of Hanjiang River dike, Wuhan Hubei, China, vetiver was planted along with other grasses Bahia and St Augustus to decrease the erosion due to wave boats. Ke et al (2003). Vetiver systems have been successfully used in Nepal for Embankment stabilisation, in South Africa for mine dump stabilisation and rail road embankment, in Bangladesh to stabilise flood, canal and river embankments, in China for reclamation of river beds, in Zimbabwe for dam spillways. Grimshaw. (1994). The Department of Highways (1994) has developed a Standard Drawing- SP-204, 1994 and SP 206, 1996 (Revision) called "Vetiver grass planting for highway slope protection" which consists of detailing pattern for vetiver to

be grown on back slope, side slope, and bridge slope Sanguankaew *et al.* (2003).

The shear strength of the soil penetrated by vetiver roots were analysed. According to the root reinforced model, in root reinforced soil subjected to direct shear the tangential component of tension in root resists the shear along the slope and the normal component of the tension in root increases the confining stress on shear plane. Wu. (1976). It is observed that roots with lower cross section area have high tensile strength than those with higher cross sectional area. Hengchaovanich and Nilaweera (1998). The tensile strength and shear strength properties of soil penetrated by vetiver roots were studied by Hengchaovanich and Nilaweera and the average tensile strength of the root was found to be 75MPa at a root diameter of 0.7mm-0.8mm which is most common diameter of the roots. The average tensile strength of the vetiver roots is very high compared to average tensile strength of many hardwood roots. According to the study of Cheng *et al* (2003) the average tensile strength of vetiver root was found to be 85MPa. This disparity between the two authors' observation is due to the varying root diameters. The tensile strength of vetiver root at different cross section was analysed by Cheng *et al* and is given in Table 1. Among the different grass roots tested by Cheng *et al* vetiver was found to have the highest tensile strength. It is found that the increase in shear strength at a depth of 0.25mm is 90.2% with the bulk weight of root in unit soil volume being 1.522 kg/m³. Hengchaovanich and Nilaweera (1998). The shear strength increase at various depths tested by Hengchaovanich and Nilaweera is given in Table 2.

3. SPECIAL FEATURES OF VETIVER

3.1 Morphological characters:

The ability of the grass to grow roots upto 2-4m long within a year without much maintenance makes it a very good material for slope stability. The vetiver roots act in same way as the soil nails used in civil engineering and therefore they are called "living nails" (Hengchaovanich, 1998). The dense hedgerow of the plant helps in decreasing

the hydraulic force and velocity of surface water on steep slope, and also acts as sediment filter there by controlling sheet erosion.

3.2 Climate and soil:

The plant can grow in any extreme conditions like droughts, floods and can even penetrate through hard rocks and can grow in any soil type like sandy, clayey, gravelly, loamy and has the ability to regrow quickly after being affected by salinity, alkalinity, frost and any other adverse conditions after the weather improves. It can tolerate NaCl at a level 15 times as high any other normal plant. Nanakorn et al. (1996) and therefore it can be used in coastal protection. It doesn't even require soil with too much fertility, in turn it increases the fertility and also increases water infiltration of the soil it is planted in, therefore this can be used in terrace farming on slopes to serve purposes of slope stability, erosion control, water retention and fertility. The grass has aerenchyma tissues and therefore can survive under water for almost a year and therefore isn't disturbed by conditions of floods.

3.3 Fire and frost resistance:

The plant is even fire resistant so it can be used in slope stability issues in places ...where there is issues of forest fire. The plant can even tolerate frost to some extent but the growth of the plant is stunted in case of heavy frost. Cold conditions decrease the shoot growth to a large extent than the root growth. In Australia the vetiver growth wasn't affected at a temperature of -11°C and in China it survived for a short time at 22°C . Xu and Zhang. (1999). The main requirement of the plant is sunlight and therefore can be commonly found in tropical and subtropical climates.

3.4 Mechanical properties:

The vetiver root's tensile strength is comparable with tensile strength of other hard woods and vetiver can be preferred over the hard wood trees for slope stability as it grows its roots faster and also the shoot will be comparatively lighter than the tree's and will contribute to lower driving force of the slope and the shoot structure also controls sheet erosion due

to surface runoff of water. The tensile strength of the root is $1/6^{\text{th}}$ of tensile strength of mild steel. Hengchaovanich. (1998).

4. EXPERIMENT ON VETIVER SYSTEM ON HIGHWAY SLOPES

(Reviewed from "Improving the efficiency of the vetiver system in the highway slope stabilisation for sustainability and saving of maintenance cost" by Sanguankaeo et al.) In Kanchanaburi province of Thailand vetiver systems were used to prevent shallow seated mass failure of highway slopes. Vetiver tillers raised in nursery were planted during June- July during the start of monsoon. Alternate rows of Arachis pinto as grown in between Vetiver rows to decrease the weed growth that would replace the vetiver. It was observed that Vetiver systems were very effective in countering shallow mass failures. It was even noted that vetiver grows well on slope of angle less than 60° and may not grow on slope angle above 70° .

5. VETIVER FOR EMBANKMENT STABILITY OF INDIAN RAILWAY

The Mangalore-Bangalore railway line via Hassan has implemented the concept of slope stability by using vetiver systems for embankment slopes in Yediyur town. A total area of 20,234 square metres was planted with vetiver tillers. The planting operation started in September 2014 on embankment slope of 14 metres height and inclination of 45 degrees. The project was undertaken by South-Western Railways.

Soil and climatic conditions: The soil in the area is gravel sand. Yediyur has tropical climate with highest rainfall in the month of October. The annual average rainfall of the place is 649mm and average temperature is 24.8°C

Planting technique: The planting operation started in September 2013 as October is the month in which Yediyur receives highest rainfall. Vetiver tillers raised in vetiver farm at Muddur were planted at the slope location. The vetiver hedgerows were planted with a spacing of 75cm and the spacing between each vetiver tiller within each hedgerow was 20cm. Chicken manure, DAP and NPK fertilisers were used in initial stages of planting.

6. SLOPE STABILITY ANALYSIS USING SLIDE SOFTWARE

A simple slope was modelled using Slide software to find the increase in Factor of Safety of the slope when vetiver was used in the slope.

6.1 Details of the slope:

A slope of elevation (H:V) 1:0.72 was modelled using Slide software. The angle of friction of the foundation bed was given as 0° and that of the slope was given as 33° . The cohesion for foundation bed was given as 23kPa and for slope was given as 30kPa.

6.2 Details of the Vetiver roots:

The vetiver roots were modelled in the slope as soil nail with the properties of tensile strength of vetiver root. The hedgerow spacing was given as 2m, 1m, 0.5m and the out of plane spacing was 10cm. The figures of the analysis are shown below for simple slope (fig. 4), slope with vetiver root reinforcement with hedgerow spacing of 1m (fig.5), for a root length of 4m. The Factor of Safety (FoS) for simple slope is 0.905. Slope with vetiver reinforcement with hedgerow spacing of 2m, 1m, 0.5m, FoS are 1.43, 1.5, 1.56 respectively for root length of 4m. When length of root is varied for hedgerow spacing of 1m, FoS for root length 2m, 3m, and 4m are 1.23, 1.31, and 1.5 (fig.5) respectively.

7. RESULTS AND DISCUSSION

According to the Slide analysis the simple slope without any root reinforcement has a factor of safety of 0.905. With Vetiver reinforcement of Vetiver, FoS can be increased above 1.5. The area coverage of the root at different depth depends on various factors like climate, fertilizers, soil type, external vegetation, so first a trial must be done for a small area and then applied to the rest of the slope.

8. CONCLUSION

Vetiver system can be used as a cost effective, long lasting and eco-friendly solution to avoid shallow slope failure due to erosion and surface water runoff which is a common problem in India.

- 1) Vetiver are very effective in slope stability and erosion control as it is a fast growing grass with root depth of 2-4m. It is also long lasting as the vetiver

grass survives for a maximum of 100 years under suitable environmental conditions.

- 2) India being a tropical country and the vetiver root being native to India has a huge potential to use it in shallow seated slope stability problems
- 3) A proper design and detailing is required to be done before planting the vetiver on slope based on the steepness, soil type, climate conditions and the vegetation of the area.

9. REFERENCES

- 1.Cheng, H., Yang, X., Liu, A., Fu, H., Wan, W. 2003. An experimental study on mechanic performance and mechanism of soil-reinforcement by herb root system, Proceedings of the Third International Conference on Vetiver and Exhibition, Guangzhou, China.
2. Grimshaw, R. G. 1994. Vetiver grass—its use for slope and structure stabilization under tropical and semitropical conditions, *Vegetation and Slopes*, Institution of Civil Engineers, London, 26-35.
- 3.Hengchaovanich, D. and Nilaweera, N. S. 1996. An assessment of strength properties of vetiver grass roots in relation to slope stabilization, Proceedings of the First International Conference on Vetiver. Office of the Royal Development Projects Board, Bangkok. 153-158.
- 4.Hengchaovanich, D. 1998. Vetiver Grass for Slope Stabilization and Erosion Control, Tech. Bull. No. 1998/2, PRVN / ORDPB, Bangkok, Thailand.
- 5.Ke, C., Feng, Z., Wu, X., Tu, F. 2003. Design Principles and Engineering Samples of Applying Vetiver Eco-engineering Technology for Steep Slope and River Bank Stabilisation, Proceedings of the Third International Conference on Vetiver and exhibition, Guangzhou, China.
- 6.Nanakorn, M., Surawattananon, Namwongporm, N., Sangnil, K., Suwannachitr, S. 1996. Vitro selection of NaCl tolerance in vetiveria species. Paper presented at First Int. Conference on Vetiver, Chiang Rai, Thailand.
- 7.Sanguankaew, S., Chaisintarakul, S., Veerapunth, E. 2003. The Application of the Vetiver System in Erosion Control and Stabilization for Highways Construction and Maintenance in Thailand. Proceedings of the Third International Conference on Vetiver and exhibition, Guangzhou, China.
- 8.Sanguankaew, S., Sawasdimongkol, L., Veerapunth, E. 2006. Improving the efficiency of vetiver system in the highway slope stabilisation for sustainability and saving of maintenance cost. Proceedings of the Fourth International Conference on Vetiver, Caracas, Venezuela.
- 9.Wu, T.H. 1976. Investigation of landslides on Prince of Wales Island, Alaska. Department of Civil Engineering, Ohio State University, Columbus. Geotech. Eng. Rep. No. 5.
- 10.Xu LY, and Zhang J. 1999. An overview of the use of vegetation in bioengineering in China. *Proc. Ground and Water Bioengineering for Erosion Control and Slope Stabilisation*, Manila.

Table 1. Result of the experiment of tensile strength of Vetiver

Diameter (mm)	Max.tensile force (kg)	Max.tensile strength(MPa)	Diameter (mm)	Max.tensile force (kg)	Max.tensile strength(MPa)
0.20	0.60	186.69	0.63	2.73	85.6
0.35	1.20	121.90	0.65	2.70	76.7
0.40	1.50	116.70	0.70	2.95	74.9
0.45	1.38	97.10	1.30	4.90	36.1
0.55	2.23	91.70	1.50	5.10	28.2
0.60	2.61	90.20	1.70	5.30	22.9

Courtesy: Cheng et al, 2003

Table 2. Shear strength increase in soil profile due to root penetration of two year old vetiver with spacing 15cm and hedge row length 50cm.

Depth(m)	D_r (kg/m ³)	A_r (mm ²)	$A_r/A \times 10^{-4}$	Δs (kN/m ²)	% Δ_s
0.25	1.522	331.0	3.31	8.92	90.2
0.50	0.701	176.2	1.76	4.17	39.3
0.75	0.521	137.8	1.38	3.46	34.6
1.00	0.378	106.8	1.07	2.61	26.3
1.25	0.181	71.2	0.71	1.94	19.0
1.50	0.135	51.6	0.52	1.28	12.5

Courtesy: Hengchaovanich and Nilaweera, 1998

D_r :Bulk weight of root in soil of unit volume, A_r :Root area on the shear surface, A :Area of the shear surface, Δ_s :Shear strength increase in the soil due to the roots.

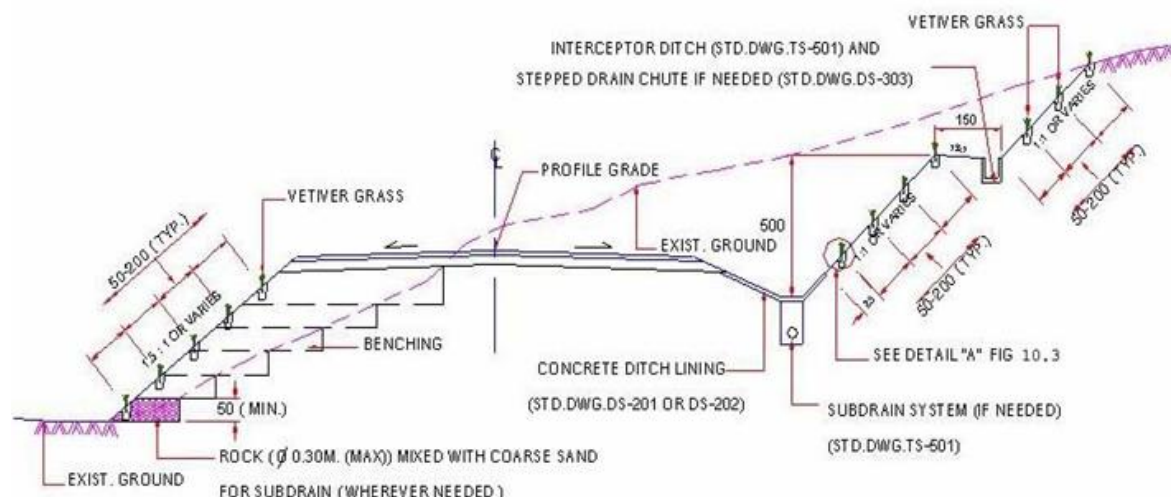


Fig.1 Cross section, Vetiver grass on back slope and side slope

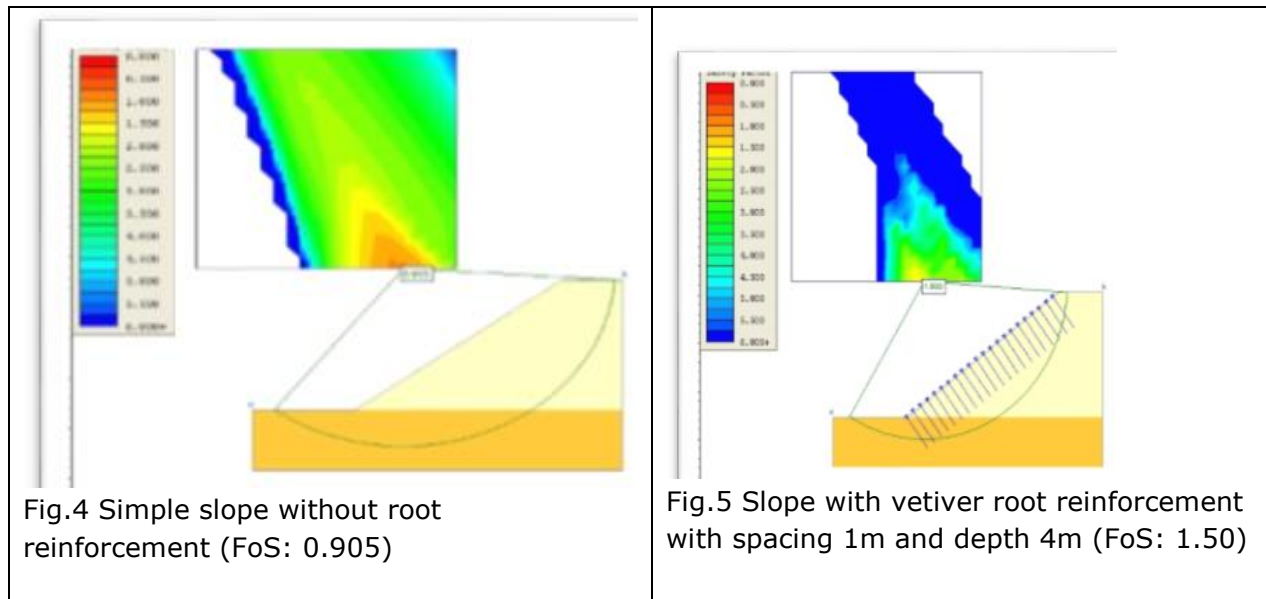
Courtesy: Sanguankaeo et al, 2006.



Fig. 2 Vetiver grass
Courtesy:aromaticwisdominstitute.com



Fig.3 Vetiver planted on embankment slope in Yediyur; Courtesy L. V. Pai



RELIABILITY ANALYSIS OF SLOPE STABILITY USING RSM METHOD

¹S.Subhashree, ²L.G.Santhosh and ³G.L.Sivakumar Babu

¹ Department of Civil Engineering, NITK, subhashree.doss@gmail.com

² CST, IISc Bangalore, lgsanthu2006@gmail.com

³Department of Civil Engineering, IISc Bangalore, glsivakumar@gmail.com

ABSTRACT It is observed that the Soil parameters are highly variable in nature so the determination of the stability and reliability of landfill slopes is crucial. Limit equilibrium method for slope failure analysis is a conventional factor of safety approach. By using probabilistic approach, the uncertainties in soil properties are overcome. Response Surface method is used in this study to optimize the uncertainties in soil properties. Hasofer-Lind reliability index gives the reliability index value. It is found that for a factor of safety 1.5, the reliability index (β_{HL}) is 2.21 and probability of failure of slope (P_f) is 1.3%. The study also presents the significant parameters which influence the stability of slopes.

KEYWORDS

Slope stability, Reliability index, Response Surface method (RSM), Probability, Landfills.

INTRODUCTION

The failure of landfill slope depends on the geotechnical properties and the environmental conditions of the landfills. The slope failures are either due to a sudden or gradual loss of strength by the soil or to a change in geometric conditions, for example steepening of an existing slope. Factor of safety (FS) is based on the limit equilibrium approach which is used to determine the degree of safety of the slopes, which is expressed as the ratio of the summation of restoring forces(or moment) to the summation of disturbing forces(or moment). To ensure long-term stability, it is suggested that the calculated FS should be in the range of 1.5-3.0. When the calculated FS value falls below 1, the slope is said to be unstable. Thus a value of greater than 1.0 must be targeted. But this conventional method does not take into account the variability of soil properties in an appropriate manner.

On the other hand, in a probabilistic approach, the stability of landfill slope is expressed in terms of probability failure (p_f)

or in terms of reliability index (β_{HL}). USACE (1997) made specific recommendations on target probability of failure (p_f) and reliability indices (β_{HL}) in geotechnical and infrastructure projects and suggests that a reliability index (β_{HL}) value of at least 4.0 is required for a good performance of the system while a value of at least 3.0 is needed for an above average performance. The uncertainty in the measured soil parameters is expressed in terms of sample mean (μ) and variance (σ^2). The coefficient of variation (CoV%) which is obtained by dividing the sample standard deviation(σ) by the sample mean (μ), is commonly used in quantifying the geotechnical uncertainty analysis.

Response Surface Method can be efficiently adopted to derive an explicit relationship between the considered input variables and output responses. For this, the most important soil parameters such as unit weight (γ), frictional angle (ϕ), cohesion (c), slope angle (β) and interface frictional angle (δ) are considered. The Second Order Reliability index formulated by Hasofer and Lind (1974)

is a most popular technique to calculate the reliability index (β_{HL}) of a system using the mean values of each parameter and their intrinsic variations. The acceptable reliability index (β_{HL}) values ranges from 3.0 to 5.0.

OBJECTIVE OF THE STUDY

The aim of the study is to evaluate the reliability of the slopes at a typical municipal solid waste landfill cover slope considering the geotechnical properties pertaining to the geotechnical properties of cover soil and geomembrane.

METHOD

The methodology followed in the reliability analysis is shown in the Figure 1. This can be divided into 3 sections; Limit equilibrium method for stability analysis of slopes due to gravitational forces, Response Surface Method (RSM) for developing explicit relationship and Reliability analysis to evaluate the reliability of slope considering uncertainty. Each section is briefly explained.

SLOPE FAILURE DUE TO GRAVITATIONAL FORCES

There are various causes of slope failures such as gravitational force, seismic force, seepage force and veneer reinforcement slopes. In the present study, stability of slope due to gravitational force exerted due to self-weight of the soil slope is analyzed. Slope failure occurs when the gravitational force acting on slope exceeds its resisting force. The shear strength characteristic of soil greatly influences the resistive forces against shear stresses which lead to failure of slope. The various forces acting on a MSW landfill slope provided at an angle β is shown in the Figure 2. It includes a passive wedge at the toe and has a tension crack of the crest (Koerner and Soong 1998).

Where W_A = total weight of the active wedge; W_P = total weight of passive wedge; N_P = effective force normal to the failure plane of the passive wedge; N_A = effective force

normal to the failure plane of the active wedge; E_A = inter wedge force acting on the active wedge from the passive wedge; E_P = inter wedge force acting on the passive wedge from the active wedge; C_a = adhesive force between cover soil of the active wedge and the geomembrane; c_a = adhesion between cover soil of the active wedge and geomembrane; C = cohesive force along the failure plane of the passive wedge; γ = unit weight of the soil cover; h = thickness of cover soil; L = length of the cover soil; β = soil slope angle beneath the geomembrane; ϕ = frictional angle of the cover soil; δ = interface frictional angle between cover soil and the geomembrane; FS= factor of safety against cover soil sliding on the geomembrane. The FS-value is then obtained from the solution of the quadratic Equation (1) as given below.

$$FS = \frac{-b \pm \sqrt{b^2 - 4ac}}{2a} \quad (1)$$

Where:

$$a = (W_A - N_A \cos\beta) \cos\beta$$

$$b = -[(W_A - N_A \cos\beta) \sin\beta \tan\phi + (N_A \tan\delta + C_a) \sin\beta \cos\beta + (C + W_P \tan\phi) \sin\beta]$$

$$c = (N_A \tan\delta + C_a) \sin 2\beta \tan\phi$$

Statistical description of Random Variables

There are various factors which influences the stability of slopes as shown in Figure 2. In this study five important factors are considered to be random variables and their statistical descriptions are given in Table 1.

Response Surface Method (RSM)

The term response surface means approximating an unknown function by a suitable graduating function. This leads to the idea that response surface methods can be used to create an approximating function for a long running system model. It defines the explicit relationship between the output

response y and the input model parameters $x_1, x_2, x_3, x_4 \dots, x_n$. The general form the relationship is by Equation (2).

$$y = f(x_1, x_2, x_3, \dots, x_n) \quad (2)$$

The advantage of this method is that getting results are compatible with computationally demanding approaches. It also analyses the effect of the important factors on the results. In this study, the uncertainties of the soil parameters are optimized by using 2^n factorial method where n refers to number of parameters considered. Accordingly, $2^n=2^5=32$ combinations exists. The combinational Matrix Table is given in Table 2."-" indicates the minimum value of the variable and "+" indicates the maximum value of the variable is shown in Table 1. The outcome Y is computed using conventional factor of safety approach as explained earlier. The RSM is well explained by Myers and Montgomery (2002).

RELIABILITY ANALYSIS

A limit equilibrium method produces the factor of safety that is used to measure the performance of the slopes. However, the safety factor cannot explicitly reflect the uncertainties of the design parameters involved in any slope problems. A better alternative is to use a reliability index which depends on mean values of each parameter and their intrinsic variations. The reliability index formulated by Hasofer and Lind (1974) is one of the popular techniques to calculate the reliability of a system. The Hasofer Lind reliability index (β_{HL}) is expressed in matrix form as:

$$\beta_{HL} = \min \sqrt{\left[\left(\frac{x - m}{\sigma} \right)^T [R]^{-1} \left(\frac{x - m}{\sigma} \right) \right]} \quad (3)$$

Where x is the vector representing the set of normally distributed random variables, m their mean values, σ their standard deviations, R the correlation matrix and F the failure region. It is noted the β_{HL} is basically the shortest distance in units of standard deviation of the failure surface to the point

where the mean values of the random variables are located.

RESULTS

In order to develop a multi-linear response surface model between input and output variables, $2^5 = 32$ sample points are used. Regression analysis with the least-squares error method is adopted to fit the response surface model. Coefficients of multiple determination R^2 and adjusted coefficients of multiple determination R^2_{adj} defining the adequacy of the fitted linear model are evaluated. The performance function obtained by RSM method is given in Equation (4). The RSM is carried out using the "Design Expert Version 9" commercial software package.

$$FS = 1.22 + (0.1 \times \gamma) - (0.023 \times c) + (0.0046 \times \varphi) + (0.179 \times \beta) - (0.0367 \times \delta) \quad (4)$$

$$R^2=0.955; R^2_{adj} \text{ value}=0.946$$

Residual analysis is also performed to check the normality assumption. A normal probability plot of residuals is shown in Figures 3. Normal probability plot approximately follow a straight line, indicating that the assumption of normality is satisfactory.

Reliability analysis is carried out using an excel spread sheet program given by Low and Tang (2007) which is based on object-oriented constrained optimization. The performance function $g(x)$ used in the reliability analysis is given in Equation (5). Corresponding probability of failure P_f can be obtained from normal probability table using the Equation (6). The reliability index (β_{HL}) is calculated for different Factor of safety values and the result is presented in Figure (4). It can be observed that for FS of 1.5, the reliability index (β_{HL}) value is 2.21 and probability of failure of slope P_f is 1.3×10^{-2} .

$$g(x) = FS_{req} - FS \quad (5)$$

$$P_f = 1 - \varphi(\beta) \quad (6)$$

SUMMARY AND CONCLUSIONS

4th International Engineering Symposium – IES 2015

March 4-6, 2015, Kumamoto University, Japan

This paper provides an approach to assess the reliability of failure of MSW landfill slopes due to gravitational forces, using RSM. Dry Unit weight (γ), Cohesion (c), Frictional angle (ϕ), Slope angle (β) and Interface frictional angle (δ) are considered as random variables for the analysis. Among the considered parameters, Dry Unit weight (γ), Cohesion (c), Slope angle (β) and Interface frictional angle (δ) were observed to be significant factors which influence the stability of slopes. Reliability index β_{HL} of 2.21 is obtained for a required FS of 1.5 which intern gives probability of failure of slope P_f of 1.3%.

REFERENCES

- G.L.Sivakumar Babu, Krishna R.Reddy and Amit Srivastava (2014). "Influence of Spatially Variable Geotechnical Properties of MSW on Stability of Landfill Slopes" *Journal of Hazardous, Toxic and Radioactive Waste*.18(27-37).
- V.Tandjria, C.I.Teh and B.K.Low (2001). "Extension to generalized method of slices for reliability analysis of reinforced slopes" Proc. Of 10th int. conf. *Computer Methods and Advances in Geomechanics*.(231-234)
- Robert M.Koerner and Soong (1998). "Analysis and design of veneer soils" 6th International Conference on Geosynthetics. (1-23)
- B.K.Low (2003). "Practical Probabilistic slope stability analysis" Proc. *Soil and Rock America 2003, 12th Panamerican conference on Soil mechanics and geotech. Engg. and 39th U.S.Rock Mechanics Symposium ,M.I.T., Cambridge, Massachusetts* (2777-2784)
- Griffiths & Lane (1999). " Slope stability analysis by finite elements" *Geotechnique* 49,No. 3(387-403)
- Felix.S.Wong (1985). "Slope reliability and response surface method" *Journal of Geotech. Engg. Vol.111*(32-53)
- G.L.Sivakumar Babu Et.al (2010). "Reliability analysis of municipal solid

waste landfill slopes" *International Congress on Environmental Geotechnics, New Delhi, India*(1711-1716)

- Myers RH and Montgomery DC (2002) Response Surface Methodology, 2nd edn. Wiley, New York, NY, USA.
- Hasofer AM and Lind NC (1974). "Exact and invariant second moment code format" *Journal of Engineering Mechanics* 100(1)(111-121)
- USACE. (1997). "Risk-based analysis in geotechnical engineering for support of 544 planning studies, engineering and design" Dept. of Army, USACE, Washington, D.C.,545 20314-100.

Table1. Statistical description of Random Variables used in this study obtained from published data.

Statisti cal param eters	Dry Unit weig ht(γ) kN/m^3	Coh esi on (c) kPa	Fricti onal angle (ϕ) degr ees	Slop e (β) degr ees	Interf ace frictio nal angle (δ) degre es
Mean (μ)	11.13	18. 23	32.27	18.4	22
Std. Dev(σ)	1.0	7.0 3	2.83	1.5	2
Cov%	23.4	68. 9	24.16	12.2	11
Minimu m value(μ - 1.65σ)	9.17	6.6 3	27.6	15.9	18.7 2
Maximu m value(μ + 1.65σ))	13.09	29. 83	36.94	20.8	25.3 7
Distribu tion	Norm al	Norm al	Norm al	Norm al	Norm al

Table 2. Combinational Matrix for RSM

Sl.No.	X ₁	X ₂	X ₃	X ₄	X ₅	Y
1	-	-	-	-	-	FS ₁
2	-	-	-	-	+	FS ₂
3	-	-	-	+	+	FS ₃
4	-	-	+	+	+	FS ₄
5	-	+	+	+	+	FS ₅
.
.
.
32	+	+	+	+	+	FS ₃₂

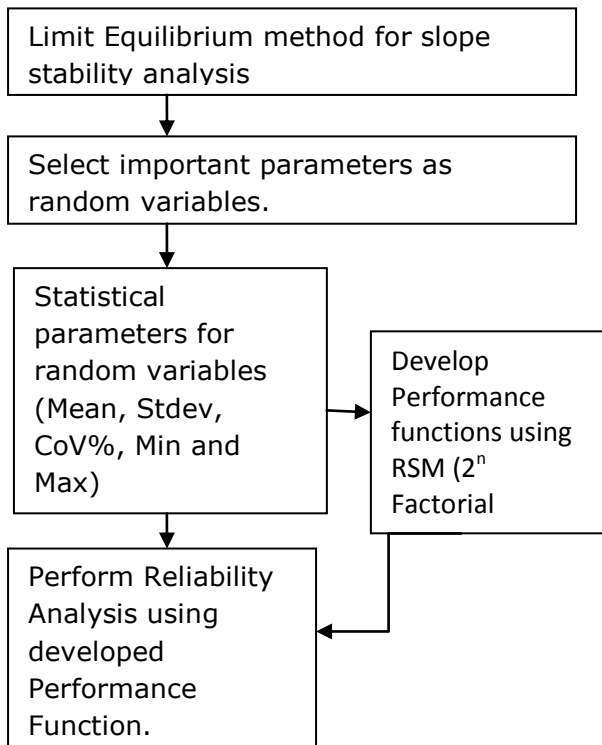


Figure 1. Flow chart of method used in the study

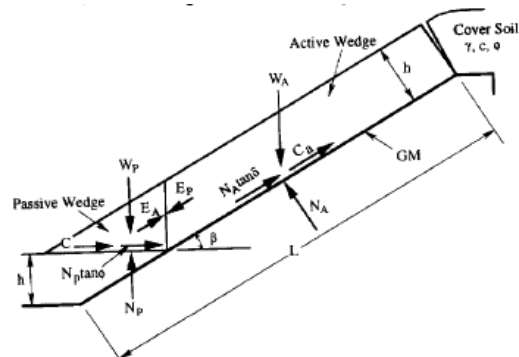


Figure 2. Forces acting on the active and passive wedges on the slope

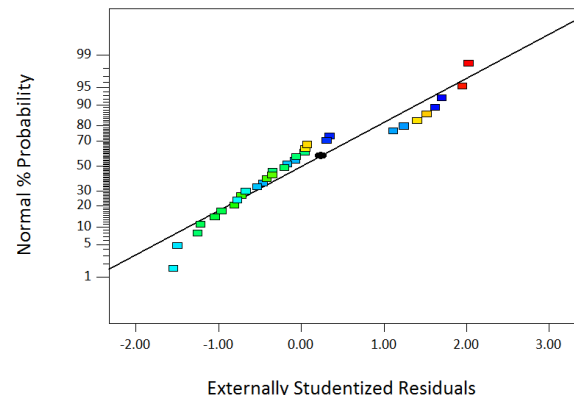


Figure 3. Normal probability plot of standardized residuals obtained from RSM

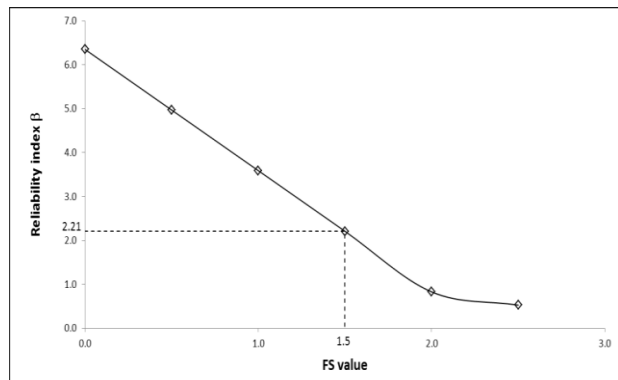


Figure 4. The plot between FOS and Reliability index (β_{HL})

Assessment of Dynamic properties of Municipal Solid Waste Sites using Multichannel Analysis of Surface Waves

B.P.Naveen, T.G.Sitharam and P.V.Sivapullaiah

*1 Department of Civil Engineering, Indian Institute of Science, Bangalore 560012, India.
e-mail: bpnaveen@civil.iisc.ernet.in*

ABSTRACT: Dynamic properties of municipal solid waste are necessary for the landfill design. The landfill needs to be safe not only under static conditions, but also under dynamic loading conditions. For the performance of seismic analysis, the selection of material properties is an important step. In recent years, geophysical surveys are becoming popular mainly to understand the profiles within the landfills and estimate its dynamic properties like shear wave velocity, shear modulus and Poisson's ratio. Geophysical tests provide a measurement of shear wave velocity (V_s) and hence widely accepted for the seismic site characterization purpose. MASW testing for characterizing municipal solid waste site has been very recent and very recently some researchers have attempted this technique for characterizing the waste in a municipal solid waste site. This paper describes the geophysical testing using MASW tests were conducted on Mavallipura landfill site, Bangalore. The typical MASW test setup used for the present study consists of 24-channel geode seismograph and 24 geophones of 4.5 Hz capacity. The geophones were placed at uniform interval of 1m. The source was created by striking the ground with a sledge hammer against the metal plate used. The generated surface waves that propagate through the soil and waves are measured by distant receivers aligned in an array and connected to a seismograph. The landfill was surveyed up to a length of about 25m at the top level. The deposit consisted of un-compacted waste up to a depth 6m. Results show that the shear wave velocity increases with depth from approximately 74 to 150m/s. Series of 1-D MASW tests have been carried out to map the entire solid waste site and new empirical correlation between (SPT) corrected N values versus measured shear wave velocity has been developed for the site in Mavallipura near Bangalore. The MASW survey results along with correlation with conventional geotechnical investigation will be presented in this paper.

Keywords: Geophysical test, Shear wave velocity, Seismograph

INTRODUCTION

Solid Waste Management is a challenging problem not only in developing countries but in developed countries as well. Various activities of the society lead to the generation of waste materials that include both organic and inorganic wastes. Due to increase in population, the amount of solid waste generated is increasing day by day. The wastes that are generated in cities dispose their wastes in different ways. Historically waste is disposed of unscientifically leading to the development of many waste dumps around. Scientific

disposal of large quantities is a challenging problem at all levels - global, regional and local levels, creating nuisance in the cities.

In Bangalore city, the municipal solid waste generation presently is about 4500 Metric tons and the waste generation is likely to grow over the coming years.

Going by the present trend of increase in the quantity of waste the waste quantity is projected to be around 12000 MT by 2032. At the same time, the strict environmental criteria for the zonation of landfills, the extensive urbanization and the

4th International Engineering Symposium - IES 2015

March 4-6, 2015, Kumamoto University, Japan

unwillingness of people to live near a landfill reduce significantly the locations where landfills could be constructed and operated. This situation applies great pressure at existing landfills to place more waste than was specified in the original design. Hence engineers need to find innovative ways to accommodate more waste in existing landfills (Zekkos, 2005).

Geophysical testing methods were developed by petroleum and mining geologist searching for oil deep and mineral below the earth surface. There were able to distinguish between different geological strata by observing the physical properties. Hence it is most promising sites for mining and drilling. Later engineering geologist and geotechnical engineer began to use some of these methods to assist in site characterization studies. Geophysical testing is not nearly as precise as drilling borings and obtaining samples, it has the benefit of covering large areas at small costs and sometimes can locate features that might be missing by conventional borings. Geophysical investigation is important to determine key insitu subsurface information for earthquake engineer and other geotechnical site investigations. The basic principles to recognize geological profile and to measure properties of the ground.

In 1885 Lord Rayleigh predicted the existence of surface waves (Rayleigh, 1885). The researchers are attracted in various disciplines as diverse as micro wave engineering, solid-state physics, geotechnical engineering, nondestructive testing, seismology, geophysics, ultrasonic acoustic and material science, these disciplines share the goal of exploiting surface waves propagation along the boundary of a domain to obtain information about the interior of that domain.

Surface waves are ideal for the development of noninvasive techniques for material characterization from very small scale (less than millimeter), to a very large scale (more than a kilometer). The geotechnical engineers and geophysicists use surface waves for the geo material

characterization. The basic principle is the same for all these applications: to use the geometric dispersion of surface waves to infer the relevant medium properties by solving an inverse problem for parameter identification (Robert and Wride, 1997).

Solid Waste dumped site materials are multiphase, complex, particulate and discontinuous with different constituents of municipal solid waste like glass, paper, organic waste, inert materials, etc.,. Material behavior cannot be described using simple models. From the initial stage of loading, municipal solid waste exhibit nonlinear and irreversible behavior. The wave travel through such materials and the two types of body wave propagate in an unbounded, homogeneous, and linear elastic medium namely P-waves (Primary or longitudinal or compression waves) and S-waves (Secondary or distortional or shear or equivoluminal waves). Primary waves propagate with particle motion in the same direction of the propagation and cause volume change without distortion. Secondary wave propagate with the particle motion is perpendicular to the direction of propagation. The propagation of velocities of seismic waves in a linear elastic solid are associated with the medium's mechanical parameters through relationships. The two elastic constants are used for the mechanical response of an elastic medium namely Lame's constants λ and μ , the latter being the shear modulus G in engineering notation. Seismic wave velocities can be expressed with relationships between such constants and the material density ρ

$$V_p = \sqrt{\frac{\lambda + 2G}{\rho}} \quad (1)$$

$$V_s = \sqrt{\frac{G}{\rho}} \quad (\text{Or}) \quad G = V_s^2 \rho \quad (2)$$

4th International Engineering Symposium - IES 2015

March 4-6, 2015, Kumamoto University, Japan

ρ = Density; V_s = Shear wave velocity;

G = Shear modulus

A change in density with depth is usually small in comparison to the change in shear modulus (G) and is normally ignored (or) assumed as constant. With known or assumed Poisson's ratio, one can also obtain P-wave velocity (V_p) profile from V_s profile. In body waves, the velocity of propagation is directly related to the stiffness of the medium and is not frequency dependent (in linear elastic materials). P-waves is associated with the young's modulus, where as S-waves is associated with the shear modulus (Sebastian et al 2014).

PROJECT SITE DETAILS

The seismic surveys were conducted at the Mavallipura Landfill site, at Hesaraghatta Hobli, Bangalore North. Fig 1. shows the Mavallipura site location in Bangalore. Waste was placed in the landfill from 2007 to 2013 at the rate of approximately 4,500 tons per day. The waste consisted of approximately 60% biodegradable waste and 40% non biodegradable waste. The typical height of solid waste dumping is 6m and the deposit consisted of uncompacted waste. 8 Borehole drilling were performed at the Mavallipura landfill. Aerial photo of the landfill shown in the fig 1. The GPS coordinate of the landfill are Latitude 13°50'North and Longitude 77°36' East. Fig.2 shows the Bore hole location on Mavallipura landfill site. Auger drilling operation using a 150mm diameter is carried out in landfill site. The purpose of the auger drilling operation was to characterize the municipal solid waste visually, to retrieve bulk samples of waste from different depths, of different degree of degradation and different age as shown in fig 3.



Fig.1 Area map of Mavallipura site

(Courtesy: google earth images,
<https://maps.google.com/map>)



Fig. 2 Bore hole location on Mavallipura landfill site

Bore Hole Bh-1		Water Table: Nil		Boring > Auger 150mm		SAMPLE DESCRIPTION	
RL	THICKNESS- cm	SAMPLE	SOIL DESCRIPTION	DEPTH- cm	SPT-N [*]	SPT, DS	UDDS
1.5		Waste		0.5			
				1.0			
				1.5	6	8	SPT
				2.0			
1.5		Waste		2.5			
				3.0	A	12	SPT
				3.5			
				4.0			
1.5		Waste		4.5	A	12	SPT
				5.0			
				5.5			
				6.0	A	14	SPT



Fig. 3 Typical bore log data & auger drilling for collection of waste samples

ESTIMATION OF UNIT WEIGHT

The unit weight of municipal solid waste MSW is an important parameter in engineering analyses of landfill performance, but significant uncertainty currently exists regarding its value. Unit weight of MSW is very essential for many engineering analyses of landfill systems, including static and dynamic slope stability, geomembrane puncture, pipe crushing, and landfill capacity evaluation. The value of MSW unit weight continues to be major source of uncertainty in landfill performance analyses. The primary method used to evaluate the unit weight of MSW is In situ large-scale methods: In situ large-scale methods generally the 150mm diameter boreholes at depth are excavated and the excavated waste material is weighed. The excavated cavity's volume is estimated by replacing the waste material with calibrated material of known unit weight such as uniform gravel. The unit weight of MSW is calculated by dividing the measured weight of the excavated MSW by the estimated volume of the cavity as shown in fig 4.



Fig.4 Estimation of unit weight with depth in Mavallipura landfill site

Based on the in-situ weight data indicate that MSW unit weight is governed by the waste composition and compaction effort applied when first placed, and the effective confining stress currently acting on it, which is largely a function of its current depth in the landfill. From the fig 5 shows the unit weight tended to increase with depth. The unit weight profile with depth

ranging from a low unit weight of 2.48 kN/m³ near the surface and a highest value of approximately 9.02 kN/m³ at a depth of 6 m.

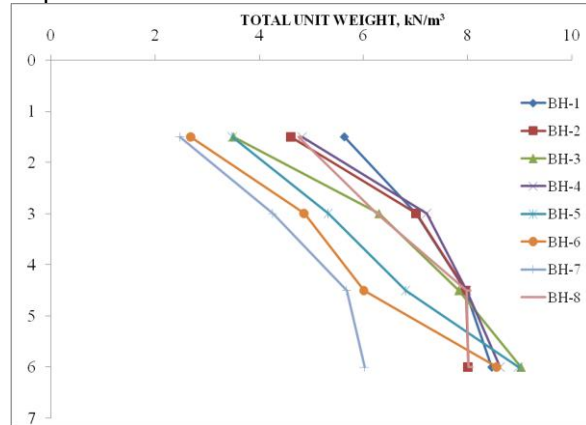


Fig.5 Variation in the total unit weight with depth for the Mavallipura landfill

SEISMIC SURVEY CARRIED OUT IN MAVALLIPURA LANDFILL SITE

The typical MASW test setup used for the present study consists of 24-channel geode seismograph and 24 geophones of 4.5 Hz capacity. Seismic data were recorded using Geode seismograph with sledge hammer source on one side of the landfill and geophones on the other side with different spacing of geophones (1m). The landfill was surveyed up to a length of about 25m at the top level. The deposit consisted of uncompacted waste up to a depth 6m. Fig.6 shows the MASW testing arrangement in landfill site. Fig.7 shows the shear wave velocity increases with depth from approximately 74 to 150m/s.



Fig. 6 MASW carried out in landfill site

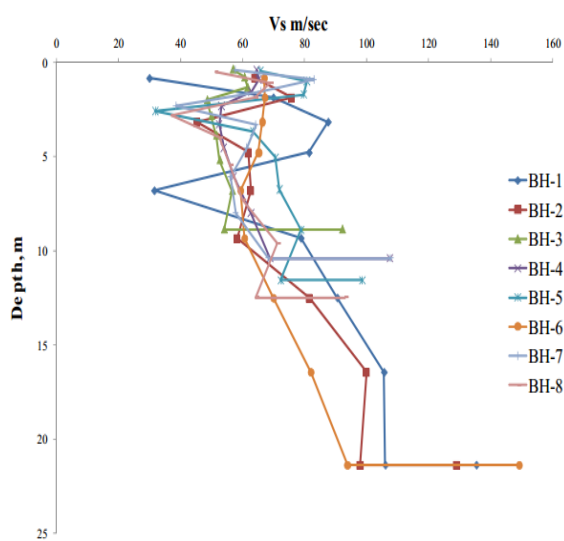


Fig. 7 Shear wave velocity vs. Depth

At present, the direct way to estimate the shear wave velocity (V_s) profile is from bore hole uphole/down hole geophysical tests, which is not feasible to make V_s measurements at all locations. Hence it will be advantageous to deduce the shear wave velocity values from the conventional geotechnical field tests like SPT which are very common. In the present study a correlation between shear wave velocity and SPT-N value is developed for the Mavallipura municipal solid waste landfill site. The N-values measured in the field were subjected to various corrections such as (a) Overburden pressure correction (C_N), (b) Hammer energy correction (C_E), (c) Borehole diameter correction (C_B), (d) liner correction (C_S), (e) Rod length correction (C_R) (Seed et al., 1983; Skempton, 1986; Youd et al., 2001; Zekkos et al., 2011). The SPT value corrected for 60 percent energy efficiency and 100KPa overburden pressure (N_{60}) was evaluated using equation 3 (Robert and Wride, 1997).

$$(N_{60})_{60} = N \times [C_N \times C_E \times C_B \times C_S \times C_R] \quad (3)$$

N-value, provided by the SPT field measurement technique, is one of the most common parameters for the evaluation of geotechnical properties of soils, and has been utilized as an indispensable index for the design

although it's empirical and rough attribute. Fig. 8 shows shear wave velocities vary from 45 m/s to 65 m/s at the portion where N-values are below 10. This means the N-value does not have enough sensitivity to unconsolidated waste material. Each bore hole location might have different waste material characteristics. If N-values are below 4 then correlation is weak. Correlation reasonable to be good if N-values are above 4.

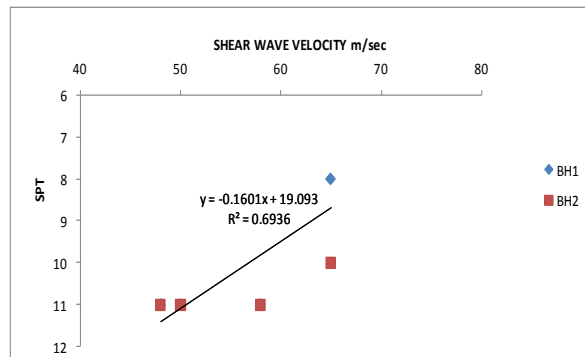


Fig. 8 BH-1, BH-2

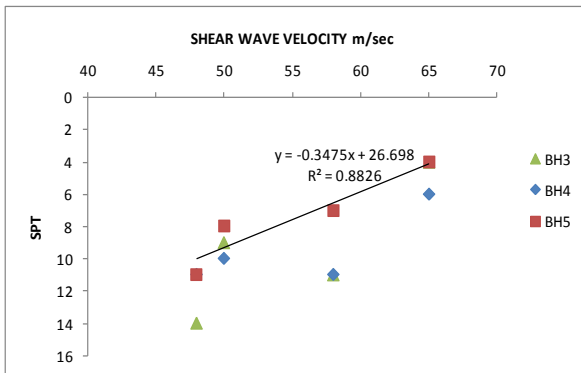


Fig. 8 BH-3, BH-4, BH-5

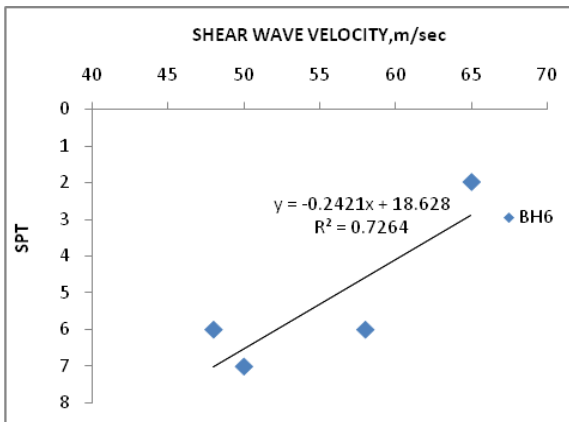


Fig. 8 BH-6

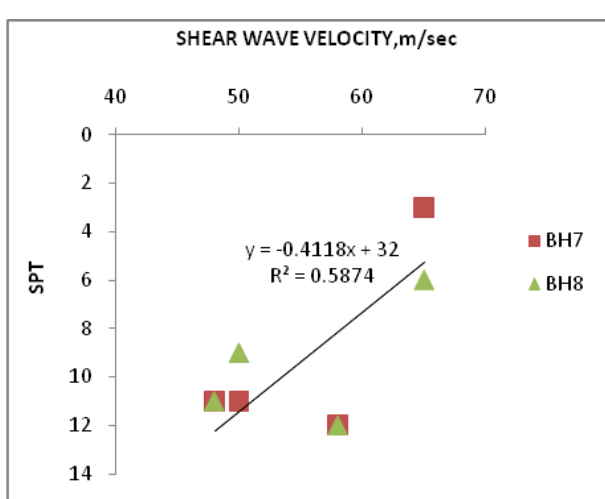


Fig. 8 BH-7, BH-8

Fig.8 Vs versus Corrected SPT-N values for Mavallipura landfill

CONCLUSIONS

In the present study, the seismic site characterization for the Mavallipura landfill site at Bangalore was performed using MASW and SPT data. Major conclusions of this paper are as follows.

- Based on the site characterization at landfill site, it was found that the Mavallipura landfill site can be categorized as very loose and it is still in a degradation process.
- Shear wave and P-wave velocity profile for 8 major locations in the study area were determined and variation of waste material stiffness (shear modulus) corresponding to the in-situ state with depth, was also evaluated. The waste material stiffness of waste strata corresponding to the undisturbed in-situ state is very essential for the ground response analysis.
- The characteristic profile, landfill-specific values of MSW unit weight depend primarily on waste composition, operational practices i.e., compaction, cover soil placement, and liquids management, and confining stress.
- The unit weight profile with depth ranging from a low unit weight of 2.48 kN/m³ near the surface and a

highest value of approximately 9.02 kN/m³ at a depth of 6 m.

- A correlation between shear wave velocity (Vs) and corrected SPT-N value was developed for the Mavallipura landfill site.
- Correlation reasonable to be good if N-values are above 4.

REFERENCES

- [1].Park, C.B., Miller, R.D., & Xia, J. (1999) Multichannel analysis of surface waves MASW, Geophysics 64(3):800–808.
- [2].Rayleigh, L., 1885, On waves propagated along the plane surface of an elastic solid: Proc. Lond. Math. Soc., 17, 4.
- [3].Robertson, P.K. & Wride, C.E. (1997) Cyclic liquefaction and its evaluation based on the SPT and CPT In In Proceedings of the NCEER Workshop on Evaluation of Liquefaction Resistance of Soils, Technical Report NCEER-97-0022, National Center for Earthquake Engineering Research, Buffalo, pp. 41–87.
- [4].Sebastiano Foti, Carlo G. Lai, Glenn J. Rix, Claudio Strobbia (2014) Surface Wave Methods for Near-Surface Site Characterization.
- [5]. Seed, H.B., Idriss, I.M., & Arango, I. (1983) Evaluation of liquefaction potential using field performance data ,Journal of Geotechnical Engineering 109(3):458–482.
- [6]. Skempton, A.W. (1986) Standard penetration test procedures and the effects in sands of overburden pressure, relative density, particle size, ageing and overconsolidation, Geotechnique 36(3).
- [7]. Youd, T.L., Idriss, I.M., Andrus, R.D., I., Arango, Castro, G., Christian, J.T., Dobry, R., W.D., Liam Finn, Harder, L.F., Hynes, M.E., Ishihara, K., Koester, J.P., Laio, S.S.C., Marcuson, W.F., Martin, G.R., Mitchell, J.K., Moriwaki, Y., Power, M.S., Robertson, P.K., Seed, R.B., & Stokoe,K.H. (2001) Liquefaction resistance of soils. summary report from the 1996 NCEER and1998 NCEER/NSF workshops on evaluation of liquefaction resistance of soils, Journal of Geotechnical and Geoenvironmental Engineering 127(10):817–833.
- [8]. Zekkos.D.P (2005). Evaluation of Static and Dynamic Properties of Municipal SolidWaste. Doctral of Philosophy. University of California. Berkeley.
- [9].Zekkos, D., Matasovic, N., El-Sherbiny, R., Athanasopoulos-Zekkos, A.,Towhata, I., andMaugeri, M. (2011) Dynamic properties of municipal solid waste, Geotechnical special publication, geotechnical characterization, field measurement and laboratory testing of municipal solid waste, Vol. 209, American Society of Civil Engineers, Reston, VA,112–134.

Ground Water Quality- Hurdles and Remedies at Solid Waste Processing site in Mysore City, India

C Nanjunda Swamy¹ and Lokeshwari M²

1 Dr. Ambedker Institute of Technology, Bengaluru, India.

E-mail: swamy_vtu@yahoo.com

2 Department of Civil Engineering, R.V.College of Engineering, Bengaluru- 560059, India. Email: eshwarienv08@gmail.com, lokeshwarim@rvce.edu.in

ABSTRACT: Around the world, groundwater pollution is a very serious and costly problem. Studies were conducted on Ground water quality analysis by collecting samples in and around the solid waste processing plant at Mysore during 2012. Results of physico – chemical characteristics revealed that, the concentration of most of the critical parameters like BOD, COD etc. exceeds the permissible limit near waste processing area. In view of this, shortcomings in the Municipal waste management practices were identified and linked with ground water pollution. Based on the study mitigative measures were suggested. So the ground water quality improved and the parameters were well within the limit during the study in the year 2014.

Key words: Solid waste, Ground water, Compost plant, landfill.

INTRODUCTION

Ground Water is that occurs below the surface of the Earth, where it occupies spaces in soils or geologic strata. Most groundwater comes from precipitation, which gradually percolates into the Earth. Leachate is the liquid that drains or 'leaches' from a Municipal waste processing site. It varies widely in composition regarding the age of processing site and the type of waste it contains. Uncontrolled disposal of municipal solid waste (MSW) in processing site is a common practice in most of the cities. As a result of which waste accumulates and produces leachate, if no proper collection system for leachate, it leads to ground water pollution.

Groundwater pollution is a very serious and costly problem and many governments have started to take aggressive action to address it. Once contaminated, groundwater is very expensive to clean up and make usable again.

Erode city, the headquarters of Erode district is located on the bank of Cauvery river in Tamil Nadu state. In addition to Cauvery river water, people in this region

also depend on the groundwater. Municipal solid waste of the city disposed as open landfills at three different sites namely vendialyam, vairapalyam and semur. Leachate of the open dump yards directly contaminates the groundwater leading unsuitability of water for drinking. (Rajkumar et.al, 2010)

Delhi generates 8567 tons of MSW every day. Physio-chemical characteristics of ground water samples in the proximity of Gazipur landfill site exceeded the permissible limits of ground water standards and it does not confirm to the drinking water standard. It is noticed that pollution is more in the areas near landfill and it reduces gradually with the distance in the north and west direction, which indicates that the landfill leachate contaminated ground water in proximity of landfill. (Suman et.al., 2013). Likewise Many literature shows ground water pollution in and around Municipal waste processing sites. So it is better to prevent ground water pollution near waste processing sites like compost plant and landfill by adopting proper waste management system.

4th International Engineering Symposium - IES 2015

March 4-6, Kumamoto University, Japan

STUDY AREA

Mysore is one of the historic city of south India and ex-capital of Mysore state (Fig1). It is one amongst few cities which had the privilege of serving as royal seats under the rulers, who devotedly contributed their own classic beauty to the architectural monuments of the city. Mysore city is a district headquarters which is 150 km away from the capital of Karnataka state in India. It is also called as cultural capital of Karnataka. Population of Mysore city is 9, 38,386 as per 2011 census. Total area of Mysore city limit is 128.42 sq.km. Mysore city is having most famous tourist places like palaces, zoo, temples heritage buildings etc., which attracts more tourists and also connecting city to Kerala and Tamilnadu, so causes high floating population.

Solid waste management in Mysore city is the obligatory function of Mysore City Corporation (MCC). MCC comprises of 65 wards, which consists of 2,06,370 households. Solid waste management of some of the wards, 4 markets and main roads are privatized due to the shortage of workers. Mysore city generates about 450 Tonnes of Municipal solid waste daily. Mysore city is having a centralized compost plant at Vishveshwara Nagar which is of 200 Tonnes per day capacity. It was established in the year 2002. Major part of the waste generated in Mysore city is transported to this plant where composting is done by windrow method. Excess waste without treatment is being dumped in the surrounding open spaces and spreading area of the compost plant.

MATERIALS AND METHODS

Groundwater samples collected from the bore wells in and around the compost plant, as per the standard methods procedure. During the study period (2012 & 2014) total 30 water samples in five intervals were collected from all the 6 pre-determined sampling stations (Table 1 and fig 2) and analyzed for water quality parameters like pH, EC, Alkalinity, Chloride, Sulphate, Phosphate, Nitrate, COD ,BOD, TDS, Hardness etc as per Indian Standards. Leachate sample collected from the leachate discharge point and analysed as per standard methods.

Results and Discussions:

Water quality analysis data are summarized in Tables 2 and 3. Characteristics of the leachate are given in Table 4.

The extent of contamination of ground water due to leachate percolation depends upon number of factors like leachate composition, rainfall, depth and distance of the water source (borewell) from the pollution source (Vennile.G, et.al., 2012). Water samples collected from the borewell situated close to the waste dump place was found to be more contaminated than that of the borewell situated farther away. It obviously follows the fact of gravitational movement of the viscous fluid. Leachate is hindered due to the mass of solid soil matter. With increasing time the viscous fluid penetrates deeper and spreads over a longer distance. The sampling point S3(Bore well) which is just 50m from the dumping indicates high concentration levels of major pollutants like BOD, COD, Chloride, Sulphate and Nitrates when compared to other 5 sampling points. Strictly speaking one should avoid using ground water drawn from the wells located in proximity of waste dumping site. If this is unavoidable, deeper drilling and frequent analysis of water samples are desirable.

Analysis of leachate (table 4) shows relatively high value of EC of 13,786 μ S/cm indicates the presence of inorganic material in the samples. The higher value of about 1,570 mg/L alkalinity in leachate imparts water an unpleasant taste and may be deleterious to human health with high pH, TDS and Total Hardness. Sulphate if exceeds the maximum allowable limit of 400mg/L, causes laxative effect on humans. Sulphate concentration in leachate is found to be 562mg/L. Sulphate concentration due to groundwater contamination from leachate and septic tank was considerably higher during rainy season than in dry season. Phosphate concentration of leachate is 23mg/L which is very high; usually constitute pollution by infiltration through groundwater. Phosphate is often the limiting nutrient for growth of many organisms in water. Presence of high COD (8,250 mg/L) indicates the high organic

4th International Engineering Symposium - IES 2015

March 4-6, 2015, Kumamoto University, Japan

strength. Indication of organic contaminants through leachate in ground water can be used as organic indicators to assess the ground water pollution.

CONCLUSIONS

- Field observations indicates that, Solid waste generated in Mysore city is around 350- 450 Tpd. Compost plant is designed for 200Tpd (2002).It will not meet the present demand, so the excess waste were dumped in compost plant on open space (spreading area) since 2005 and dosed to compact the waste without treatment. This is the main reason for ground water contamination.
- Sample S3, which is nearer to the dump place (50m) is more contaminated, also Sample S2(250m downstream),shows considerable contamination.
- Hence transportation of excess waste than the capacity of the processing compost plant should be avoided.
- Thus the study suggests 7 clusters of decentralized solid waste management systems in the peripheral area and also the development of landfill site away from residential area to improve the efficiency of existing central compost plant.
- Starting Decentralised Solid Waste management and clearing off the excess waste from compost plant reduced the leachate production and percolation. Thus the analysis in the year 2014, ground water samples shows lesser contamination than 2012.
- However landfill site should be away from the habitat and water source. Development of landfill site inside the compost plant expects again the ground water contamination in near future, if it is not maintained properly.

REFERENCES

- [1] CPHEEO. 2000, Manual on municipal solid waste management. New Delhi: Central Public Health and Environmental Engineering Organisation, Ministry of Urban Development.
- [2] Rajkumar N, et.al., 2010, 'Groundwater Contamination Due to Municipal Solid Waste Disposal – A GIS Based Study in

Erode City', International Journal of Environmental Sciences, Volume 1, No1, pp 45-48.

[3]Suman et.al., 2013 "Leachate characterization and assessment of Ground water pollution near Municipal Solid waste landfill site". Pollution research, Vol2, No3,pp 26-32.

[4]Vennile.Get.al.,2012.'GIS Based Ground Water Quality Assessment of Vattamalaikarai Basin, Tamil Nadu, India', Nature Env and Pollution Technology, Vol 4, pp 585-592.

[5] Indian Standards for drinking water quality, IS 10500-2012.

Mysore City in India

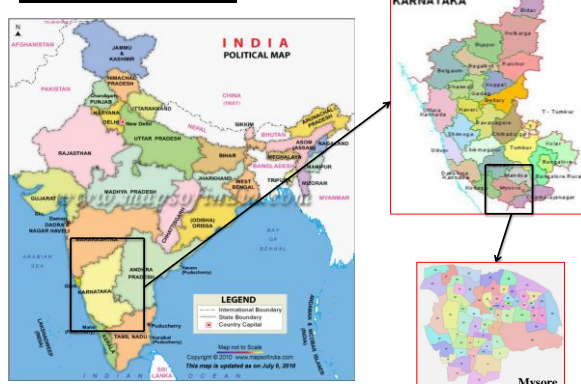


Fig 1: Study area

Table 1: Details of Sampling Points

Type of sample	Approximate distance of processing site from waste dump (m)
Bore well (S 1)	500
Bore well (S 2)	250
Bore well (S 3)	50
Bore well (S 4)	150
Bore well (S 5)	300
Bore well (S 6)	500



Fig 2: Location of sampling points

Table 2: Average values of Water Quality Parameters in the year 2012

Location	pH	EC μS/cm	Alkalinity mg/l	Chloride mg/l	Sulphate mg/l	Phosphate mg/l	Nitrate mg/l	COD mg/l	BOD mg/l	TDS mg/l	Hardness mg/l
S1	7.42± 0.45	1910± 700	670± 50	45 ± 8	50 ±6	0.160± 0.35	1.0± 3	9 ± 6	4± 1	554± 40	360 ±8
S2	7.37± 0.35	4610 ± 600	510 ± 30	316 ± 10	180 ± 15	0.980± 0.3	38± 5	49 ± 5	30± 5	600± 35	570±20
S3	7.26± 0.28	6110± 300	510 ±25	386 ± 5	181± 20	1.910 ± 0.2	42 ± 4	53 ± 8	17 ± 5	1660± 25	750±35
S4	7.78± 0.40	3110± 600	470± 35	59 ± 6	55 ± 5	0.360 ± 0.02	2.91± 5	25 ± 5	8± 3	600± 20	600±15
S5	7.15± 0.35	2990± 400	450±30	75±9	61 ± 9	0.182± 0.02	3.66± 4	8 ± 7	4 ± 2	1200± 30	500±25
S6	7.36 ± 0.3	3000± 500	500 ±45	69 ± 4	38 ± 8	0.380± 0.15	Nil	6 ± 4	4± 3	700± 35	640±30

4th International Engineering Symposium - IES 2015
March 4-6, Kumamoto University, Japan

Table 3: Average values of Water Quality Parameters in the year 2014

Location	pH	EC μS/cm	Alkalinity mg/l	Chloride mg/l	Sulphate mg/l	Phosphate mg/l	Nitrate mg/l	COD mg/l	BOD mg/l	TDS mg/l	Hardness mg/l
S1	7.77 ± 0.35	1410 ± 700	620± 50	37 ± 8	44 ± 6	0.210± 0.35	1.0± 3	2 ± 1	1± 1	504 ± 40	380 ± 6
S2	7.4± 0.4	3610 ± 600	500 ± 30	216 ± 10	110 ± 15	1.040± 0.3	25± 5	5 ± 2	4± 1	550 ± 35	560±10
S3	7.59 ± 0.45	4210 ± 300	470 ±25	246 ± 5	121± 20	1.030 ± 0.2	38 ± 4	5 ± 2	2 ± 2	960 ± 25	780±25
S4	7.78 ± 0.35	2110 ± 600	460± 35	53 ± 6	54 ± 5	0.360 ± 0.02	29± 5	3± 2	1± 1	700 ± 20	700±10
S5	7.55 ± 0.45	2490 ± 400	440±30	72+9	60 ± 9	0.282± 0.02	3.5± 4	3 ± 2	1 ± 2	950 ± 30	600±15
S6	7.86 ± 0.2	2600 ± 500	450 ±45	61 ± 4	29 ± 8	0.280± 0.15	0.5±2	3 ± 2	1± 1	650 ± 35	600±10

Table 4: Results of Leachate Analysis

Sample	pH	EC μS/cm	Alkalinity mg/l	Chloride mg/l	Sulphate mg/l	Phosphate mg/l	Nitrate mg/l	COD mg/l	BOD mg/l	TDS mg/l
Leachate	7.32 ±3	13,786 ±200	1,570 ±50	1,823 ±30	562±10	23± 8	163±15	8,250± 50	263 8 ±60	8,960± 160

4th International Engineering Symposium - IES 2015
March 4-6, 2015, Kumamoto University, Japan

ASSESSING CHANGE-OUTCOME AND IMPACT EVALUATION OF DABASPET-SOMPURA AREA BY REIA

**Ramya R, Rajesh Gopinath, Akash Sirsikar, Amar, Balaji Biradar
and Jai Prakash Reddy**

*Department of Civil Engineering, Acharya Institute of Technology, Bangalore, INDIA
e-mail:ramya.r@acharya.ac.in, ramyarkoundinya@gmail.com*

ABSTRACT: Environmental Impact Assessment (EIA) is broadly defined as a systematic process that proactively examines the potential consequences of developmental actions. As a planning process, the long-term objective of EIA is to contribute to sustainable development of the environment. Bangalore City as the principal administrative, commercial, industrial and educational Capital of Karnataka state has become extremely urbanised in an unorganised manner, therewith facing perils of urbanisation and environmental pollution. As the existing city has run out of spaces, now the focus has shifted to its rural fringes with newer industrial zones adding on to its existing spatial extent. Amidst this requisite for development, the governance fails to acknowledge the need for sustainable growth in town-planning as unplanned addition of industries aggravates the existing problems. Thereby this study proposes inception of EIA during town-planning in conceptual stages itself. In this context, the present research envisages the assessment of Change-Outcome and Impact evaluation for Dabaspet-Sompura Area by Rapid EIA (REIA). The study advents the Simple Checklist and 'Look Alike' approach to achieve the objectives, by studying industrial belts of Whitefield, Bidadi and Nelamangala.

Keywords: Dabaspet, Sompura, Environmental, Checklist, Assessment

INTRODUCTION

The Bangalore city as the principal administrative, commercial, educational and cultural capital of Karnataka state, is witnessing large scale industrial urbanization as the existing city has run out of spaces, now the focus has shifted to its rural fringes with newer industrial zones adding on to its existing spatial extent. Consequently Bangalore city has become extremely urbanised in an unorganised manner, therewith facing perils of urbanisation and environmental pollution [1]. Hence before embarking on the newer industrial projects, the associated short term or long term environmental impacts need to be seriously examined. One such tool which aids in this is Environmental Impact Assessment (E.I.A.), which evaluates the existing pre-operational baseline status by field studies and data

collection, and then carries out an objective assessment of the various impacts on the environment as a result of the proposed industrial activities [3].

METHODOLOGY

The Primary data about the observatories comprises of ambient air quality, water quality, noise levels, traffic volume, wind speed & wind direction, ambient air temperature and relative humidity. These data's were collected at Observatories encompassing an industrial belt, a market place, a residential area and green cover/water cover near dabaspet-sompura area as shown in Fig. 1. The Secondary data was collected from publications and by interacting with the stakeholders at Taluk & District levels.

The Ambient Air Quality Assessment ascertained for each observatory for the

4th International Engineering Symposium - IES 2015

March 4-6, 2015, Kumamoto University, Japan

parameters included Lead, Carbon Monoxide, Oxides of Nitrogen (NO_x), Suspended Particulate Matter and Sulphur di-oxide for 8 hourly mean by employing services of Respirable Dust Sampler - APM 460. The 'Water Quality Assessment' was determined about each observatory for the parameters pH, Total Alkalinity, Total Hardness, Calcium, Magnesium, Chloride, Total Dissolved Solids and Total Suspended Solids. Both surface water and sub-surface water samples were collected to ascertain the water quality. The water quality was then assessed by referring to 'Standards Methods' [2]. Hourly noise levels were measured using calibrated sound-level meter, alongside which simultaneously Hourly Traffic volume survey was carried out. The air temperature and relative humidity were also measured. The measurements were restricted to sunny days with monitoring interval limited to ½ hour, with the height of sensor during monitoring maintained at 1.5m above ground level, due to its representativeness with the human environment. Subsequently Checklist' Method was made use of in extraction of critical environmental attributes which ought to be constantly monitored and managed. Finally with the help of 'Look Alike' Approach, the future trend of development of study area with its probable environmental degradation was predicted.

RESULTS AND DISCUSSIONS

The observations of ambient air quality monitoring are much evident that amidst all pollutants, suspended particulate matter was found to be higher across all stations. The probable reasons for high suspended particulate matter may be attributed to the rising traffic count, flue gases from the chimney of industries and open combustion occurring in the vicinity. From Fig. 2, it's also clear that none of the stations have any significant levels of lead in them.

Results for water quality analysis as can be observed from Fig. 3, indicates all the parameters to be within the standards, except Total Dissolved Solids which was found to be in elevated levels across all stations.

The noise survey is plotted in Fig. 4. It was observed that maximum exposure to noise was during 9AM, 2PM and 5PM.

The Traffic volume analysis which is observed from Fig. 5, for the vehicular count encompassing traffic contributed by Two Wheelers, Three Wheelers, Four Wheelers and Bus, Truck / HLV indicates that 4 Wheelers was highest throughout the monitoring period, followed by 2-Wheelers and 3-Wheelers respectively.

The Relative Humidity made known in Fig. 6, shows that amidst all stations residential areas had least humidity.

The Air temperature at all observatories had risen as day progressed with sun and is revealed in Fig. 7. The consequent wind speed is shown in Fig. 8.

An attempt has also been made to know the percentage increase in population of that area. For in case of growth rate, it was found that there has been an increase of 21.59% in population of the study area from 2001 to 2011 owing to rapid increase in the development of its area.

With the Look Alike survey it was observed that the study area is following a spatial growth as similar to that of Whitefield.

CONCLUSIONS

While the study area is following a spatial growth as similar to that of Whitefield, what makes the matter graver is the fact that while Whitefield was mostly a non-manufacturing industrial belt, the study area is more of manufacturing sector highly linked with environmental pollution. To conclude, this unplanned town planning aspects depicts probable unforeseen and foreseen impacts at magnified scale. This hence mandates the inclusion of EIA studies while planning new townships.

REFERENCES

- [1] Rajesh Gopinath et al. "Distinguishing between Global Warming and Urban Warming for Bangalore with the aid of Statistical Analysis", American International Journal of Research in Science, Technology, Engineering & Mathematics, 6 (1), 2014, pp. 57-60.

4th International Engineering Symposium - IES 2015

March 4-6, 2015, Kumamoto University, Japan

[2] Standard Methods for the Examination of Water and Waste Water, American Public Health Association, 1015, 15th Street, N.W., Washington D.C., 2005.

[3] Ting-Fei Shu et al., "Framework for integration of and ecological planning for urban sustainability within the context of China", Environmental Impact Assessment Review, 31, 2011, pp. 549-560



Fig.1 Observatories in dabaspet sompura area

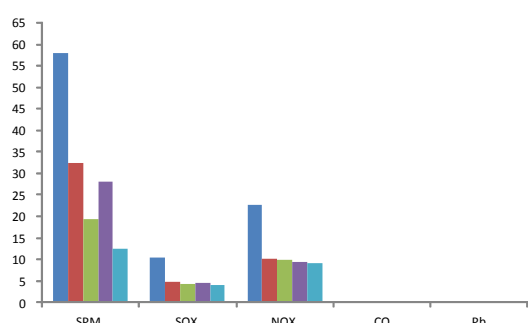


Fig. 2 Air Quality across study area

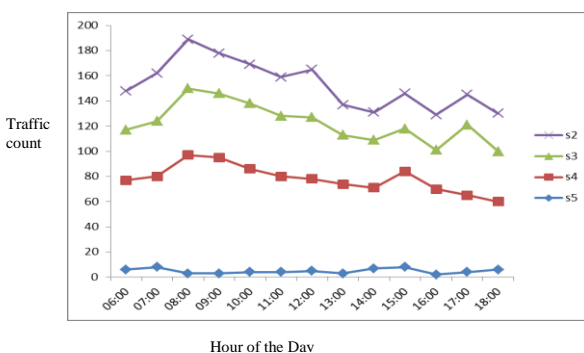


Fig. 4 Noise Volume across study area

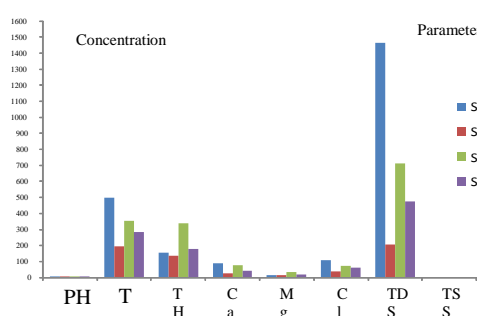


Fig. 3 Water Quality across study area

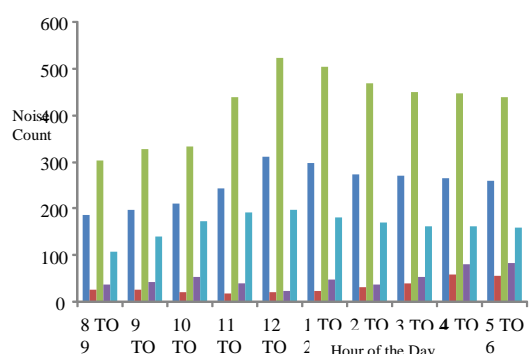


Fig. 5 Traffic volume across study area

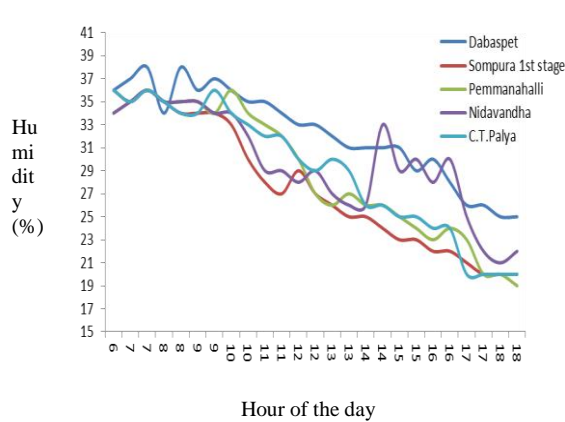


Fig. 6 Relative Humidity across study area

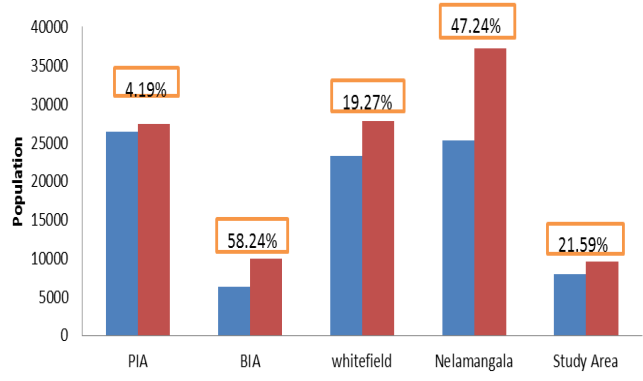


Fig. 9 Percentage change in growth rate

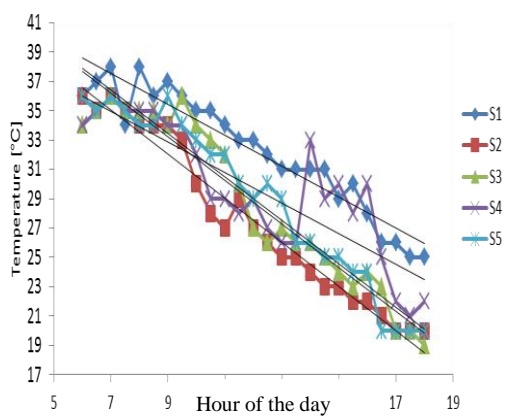


Fig. 7 Air temperature across study area

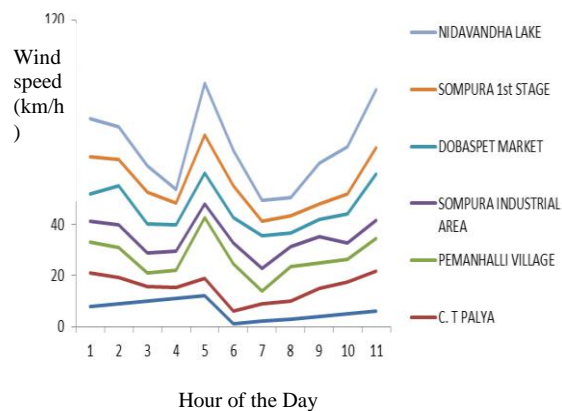


Fig. 8 Wind speed across study area

GROUNDWATER FLOW AND MASS TRANSPORT MODELLING – A CASE STUDY

¹B.V.Sai Charitha, ²M.J.Nandan and ³V.V.S Gurunadha Rao

¹ Department of Civil Engineering, NITK, bvsaicharitha@gmail.com

² Principal Scientist, CSIR-NGRI, Hyderabad, mjnandan@gmail.com

³Ex-chief Scientist, CSIR-NGRI, Hyderabad, gurunadharaovvs@gmail.com

ABSTRACT: A site consisting of two granite quarry pits is chosen for disposal of non-hazardous sediments dredged from Hussainsagar Lake in Hyderabad. Geo physical investigations, hydro geological investigations, in situ infiltration measurements and mass transport modelling study for likely contaminant migration from the Quarry pits is carried out. These studies indicate that the proposed granite Quarry Pit 1 & Pit 2 are ideal sites for disposal. Little engineering on side walls of the Pits have to be undertaken to close the open joints occurred during quarrying of granite material and drilling of 5 observation wells up to 50 m depth at <10 m from the Quarry pits in the South and South Eastern part is suggested.

KEYWORDS: Lake bed sediments, watershed, groundwater level contours (bgl), groundwater velocity, TDS concentration, Electrical resistivity.

INTRODUCTION

The existing pleasant lakes like Hussainsagar in Hyderabad are being polluted heavily due to dumping of municipal wastes. Safe disposal of these lake sediments is one of the important measure to be maintained to restore the original sanctity and cleanliness of the lakes. For safe disposal of garbage, proper sites are to be selected which should not contaminate the surroundings as well as groundwater. This paper is about the geological and hydro geological study of the site chosen nearby the lake to dump these lake bed sediments. The area is of granitic terrain consisting of two Quarry pits where groundwater recharge occurs due to rainfall.

GEOLOGY AND GROUND SURFACE ELEVATION

The watershed is in the granite and granite gneiss rock. The area is mostly covered with pediment inselberg complex (PIC 812), Pedi plain shallow (PPS 83) and Valley fill Shallow (VFS 83). On pediment inselberg complex limited recharge potential along fracture zone could be possible and occurrence of groundwater at depths > 80 m in sheet fractures may be noticed. The groundwater exploration was carried out in the adjacent area indicates fractures below

60-80 m depth (NRSC, ISRO, GWP Map). No fault/fracture zone could be seen near the Quarry pits. The topographic elevation of quarry pits are varying from 588 m(amsl) to 595 m (amsl)(Fig.1). All the streams originating in the watershed join the Ellammabanda tank in the downstream.

GROUNDWATER CONDITIONS

Groundwater monitoring was carried out on 34 selected observation bore wells during July 2013. Groundwater in the watershed occurs under water table conditions and the movement is in the weathered, semi-weathered and fractured zones. Groundwater is tapped by shallow to deep bore wells with depths ranging from 30 to 100 m below ground level (bgl)(Fig.2). The depth of the water levels ranges from 10 to 30 m bgl. The permeability in these rocks is 0.50-25 m/day, specific yield is 0.005 – 0.040 m/day and the yield prospects are 15 m³/hr. The fractures controlling the groundwater mainly trend NW-SE and North – South.

IN SITU FILTRATION TESTS

In situ infiltration measurements on the groundwater surface as well as in the quarry pit bottom were made using a double ring infiltrometer. The in situ infiltration rate

varied from 0.09 cm/hr to 15.36 cm/hr. The lowest infiltration could be found from the quarry pit bottom as 0.09 cm/hr at a depth of about 15 m from ground surface. The highest infiltrate rate was reported from ground adjacent to a stream course.

GEOPHYSICAL INVESTIGATIONS

Electrical Resistivity Topography (ERT) Imaging

Groundwater potential zones in the watershed covering the proposed granite quarry pits was assessed by Electrical Resistivity Topography imaging surveys at 22 locations using Wenner – Schlumberger Configuration with inner electrode spacing of 5 m to determine the aquifer geometry (*Fig.3*). The processing and interpretation of geo electrical data was performed using the RES2DINV algorithm, which generates a two dimensional (2D) resistivity depth model of the subsurface resistivity distribution. The 2D resistivity model is obtained by using the standard Gauss-Newton method to the measured data.

ERT profiles were laid at southern boundary of quarry pit 1 and pit 2 and at 10 m, 20 m, 30 m, 100 m, 200 m and 300 m away from both the pits. The ERT image shows a low resistivity in the weathered zone ranging from 16-95 ohm-m confining very much to a shallow depth (<3). The fracture zone represented by resistivity ranging from 100-300 ohm-m, extending up to 6m depth. The fracture zone is underlain by a high resistivity >1000 ohm-m representing hard granite basement. These geophysical investigations concluded that the quarry consist of hard granitic terrain.

GROUNDWATER FLOW AND MASS TRANSPORT MODELLING

Groundwater Flow

The groundwater flow model in the watershed covering quarry pits was conceptualized as a two layer weathered and fractured aquifer system spread over 4200 m x 4700 m (*Fig. 4*) The permeability of saturated weathered and fractured zone assumed as 1 m/day and was assigned in the model. Accordingly 0.1 m/day and 0.3 m/day were assigned to cells close to quarry pits and in the adjacent area. The permeability has been assumed to be one

tenth of the horizontal permeability in the vertical direction. The simulated vertical cross sections indicates that the weathered zones has 20 m thickness. The groundwater withdrawal from nearby villages reported poor yield.

Flow and Transport Processes

The process of groundwater flow is generally assumed to be governed by the relations expressed in Darcy's law and the conservation of mass. The purpose of Mass transport model in groundwater is to compute the concentration of a dissolved chemical species in an aquifer at any specified time and place. The changes in chemical concentration occur within a dynamic groundwater system primarily due to four distinct processes:

1. Advective transport, in which dissolved chemicals are moving with the flowing groundwater.
2. Hydrodynamic dispersion, in which molecular and ionic diffusion and small-scale variations in the flow velocity through the porous media cause the paths of dissolved molecules and ions to diverge or spread from the average direction of groundwater flow.
3. Fluid sources, where water of one composition is introduced into and mixed with water of a different composition.
4. Reactions, in which some amount of a particular dissolved chemical species may be added to or removed from the groundwater.

Governing Equations

The subsurface environment constitutes a complex, three dimensional heterogeneous hydro geologic setting. The variability strongly influences groundwater flow and transport. The mathematical equations that describe groundwater flow and transport processes may be developed from the fundamental principle of conservation of mass of solute.

A general form of the equation describing the transient flow of a compressible fluid in a non-homogeneous anisotropic aquifer may be derived by combining Darcy's law with the continuity equation. A general groundwater flow equation may be written in Cartesian tensor notation as:

$$\frac{\partial}{\partial x_i} \left(K_{ij} \frac{\partial h}{\partial x_i} \right) = S_s \frac{\partial h}{\partial t} + W^* \longrightarrow (1)$$

Where S_s is the specific storage, L^{-1} ; t is time, T ; W^* is the volumetric flux per unit volume (+ for outflow and - for inflow), T^{-1} ; K_{ij} is coefficient of permeability and x_i is Cartesian coordinate, L , h is head of water, L . Darcy's law applies and fluid properties (density and viscosity) are homogeneous and constant. Aquifer properties can vary spatially and fluid stresses (W^*) can vary in space and time.

If the aquifer is relatively thin compared to its lateral extent, it may be appropriate to assume that groundwater flow is aerially two-dimensional. This allows the three-dimensional flow equation to be reduced to the case of two dimensional aerial flows, which requires shorter computation time to achieve numerical solutions.

In an unconfined system, the saturated thickness changes as the water table elevation (head) changes. Thus, the transmissivity also can change over space and time (i.e. $T_{ij} = K_{ij} b$, where $b(x,y,t) = h - h_b$ and h_b is the elevation of the bottom of the aquifer).

The cross-product terms of the hydraulic conductivity tensor drop out when the coordinate axes are aligned with the principal axes of the tensor; i.e. $K_{ij} = 0$ when $i = j$. Therefore, the only hydraulic conductivity terms with possible nonzero values are K_{xx} and K_{yy} . The eq 1 may be modified to

$$\frac{\partial}{\partial x} \left(T_{xx} \frac{\partial h}{\partial x} \right) + \frac{\partial}{\partial y} \left(T_{yy} \frac{\partial h}{\partial y} \right) = S \frac{\partial h}{\partial t} + W \longrightarrow (2)$$

Where T_{ij} is the transmissivity, $L^2 T^{-1}$; $T_{ij} = K_{ij} b$; b is the saturated thickness of the aquifer, L ; S is the storage coefficient (dimensionless) and $W = W^* b$ is the volume flux per unit area LT^{-1} .

In some filed problems, fluid properties such as density and viscosity may vary significantly. When the fluid properties are heterogeneous and transient, the relations among water levels, hydraulic heads, fluid pressures, and flow velocities are neither

simple nor straightforward. In this situation, the flow equation is written and solved in terms of fluid pressures, fluid densities, and the intrinsic permeability of the porous media.

Groundwater Velocity

The migration and mixing of chemicals dissolved in groundwater will obviously be affected by the velocity of the flowing groundwater. The actual seepage velocity of groundwater is computed as

$$V_i = \frac{q_i}{\varepsilon} = - \frac{K_{ij}}{\varepsilon} \frac{\partial h}{\partial x_j} \longrightarrow (3)$$

Where V_i is the seepage velocity q is discharge per unit time, K_{ij} is coefficient of permeability and ε is the effective porosity of the porous medium.

Mass Transport Equation

An equation describing the transport and dispersion of a dissolved chemical in flowing groundwater may be derived from the principle of conservation of mass by considering all fluxes into and out of a representative elementary volume (REV).

A generalized form of the solute transport equation, in which terms are incorporated to represent chemical reactions and solute concentration both in the pore fluid and on the solid surface, as:

$$\frac{\partial(\varepsilon C)}{\partial t} = \frac{\partial}{\partial x_i} \left(\varepsilon D_{ij} \frac{\partial C}{\partial x_j} \right) - \frac{\partial}{\partial x_i} (\varepsilon C V_i) - C' W^* + CHM \longrightarrow (4)$$

Where CHM equals one or more of the following:

$-\rho_b \frac{\partial \bar{C}}{\partial t}$ for linear equilibrium controlled sorption or ion-exchange reactions

$\sum_{k=1}^s R_k$ for s chemical rate-controlled reactions, and (or)

$-\lambda \left(\varepsilon C + \rho_b \bar{C} \right)$ for decay

and where D_{ij} is coefficient of hydrodynamic dispersion (a second order tensor) which is sum of mechanical dispersion and molecular diffusion, $L^2 T^{-1}$, C' is the concentration of the solute in the source or sink fluid, C is the concentration of the species adsorbed on

the solid (mass of solute/mass of solid), ρ_b is the bulk density of the sediment ML^{-3} , R_k is the rate of production of the solute in reaction k , $ML^{-3}T^{-1}$, and λ is the decay constant T^{-1} . The first term on the right hand side of equation (4) represents the change in concentration due to hydrodynamic dispersion.

GROUNDWATER FLOW MODEL

The mathematical solute-transport model requires at least two partial differential equations. One is the equation of flow, from which groundwater flow velocities are obtained, and the second is the solute transport equation, whose solution gives chemical concentration in groundwater. If the properties of water are affected significantly by changes in solute concentration, as in a sea water intrusion problem, then the flow and transport equations should be solved simultaneously otherwise it can be solved sequentially. The numerical approaches for solving mass transport equations are based on computer-based particle tracking methods. They are approximate forms of the advection-dispersion equation (2) as a system of algebraic equations. Second step is to provide boundary condition at a large number of node points and assign values of concentration or loading rates defining various boundary conditions for all nodes located along boundary of the domain. Continuity consideration of numerical solutions of solute transport requires a smooth and accurate representation of velocity field, which was obtained by simulation of groundwater flow model. Velocity values are computed from calculated hydraulic heads and porosity values by applying Darcy's equation. The transport model was coupled to the flow model by velocity terms. The water level configuration of particular time period will be considered for solving groundwater flow equation under steady state and thereby a single velocity field determined for the mass transport simulation for all times. The mean concentration for each grid block was calculated as the sum of the mass carried by all the particles located in a given block divided by the total volume of water in the block. The head solution is obtained using visual MODFLOW.

The computed groundwater level contours in the groundwater flow model has been showing groundwater flow direction towards the stream joining the Ellammabanda lake and following closely the observed water level contours (Fig. 5). The groundwater velocity field has been computed from the flow model using the hydraulic gradient and by assuming an effective porosity of 0.1. The computed groundwater velocity field represents maximum groundwater velocity < 20 m/year.

MASS TRANSPORT MODEL

Using the computed velocity field from the groundwater flow model, the mass transport model simulation was carried out using the MT3D software. The source concentration was assigned an assumed TDS concentration of 1500 mg/l to the granite quarry pits (Fig 6). The initial concentration of groundwater was assumed as 600 mg/l. The vertical migration of TDS concentration from two Quarry pits along Rows 19 and column 17 for 10, 20 and 50 years indicates that predicted TDS plume will be confined within the weathered Zone adjacent to the Quarry pits only during next 50 years and limited to maximum distance of about 200 m from the Quarry pits.

CONCLUSIONS AND RECOMMENDATIONS

Groundwater level monitoring carried out in 34 observation wells in the watershed covering granite quarry pits indicated that there exists a steep hydraulic gradient with regard to the groundwater movement around the quarry pits which indicate poor groundwater potential in the wells located in the immediate vicinity of the quarry pits and there is very little possibility of groundwater entering from upstream area into the quarry pits. The Geophysical Resistivity Imaging survey results inside the Quarry pits as well as in the surrounding areas projected extension of high resistivity granite rocks from quarry pits. Further, the groundwater flow and mass transport modeling study has quantified the likely TDS plume migration confining to maximum of 200 m only from the Quarry pit boundary in the downstream towards south and southeast during next 50 years.

Based on the resistivity inferred from Electrical Resistivity tomography imaging, hydro geological investigations, in situ infiltration measurements and mass transport modeling study for likely contaminant migration from the Quarry pits study, it is recommended that the proposed granite Quarry Pit 1 & Pit 2 are ideal sites for disposal of non-hazardous sediments dredged from Hussainsagar Lake. Little engineering on side walls of the Pits have to be undertaken to close the open joints occurred during quarrying of granite material for arresting lateral migration of leachate through them. Drilling of 5 observation wells up to 50 m depth at <10 m from the Quarry pits in the South and South Eastern part is suggested. Periodical monitoring of groundwater quality in the suggested monitoring wells adjacent to Quarry pits is required for ascertaining and assessing functioning of the land fill.

REFERENCES

- BIS (1991). Indian Standard for Drinking water specifications. Bureau of Indian Standards IS10500, Indian Standard Institute, India.
- Jupp D.L.B. and Vozoff K. 1975. Stable iterative methods of inversion of geophysical data. Geophy.J.RAS, 4, (Implemented by T. Harinarayana on VAX 11/750 at NGRI)
- WHO (1984). Guidelines for drinking water quality in Health Criteria and other supporting information. Vol. 2, 336 p.
- Orellana E. and Mooney H.M. 1966. Master tables and curves for vertical electrical sounding over layered structures. Interciencia, Madrid, Spain, p.150 (66 tables).
- Harbaugh, AW, ER Banta, MC Hill and MG McDonald, 2000. MODFLOW -2000. the US Geological Survey modular groundwater model: User Guide to modularization concepts and the groundwater flow process. USGS Open File Report 00-92. USGS.
- Langevin, CD and Weixing Guo, 2006. MODFLOW/MT3DMS-Based simulation of variable
- Guo. W and C.D.Langevin, 2002. User's guide to SEAWAT: A computer program for simulation of three dimensional variable density groundwater flow.US

Geological Survey TWRI Book 6, Chapter 7, 79p.

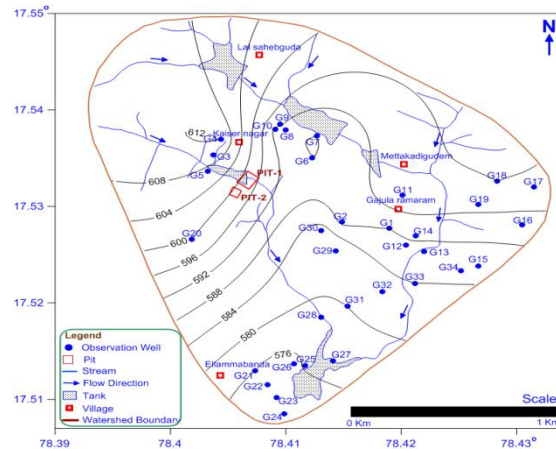


Fig.1: Topography Elevation Contours in m (amsl) in the watershed area, Hyderabad (source - NGRI)

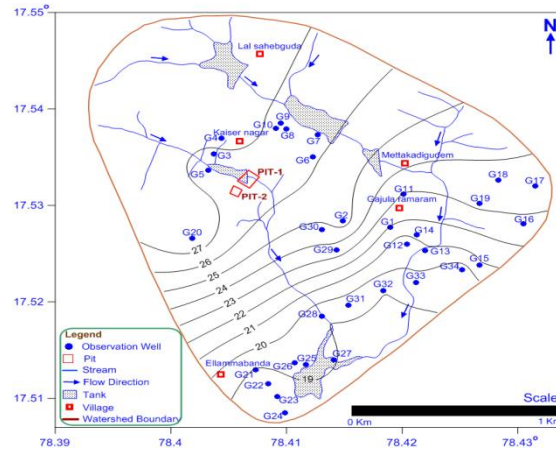
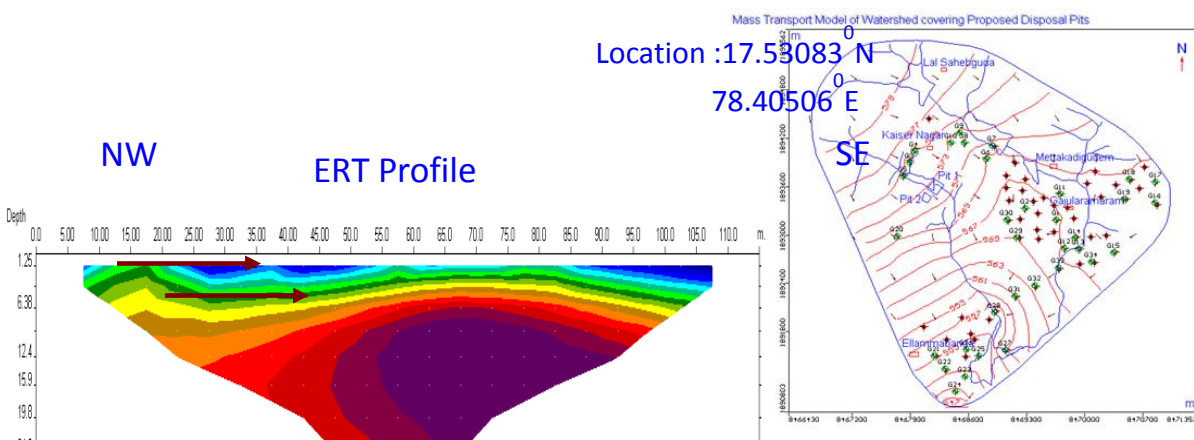


Fig.2: Depth to Groundwater Level Contours in m (bgl) in watershed covering granite quarry , Hyderabad (source - NGRI)



Inverse Model Resistivity Section

Resistivity in ohm.m

16.4 39.4 94.9 208 550 1323 3185 7666

Fig.3: Electrical Resistivity Tomography Image along ERT Profile in side proposed granite Quarry Pit 1 (North East), Hyderabad (source - NGRI)

Groundwater Flow & Mass Transport Model of watershed covering Granite Quarry near Hyderabad

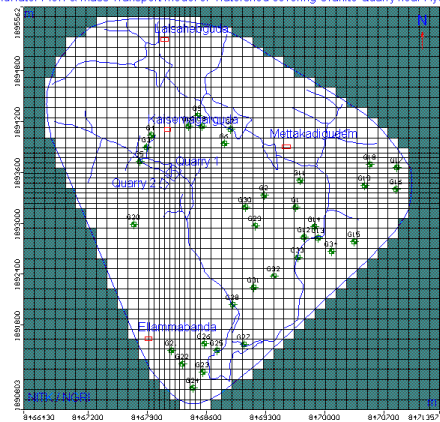


Fig.4: Groundwater Flow Model Domain in the watershed covering proposed Granite Quarry pits, Hyderabad

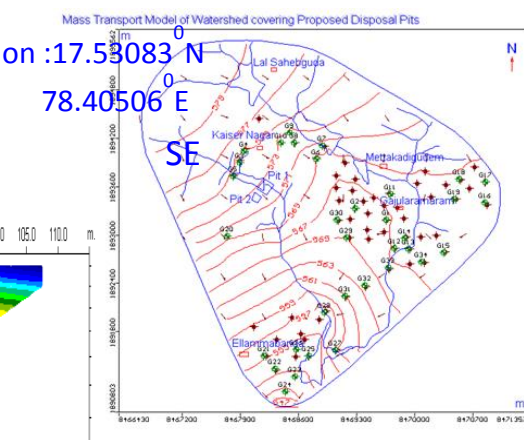


Fig.5: Computed Groundwater contours m(amsl) in Groundwater Flow Model in the watershed covering proposed Disposal pits, Hyderabad

↓ Groundwater Flow & Mass Transport Model of watershed covering Granite Quarry near Hyderabad

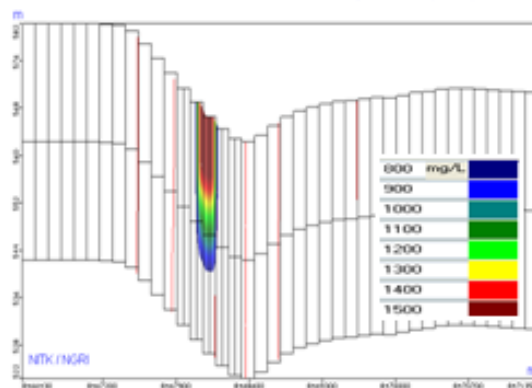


Fig.6: TDS Plume concentration from Mass Transport Model in the watershed covering proposed Disposal pits, Hyderabad – After 50 Years (Row 19)

Prediction of air temperature by conjunctive method (Wavelet-ANFIS) using subseries of wavelet decomposed data

Karthika B S and Paresh Chandra Deka

Department of Applied Mechanics & Hydraulics
National Institute of Technology Karnataka, Surathkal, Karnataka, India.
E-mail: bskarthikgowda@gmail.com

Abstract :- Prediction of reliable air temperature is a key element towards taking decision regarding climate monitoring, drought detection and environmental issues. In this study a new conjunctive method (wavelet-ANFIS) for prediction of air temperature is proposed. Observed meteorological data with air pollution data (PM_{10}) of the Bhadra station of Karnataka, located in India is used for the study. Data is decomposed into subseries using wavelet and from that subseries approximated data are used as input for Adaptive Neuro Fuzzy Inference system (ANFIS). An attempt is made to compare the output results of the conjunctive method with Gbell membership and Gauss membership function and ANFIS model. The benchmark results showed that the conjunctive model with Gbell membership function shows better results when compared to the other conjunctive model with Gauss membership and single ANFIS model only.

Key words: ANFIS, Wavelet, Air temperature, Conjunctive method, PM_{10} .

1. Introduction

Fluctuation of air temperature has attracted the researcher attention in recent years. Prediction of air temperature is an important meteorological parameter. Many applications like agriculture (Abdel-Aal., 2004), vector borne diseases (Thomson et al., 1996; Goetz et al., 2000), epidemic forecasting (Bian et al., 2006), weather forecasting, climate change(Bocchiola et al., 2010; Kittel et al., 2011) depends on air temperature.

In the last few decades, many soft computing models are being applied for temperature prediction problems. Neural computing techniques are majorly used for fast and accurate results. Adaptive Neuro-Fuzzy Inference System (ANFIS) is a better approach in improving of Neuro-fuzzy in case of modeling nonlinear functions. The ANFIS learns the features by example data set and adjusts the system parameters according to a given error criterion (Jang J-SR., 1992., and Jang J-SR., 1993). Wavelet decomposition

decomposes time series data into a different time and scale of wavelet transformation. But in recent times, many hybrid models are performing better and faster compared to single model approach (Moosavi et al., 2013).

In this study, it is intended to check the conjunctive models for the prediction of air temperature for the Bhadra station of Karnataka located in India.

2. Methodology

2.1 Wavelet Analysis

The Wavelet Series are just like Continuous Wavelet Transform (CWT) and it requires a significant amount of time and resources, depending on the results required. $\psi(t)$ is the mother wavelet or the basis function (Eq. 1). The CWT is provided by Eq. (2), where $f(t)$ is the signal to be analyzed. The transformation used in the wavelet functions are derived from the mother wavelet through translation

(shifting) and scaling (dilation or compression) (Yarar., 2014).

$$\psi_{a,b}(t) = \frac{1}{\sqrt{|a|}} \psi \left(\frac{t-b}{a} \right) \quad (1)$$

$$X_{WT}(a,b) = \frac{1}{\sqrt{|a|}} \int f(t) \psi^* \left(\frac{t-b}{a} \right) dt \quad (2)$$

Where $\psi_{a,b}(t)$ is the successive wavelet, a is the frequency factor, b is the time factor and ψ^* is the complex conjugate functions of $\psi(t)$.

The Discrete Wavelet Transform (DWT), which is based on sub-band coding, is found to be best for computation of Wavelet Transform. Implementation of this method is easy and works better in terms of computation time and resources required. Discrete wavelet transform of $f(t)$ can be written as (Eq. 3);

$$X_{WT}(j,k) = \frac{1}{\sqrt{1/a_1}} \int f(t) \psi^* \left(\frac{t-a_0^{-j}-kb_0}{a_0^{-j}} \right) dt \quad (3)$$

The most frequent choice of the parameters a_0 and b_0 is 2 and 1 time steps, respectively (wei., 2012). This power of two logarithmic scaling of the time and scale is known as a dyadic grid arrangement and is the simplest and the most efficient case for practical purposes (Mallat S., 1998).

DWT operates on two sets of function like high-pass and low-pass filters. The original time series is passed through high-pass and low-pass filters and separated at different scales. The time series is decomposed into one comprising its trend (the approximation) and one comprising the high frequencies and the fast events (the detail) (Figure. 1).

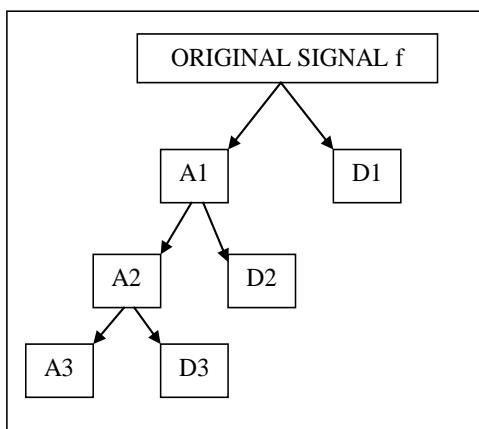


Figure 1 Architecture of wavelet transforms

2.2 The Adaptive Neuro-Fuzzy Inference Systems (ANFIS) models

ANFIS incorporates the self-learning ability of NN with the linguistic expression function of fuzzy inference. It combines least-squares and backpropagation gradient descent methods train. Takagi-Sugeno type fuzzy inference system leads to search for the optimal parameters. The ANFIS architecture is shown in Figure. 2. The ANFIS network contains five layers. Each layer contains several nodes described by the node function.

In layer one; every node is an adaptive node with a node function such as a generalized bell membership function or a Gaussian membership function. In layer two, each node multiplies incoming signals and the output is the product of all the incoming signals. Each node output represents the firing strength of a rule. In layer three, each node calculates the ratio of the i^{th} rules firing strength to the sum of all rule's firing strengths. The normalized firing strengths are the output from this layer. In layer four, each node calculates the contribution of the i^{th} rule to the overall output. In layer five, the single node calculates the final output as the summation of all input signals. (Jang and Sun., 1995)

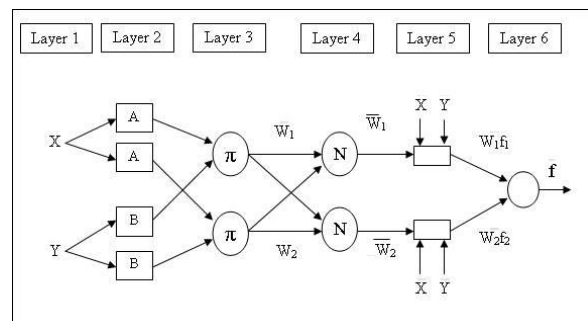


Figure 2 Architecture of ANFIS model

3. Study area

The meteorological data and air pollution data (PM_{10}) were collected from the station located in B. R. Project (Bhadra station) of Karnataka (between $13^{\circ}42'0''$ North latitude and $75^{\circ}38'24''$ East longitude) of India (Figure 3). The area receives an average annual rainfall of 2320 mm with rainfall occurring during monsoon period (June to November). The rainfall is experienced both during the Southwest Monsoon and North East monsoon.

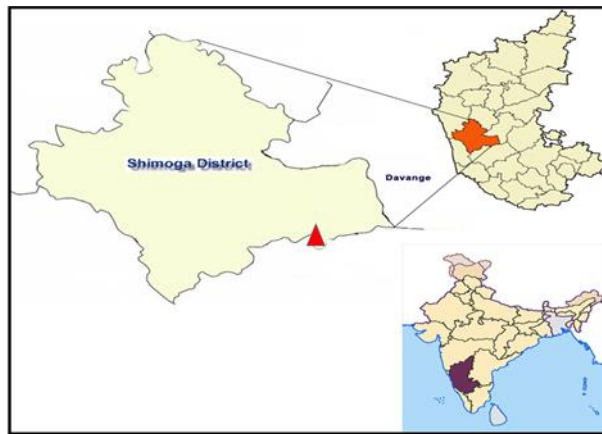


Figure 3 Bhadra location of the gauge stations

4. Input Data

Basic input monthly averaged data like rainfall, wind speed, humidity, sunshine hour, PM_{10} were used for the present study collected from January 2009 to July 2012.

5. Results and Discussion

To study the effectiveness of the approach, The Correlation Coefficients (CCs) between desired output and network predicted outputs were calculated by using Eq. (5). The Root Mean Square Error (RMSE) and Scatter Index (SI) between target output and network predicted output is calculated by using Eqs. (4) and (6).

Root mean square error

$$RMSE = \sqrt{\frac{1}{n} \sum_{i=1}^n \left(\frac{o_i - p_i}{p_i} \right)^2} * 100\% \quad (4)$$

Correlation coefficient

$$CC = \frac{\sum_{i=1}^n p_i o_i}{\sqrt{\sum_{i=1}^n p_i^2 \sum_{i=1}^n o_i^2}} \quad (5)$$

Scatter index

$$SI = \frac{\sqrt{\frac{1}{n} \sum_{i=1}^n ((p_i - \bar{p}) - (o_i - \bar{o}))^2}}{\bar{o}} \quad (6)$$

Where, O and P are observed and predicted damage level respectively, n is the number of data set used and \bar{P} & \bar{O} are average predicted and observed damage level respectively.

5.1 ANFIS model:-

As mentioned earlier, ANFIS model was tested for six different parameters (rainfall, wind speed, humidity, sunshine hour, PM_{10}) with 2 Membership Functions and 50 iterations. Monthly averaged air temperature was output and monthly averaged above mentioned six parameters as input data for ANFIS model. Within Gauss and Gbell membership function the Gauss membership works better when compared to Gbell membership function. For Gauss and Gbell membership functions an R^2 of 0.38, 0.33, RMSE of 2.76, 2.88 and SI of 0.11, 0.11 respectively was observed (Table 1).

4th International Engineering Symposium - IES 2015

March 4-6, 2015, Kumamoto University, Japan

Table 1 Results of ANFIS model

PM ₁₀	ANFIS model	
	Gbell	Gauss
R ²	0.33	0.38
RMSE	2.88	2.76
SI	0.11	0.11

5.2 Wavelet- ANFIS model:-

In this part the wavelet - ANFIS model was tested in the same area. The data were decomposed to 1, 2, 3, 4 and 5

levels for all Db1, Db2, Db3, Db4, and Db5. For Badra area conjunctive Wavelet-ANFIS model worked better when compared to ANFIS model alone. Results show that Db5 with level4 (2MF) with Gbell membership function works better compared to other combination as mentioned in the Table 2. The combination of artificial neural network, fuzzy logic and wavelet transformation work better to get the best output.

Figure 4 shows the time series and a scatter plot of observed and predicted average temperature for the Wavelet-ANFIS model of the Bhadra station. Db5 with level4 (2MF) with Gbell membership function R²=0.95; RMSE= 0.66; SI=0.03) works better.

Table 2 Results of conjunctive model (Wavelet-ANFIS)

	Wavelet-ANFIS model														
	Db1			Db2			Db3			Db4			Db5		
	R ²	RMSE	SI	R ²	RMSE	SI	R ²	RMSE	SI	R ²	RMSE	SI	R ²	RMSE	SI
	Gbell			Gbell			Gbell			Gbell			Gbell		
Level 1	0.72	1.84	0.08	0.28	4.67	0.19	0.69	3.99	0.16	0.17	3.23	0.13	0.15	2.75	0.11
Level 2	0.16	3.28	0.14	0.68	1.54	0.06	0.30	3.75	0.15	0.80	1.27	0.05	0.74	1.38	0.06
Level 3	0.03	2.86	0.12	0.75	1.54	0.06	0.76	1.53	0.06	0.93	0.79	0.03	0.57	1.83	0.08
Level 4	0.11	2.91	0.12	0.70	1.50	0.06	0.86	1.27	0.05	0.10	4.00	0.16	0.95	0.66	0.03
Level 5	0.03	2.84	0.12	0.88	1.01	0.04	0.84	1.29	0.05	0.88	1.18	0.05	0.91	0.94	0.04
	Gauss			Gauss			Gauss			Gauss			Gauss		
Level 1	0.72	1.84	0.08	0.12	6.80	0.28	0.71	2.78	0.11	0.51	2.05	0.08	0.65	1.58	0.07
Level 2	0.16	3.28	0.14	0.87	1.28	0.05	0.14	5.50	0.23	0.75	1.35	0.06	0.72	1.54	0.06
Level 3	0.03	2.86	0.12	0.84	1.36	0.06	0.45	2.45	0.10	0.85	1.16	0.05	0.73	1.50	0.06
Level 4	0.11	2.91	0.12	0.79	1.51	0.06	0.86	1.13	0.05	0.28	2.53	0.10	0.93	0.74	0.03
Level 5	0.03	2.84	0.12	0.46	2.32	0.10	0.76	1.65	0.07	0.81	1.24	0.05	0.69	1.50	0.06

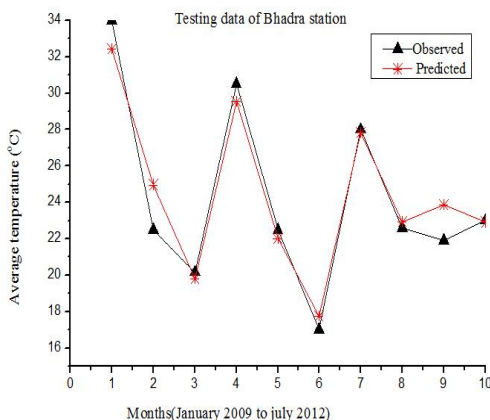


Figure 4 Time Series and scatter plot of observed and predicted average temperature of Bhadra station (Db5-level 4, Gbell membership)

6. Conclusion

The ability of conjunctive Wavelet-ANFIS model was compared with ANFIS model for prediction of temperature. Results showed that data pre-processed by Wavelet and used as input for ANFIS model works better compared to ANFIS model alone. By referring to the work, it is concluded that conjunctive Wavelet-ANFIS model have the best capability to predict air temperature than ANFIS model alone.

7. Acknowledgements:

The authors are grateful for the assistance provided by the Department of Applied Mechanics and Hydraulics, National Institute of Technology Karnataka, India. We would also like to thank all the Government Departments and Organizations for providing required data.

8. References:

- [1] Abdel-Aal, R. E., (2004). "Hourly temperature forecasting using abductive networks." *Engineering Applications of Artificial Intelligence* 17.5 543-556.
- [2] Bocchiola, D., & Diolaiuti, G., (2010). Evidence of climate change within the Adamello Glacier of Italy. *Theoretical and applied climatology*, 100(3-4), 351-369
- [3] Bian, L., Li, L., & Yan, G., (2006). Combining global and local estimates for spatial distribution of mosquito larval habitats. *GIScience & Remote Sensing*, 43(2), 128-141.
- [4] Goetz, S. J., S. D. Prince, and J. Small.,(2000) "Advances in satellite remote sensing of environmental variables for epidemiological applications." *Advances in Parasitology* 47 : 289-307.
- [5] Immerzeel, W. W.,(2008). and Droogers, P., "Calibration of a distributed hydrological model based on satellite evapotranspiration," *Journal of Hydrology*, vol. 349, pp. 411-424.
- [6] Jang J-SR., (1992). Self-learning fuzzy controllers based on temporal backpropagation. *IEEE Trans Neural Netw* .3(5):714–23.
- [7] Jang J-SR., (1993). ANFIS: Adaptive-network-based fuzzy inference system. *IEEE Trans Syst Man Cybern* .23(3):665–85.
- [8] Jang, J. S., & Sun, C. T. (1995). Neuro-fuzzy modeling and control. *Proceedings of the IEEE*, 83(3), 378-406
- [9] Kittel, T. G., Baker, B. B., Higgins, J. V., & Haney, J. C., (2011). Climate vulnerability of ecosystems and landscapes on Alaska's North

4th International Engineering Symposium - IES 2015

March 4-6, 2015, Kumamoto University, Japan

Slope. *Regional Environmental Change*, 11(1), 249-264.

- [10] Paniagua-Tineo, A., Salcedo-Sanz, S., Casanova-Mateo, C., Ortiz-García, E. G., Cony, M. A., & Hernández-Martín, E., (2011). Prediction of daily maximum temperature using a support vector regression algorithm. *Renewable Energy*, 36(11), 3054-3060.
- [11] Mallat S., (1998). A theory for multiresolution signal decomposition—The wavelet representation. *IEEE Trans. Pattern Anal. Mach. Intell.*, vol.11, no. 7, pp. 674–693.
- [12] Moosavi, V., Vafakhah, M., Shirmohammadi, B., & Behnia, N., (2013). A wavelet-ANFIS hybrid model for groundwater level forecasting for different prediction periods. *Water resources management*, 27(5), 1301-1321.
- [13] Thomson, M. C., Connor, S. J., Milligan, P. J., & Flasse, S. P., (1996). The ecology of malaria--as seen from Earth-observation satellites. *Annals of tropical medicine and parasitology*, 90(3), 243-264.
- [14] Wei S, Song and J., Khan NI .,(2012). Simulating and predicting river discharge time series using a wavelet-neural network hybrid modelling approach. *Hydrol Process* 26:281–296.
- [15] Yarar, A. (2014). A Hybrid Wavelet and Neuro-Fuzzy Model for Forecasting the Monthly Streamflow Data. *Water Resources Management*, 28(2), 553-565.

Analysis of spatial and temporal trend in rainfall of Mangalore region using Mann-Kendall Test

Aparna P and B M Dodamani

*Department of Applied Mechanics & Hydraulics
NITK Surathkal, India
Email: 13wr03f.aparna@nitk.edu.in*

Trend Analysis is the practice of collecting information and attempting to spot a pattern and is often used to predict future events. The study is mainly concerned with trend analysis of rainfall in Mangalore Karnataka India. 20 years data from 1990 to 2010 has been processed to find out the monthly variability of rainfall for which Mann-Kendall Test has been used to identify significant positive and negative trends together with the Sen's Slope Estimator for determination of trend and slope magnitude. Monthly precipitation trend has been identified and there are rising rates of precipitation in some months and decreasing trend in other months. From the monthly precipitation variables, June, July and especially August were determined to have strong increasing trends, as opposed to other months which affected the results of annual series. Overall trend analysis reveals stations in the north shows an increasing trend and rest shows a decreasing trend.

The Influence of Policy Decisions on the Wetlands of Bangalore

Fathima Samana. S¹ and K. S. Anantha Krishna³

1 Acharya's N R V School of Architecture, Bangalore 560090, India.

e-mail:samanafathima@gmail.com

2 R V College of Architecture, Bangalore 560062, India. Email: ka12rvsa@gmail.com

ABSTRACT: Bangalore's urbanization process has impacted its natural wetlands, reducing number drastically. The conservation efforts started with the 1965-Master Plan, aiming to preserve certain lakes, developing them as parks and recreational spaces, where lake-restoration measures treated water-bodies as isolated elements and not as a part of the larger system. The government's policy decisions over the past, has led to the displacement of lakes for different infrastructural facilities like bus-terminals, golf-courses, stadiums, hospitals, parks and residential developments. Due to this indifferent attitude of the government, even the public movements to safeguard the lakes have failed. Hence, there is a need for sustainable policies to conserve the water-network as a continuous system and not just preserve it.

Keywords: urbanisation, Bangalore, fabric, lakes, sustainable

INTRODUCTION

Bangalore is a city, with no natural perennial source of surface water. The topography of the city is characterized by hills, plains, valleys & undulating terrain. It is located in the Deccan Plateau. The city has taken advantage of the natural features – topography and climatic conditions of the area and evolved a system of tanks or lakes, considering the watersheds and catchments; earning itself an identity as a "City of lakes". The city depended on a system of tanks that were constructed identifying the natural ridges and valleys, considering its topography. The construction of tank system was based on the principle of cascading.

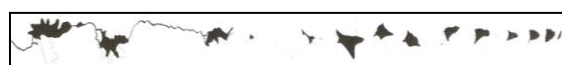


Fig.1 Cascading System of tanks

WATER AND ITS RELATION TO SETTLEMENTS

These tanks were initially the life-line of the city. They were constructed to cater to the agricultural and domestic needs of the settlements. The city is an agglomeration many small settlements. Each settlement happens at the ridge, while the lake occupies the valley zone. Both the settlement and the lake share a common name or identity. For example: Mathikere settlement and Mathikere (kere means lake), Bellandur village and Bellandur lake, Madiwala lake and Madiwala area, Hebbal

4th International Engineering Symposium - IES 2015

March 4-6, 2015, Kumamoto University, Japan

lake and Hebbala Village, etc. The tanks are connected to other tanks at higher and lower elevations, through connectors or nalas. In Bangalore, there existed a system of water tanks, constructed identifying the natural valley systems in the region. These tanks were fed by the valleys (nalas), which carried surface run-off during rains. The tanks stored the run-off water during monsoons, to be used during lean period. The tank system worked on the principle of cascading. The tanks formed chains, situated in the same catchment area, which depended on surplus water from the tanks at higher elevation and the run-off from their catchment. Most of these – the tanks and their nalas, had institutional land uses abutting them. But in the present times, the demand for land has engulfed tank beds and the unplanned developments have converted nalas into sewage corridors. The tank system, which was a man-made feature, has acquired diverse roles in the urban landscape, and is an integral part of the cityscape since four centuries.

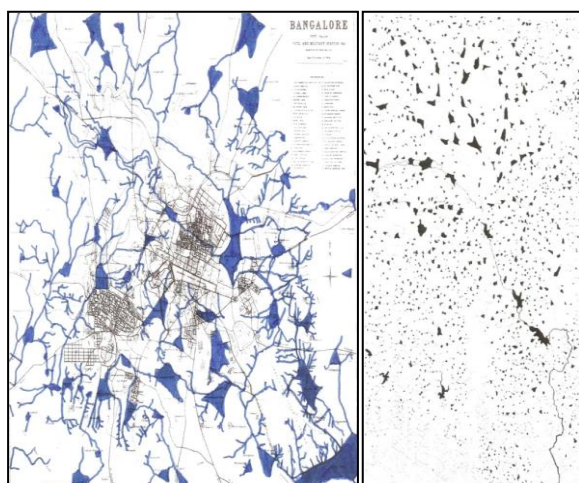


Fig.2 Cascading System of tanks

THE CITY OF BANGALORE

The region of Bangalore has Nandi Hills at the apex of the ridge, from where water flows in different directions [1]. Within the city of Bangalore, the main ridge-line runs North-west and South-east direction dividing the city into two river basins – Arkavathi river basin and Pinakini river basin. Arkavathi river basin is to the west with steep slope and undulating terrain.

But the Pinakini river basin is to the east with gentle slopes and valleys.

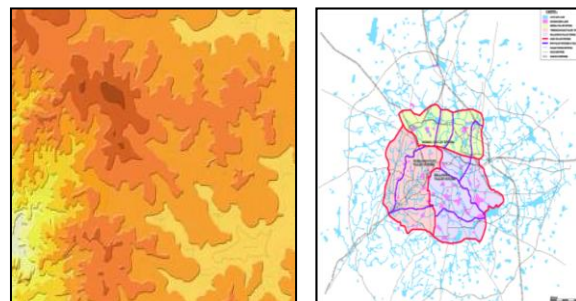


Fig.3 Contour map and Valley Systems of Bangalore

The contour map of the city shows a radial pattern, from the High-Grounds at the apex, occupying the highest position [2]. The water is drained off into the low-lying plains or the valley zones – Vrishabhavathi (south-west), Hebbal (north east) and Bellandur (south-east).

THE PHASED GROWTH OF THE CITY

Chronologically, the evolution of the city of Bangalore can be classified as:

The Pre-colonial phase

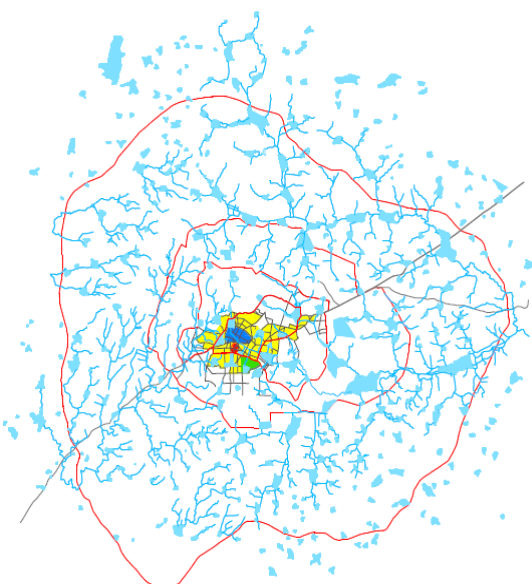


Fig.4 Growth of the city – phase I

After 1537, the tanks were constructed for agricultural and domestic needs of the settlements. Kempambudhi tank in Basavanagudi area, Dharmambudhi tank in Majestic area, Ulsoor tank in Shivajinagar area, Sampangi tank in Corporation area and Siddikatte tank near

City Market area, built by Kempegowda-I and Kempegowda-II.

In 1759, Haider Ali and Tipu Sultan created Lal-Bagh, which comprised of a garden and a lake.

During this period, the settlements happened along the ridges and the series of tanks were built in accordance with the natural valley systems [3].

The Colonial Phase

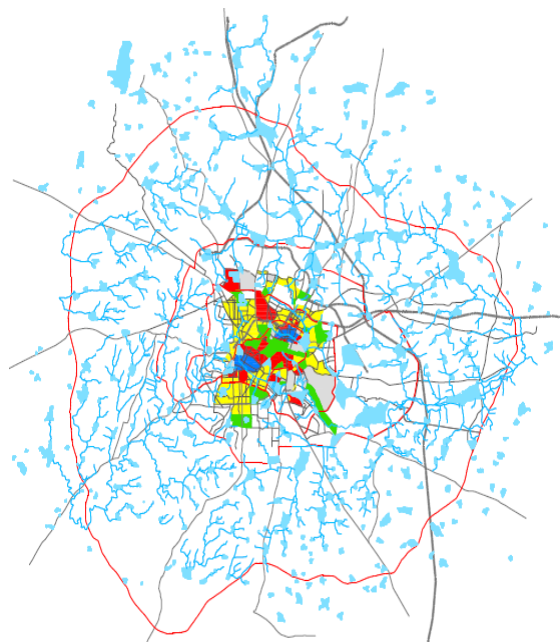


Fig.5 Growth of the city – phase II

In 1809, the Ulsoor lake and its precinct was developed for the cantonment settlement. In 1831, the British shifted from Mysore to Bangalore, promoting the image of Bangalore as a "Garden City". The establishment of the cantonment, its residential quarters and a commercial center, triggered the city's growth eastward in the Pinakini river basin, strengthening its connections with the British base at Madras.

A large area was made a buffer zone between the cantonment and the old city. Cubbon Park, Golf Course and Race Course were built in the high grounds region, which was the apex of the ridge, in the city.

By 1873, a string of three tanks known as 'The Millers Tanks' were erected in a huge area, as the primary source of piped water to the Cantonment area, along with the Ulsoor tank. The influx of people from

various regions accelerated the ever-increasing demand for water and the authorities had to look for new source of water supply. Sankey Tank was constructed at Sadashivanagar in 1882, by Col. Richard Sankey, to supply water to the Civil and Military Station in Bangalore. This was connected with Millers Tank and onwards to Dharmambuddhi Tank through contour channels. When Sankey Tank overflowed, water would flow into Millers Tank and then to Dharmambuddhi. In 1896, Hesaraghatta reservoir was constructed across Arkavathi River, 20kms to the north-west of Bangalore, to supply piped water through meters. The transportation network, with roads along lakes, isolated the tanks as traffic islands. The supply of piped water from reservoir led to the neglect of water bodies, in the city. The sewer lines and storm water drains ran along the natural valleys, which resulted in mixing of the two. Thereby, turning the seasonal storm water drains into perennial sewage channels, with sewers directly opening into them.

The Pre-independence Phase

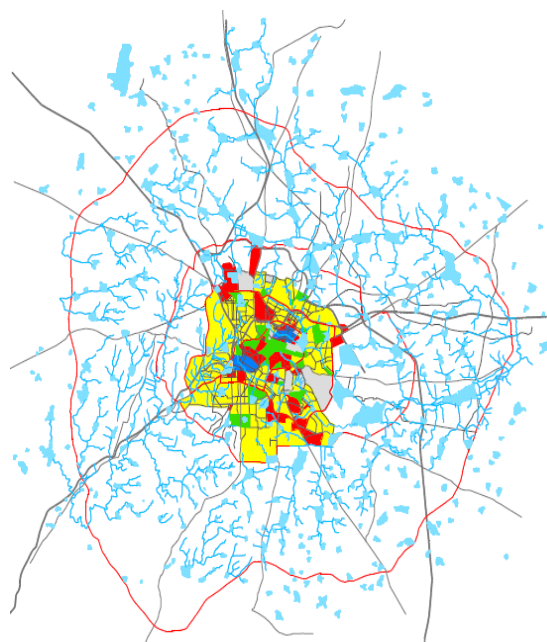


Fig.6 Growth of the city – phase III

In 1925, Hesaraghatta reservoir dried up completely. Efforts were made to restore water supply to the city from Yelemallappa Chetty Tank, Byatha and Kakol tanks.

Hence, Tippegondanahalli dam was constructed across the Arkavathi River in 1933, to bring treated water into the city. To cater to the growing city and its increasing density, recreational spaces were laid on dry tank-beds - a part of Ulsoor and Domlur tanks, Dharmambuddi, Shule & Sampangi tanks. These were the initial governmental decisions taken to encroach upon the existing lakes. Recreational spaces were planned over the tank beds, which remained empty, during the dry season. Koramangala tank was breached to be used as a vegetable garden.

The Post-independence phase

In 1950s, five satellite towns were established as industrial townships - H. A. L., H. M. T., I. T. I., Banaswadi and north of Tannery Road. With industrialization, there was migration and a sudden influx of people from different parts of the country, leading to water-scarcity again. Hence, Bangalore Water Supply Sewerage Board (BWSSB) was set up in 1974. The BWSSB depended on Cauvery River, as the main source, to tap water for the city.

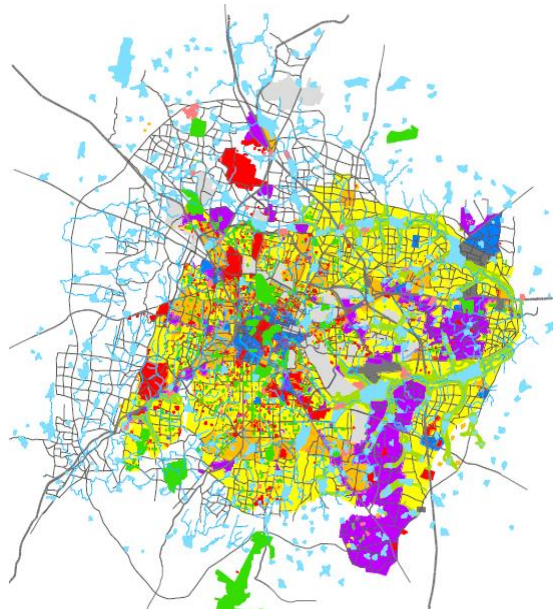


Fig.7 Growth of the city – phase IV

The Master Plan of 1965 initiated strategies to conserve the existing lakes in Bangalore. It proposed to conserve Sankey tank, Hebbal tank, Nagawara tank, Challaghatta tank, Bellandur tank,

Madiwala tank, Sarakki tank and Kempambuddhi tank. Industrialization led to alternate employments, reducing the dependency on tanks. It also encouraged migration of people into the city. This directly increased the population and the demand for land. This led to the further negligence tanks and encroachment of the seasonally dry tanks-beds.

The Current phase

The land uses along valleys and ridges, initially sought to protect the watershed zones. The ridges and valleys abutted institutions, parks, gardens etc along their edges. But later, with the ever-increasing demand for land, the tank beds were encroached upon to house major infrastructure facilities for the city, like transportation terminals, residential layouts, educational institutes, sports stadiums and complexes, hospitals, public offices, industries, community halls, markets, regional parks, textile mills, slum rehabilitation, exhibition and demonstration grounds etc.

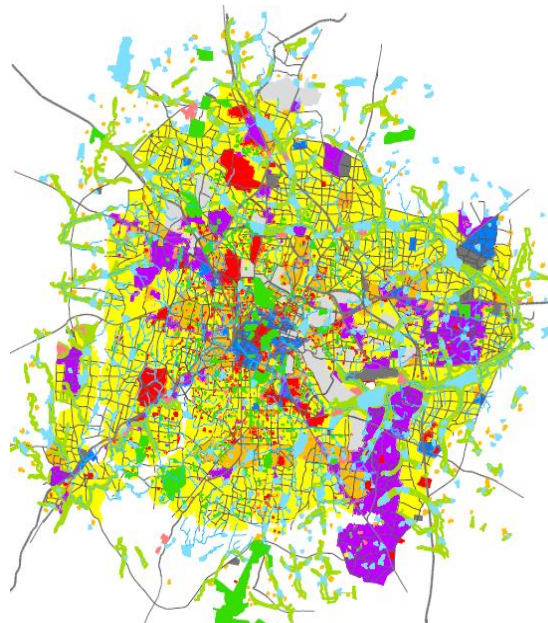


Fig.8 Growth of the city – phase V

The table below gives examples of a few tank-beds encroached upon to facilitate urban growth and development. These encroachments by certain governmental policy decisions to provide infra-structure facilities to the people.

4th International Engineering Symposium - IES 2015

March 4-6, Kumamoto University, Japan

Table 1 Encroachment of Lakes

Encroachment of Lakes			
Sl. No	Lake Name	Location	Present Land-Use
1	Dharmambuddhi Tank	Gandhi nagar	Kempegowda Bus Terminal
2	Karanji Tank	Chamaraj pet, Gandhi Bazaar, Basavanagudi	National High School, Residential Layouts
3	Sampangi Tank	Corporation	Kanteerava Stadium, parks & institutions
4	Siddikatte Tank	Kalasi palyam	Krishna Rajendra Market
5	Miller's Tank	Vasant nagar, Shivaji nagar	Ambedkar Bhavan, IT & office Buildings, Jain Hospital, Marriage Halls, Other Public Organisation
6	Mathikere Tank	Yeshwantpur	Regional Park (J. P. Park)
7	Challaghatta Tank	Kora-mangala	K. G. A. Golf Course
8	Kora-mangala Tank	Kora-mangala	N. D. R. I., Sports Complex
9	Shule Tank	Ashoknagar	Commercial Establishment, Football & Hockey Stadium
10	Tumkur Tank	Yeshwantpur	Mysore Lamps Factory
11	Ganga shetty Tank	Minerva	Minerva Mills, Open Ground
12	Sunkal Tank	Shanti nagar	Shantinagar Bus Stand, Slums, K. S. R. T. C. Regional Workshop

But now, there have been measures taken by the governing authorities to conserve this sensitive layer, which structures the city.

THE PRESENT DEVELOPMENT TRENDS

With the change in lifestyles and occupations after industrialization, the relationship between settlements and water has changed. With alternate sources of water in the city, the dependency on these tanks has declined. With globalization and urbanization, the present trends of development have resulted in negation of this sensitive water network structuring the city. The growing cities have encroached upon tank-beds and nallas for provision of housing, infra-

structure, services etc. But the existence of these tanks, forming the softscape of the city, from past four centuries, has a deep impact on the environment & climatic conditions of the city. Now, the tank system is an inseparable part of the urban landscape.

THE IMPORTANCE OF TANK SYSTEM

The importance of this layer is emphasized by the various roles it plays in the present context. The water layer of the city is super-imposed by other layers, like road network, rail network, commercial network, industrial network, open space/landscape network etc.

4th International Engineering Symposium - IES 2015

March 4-6, Kumamoto University, Japan

Table 2 Importance of Lakes

ROLE OF TANKS	FUNCTION OF TANKS	IMPACT OF DISTURBANCE
ECOLOGICAL	Wet-land ecosystems	Ecological imbalance
HYDROLOGICAL	Regulating run-off	Flash floods & soil erosion
CLIMATOLOGICAL	Control surface radiation, humidity, soil moisture	Reduced water-spread area, changing climatic surface & atmospheric temperature conditions & increase in temperatures
RECREATIONAL	Parks, gardens, boating, bird watching clubs, water-sports, etc.	Deficiency of recreational & open spaces in cities
RELIGIOUS	Embanked by institutions	Loss of attachment of faith & belief to water
SOCIO-ECONOMICAL	Cultivation, fisheries, recreation, hawking along lake promenades, etc	Generate employment & economy
EDUCATIONAL	Biological study of ecosystems, flora, fauna, water supply, sewage treatment, botanical & horticultural	Loss of many rare species of organisms, opportunity to understand & respect other aspects activities in adjacent parks, etc. of water
INFRA-STRUCTURAL	setting-up of water treatment plants and sewage effluent treatment plant along tanks for re-use the water for landscaping, etc.	Loss of alternate sources of water, lack of recharge points for the under-ground water-table
STRUCTURAL	Structures the city	Disturbs other structuring networks also

CONCLUSIONS

The lack of understanding of the water network is the main reason for its present state. The network lost its importance with changes in life style and trends in development. But now, the importance of this network has been understood, where the efforts of restoration and de-silting of tanks are seen. But, for the proper working of the system, a holistic approach should be adopted in trying to understand, analyze its working and initiate its revival. Hence, there is a dependency of the city on this network. However, if this is emphasized with the various roles it performs along with the change in the attitude of development, then the sense of responsibility, pride and ownership will be induced among the citizens, towards uniqueness of Bangalore city. The approach towards these lakes and their

nalas should be of Conservation and not just Preservation.

An understanding of the tank system as a whole and its influence on the city may help to invoke a sense of responsibility and pride in possession of this sensitive layer of the city.

REFERENCES

- [1] Mathur, Anuradha, and Da Cunha, Dilip, Deccan Traverses, Rupa & Co., Delhi, 2004.
- [2] Mahalakshmi, K., "Trends in Urban Development around Water Tanks in Bangalore", Paper Presented in Symposium – Lake 2002, I.I.Sc., Bangalore, 2002.
- [3] Rice, Lewis, Mysore: A Gazetteer Compiled For Government, Vol. II, Archibald Constable & Company, Westminster, 1897.

Analysis of morphometry and flow pattern of Chalakudy river basin, Kerala with GIS tools

Nigee K, K Subrahmanyam, Aparna P, Shimna P and Drissia T K

*Department of Applied Mechanics & Hydraulics
NITK Surathkal, India
Email: nigee311@hotmail.com*

Morphometry and terrain analyses are important in geomorphology where quantitative measurements are made on physical characteristics of landforms. Analysis of the flow pattern in a basin helps to relate the runoff characteristics to the morphometric parameters. This research work attempts to study the morphometric aspects of streams and terrain characteristics of Chalakudy river basin of Kerala, India. Topographic maps were used for extracting the vector maps using GIS software like MapInfo and ArcGIS and linear, areal and relief aspects calculated for three sub-basins of Chalakudy river basin, namely Ambalakkadavu, Peringalkuthu and Sholayar were related to the mean discharge and peak runoff. The results confirm that Horton's laws with reference to quantitative geomorphology are applicable to the regions of Chalakudy river basin, situated in the highland and midland. However the law doesn't hold good for lowland or coastal belt. The reason may be the presence of non homogenous nature of bed rock in the sub-basins.

Application and Test of the SWAT Model in the Upper Cauvery River Basin, Karnataka, India

Kumar Raju B C and Lakshman Nandagiri

Department of Applied Mechanics & Hydraulics, National Institute of Technology Karnataka, Surathkal, Karnataka, India, e-mail: kumarrajubc@gmail.com

ABSTRACT: With increased availability of spatial data-sets of catchment characteristics and hydrometeorological variables, distributed hydrological models are being applied to solve a variety of problems related to catchment hydrology and water resources management. In this study, we explore the applicability of the distributed Soil and Water Assessment Tool (SWAT) hydrological model to map the spatial distribution of hydrological processes in the Upper Cauvery basin (36682 km^2) located in Karnataka State, India. SWAT was applied to the basin using input data of daily rainfall from 33 influencing rain gauges, climatic variables from 6 climate stations, land use-land cover and topography information derived from satellite imagery and soil characteristics from a map. Daily streamflow records of the Billigundulu gauging site was used for model calibration and validation. Model sensitivity analysis, to identify the most critical parameters was performed using the Latin Hypercube (LH) and One-factor-At-a-Time (OAT) sampling approach. SWAT performance in simulating streamflow at the Billigundulu gauge site was good as indicated by coefficient of determination (R^2) of 0.81 and Nash-Sutcliffe efficiency (ENS) of 80% between simulated and observed daily flows. Results of this study prove that SWAT is an effective modeling tool for hydrologic analyses in large heterogeneous tropical catchments.

Key words: *SWAT, Hydrological modeling, Sensitivity analysis, Surface runoff, Cauvery basin*

1. INTRODUCTION

Hydrological models are used to represent temporal and spatial processes of the hydrological cycle at a basin scale. These models are also useful in identifying sensitive parameters for basin response for the sub hydrological process. A variety of distributed hydrological models are available of which some are integrated within a Geographical Information System (GIS) environment for predicting watershed water balance components (Arnold et al., 1998; Beasley and Huggins, 1981; Beven and Kirkby, 1979; Young et al., 1989).. Among these, Soil Water Assessment Tool (SWAT) has been widely used in various regions of the world and in different climatic zones at daily, monthly and annual time steps and also it has been

successfully implemented at spatial scales ranging from small watersheds to large river basins (Arnold et al., 1998). SWAT is also suitable in the quantification of relative impact using alternative input data on water balance components, land use changes and water quality assessment (Tripathi et al., 2003; Xu et al., 2011). For Indian climatic condition SWAT has been effectively implemented to predict streamflow, sediment yield and water quality of a catchment (Dhar and Mazumdar, 2009; Gosain et al., 2006; Immerzeel and Droogers, 2008; Wagner et al., 2013). In this study, it is intended to test a SWAT model for the upper Cauvery basin, Karnataka, India. Also, this study aims at identifying sensitive parameters which govern water yield of the basin.

2. SWAT MODEL DESCRIPTION

The SWAT model has been used for investigating the impact assessment of water availability, erosion, sediment and nutrient transport at the basin scale (Arnold et al., 1998). SWAT requires rainfall, climate, land use, soil data and elevation data for delineating the watershed boundaries, streams and flow routing. In SWAT the watershed is subdivided into a number of sub watersheds. These sub watersheds are further divided into Hydrologic Response Units (HRUs), which are units of unique intersections of land use and soils and it simulates water balance components for each HRU by using a water balance equation. The hydrologic cycle is simulated by the water balance equation:

$$SW_t = SW_0 + \sum_{i=1}^t R_{day} - Q_{surf} - E_a - w_{seep} - Q_{gw} \quad (1)$$

where SW is the soil water content, i is time in days for the simulation period t , and R_{day} , Q_{surf} , E_a , w_{seep} , and Q_{gw} respectively are the daily precipitation, surface runoff, evapotranspiration, percolation and return flow. Surface runoff (Q_{surf}) for each HRU is calculated by using SCS-CN method. The general form of the SCS-CN method (USDA, 1972), is given by the following equation:

$$Q_{surf} = \frac{P_e^2}{(P_e + S)} \quad (2)$$

Where P_e (mm) is the depth of effective precipitation (precipitation minus initial abstraction), S (mm) is the amount of water storage available in the soil profile or the retention parameter and it is defined as:

$$S = 25.4 * \left(\frac{1000}{CN} - 10 \right) \quad (3)$$

The CN is a function of the soil's permeability, land use and antecedent soil water conditions.

3. STUDY AREA

The Cauvery River, also known as the Dakshin Ganga, is one of the major interstate peninsular rivers of South India. The Cauvery River rises in the Western Ghats and flows in an eastwardly direction passing through the states of Karnataka, Tamil Nadu, Kerala and Pondicherry before it drains into the Bay of Bengal. The present study was taken up to the Billigundulu gauge site of the Cauvery basin to simulate the water yield. The basin up to the Billigundulu gauge site has an area of 36682 km² with many tributaries, including the Shimsha, Hemavathi, Harangi, Arkavati, Lakshmanathirtha and Kabini (Table 1). The south-west monsoon covers most of the annual precipitation. The recorded maximum and minimum temperatures are 39.1°C and 4.8°C respectively. There are many major and medium projects in the upper Cauvery basin located in Karnataka state from which water is utilized for irrigated areas in many districts. A few of the selected major water resources projects in the upper Cauvery basin are KRS dam, Harangi dam, Hemavathi dam, and Kabini dam. The larger part of the upper Cauvery basin is comprised of irrigated agriculture. More than 70,000 ha of land is irrigated from canals, groundwater wells and tanks. Irrigated agriculture in this basin provides livelihood to a large population and contributes significantly to the food production of Karnataka State. An assessment of the basin is important because it provides a statistic on the water yield of the basin, especially under the impacts of significant human-induced land use/cover and climate changes. The topography map of the upper Cauvery basin is shown in Fig. 1.

Table 1 Sub basins in the Upper Cauvery Basin

Sl. No.	Sub basin Name	Drainage Area (km ²)
1	Hemavathy	5548.32
2	Harangi	3209.20
3	Lakshmanathirtha	1912.45
4	Kabini	7021.33
5	Shimsha	8646.89
6	Arkavathy	4123.84
	Upper Cauvery	36682.00

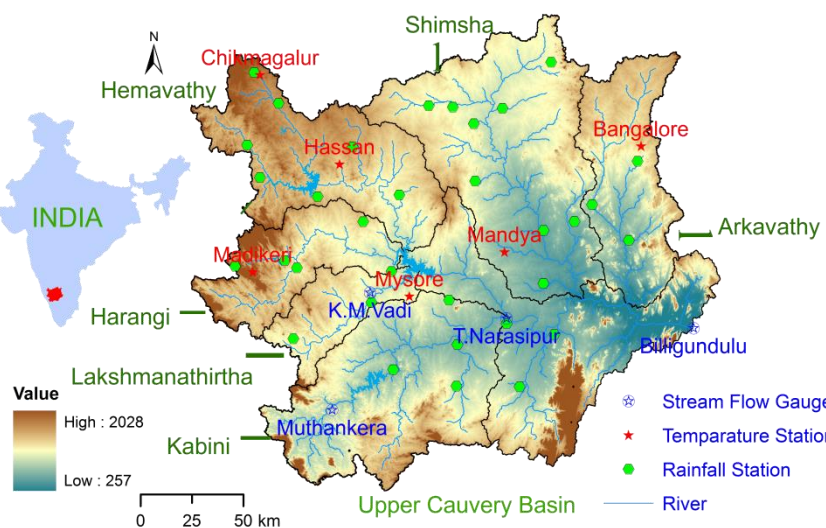


Fig. 1 Topography of Upper Cauvery basin and the location of the rain gauge stations

4. INPUT DATA

Basic input data required for the SWAT hydrological model includes topography, weather, rainfall, land use and soil data. Topographic data was obtained in the form of DEM (Digital Elevation Model) at 90 m resolution from the SRTM (Shuttle Radar Topography Mission) and it was used to delineate a basin into multiple sub basins and calculate topographic related parameters such as slope class, stream length and locate monitoring points. 1:50,000 scale land use data was collected from Karnataka State Remote Sensing Application Centre (KSRSAC) and soil map and its physical properties database were obtained from the National Bureau of Soil Survey and Land Use Planning (NBSS and LUP). Daily precipitation data was collected from Karnataka Irrigation Investigation Division (KIID) for 33 rain gauge stations located in and around the basin. Daily climate data were collected from the Indian Meteorological Department (IMD) climate stations.

4.1 LAND USE AND SOIL

The predominant land use in the basin is agriculture. Agricultural fields and forest areas cover more than 64.17% and 24.47% of the basin respectively. The water bodies include reservoirs and tanks cover 3.9% of the basin. The barren rocky and scrub land cover 4.51% of the basin. The urban areas, industrial area and villages cover 2.95% of the basin. The

map and distribution of the land use obtained from KSRSAC are shown in Fig. 2.

5. SENSITIVITY ANALYSIS

Sensitivity analysis can give a better understanding of the impact of change in an individual input parameter of the model response and can be performed using various methods. The method in the ArcSWAT interface combines the Latin Hypercube (LH) and One-factor-At-a-Time (OAT) sampling. Van Griensven et al. (2006), characterized Global rank 1 as "very important", rank 2 to 6 as "important", rank 7 to 19 as "slightly important" and rank 28 as "not important". Sensitivity analysis was performed on 16 different SWAT model parameters for the upper Cauvery basin. Parameters and parameter ranges used in the sensitivity analysis are shown in Table 2. By using default upper and lower boundary parameter values, the parameters were tested for sensitivity using without observed streamflow data. Results of sensitivity analysis for the upper Cauvery basin are presented in Fig. 3 with parameters ranked according to their magnitude of response. The most sensitive factor governing the streamflow for the upper Cauvery basin was base flow alpha factor (Alpha_Bf). This indicates that base flow is very significant in the water yield. The SCS runoff curve number for moisture condition II (CN2), Effective hydraulic

4th International Engineering Symposium - IES 2015

March 4-6, 2015, Kumamoto University, Japan

conductivity in main channel alluvium (Ch_K2), threshold depth of water in the shallow aquifer required for return flow to occur (Gwqmn), available water capacity (Sol_Awc) and soil evaporation compensation factor (Esco) are also important parameters. Alpha_Bf and Sol_Awc were correlated to base flow and

that could be the reason for their higher ranking in the sensitivity analysis. Sol_Z, Canmx, Blai, Gw_delay and Sol_K were the next sensitive parameters. Ch_N2, Gw_revap, Surlag, Epco and Revapmn parameters had very less influence on the streamflow.

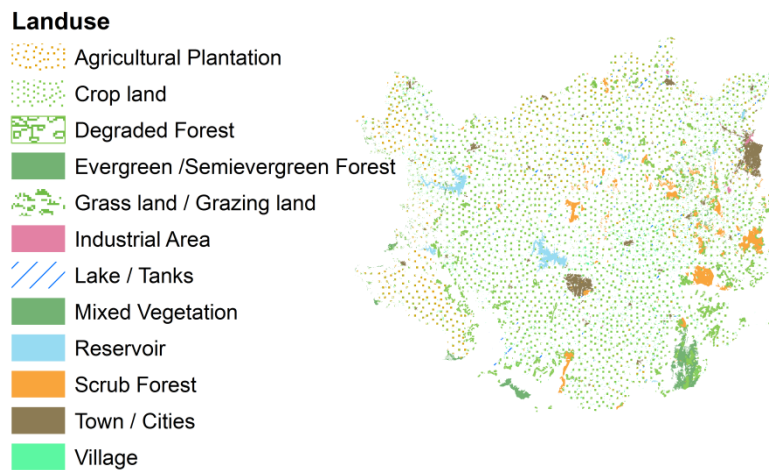


Fig. 2 Land use/Land cover map of the upper Cauvery basin

Table 2 Parameters and their ranges considered for the sensitivity analysis
(Gw. = groundwater, Evap. = evaporation, Geom. = geomorphology)

Name	Min	Max	Definition	Process
Alpha_Bf	0	1	Base flow alpha factor (days)	Gw.
Blai	-20	20	Leaf area index for crop *	Crop
Canmx	0	10	Maximum canopy index	Runoff
Ch_K2	0	150	Effective hydraulic conductivity in main channel alluvium (mm/hr)	Channel
Ch_N2	-20	20	Manning coefficient for channel	Channel
CN2	-20	20	SCS runoff curve number for moisture condition II *	Runoff
Epco	-20	20	Plant evaporation compensation factor *	Evap.
Esco	0	1	Soil evaporation compensation factor	Evap.
Gw_delay	0	100	Groundwater delay (days)	Gw.
Gw_revap	0.02	0.2	Groundwater "revap" coefficient	Gw.
Gwqmn	0	1000	Threshold depth of water in the shallow aquifer required for return flow to occur (mm)	Soil
Revapmn	0	500	Threshold depth of water in the shallow aquifer for "revap" to occur (mm)	Gw.
Sol_Awc	-20	20	Available water capacity (mm/mm soil)*	Soil
Sol_K	-20	20	Soil conductivity (mm/h) *	Soil
Sol_Z	-20	20	Soil depth *	Soil
Surlag	0	10	Surface runoff lag coefficient	Runoff

*Relative percent change.

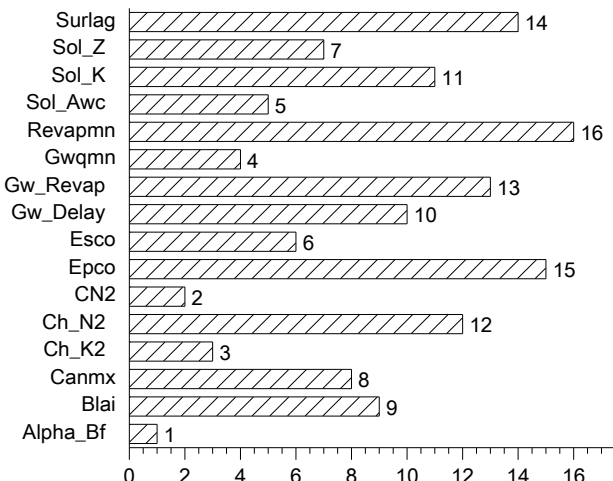


Fig. 3 Sensitivity ranking for hydrology over the upper Cauvery basin for SWAT model

6. CALIBRATION OF THE SWAT PARAMETERS

Model calibration involves the adjustment of parameter values and comparison of simulated streamflow, to observe data until a defined objective function is attained. In this study, automatic calibration was carried out using a dataset of daily streamflow records. The parameters obtained from the sensitivity analysis using LH-OAT were chosen for automatic calibration. To calibrate the SWAT model, auto-calibration tool in the ArcSWAT interface was used with Parasol mode. The model predictions are evaluated for the calibration periods using three statistical methods: Nash-Sutcliffe efficiency coefficient (ENS), Percent BIAS (PBIAS) and coefficient of determination (R^2).

7. RESULTS AND DISCUSSION

Streamflow was estimated based on calibrated model parameters. The SWAT model was calibrated using the daily observed streamflow data on Billigundulu gauge site. The calibration period was chosen between 1/6/2005 to 31/12/2005. Fig. 4 shows the time series and a scatter plot of simulated and observed flows (m^3/s) for the SWAT model at the gauging site of the basin. The model was also capable of simulating the pattern of flow during dry and wet period reliable with the climate data inputs. From these Figure it is noticed that observed streamflow are simulated well, which implies that the performance of SWAT model is good. The ENS, R^2 and PBAIS values of the SWAT model for the basin was 0.80, 0.81 and -2.73 respectively.

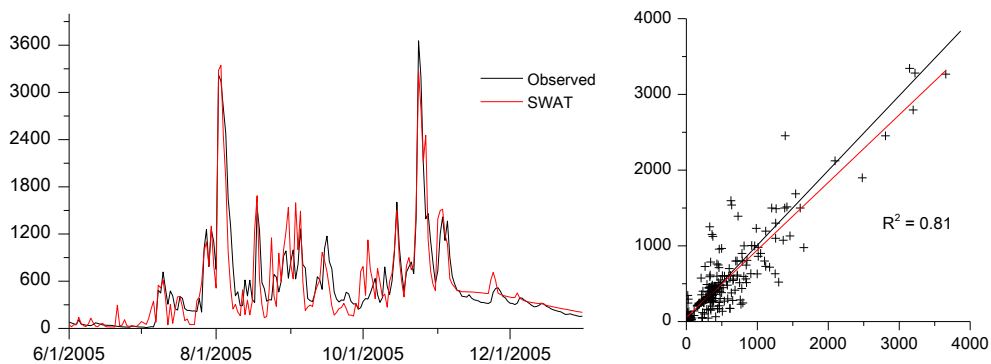


Fig. 4 Time Series and scatter plot of observed and simulated daily streamflow in the upper Cauvery basin

4th International Engineering Symposium - IES 2015

March 4-6, 2015, Kumamoto University, Japan

8. CONCLUSION

The present study was able to interpret the physically based SWAT model for agricultural dominated basin like upper Cauvery. The behavior of the basin in terms of response to streamflow at the gauge site was successfully assessed by identifying the sensitive parameters. The sensitivity analysis of the model showed that the base flow alpha factor was the most sensitive parameter. The model was successfully calibrated using observed daily flow data on the Billigundulu gauge site using auto-calibration tool. The results showed that the major part of flow was from the aquifer zone nearer to the gauge site that reaches up to 40% of the streamflow contribution. The statistics of model performance in simulating temporal variations in the Billigundulu gauge site are good. In view of the results obtained in this study, it may be concluded that SWAT is an effective modeling tool for hydrologic analyses and water resources management in the upper Cauvery basin.

ACKNOWLEDGEMENTS

The authors are grateful for the financial assistance provided by the Department of Applied Mechanics and Hydraulics, National Institute of Technology Karnataka, India. We would also like to thank all the Government Departments and Organizations for providing required data.

REFERENCES

- [1] Arnold, J. G., et al., (1998), Large area hydrologic modeling and assessment part i: model development, JAWRA Journal of the American Water Resources Association, vol. 34, pp. 73-89.
- [2] Beasley, D. B. and Huggins, L. F., (1981), ANSWERS users manual, Chicago: United States Environmental Protection Agency,
- [3] Beven, K. J. and Kirkby, M. J., (1979), A physically based, variable contributing area model of basin hydrology, Hydrological Sciences Bulletin, vol. 24, pp. 43-69.
- [4] Dhar, S. and Mazumdar, A., (2009), Hydrological modelling of the Kangsabati river under changed climate scenario: case study in India, Hydrological Processes, vol. 23, pp. 2394-2406.
- [5] Gosain, A., et al., (2006), Climate change impact assessment on hydrology of Indian river basins, Current Science, vol. 90, pp. 346-353.
- [6] Immerzeel, W. W. and Droogers, P., (2008), Calibration of a distributed hydrological model based on satellite evapotranspiration, Journal of Hydrology, vol. 349, pp. 411-424.
- [7] Tripathi, M. P., et al., (2003), Identification and prioritisation of critical sub-watersheds for soil conservation management using the SWAT Model, Biosystems Engineering, vol. 85, pp. 365-379.
- [8] USDA, S., (1972), National Engineering Handbook, Section 4: Hydrology, Washington, DC,
- [9] Wagner, P. D., et al., (2013), An assessment of land use change impacts on the water resources of the Mula and Mutha Rivers catchment upstream of Pune, India, Natural Hazards and Earth System Sciences, vol. 17, pp. 2233-2246.
- [10] Xu, H., et al., (2011), Quantifying uncertainty in the impacts of climate change on river discharge in sub-catchments of the Yangtze and Yellow River Basins, China, Natural Hazards and Earth System Sciences, vol. 15, pp. 333-344.
- [11] Young, R. A., et al., (1989), AGNPS: A nonpoint-source pollution model for evaluating agricultural watersheds, Journal of Soil and Water Conservation, vol. 44, pp. 168-173.

Study on the Utilization of Unconventional Materials as a Substitution Material for Fine Aggregates in Concrete

B.M. Sunil¹, Madhura¹ and Balasubramanya M²

¹*Department of Civil Engineering, National Institute of Technology Karnataka, Surathkal, Mangalore - 575 025, India. E-mail: bmsunil@gmail.com*

²*Consulting Engineer, Mangalore, India*

ABSTRACT: Mine tailings and fly ash are a major category of industrial wastes whose disposal is problematic from environmental point of view. The present study was motivated by the possibility of using iron ore tailings as a possible substitute for fine aggregates in concrete mixes. Accordingly this study presents the results of a treatability study of mine tailings with replacement of fine aggregates in mix designs and with fly ash and cement blends in different proportions. The iron ore tailings consisted of soil excavated/sampled from the tailing dam facility in Kudremukh, Karnataka state, India, having an in situ moisture content of approximately 6-7 % (during dry conditions) and void ratio of 0.90. Mix designs were prepared by complete replacement of conventional fine aggregates (river sand) with tailings and also tailings with blends of fly ash and cement (by substituting 15% and 30% of cement with fly ash). The results showed that the 28 days cured specimens of tailings mixed with cement and coarse aggregates had compressive strength values up to 28 MPa. The results were compared with 28 days cured trial mix concrete specimens prepared using cement, fine aggregates and coarse aggregates. Overall, test results suggest that it may be possible to use concrete mix prepared with tailings and blends of tailing and fly ash, in the infrastructure projects.

Keywords: Industrial waste; Tailing; Cement; Fly ash; Concrete mix; Laboratory tests.

INTRODUCTION

Shortage or inadequate supply of natural sand may affect construction projects. Worldwide concrete is abundantly used by the construction industry. Non-availability of natural sand (fine aggregate) may arise because of various reasons. Shortage of fine aggregates could jeopardize construction projects. In such cases substitute/alternate materials have to be chosen based on the relevant studies. This study was motivated by the possibility of using mine tailings and fly ash as potential materials to replace fine aggregates in concrete mix. Mine tailings produced during processing have traditionally been treated as a waste material and require special attention at disposal. This tradition

is however changing as tailings are being used as a useful material (Zou and Sahito, 2004). Shansai et al (2007) conducted a series of geotechnical experiments on copper mine tailings in order to investigate the suitability of tailings for construction purposes. Kudremukh iron ore facility called as Kudremukh iron ore Company limited (KIOCL) mines occur in the semi-arid region in the Northern part of Karnataka.

The region is characterized by annual rainfall of 7000 mm spread over June – September in a year and has temperatures in excess of 32°C during summers (32°C to 37°C). Winters (November to February) witness a pleasant season with average temperature lying in the band of 14°C to 33°C, even though minimum can touch to

4th International Engineering Symposium - IES 2015

March 4-6, 2015, Kumamoto University, Japan

10°C. Storage and handling of these tailings is a serious environmental concern and on the other hand utilization of disposed tailings is a technological challenge. In the past attempts have been made to study the utilization of mine tailings for different purposes such as aggregates for asphalt pavements, making bricks, as fill material for road construction, etc ([Zhang et al., (2006); Mahmood and Mulligan (2007); Roy et al (2007); Fang et al (2010); Cheng et al (2010); Li et al (2010); Shun et al (2011); Sivakugan et al (2006)]. Successful utilization of tailings makes the construction activity economical and also results in resolving certain environmental problems such as disposal and leaching of heavy metals etc (Rao and Reddy, 2006). Leaching of soluble toxic substances by the infiltrating rainwater may contaminate groundwater resources (Rao and Reddy, 2006). One method that is generally used to prevent migration of toxic constituents into the subsurface is by stabilization and solidification (S/S) process (Nehdi and Tariq, 2005).

MATERIALS AND METHODS

In this study mine tailings and the blends of mine tailings were used as substitution material for fine aggregates in concrete mix designs. Cement and fly ash were used as blend materials, with source material, tailing. Trial concrete mix designs were made with iron ore tailings as fine aggregate by completely substituting sand with different mixture proportion. Trial mix designs were also made using tailings by substituting 15% and 30%, of cement with fly ash. Fly ash was acquired from the nearby thermal power plant situated at Padubidri (Udupi District) Karnataka. The experiments were performed by mixing of all the materials manually in the laboratory at room temperature. The fresh concrete was used to cast cubes of size 150 x 150 x 150 mm to determine its compressive strength. Each concrete cube specimen was cast in three layers by using vibrating table. After casting, the specimens were left for about 24 hours and then immersed into curing tank for further curing. The concrete cube specimens were cured for 7 days and 28 days and then tested for

compressive strength. To compare the test results trial concrete mix designs were also made using conventional materials (i.e. using Portland cement, river sand, as fine aggregate and coarse aggregate, maximum nominal size of 20 mm). Mixing and casting of cube specimens were performed in accordance with ASTM C192/C192M standards for concrete testing.

Non-destructive Testing

During this study the quality of the hardened concrete is assessed through rebound hammer test and Ultrasonic Pulse velocity test.

Mine Tailings

Fresh tailing material classifying as SP was sampled from the tailing pond. The tailing material is obtained from, 15 cm below the surface crust and had the moisture content of 6-7 % and insitu void ratio of 0.90. The tailing material used in the testing program is non-plastic (NP) with approximate fines (silt and clay) on the order of 2-3% and a specific gravity (G_s) on the order of 3.10 to 3.30. Basic properties of tested tailing samples are shown in Table 1.

Table 1 Basic properties of tested tailing samples

Sam ple	G_s	Atterberg limits			Grain-size distribution (%)		
		w_L	w_p	I_p	G	S	Fines
A	3.3	NP	NP	0	5	93	2
B	3.1	NP	NP	0	5	92	3

G_s - Specific gravity of tailing; w_L - Liquid limit; w_p - Plastic limit; I_p - Plastic index; G-gravel; S-Sand; Fines-Silt & Clay.

RESULTS AND DISCUSSIONS

The effective utilization of mine tailings in concrete mix designs were studied through a series of experiments.

Mix Designs

Mix designs were prepared with iron ore tailings as fine aggregate by completely replacing sand with tailings. Mix designs

were also prepared with the tailings by substituting 15%, and 30%, of cement with fly ash. The results were compared with the compressive strength of concrete specimens prepared using conventional civil engineering materials (i.e. cement, sand and coarse aggregates). Compressive strength and theoretical flexural strength test results obtained for the trial mix are presented in Table 2 (appendix). The compressive strength and flexural strength of 28 days cured specimens are on the order of 42.3 to 47.0 MPa and 4.6 to 4.8 MPa. Rebound hammer test was performed on the concrete cube specimens to correlate the data with the compressive strength. From Table 2 it is observed that the rebound number had a good correlation with the compressive strength, which varied from 42-45. The results of nondestructive test using rebound hammer conform well as per BIS standards. The results of the ultrasonic pulse velocity test by direct transmission are shown in Table 2. The pulse velocity of the concrete specimens is above 4500 m/s which indicates that the concrete is of excellent quality (as per IS: 13311-Part I).

Concrete mix design using tailings

Utilization of mine tailings in concrete mix designs was studied by substituting fine aggregates with tailings. Accordingly the fine aggregate portion was completely replaced with mine tailings. In order to compare the test results and to study the variation, tailings were mixed in different proportions with cement and coarse aggregates (see Tables 3 to 5 in appendix). Concrete cube specimens (15 cm x 15 cm x 15 cm) were tested for each mix proportion. The results obtained were compared with concrete cube specimens prepared with conventional materials (see Table 2). When the mix design proportion is 1:3.11:4.53, the compressive strength of 7 days and 28 days cured specimens is shown in Table 3 (on the order of 8 MPa to 11 MPa and 15.5 to 18 MPa). The rebound number of 28 days cured specimens vary from 19 to 26 and the ultrasonic pulse velocity is about 4687 m/s.

The test results of compressive strength, flexural strength, rebound hammer and ultrasonic pulse velocity of 1: 1.65: 2.92

mixes are shown in Table 4 (appendix). The values of compressive strength and flexural strength of 28 days cured specimens are on the order of 15.0 to 21.7 and 2.7 to 3.1 MPa respectively. The test results of 7 days and 28 days cured specimens of concrete mix corresponding to 1: 1.05: 2.3 are shown in Table 5 (appendix). By comparing the results of different mix proportions using tailings (see Tables 3 to 5) improvement in compressive strength and flexural strength results is observed as we reduce the quantity of tailings in the mix designs. However it can be concluded that when fine aggregates are replaced completely by tailings the concrete specimens fails to achieve the desired compressive strength of a particular mix or the design mix strength of M40 obtained using fine aggregates. This is also true with the flexural strength, which decreases due to addition of tailings. Therefore it can be said that the tailings (alone) cannot be an alternative or a complete substitute for the fine aggregates in concrete mix. The decrease in strength of the concrete cube specimens may be attributed due to the presence of deleterious materials (Aubertin et al., 1995).

Mix designs using tailing and fly ash

Mix designs were performed by partial replacement of cement with the fly ash by substituting 15%, and 30%, of cement with fly ash. Six concrete cube specimens of size 15cm x 15cm x 15cm for each trial mix were tested in the laboratory. The test results of 7 days and 28 days cured concrete specimens (for different mix proportions) are presented in Tables 6 and 7 in appendix. Compressive strength of specimens obtained by substituting cement with 15 % of fly ash was found to be very poor (Table 6). Compressive strength varied from 2.2-3.0 MPa and 2.2-8.8 Mpa for 7 days and 28 days of curing period respectively. Theoretical flexural strength varied from 1.0-1.2 Mpa and 1.0-2.1 Mpa for 7 days and 28 days cured specimens respectively. The rebound number correlated well with the compressive strength. However, the pulse velocity showed that the sample specimens were of poor quality (i.e. the

4th International Engineering Symposium - IES 2015

March 4-6, 2015, Kumamoto University, Japan

ultrasonic pulse velocity <4500 m/s [see Table 6]). When compared to both the concrete mixes i.e involving cement, fine aggregates and coarse aggregates and concrete mix involving cement, tailings and coarse aggregates, the fly ash based concrete also possess fairly good compressive strength which can be used in many structural applications. Thus fly ash based concrete along with tailings can be a good substitute for natural sand in concrete mix designs. This type of concrete can be a good substitute for many of the civil engineering applications.

SUMMARY AND CONCLUSIONS

The findings of this study are as follows:

- i) The concrete specimens prepared with tailings (complete replacement of fine aggregates) failed to achieve the desired compressive strength. This may be due to the presence of deleterious material in tailings. Presence of silt and clay hinders the solidification process and hydration of concrete. However, appreciable strength of 28 MPa was achieved. Hence it can be used for building construction such as partition walls, and in other infrastructure projects etc. Sieving and washing of tailings prior to its utilization will remove the unwanted constituents that may subsequently increase the strength of concrete.
- ii) The 28 days cured concrete specimens prepared with cement, 30% fly ash, tailings and coarse aggregates showed a fairly good compressive strength. When compared to both the concrete mixes i.e involving cement, fine aggregates and coarse aggregates and concrete mix involving cement, tailings and coarse aggregates, the fly ash based concrete possess good compressive strength and flexural strength. To economize the use of cement and to get rid of disposal problems of tailings and fly ash this may be the best option.
- iii) Addition of fly ash acted as pozzolanic material which increased the strength since fly ash arrests alkali-aggregate reaction and it acts as a pozzolanic material in binding the aggregates with cement.
- iv) Using tailings and fly ash in infrastructure projects proves to be economical when compared with natural sand or fine aggregates. The use of tailings and fly ash as admixture not only extends technical advantages to the properties of concrete but also contributes to the environmental pollution control.

REFERENCES

- [1] Mahmood A.A, Mulligan C.N., (2007), "Investigation of the use of mine tailings for unpaved road base, Proceedings of the Annual International Conference on soils, sediments", *water and energy*, 12 (1), 107-117.
- [2] Jagdish Krishnaswamy Milind Bunyan, K. Vishal Mehta, Niren Jain, K. Ullas Karanth, (2006), "Impact of iron ore mining on suspended sediment response in a tropical catchment in Kudremukh, Western Ghats, India", *Journal of forest ecology and management*, 187-198.
- [3] Li Chao, Sun Henghu, Bai Jing, Li Longtu, (2010), "Innovative methodology for comprehensive utilization of iron ore tailings Part 1. The recovery of iron ore tailings using magnetic separation after magnetizing roasting", *Journal of hazardous materials*, 174, 71-77.
- [4] Liyang Zhang, Saeed Ahmari, Jinhong Zhang, (2011), "Synthesis and characterization of fly ash modified mine tailings-based geopolymers", *Journal of construction and building materials*, 3773-3781.
- [5] M. Aubertin, B. Bussiere, P. Chapuis Robert, (1996), "Hydraulic conductivity of homogenized tailings from hard rock mines", *Canadian Geotechnical Journal*, 33, 470-482.
- [6] M. Nehdi, A. Tariq, (2005), "Stabilization of sulphidic mine tailings for prevention of metal release and acid drainage using cementitious materials: a review", *Journal of Environ. Eng.*, 6, 423-436.
- [7] N. Sivakugan, R.M. Rankine, K.J. Rankine, K.S. Rankine, (2006), "Geotechnical considerations in mine backfilling in Australia", *Journal of Cleaner Production*, 14, 1168-1175.
- [8] S. Roy, G.R. Adhikari, R.N. Gupta, (2007), "Use of gold mill tailings in making bricks: a feasibility study", *Waste Management & Research*, 25, 475-482.
- [9] S.M. Rao, B.V.V. Reddy, (2006), "Characterization of kolar gold field mine tailings for cyanide and acid drainage", *Journal of Geotechnical and Geological Engineering*, 24, 1545-1559.
- [10] Shamsai, A. Pak, S.M. Bateni, S.A. Ayatollahi, (2007), "Geotechnical characteristics of copper mine

4th International Engineering Symposium - IES 2015

March 4-6, 2015, Kumamoto University, Japan

tailings: A case study”, *Journal of Geotechnical and Geological Engineering*, 25, 591-602.

[11] Yonghao Fang, Yamin Gu, Qiubo Kang, Quan Wen, Pin Dai, (2010), “Utilization of copper tailing for autoclaved sand-lime brick”, *Journal of construction and building materials*, 867-872.

[12] Yongliang Chen, Yimin Zhang, Tiejun Chen, Yunliang Zhao, Shenxu Bao, (2010), “Preparation of eco-friendly construction bricks from hematite tailings”, *Journal of construction and building materials*, 2107-2111.

APPENDIX

Table. 2 Strength characteristics of concrete specimens using cement, sand and coarse aggregates

Specimen size (cm)	Compressive strength (MPa)		Theoretical flexure strength		Rebound number (for 28 days cured specimens)	Time (μs)	Pulse velocity (m/s)
	7 days	28 days	7 days	28 days			
15x15x15	35.1	46.7	4.2	4.8	44	30	5000
15x15x15	34.3	47.0	4.1	4.8	45	30	5000
15x15x15	35.9	42.3	4.2	4.6	43	32	4687

Table 3 Strength characteristics of concrete specimens using cement, tailings and coarse aggregates

Specimen size (cm)	Compressive strength (MPa)		Theoretical flexure		Rebound number (for 28 days cured specimens)	Time (μs)	Pulse velocity (m/s)	Remarks
	7 days	28 days	7 days	28 days				
15x15x15	8.9	18.0	2.1	2.9	26	33	4545	Design Mix proportion (1: 3.11: 4.53)
15x15x15	11.1	17.8	2.3	2.9	25	32	4687	
15x15x15	8.0	15.5	1.9	2.8	19	32	4687	

Table 4 Strength characteristics of concrete specimens using cement, tailings and coarse aggregates

Specimen size (cm)	Compressive strength (MPa)		Theoretical flexure strength (MPa)		Rebound number (28 days cured specimens)	Time (μs)	Pulse velocity (m/s)	Remarks
	7 days	28 days	7 days	28 days				
15x15x15	11.6	21.7	2.4	3.3	28	33	4545	Design Mix proportion (1: 1.65: 2.92)
15x15x15	11.1	20.0	2.3	3.1	28	34	4411	
15x15x15	13.9	15.0	2.6	2.7	20	38	3947	

Table 5 Strength characteristics of concrete specimens using cement, tailings and coarse aggregates

4th International Engineering Symposium - IES 2015
March 4-6, 2015, Kumamoto University, Japan

Specimen size (cm)	Compressive strength (MPa)		Theoretical flexure strength (MPa)		Rebound number (for 28 days cured specimens)	Time (μs)	Pulse velocity (m/s)	Remarks
	7 days	28 days	7 days	28 days				
15x15x15	19.6	26.7	3.1	3.6	32	31	4838	Design Mix proportion (1: 1.05: 2.3)
15x15x15	18.7	24.8	3.0	3.5	31	30	5000	
15x15x15	20.0	28.3	3.1	3.7	30	30	5000	

Table 6 Strength characteristics of concrete specimens using cement, 15% fly ash, tailings and coarse aggregates

Specimen size (cm)	Compressive strength (Mpa)		Theoretical flexure strength (Mpa)		Rebound number (for 28 days cured specimens)	Time (μs)	Pulse velocity (m/s)	Remarks
	7 days	28 days	7 days	28 days				
15x15x15	2.7	8.8	1.1	2.1	14	55	2727	Design Mix proportion (1: 1.65: 2.92)
15x15x15	3.0	5.0	1.2	1.6	15	50	3000	
15x15x15	2.5	8.3	1.1	2.0	17	56	2678	

Table 7 Strength characteristics of concrete specimens using cement, 30 % fly ash, tailings and coarse aggregates

Specimen size (cm)	Compressive strength (Mpa)		Theoretical flexure strength (Mpa)		Rebound number (for 28 days cured specimens)	Time (μs)	Pulse velocity (m/s)	Remarks
	7 days	28 days	7 days	28 days				
15x15x15	22.2	28.0	3.3	3.7	31	31	4839	Design Mix proportion (1: 1.65: 2.92)
15x15x15	22.2	28.4	3.3	3.7	35	32	4687	
15x15x15	15.0	28.0	2.7	3.7	36	32	4687	

USE OF RECYCLED COARSE AGGREGATES AS AN ALTERNATIVE IN CONSTRUCTION INDUSTRY – A REVIEW

Suman Saha ¹, C. Rajasekaran ² and T. Vinayak Pai ³

¹ Department of Civil Engineering, National Institute of Technology Karnataka Surathkal, Mangalore-575025, India. Email:sumansaha.civil@gmail.com

² Department of Civil Engineering, National Institute of Technology Karnataka, Surathkal, Mangalore 575025, India. Email:bcrrajasekaran@gmail.com

³ Proprietor, M/S Thodarkas, Mangalore 575006, India. Email: thodarkas@gmail.com

ABSTRACT: The quantity of construction & demolition wastes and the scarcity of natural resources are increasing day by day. To promote sustainability in construction industry, the use of recycled concrete aggregates, resourced from construction & demolition wastes is very important and useful solution for the production of concrete. From a systematic literature review, the paper explains the physical and mechanical properties of recycled concrete aggregates for the production of concrete. This paper also describes the properties of concrete made of recycled coarse aggregates. More experiments are to be done to find the maximum possibilities to use recycled coarse aggregates to produce concrete. The use of recycled coarse aggregates will help to protect environment and will lead to sustainable development.

Keywords: Construction Demolition, Sustainability, Recycled Aggregates, Concrete.

INTRODUCTION

In this 21st century, sustainable development and environmental protection become key goals of modern society. Important role in the sustainable development of the built environment, reduction of pollution, conservation of natural resources and energy savings certainly has the entire civil engineering, especially construction materials. The protection of the environment is a basic factor, which is directly connected with the survival of the human beings. Parameters like environmental consciousness, protection of natural recourses, sustainable development play an important role in modern requirements for construction works. But development has done severe damages on the environment and may endanger its sustainability. Main problems regarding construction materials are as follows:

- ✓ Depletion of natural resources.

- ✓ High consumption of Portland cement and associated high emission of carbon dioxide.
- ✓ Large amount of generated construction and demolition (C&D) waste and land fill space depletion.

Concrete is the premier construction material across the world and the most widely used in all types of civil engineering works including infrastructure, low and high-rise buildings, defence installations, environmental protection facilities etc. The protection of the environment concerns three following points mainly:

- ✓ Use of high amounts of raw materials (aggregates for the production of cement and concrete) which result in the decrease of available natural resources which is continuously sub-graded.
- ✓ Consumption of high amounts of energy for the production,

4th International Engineering Symposium - IES 2015

March 4-6, Kumamoto University, Japan

- ✓ transport, use of raw materials and final ones, as cement and concrete.
- ✓ Creation of big volumes of old concrete from old construction works (demolition wastes).

The main reasons for the increase of the volume of demolition concrete waste are:

- ✓ Many old buildings and other structures have overcome their limit of use and need to be demolished;
- ✓ structures even adequate to use, are under demolition, because there are new requirements and necessities;
- ✓ Creation of building wastes which result from natural destructive phenomena (earthquakes, storms, etc). Nik. D. Oikonomou. et al. (2005) gave the approximate percentage of various construction materials in demolition waste (DW) shown in Fig. 1.
- ✓ New construction for better economic growth;
- ✓ Creation of building waste resulting from manmade disaster/war.

The recycled concrete aggregates (RCA) are the main components of old concrete and for many reasons there is a need to re-use them.

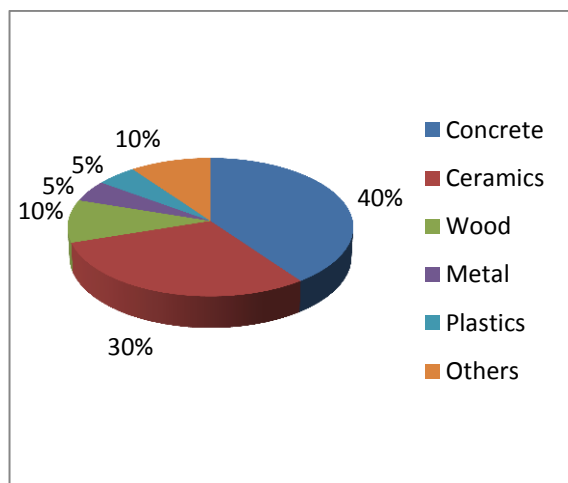


Fig 1. approximate percentage of various construction materials in demolition waste (DW)

SIGNIFICANCE FOR THE USE OF RCA

Since aggregate represents about 70-80 % of concrete components, the use of recycled aggregates in concrete opens a whole new range of possibilities in the reuse of materials in the construction industry. The utilization of recycled aggregates is a good solution to the problem of an excess of construction demolition waste materials, provided that the desired final product will fit the standards. The use of RCA will lead the followings:

- ✓ Protection of natural sources of a country.
- ✓ Decrease of high volumes of fresh concrete wastes, which illegally end up in uncontrolled areas of deposition.
- ✓ Sustainable development in the construction industry.
- ✓ To protect the environment.

INTERNATIONAL SCENARIO ON RECYCLED CONCRETE AGGREGATES

Now-a-days each and every country, high priority has been given to use the recycled materials in the construction industries. Indicatively, Collins RJ. et al. (1996) 10% of used aggregates in Great Britain are RCA and De Vries, P et al. (1996) 78,000 tonnes of RCA were used in Holland in 1994 as the corresponding national organization admitted that the use of 20% of coarse RCA result in no differentiation of the properties of fresh or hardened concrete. Acker Av et al. (1996) additionally, the recycling of building demolition waste at 40% has been set as an aim in Germany since 1991. A recent report by US Department of Transportation (2000) refers that the Dutch government has a policy that minimizes the use of natural materials and promotes the use of recycled materials within a market system. The government cooperates with industry by sharing risk and profit and providing unambiguous technical and environmental standards. High degrees of recycling are seen, especially for construction and demolition (C&D) aggregates, blast furnace slag, recycled asphalt pavements (RAP), coal fly ashes, steel slag, and municipal solid waste waste-to-energy bottom ash. For example, the Construction

4th International Engineering Symposium - IES 2015

March 4-6, 2015, Kumamoto University, Japan

Materials Recycling Association (CMRA) et al. (2013) has accounted for approximately 140 million tonnes of concrete waste, which are recycled yearly in the United States. The 2010 European Aggregates Association (UEPG) et al. (2012) reported in Annual Review that recycled aggregates are generated approximately 5% of the production of aggregates in the European Union (EU). European Aggregates Association et al. (2012) Germany is the greatest producer of recycled aggregates, with a production of approximately 60 million tonnes. The United Kingdom follows with approximately 49 million tonnes; the Netherlands has approximately 20 million tonnes; and France produces 17 million tonnes. Tam VWY et al. (2009) in Australia, more than 50% of the total concrete residue generated from C&D activities is recovered for recycling, while the rest goes to landfills. Dosho Y. et al. (2007) reported that Japan has reached approximately a 98% rate for processing concrete waste to recycled aggregates.

PHYSICAL PROPERTIES OF RECYCLED CONCRETE AGGREGATES:

The physical Properties of Recycled Concrete Aggregates are influenced by the procedure of recycling, the quality of the original material, size and shape of the aggregates etc.

Density

The simplest and commonest method for characterizing aggregates is in terms of their specific gravity. The aggregate particle density is an essential property for concrete mix design and also for calculating the volume of concrete produced from a certain mass of materials. Sallehan Ismail, Mahyuddin Ramli. et al. (2013) conducted experiments and the particle density of recycled coarse aggregate (oven dry condition) of 20mm and 10 mm is generally found to be 2.33 Mg/m³ and 2.23 Mg/m³. These figures are lower than the particle density of coarse natural aggregates.

Water Absorption

The most significant difference in the physical properties of recycled coarse aggregates reflected in most studies is its higher water absorption capacity as compared to natural coarse aggregates. This is largely due in part to higher porosity of the mortar phase than aggregate phase. Generally, normal coarse aggregates have water absorption (WA) values between 0.5% and 1.5%, which is normally omitted for most concrete applications. However, more precautions must be taken when using recycled coarse aggregates because of their greater porosity. Recycled coarse aggregate will almost always exhibit higher WA values than normal coarse aggregates. For that reason extra amount of water is to be calculated in mix design to obtain desired workability of the concrete made of recycled coarse aggregates.

MECHANICAL PROPERTIES OF RECYCLED COARSE AGGREGATE

The mechanical properties of RCA are generally provided by the Aggregate Crushing Value, Aggregate Impact Value and the LA abrasion value. These properties are greatly influenced by the relative weakness of the mortar adhered onto the aggregate in the RCA. Aggregate Crushing Value test determine the ability of aggregate to resist crushing under static load. Natural coarse aggregate is better able to withstand crushing compared to RCA. However, the degree to which the performance differs may vary with different sources of RCA. Aggregate Impact Value test determine the ability of aggregate to resist crushing under impact load. The abrasion resistance of aggregates can be defined as the resistance to degradation caused by loads, stockpiling, mixing, placing and compacting of concrete, and is measured by Los Angeles (LA) abrasion value. Large variations in the mechanical properties of RCA seems to suggest that unlike the cases with natural aggregate where the performance of concrete depends primarily on the mix design, performance of concrete with RCA will experience greater variability in view of the variation of mechanical properties of the RCA. The mechanical properties of RCA may have to

4th International Engineering Symposium - IES 2015

March 4-6, Kumamoto University, Japan

be taken into consideration when designing concrete.

PROPERTIES OF CONCRETE USING RCA

A continuous study on the properties of concrete containing various proportions of recycled concrete aggregates is been carried out over the time of last decade. The results of that study describe the properties of the concrete i.e. workability, density, compressive strength etc.

Workability

Workability of the concrete is measured using slump test. It is revealed that the workability of concrete is significantly influenced by RCA content. Sallehan Ismail, Mahyuddin Ramli. et al. (2013) conducted tests and found a linear decrease causes an increase in the addition of RCA in concrete. This may be attributed to the effects of the physical characteristics of RCA. The properties of RCA are more angular and rougher in the surface because of the presence of adhered mortar. The angular and rougher surface of RCA particles compared with normal concrete aggregates decreases the workability of the fresh concrete mix. Thus, workability is decreased. In addition, the presence of porous adhered mortar in the RCA increases water absorption. Hence, RCA affects the workability of the fresh mix. Carmine Lima et al. (2013) concluded that due to the rougher surfaces and to the more irregular shapes of the recycled concrete aggregates with respect to the normal ones, the replacement of NAs with RCAs has caused a significant reduction in workability. On the contrary, the addition of fly ash in the mixture has produced clear increase in the work of the total volume ability. Carmine Lima et al. (2013) observed although concretes made with 100% of recycled concrete aggregates (RAC 100%) were prepared with higher amounts of super-plasticizer (up to 0.6%) a significant reduction in their workability.

Density of Concrete

It was found that a loss in concrete density is accompanied by an increase of the replacement percentage of recycled

concrete aggregates. Such behaviour occurs due to the presence of porous adhered mortar attached to physical properties of recycled coarse aggregates. Thus, an increase in the replacement content of coarse natural aggregate by RCA has significant effect on the reduction of concrete density. Carmine Lima (2013) found through his research work that reduction in density of concrete is almost negligible in the case of concretes with only 30% of RCAs.

Compressive strength

The compressive strength of the concrete is analysed of the mix having different percentage replacement of natural coarse aggregate by recycled coarse aggregates at 3 days, 7 days, 28 days etc. it has been found that higher percentage replacement of natural coarse aggregate by recycled coarse aggregate results in lower concrete compressive strength. This is because of the presence of adhering mortar on surface recycled coarse aggregates which is porous and weaker than the natural aggregate. Carmine Lima et al. (2013) conducted tests on several cubic samples made of the thirteen concrete mixes under consideration at different curing times. Results concluded a progressive reduction of the concrete compressive strength as a result of an increased percentage of recycled aggregates in the mix. Isabel Martínez-Lage et al. (2012) found that the decline in compressive strength, also approximately linear with rising replacement rates, ranges from 20% to 30% in concrete containing 100% recycled aggregate. Failure strain rises with the replacement rate, with a value of 2.1% for concrete with natural aggregate only to 2.3% for material with 50% recycled aggregate and 2.5% for mixes in which all the coarse aggregate is recycled. Isabel Martínez-Lage et al. (2012) observed an increment of failure strain with the replacement rate.

RESEARCH WORK TO BE DONE

Many research works on the physical and mechanical properties of recycled concrete aggregates are going on since past few years. Experimental studies on the properties of the concrete (i.e. workability,

4th International Engineering Symposium - IES 2015

March 4-6, 2015, Kumamoto University, Japan

compressive strength, split tensile strength, durability etc.) made by recycled coarse aggregates have been also done by researchers. According to that study, the properties of the concrete depends on the percentage of replacement of natural coarse aggregates by recycled coarse aggregates. In future, experimental studies on the concrete made by recycled coarse aggregates with varying the different parameters i.e. quantity of recycled coarse aggregates, with the addition of admixtures will be done to analyse the properties of recycled coarse aggregates. This research aims to find the possibilities of using recycled aggregates to produce concrete with proper strength in the construction industry. Use of recycled concrete aggregates will lead to reduce the environmental problems generated from dumping the construction and demolition wastes. This aim can be achieved by recycling the construction and demolition wastes to produce concrete mixes for structural elements with high performance as natural aggregates.

CONCLUSION

The following conclusions are deduced from this study:

- Use of recycled coarse aggregates is given priority in construction industry throughout the world.
- The density of recycled coarse aggregates is lower than the normal aggregates.
- Water absorption rate is high for recycled coarse aggregates than normal coarse aggregates.
- The properties of concrete depend on the percentage of replacement of normal coarse aggregates by recycled coarse aggregate.
- Workability, compressive strength, density of the concrete made of recycled coarse aggregates is lower than the concrete made of normal coarse aggregates.

At present, the quantity of the construction demolition waste is increasing day to day due to some reasons. So, one of the most environmentally responsible ways of meeting the challenges of sustainability in construction is the use of

recycled construction and demolition waste in new construction. The reuse of recycled materials derived from construction and demolition waste is growing all over the world. Many governments are actively promoting policies aimed at reducing the use of primary resources and increasing reuse and recycling. Research and experimental works on the use of recycled aggregates have proven that good quality concrete could also be produced with recycled aggregates.

REFERENCES

- [1] Acker Av. Recycling of concrete at a precast concrete plant. *Betonwerk+Fertigteil-Tech* 1996; 6:91–101.
- [2] Ashraf M. Wagih, Hossam Z. El-Karmoty, Magda Ebied , Samir H. Okba. (2013) Recycled construction and demolition concrete waste as aggregate for structural concrete. *HBRC Journal* 9, P193–200.
- [3] Carmine Lima, Antonio Caggiano, Ciro Faella, Enzo Martinelli, Marco Pepe, Roberto Realfonzo. (2013) Physical properties and mechanical behaviour of concrete made with recycled aggregates and fly ash. *Construction and Building Materials* 47, P547–559
- [4] Collins RJ. Increasing the use of recycled aggregates in construction. In: Proc. of the International Conference: Concrete in the Service of Mankind. I. Concrete for Environment Enhancement and Protection, Dundee, Scotland; 1996. P 130–139.
- [5] Construction Materials Recycling Association. *Concrete Recycling*; 2013. Website:<http://www.cdrecycling.org>
- [6] D. Matias, J. de Brito, A. Rosa, D. Pedro. (2013) Mechanical properties of concrete produced with recycled coarse aggregates – Influence of the use of superplasticizers. *Construction and Building Materials* 44, P101–109
- [7] De Vries, P. Concrete recycled: crushed concrete aggregate. In: Proc. of the International Conference: Concrete in the Service of Mankind. I. Concrete for Environment Enhancement and Protection, Dundee, Scotland; 1996. P 121–130.
- [8] Dosho Y. Development of a sustainable concrete waste recycling system application of recycled aggregate concrete produced by aggregate replacing method. *J Adv Concr Technol* 2007;5(1):27–42
- [9] European Aggregates Association. Annual review 2011–2012. Brussels, Belgium; 2012. Website:<http://www.uepg.eu>
- [10]Isabel Martínez-Lage, Fernando Martínez-Abella, Cristina Vázquez-Herrero, Juan Luis Pérez-Ordóñez, 2012. Properties of plain concrete made with mixed recycled coarse aggregate. *Construction and Building Materials* 37, P171–176.

4th International Engineering Symposium - IES 2015

March 4-6, 2015, Kumamoto University, Japan

-
- [11]Nik. D. Oikonomou. (2005) Recycled concrete aggregates. *Cement & Concrete Composites* 27 ,P315–318
 - [12]R.V. Silva, J. de Brito , R.K. Dhir. (2014) Properties and composition of recycled aggregates from construction and demolition waste suitable for concrete production. *Construction and Building Materials* 65 , P201–217
 - [13]Sallehan Ismail, Mahyuddin Ramli. (2013) Engineering properties of treated recycled concrete aggregate (RCA) for structural applications. *Construction and Building Materials* 44, P464–476
 - [14]Sonawane Tushar R, Pimplikar Sunil S.(2013) Use Of Recycled Aggregate In Concrete. *International Journal of Engineering Research & Technology (IJERT)* ISSN: 2278-0181. Vol. 2 Issue 1, January-2013.
 - [15]Surya M., Kanta Rao, VVL , Lakshmy, P. (2013) Recycled aggregate concrete for Transportation Infrastructure. *Procedia - Social and Behavioral Sciences* 104 , P1158 – 1167
 - [16]Tam VWY. Comparing the implementation of concrete recycling in the Australian and Japanese construction industries. *J Cleaner Prod* 2009; 17(7):688–702.
 - [17]US Department of Transportation. Recycled materials in European highway environment. Uses, technologies and policies. International Technology Exchange Program, 2000. Website:<http://www.international.fhwa.dot.gov>
 - [18]Vlastimir Radonjanin, Mirjana Malešev, Snežana Marinković, Ali Emhemd Saed Al Malty. (2013) Green recycled aggregate concrete. *Construction and Building Materials* 47, P1503–1511.
 - [19]Zhen Hua Duan, Chi Sun Poon. (2014) Properties of recycled aggregate concrete made with recycled aggregates with different amounts of old adhered mortars. *Materials and Design* 58 , P19–29.

Studies on Fly Ash Mixed Concrete in Aggressive Environment

G. Vijayakumar ¹, C. Rajasekaran ² and Muralidhara ³

1 Department of Civil Engineering, Pondicherry Engineering College, Puducherry, India.
Email: gvk@pec.edu

2 Department of Civil Engineering, National Institute of Technology Karnataka, Surathkal, India. Email: bcrajasekaran@gmail.com

3 Consulting Engineer, Mangalore, India. Email: murli18@yahoo.com

ABSTRACT: In the severe environment exposure condition such as marine environment, durability is the most important factor which concerns the service life of most concrete structure, both in terms of economy and safety. This study emphasise on the selection of a suitable material which can contemplate the above phenomenon. For the present study, flyash was selected and used as partially replacement of cement in concrete and subjected to continuous monitoring on its behaviour in simulated aggressive and actual marine exposure condition. The results of various investigation such as determination of chloride, alkalinity, compressive strength, carbonations of concrete for plain and partially replaced flyash based concrete (10%, 20% and 30% replacement of cement) exposed to various aggressive environment, are presented.

Keywords: Flyash, Marine, Concrete, Carbonation

INTRODUCTION

Concrete exposed to marine environment both on and offshore undergo deterioration both by physical and chemical processes. The physical actions consisting of various loadings caused due to cyclic sea waves, high and low tides, ocean currents, hydrostatic pressure, freeze thaw cycles, temperature gradient etc, have their own independent damaging effects on the exposed concrete structures. While the chemical actions consist of slow decomposition of cement mortar matrix and corrosion of the embedded reinforcement due to the reaction of various salt ions present abundantly in sea water. The external action includes physical actions like freezing-thawing, alternate wetting-drying and also the mechanical actions like abrasion, salt water spray, cyclic drag etc. The internal actions cause the deterioration of concrete due to penetration of salt ions into its various depths. The impact of these events are severe in concrete structures which are in the splash zone, high in tidal zone and moderate in front structures. Sea

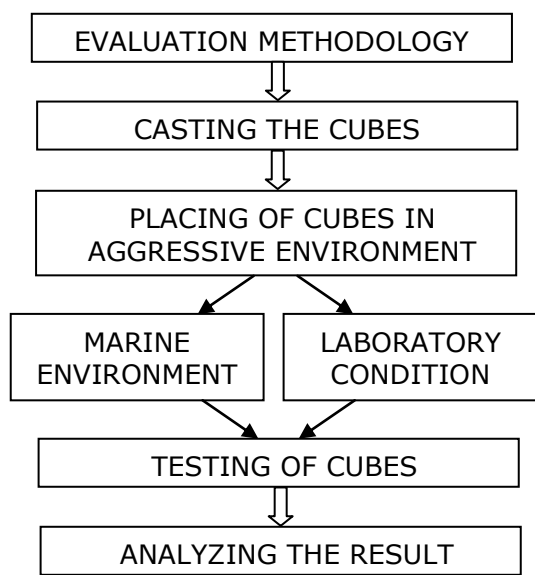
water generally consists of salts such as Chlorides and sulphates which contributes around 3.5% by weight. The pH of seawater varies between 7.5 to 8.4 which is alkaline in nature. Also, the sea water contains some amount of CO₂. These salts and oxides are primarily responsible for the chemical attack on concrete exposed to marine environment. As a part of chemical deterioration, the concrete in sea water is subjected to chloride induced corrosions on steel, due to the presence of high chloride concentrations and humid or saturated conditions.

Hence it is very much necessary to formulate steps in order to improve the durability of concrete in sea water either by making the concrete more impervious to the attack of seawater. Moreover effective utilization of pozzolanic materials is yet another desirable step that could be taken to improve durability against sea water.

4th International Engineering Symposium - IES 2015

March 4-6, 2015, Kumamoto University, Japan

METHODOLOGY



MIX PROPORTIONS

M35 grade mix was suggested in this study for better performance in aggressive conditions such as Marine environment where cement posses durability and serviceability problem due to continuous wave action, salt spray and splitting. Reference mix was prepared using OPC and conventional ingredients in accordance with IS 10262:1982 to achieve the target strength of 35MPa (Table 1). Using the same mix proportion, Concrete cube for aggressive environment were casted as partial replacement of cement by flyash in terms of 10%, 20%, 30% on volume basis.

The concrete cube of sizes (150 x 150 x 150) is casted in the laboratory. Totally 96 cubes were casted where placed in actual marine environment such as Atmosphere, splash, tidal and fully submerged (Table.2). Then the samples are periodically collected from the site and tested for physical and chemical properties such as compressive strength , chloride, pH, X-ray diffraction, weight loss , carbonation depth and Ultrasonic pulse velocity test. These tests are periodical conducted 28, 90 and 150 days. The location of cubes placed in the site conditions and lab conditions is shown in Fig. 1 to 6.

Table 1 Mix Design

Cement (Kg/m ³)	Water (liter)	Fine aggregate (Kg/m ³)	Coarse aggregate (Kg/m ³)
400	159	630	1175
1	0.40	1.57	2.93

Table 2 Cubes Casted Details in Marine Environment

Sl. No	Concrete-Mix	Marine Environment zones				Total
		(a)	(b)	(c)	(d)	
1	OPC	6	6	6	6	24
2	FA10	6	6	6	6	24
3	FA20	6	6	6	6	24
4	FA30	6	6	6	6	24

(a) Atmosphere
(c) Tidal zone

(b) Splash zone
(d) Submerged zone



Fig. 1 Atmosphere Zones



Fig.2 Tidal Zones



Fig. 3 Splash zones



Fig. 4 Submerged Zones



Fig. 5 H₂SO₄ Curing in Lab Conditions



Fig. 6 NaCl Curing in Lab Conditions

RESULTS AND DISCUSSION

Carbonated Depth

Phenolphthalein indicator was used to determine the carbonation effect on the cubes. It was found that both conventional and flyash concrete cubes placed at sea environment were affected by carbonates over the surface, when analysed for 28, 90 and 150 days of exposure condition. The effect of carbonation has reach a depth of 2mm for the flyash based concrete cubes and 4mm depth for conventional concrete when tested on 28th day aging of concrete. At 90 days of testing the depth of carbonation in flyash based concrete has increased to 4mm and in conventional concrete it has reached to 6mm. On 150 days aging of concrete the depth of carbonation in flyash based concrete has still increased to 7mm and in conventional concrete it has propagated to 9mm.

Compressive Strength Values

The compressive strength of concrete specimens cured in alkaline, acidic conditions and marine environment were tested at 28, 90, 150 days and the result are shown in Fig 7 and Fig 8. The compressive strength of flyash concrete ranged from a minimum 28 MPa to a maximum of 56 MPa for 10%, 20% and 30% replacement of cement by flyash. The compressive strength of conventional concrete ranged between 21 MPa and 50 MPa.

References

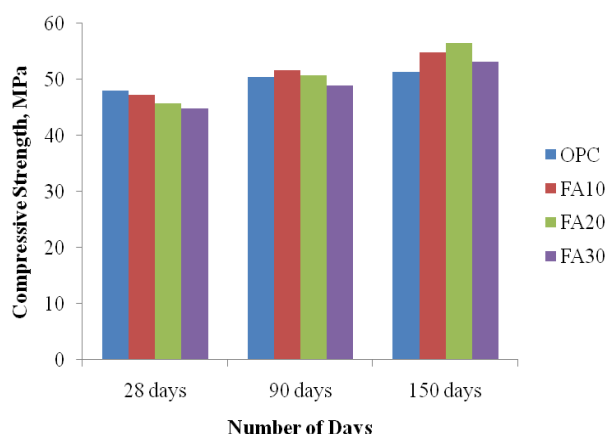


Fig. 7 Compressive Strength Value for Reference

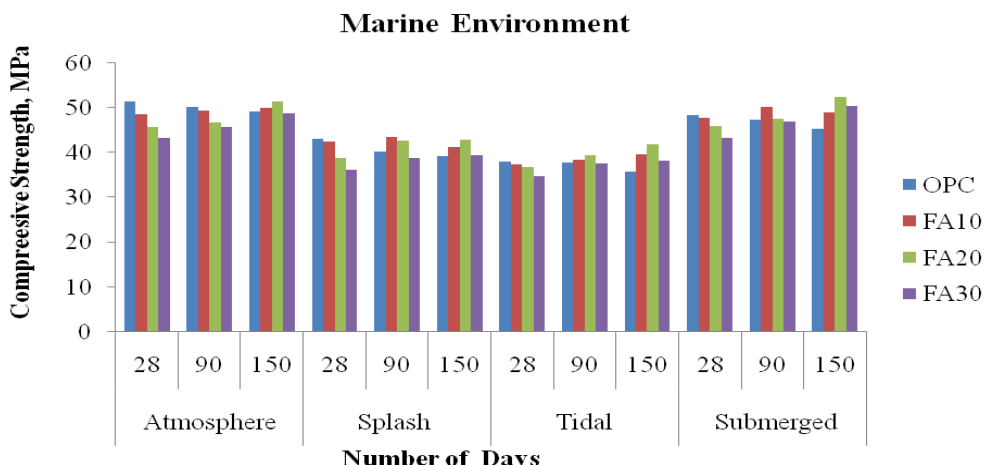


Fig 8 Compressive Strength Value for Marine Environment

Chloride Visual Testing

Traces of chloride was found in the cubes placed in partially submerged marine environment .The cubes which were placed near the coast and cubes which were placed under fully submerged condition was found to be unaffected by chlorides for all the observation period

Weight Loss Comparison

For the concrete cubes in marine environment, the weight loss was found to be more predominant for the concrete cubes kept under partially submerged condition when compared to fully submerged and atmosphere which pertain to both flyash based and conventional concrete. The percentages of weight loss in various conditions are shown in Fig 9 – 11.

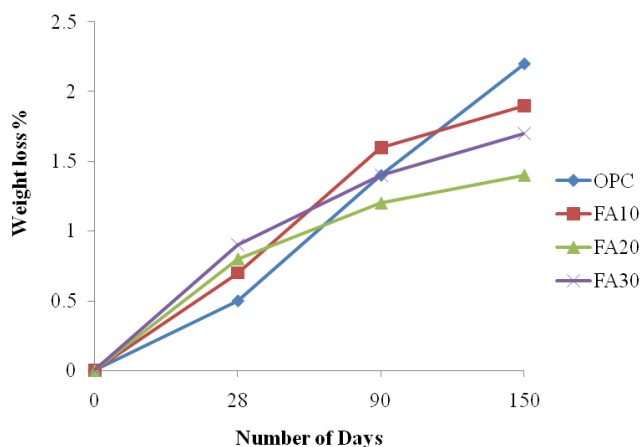


Fig. 9 Weight Loss on NaCl Cured Concrete Cubes

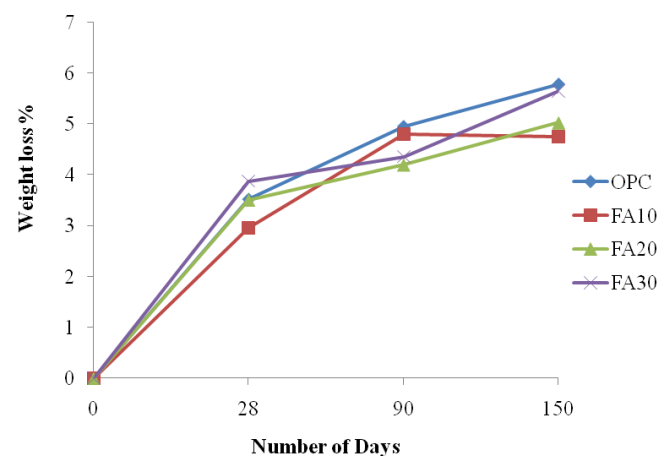


Fig. 10 Weight Loss on H₂SO₄ Cured Concrete Cubes

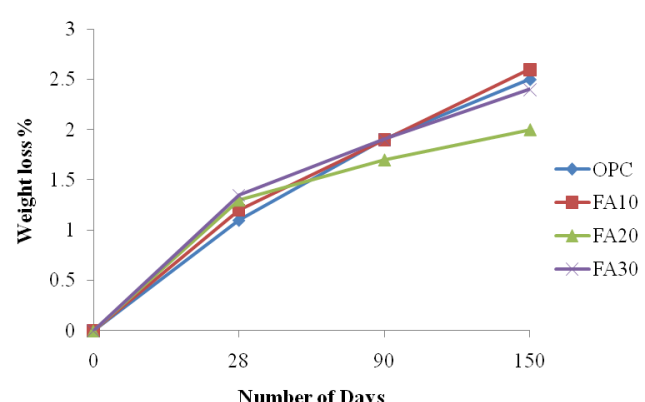


Fig. 11 Weight Loss on Tidal Zones in Marine Environment

4th International Engineering Symposium - IES 2015

March 4-6, Kumamoto University, Japan

CONCLUSION

Based on the observations from accelerated laboratory cured sample and sample placed at various conditions in actual marine environment the following conclusion was drawn.

1. The effect of carbonation for 20% replacement of cement by flyash concrete cubes was found to be less when compared to all the cubes under various marine environmental exposure condition.
2. The durability of concrete is ascertained by its compressive strength. 20% replacement of cement by flyash given a better compressive strength when compared to all the cubes placed under marine environments.
3. The flyash based concrete cubes placed in submerged marine environment were less affected by chloride attack. Traces of chlorides were found in partially submerged flyash based concrete cubes which are more for conventional concrete cubes when compared to flyash based concrete.
4. Weight loss in conventional concrete was observed to be 5% more in simulated acidic environment and 2% more for concrete cubes in partially submerged marine environment, when compared with flyash based concrete cubes.
5. On the basis of the experimental results regarding the conventional concrete and Flyash based concrete when subjected to aggressive and marine environment it has been concluded that Utilization of 20% replacement of cement by flyash has been proved to be an effective material which can be confidently used in aggressive environmental conditions.

REFERENCES

- [1] Code of practice for plain and reinforced concrete (fourth edition), IS 456:2000, Bureau of India Standard, New Delhi.
- [2] Md. Moinul Islam et al (2010), Strength behavior of concrete using slag with cement in sea water environment, Journal of Civil Engineering (IEB), vol. 38 (2), pp. 129-140.
- [3] Mehta, P.K., (1980), Durability of concrete in marine environment - A review, Performance of Concrete in Marine Environment, , ACI Pub., SP-65, pp. 1-20.
- [4] Mehta, P.K., (1986), Durability, Chapter-5, Concrete structure, Properties and Materials, Prentice-Hall, Eaglewood Cliffs , New Jersey.
- [5] Handbook on concrete mixes (based on Indian Standards), SP: 23-1988, Bureau of Indian Standards, New Delhi, India.
- [6] Indian standard, recommended guidelines for concrete mix design, IS 10262:1982, Bureau of India Standard, New Delhi.
- [7] Indian standard concrete mix proportioning - Guidelines (First revision) IS 10262:2009, Bureau of India Standard, New Delhi, India.
- [8] Reddy, D.V. et al (2011), Durability of Reinforced Fly Ash-Based Geopolymer Concrete in the Marine Environment, Proc. 36th Conf. on Our World in Concrete & Structures, Singapore.
- [9] Sri Ravindrarajah, R et al (2002), Properties Of High-Strength High-Performance Concrete For Marine Environment, Proc. Int. Conf. on Concrete in Marine Environment, Hanoi, Vietnam.

IMPROVEMENT OF FLY ASH CONCRETE STRENGTH BY BACTERIAL MINERAL PRECIPITATION

M. Suren Babu ¹, M. Jyothi ², C. Rajasekaran ³ and K.V. Arun Raj ⁴

- 1 Department of Civil Engineering, National Institute of Technology Karnataka, Surathkal, India. Email: surenmaddipoti8@gmail.com
- 2 Department of Civil Engineering, VNRV Jyothi Institute of Engineering & Technology, Secunderabad, India. Email: jyothi_manik@vnrvjet.in
- 3 Department of Civil Engineering, National Institute of Technology Karnataka, Surathkal, India. Email: bcrajasekaran@gmail.com
- 4 Consulting Engineer, Mangalore, India. Email: advitha_raj@yahoo.com

ABSTRACT: The objective of this research paper was to obtain the performance of the concrete by the microbiologically induced special growth/filler. One such thought has led to the development of a very special concrete known as Bacterial Concrete where bacteria is induced in the mortars and concrete to heal up the faults. Here an attempt was made by using the bacteria "Bacillus subtilis" is a model laboratory bacterium, which can produce calcite precipitates on suitable media supplemented with a calcium source. Experimental investigation carried out to evaluate the influence of Bacillus Subtillis on the compressive strength and Split Tensile Strength of concrete made without and with fly ash. Cement was replaced with three percentages (10%, 20% and 30%) with fly ash by weight. Through this study a significant increase in the compressive strength and split tensile strength was observed due to the addition of bacteria for a cell concentration of 10^5 cells per ml of mixing water.

Keywords: Bacterial concrete, bacillus subtilis, compressive strength, fly ash,

INTRODUCTION

Concrete is the most widely used construction material. Despite its versatility in construction, it is known to have several limitations. It is weak in tension, has limited ductility and little resistance to cracking. Based on the continuous research carried out around the globe, various modifications have been made from time to time to overcome the deficiencies of cement concrete. The ongoing research in the field of concrete technology has led to the development of special concrete considering the speed of construction, the strength of concrete, the durability of concrete and the environmental friendliness with industrial material like fly ash, blast furnace slag, silica fume, metakaoline etc. Recently, it is found that microbial mineral precipitation resulting from metabolic activities of favourable microorganisms in concrete improved the overall behaviour of

concrete. The process can occur inside or outside the microbial cell or even some distance away within the concrete. Often bacterial activities simply trigger a change in solution chemistry that leads to over saturation and mineral precipitation. Use of these bio mineralogy concepts in concrete leads to potential invention of new material called —Bacterial Concrete.

GENERAL

The main objective of the present experimental investigations is to obtain specific experimental data, which helps to understand the Bacterial concrete and its characteristics (Strength). In the present experimental investigation, studies have been carried out on the behaviour of fresh and hardened properties of standard grade concrete with and without addition of bacteria with varying percentages of fly ash. The hardened properties, compressive strength and split tensile strength of concrete are determined by

4thInternational Engineering Symposium - IES 2015

March 4-6, 2015, Kumamoto University, Japan

conducting suitable laboratory tests on concrete in hardened state. Researchers with different bacteria proposed different Bacterial concretes. The various bacteria used in the concrete are *Bacillus pasteurii*, *Bacillus sphaericus*, *E.coli* etc. In the present study an attempt was made by using the bacteria *Bacillus subtilis* strain no. JC3.

LITERATURE REVIEW

The concept of Bacterial concrete was first introduced by V. Ramakrishnan et al, (2001). A novel technique is adopted in remediating cracks and fissures in concrete by utilizing microbiologically induced calcite (CaCO_3) precipitation. Microbiologically induced calcite precipitation (MICP) is a technique that comes under a broader category of science called bio mineralization. *Bacillus subtilis* JC3, a common soil bacterium can induce the precipitation of calcite. Calcite formation by *Bacillus subtilis*, was studied by Chiara Barabesi et al, (2007) in order to identify genes involved in the bio mineralization process. Day J L et al, (2003) described the results of an innovative approach in concrete crack remediation utilizing microbiologically induced calcite. The basic principles for this application are that the microbial urease hydrolyzes urea to produce ammonia and carbon dioxide, and the ammonia released in surroundings subsequently increases pH, leading to accumulation of insoluble calcite. Microbiologically enhanced crack remediation was evaluated by comparing the compressive strengths of the treated concrete specimens and those of the control. X-ray diffraction analysis quantified calcite distribution in the region of the treated cracks. According to H.S. Patil et al, (2008) MECR increases compressive strength of treated cubes specimens by 12 -13% and remarkable potential as sealant for concrete cracks.

METHODOLOGY

Cubes of 150X150X150 mm and cylinders of 150X300 mm with bacteria concentration of 10^5 cells per ml of mixing water with varying percentages of fly ash as 0%, 10%, 20%, 30% are casted and

tested. The proportion of cement, fine aggregate and coarse aggregate is 1:1.2:2.5. In addition, controlled concrete specimens were casted and tested without bacteria and fly ash. The water cement ratio is taken as 0.42.

CULTURE OF BACTERIA – *Bacillus subtilis* JC3

The pure culture was isolated from the soil sample of JNTUH and is maintained constantly on nutrient agar slants. It forms irregular dry white colonies on nutrient agar plate. Whenever required a single colony of the culture is inoculated into nutrient broth of 25 ml in a 100 ml conical flask and the growth conditions are maintained at 370° C temperature and placed in 125 rpm orbital shaker.

COMPRESSIVE STRENGTH OF CONCRETE

The investigation is carried out to study the compressive strength of concrete of standard grade concrete (M30). A total of 30 cubes are cast with optimized concentration of bacteria and without bacteria with varying percentages of fly ash and tested to study the compressive strength under axial compression. Concrete cubes of 150mm x 150 mm x 150 mm are cast. Tests are conducted on concrete specimens for compressive strength on completion of 7 days, 28days.

SPLIT TENSILE STRENGTH OF CONCRETE

The tensile strength is one of the basic and important properties of the concrete. The concrete is not usually expected to resist the direct tension because of its low tensile strength and brittle nature. However, the determination of tensile strength of concrete is necessary to determine the load at which the concrete members may crack. The investigation is carried out to study the tensile strength of concrete of standard grade concrete (M30). A total of 30 cylinders are cast with optimized concentration of bacteria and without bacteria with varying percentages of fly ash and tested to study the tensile strength. Concrete cylinders of 150 mm x 300 mm are cast. Tests are conducted on

4th International Engineering Symposium - IES 2015

March 4-6, 2015, Kumamoto University, Japan

concrete specimens for tensile strength on completion of 7 days, 28days.

MIX DESIGN

Mix design can be defined as the process of selecting suitable ingredients of concrete such as cement, aggregates, water and determining their relative proportions with the object of producing concrete of required minimum strength, workability and durability as economically as possible. The purpose of designing can be seen from the above definitions, as two-fold. The first objective is to achieve the stipulated minimum strength and durability. The second objective is to make the concrete in the most economical manner. The grade of concrete used in the present concrete and investigation is standard grade concrete. The mix proportions for standard grade concrete are designed using IS: 10262-1982. The proportions of the mixes are

The mix proportion is obtained by the following steps

Step 1: Target strength for proportioning from 3.2 of the code book

$$f_{ck}^1 = f_{ck} + 1.65 \times S \quad (1)$$
$$= 30 + 1.65 \times S$$

Where f_{ck}^1 = target average compressive strength at 28 days

f_{ck} = characteristic compressive strength at 28 days, and

$$S = \text{standard deviation.}$$
$$= 30 + 1.65 \times 5 \quad (\text{standard deviation is taken as 5 from table 1})$$

$$f_{ck}^1 = 38.25 \text{ N/mm}^2$$

Step 2: Selection of W/C ratio from table 5 of IS: 456-2000

$$W/C = 0.42$$

From IS 456 maximum W/C = 0.5
 $0.42 < 0.5(\text{ok})$

Step 3: Selection of water content

From table 2 IS: 10262-2009
For 20mm aggregate water content
 $= 186 \text{ liters}$

Step 4: Selection of cement content

$$W/C = 0.42$$

$$186/0.42 = c$$

$$\text{Cement} = 443 \text{ Kg/m}^3$$

Step 5: Proportioning of fine and coarse aggregates

The percentage of fine aggregate for W/C ratio 0.35 for Zone I sand is 30%

But present W/C ratio is 0.42, thus the fine aggregate is increased at rate 0.01 for every 0.05 change in W/C ratio

For 0.05 increase – 0.1% increase

For 0.7 increase – 1.4% increase

For Zone I sand there must be 1.5% increase of fine aggregate

Therefore a total of 2.9% is increased

Thus, the final fine aggregate proportion is 32.9%

Thus, the coarse aggregate proportion is $100 - 32.9 = 67.1\%$

$$V * 1000 = w + \frac{c}{s_c} + \frac{f_a}{p * s_{fa}} \quad (2)$$

$$0.98 * 1000 = 186 + \frac{443}{2.745} + \frac{f_a}{0.329 * 2.508}$$

$$f_a = 520 \text{ Kg/m}^3$$

$$V * 1000 = w + \frac{c}{s_c} + \frac{c_a}{(1-p) * s_{ca}} \quad (3)$$

$$0.98 * 1000 = 186 + \frac{443}{2.745} + \frac{c_a}{0.671 * 2.61}$$

$$c_a = 1107 \text{ Kg/m}^3$$

Materials required for 1 cubic meter of concrete standard grade concrete are:

Standard grade concrete (M30)

Mix proportion 1: 1.2: 2.51: 0.42

Cement : 443 Kgs

Fine aggregate : 520 Kgs

Coarse aggregate : 1107 Kgs

Water : 186 Liters

MIXING OF CONCRETE:

The mixing process is carried out by machine mixing. The materials are laid in uniform layers, one on the other in the order – coarse aggregate, fine aggregate and cementitious material and Fly Ash. The amount of Fly Ash added for different concrete types are tabulated in Table 1. Dry mixing is done to obtain a uniform colour. Required amount of bacteria (*Bacillus subtilis* JC3) are added along with the water. The workability tests are carried out immediately after mixing of concrete using the compaction factor testing apparatus in accordance with IS: 10510-1983.

4thInternational Engineering Symposium - IES 2015

March 4-6, 2015, Kumamoto University, Japan

RESULTS

The results of the test conducted on the concrete obtained by using bacteria and varying percentages of fly ash have been calculated as:

$$\text{Compressive strength} = P/A$$

$$\text{Tensile strength} = 2P/\pi l d,$$

P – Load in KN,

A – Area of the cube,

L – Length of the cylinder,

D – Diameter of the cylinder,

Computed results are tabulated in Table 2 and Table 3

CONCLUSIONS

CULTURE OF BACTERIA

- *Bacillus subtilis JC3* is a soil bacterium.
- *Bacillus subtilis JC3* can be produced in the laboratory which is proved to be safe and cost effective.

STRENGTH STUDIES

- In standard grade concrete with 10% fly ash, from Table 2 it is evident that there was a significant increase in compressive strength by 8.75% at 28 days by addition of *Bacillus Subtilis JC3* bacteria when compared to Conventional concrete.
- In standard grade concrete, with the addition of bacteria and with the addition of fly ash, from Fig. 1it is evident that the percentage of improvement in the compressive strength decreases with increase in fly ash percentage.
- In standard grade concrete with 10% fly ash, from Table3 it is evident that there was a significant increase in split tensile strength by 10.9% at 28 days by addition of *Bacillus subtilis JC3* bacteria when compared to conventional concrete.
- In standard grade concrete, with the addition of bacteria and with the addition of fly ash, from Fig. 2 it is evident that the percentage of split tensile strength improvement decreases with increase in fly ash percentage.

ACKNOWLEDGEMENTS

The project was undertaken by a group Of six students under valuable guidance. Special thanks for the help from B. Poornima, B. Shravya, E. Saketh Reddy, G. Harish, G. Snigdhafor the completion of this project.

REFERENCES

- [1] M.S.SHETTY-Concrete technology
- [2] IS code book- 10262-2009 – Mix design
- [3] IS code book-456-2000 – W/C ratio determination
- [4] IS code book – 2386-1963 – Tests on coarse aggregates
- [5] 5. IS code book – 2720 – 1973 - Tests on fine aggregates
- [6] IS code book – 4031 -1988 – Tests on cement
- [7] IS code book – 383 -1970 – fine aggregate zone determinations
- [8] Appa Rao.G. –Role of water binder ratio on the strength development in mortars incorporated with Silica Fumell. Cement and Concrete Research, 2001, Vol.31, pp.443-447
- [9] Annie Peter.J, Lakshmanan.N, Devadas Manoharan.P, Rajamane.N.P& Gopalakrishnan.S –Flexural Behaviour Of RC Beams Using Self Compacting Concretell. The Indian Concrete Journal, June 2004, PP 66-72.
- [10] Antony Jeyasehar, Balamuralikrishnan, –Flexural Behaviour of RC Beams Strengthened with Carbon Fiber Reinforced Polymer (CFRP) Fabrics, International Conference on Advances in Construction Materials, Methodologies & Management (AC3M-'09), January 21-22,2009, CBIT, Hyderabad, pp.353-366.
- [11] Bachmeier K, Williams A E, Warminton J and Bang, S.S. –Urease activity in microbiologically – induced calcite precipitation II. Journal of Biotechnology, 93: 171-181, 2002
- [12] Badawe.B.R. And Kumbhar.P.D. –Deterioration of concrete-Experimental studies and RemediesII. International conference on Maintenance and Durability of concrete structures, March 4-6, 1997, JNTU, Hyderabad. Pp.88-92.
- [13] Bang, S.S., Galinat, J.K. & Ramakrishnan,V. –Calcite precipitation induced by polyurethane immobilized *Bacillus pasteurii* II Enzyme and Microbial Technology 28 (2001) 404-409.
- [14] Bang, S.S. and Ramakrishnan, V., "Microbiologically-Enhanced Crack Remediation (MECR)," Proceedings of the Microbiological Society of Korea, Seoul, Korea, 2001.
- [15] Bang, S.S. and Ramakrishnan, V., "Bacteria for Repair of Cracks in Concrete," the Transportation Research Board, Washington, DC, 2000
- [16] Bishwajit Bhattacharjee and Shamsad Ahmad, –Influence of chloride content, cover and concrete mix parameters on post de-passivation service life of chloride contaminated Reinforces Concrete Structures II. International Conference on Maintenance and Durability of concrete structures, March 4-6, 1997, JNTU, Hyderabad. Pp.68-72.
- [17] Bouzoubaa.N., Zhang.M.H. And Malhotra.V.M. –Mechanical properties and durability of concrete made with HVFA blended cements using a coarse FA II. Cement and Concrete Research.2001. Vol. 31, pp.1393-1402.

4th International Engineering Symposium - IES 2015

March 4-6, 2015, Kumamoto University, Japan

- [18] Carreira.D and Chu, K-H (1985), –Stress-Strain Relationship of plain concrete in compression II, Journal of ACI .vol.82.No6. Nov-Dec. pp 797-804.
- [19] Chandraprasirt. P and Hovichitr.I. –Portland Pozzolana Cement – A Cheaper Alternative for Thailand II, proc.Symposium on building materials for low income housing, U.N. Building, Bangkok, 1987.
- [20] Chan.W.W.J. And Wu.C.M.L. –Durability of concrete with high cement replacement II. Cement and Concrete Research. 2000, Vol.30, pp 865-879.
- [21] Chiara Barabesi, Alessandro Galizzi, Giorgio Mastromei, Mila Rossi, Elena, Tamburini and Brunella Perito Pavia, Italy
- [22] Gopala Krishnan.S., Annie Peter.J., Rajamane.N.P. –Effect of coarse aggregate type on mechanical properties of HPC II, 2003, Vol.31, pp 1421-1425.

Table 1. Classification of concrete types used for determining the strength properties

CONCRETE TYPE	% FLYASH	BACTERIA (cells/ml)
M ₀₀	0	0
M _{0B}	0	10 ⁵
M _{10B}	10	10 ⁵
M _{20B}	20	10 ⁵
M _{30B}	30	10 ⁵

Table 2. Compressive strength at 7 and 28 days in N/mm²

	7 DAYS	28 DAYS
Conventional (M₀₀)	12.8	32.0
0% fly ash (M_{0B})	13.9	34.8
10% fly ash (M_{10B})	13.7	34.4
20% fly ash(M_{20B})	13.3	33.3
30% fly ash(M_{30B})	12.6	31.4

Table 3. SPLIT TENSILE STRENGTH AT 7 AND 28 DAYS IN N/mm²

	7 days	28 days
Conventional (M₀₀)	0.54	1.34
0% fly ash (M_{0B})	0.59	1.49
10% fly ash (M_{10B})	0.58	1.45
20% fly ash(M_{20B})	0.57	1.44
30% fly ash(M_{30B})	0.53	1.32

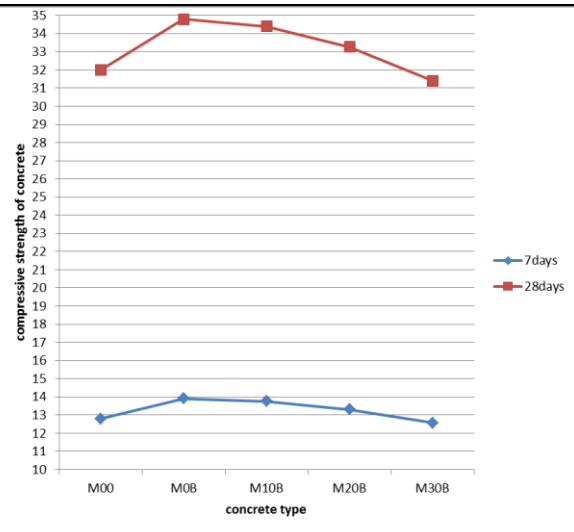


Fig 1. Compressive strength of concrete v/s concrete type

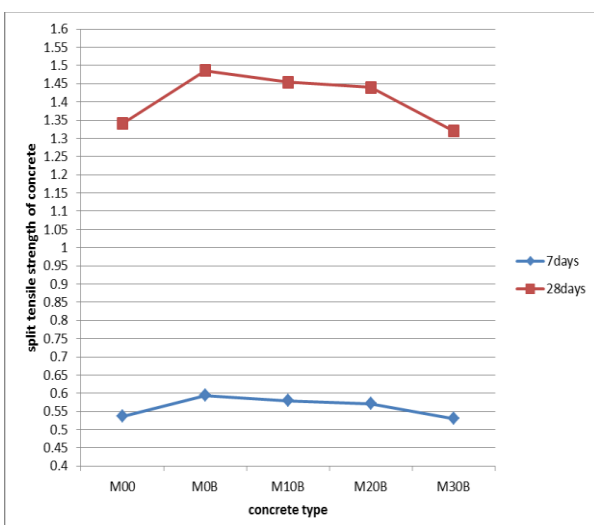


Fig 2. Split tensile strength of concrete v/s concrete type

An Experimental study on the Hardened Property of concrete by partial replacement of cement with sugarcane bagasse ash

K. Vinay¹, Y.M. Vijayakumar², C. Rajasekaran³ and Gokulraj⁴

- 1 Department of Civil Engineering, National Institute of Technology Karnataka, Surathkal, India. email: vinaykudlur1@gmail.com
 - 2 Department of Civil Engineering, Adichunchanagiri Institute Of Technology, Chikmagalur, Karnataka, India.
 - 3 Department of Civil Engineering, National Institute of Technology Karnataka, Surathkal, India. Email: bcrajasekaran@gmail.com
 - 4 Consulting Engineer, Mangalore, India. Email: gokulrajassociates@gmail.com
-

ABSTRACT: Sugarcane bagasse ash is a by-product of the sugar factories found after burning sugarcane bagasse which itself is found after the extraction of all economical sugar from sugarcane. This research was conducted to examine the potential of bagasse ash as a cement replacing material. Ordinary Portland cement was replaced by ground bagasse ash. Normal consistency and setting time of the pastes were investigated. The compressive strength and tensile strength of the concrete(M20 grade) containing Ordinary Portland cement and bagasse ash from 5% to 15% replacements was investigated. The results of the concrete work have shown that, up to 5% replacement of the Ordinary Portland cement by bagasse ash achieved a higher strengths at all test ages i.e. 7 and 28 days, whereas the 10% and 15% replacement of the cement by bagasse ash in the concrete have shown a slightly lower strength. The results were compared with normal concrete; it was observed that the 5% replacement of the bagasse ash shows good results.

Keywords: Sugarcane bagasse ash; Concrete; Strength; Ordinary Portland cement

INTRODUCTION

Concrete is the most commonly used construction material in the world. It is basically composed of two components: paste and aggregate. The paste contains cement and water and sometimes other cementitious and chemical admixtures, whereas the aggregate contains sand and gravel or crushed stone. The paste binds the aggregates together. The aggregates are relatively inert filler materials which occupy 70% to 80% of the concrete and can therefore be expected to have influence on its properties. The proportion of these components, the paste and the aggregate is controlled by; the strength and durability of the desired concrete, the workability of the fresh concrete and the cost of the concrete. Manufacturing of

cement is already causing pollution apart from several pollution caused by different industrial waste , etc. Researchers all over the world today are focusing on ways of utilizing either industrial or Agricultural waste, as a source of raw materials for industry. Aigbodion et al., (2010) suggests this waste, utilization would not only be economical, but may also result in foreign exchange earnings and environmental pollution control. Industrial wastes, such as blast furnace slag, fly ash and silica fume are being used as supplementary cement replacement materials. Committee Board of sugar cane and sugar et al., (2004) has been an attempted to utilize the large amount of bagasse ash, the residue from an in-line sugar industry and the bagasse-biomass fuel in electric generation industry. Aigbodion et al.,

4th International Engineering Symposium - IES 2015

March 4-6, 2015, Kumamoto University, Japan

(2010) mentions how SCBA is usually obtained under controlled burning conditions in the boilers of the cogeneration processes and also Baguant et al., (1995) mentions that when this bagasse is burned under controlled conditions, it also gives ash having amorphous silica, which has pozzolanic properties. Few studies have been carried out on the ashes obtained directly from the industries to study pozzolanic activity and their suitability as binders, partially replacing cement. Therefore it is possible to use sugarcane bagasse ash (SCBA) as cement replacement material to improve quality and reduce the cost of construction materials such as mortar, concrete pavers, concrete roof tiles and soil cement interlocking block. R.Srinivasan et al., (2010) conducted experiment by replacing cement with different percentage of bagasse ash and found out that the upto 10% of replacement the strengths are increased.

The present study was carried out on SCBA obtained by controlled combustion of sugarcane bagasse, which was procured from sugar factory in Kukwada near Davangere. Sugarcane production in India is about 300 MT/year leaving about 10 MT of as unutilized so it left as waste material. This report analyzes the effect of SCBA in concrete by partial replacement of cement at the ratio of 0%, 5%, 10%, and 15% by weight. The experimental study examines the compressive strength, split tensile strength. The main ingredients consist of Portland cement, SCBA, river sand, coarse aggregate and water. After mixing, concrete specimens were casted and subsequently all test specimens were cured in water at 7 and 28 Days.

EXPERIMENTAL DETAILS

Materials

Cement:

Cement is a fine powder, which when mixed with water and allowed to set and harden, is capable of uniting fragments or masses of solid matter together to produce a mechanically strong material. The most common cement is used is ordinary Portland cement. Many tests were conducted to cement some of them

are consistency tests, setting tests, soundness tests, etc.

Cement brand : ACC cement
Type of cement : Ordinary Portland cement
Grade of cement : 43 grade.

Table 1 Composition of Ordinary Portland Cement

Oxides	% By Mass
SiO ₂	20.98
Al ₂ O ₃	5.42
Fe ₂ O ₃	3.92
CaO	62.85
MgO	1.76
Na ₂	0.28
K ₂ O	0.53
SO ₃	2.36
Loss of ignition	1.90

Fine Aggregate:

Locally available free of debris and nearly riverbed sand is used as fine aggregate. The sand particles should also pack to give minimum void ratio, higher voids content leads to requirement of more mixing water. In the present study the sand conforms to zone I as per the Indian standards (IS:383-1970,Reaffirmed 2007).The specific gravity of sand is 2.59.Those fractions from 4.75 mm to 150 micron are termed as fine aggregate.

Coarse Aggregates: The crushed aggregates used were 20mm nominal maximum size and are tested as per Indian standards (IS:383-1970,Reaffirmed 2007) and results are within the permissible limit. The specific gravity of coarse aggregate is 2.67.

Water: Water used in this project is conforming to the requirements of water for concreting and curing as per IS: 456-2000.Water available in the college campus is used.

Sugarcane Bagasse Ash: The sugarcane bagasse consists of approximately 50% of cellulose, 25% of hemicellulose and 25% of lignin. Each ton of sugarcane generates approximately 26% of bagasse (at a moisture content of 50%) and 0.62% of

4th International Engineering Symposium - IES 2015

March 4-6, 2015, Kumamoto University, Japan

residual ash. The residue after combustion presents a chemical composition dominates by silicon dioxide (SiO_2). Inspite of being a material of hard degradation and that presents few nutrients, the ash is used on the farms as a fertilizer in the sugarcane harvests. In this sugarcane bagasse ash was collected during the cleaning operation of a boiler operating in the Sugar Factory in Kukwada near Davangere, located in Karnataka.

Table 2 Composition of Bagasse ash

Oxides	% By mass
SiO_2	67.81
Al_2O_3	19.41
Fe_2O_3	3.85
CaO	4.03
MgO	1.11
Na_2	0.35
K_2O	1.69
SO_3	0.66
Loss of ignition	1.09



Fig.1 Bagasse ash

MIX PROPORTIONING

The mix proportion is done as per IS: 10262-2009 for M20 grade concrete. Different tests were conducted on the materials as per standards before mix proportioning. All the tests are conducted on materials in institution laboratory as per IS standards. The results were as follows.

Table 3 Properties of Fine aggregate.

Particulars	Obtained values
Fineness modulus	2.555
Maximum size	2.36
Specific gravity	2.59
Water absorption	1.3%

Table 4 Properties of Cement

Particulars	Obtained values
Specific gravity	3.10
Fineness of cement by IS sieve method	
a) By hand sieve	7.9%
b) By mechanical sieve	7.6%
Setting time of cement	
a) Initial setting time	30 min
b) Final setting time	285 min

Table 5 Properties of Coarse aggregate.

Particulars	Obtained values
Fineness modulus	2.26
Maximum size	20mm
Specific gravity	2.67
Water absorption	0.8%

Table 6 Properties of Bagasse ash.

Particulars	Obtained values
Specific gravity	2.06
Fineness of bagasse ash by IS Sieve method	
a) By hand sieve	9.6%
b) By mechanical sieve	8.4%

TESTS ON FRESH CONCRETE

SLUMP TEST

Slump test is conducted on fresh concrete to determine the workability of concrete

Table 7:Slump values

W/C Ratio	Type of slump	Slump value
0.45	True slump	0
0.50	-	30
0.55	Shear slump	69
0.60	Collapse	94

Table 7 Final mix proportion for different percentage of replacement

	0% SCBA	5% SCBA	10% SCBA	15% SCBA
Cement, kg/m ³	383.2	364.04	344.88	325.72
Bagasse ash, kg/m ³	0	19.16	38.32	57.48
Water, kg/m ³	191.6	209.34	209.34	209.34
Fine aggregate	673.98	662.2	662.2	662.2
Coarse aggregate	1133.62	1119.46	1119.46	1119.46
Water-cement ratio	0.5	0.54	0.54	0.54

EXPERIMENTAL WORK

In this experimental work, a total of 48 numbers of concrete specimens were casted. Out of these 24 numbers of cubes and 24 numbers of cylinders were casted by replacing cement with bagasse ash replaced by 5%, 10% and 15% for 0.54 water cement ratio. For each replacement 6 cubes and 6 cylinders were cast and its average compressive strength and tensile strength were tabulated for 7 days and 28 days. All the materials used were batched by weight proportions. Concrete were mixed in tray in the laboratory. Before starting mixing the tray was fully washed using potable water and allowed to dry for 5 minutes. The coarse aggregate calculated should be placed first and allowed to mix for a minute. Then sand and coarse aggregate were mixed continuous for 2 minutes in a dry condition. Finally cement, SCBA and remaining water was added and mixing continued until the concrete gets homogeneous. The same procedure was followed for various mixes. 150 mm cube moulds and cylinders of size (100 mm dia and 200 mm length) were used to cast the specimen and a tamping rod was used to compact the concrete. Immediately after casting the specimens were leave for 24Hrs. They were demolded after 24hrs and cured in water under ambient temperature until they were tested.

5. Results and discussion

Determination of Compressive strength & Tensile strength of concrete is very important, because the compressive strength is a criteria of concrete quality.

This strength will help us to arrive the optimal proportion of replacement. The tests are conducted as per IS 516-1959. The strength results obtained from the experimental investigations are shown in tables. All the values are the average of the three trials in each case in the testing program of this study. The test results shown that the compressive strength & tensile strength of the concrete specimens increased as the bagasse ash content increased up to 5%. But when the bagasse ash was replaced at 10%, 15%, of cement, the compressive strength & tensile strength was found to decrease.



Fig.2 Compressive Strength Test



Fig.3 Tensile Strength Test

The strength results obtained for different specimens cured for 7 and 28 days are tabulated below

4th International Engineering Symposium - IES 2015

March 4-6, 2015, Kumamoto University, Japan

Table 8 Strength results of scba concrete at 7 days

SCBA replacement by weight of cement in %	Compressive strength N/mm ²	Split tensile strength N/mm ²
0	14.12	1.38
5	15.33	1.57
10	13.52	1.4
15	7.53	1.1

Table 9 Strength results of scba concrete at 28 days

SCBA replacement by weight of cement in %	Compressive strength N/mm ²	Split tensile strength N/mm ²
0	22.63	2.73
5	23.48	3.06
10	20.62	2.47
15	15.92	1.97

On comparing the above results we can observe that the compressive and split tensile strength of concrete with SCBA replaced 5% shows increased strength than the conventional concrete and for other replacements percents strengths are decreasing.

CONCLUSIONS

The following conclusions are deduced from this study:

- At the replacement of Ordinary Portland Cement by bagasse ash from 5% to 10% results in a better compressive and tensile strength.
- The compressive strength results of the concrete have revealed that the concrete with 5% cement replacement by bagasse ash have shown a compressive strength improvement at 28 days over the control concrete with the 100% Ordinary Portland Cement.
- Partial replacement of cement by SCBA increases workability of fresh

concrete, therefore use of super plasticizers is not substantial.

- The workability of concrete containing bagasse ash decreases slightly as the bagasse ash content increases which is due to the higher water demand of bagasse ash.

ACKNOWLEDGEMENTS

This project is undertaken by the group of four students.I like to thank Pramod H P, Sindhu Rashmi B M and D.Wasambhasaka Rymbai for their help for the completion of project.

REFERENCES

- [1.] Aigbodion, V. S, Hassan, S. B, Ause, T. and Nyior, G. B.: Potential Utilization of Solid Waste (Bagasse Ash), Journal of Minerals & Materials Characterization & Engineering, 9, pp. 67-77, 2010
- [2.] Baguant,K., Properties of concrete with bagasse ash as fine aggregate, In Proc 5th CANMET/ACI Intl. conf. on fly ash, silica fume, slag and natural pozzolans in concrete, Ed by Malhotra VM, USA, ACI SP, (1995)153(18), 315-337.
- [3.] R.Srinivasan , K.Sathiya Experimental Study on Bagasse Ash in Concrete, International Journal for Service Learning in Engineering Vol. 5, No. 2, pp. 60-66, Fall 2010ISSN 1555-9033
- [4]. IS 383 -1970 "Specifications for Coarse and Fine Aggregates from Natural Sources for Concrete", Bureau of Indian Standards, New Delhi.
- [5]. IS 10262 -2009 "IS Method of Mix Design", Bureau of Indian Standards, New Delhi
- [6]. IS 516 -1959 "Methods of Tests for strength of concrete", Bureau of Indian Standards, New Delhi
- [7] IS 456 -2000 "Code of Practice for Plain and Reinforced Concrete", Bureau of Indian Standards, New Delhi

CRITICAL ANALYSIS ON RANKING OF DELAY FACTORS WITH REFERENCE TO THE INDIAN CONSTRUCTION INDUSTRY

C. Rajasekaran¹, Hashim Yousuf² and Gregory D'Silva³

¹ Department of Civil Engineering, National Institute of Technology Karnataka, Surathkal, Mangalore 575025, India. email:bcrajasekaran@gmail.com

² Department of Civil Engineering, National Institute of Technology Karnataka, Surathkal, Mangalore 575025, India. email: hashim_zz@hotmail.com

³ Proprietor, ACE Developers, Mangalore 575003, India. Email: gregords@yahoo.com

ABSTRACT: Experience and literature studies revealed that for a construction project to be considered successful, it should be completed within time and within the budget. The factors that cause time delay are then of critical importance to the profitability of most construction projects. Many researchers, in the literature, have identified the most common problems that affect and cause delays in construction projects. These affect the company's performance and also have a drastic impact on the overall economy of the country. A deeper understanding of these factors is necessary as it is critical to understand which factors are more detrimental to the project than others. From the literature reviews the most common delay causing factors were identified and a questionnaire was prepared. The inputs from the engineers and other experts in the construction industry were then collected. The data was analyzed using the Relative Importance Index and simple percentages. According to the results the most contributing factors were then discussed and recommendations were made in order to minimize and control them. Also this paper can serve as a guide for all parties in construction projects who desire to achieve a competitive level of quality and a time effective project.

Keywords: Delays, Construction Industry, Relative Importance Index, Ranking Survey.

INTRODUCTION

If a construction project is to be considered successful, it must be completed within budget and before the project due dates. Therefore the causes of time delay are of critical importance. In the literature, many authors have identified these factors that affect or cause delays in construction projects and their evaluation have been carried out. But such an exercise has never been undertaken in the Indian scenario. The Indian construction industry is notoriously known for huge time over-runs in projects especially government projects. Construction projects may differ in terms of size, duration, complexity and other dimensions. A delay in the construction industry is defined as non-completion of the project within the specified duration

agreed upon in contract. The common results of delays are

- (i) Increased cost
- (ii) Late completion of project
- (iii) Loss of productivity
- (iv) Disputes
- (v) Termination or abandonment of contracts.

Many researchers agreed that the financial difficulties faced by the contractor and too many change of orders by the owner are the leading causes of construction delay. The construction industry has a very poor reputation when it comes to coping with delays. This is especially great in India, where delay analysis is usually ignored or done subjectively by simply adding a contingency. As a result a majority of the major projects fail to meet the schedule deadlines. Also some factors are obviously

4th International Engineering Symposium - IES 2015

March 4-6, 2015, Kumamoto University, Japan

more severe in their impact on the project than others and a ranking system based on a Relative Importance Index will help us to identify the causes that are perceived to be the most severe.

Literature Review:

There have been a lot of papers on delays in construction projects over the years. Several projects experiencing time and cost over-runs were reviewed by Chidambaram Ramanathan (2009). He has tried to review and evaluate the efforts of his previous authors with an aim to get a deeper understanding about the factors responsible for causing delays in construction projects. The authors identified 113 causes of delays in construction projects and grouped them into 18 groups. All the studies reviewed by Chidambaram Ramanathan et al. were questionnaire surveys where the researchers prepared questionnaires and sent them to engineers and others related in the construction industry. From these studies it was clear that the rankings given by various researchers were not similar. It was also noted that the most delays occur in the package of the project awarded to the lowest bidder. The questionnaires used in these surveys were designed to evaluate the frequency of occurrence, severity and the perceived importance of the identified causes. It was also noted that the groups which are highly relevant do change with time. Although the parties associated with the project agree upon the extra time and cost associated with a particular delay, it is often a big question as to whether the contractor is entitled to that extra cost and time. Delays invariably cause disputes between the contractor and owner and claims usually take time to get cleared at least in the Indian scenario. The time taken to clear the claims usually is a big problem, especially in Indian projects. The most important thing that one must realize here is that if the project gets delayed, everybody loses. If the owners and the contractor do not realize this, it results in a dead lock and in the end the project will suffer enormous time and cost over-runs and might even have to be abandoned. It becomes absolutely crucial that the contractor and the project

management team identify the causes that can affect the success of the project. The probability of these causes occurring and causing the project to go haywire must be understood carefully by the contractors if they are to make a proper bid for the project package.

Shamil G. Naoum et al. (1994) does a critical analysis of time and cost management in traditional contracts. Broadly speaking, the problems during the building process have been considered in relation to:

- (i) Separation of design from construction
- (ii) Lack of integration
- (iii) Lack of effective communication
- (iv) Uncertainty
- (v) Changing environment, and
- (vi) Increasing project complexity.

These, together with economic changes (e.g. inflation and recession), have led construction professionals and the industry to offer alternative methods of building procurement, including management contracting, and design and build, and project management.

From the literature reviews it was clear about the impacts of delays in construction projects and the associated time and money loss to all the stakeholders involved. The most basic reasons being an improper understanding of the factors that cause these delays in construction projects. In the Indian scenario, where planning is not given sufficient importance, delays and over-runs tend to become a common occurrence. It was important to understand the impact of these delay causing factors in the Indian scenario, and also imperative that the factors be ranked so that planners can get a fair idea about the factors they have to look out for in the Indian scenario.

Methodology:

This study aims to find and rank the factors that cause time over-runs in construction projects in India. A detailed literature review gave the most common categories of factors causing delays in projects. By combining the inputs from professionals in the construction industry, these factors can then further be reduced

4th International Engineering Symposium - IES 2015

March 4-6, 2015, Kumamoto University, Japan

to the ones most prominent in the Indian scenario. A detailed questionnaire survey was prepared. The factors that cause delays in projects as obtained from the literature reviews were divided into categories. The participants in the survey were asked to rate the severity of these factors. From their inputs the factors were then sorted out based on their Relative Importance Index. From this index we get a fair idea of the factors which tend to cause the most delays in projects. The Relative Importance Index of these factors are then calculated using the weighted average method. This helps to rate which factor is considered the most severe in the group and on the whole list of factors. From these survey results we will get a greater understanding of factors which we are supposed to avoid from a project management perspective in order to avoid time over-runs in the project.

The Relative Importance Index of each of the factors are calculated using the following formula

$$\text{Relative Importance Index} = \frac{(n_1 \times 1) + (n_2 \times 2) + (n_3 \times 3) + (n_4 \times 4) + (n_5 \times 5)}{\text{Total Number of respondents}}$$

n1: Number of respondents who checked "Very little effect"

n2: Number of respondents who checked "Little effect"

n3: Number of respondents who checked "Average effect"

n4: Number of respondents who checked "High effect"

n5: Number of respondents who checked "Very high effect"

The results from these surveys are tabulated and discussed in detail in the proceeding chapters. All the factors which were selected for the questionnaire survey were categorized into the following 7 groups.

(i) Consultant related factors

(ii) Contractor related factors

(iii) Equipment related factors

(iv) External factors

(v) Labour related factors

(vi) Materials related factors

(vii) Owner related factors

Survey Results:

The questionnaire survey was distributed to various industry experts and engineers.

Crucial Factors

From the survey conducted, the most crucial factors as perceived by the industry experts were found out. These are the factors which were considered by the industry experts to be the most contributing towards the time over-runs occurring in projects. Crucial factors are showing in the figure 1 with their relative important index.

Delay in payments is the most crucial factor as indicated by literature reviews and the survey itself. It falls in the owner category as it is the direct result of the actions of the owner. The owners must realize that they are the people who stand to lose the most if the project goes haywire. This is a common occurrence in government projects where the payments regularly gets tangled up in bureaucratic procedures.

The next crucial factor was the Shortage of equipment. This falls in the equipments category, but is the direct responsibility of the contractor. The prime reason however being that the contractor not being self-sufficient in the case of equipments. If he depends on others to procure his equipment, this can happen regularly on the site. Also the contractor dividing his equipments among all his projects in an inefficient way can result in this.

Ineffective planning and scheduling comes under the consultant category. Ineffective planning and scheduling means an incompetent project team, which also comes in the most crucial factors. Ineffective planning and scheduling as pointed earlier can lead to unrealistic time

4th International Engineering Symposium - IES 2015

March 4-6, 2015, Kumamoto University, Japan

tables and schedules which cannot be met by the contractors undertaking the project.

The next factor which is poor financial control on the site also is a result of the incompetency of the contractor. The contractor must realize that poor financial control on site means that he is eating away his own profits. Also another crucial factor was the poor site management and supervision. This indicates a general incompetency on the contractor side. This can further lead to claims and disputes between the contractor and owner which can result in delays to payments for the completed work which is the most crucial delay causing factor.

Conclusion

Time over-runs are a very important aspect from the project management perspective. It must be avoided at all costs. However for this a thorough understanding of the factors that can cause time over-runs in projects must be known. The survey provided us with a good idea about the factors that are perceived to be the most serious culprits in causing delays in the Indian scenario.

Future scope of work

From the literature reviews it was clear that the factors that were considered to be the most severe in terms of causing delays to projects keeps changing. With new advances in technology and the usage of better construction practices, some factors will become obsolete while others may contribute more. Also the sample selected for the survey can be increased to get a more clearer idea about the delay causing factors in the Indian construction industry.

REFERENCES

- [1] Akinci, B., and Fischer, M. (1998). "Factors Affecting contractor's risk of cost overburden." *J. Manage. Eng.*, 14(1), 67–76.
- [2] Alkass, S., Mazerolle, M. and Harris, F. (1994). "Construction delay analysis techniques", *Journal of Construction Management Economics*, 14 (5) 375–94
- [3] Ashan, K., and Gunawan, I. (2010). "Analysis of cost and schedule performance of international development projects." *International Journal Project Management*, 28(1), 68–78.
- [4] Shamil G. Naoum, "Critical analysis of time and cost of management in traditional contracts", *Journal of Construction Engineering and Management*, ASCE, 1994.120:687-705.
- [5] Chidambaram Ramanathan, SP Narayanan and Arazi B Idrus, " Construction Delays causing risks on time and cost – A critical review", (Universiti Teknologi Petronas, Malaysia), 2009

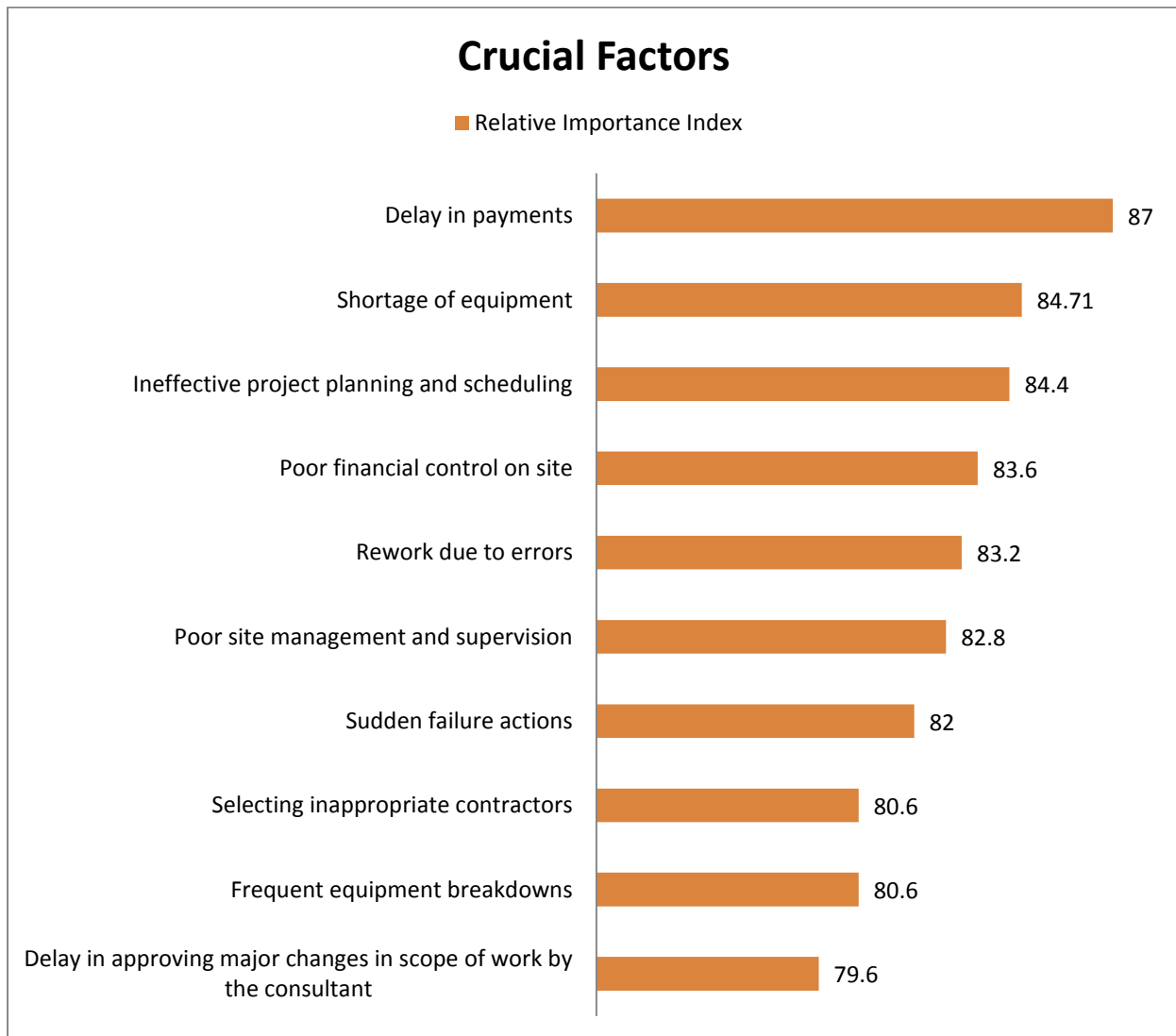


Fig.1 Relative Important Index for crucial factors

Procurement System Integrated With Building Information Modelling (BIM)

C. Rajasekaran ¹, A. Girish Baburao ² and B. Madhukar ³

¹ Department of Civil Engineering, National Institute of Technology Karnataka, Surathkal, Mangalore 575025, India. Email:bcrajasekaran@gmail.com

² Department of Civil Engineering, National Institute of Technology Karnataka, Surathkal, Mangalore 575025, India. Email:girishppt@gmail.com

³ Consulting Engineer, MR Consultants Ltd, Mangalore 575003, India.
Email: madhukar08@gmail.com

ABSTRACT: Economic growth of any nation is signified by its development in infrastructure. However, larger investment on infrastructure postulates construction and consequently for construction engineers and technicians. But the strength of skilled manpower has been consistently and substantially going down. Some estimates reckon as 16% of total cost of project is for procurement; whereas it accounts for 22% if we also conceive monitoring and indirect costs. Moreover all the projects protract a lot of risk. This paper deals with development of standard contract procedure along with appropriate procurement route; which when incorporated with BIM promotes transparency and collaboration between client and players; thus reducing wastage of resources at all levels of procurement system. This new system has been examined with few case studies for on-going projects and survey with construction personnel. It was thus incurred with extravagant benefits to stakeholders there to savings in time, capital and resources; further more subduing the risk.

Keywords: Procurement Model, Building Information Modelling (BIM), Risk Assessment, Construction Survey

BACKGROUND

The construction industry is posited as an economical backbone for any nation because it accounts 7-10 percentage of the Gross Domestic Product, Winch (1996), Voordijk et al. (2000). But this industry has always been affected by the uncertainties, complexity and various pressures at different levels of project. Due to which it has always been prostrated to its inefficiency. As per the report of Construction Industry Institute (CII) it is stated that construction industry produces twice the waste of manufacturing industry, Chuck Eastman et al. (2008). Hence resulting to time and cost over runs signifying low productivity. Furthermore poor quality of work is ascertained which falls short of customer satisfaction. Thus all the above factors have increased the

need for cooperation among different stakeholders or players of the project. Traditionally, relationships are very competitive and adversarial in the construction industry Cheung et al. (2003). If these problems are affected to a large extent, due to the customary procurement procedures; it may potentially induce many problems in all stages of the buying process, Eriksson and Laan, (2007). Therefore, procurement procedures for coaction are one such fundamental area which can not only conduce but also improve the governance of the project substantially. Thus in order to achieve successful governance of construction projects a holistic and systemic approach to procurement procedures is crucial, Cox and Thompson, (1997), Eriksson and Pesamaa, (2007).

After assessing all the models of procurement authors have developed a new testable procurement route where the players are redeemed to have an ameliorate relationships and genial cooperation. To be more effective evincing using computer aided approach i.e. BIM is proved to be more beneficiary in a procurement system.

NEW PROCUREMENT MODEL (PCP)

This procurement model has been entitled as "Project Contemplating Panel" (PCP). In this system the client will first chose an architect who will be preparing the schematic design and thereafter relies entirely on a project management consultancy (PMC) who will undertake the work as per Guaranteed Maximum Price (GMP) contract. This PMC along with the architect will be responsible for selecting the Design consultant in order to avoid the build ability problems whose payment modality will be percentage of total cost of project. As per the design, PMC will

prepare the documentation and the scope of work to be done. In order to carry the execution he will be opting for a main contractor as per selective tendering and further negotiating for awarding contract. The main contractor will open the tenders by dividing the work to the sub-contractors based on their expertise for a lump-sum payment. But what is different when compared to contemporary procurement models is that; it comprises of a PCP whose payment modality would be fixed salary; which is a jury of 3 members each one representing the design consultant, client and the main contractor. Moreover this component is termed as heart of the procurement system. In addition to this any project is subject to three important parameters for its completion i.e. to required quality, within stipulated time and optimum capital. But in addition it also considers as completion of project with maximum productivity.

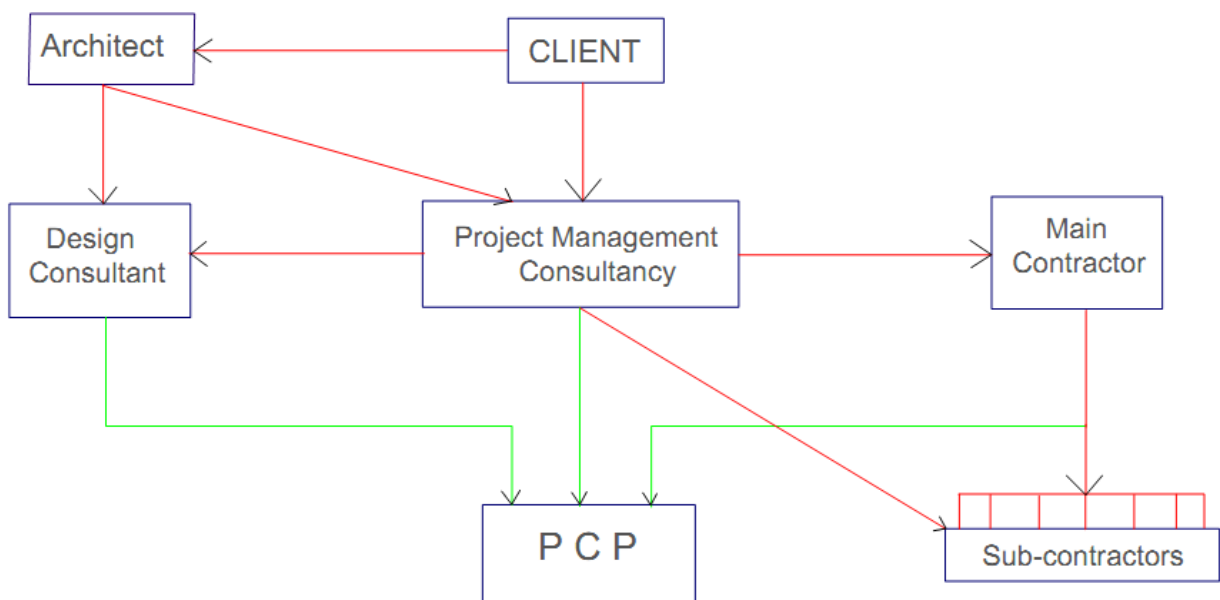


Fig.1 Flow chart of PCP based Procurement system

PCP INCORPORATED WITH BIM

The various elements of any construction project are drawings and specifications, equipment's used, bill of quantities (BOQ), planning and scheduling, allocation of resources, etc. All these factors are subjected to have some coefficient of misconstrue. This divagation is much

higher in infrastructure projects where the resources are more exploited compared to small scale industries. Such inevitable transfer of data may lead to non-performance of project due to conflicts between contractor, consultant and client. Therefore it is important to have software which can encounter problems like

4th International Engineering Symposium - IES 2015

March 4-6, 2015, Kumamoto University, Japan

clashing of components (structural or non-structural), carelessness in design, misreckoning of BOQ, etc.

Role of BIM

BIM consists of various models as mentioned below in table 1. So on incorporating it with PCP following are the advantages:

- a. It is easier for architect/design consultant to identify the more queer and conciliatory design for different methods of construction.
- b. It could identify the specification automatically using Master Format, CSI Uni Format and Omni Class.
- c. It sights the scope of value engineering (completing the project within the budget without wastage of resources) using 3D simulations and visualize the constructability.
- d. It can calculate the BOQ as per geometrical configuration and can calculate the cost. Moreover it also shows the relation between the information of time and cost. Automatically schedule (4D) and cost (5D) table can be updated.
- e. Life cycle considerations i.e. building sustainability analyses (6D) of harnessing solar energy, savings in energy, reduction of carbon content, etc. This can also

look after the characteristics required for LEED

- f. BIM master model consists of various other models as mentioned in table 1 which can be modelled individually. These models can then be integrated into the master model by Web Meeting. Thus enhancing the co-operation between the players.
- g. Using a BIM master model we can also detect the clashes between the components with the help of different variation in colours.
- h. This software has the ability to store a lot of knowledge along with the progress of project life-cycle.

Table 1 Types of BIM models

Type of BIM Model	Application
Site model	Land, Buildings, Landscape, etc.
Architectural model	Walls, Floors, Roofs, etc.
Structural model	Structural systems
MEP models	Mechanical, Electrical, Plumbing
FP model	Fire Protection model
Speciality models	Equipment, Finishes, temporary construction-Scaffolding, Form work, trenching, etc.



Fig. 2 Ranked benefits of BIM adoption, Open BIM Network, (2012)



Fig.3 Ranked feedback to industry, Open BIM Network, (2012)

PCP PROCUREMENT-METHODOLOGY

The primary work in this procurement constitutes is preparing a BIM estimate by the PMC with respect to time, cost, quality and productivity. Thereafter the PMC will invite some selective contractors for tendering (not more than six). All these tenders will be assessed for technical content of doing the project. The top four technical bids will be negotiated and some grading will be done for awarding the project to an appropriate contractor. Thus the grading allotted is based on four basic objectives of construction namely cost, productivity, time and quality. Each of these objectives will be carrying equal points and the contractor with highest grade will be allotted the project. Thus all the elements of grading have been defined accordingly:

Cost Factor and Time Factor

These factors have been evaluated to check how realistic the bids have been in terms of time and cost. It comprises of a step by step procedure:

- Estimation as per the PMC (O)
- Calculating the mean (M) and standard deviation (S) of the contracting bids.
- Now there are two cases whether the difference between the M and O (D) may or may not be greater than S .
- If the value (D) is greater than S ; then the PMC presumes that bids were not realistic and considers O as the reference bid (A).

- But if the value (D) is less than or equal to S ; then it is presumed that the bids were realistic and considers M as the reference bid (A).
- Reference bid also states that the minimum amount of capital that the PMC would invest on the project also known as Guaranteed Minimum Price ($GM'P$).
- Thus the range of consideration of bid will be from $(A-S)$ to $(A+S)$.
- Cost Factor:** If it is considered that the capital spent for completing project is (C). Now four cases arises of completion of total cost of project:
 - $(C) < (A-S)$: Then the entire profit share will be $(A-C)$ that belongs to the main contractor.
 - $(A-S) < (C) < (A)$: Then the profit share will be in a ratio higher to the main contractor than the PMC.
 - $(A) < (C) < (A+S)$: Then the profit share will be in a ratio higher to the PMC than the Main contractor.
 - $(C) > (A+S)$: Then the PMC will not bear any capital exceeding and it has to be paid by the contractor himself.
- Time factor:** If time required for completing the project is (T). Now the maximum time that should be allotted for completion of project is $(A+S)$. Thus there could be three

4th International Engineering Symposium - IES 2015

March 4-6, 2015, Kumamoto University, Japan

different time estimates that can adhere:

- i. (A-S): This can be the minimum time required for completion of project.
- ii. (A): This is the mean time that can be expected to complete the project. If the work does not complete within this time a cautionary message is provided to the main contractor by the PCP.
- iii. (A+S): If the work exceeds the maximum limit then the security deposit will not be refunded. Moreover he will be exercised with heavy duties as decided by the PCP.

Thus based on the above two factors negotiation will undergo between the PMC and the main contractor.

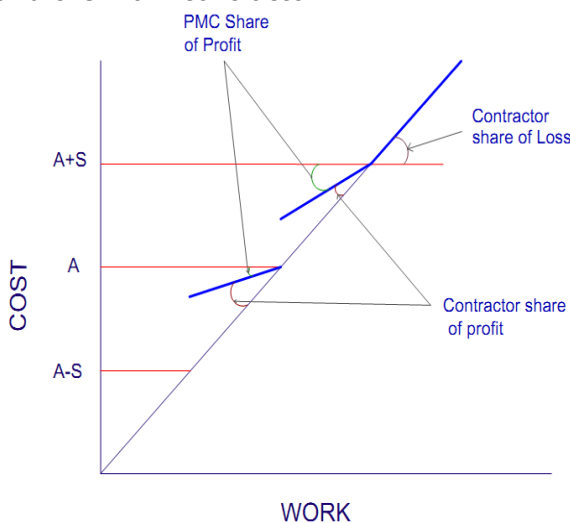


Fig.4 Role of Cost factor in PCP

Productivity Coefficient (PC)

It implies that how optimised are the resources i.e. equipment and man power being used. Author defines this considering the principle that no work pressure should be given; but he should be able to get the work done i.e. possible by the labour to his capability when works for 8hrs a day. This can be stated as the time required to complete a process of work in standard using a particular resource should be well defined. Thus considering a factor of safety (1.25 as considered by author) time required for completing the given work done can be known. In simple words it is

calculated as the ratio of the actual work done to the factored estimate of work done.

Quality Coefficient (QC)

This coefficient is to determine the clients past experience in similar projects. It will be assessing the project for time, cost and quality parameters. After the end of each project government should give some grading to each project based upon its deviation from the estimate. If there are any disputes for which contractor was liable then negative grades should be given.

ROLE OF PCP

The main objective of PCP is:

- a. To check whether the work is going as per the required schedule; if not find out the reasons and penalizes the stakeholder, liable for it.
- b. To solve the disputes whenever encounters and does not take any time for arbitration. As he is thorough with the sequential activities from the signing of contract.

In order to meet the first objective daily schedule of work (DSW) is to be made in cross with its daily progress report (DPR). If there is any delay implies that it lacks in productivity coefficient. In such cases PCP has a vital role to play which will analyse the factors of low productivity.

If the contractor is liable for low productivity then he will be given three weeks time to complete the work or else he has to pay the penalty within one week. In order to avoid the cash flow issues the amount will be deducted from the security deposit. But if the delay is prevailing and contractor is neglecting the penalties; the point where the contractor has already been penalised with more than seventy percentage of security deposit tends the contract to be terminated. If a contractor amends over the delay and copes up to the normal schedule then all the penalties will be cancelled.

CONCLUSIONS

After the entire research authors have come to a conclusion that BIM is expensive software when purchased for the first time. But can be implemented for public

4th International Engineering Symposium - IES 2015

March 4-6, 2015, Kumamoto University, Japan

procurement projects; because thereafter it can be used for several projects in future. In construction survey it was found that the construction personnel lack in knowledge of BIM. Hence here it is the duty of government to train the personnel. This may lead to incurring huge profits in future. BIM preponderates the drawbacks with its benefits.

As the contemporary procurement models when incorporated with BIM; it thus becomes poor in management. Hence author has developed PCP model of procurement which can have a strong base over management; and scope of completing the work within stipulated time and cost with optimum productivity and quality.

It was also observed that as the BIM models were only accepted by the PMC from the main contractors; it becomes pretty easy job to decide whose analysis is more realistic without any burden of work.

FUTURISTIC APPROACH

The software industry has to be incorporated furthermore in construction industry. In order to reduce the further more complexity and time span of procurement process; E-Procurement should be done along with PCP which is again integrated with BIM.

REFERENCES

- [1] Winch G (1996), Contracting Systems in the European Construction Industry: A Sectoral Approach to the Dynamics of Business Systems. IN KRISTENSEN, R. W. A. P. H. (Ed.) The Changing European Firm: Limits to Convergence. London, Routledge.
- [2] Voordijk, et al. (2000), Changing Governance of Supply Chains in the Building Industry: A Multiple Case Stud, European Journal of Purchasing &Supply Management, 6 (3-4), 217-225.
- [3] Cheung, et al. (2003), Behavioral Aspects in Construction Partnering, International Journal of Project Management, 21 (5), 333-343.
- [4] Eriksson, P. E. and Laan, A. (2007), Procurement Effects on Trust and Control in Client-Contractor Relationships, Engineering, Construction and Architectural Management, 14 (4), 387-399.
- [5] Eriksson, P. E. and Pesämaa, O. (2007), Modelling Procurement Effects on Cooperation, Construction Management and Economics, 25 (8), 893-901.
- [6] Cox, A and Thompson, I (1997), Fit for Purpose Contractual Relations: Determining a Theoretical Framework for Construction Projects, European Journal of Purchasing and Supply Management, 3 (3), 127-135.
- [7] Chuck, Eastman et al. (2008). BIM Handbook: A Guide to Building Information Modelling for Owners, Managers, Designers, Engineers, and Contractors, John Wiley & Sons, Inc., New Jersey.

Lime fly-ash soil bricks

**Anvin Sebastian¹, S. Latheswary², C. Rajasekaran³ and
Shankarnarayanan Kotian⁴**

- ¹ Department of civil Engineering, National Institute of Technology Karnataka, Surathkal, Mangalore 575025, India. Email:anvinsebastian@gmail.com
² Department of Civil Engineering, College of Engineering, Trivandrum, Thiruvananthapuram, Kerala 695016, India. Email:lathahayagreev@yahoo.co.in
³ Department of civil Engineering, National Institute of Technology Karnataka, Surathkal, Mangalore 575025, India. Email:bcrajasekharan@gmail.com
⁴ Consulting Engineer, Mangalore, India, Email: kotianshankarnarayanan@yahoo.com
-

ABSTRACT: The country consumes about 180 billion tonnes bricks, exhausting approximately 340 billion tonnes of clay every year, raising concerns about excessive consumption of soil for the production of massive amounts of bricks. Fly ash accumulating as waste product can cause serious environmental problems. Hence its use as construction material can not only reduce its adverse effect on environment but also can act as effective means of disposal of this waste material from thermal power plants. Fly ash bricks were studied in a detailed manner. Various properties of constituent materials used, properties of bricks were studied. The use of fly ash in various fields was studied from various journals. Various mixes were prepared with different proportions of lime, fly ash and soil. The properties such as compressive strength, percentage of water absorption were determined using standard test procedures and feasibility of its use were analysed and a comparison was done.

Keywords: compressive strength, water absorption, feasibility

INTRODUCTION

The ever developing construction industry requires replacement of costly and scarce conventional building materials by innovative, cost effective and environment friendly alternate building materials. The use of clay for brick construction has led to huge consumption of soil. The country consumes about 180 billion tonnes bricks, using up approximately 340 billion tonnes of clay every year. The use of fly ash for brick manufacture can solve various problems associated with disposal of fly ash and reduce its harmful effects on environment. For fly ash bricks to be used in construction, they must have properties such as strength and other properties similar to that of burnt clay bricks. Fly ash is a heterogeneous material. Silicon Dioxide (SiO_2), Aluminium Oxide (Al_2O_3), Iron Oxide (Fe_2O_3) and occasionally

Calcium Oxide (CaO) are the main chemical components present in fly ash. Two classes of fly ash are defined by ASTM C618: Class F fly ash and Class C fly ash. Nearly 65% power in India is generated through Thermal Power Plants (TPP). The high ash content of Indian coal (30% to 40%) is contributing high volume of fly ash.

OBJECTIVES

Objectives of the present study are:
To determine the strength and water absorption characteristics of lime fly ash soil bricks.
To compare the properties of lime fly ash soil bricks with burnt clay bricks.
To determine the optimum composition of the lime fly ash soil bricks.

LITERATURE SURVEY

In the research article presented by Kitzume et al. (1996), the cost

4th International Engineering Symposium - IES 2015

March 4-6, Kumamoto University, Japan

effectiveness of fly ash and its feasibility in using it as a construction material has been studied. The study has revealed that fly ash could be used as a fill material for water front structures and also as a low cost, light weight, self-hardening construction material for various applications in port and harbour areas. Naik et al. (2010) conducted a further study on the feasibility of fly ash, which explains the effect of using gypsum on fly ash and lime. The slow chemistry of fly ash and lime could be manoeuvred by tapping the "ettringite" phase to its threshold limits through sufficient limit of gypsum.

A study on the mechanical properties of fly ash bricks with various fibres has been carried out by Akthar et al. (2010). It has been reported that the compressive strength of plain fly ash bricks (FAB) and treated fly ash bricks (TFAB) increases linearly reaching maximum with 5% coarse sand and 15% sand combination with 10% cement. The addition of lime enhanced the cementitious property of fly ash and the use of fibres with lime improved the strength as well as the mechanical properties of the brick. Also when the amount of treated fly ash has been changed with respect to the stone dust and sand replacement, the compressive strength increased to maximum, nearly close to Indian standard first class bricks at 25% stone dust-sand combination with 50% treated fly ash. Studies conducted by Lopez et al. (2011), suggest that additional fly ash and hemihydrate gypsum improve the mechanical properties of lime fly ash bricks.

Studies have revealed that, compared to conventional clay bricks, fly ash bricks have greater compressive strength (about 40%-80% greater than conventional clay brick strength), and almost 10% lighter than normal bricks. Also the bricks have proved to be energy efficient, environmental friendly and cost effective (Christy and Tensingb, 2011; Mistry et al., 2011). Another study conducted by Mistry et al. (2011) has emphasised on the significance of FAL-G bricks, which are composed of fly ash, lime and gypsum, and concluded that these bricks have greater strength and are more

economical compared to normal burnt clay bricks. The research work also describes the use of rap-trap bond in FAL-G brick masonry prism test study. Rushad et al. (2011) conducted experiments to study the strength and water absorption characteristics of Lime Fly Ash Soil (LFAS) bricks. The tests were conducted on hand moulded and pressure moulded fly ash bricks. It has been reported that none of the LFAS bricks satisfied all the requirements of Indian Standard code (IS: 12894-2002), while lime fly ash bricks of proportion 40:60, satisfied the provisions in respect of strength.

METHODOLOGY

Raw Materials:

Fly ash for the present investigation was procured from HitecFlyash, Tuticorin, TamilNadu and was of Class F. Lime manufactured by Sankar cements were used and of specific gravity 2.65. The soil was obtained from Thiruvananthapuram region in Kerala. The specific gravity of the soil was 2.62. Its liquid limit, plastic limit and plasticity index were 20%, 0%, 20% respectively. The modular brick samples of size 190mm x 190mm x 90mm (IS: 12894-2002) were cast in the laboratory using lime (L), fly ash (FA) and soil(S) in various proportions as presented in Table1.

Table 1 Arbitrary proportions of mix adopted

Sl. No.	Designation	% Lime	% Fly ash	% Soil
1	LFAS1	10	80	10
2	LFAS2	15	80	5
3	LFAS3	20	60	20
4	LFAS4	25	70	5
5	LFAS5	30	65	5
6	LFA1	20	80	0
7	LFA2	40	60	0

Needle vibration was used in each of the mixes. The green bricks were air dried for 48 hours and then placed in hot air oven at 100° C for 24 hours. The mixing was done uniformly in all the mixes. About 6 samples of each composition were considered and average values are given Table 2 and Table 3.

4th International Engineering Symposium - IES 2015

March 4-6, Kumamoto University, Japan

TESTS CONDUCTED

Water absorption test: The dried specimen of weight (W_1) was completely immersed in clean water at a temperature of 27 ± 2 °C for 24 hours. The specimen was then removed and any trace of water was wiped out using a cloth and it was weighed (W_2). Water absorption after 24-hour immersion in cold water is given by the following formula and the results are given in Table 2. The IS specification states that water absorption of bricks must not exceed 20%. The water absorption is determined by

$$\text{Percentage water absorption} = \frac{W_2 - W_1}{W_1} * 100 \quad (1)$$

Table 2: Results of water absorption test

Designation of sample	Percentage water absorption (%)
LFAS1	22.7
LFAS2	19.57
LFAS3	16.9
LFAS4	9.62
LFAS5	17.76
LFA1	17.83
LFA2	14.06

Compressive strength test:

i. The specimen was placed with flat faces horizontal between two plywood sheets and centred carefully between plates of testing machine.

ii. Load was applied axially at a uniform rate 14 N/mm^2 per minute till it failed. The maximum load at failure was noted. Though eight specimens were cast under each category, some specimens have lost their shape after curing and accordingly the available bricks (six in all cases reasonably) having perfect shapes were tested. These observations giving reasonably consistent values are presented in Table 3.

The bricks of class designation 5 can be used in masonry constructions.

Table 3: Compressive strength of LFAS bricks

Designation	Compressive strength(N/mm^2)
LFAS1	1.16
LFAS2	0.97
LFAS3	7.8
LFAS4	5.93
LFAS5	2.92
LFA1	2.24
LFA2	5.26

DISCUSSIONS

It is evident from table 3 that except LFAS1 (10:80:10), all other samples satisfy the requirements for water absorption as mentioned in IS 12894-2002. The least water absorption is shown by LFAS4 (25:70:5). It can also be seen that seen that percentage water absorption decreases with increase in lime content for LFAS bricks except LFAS5 (30:65:5) which may be due to the low soil content.

Table 3 shows the average compressive strength of LFAS bricks of different mixes. From the chart, it is see that LFAS1 and LFAS2 are very weak in compression. Mixes LFAS4 (25:70:5), LFAS3 (20:60:20) and LFA2 (40:60), have compressive strength greater than 5 MPa. Bricks having fly ash content in the range of 60%-70% have high compressive strength. LFAS5 (30:65:5) has comparatively low compressive strength, this could probably be due to very low soil content. From this, it is also clear that by increasing the lime content in LFA bricks there is a tremendous increase in compressive strength. By studying the table, we see that LFAS3 has the highest compressive strength and fall under class 7.5 bricks while LFAS4 and LFA2 falls under class 5 bricks.

From the present study the following conclusions are made

- Compressive strength of LFA bricks increases with increase in lime content.
- Most of the LFAS and LFA bricks satisfy the water absorption criteria.

4th International Engineering Symposium - IES 2015

March 4-6, Kumamoto University, Japan

- Bricks prepared with lime: fly ash: soil in the ratio 20:60:20 give compressive strength equivalent to class 7.5 bricks, which is reasonably good.
- Reasonably good strength, around 5MPa, could be attained with lime: flyash in the proportion 40:60, thereby eliminating the soil completely.

From the study, it can be seen that by using 60% fly ash, bricks similar or better than ordinary burnt clay bricks can be produced. By increasing the lime content to 40% we can completely replace soil from the bricks. No carbon footprints study was done in this project. There is hence further scope for improved studies.

CONCLUSION

Based on the studies conducted it can be inferred that lime fly ash soil bricks prepared by mixing the ingredients in proper proportion are better than ordinary burnt clay bricks with regard to compressive strength and water absorption. Moreover, from the cost analysis it is seen that LFAS bricks are much more economical than ordinary burnt clay bricks. Moreover, LFAS bricks are environment friendly as they use up waste products from thermal power plants. Compressive strength up to 7.8 MPa was obtained and percentage water absorption as low as 9.2% was obtained.

Further fly ash bricks have many advantages like:

- Light weight
- Economical
- Environmental friendly
- Saving of fertile land
- Higher compressive strength

REFERENCES

- [1] Akhtar,N. J.,Alam, J. and Akhtar, M. N. (2010), "An Experimental Study on Fibre Reinforced Fly Ash Based Lime Bricks", *International Journal of the Physical Sciences*, 5(11), pp 1688-1695.
- [2] Akhtar,N. J.,Alam, J. and Akhtar, M. N. (2011), "Bricks With Total Replacement of Clay by Fly Ash Mixed with Different Materials", *International Journal of the Physical Sciences*, 6(12) pp 1245-1249.
- [3] Carlos, Marín, López, José, Luis, Reyes, Araiza, Alejandro, Manzano-Ramírez (2011), "Effect of fly ash and hemihydrate gypsum on the properties of unfired compressed clay bricks", *International Journal of the Physical Sciences*, 6(4), pp 135-146.
- [4] Freeda, Christy, C. and D., Tensingb(2011), "Greener building material with fly ash", *Asian Journal of Civil Engineering*, 12(6), pp 87-105.
- [5] IS 12894: 2002 Pulverised Fuel Ash-Lime Bricks – Specifications (first Revision), Bureau of Indian Standards, New Delhi.
- [6] IS: 1077-1992, Common Burnt Clay Building Bricks—Specification, Bureau of Indian Standards, New Delhi.
- [7] IS: 2720-1983, Methods of tests for Soils—Specification, Bureau of Indian Standards, New Delhi.
- [8] IS: 3495 (Part 1 and 2)-1992, Methods of tests of Burnt Clay Building Bricks—Specification, Bureau of Indian Standards, New Delhi.
- [9] IS: 6932-1973, Methods of tests for building lime—Specification, Bureau of Indian Standards, New Delhi.
- [10] Sameer, Mistry, Samip, Patel and Jayesh, Pitroda (2011), "Fly Ash Bricks Masonry: An Experimental Study", Proceedings of the National Conference on Recent Trends in Engineering and Technology, pp 54-59.
- [11] Tabin, Rushad, S., Abhishek, Kumar, Duggal, S. K., Mehta, P. K. (2011), "Experimental Studies on Lime-Soil-Fly Ash Bricks", *International Journal of the Physical Sciences*, 1(4).
- [12] www.Wikipedia.com
- [13] www.MRFbricks.in

ACKNOWLEDGEMENTS

The project was undertaken by a group of five students under valuable guidance. Special thanks for the help from Aju Elias Basil, Feby Abraham, Ismail PCP, Joseph V. Puthuserry for the completion of this project.

Heavy metal contamination of Soils

B.M. Sunil¹, and Vijaya Vishnu Mayya²

¹ Department of Civil Engineering, National Institute of Technology Karnataka, Surathkal, Mangalore - 575 025, E-mail: bmsunil@gmail.com

² Proprietor, Anubhav Designers, Mangalore, India.

ABSTRACT: The presence of toxic constituents in discarded waste materials and subsequent leaching cause significant damage to the environment and human health due to their mobility and solubility in soil and groundwater resources. Ingestion of heavy metals through drinking water represents a great problem of human health due to its toxicity. The present study investigates heavy metal contamination of soil near a municipal solid waste (MSW) disposal site. The soil near the site was found to be contaminated by heavy metals. About twenty one soil samples analyzed from the waste disposal yard showed that the retention of trace metals varied significantly with sampling locations. The heavy metal concentrations in soil samples analyzed varied from 0.0-0.7 mg/kg for Cadmium, 14.40-127.80 mg/kg for Copper, 12.0-174.00 mg/kg for Zinc, 2.0-659.40 mg/kg for Lead and 1.81-17.20 mg/kg for Manganese. The heavy metals were extracted using Diethylene triamine penta acetic acid extraction technique and analyzed using Atomic Absorption Spectrometry.

Keywords: Soil; Solid waste disposal; Laboratory tests; Heavy metal; Contamination

INTRODUCTION

Contamination of soil and groundwater is an issue of major concern in residential areas which may occur as a result of spillages of hazardous chemicals, dumping of toxic waste, landfills, waste water, or industrial discharges (Javadi et al., 2008). A thorough assessment of the distribution and retention of heavy metals in soil in municipal solid waste (MSW) disposal areas is of great importance in the context of environmental pollution and any systematic hazard evaluation program. The presence of toxic constituents in the discarded waste may get accumulated or retained onto the soil particles. Toxic metals can cause significant damage to the human health and from socioeconomic point of view remediation of the disposal sites may be required. Before remediation work could be taken up data pertaining to the type and extent of heavy metal contamination is required. Therefore there is a need to assess contaminant retention by soils near the waste dump yard. Heavy metal retention by soils have been investigated by several researchers

(Mohamed et al. 1997; Darban et al. 2000; Elzahabi et al. 2001; Yong et al. 2001; Li et al. 2001; Coles et al. 2006). Toxic metals are released into the environment by a wide variety of sources such as waste disposal, disposal of domestic and industrial effluents (Mulligan and Wang 2006). Leaching of heavy metals from unlined landfills could take place due to infiltration of rain water. The transport of the leached metals significantly depends on the hydraulic conductivity of the surrounding soil. Landfill leachate normally contain lead (Pb), copper (Cu), zinc (Zn) due to disposal of various household products. Several studies have demonstrated that land application of waste containing heavy metals will also result in increased plant uptake of heavy metals (Mullin and Mitchell 1994). Yong et al. (2001) studied the retention mechanisms of heavy metals in the soil columns from leaching experiments. Elzahabi et al. (2001) studied pH influence on the sorption characteristics of heavy metal from leaching tests using illitic soil. The results showed that the presence of carbonates in

4th International Engineering Symposium - IES 2015

March 4-6, 2015, Kumamoto University, Japan

the soil increases the retention of heavy metals at high pH and also enhances the buffering capacity of the soil. Li et al. (2001) studied the interaction between heavy metal contaminants and surface forces in order to explain the sorption and desorption phenomena using a mathematical model. Coles et al. (2006), modeled retention of Pb and Cd in soils using Freundlich isotherms from the experimental results of batch tests.

The heavy metal analysis of contaminated soils from the disposal area was carried out using DTPA extraction technique. Table 1 shows the index properties of the typical original lateritic soil. Table 2 and Table 3 show the chemical composition and mineralogical composition of these soils.

Table 1 Index and compaction characteristics of lateritic soils

G _s	Atterberg limits			Grain-size distribution				Compaction characteristics	
	w _L (%)	w _P (%)	w _S	Gravel (%)	Sand (%)	Silt (%)	Clay (%)	w _{opt} (%)	γ _{dmax} (kN/m ³)
2.72	42	24	20	20	69	8	3	12	19

G_s- Specific gravity of soil solids; w_L- Liquid limit; w_P- Plastic limit; w_S- Shrinkage limit; (w)_{opt} - Optimum moisture content; γ_{dmax} - Maximum dry density

Table 2 Chemical characteristics of original lateritic soil

pH of soil, 25 °C	EC of soil solution (µS)	CEC (meq/100 g)	CaCO ₃ (%)	SO ₄ ×10 ⁻³ (%)	Fe ₂ O ₃ (%)	SiO ₂ (%)	Al ₂ O ₃ (%)
5.2	40	9.5	1.0	1	3	72	10

Table 3 Mineralogical composition of soil

Sample	Clay minerals	Non clay minerals
Lateritic soil	Kaolinite and illite	Quartz, goethite, hematite,gibbsite

STUDY AREA

The study area has tropical climate. It receives heavy rainfall (average annual rainfall of 4000mm) during monsoon and high temperature and humidity in summers. The mean temperature varies between 22° C to 36° C. The average relative humidity is very high during June, July and August. The maximum average humidity recorded was 96 per cent in month of July and minimum average relative humidity recorded was 20.5 per

cent in the month of January. The South-West monsoon sets in from June and continues to September. The geology of the area consists of laterite formations. The dumping site chosen for the study (city of Udupi in Karnataka, India) is in use for more than two decades which has an area of 2.2 Ha.

Methodology

All the municipal waste and other debris are dumped at waste disposal yard, which is located at the southwestern side of the

Udupi city. A preliminary survey was conducted to study the topography of the disposal site and its accessibility from different directions. The objective was to obtain soil samples that could be contaminated by the landfill leachate. Twenty one soil samples were sampled from the locations shown in Fig. 1 with

visual inspection of most likely contaminated points. These samples were collected from two depths: one from the surface (0-10 cm) and the other from 20-30 cm deep. The natural soil at these locations being of laterite origin, dark grey soils to black coloured soils could be assumed to be most likely contaminated.



Fig. 1 Soil sampling locations at waste disposal yard

The pH and electrical conductivity of soil samples were determined as per IS: 2720 (Part 26)-1987 by mixing distilled water and soil (3:1 range, and with a one-hour wait before measuring). The organic matter was estimated as per IS: 2720 (Part 22)-1972 (Reaffirmed 1978) using potassium dichromate for digestion and ferrous sulphate for titration. The extraction of heavy metals required for the analysis was carried out using DTPA extraction technique. 25g of soil sieved through IS 2mm sieve was extracted in 50 ml DTPA extractant solution. The extracted samples were collected in PPE bottles of 125 ml capacity that were pre washed thoroughly in 1:1 HNO₃ & rinsed with ultra pure water to eliminate any back ground contamination. All the extracted samples

were analysed using GBC-932 plus Atomic Absorption Spectrometer (AAS). The experimental analysis took place in the laboratories of National Institute of Technology Karnataka Surathkal, (India).

RESULTS AND DISCUSSION

The variation in pH and electrical conductivity of contaminated soil samples are shown in Figs. 2 and 3. The pH of the soil was measured by mixing the soil sample with distilled water in the ratio of 1:3. It is then filtered and the solution was used to measure soil pH. The soil pH from 0-10 cm and 20-30 cm depth at the landfill site was found to vary from 6.9 to 8.1. This variation is significant when the pH of contaminated soil is compared with pH of original lateritic soil. It is observed that the pH of original lateritic soils is acidic. The

acidic nature of soil is mainly due to two reasons. First, leaching of appreciable amounts of exchangeable bases from the soils due to high precipitation. Second, due to the decomposition of organic matter. Increase in soil pH may be attributed due to leachate characteristics Fig. 3 shows the variation in electrical conductivity of soils. The general increase in electrical conductivity of soil might be due to dissolution of soluble salts from the soils due to interaction with leachate.

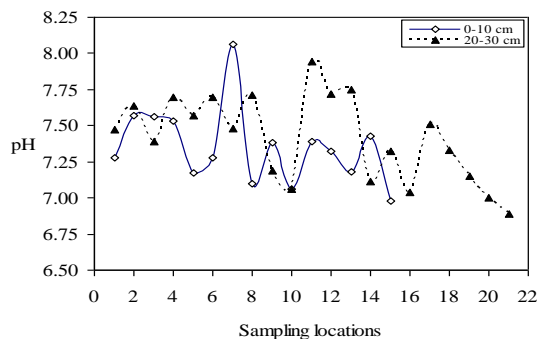


Fig. 2 Variation of soil pH

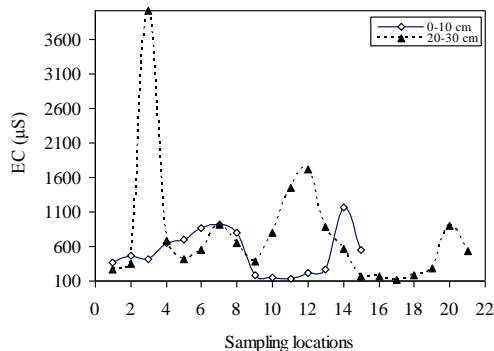


Fig. 3 Variation of EC in contaminated soil samples

The sorption of the contaminant onto the soil is directly proportional to organic carbon fraction. The organic matter content of the contaminated soil samples varies from 4.47 % to 23.58 %. This variation in organic matter of contaminated soils is significant when compared with the organic matter content of original soil. Gidigasu (1976) reports presence of excessive organic matter (above 4%) in soils affect the physical characteristics of soils. The variation of organic matter with depth is shown in Fig. 4.

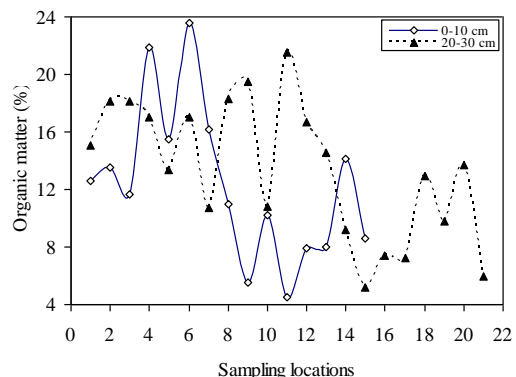


Fig. 4 Variation of organic matter in soil samples

Fig. 5 shows the variation of copper (Cu) with sample locations. It is observed that copper concentrations in 0-10 cm layer and 20-30 cm layer ranged from 14.40 to 127.80 mg/kg. The variation is significant at different locations. However this is less than the background concentration level but the copper content in some samples is near the threshold limit.

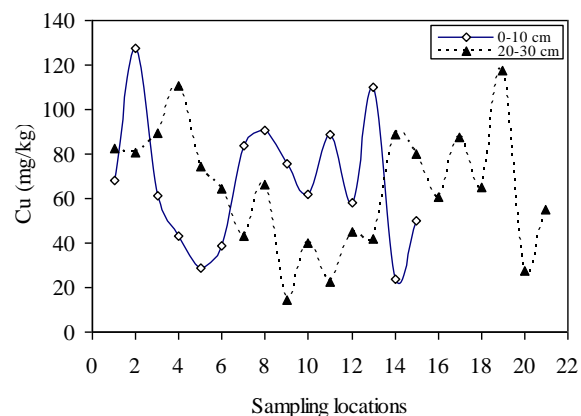


Fig. 5 Variation of copper in contaminated soil samples

Lead is potential source of danger to human health and vegetation. The threshold limit for lead (Pb) in soils as per IS standards is 250-500 mg/kg. The lead content in one sample (sample 7) exceeds limit with very high concentration as 659.4 mg/kg. The dominant mechanisms responsible for accumulation of heavy metal pollutants are sensitive to pH of the immediate environment. Anionic organic content complex the cationic heavy metals into a strong bond not allowing its extractability consequently high organic

matter present in the soil also bind the Pb strongly. The variation of Pb content in soils is shown in Fig. 6. For better representation of values of other samples, Fig. 6 has been modified to exclude sample 7 and is presented in Fig. 7.

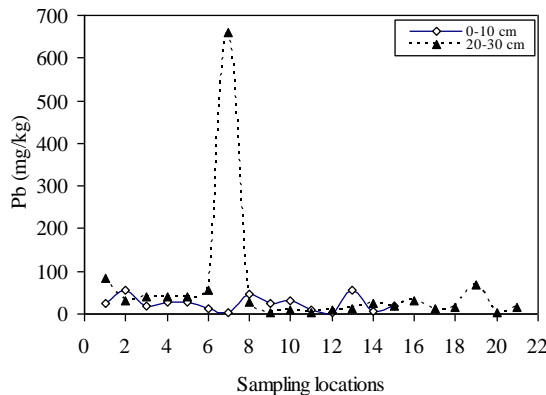


Fig. 6 Variation of lead in soil samples

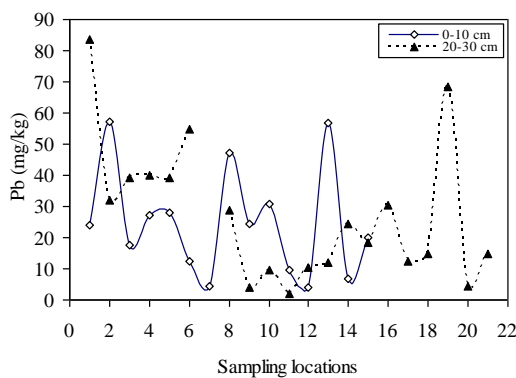


Fig. 7 Variation of lead in contaminated soil samples (excluding sample 7)

The variation of zinc in 0-10 cm soil layer and that in 20-30 cm soil layer is presented in Fig. 8. It is observed that the concentration of zinc is less than the background concentration. Zinc concentrations in the soil layer 0-10 cm and 20-30 cm layer ranged from 12 to 174 mg/kg. Chromium was not detected in any of the extracted samples tested using atomic absorption spectrometer technique.

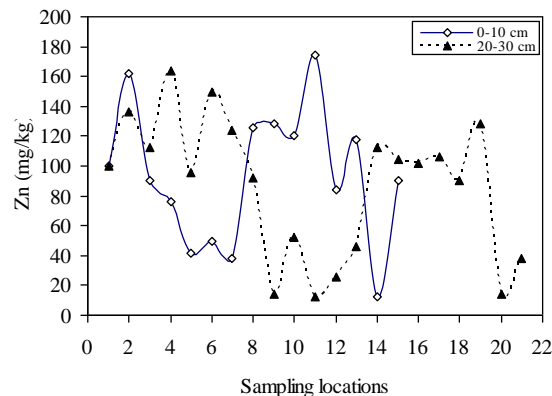


Fig. 8 Variation of zinc in soil samples (excluding sample 7)

Cadmium compounds are used in various applications such as stabilizers in PVC products, colour pigment, several alloys and, in re-chargeable nickel-cadmium batteries. When cadmium containing products are dumped together with household waste it tends to accumulate in soil and groundwater due to leaching. Cadmium in the soil samples analyzed was detected in the range from 0.0 – 0.70 mg/kg. For analyses soil samples with particle size less than 2mm was sieved and extracted with DTPA. The variation of cadmium in 0-10 cm and 20-30 cm layer is plotted in Fig. 9.

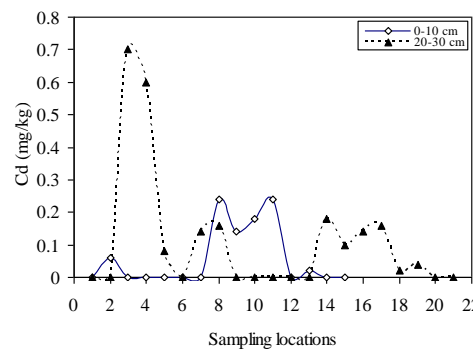


Fig. 9 Variation of cadmium in soil samples

All the soil samples analyzed found to contain manganese with a minimum value of 1.81 mg/kg in 0-10 cm soil layer and a maximum value of 17.20 mg/kg in 20-30 cm soil layer. The variation of manganese with sample location is shown in Fig. 10.

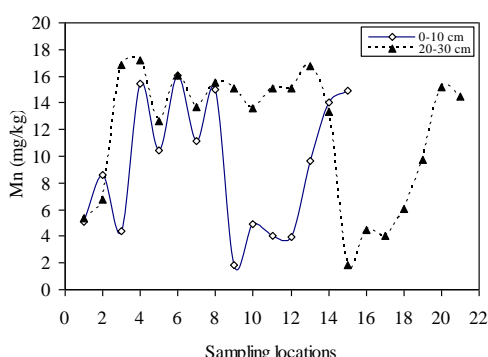


Fig. 10 Variation of manganese contaminated in soil samples.

Summary and conclusions

The capacity of the soils to retain toxic constituents, such as heavy metals, due to percolation of leachate in the dumpsite has been studied in this preliminary work. It is observed that the organic matter content of the contaminated soils is much higher than the original soil. This may be attributed due to leachate characteristics. The contaminated soils showed remarkable increase in pH, EC and organic matter content values. The results of the study show that, heavy metal contamination of soil in the MSW disposal area varies at different sampling points. Since lateritic soils are highly permeable leaching of metals of concern may take place due to very high precipitation. No direct relationship between pH and heavy metal content of soil was observed during this investigation. Chromium was not detected in the soil samples analyzed. In this preliminary work it is observed that at some locations the soil is contaminated with high concentration of lead. Since lead is potential source of danger to human health and vegetation translocation into the food chain through plant uptake or into solution through leachate is possible.

The following are the important conclusions drawn based on the test results:

- i) All the soil samples analyzed from the municipal solid waste disposal yard showed the presence of heavy metal. Some samples showed very high concentration of lead contamination.
- ii) In soil where the fines content is very small the retention mechanism may not be predominant and there is possibility of

heavy metals, being leached out due to percolation of rain water. Hence no significant correlation was observed in the present study between the pH and heavy metal content of soils analyzed.

ACKNOWLEDGEMENTS

The above research work was conducted with the financial assistance (seed money grant) from National Institute of Technology grant (National Institute of Technology Karnataka Surathkal, PO Srinivasnaga, Mangalore – 575025, India).

REFERENCES

- [1] Andreottola, G. and Cannas, P. (1992) Chemical and biological characteristics of landfill leachate Edited by Christensen T.H., Cossu R., and Stegmann R. Landfilling of Waste Leachate (pp. 65-88). E & FN Spon, UK.
- [2] Coles C.A. and Yong R.N. (2006) Humic acid preparation, properties and interactions with metals lead and cadmium. Journal of Engineering Geology, 85, 26-32.
- [3] Darban A.K., Foriero A. and Yong R.N (2000) Concentration effects of EDTA and chloride on the retention of trace metals in clays, Journal of Engineering Geology, 57, 81-94.
- [4] Elzahabi M. and Yong R.N. (2001) pH influence on sorption characteristics of heavy metal in the vadose zone, Journal of Engineering Geology, 60, 61-68.
- [5] Frempong Eric M. and Yanful E. K. (2008) Interactions between three tropical soils and municipal solid waste landfill leachate. Journal of Geotechnical and Geoenvironmental Engineering, 134(3), 379-396.
- [6] Gidigasu M.D. (1976) Physico-chemical characteristics of laterite soils, Laterite soil engineering (pp.178-191), Elsevier Publishing Company, Amsterdam.
- [7] IS: 10500 -2004 Drinking water specification, Bureau of Indian Standards, 239-242.
- [8] IS: 2720 (Part 26)-1987 Methods of test for soils-Determination of pH value, SP: 36 (Part 1) – 1987, Bureau of Indian Standards, 239-242.
- [9] IS: 2720 (Part 22)-1972 Methods of test for soils-Determination of organic matter, SP: 36 (Part 1) – 1987, Bureau of Indian Standards, 258-261.
- [10] Li R.S., Yong R.N. and Li L.Y. (2001) Mathematical prediction of lead removal from carbonate-rich illite. Journal of Engineering Geology, 60, 159-171.
- [11] Mohamed Abdel M.O., Shooshpasha I and Yong R.N. (1997) Diffusion of metal ions in frozen capillary barriers. Journal of Engineering Geology, 47, 1-15.
- [12] Mulligan C.N., Yong R.N. and Gibbs B.F. (2001) Remediation technologies for metal-contaminated soils and groundwater: an evaluation. Journal of Engineering Geology ,60, 193-207.

Hazardous Waste Management

B.M. Sunil¹, and Ranganath Aithal P²

¹ Department of Civil Engineering, NITK, Surathkal, Mangalore-575025, India. E-mail: bmsunil@gmail.com

² Aithal Associates, 2nd Floor, Grace Towers, Bejai-Kapikad Road, Bejai, Mangalore-575 004, India Email: prraithal@gmail.com

ABSTRACT: Increasing quantity of waste generation and its effects on the surrounding environment has led to adopt several safe disposal techniques that are assumed to cause less harm to the environment. Hazardous wastes are considered highly toxic and therefore disposal of such wastes needs proper attention so as to reduce possible environmental hazards. This paper presents general background information on management and disposal of hazardous wastes. It describes the characteristics of different groups or types of hazardous wastes and their disposal methods.

Keywords: Hazardous wastes, Management, Disposal, E-waste.

INTRODUCTION

Environmental management of hazardous wastes has become a major concern as irresponsible dumping of hazardous wastes results in severe environmental impairment (Dutta et al., 2006). The adverse effects of hazardous wastes as well as the significant potential risks posed by them to the life and its supporting systems are increasingly recognized. This is because of increased industrial activity that resulted in generation of increasing volume of hazardous wastes.

There are numerous examples of waste disposal practices in the past when wastes were disposed of without much care to the environment. Until legislation was enacted in the 1970s to regulate waste disposal and protect the air and water from contamination, wastes of all kinds were discarded with little concern for human health and the environment. Hazardous wastes were simply dumped on vacant lots and along roadways (Fig.1). Such disposal practices have led to severe contamination of soil and ground water systems. In certain cases contamination is so extensive that complete cleanup may never be possible. Some of the household items (Fig. 2) may be harmful to living beings

and the environment if disposed of improperly.



Fig. 1 Discarded hazardous waste drums



Fig. 2 Hazardous household items

According to Environmental Protection Agency (EPA), Solid waste includes garbage, refuse, sludge from waste treatment plants, waste from air pollution control facilities and any other discarded

4th International Engineering Symposium - IES 2015

March 4-6, Kumamoto University, Japan

material. Municipal solid waste includes garbage (food wastes), paper, glass, plastics, yard waste and other household items. Until 1960s most municipal solid waste was dumped in open yards called as dump yards (this method of disposal is still practiced in some countries). Due to environmental concern and the passage of solid waste disposal Act in 1965 management and disposal of solid waste have been subject to environmentally strict controls. Currently solid waste is disposed in the engineered containment systems (in the ground) called landfills. In landfills each day load (called reuse) is spread and compacted by appropriate type of rollers and then the reuse is covered with layer of soil.

Hazardous waste is waste that poses substantial or potential threats to public health or the environment. Hazardous wastes can be liquids, solids, gases, or sludges. They can be discarded commercial products, like cleaning fluids or pesticides (Fig.2), or the by-products of manufacturing processes.

EPA began regulating hazardous waste in 1976. In the present scenario management and disposal of hazardous waste is a challenging task. To avoid any significant impact in living organisms or surrounding environment its proper management is crucial. According to Resource Conservation and Recovery Act (RCRA) wastes are described as hazardous if they pose a potential hazard to human health or the environment. According to EPA a waste is also hazardous if it exhibits the characteristics of ignitability, corrosivity, reactivity and toxicity. Once a waste has been identified as hazardous, the proper method for disposing of it must be selected.

HAZARDOUS WASTE CHARACTERISTICS

Wastes that present significant fire hazard, acidic aqueous wastes with $\text{pH} \leq 2$ and basic aqueous wastes with $\text{pH} \geq 12.5$, reactive wastes (e.g. $\text{Na} + 2\text{H}_2\text{O} \rightarrow \text{NaOH} + \text{H}_2$) and wastes that present toxicity are characteristics of hazardous waste. Toxic wastes are of concern because they cause significant hazard to living organisms by

interfering with normal physiological process. The major concern with regard to the disposal of toxic waste on land is contamination of soil and ground water due to environmental leaching. About 10 to 15 percent of wastes produced by industry are hazardous and the generation of hazardous wastes is increasing at the rate of 2 to 5 percent per year (Trehan, 1992).

SOURCES OF HAZARDOUS WASTE

Worldwide millions of tons of solid waste are produced annually. Most of these wastes are produced by chemical/petroleum/metal related industries. Some of the hazardous waste produced by the industries is shown in Table 1.

Table 1 Hazardous wastes produced by Industry*

Industry	Hazardous Wastes
Fertilizers	Sulfuric, nitric and phosphoric acids; sodium hydroxide, ammonia
Electro plating	Toxic metals, cyanide
Iron and steel	Acids (including hydrofluoric acid), bases, phenols, benzene, toluene
Medicines	Toxic metals, organic solvents
Paints	Toxic metals, pigments (chrome yellow),

*Other industries include Electro plating, Insecticides and herbicides, Leather, Organic chemicals, Petroleum refining, Plastics, Power industry, Soaps and detergents, Synthetic rubber, Textiles etc.

As observed from the above table toxic metals and chlorinated hydro carbons are produced by various industries and are of greater concern whenever such hazardous waste are disposed off irresponsibly. Different processes are used by the petrochemical industry in refining crude oil and processing the synthetic organic chemicals needed for manufacturing polymers, pesticides, medicines and other consumer products. All these processes inevitably

4th International Engineering Symposium - IES 2015

March 4-6, Kumamoto University, Japan

produce waste and it has been estimated that 10-15% of them are hazardous.

MANAGEMENT AND DISPOSAL OF HAZARDOUS WASTE

In order to have better control over the management and disposal of hazardous waste 3 policies have been described by National Academy of Sciences, United States -1983. i) Minimize the amount of hazardous waste produced ii) Convert the waste to less hazardous or non-hazardous form iii) isolate in a secure perpetual storage site.

Disposal of hazardous waste in compliance with EPA regulations maybe very costly. Therefore it is better to adopt recycling strategy to reduce or minimize waste production. In order to minimize hazardous waste production process manipulation (during manufacturing stage) may be economical and it is believed that over the years many industries have adopted this technique. As an example, electro plating plants use ion exchange resins to remove the contaminant metal from electro plating baths. Many industries recover chemicals that can be reused, recycled or sold to other industry as a raw material. For example hydrochloric acid (HCl) is recovered from chlorinated waste from pesticide industry to sell it to other industries. Several options are available for better management of hazardous waste but the choices depends on the type of waste to be treated.

OPTIONS FOR DISPOSAL OF HAZARDOUS WASTE

A number of hazardous waste can be successfully treated by using thermal treatment method (incineration). For this to achieve the industry should have adequate air pollution controlling devices to purify the flue gases. At sufficiently high temperature incineration destroys hazardous waste converting them to CO₂, H₂O and various gases. At some point of time the volume of waste is greatly reduced and the energy released can be used either as a source of heat or to generate electricity. Combustible liquid and solid hazardous wastes in petroleum refinery are destroyed by incineration.

Hazardous organic wastes can be treated by microorganisms in doing so it must be ensured that the waste do not contain toxic metals. Another commonly used treatment of hazardous waste is cement based solidification and stabilization. Cement is used because it can treat a range of hazardous wastes by improving physical characteristics and decreasing the toxicity and transmission of contaminants. Most of the medical waste is treated by incineration process.

PERPETUAL STORAGE OF HAZARDOUS WASTE

Treatment of hazards depends on the type of waste. Hazardous waste that cannot be recycled are converted to non-hazardous form must be stored in secured landfills (Fig.3), deep well injection and surface impoundment. Deep well injection (Fig.4) is a liquid waste disposal technology. This alternative uses injection wells to place treated or untreated liquid waste into geologic formations that have no potential to allow migration of contaminants into potential potable water aquifers. Surface impoundment is a lagoon or pond designed to hold waste materials and prevent their escape to the environment.

However none of the above methods provides secure storage for dangerous hazardous waste. Because we are not fully aware of the later consequences arising from such disposal practices.

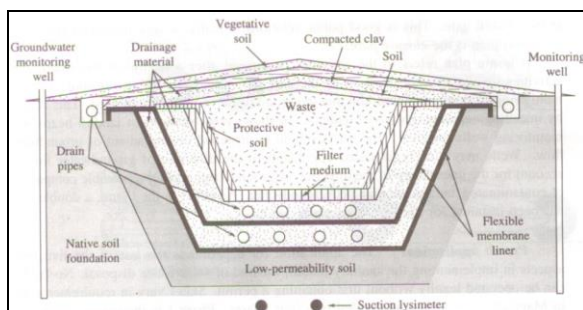


Fig.3 A secured landfill for the long-term storage of hazardous wastes

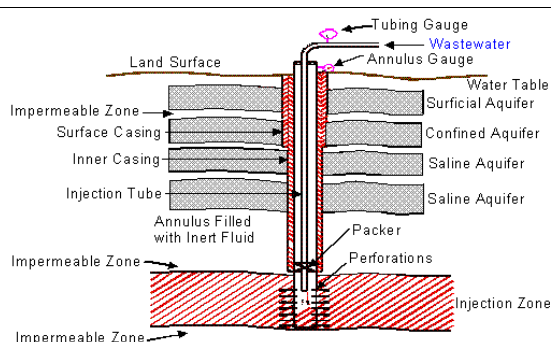


Fig.4 Deep-well injection for the disposal of hazardous liquid wastes

E-WASTE

In the recent years, our dependence on the electronic products has grown significantly, both for domestic and for office uses, and this has resulted in generation of large quantities of electronic wastes (E-waste) all over the world. On an average, E-waste makes up approximately one percent of municipal solid waste (MSW) stream (EPA, USA). Many municipal corporations are facing problems with the proper disposal of E-waste because rapid changes in computer technology attract the people to throw the gadgets of old technology. Obsolete computers, color cathode ray tubes (CRTs) and other electronic appliances form the electronic waste or E-waste. These E-wastes contain hazardous substances, such as lead, mercury, chromium, etc. A television and CRT monitor contains about four pounds of lead on an average⁸. E-waste may contribute high level of Hg contamination in municipal solid waste.

RADIOACTIVE WASTE

Radioactive wastes are hazardous to human lives and environment and require special techniques to dispose of the same. Nuclear power plants and nuclear weapons manufacturing facilities are the principal sources of radioactive waste. The amount of radioactive waste is very small relative to waste produced by fossil fuel and its final disposal is a challenging task. Based on the mode of generation, radioactive wastes are classified into high level waste and low level waste. High level wastes are produced by nuclear reactors and weapon plants. Low level wastes are produced by

hospitals, research laboratories and certain industries.

Technologies for radioactive waste disposal

Disposal methods of radioactive wastes vary depending on whether the wastes are high-level or low-level wastes. Non-hazardous wastes are normally disposed of in landfills. On the other hand landfills are not a better option to store materials that retain their hazardous properties indefinitely. This is due to the fact that all landfills will eventually leak in the long run due to various reasons.

Currently, the recommended procedure for the disposal of high-level wastes is disposal in deep geological formation along with the confinement of the canisters containing the waste. While adopting such techniques the radioactive waste is incorporated into a glass or ceramic material, seal the glass or ceramic product in a corrosion-resistant steel canister and then bury the canister in a concrete vault deep underground in a stable geologic formation.

ISSUES OF CONCERNs

The major issues of concern for hazardous wastes are import (in some countries), illegal dumping sites and in-complete data on generation and disposal of hazardous wastes in the country. In some cases industrial incinerators in use are generally not efficient and are merely a combustion chamber and source of emission of dioxins and toxic substances. According to Dutta et al. 2006, environmentally sound management of hazardous wastes would require Common Hazardous Waste Management Facility (CHWMF) for industrial clusters spread all over the country, as it is not possible to have hazardous waste management facility for each unit, particularly in the case of small and medium scale units.

4th International Engineering Symposium - IES 2015

March 4-6, Kumamoto University, Japan

CONCLUSIONS

Compatible techniques for the management and disposal of hazardous wastes are presented in this paper. The basic policy of any waste management system is to reduce the quantity of waste generated. This is also true with hazardous wastes. Best available options to produce less hazardous waste are process manipulation and recycle and reuse. But the cost is very while adopting these techniques. In developed countries process manipulation (during manufacturing) and recycle and reuse are adopted while maintaining stringent regulations for the disposal of hazardous wastes. Developing countries still have to catch up with these techniques. Also, In developing countries, the thrust on economic development is often given priority to production costs than the best available technology and this results in more wastes generation (inspite of technical knowledge available in the country).

REFERENCES

[1] CPCB, Inventorisation of Hazardous Waste Generating Units in Orissa, Hazardous Waste Management Series : Hazwams / 21/ 2002-03, p93. (2003)

[2] EPA, Electronics: A New Opportunity for Waste Prevention, Reuse and Recycling, <http://www.epa.gov/epr> (2001)

[3] Shantanu K Dutta, U.P. Upadhyay and U Sridharan (2006), Environmental management of industrial hazardous wastes in India, J Environ. Sci. and Engg. Vol. 48(2), 143-150, April 2006.

[4] Trehan, N.C., Environmental aspects of hazardous wastes disposal in India, Environmental impact assessment of developing countries (1992).

[5] USEPA, Electronics : A new opportunity for waste prevention, reuse and recycling, <http://www.epa.gov/epr> (2005).

[6]<https://www.denvergov.org/trashrecycling/TrashandRecycling/HazardousWaste/tabid/438319/Default.aspx>

[7]<http://environment.nationalgeographic.com/environment/global-warming/toxic-waste-overview/>

[8]<http://web.deu.edu.tr/atiksu/ana58/deepwell.html>

[9] www.cpcb.nic.in

Study on unlined rock caverns for storage of crude oil and stability analysis using numerical methods

B.M Sunil¹, Deepthi K. Achar² and Anil S D'Souza³

¹ Department of Civil Engineering, National Institute of Technology Karnataka, Surathkal, Mangalore - 575 025, India, E-mail: bmsunil@gmail.com

² Formerly Department of Civil Engineering, National Institute of Technology Karnataka, Surathkal, Mangalore 575025, India.

³ Consulting Engineer, Mangalore, India

ABSTRACT: A cavern is a large underground structure, lined or unlined, having rock mass as an extra barrier for protection of strategic infrastructure, defence and variety of other purposes. A general study has been done on construction and operation of unlined rock cavern project for storage of crude oil. The underground storage scheme comprises of 4 horseshoe shaped storage caverns each of 20m span and 30m height, 3 parallel water galleries of span 6.5 to 9m and height 6.5m and access tunnel 12m wide and 8m high. In this study based on the type of rock, in-situ stress conditions and construction sequence, construction stages were simulated for water gallery using PLAXIS 3D tunnel, finite element modelling. The displacements closely matched the convergence readings monitored at site and was found to be having ideal confining stresses.

Keywords: Rock caverns, Crude oil, Storage, Stability Analysis, Numerical methods.

INTRODUCTION

Large underground caverns are used for a variety of purposes. These include for hydroelectric projects, caverns for storing liquid or gaseous fuels in unlined or lined caverns, underground sports facilities, water treatment plants, subway stations, military and civil defence installations, underground car parking, aircraft hangars, caverns for conventional or cold storage etc. Such caverns have been excavated in recent years with widths of 20 to 30m and heights of 30 to 40m. With the rock mass as extra barrier, the underground alternative is excellent for protection of strategic infrastructure, defence and civil defence facilities. Underground storages included concepts such as: aquifer storage, saltdome storage, mine storage, depleted oil and gas field, rock cavern storage. In this paper a general study has been done on construction and operation of unlined rock cavern project for storage of crude oil.

SITE INVESTIGATION

Site study and reconnaissance indicates the site had metamorphosed granitic gneiss, also called worked granite at relatively shallow depth. The rock strength from compressive strength result indicates strong to very strong. Table 1 shows intact rock mass properties. From the in-situ stress parameters by hydro fracture tests it was found that for overburden of 68.5 m with density of rock as 27kN/m³: maximum horizontal stress (σ_H)_{max} = 5.84 MPa; minimum horizontal stress (σ_H)_{min} = 2.92 MPa; orientation of the maximum horizontal stress (σ_H) = N150° and k = 2.42. Based on site investigations, horizontal caverns of sizes up to 20 m in span and 25 to 32 m high are envisaged.

Table 1 Intact rock properties

4th International Engineering Symposium - IES 2015

March 4-6, 2015, Kumamoto University, Japan

SI No.	Properties	Result	
1	Uniaxial compressive strength (σ_c)	150-300 MPa	introduced to prevent rockburst conditions near the entrance of access tunnel. This was followed by application of fibrecrete.
2	Density	26~27 kN/m ³	
3	Specific gravity	2.73	
4	Young's modulus (GPa)	40~200 GPa	Construction of water gallery tunnel D-shaped tunnel of size 6.5 m x 6.5 m has to be excavated for a length of 3500 m which is the total length of three water gallery tunnel with connecting tunnels. The construction of three parallel water gallery tunnels was required to achieve hydrodynamic control. By hydrodynamic control it means that there should be groundwater present in discontinuities (joints and cracks) in the rock mass and that this groundwater has a static head that exceeds the internal storage pressure.
5	Poisson's ratio	0.15-0.40	

CONSTRUCTION

The rock storage caverns have a cross-section of approximately 500 m². In practical terms this means that the caverns cannot be excavated in one blast round, but must be split into a top heading and several benches. Norwegian Method of Tunnelling (NMT) has been adopted for excavation in these hard rocks. Excavation cycle followed is as shown in the flowchart (Fig.1). Mode of excavation chosen in this project is the drill and blast method. A Jumbo is used for drilling starting with the top heading. The holes are charged with explosives after drilling and controlled blasting is carried out. These drilled holes some of which are fully charged and some are partially charged to have controlled blasting. After excavation followed application of fibrecrete and provision of rockbolts.

ACCESS TUNNEL CONSTRUCTION

This involves excavation of D shape tunnel of size 12 m x 8 m for a length of 400 m. Rock mass characterization indicated that poor rock would be encountered during the excavation for access tunnel. The rock encountered here possessed Q value of 1-0.1 rated as very poor. To begin with the first excavation phase for access tunnel forepoling had to be done to ensure support prior to excavation. Because the time available for support, after excavation (stand-up time) was so little support had to be secured prior to excavation. In this case it was seen that at the initial excavation face for access tunnel there was fragmented and squeezing rock. After forepoling, drilling and blasting followed and next reinforced ribs had to be

CAVERN CONSTRUCTION

The excavation shall take place in a fully saturated environment; the artificial water gallery has to be installed prior to allowing the cavern top heading and benches to advance. All the caverns are 20 m wide and 30 m in height. Hence excavation is done in three stages top heading of first 10 m which would be followed by bench of next 10 m and then invert being 10 m. A probe hole of 11-15 m is drilled ahead of blasting to forecast rushing water, bad roof conditions, explosive gas, or change in rock strength. If the water gushing out of probe holes is greater than 3l/min packers were installed and pre-grouting was executed..

DESIGN OF ROCK SUPPORTS

The design of supports steel reinforced shotcrete, rockbolt length and interval are provided based on NMT based Q system.

Rock bolt

Fully grouted cement based rock bolts are installed and this also helps in corrosion protection for rockbolts inside the rock mass by having 10mm grout around rock bolt. The cavern span dominates the determination of bolt length. Rock bolts placed systematically are in general located normal to the theoretical excavation line.

4th International Engineering Symposium - IES 2015

March 4-6, 2015, Kumamoto University, Japan

MONITORING READINGS FOR CHAINAGE AT 5M IN WATER GALLERY TUNNEL

It can be observed from Fig.1-3, that convergence readings range between 3 mm to -1.5 mm in October 2010 and 1.5 to -1.5mm in April 2011. The crown sag (CS) seen from graph shows upward displacement of crown in April 2011 as against maximum of 0.5mm in October 2010 indicating good stability of the region. Maximum convergence of wall to wall is 2 mm and wall to crown is 3 mm during the initial excavation period.

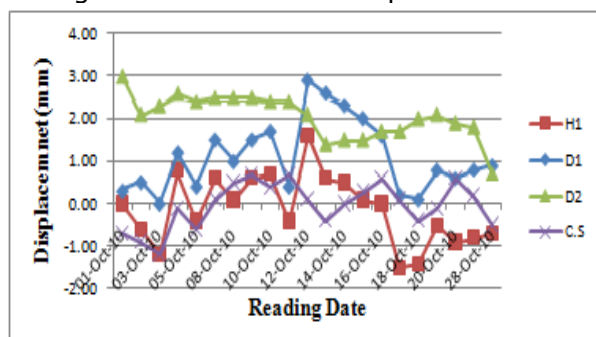


Fig. 1 Convergence measurements at chainage 5m (October 2010)

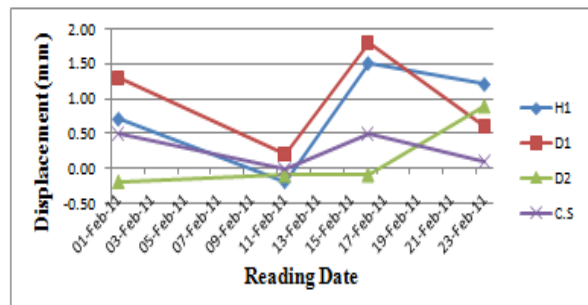


Fig. 2 Convergence measurement at chainage 5m (February 2011)

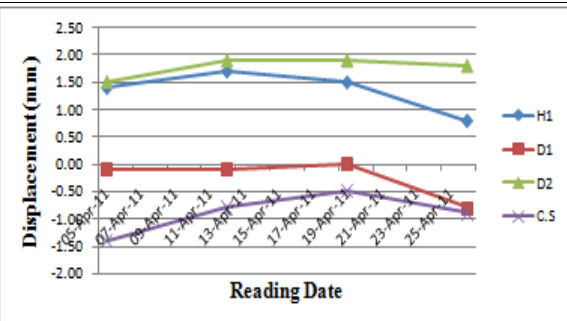


Fig. 3 Convergence measurements at chainage 5m (April 2011)

NUMERICAL MODELING IN PLAXIS 3D TUNNEL

3D FEM package "Plaxis 3D Tunnel" has been utilized in order to simulate the construction phases during excavation for water gallery. The investigations were carried out to study the water gallery tunnel modelled with and without support for a length from chainage 0 to chainage 50 m under the similar construction phases as executed in site. The rock type at the site was granitic gneiss with rock cover of 70 to 80 m. Finite element modelling study was conducted for analysing the stress distribution for 50 m chainage length of water gallery, prior to excavation, after excavation but without any supports and after provision of supports of fibrecrete (thickness 50 mm) along with patterned rockbolting of 3 m length. The material model type was chosen as Jointed Rock model. The input properties of the rock mass considered is shown in Table 2. The input properties for rock bolts and fibrecrete are shown in Table 3.

Table 2 Input properties of the rock mass considered in the Plaxis 3D Tunnel

Material Type	γ_{unsat} (kN/m ³)	γ_{sat} (kN/m ³)	E_1	v_1	E_2	v_2	c (MPa)	ϕ (degree)
Drained	26	27	28	0.27	17	0.28	8.7	43

The rock bolt length was modelled to be 3 m for roof and sidewalls as at site for water gallery tunnel. Node-to-node anchor was used for modelling rockbolts whose material set was considered as elastoplastic with maximum anchor force of 180 kN and plate elements for fibrecrete whose material set was taken as elastic. k_0 condition of 2.4 was applied for the analysis as in the site condition. First the analysis was conducted without having any excavation that is the stresses in the region prior to excavation for a chainage length of 50m was modelled based on the rock cover and rock structure as found at site in Mangalore. Fig. 4 shows 2D mesh and 3D mesh generated in PLAXIS 3D tunnel for 50 m chainage

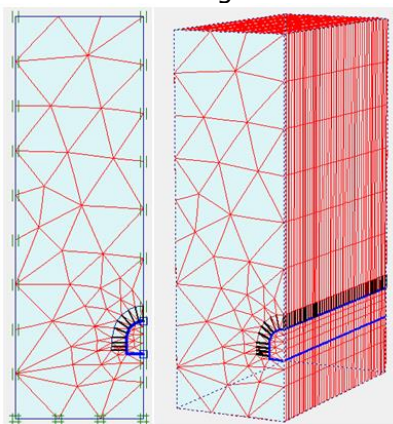


Fig. 4 2D mesh and 3D mesh generated in PLAXIS 3D tunnel for 50m chainage

ANALYSIS PRIOR TO MAKING EXCAVATION FOR WATER GALLERY TUNNEL

The deformed mesh for the model of jointed rock is as shown in Fig. 5. Fig. 6 gives the in-situ stress before excavation. Different colours in the Fig. 7 is a representation to indicate various dip and strike angle that have been input for different planes as at site. The total displacement before the excavation is nil.

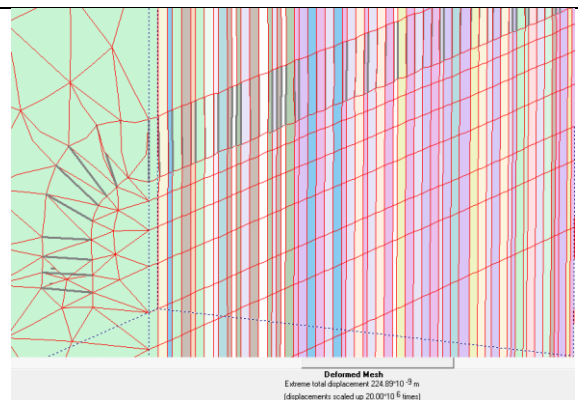


Fig.5 Deformed mesh of the excavation region

At a depth of 70 m where the excavation for water gallery tunnel is done it is observed from effective mean stress analysis (Fig. 6) that this region is found to have compressive stresses of 3.62 MPa. A moderate vertical stress of 1.87 MPa is seen from the analysis which is adequate to have rock caverns (Fig.7).

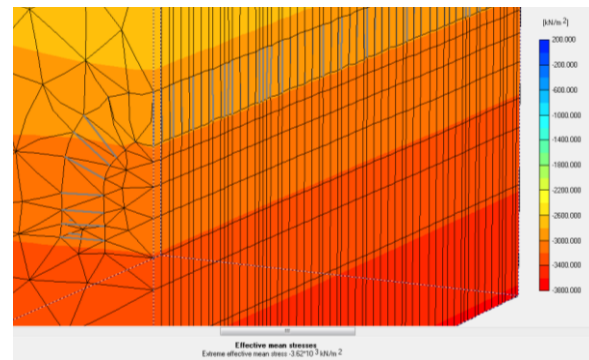


Fig. 6 Effective mean stress in the excavation region

Adequate confining horizontal stress of 4.5 MPa is found in this region (Fig.8). Because of the prevailing higher confining stresses in the region, numerical modelling also confirms the chosen site is ideal to have water gallery tunnel.

Table 3 Input properties for rockbolts and fibrecrete in Plaxis 3D Tunnel

Rock bolts	Fibrecrete
Elastic module of steel Es = 207000 MPa	Primary lining thickness $d = 0.05 \text{ m}$
Rock bolt cross section $A_b = 6.16 \times 10^{-4} \text{ m}^2$	Elastic module of fibrecrete Es = 10000 MPa
Axial rigidity of the rock bolt $Es A_b = 1.275 \times 10^5 \text{ kN}$	Axial rigidity of the primary lining $4.28 \times 10^8 \text{ kN/m}$
Maximum force in the anchor 180 kN	Bending rigidity of the primary lining $EI = 8.93 \times 10^4 \text{ kN m}^2/\text{m}$
	Poisson's ratio $\nu = 0.1$

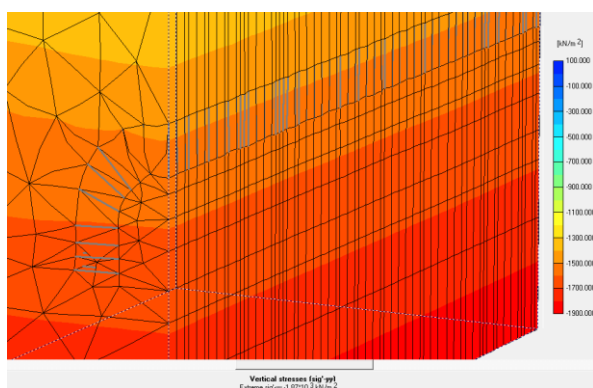


Fig. 7 Vertical stresses in the excavation region

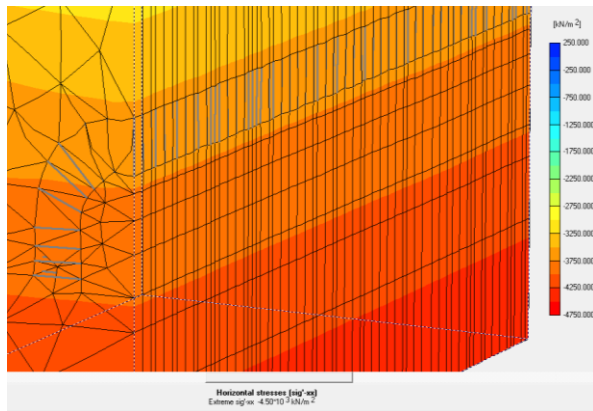


Fig. 8 Horizontal stresses in the excavation region

Analysis after excavation but without providing any supports

Sequential excavation was modelled having 19 phases each of advancement length 2.5 m excavated with time interval of one day for each phase in Type 2 class of rock. The extreme total displacements are found to be 0.7 mm. Fig. 11(9) shows the deformed mesh after the excavation and Fig. 12(10) shows the downward displacement of roof wall and convergence of excavation.

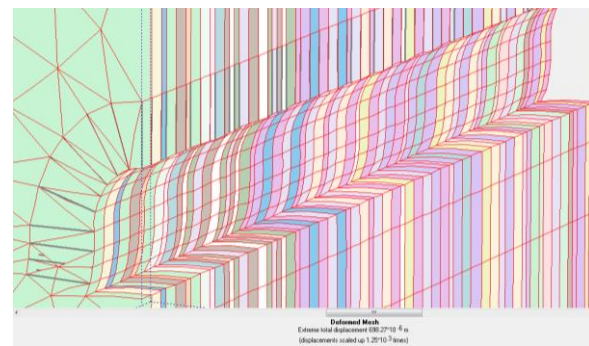


Fig. 9 Deformed mesh after excavation

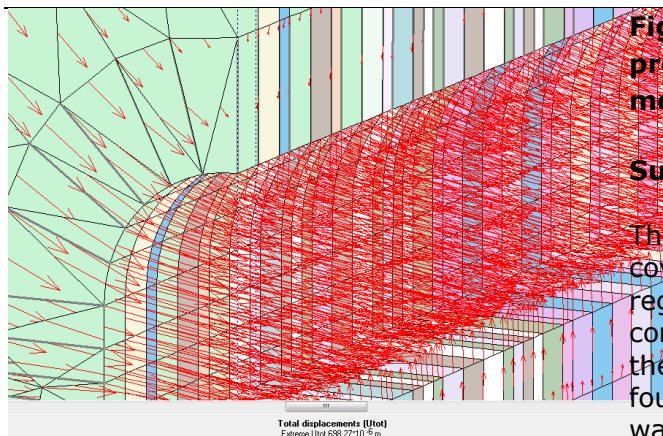


Fig. 10 Downward displacement of roof wall and convergence of excavation

Analysis on provision of supports:

On provision of supports fiber reinforced shotcrete and rock bolt the extreme total displacement here is found to decrease to 0.5 mm. Fig. 17 (11) shows the deformed mesh after provision of supports. Fig. 18 (12) shows that there is upward movement of the roof indicating good stability of tunnel after provision of supports.

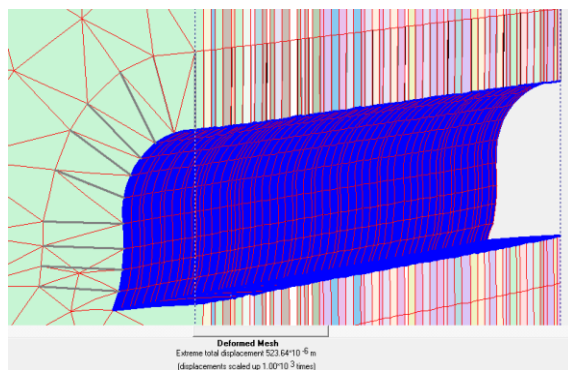


Fig. 11 Deformed mesh after provision of supports

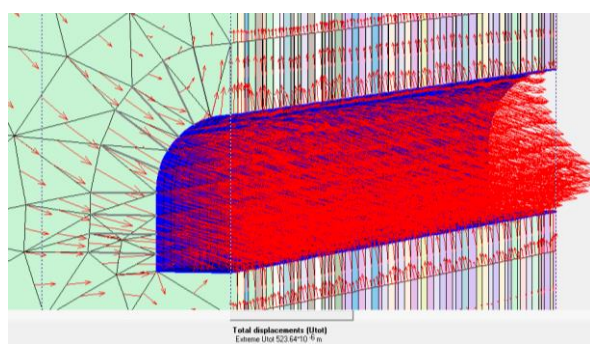


Fig. 12 Total displacement after provision of supports and upward movement of roof wall

Summary and conclusions

The site studies showed competent rock cover with massive granitic gneiss in the region having ideal in-situ stress conditions to have rock caverns and hence the storage scheme was proposed with four horseshoe shaped caverns and three water gallery tunnels. From the study made on the cavern project, numerical modelling studies were done and the following conclusions can are made:

- i) The numerical modelling of water gallery tunnel in Plaxis 3D Tunnel under in-situ stress conditions having k_o as 2.4 showed displacements of 0.7mm independent of provision of supports which is nearly the same as convergence measurement reading taken at site.
- ii) Also with the provision of supports, upward movements of the roof has been observed in Plaxis 3D Tunnel analysis thus indicating good stability with an overall self supporting arch having corresponding horizontal stress of 5 MPa in the crown region. This would be the required confining stresses for upward displacements. Similar upward movements are also seen from the convergence monitoring in the crown level.

REFERENCES

- [1] Adhikary, D. P. and Dyskin, A. V., (1997), Modeling the Deformation of Underground Excavations in Layered Rock Masses: *International Journal of Rock Mechanics and Mining Science*, vol. 34 (3-4), p. 714.
- [2] Bieniawski, Z. T. (1984). *Rock Mechanics Design in Mining and Tunneling*. Rotterdam and Boston: A.A. Balkema.
- [3] Brady, B. H., & Brown, E. T. (1993). *Rock Mechanics for Underground Mining*. London: George Allen & Unwin.
- [4] Bray, J. W. (1987). Chapter 2: Some Applications of Elastic Theory. In E. T. Brown, *Analytical and Computational Methods in Engineering Rock Mechanics* (pp. 32-94). London: Allen & Unwin.
- [5] Cristescu, N. D. and Paraschiv, I., 1995, The optimal shape of rectangular-like caverns:

4th International Engineering Symposium - IES 2015

March 4-6, Kumamoto University, Japan

International Journal of Rock Mechanics and Mining Sciences & Geomechanics Abstracts, v. 32 (4), p. 285-300.

[6] Esaki, Tetsuro. (2005). *Underground Space Design and Practice*.

[7] Goel, R. K., Swarup A., & Sheorey, P. R. (2006), Bolt Length Requirement in Underground Openings: *International Journal of Rock Mechanics & Mining Sciences* (44). Elsevier, 802-811.

[8] Grov, Eivind., Rohde, Jan K.G., Roren, Nils., & Ravlo, Aslak. (2006). Sustainable Underground Concepts. *Norwegian Tunnelling Society* , 15, pp. 9-99.

[9] Hoek, E., & Brown, E. T. (1997, December). Practical Estimates of Rock Mass Strength. *International Journal of Rock Mechanics and Mining Sciences* , 1165-1186.

[10] Lindblom, U. E. (1986). Developments in Design Methods for Large Rock Caverns. In K. H. Saari, *Large Rock Caverns Proceedings of the International Symposium Helsinki* (Vol. 3, pp. 1835-1852). Finland: Pergamon Press

Water Quality Modelling using GIS

Devatha C P¹, Bharat J²

1 Department of Civil Engineering, National Institute of Technology Karnataka, Surathkal, Mangalore 575025, India. email:revacp@gmail.com

2 Consulting Engineer, Mangalore, India, Email: bharathj_er@yahoo.com

ABSTRACT: Groundwater is an important component of our nation's fresh water resources. It plays a key role in meeting the water needs of various user-sectors in the world. The natural resource cannot be optimally used and sustained unless the quality of water is assessed. Present work is aimed at assessing and mapping of ground water quality in the National Institute of Technology-Surathkal (NITK) using ArcGIS. For the study, data collection includes water samples, well locations and NITK boundary map is delineated from the google earth as a base map. Water Quality Index has been calculated for various parameters such as pH, Turbidity, Total hardness(TH), Chloride, Total dissolved solids(TDS), Calcium, Nitrate, Iron, and Fluoride. Water Quality Index map is also developed.

Keywords: Ground water, GIS, Water Quality Index, Interpolation.

INTRODUCTION

Groundwater is almost globally important for human being consumption as well as for the support of habitat and for maintaining the quality of base flow to rivers. Usually they are of excellent quality. Being naturally filtered in their way through the ground, they are generally clear, colourless, and free from microbial contamination and require minimal treatment. A threat is now posed by an ever-increasing number of soluble or dissolved chemicals from urban, industrial activities and from modern agricultural practices. Nevertheless, landslides, fires and other surface processes that increase or decrease infiltration or that expose or blanket rock and soil surfaces, which interact with downward-moving surface water, may also affect the quality of Shallow groundwater. The chemical concentration of groundwater is a measure of its suitability as a source of water for human and animal consumption, irrigation, and for industrial and other purposes. The definition of water quality is therefore not objective, but is socially defined depending on the desired use of water. Different uses require different standards of water quality. Water quality should be taken to

summarize the "physical, chemical, and biological characteristics of water necessary to sustain desired water uses". The transport of pollutants from the point of application to the groundwater system is a function of the properties of the soil-rock strata above the aquifer and the type of pollutant. Once the groundwater is polluted, its quality cannot be restored by stopping the pollutants from the sources. There is need for a definite strategy and guidelines which would focus on specific part of a groundwater management, means the protection of ground water from contamination. Therefore, monitoring the quality of water is necessary and important as clean water is required for human health. It becomes important for the assessment and management of ground water.

Various literatures, data were collected and reviewed keeping the prospect and requirement of the study. India is a large country which supports about 1/6th of the world's population, 1/50th of the world's land and 1/25th of world's water resources (water management forum, 2003). Water is a dynamic renewable natural resource. In the last few decades there has been a tremendous increase in the demand for

4th International Engineering Symposium - IES 2015

March 4-6, Kumamoto University, Japan

fresh water due to rapid growth of population and the accelerated pace of industrialization (K.H.Lateef et al., 2011). In India, most of the population is dependent on groundwater as the only source of drinking water supply (Mahmood and Kundu, 2005; Phansalkar et al., 2005). Its availability with good quality and adequate quantity is very important for human life and other activities. The quality of water is a vital concern for mankind since it is directly linked with human welfare (P.Balakrishnan et al; 2011).

Groundwater can become contaminated naturally or because of numerous types of human activities; residential, municipal, commercial, industrial, and agricultural activities can all affect groundwater quality (U.S. EPA, 1993; Jalali, 2005a; Rivers et al., 1996; Kim et al., 2004., Srinivasamoorthy et al., 2009; Goulding, 2000; Pacheco and Cabrera, 1997). Common sources of groundwater pollution from industry (Morris et al., 2003) are underground and surface storage tanks, effluent pipe work, industrial sewers/collectors, waste injection wells, Bulk chemical storage areas, liquid effluent and process lagoons, solid process-waste disposal sites etc.

A wide variety of materials have been identified as contaminants found in groundwater. These include synthetic organic chemicals, hydrocarbons, inorganic cation, inorganic anions, pathogens, and radionuclides (Fetter, 1999). According to WHO organization, about 80% of all the diseases in human beings are water borne. Further the groundwater, and the pollutants it may move with a very low velocity that it may take long period for the contaminants to move away from the source of pollution and also degradation in the groundwater quality may remain unpredicted for years.

Ground Water Quality Assessment

Quality of ground water refers to physical, chemical and biological characteristics which are essential for various uses such as drinking, domestic, agricultural, industrial uses etc. Among the available methods for ground water quality assessment, Water Quality Index method

is most widely used to detect the existing scenario of ground water quality. Water quality index is an important factor to specify its suitability for drinking water.

Water Quality Index (WQI)

WQI is an important parameter for ascertaining groundwater quality and its suitability for drinking purpose (Hema Latha.T et al., 2012). Water Quality Index is one of the most effective tools to communicate information on overall quality status of water to the concerned user community and policy makers (Subba Rao N et al., 1999, Tiwari TN, Mishra MA et al., 1985). It helps to understand water quality issues by integrating complex data and generating an index that describes present water quality status. It is a rank that provides the influence of water quality parameters on the overall quality of water for drinking purpose. Water quality index is a dimensionless number that add multiple water quality factors into a single index by normalizing values to subjective rating curves. WQI is defined as a rating reflecting the composite influence of different water quality parameters (Ramakrishnalah et al., 2009). Factors to be included in WQI model can deviate depending upon the designated water uses and local preferences. Water quality indices (WQIs) have been developed to integrate water quality variables (Liou, S., et al. 2004). A WQI summarizes large amounts of water quality data into simple terms (excellent, good, bad, etc) for reporting to managers and the public in a consistent manner (Hulya, B et al., 2009). Thus it is an important parameter for the assessment and mapping of ground water. Thus the overdependence on groundwater to meet ever-increasing demands of domestic, agriculture, and industry sectors has resulted in overexploitation of groundwater resources in several states such as Gujarat, Rajasthan, Punjab, Haryana, Uttar Pradesh, Tamil Nadu, among others (CGWB 2006; Garg and Hassan, 2007; Rodell et al., 2009).

Ground water quality assessment and mapping using GIS

GIS has emerged as a powerful tool for storing, analysing, and displaying

4th International Engineering Symposium - IES 2015

March 4-6, 2015, Kumamoto University, Japan

spatial data and using these data for decision making in several areas including engineering and environmental fields (Stafford, 1991; Goodchild, 1993; Burrough and McDonnell, 1998; Lo and Yeung, 2003). It can be characterized as a software package that efficiently relates graphical information to attribute data stored in a database and vice-versa (Kurt et al., 1993).

GIS has been used in the map classification of groundwater quality, based on correlating total dissolved solids (TDS) values with some aquifer characteristics (Butler et al., 2002) or land use and land cover (Asadi et al., 2007). Other studies have used GIS as a database system in order to prepare maps of water quality according to concentration values of different chemical constituents (Skubon, 2005; Yammani, 2007). A similar approach was adopted by Rangzan et al. (2008) where GIS was used to prepare layers of maps to locate promising well sites based on water quality and availability. Babiker et al. (2007) proposed a GIS-based groundwater quality index method which synthesizes different available water quality data (for example, Cl, Na, Ca) by indexing them numerically relative to the WHO standards. Nas and Berkay (2010) have mapped urban groundwater quality in Konya, Turkey, using GIS.

Ahn and Chon (1999) studied groundwater contamination and spatial relationships among groundwater quality, topography, geology, land use, and pollution sources using GIS in Seoul. Ducci (1999) produced groundwater contamination risk and quality maps by using GIS in Southern Italy. Hong and Chon (1999) investigated groundwater contamination and spatial relationships among groundwater quality, topography, geology, land use and pollution sources in two sites namely Asan area and Gurogu area of Seoul city, Korea. Another interesting work was done by Anbazhagan and Nair (2005), in which they conducted groundwater quality mapping using the GIS, in Panvel basin of Raigarh district, Maharashtra, India for agricultural and drinking purposes. Ground water quality maps may be used to assist planners, managers, and local officials in evaluating

the current scenario on whole ground water quality parameters.

Study area

In order to perform the objective of the present study assessment & mapping of ground water quality NITK Surathkal Mangalore, Karnataka, India has been selected. NITK campus boundary has been delineated from google earth and five open wells were located. Figure 1 shows the NITK campus boundary and well location map.

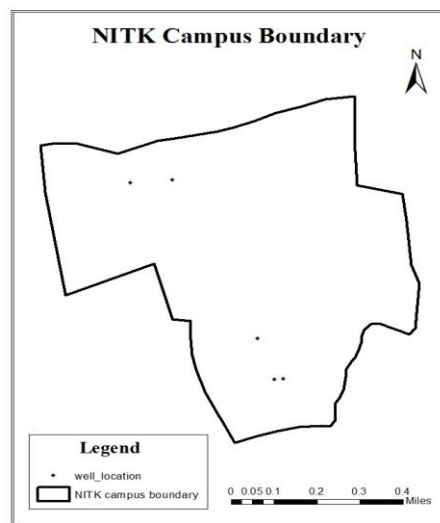


Fig. 1 NITK Boundary and Well Location Map

Methodology

In the present study, base map of NITK campus is delineated. In the campus boundary, five open wells are located. water samples were collected from the wells in the pre and post monsoon seasons. water samples were analysed using standard laboratory procedures. the parameters analysed were pH, chloride, hardness, iron, turbidity, conductivity, alkalinity and sulphates. Spatial distribution of each parameter is shown using interpolation technique for the study area using GIS.

WQI is calculated by using the Weighted Arithmetic Index Method as described by (Cude, c et al., 2001). In this method, the water quality components are multiplied by weighting factor and then aggregated by simple arithmetic mean. For

assessing the water quality in this study, first of all, the quality rating scale (Q_i) for each parameter was estimated by using the equation

Where, Q_i =Quality rating of i^{th} parameter
for total of n water quality parameters

Vact = Actual value of water quality parameter obtained from laboratory test

Videal = Ideal value of that same water quality parameter can be obtained from

Videal for pH = 7 and for other parameters

V_{std} = Recommended BIS standard of

vstd = Recommended BIS standard of water quality parameter (BIS 10500., 1991).

Overall WQI was determined by aggregating the quality rating with the relative weight linearly by using the following expression;

The maximum WQI for the drinking water was considered as 100 score. Based on the above WQI values, the ground water quality is rated as excellent, good, poor, very poor and unfit/unsuitable for drinking.

Results and Discussion

The water samples are collected manually from open wells. All the water quality parameters are expressed in mg/l except pH and turbidity. Each parameter was compared to desirable standard limit of that parameter stipulated for drinking water as prescribed by BIS Standards(1991) and WHO(1983) for drinking and public health purposes.

The samples were tested using standard procedures in the laboratory. The ground water quality data thus obtained forms the non spatial database for the present study. Thematic layers for all the parameters were developed using GIS.

pH is one of the most important operational water quality parameters with the optimum pH required within the range from 6.5 -8.5.Usually pH has no direct effect on consumers. Ground water of study area is mainly acidic. Spatial

distribution of pH concentrations are shown in fig 2.

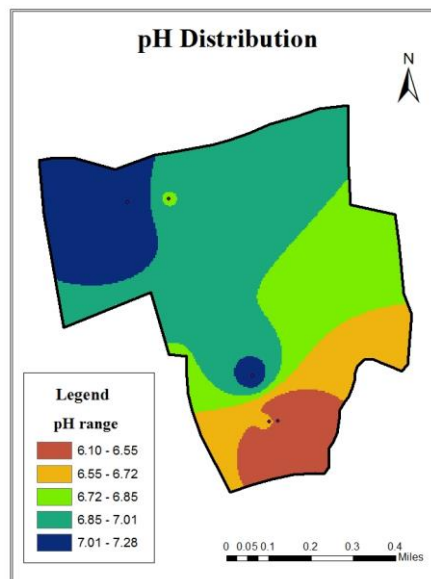


Fig.2 Distribution of pH

Turbidity values are well within the limits. Chloride is present at varying concentration in all natural waters depending upon the geochemical conditions. Chloride concentrations may occur due to industrial waste, sewage disposal, leaching of saline residues in the soil. Water quality data collected indicates that chloride concentration ranges from 0 mg/l to 40 mg/l which is within desirable limit. Spatial distribution of Chloride is shown in fig 3. Total hardness is a measure of calcium(Ca^{2+}) and magnesium(Mg^{2+}) content in water and is expressed as equivalent of calcium carbonate (CaCO_3). Presence of total hardness is also well within the limits and is shown in fig 4.

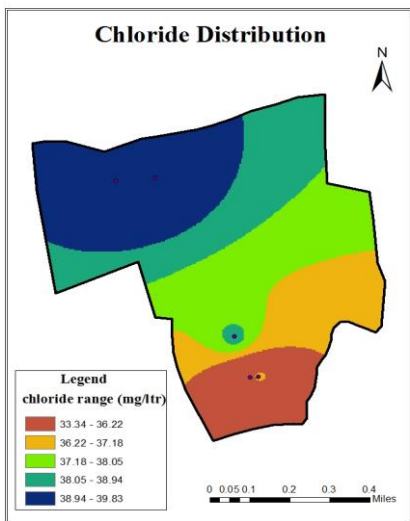


Fig.3 Distribution of Chloride content

reflects the overall status of GWQ for drinking purposes. The overall view of WQI of the present study area is shown in Figure 4.

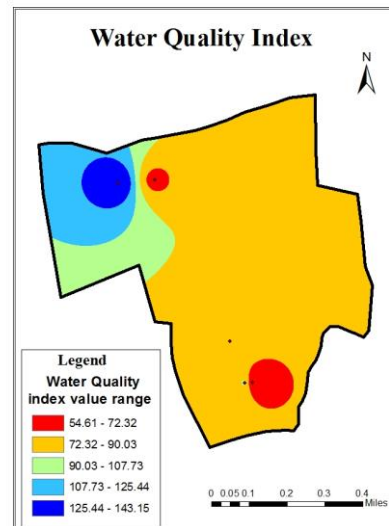


Fig.4 Map showing WQI for the NITK Campus

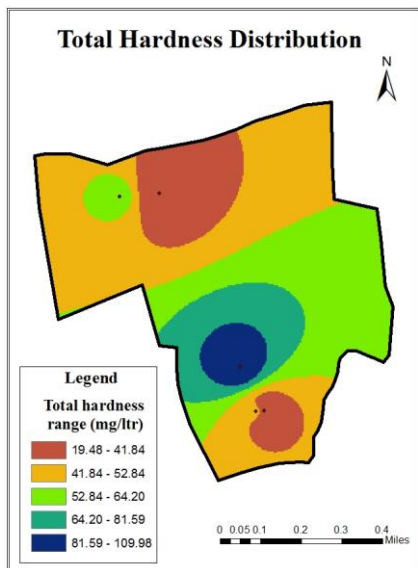


Fig.4 Distribution of Total Hardness
Similarly for other parameters, thematic layers have been prepared for spatial analysis. Overall water quality is classified as good condition. But it needs atleast 10 years data to exactly examine the status of water quality. In this study, only the present scenario is analysed and presented as reference for future analysis.

Water Quality Index Map

WQI indicates the quality of water with reference to an index number which

CONCLUSIONS

In the present work, an attempt was made to evaluate and to map the groundwater quality in NITK Campus. The present study demonstrates that use of GIS and WQI could provide element wise thematic information for water quality assessment and mapping. The estimated WQI provides an easy way of understanding the overall portability of water quality. The integration of various thematic layers with the help of ArcGIS is of immense help in determining suitability of ground water quality for drinking purpose.

REFERENCES

- [1] Ahn, H., and Chon, H. (1999). Assessment of groundwater contamination using geographic information systems. Environ. Geochem. Health, 21: 273-289 .
- [2] Anbazhagan, S., and Nair, A., M. (2004). Geographic information system and groundwater quality mapping in Panvel Basin, Maharashtra, India. Environmental Geology , 45(6), 753-761.
- [3] Asadi, S. S., Vuppala, P., Reddy, M. A. (2007). Remote sensing and GIS techniques for evaluation of groundwater quality in Municipal Corporation of Hyderabad (Zone-V), India. Int. J. Environ. Res. Public Health, 4(1): 45-52 .
- [4] Babike, I. S., Mohamed, A. M., Hiyama, T. (2007). Assessing groundwater quality using GIS. Water Resour. Manage., 21(4): 699 -715.

4th International Engineering Symposium - IES 2015

March 4-6, 2015, Kumamoto University, Japan

-
- [5] Balakrishnan, P., Salaam A., and Mallikarjun, N. D. (2011). Groundwater quality mapping using geographic information system (GIS): A case study of Gulbarga City, Karnataka, India. African Journal of Environmental Science and Technology. Vol. 5(12), pp. 1069-1084.
- [6] Burrough, P. A., McDonnell, R. A. (1998). Creating continuous surfaces from point data. Principles of Geographic Information Systems. Oxford University Press, Oxford, UK.
- [7] Butler, M., Wallace, J., Lowe, M. (2002). Groundwater quality classification using GIS contouring methods for Cedar Valley, Iron County, Utah. In: Digital mapping techniques, 2002, Workshop Proceedings, US Geological Survey Open-File Report 02-370.
- [8] Cude, C. (2001). Oregon water quality index: A tool for evaluating water quality management effectiveness. Journal of the American Water Resources Association, 37, 125-137.
- [9] CGWB (2006). Central Ground Water Board (CGWB), Ministry of water resources. New Delhi: Government of India, p. 120.
- [10] Ducci, D. (1999). GIS techniques for mapping groundwater contamination risk. Natural Hazards, 20: 279-294 .
- [11] Fetter, C. W. (1999). Contaminant Hydrogeology. Prentice-Hall, Englewood Cliffs, NY.
- [12] Garg, N. K., Hassan Q (2007). Alarming scarcity of water in India. Current Sci., 93: 932-941.
- [13] Goulding, K. (2000). Nitrate leaching form arable and horticultural land. Soil Use Manage., 16: 145-151.
- [14] Goodchild, M.F., (1993). The state of GIS for environmental problem-solving. Environ. Modeling GIS, New York": Oxford University Press, pp. 8-15.
- [15] Hema Latha. T., Pradeep Kumar G.N., Lakshminarayana, P., Anil, A. (2012). Assessment of Groundwater Quality Index for Upper Pincha Basin, Chittoor District, Andhra Pradesh, India using GIS. International Journal of Scientific & Engineering Research Volume 3, Issue 7.
- [16] Hong, I. A., & Chon, H. T. (1999). Assessment of groundwater contamination using geographic information systems. Environmental Geochemistry and Health , 21(3), 273-289.
- [17] Hulya, B. (2009). Utilization of the Water Quality Index method as a classification tool, Environmental monitoring and assessment.
- [18] Jalali, M. (2005a). Nitrates leaching from agricultural land in Hamadan, western Iran. Agric. Ecosystem. Environ., 110: 210-218.
- [19] Kim, K. N., Rajmohan, H. J., Kim, G. S., Hwang, Cho M. J. (2004). Assessment of groundwater chemistry in a coastal region (Kunsan, Korea) having complex contaminant sources: A stoichiometric approach. Environ. Geol., 46(6-7): 763-774.
- [20] Lateef, K.H., (2011). Evaluation of Groundwater Quality for Drinking Purpose for Tikrit and Samarra Cities using Water Quality Index. European Journal of Scientific Research ISSN 1450-216X Vol.58 No.4 (2011), pp.472-481.
- [21] Liou, S., Lo,S.,Wang S. (2004). A generalized Water Quality Index for Taiwan. Environmental monitoring and assessment, 96, 35-52.
- [22] Mahmood, A., Kundu, A. (2005). India's demography in 2050: size, structure and habitat. Discussion Paper, IWM-TATA partners meet - 2005, Anand, Gujarat.
- [23] Morris, B. L., Lawrence, A. R., Chilton, P. J., Adams., B,Calow, R., and Klinck, BA., 2003. Groundwater and its susceptibility to degradation: A global assessment of the problems and options for management. Early Warning and Assessment Report Series. RS, 03-3. United Nations Environment Programme, Nairobi, Kenya.
- [25] Nas, B. and Berkay, A. (2010). Groundwater quality mapping in urban groundwater using GIS. Environ. Monitor. Assess., 160(1-4): 215-227.
- [26] Phansalkar, S. J. Kher, V. Deshpande, P. (2005). "Expanding Rings of Dryness: Water Imports from Hinterlands to Cities and the Rising Demands of Mega-Cities", in IWMI-Tata Annual Partner's Meet, Anand.
- [27] Pacheco, J. Cabrera, S. (1997). Groundwater contamination by nitrates in the Yucatan Peninsula, Mexico. Hydrogeol. J., 5(2): 47-53.
- [28] Ramakrishnaiah, C. R., Sadashivaiah, C. and Ranganna, G. (2009). Assessment of Water Quality Indexfor the ground water in Tumur Taluk.E-Journal of Chemistry.6(2),523-530.
- [29] Rangzan K, Charchi A, Abshirini E, Dinger J (2008). Remote sensing and GIS approach for water-well site selection, Southwest Iran. Environ. Eng. Geosci., 14(4): 315-326 .
- [30] Rodell M., Velicogna I, Famiglietti J. S.(2009). Satellite-based estimates of groundwater depletion in India. Nature, 460: 999-1002.
- [31] Rivers C. N., Hiscock KM., Feast NA., Barrett MH. Dennis P. F. (1996). Use of nitrogen isotopes to identify nitrogen contamination of the Sherwood sandstone aquifer beneath the city of Nottingham UK. Hydrogeol. J., 4(1): 90-102.
- [32] Srinivasamoorthy K, Nanthakumar C, Vasanthavigar M, Vijayarag havan K, Rajivgan dhi R, Chidambaram S, Anandan P, Manivannan R, Vasudevan S. (2009). Groundwater quality assessment from a hard rock terrain, Salem district of Tamilnadu, India, Arabian J. Geoscience.
- [33] Skubon B. A. (2005). Groundwater quality and GIS investigation of a shallow sand aquifer, Oak opening region, North West Ohio. Geological Society of America. Abstracts Programs, 37(5): 94.
- [34] Stafford, D. B. (1991). Civil engineering applications of remote sensing and geographic information systems. New York, ASCE.
- [35] Subba Rao, N., (1997). Studies on the water quality index in hard rock terrain of Guntur district, Andhra Pradesh, India. National Seminar on Hydrology of Precambrian Terrains and hard rock areas, pp 129-134.
- [36] Tiwari, T. N., Mishra, M. A., (1985). A preliminary assignment of water quality index of major Indian rivers. Indian J Environ Proc, 5:276-279.
- [37] U.S. EPA., (1993). A review of methods for assessing aquifer sensitivity and ground water Vulnerability to pesticide contamination. U.S. EPS. EPA/813/R-93/002.
- [38] Yammani, S. (2007). Groundwater quality suitable zones identification: application of GIS, Chittoor area, Andhra Pradesh, India. Environ. Geol., 53(1): 201-210.

Ground Water Treatment Methodologies - Review

Devatha C P¹, Suresh A V²

1 Department of Civil Engineering, National Institute of Technology Karnataka, Surathkal, Mangalore 575025, India. email:revacp@gmail.com

2 Proprietor, S.Consultants, Mangalore, India

ABSTRACT: Groundwater is an important component of fresh water resources. It plays a key role in meeting the water needs of various user-sectors in the world. Contamination of aquifers has become a great concern in many countries where population relies on groundwater resources for drinking water supply. Ground water contaminants are subjected to physical, chemical and biological processes that can act individually or in combination to alter the fate of contaminants. Therefore main objective of the study is to provide broad spectrum of in-situ treatment technologies available in the field and it is discussed through various literatures. The study deals mainly with activated carbon, air sparging, permeable reactive barriers (PRBs), nanofiltration, reverse osmosis, bioremediation treatment processes.

Keywords: ground water, contamination, air sparging, activated carbon, PRBs, reverse osmosis, bioremediation

INTRODUCTION

In India, the surface water resources are inadequate to fulfill the water demand and so, the productivity through ground water is high compared with surface water. Over the years, increasing population, urbanization and expansion in agriculture has exerted tremendous pressure on the ground Water and is depleting this valuable resource at a high rate. It can be defined as possibility of percolation and diffusion of contaminants from the ground surface in to the ground water system. Sources of contamination include: gasworks, coal gasification plants, refineries, abandoned industrial areas, storage tank areas, military areas, bus-stations and airports.

The movement of contaminant as it progress downwards into the ground before it encounters the aquifer will undergo following process like adsorption on the soil particles, biological degradation, oxidation, reduction, hydrolysis volatilization. Movement of contaminant in the aquifer is slow than in water due to adsorption to the soil particles. The chemistry of groundwater reflects inputs from the atmosphere, from

soil and water-rock reactions, as well as from pollutant sources such as mining, land clearance, agricultural practices, and acid rainfall, domestic and industrial wastes. The transport of pollutants from the point of application to the groundwater system is a function of the properties of the soil-rock strata above the aquifer and the type of pollutant. Once the groundwater is polluted, its quality cannot be restored by stopping the pollutants from the sources. Hence prevention of ground water pollution is necessary for effective ground water resource management and ground water vulnerability assessment is important for such ground water protection.

Numerous site remediation processes have been used for the saturated and unsaturated zones. Saturated zone technologies include air sparging and permeable reactive barriers, and common technologies for the unsaturated zone include soil vapor extraction and bioventing. The main objective of the study is to discuss the treatment technologies available to remove/reduce ground water contamination in the field in a detailed manner and to analyze its

suitability based on the case studies dealt in the literature.

Activated Carbon (AC)

Activated carbon is proven to be an effective removal technology for organic and inorganic pollutants from aqueous and gaseous media. It is a widely used method due to its high surface area for treatment of water. Solvents, pesticides, industrial wastes, and leaking underground storage tanks are some sources of this contamination. Basic process involved in AC principle is shown in Figure 1. Bhatnagar et. al (2013) defined AC as a common term used to describe carbon based materials which contains well developed internal pore structure. AC is produced from a variety of carbonaceous rich materials such as wood, coal, lignite and coconut shell. There are two basic types of water filters: particulate filters and adsorptive/reactive filters. Particulate filters exclude particles by size, and adsorptive/reactive filters contain a material (medium) that either adsorbs or reacts with a contaminant in water. The principles of activated carbon filtration are the same as those of any other adsorption material. The contaminant is attracted to and held (adsorbed) on the surface of the carbon particles. The characteristics of the carbon material (particle and pore size, surface area, surface chemistry, density, and hardness) influence the efficiency of adsorption.

The two main types of activated carbon used in water treatment applications are granular activated carbon (GAC) and powdered activated carbon (PAC). GAC is made from organic materials with high carbon contents such as wood, lignite and coal. The primary characteristic that differentiates GAC to PAC is its particle size. While the effectiveness of ACs to act as adsorbents for a wide range of contaminants is well documented, research on AC modification is gaining prominence due to the need to develop the affinity of AC for certain contaminants to facilitate their removal from water. Most of research studies revealed that H₂O₂ treatment produces minimal textural modifications (Qiao et. al 2002; Garcia et. al 2004 and Pereira et. al 2003). In some cases, it is

reported as increased surface area by Garcia et. al 2000 and decreased by Pradhan and Sandle, 1999.

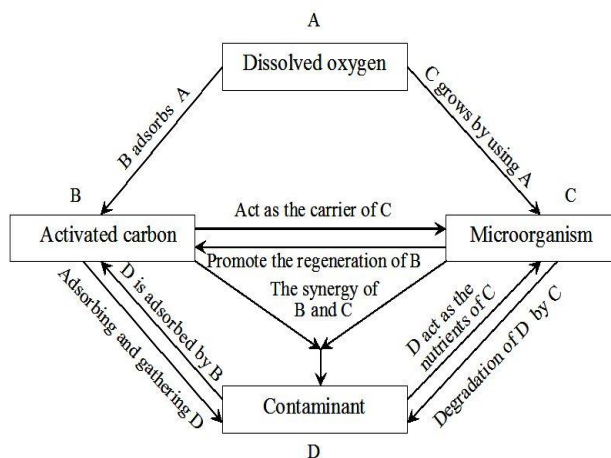


Figure. 1 Process involved using AC

Air Sparging

In situ air sparging technique is developed in late 1980s for treating dissolved volatile organic compounds (VOCs) in groundwater. Air sparging involves the injection of air under pressure into saturated zone soils. The injected air displaces water and creates air-filled porosity in the saturated soils, volatilizes and removes dissolved and adsorbed phase VOCs, and transfers oxygen into the groundwater. As a result, both physical removal and aerobic biodegradation of contamination in groundwater and saturated zone soil are enhanced. Air sparging has been used to remediate both chlorinated solvents and petroleum hydrocarbons. (Bass and Brown, 1991; Leonard and Brown, 1992; Marley et. al, 1992 and Noonan et. al 1993). Figure 2 shows the principle involved in air sparging technique. Process explained in the figure is by injecting air beneath a ground water aquifer, air sparging operations can induce aquifer mixing, and promote the volatilization or biodegradation of dissolved organic contaminants. vapor extraction wells create a vacuum in the subsurface, to direct the flow of liberated vapors to recovery or monitoring wells.

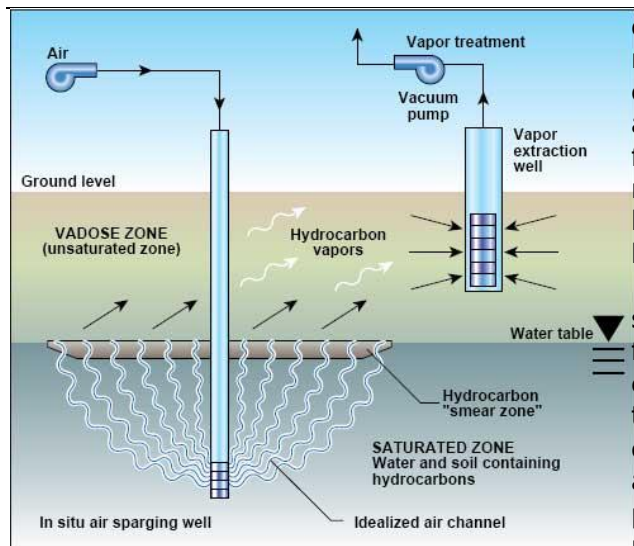


Figure 2. Air Sparging Technique

Bass et. al (2000) studied about the performance of 49 case studies of air sparging technique to explain clearly under which circumstance the technique achieves permanent reduction in ground water contamination. Results indicates that 21 sites(48%) produced permanent reductions greater than 90% averaged over all monitoring wells, with no monitoring well showing a permanent reduction of less than 80%. An additional 13 sites (29%) had averaged permanent reductions somewhat less than 90%, but this was still sufficient to effect site closure. The performance at the remaining 10 sites (23%) was unsatisfactory. The study concluded that before installing the sparge system, pilot study is to be conducted and tested to test the efficiency of the system. Benner et. al (2000) studied the in situ air sparging for drum surface area and the study found to be successful and subsequent evaluation of several remediation system design parameters through numerical modelling.

Permeable Reactive Barriers (PRBs)

PRBs are one of widely accepted technology for treating groundwater. A permeable reactive barrier (PRB) is a zone of reactive material that extends below the water table to intercept and treat contaminated groundwater. Franklin et. al (2014) explained that it is a concept of the technology involves the emplacement

of a permeable barrier containing reactive materials across the flow path of the contaminated groundwater to intercept and treat the contaminants as the plume flows through it under the influence of the natural hydraulic gradient. it is not a barrier to the ground water but it is a barrier to contaminants.

PRBs immobilize the contaminants in situ without taking them to surface for further treatment. it does not require excess energy input for treatment because the flow occurs under gravity so that the contaminants reaches the reactive zone along with ground water flow. Only periodic replacement of reactive medium is required. contamination degradation is achieved though a simple means of change of phase of contaminants. Figure 3 explains the principle involved in PRBs. It is widely used technology for reducing ground water contamination (Thiruvenkatachari et. al 2008).

From the last decades, most of the studies have been focused on the development of passive methods such as permeable reactive barriers for the removal of contaminants from waters (Jun et. al 2009; Bartzasaand Komnitsasb, 2010; Giberta et. al 2011 and Xina et. al 2013)

Nanofiltration and Reverse Osmosis

Konstantine and Karabelas (2012) reviewed various literature to assess the performance of nanofilters and reverse osmosis process for removal of pesticides from water. The objective is to critically assess the performance of nanofilters and reverse osmosis in relation to in relation to the currently in-force strict regulations for potable water characteristics. Pesticide removal by nanofiltration and reverse osmosis membranes is so complicated because of the involvement of several membranes and solute parameters plays vital role in purification. This paper discusses about more optimistic models based on irreversible thermodynamics, mass transport models and artificial neural networks regarding its advantages and disadvantages. The study also finds that use of membranes rejection can vary depending on pesticide affinity for the membrane.

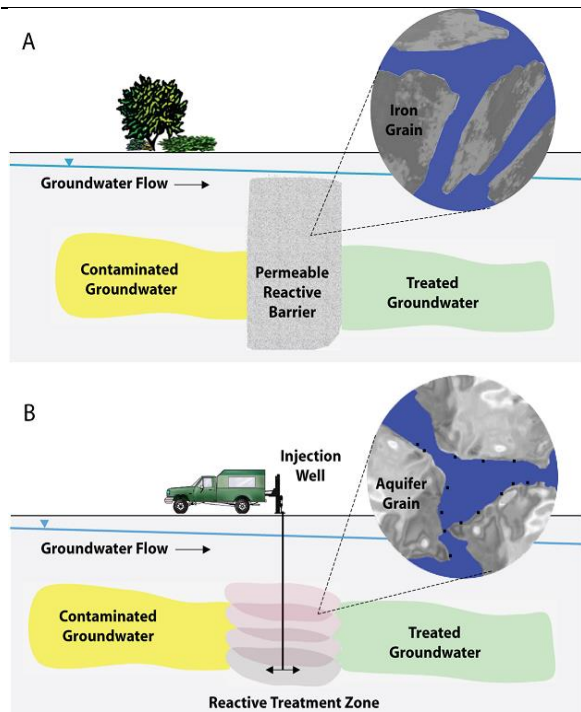


Figure 3. Permeable Reactive Barrier

Hence it is of utmost importance to identify the type of organic and other species which deposits on the membrane to improve the efficiency of removal system. Also study concluded that nanofiltration as a reliable operation for pesticides removal from water sources, which provides the basis for developing effective potable water treatment processes. However, nanofilters alone cannot be used the water purification but it should be used along with operational procedures to increase its effectiveness.

Extensive research had been carried for the past two decades for complete assessment of reverse osmosis and nanofiltration process, regarding removal of pesticide residues from various aquatic matrices in many laboratories (Jung et. al 2005; and Bhattacharya et. al 2006), to pilot tests (Miltner et. al 1989; Kruithof, 1997 and Berg et. al 1997) and to industrial scale experiments (Ventrisque et. al 2000; Cyna et. al 2002).

Zero-valent iron

Zero-valent iron is the most common reactive material used in field application. ZVI tend to be oxidised, passing its electron to contaminants (organic-

halogenated hydrocarbons, inorganic-some metal; U(VI), Cr(VI), etc., which undergo reductive mechanism resulting in precipitation or degradation. The mechanism for metal precipitation and degradation of halogenated hydrocarbon by ZVI is given elsewhere by Ott 2000.

Vast literature is available based on the type of materials used like alkalin complexing agents, phosphate reducing minerals, zeolites, clay, metal oxides, microorganisms and polymers containing iron is evaluated.

Bioremediation

Bioremediation is defined as the process whereby organic wastes are biologically degraded under controlled conditions to an innocuous state, or to levels below concentration limits established by regulatory authorities. The control and optimization of bioremediation processes is a complex system of many factors. The factors include: the existence of a microbial population capable of degrading the pollutants; the availability of contaminants to the microbial population; the environment factors (type of soil, temperature, pH, the presence of oxygen or other electron acceptors, and nutrients).

In situ bioremediation creates subsurface environmental conditions (without withdrawing the contaminated water from under the ground), typically through the principle of oxidation-reduction manipulation, which induce the degradation of chemicals via microbial catalyzed biochemical reactions.

Not all compounds are susceptible to rapid and complete degradation. There are some concerns that the products of biodegradation may be more persistent or toxic than the parent compound. Important site factors required for success include the presence of metabolically capable microbial populations, suitable environmental growth conditions, and appropriate levels of nutrients and contaminants. It is difficult to extrapolate from bench and pilot-scale studies to full-scale field operations. Research is needed to develop and engineer bioremediation technologies that are appropriate for sites with complex mixtures of contaminants

4th International Engineering Symposium - IES 2015

March 4-6, 2015, Kumamoto University, Japan

that are not evenly dispersed in the environment. Contaminants may be present as solids, liquids, and gases. Bioremediation often takes longer than other treatment options, such as excavation and removal of soil or incineration.

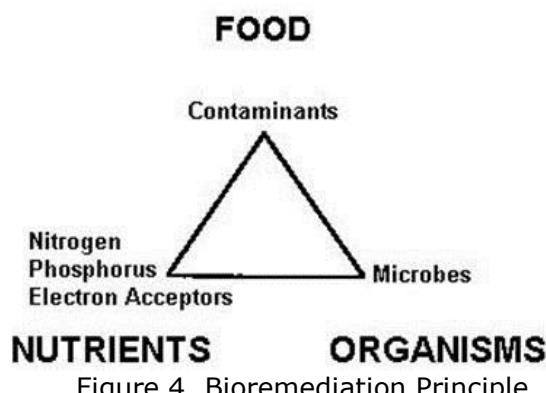


Figure 4. Bioremediation Principle

Main factors affecting in situ bioremediation of contaminated ground water have been widely described in the literature (Kampbell et al., 1996; MacDonald et al., 1999; Boopathy, 2000; Andreoni and Gianfreda, 2007). In situ bioremediation has been successful for the treatment of groundwater contaminated with mixtures of chlorinated solvents (Dyer et al., 2003; Kao and Prosser, 1999; Schmidt et al., 1999) petroleum hydrocarbons (Hunkeler et al., 1998, 1999; Bolliger et al., 1999; Chapelle, 1999; Kao et al., 2006).

CONCLUSIONS

The following conclusions are deduced from the present study:

Modified AC (oxidation, nitrogenation, sulfurization, ligands) shows increased efficiency for removing contaminants compared to conventional ACs. Altogether, surface modified ACs is still an emerging field for research to further develop the innovative methods to improve the efficiency of ACs.

Pilot plant studies is to conducted before insitu treatment to exactly determine its removal efficiency.

Generally conventional PRB is suitable for shallow depths. The limitation can be overcome by employing new technique like hydro-fracturing, which is applicable to

deeper depths. and also long term performance of PRBs is not dealt systematically.

Since bioremediation depends on many factor to achieve to high efficiency of removal, still there is a need of research which can be dealt to identify the significant parameter. Moreover engineered in situ bioremediation is needed to increase the rate of organic pollutant biodegradation.

REFERENCES

1. Andreoni, V., and Gianfreda, L., (2007). Bioremediation and monitoring of aromatic-polluted habitats. *Appl. Microbiol. Biotechnol.* 76, pp. 287–308.
2. Bartzasa, G., and Komnitsasb, K., (2010). Solid phase studies and geochemical modelling of low-cost permeable reactive barriers, *J. Hazard. Mater.*, 183, pp. 301–308.
3. Bass, D. H., and Brown, R. A., (1991). In Situ Air Sparging for Remediation of Contaminated Saturated Zone Soils, in: Proceedings of the New Jersey Environmental Expo, Seacaucus.
4. Benner, M. L., Stanford, S. M., Lee, L. S., and Mohtar, R.H., (2000). Field and numerical analysis of in-situ air sparging: a case study, *Journal of Hazardous Materials*, 72, pp. 217–236.
5. Berg, P., Hagmeyer, G., and Gimbel, R., (1997). Removal of pesticides and other micropollutants by nanofiltration, *Desalination*, 113, pp. 205–208.
6. Bhatnagar, A., Hogland, W., Marques, M., and Sillanpaa, M., (2013). An overview of the modification methods of activated carbon for its water treatment applications *Chemical Engineering Journal*, 219, pp. 499–511.
7. Bhattacharya, A., Ray, P., Brahmabhatt, H., Vyas, K. N., Joshi, S. V., Devmurari, C.V., and Trivedi, J. J., (2006). Pesticides removal performance by low-pressure reverse osmosis membranes, *J. Appl. Polym. Sci.*, 102, pp. 3575–3579.
8. Bolliger, C., Ho'hener, P., Hunkeler, D., Ha'berli, K., and Zeyer, J., (1999). Intrinsic bioremediation of a petroleum hydrocarbon-contaminated aquifer and assessment of mineralization based on stable carbon isotopes. *Biodegradation* 10, pp. 201–217.
9. Boopathy, R., (2000). Factors limiting bioremediation technologies. *Biores. Technol.* 74, pp. 63–67.
10. Chapelle, F. H., (1999). Bioremediation of petroleum hydrocarbon-contaminated ground water: the perspectives of history and hydrology. *Ground Water* 37, pp. 122–132.
11. Cyna, B., Chagneau, G., Bablon, G., and Tanghe, N., (2002). Two years of nanofiltration at the Méry-sur-Oise plant, France, *Desalination*, 147, pp. 69–75.
12. Domingo-Garcia, M., Lopez-Garzon, F. J., Perez-Mendoza, M., (2000). Effect of some oxidation treatments on the textural characteristics and surface chemical nature of an AC, *J. Colloid Interf. Sci.*, 222, pp. 233–240.

4th International Engineering Symposium - IES 2015

March 4-6, 2015, Kumamoto University, Japan

13. Dyer, M., Heininen, E. V., and Gerritse, J., (2003). A field trial for in-situ bioremediation of 1,2-DCA. *Eng. Geol.* 70, pp. 315–320.
14. Franklin Obiri-Nyarko, Johana Grajales-Mesa, S., and Malina, G., (2014). An overview of permeable reactive barriers for in situ sustainable groundwater remediation, *Chemosphere*, Volume 111, pp. 243–259.
15. Garcia, T., Murillo, R., Cazorla-Amoros, D., Mastral, A. M., and Linares-Solano, A., (2004). Role of the AC surface chemistry in the adsorption of phenanthrene, *Carbon* 42, pp. 1683–1689.
16. Giberta, O. Röttingb, T., Cortinaa, J. L., de Pabloa, J., Ayorac, C., Carrerac, J., and Bolzicco, J., (2011). In-situ remediation of acid mine drainage using a permeable reactive barrier in Aznalcóllar (Sw Spain), *J. Hazard. Mater.*, 191, pp. 287–295.
17. Hofman, J. A. M. H., Beerenddonk, E. F., Folmer, H. C., and Kruithof, J. C., (1997). Removal of pesticides and other micropollutants with cellulose-acetate, polyamide and ultra-low pressure reverse osmosis membranes, *Desalination*, 113, pp. 209–214.
18. Hunkeler, D., Hohener, P., and Zeyer, J., (2002). Engineered and subsequent intrinsic in situ bioremediation of a diesel fuel contaminated aquifer. *J. Contam. Hydrol.* 59, pp. 231–245.
19. ITRC, A Systematic Approach to In situ Bioremediation in Groundwater, Including Decision Tree on In situ Bioremediation for Nitrates, Carbon Tetrachloride, and Perchlorate, ITRC, USA, 2002.
20. Jun, D., Yongsheng, Z., Weihong, Z., and Mei, H., (2009). Laboratory study on sequenced permeable reactive barrier remediation for landfill leachate-contaminated groundwater, *J. Hazard. Mater.*, 161, pp. 224–230
21. Jung, Y. J., Kiso, Y., Othman, R. A. A., Ikeda, A., Nishimura, K., Min, K. S., Kumano, A., and A. Ariji, A., (2005). Rejection properties of aromatic pesticides with a hollow-fiber NF membrane, *Desalination*, 180, pp. 63–71.
22. Kampbell, Don H., Wiedemeier, T. H., and Hansen, J. E., (1996). Intrinsic bioremediation of fuel contamination in ground water at a field site. *J. Hazardous Mater.* 49, pp. 197–204.
23. Kao, C. M., Huang, W. Y., Chang, L. J., Chen, T. Y., Chien, H. Y., and Hou, F., (2006). Application of monitored natural attenuation to remediate a petroleum-hydrocarbon spill site. *Water Sci. Technol.* 53, pp. 321–328.
24. Kao, C. M., and Prosser, J., (1999). Intrinsic bioremediation of trichloroethylene and chlorobenzene: field and laboratory studies. *J. Hazardous Mater.*, 69, pp. 67–79.
25. Konstantinos V. P., and Karabelas, A. J., (2012). Removal of pesticides from water by NF and RO membranes — A review, *Desalination*, 287, pp. 255–265
26. Leonard, W. C., and Brown, R. A., (1992). Air sparging: an optimal solution, in: *Proceedings of Petroleum Hydrocarbons and Organic Chemicals in Ground Water: Prevention, Detection, and Restoration*, NGWA, Dublin, OH.
27. MacDonald, T. R., Kitanidis, P. K., McCarty, P. L., and Roberts, P. V., (1999). Effects of shear detachment on biomass growth and in situ bioremediation. *Ground Water* 37, pp. 555–563.
28. Marley, M. C., Hazebrouk, D. J., and Walsh, M. T., (1992). The application of in situ air sparging as an innovative soil and groundwater remediation technology, *Groundwater Monitoring Review Spring*.
29. Miltner, R. J., Baker, D. B., Speth, T. F., and Fronk, C. A., (1989). Treatment of seasonal pesticides in surface waters, *J. Am. Water Works Assoc.*, 81, pp. 43–52.
30. Noonan, D. C., Glynn, W. K., and Miller, M. E., (1993). Enhance performance of soil vapor extraction, *Chemical Engineering Progress*, 6(89).
31. Ott, N., (2000). Permeable Reactive Barriers for Inorganics, USEPA, Washington, DC, Report obtained from website <http://www.clu-in.org>, 2000.
32. Pereira, M. F. R., Soares, S. F., Orfao, J. J. M., and Figueiredo, J. L., (2003). Adsorption of dyes on ACs: influence of surface chemical groups, *Carbon* 41, pp. 811–821.
33. Pradhan, B. K., and Sandle, N. K., (1999). Effect of different oxidizing agent treatments on the surface properties of ACs, *Carbon* 37, pp. 1323–1332.
34. Qiao, W., Korai, Y., Mochida, I., Hori, Y., and Maeda, T., (2002). Preparation of an AC artifact: oxidative modification of coconut shell-based carbon to improve the strength, *Carbon* 40, pp. 351–358.
35. Richard, J., Watts, and Teel, L., (2006). Treatment of Contaminated Soils and Groundwater Using ISCO 2, Practice Periodical of Hazardous, Toxic, and Radioactive Waste Management, Vol. 10, No. 1, January 1, ©ASCE.
36. Rivera-Utrilla, J., Sanchez-Poloa, M., Gomez-Serrano, V. Alvarezc,P.M., Alvim-Ferraz, M. C. M., and Dias, J. M., (2011). Activated carbon modifications to enhance its water treatment applications- An Overview. *Journal of Hazardous Materials* 187, PP. 1–23.
37. Schmidt, L. M., Delfino, J. J., Preston, J. F., and Laurent, G. S., (1999). Biodegradation of low aqueous concentration pentachlorophenol (PCP) contaminated groundwater. *Chemosphere* 38, pp. 2897–2912.
38. Shevah, Y., and Waldman, M., (1995). In-Situ and On-Site treatment of ground water, Technical Report, Pure & App/. Chern., Vol. 67, Nos 8/9, pp. 1549–1561.
39. Thiruvenkatachari, R., Vigneswaran, S., and Naidu, R., (2008). Permeable reactive barrier for groundwater remediation, *Journal of Industrial and Engineering Chemistry* 14, pp. 145–156.
40. Ventresque, C., Gisclon, V., Bablon, G., and Chagneau, G., (2000). An outstanding feat of modern technology: the Mery-sur-Oise nanofiltration treatment plant (340,000 m³/d), *Desalination*, 131, pp. 1–16.
41. Xina, B. P., Wub, C. H., and Linc, C. W., (2013). Bioaugmented remediation of high concentration BTEX-contaminated groundwater by permeable reactive barrier with immobilized bead, *J. Hazard. Mater.*, pp. 765–772.

Structural and vibroacoustic Analysis of Aircraft fuselage section with passive noise reducing materials : A material performance study

Balakrishnan B ¹, Divyadev C M ², Raja S ³ and Katta Venkataramana ⁴

- 1 *Scientist, Structural Technologies Division, CISR-National Aerospace Laboratories, Bangalore 560017, India. e-mail:balki06@nal.res.in*
 - 2 *Lecturer, Government Engineering college, westhill, Kozhikode 673005, India. email: divyadevc.m@gmail.com*
 - 3 *Senior Principal Scientist, Structural Technologies Division, CISR-National Aerospace Laboratories, Bangalore 560017, India. e-mail:raja@nal.res.in*
 - 4 *Professor, Department of Civil Engineering, National Institute of Technology Karnataka, Surathkal, Mangalore 575025, India. email: ven.nitk@gmail.com*
-

ABSTRACT: In the present work, vibroacoustic (VA) modeling and analysis of an aluminum fuselage section with acoustic insulations made up of porous elastic material(PEM) is carried out. The work aims at studying the VA performance of various materials as fuselage skin; for this a numerical model using finite element method is developed and noise absorption blankets are modelled. The sound transmission loss (STL) analysis from exterior to interior cabin of fuselage section is carried out using finite element analysis to examine the VA phenomenon and it is compared with fuselage skin embedded with PEM melamine foam. The STL characteristics of foams of various thickness on different aircraft materials like Aluminium, Glass Fiber Reinforced Plastics (GFRP), Carbon Fiber Reinforced Plastic (CFRP) and Fiber Metal Laminate (FML) are evaluated through simulation case studies.

Keywords: Vibroacoustics, Sound Transmission Loss, Sound Pressure Level.

INTRODUCTION

In recent years the stringent norms on noise emission levels and the customer demand in the comfort level in the automobiles and aircraft have made the vibroacoustic behaviour into an important criterion in many design problems. Noise and vibration inside an aircraft cabin cause increasing risks in health and performance of flight and cabin crews besides the discomfort to the passengers. After continuous exposure to high noise, typically exceeding 60 to 80 decibels (dB) of a weighted sound level, people will start to experience a temporary threshold shift, which is the primary hearing loss. Sound

pressure level (SPL) outside the fuselage of multi-engine transport aircraft is typically in the order of 130 dB at the blade-passage frequency. However FAR (Federation of Aviation Regulation) authority has laid stringent norms on the noise levels to be less than 75 dB inside the fuselage cabin [4]. Many aircraft industries are therefore striving hard in achieving a higher comfortable level. The great deal of effort has been put into studying the method of reducing noise inside aircraft cabin [6-8].

In order to reduce the acoustic noise level inside the aircraft cabin, the primary and secondary structural elements inside

4th International Engineering Symposium - IES 2015

March 4-6, 2015, Kumamoto University, Japan

an aircraft need to be designed with superior acoustic properties. The structural components of the aircraft require high stiffness with minimum weight in order to maximize the aircraft's performance and ensure the safety of the passengers. Keeping all these criteria, an segmented fuselage structure was modelled using FEM for VA analysis by using different materials for skin namely aluminium, glass fiber reinforced plastics (GFRP), carbon fiber reinforced plastic (CFRP) and fiber metal laminate (FML). By including the PEM foam with varying thickness and density, its effect on the STL in fuselage section inner cabin is studied.

POROELASTIC MODELLING

Porous materials are commonly used to suppress acoustic waves; this attenuating effect arises from a number of effects as the acoustic fluid interacts with the solid matrix. For many categories of materials, the solid matrix can be approximated as either fully rigid compared to the acoustic fluid or fully limp.

The most widely used theory for porous materials is due to Biot, who came up with general three-dimensional continuum theory for elastic porous media.

The Biot model [1] applied to the poroelastic foam consists of two homogeneous and continuum mediums (a solid phase and fluid phase) which are coupled by inertial and viscous forces developed into the porous medium owing to the relative motion of the solid and fluid particles.

The Biot formulation of the constitutive equations[9] for a fluid-filled porous material is based on the assumptions of linearity between the stress (δ_{ij}, p) and the strain (ε_{ij}, ζ) and reversibility of the deformation process. The most general form for isotropic material response is

$$\varepsilon_{ij} = \frac{\sigma_{ij}}{2G} - \left(\frac{1}{6G} - \frac{1}{9K} \right) \delta_{ij} \sigma_{kk} + \frac{1}{3H'} \delta_{ij} p \quad (1)$$

$$\zeta = \frac{\sigma_{kk}}{3H''} + \frac{p}{R'} \quad (2)$$

The parameters K and G are the bulk and the shear modulus of the drained elastic solid. The additional constitutive constants H' , H'' and R' characterize the

coupling between the solid and fluid stress and strain.

To predict the behaviour of Poro-elastic materials, finite element model (FEM) based on Biot's theory can be employed. The propagation of sound in a porous material is a phenomenon that is governed by physical characteristics like Young's Modulus, structural damping, Poisson's Ratio, density of the solid frame, porosity, tortuosity, airflow resistivity and the viscous and thermal characteristic lengths[5]. Hence melamine poro-elastic material is analyzed here with different thickness and densities to study their effect with respect to acoustic behavior.

FINITE ELEMENT MODELLING OF FUSELAGE SECTION

The finite element based vibro-acoustic model of fuselage section is created using commercially available general purpose software HYPERMESH to discretize the structure. The physics of this problem involves coupled fluid structure interaction between the acoustics cavity representing the aircraft interior (fluid) and the vibrating fuselage (structure); to solve this coupled fluid structure problem MSC NASTRAN solver is used. Fig.1a illustrates the FEM surface mesh of the aircraft fuselage section with skin segment, stringers, bulkhead, floor board, cargo board stiffeners and windows. The mesh was composed of 4 noded quadrilateral elements and 3 noded triangular elements. Fig.1b shows the acoustic cavity model of the interior of the aircraft. Fluid is modelled using 8 noded brick element. The material properties used in fuselage model is tabulated in Table 1.

The interior fluid volume is modelled using conventional MSC Nastran fluid finite elements connected to a special set of GRID points. The structural interface simply requires that the nodes of finite elements lay on the exterior fluid boundaries. The coupled interactions between the fluid and structural model are generated internally using the geometry definitions of the elements of the two domains (fluid and structure).

4th International Engineering Symposium - IES 2015

March 4-6, Kumamoto University, Japan

FINITE ELEMENT MODELLING OF POREOELASTIC MATERIAL (PEM)

Porous materials are used in a wide range of applications such as automotive, marine and aircraft to improve the acoustic properties at mid and high frequencies without adding an excessive mass. Open-cell surface of the PEM guarantees that sound waves are not reflected as an echo but can penetrate the cell structure unhindered thus sound energy is reduced in the cell structure.

According to Biot's theory several parameters are necessary to represent a poro elastic material. The Biot properties for the Melamine PEM are tabulated in Table 2.

Acoustic and structure models are modelled using HYPERMESH. Passive PEM is idealized using poroelastic trim components, which involves complex multi-physics in terms of the solid fluid interaction at the microscopic level, as well as its unique applications in finite-element based analysis; refer to Fig.2. Poro-elastic foam properties are applied via MATPE1 material card of MSC NASTRAN solver; it is a combination of material cards like MAT1 (for the solid-phase) and MAT10 (for the fluid phase) and additional material parameters unique to the porous medium are considered. In MAT10 card the properties of air is assigned; since we assume air cavities inside the poroelastic material. To define the PEM interface coupling types, ACPEMCP card is used. Interface properties are assigned through TRMCPL. Here the interface between foam and air inside the cabin is made impervious and the interface between foam and outside skin of fuselage material is made glued. In some case even the interface between foam and outer skin of the fuselage is made slip but it is seen that glued interface performs better compared to the slipped one.

NUMERICAL SIMULATION AND VIBROACOUSTIC ANALYSIS

To assess the vibroacoustic performance of fuselage skin, materials like Aluminium, GFRP, CFRP and FML are chosen. The fuselage section is built and the inner air cavity of the fuselage is also modelled. Dynamic analysis like normal mode

analysis is carried on the structure and fluid separately to know their natural frequencies (refer Fig.3). Coupled Frequency response analysis is then carried on the fuselage section with inner cabin air to identify the critical fluid structure coupling modes (refer Fig.4). The propeller noise is introduced as external load in the form of Power Spectral Density (PSD) on to the structure. Sound transmission loss analysis is performed for the fuselage section with all selected skin materials separately in the frequency band of 130 Hz to 260 Hz. The output such as sound pressure level (SPL) and the overall sound pressure level (OASPL) are computed, accordingly.

EVALUATION OF MELAMINE PEM IN NOISE REDUCTION

Acoustic performance of the melamine PEM in sound transmission is analysed. The evaluation is done in two ways; first by varying its thickness i.e Melamine foam of 65 mm and 75 mm respectively are employed. Secondly by varying its density, with Low and high values and their effect in sound transmission is studied.

The finite element model of the melamine PEM is placed between the fuselage outer skin and the inner skin of the fuselage FE model. Necessary coupling between the PEM, structure and the fluid as mentioned earlier is applied. The SPL and the OASPL with different fuselage skin materials with and without Melamine PEM is plotted (refer Fig.6 & Fig.7). The passenger ear position inside the cabin next to the window is selected to plot the SPL and the OASPL plots.

RESULTS AND DISCUSSION

The sound pressure levels in terms of dB are extracted from the frequency response analysis, performed on the structure with propeller loading. From the SPL and OASPL plots, following are the observations made for various fuselage skin materials with and without foam. From the OASPL plot (refer Fig.7a), a difference of 40 dB is seen in FML compared to CFRP.

When 65mm foam is used with aluminium fuselage , the sound pressure reduces to 24 dB and for 75mm foam it reduces to 30 dB (refer Fig.7b). Similarly, for FML as

4th International Engineering Symposium - IES 2015

March 4-6, 2015, Kumamoto University, Japan

fuselage material, addition of foam of thickness 65mm,gives a reduction of 9 dB and with 75mm foam there is a reduction of 19 dB noticed (refer Fig.7c.) For composite materials like CFRP a reduction of 35 dB and 41 dB is seen for 65mm and 75mm foam thickness, respectively (refer Fig.7d). In case of GFRP there is a reduction of 35 dB and 68 dB is observed with 65mm and 75mm thickness foams, respectively (refer Fig.7e)

Sound Pressure contour plots for cabin fluid with FML as skin material is presented in Fig.5. It shows the contour plot of sound pressure, sound pressure level distribution inside the cabin. At a frequency of 167 Hz, (see the figure), a reduction of 10 dB in sound pressure level is observed, when the fuselage is treated with 75mm foam. The SPL plots with foams having high and low density for FML and AL skin are shown in Fig.8; a very minimal SPL change is observed in this case.

CONCLUSION

In this work, the vibro acoustic performance of various fuselage materials with and without acoustic foam is analyzed. Normal mode analysis is carried out to check the natural frequency of the structure and the fluid. Coupled Eigen analysis is performed to obtain the fluid and structure interaction modes. To obtain the sound pressure level inside fuselage cabin for various materials as skin, a frequency response analysis is performed with propeller noise as load. From the analysis it is found that, out of all the materials that have been assessed for vibro-acoustic performance, FML performs better, followed by Aluminium. The thickness of foam has got a drastic effect in reducing the of sound pressure level. Increase in foam thickness gives an improved VA performance. The variation in density of the foam material has very little effect on the VA characteristics of the fuselage structure.

REFERENCES

- [1] Biot. M (1962), Generalized theory of acoustic propagation in porous dissipative media. Journal of the Acoustical Society of America Vol 34, pp.168-178.

- [2] Carl Howard (2000), coupled structural acoustic analysis using Ansys, Department of Mechanical Engineering, The University of Adelaide
[3] Doutres O et al., (2007), Porous layer impedance applied to a moving wall: Application to the radiation of a covered piston. Journal of the Acoustical Society of America, Vol.121, No.1, pp.206-213
[4] GPO's Federal Digital System (2014), Electronic Code Of Federal Regulations, Title 14: Aeronautics And Space, Part 36-Noise Standards: Aircraft Type and Airworthiness Certification. subpart B, 36.103.
[5] Jean-Daniel Chazot and Erliang Zhang (2012). Acoustical and mechanical characterization of poroelastic materials using a Bayesian approach", Acoustical Society of America, Vol.131, No.6, pp. 4584-4595.
[6] Krakens L A (2009), parametric fuselage design integration of mechanics, acoustics and thermal insulation, voorzitter van het college voor promoties.
[7] Mejdi A and Atalla N (2012). Vibroacoustic analysis of laminated composite panels stiffened by complex laminated composite stiffeners. International Journal of Mechanical Sciences; Vol.58, No.1, pp.13-26.
[8] Rajesh Arjunan (2007), vibro-acoustic parametric analysis of honeycomb composite fuselage for improved transmission loss. M.Sc Thesis, Department of Mechanical Engineering, Wichita state university.
[9] Raymond P and Noureddine A (1996), Numerical prediction of sound transmission through finite multilayer systems with poro-elastic materialas, Journal of Acoustical society of America, Vol.100, No.1, pp. 346-354.

Table 1 Material properties

Material	Young's modulus (Gpa)	Poisson ratio	Density (kg/m ³)
Al	70	0.3	2500
CFRP	336.391	0.2	1400
GRPF	132.926	0.2	2000
Acrylic	4.5	0.35	1170
Glass			
Air			1.2

Table 2 Material Properties of Melamine PEM

viscosity	1.84E-8
Gamma	1.40
Prandtl length	7.13E-1
Porosity	9.5E-1
Tortuosity	1.4
airflow resistivity	2.5E-5
VLE	9.32E-2

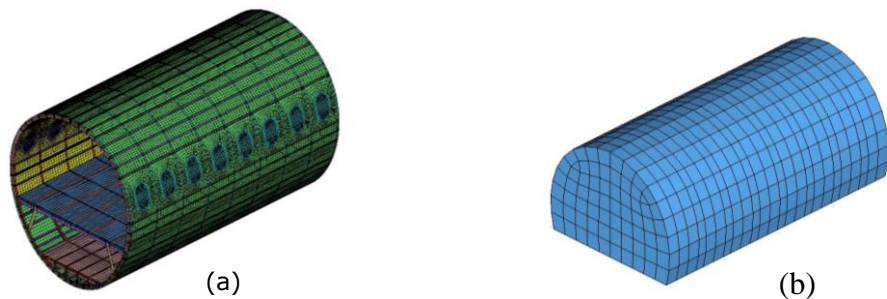


Fig.1 FEM model (a) Fuselage section (b) acoustic cavity

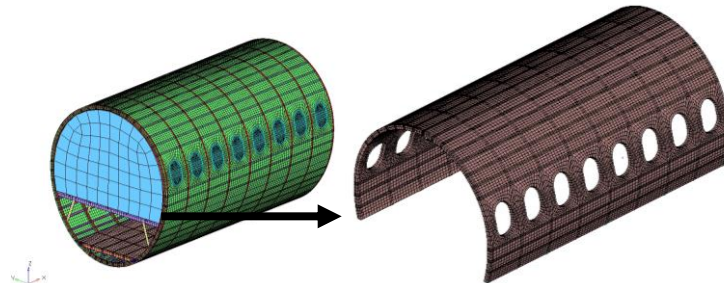


Fig.2 FEM model of Poroelastic material FOAM

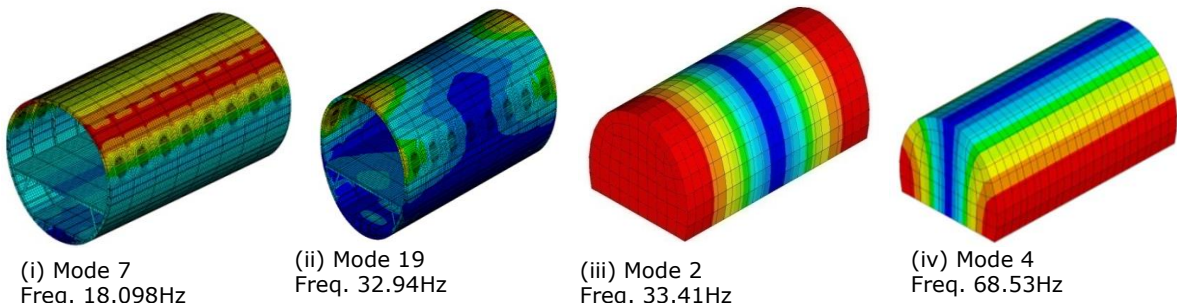


Fig.3 Displacement contours (i)& (ii) Fuselage section (iii)& (iv) acoustic cavity

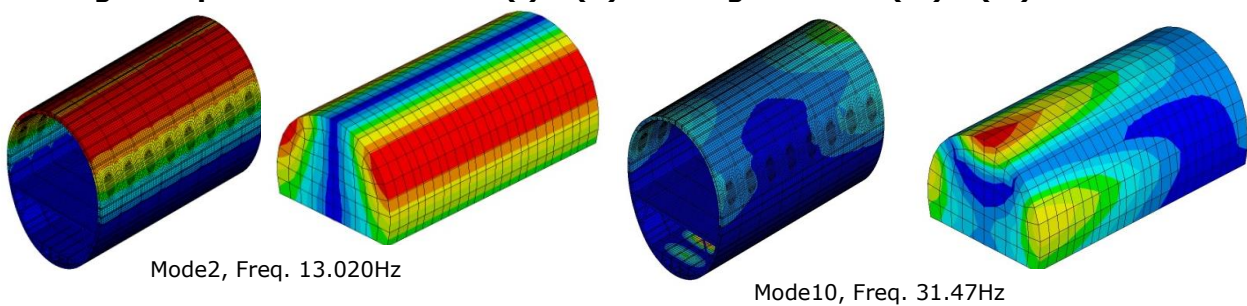


Fig.4 coupling modes displacement contours

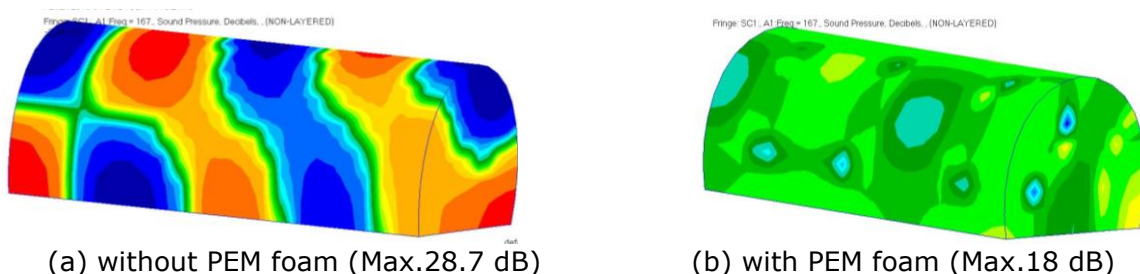


Fig.5 Sound Pressure Level (SPL) inside cabin for FML skin

4th International Engineering Symposium - IES 2015
 March 4-6, 2015, Kumamoto University, Japan

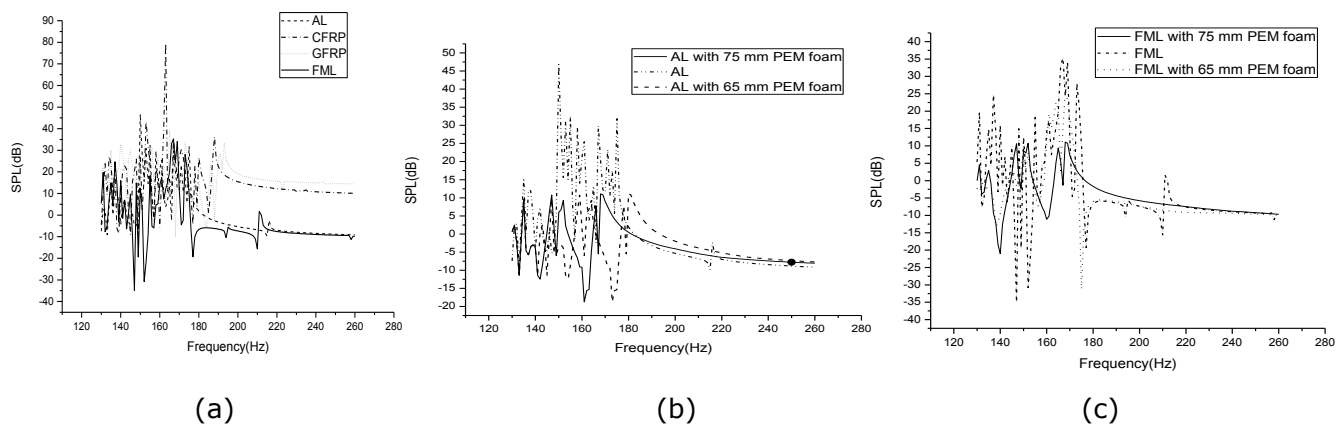


Fig.6 Sound Pressure Level plots

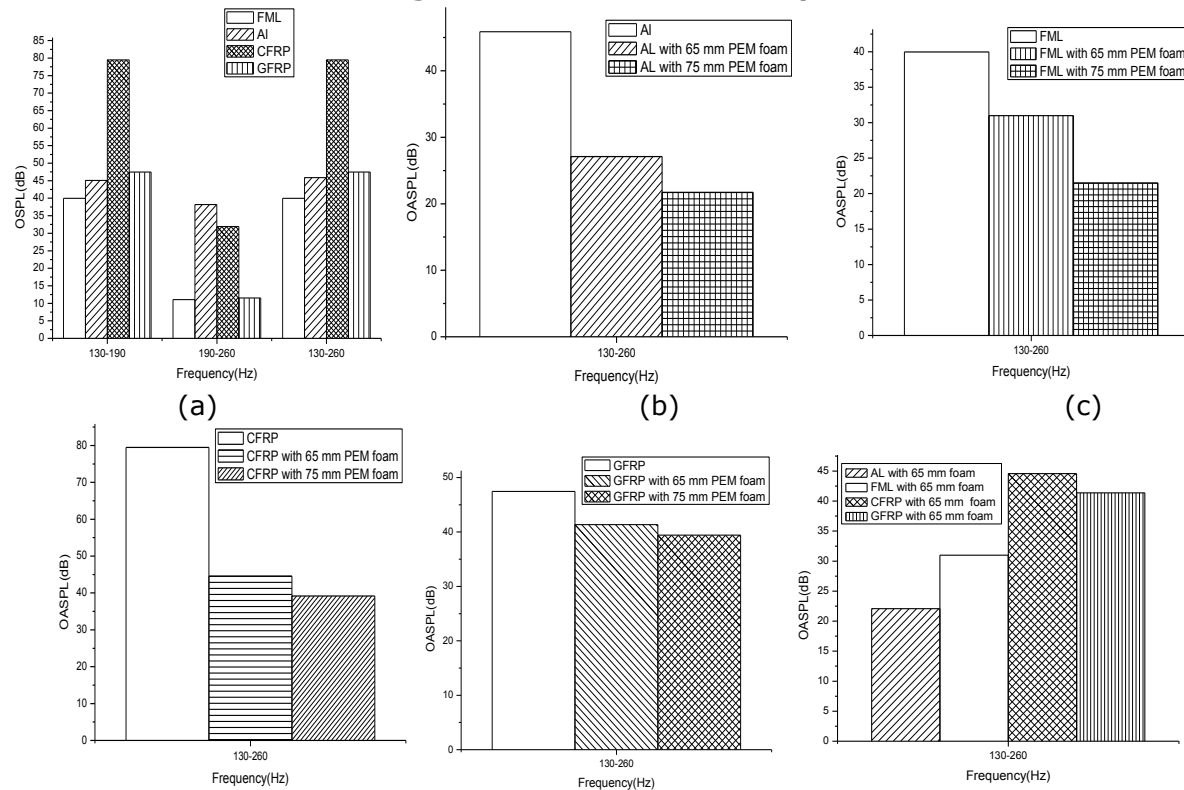


Fig.7 Over All Sound Pressure Level plots

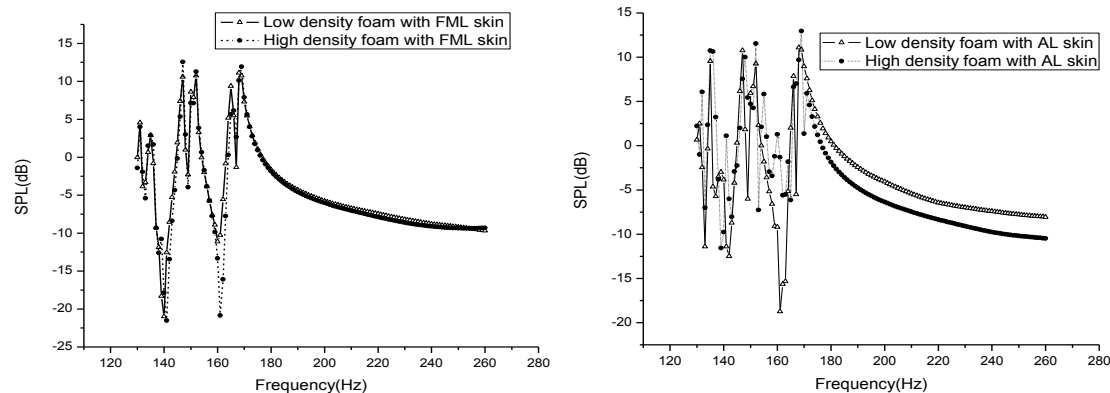


Fig.8 Sound Pressure Level plots with density variation for FML & AL

INTEGRITY EVALUATION OF BORED CAST-IN-SITU PILES – A NON DESTRUCTIVE APPROACH

Rao Katapadi Anirudh¹, Rao Arun Prabha Katapadi Sripathi²

1 *Sahyadri College of Engineering & Management, Affiliated to Visvesvaraya Technological University, Mangalore – 575007, India.
email:katapadianirudh@gmail.com*

2 *Principal Consultant – Construction, Projectile, Mangalore – 575006, India
email:arunprabha1@gmail.com*

ABSTRACT: Pile foundations generally offer no visual inspection for reasonable estimate of the condition of the pile. Confirmation of the structural integrity of a pile is a fundamental requirement. Low Strain Pile Integrity Testing (LSPIT) is a simple, quick, accurate method of evaluation of qualitative and quantitative information of the pile which is the very reason for its widespread acceptance. Test requires impact induced by a small hand held hammer on the shaft top and the measurement of the shaft top motion. The input compression wave from the hammer is reflected from pile toe and returns to the pile top at a time related to the speed of travel of the wave in the pile material. This evaluation provides the integrity aspects of the as-built pile on a real-time basis.

This paper envisages the use of LSPIT in bored cast-in-situ pile. The method of testing, interpretation of the results, acceptance and rejection criteria, remedial action and limitations of testing are also discussed.

Keywords: *LSPIT, Pile, Shock Wave, Strain, Velocity Curve, Accelerometer*

INTRODUCTION

Over the last twenty to twenty five years Non-Destructive Integrity Testing techniques have been in use world over. Today, this is commonly acknowledged as a useful tool for the evaluation of the quality and acceptance of pile foundations. Although, this is a very economical method even for assessing the total number of piles at a site, it is limited in scope to testing the integrity of the shaft and is not intended to replace the use of static load testing. Integrity testing is relatively simple and

quick and enables large number of piles to be examined in a single working day. The method does not identify all imperfections in a pile, but provides information about continuity, defects such as cracks, necking, soil incursions, changes in cross section and approximate pile lengths. LSPIT apparatus consists of a small metal/hard rubber/nylon tipped hammer to produce a light tap on top of the pile. The shock traveling down the length of the pile is reflected back from the toe of the pile and recorded through a suitable transducer/accelerometer fed onto a

hand held computer. The primary shock wave which travels down the length of the shaft is reflected from the toe by the change in density between the concrete and sub-strata. However, if the pile has any imperfections or discontinuities within its length these will set up secondary reflections which will be added to the return signal. The test has been standardized as per ASTM D5882. The result for each pile tested is a velocity curve plotted as a function of time. This curve is investigated for any wave reflections, which indicate a change in pile properties. Low Strain Pile Integrity Test is a very cost-effective method of evaluating integrity of the pile. For a successful pile foundation it is imperative that the piles constructed are of sound quality and of design shape and dimensions that is 'structural integrity'. The routine vertical load tests carried out on working piles do not provide direct information on structural integrity of piles. Also, in view of the very limited number of load tests (0.5 to 2 percent) carried out at a particular project site, it is not possible to reliably testify structural quality of piles. However, it is also true that all the piles cannot be tested in this way because of both economic and time constraints. It is a firm belief that cast-in-situ piles in majority of cases fail because of defective pile shaft necking, discontinuity of concrete, intrusion of foreign matter and improper toe formation due to contamination of concrete at base with soil particles, washing of concrete due to high water current, adoption of improper construction method, poor quality control on concreting or any other reason, cracks developed while handling and installing precast piles can also be a cause of failure. If pile integrity can be assessed before completion of pile caps then this will go a long way to certification of pile integrity. Integrity tests provide an indication of the soundness of concrete but they should be undertaken by persons experienced in the method and capable of interpreting the results with specific regard to piling.

GENERAL REQUIREMENTS OF THE TEST

Piles shall be trimmed to cut off level or sound concrete level before the test with all laitance removed. No pile cap work should be undertaken prior to the test. The area surrounding the pile should be free from standing water and kept dewatered during the tests. The pile head should be accessible. Testing should be free of work likely to cause disturbance. The cast-in-situ piles should not be tested normally before 14 days of casting. The test piles, if available at site, can be used to determine the pulse velocity and characteristic or reference signal generated. Where no test pile is available information can be obtained from cast piles whose length is accurately recorded.

METHOD OF TESTING

The LSPIT processor provides signal conditioning, digital signal processing, digital signal storage and for output an LCD screen. The first and sometimes most important step for any low strain test is the preparation of the pile top surface. In fact, depending on the construction method it may be necessary to remove several inches of the upper concrete if it is contaminated with soil, bentonite slurry or any other foreign materials during construction. After a clean, healthy and hard concrete top surface is exposed, the accelerometer is attached to the pile surface with a thin layer of soft paste like vaseline, petro-wax etc. After this preparation, an impact with the hand held hammer is applied. The impact typically generates pile strains around 10^{-5} , and displacements less than 0.03mm. Accelerations produced by several hammer blows are integrated and displayed as velocities on the processor's screen. Consistent records are selected, averaged, scaled and then redisplayed. Averaging reinforces repetitive information from pile or soil effects while reducing random noise effect. Image below shows schematic representation and the PIT tester.

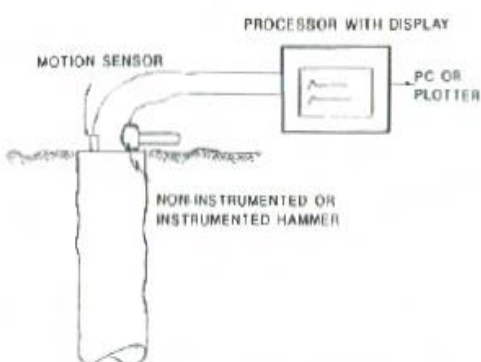


Fig. 1 Schematic of Pile Integrity Testing



Fig. 2 Pile Integrity Tester

WAVE SPEED AND PILE LENGTH CALCULATIONS.

The low strain test method has two unknowns, the length and the wave speed and one of them has to be known in advance. The test engineer to determine the length or wave speed uses the following two procedures.

- Assuming that the pile or shaft length is known accurately, the wave speed is back calculated from the time between impact and pile toe reflection.
- If the shaft length is not known then a wave speed is assumed based on the experience, and the pile length is then calculated from time of toe reflection. Since wave speeds of the piles in the same site normally fluctuate within $\pm 5\%-10\%$, similar variation in predicted length must be expected.

STRESS WAVE PROPAGATION IN A PILE

The linear one dimensional wave equation represents a pile that is long compared to its width or diameter and which consists of linearly elastic material. A violation of this basic condition may imply an L/D ratio less than 10 or poor concrete quality inside the pile. As a compressive downward travelling wave encounters a cross sectional reduction, an upward travelling tensile wave is generated which can be observed at the pile top at a time equal to twice the distance of disturbance from the pile top divided by the wave speed. Thus a wave form travelling through a pile will reflect due to three reasons: changes in cross section, changes in soil properties and changes in material property of the pile. Thus reflections are primarily due to change in impedance Z or soil strata changes. This pile impedance, Z is the product of cross sectional area, and elastic modulus divided by the wave speed, a decrease in either the cross sectional area or elastic modulus can result in a tensile toe reflection, while an increase of either cross sectional area or elastic modulus will produce a compressive reflection. Typical Velocity curve for good pile and for damaged pile are given below.

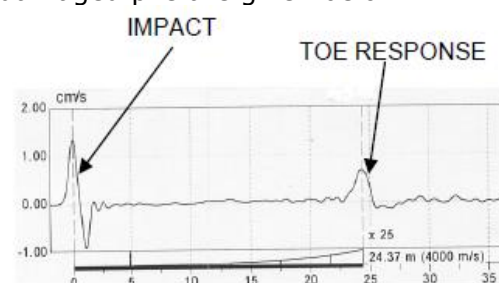


Fig. 3 Typical Velocity Curve—Good Pile

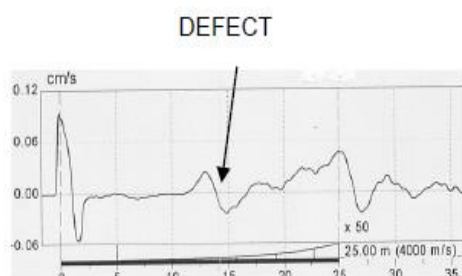


Fig. 4 Typical Velocity Curve—Defect Pile

BENEFITS OF PILE INTEGRITY TESTING

The test is simple, reliable and can be easily performed. The test determines defects in pile and with additional field information, it is possible to ascertain the nature of defect, viz. reduction in cross section, cold joint, poor concrete quality etc.

The test can be used to identify piles for further static or dynamic testing instead of random selection thus ensuring better quality control.

The test can be used to ascertain pile length with reasonable accuracy.

The test can also be used as a quality control tool for both offshore and onshore structures.

Cost of test is fraction of the entire cost of piling.

ACCEPTANCE AND REJECTION CRITERIA

It is for the engineers to decide whether results of the tests point to the likelihood of defects being present of such significance as to affect materially the long term load carrying capacity of the pile.

The engineer should then decide whether to carry out further examination of the pile or to take remedial action for which a sound engineering judgement is called for.

LIMITATIONS OF THE TEST

Non-Destructive Testing of piles does not provide the load carrying capacity of piles.

It does not provide information regarding verticality or displacement in position of piles.

Minor deficiencies like local loss of cover, small intrusions or type of conditions of materials at the base of piles are undetectable. Integrity testing may not identify all imperfections, but it can be useful tool in identifying major defects within the effective lengths. The test may identify minor impedance variations that may not affect the bearing capacity of piles. In such cases, the engineer should use judgment as to the acceptability of these piles considering other factors such as load redistribution to adjacent pile, load transfer to the soil

above the defect, applied safety factors and structural load requirements.

Based on the latest information available, the limitations relating to the depths up to which the integrity tests can be carried on piles, depends on the surrounding strata and damping within the concrete.

Soil stiffness or founding on rock of similar density as the pile will attenuate the signals such that there will be little or no toe reflection.

The low strain integrity method is applicable to cast-in-situ concrete bored and driven piles. Conclusive results are rarely obtained in case of segmented precast reinforced concrete driven piles or precast piles in prebored holes.

REFERENCES

- [1] Likins, G. E., Rausche, F., September 2000. Recent Advances and Proper Use of PDI Low Strain Pile Integrity Testing. Proceedings of the Sixth International Conference on the Application of Stress-wave Theory to Piles 2000: São Paulo, Brazil, pp.211-218.
- [2] Rausche F, Likins G E and Hussain M, "Pile Integrity by Low and High Strain Impacts", Proceedings of the Third International Conference on Stress Wave Theory on Piles, Ottawa, Canada, May 1998.
- [3] Ravikiran Vaidya, D L Shah, (2001), Pile Diagnostics by Low Strain Integrity Testing, IGC 2001, "The New Millennium Conference", 14-16 Dec.. 2001, Indore.

POTENTIAL APPLICATION OF EXPERIMENTAL PREDICTION EQUATION IN ESTIMATING THE CORROSION OF RC STRUCTURES

Akshatha Shetty¹, Katta Venkataramana², Babu Narayan K. S.³ and Srinath Shetty⁴

¹ Department of Civil Engineering, NMAMIT Nitte, Karnataka India. e-mail:akshathashetty16@gmail.com

^{2 &3} Department of Civil Engineering, National Institute of Technology Karnataka, Surathkal, Mangalore 575025, India. email:ven.nitk@gmail.com, srilalisutha@gmail.com

³ Department of Civil Engineering, NMAMIT Nitte, Udupi 574110, India. Email: shettsrinath@nitte.edu.in

ABSTRACT: Corrosion is one of the factors affecting the structures in coastal environment. Corrosion is defined as destruction or deterioration of material because of its reaction with environment. Corrosion ultimately affects the strength and serviceability of RC structure. Hence the present study aims to investigate the real life structures for corrosion rate using applied corrosion monitoring instrument. Based on the prediction equation of experimental data, bond strength of RC structures can be determined.

Keywords: corrosion rate, bond strength, reinforcement, concrete

INTRODUCTION

Chloride ingress into the concrete is a major cause of steel corrosion. Presence of chloride ions at the rebar level leads to the breakdown of passive film layer and consequently initiates the corrosion (Pradhan and Bhattacharjee, 2009). In case of corrosion formation, an oxide of iron due to oxidation of the iron atoms in solid solution is a well-known example of electrochemical corrosion, commonly known as rusting. These oxides are usually weaker than steel. Rust produced as a result of corrosion increases its volume 2 to 6 times than that of original steel; it causes increase in volume of tensile stresses in concrete (Bhaskar et al. 2010).

The process of corrosion is initially slow and later it progresses exponentially. To understand and

appreciate the effects of natural conditions causing corrosion, tremendous amount of time and resource are needed. Hence for the present study, simulation of condition in an accelerated way (using impressed current technique) is considered; whereby time can be saved and existing structures performance can be better understood.

Corrosion of reinforcement is a prime concern as stability, strength, safety, serviceability, and durability and economy of RC structures are severely affected. One of the most important prerequisites of reinforced concrete construction is adequate bond between the reinforcement and the concrete.

SIGNIFICANCE OF BOND STRENGTH

Reinforced steel bar can receive its external loads only from the

4th International Engineering Symposium - IES 2015

March 4-6, 2015, Kumamoto University, Japan

surrounding concrete, because external loads are very rarely applied directly on it. Composite action between concrete and reinforcing steel cannot occur without proper bond (Shetty A. et.al. (2013).

EXPERIMENTAL STUDY

National Bureau of Standard (NBS) beam specimens of size 2.44mx0.457mx0.203m were used. Concrete grade of M30 and water cement ratio of 0.45 was adopted for the study. Mix proportion of 1:1.77:2.87 selected after the trial mix design both for OPC and PPC concrete specimen.

After casting beam specimens were cured for 28 days and accelerated corrosion was achieved using impressed current technique. Amount of current required to induce corrosion levels are calculated from Faradays Eq. 1, (ahmad, 2009).

$$i_{corr} = i_{app} = \frac{\rho \times W_i \times F}{100 \times \pi \times d \times l \times w \times t} \quad (1)$$

i_{app} = Applied Current

F = 96487 Amp – sec

l = Length of the bar (= 85cm)

w = Equivalent weight of iron (= 27.925g)

$\pi d l = \pi \times 1.6 \times 85 = 427.6 \text{ cm}^2$

t = Time in seconds

ρ = Degree of corrosion percentage

Once the corrosion process is achieved measurement of corrosion level is carried out using Applied Corrosion Monitoring (ACM) Instrument.

ACM INSTRUMENT MEASUREMENT PROCEDURE

Measurement of corrosion using guard ring

In LPR method, reinforcing steel bar was polarised potentiostatically by an inner auxiliary electrode and the real time plot of current response was displayed on a laptop screen which controls the guard ring device. Area of steel polarised was confined by a current applied from an outer guard ring electrode. Area of steel was controlled by two sensor electrodes positioned between the inner auxiliary and outer guard ring electrode (Law et al. 2000).

Linear polarization resistance technique

LPR procedure is based on Stern-Geary characterization of typical polarization curve for the corroding metal. In this method, a linear relationship is described mathematically for a region on the polarization curve in which slight change in current applied to corroding metal causes corresponding change in potential of the metal. In other words, if a large current was required to change potentials by a given amount, the corrosion rate will be high and on the other hand, if only a small current was required, then corrosion rate will be low.

Corrosion cell consists of a guard ring with reference electrode and reinforcing steel embedded inside concrete specimen functions as working electrode. Reinforcing steel bar was polarized by applying a small potential shift to it (ΔE) and resultant current (ΔI), between working electrode and counter electrode (Ha-Won song and Saraswathy 2007). Measurement of corrosion set up is shown in Fig. 1. The corrosion current density was then calculated by using the Stern-Geary formula from Eq. 2, (Fontana, 2005).

$$i_{corr} = \frac{B}{R_p} \quad (2)$$

where, i_{corr} = Corrosion current density ($\mu\text{A}/\text{cm}^2$); R_p = Polarization resistance

4th International Engineering Symposium - IES 2015

March 4-6, 2015, Kumamoto University, Japan

($\text{k}\Omega \text{ cm}^2$); $B = 26 \text{ mV}$ for steel in active condition

After measurement of corrosion process beam specimens were tested using two point flexural strength test. Test set up is shown in Fig. 2. After analysing results using bond strength Eq. 3, the following regression equations are suggested:

OPC concrete

$$y = -0.076x + 3.099 \quad R^2 = 0.992 \quad (3)$$

PPC Concrete

$$y = -0.084x + 3.269 \quad R^2 = 0.990 \quad (4)$$

where, x =corrosion levels (%) and y = bond stress (N/mm^2).

POTENTIAL APPLICATIONS OF PREDICTION EQUATIONS-ILLUSTRATIONS

The potential application of the findings in real time health monitoring of structures is presented in the sections that follow.

Illustration I: Element Assessed-An RC beam in the swimming pool complex at NITK Surathkal.

Beam has a width of 230mm and depth of 300 mm. Main bar 3 No's-16mm have been provided at a clear cover of 25mm. Concrete grade used is M15. Corroded rebar inside beam element is shown in Fig. 3

Test set up of field data acquisition set up for corrosion current density (i_{corr} , $\mu\text{A}/\text{cm}^2$) determination using ACM instrument as shown in Figs. 4 and 5 Real time plot of Potential (mV) vs current (mA/cm^2) for corroded beam is shown in Fig. 6. For the polarisation value obtained from the plot, corrosion current density value is determined using Stern-Geary formula Eq. 2. Table 1 represents the values of corrosion current density.

Degree of corrosion percentage (ρ) can be determined using Faradays law as detailed in Eq. (3.1).

For the beam in question the required data for corrosion percentage determination are as under:

W_i = Initial weight of steel reinforcements =93,469g

F =Faradays Constant=96487 Amp-sec

w = equivalent weight of iron=27.925 g

Πdl =Surface area=73,915cm²

t = Time in seconds, from field test
=19×365×24×3600

And substitution in Eq. 1 yield corrosion % as

$$(0.576 \times 10^{-6}) = \frac{\rho \times 93469 \times 96487}{100 \times 73915.39 \times 27.925 \times 19 \times 365 \times 24 \times 3600}$$
$$\therefore \rho = 7.9\%$$

Based on proposed prediction equation for M30 grade concrete from Eq. 3:

$$\text{Bond Strength} = 2.5 \text{ N/mm}^2$$

Corresponding bond strength for M15 grade concrete:

$$\text{Bond strength} = 2.5 \times 0.707 = 1.77 \text{ N/mm}^2$$

Similarly different illustrations in NITK Campus were carried out and bond strength values are determined for the corresponding corrosion levels and are shown in Table 2.

CONCLUSIONS

The following conclusions are drawn from this study:

- Proposed regression equation is very much useful for quick assessment to predict the bond strength values for different corrosion levels in structures. Structures can be monitored for different corrosion levels by using the applied corrosion monitoring instrument. Based on measured corrosion current density values, corrosion percentage can be

4th International Engineering Symposium - IES 2015

March 4-6, Kumamoto University, Japan

determined. With the help of empirical prediction equation for different corrosion percentage, drop in bond strength values can be determined

- Versatility of the results is applicable to the RC beam structures for the different levels of corrosion within the experimental data (0% to 10% variation).

REFERENCES

- [1] Ahmad, S (2009). Techniques for inducing accelerated corrosion of steel in concrete, ARABIAN SCIENCE AND ENGINEERING, Vol. 34, No. 2C pp.1-11.
- [2] Bhaskar, S et al (2010), Effect of corrosion on the bond behavior of OPC and PPC concretes, JOURNAL OF STRUCTURAL ENGINEERING, Vol. 37 No. 1, pp. 37-42.
- [3] Fontana, M G, (2005). Corrosion Engineering. Tata McGraw-Hill Education Private Limited, New Delhi.
- [4] Ha-Won song and saraswathy, V (2007). Corrosion Monitoring of Reinforced Concrete Structures – A Review. INTERNATIONAL JOURNAL OF ELECTROCHEMICAL SCIENCE, Vol, pp. 21-28.
- [5] Law, D W, et al (2000). Linear polarisation resistance measurements using a potentiostatically controlled guard ring. NDT AND E INTERNATIONAL, 33, 15-21.
- [6] Pradhan, B and Bhattacharjee, B (2009). Performance evaluation of rebar in chloride contaminated concrete by corrosion rate, CONSTRUCTION AND BUILDING MATERIALS, Vol. 23, pp. 2346-2356.
- [7] Shetty, A. et al (2013). Bond strength behaviour in reinforced concrete members exposed to corrosive environment-an overview. INTERNATIONAL JOURNAL OF EARTH SCIENCES AND ENGINEERING, Vol. 5, NO. 3(1), pp. 530-535.

Tables and Figures

Table 1: Corrosion current density ($\mu\text{A}/\text{cm}^2$) of corroded RC beam

Corrosion current density (i_{corr})			
Grid-1	Grid-2	Grid-3	Average
0.583	0.563	0.582	0.576

Table 2: Effect of corrosion on bond Strength

Location of Beam Member	Age years	Corrosion (%)	Grade of concrete	Bond Strength (N/mm ²)
Naturally exposed	3	1	M20	2.5
Civil Department (FF)	8	2.89	M15	2.0
Civil Department (GF)	14	5.16	M15	1.9
Swimming Pool Complex	19	7.9	M15	1.8

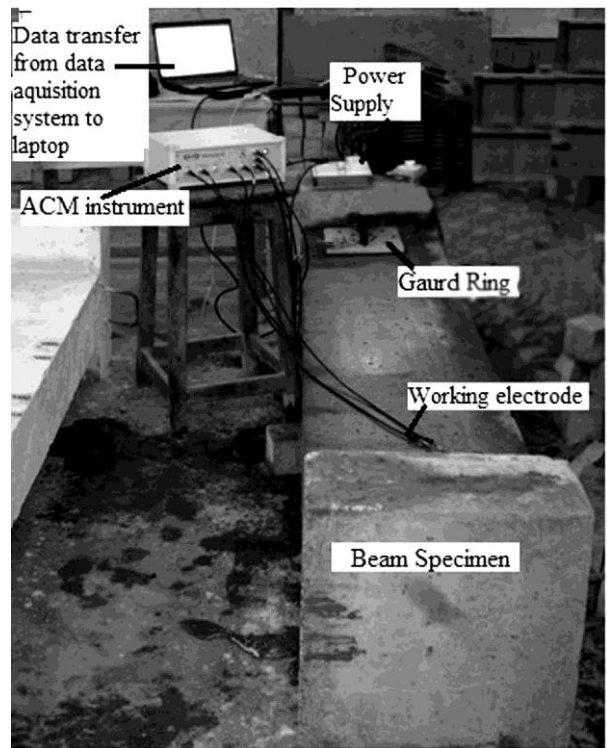


Fig. 1: Corrosion monitoring set up

4th International Engineering Symposium - IES 2015
March 4-6, 2015, Kumamoto University, Japan

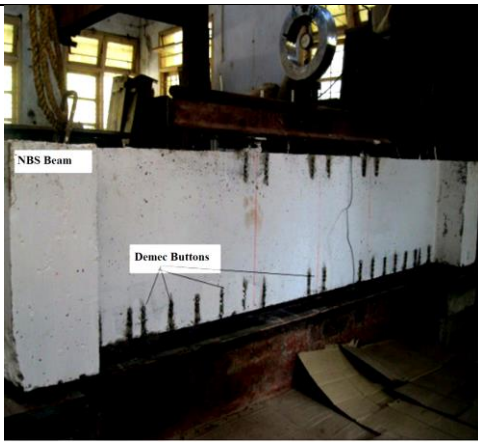


Fig. 2: Flexural strength test set up



Fig. 3: Corroded rebar inside beam



Fig. 4: View of working electrode connection to rebar



Fig. 5: Monitoring of beam specimen with guard ring

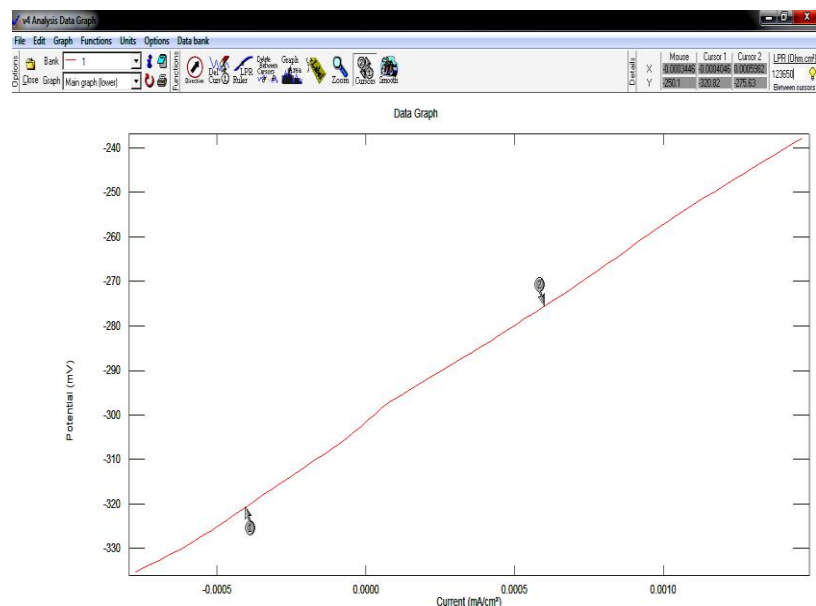


Fig. 6: Real time plot of corroded beam using ACM instrument

CRYSTAL HEATED COMFORT JACKET

Saudamini Rao Katpadi¹, Arun Prabha K S², Vishnuprasad P V³

-
- 1 *Sahyadri College of Engineering & Management, Affiliated to Visvesvaraya Technological University, Mangalore – 575007, India. email:sweety2993@gmail.com*
 - 2 *Principal Consultant – Construction, Projectile, Mangalore – 575006, India email:arunprabha1@gmail.com*
 - 3 *Sahyadri College of Engineering & Management, Affiliated to Visvesvaraya Technological University, Mangalore – 575007, India. email:vishnuprasadparppuram@gmail.com*
-

ABSTRACT: In the proposed paper, by employing the Pyro electric effect of Bismuth crystals, we are making a jacket which can warm the body at low temperatures. The Bismuth crystals will produce voltage across the jacket when there is a temperature difference between the surroundings and body. By using the voltage which is generated from the crystal a coil embedded in the jacket is heated. The cold air penetrating from outside of the jacket passes through the heated coil and the air which becomes hot, heats the wearer's body. These jackets can be extensively used in the army; thereby soldiers who are the fighting and guarding force of a nation to all its external threats can work in any extreme climatic conditions. As the gadget designed does not need any external source to work; the maintenance charges will be low. The electronic circuit proposed is simple and hence low cost.

KEYWORDS: *Pyro electric effect, Bismuth crystals, temperature difference, amplified voltage, rechargeable battery.*

INTRODUCTION:

Bismuth is a chemical element with the symbol Bi and an atomic number of 83. Bismuth is a pentavalent post-transition metal, chemically resembles arsenic and antimony. Elemental bismuth may occur naturally, although its sulfide and oxide from important commercial ores. The free element is 86% as dense as lead. It is a brittle metal with a silvery white color when freshly produced, but is often seen in air with a pink tinge owing to surface oxidation. Bismuth is most naturally diamagnetic element and has one of the

lowest values of thermal conductivity among metals.

PHYSICAL CHARACTERISTICS:

The spiral, stair-stepped structure of bismuth crystals is the result of higher growth rate around the outside edges than on the inside edges. The variations in the thickness of the oxide layer that forms on the surface of the crystal causes different wavelengths of light to interfere upon reflection, thus displaying rainbow of colors. When burned in oxygen, bismuth burns with a blue flame and its oxide

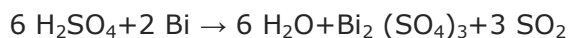
forms yellow fumes. Its toxicity is much lower than that of its neighbors in the periodic table, such as lead, antimony and polonium.

CHEMICAL CHARACTERISTICS:

Bismuth is stable to both dry and moist air at ordinary temperatures. When red hot it reacts with water to make bismuth (III) oxide.



Bismuth dissolves in concentrated sulfuric acid to make bismuth (III) sulfate and sulfuric dioxide.



It is used as a transmetalating agent in the synthesis of alkaline-earth metal complexes.



The price of the bismuth metal has been relatively stable through most of the 20th century, except for a spike in the 1970s. Bismuth has always been produced mainly as a byproduct of lead refining and thus the price usually reflected the cost of recovery and the balance between the demand and production. Though it is a byproduct, it is substantially more dependent on recycling.

BISMUTH CRYSTAL:



Fig1: Bismuth Crystals

Bismuth has a few commercial applications, none of which is particularly large. Taking the US as an example, 884 tonnes of bismuth were consumed in 2010, of which 63% went into chemicals, 26% into metallurgical additives for casting and galvanizing, 7% into bismuth alloys, solders and ammunition, and the balance into research and other uses.

PYRO ELECTRIC EFFECT:

When certain materials are heated or cooled, generate a temperature voltage. This particular ability of the material is known as the Pyro electric effect. The change in temperature modifies the position of the atoms slightly within the crystal structure, such that the polarization of the metal changes. Usually, there is a slight confusion between pyro electricity and thermo electricity. In a typical demonstration of Pyro electricity, the whole crystal is changed from one temperature to another and thus the result is temporary voltage across the crystal. Whereas in a typical demonstration of Thermo electricity, one part of the device is kept at one temperature and the other part at a different temperature, and the result is a permanent voltage across the device as long as there is a temperature difference. The property of pyro electricity is the measure change in net polarization proportional to a change in temperature. Pyro electric materials have the potential to generate electrical power from thermal fluctuations.

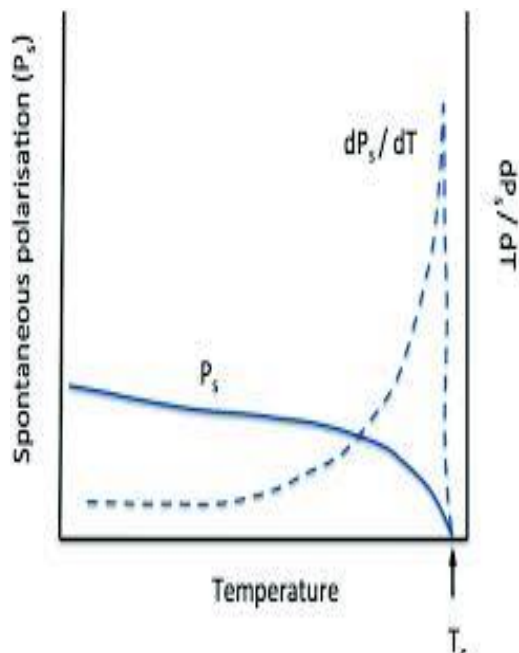


Fig2:The change of Spontaneous Polarisation

Pyroelectric property

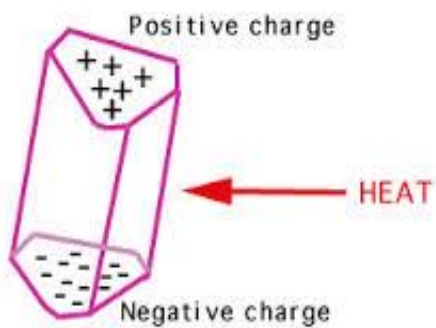


Fig3: Pyroelectric Effect

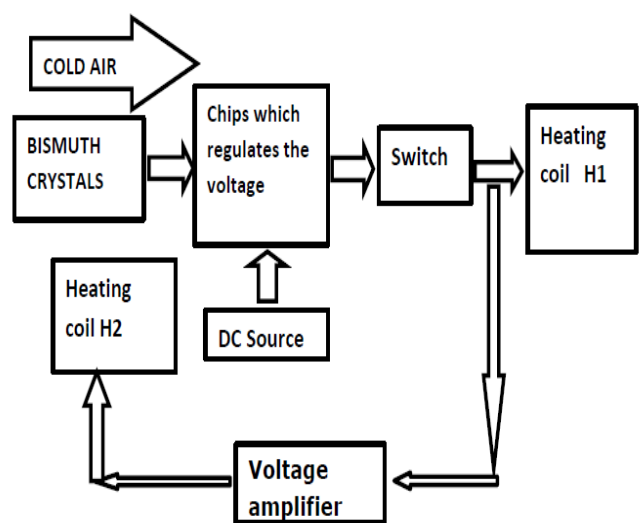


Fig4:Schematic drawing of Comfort Jacket

BASIC PRINCIPLE:

Pyro electric crystals are the crystals which generate voltage when there is temperature difference. The previously used methods to keep the body warm are complex.

WORKING:

The Bismuth crystal is cooled by cold air. Since there is temperature change, the crystal will produce a voltage. This produced voltage is then passed to the chip's input. Here the chip compares the voltage with the voltage which is necessary to produce the required body temperature by the heating coil, and its controls the switch. Finally the voltage V_2 flows through the heating coil H_1 and heats the cold air entering from outside the jacket until it matches with the wearer's body temperature. Thus the voltage V_1 acts as a feedback which is amplified by the voltage amplifier and then passed through the heating coil H_2 .

PROPOSED METHOD

When the crystal's temperature remains constant, the voltage generated gradually becomes voltage produced is in the range of millivolt. This voltage needs to be amplified before applying to both the coils. The dc required for the amplifier, chip can be provided from a zero. At that time, the heating coil H2 heats the crystal and the temperature difference is created and again the voltage is generated. Hence this cycle keeps on repeating. The rechargeable battery which can be charged from solar or from boots of the soldiers in which the pressure applied is converted into piezoelectric voltage by quartz crystal with the help of a small damper.

CONCLUSIONS:

The proposed crystal heated comfort jacket can be used by the Army personals at the World's largest battle field Siachen.

Siachen Glacier is located in the eastern Karakoram range in the Himalaya Mountains where the line of control between India and Pakistan ends. Most of the casualties in Siachen has been due to the weather.

REFERENCES:

- [1].Brewster David (1824). Observations of the pyro-electricity of minerals.
- [2]. "Bismuth line", The Fee Dictionary's Medical Dictionary.
- [3].Norman, Nicholas C (1998). Chemistry of arsenic, antimony and bismuth.
- [4].Taylor Harold A (2000). Bismuth Financial Times Executive Commodity Reports.
- [5].Webster, John G (1999). The measurement, instrumentation and sensors handbook.
- [6].William Thomson (1878),"On the thermoelastic, thermomagnetic and pyroelectric properties of matter".

ANALYSIS OF FLOATING OFFSHORE WIND TURBINE

Jobil Varghese 1, Freeda Christy 1 and Katta Venkataramana 2

*1 School of Civil Engineering, Karunya Institute of Technology and Sciences,
Karunya Nagar, Coimbatore 641114, India. email: jobilvarghese@gmail.com,
freeda@karunya.edu*

*2 Department of Civil Engineering, National Institute of Technology Karnataka,
Surathkal, Mangalore 575025, India. email: ven.nitk@gmail.com*

ABSTRACT: The quest for safe energy is pushing the wind turbines to deeper waters. The innovations in floating structures that will not capsize even in the most unfavorable climatic condition resulted in the revelation of the spar structure (deep draught floater). The generated power of the wind turbine has a cubic relation with the velocity of wind. This fact together with the increased wind velocity, less turbulence and surface roughness in the offshore environment makes floating offshore wind turbine a more viable option for energy generation. The paper analyses the response of the spar structure off the coast of Bay of Bengal, the eastern coast of India. The literature pertaining to the analysis and the computer programs developed for the analysis were discussed. The various environmental forces acting on the wind turbine and spar structure such as wind force and wave force were calculated. The analysis is done using commercial finite element analysis software Ansys. The study reiterates the necessity of installing wind turbines offshore.

Keywords: : Spar structure, Environmental Forces, Response, Finite Element Analysis, Offshore

INTRODUCTION

The improvement in the living standards of the people around the world together with the dependence on industrialization to sustain country's growth rate led to the increase in the energy demand. The fossil fuels like oil and natural gas is depleting day by day and the environmental threats they pose are considerable. Under these circumstances it is imminent to turn to renewable energy source like the wind and solar energy. Proven technology is available to harness wind energy onshore but some constraints like visual pollution and threat to avian population restricts its substantial deployment. Offshore wind turbines does not possess any of the disadvantages that onshore wind turbine

possess, but have the added advantage that the quality of wind in terms of velocity, turbulence and surface roughness are more favourable for power generation in the offshore environment. The generated power have a cubic relation with the wind velocity. Due to surface roughness the velocity of the wind is comparatively less at lower levels onshore. It have less effect on the offshore environment and turbines can be installed at less height. Less turbulence means more uniform loading on the turbine and tower and more life to the unit. The complexities involved in the marine soil structure interaction, installation and ill effects of scouring can be avoided by providing floating platforms for wind turbine installation. The details of the

4th International Engineering Symposium - IES 2015

March 4-6, Kumamoto University, Japan

turbine selected is furnished in Table 1. The platform chosen for installation is the spar structure that will not capsize even in the worst environmental condition.

SPAR STRUCTURE

The structure designed for the purpose consists of two cylindrical hulls. The diameter of the inner hull is made to match with diameter of the tubular tower for wind turbine installation. The gap between the hulls is made into empty compartments that will provide buoyancy and additional rigidity to the structure. The central hull is taken to a lower level and at the bottom soft tank is provided that accommodates the fixed ballast (high density material). Because of the high density material at the bottom, the centre of gravity of the structure is always lower than the centre of buoyancy and this makes the spar structure unconditionally stable. The location chosen for installation is the bay of Bengal that posses potential challenges to the operation of wind turbine due to the frequent occurrence of cyclones. The structure is fixed to the ocean floor by means of taut catenary moorings.

LITERATURES OVERVIEW

Load and stability requirements are governed by the procedures of the International Electro Technical Commission [(IEC) 61400-3]- offshore wind turbine design standard. The method of stabilizing the floating platform is more important in dynamic response than the design features. The offshore wind turbines experience more load on their components than their counterpart onshore due to the coupling between the turbine and the floating platforms. Robertson and Jonkman (2011) modeled different types of floating structure installing 5MW wind turbine at two different water depths. The platforms model included Barge that maintains stability with the help of large water plane area and shallow draught, Semi-submersible a hybrid system that use a combination of large water plane area deep draught and ballasting for its stability, Tension leg platform (TLP) maintains stability by mooring lines and excess buoyancy and Truss spar maintains

stability by deep draught and fixed ballast. Agarwal and Jain (2003) modeled spar as a rigid body with 6 degrees of freedom, connected to the sea floor by multi-component catenary mooring lines.

Moriarty and Butterfield (2009) said that floating wind turbine modeling can be broken into the related areas on aerodynamics, hydrodynamics, turbulent inflow, foundation dynamics and structural dynamics. Heege et al (2011) discretized the wind turbine models by more than 3000 degrees of freedom that accounted for all the coupling effects. He formulated offshore loads in terms of hydrostatic buoyancy and hydrodynamic wave loads which are approximated through Morison's equation. Wang and sweetman (2011), computed large amplitude translational motion of floating wind turbine from the theorem of motion of mass centers and rotational motion by the sequenced Euler angles and the law of conservation of angular momentum. Ran and Kim (2001), presented the response of spar platform in random waves and currents after conducting experiments with 1:61 scale model. Wang et al (2007), validated the time domain and frequency domain hydrodynamic analysis of geometric spar by physical and model test results. They pre-generated irregular wave excitation time series by means of the Fast Fourier Transform and the motion equations were solved directly by numerical integration to obtain the six degree of freedom motion and wave force series. Ran et al (1999) generated total wave force time series based on a 2- term volterra series model. The hull/mooring coupled dynamics were solved by time domain. Bir and Jonkman (2008), presented modal dynamics of floating platform-supported and mono pile-supported offshore turbines. Ran et al. (1999), coupled the mooring lines to the platform through generalized springs and dampers and showed that dynamic effects are very important for mooring design. Zhang et al. (2007), modeled mooring lines consisting of bar elements only (bending stiffness and torsional stiffness were neglected). Matha et al. (2006), outlined different techniques for the representation of mooring-line dynamics, including quasi-static, finite element, and

4th International Engineering Symposium - IES 2015

March 4-6, Kumamoto University, Japan

multi-body methods, and investigated their impact on global system loads. Karimirad (2010), suggested that wind turbines are to be designed for operational and survival conditions. Fylling and Berthelsen (2011), in their optimization of floating support structure for deep water, fixed parameters for design as floater motions, heel angle, nacelle acceleration, capacity, offset limitations etc and the design variables as spar diameter and length, mooring line diameter, length and pretension. Chen et al. (2006), developed numerical code 'COUPLE' for computing the motions and tensions pertaining to a moored floating structure and developed a code for computing dynamics of mooring/tendon/riser system which is based on a slender body assumption and employs a non linear finite element method known as 'CABLE3D'. Wayman et al. (2006), coupled the aerodynamics and structural dynamics code 'FAST' with the wave load and response simulation code WAMIT(Wave Analysis at MIT). Wang et al. (2007), did numerical simulation of wave loads and motion response in a specified wave condition by commercial program 'SESAM'. Bir and Jonkman (2008), used program 'Bmodes' to provide modes for flexural towers to carry head mass (rotor-nacelle subassembly modeled as rigid body). Manenti et al. (2008), developed smoothed particle hydrodynamics (SPH) for simulating wave induced loads on support structure for offshore wind turbines. Montasir and Kurian (2011), developed a MATLAB program 'TRSPAR' to predict the dynamic response in time domain.

IEC RECOMMENDATIONS

The wind turbine and the support structure should withstand the load and load effects prescribed in the (International Electro-Technical Commission) IEC-61400-1 for the site specific wind characteristics. IEC-61400-1 divides the wind turbine into three classes I, II and III depending upon the wind velocity of the location 50m/s, 42.5m/s and 37.5m/s. The various design situations to be considered are power production plus occurrence of fault, start up, normal shut down, emergency shut down, (control failure or network failure)

parked condition, parked and fault condition (yaw error), during transport, assembly maintenance and repair. The wind conditions normally encountered are extreme wind, wind distribution, turbulence, wind shear, dynamics events. The load types are fatigue and ultimate load. The check list for site assessment includes extreme winds shear of vertical wind profile, flow inclination, background turbulence, wake turbulence, wind speed distribution etc. Partial safety factors for favorable and un favorable loads for the various design situation such as normal, abnormal, transport and erection are considered for both ultimate and fatigue design. Pretension and gravity loads that significantly relieve the load response are considered to be favorable.

BAY OF BENGAL

Bay of Bengal is the largest bay of the world covers a watery of 2.2 million square kilometres and reaches a depth of up to 5258 meters [1]. It is a northern extended arm of the Indian ocean. It is a 'U' shaped basin with its south opening to the Indian ocean along with a thick uniform abyssal plain gently sloping towards southward direction. The upper fan extend between 1000m and 2250m water depth. The continental slope extend between 100m and 2000m with the depth increasing gently towards southwest part. From the data collected at longitude 92 east and latitude 21 north the significant wave height observed for the years 2010, 2011, 2012 & 2013 shows a maximum value of 4m. The environmental parameters of the location considered in the analysis are furnished in table.2.

WIND FORCE

The thrust force experienced by the exposed parts of the platform, tower and turbine can be expressed as

$$F = \frac{1}{2} \rho_a A_T V^2 \quad (1)$$

Wind speed increases with the height in a logarithmic pattern. If the wind data is available at a height Z and the roughness height is Z₀, Then the velocity at height Z_R is given by

4th International Engineering Symposium - IES 2015

March 4-6, 2015, Kumamoto University, Japan

$$V(Z_R) = V(Z) \frac{\ln \frac{Z_R}{Z_0}}{\ln \frac{Z}{Z_0}} \quad (2)$$

Where $V(Z_R)$ and $V(Z)$ are the velocities at heights Z_R and Z respectively.

WAVE FORCE

Wave loads are dynamic in nature. For most design water depths encountered these loads may be adequately represented by their static equivalents. For deep water or platforms that tend to be more flexible, the static analysis may not adequately describe the true dynamic load induced on the platform. Correct analysis of such platform requires a load analysis involving the dynamic action of the structure.

Wave loads on a platform can be calculated by the Morison's equation which was originally developed for vertical piles in shallow water. For engineering purpose it is assumed to be valid for cylinders of arbitrary orientation in deep and shallow water with the proviso that the coefficients C_m and C_d are chosen experimentally for the appropriate condition. The computation of wave force on cylindrical objects depends on the ratio of wave length to the member diameter(λ/D). When the ratio is large the member does not significantly modify the incident wave. The wave force can then be calculated as the sum of drag force and inertia force. The calculation of drag and inertia components depend on the apparent wave period, two dimensional wave kinematics, wave kinematics factor, drag and inertia coefficients, The total force acting on the structure by Morrison' is equation is given by

$$F = C_m \rho \pi r^2 \int_{-d}^0 u dy + C_d \rho r \int_{-d}^0 |u| u dy \quad (3)$$

Linear wave theory is used to describe the kinematics of the design wave. In using the linear wave theory it is assumed that the waves are sinusoidal that is wave height is small compared to wave length and water depth (d). Also the free surface kinematic and the dynamic boundary conditions are satisfied at the mean sea level rather than at the oscillating free surface.

$$\text{Wave length } (\lambda) = \frac{g T^2}{2\pi} \quad (4)$$

Since(λ/D) is small, the diameter of the structure being 9m, the wave properties are not altered by the presence of the structure and Morison's equation can be used in the wave force computation.

The instantaneous wave particle horizontal velocity based on linear wave theory for deep water condition is given by

$$u = \frac{g k a \cosh ky}{\omega \cosh kd} \cos[k(x - ct)] \quad (5)$$

The wave particle acceleration is given by

$$u'' = \frac{g k a \cosh ky}{\cosh kd} \cos[k(x - ct)] \quad (6)$$

where k is the wave number($2\pi/\lambda$)

$$\omega = 2\pi/T; c = gT/2\lambda \text{ (wave celerity)}$$

When the wave particle is having a maximum horizontal velocity its vertical velocity is equal to zero.

The hydrodynamic coefficients that is, the inertia coefficient and drag coefficients are determined experimentally either in the laboratory or from field measurements. The hydrodynamic coefficients determine the relative contributions of the drag and inertia forces which are given in terms of non dimensional parameters the Keulegan-Carpenter number $kc = U_0 T/D$ and the

Reynolds number $Re = U_0 D/\nu$. Based on their values c_m and c_d can be obtained from Table 3.

ANALYSIS OF THE STRUCTURE

Analysis of the structure requires its idealization into a form that can be solved. Mathematical equations can be formulated for the idealized structure, the solution of which gives the variation of the unknown quantities in the structure. The structure can be represented either as a lumped parameter model or as a continuous system. Finite element analysis is called upon since it is tedious to obtain the analytical solution. The finite element modeling of the structure and subsequent formulation and solution of finite element equations provide approximate but acceptable values for the unknowns using numerical techniques. The structure is represented by an assemblage of subdivisions interconnected at the joints called nodes. The loads are classified to

4th International Engineering Symposium - IES 2015

March 4-6, 2015, Kumamoto University, Japan

nodal loads applied directly at the nodes and element loads applied to elements. The element loads are transformed into equivalent nodal forces. The element loads are applied as uniform or non uniform pressure to faces of elements. Gravity loads and inertia loads may be applied to any element which has a mass density. The inertia properties of the system can be modeled by specifying a non zero material density. The loads that the structure is subjected are dynamic in nature. The dynamic load is any load of which the magnitude, direction or position varies with time. The structural responses to dynamic load like the resulting deflection and stresses are also time varying. The variation of loads with respect to time can be expressed by means of time amplitude curves.

CONCLUSIONS

The following conclusions are deduced from this study:

- The transportation and installation can be done cost effectively by making use of the buoyant substructure
- The coupled effect of the loads creates more stresses on the tower and the turbine components unless the various motions of the structure are prevented.
- The effect of the reduction of diameter of the tower towards the top and the increase in the wind velocity as height increases results in a non uniform wind load distribution.
- The contribution of drag in the computation of total wave force acting on the structure is not significant.

REFERENCES

- [1] Abdul Kader et al (2013), Bathymetric Study of the Bay of Bengal Based on Open Source Satellite and Sounding Data, International Journal of Geomatic and Geosciences, vol. 4, No.1, pp. 116-124.
- [2] Agarwal, A.K., Jain, A.K (2003), Dynamic Behaviour of Offshore Spar Platforms Under Regular Sea Waves. International journal of ocean engineering USA 30(4), pp. 487-516
- [3] Bert Sweetman., Lei Wang (2011), Floating Offshore Wind Turbine Dynamics: Large-Angle Motions in Euler-Space, Journal of offshore mechanics and arctic engineering, April
- [4] Berthelsen P. A (2011), Optimization of Floating Support structures for Deep Water Wind Turbines, Europe's premier wind energy event EWEA.
- [5] Chen Z.Z, Tarp-Johansen N.J, and Jensen J.J (2006), Mechanical Characteristics of Some Deep Water Floater Designs for Offshore Wind Turbines", Wind Engineering, 30(5), pp. 417-430
- [6] Fan Z, Jian-min, Run Pei, Gang. (2008), Coupling Effects for a Deepwater Spar Platform: Comparison of Frequency and Time Domain Analysis with Model tests, Journal of Hydrodynamics , Vol. 20(4) pp. 424 - 432.
- [7] Halkyard, J.E (1996), Status of Spar Platforms for Deep Water Production Systems, Proceedings of Sixth International Offshore and Polar Engineering Conference, vol. 1, pp. 262-272.
- [8] Hege A., Betran J., Radovcic Y (2007), Fatigue Load Computation of Wind Turbine Gearboxes by Coupled Finite Element, Multi Body System and Aerodynamic Analysis. Wind Energy, Vol.10, pp.395-413,
- [9] Henderson, A.R. and Patel, M.H (2003), On The Modelling of a Floating Offshore Wind Turbine, Wind energy, Vol. 6, No.1, pp. 53-86.
- [10] International Electro-Technical Commission (2009). IEC 61400-3, Wind turbines-Part 3: Design Requirements for Offshore Wind Turbines.
- [11] Jason M Jonkman (2009), Dynamics of Offshore Floating Wind Turbines-Model Development and Verification. Wind energy, Vol. 12, pp. 459-492
- [12] Jonkman J and Matha D (2011), Dynamics of Offshore Floating Wind Turbines - Analysis of Three Concepts", NREL, Wind Energy Journal
- [13] Karimirad, T Moan (2011), Extreme Dynamic Structural Response Analysis of Catenary Moored Spar Wind Turbine in Harsh Environmental Conditions, Journal of Offshore Mechanics and Arctic Engineering, Vol. 133 (4)
- [14] Kim M.H, Ran Z and Zheng W (2001), Hull/Mooring Coupled Dynamic Analysis of a Truss Spar in Time Domain, International journal of Offshore and Polar Engineering, Vol. 11, No. 1.
- [15] Kourosh Shoele et al (2011), Dynamic and Structural Modelling of a Floating Wind Turbine, International Journal of Offshore and Polar Engineering Vol. 21(2), June, pp. 155-160.
- [16] Lei Wang, Bert Sweetman (2012) Simulation of Large Amplitude Motion of Floating Wind Turbines Using Conservation of Momentum, Ocean Engineering, Vol. 42 , pp. 155-164.
- [17] Md. Arefin kowser et al (2014), Feasibility Study of Ocean Waves of the Bay of Bengal to Generate Electricity as a Renewable Energy with a Proposed Design of Energy Conversion System, International Journal of Renewable Energy Research, Vol. 4, No.2, pp. 445-452.
- [18] Montaiser O.A, KurianV.J (2011), Effect of Slowly Varying Drift Forces on the Motion Characteristics of Truss Spar Platforms, Ocean Engineering, Vol. 38, pp. 1417-1429.
- [19] Ostergaard and Schellin (1987), Comparison of Experimental and Theoretical Wave Actions on Floating Compliant Offshore Structures, Applied ocean research, Vol. 9, pp. 192-213
- [20] Ran, Z., Kim, M.H., Zheng, W (1999), Coupled Dynamic Analysis of a Moored Spar in Random Waves and Currents (Time domain vs Frequency Domain Analysis), Journal of Offshore Structure and Arctic Engineering Vol. 121, pp. 194-200.

4th International Engineering Symposium - IES 2015

March 4-6, 2015, Kumamoto University, Japan

- [21] Robertson A.N. , J.M. Jonkman (2011), Loads Analysis of Several Offshore Floating Wind Turbine Concepts, International Society of Offshore and Polar Engineers Conference.
- [22] Swain J (1997), Simulation of Wave Climate for Arabian Sea and Bay of Bengal, Doctoral Thesis, Cochin University of Science and Technology.
- [23] Tang You-gang, Zhang Su-xia, Zhang Ruo-yu and LIU Hai-xiao (2007), Development of Study on Dynamic Characteristics of Deep Water Mooring System. Journal of Marine Science and Application, Vol. 6, no.3, pp. 17-23
- [24] Wang Ying, Yang Jian-min, Hu Zhi-qiang, Xiao Long-fei (2008), Theoretical Research on Hydrodynamics of a Geometric Spar in Frequency and Time Domains, Journal of Hydrodynamics, 20(1), pp. 30-38
- [25] Xiaohong et al (2006), Coupled Dynamic Analysis of a Mini TLP: Comparison with measurements, Ocean engineering, Vol. 33, pp. 93-117
- [26] Zhang Fan, Yang Jian-min, Li Run-pei, Chen Gang (2006), Experimental Investigation on the Hydrodynamic Behaviour of Geometric Spar Platform", China Ocean Engineering, Vol. 20(2) pp. 213-224
- [27] Zhang Fan, Yang Jian-min, Li Run-pei, Chen Gang (2007), Numerical Investigation on the Hydrodynamic Performance of a New Spar Concept, Journal of Hydrodynamics, Ser.B19(4), pp. 473-481

Table1 Turbine Specification

Rotor Power	5 MW
Rotor Orientation	upwind
Rotor Configuration	3 Blades
Rotor Diameter	126 m
Hub Diameter	3 m
Hub Height	90 m
Tower Base Diameter	6 m
Tower Top Diameter	3.87 m
CM Coordinate Location	-0.2, 0, 64
Rated Tip Speed	80 m/s
Rotor Mass	110,000 kg
Nacelle Mass	240,000 kg
Tower Mass	347,460 kg
Cut-in Wind Speed	3m/s
Rated Wind Speed	11.4 m/s
Cut-out Wind Speed	25 m/s
Cut-in Rotor Speed	6.9 rpm
Rated Rotor Speed	12.1 rpm

Table 2 Environmental parameters

Wave Period	10 s
Wind Speed	15 m/s
Wave height	4m
Current Speed	0.3 m/s
Water Depth	450 m

Table 3 Values of C_m & C_d

	C_m	C_d
$K_c < 5$	2.0	negligible
$5 < K_c < 25$ $Re > 1.5 \times 10^6$	1.8	0.62
$K_c > 25$ $Re > 1.5 \times 10^6$	1.8	0.62
$K_c > 25$ $10^5 < Re < 1.5 \times 10^6$	1.8	1.0~0.6

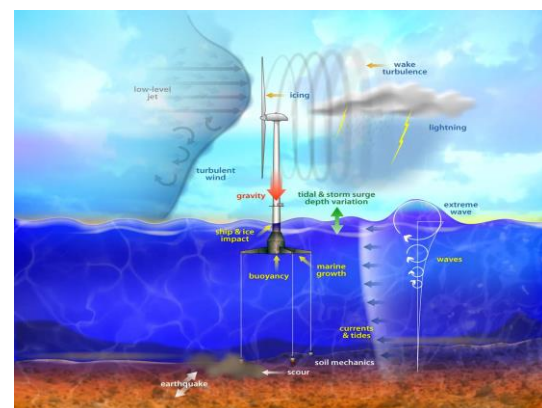


Fig.1 Loads on Offshore Structure

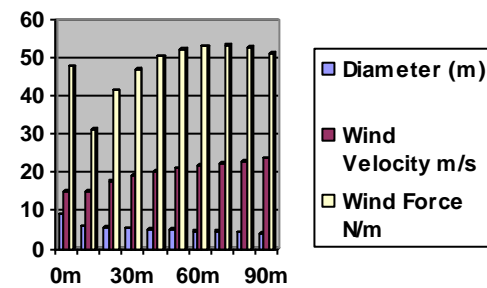


Fig.2 Variation of diameter, Wind velocity and Wind Force

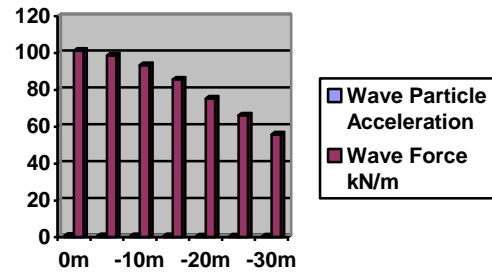


Fig.3 Variation of Wave Force

An Overview of MeshFree Methods and its Advancements

Bhavana Patel S.S.¹, K.S. Babu Narayan² and Katta Venkataramana²

- ¹ Research Scholar, Department of Civil Engineering, National Institute of Technology Karnataka, Surathkal, Mangalore 575025, India. email:bhavana8patel@gmail.com
- ² Profesor, Department of Civil Engineering, National Institute of Technology Karnataka, Surathkal, Mangalore 575025, India. email:shrilalisuta@gmail.com
-

ABSTRACT: The development of Finite Element Method (FEM) for mathematical modeling has been one of the greatest advancement in the engineering field. FEM has given birth to advanced techniques, of which Extended Finite Element Method (XFEM) and MeshFree methods have received potential applications in modeling real time challenges. The method has the advantage of solving problems involving high stress gradient and introducing damage within the element which was difficult in mesh based methods. The paper discusses various MeshFree methods adopted in the engineering with their advantages. Also its advancement called extended MeshFree technique, used particularly in studies related to crack growth and propagation are addressed.

Keywords: *MeshFree method, Finite Element Method, adaptive refinement, coupled techniques*

INTRODUCTION

Mathematical modeling and simulation of physical systems has greatly advanced in the last three decades. Numbers of numerical methods adopted are discussed in Fig. 1. In structural dynamics, the development of Finite Element Method (FEM), which is adopted to solve Partial Differential Equations (PDE), has been one of the greatest advancement in the engineering sector. Continuous research is still being pursued to develop this method, and has given birth to more advanced techniques such as the Extended Finite Element Method (XFEM) and MeshFree methods; and has received potential applications in modeling and simulation of crack propagation.

The XFEM method is the extended form of FEM, where discontinuous field functions can be defined within the element for modeling holes, cracks and material / boundary interfaces. Hence, re-meshing is avoided and the nodes of the finite element are enriched that includes the asymptotic crack tip field and Heaviside function to define discontinuity. But, even

with the incorporation of discontinuity in the element, XFEM fails to model component with high stress gradient, as the order of the interpolation function doesn't change. Hence, in-order to capture stress gradients accurately, advanced technique such as MeshFree method coupled with the extended features of XFEM needs to be adopted.

The method of arriving at the algebraic equations for the whole domain without having a predefined mesh or automated mesh is called MeshFree method (Liu, 2009). MeshFree is the solutions to overcome the dependency on meshes, where automated meshes are sufficient for the analysis.

The term MeshFree as discussed refers to automated mesh, where the meshes are not of much importance as that in FEM. Simple basic mesh such as triangular shaped in case of 2D element or tetrahedral in case of 3D element are used, which are easy to be implemented in automated meshing. These meshes are called as background mesh, usually used for integration purpose only. The whole of the structure is divided into domains which

4th International Engineering Symposium - IES 2015

March 4-6, 2015, Kumamoto University, Japan

can be circular, rectangular or any shape as shown in Fig. 2. The set of nodes are spread in and on the boundaries of the domain. Based on the number of nodes in the domain, the field function is chosen, which is of higher order polynomial and can interpolate the stresses in a smoother sense. Shape functions are constructed using Moving Least Square (MLS) technique, wherein weightages are assigned to the nodes using weight functions shown in Fig. 3. This paper discusses various types of MeshFree methods developed (Daxini and Prajapati, 2014) in the two decades. Further the coupled techniques i.e. use of FEM and XFEM with MeshFree methods are presented.

Meshfree Method

FEM has dominated the numerical analysis since its genesis. Some of the drawbacks like re-meshing at each stage, singularity issues and dealing with discontinuity have led to the new method without meshes known as MeshFree method. Some of the methods for constructing shape functions in MeshFree method are kernel approximation and moving least square methods. Various methods and its application with the effect of computation and accuracy are discussed by Belytschko et al. (1996). Some of the most commonly adopted MeshFree techniques such as Smoothened Particle Hydrodynamics (SPH), Element Free Galerkin (EFG) method, Point Interpolation Method (PIM), and Collocation methods are discussed in detail with their advantages and disadvantages in Vinh et al. (2008).

SPH is one of the oldest MeshFree methods. In this method, a system is represented by particles and these particles are controlled by weighting or smoothing functions. It was first used in astro-physics. The movement of the particles in this method is same as liquid or gas; these are solved using hydrodynamics. Some of the difficulties faced by SPH are enforcing boundary condition, instabilities, consistency and presence of zero energy modes. Shaofan and Wing (2002) have suggested some of the improvements for the SPH drawbacks such as to use stress point interpolation so as to overcome the disadvantage of zero energy

mode. Modeling methods for discontinuities are discussed in Antonio et al. (2004).

Modeling of crack using SPH method with arbitrary orientation is discussed in Rabczuk et al. (2007) by considering enrichment of displacement field. The method is formulated for large deformations and for arbitrary nonlinear materials. Further the authors have extended it for shear bands which undergo large strains. Though the results and accuracy were reasonable but it lacked computational efficiency. Stress point integration method was adopted by Thomas and Ted (2008), wherein additional particles called slave particles are added as stress points and used for interpolation. In general, number of stress points is taken equal to that of number of particles in the structure. Stress point integration leads to the faster convergence and stability.

Extension of SPH method in geotechnical engineering for the design of elasto-plastic flow of soil has been tried but this causes tensile instability. Hence, Ha et al. (2008) have adopted artificial stress method in order to remove instability. Further, Liu and Liu (2010) have carried out extensive survey on SPH method and discussed on improvements and approximation techniques such as Kernel approximation, particle approximation. The recent developments, applications, consistency restoring approaches have been reviewed. The researchers give the scope for improvement of feasibility of discontinuous functions, computational cost and efficiency in this method.

Point Interpolation Method (PIM) PIM is one of the series representation methods for the approximation of the shape function. Other MeshFree methods such as Boundary element method, collocation methods and RKPM are discussed in Thomas and Hermann (2004). The paper also discusses about different types of integrations carried out, like direct nodal integration, background cell integration and integration over supports. Further ideas of coupling of MeshFree method with FEM and with other MeshFree methods are put forth.

4th International Engineering Symposium - IES 2015

March 4-6, 2015, Kumamoto University, Japan

The method of locally smoothing strain field for PIM using triangular background meshes are discussed in Xu et al. (2010). This method assures good convergence and also solutions obtained are bound from both the sides. But in this method, problem of singularities are observed and hence in order to overcome this issue radial basis functions are adopted by Chen et al. (2010) and Cui et al. (2011). First paper discusses different types of smoothing operations and also their advantages. Use of node based strain smoothing provides upper bound solution; edge based strain smoothing with triangular background mesh are more accurate and have higher convergence. The second paper discusses on edge based strain smoothing with linear interpolation technique which provides computational efficiency. This method proves to be more accurate than the traditional FEM and PIM. Solution to some of the strong forms is obtained by using collocation methods. Use of localized radial basis approximation for the shape function construction in Chen et al. (2011) proved to be accurate though it is unstable. In order to obtain stability, Mohamed et al. (2012) have adopted shape function construction by using a linear interpolation function using moving least square and radial basis function. This method proves to be efficient for the boundary value problem.

Combinations of some of the MeshFree method are adopted in order to increase the efficiency by decreasing the computational time. Hence some of the methods like EFG (Someshar et al., 2013), SPH, Reproducing Kernel Particle Method (RKPM), and PIM are coupled together and applied to some kind of problem. One such combination was adopted by Chinesta et al. (2007). They considered some enrichment method to RKPM and coupled with RKPM which did not result in efficient results. Later moving least square was adopted to obtain the shape functions for NE method and this was fused with the RKPM enrichment. This method was adopted for several numerical examples and they proved to be efficient.

In recent years, development of different materials has led to the demand of developing efficient numerical technique

for their analysis. Composites and functionally graded materials are efficiently modeled using MeshFree methods which are difficult using FEM. Liew et al. (2011) have reviewed on different types of analysis used for such materials and application to three dimensional problems are given as future scope.

The other advancements of MeshFree methods are by introducing the change in the shape of the influence domain by Xiao et al. (2012). Usually influence domains are circular or rectangle; they have suggested arbitrary convex polygon shape. This approach helps in reducing the band width of stiffness matrix and also boundary condition implementation has been made easy. Change in shape of influence domain promises accurate results with lesser computational time. Use of elliptical shape functions instead of linear, quadratic functions and adopting moving least square method with penalty function by Hae-Soo (2012) proved to be efficient. Higher order polynomials are used and use of this function has been efficient when applied to different shapes of plate under different loading and boundary conditions.

COUPLED TECHNIQUES

Hence, from the above surveyed literatures, it is clear that, the capabilities of FEM or MeshFree method can greatly be improved by their inter-coupling or adopting extended features such as discontinuous functions and asymptotic crack tip function. The coupling of XFEM and FEM gives much more accurate results without much re-meshing. But it is difficult to adopt in case of complex geometries. Coupling of FEM and MeshFree methods are also discussed, which proves to be efficient in some cases.

Coupling FEM and XFEM

Modeling cracks in finite element framework by enriching displacement function by discontinuous field and near tip asymptotic field is presented in Nicolas (1999). Same idea was extended by Sukumar et al. (2003) to solve three dimensional crack propagation problems. Since the results obtained are not satisfactory the method has been coupled with fast marching method. Quasi static

4th International Engineering Symposium - IES 2015

March 4-6, 2015, Kumamoto University, Japan

analysis of three dimensional crack propagation studies was carried out by Pedro et al. (2005). The authors have combined XFEM with FEM and have used linear tetrahedral elements for modeling. The method allows closed form integration and damage is introduced when consecutive model loses its stability.

Further, studies are carried out on the different shapes of crack propagation such as elliptical and circular. Stress intensity factor has been computed numerically and these results have shown good agreement with the theoretical solutions. Elie et al. (2007) have compared the results of coupled technique with and without enrichment. With smoothened enrichment, the accuracy increased with the rate of convergence.

Mapping is another disadvantage while modeling in FEM. Using XFEM mapping of solution between the mesh is avoided so it is advantageous to use it in nonlinear and time dependent problems. Armando et al. (2007) have studied on three dimensional problems without mapping and have given good correlation with the experimental results. Orthotropic crack propagation has been studied by Asadpoure and Mohammadi (2007).

Coupling FEM and MeshFree Method

MeshFree methods have proved their ability in giving accurate results but lack computational efficiency. Therefore researchers have put their effort to adopt FEM and combine it with MeshFree method in order to get the full advantage of these methods by minimizing their disadvantages. FEM can be used in the entire structure and in the sub-domain where meshes play a major role can be replaced with MeshFree methods. Thereby improving the results in case of problems like crack propagation which aids in proper stress distribution.

FEM and EFG method are combined together to obtain continuity and consistency between interface elements. Belytschko et al. (1995) have implemented this on one-dimensional cantilever beam and wave propagation problem for elasto-static and elasto-dynamic problems. Though the accuracy has improved, it lacks faster convergence due to the errors.

But in case of fracture problems it proved to be efficient with reduced computational cost. Application of Dirichlet boundary condition was carried out by Yury (1997). He has adopted a method where shape functions from weighted MeshLess method and FEM are adopted on the boundary. These shape functions are continuous and possess linear variation. Rao and Rahman (2001) adopted FEM to model the region away from cracks whereas near the cracks EFG was used. This showed accurate results when compared with fully MeshLess method. In the interface nodes, shape functions from both the methods are used, the crack region or the domain of interest is modeled only by nodal points. This method has given accurate result with significant reduction in computational time. The study on crack propagation is carried out by extending the free surface and the crack propagated same as predicted. Huerta et al. (2004) improved the same idea by adopting different interpolations methods in various regions and further in place of transition, linear interpolation is carried out. Bridging scale and continuous blending techniques is discussed in this paper, which addresses various approaches for nodal interpolation and convergence.

Material point method (MPM) is one of the MeshFree methods which are used for modeling extreme deformation. While modeling problem with small deformation, FEM is more efficient than MPM because of problems with mapping. Lian et al. (2012) have combined FEM and MPM for problems with small deformation. Eulerian particle is used for background meshing and Lagrangian is used to represent state variables of particles in the material domain. Further, authors have verified this method using numerical problems and have obtained agreeable experimental results. Another MeshFree technique RKPM has been coupled with FEM by Wu et al. (2013) in order to avoid the transition at the interface. Unique domain and nodal integrations are performed for both the methods and state variables are stored directly at the nodal points. This method has been tested for different loading conditions such as quasi-static, impact and

4th International Engineering Symposium - IES 2015

March 4-6, 2015, Kumamoto University, Japan

blast loading, and realistic results were obtained.

CONCLUSIONS

From the literatures published in the last three decades, it is clear that, one cannot identify an analysis tool that can simulate crack propagation phenomenon which is computationally efficient and numerically very accurate. In the literature survey carried out, two methods were identified to model crack propagation phenomenon, namely FEM and MeshFree method. FEM has the advantage of being computationally very efficient, but very inefficient in interpolating the high stress gradients. The method when coupled with XFEM, which includes modeling discontinuous field function, could handle the crack propagation phenomenon much more efficiently due to reduction in remeshing. But, both these methods lack in efficiently interpolating the high stress gradients, which is a basic requirement of crack propagation phenomenon. On the other hand, the MeshFree method could handle the interpolation of high stress gradients very efficiently, but the computational time of this method is very high, which is in the range of 50 times as stated by Liu (2009). This is because of the basic reason of constructing shape functions independently for each unit cell and also in forming the unit cell. Hence, a very good research opportunity is available in improving the computational efficiency of the MeshFree method and is one of the possible and potential topics for carrying out research work.

In the recent years it can be seen that use of advanced methods such as XFEM and MeshFree methods in the area of damage diagnosis and prognosis have proved to be much better than the traditional methodologies. But still these techniques are in the initial stage of developments. Hence this is one of the hot spot for the researchers to throw light on.

ACKNOWLEDGEMENTS

The authors are grateful to Technical Education Quality Improvement Programme (TEQIP) for funding this study.

REFERENCES

- [1] Antonio Huerta, Ted Belytschko, Sonia Fernandez Mendez and TimonRabczuk (2004), MeshFree Methods, Encyclopaedia of Computational Mechanics, John Wiley & Sons, Ltd.
- [2] Armando Duarte C, Dae-Jin Kim and Ivo Babuska (2007), A Global-Local Approach for the Construction of Enrichment Functions for the Generalized FEM and Its Application to Three-Dimensional Cracks, Advances in MeshFree techniques, Springer, pp.1-26
- [3] Asadpoure A. and Mohammadi S. (2007), Developing new enrichment functions for crack simulation in orthotropic media by the extended finite element method, International Journal for Numerical Methods in Engineering, No.69, pp. 2150-2172
- [4] Belytschko T., D. Organ and Y. Krongauz (1995), A coupled Finite element-element-free Galerkin method, Computational Mechanics, No.17, pp. 186-195
- [5] Belytschko T., Y. Krongauz, D. Organ, M. Fleming, I. Krysl (1996), MeshLess methods: An overview and recent developments, Computer methods in applied mechanics and engineering, No.139, pp. 3-47
- [6] Chen Jiun-Shyan, Sheng-Wei Chi and Hsin-Yun Hu (2011), Recent developments in stabilized Galerkin and collocation MeshFree methods, Computer Assisted Mechanics and Engineering Sciences, No.18, pp. 3-21
- [7] Chen L., H. Nguyen-Xuan, T. Nguyen-Thoi, K. Y. Zeng and S. C. Wu (2010), Assessment of smoothed point interpolation methods for elastic mechanics, Int. J. Numer. Meth.Biomed.Engng., No.26, pp. 1635-1655
- [8] Chinesta F., J. Yvonnet, P. Villon, P. Breitkopf, P. Joyot, I.Alfarro and E. Cueto (2007), New Advances in MeshLess Methods: Coupling Natural Element and Moving Least Squares Techniques, Advances in MeshFree techniques, Springer, pp. 97-121
- [9] Cui X.Y., G. R. Liu, G. Y. Li, and G. Y. Zhang (2011), A thin plate formulation without rotation DOFs based on the radial point interpolation method and triangular cells, Int. J. Numer. Meth.Engng, No.85, pp. 958-986
- [10] Daxini S. D. and Prajapati J.M. (2014), A Review on Recent Contribution of MeshFree Methods to Structures and Fracture Mechanics Application, The Scientific World Journal, Article ID 247172.
- [11] Huerta Antonio, Sonia Fernandez-Mendez and Wing Kam Liu (2004), A comparison of two formulations to blend finite elements and mesh-free methods, Journal of Computer Methods in Applied Mechanics and engineering, No.193, pp. 1105-1117
- [12] Lian Y.P., X. Zhang, Y. Liu (2012), An adaptive finite element material point method and its application in extreme deformation problems, Computer Methods in Applied Mechanics and Engineering, No.27, pp. 275-285
- [13] Liew K.M., Xin Zhao and Antonio J.M. Ferreira (2011), A review of MeshLess methods for laminated and functionally graded plates and shells, Composite Structures, No.93, pp. 2031-2041
- [14] Liu G.R. (2009), MeshFree Methods Moving beyond the Finite Element Method, Second edition, CRC press, Taylor and Francis group, New York
- [15] Liu M.B. and Liu G.R. (2010), Smoothed Particle Hydrodynamics (SPH): an Overview and Recent Developments, Arch Computer Methods in Engineering, No.17, pp. 25-76
- [16] Mohamed H. A., A.E.Bakrey and S.G.Ahmed (2012), A collocation MeshFree method based on

4th International Engineering Symposium - IES 2015

March 4-6, 2015, Kumamoto University, Japan

- multiple basis functions, *Engineering Analysis with Boundary Elements*, No.36, pp. 446–450
- [17] Nicolas Moesly, John Dolbow and Ted Belytschko (1999), A finite element method for crack growth without re-meshing, *International Journal for Numerical Methods in Engineering*, No.46, pp. 131–150
- [18] Rabczuk T., P. M. A. Areias and T. Belytschko (2007), A simplified mesh-free method for shear bands with cohesive surfaces, *Int. J. Numer. Meth. Engng.*, No.69, pp. 993–1021
- [19] Rao B.N. and Rahman S. (2001), A coupled MeshLess finite element method for fracture analysis of cracks, *International Journal of Pressure Vessels and Piping*, No.78, pp. 347–357
- [20] Shaofan Li and Wing Kam Liu (2002), MeshFree and particle methods and their applications, *American society of Mechanical Engineers*, No.55, pp. 1-34
- [21] Someshwar S. Pandey, Paresh K. Kasundra and Sachin D. Daxini (2013), Introduction of MeshFree methods and implementation of EFG methods to beam problem, *International Journal on Theoretical and Applied Research in Mechanical Engineering*, No.2, pp. 2319 – 3182
- [22] Sukumar N., D.L. Chopp and B. Moran (2003), Extended finite element method and fast marching method for three-dimensional fatigue crack propagation, *Engineering Fracture Mechanics*, No.70, pp. 29–48
- [23] Thomas-Peter Fries and Hermann-Georg Matthies (2004), Classification and Overview of MeshFree Methods, Technical report, Institute of Scientific Computing Technical University Braunschweig, Brunswick, Germany
- [24] Thomas-Peter Fries, and Ted Belytschko (2008), Convergence and stabilization of stress-point integration in mesh-free and particle methods, *International Journal for Numerical Methods in Engineering*, No.74, pp. 1067–1087
- [25] Wu, Y., Magallanes, J., Choi, H., and Crawford, J. (2013), Evolutionarily Coupled Finite-Element Mesh-Free Formulation for Modeling Concrete Behaviors under Blast and Impact Loadings, *J. Eng. Mech.*, No.139(4), pp. 525–536
- [26] Xiao HuaZhang, Ping Zhang and Lin Zhang (2012), A simple technique to improve computational efficiency of MeshLess methods, *International Conference on Advances in Computational Modeling and Simulation, Procedia Engineering*, No.31, pp. 1102 – 1107
- [27] Xu,X, G.R.Liu, Y.T.Gu, G.Y.Zhang, J.W.Luo and J.X.Peng (2010), A point interpolation method with locally smoothed strain field (PIM-LS2) for mechanics problems using triangular mesh, *Finite Elements in Analysis and Design*, No.46, pp. 862–874
- [28] Yury K. Krongauz (1996), Application of MeshLess methods to solid mechanics, PhD. thesis, Northwestern University, Illions

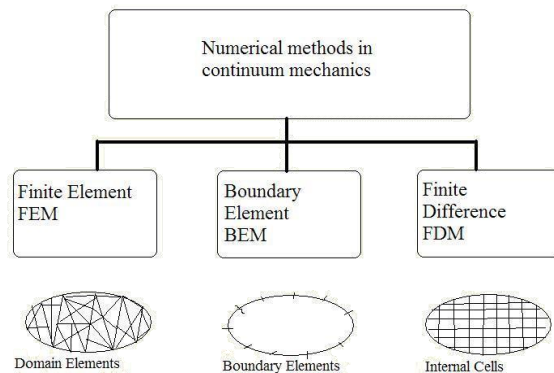


Figure 1 – Numerical methods in continuum mechanics

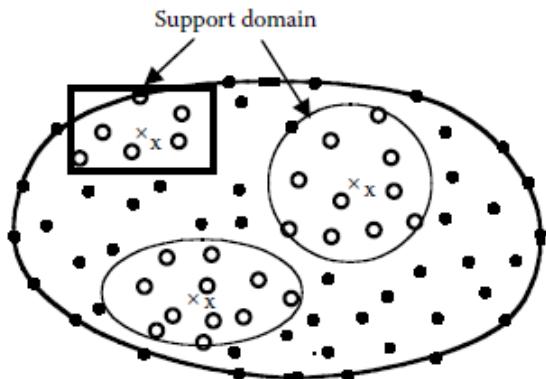


Figure 2 - Support domain of different shapes

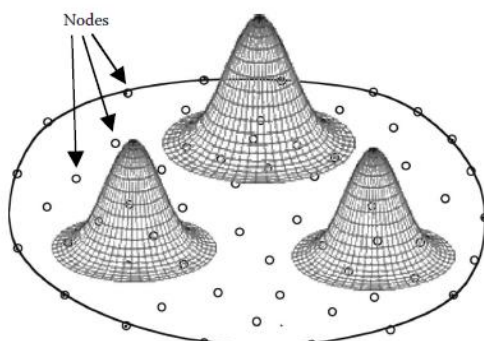


Figure 3 – Support domain weight function distribution

Pyroclastic Flow Deposit Called Shirasu as Aluminosilicate Source in Geopolymer

Dhruva Narayana Katpady, Koji Takewaka and Toshinobu Yamaguchi

*Department of Ocean Civil Engineering, Kagoshima University
Korimoto, 1-21-40, Kagoshima 890-0065, Japan
e-mail:dnkata@gmail.com*

ABSTRACT: Geopolymer has lately attracted considerable attention as one of the CO₂ free construction materials, because of concrete free from any cementitious material. The paper presents an attempt to study the behavior of Shirasu, a pyroclastic flow deposit, as aluminosilicate source in geopolymer. Shirasu is characterized by high percentage of volcanic glass in its mineral composition and has been confirmed to show pozzolanic reaction. Geopolymer mortar is made with Shirasu and mixture of alkaline activators and heat cured under oven dry condition. The performance of Shirasu geopolymer in terms of strength is analyzed and the strengths are compared with geopolymer mortar using fly ash as aluminosilicate source. Mix proportions are considered based on variations in ratio of alkaline activators to aluminosilicate, keeping the total amount of alkaline activators constant in all the mix. The parameters like temperature, fineness of source particles, porosity and silica to hydroxide balance in the mix that influence the strength properties of geopolymer mortars are considered as important factors in strength development of geopolymer.

Keywords: geopolymer, shirasu, pyroclastic flow, aluminosilicate, polymerization

INTRODUCTION

The contribution of cement to global CO₂ increase has been a concern lately. A new technology called Geopolymer concrete has proved to solve this problem to a great extent if not completely. Geopolymerization involves the reaction of an aluminosilicate with a mixture of highly concentrated aqueous alkali hydroxide and silicate solution to produce a synthetic polymer, alkali aluminosilicate material (-Si-O-Al-O) (Duxson 2007). These materials are comparable to traditional cementitious binders for a wide range of applications, but with the added advantage of significantly reduced greenhouse emissions (Louise et al. 2013). Geopolymers can exhibit a wide variety of properties and characteristics depending on the raw material selection, mix design and processing conditions. High compressive strength, low shrinkage, fast or slow setting and low thermal conductivity are some of the attributes

(Daniel et al. 2010). The geopolymerization mechanism is very complex in nature and initially involves dissolution of silica and alumina in aluminosilicate source by alkaline hydrolysis which triggers polymerization at high pH conditions followed by gelation. Further rearrangement and reorganization increases the connectivity of the gel network resulting in the three-dimensional aluminosilicate network commonly attributed to geopolymer. There are several models proposed on different types of networks formed during polymerization. The characteristics and structure of polymers formed largely depends on aluminosilicate source used, alkalinity and temperature. The salient parameters affecting the compressive strength of geopolymer concrete are as listed below (Hardjito et al. 2004):

1. Silicon oxide (SiO₂)-to-aluminum oxide (Al₂O₃) ratio by mass of the source material (preferably 2.5 to 5).

4th International Engineering Symposium - IES 2015

March 4-6, 2015, Kumamoto University, Japan

2. Activator liquids to source material ratio by mass (around 0.3-0.7).
3. Molar concentration of sodium hydroxide (NaOH) liquid (Molarity, M), in the range of 8 to 16 M.
4. Sodium silicate to sodium hydroxide liquid ratio by mass (ranging from 1 to 2.5, and 2.5 is found to be optimum).
5. H₂O/Na₂O molar ratio (preferably between 10-13)
6. Curing temperature in the range of 60°C to 90°C.
7. Water to geopolymer solids ratio (ranging from 0.15-0.25).
8. Curing time and curing methods (Steam curing is known to be most effective).

Shirasu in Geopolymer

Extensive research is carried out on geopolymer with fly ash, metakaolin and blast furnace slags as aluminosilicates. The present study is an attempt to utilize unused natural resource called Shirasu as aluminosilicate source in geopolymer. "Shirasu", a kind of volcanic ash abundantly deposited due to a big pyroclastic flow in the southern part of Kyushu Island, Japan, in 20 to 100 thousand years ago, is one of the unused natural resources. Shirasu is sandy but porous material with large amount of very fine particles. It has about 80% density of that of sea sand and three times higher water absorption capacity when compared to sea sand. It also has high quantity of volcanic glasses in its mineral composition and has been confirmed to show pozzolanic reaction (Takewaka et al. 2004). Shirasu concrete (Shirasu as fine aggregate) is successfully applied to the concrete foundation for piers constructed in hot spring environment and investigations have proved that Shirasu concrete behaves well in hot conditions and is resistant to sulfate attacks (Takewaka 1991). As Shirasu is rich in silica and alumina, it can be potentially used as aluminosilicate source in geopolymer. The present investigation is an attempt to study the performance of geopolymer with Shirasu as aluminosilicate source. The behavior of Shirasu geopolymer is compared with that of geopolymer mortars prepared with fly ash.

Past researches have proved that fly ash geopolymer are generally more strong and durable (Duxson 2007). With this knowledge, Shirasu geopolymer with different mix proportions is tried. As Shirasu and fly ash have different characteristics, an attempt to study the strength development of mortars and to obtain optimum strength is done assuming silica to hydroxide ratio (here-in-after called "Si/OH") in the mix to be one of the important parameters.

Materials and Methods

Geopolymer mortar is made with following materials:

- 1 Aluminosilicate source (Binder): Shirasu of size under 75µm and fly ash are used. The physical and chemical characteristics of Shirasu and fly ash are shown in Table 1.
- 2 Fine aggregate: River sand with a specific gravity of 2.6.
- 3 Alkaline activators: Sodium hydroxide solution (14N) ("NH") and sodium silicate solution (52% assay) ("NS") are used under the condition of Sodium silicate/Sodium hydroxide=2.5 by volume.

Two main types of geopolymer mortars are made, namely

1. Shirasu geopolymer (GSH): Shirasu as aluminosilicate source and river sand as fine aggregate.
2. Fly ash geopolymer (GFA): Fly ash as aluminosilicate source and river sand as fine aggregate.

Table 2 and Table 3 show the mix proportions for geopolymer mortars with Shirasu and fly ash as aluminosilicate sources, respectively. The total amount of alkaline activators is kept constant in all the mix while the ratio of alkaline activators to aluminosilicate (here-in-after referred as "GPA/B", where GPA means geopolymer alkalis and B is for aluminosilicate source) is varied, as, 0.56, 0.7 and 0.84.

4th International Engineering Symposium - IES 2015

March 4-6, 2015, Kumamoto University, Japan

Table 1 Properties of aluminosilicates used

Mass%	Aluminosilicate source	
	Shirasu	Fly ash
SiO ₂	76.6	63.3
Al ₂ O ₃	12.2	22.41
CaO	1.08	1.93
Na ₂ O	3.43	-
K ₂ O	3.54	-
MgO	-	1.01
Fe ₂ O ₃	1.48	5.74
Specific gravity	2.4	2.25
Blaine specific surface area (cm ² /g)	2200 (-75µm)	3990
Water absorption (%)	7.52	-

Table 2 Mix proportion for GSH

Mix No.	GPA/B	Materials (kg/m ³)			
		Shirasu	Sand	NH	NS
GSH-1	0.56	457	1655	78	176
GSH-2	0.7	365	1756	78	176
GSH-3	0.84	304	1823	78	176

Table 3 Mix proportion for GFA

Mix No.	GPA/B	Materials (kg/m ³)			
		Fly ash	Sand	NH	NS
GFA-1	0.56	456	1624	78	176
GFA-2	0.7	365	1729	78	176
GFA-3	0.84	304	1803	78	176

The ratios were selected based on trials to obtain consistent mix for easy handling since geopolymer mortars are generally very sticky in nature. Shirasu geopolymer is named as "GSH" and fly ash geopolymer as "GFA" in the experimental study. The required water is contained in the alkaline activator solutions and no extra water is added. All mix proportions are in unit weight to volume basis. Cylindrical specimens of diameter 5cm and length 10cm are cast and subjected to temperature of 90°C for all mix proportions.

Porosity test

The geopolymer mortars are analyzed for porosity based on the principle of mercury porosimetry. The tests are conducted on all samples subjected to a temperature of 90°C for 7 days.

Silica to hydroxide ratio (Si/OH)

Shirasu and Fly ash are two different materials with different origin, chemical characteristics and so on. So, the mix proportion based on silica to hydroxide ratio makes both Shirasu and fly ash mixes similar for better comparison of their strength properties. Si/OH of GSH and GFA are varied from 6 to 12. Si/OH was calculated as follows:

$$\text{Si} = (\text{Silica in Shirasu/fly ash}) + (\text{Silica in sodium silicate}), \text{ grams}$$

OH = NaOH solution, grams

$$\text{That is, } [(\text{Silica in Shirasu/Fly ash}) + (\text{Silica in Na}_2\text{SiO}_3)]/\text{NaOH}$$

The mix proportions based on Si/OH in GSH and GFA are shown in Table 4 and Table 5 respectively. The paste volume in all the mixes is kept constant. The compressive strength tests are carried out for both GSH and GFA mortars heat cured at 90°C.

Table 4 Mix proportion for based on Si/OH for GSH

Si/OH	Materials (kg/m ³)			
	Shirasu	Sand	NH	NS
12	401	1716	78	177
10	354	1716	87	195
9	326	1716	92	207
8	295	1716	97	219
6	221	1716	110	249

Table 5 Mix proportion for based on Si/OH for GFA

Si/OH	Materials (kg/m ³)			
	Fly ash	Sand	NH	NS
12	414	1716	71	160
10	369	1716	80	179
9	343	1716	85	191
8	313	1716	90	204
6	278	1716	97	218

Results and Discussion

Shirasu geopolymers (GSH)

Geopolymer mortar with Shirasu of size under 75µm as aluminosilicate source is made with mix proportions given in Table 2 and heat cured at 90°C. Compressive strength test is carried out for specimens for each set of mix proportions. The compressive strengths of specimens are shown in Fig.1. At all ages of heat curing, higher the alkali activator to aluminosilicate ratio (GPA/B), lower the compressive strength. However, the strength develops only after 6 days at 90°C heat curing. Shirasu shows lower reactivity and initiation of hardening. This may be attributed to the fact that Shirasu has been deposited over thousands of years. Hence, impurities and oxides coating on the surface of particles reduces the rate of polymerization and delays initiation of hardening. Even though such case arises, Shirasu clearly shows good performance in polymerization and the maximum compressive strength is up to 20MPa. Degree of amorphousness is also one of the main factors governing the development of strength. Shirasu particles may be less amorphous in nature and percentage of reactive silica in Shirasu may also affect the strength gain. Decrease in the compressive strength of Shirasu geopolymers is observed with increase in ratio of alkaline activators to Shirasu, unlike fly ash geopolymers. But, the decrement is insignificant. One of many other possibilities of delayed hardening and strength gain of Shirasu mortar is the fineness. Shirasu particles of size under 75µm has Blaine specific surface area of 2200cm²/g which is much lower than that of fly ash with 3990cm²/g.

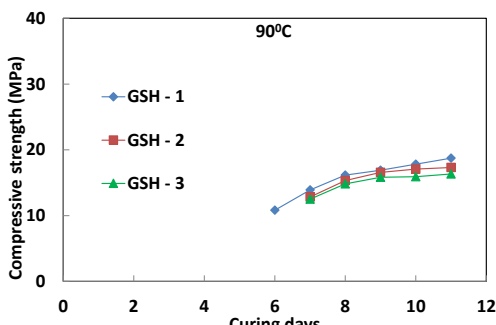


Fig.1 Strength variation with age

Fly ash geopolymer (GFA)

Fly ash geopolymer mortar is prepared with mix proportion as shown in Table 4. The amount of alkaline activators is kept constant similar to Shirasu geopolymers to study the relative performance of Shirasu polymerization when compared to fly ash. The compressive strengths of fly ash geopolymers heat cured at 90°C are given in Fig.2. Increase in ratio of alkaline activators to aluminosilicate shows increase in strength, unlike Shirasu geopolymers. The results are compliant with several other researches carried out on fly ash geopolymers. As the alkaline activators increase, dissolution of aluminosilicates in pozzolans becomes easier. Also, fly ash is more amorphous in nature than Shirasu and silica and alumina are readily available for reaction in the case of fly ash. Even though the amount of silica in fly ash is lesser than Shirasu, reactive silica and alumina in fly ash are higher in content. Maximum strength of around 35MPa is achieved. But maximum strength of Shirasu geopolymers are comparable to fly ash geopolymers.

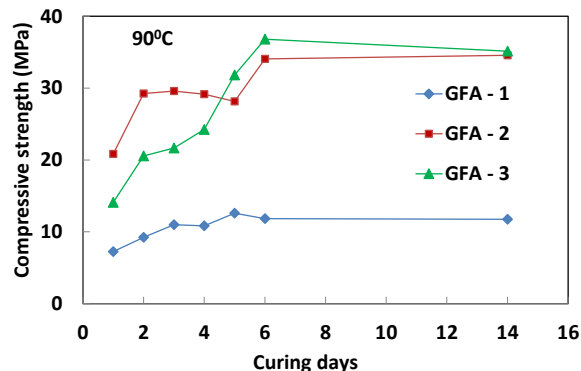


Fig.2 Strength variation with age

The only major difference between Shirasu and fly ash geopolymers is that the fly ash geopolymers gain strength within 1 day of heat curing, whereas strength development of Shirasu geopolymers is after 6 days. The contrast in result is the effect of the nature of Shirasu and fly ash. Even if both are pozzolans and have similar characteristics, Shirasu is a deposit and fly ash is a by-product. Shirasu was deposited several thousand years ago and has been subjected to various natural

conditions which change the particle surface nature. The demand for sufficient alkali may not have been met in these mix designs. Moreover, Blaine specific surface area of Shirasu used is much less than fly ash. The fineness affects the reactive, overall strength and initiation of hardening. Overall results show that Shirasu can be potentially used in geopolymers.

Porosity of geopolymer mortars

Porosity of GSH and GFA subjected to 90°C for 7 days was determined for clear understanding of the variation in strengths. The results of porosity are given in Fig.3. GSH mortars have highest volume of pores at 100μm and above. On the other hand, GFA-1 has high volume of pores at 100μm, GFA-2 at 1μm and GFA-3 at 10nm. Therefore, as the ratio of alkaline activators to aluminosilicate increases, porosity reduces while reducing large pores and simultaneously increasing micro pores. Geopolymer mortars where Shirasu is used as aluminosilicate source (GSH) show higher porosity compared to that of fly ash geopolymers (GFA). This trend in porosity of mortars is similar to the trend in strength development. The pore volumes and pore distribution in each mix of GSH and GFA match with the compressive strength results and explain the contradicting results of strength.

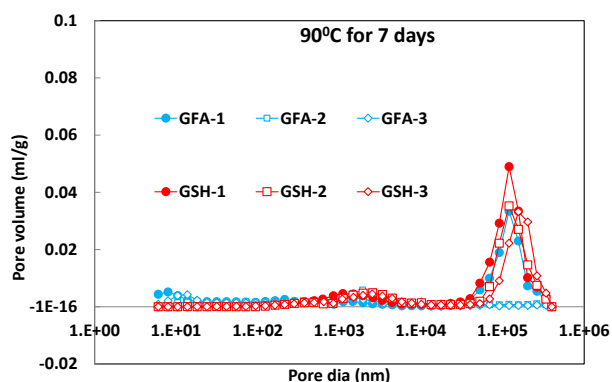


Fig.3 Pore distribution of all geopolymers mortars subjected to temperature of 90°C for 7 days

Silica to hydroxide ratio (Si/OH)

In the previous investigations of geopolymers with Shirasu and/or fly ash, it was observed that changes in

compressive strength with variation in ratio of alkaline activators to aluminosilicate were not similar. Difference in nature of Shirasu and fly ash, like, amount of silica and reactive silica content, degree of amorphousness and origin, processing of aluminosilicates and specific surface area are governing factors. For this purpose, the ratio of silica to sodium hydroxide in the mix is made equal for both Shirasu and fly ash geopolymers and compressive strengths are compared. In this way, by creating a balance in silica and alkaline conditions in the mix, comparative study can be easily possible. The compressive strength results of GSH and GFA mortars with mix proportions shown in Table 4 and Table 5, heat cured at 90°C are shown in Fig.4 and Fig.5 respectively. The graphs illustrating the compressive strength depending on Si/OH clearly shows that Si/OH has a great influence on the strength properties of mortar. The peak compressive strength is obtained at Si/OH=9 in both aluminosilicates. This indicates a clear effect of silica to hydroxide balance in the mix. The condition of Si/OH<9 has fewer amount of aluminosilicate source necessary for polymerization. On the contrary, the condition of Si/OH>9 has higher amount of alkaline activators in the mix which does not have enough aluminosilicate source necessary for polymerization. Higher amount of alkaline activators also increase the cost of preparation of mortars and causes adverse conditions like expansion and cracking. Hence, Si/OH is an important parameter for development of strength and also one of the factors to be considered for design of mix proportions.

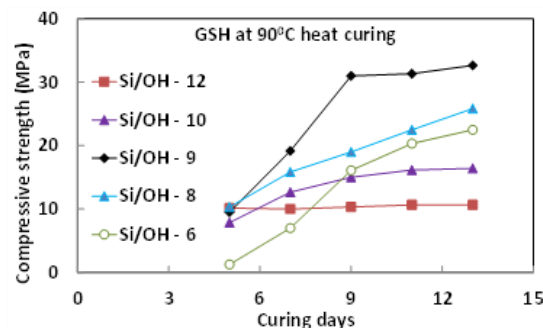


Fig.4 Compressive strength versus Si/OH for Shirasu geopolymers

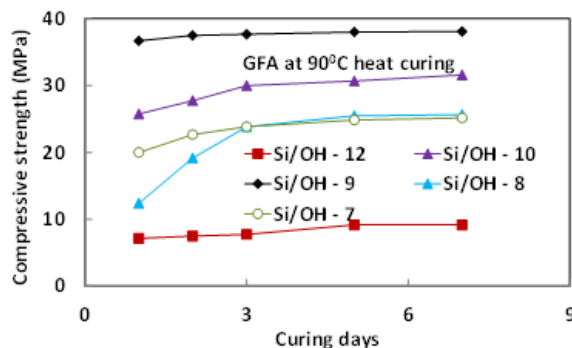


Fig.5 Compressive strength versus Si/OH for Fly ash geopolymers

CONCLUSIONS

Shirasu in geopolymer gave considerably good results when compared to fly ash. The variations in ratio of alkaline activators to aluminosilicate show contrasting results between different geopolymers. These results are attributed to the effect of different parameters like property of silica and its content in Shirasu or fly ash, specific surface area of particles (fineness) and also the balance between aluminosilicates and alkalinity. Shirasu is a pyroclastic flow deposit and fly ash is an industrial by-product. Hence, the chemical characteristics of silica and alumina vary in these pozzolans. Silica and alumina in Shirasu particles may not be easily available for dissolution process with alkaline medium to form polymer at high temperatures. Silica to hydroxide balance in the mix has an effect on the compressive strength of the mortar. It can be considered as one of the important factors in formulations of mixes. Strength of Shirasu geopolymer is lesser when compared to fly ash geopolymer. But the peak compressive strength for Si/OH=9 matched the strength of fly ash geopolymer. The initial hardening of Shirasu geopolymer is delayed up to 5-6 days of heat curing. Dissolution process in the case of Shirasu may be lower because of possible impurities and oxide content over the years of deposition which delays the succeeding gelation and polymerization process. Since concrete with no cement is possible in geopolymer technology, wide range of applications with significant reduction in cost, energy and greenhouse emission can be achieved using Shirasu in

geopolymer while contributing to sustainable concrete and environment. Processing of Shirasu or using finer Shirasu (Blaine specific surface area > 4000cm²/g) would increase the reactivity in polymerization and possible scope for future work.

REFERENCES

- [1] B. Vijaya Rangan, Fly Ash-Based Geopolymer Concrete, Proceedings of the International Workshop on Geopolymer Cement and Concrete, Allied Publishers Private Limited, Mumbai, India, December 2010, pp 68-106.
- [2] Daniel L.Y. Kong, Jay G. Sanjayan, Effect of elevated temperatures on geopolymer paste, mortar and concrete, Cement and Concrete Research, Volume 40, Issue 2, February 2010, Pages 334-339
- [3] Djwantoro Hardjito, Steenie E. Wallah, Dody M. J. Sumajouw, and B.Vijaya Rangan, On the Development of Fly Ash-Based Geopolymer Concrete, ACI Materials Journal, V. 101, No. 6, November-December 2004, pp. 467-472.
- [4] Duxson, P (2007), Geopolymer Technology: The Current State of the Art, Journal of Material Science, Vol. 42, No.9, pp. 2917-2933.
- [5] E. Arioza, O. Arioza, O. Mete Kockar, An experimental study on the mechanical and microstructural properties of geopolymers, 20th International Congress of Chemical and Process Engineering CHISA 2012, 25 – 29 August 2012, Prague, Czech Republic
- [6] G. Habert, J.B. d'Espinose de Lacaillerie, N. Roussel, An environmental evaluation of geopolymer based concrete production: reviewing current research trends, Journal of Cleaner Production, Volume 19, Issue 11, July 2011, Pages 1229-1238.
- [7] Louise K. Turner, Frank G. Collins, Carbon dioxide equivalent (CO₂-e) emissions: A comparison between geopolymer and OPC cement concrete Construction and Building Materials, Volume 43, June 2013, Pages 125-130.
- [8] Maeda, S et al (2006), Exposure Tests on Durability of Concrete using Pyroclastic Flow Deposit "SHIRASU", Tenth East Asia-Pacific Conference on Structural Engineering and Construction.
- [9] Monita Olivia, Hamid Nikraz, Properties of fly ash geopolymer concrete designed by Taguchi method, Materials & Design, Volume 36, April 2012, Pages 191-198
- [10] Takewaka K and Kawamata K (1991), Durability of Concrete using Pyroclastic Flow Deposit for Fine Aggregates, Proceedings of Second Canada/Japan workshop, Ottawa, August.
- [11] Takewaka, K (2004), State-of-Art-Report on Characteristics of SHIRASU Concrete and its Practical Use, Concrete Journal, Vol. 42, No.3, pp. 38-47 (in Japanese).

MeshFree Method for Beam Convergence

Bhavana Patel S.S., K.S. Babu Narayan and Katta Venkataramana

Department of Civil Engineering, National Institute of Technology Karnataka, Surathkal, Mangalore 575025, India. email: bhavana8patel@gmail.com

ABSTRACT: Finite Element Method (FEM) is one of the well developed techniques to solve majority of the engineering problems. The major disadvantage of this method is its requirement for quality mesh and its difficultly in computing smother stress values across the elements. In order to overcome these issues MeshFree methods were developed, where nodes are present without predefined mesh. In this paper, shape function is constructed by Moving Least Square (MLS) technique and the strain-displacement matrix is derived for a beam using Element Free Galerkin (EFG) method. Further computed displacements and stresses using EFG are compared with that of traditional FEM. The result shows the better and faster convergence of MeshFree method in comparison with the FEM.

Keywords: MeshFree, element free Galerkin method, convergence studies, moving least square technique

INTRODUCTION

Advancement in structural engineering has led to the rapid development of numerical methods such as, Boundary Element Method (BEM), Finite Difference Method (FDM), and Finite Element Method (FEM) (Robert D.C et al., 2001). But all these methods are based on discretization of the structure into smaller elements also called as meshes for the analysis. The accuracy of mesh based structures is based on refinement and quality of mesh and requires a lot of human effort. Further it is also difficult to discretize the structure which deals with large deformations and high stress gradients.

In order to overcome these disadvantages of mesh based techniques, MeshFree methods (Daxini S. D. and Prajapati J.M., 2014) are evolved. Arriving at the set of algebraic equation without predefined mesh is called as MeshFree method (Liu G.R., 2009). The method is well suited for adaptive refinement methods (Liu G.R. and Gu Y.T., 2005) wherein nodes can added or removed when and where required.

In the present work Element Free Galerkin (EFG) method (Belytschko T. et al., 1994),

one of the MeshFree methods is adopted for deriving stiffness matrix. Interpolation of the field variables is carried out using Moving Least Square (MLS) technique (Kushawaha J. S., 2012). The formulated procedure has been verified for a cantilever beam loaded at free end. Computed displacements and stresses using MeshFree method are compared with FEM for their convergence. Results show faster convergence of EFG method compared to that of FEM. The results obtained for beam are also discussed in Slokarth Dash and Roshan Kumar (2011) and Someshwar S. P. et al. (2013).

MATERIAL MODEL

The constitutive relation (Timoshenko S.P. and Goodier J.N., 1970) can be written as,

$$\begin{Bmatrix} \sigma_{xx} \\ \tau_{xy} \end{Bmatrix} = \begin{bmatrix} C_{11} & 0 \\ 0 & \frac{C_{11}-C_{12}}{2} \end{bmatrix} \begin{Bmatrix} \varepsilon_{xx} \\ \gamma_{xy} \end{Bmatrix} = \begin{bmatrix} E & 0 \\ 0 & G \end{bmatrix} \begin{Bmatrix} \varepsilon_{xx} \\ \gamma_{xy} \end{Bmatrix} \quad \dots (1)$$

where, σ_{xx} is the normal stress; τ_{xy} is the shear stress; ε_{xx} is the normal strain; γ_{xy} is the shear strains; C_{11} and C_{12} are the material constants.

KINEMATIC RELATIONS

The kinematic relation can be written as,

$$\left. \begin{array}{l} u = u_0 - y\theta_z \\ v = v_0 \end{array} \right\} \quad \dots (2)$$

where, u_0 and v_0 are mid-plane displacements along x and y directions respectively, and θ_z is the mid-plane rotations.

FORCE AND MOMENT EQUATION

The strains are obtained from the kinematic relation (Eq. 3) as,

$$\left. \begin{array}{l} \varepsilon_{xx} = \frac{\partial u}{\partial x} = \varepsilon_{xx}^0 + y\kappa_x \\ \gamma_{xy} = \frac{\partial u}{\partial y} + \frac{\partial v}{\partial x} = \frac{\partial v_0}{\partial x} - \theta_z \end{array} \right\} \quad \dots (3)$$

where, $\varepsilon_{xx}^0 = \frac{\partial u_0}{\partial x}$ is the in-plane strain;

$\kappa_x = -\frac{\partial \theta_z}{\partial x}$ is the curvature strain.

The relation between the force and moment with stresses can be expressed as,

$$\left. \begin{array}{l} N_x = \int_{-h/2}^{h/2} \sigma_{xx} b dy \\ M_x = \int_{-h/2}^{h/2} \sigma_{xx} y b dy \\ Q_x = \int_{-h/2}^{h/2} \tau_{xy} b dy \end{array} \right\} \quad \dots (4)$$

where, N_x is force, M_x is moment, Q_x is shear force and b , h are the cross-sectional dimensions of the beam.

Substituting Eq. 1 & 3 in Eq. 4, we get,

$$\begin{Bmatrix} N_x \\ M_x \\ Q_x \end{Bmatrix} = [MAT] \begin{Bmatrix} \varepsilon_{xx}^0 \\ \kappa_x \\ \gamma_{xy} \end{Bmatrix} = \begin{bmatrix} EA & 0 & 0 \\ 0 & EI & 0 \\ 0 & 0 & GA \end{bmatrix} \begin{Bmatrix} \varepsilon_{xx}^0 \\ \kappa_x \\ \gamma_{xy} \end{Bmatrix} \quad \dots (5)$$

where, E is the Young's modulus of a material, I is area moment of inertia and A is the cross-sectional area.

SHAPE FUNCTION BY MLS TECHNIQUE

Shape function or interpolation of field variables decides the accuracy of the results. $u(x)$ is the function of field variable defined in the domain. The approximation of $u(x)$ at a point can be given as $u^h(x)$. MLS approximation can be represented in series form as,

$$u^h(x) = \sum_j^m p_j(x) a_j(x) = p^T(x) a(x) \quad \dots (6)$$

where, m is the number of basis function, $a(x)$ is the vector of coefficients, which is a function of x and is given as by $a^T(x) = \{a_0(x), a_1(x), \dots, a_m(x)\}$, $p(x)$ is a basis function of the spatial coordinates.

In one-dimensional polynomial basis of order m can be written as,

$$p^T(x) = \{p_0(x), p_1(x), \dots, p_m(x)\} = \{1, x, x^2, x^3, \dots, x^m\} \quad \dots (7)$$

By solving the linear relation as given in Eq. 8, $a(x)$ is obtained

$$A(x) a(x) = B(x) d \quad \dots (8)$$

where,

$$A(x) = \sum_l^n W_l(x) p^T(x_l) p(x_l)$$

$$B(x) = [B_1, B_2, \dots, B_n]$$

$$B_l = W_l(x) p(x_l)$$

$$d = \{u_1, u_2, \dots, u_n\}^T$$

d is the vector that collects the discrete nodal parameters of the field variables for all the nodes in the support domain.

Substituting Eq. 8 in Eq. 7, we get

$$u^h(x) = \sum_l^n \sum_j^m p_j(x) (A^{-1}(x) B(x))_{jl} d \quad \dots (9)$$

Eq. 9 can be written as,

$$u^h(x) = \sum_l^n N_l(x) d \quad \dots (10)$$

where,

$$N_l(x) = \sum_j^m p_j(x) (A^{-1}(x) B(x))_{jl} = p^T A^{-1} B_l ,$$

$N(x)$ is the matrix of MLS shape function corresponding to n nodes in the support domain, $N(x) = [N_1(x), N_2(x), \dots, N_n(x)]$.

Exponential weight function (Suzhen Liu et al., 2008) is adopted as it gives higher importance to neighboring nodes, which will be important in locating the high stress point in the problems such as crack initiation and propagation. Also, the first and second order differential of the exponential weight function follows continuity in the field variable interpolation.

$$W(x - x_l) = W(d) = \begin{cases} e^{-(d/\alpha)^2} & \text{for } d \leq 1 \\ 0 & \text{for } d > 1 \end{cases} \quad \dots (11)$$

where, a is constant and taken as 0.3; $d = \frac{|x-x_I|}{d_w}$ and x is any point in the domain, x_I is the node of interest and d_w is the smoothing length.

STRAIN-DISPLACEMENT AND STIFFNESS

The strain-displacement matrix is obtained by substituting the shape functions derived from Eq. 10 as,

$$\begin{bmatrix} \varepsilon_{xx_0} \\ k_x \\ v_{xy_0} \end{bmatrix} = \sum_{i=1}^n B_i \begin{bmatrix} u_i \\ v_i \\ \theta_{zi} \end{bmatrix} = \sum_{i=1}^n \begin{bmatrix} \frac{\partial N_i}{\partial x} & 0 & 0 \\ 0 & 0 & \frac{\partial N_i}{\partial x} \\ 0 & \frac{\partial N_i}{\partial x} & N_i \end{bmatrix} \begin{bmatrix} u_i \\ v_i \\ \theta_{zi} \end{bmatrix} \quad \dots (12)$$

By the stationary minimum potential energy principle, the stiffness K can be derived as,

$$K = \int_{-1}^1 B^T [Mat] B |J| d\xi \quad \dots (13)$$

where, $J = \sum_{i=1}^n \frac{\partial N_i}{\partial x} X_i$ and X_i are the coordinates of the nodes in the domain.

Eq. 13 is numerically integrated by applying Gaussian quadrature, which is represented in terms of Gauss points and weights as,

$$K = \sum_{i=1}^{N_g} w_i B^T(\xi_i) [Mat] B(\xi_i) J(\xi_i) \quad \dots (14)$$

where, N_g is the number of Gauss points

RESULTS AND DISCUSSIONS

The formulation discussed in the previous section is verified on a steel cantilever beam of length 1000 mm, cross-sectional area $100 \times 100 \text{ mm}^2$ and point load (P) of 1000N as shown in Fig. 1. Convergence of Displacements and stresses to the exact solution are illustrated. Exact solutions of Timoshenko (higher order) and Euler-Bernouli's (first order) theories are considered to verify the results of FEM and MeshFree method.

Fig. 2 shows the comparison of displacements obtained from the numerical methods with the exact solution. MeshFree method converges with the Timoshenko's values with lesser nodes than that of FEM.

Fig. 3 shows the comparison of the computed stress values with the exact solution. Results obtained using MeshFree method exactly coincides with the exact solution.

CONCLUSIONS

FEM is one of the well developed numerical techniques, but the method fails to interpolate displacements and stresses accurately with lesser number of nodes. The accuracy of mesh based methods depends on the finer discretization, whereas EFG method interpolates displacements and stresses much smoother using MLS (based on weightage). The results shows convergence of displacements and stresses using MeshFree method is superior compared to that of FEM.

ACKNOWLEDGEMENTS

The authors are grateful to Technical Education Quality Improvement Programme (TEQIP) for funding this study.

REFERENCES

- [1] Belytschko T. et al. (1994), Element-free Galerkin method, International Journal For Numerical Methods In Engineering, 37, 229-256.
- [2] Daxini S. D. and Prajapati J.M. (2014), A Review on Recent Contribution of MeshFree Methods to Structures and Fracture Mechanics Application, The Scientific World Journal, Article ID 247172.
- [3] Kushawaha J. S. (2012), MeshFree shape function from moving least square, e-Journal of Science and technology, 29-41
- [4] Robert D.C et al. (2001), Concepts and Application of Finite Element Analysis, Fourth edition, John Wiley and sons, INC.
- [5] Liu G.R. and Gu Y.T. (2005), An Introduction To Meshfree Methods And Their Programming, Springer, AA Dordrecht, The Netherlands.
- [6] Liu G.R. (2009), MeshFree Methods Moving beyond the Finite Element Method, Second edition, CRC press, Taylor and Francis group, New York.
- [7] Slokarth Dash and Roshan Kumar (2011), Analysis of Beams and Plates Using Element Free Galerkin Method, B.Tech Thesis, Indian Institute of Technology, Rourkela.
- [8] Someshwar S. P. et al. (2013), Introduction of MeshFree methods and implementation of EFG methods to beam problem, International Journal on Theoretical and Applied Research in Mechanical Engineering, 2, 2319 – 3182.
- [9] Suzhen Liu et al. (2008), Study of Weight Functions in the Element-Free Galerkin Method, ICEMS Proceeding, Hebei University of Technology
- [10] Timoshenko S.P. and Goodier J.N. (1970), Theory of Elasticity, 3rd edition, McGraw-Hill, New York.



Figure 1 – Cantilever Beam

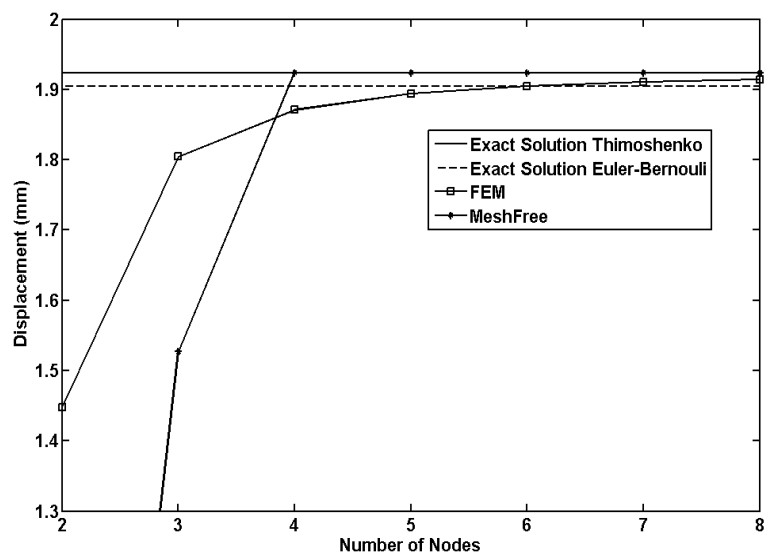


Figure 2 - Displacement plot for cantilever beam

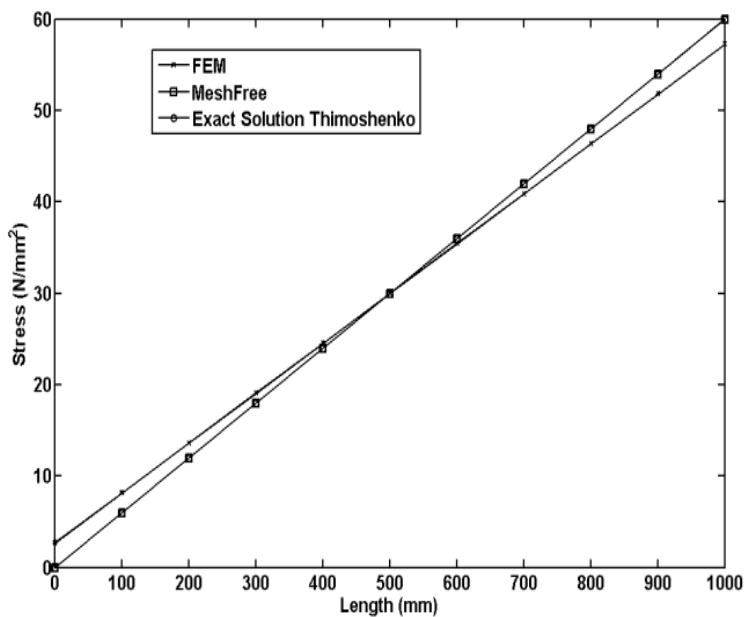


Figure 3 - Stress plot for cantilever beam

INFLUENCE OF GEOMETRIC PARAMETERS ON THE IN-PLANE RESPONSE OF MASONRY WALLS – ANALYTICAL STUDIES

Ashwin Thammaiah K¹, Raghunath S² and Aswath M U³

1. Post Graduate Engineer Trainee, L&T Construction, Chennai and formerly Post Graduate (M.Tech Structural Engineering) student, Department of Civil Engineering, Bangalore Institute of Technology, Bangalore – 560004, India. email: ashwintk_18@yahoo.com
 2. Department of Civil Engineering, BMS College of Engineering, Bangalore – 560019, India. email: raghunath.smrc@gmail.com
 3. Department of Civil Engineering, Bangalore Institute of Technology, Bangalore – 560004, India. email: aswathmu@yahoo.com
-

ABSTRACT: Multi-storeyed load bearing masonry is generally configured by giving special considerations to the location and geometry of shear walls, followed by strength-based design for gravity loads and lateral loads. The aspect ratio of walls and openings present in them, influence the lateral load response significantly. In this paper, the results of parametric studies carried out to understand the influence of above mentioned parameters, is presented. Also included is the stress analysis of two special types of shear walls known as perforated shear walls and coupled shear walls. The masonry wall has been modelled using finite element technique, whose properties were evaluated through experimental studies. In the present study, the influence of provision of reinforcement through cores of engineered hollow blocks is highlighted. The studies reveal that the provision of grouted masonry cores greatly benefits in contributing to the lateral load response.

Keywords: Multi-storeyed load bearing masonry, aspect ratio, stress analysis, perforated shear walls and coupled shear walls, finite element technique and engineered hollow blocks.

INTRODUCTION

The concept of reinforced masonry as a form of construction has been identified as early as 18th century along the same time as the invention of cement. In spite of which either due to lack of exhaustive experimental evidences, lack of confidence in designers, lack of well defined codal provisions, etc this form of construction has taken a backburner and is mainly restricted to academic interests and certain sections of countries.

From the observation on the lateral load response of masonry, it is

evident that unreinforced masonry in particular is highly vulnerable to lateral loads and thus, leading to catastrophic failures or even total collapse of load bearing walls. This has been attributed to major share of fatalities recorded due to earthquake (Fig 1 and Fig 2)

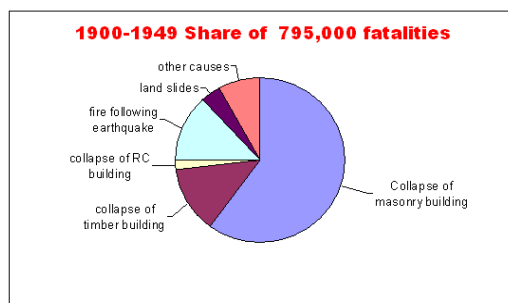


Fig 1 Pie chart on fatalities 1900-1949
(Courtesy: Coburn and Spence)

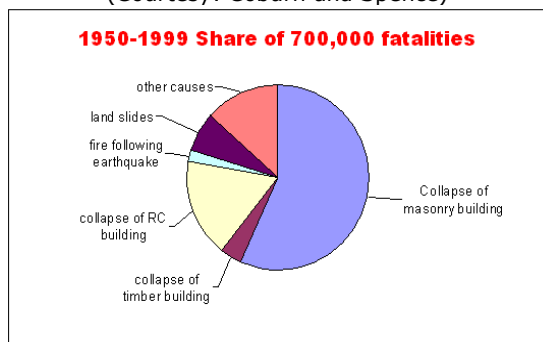


Fig 2 Pie chart on fatalities 1950-1999
(Courtesy: Coburn and Spence)

The limitation with unreinforced masonry lies due to the lack of unison action between the load resisting members as well as the inherent brittle nature of masonry. Also, the vulnerability to lateral loading is enhanced by unsymmetrical plan, discontinuity in load transfer path, effect of geometric characteristics and presence of openings, etc.

In a typical box type of masonry walls with plane normal to seismic excitation is referred to as cross walls and that parallel to direction of excitation as shear walls. The shear walls in general are known to share a majority of lateral load owing to relatively higher inherent stiffness along the plane of wall. However, even a typical box type of masonry is very complex for analytical modelling due to orthotropic nature, brittle behaviour, non-linear stress-strain characteristics, effect of joints and interaction between the mentioned parameters. Experimental and analytical studies have revealed that the non-linearity in masonry is governed by effect of perpend joint and hence the failure, due to which crack propagation

on progressive loading leads to an increase in Poisson's ratio [1].

In Indian context until recent times the qualities of materials have not been up to the required standards. However, experimental and analytical studies on masonry have revealed that the shear strength and ductility in masonry is a parameter dependent on both the elastic properties as well as the laying course configuration of the constituent materials [2].

The parameters governing the modes of failure and crack propagation in masonry can in general be related to geometric characteristics of masonry and elastic properties of constituent materials. The modes of failure may be classified into flexural rocking with toe crushing in case of slender walls, sliding shear in case on squat walls and diagonal X-type of shear crack with crack propagation through units or mortar based on their relative strengths in case of walls which are neither too slender nor squat [3].

Also in estimation of stiffness of masonry, the existing methods are specified for strong spandrel weak pier configuration, the vice versa case has overestimated the stiffness with existing methods. The shear interaction effect between cross wall and shear wall leading to a probable transformation in nature of stresses is known to have a significant effect on the stiffness estimation [4].

A variety of reinforced masonry buildings have been evaluated for performance under lateral dynamic load using shock table tests. These include reinforced masonry in the form of vertical corner reinforcement [5], containment reinforcement [6], reinforced concrete bands at different levels (with inclusion of sill band which is not specified in Indian Standard: 4326 – 1993) [7], post tensioning of walls, steel mesh plastering [8], providing reinforcement bars through hollow cores of units followed by grouting [9] and/or a system with combinations of above

mentioned configurations. The inherent superiority of reinforced masonry is clearly evident over unreinforced masonry.

OBJECTIVES OF PRESENT STUDY

To study the influence of geometric / elastic properties on the in-plane response (viz., lateral stiffness, peak deformation and nature of stresses induced) of masonry. The following parameters were considered.

- i. Variation in Aspect ratio (h/l) of masonry. (Fig 3)
- ii. Openings in masonry. (Fig 4)
- iii. Perforated and Coupled shear wall. (Fig 5)
- iv. Influence of reinforced masonry. (Fig 5)

Also, as a part of this study, a comparison on the performance of unreinforced and reinforced masonry (with reinforcement at the wall corners and / or on adjacent sides of openings) of identical dimensions was carried out.

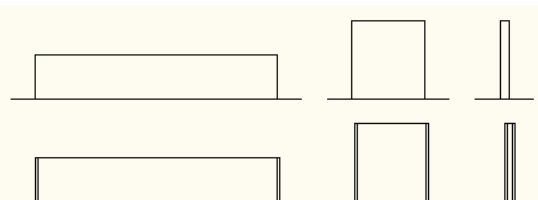


Fig 3 Typical representation of variation in aspect ratio (0.18-8) considered in unreinforced and corner reinforced masonry respectively

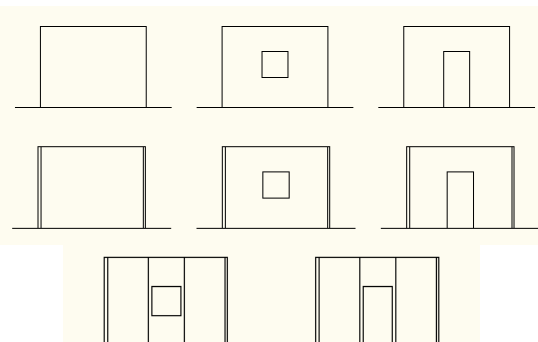


Fig 4 Typical representation of unreinforced masonry, corner reinforced masonry and masonry with corner as well as opening reinforced respectively

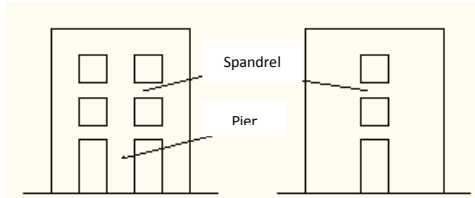


Fig 5 Typical representation of perforated and coupled shear wall respectively

ANALYTICAL MODELLING OF SPECIMENS

The specimens were modelled in finite element software package NISA ver 15.0. The masonry walls were modelled as a four noded three dimensional, orthotropic shell element of 0.2 m thick each with necessary discretization. The boundary condition adopted was fixed at base. The common nodes were merged and compacted to ensure displacement compatibility & non duplication of nodes.

To evaluate the in-plane performance, loads were applied at the top end of specimen and then normalized after analysis. For the case of perforated and coupled shear walls, the loads were applied based on calculations related to equivalent lateral load method specified in IS: 1893-2002 and again normalized as required.

RESULTS AND DISCUSSIONS

1) With reference to the parameter aspect ratio, there appears to be minimal variation in stiffness for both reinforced and unreinforced masonry for low values of aspect ratio. However, as the slenderness increases with aspect ratio, the stiffness of reinforced masonry exceeds unreinforced masonry significantly. The vice versa relation is evident in peak displacement experienced by reinforced and unreinforced masonry (as shown in Fig 6 & 7 respectively).

4th International Engineering Symposium - IES 2015

March 4-6, 2015, Kumamoto University, Japan

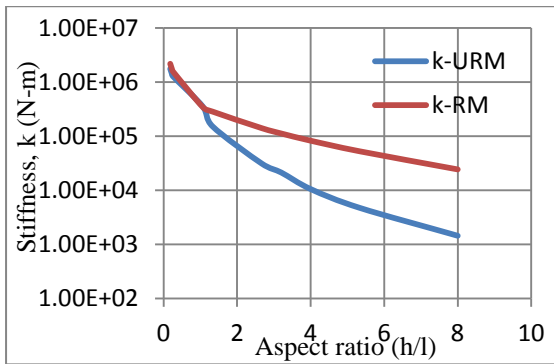


Fig 6 Plot of variation of stiffness versus aspect ratio

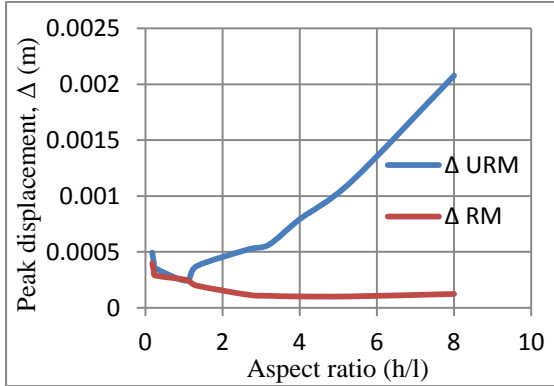


Fig 7 Plot of variation of peak displacement versus aspect ratio

2) With reference to maximum stress induced, unreinforced masonry exceeds reinforced masonry with respect to compression, tensile and shear. Also, there appears to be peculiarity in the behaviour of masonry (point of inflection) corresponding to aspect ratio of $5/3$ (2.667) which requires further investigation (as shown in Fig 8, 9 & 10).

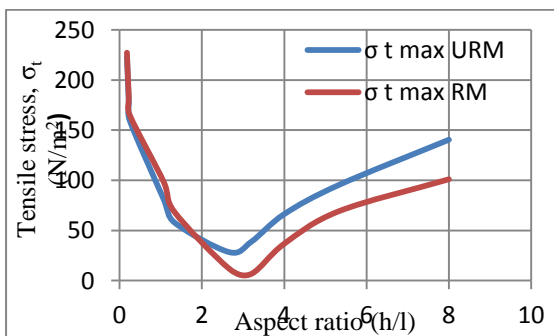


Fig 8 Plot of variation of tensile stress induced versus aspect ratio

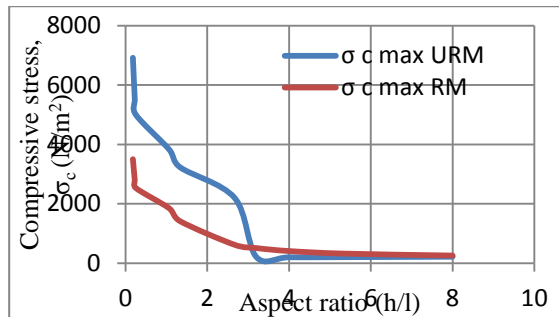


Fig 9 Plot of variation of compressive stress induced versus aspect ratio

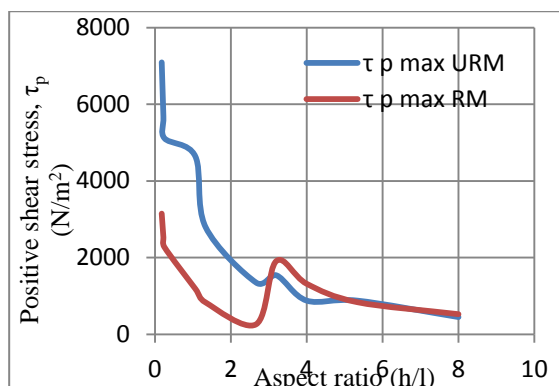


Fig 10 Plot of variation of positive shear stress versus aspect ratio

3) The typical shear transformation (positive and negative shear stress) is evident in squat walls with shear tendency and not in slender walls with flexure tendency (as shown in Fig 11).

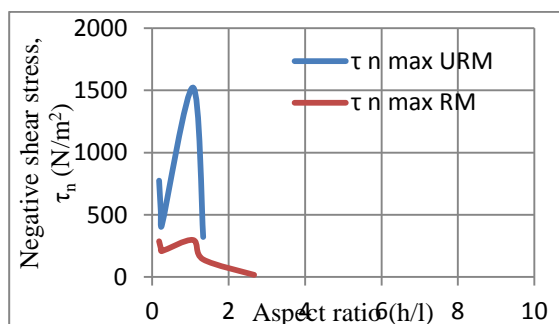


Fig 11 Plot of variation of negative shear stress versus aspect ratio

4) With reference to effect of openings, it is known that stiffness reduces with increase in dimensions of opening. However, in case of masonry wherein the openings are reinforced on either boundary, there seems to be an

improvement in stiffness and a vice versa relation is evident with respect to peak displacement experienced (as shown in Fig 12 & 13).

5) With reference to maximum stress induced, stresses induced in unreinforced masonry exceed reinforced masonry. Also, by reinforcing the openings on boundary, there appears to be negligible variation in stress induced even with changes in area of opening (as shown in Fig 14, 15, 16 & 17).

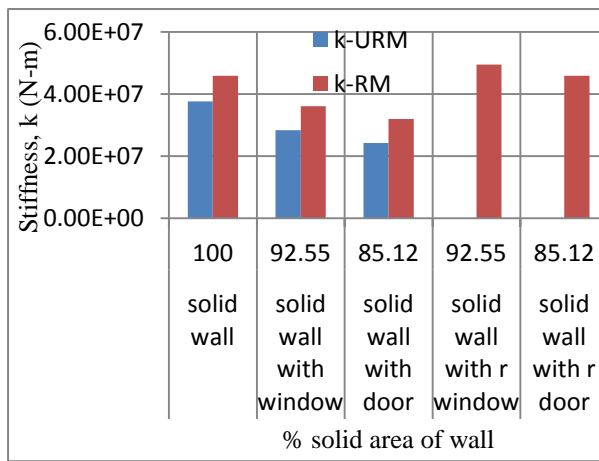


Fig 12 Plot of variation of stiffness versus % solid area of wall

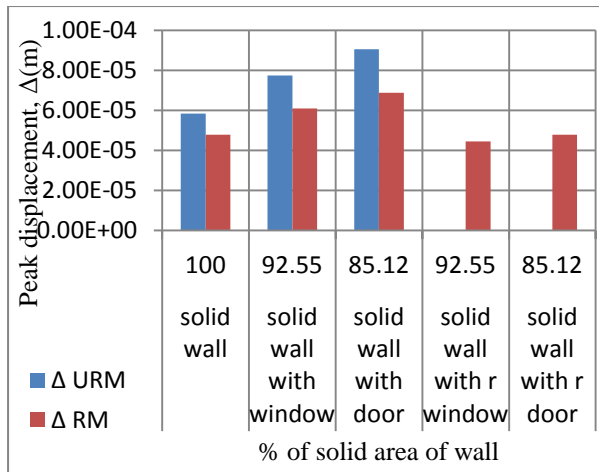


Fig 13 Plot of variation of peak displacement versus % solid area of wall

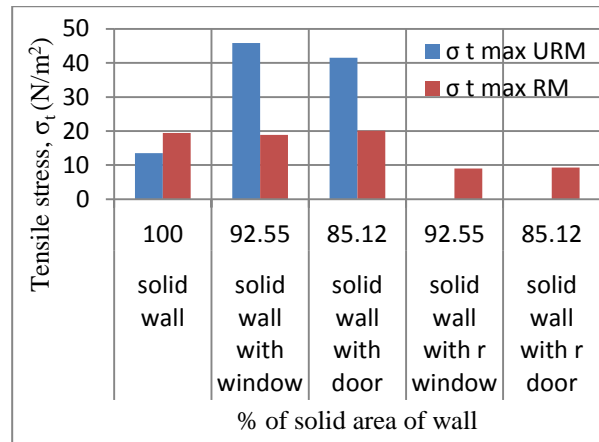


Fig 14 Plot of variation in tensile stress induced versus % solid area of wall

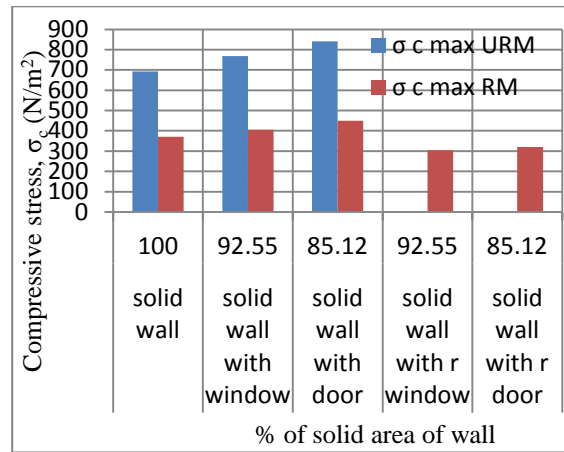


Fig 15 Plot of variation of induced compressive stress versus % solid area of wall

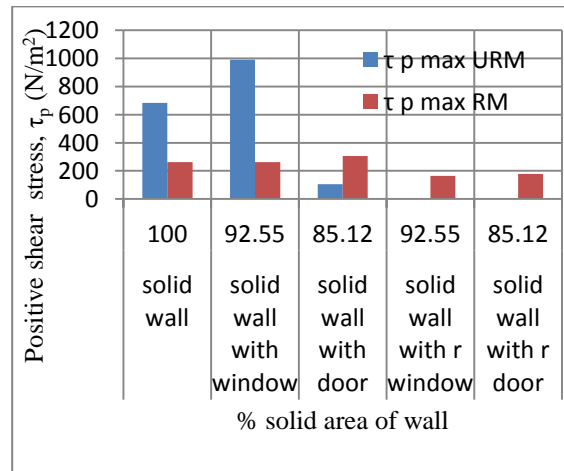


Fig 16 Plot of variation of induced positive shear stress versus % solid area of wall

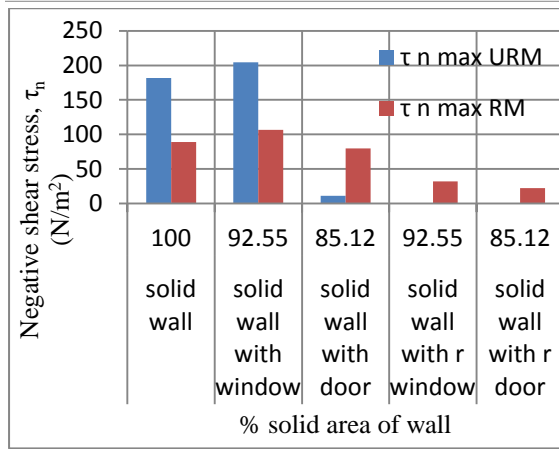


Fig 17 Plot of variation of induced negative shear stress versus % solid area of wall

6) The enhanced performance of coupled shear wall over perforated wall may be as the former has a discontinuity within the element itself, whereas in the latter, the discontinuity appears in between continuous elements bound by structural system (as shown in Fig 18, 19, & 20).

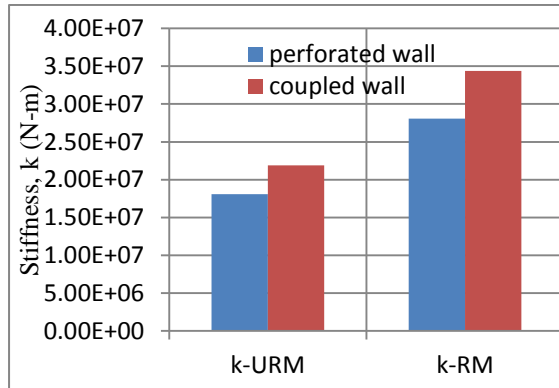


Fig 18 Plot of stiffness of unreinforced and reinforced masonry respectively

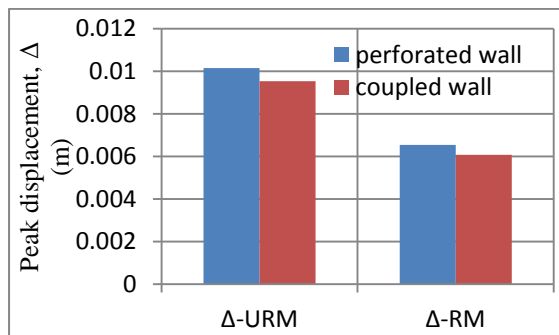


Fig 19 Plot of peak displacement of unreinforced and reinforced masonry respectively

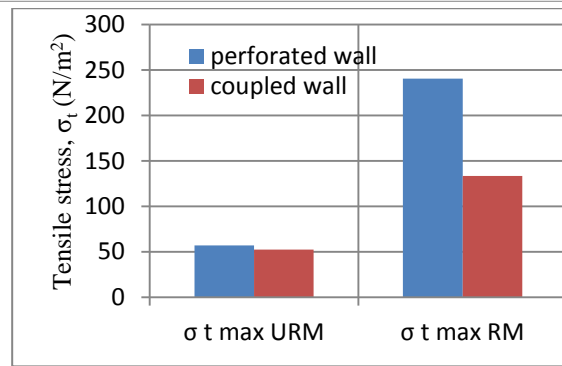


Fig 20 Plot of induced tensile stress in unreinforced and reinforced masonry respectively

7) At instances where in the stress in reinforced exceeds unreinforced masonry or wherein stress in coupled shear walls exceeds that in perforated walls, the stresses appear to be concentrated within the reinforced cores and not in walls within the reinforced cores.

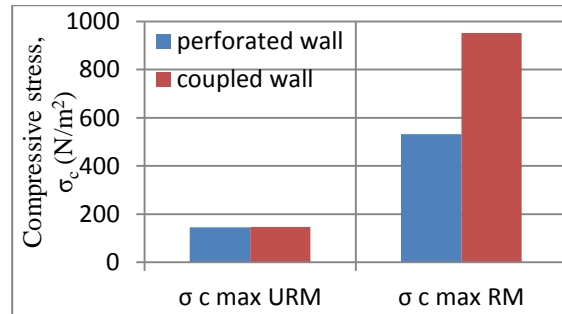


Fig 21 Plot of induced compressive stress in unreinforced and reinforced masonry respectively

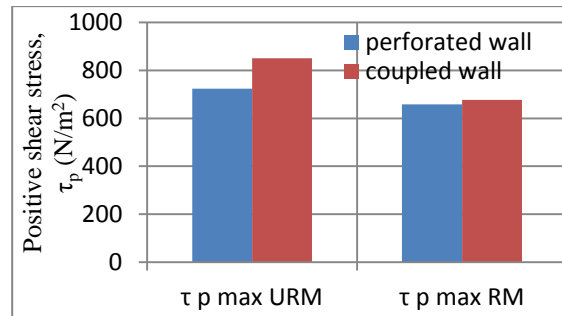


Fig 22 Plot of induced positive shear stress in unreinforced and reinforced masonry respectively

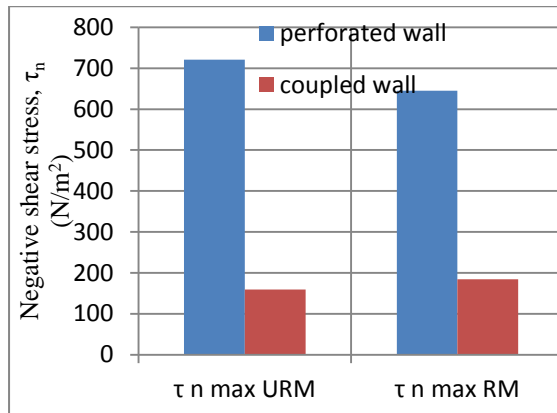


Fig 23 Plot of induced negative shear stress in unreinforced and reinforced masonry respectively

CONCLUSIONS

The following conclusions are deduced from this study:

- 1) The significance of reinforced masonry is realized in case of slender walls with flexural tendency as opposed to squat walls with dominant shear tendency. Also, the intrinsic negligible tensile strength of masonry necessitates the need for reinforced masonry in slender walls.
- 2) In case of squat walls loaded in-plane, majority of stresses induced is compressive in nature with negligible tension at loaded edges. Whereas, in slender walls the stress induced is significantly both compressive and tensile in nature.
- 3) The openings which serve as a discontinuity within walls lead to reduction in stiffness, increased displacement and localized stress concentration. However, reinforced masonry (in particular when boundary of opening is reinforced) tends to relatively enhance the integrity of piers and spandrels, the whole of structural system in general and hence comparatively improves the above mentioned parameters irrespective of dimension of openings (either the presence of door or window).
- 4) The coupled shear walls clearly exhibit an enhanced performance over perforated walls when subjected to in-

plane loads and hence, from a point of view of seismic design, it can be considered for construction of multi storeyed masonry.

LIST OF NOTATIONS

URM :	Un-reinforced masonry
RM :	Reinforced masonry
$\sigma_c \max$:	Maximum compressive stress
$\sigma_t \max$:	Maximum tensile stress
T_p :	Maximum positive shear stress
T_n :	Maximum negative shear stress
r-window :	reinforcement around window opening
r-door :	reinforcement around door opening

REFERENCES

- [1] Mohamad, Gihad; Lourenço, Paulo Brandão; Rizzato, Eduardo; Roman Humberto Ramos; Nakanishi, Elizabete Yukiko, "Failure mode, deformability and strength of masonry walls" 15th International Brick and Block Masonry Conference Florianópolis – Brazil – 2012
- [2] Jelena Milosevic, Antonio S Gago, Maria Lopes and Rita Bento. "Rubble stone masonry walls – Evaluation of shear strength by diagonal compression tests" Proceedings of 8th International Conference of SAHC (2012) Wroclaw Poland
- [3] Miha Tomozavic, "Shear resistance of masonry walls and Euro code 6: Shear versus tensile strength of masonry" Materials and structures (2009) 42:889-907
- [4] Balasubramanian S. R., Balaji Rao K., Dhiman Basu, Anoop M. B., and Vidyanathan C. V, "An improved method for estimation of elastic lateral stiffness of brick masonry shear walls with openings" KSCE Journal of Civil Engineering (2011) 15(2):281-293
- [5] Biswarup Saikia, "Analytical and experimental investigations on earthquake resistant low-rise brick masonry buildings", Phd thesis submitted to VTU (2012)
- [6] Raghunath S, "Static and dynamic behaviour of brick masonry with containment reinforcement", PhD thesis submitted to IISc
- [7] Dharshan K, "Shock table studies on masonry building with rigid RC roof", M.Tech thesis submitted to VTU (2007)
- [8] F Ersubasi and H H Korkmaz, "Shock table tests on strengthening of masonry structures against earthquake hazard". NHESS, 10, 1209-1220, 2010
- [9] Ashwin Thammaiah K, Anush K C, Pratyusha M Naik and Srikanth P, "Seismic evaluation of reinforced hollow concrete block masonry building model", B.E. project work submitted to VTU (2012)

4th International Engineering Symposium - IES 2015

March 4-6, 2015, Kumamoto University, Japan

**ELECTRICAL, ELECTRONICS,
COMPUTER ENGINEERING
&
RELATED FIELDS**

Real-Time Pedestrian Detection and Tracking

Anmol J Bhattad¹, Sharukh S Shaikh¹, Sumam David S.¹,
K. P. Anoop² and Venkat R Peddigari²

¹ Department of Electronics and Communication Engineering, National Institute of Technology Karnataka, Surathkal, Mangalore 575025, India. Email: sumam@ieee.org

² Formerly with Texas Instruments (India) Pvt. Ltd., Bangalore, India.

ABSTRACT: Pedestrian detection is a key problem in computer vision, with several applications that have the potential to positively impact the quality of life. This paper describes a comprehensive combination of feature extraction methods for vision-based pedestrian detection and tracking in Intelligent Systems based on monocular vision. First, we detect the pedestrian using Integral Channel Features and AdaBoost classifier, which is implemented with Modified Soft Cascade to achieve robust thresholds. Later we track the pedestrian for the next few frames based on Lucas Kanade features. The experiment results show that the method can detect and track pedestrian ahead of vehicle in spite of different sizes and postures. The algorithms have been tested on Inria database for the detection system and Caltech and Daimler datasets for the detection and tracking system.

Keywords: Pedestrian Detection, Pedestrian Tracking, Integral Channel Features, Lucas Kanade features

INTRODUCTION

Detecting and tracking people is an important area of research, and machine vision is bound to play a key role. Its applications include traffic control, robotics, entertainment, surveillance, care for the elderly and disabled, and content-based indexing. Our study aims to address these questions by detecting and tracking the pedestrians in the video which is at the rate of around 30 frames/second captured with a monocular camera mounted on the car. Fig. 1. shows the block diagram of the detection and tracking system.

Many interesting pedestrian detection approaches have been proposed in the literature. The Histogram of Oriented Gradients (HOG) detector proposed by Dalal and Triggs (2005), is a combination of edge orientation histograms, shape contexts and Scale-invariant feature transform (SIFT) descriptors. Histogram of Optical Flow (HOF) introduced by Dalal N. et. al. (2006), is based on motion features. HOF, is not affected by movements in camera and background, which makes it robust. In

Stefan W. et. al. (2010), HOF is used in combination with HOG, and the model was trained using SVM.

Unlike features such as Haar, HOG, HOF, Sabzmeidan and Mori (2007) uses mid-level features called Shapelets to train the classifier. These features focus on local regions of the image and are built from low-level gradient information.

A multi cue approach suggested in Wojek and Schiele (2008) combines various features like Haar Wavelets, Haar-like HOG features, Shapelets and Shape Context and shows that a multi-cue pedestrian detection approach performs better than using single feature. The combination of modified HOG and HOF in Stefan W. et. al. (2010) performs better than any individual feature.

Viola P. et.al. (2005) is an extension of the rectangle filters from Viola and Jones (2004) to the motion domain. It describes a pedestrian detection system that integrates image intensity information with motion information. ChnFtrs, Dollar P. et. al. (2009) coupled the integral channel features with

soft cascade AdaBoost algorithm which outperformed existing methods for pedestrian detection. Multiple image channels are computed using linear and non-linear transformations of the input image, and then features such as local sums, histograms, and Haar features are computed to get integral channels.

The overview of state-of-art pedestrian detectors brings out the following facts. HOG is a very basic and effective feature, but bare HOG can't give the best results. Hence, a multi cue pedestrian detection is favorable. Mid-level features such as Shapelets are computationally expensive and hence unsuitable for real-time detector implementation. The need to calculate the Optical Flow channels makes the computation of HOF features very slow. Thus, HOG+HOF, Stefan W. et. al. (2010), is not good for real-time applications, inspite of having good accuracies. The integral channel features (ICF), Dollar P. et. al. (2009), obtained from color channels, gradient histograms etc. are computationally efficient, capture thorough information and offer faster detection. The ChnFtrs utilizing ICFs detector has high accuracy but, has a rate of 1.18 fps. But for real-time implementation we need faster detectors. Higher computational time requirement makes the non-linear SVM kernels unsuitable for real-time pedestrian detection. Though SVM is universally known for good accuracies, AdaBoost is quite comparable. AdaBoost along with soft cascade is much faster than linear SVM, at the cost of marginal decrease in the performance and hence, it is chosen as the basic classifier in our implementation.

PEDESTRIAN DETECTION

Given an input image I , channels can be computed using linear or non-linear transformation of I . We consider the following channels for our detector:

LUV Colour Channels

The Fig. 3 shows the LUV channels of the original image shown in Fig. 2. In case of 8-bit images the values of R, G and B are converted to the floating-point format, scaled to fit 0 to 1 range and then converted into LUV channels.

Gradient Magnitude

The Gradient Magnitude measures the strength and distribution of the gradients within an image. Let $I(i,j)$ denote an $m \times n$ discrete signal, and $\delta I/\delta x$ and $\delta I/\delta y$ denote the discrete derivatives of I (typically 1D centred first differences are used). Gradient magnitude $M(i,j)$ and orientation $O(i,j)$ are given by

$$M(i,j) = \sqrt{\frac{\delta I(i,j)}{\delta x}^2 + \frac{\delta I(i,j)}{\delta y}^2} \quad (1)$$

$$O(i,j) = \arctan\left(\frac{\frac{\delta I(i,j)}{\delta y}}{\frac{\delta I(i,j)}{\delta x}}\right) \quad (2)$$

Fig. 4 is the Gradient Magnitude of the original image shown in Fig. 2. Let the horizontal changes given by $\delta I/\delta x$ be denoted by G_x and the vertical changes given by $\delta I/\delta y$ be denoted by G_y . The actual gradient magnitude is given by

$$G = \sqrt{G_x^2 + G_y^2} \quad (3)$$

To avoid the computational burden of calculating the square root for each pixel we adopt an approximation given by

$$G = |G_x| + |G_y| \quad (4)$$

Gradient Orientation Channels

The Gradient Orientations $O(i,j)$, Dollar P. et. al. (2009) are distributed in the range $[0, \pi]$. The range is divided into equal sized six bins and the orientation channels are computed as

$$G_\theta(i,j) = M(i,j) \cdot \mathbf{1}[O(i,j) \in (\theta_1, \theta_2)] \quad (5)$$

where $G_\theta(i,j)$ is the gradient orientation channel within range $[\theta_1, \theta_2]$, $M(i,j)$ the gradient magnitude and $O(i,j)$ is the gradient angle, respectively, at $I(i,j)$. Fig. 5 shows the gradient orientation channels along six orientations within six equal sized bins. The six bins for the images shown are $[0, \pi/6]$, $[\pi/6, \pi/3]$, $[\pi/3, \pi/2]$, $[\pi/2, 2\pi/3]$, $[2\pi/3, 5\pi/6]$ and $[5\pi/6, \pi]$. The gradient orientations are computed over these bins and are used for obtaining integral channel features.

Gradients are computed over the channels using the discrete derivative mask $d^2x = [1, -2, 1]$ and $d^2y = [1, -2, 1]'$. These provide the second order gradients which have strong response near edges and other sharp transitions.

4th International Engineering Symposium - IES 2015

March 4-6, 2015, Kumamoto University, Japan

Using the above mentioned linear and non-linear transforms on the input image, we get different channels. Further we compute the features of each channel by taking the sum over randomly selected rectangular regions. These features are computed efficiently from the channels by using integral images. Such features are called as integral channel features.

Each feature has three parameters that are generated randomly. Given that we compute different channels of our detection Window, a feature is calculated on a random channel, over a rectangle whose dimensions and position is also random.

Soft Cascade AdaBoost Classifier

In AdaBoost, weak classifiers are cascaded to produce strong classifier, John Lu (2010). The weak classifiers are very simple and are computationally inexpensive. The weak classifiers used here are 2-depth decision tree. Bourdev & Brandt's (2005) thresholding technique after every weak classifier is better than thresholding at the end, helping us remove negative samples at an early stage. Given the large number of negative windows in an image, this feature called as soft cascade makes AdaBoost faster.

Modified Soft Cascade

In the proposed method, a modified version of soft cascade is suggested. Instead of thresholding at the end of every weak classifier, it is performed only after a few weak classifiers, separated by a regular interval n . Consider an AdaBoost classifier consisting of T weak classifiers. Let, $c_t(x)$ denote the confidence by the weak classifier t for a sample x . Then, the thresholding is shown by the following algorithm,

```
d ← 0
for t = 1 ... T
    d ← d + ct(x)
    if t % n == 0 then
        if d < ri return false
return true
```

To determine the threshold, consider a set of positive test images $i = 1, 2, 3, \dots$. We run it over the trained AdaBoost. Let $c_j(i)$ be the value of the j^{th} weak classifier for the i^{th} image, where $i = n, 2n, 3n, \dots, N$.

Let, $M_j = \sum_i c_j(i)$ and $\sigma_j = \sum_i (c_j(i) - M_j)^2$. Then, the threshold r_j is given by,

$$r_j = M_j - k\sigma_j \quad (6)$$

To get the thresholds, test images are used instead of training images because, the AdaBoost will fit over the training data very well when compared to the test data, resulting in higher thresholds. Thus, the modified soft cascade helps us achieve speed like that of soft cascade and results in more robust thresholds.

Detection over full images

To implement the detector over the complete image, downscale the image from its original size and keep on placing them one upon the other. Scale down until, $[\text{ImageHeight}/\text{Scale}] > 128$ and $[\text{ImageWidth}/\text{Scale}] > 64$.

Between the two consecutive levels of the pyramid the scale factor is chosen to be 1.2. And between the two consecutive windows the distance (window stride) is 8 pixels. New height and new width of the image are given by,

$$\begin{aligned} \text{NewHeight} &= [\text{OrigHeight}/\text{Scale}] \\ \text{NewWidth} &= [\text{OrigWidth}/\text{Scale}] \end{aligned} \quad (7)$$

Scanning-window style classification of image patches typically results in multiple responses around the target object. We circumvent this by removing any detector responses in the neighborhood of detections with the locally maximal confidence score. This technique is known as Non-Maximal Suppression (NMS), Rosten E. et. Al. (2006).

PEDESTRIAN TRACKING

The tracking phase assumes that the person has already been detected. Since, the displacement of the pedestrian is not huge in short interval of time (10-15 frames), the tracking system need not be robust. Hence, we consider the point and kernel tracking algorithms, Li X. et. al. (2013), that are not computationally intensive.

Lucas Kanade (LK) feature tracker

- Detection of the feature points: Shi-Tomasi feature detector, Shi and Tomasi (1994), is used to detect the feature

4th International Engineering Symposium - IES 2015

March 4-6, 2015, Kumamoto University, Japan

points in the bonding box provided by the pedestrian detector.

- Pyramidal Implementation Feature Tracker: The pyramidal implementation, Bouquet J. (2001), of the LK optical flow is used, Dollar P. et. al. (2009), to evaluate the position of the feature points in the consecutive frames.
- Evaluate the final position of the bonding box: The position of the feature points in the consecutive frames is known. The outlier points which do not lie on the pedestrian and the points which move insignificantly are eliminated. By computing the velocities of the remaining points the shift in the bonding box is calculated.

RESULTS

The experiments were carried out on INRIA database [9] which comprises of 2,416 positive training samples of size 96x160 and 1,126 positive testing samples of size 70x134 and 1,218 negative training images and 453 negative testing images. The performance of the detector is evaluated by obtaining the Miss Rate Vs False Positive per Window (FPPW) plots. Miss Rate is the ratio of positive samples mispredicted to the total number of positive samples in the dataset. All the accuracies are measured at 10^{-3} FPPW.

For pre-processing, we applied a 3×3 Gaussian smoothening on the images. After multiple experiments, (Fig.6) we conclude that 12,000 features, 5-15 pixel rectangle size and AdaBoost with 1000 weak classifiers give the most promising results, with an accuracy of 93.82% (Fig. 7). A few snap shots are given in Fig. 8 and Fig. 9.

The tracking system assumes that the pedestrian has already been detected and the pedestrian detector gives the bonding box coordinates centering the pedestrian. The tracking system is then expected to track the pedestrian for next 10 to 15 consecutive frames i.e. around 0.3-0.5 seconds. We have run the algorithm on video clips from Caltech datasets, Dollar P. et.al. (2012), and Daimler, Enzweiler M. (2009). These video samples can be seen at <http://goo.gl/SKV59Z>.

CONCLUSIONS

Based on the literature survey on the state of the art detection systems ChnFtrs Filter detector which uses ICFs with Soft Cascade AdaBoost classifier is a milestone in real-time pedestrian detection. Integral Channel Features extracted from LUV, Gradient magnitude and Gradient Orientation channels are chosen for our system because they offer better speed and performance. AdaBoost classifier, with soft cascade feature is proven to be faster than other classifiers like SVM, NN, etc. The proposed, modified soft cascade helps us achieve speed similar to that of soft cascade and resulted in more robust thresholds. Once the pedestrian in the frame is detected, the detected pedestrian is tracked using Lucas Kanade feature based tracking. In future, we can build an optimized real-time VLSI design/ FPGA / microprocessor based implementation for pedestrian detection and tracking system.

ACKNOWLEDGEMENTS

The authors gratefully acknowledge Texas Instruments India Ltd, Bangalore, for their support to this work.

REFERENCES

- [1] Bouquet, Jean-Yves. (2001), Pyramidal implementation of the affine lucas kanade feature tracker description of the algorithm, Intel Corporation.
- [2] Bourdev, Lubomir, and Jonathan Brandt, (2005), Robust object detection via soft cascade, IEEE Computer Society Conference on Computer Vision and Pattern Recognition, vol. 2, pp. 236-243.
- [3] Dalal Navneet, and Bill Triggs, (2005), Histograms of oriented gradients for human detection, IEEE Conference on Computer Vision and Pattern Recognition, vol. 1, pp. 886-893.
- [4] Dalal, Navneet, Bill Triggs, and Cordelia Schmid, (2006), Human detection using oriented histograms of flow and appearance, ECCV, pp. 428-441.
- [5] Dollar, Piotr, Christian Wojek, Bernt Schiele, and Pietro Perona, (2012), Pedestrian detection: An evaluation of the state of the art, IEEE Transactions on Pattern Analysis and Machine Intelligence.
- [6] Dollár, Piotr, Zhuowen Tu, Pietro Perona, and Serge Belongie, (2009), Integral Channel Features, BMVC, vol. 2, no. 4, p. 5.
- [7] Enzweiler M. and D. M. Gavrila, (2009), Monocular Pedestrian Detection: Survey and Experiments, IEEE Trans. on Pattern Analysis and Machine Intelligence, vol.31, no.12, pp.2179-2195.
- [8] John Lu, Z. Q, (2010), The elements of statistical learning: data mining, inference, and prediction, Journal of the Royal Statistical Society: Series A (Statistics in Society) 173, no. 3, 693-694.
- [9] Li, X., Hu, W., Shen, C., Zhang, Z., Dick, A., & Hengel, A. V. D. (2013), A survey of appearance models in visual object tracking, ACM Transactions on Intelligent Systems and Technology (TIST), 4(4), 58.

4th International Engineering Symposium - IES 2015

March 4-6, 2015, Kumamoto University, Japan

-
- [10] Piotr's Image & Video Matlab Toolbox, <http://vision.ucsd.edu/~pdollar/toolbox/doc/index.html>
 [11] Rosten, E., & Drummond, T. (2006), Machine learning for high-speed corner detection, Computer Vision-ECCV, Springer Berlin Heidelberg, pp. 430-443.
 [12] Sabzmeydani, Payam, and Greg Mori, (2007), Detecting pedestrians by learning shapelet features, IEEE Conference on Computer Vision and Pattern Recognition, pp. 1-8.
 [13] Shi, Jianbo, and Carlo Tomasi, (1994), Good features to track, 1994 IEEE Computer Society Conference on Computer Vision and Pattern Recognition, pp. 593-600.
 [14] Viola, Paul, and Michael J. Jones, (2004), Robust real-time face detection, International journal of computer vision 57, no. 2: 137-154.
 [15] Viola, Paul, Michael J. Jones, and Daniel Snow, (2005), Detecting pedestrians using patterns of motion and appearance, International Journal of Computer Vision63, no. 2: 153-161.
 [16] Walk, Stefan, Nikodem Majer, Konrad Schindler, and Bernt Schiele. (2010), New features and insights for pedestrian detection, IEEE Conf. Computer Vision and Pattern Recognition, pp. 1030-1037.
 [17] Wojek, Christian, and Bernt Schiele, (2008), A performance evaluation of single and multi-feature people detection, In Pattern Recognition, pp. 82-91. Springer Berlin Heidelberg.

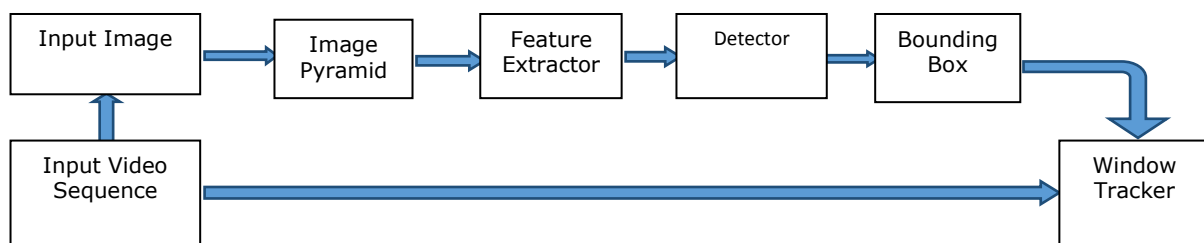


Fig.1 Block Diagram of the detection and tracking system



Fig. 2 Original Image



Fig. 3 Gradient Magnitude



Fig. 4 CIE LUV Channels

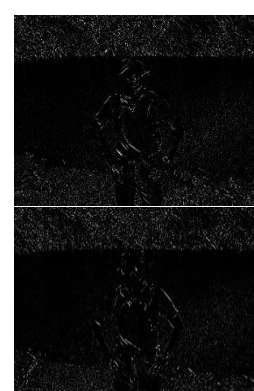


Fig. 5 Gradient Histogram Orientation along six orientation bins

4th International Engineering Symposium - IES 2015

March 4-6, 2015, Kumamoto University, Japan

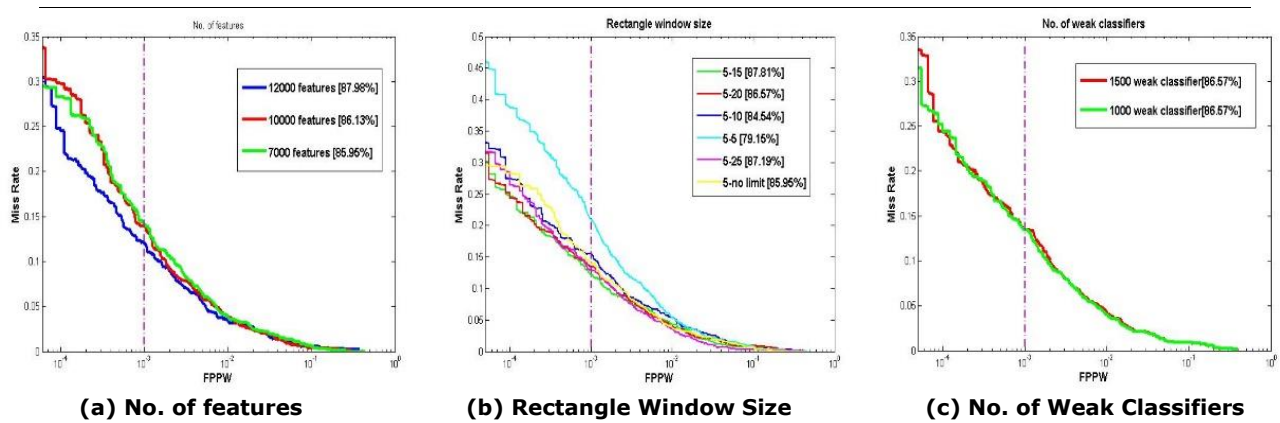


Fig. 6 Detector Performance Evaluation

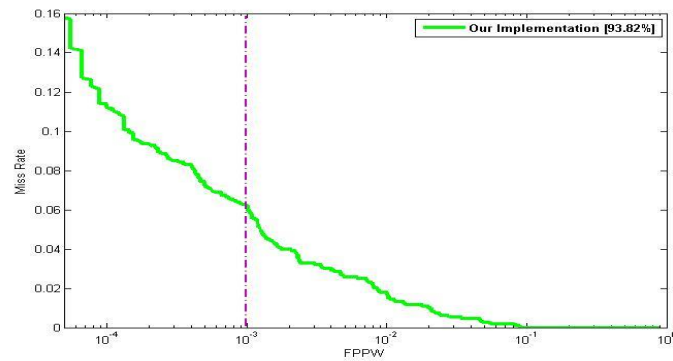


Fig. 7 Final Performance of the Detector

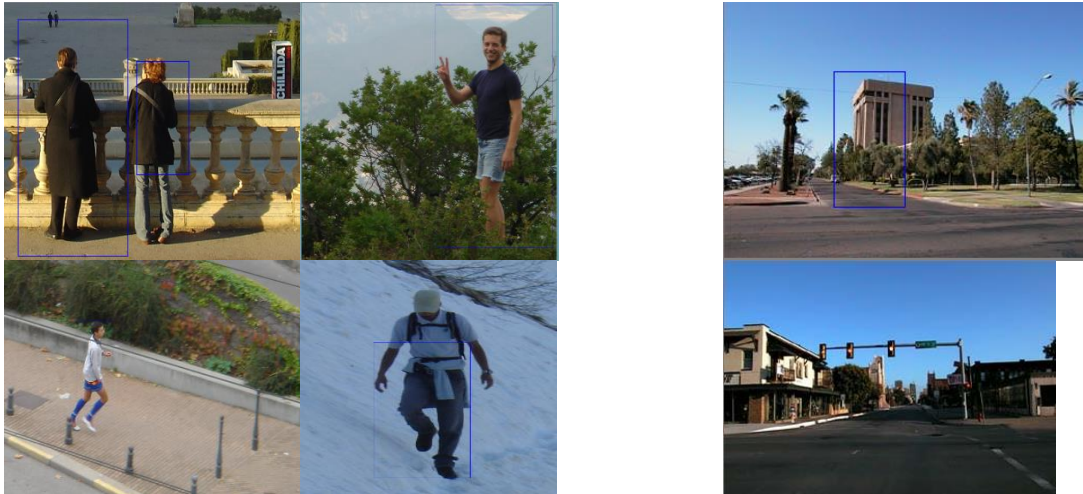


Fig. 8 Images with pedestrian

Fig. 9 Images without pedestrian

Analysis of Emerging Workflow Scheduling Algorithms in Cloud

S. Raghavan¹ and K. Chandrasekaran²

¹ Department of Computer Science and Engineering, National Institute of Technology Karnataka, Surathkal, Mangalore, India, e-mail:raghavan.sm2005@gmail.com

² Department of Computer Science and Engineering, National Institute of Technology Karnataka, Surathkal, Mangalore, India. email:kchnitk@gmail.com

ABSTRACT: Workflow has a great impact on several diverse fields of science such as Physics, Bioinformatics, Astronomy etc. The computational requirements of the world is increasing exponentially and so the use of workflows. These requirements are expected to increase further. Thus workflow can be considered as one of the important areas to be explored. Workflow is used extensively by the scientific community for automation. Similarly these workflows have a significant impact on grid computing, cloud computing and other distributed environments. Moreover it is because of grid computing technology that power of workflow is realizable. Similarly cloud computing also supports workflows. Workflow scheduling is considered to be the core when it comes to workflows thus, it is highly important to know what are workflow scheduling algorithms available for scheduling workflow in cloud. This paper gives an overview about workflow, the impact of workflows on cloud and other important issues related to it are presented. This paper primarily focuses on Workflow scheduling algorithms in cloud and analysis of the same is presented.

Keywords: Workflow, Cloud, Scheduling, Scheduling Algorithms, Workflow Scheduling

INTRODUCTION

Workflow can be defined as a collection of sequential tasks or sequential steps which collectively solves a single problem. A workflow can be considered as a process which consists of several sequential subprocesses, these sub processes are usually tasks. These tasks combine to give a workflow which on the whole has a single purpose and is automated based on certain rules. Workflows are in use from several decades and has become as an integral part of computer science. Workflow is considered to be one of the major segment which is continuously being studied for its application and working. Initially people used to have a single high end computer and would usually share the system time to accomplish the task. By the time these things changed and people started using a separate personal computer for their use. Each computer was capable of doing several computationally

intensive tasks but very complex and high end computations were not possible. For that something more than a single computer was required. At this time distributed computing was introduced. With the advent of distributed computing the whole scenario has changed. Now there are some applications where you need very high computational power and this is usually provided distributed technology. This is the place where workflows are extensively used, the computationally intensive tasks are divided into complex workflows which in turn use the computational infrastructure to execute it. This is one of the important applications of workflow which is driving the whole world, from computer science to basic science, towards it.

There are numerous applications of workflows. Basically, the workflows are used for extensive scientific computations. By the 90's the computational requirements for scientific applications in

areas like Physics, Bioinformatics etc. grew exponentially and to address this issue workflows were used.

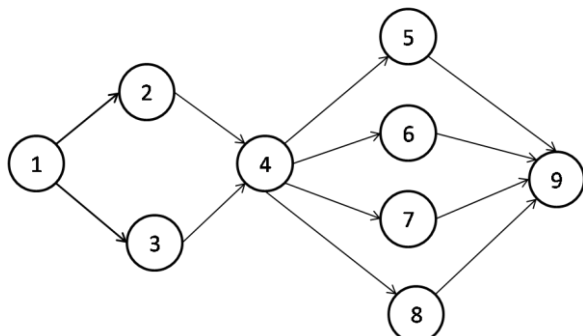


Figure 1 A Simple Workflow

This paper is further divided into four more sections. The second section explains the relation between cloud workflow, its properties and discusses about scheduling in cloud. Then cloud workflow scheduling algorithms are compared in the next section. These algorithms are compared by taking several parameters into account. After that an analysis of all the cloud workflow scheduling algorithms is made and our viewpoint is presented. The final section concludes the paper and lists some of the future works that can be done.

CLOUD WORKFLOW SCHEDULING

Today cloud computing is one of the most popular and one of the extensively used technology. The number of cloud users is increasing at a very faster rate. According to Gartner, it is one of the fastest growing market segments and by the end of 2015 the public cloud market would touch a whooping 160 Billion dollars (www.gartner.com) . Usually the scale at which cloud operates is very large. The system is distributed and due to cloud's service oriented nature the usage of workflow becomes inevitable. The Service Oriented and on-demand Nature of cloud makes it different from others (Liu et al. (2011)).

Workflow scheduling is a process of mapping the tasks and services in a workflow (Yu, Jia et al. (2005)). As there are several tasks and services involved, the mapping of tasks and services is considered to be a complex operation. Usually, sophisticated algorithms are designed for scheduling the workflow.

These are called as workflow managers. The workflow managers are responsible for managing the whole workflow. Scheduling problem is a NP-complete problem (Yu, Jia et al. (2005)) and in a standard complex workflow the number of services and tasks are very large in numbers. Usually for scheduling these kinds of algorithm meta-heuristic and heuristic approaches are used and exhaustive approaches are avoided (Yu, Jia et al. (2005)). This is because the meta-heuristic or Heuristic approaches find the optimal solution by taking lesser time as compared to other exhaustive searches which find the best solution but take more time.

WORKFLOW SCHEDULING ALGORITHMS IN CLOUD

There are several algorithms that have been proposed for workflow scheduling in cloud. There are several factors that need to be considered for scheduling workflows in cloud. The most important parameters include makespan and cost. Here a detailed study of all the scheduling algorithms is made. All the algorithms are compared based on certain parameters and properties; these include makespan, Cost, Deadline, Budget, Type of Cloud, Type of Deployment, Reliability, Details about experimentation and Energy efficiency. A detailed description is given in the Table 1.

ANALYSIS

The design of scheduling algorithms for the cloud workflows is a new domain that has garnered attention just half a decade before. Though there are several algorithms available for Grid, they cannot be directly used for cloud as there are specific differences between grid and cloud. There are several additional parameters needed to be considered for cloud scheduling. Based on the algorithms that are proposed, each algorithm considers either one or several QoS parameters. The most prominent QoS parameters considered are makespan and cost. All the algorithms proposed consider either of the two QoS parameters or both.

4th International Engineering Symposium - IES 2015
 March 4-6, 2015, Kumamoto University, Japan

Workflow Scheduling Algorithm	Cost Efficiency	Make Span	Energy Efficient	Multiple Workflows	Deadline Constrained	Budget Constrained	Reliable	Cloud Type	Service	Approach	Implementation	Year of Publication
Optimizing Makespan and Reliability for Workflow Applications with Reputation and Look-ahead Genetic Algorithm (Wang et al. (2011))	✗	✓	✗	✗	✗	✗	✓	Private	IaaS	Look Ahead Genetic Algorithm	GridSim	2011
Workflow Scheduling for SaaS/PaaS Cloud providers considering two SLA (Genez et al. (2012))	✓	✗	✗	✗	✓	✗	?	?	SaaS/ PaaS	Integer linear programming formulation	Simulation Java and IBM Cplex optimizer	2012
A market-oriented hierarchical scheduling strategy in cloud workflow systems (Wu et al. (2013))	✓	✓	✗	✗	✓	✓	?	Private	IaaS	Hierarchical Scheduling Strategy	SwinDew -C	2013
Cost- and Deadline-Constrained Provisioning for Scientific Workflow Ensembles in IaaS Clouds (Malawski et al. (2012))	✓	✗	✗	✓	✓	✓	?	?	IaaS	Dynamic Provisioning Dynamic Scheduling(DPDS), Static Provisioning, Static Scheduling and Workflow aware DPDS	Cloudsim	2012
Ordinal Optimized Scheduling of Scientific Workflows in Elastic Compute Clouds (Zhang fan et al. (2011))	✗	✓	✗	✗	✗	✗	?	?	IaaS	Iterative Ordinal optimization approach -Heuristic	Simulation	2011
A Particle Swarm Optimization-based Heuristic for Scheduling Workflow Applications in Cloud Computing Environments (Suraj Pandey et al. (2010))	✓	✗	✗	✗	✗	✗	?	Public	IaaS	Particle Swarm Optimization	Amazon EC2	2010
Scheduling Scientific Workflows Elastically for Cloud Computing (lin et al. (2011))	✗	✓	✗	✗	✗	✗	?	?	IaaS	Scalable Heterogeneous Earliest Finish Time Heuristic	?	2011
A Revised Discrete Particle Swarm Optimization for Cloud Workflow Scheduling (Wu Zhangjun, et al. (2010))	✓	✓	✗	✗	✓	✗	?	?	IaaS	Revised Discrete Particle Swarm Optimization	?	2010
Deadline-constrained workflow scheduling algorithms for Infrastructure as a Service Clouds (Abrishami et al. (2013)).	✓	✓	✗	✗	✓	✗	?	Private	IaaS	IaaS Cloud Partial Critical Paths (IC-PCP) and ICPCP with Deadline Distribution	Private cloud testbed	2013
HCOC: a cost optimization algorithm for workflow scheduling in hybrid clouds (Bittencourt et al. (2011))	✓	✓	✗	✗	✓	✗	?	Hybrid	IaaS	The Hybrid Cloud Optimized cost Algorithm	Hybrid Cloud Test Bed	2011
Cost-Minimizing Scheduling of Workflows on a Cloud of Memory Managed Multicore Machines (Grounds et al. (2009))	✓	✗	✗	✗	✓	✗	?	?	?	Cost minimizing Scheduling algorithm (CMSA) - Heuristic	Simulation	2009

4th International Engineering Symposium - IES 2015
March 4-6, 2015, Kumamoto University, Japan

A Compromised-Time-Cost Scheduling Algorithm in SwinDeW-C for Instance-Intensive Cost-Constrained Workflows on a Cloud Computing Platform (Liu Ke et al. (2010))	✓	✓	✗	✗	✓	✓	?	Private	IaaS	Compromised Time cost Scheduling Algorithm	SwinDew C Simulation	2010
A Bi-Criteria Truthful Mechanism for Scheduling of Workflows in Clouds (Fard et al. (2011))	✓	✓	✗	✗	✗	✗	?	Public	IaaS	Bi-Objective Scheduling Strategy (BOSS)	Gridsim	2011
Multi-Objective Approach for Energy-Aware Workflow Scheduling in Cloud Computing Environments (Yassa et al. (2013))	✓	✓	✓	✗	✓	✗	?	?	IaaS	DVFS, Multi Objective Discrete Particle Swarm Optimization	Simulation	2013
Deadline-constrained workflow scheduling in software as a service Cloud (Abrishami S et al. (2012))	✓	✗	✗	✗	✗	✗	?	?	SaaS	SaaS Cloud partial Critical Path (SC-PCP)	Simulation	2012
Agent -based cloud workflow execution (Gutierraz-Garcia et al.(2012))	✓	✓	✗	✗	✗	✗	?	?	IaaS	Agent Based Dynamic Resource allocation and Composition	Agent based TestBed, Simulation	2012
An Iterative Optimization Framework for Adaptive Workflow Management in Computational Clouds (Wang et al. (2012))	✓	✓	✗	✗	✗	✗	?	Private	IaaS	Iterative Optimization	Testbed	2013
Cost-Aware Scheduling of Deadline-Constrained Task Workflows in Public Cloud Environments (Moens et al. (2013))	✓	✓	✗	✗	✓	✗	?	Public	IaaS	Integer Linear Programming and Two other Heuristic Approaches	AWS Amazon EC2	2013
A Multiple QoS Constrained Scheduling Strategy of Multiple Workflows for Cloud Computing (Xu, Meng et al. (2009))	✓	✓	✗	✓	✗	✗	?	?	IaaS	Multiple QoS and Multiple Workflows Algorithm -Heuristic	Simulation	2009
Budget Constrained Resource Allocation for Non-Deterministic Workflows on a IaaS Cloud (Caron et al. (2012))	✓	✓	✗	✗	✓	✓	?	?	IaaS	Original allocation strategy for deterministic workflows - Heuristic	Simulation	2012
A Provenance-based Adaptive Scheduling Heuristic for Parallel Scientific Workflows in Clouds (de Oliveria et al. (2012))	✓	✓	✗	✗	✓	✓	?	Public	IaaS	3 Objective weighted cost model and greedy algorithm	Amazon EC2 Scimulus	2012
Probabilistic Scheduling of Scientific Workflows in Dynamic Cloud Environments (Zhou et al. (2013))	✓	✓	✗	✗	✓	✗	?	Public	IaaS	Probabilistic Scheduling Framework called Dyna	Amazon EC2	2013
HSGA: a hybrid heuristic algorithm for workflow scheduling in cloud systems (Delavar et al. (2013))	✓	✓	✗	✗	✗	✗	?	?	IaaS	Hybrid Heuristic algorithm based on Genetic Algorithm	Simulation	2013
An Energy-Aware Heuristic Scheduling for Data-Intensive Workflows in Virtualized Datacenters (Xiao et al. (2013))	✗	✓	✓	✗	✗	✗	?	?	IaaS	Minimized Energy Consumption in Deployment and Scheduling (MECDS)-Heuristic	Test Bed, XCP and Oprofile toolkit	2013
Bi-criteria workflow tasks allocation and scheduling in Cloud computing environments (Bessai, et al (2012))	✓	✓	✗	✗	✗	✗	?	?	IaaS	Cost Based Approach, Time based approach and cost-time based approach	Simulation	2012

Table 1 Cloud Workflow Scheduling

Apart from these parameters there are several other issues on the basis of which algorithms are designed. Usually a workflow design involves several constraints like Budget constraints and Time constraint (Deadline constraints). So an algorithm should consider these constraints, though not always required. Based on the analysis it is found that nearly 18% of the algorithms consider budget constraint and nearly 52% of algorithms are deadline constrained. Further analysis involves considering the tools using which the algorithms are implemented, Figure 2. shows the details.

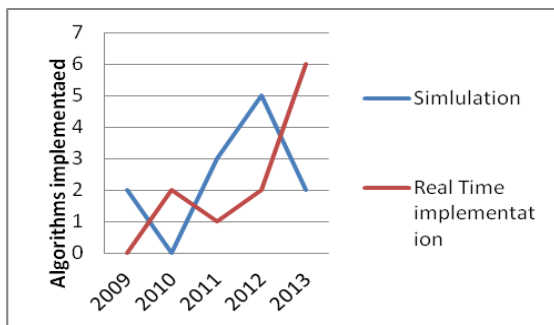


Figure 2. Year wise Implementation

As seen there has been a gradual increase in the real-time implementation. Initial years show that simulation was a better choice for researchers. But by time it is changing and people are more focused towards realtime implementation, i.e. a private cloud or public cloud.

Energy Efficiency:

Energy efficiency is another important issue that has led a new area of computing called green computing. As workflows are considered to be important and their scheduling has a considerable impact on the way the cloud is used, designing an algorithm which considers energy is a good approach. According to the analysis this area is picking up and researchers have started proposing energy efficient algorithms. Even for Cloud workflow scheduling there has been attempt to reduce the energy consumption by use of efficient algorithms. According to analysis only 8 % of algorithms designed consider energy for Scheduling workflows and all of these algorithms were proposed in 2013. Signifying that the world is going for green

computing and so are the workflows. Thus more energy aware algorithms are expected for cloud workflow scheduling.

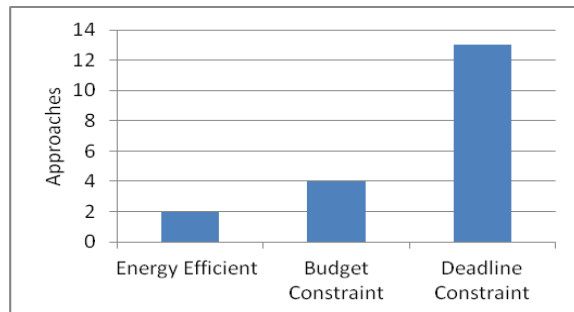


Figure 3. Classification of Approaches

CONCLUSION AND FUTURE WORK

The workflows have changed the way the data is processed. According to the way it has been till now we can see that there will never be a decrease in the use of workflow but there will either be a linear or exponential increase in its use. Scientists are able use workflow from complex astronomical data to earthquake science. All the success that scientific workflow has achieved is because of the grid computing resources that were used at the back end. For example, Large Hadron collider which is considered to be one of most high level complex project used grid infrastructure for computing more than thirty percent of its computational processes (www.uslhc.us) . Grid has transformed the concept of computing using workflow, similarly cloud can also be considered for workflow. Though both Grid and cloud are distributed in nature and have several similarities between them, there are some specific issues related to cloud which need to be considered for designing and scheduling workflows in cloud. All the scheduling algorithm proposed till now try to give a best optimal solution and some of them have been really successful.

REFERENCES

- [1] Abrishami, S., and M. Naghibzadeh. "Deadline-constrained workflow scheduling in software as a service Cloud." *Scientia Iranica* 19.3 (2012): 680-689.
- [2] Abrishami, Saeid, Mahmoud Naghibzadeh, and Dick HJ Epema. "Deadline-constrained workflow scheduling algorithms for Infrastructure as a Service Clouds." *Future Generation Computer Systems* 29.1 (2013): 158-169..
- [3] Bessai, Kahina, et al. "Bi-criteria workflow tasks allocation and scheduling in Cloud computing

4th International Engineering Symposium - IES 2015

March 4-6, 2015, Kumamoto University, Japan

- environments." Cloud Computing (CLOUD), 2012 IEEE 5th International Conference on. IEEE, 2012.
- [4] Bittencourt, Luiz Fernando, and Edmundo Roberto Mauro Madeira. "HCOC: a cost optimization algorithm for workflow scheduling in hybrid clouds." *Journal of Internet Services and Applications* 2.3 (2011): 207-227.
- [5] Buyya, Rajkumar, et al. "Cloud computing and emerging IT platforms: Vision, hype, and reality for delivering computing as the 5th utility." *Future Generation computer systems* 25.6 (2009): 599-616.
- [6] Caron, Eddy, et al. "Budget constrained resource allocation for non-deterministic workflows on an IaaS cloud." *Algorithms and Architectures for Parallel Processing*. Springer Berlin Heidelberg, 2012. 186-201.
- [7] de Oliveira, Daniel, et al. "A provenance-based adaptive scheduling heuristic for parallel scientific workflows in clouds." *Journal of Grid Computing* 10.3 (2012): 521-552.
- [8] Delavar, Arash Ghorbannia, and Yalda Aryan. "HSGA: a hybrid heuristic algorithm for workflow scheduling in cloud systems." *Cluster Computing* (2013): 1-9.
- [9] Fard, Hamid Mohammadi, et al. "A Bi-Criteria Truthful Mechanism for Scheduling of Workflows in Clouds." *Cloud Computing Technology and Science (CloudCom)*, 2011 IEEE Third International Conference on. IEEE, 2011.
- [10] Genez, Thiago AL, Luiz F. Bittencourt, and Edmundo RM Madeira. "Workflow scheduling for SaaS/PaaS cloud providers considering two SLA levels." *Network Operations and Management Symposium (NOMS)*, 2012 IEEE. IEEE,
- [11] Grounds, Nicolas G., John K. Antonio, and Jeff Muehring. "Cost-minimizing scheduling of workflows on a cloud of memory managed multicore machines." *Cloud Computing*. Springer Berlin Heidelberg, 2009. 435-450.
- [12] Gutierrez-Garcia, J. Octavio, and Kwang Mong Sim. "Agent-based cloud workflow execution." *Integrated Computer-Aided Engineering* 19.1 (2012): 39-56.
- [13] Hoffa, Christina, et al. "On the use of cloud computing for scientific workflows." *eScience, 2008. eScience'08. IEEE Fourth International Conference on*. IEEE, 2008.
- [14] IaaS Continues as Fastest-Growing Market Segment [Online]. Available <http://www.gartner.com/newsroom/id/2352816>.
- [15] Lin, Cui, and Shiyong Lu. "Scheduling scientific workflows elastically for cloud computing." *Cloud Computing (CLOUD)*, 2011 IEEE International Conference on. IEEE, 2011.
- [16] Liu, Ke, et al. "A compromised-time-cost scheduling algorithm in swindew-c for instance-intensive cost-constrained workflows on a cloud computing platform." *International Journal of High Performance Computing Applications* 24.4 (2010): 445-456.
- [17] Malawski, Maciej, et al. "Cost-and deadline-constrained provisioning for scientific workflow ensembles in IaaS clouds." *Proceedings of the International Conference on High Performance Computing, Networking, Storage and Analysis*. IEEE Computer Society Press, 2012.
- [18] Moens, Hendrik, Koen Handekyn, and Filip De Turck. "Cost-aware scheduling of deadline-constrained task workflows in public cloud environments." *Integrated Network Management (IM 2013)*, 2013 IFIP/IEEE International Symposium on. IEEE, 2013.
- [19] Pandey, Suraj, et al. "A particle swarm optimization-based heuristic for scheduling workflow applications in cloud computing environments." *Advanced Information Networking and Applications (AINA)*, 2010 24th IEEE International Conference on. IEEE, 2010.
- [20] The US and the LHC [Online]. Available: http://www.uslhc.us/The_US_and_the_LHC/Computing
- [21] Wang, Long, et al. "An Iterative Optimization Framework for Adaptive Workflow Management in Computational Clouds."
- [22] Wang, Xiaofeng, et al. "Optimizing the makespan and reliability for workflow applications with reputation and a look-ahead genetic algorithm." *Future Generation Computer Systems* 27.8 (2011): 1124-1134.
- [23] Wu, Zhangjun, et al. "A market-oriented hierarchical scheduling strategy in cloud workflow systems." *The Journal of Supercomputing* 63.1 (2013): 256-293.
- [24] Wu, Zhangjun, et al. "A revised discrete particle swarm optimization for cloud workflow scheduling." *Computational Intelligence and Security (CIS)*, 2010 International Conference on. IEEE, 2010.
- [25] Xiao, Peng, Zhi-Gang Hu, and Yan-Ping Zhang. "An Energy-Aware Heuristic Scheduling for Data-Intensive Workflows in Virtualized Datacenters." *Journal of Computer Science and Technology* 28.6 (2013): 948-961.
- [26] Xu, Meng, et al. "A multiple QoS constrained scheduling strategy of multiple workflows for cloud computing." *Parallel and Distributed Processing with Applications*, 2009 IEEE International Symposium on. IEEE, 2009.
- [27] Yassa, Sonia, et al. "Multi-Objective Approach for Energy-Aware Workflow Scheduling in Cloud Computing Environments." *The Scientific World Journal* 2013 (2013).
- [28] Yu, Jia, and Rajkumar Buyya. "Scheduling scientific workflow applications with deadline and budget constraints using genetic algorithms." *Scientific Programming* 14.3 (2006): 217-230.
- [29] Yu, Jia, Rajkumar Buyya, and Chen Khong Tham. "QoS-based scheduling of workflow applications on service grids." *Proceedings of the 1st IEEE International Conference on e-Science and Grid Computing (e-Science 2005*, IEEE CS Press, Los Alamitos, CA, USA). 2005.
- [30] Zhang, Fan, et al. "Ordinal Optimized Scheduling of Scientific Workflows in Elastic Compute Clouds." *Cloud Computing Technology and Science (CloudCom)*, 2011 IEEE Third International Conference on. IEEE, 2011.
- [31] Zhou, Amelie Chi, Bingsheng He, and Cheng Liu. "Probabilistic Scheduling of Scientific Workflows in Dynamic Cloud Environments." arXiv preprint arXiv: 1306.6410 (2013).

Meta-Classifier Based Approach to Software Change Classification: Towards Better Performance

**Sreecharan Sankaranarayanan, Vidyashankar B Lakshman,
Swapan Bhattacharya and K Chandrasekaran**

*Department of Computer Science and Engineering,
National Institute of Technology Karnataka, Surathkal, India.
Email: kchnitk@ieee.org*

ABSTRACT: Software Change Classification provides a technique for finding latent software bugs in a new software change using a method called Change Classification. It uses a machine learning classifier to determine whether a new change is more similar to prior buggy or clean changes thus allowing us to flag the existence of a bug. Although significant advances have been made in both machine learning based approaches as well as others, there are still performance issues that limit the development of a practical tool for the same. Our contribution is to provide a Meta-Classifier based algorithm that not only gives relatively high accuracy, but also provides a high precision, recall and kappa statistic. We also describe attribute selection approaches with the aim of improving the generalization of the algorithm. We have validated our approaches on the NASA Software Defect Dataset.

Keywords: *Software Change Classification, Machine Learning, Attribute Selection, Bug Classification, Meta-Classifier, Cost-Sensitive Classifier*

INTRODUCTION

Bug Classification has become an important research field in Software Engineering as the time, effort and expenditure required to fix bugs is usually quite large. Software Change Classification or Software Defect Detection in particular, can be modeled as a supervised machine learning problem to predict defective software changes by learning over the features of prior changes [12].

Change Classification first described in Kim et.al. [12] learns from software change history to classify future changes as Clean(Normal) or Buggy(Defective). Features are first extracted from all the source information of the project using

change log messages, complexity metrics, author, time and day of submission, file and directory names etc. to create a corpus that the classifier can train on. The NASA Software Defect Dataset [9] used to validate our approach provides the following features among others - Number of Branches, Number of Conditions, Number of Lines of Code, Percentage of Comments and Software Metrics such as Cyclomatic Complexity [15], Cyclomatic Density, Decision Density, Essential Complexity, Halstead Complexity Metrics [4] and Maintainability Index. Software Change Classification problem reduces to training our algorithm on the features provided and predicting whether a new set of features is Defective or Normal.

4th International Engineering Symposium - IES 2015

March 4-6, 2015, Kumamoto University, Japan

Even though most of the approaches described in the following sections report very high accuracies, they do not consider other performance metrics such as precision, recall or kappa statistic [3]. We have described a Meta-Classifier based approach as well as attribute selection techniques which produce relatively high accuracies while improving the precision, recall and kappa statistic significantly.

The rest of the paper is organized as follows. Section 2 describes Related Work. Section 3 illustrates the current approach to solving the Software Change Classification problem. Section 4 describes our approach to the problem including Attribute Selection and the Meta-Classifier based algorithm. Section 5 describes the results of applying our algorithm to the NASA Software Defect Dataset [9]. Section 6 summarizes the results. Section 7 concludes with sections describing the Conclusion, Future Work and References.

RELATED WORK

Many techniques have emerged for detecting and predicting bugs in software. Few are based on Static and Dynamic Analysis of programs [2], [7], [5]. They primarily use classification and regression based algorithms over features such as complexity metrics, number of lines of code and bug counts to flag possibly defective entities [20], [8], [1], [17], [16], [11], [6], [18]. Ramani et.al. [20] provided an evaluation of 20 machine learning algorithms over the NASA Software Defect Dataset [9] and concluded that the Random Tree algorithm is the most accurate. Even though high accuracies of over 92% were reported for certain datasets, their evaluation does not generalize well for real datasets. This issue is apparent in the currently available tool for bug classification developed by J.T.Madhavan et.al. [14] which reports an accuracy between 63% and 92%, a buggy change recall between 43% and 86% and a buggy change precision between 44% and 85% where a support vector machine based algorithm has been implemented. Most of these algorithms do not consider all the performance parameters.

MACHINE LEARNING APPROACHES TO SOFTWARE CHANGE CLASSIFICATION

We describe here the machine learning approaches that have been used in most of the past work in the area. We validate these approaches on the NASA Software Defect Dataset [9] and evaluate the performance of the classifiers using the Cross Validation [13] technique so as to enable comparison with our classifier. We have in particular, used a method called 10-fold Cross-Validation. Over each of the k runs or folds of the algorithm, one of the k randomly obtained subsets is chosen for validation and the remaining k-1 subsets are used for training. This ensures that all the observations are used for both training and validation. In our case k = 10. The results of applying basic classification algorithms on the NASA Software Defect Dataset [9] are shown in the Tables 2-8.

TABLE I

PERCENTAGE OF CORRECTLY CLASSIFIED INSTANCES - Shows the accuracy of the basic classification algorithms over all the datasets in the NASA MDP Corpus. The classifiers produce very high accuracies primarily because the dataset is highly skewed or unbalanced.

Dataset	Bayesian Logistic Regression	Sequential Minimal Optimization	Random Forest
CM1	87.7907%	87.7907%	84.3023%
JM1	81.7367%	81.7471%	80.7672%
KC1	84.5897%	84.8282%	84.4943%
KC3	82%	83%	80%
MC1	99.267%	99.2454%	99.558%
MC2	37.7953%	72.4409%	62.9921%
MW1	89.7727%	89.7727%	89.0152%
PC1	91.9631%	91.9631%	91.4361%
PC2	98.99%	98.9905%	98.8644%
PC3	87.5556%	87.556%	86.9333%
PC4	87.2766%	88.5633%	90.0643%
PC5	97.1884%	97.2237%	97.5237%

TABLE II

PRECISION FOR DEFECTIVE CLASS - Shows the precision values for the defective class. Most of these values are zero indicating that no sample falls into the defective class. Values close to 1 are desirable.

Dataset	Bayesian Logistic Regression	Sequential Minimal Optimization	Random Forest
CM1	0	0	0.227
JM1	0.733	0.9	0.463
KC1	0.583	0.652	0.5
KC3	0	1	0.4
MC1	0	0	0.829
MC2	0.358	0.765	0.457
MW1	0	0	0.429
PC1	0	0.5	0.417
PC2	0	0	0
PC3	0	0	0.462
PC4	0	0.846	0.638
PC5	0.644	0.754	0.590

4th International Engineering Symposium - IES 2015

March 4-6, 2015, Kumamoto University, Japan

TABLE III

PRECISION FOR NORMAL CLASS - Shows the precision values for the normal class. Values close to 1 are desirable.

Dataset	Bayesian Logistic Regression	Sequential Minimal Optimization	Random Forest
CM1	0.878	0.878	0.885
JM1	0.817	0.817	0.856
KC1	0.847	0.85	0.891
KC3	0.82	0.828	0.844
MC1	0.993	0.993	0.996
MC2	1	0.718	0.696
MW1	0.898	0.898	0.916
PC1	0.92	0.921	0.931
PC2	0.99	0.99	0.99
PC3	0.876	0.876	0.905
PC4	0.873	0.886	0.930
PC5	0.974	0.973	0.986

TABLE IV

RECALL FOR DEFECTIVE CLASS - Shows the recall values for the defective class. Most of the values are close to zero indicating that very few samples fall into the defective class. Values close to one are desirable

Dataset	Bayesian Logistic Regression	Sequential Minimal Optimization	Random Forest
CM1	0	0	0.119
JM1	0.006	0.005	0.31
KC1	0.022	0.046	0.382
KC3	0	0.056	0.222
MC1	0	0	0.5
MC2	1	0.295	0.364
MW1	0	0	0.222
PC1	0	0.016	0.164
PC2	0	0	0
PC3	0	0	0.3
PC4	0	0.124	0.506
PC5	0.111	0.091	0.533

From the Tables 2-7, it is abundantly clear that the high accuracy obtained in all the classifiers is a gross misrepresentation of their performance. The accuracy is high because the dataset is highly skewed towards normal changes and very few instances of buggy changes are present. In fact, in many cases, the classifier simply outputs normal for all instances and declares that there are no buggy instances still achieving very high accuracy. One such scenario is shown in Table 8. The Bayesian Logistic Regression based classifier simply outputs normal for all instances and still manages an accuracy of 87.7907%. It is this issue that we would like to address.

The Meta-Classifier based algorithm not only provides better precision, recall and kappa statistic but also retains accuracy at the same level.

TABLE V

RECALL FOR NORMAL CLASS - Shows the recall values for the normal class. Values close to 1 are desirable.

Dataset	Bayesian Logistic Regression	Sequential Minimal Optimization	Random Forest
CM1	1	1	0.944
JM1	0.999	1	0.919
KC1	0.997	0.995	0.93
KC3	1	1	0.927
MC1	1	1	0.998
MC2	0.048	0.952	0.771
MW1	1	1	0.966
PC1	1	0.999	0.980
PC2	1	1	0.999
PC3	1	1	0.95
PC4	1	0.997	0.958
PC5	0.998	0.999	0.989

TABLE VI

KAPPA STATISTIC - Shows the kappa statistic values for the classification algorithms. Most of the algorithms produce very low values as they do not perform any better than chance. Values close to one are desirable

Dataset	Bayesian Logistic Regression	Sequential Minimal Optimization	Random Forest
CM1	0	0	0.0789
JM1	0.0093	0	0.2635
KC1	0.0308	0.0671	0.3449
KC3	0	0.088	0.1803
MC1	0	0	0.6218
MC2	0.0339	0.2889	0.1415
MW1	0	0	0.2396
PC1	0	0.0268	0.12
PC2	0	0	-0.0022
PC3	0	0	0.2945
PC4	0	0.1894	0.509
PC5	0.1827	0.1577	0.5474

TABLE VII

CONFUSION MATRIX FOR BAYESIAN LOGISTIC REGRESSION OVER DATASET CM1 - Shows the confusion matrix obtained after applying the Bayesian Logistic Regression algorithm on the CM1 dataset. The classifier simply classifies every instance as normal still managing a high accuracy of 87.7907%. Accuracy therefore, is not an accurate measure of performance.

Predicted Class Defective	Predicted Class Normal	
0	42	True Class Defective
0	302	True Class Normal

OUR APPROACH

The NASA Software Defect Dataset therefore is highly imbalanced. An imbalanced dataset is a special case of the classification problem where the class distribution is not uniform [19]. The problem in this case has been solved using a combination of attribute selection and a Meta-Classifier based approach called Cost-Sensitive Classification.

4th International Engineering Symposium - IES 2015

March 4-6, 2015, Kumamoto University, Japan

A. Attribute Selection for Better Precision and Recall

As was seen in the earlier section, the distinguishability of the features given in the NASA Software Defect Dataset [9] is highly skewed toward normal observations. Therefore, there is a need to improve the existing features or choose a subset of the existing features. One such method for attribute selection is the Chi-Squared(χ^2) test for attribute selection [10]. Chi-Squared evaluates the worth of a feature by computing the value of the chi-squared statistic with respect to the class.

$$\chi^2 = \sum_{i=1}^r \sum_{j=1}^c \frac{(O_{ij} - E_{ij})^2}{(E_{ij})} \quad (1)$$

where r is the number of rows, c is the number of columns, O_{ij} is the observed frequency and E_{ij} is the expected frequency as asserted by the null hypothesis.

The results obtained from running the Bayesian Logistic Regression algorithm after Chi-Squared attribute selection is shown in Table 9. As can be seen, the accuracy, precision, kappa statistic and recall can be improved with attribute selection techniques.

B. The Meta-Classification Algorithm

A Meta-Classifier is one that doesn't implement a classifier on its own, but uses another classifier to do the actual work. In addition, the Meta-Classifier adds another processing step that is performed before the actual Base-Classifier sees the data. One such Meta-Classifier is the Cost-Sensitive Classifier [23], [22]. The Cost-Sensitive classifier is one that takes misclassification costs into consideration. The goal of this classifier is to minimize the total cost. The classifier uses a cost-matrix to assign different weights to different cells in the confusion matrix. The cost-matrix is considered a hyper-parameter and its value is fixed manually or by other learning approaches.

TABLE VIII

PERFORMANCE METRICS OBTAINED FROM APPLYING THE BAYESIAN LOGISTIC REGRESSION ALGORITHM TO ALL DATASETS AFTER CHI-SQUARED ATTRIBUTE SELECTION - The accuracy, precision, recall and the kappa statistic have improved when compared to the basic classification algorithm.

Dataset	Accuracy	Weighted Avg. Precision	Weighted Avg. Recall	Kappa Statistic
CM1	87.7907%	0.771	0.878	0
JM1	81.7471%	0.8	0.817	0.011
KC1	84.7328%	0.813	0.847	0.0612
KC3	82%	0.6728	0.82	0
MC1	99.267%	0.985	0.993	0
MC2	37.7953%	0.777	0.378	0.0339
MW1	89.7727%	0.806	0.898	0
PC1	91.9631%	0.846	0.92	0
PC2	98.9905%	0.98	0.99	0
PC3	87.5556%	0.767	0.876	0
PC4	87.2766%	0.762	0.873	0
PC5	97.1884%	0.963	0.972	0.1827

TABLE IX

WEIGHTS OF THE RELATIVE POSITIONS IN THE COST MATRIX - This hyper-parameter was fixed as shown to reduce the number of false negatives.

Predicted Class Defective	Predicted Class Normal	
0	14	True Class Defective
5	0	True Class Normal

Given the cost-matrix, a feature must be classified into the class that has minimum expected cost. This is the minimum expected cost principle. The expected cost $R(i|x)$ of classifying an instance x into class i is given by the following formula.

$$R(i|x) = \sum_j P(j|x)C(i,j) \quad (2)$$

where $P(j|x)$ is the probability estimation of classifying an instance into class j .

TABLE X

Performance Metrics obtained from applying the Meta-Classifier Cost-Sensitive Classifier and the Base-Classifier Random Forest to all the datasets.

Dataset	Accuracy	Weighted Avg. Precision	Weighted Avg. Recall	Kappa Statistic
CM1	83.7209%	0.827	0.837	0.1909
JM1	77.5357%	0.785	0.775	0.2814
KC1	81.6794%	0.831	0.817	0.3513
KC3	77.5%	0.777	0.775	0.246
MC1	99.4395%	0.994	0.995	0.571
MC2	59.055%	0.613	0.591	0.1417
MW1	87.1212%	0.875	0.871	0.3209
PC1	90.5138%	0.895	0.905	0.2832
PC2	98.612%	0.982	0.986	0.0771
PC3	84.6222%	0.853	0.846	0.3253
PC4	89.3495%	0.9	0.893	0.5476
PC5	97.2355%	0.975	0.972	0.5639

4th International Engineering Symposium - IES 2015

March 4-6, 2015, Kumamoto University, Japan

ALGORITHM 1: Pseudo Code for Random Forest Algorithm

```
To generate c classifiers:  
for i=1 to c do  
    Randomly sample the training data D with  
    replacement to produce Di.  
    Create a root node Ni containing Di.  
    Call BuildTree(Ni)  
end  
BuildTree(N):  
if N contains instances of only one class then  
    return  
end  
else  
    Randomly select x% of the possible splitting features  
    in N.  
    Select the feature F with highest information gain to  
    split on.  
    Create f child nodes of N, N1 .. Nf where F has f  
    possible values, F1 .. Ff  
    for i=1 to f do  
        Set the content of Ni to Di where Di is all the  
        instances in N that match Fi.  
        Call BuildTree(Ni)  
    end  
end
```

Our Meta-Classifier uses the Random Forest classification algorithm as the Base-Classifier. The Random Forest classification algorithm [21] is shown as Algorithm 1. Using Random Forest as the Base-Classifier, the Cost-Sensitive Classifier applies the minimum expected cost principle to obtain the classification that minimizes the total expected cost.

EXPERIMENTS AND ANALYSIS

The algorithm described in the previous section has been applied to the NASA Software Defect Dataset [9] for validation. In our case, a large number of false negatives were being obtained, we have thus penalized that position with a higher cost in order to reduce the number of false negatives. The cost matrix for the Cost-Sensitive Classifier is shown in Table 10. The results obtained after classification using the Cost-Sensitive Classifier as the Meta-Classifier and the Random Forest Algorithm as the Base-Classifier are shown in Table 11.

RESULTS

As can be seen from Table 11, the accuracy levels have been maintained while significantly improving the precision, recall and kappa statistic. This provides a significant practical performance improvement over the existing methods thus fulfilling our objectives. Our approach

has handled the imbalance in the data to produce high precision, recall and kappa statistic regardless of the dataset. The precision and recall have increased significantly towards the desirable value of 1 while the kappa statistic has also increased compared to the basic classification algorithms. The graph in Figure 1 shows the variation of kappa statistic for different algorithms over the provided dataset.

CONCLUSION AND FUTURE WORK

The drawbacks of the existing methods have been successfully addressed while providing an improvement in terms of generalization of the algorithm to real datasets. Generalization issues were addressed by improved values of precision, recall and kappa statistic. There is always however, a tradeoff between the performance of Machine Learning based classifiers and the generalization. Other approaches therefore, carry more promise to improve both the accuracy and the generalization. We would like to extend the same to a bug taxonomy classification problem.

The problem would then be to classify bugs into various categories such as Structural, Data, Coding or Integration Bugs. A dataset for this however, is presently unavailable, we will therefore update the NASA Software Defect Dataset with these classes and present it as a multi-class classification problem.

REFERENCES

- [1] Y. Brun and M. D. Ernst. Finding latent code errors via machine learning over program executions. In Proceedings of the 26th International Conference on Software Engineering, ICSE '04, pages 480–490, Washington, DC, USA, 2004. IEEE Computer Society.
- [2] W. R. Bush, J. D. Pincus, and D. J. Sielaff. A static analyzer for finding dynamic programming errors. Softw. Pract. Exper., 30(7):775–802, June 2000.
- [3] J. Carletta. Assessing agreement on classification tasks: The kappa statistic. Comput. Linguist., 22(2):249–254, June 1996.
- [4] B. Curtis, S. Sheppard, P. Milliman, M. A. Borst, and T. Love. Measuring the psychological complexity of software maintenance tasks with the halstead and mccabe metrics. Software Engineering, IEEE Transactions on, SE-5(2):96–104, March 1979.

4th International Engineering Symposium - IES 2015

March 4-6, Kumamoto University, Japan

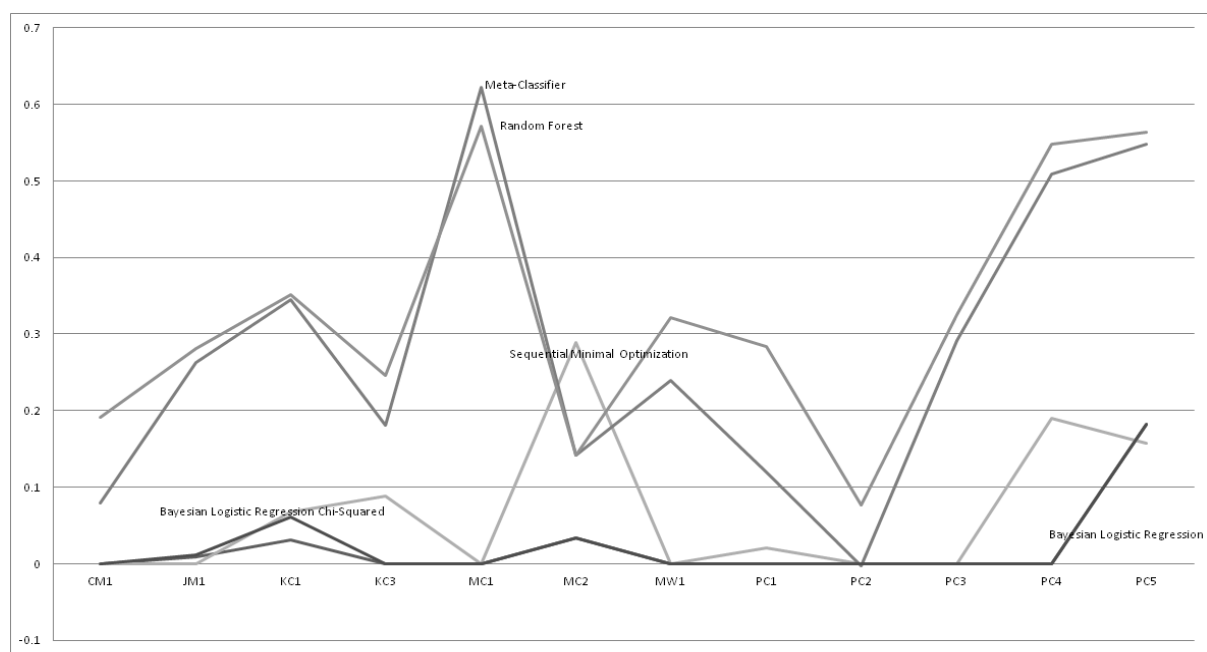


Fig. 1. Shows the variation of the kappa statistic for different algorithms over the provided datasets.

- [5] M. D. Ernst, J. Cockrell, W. G. Griswold, and D. Notkin. Dynamically discovering likely program invariants to support program evolution. In Proceedings of the 21st International Conference on Software Engineering, ICSE '99, pages 213–224, New York, NY, USA, 1999. ACM.
- [6] G. Evgeny. Automated source code changes classification for effective code review and analysis. Proceedings of the Spring/Summer Young Researchers Colloquium on Software Engineering, 2, 2008.
- [7] C. Flanagan, K. R. M. Leino, M. Lillibridge, G. Nelson, J. B. Saxe, and R. Stata. Extended static checking for java. In Proceedings of the ACM SIGPLAN 2002 Conference on Programming Language Design and Implementation, PLDI '02, pages 234–245, New York, NY, USA, 2002. ACM.
- [8] T. Gyimothy, R. Ferenc, and I. Siket. Empirical validation of object-oriented metrics on open source software for fault prediction. Software Engineering, IEEE Transactions on, 31(10):897–910, Oct 2005.
- [9] T. Hall, S. Beecham, D. Bowes, D. Gray, and S. Counsell. A systematic literature review on fault prediction performance in software engineering.
- [10] N. Jasmina, S. Perica, and B. Dusan. Toward optimal feature selection using ranking methods and classification algorithms. Yugoslav Journal of Operations Research, 21(1):119–135, 2011.
- [11] T. Khoshgoftaar and E. Allen. Ordering fault-prone software modules. Software Quality Journal, 11(1):19–37, 2003.
- [12] S. Kim, E. J. Whitehead, Jr., and Y. Zhang. Classifying software changes: Clean or buggy?, 2008.
- [13] R. Kohavi. A study of cross-validation and bootstrap for accuracy estimation and model selection. pages 1137–1143. Morgan Kaufmann, 1995.
- [14] J. T. Madhavan and E. J. Whitehead, Jr. Predicting buggy changes inside an integrated development environment. In Proceedings of the 2007 OOPSLA Workshop on Eclipse Technology eXchange, eclipse '07, pages 36–40, New York, NY, USA, 2007. ACM.
- [15] T. J. McCabe. A complexity measure. In Proceedings of the 2Nd International Conference on Software Engineering, ICSE '76, pages 407–, Los Alamitos, CA, USA, 1976. IEEE Computer Society Press.
- [16] A. Mockus and D. M. Weiss. Predicting risk of software changes. Bell Labs Technical Journal, 5:169–180, 2000.
- [17] K. Pan, S. Kim, and E. J. Whitehead, Jr. Bug classification using program slicing metrics. In Proceedings of the Sixth IEEE International Workshop on Source Code Analysis and Manipulation, SCAM '06, pages 31–42, Washington, DC, USA, 2006. IEEE Computer Society.
- [18] J. Peters and S. Ramanna. Towards a software change classification system: A rough set approach. Software Quality Journal, 11(2):121–147, 2003.
- [19] F. Provost. Machine learning from imbalanced data sets 101 (extended abstract).
- [20] R. Ramani, S. Kumar, and S. Jacob. Predicting fault-prone software modules using feature selection and classification through data mining algorithms. In Computational Intelligence Computing Research (ICCIC), 2012 IEEE International Conference on, pages 1–4, Dec 2012.
- [21] N. Sirikulviriya and S. Sinthupinyo. Integration of rules from a random forest.
- [22] Y. Sun, M. S. Kamel, A. K. Wong, and Y. Wang. Cost-sensitive boosting for classification of imbalanced data. Pattern Recognition, 40(12):3358 – 3378, 2007.
- [23] N. Thai-Nghe, Z. Gantner, and L. Schmidt-Thieme. Cost-sensitive learning methods for imbalanced data. In Neural Networks (IJCNN), The 2010 International Joint Conference on, pages 1–8, July 2010.

CLUSTER BASED ROUTING IN NDN

Arun Nandewal and K Chandrasekaran

*Department of Computer Science and Engineering, NITK Surathkal, India
Email: arunnendewal198@gmail.com*

Named Data Networking (NDN) being a potential future technology designed as a distribution network alternative to the present day host oriented IP-based host-oriented Internet architecture. Some arguments against NDN implementation over other candidate architectures are as mentioned. (1) Availability of extensive content which needs to be comprehended in accordance with its relevance and type. (2) Scalability and maintenance of burgeon networks on the subject of considering each bridging device as an independent node. This paper proposes a reliable and scalable ad-hoc routing protocol for NDN wireless networks. Functionality of protocol requires initial associating of each node with virtual coordinates and then distributing them among clusters or cliques. We focus on reducing the searching space for the route reliant to the number of nodes. Proposed protocol feasibility has been instituted with theorem and resulting graphs. This work proposes the idea of a protocol positioned to reduce the searching space and endure node failure within a network. As padding to the protocol perks consideration to reduce numbers of routers and caching the content packets are also compassed.

TRANSPORT LAYER PROTOCOLS FOR NETWORK BASED GAMING

Aditya Hendre, Gaurav Choudhary, Yash Kedia and B R Chandavarkar

*Department of Computer Science and Engineering, NITK Surathkal, India
Email: yash.kedia2694@gmail.com*

Today, with the advancement of efficient cloud based data storage technology and cryptographically secured data transfer, as also the cheap, easy and widespread availability of high speed and robust networks, network based (cloud based) data sharing applications are fast gaining popularity among the online population. Network based games are among the most popular category of such applications. The persistent online presence of the younger, technology savvy generation has created a massive demand for such gaming applications. The market for network based games and one category in particular known as Massively Multiplayer Online Games or MMOGs for short, has as a result, grown into a multibillion dollar industry and an area of growing research interest. The chief challenge in these games is that real time instantaneous response is required by several thousand if not millions of concurrently active users. An integral resource contributing to the required network efficiency is the transport protocol used for data sharing among the various peers and connected servers. The most popular protocols used today are TCP (Transmission Control Protocol) and UDP (User Datagram Protocol). The chief objective of this study is to understand the performance of TCP and UDP in the various gaming scenarios and suggest the superior of them for each of the game genre.

Clique-Clique Domination Number of a Graph

R.S.Bhat¹, Smitha Holla² Sayinath Udupa N³ and Surekha R Bhat⁴

1,2,3 Department of Mathematics, Manipal University, Manipal, 576104, Karnataka, India. e-mail:rs.bhat@manipal.edu

4 Department of Mathematics, Milagres College, Kallianpur, Udupi, 576114, India. email:surekharbhat@gmail.com

ABSTRACT: A maximal complete subgraph of a graph G is called a clique of G . Let $K(G)$ denote the set of all cliques of G . Two cliques $k_1, k_2 \in K(G)$ are said to be adjacent if there is a common vertex incident on k_1 and k_2 . A set $L \subseteq K(G)$ is said to be a clique-clique dominating set if every clique not in L is adjacent to at least one clique in L . The *clique-clique domination number* $\gamma_{cc} = \gamma_{cc}(G)$ is the cardinality of a minimum clique-clique dominating set of G . In this paper we initiate a study of new parameter clique-clique domination number giving some bounds on the new parameter.

Keywords: Clique-clique domination number, independent clique-clique number, minimum clique number, clique degree.

1. INTRODUCTION

For any undefined terminologies we refer Diestel R (2000), West D.B (1996) and Harary F (1969). By a graph we mean a connected finite simple graph $G = (V, X)$ with $|V(G)|=p$ and $|X(G)|=q$ called the order and size of the graph respectively. A vertex $v \in V$ is a *cut-vertex* of a graph G , if $G-v$ is disconnected and such an edge is a *bridge* or a *cut-edge*. A graph G is *separable* if it has a cut-vertex otherwise it is *nonseparable*. A maximal nonseparable subgraph is a *block* of G . The concept of mixed block domination is introduced by Surekha and Bhat P G (2011) and further studied by Bhat P G et al. (2013) and Bhat R S et al.(2013 and 2014). Let $B(G)$ and $C(G)$ denote the set of all blocks and cut-vertices of G respectively. Let $|B(G)|=m$ and $|C(G)|=n$. A maximal complete subgraph of G is called a *clique* of G . For a survey of clique related results one can refer Bo-Jr-Li and Chang G J (2007), Brigham and Dutton R D (1983), Cacetta and Pullman N J (1983), Chariya U (2003),

Choudum et al. (1975), Erdos P et al. (1988), Parthasarathy K R and Choudum S A (1976), Pullman et al. (1988). An application of cliques in sociology is studied in Alba R (1973).

A vertex v is called *uniclinal* if it is incident on only one clique in G otherwise v is called *polyclical*. Similarly a uniclinal edge is defined. Let $K(G)$ denote the set of all cliques of G . Let $P_c(G)$ denote the set of all polyclical vertices of G . and $|K(G)|=k$ and $|P_c(G)|=p_c$. Two cliques k_1 and k_2 are adjacent if there is a common vertex incident on k_1 and k_2 . A *clique graph* $K_G(G)$ is a graph with vertex set $K(G)$ and any two vertices in $K_G(G)$ are adjacent if corresponding cliques in G have a vertex in common. A *polyclical vertex graph* $PV(G)$ is a graph with vertex set $P_c(G)$ and any two vertices in $PV(G)$ are adjacent if corresponding polyclical vertices in G have a clique in common. Infact, a *polyclical vertex graph* is a subgraph induced by the set $P_c(G)$. For any graph G , $PV(G) \cong G$ if and only if $P_c(G) = V(G)$. For

example, for any cycle C_n with n vertices $PV(C_n) \equiv C_n$. Further a *clique polycliqual vertex graph* (CPV-graph) $CPV(G)$ is a bigraph with vertex set $K(G) \cup P_c(G)$ and a polycliqual vertex $u \in P_c(G)$ and a clique $l \in K(G)$ are adjacent if and only if u is incident on the clique l . A *clique vertex graph* (CV-graph) $CV(G)$ is a bigraph with vertex set $K(G) \cup V(G)$ and a vertex $u \in V(G)$ and a clique $l \in K(G)$ are adjacent if and only if u is incident on the clique l . The $PV(G)$ of the graph G in Fig.1 is the graph induced by the polycliqual-vertices $\{u_1, u_2, u_3, u_4, u_5\}$. The Clique graph, CPV-graph and CV-graph of the graph G are illustrated in the Fig.1.

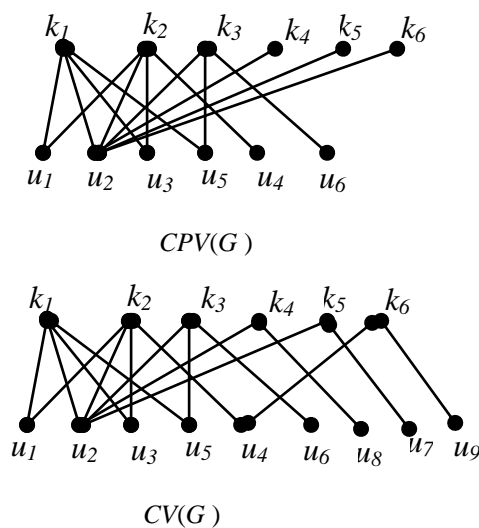
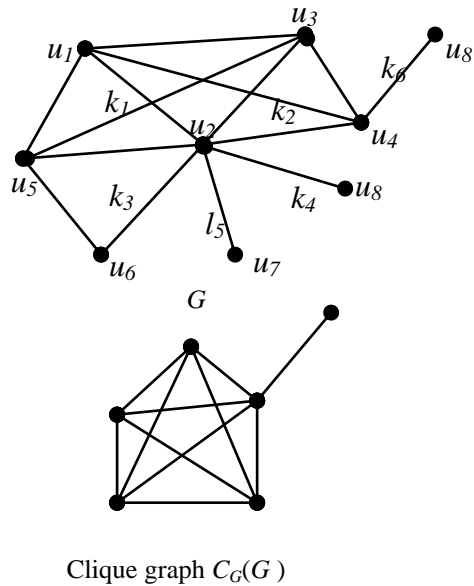


Fig.1

2. NEW CLASS OF GRAPHS

2.1 Clique paths and clique cycles

A *clique-walk* (C-walk) is a sequence of cliques and polycliqual vertices say, $l_1, u_2, l_3, u_4, l_5, \dots, l_{m-2}, u_{m-1}, l_m$ beginning and ending with cliques in which each polycliqual vertex u_i is incident with the cliques l_{i-1}, l_{i+1} . If all the polycliqual vertices are distinct in a clique walk, then such a walk is called a *clique path*. The *length* of a clique path is the number of polycliqual vertices in a clique path sequence. We observe that clique graph of a clique path is a path. A graph G is called a *clique cycle*, if $K_G(G)$ is a cycle. A clique path with 5 cliques and a clique cycle with 11 cliques are shown in the Fig.2

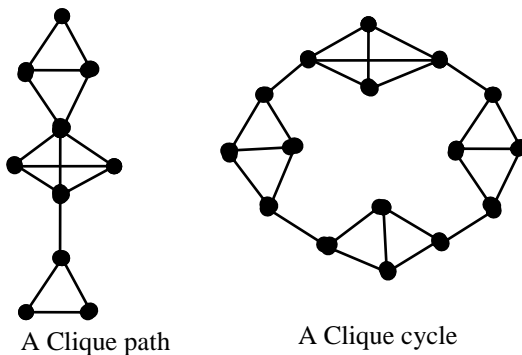


Fig. 2

2.2 Clique complete graphs and clique stars

A graph G is a *block-graph* if every block of G is a clique. A graph G is a *clique tree*, if $K_G(G)$ is a block graph. Therefore any block graph is a clique tree. But not conversely. A graph G is said to be *Clique-Complete*, if $K_G(G)$ is complete. A graph G is a *Clique-Star*, if $K_G(G)$ is a clique complete graph. A graph G with k cliques is said to be a generalized star if K_r (a complete graph with r vertices) is a common subgraph between all the cliques of G . Friendship graph, Hajo's graph and generalized star graphs are the examples of clique complete graphs which are shown in Fig.3

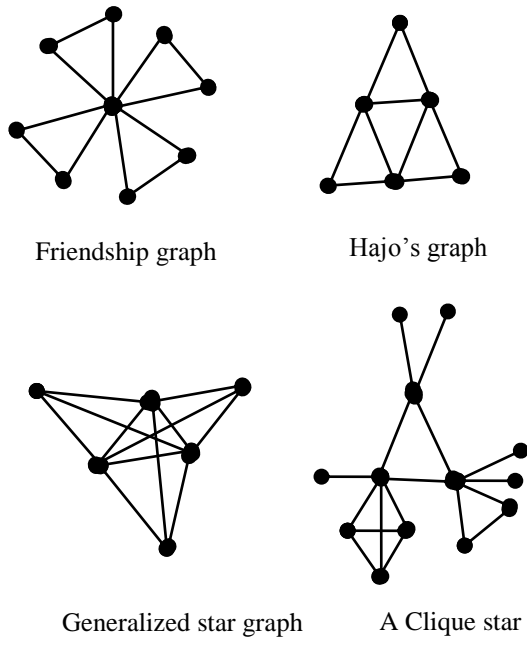


Fig. 3.

3. CLIQUE DEGREES

Different types of degrees are defined by Kamath S S and Bhat R S (2006 and 2007). Bhat R S et al. (2013) also studied block degree concepts and obtained the expressions for the sum of block degrees. Motivated by these papers, we define following degrees in a graph. The *vc-degree* $d_{vc}(u)$ of a vertex u , is the number of cliques incident on u . The *cv-degree* $d_{cv}(l)$ of a clique l , is the number of vertices in clique l . The *polyclique vertex-degree* $d_{pc}(l)$ of a clique l , is the number of polyclique vertices in the clique l . The *cc-degree* of a clique l , $d_{cc}(l)$ is the number of cliques adjacent to l . Let $\Delta_{vc}(G)$ and $\delta_{vc}(G)$ denote the maximum and minimum vc-degrees of G respectively. Then $\Delta_{cv}(G)$, $\delta_{cv}(G)$, $\Delta_{pc}(G)$, $\delta_{pc}(G)$, $\Delta_{cc}(G)$ and $\delta_{cc}(G)$ are defined similarly. The *minimum clique number* $\vartheta = \vartheta(G)$ is the order of a minimum clique of G , while the *maximum clique number* $\omega = \omega(G)$ is the order of a maximum clique of G . We observe that $\Delta_{cv}(G) = \omega(G)$ and $\delta_{cv}(G) = \vartheta(G)$.

Proposition 3.1. For any graph G with k cliques and p_c polyclique vertices,

$$p_c + k - 1 \leq \sum_{u \in P_c(G)} d_{vc}(u) = \sum_{l \in K(G)} d_{pc}(l) \leq \Delta_{vc}k \quad (1)$$

$\sum_{u \in P_c(G)} d_{vc}(u) = p_c + k - 1$ if and only if

$CPV(G)$ is a tree.

Further, $\sum_{u \in P_c(G)} d_{vc}(u) = \Delta_{vc}k$ if and only if $CPV(G)$ is a complete bipartite graph.

Proof. First we note that $d_{vc}(u) = d(u)$ in $CPV(G)$. Therefore $\sum_{u \in P_c(G)} d_{vc}(u)$ gives the number of edges in $CPV(G)$ which is a bipartite graph with partition V_1 = set of all cliques of G and V_2 = set of all polyclique vertices of G . Similarly, $d_{pc}(l) = d(l)$ in $CPV(G)$.

$$\text{Therefore } \sum_{u \in P_c(G)} d_{vc}(u) = q(CPV(G)) = \sum_{l \in K(G)} d_{cv}(l)$$

If $CPV(G)$ is a tree then it has $p_c + k - 1$ edges and if $CPV(G)$ is a complete bipartite graph then it has $\Delta_{vc}k$ edges. Therefore $p_c + k - 1 \leq \sum_{u \in P_c(G)} d_{vc}(u) \leq \Delta_{vc}k$.

Proposition 3.2 For any graph G with k cliques,

$$p + k - 1 \leq \sum_{u \in V(G)} d_{vc}(u) = \sum_{l \in K(G)} d_{cv}(l) \leq \omega k \quad (2)$$

and
 $\sum_{l \in K(G)} d_{cv}(l) = p + k - 1$ if and only if $CV(G)$ is a tree.

$\sum_{l \in K(G)} d_{cv}(l) = \omega k$ if and only if $CV(G)$ is a complete bipartite graph.

Proof. As in the above proposition, first we note that $\sum_{l \in K(G)} d_{cv}(l)$ gives the number of edges in $CV(G)$ which is a bipartite graph with partition V_1 = set of all cliques of G and V_2 = set of all polyclique vertices of G .

Therefore $\sum_{l \in K(G)} d_{cv}(l) = q(CV(G)) = \sum_{u \in V(G)} d_{vc}(u)$.
If $CV(G)$ is a tree then it has $p + k - 1$

4th International Engineering Symposium - IES 2015

March 4-6, Kumamoto University, Japan

edges and if $CV(G)$ is a complete bipartite graph then it has $\Delta_{cv}k = \omega k$ edges.

$$\text{Therefore } p+k-1 \leq \sum_{l \in K(G)} d_{cv}(l) \leq \Delta_{cv}k = \omega k$$

Corollary 3.2.1 For any graph $\frac{p-1}{\omega-1} \leq k$.

Proof. From Proposition 3.2,

$$p+k-1 \leq \sum_{l \in K(G)} d_{cv}(l) \leq \omega k$$

This implies $\frac{p-1}{\omega-1} \leq k$.

$$\frac{p-1}{\omega-1} \leq k$$

Which gives

Corollary 3.2.2 If G is a block graph, then

$$k \leq \frac{p-1}{\omega-1}$$

Proof. From Proposition 3.2, for any block graph,

$$9k \leq \sum_{l \in K(G)} d_{cv}(l) = p+k-1. \text{ Then the result}$$

follows.

4. CLIQUE-CLIQUE DOMINATION

A set $S \subseteq V$ is a dominating set if every vertex not in S is adjacent to at least one vertex in S . The domination number $\gamma = \gamma(G)$ is the cardinality of a minimum dominating set of G . The concept of domination is well studied in Haynes T W et al. (1997 and 1998), Bhat R S et al. (2012 and 2013), Allan R B and Laskar R (1978). Recently, Surekha and Bhat P.G (2011) introduced bb-domination. Two blocks $b_1, b_2 \in B(G)$ are said to *bb-dominate* each other if there is a common cutvertex incident with b_1 and b_2 . A set $L \subseteq B(G)$ is a *bb-dominating set* (BBD set) if every block not in L is bb-dominated by some block in L . The *bb-domination number* $\gamma_{bb} = \gamma_{bb}(G)$ is the minimum cardinality of a BBD-set of G . Similar to bb-domination we define cc-domination. Two cliques $k_1, k_2 \in K(G)$ are said to *clique dominate* each other if there is a polycliquial vertex incident with k_1 and k_2 . A set $L \subseteq K(G)$ is said to be a *clique-clique dominating set* (CCD-set) if every clique in G is clique dominated by some clique in L . The *clique-clique domination number* $\gamma_{cc} = \gamma_{cc}(G)$ is the

cardinality of a minimum clique-clique dominating set of G . It is immediate that $\gamma_{cc}(G) = \gamma(K_G(G))$. Cozzens M B and Kelleher L L (1990) introduced another parameter called clique domination number of a graph which is different from our parameter.

A set $L \subseteq K(G)$ is *cc-full* if every clique in L is adjacent to some clique in $K(G) - L$. The *cc-full number* $f_{cc} = f_{cc}(G)$ is the cardinality of a maximum cc-full set of G . For the graph G with 15 cliques in Fig.4, $\gamma_{cc} = 4$, $f_{cc} = 11$

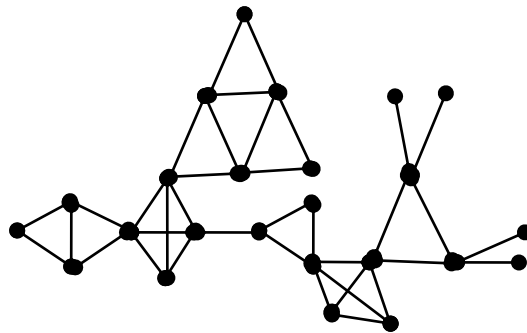


Fig.4 Graph G with 15 cliques

Next we give cc-domination number for newly defined graphs. Since the results can easily be verified, we omit the proof.

Proposition 4.1.

- i) If G is a clique path, $\gamma_{cc}(G) = \left\lceil \frac{k}{3} \right\rceil$
- ii) If G is a clique cycle $\gamma_{cc}(G) = \left\lceil \frac{k}{3} \right\rceil$
- iii) If G is a clique complete graph, $\gamma_{cc}(G) = 1$
- iv) If G is a clique star with c cutvertices, $\gamma_{cc}(G) = c$

Proposition 4.2

For any connected graph G with k cliques, $\gamma_{cc}(G) \leq \left\lfloor \frac{k}{2} \right\rfloor$ (3)

Proof. Let L be a minimal CCD set of G . Then $\gamma_{cc}(G) \leq |L|$. We also see that for any connected graph, if L is a minimal CCD set of G , then $K-L$ is also a CCD set of G .

4th International Engineering Symposium - IES 2015

March 4-6, 2015, Kumamoto University, Japan

Hence $\gamma_{cc}(G) \leq |K(G) - L|$. Adding the above two equations we get,

$$\begin{aligned} 2\gamma_{cc}(G) &\leq |L| + |K(G) - L| \\ &\leq |L| + |K(G)| - |L| \\ &\leq |K(G)| = k \end{aligned}$$

Then the result follows.

Proposition 4.3 For any connected graph G with k cliques,

$$\gamma_{cc} + f_{cc} = k \quad (4)$$

Proof. Let L be a γ_{cc} -set of G . Then, $K(G) - L$ is a cc-full set of G . Hence $f_{cc} \geq |K(G) - L| = k - \gamma_{cc}$.

Therefore $\gamma_{cc} + f_{cc} \geq k$ (A)

On the other hand let D be a maximum cc-full set of G . Then $K(G) - D$ is CCD set of G .

Hence $\gamma_{cc} \leq |K(G) - D| = k - f_{cc}$.

Therefore $\gamma_{cc} + f_{cc} \leq k$. (B)

Then the result follows from (A) and (B).

In what follows, we use the following notations. For any clique $l \in K(G)$, cc-neighbor of l ,

$$N_{cc}(l) = \{k \in K(G) \mid l \text{ and } k \text{ are adjacent}\}$$

Proposition 4.4 For any graph with maximum cc-degree Δ_{cc} ,

$$\frac{k}{1+\Delta_{cc}} \leq \gamma_{cc} \leq k - \Delta_{cc} \quad (5)$$

Further, the bound is sharp.

Proof. Since a clique can cc-dominate atmost Δ_{cc} cliques and itself, to cc-dominate k cliques we need atleast $\frac{k}{1+\Delta_{cc}}$ cliques. For the upper bound, let l be a clique of maximum cc-degree Δ_{cc} . Then $K(G) - N_{cc}(l)$ is a cc-dominating set of G . Hence $\gamma_{cc} \leq |K(G) - N_{cc}(l)| = k - \Delta_{cc}$.

Any clique star and clique complete graph attain both upper and lower bounds.

5. INDEPENDENT CC-DOMINATION

A set $L \subseteq K(G)$ is said to be cc-independent if no two cliques are adjacent. The cc-independence number $\beta_{cc} = \beta_{cc}(G)$ is the cardinality of a maximum cc-independent set of G . A CCD set which is

cc-independent is called independent clique-clique dominating set (ICCD set). The *independent clique-clique domination number* $\gamma_{icc} = \gamma_{icc}(G)$ is the cardinality of a minimum ICCD set of G . A set $L \subseteq X$ is a line dominating set if every edge not in L is adjacent to some edge in L .

The *edge domination number* $\gamma' = \gamma'(G)$ is the cardinality of a minimum edge dominating set of G . The *independent edge domination number* $i' = i'(G)$ is the cardinality of minimum edge independent dominating set of G . For any triangle free graph, $\gamma_{cc} = \gamma'$ and $\gamma_{icc} = i'$. Allan R B and Laskar R (1978) proved that for any graph G , $\gamma' = i'$. The *edge independence number* $\beta_1 = \beta_1(G)$ is the cardinality of a maximum edge independent set of G . The *edge covering number* $\alpha_1 = \alpha_1(G)$ is the cardinality of a minimum edge covering of G .

The inequality chain stated in the next proposition relates the new domination parameter with the existing graph parameters.

Proposition 5.1 For any graph G ,

$$\gamma_{bb} \leq \gamma_{cc} \leq \gamma_{icc} \leq \beta_{cc} \leq \beta_1 \leq \alpha_1 \quad (6)$$

Proof. Since every cc-independent set is a ICCD set and every ICCD set is a CCD set, and every CCD set is a BBD set we have

$$\gamma_{bb} \leq \gamma_{cc} \leq \gamma_{icc} \leq \beta_{cc}$$

To prove $\beta_{cc} \leq \beta_1$. Let D be a maximum cc-independent set of G . Let L be the set of edges formed by choosing one edge from each of the cliques. Since the cliques are cc-independent, the edges in L are necessarily independent and has β_{cc} edges. Therefore $\beta_{cc} = |D| = |L| \leq \beta_1$. We already know that $\beta_1 \leq \alpha_1$ (see West D.B (1996)). This completes the proof.

Corollary 5.1.1 For any graph G ,

$$\gamma_{cc} \leq \gamma_{icc} \leq \beta_{cc} \leq \frac{p}{2} \quad (7)$$

Proof. From Proposition 5.1, we have $\gamma_{bb} \leq \gamma_{cc} \leq \gamma_{icc} \leq \beta_{cc} \leq \beta_1$. It is well known that

4th International Engineering Symposium - IES 2015

March 4-6, 2015, Kumamoto University, Japan

$\beta_1 \leq \frac{p}{2}$ (see West D B (1996)). Then the result follows.

Bhat R S et al. [2012] defined the edge –edge domination number as follows. By $N(v) = \{u \in V \mid u \text{ is adjacent to } v\}$ and $N[v] = N(v) \cup \{v\}$. Let $\langle N[v] \rangle$ denote the induced subgraph induced by the set $N[v]$. For any edge $x = uv$, let $\langle N[x] \rangle = \langle N(u) \cup N(v) \rangle$. We say that an edge y is ee-adjacent to the edge x if $y \in \langle N[x] \rangle$. A set $L \subseteq X(G)$ is said to be edge-edge dominating set (EED-set) if every edge in $X-L$ is ee-dominated by an edge in L . The edge-edge domination number $\gamma_{ee} = \gamma_{ee}(G)$ is the cardinality of a minimum EED set of G . We observe that γ_{ee} and γ_{cc} are not comparable. For example, for any cycle C_4 , $\gamma_{cc}(C_4) = 2 > 1 = \gamma_{ee}(C_4)$ and for the clique star G , shown in the Fig.3, $\gamma_{cc}(G) = 1 < 2 = \gamma_{ee}(G)$.

CONCLUSIONS

The following conclusions are deduced from this study:

- Conclusion 1. New class of graphs such as clique path, clique cycle and clique complete graphs are defined.
- Conclusion 2. Various types of clique degrees are defined.
- Conclusion 3. cc-domination is defined and bounds in terms of clique degree is obtained. We also compared the cc-domination number with the existing graph parameters such as line domination number and cc-independence number of a graph.

ACKNOWLEDGEMENTS

We thank the unknown referee for giving suggestions to improve the presentation of the paper.

REFERENCES

- [1] Alba D R (1973), A graph theoretic definition of sociometric clique, J. Math.sociology, Vol.13, 113-126.
- [2] Allan R B and Laskar R (1978), On Domination and Independent domination number of a graph, Discrete Math., 23, 73-76.
- [3] Bhat P G, Bhat R S and Surekha (2013), Relationship between block domination parameters of a graph, Discrete Math. Algorithms and Applications, Vol. 5, No. 3, 1350018.
- [4] Bhat R S, Kamath S S and Surekha (2012), Strong (Weak) Edge- Edge Domination Number of a Graph, Applied Math. Sciences, Vol.6, no.111, 5525-5531.
- [5] Bhat R S, Bhat P G and Surekha (2013), Sum of block degrees, submitted
- [6] Bhat R S, Bhat P G and Surekha (2014) Block Regular Graphs -Proc. National Seminar on Emerging Trends in Graph Connections, 214-218.
- [7] Bhat R S, Kamath S S and Surekha (2013), An Improved Bound on Weak Independence Number of a Graph, Proc. World Congress on Engineering, WCE 2013, London, U.K., Vol 1, 208-211.
- [8] Bo-Jr-Li and Chang G J (2007), Clique coverings and partitions of line graphs, Discrete Math. 2075-2079.
- [9] Brigham R C, and Dutton R D (1983), On clique covers and Independence numbers of graphs, Discrete Math., 44, 139-144.
- [10] Caccetta and Pullman N J (1983), On Clique covering numbers of regular Graphs, Ars combinatoria, 15, 201- 230
- [11] Chariya U (2003), Maximal clique partitions, Ph.D Thesis, University of Colorado.
- [12] Choudam S.A, Parthasarathy K R and Ravindra G, (1975), Line-clique Cover Number of a graph, Proceedings of INSA, Vol.41 Part A, No.3, 289-293.
- [13] Cozzens M B and Kelleher L L (1990), Dominating Cliques in graphs, Discrete Math., 86, 145-164.
- [14] Diestel R (2000) Graph Theory, Springer Verlag Neyork, electronic Edition 2000.
- [15] Erdos P, Faudree R and Edward T O (1988), Clique partitions and clique coverings, Discrete Math. 72, 93-101
- [16] Harary F, (1969), Graph Theory, Addison Wesley.
- [17] Haynes T W, Hedetniemi S T and Slater P J (1997), Domination in Graphs, Advanced Topics, Marcel Dekker, Inc., N. Y.
- [18] Haynes T W, Hedetniemi S T and Slater P J (1998), Fundamentals of Domination in Graphs, Marcel Dekker, Inc, N.Y.
- [19] Kamath S S and Bhat R S (2006), Some New Degree Concepts in Graphs, Proc. of ICDM 2006, 237-243.
- [20] Kamath S S and Bhat R S (2007), Strong (Weak) Independence and Covering Numbers of a Graph, Discrete. Math. , Vol. 307, 1136 - 1145.
- [21] Parthasarathy K R and Choudam S.A (1976), Edge-clique Cover Number of Product Graphs, J. Math. and Phy. Sci., Vol 10, No.3, 255-261.
- [22] Pullman N J, Shank H and Wallis W D (1982), Clique coverings of Graphs, Discrete Math., 72, 93-101.
- [23] Surekha and Bhat P G (2011), Mixed Block Domination in Graphs, J. of International Academy of Physical Sciences, 15, 345-357.
- [24] West D B (1996), Introduction to Graph Theory, Prentice Hall, 1996.

Phase Balancing Techniques

Swapna M and Udaykumar R Y

*Department of Electrical and Electronics Engineering,
National Institute of Technology Karnataka, Surathkal, Mangalore 575025, India.
email:swapna44@gmail.com*

ABSTRACT: In practice, engineers use empirical methods for phase balancing to reduce the loss incurred by load unbalance; which are laborious, time-consuming and involve lot of power interruptions. These issues can be simplified by using phase balancing algorithm, which provides optimal phase lateral arrangements with minimum power loss, phase moves, interruptions and cost, thereby making system more efficient. This paper reviews different existing phase balancing formulation techniques for secondary distribution system.

Keywords: Phase Balancing, Re-phasing, Phase swapping, Techniques

INTRODUCTION

The gap between generation and demand is increasing day by day due to increasing demand and limited availability of fossil fuels. It can be reduced either by increasing the generation capacity or by minimizing the system losses. Energy management is the key tool to minimize the loss. In power system, the percentage of distribution loss is more compared to generation and transmission losses. The major losses in power distribution network are

- Unbalanced loading
- Distribution transformer core and winding losses
- Energy Metering losses
- I^2R loss
- Improper Earthing
- Protection and monitoring device internal losses
- Network designing
- Low power factor
- Bad workmanship and
- Pilferage

Practically, except load balancing other loss parameters are nearly optimized by network design, new equipments and regular inspections. Phase balancing is one of the technique to reduce the losses incurred by load unbalance. It is a concept

of re-phasing (Phase swapping) of service laterals on the feeder such that load on three phases is balanced. The system performs efficiently when loads are evenly distributed on three phases.

The power interruptions and loss due to load unbalance can be minimized or optimized by phase balancing algorithm.

PHASE BALANCING EFFECTS

Electric power distribution companies expect to have approximately equal loads on each phase. Even if the loads are initially balanced, time varying loads cause unbalance problem. The effects of load unbalance on system performance are

- The loaded phase when reaches maximum allowable capacity of the serving equipment or conductor, effects the system peak load supplying capability.
- If one phase is overloaded because of unbalance, it deteriorates life span of transformer and other equipments.
- Loss in the heavily loaded phase rapidly increases since loss is proportional to the square of the current; this unbalance further leads to increase in neutral current which further increases conductor loss.

4th International Engineering Symposium - IES 2015

March 4-6, 2015, Kumamoto University, Japan

- The circuit results in excessive voltage drop in the heavily loaded phase giving rise to poor voltage regulation.
- System protection is also affected.

An unbalanced feeder increases the energy loss and electricity price along with the risk of overload situations thereby effecting power quality issues. In terms phases , direct and effective way to balance a feeder is by phase swapping.

In practice, engineers use phase swapping to balance phase load based on the empirical methods. The process is laborious, time-consuming and involves lot of power interruptions. The phase balancing algorithm will give the solution for optimal phase lateral arrangements considering constraints like minimum power loss, phase moves, interruptions and cost.

PHASE BALANCING TECHNIQUES

The following are the different phase balancing formulation techniques existing in the literature

Difference of flow currents in phase

Maximum unbalanced flow of branch current is computed from difference of phase currents and it is optimised by considering following constraints

- Each Phase has a load assigned
- Each load is only assigned to a phase
- Line capacity constraints

Jinxiang Zhu et al(1998) and Khodr et al(2006) considered critical branch phase balancing only single phase loads.

Minimize U_j

Subject to

$$\max\{|I_{j,a} - I_{j,c}|, |I_{j,b} - I_{j,c}|, |I_{j,a} - I_{j,b}|\} = U_j \quad (1)$$

$$I_{j,\Phi} = \sum_k I_{k,\Phi} + \Pi_{\Phi,1}^i d_{\Phi,1} + \Pi_{\Phi,2}^i d_{\Phi,2} + \Pi_{\Phi,3}^i d_{\Phi,3} \quad (2)$$

$$\Pi_{\Phi,1}^i + \Pi_{\Phi,2}^i + \Pi_{\Phi,3}^i = 1 \text{ for all } \Phi = a, b, c \quad (3)$$

$$\Pi_{a,\omega}^i + \Pi_{b,\omega}^i + \Pi_{c,\omega}^i = 1 \text{ for all } \omega = a, b, c \quad (4)$$

$$I_{j,\omega} \leq C_j \quad (5)$$

$$\Pi_{\Phi,\omega}^i \in \{0,1\} \text{ for all } i \quad (6)$$

where

j is any monitored branch

U_j is the unbalanced flow on branch j

$I_{j,\Phi}$ is the Φ phase flow on branch j

$\Pi_{\Phi,\omega}^i$ is the decision variable for ω^{th} load tapping to phase Φ at node i

C_j is the phase line capacity of branch j

Average Unbalance per phase

Siti et al(2007) and Abhisek Ukil et al(2008) calculated average unbalance per phase as per Eq.7 and compared it with threshold value. If value is below threshold value further phase balancing is not required else diverted to fuzzy logic based load balancing.

$$AU/\text{ph} = \frac{|L_{\text{pha}} - L_{\text{phb}}| + |L_{\text{phb}} - L_{\text{phc}}| + |L_{\text{phc}} - L_{\text{pha}}|}{3} \quad (7)$$

where

$L_{\text{pha}}, L_{\text{phb}}, L_{\text{phc}}$ are the loads (power) drawn from the phase A,B,C.

Input given to fuzzy is total phase load(KW) for each one of 3 phases, the resulted output of the fuzzy step is the load change values i.e., negative value for load releasing and positive value for load receiving.

Power Loss

1. Gandomkar (2004) discussed about Minimize power loss F subjected to

- Node voltage between upper and lower limit
- Conductors capacity
- Load phase either Single or double phase.
- Re-phasing number(s).

$$F = \sum_{i=1}^I (I_{ai}^2 R_{ai} + I_{bi}^2 R_{bi} + I_{ci}^2 R_{ci} + I_{ni}^2 R_{ni}) \quad (8)$$

where

I_{ai}, I_{bi}, I_{ci} are current of i^{th} segment of LV network for A,B,C phases

R_{ai}, R_{bi}, R_{ci} are Resistance of i^{th} segment of Lv network for A,B,C phases

I_{ni}, R_{ni} are neutral current and resistance of i^{th} segment

I is maximum segment number of LV network

4th International Engineering Symposium - IES 2015

March 4-6, 2015, Kumamoto University, Japan

Mauricio Granada Echeverri et al (2012) objective function is as follows

$$\min \sum_{t=1}^{N_t} \sum_{i=1}^{N-1} R_i \frac{P_{it}^2 + Q_{it}^2}{V_{it}^2} \quad (9)$$

$$P_{kt}^{Spe} - P_{kt}^{Calc}(V_{kt}, \theta_{kt}, \beta, H) = 0 \quad (10)$$

$$Q_{kt}^{Spe} - Q_{kt}^{Calc}(V_{kt}, \theta_{kt}, \beta, H) = 0 \quad (11)$$

$$V_k^{\min} < V_k < V_k^{\max} \quad (12)$$

$$P_{it}^{\min} < P_{it} < P_{it}^{\max} \quad (13)$$

Where

P_{it} and Q_{it} are the active and reactive power flow in line i for load level t

R_i is the resistance of line i

P_{kt}^{Spe} and Q_{kt}^{Spe} are the specified values of the active and reactive power injections in node k for load level t

V_{kt} and θ_{kt} represent voltage magnitude and angle in node k for load level t

N_t is number of load levels considered in load duration curve

$N - 1$ is the number of lines of the system,

Phase current deviation

Murat Dilek et al(2001) and Sathiskumar et al(2012) have carried out phase current deviation objective function. Deviation is computed for each phase and it ranges from -1 to 2. Negative sign indicates below average and positive sign for above average. If deviation is 2, it implies 200% above average and that particular phase carries total current.

$$C = \min(DI_m) \quad (14)$$

Subject to

$$|V_{\min}| < |V_{nb}| \leq |V_{\max}| \quad (15)$$

$$|I_{\max}| > |I_k| \quad (16)$$

where

$$DI_j = \max(|Dev_a^j|, |Dev_b^j|, |Dev_c^j|) \quad (17)$$

$$Dev_i^j = \frac{I_{ph,i}^j - I_{ave}^j}{I_{ave}^j} \quad (18)$$

$$I_{ave}^j = \frac{I_{ph,a}^j + I_{ph,b}^j + I_{ph,c}^j}{n_p} \quad (19)$$

Where

Dev_a , Dev_b , Dev_c are the phase current deviations of the phases A,B,C

DI_j refers to maximum deviation index of j^{th} node

$I_{ph,a}$, $I_{ph,b}$, $I_{ph,c}$ are the phase currents of the phases A,B,C

i = phases A,B,C

j = nodes m, n, k, . . . , nb

$k = 1, 2, 3, 4, \dots, n_l$

n_p = number of phases

n_b = total number of buses in the system

n_l = total number of lines in the system

V_{\max} = maximum bus voltages limit

V_{\min} = minimum bus voltages limit

Phasing unbalance index (PUI)

Lin et al(2003), Chia-Hung Lin et al(2005) and Kai Wang et al(2013) used PUI for phase balancing with a assumption of one service lateral at each node. Maximum PUI lateral is rephrased by considering minimum PUI later as base branch.

$$PUI_j = \frac{\max(|I_a^j - I_{avg}^j|, |I_b^j - I_{avg}^j|, |I_c^j - I_{avg}^j|)}{I_{avg}^j} * 100\% \quad (20)$$

where

I_a^j, I_b^j, I_c^j are current loadings of phase A,B,C at node j

I_{avg}^j is average phase current

The following operation constraints are considered for rephasing.

- No main transformers, feeders and line switches are overloaded after rephasing.
- Radial network configuration must be maintained for distribution feeders.
- All service zones are connected and served by the feeder.

Multi objective optimization

- Schweickardt et al(2011) proposed a formulation to the general problem of Phase Balancing as

$$\text{Min} \left\{ \text{Loss}_r; I(\Delta u); |I_{[o]}|_f \right\} \quad (21)$$

where

$$|I_{[A]}|_f \leq I_{\max} \quad (22)$$

$$|I_{[B]}|_f \leq I_{\max} \quad (23)$$

$$|I_{[C]}|_f \leq I_{\max} \quad (24)$$

where

the subindex f is the output of substation connected to the principal feeder of the system

Loss_T is the total active power loss of the system

$I(\Delta)$ is voltage drop based index

$I_{[0]f}$ (homopolar component) satisfy the equation

$$|I_{[R]_f}| + |I_{[S]_f}| + |I_{[T]_f}| = 3X|I_{[0]_f}| \quad (25)$$

If system is balanced, then $|I_{[0]f}| = 0$

2. Willy Mukwanga Siti et al(2011) proposed the multi objective optimization function as

$$\text{Minimize } J_{\text{obj}} = J + J_n + \lambda I_{\text{phs}}^0 + \lambda I_{\text{phs}}^- \quad (26)$$

Where

J: Phasor current unbalance relationship

J_n : Neutral current of an unbalanced circuit

I^0_{phs} and I^-_{phs} : Zero and negative sequence currents of an unbalanced circuit

$$\text{Minimize } J = \begin{vmatrix} I_{\text{ph1k}} - I_{\text{ph2k}} \\ I_{\text{ph1k}} - I_{\text{ph3k}} \\ I_{\text{ph2k}} - I_{\text{ph3k}} \end{vmatrix} \quad (27)$$

$$\text{Minimize } J_n = \left[I_N^2 - \left(\left(I_{\text{phak}} - I_{\text{phbk}} \right)^2 + \left(I_{\text{phak}} - I_{\text{phck}} \right)^2 + \left(I_{\text{phbk}} - I_{\text{phck}} \right)^2 \right) \right]^2 \quad (28)$$

3. Rahmat Allah Hooshmand et al(2012) proposed the objective function including the neutral current of the supporting feeder, the rephasing cost, the voltage drop, and the line losses.

The four objectives are fuzzified and then integrated as the fuzzy multi-objective function

Neutral Current of Supporting Feeder

$$I_N = I_a + I_b + I_c \quad (29)$$

Average Voltage Drop of i th node

$$(V_d)_i = \frac{1}{3} \sum_{k=a}^c (V_n - (V_k)_i) / V_n \quad (30)$$

Average Voltage Drop

$$(V_d)_{AV} = \frac{1}{n} \sum_{i=1}^n (V_d)_i \times 100\% \quad (31)$$

Rephasing Cost, customer service interruption cost at node i is

$$CIC_i = (\sum_{j=1}^k c_j x L_j) X t_i \quad (32)$$

where k is the number of nodes under the effect of rephasing at node i

C_j is the interruption cost of each kWh for j node on

$$CIC_t = \sum_{k=1}^p CIC_k \quad (33)$$

$$RC_t = CIC_t + CL_t \quad (34)$$

where CL_t is the labor cost in the whole nodes in which rephasing is performed.

Power Losses Cost

$$P_{\text{loss}} = \sum_{j=1}^b I_j^* \times R_j \times i_j \quad (35)$$

Proposed Objective Function

$$of = \omega_1 \times I_N + \omega_2 \times (V_d)_{AV} + \omega_3 \times P_{\text{loss}} + \omega_4 \times RC_t \quad (36)$$

$$\omega_1 + \omega_2 + \omega_3 + \omega_4 = 1 \quad (37)$$

$$V_{K_{\min}} < V_K < V_{K_{\max}}, \quad K = 1, 2, \dots, n \quad (38)$$

CONCLUSIONS

The paper has reviewed different phase balancing formulation techniques in the literature. It is observed phase balancing play a major role in the reduction of distribution system losses. Power interruptions and number of phase rephasing can be reduced by using phase balancing techniques rather than empirical or trial and error method.

REFERENCES

- [1] Dilek, M., Broadwater, R.P., (2001). "Simultaneous phase balancing at substations and switches with time-varying load patterns." IEEE Trans. Power Systems., 16(4), 922-928.
- [2] Gandomkar, M (2004)."Phase balancing using genetic algorithm"39th international Universities Power Engineering Conference, 377-379
- [3] Hooshmand, R.A., Soltani, S.,(2012)."Fuzzy optimal phase balancing of radial and meshed distribution networks using bf-psos algorithm." IEEE Trans. Power Systems., 27(1), 47-57.
- [4] Khodr, H.M., Zerpa, I.J., De Jesus, P.M (2006) ."Optimal Phase Balancing in Distribution System Using Mixed-Integer Linear Programming" Proc., IEEE PES Transmission and Distribution Conference and Exposition Latin America, Venezuela, 1-5.
- [5] Lin, C.H., Chen, C.S., Chuang, H.J., Cheng, Y.H.,(2005)." Heuristic rule-

4th International Engineering Symposium - IES 2015

March 4-6, 2015, Kumamoto University, Japan

-
- based phase balancing of distribution systems by considering customer load patterns." IEEE Trans. Power Systems., 20(2), 709-716.
- [6] Sathishkumar, M., Nirmal kumar, A., Lakshminarasimman, L., Thiruvenkadam, S.,(2012)." A self-adaptive hybrid differential evolution algorithm for phase balancing of unbalanced distribution system." J. Electric Power Systems Research., 42, 91-97.
- [7] Schweickardt, G.A., Miranda, V., Wiman, G.,(2011)." A comparison of metaheuristics algorithms for combinatorial optimization problems. Application to phase balancing in electric distribution systems." J. Latin America Applied Research., 41, 113-120.
- [8] Siti, M.W., Nicolae, D.V., Jimoh , A.A., (2007)." Reconfiguration and load balancing in the lv and mv distribution networks for optimal performance." IEEE Trans. Power Delivery., 22(4), 2534-2540.
- [9] Siti, W., Jimoh, A., Nicolae, D.,(2011)." Distribution network phase load balancing as a combinatorial optimization problem using fuzzy logic and Newton-Raphson." J. Electric Power Systems Research., 81, 1079-1087.
- [10] Siti, W., Jimoh, A., Nicolae, D.,(2011)." Distribution network phase load balancing as a combinatorial optimization problem using fuzzy logic and Newton-Raphson." J. Electric Power Systems Research., 81, 1079-1087
- [11] Wang, K., Skiena, S., Robertazzi, T.G.,(2013)." Phase balancing algorithms." J. Electric Power Systems Research., 96, 218-224.
- [12] Zhu, J., Chow, M.Y., Zhang, F.,(1998)." Phase balancing using mixed-integer programming." IEEE Trans. Power Systems., 13(4), 1487-1492.

4th International Engineering Symposium - IES 2015

March 4-6, 2015, Kumamoto University, Japan

**CHEMISTRY,
CHEMICAL ENGINEERING,
ENVIRONMENT
&
RELATED FIELDS**

Enzymatically Derived Chitosan Hydrogels: Preparation and Application

Ritu Raval¹, Stephan Kolkenbrock², Bruno Moerschbacher³

1 Department of Biotechnology, Manipal Institute of Technology, Manipal University, Manipal, Karnataka-576104, India. e-mail: ritu.raval@manipal.edu

2 Institute of Biochemistry and Biotechnology of Plants, WWU Muenster-48143, Germany. e-mail: Stephan.Kolkenbrock@uni-muenster.de

3 Institute of Biochemistry and Biotechnology of Plants, WWU Muenster-48143, Germany. e-mail: moersch@uni-muenster.de

ABSTRACT: Chitosan, one of the most abundant biopolymers, is the partially deacetylated product obtained from chitin. On a commercial scale, this conversion is performed chemically using sodium hydroxide. This chemical conversion not only pollutes the environment unless the waste water is treated extensively, but also results in a randomized pattern of acetylation (PA) on the chitosan. This might be different if an enzymatic pathway towards the conversion can be established. This inclusion of an enzyme may not only produce chitosan with a non-random pattern of acetylation on its surface but could also reduce the pollution from the environmental dumping of the chemicals during the conversion process. The PA is in particular of potential influence for applications in the medical, agricultural and food sector. In this paper, we report the expression of a *Bacillus* chitin deacetylase gene in *E.coli* Rosetta pLyS cells and the subsequent purification of the recombinant protein. The enzyme was later utilized for chitosan modification. We report the application of the enzymatically modified chitosan as hydrogels for chloride sequestering. This is a first report on hydrogels based on enzymatically derivatized chitosan and the work can be further extended towards water treatment.

Keywords: Chitin deacetylase, Expression, *E.coli*, Purification, Enzymatically derivatized chitosan, Hydrogels,

INTRODUCTION

Chitosan, one of the most abundant biopolymers, is the partially deacetylated product obtained from chitin. This chemical is converted chemically on a commercial scale. The other mode of conversion viz, enzymatic is not explored on the large scale. On the contrary it holds many advantages, one of the main being the high Degree of Acetylation (DA) that is achieved and molecular weight homogeneity of the final chitosan when compared to the chemical deacetylation. In addition the chemical mode is considered as a random and harsh conversion process (Cabrera J C, and Van Cutsem P 2005, Zhao Y et al 2010, Pareek N et al 2013). The enzymatic conversion

reaction also allows a regioselectivity during deacetylation (which is hard to achieve by chemical N-acetylation). This offers a possibility of a good control of the final chemical structure of chitosan [Tokuyasu K et al (2000)]. Due to these properties, the enzyme deacetylated chitosan (EDC) would display potential application in advanced technologies where a high chitosan quality is required, such as in medicine, food, agriculture and pharmaceutical formulation (Tsigos I et al 2000). One such field of application is environmental wherein the chitosan offers usage in waste water treatment.

The structure of Chitosan in solution exists in the form of quasi-globular conformation stabilized by extensive intra and intermolecular hydrogen bonding. The high

viscosity of the chitosan solution is also attributed to the hydrogen bonding between the amine and hydroxyl groups. According to Chen RH et al 1994), the DA determines the number of intermolecular hydrogen bonds which in turn affects the rigidity of the polymer film. In the case of chitosan hydrogels, the extent of dissociation of the hydrogen bonding may affect the swelling kinetics of the gels. At low pH, the hydrogen bonding dissociates due to the protonation of the amine groups leading to faster swelling. In this paper , an attempt to obtain an enzymatically derivatized chitosan has been made. The derivatized chitosan has also been studied for its ion sequestering properties.

METHODS

(3.1.1). Transformation of Gene in *E.coli*

The gene responsible for the chitin deacetylase (CDA) activity was cloned from *Bacillus licheniformis*. The gene was transformed into *E.coli* pLsS cells with pET22b vector for expression using the heat shock method. The *E.coli* cells were grown at 37° C to obtain the expressed protein for further studies.

Purification of Chitin deacetylase

The protein was obtained after growing the *E.coli* t 37° C for 8 h after inducing with 1mM IPTG. The culture broth was centrifuged at 10,000 rpm for 20 min. The pellet containing the cells was subjected to sonication after resuspending them in lysis buffer (50 mm sodium phosphate, pH- 8.0, 2 M NaCl, 40 mm imidazole). The cells were subjected to sonication for 2.5 min with a on -off cycle of 10 and 15 sec respectively. The lysates were centrifuged at 10,000 rpm for 10 min. the resultant supernatants, containing the His6-tagged protein, were loaded to nickel-NTA columns for purification (Qiagen).

Spectrometry based Enzyme assay for Chitin deacetylase activity

The protocol was a slight modification of Pareek et al, 2011 The assay mixture in a total volume of 500 μ l was prepared in test tubes including 50 μ l suitably diluted enzyme solution, 200 μ l of substrate (Glycol Chitin) and 250 μ l Tris buffer (pH 7.0). The mixture was incubated in 30°C for 30 min. The reaction was terminated by adding 0.5 mL of 5% KHSO₄. For deamination 0.5 mL of 5% NaNO₂ were added then mixture was then left standing with occasional shaking at room temperature for 15 min. The excess nitrous acid was then removed by adding 0.5 mL of 12.5% NH₄SO₃NH₂ and repeatedly shaking the mixture for periods of 5 min. To the deaminated mixture 0.5 mL of 5% MBTH was added and the mixture was allowed to stand for 60 min or heated in boiling water bath for 3 min and cooled. Finally 0.5 mL of 5% FeCl₃ was added. After standing for 30 min, the optical density at 650 nm was read. Standard solution of glucosamine (0-50 μ g) were added into each assay and results expressed as μ g glucosamine. One unit of enzyme activity was defined as the amount enzyme required producing 1 μ g glucosamine per min.

Modification of Chitosan using Chitin deacetylase

A chitosan solution of 1mg/ml was prepared with 0.5% acetic acid. The reaction mixture to subjected to 200 U of enzyme at 37°C for 8 hours. The activity was terminated by heating it for 30 min. The modified chitosan was used for further experiments.

Chloride sequestering ability of Enzymatically Derived Chitosan Hydrogels

This procedure was proposed for determining chloride ions based on titration with a silver nitrite solution in the waste water using chitosan gels at different pH. A known stock solution (300mg/L) of chloride ions was prepared and filtered through the chitosan gels. The filtrate obtained was titrated with 0.025N silver nitrate in the presence of potassium chromate indicator to calculate the chloride ions concentration.

4th International Engineering Symposium - IES 2015

March 4-6, Kumamoto University, Japan

Results and Discussion

The *E.coli* pLysS was transformed using pET22b expression vector with the CDA gene inserted (Fig 1). The transformed cells were grown in LB Broth media at 37°C and 250 rpm. The growth profile of *E.coli* followed the sigmoidal curve (Fig 2). The expressed protein from the intracellular fraction was subjected to sonication followed by Ni-NTA purification which involved two step approach of elution elution initially at 250 mM Imidazole followed by 500 mM Imidazole treatment (Fig. 3). The purified enzyme was later utilized for the chitosan modification. The enzymatically modified chitosan was made use in the hydrogel formation. The hydrogel made in conjunction with agar was at all pH was soft giving more colouration at the acidic pH as compared to the alkaline pH used of 8.0. The work is in lines with the earlier works of Bhavani and Dutta, 1999 and Sridhari and Dutta 2000 wherein it was proposed that the cationic property of the chitosan can be used for flocculating the negative ions. In the present study its was found that the chelating ability of the hydrogel was dependent on the pH at which it was formed with the acidic hydrogels being able to scavenge chloride to a better capacity than the alkaline hydrogels (Table1). The initial chloride concentration was 300 mg/L and the corresponding removal gradually increased from 58% to 82% with gradually decrease pH due to protonation of chitosan. In this result 3% chitosan gel have capacity to absorbed 58.64% chloride ions at 8.0 pH. If pH gradually decreases absorbing capacity increases due to protonation to 82%.

CONCLUSIONS

The aim of the present study was to express the gene responsible for CDA from *Bacillus licheniformis* with the pET 22b vector into *E. coli* pLysS cells. The purified protein was utilized in the chitosan modification. The enzymatically derivatized hydrogels was tested for the chelating ability for chloride ions. The report is an

initiative towards the utilization of these derivatized chitosan hydrogels for waste water treatment.

REFERENCES

- [1] Cabrera J C, and Van Cutsem P. (2005), Preparation of chitooligosaccharides with degree of polymerization higher than 6 by acid or enzymatic degradation of chitosan. Biochemical Engineering Journal, Vol 25,pp. 165-172.
- [2] Pareek N et al (2013), Bioconversion to chitosan: A two stage process employing chitin deacetylase from *Penicillium oxalicum* SAEM-51. Carbohydrate Polymers, Vol 6, pp. 417-425.
- [3] Zhao Y et al (2010), Chitin deacetylases: Properties and applications. Marine Drugs, Vol.8,pp. 24-46.
- [4] Tokuyasu K et al (2000), Synthesis of a chitosan tetramer derivative, $\text{I}^2\text{-d-GlcNAc-(1}\overset{\text{Ac}}{\text{+4}}\text{-)}\text{I}^2\text{-d-GlcNAc-(1}\overset{\text{Ac}}{\text{+4}}\text{-)}\text{I}^2\text{-d-GlcNAc-(1}\overset{\text{Ac}}{\text{+4}}\text{-)}\text{I}^2\text{-d-GlcN}$ through a partial N-acetylation reaction by chitin deacetylase. Carbohydrate Research, Vol 325,pp. 211-215
- [5] Tsigos I et al (2000), Chitin deacetylases: new, versatile tools in biotechnology. Trends in Biotechnology, Vol 18 pp. 305-312
- [6] Chen RH et al (1994), Relationships between the chain flexibilities of chitosan molecules and the physical properties of their casted films, Carbohydrate Polymers, Vol 24 pp. 41-46
- [7] Pareek N et al (2011), *Penicillium oxalicum* SAEM-51: a mutagenised strain for enhanced production of chitin deacetylase for bioconversion to chitosan, New Biotechnology, Vol 28 pp.118-24
- [8] Bhavani K D, and Dutta P K (1999) Physico-chemical adsorption properties on chitosan for dyehouse effluent, American Dyestuff Reporter, Vol 88 pp.53-58
- [9] Sridhari T R and Dutta P K (2000) Synthesis and characterization of maleilated chitosan for dye house effluent , Indian Journal of Chemical Technology, Vol 7 pp. 198-203

Table 1 Comparison of chelating ability of chitosan and enzymatically derivatized chitosan towards chloride ions

Material	pH	Absorbing capacity of chloride ions (%)
Chitosan hydrogel	4.5	82.77
Chitosan hydrogel	6.0	80.13
Chitosan hydrogel	8.0	58.64
Enzymatically derived Chitosan hydrogel	4.5	82.71
Enzymatically derived Chitosan hydrogel	6.0	72.43

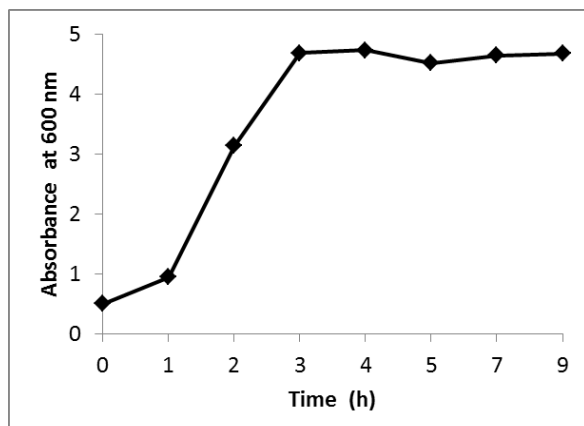


Fig.1 Growth Profile of E.coli pLysS cells supplemented with Ampicillin and Chloroamphenicol. The cells were grown at 37C , 250 rpm and absorbance measured at 600 nm.

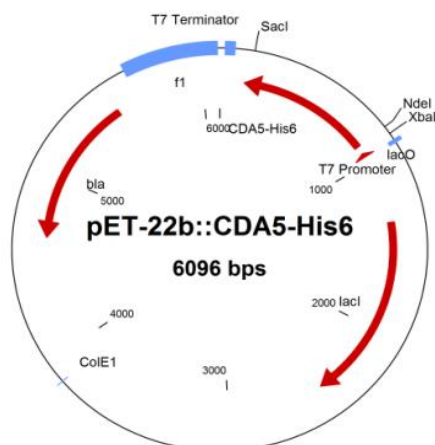


Fig. 1 The vector map of pET 22b construct with the inserted CDA gene



Fig.2 Purification of CDAHis6 with the Ni-NTA resin using batch mode of purification. The column bed volume was 2 ml. The resin was bound to the protein at 4°C for 20 h and then washed with 20 mM Imidazole and then eluted with two batches of 250 mM and 500 mM imidazole. From Right to left Lane 1: Marker (M), Lane 2: Elution 1 (E1), Lane 6: Elution 2 (E2), Lane 7: Elution 3 (E3), Lane 8: Elution 4 (E4), Lane 9: Elution 5 (E5), Lane 10: Elution 6 (E6)

Bioprocess development of Chitin Deacetylase production from recombinant *E. coli* pLysS cells

Keyur Raval¹, Ritu Raval², Nitasha Chinaan³, Stephan Kolkenbrock⁴ and Bruno Moerschbacher⁵

- 1 Department of Chemical Engineering, National Institute of Technology Karnataka, Surathkal, Mangalore, 575025 India. e-mail : keyurnraval@gmail.com
 - 2 Department of Biotechnology, Manipal Institute of Technology, Manipal, 576104 India. email: ritukraval@gmail.com
 - 3 Department of Chemical Engineering, National Institute of Technology Karnataka, Surathkal, Mangalore, 575025 India. Email: nithashzzz@gmail.com
 - 4 Institute of Biology and Biotechnology of Plants, WWU Muenster, Germany. Email: moersch@uni-muenster.de
 - 5 Institute of Biology and Biotechnology of Plants, WWU Muenster, Germany. Email: moersch@uni-muenster.de
-

ABSTRACT: Chitosan is one of the classes of polysaccharide with a promising economic potential because of its biological activities and many roles in the life of bacteria, fungi and animals. Chitosan is produced from second most abundant biopolymer, Chitin by chemical methods such as acid and alkali treatment. The chemical methods produce lower yields and variable degrees of chitosan. Moreover, the effluent produced by chemical method is hazardous to environment. Alternative and/or complementing enzymatic modifications of chitin using chitin deacetylase can reduce energy input and environmental impact while at the same time offering the advantage of higher specificity and, thus, potentially yielding novel polymers and/or oligomers with advanced physico-chemical properties and biological functionalities. Chitin deacetylase (CDA) catalyzes the conversion of chitin to chitosan by the deacetylation of N-acetyl-D-glucosamine residues. This research work involved production of CDA, from a recombinant *E. coli* Rosetta pLysS. This is the first report of media design and scale up of CDA production process from recombinant *E. coli*. Various media components were investigated to enhance the production of CDA. The CDA productivity was improved tremendously at shake flask level by changing operating conditions. The final medium was designed with glycerol as the sole carbon source. The bioprocess was further scaled-up to 3 liter stirred tank bioreactor.

Keywords: Chitin deacetylase, recombinant, media development, scale-up

INTRODUCTION

Chitin is a homopolymer of β (1,4)-linked N-acetyl-glucosamine, is one of the most abundant, easily obtained, and renewable natural biopolymers. Chitin is present in marine invertebrates, insect, fungi, yeast (Tharanathan and Kittur 2003). Chitin is not water soluble or majority of organic solvents and therefore its uses are restricted. On the other hand, Chitosan, a derivative of chitin is easily soluble in

water and has potential applications in the environmental, biomedical as well as the pharmaceutical industries (Araki and Ito 1975). Commercially chitosan is produced from chitin, the ingredient present in the shells of the arthropods using chemical process of acid/base hydrolysis (Chang, Tsai et al. 1997). This process delivers chitosan of variable specificity requiring troublesome purification steps and loading the environment with the unsafe chemicals in the process and making it unsustainable.

4th International Engineering Symposium - IES 2015

March 4-6, 2015, Kumamoto University, Japan

On the other hand, chitin deacetylase (CDA), hydrolyses the acetamido groups of N-acetylglucosamine in chitin and converts into chitosan (Tsigos, Martinou et al. 2000). This enzymatic process is highly specific, environmental friendly and sustainable. CDA, a member of carbohydrate esterase family of proteins was first discovered from extracts of the fungus *Mucor rouxii* and it was further found that the enzyme was associated with cell wall synthesis by converting nascent chitin into chitosan (Araki and Ito 1975). Other sources of CDA are bacterial, fungal and insects (Šimůnek, Tishchenko et al. 2004, Kadokura, Rokutani et al. 2007, Pareek, Vivekanand et al. 2011). However, the enzyme yield is low in wild type microorganisms which required high yielding recombinant organisms for production of CDA (Tokuyasu, Kaneko et al. 1999). Group of Professor Bruno Moerschbacher extensively researched on recombinant CDA expressed in various eukaryotic and prokaryotic platforms (Govinda Rajulu, Thirunavukkarasu et al. 2011). One such promising platform is recombinant CDA from *E.coli* pLysS.

This research work focuses on bioprocess development using the recombinant *E.coli* cells obtained from the group of Professor Moerschbacher.

MATERIALS AND METHODS

All media were purchased from HiMedia and chemical were purchased from Merck India Ltd. All the shake flask experiments were conducted in 250 mL shake flasks. The shaker used was from LEAD Instruments, India having 25 mm orbital shaking diameter.

STARTING MATERIAL AND SHAKE FLASK STUDIES

The recombinant *E. coli* pLysS were obtained from the group of Professor Moerschbacher, WWU Muenster, Germany.

The culture was maintained on LB Agar medium at 37°C. Chloramphenicol (35 µg/ml) and ampicillin (200 µg/ml) were used to maintain antibiotic pressure on plasmid.

One loop of culture was inoculated in 3 mL LB medium in test tubes for preparation of

inoculum for shake flask experiments. The test tubes were kept overnight at 37°C. The broth from the test tube was used to inoculate shake flask medium with 2% (v/v) inoculum. The broth was induced with 1 mM Isopropyl-1-thio-beta-D-galactopyranoside (IPTG) when optical density of the broth (660 nm) reached 0.5. The experiments were conducted at various shaking frequencies ranging from 100 to 250 rpm and various filling volumes (40% to 5%) to investigate effect of oxygen transfer rate and power consumption on biomass and CDA production.

EFFECT OF CARBON AND NITROGEN SOURCE ON CDA PRODUCTION.

Effect of five different carbon sources, namely, glucose, maltose, sucrose, lactose and glycerol was investigated on CDA production. Each carbon source was added to maintain 0.5% (w/v) concentration in LB medium. The 250 mL shake flasks were used with 5% filling volume and 250 rpm shaking frequency.

Similarly effect of five different complex nitrogen sources, namely, yeast extract, meat peptone, bacteriological peptone, high veg peptone and soya casein digest was investigated at 0.5% (w/v) concentration.

SCALE-UP STUDIES

The bioprocess was scaled up to 3L stirred tank bioreactor (Scigenics India Pvt. Ltd, India) with 1.5 L filling volume. The bioreactor had height to diameter ratio of 1.5 and was equipped with six blade rushton turbine. The bioreactor was inoculated with 2% inoculum.

CDA ASSAY

Extracellular CDA activity was estimated using ethylene glycol chitin as the substrate which was prepared from ethylene glycol chitosan. Briefly, ethylene glycol chitosan (EGC, 40 mg) was treated with a mixture containing NaHCO₃ (400 mg) and acetic anhydride (4.5 ml) and kept at 4°C for 24 hours. Following incubation, 200 ml of acetic anhydride was added and the mixture was

further incubated at 4°C for 24 hours. It was then dialysed against deionized water and acetylated ethylene glycol chitosan (1 mg/ml) thus recovered was used as a substrate for the assay of CDA.

The extracellular CDA was assayed as described by Kauss and Bauch (Kauss and Bauch 1988). Briefly, the assay mixture in a total volume of 250 µl contained 100 µl of EGC (1 mg/ml) and 100 µl of 50mM sodium tetraborate buffer (pH 6.5) along with suitably diluted fermentation broth as a source of enzyme. The mixture was incubated at 37°C for 30 min with constant shaking. The reaction was terminated by the addition of 250 ml of potassium hydrogen sulfate (5%). For color development, 250 ml of 5% sodium nitrite was added, allowed to stand for 15 min and then followed by the addition of 250 ml of 12.5% ammonium sulfamate. After 5 min, 250 ml of freshly prepared 3-methyl-2-benzothiazolinonehydrazone hydrochloride (0.5%) was added and the mixture was heated in boiling water bath for 3 min. The tubes were cooled and 250 ml of 0.5% ferric chloride was added. Absorbance was read at 650 nm after 30 min. One unit of enzyme was defined as the activity which released 1 µmol of acetate from ethylene glycol chitin per minute.

RESULTS AND DISCUSSION

Effect of different shaking frequencies and filling volume on biomass and CDA production.

Fig.1 shows the effect of various shaking frequencies on biomass and CDA production. As expected, as the shaking frequency increased the biomass as well as CDA production increased. Maximum biomass and CDA production was found at 250 rpm. Power consumption and oxygen transfer rate increase as shaking frequency is increased in shake flasks. Power consumption and oxygen transfer rate are proportional to shaking frequency with exponents of 2.8 and 1.16, respectively. This lead to ca. 20% increase in CDA activity from 220 U/L at 150 rpm to 260 U/L at 250 rpm. It was not possible to

operate shaker at more than 250 rpm due to mechanical instability.

Filling volume indicates the amount of liquid medium in the shake flask. As shown in Fig.2, as filling volume decreased, the biomass as well as CDA production increased. Power consumption and oxygen transfer rate are inversely proportional to filling volume, with exponents of -0.6 and -0.83, respectively. Thus there was ca. 31% increase in CDA activity; from 220 U/L at 100 ml to 360 U/L at 12.5 mL of broth. Hence, all experiments were conducted at 250 rpm and 12.5 mL filling volume in 250 mL shake flask. Overall there was ca. 51% increase in CDA activity at this optimized operating condition as compared to the routinely used operating condition of 250 ml shake flask 100 ml filling volume and 150 rpm. The growth curve was also completed in 12 to 15 hours at optimized operating conditions as compared to 27 hours in unoptimized operating condition.

Effect of different carbon and nitrogen sources on biomass and CDA production.

Fig.3 shows the effect of various carbon sources on CDA productivity. Maximum productivity was achieved using glycerol as the carbon source. Glucose and lactose induces catabolite repression and hence, reduces the recombinant protein expression based on any lac operon vector system. Maltose and sucrose also are converted to glucose during their metabolism in *E. coli* and hence they also reduce protein expression. This behavior explains lower levels of CDA in all carbon sources except glycerol.

As shown in Fig. 4, Soyabean casein digest gave lowest CDA production. Other three nitrogen sources did not alter CDA activity significantly. Soybean casein digest has glucose as one of the constituents which reduced CDA activity due to its catabolite repression effect on plasmid.

Scale-up studies

4th International Engineering Symposium - IES 2015

March 4-6, 2015, Kumamoto University, Japan

Fig.5 compares the growth and production profile of *E. coli* pLysS cells in 250 ml shake flask and 3 L stirred tank bioreactor.

The growth rate was more in stirred tank bioreactor as compared to that in shake flasks. The dissolved oxygen level in stirred tank bioreactor was always maintained above 70% oxygen saturation. The medium pH was also maintained at 7. Whereas shake flask studies were carried out without uniform maintenance of dissolved oxygen level and pH which lead to less growth and CDA activity. The extracellular recombinant enzyme activity reported in this study is one of the highest enzyme activity reported in the literature so far. Kadokura et al. (2007) observed 15 times higher recombinant enzyme activity than wild type *Vibrio parahaemolyticus* (Kadokura, Sakamoto et al. 2007). Other authors reported recombinant CDA activity in the range of 20 to 140 U/L (Tokuyasu, Kaneko et al. 1999, Martinou, Koutsoulis et al. 2003).

Conclusion

A bioprocess for recombinant Chitin deacetylase production was successfully developed. Results indicated that use of high shaking frequencies and low filling volume can tremendously increase productivity of CDA at shake flask level. Glycerol and so casein digest were the best carbon and nitrogen sources for CDA production. Catabolite repression was observed when glucose and similar carbon sources were used in the medium.

REFERENCES

- Araki, Y. and E. Ito (1975). "A Pathway of Chitosan Formation in *Mucor rouxii*." European Journal of Biochemistry, Vol. **55**, No. (1): pp. 71-78.
- Chang, K. L. B., et al. (1997). "Heterogeneous N-deacetylation of chitin in alkaline solution." Carbohydrate Research, Vol. **303**, No. (3): pp. 327-332.
- Govinda Rajulu, M., et al. (2011). "Chitinolytic enzymes from endophytic fungi." Fungal Diversity, Vol. **47**, No. (1): pp. 43-53.
- Kadokura, K., et al. (2007). "Purification and characterization of *Vibrio parahaemolyticus* extracellular chitinase and chitin oligosaccharide deacetylase involved in the production of heterodisaccharide from chitin." Applied Microbiology and Biotechnology, Vol. **75**, No. (2): pp. 357-365.
- Kadokura, K., et al. (2007). "Production of a recombinant chitin oligosaccharide deacetylase from *Vibrio parahaemolyticus* in the culture medium of *Escherichia coli* cells." Biotechnology Letters, Vol. **29**, No. (8): pp. 1209-1215.
- Kauss, H. and B. Bauch (1988). Chitin deacetylase from *Colletotrichum lindemuthianum*. Methods in Enzymology. S. T. K. Willis A. Wood, Academic Press. **Volume 161**: 518-523.
- Martinou, A., et al. (2003). "Cloning and expression of a chitin deacetylase gene (CDA2) from *Saccharomyces cerevisiae* in *Escherichia coli*: Purification and characterization of the cobalt-dependent recombinant enzyme." Enzyme and Microbial Technology, Vol. **32**, No. (6): pp. 757-763.
- Pareek, N., et al. (2011). "Penicillium oxalicum SAEM-51: a mutagenised strain for enhanced production of chitin deacetylase for bioconversion to chitosan." New Biotechnology, Vol. **28**, No. (2): pp. 118-124.
- Šimůnek, J., et al. (2004). "Chitinolytic enzymes from *Clostridium aminovalericum*: Activity screening and purification." Folia Microbiologica, Vol. **49**, No. (2): pp. 194-198.
- Tharanathan, R. N. and F. S. Kittur (2003). "Chitin — The Undisputed Biomolecule of Great Potential." Critical Reviews in Food Science and Nutrition, Vol. **43**, No. (1): pp. 61-87.
- Tokuyasu, K., et al. (1999). "Production of a recombinant chitin deacetylase in the culture medium of *Escherichia coli* cells." FEBS Letters, Vol. **458**, No. (1): pp. 23-26.
- Tsigos, I., et al. (2000). "Chitin deacetylases: new, versatile tools in biotechnology." Trends in Biotechnology, Vol. **18**, No. (7): pp. 305-312.

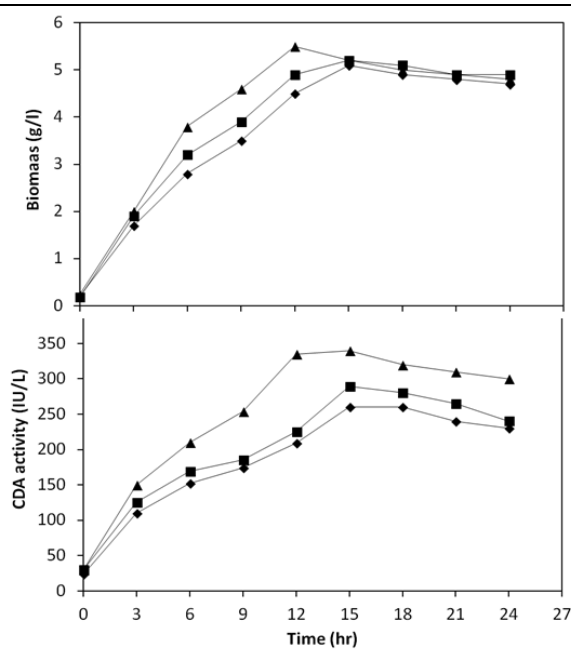


Figure 1: Biomass and CDA activity at (◆) 150, (■) 200 and (▲) 250 rpm.

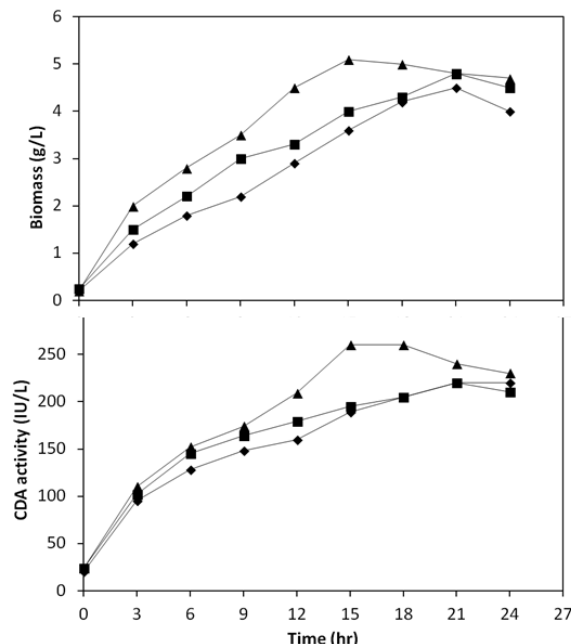


Figure 2: Effect of filling volume on biomass and CDA production in 250 ml shake flask, 250 rpm and, (◆) 100 ml, (■) 50 ml and (▲) 12.5 ml filling volume.

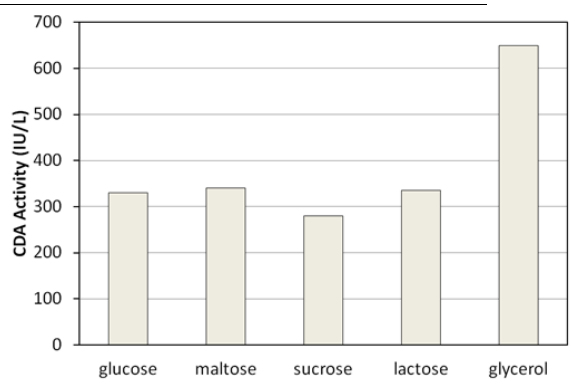


Figure 3: Effect of various carbon sources on CDA activity.

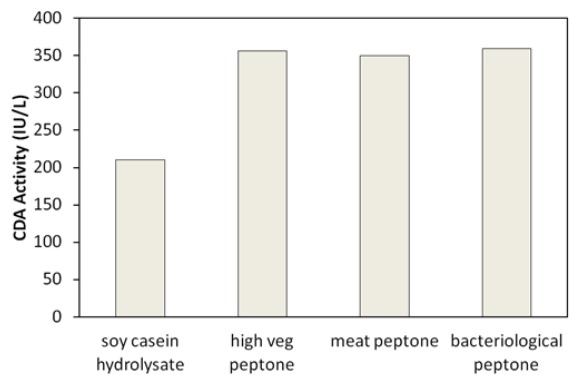


Figure 4: Effect of various complex nitrogen sources on CDA activity.

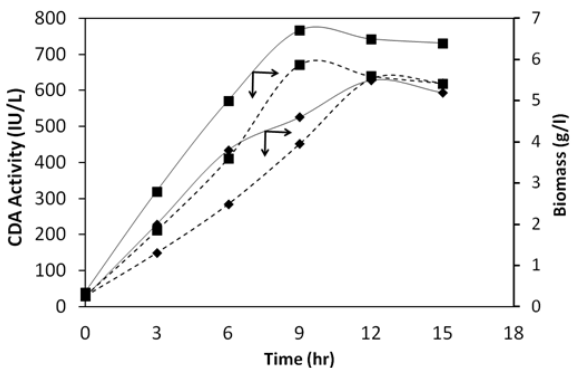


Figure 5: Growth and CDA production profile in (◆) 250 ml shake flask, (■) 3 L stirred tank reactor. Solid lines indicate biomass and dotted lines indicate CDA activity.

Design, Synthesis and Characterization of Colorimetric Receptors for Fluoride ion Detection in Competitive Media

Vijil A T V, Madhuprasad and Darshak R. Trivedi

*Supramolecular Chemistry Laboratory, Department of Chemistry,
National Institute of Technology Karnataka, Surathkal, Mangalore, Karnataka. INDIA
Email: darshak_rtrivedi@yahoo.co.in*

ABSTRACT: Four new receptors R1-R4 based on simple Schiff base were designed and synthesised for the colorimetric detection of fluoride ions in aqueous media. The receptors were characterized by FT-IR, UV-Visible and ¹HNMR spectroscopic techniques. The receptors R1, R2 and R3 are highly selective towards fluoride ion over other anions. The receptors R1, R2 and R3 showed significant colour change from light yellow to blue, colourless to dark pink and colourless to orange in DMSO solvent for TBAF with a $\Delta\lambda_{\max}$ of 150 nm, 135 nm and 130 nm respectively. Receptors R1 and R2 are able to detect inorganic fluoride such as NaF in aqueous solutions. The mechanism involved in the colour change was initially hydrogen bond followed by deprotonation and stabilization of complex through Intramolecular Charge Transfer (ICT). This was further confirmed by ¹H NMR titration. The receptor R1 proved itself to be potentially useful for real-life applications by detecting fluoride ion quantitatively in sea water and commercially available mouth wash.

Keywords: Anion receptor, Aqueous detection, Hydrogen bonding, Supramolecular chemistry, Naked eye detection

INTRODUCTION

The design and synthesis of organic chemoreceptors for selective detection of anions and metal ions has gained attention of scientific community over past two decades due to their potential applications in chemical, agricultural, industrial, biological and environmental sciences. Nevertheless, among the wide range of anions, the detection of fluoride ion has gained greater attention because of its dual functionality. (Duke, R M et al., 2010; Gale, P A, 2010; Sessler, J L et al., 2006; Stibor, I, 2005) Though instrumental methods such as fluoride ion monitor probes are available for the detection of fluoride ion, it consumes more time and requires experienced efforts to operate. Contrary, colorimetric method of detection is instantaneous, equally selective and sensitive and hence development of

colorimetric receptors for fluoride ion is of great significance. (Bose, P et al., 2010; Piatek, P et al., 2002) However, majority of these receptors could be operated only in noncompetitive organic solvents for the detection of tetrabutylammonium fluoride (TBAF) and not in the aqueous medium. This drawback is due to the higher acidity of water than that of protons which is involved in binding process and hence the F⁻ ion readily gets solvated in aqueous solutions. On the other hand, design and synthesis of receptor molecules capable of detecting inorganic fluoride such as sodium fluoride(NaF) in aqueous medium for real-life applications is a daunting task and yet to be explored by chemists. Few receptors have been reported that are capable of detecting fluoride ion in aqueous solutions (organic/water mixture). However, majority of these detection processes are restricted either to TBAF. (Sokkaligam, P et al., 2011) or

4th International Engineering Symposium - IES 2015

March 4-6, 2015, Kumamoto University, Japan

only to test papers which requires several minutes for the detection process. (Lin,Z H et al., 2006) These drawbacks restrict the use of reported receptors for real-life applications such as detection of inorganic fluoride in ground water. However, recently Gunnlaugsson, T et al. (2005) reported the detection of NaF in aqueous solutions and Das et al. (2011) have demonstrated the extraction of inorganic fluoride ion from ground water to organic solvent. Nevertheless, the challenges of designing and synthesizing the receptors with real-life applications, such as detection of inorganic fluoride in aqueous media still remain.

Herein, we report a new receptors R1-R4 (Figure 1), based on simple Schiff base for the detection of inorganic fluoride ion in aqueous solutions. The receptor R1 encompasses hydroxyl (-OH) functional group at 4th position on naphthalene backbone and a nitro group (-NO₂) at *p*-position of the phenyl ring to facilitate the Intramolecular Charge Transfer (ICT). Receptor R2 and R3 were synthesized to verify the role of electron withdrawing nitro group (-NO₂) and electron donating hydroxyl group (-OH) at *p*- position of phenyl ring on ICT mechanism. Receptor R4 was designed to examine the role of hydroxyl group (-OH) at 4th position of naphthalene backbone as a binding site.

EXPERIMENTAL SECTION

All the chemicals were purchased from sigma Aldrich, Alfa Acer chemicals and were used without further purification. All the other solvents used were purchased commercially and used without any further purification. The uv-visible titrations were carried out using ocean optics SD2000-Fiber Optics apectrometer. The ¹H NMR was recorded on a Bruker (400 MHz) instrument using TMS as internal reference and DMSO-d6 as solvent. Infra-red (IR) spectra were recorded using Nicolet Avatar 330 FTIR (Thermo Electron Corporation) instrument. Melting point was recorded on Stuart Melting Point SMP3.

A mixture of corresponding naphthaldehyde derivatives (4-hydroxy naphthaldehyde /1- naphthaldehyde, 0.58 mmol) and various amines (4-Nitro aniline/aniline/4-hydroxy aniline, 0.58

mmol) was reacted in ethanol solvent using laboratory sonicator for 15 minutes at room temperature. The reaction was catalyzed by a drop of acetic acid. The solid product was obtained after sonication was filtered and washed with ethanol to get the target compounds (R1, R2, R3 and R4). Receptors R1-R4 were synthesized as depicted in Figure-1 and characterized using melting point determination and FT-IR analysis.

Analytical Data

4-{(E)-[(4-nitrophenyl)imino]methyl}naphthalen-1-ol (R1):

yield 85 %; MP >350° C; FT-IR: 3241 cm⁻¹ (-OH stretching), 1643 cm⁻¹ (C=N stretching), 1540 cm⁻¹ (NO₂ absorption).

4-[{(E)-(phenylimino)methyl]naphthalen-1-ol (R2):

yield 80 %; MP 170° C; FT-IR: 3066 cm⁻¹ (-OH stretching), 1584 cm⁻¹ (C=N stretching).

4-{(E imino) methyl} naphthalen-1-ol-[(4-hydroxyphenyl) (R3):

yield 83%; MP 136° C; FT-IR: 3339and 3276 cm⁻¹ and (-OH stretching), 1643 cm⁻¹ (C=N stretching).

4-[{(E)-(naphthalen-1-ylmethylidene) amino]phenol (R4):

yield 85 %; MP 154° C; FT-IR: 1643 cm⁻¹ (C=N stretching), 1540 cm⁻¹ (NO₂ absorption).

RESULTS AND DISCUSSION

Initially the receptors R1-R4 were investigated for colorimetric detection application in presence of different anions in dry DMSO solvent. The receptor solutions (2.5×10^{-5} M) were treated with different anions (1 equiv.) such as fluoride, chloride, bromide, iodide, nitrate, hydrogensulphate, dihydrogenphosphate and acetate in the form of tetrabutylammonium (TBA) salts. The Receptor R1 showed remarkable colour change from pale yellow to violet blue instantaneously only with F⁻ ion. The receptors R2 and R3 showed instantaneous colour change from colourless to dark pink and dark orange respectively only with F⁻ ion. This confirms selective binding of F⁻ ion to the receptor R1 to R3. However, no colour change was observed on addition of

4th International Engineering Symposium - IES 2015

March 4-6, Kumamoto University, Japan

other anions. Fig. 2 and Fig.3 show the change in the colour of receptor R1 and R2 respectively on addition of 1 equiv. of different anion solutions as TBA salts. The receptor R4 which lack hydroxyl (-OH) functional group as a binding site at 4th position on naphthalene backbone did not show any colour change upon addition of any anions including fluoride ions.

As a justification for selectivity, changes in UV-Vis absorption of receptor R1 were recorded in dry DMSO (2.5×10^{-5} M), after adding 10 equiv. of different anions. Only F⁻ ion induced instantaneous red shift in the absorption maxima and all other anions did not cause any change in the absorption which confirms that other anions did not show any interference with detection process.

The sensing ability of receptor R1 in dry DMSO solution (2.5×10^{-5} M) was examined using UV-Vis spectrophotometric titration experiments by gradually adding a standard solution of TBAF. Fig. 4 shows the UV-Vis spectral changes of R1 on titrating with F⁻ ions. With the constant increase in the concentration of F⁻ ion, the peak at 400 nm was decreased and new band at 550 nm formed and developed with the formation of a clear isobestic point at 434 nm, which corresponds to the stabilized structure of R1 after the addition of fluoride ion. Red shift of 150 nm was observed, which was ascribed to the formation of Intramolecular Charge Transfer (ICT) complex. The same trend was observed as shown in fig.5 in case of the receptor R2 where a red shift of 135 nm was observed.

To explore the applicability of receptor R1, UV-Vis titration was carried out in DMSO using sodium fluoride (NaF) solution in water as fluoride source. Upon increasing addition of NaF to receptor R1, the peak at 400 nm was decreased and new band at 550 nm formed and developed with the formation of a clear isobestic point at 434 nm as shown in Fig. 6. Similarly, the receptor R2 showed a new peak at 525 nm corresponding to ICT with a red shift of 135 nm. These results revealed that the titration spectra did not show much difference on addition of aqueous inorganic fluoride to receptor solution (DMSO:H₂O, 9:1; v/v) when compared to TBAF with dry

DMSO solution of R1 and R2. This indicates the same ICT mechanism was followed in case of organic and aqueous media for detection of F⁻ ion. However, Receptors R3 with hydroxyl group at p-position on phenyl ring failed to show any colour change with aqueous NaF solution. This may be attributed to the lack of ICT mechanism due to electron releasing hydroxyl group at p-position on phenyl ring. Receptor R4 which do not contain the hydroxyl group at 4th position on naphthalene scaffold did not show any colour change with either TBAF or NaF solution confirms that -OH functional group act as a binding site for fluoride ion detection in present investigation.

Presence of nitro substitution at p-position of phenyl ring made the -OH proton highly acidic (Clayden, J et al., 2001) and hence the receptor R1 readily get deprotonated in presence of basic F⁻ ion. Thus, receptor R1 can detect both organic as well as inorganic fluorides with similar and highest red shift.

Furthermore, the receptor R1 was tested for the detection of F⁻ ions in sea water, collected from Arabian Sea (latitude $13^{\circ}0'33.99''$, longitude $74^{\circ}47'17.23''$) and commercial mouthwash. When a drop of sea water/mouthwash was added to the DMSO solution of receptor R1, a permanent change in colour from colourless to light pink was observed as shown in Fig. 7. Thus, the F⁻ ion in sample water can be detected with naked eye by adding a drop of water sample containing F⁻ ion to the receptor solution. The amount of F⁻ ions in sea water/mouthwash was determined using a calibration curve which was established by plotting absorbance v/s concentration of F⁻ ions (Fig. 8). The curve showed 1.45 ppm of F⁻ ions in sea water, which is comparable with standard values (WHO Technical Report, 1994).

The $\Delta\lambda_{\max}$ for organic solutions of receptors R1-R4 upon addition of TBAF are discussed herein. In case of R1, extended conjugation was observed upon binding of F⁻ ion due to the presence of -NO₂ group at p-position to phenyl ring and as a result ICT was achieved with a maximum red shift of 150 nm. However, in case of R2, absence of -NO₂ groups at p-position

4th International Engineering Symposium - IES 2015

March 4-6, 2015, Kumamoto University, Japan

to phenyl rings did not make much difference in the sensitivity. As the receptor R3 bearing electron donating -OH group, ICT was not feasible and hence only 130 nm red shift was observed. The receptor R4 did not show any shift in absorbance on addition of F⁻ ion. This further confirms the -OH proton at 4th position on naphthalene scaffold are responsible for binding process of F⁻ ion. The stoichiometry of the F⁻ ion complexation with receptor R1 in dry DMSO was determined by Benesi-Hildebrand method (Benesi, H et al., 1948) (Fig. 9) using TBAF. This clearly confirmed the formation of a stable 1:1 stoichiometric complex between receptor R1 and F⁻ ions. The binding constant for the receptor R1 in organic medium was found to 3.92×10^4 .

From stoichiometric studies it is clear that F⁻ ion detection using receptor L1 is a two-step process. At first, a F⁻ ion binds to receptor through hydrogen bonding and thus a 1:1 adduct is generated to form a R1...F⁻ complex. (Ghosh, A et al., 2009) The second F⁻ ion causes deprotonation of -OH proton in receptor R1 which resulted in increased electron density over the complex system. This induced a charge separation in the molecule (Figure 10) and hence Intramolecular Charge Transfer (ICT) interaction was observed which resulted in the optical colour change. (Cho, E J et al., 2005) The tautomer L also form hydrogen bonding initially and get deprotonated to give the stable structure M as shown in Fig.10.

CONCLUSION

To summarize, we have designed and synthesized simple Schiff base derivative R1 for the instantaneous and selective detection of inorganic fluoride (NaF) in aqueous media by simple condensation reaction between aldehyde and amine functional group using green sonochemical process. The receptor possesses high sensitivity towards F⁻ ions. The mechanism followed for the detection process is ICT. Hence on interaction with F⁻ ion the receptor R1 showed brilliant colour change from colourless to blue with a large red shift of 150 nm. This derivative proved itself as potent colorimetric fluoride

ion receptor by detecting the presence of fluoride in sea water.

ACKNOWLEDGEMENTS

Authors acknowledge The Director, NITK for providing the research infrastructure. MP is thankful to NITK for the research fellowship. Authors thank CSMCRI-Bhavnagar and Manipal Institute of Technology-Manipal for the spectral analysis.

REFERENCES

- [1] Benesi, H et al (1948), A Spectrophotometric Investigation of the Interaction of Iodine with Aromatic Hydrocarbons, *J. Am.Chem. Soc.*, Vol. 71, pp. 2703-2707.
- [2] Bose, P et al (2010), Visible and near-infrared sensing of fluoride by indole conjugated urea/thiourea ligands, *Chem. Commun.*, Vol.46, pp. 2962-2964.
- [3] Clayden, J et al (2001), *Organic Chemistry*; Oxford University Press: New York, Chapter 8, pp.197.
- [4] Das,P et al (2011), Receptor design and extraction of inorganic fluoride ion from aqueous medium, *Chem. Commun.*, Vol. 47, pp. 7398-7400
- [5] Duke, R M et al (2010), Colorimetric and fluorescent anion sensors: an overview of recent developments in the use of 1,8-naphthalimide-based chemosensors, *Chem. Soc. Rev.*, Vol.39, pp. 3936-3953.
- [6] Cho, E J et al (2005), Visible Colorimetric Fluoride Ion Sensors, *Org. Lett.*, 2005, Vol. 7, pp. 2607-2609.
- [7] Gale, P A (2010), Anion receptor chemistry: highlights from 2008 and 2009, *Chem. Soc. Rev.*, Vol.39, No.10, pp. 3746-3771.
- [8] Ghosh, A et al (2009), Influence of urea N-H acidity on receptor-anionic and neutral analyte binding in a Ruthenium(II)-polypyridyl-based colorimetric sensor, *Eur. J. Inorg. Chem.*, pp.2496-2507.
- [9] Gunnlaugsson,T et al (2005), Colorimetric "naked eye" sensing of anions in aqueous solution, *J. Org. Chem.*, Vol.70, pp. 10875-10878.
- [10] Lin,Z H et al (2006), Naked-eye detection of fluoride ion in water: a remarkably selective easy-to-prepare test paper, *Chem. Commun.*, pp. 624-626.
- [11] Piatek, P et al (2002), A selective colorimetric anion sensor based on an amide group containing macrocycle, *Chem. Commun.*, pp. 2450-2451.
- [12] Sessler, J L et al (2006), Anion Receptor Chemistry, Royal Society of Chemistry: Cambridge, Ed. J.F. Stoddart.
- [13] Sokkalingam, P et al (2011), Highly Sensitive Fluorescence "Turn-On" Indicator for Fluoride Anion with Remarkable Selectivity in Organic and Aqueous Media, *J. Org. chem.*, Vol. 76, pp. 3820-3828.
- [14] Stibor, I (2005), Anion sensing, *Top. Curr. Chem.*, Springer: Heidelberg, Berlin, pp.255.
- [15] WHO Technical Report Series- 846, Fluoride and Oral Health, Geneva, 1994.

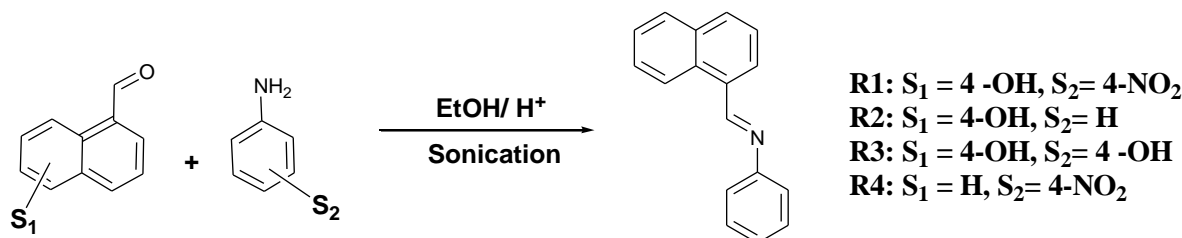


Fig.1 Syntheses of receptors R1-R4



Figure 2 Colour change of R1 (2.5×10^{-5} M) in DMSO on adding 1 equivalent of tetrabutylammonium anions: (a) free receptor (b) F^- , (c) Cl^- , (d) Br^- , (e) I^- , (f) NO_3^- , (g) HSO_4^- , (h) H_2PO_4^- , and (i) AcO^-



Figure 3 colour change of R2 (2.5×10^{-5} M) in DMSO on adding 1 equivalent of tetrabutylammonium anions: (a) free receptor (b) F^- , (c) Cl^- , (d) Br^- , (e) I^- , (f) NO_3^- , (g) HSO_4^- , (h) H_2PO_4^- , and (i) AcO^-

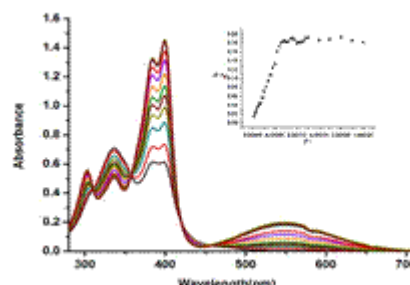


Figure 5 UV-Visible titration of R2 (2.5×10^{-5} M) in DMSO with TBAF solution from 1 to 10 equivalent. Inset: corresponding titration plot of R2 at 515 nm ($A - A_0$) vs $[\text{F}^-]$

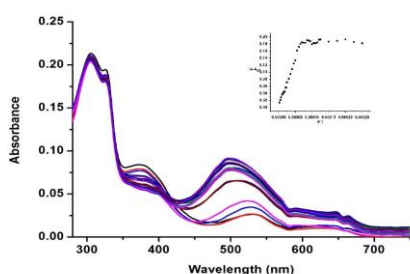


Figure 4 UV-Vis titration of R1 (2.5×10^{-5} M) with increasing concentrations of TBAF (0-10 equiv.) in dry DMSO. Inset: corresponding titration plot of R1 at 550nm ($A - A_0$) vs $[\text{F}^-]$

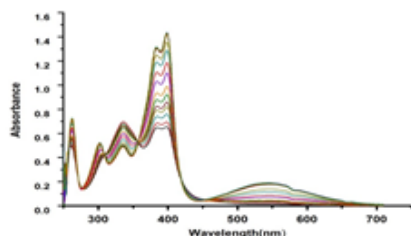


Figure 6 UV-visible titration of R1 (2.5×10^{-5} M) in DMSO with aqueous NAF solution from 1 to 10 equivalent

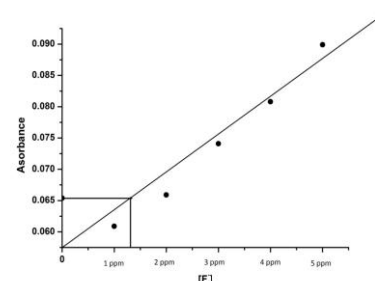


Figure 8 Calibration curve to determine the amount of F^- in sea water



Figure 7 Colour change of R1 in dry DMSO (2.5×10^{-5} M) on adding different fluoride salts (a) free receptor (b) TBAF in DMSO (c) aqueous NAF (d) one drop of mouth wash (e) one drop of sea water

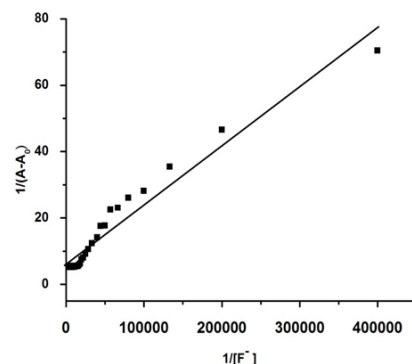


Figure 9 Benesi-Hildebrand plot of receptor R1 binding with F^- associated with absorbance change at 550 nm in dry DMSO solvent

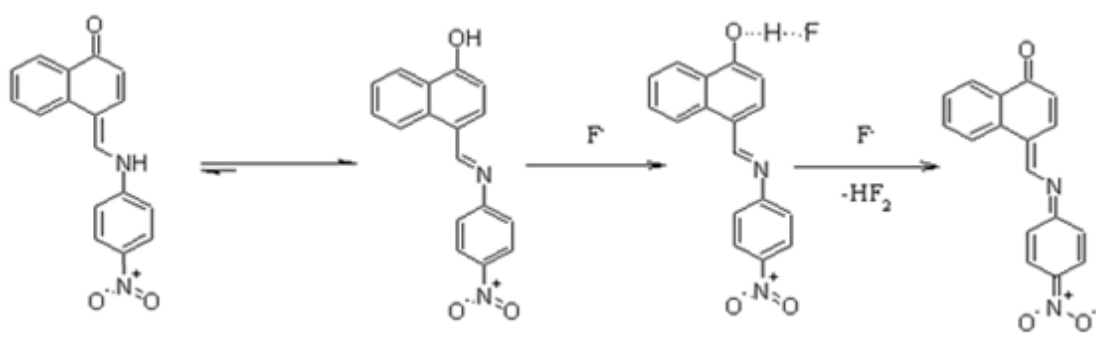


Figure 10 Detection mechanism of R1 with fluoride ion

Study on the Improved VBO model applied to NBR and on the Deterioration of NBR

**Fumiko KAWASHIMA¹, Yuma OTSUKA², Atsushi OTA³, Yasutaka MIYAZAKI³,
Kazuhito FUJIWARA² and Hidehiro HATA²**

¹ Department of advanced technology, Kumamoto University, Kurokami, 2-39-1,
Kumamoto 860-8555, Japan. e-mail:kawashima@mech.kumamoto-u.ac.jp

² Department of advanced technology, Kumamoto University.

³ Department of Mechanical System Engineering, Kumamoto University.

Abstract: Rubber is important material. The estimation of its deterioration and its constitutive equation is demanded for reliable design. In this study the improved VBO model that contains strain-acceleration term is proposed as a constitutive equation of NBR. The deterioration test in water at 60C in 1 year was carried out. NBR was softened till 9 month, and hardened after that by deterioration. The possible reason was chemical reaction against Chlorine. The mechanical properties and the variables in the proposed constitutive equation were determined with constant-strain-rate tests and relaxation tests in compression. The change of mechanical properties and variables because of deterioration were examined. Proposed model could evaluate the unique stress-strain curve observed in tests.

Keywords: NBR, constitutive equation, deterioration, VBO model, rubber

1. Introduction

Rubber is important material. The estimation of its deterioration and its constitutive equation is demanded for reliable design. In this study the improved VBO model that contains strain-acceleration term is proposed as a constitutive equation of NBR. The deterioration test in water at 60C in 1 year was carried out. NBR was softened till 9 month, and hardened after that by deterioration. The possible reason was chemical reaction against Chlorine. The mechanical properties and the variables in the proposed constitutive equation were determined with constant-strain-rate tests and relaxation tests in compression. The change of mechanical properties and variables because of deterioration were examined. Proposed model could evaluate the unique stress-strain curve observed in tests.

2. VBO model

VBO model was proposed by Kremple et al. as a constitutive equation of SUS304¹⁾.

$$\dot{\varepsilon} = \frac{\dot{\sigma}}{E} + \frac{\sigma - g[\varepsilon]}{Ek[\sigma, \varepsilon]} \quad (1)$$

where $g[\varepsilon]$ is equilibrium stress function, $k[\sigma, \varepsilon]$ is viscosity function and $X = \sigma - g[\varepsilon]$ is over stress, respectively. $g[\varepsilon]$ and $k[\sigma, \varepsilon]$ are nonlinear function. Hiroe et al. proposed eq.(2) applicable to nonlinear deformation of 2.25Cr-1Mo steel at high temperature²⁾.

$$k[\sigma, \varepsilon] = k[\varepsilon, X] = \exp \left\{ \beta_2[\varepsilon] - \frac{\beta_2[\varepsilon]}{\beta_1[\varepsilon]} X \right\} \quad (2)$$

where $\beta_1[\varepsilon]$, $\beta_2[\varepsilon]$ are viscosity control functions and assumed to be eqs.(3) and (4).

$$\beta_1[\varepsilon] = b_0 + b_1\varepsilon \quad (3)$$

$$\beta_2[\varepsilon] = c_0 + c_1\varepsilon \quad (4)$$

Figures 1 and 2 are outlines of the methods to determine $g[\varepsilon]$ and E . The $g[\varepsilon]$ is determined with relaxation test. $\dot{\varepsilon}$ and $\dot{\sigma}$ equal zero when the relaxation test finishes. Eq.(1) with $\dot{\varepsilon} = 0$ and $\dot{\sigma} = 0$ become $\sigma = g[\varepsilon]$. Therefore the stress at the end of the relaxation test equals $g[\varepsilon]$.

E is determined with $g[\varepsilon]$ and constant strain-rate test. σ equals $g[\varepsilon]$ at the intersection of stress-strain curve of constant-strain-rate test and the line of $\sigma = g[\varepsilon]$. Eq.(1) with $\sigma = g[\varepsilon]$ becomes $E = d\sigma/d\varepsilon$. Therefore the slope of the stress-strain curve at the intersection equals E .

$k[\varepsilon, X]$ is determined with eq.(1) including known variables, $g[\varepsilon]$ and E , and the constant-strain-rate test results of, $\dot{\varepsilon}$, $\dot{\sigma}$ and σ . Different strain rate under same strain gives the relation between $k[\varepsilon, X]$ and X , and the relation between $\beta_1[\varepsilon]$, $\beta_2[\varepsilon]$ and ε .

3. Test method

The test pieces were column with the diameter of 20mm and with the height of 30mm. They were sold by I.T.X Ltd as the specification No.2109. All test pieces except for pre-test pieces were in the same lot and were made in the same time.

During the deterioration test, test pieces were exposed in tap water at 60°C in the thermo bath for 0 month, 3 months, 7 months, 9months and 12 months. We named them 'not deteriorated material', '3 month material', '7 month material', '9 month material' and '12 month material',

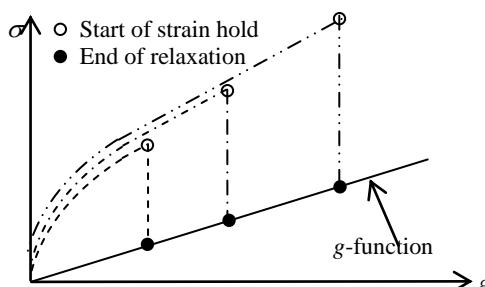


Fig. 1 Outline of the way to assume g -function

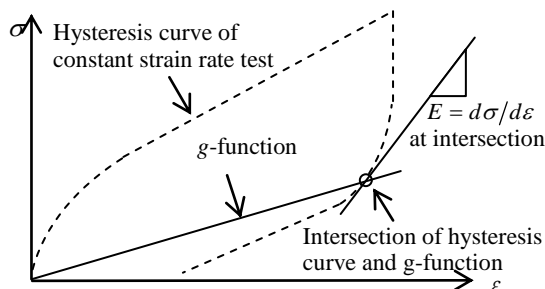


Fig.2 Outline of the way to assume E

respectively. The test machine used to the relaxation test and the constant-strain-rate test was SHIMADZU servo pulsar EHF-EG 50KN-10L. Between the test piece and the jig there was a piece of Teflon sheet to lubricate. The tests were carried out in the water at 25°C to keep the temperature of test piece.

In this essay the true strain, the true stress, the nominal strain and the nominal stress are expressed as ε , σ , ε_n and σ_n , respectively. Compression is expressed as 'plus' and tension is expressed as 'minus'. Therefore ε equals $\varepsilon = -\ln(1-\varepsilon_n)$ and σ equals $\sigma = \sigma_n(1-\varepsilon_n)$. In the relaxation test, the nominal strain rates before the strain hold were $1 \times 10^{-3}\text{s}^{-1}$ on loading process and $-1 \times 10^{-3}\text{s}^{-1}$ on unloading process. In the constant-strain-rate test, the nominal strain rate was constant (the true strain rate is not constant). Three kinds of the nominal strain rates were used;

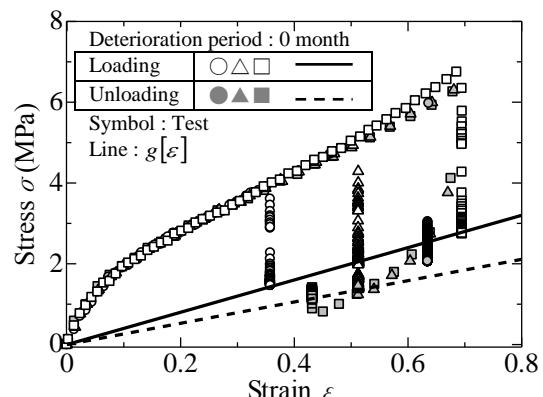


Fig.3 Example of relaxation test (stress-strain curve)

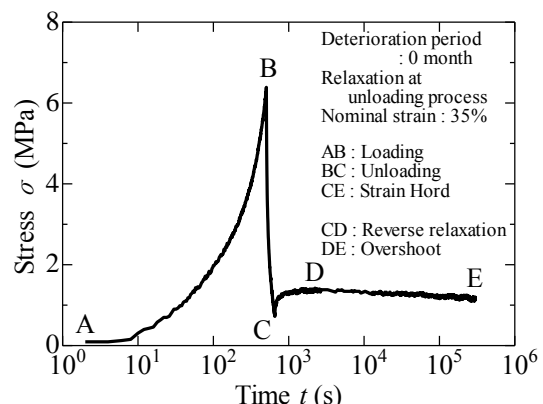


Fig.4 Example of relaxation test (the history of stress)

$\pm 1 \times 10^{-2.5} \text{ s}^{-1}$, $\pm 1 \times 10^{-3} \text{ s}^{-1}$ and $\pm 1 \times 10^{-4} \text{ s}^{-1}$. The maximum nominal strain was 50%. The absolute value of nominal strain rate of loading process and unloading process was the same.

4 test results and determined mechanical properties

The results of relaxation tests are shown in Figs.3 and 4. In the relaxation test from unloading process, there were the reverse relaxations and the overshoots; the former was the increasing stress while the strain was held, and the latter was the decreasing stress after the reverse relaxation. Figure 5 shows results of the constant-strain-rate test. The stress was influenced by the strain rate. The larger strain rate gave the larger stress. The stress decreased rapidly when the unloading began. After that the influence of the strain rate to the stress was hardly observed.

The mechanical properties and variables determined with tests are a_1 , b_0 , b_1 , c_0 and c_1 . They are shown in Table 1. $g[\varepsilon]$ was assumed to be proportional to ε ; $g[\varepsilon] = a_1 \varepsilon$. b_0 , b_1 , c_0 and c_1 are variables for X [MPa] and k [s]. The $g[\varepsilon]$ of not deteriorated material is shown in Fig.3. The $g[\varepsilon]$ was determined as the stresses of the end of the relaxation tests. It was approximated to be proportional to ε because of the test results. The $g[\varepsilon]$ of loading process and that of unloading

process after overshoots was different. To finish the relaxation test, the material deteriorated for long time took long time. The not deteriorated material needed $1 \times 10^5 \sim 3 \times 10^5$ s to finish the relaxation test. 7 month material needed more than 8.6×10^5 s, and we stopped the relaxation test. The $g[\varepsilon]$ of 9 month material and 12 month material were determined with the following assumptions.

- > $g[\varepsilon]$ is proportional to ε .
- > The difference between $g[\varepsilon]$ of the loading process and that of the unloading process is little and negligible.
- > If the reverse relaxation does not occur in the relaxation from the unloading process, then g is smaller than the stress of the beginning of the strain hold.
- > If the reverse relaxation occurs in the relaxation test from the unloading process, then $g[\varepsilon]$ is larger than the stress of the beginning of the strain hold, and is smaller than the maximum stress of the reverse relaxation.

Figure 6 shows how to determine the $g[\varepsilon]$ of 9 month material and 12 month material. $k[\varepsilon, X]$ of not deteriorated material is shown in Fig.7. A datum for every 10% was picked out in range of 20%-60%. Three data of the same strain and of the different strain rate were used to make approximate line. The X -section and the $k[\varepsilon, X]$ -section were used to determine $\beta_1[\varepsilon]$ and $\beta_2[\varepsilon]$. $k[\varepsilon, X]$ -section were used to determine $\beta_1[\varepsilon]$ and $\beta_2[\varepsilon]$.

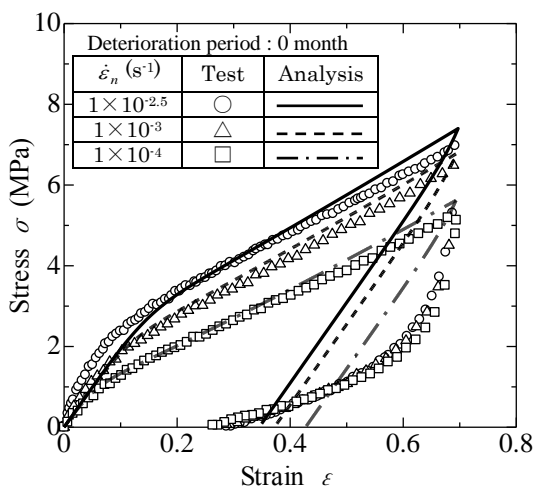


Fig.5 Example of coonstant-strain-rate test and simulation with VBO model

Table 1 Mechanical properties and variables of VBO model

	Deterioration period (month)			
	0	3	9	12
E (MPa)	19.9	13.6	9.44	10.3
a_1 (MPa) ^{*1)}	3.984	3.244	2.441	2.565
b_0 ^{*2)}	3.574	0.5658	2.409	1.211
b_1 ^{*2)}	4.447	12.86	8.199	7.775
c_0 ^{*3)}	8.043	9.357	8.876	8.592
c_1 ^{*3)}	4.297	-1.595	6.269	8.466

*1) $g[\varepsilon] = a_1 \varepsilon$

*2) b_0 and b_1 are for X (MPa)

*3) c_0 and c_1 are for k (s)

5. Influence of deterioration

The surfaces of deteriorated test pieces became white. The white became thicker with the deterioration period. The phenomenon is considered as 'whitening' because of the hydrolyzation or chlorine. The inner part of test piece was not white. The edge of test piece of 12 month material pointed. The relations between the deterioration period and the stress, the mechanical properties and the variables of VBO model are shown In Figs.8-12. $A(t)$

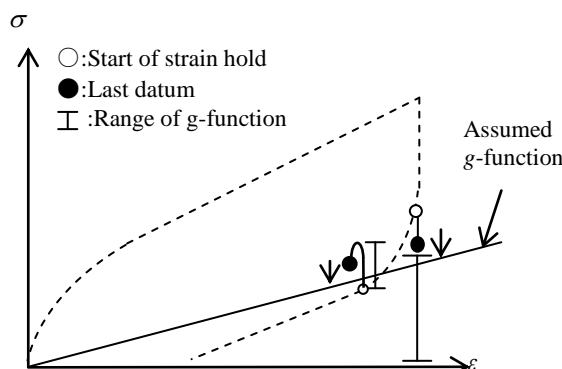


Fig.6 Outline of the way to assume $g[\varepsilon]$

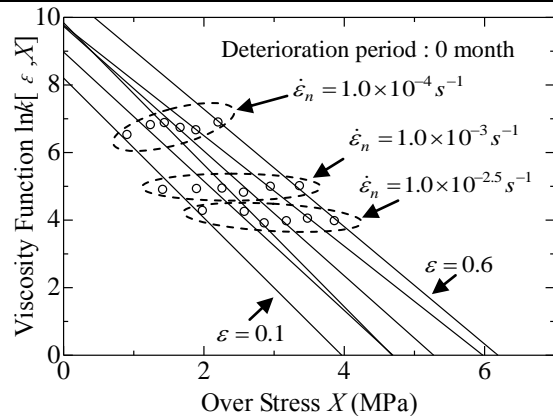


Fig.7 Method of evaluating $k[\varepsilon, X]$

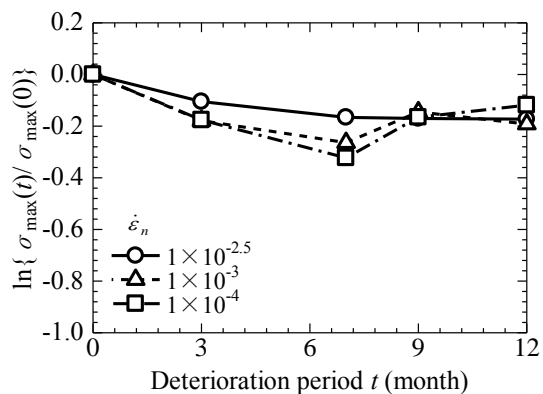


Fig.8 Deterioration of maximum stress expresses the mechanical property A deteriorated for t month. σ_{\max} in Fig.8 expresses the maximum stress at the nominal strain of 0.5 in a constant-strain-rate test. E , a_1 and σ_{\max} decreased till 9 month but increased from 9 month to 12 month. It was reported that NBR exposed to tap water containing less than 1.4ppm chlorine at room temperature for ten years was softened³⁾. Also it was reported that NBR exposed to tap water containing 200ppm chlorine at 40C in 1000 hours was hardened⁴⁾. The density of chlorine and the temperature dividing the softening and the hardening is not known. The density of chlorine on the surface of the test pieces is being measured now.

$\beta_1[\varepsilon]$ is shown in Fig.11. $\beta_1[\varepsilon]$ with the larger strain was larger. The influence of the deterioration on the average of $\beta_1[\varepsilon]$ was not clear. $\beta_2[\varepsilon]$ is shown in Fig.12. The influence of the strain on $\beta_2[\varepsilon]$ was not clear. The average of $\beta_2[\varepsilon]$ became small till 3 month and became large after that.

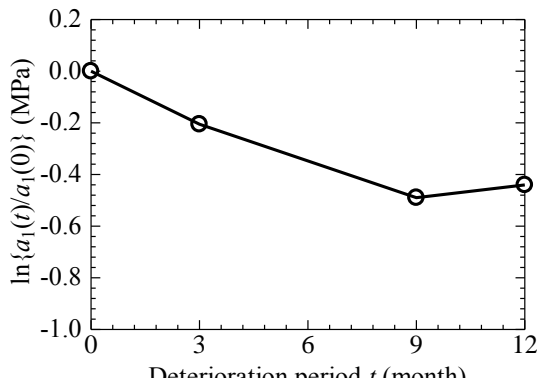


Fig.9 Deterioration of $g[\varepsilon]$

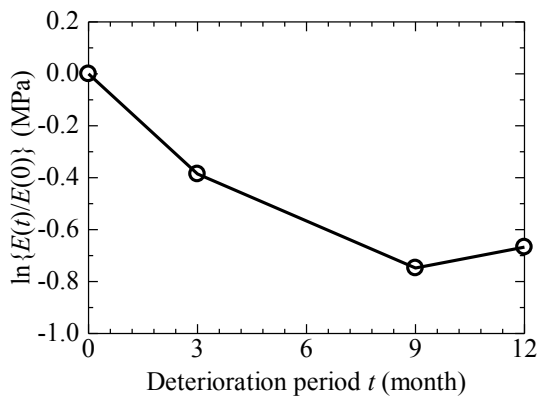


Fig.10 Deterioration of Young's modulus

6. The simulation with VBO model and with improved VBO model

To confirm the validity of VBO model, the mechanical properties and the variables, the stress-strain curves of the constant-strain-rate tests were simulated with VBO model. The examples of the results are shown in Fig.5. The simulated curves of loading process corresponded with that of the tests. However, the rapidly decrease at the start of the unloading process could not be simulated. The probable reason was that VBO model did not contain the strain acceleration term. The acceleration of strain occurred in the test at that point. On the other hand, the constitutive equations containing the strain acceleration terms could express the rapidly decrease. We proposed the improved VBO model expressed in eq.(5).

$$\dot{\varepsilon} = \frac{\dot{\sigma}}{E} + \frac{\sigma - g[\varepsilon]}{Ek[\varepsilon, X]} - C\ddot{\varepsilon} \quad (5)$$

$g[\varepsilon]$ and E can be determined with the same way mentioned in the section 2 and

they are the same as that in table 1. $k[\varepsilon, X]$ can not be determined with the way in Section 2, because of the strain acceleration of the true strain. $k[\varepsilon, X]$ in improved VBO model was determined with the relaxation test ($\dot{\varepsilon} = \ddot{\varepsilon} = 0$). E and $g[\varepsilon]$, the ε , σ and $\dot{\sigma}$ taken with the relaxation test and $\dot{\varepsilon} = \ddot{\varepsilon} = 0$ are substituted into eq.(5), then $k[\varepsilon, X]$ is determined. The results are shown in table2, Fig.13 and Fig.14.

C , the coefficient of $\ddot{\varepsilon}$, was assumed to be the constant. C was determined in order that the simulation corresponded with the test. $\ddot{\varepsilon}$ at the beginning of the unloading process in constant-strain-rate test could not be quantified. It was because the strain rate changed so fast that enough data could not be gotten. In the simulation $\ddot{\varepsilon}$ was assumed to be the constant of $-1 \times 10^{-4} \text{ s}^{-2}$. In table 3 the assumed value of C is shown. In Fig.15 the simulation with eq.(5) is shown. The rapidly decrease of the stress at the start of the unloading process could be simulated. But, in the range that the stress was less than $g[\varepsilon]$, the simulation did not correspond with the test.

7. Conclusion

- (1) VBO model is valid to express the stress-strain curve of loading process of constant-strain-rate test of NBR.
- (2) With the deterioration, the maximum stress, E and $g[\varepsilon]$ decreased till 9 month. They increase after that.
- (3) Improved VBO model containing the strain acceleration term might be able to express the stress-strain curve of the unloading process.

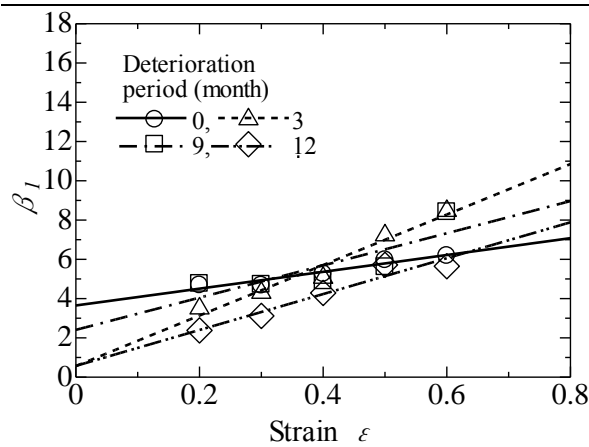


Fig.11 Deterioration of $\beta_1[\epsilon]$

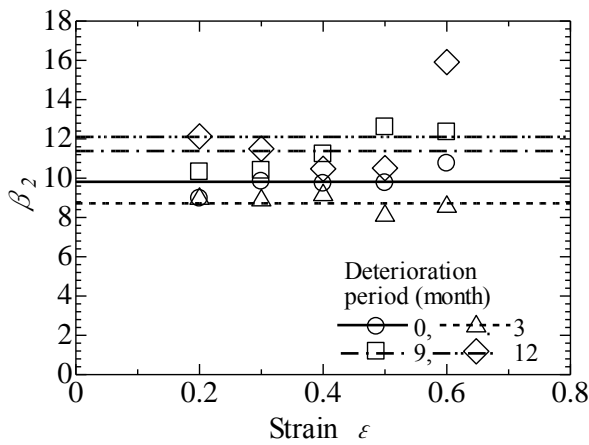


Fig.12 Deterioration of $\beta_2[\epsilon]$

Table 2 variables of improved VBO model (deterioration period : 0 month)

b_0	b_1	c_0	c_1
2.977	3.272	8.798	2.962

b_0 and b_1 are for X (MPa)

c_0 and c_1 are for k (s)

References

- 1) T. Hiroe, Y. Nakao, S. Matsumoto, K. Fujiwara and H. Hata, "Cyclic Inelastic Deformation Behavior of Solid Polymers and an Application of the Modified Overstress model to Polyethylene", Transaction of the Japan Society of Mechanical Engineers, Series A, Vol. 71, No. 705, pp.824-830 (2005).
- 2) T. Hiroe and T. Igari, "The Viscoplasticity Theory Applied to the Inelastic Analysis at Elevated Temperatures", Nuclear Engineering and Design, Vol.133, Issue 2, pp.225-238 (1992).
- 3) Y. Mitsuhashi, J. Hatakeyama, Y. Otake and M. Furukawa, "The Degradation Mechanism of NBR Invaded by Chlorine in Tap Water", Journal of the Society of Rubber Science and Technology, Japan, Vol.77, No.9, pp.301-305 (2004).
- 4) Y. Mitsuhashi, J. Hatakeyama, Y. Otake and M. Furukawa, "The Degradation Mechanism of NBR Invaded by High Concentration Chlorine Water", Journal of the Society of Rubber Science and Technology, Japan, Vol.78, No.3, pp.98-102 (2005).

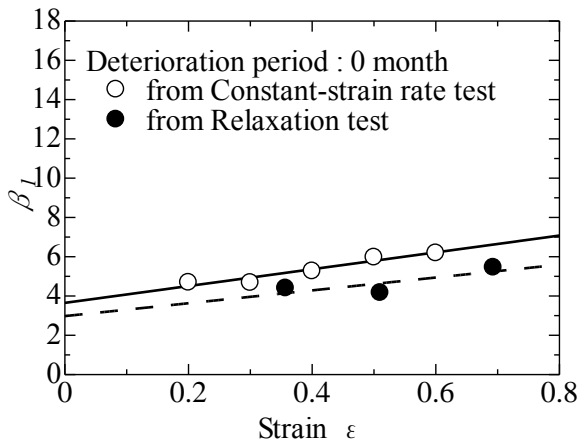


Fig.13 $\beta_1[\epsilon]$ from relaxation test
 (deterioration period : 0 month)

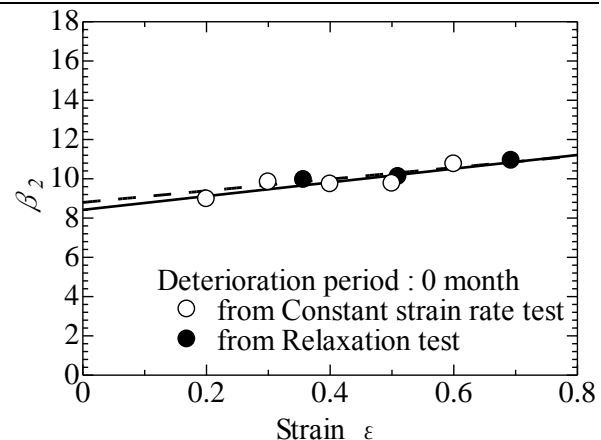


Fig.14 $\beta_2[\epsilon]$ from relaxation test
 (deterioration period : 0 month)

Table 3 C for improved VBO model

$\dot{\epsilon}_n$ (s ⁻¹)	$1 \times 10^{-2.5}$	1×10^{-3}	1×10^{-4}
C (s)	10	25	150

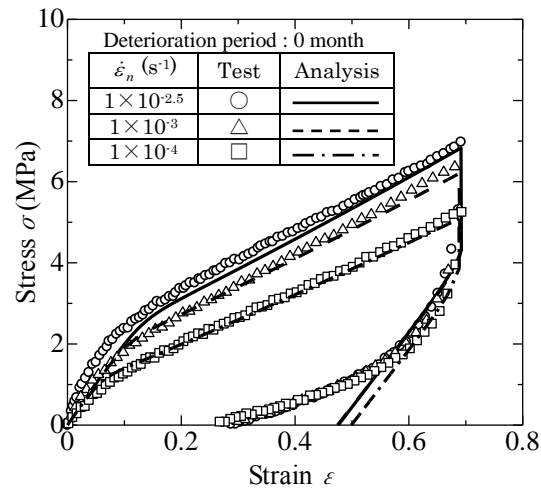


Fig.15 Simulation with improved VBO model

DECOLORISATION OF SYNTHETIC AND TEXTILE WASTEWATER BY FENTON PROCESS

Kumara Guru B. N.¹ and M. K. Krishna²

1 Assistant Manager, Safety, Health & Environment, Tata Chemicals Ltd, Ahmedabad, India

2 HOD & Assistant Professor, Department of Environmental Engineering, P.E.S.C.E Mandya, India

ABSTRACT: Wastewater from Textile industries are one among the principal sources for contamination of Aromatic Amines into the environment. The Color of these effluents is basically due to the application of reactive dyes. Predominantly, the degradation of Azo dyes contributes to about 70% of all used dyes, and its intricacy owes to their complex structure and synthetic nature. Effluents originating from dye invention & fabrication, and its subsequent application masquerades a foremost threat to surrounding ecosystems, attributable to their toxicity and potentially carcinogenic nature. In this case study, the degradation of dyes by means of proficient medium was premeditated with the Fenton process, an alternative to Advanced Oxidation Technology. The focal intent of this research was to scrutinize the optimum conditions for efficient color removal from the Textile effluent. A Bench Scale Reactor with working volume of 923.25cm³ for synthetic wastewater was set up, wherein removal efficiency achieved was a maximum of about 90.47%. The identical optimum conditions were adopted to confirm the capability of color removal in Textile wastewater. About 18% decline was observed in the amputation of color in contrast to the synthetic wastewater.

Keywords: Azo dye, Fenton, textile, wastewater, color

INTRODUCTION

Wastewater from textile industry comprises more than 10,000 dyes and 280,000 tonnes of textile dyes are discharged every year worldwide. Azo dyes which are abundantly used in the textile industry are characterized by nitrogen to nitrogen double bond (-N=N-). The color of dyes is due to azo bond and associated chromophores, hence disposal of dyes into surface water not only affects the aesthetic but also leads to bio toxicity [Nilesh P. Tantak et al. 2006].

Synthetic dyes are also employed in leather tanning industry, in paper production, in agricultural research, in photo electrochemical cells, and in hair colorings. These dyes also strongly absorb sunlight, thus impeding the photosynthetic activity of aquatic plants and seriously threatening the whole ecosystem. The

color problem in some textile wastewater is caused by the residual dyes which need more efforts for its treatment [Abo-Farha S. A et al. 2010]. Therefore, there is a clear need to treat dye wastewater prior to disposal. Most of the pollutants, except color, can be reduced by chemical, physical or biological methods. Several methods have been investigated to treat azo dye containing wastewater [Nilesh P. Tantak et al. 2006] Amongst them, Fenton process have been chosen for the current study.

Fenton's reagent has been found effective in treating various industrial wastewater components including aromatic amines and wide variety of dyes, pesticides and surfactants, as well as many other substances [Barbusinski K et al. 2001].

4th International Engineering Symposium - IES 2015

March 4-6, Kumamoto University, Japan

METHODOLOGY

Swarf was produced from metal sawing and the particle size of swarf was in the range of 0.5-2.5 mm. Chemical constitution of the steel used as catalyst (Swarf) is shown in table 1. Analytical grade H₂O₂ and H₂SO₄ were used.

A bench scale set up used for the Fenton process consists of a reactor with diameter 6.6 cm and height 50 cm with working volume of 923.25cm³.

The synthetic wastewater is prepared for selected pH with varying amount of H₂SO₄ and H₂O₂ is added as an oxidising agent. The pH 2, 3, 4, 5 and 6 are used to determine the maximum colour removal.

The prepared solution are fed into the reactor at varied flow rates i.e., 2ml, 3ml, 4ml, 5ml and 6ml/min under gravity. For every hour, the samples were tested using UV-VIS Spectrophotometer at 510 nm. Standard curve is used to determine color unit in wastewater samples.

RESULTS AND DISCUSSIONS

The experimental result signifies the effect of flow rate and pH on the removal of color by column study.

Continuous column studies conducted for synthetic wastewater at varied flow rates of 2, 3, 4, 5 and 6ml/min over a period of 5 hour are shown in fig 1-5. The maximum colour removal of 90.47% is achieved at 4ml/min after 4 hour collection time as shown in fig 3. With this optimum flow rate of 4ml/min, maximum color removal efficiency of about 90.47% is achieved under pH 3 in 4 hour duration as depicted in fig 7. Thereby, flow rate of 4ml/min and pH 3 are selected for comparison with textile wastewater. Figures 6-10 indicates variation of color and iron concentration with time at varying pH.

Under this optimum pH and flow rate about 72.72% of reduction in color is observed for raw textile wastewater as shown in table 2. About 18% decrease is observed in color removal in comparison with synthetic wastewater.

CONCLUSIONS

The removal of color from both synthetic and textile wastewater mainly depends on dissociation of iron ions in Fenton Process. Fenton's reagent is found effective in treating azo dye of textile wastewater.

REFERENCES

- [1] Abo-Farha S. A., 2010. Comparative Study of Oxidation of Some Azo Dyes by Different Advanced Oxidation Processes: Fenton, Fenton-Like, Photo-Fenton and Photo-Fenton-Like. Chemistry Department, Faculty of Science, Al-Azhar University (Girls), Nasr City, Cairo, Egypt, Journal of American Science, 6(10).
- [2] Barbusiński K, Filipek K., 2001. Use of Fenton's Reagent for Removal of Pesticides from Industrial Wastewater. Institute of Water and Wastewater Engineering, Silesian University of Technology, Konarskiego 18, 44-101 Gliwice, Department of Water Protection, Central Mining Institute, 40-166 Katowice, Poland, Vol. 10, No. 4, pp207-212.
- [3] Nilesh P. Tantak, Sanjeev Chaudhari., 2006. Degradation of azo dyes by sequential Fenton's oxidation and aerobic biological treatment. Centre for Environmental Science and Engineering, Indian Institute of Technology Bombay, Powai, Mumbai 400076, Maharashtra, India, Journal of Hazardous Materials, pp698-705.

Table 1: Chemical constitution of the steel used as a catalyst (Swarf)

En Number	Chemical Constitution (%)			
	Cu	Mn	Si	Sp. gravity
9	0.50 -	0.50 -	0.05 -	0.060
	0.60	0.80	0.35	

Table 2: Comparison of colour removal efficiency between synthetic and textile wastewater

Time (hours)	Concentration of dye (mg/l)		Color (Hazen)		Color Removed (%)		Iron Concentration (mg/l)	
	Synthetic Waste Water	Textile Waste water	Synthetic Waste water	Textile Waste water	Synthetic Waste water	Textile Waste water	Synthetic Waste water	Textile Waste water
Initial	1.85	0.94	21	11	-	-	1.14	0.74
1	0.47	0.54	5	6	76.19	45.45	2.08	1.56
2	0.38	0.42	4	5	80.95	54.54	3.78	2.14
3	0.23	0.30	3	3	85.71	72.72	4.88	2.97
4	0.16	0.28	2	3	90.47	72.72	4.95	3.46
5	-0.09	0.27	-	3	-	72.72	-	3.88
6	-0.30	0.25	-	3	-	72.72	-	4.54
7	-	0.24	-	3	-	72.72	-	4.98

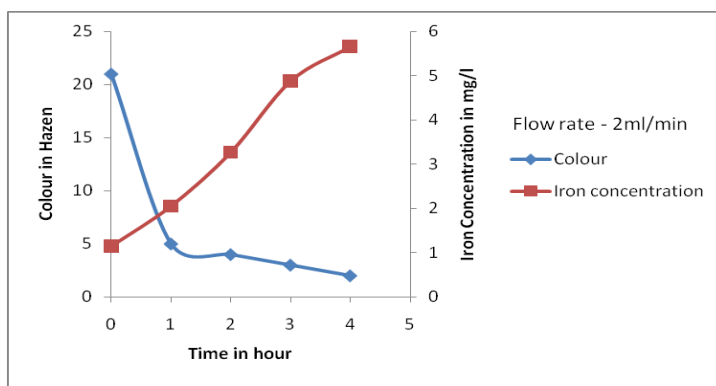


Fig 1: Variation of Color and Iron concentration with time for 2ml/min

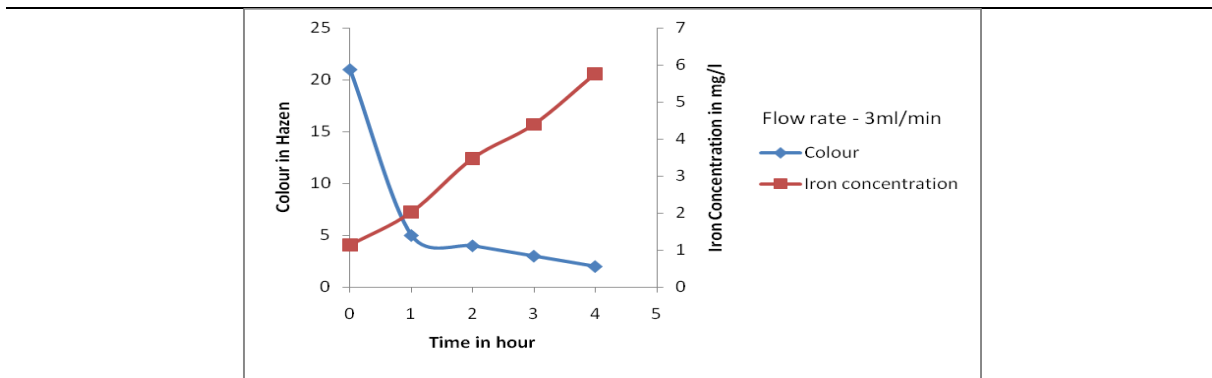


Fig 2: Variation of Color and Iron concentration with time for 3ml/min

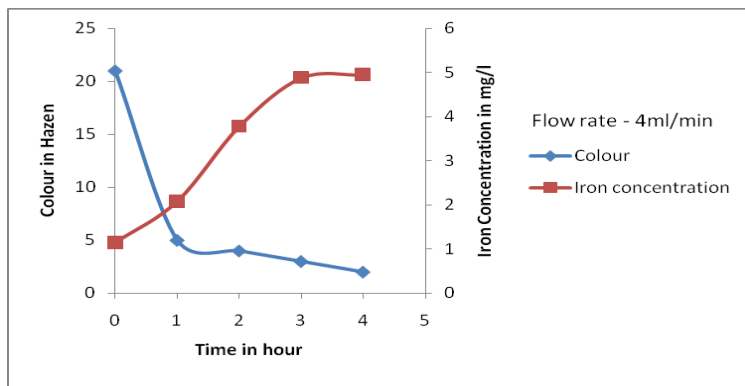


Fig 3: Variation of Color and Iron concentration with time for 4ml/min

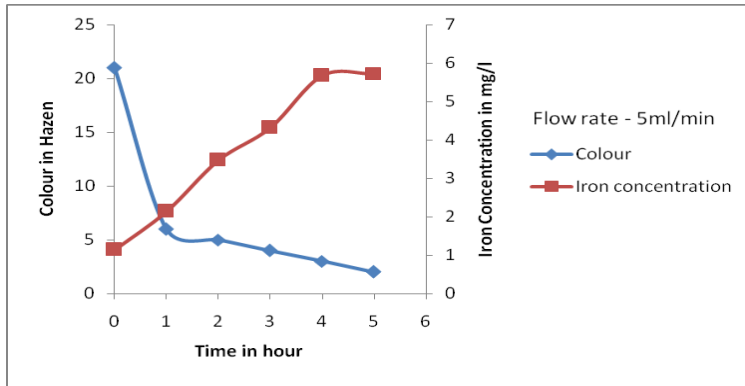


Fig 4: Variation of Color and Iron concentration with time for 5ml/min

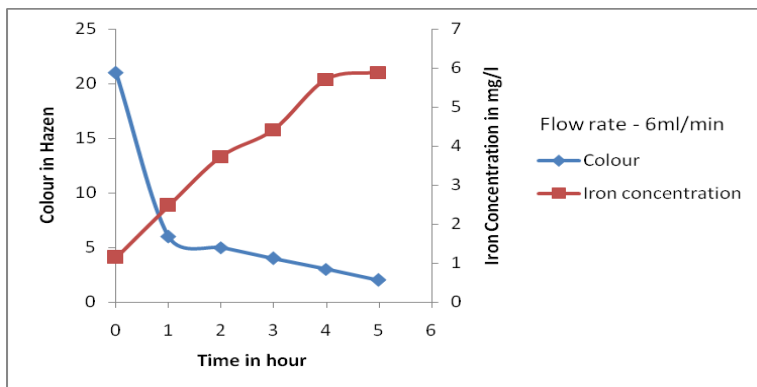


Fig 5: Variation of Color and Iron concentration with time for 6ml/min

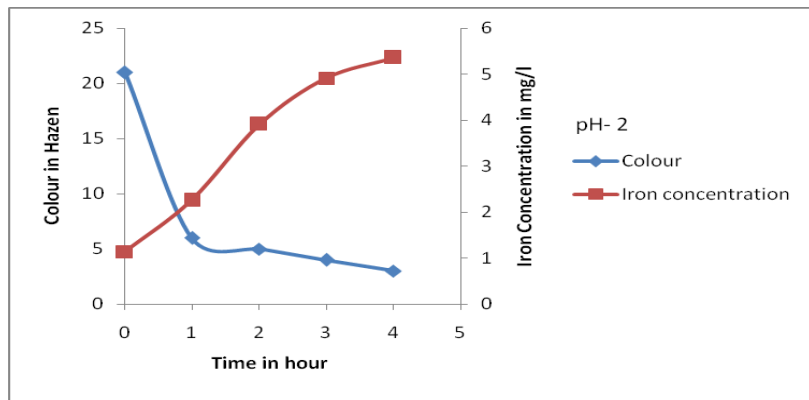


Fig 6: Variation of Color and Iron concentration with time at pH2

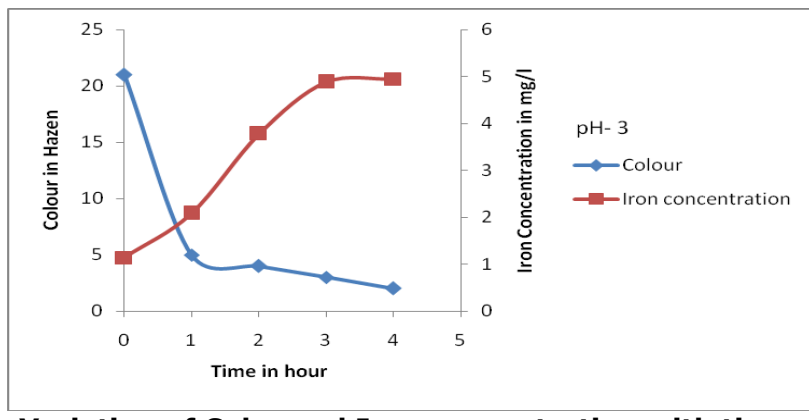


Fig 7: Variation of Color and Iron concentration with time at pH3

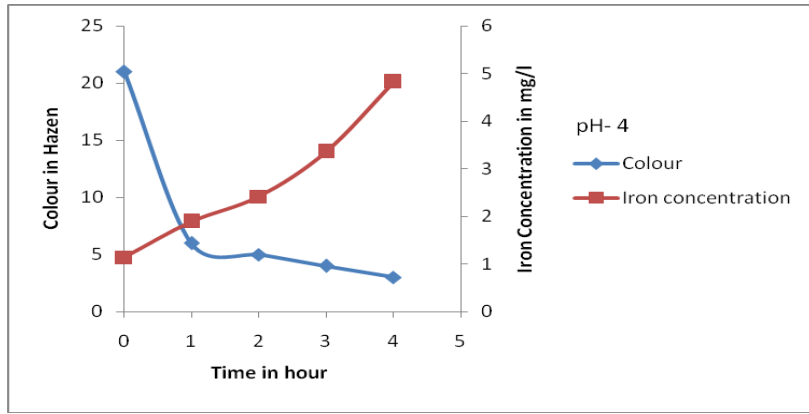


Fig 8: Variation of Color and Iron concentration with time at pH4

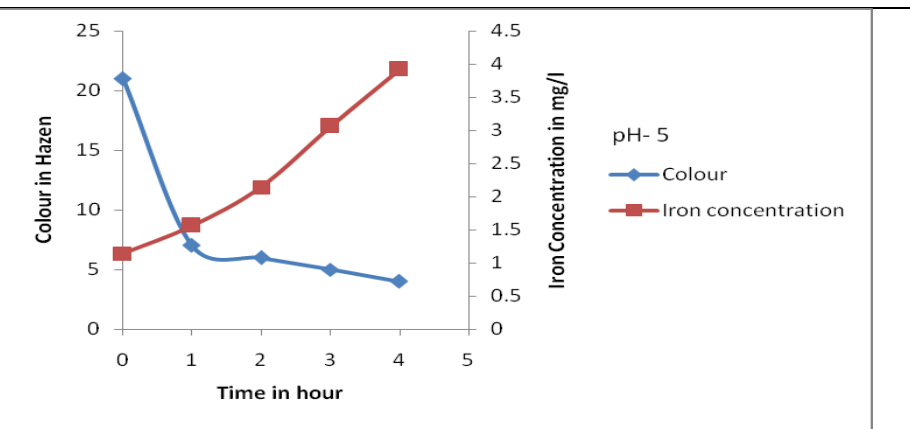


Fig 9: Variation of Color and Iron concentration with time at pH5

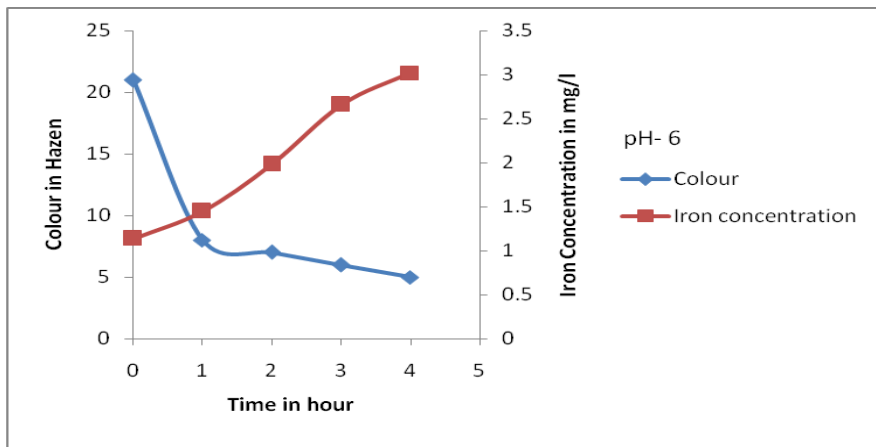


Fig 10: Variation of Color and Iron concentration with time at pH6

Synthesis of site-specifically PEGylated Uricase conjugates with improved pharmaceutical properties for the treatment of hyperuricemia

Pooja Nanda¹ and P.E. Jagadeesh Babu²

*Department of Chemical Engineering
National Institute of Technology Karnataka, Surathkal, India
Email: poojananda88@gmail.com*

ABSTRACT: Uricase, a therapeutic enzyme, used for the treatment of hyperuricemia and gout, is currently administered in its conjugated form with polyethylene glycol (PEG). PEG conjugation aids size enlargement, increased serum half-life, reduction in immunogenicity and kidney ultrafiltration rate. Though it is a highly successful therapeutic drug, the randomly PEGylated uricase molecule suffers from problems of reduced uricolytic activity, lack of selectivity, molecular heterogeneity, immunogenicity etc. In order to overcome these demerits, in the present study, the concept of site-specific modification of uricase enzyme using mPEG-maleimide via Thiol reactive PEGylation has been implemented. The residual uricolytic activity, molecular weight, number of PEG molecules attached and the extent of modification of the newly synthesized conjugates were determined and it was observed that these conjugates displayed improved properties in comparison to the currently available randomly PEGylated uricase formulations.

Keywords: Uricase, PEGylation, Improved pharmaceutical properties

INTRODUCTION

Uricase (urate: oxygen oxidoreductase, EC 1.7.3.3) is a therapeutic enzyme, which catalyzes the oxidative opening of purine ring of urate to yield allantoin, carbon dioxide, and hydrogen peroxide. [Wu X. et al. (2004)]. Uric acid is present in blood plasma and is insoluble. Excessive concentration of uric acid in the blood can lead to Gout, painful arthritis, disfiguring urate deposits (tophi) and renal failure [Lofty W. (2008)]. Gout can be cured by intravenous administration of uricase enzyme, which can convert uric acid crystals to allantoin. Allantoin being five to ten times more soluble than uric acid, gets easily eliminated through the kidneys [Pui C. et al. (2004)]. Humans do not produce enzymatically active uricase [Friedman T. et al. (1985)] and hence it is administered to hyperuricemic and gout patients in its conjugated form with PEG. Though it is a highly successful therapeutic drug, there are some associated drawbacks. The present PEGylated uricase formulations

available in the market are: Rasburicase and Pegloticase. Rasburicase has a monthly dose of 10 mg and can elicit an immune response [Vogt B. (2005)]. Pegloticase has biweekly dose of 0.14 mg/kg body weight, which is approximately 1.12 mg/kg body weight per month and elicits an immune response against mPEG [Yue C. et al. (2008)]. Considering a very interesting case of single site-specifically PEGylated Interferon α -a, only 4 μ g of weekly dosage is sufficient for the treatment of chronic Hepatitis C with reduced immunogenicity. [Foster G. R. (2010); Rodriguez T. et al. (2009)]. Hence, site-specifically PEGylated uricase can turn out to be an efficient alternative PEG therapeutic, capable of overcoming the demerits of the existing uricase therapeutics.

Also, antigenicity of randomly PEGylated PEG-uricase was reported by Ganson N. J. et al (2006). Interestingly, antibodies were directed against PEG itself rather than the uricase protein, which indicates PEG immunogenicity deserves further

4th International Engineering Symposium - IES 2015

March 4-6, 2015, Kumamoto University, Japan

investigation as it has potential implications for other PEGylated therapeutic agents in clinical use. Yang X. et al. (2013) have reported that Pegloticase, (recombinant mammalian uricase modified with methoxy PEG), after continued treatment for three months at a biweekly therapeutic dose of 0.14 mg/kg body weight, it elicited an immune response against mPEG in nearly 20% of patients. It can be assumed that reduction in the amount of mPEG attached can reduce the immunogenicity caused by mPEG.

In the present study, the concept of site-specific modification of uricase enzyme via Thiol reactive PEGylation has been implemented. The synthesis of site-specifically PEGylated conjugates of Uricase from *Bacillus fastidiosus* using Methoxy (polyethyleneglycol)-maleimide (mPEG-Mal) via Thiol modification approach has been carried out. The residual uricolytic activity, molecular weight, number of mPEG molecules attached and the extent of modification of the newly synthesized conjugates were determined and it was observed that these conjugates displayed improved pharmaceutical properties in comparison to the currently available uricase formulations.

MATERIAL AND METHODS

MATERIAL

Uricase from *Bacillus fastidiosus* (Average Mol wt 35 kDa) [specific activity: 9 U/mg], methoxyPEG-maleimide [mPEG-Mal] (Average Mol wt 5 KDa), Ellman's reagent (5,5-Dithiobis-2-nitrobenzoic acid), Bradford reagent, Dialysis membrane (20 KDa cutoff) uric acid and uric acid sodium salt were obtained from the Sigma Aldrich Company. Ethylenediamine tetra acetic acid (EDTA) sodium salt, boric acid, sodium dihydrogen phosphate, disodium hydrogen phosphate were procured from HiMedia Chemicals, (India). Millipore grade water was used for all the trials.

SDS PAGE Kit, reagents and the ready-to-load protein marker (medium range) were obtained from Bangalore Genei, India. UV-Visible Spectrophotometer (Hitachi) was used for evaluating the activity of the

native and PEGylated Uricase and also for carrying out all the colorimetric assays. A calorimeter (Systronics) was used for absorbance measurement in the visible range.

METHODS

Synthesis and purification of PEGylated conjugates:

Uricase from *Bacillus fastidiosus* (1 mg/mL) was allowed to react with mPEG-Mal (5 mg) in the ratio (Uc:mPEG-mal) of 1:5 (wt/wt) in 0.1 M sodium phosphate EDTA buffer at pH 7.2 and 4°C for 8-16 hours. After incubation, the reaction mixture was dialyzed using a pre-treated dialysis membrane (20 KDa-cutoff). Pre-treatment of the dialysis membrane was carried out by incubating the membranes for 10 minutes in boiling 1mM EDTA solution. Dialysis of the reaction mixture was carried out against 100mM Sodium phosphate buffer, pH 7.2 at 4°C. The dialyzed sample was then subjected to gel filtration chromatography at 25°C, using Sepharose 6B as the stationary column and the above mentioned buffer as the mobile phase. A flow rate of 1 ml/min was maintained. Fractions obtained were subjected to various calorimetric assays and fractions containing uricolytic activity were used as source of PEGylated Uricase.

Uricase enzymatic assay and protein estimation:

The enzymatic assay was carried out by the method described by Mahler H. et al. (1955). To a 3mL of 20mM boric acid buffer of pH 9.0, 75µL of 3.57mM uric acid solution and 20µL of uricase solution were added at 25°C. For the blank, 20µL of buffer was added, instead of the uricase solution. The blank and the test solutions were incubated at 25°C for ten minutes, after which the decrease in the uric acid concentration was measured with the aid of a UV-Visible spectrophotometer at 293nm. The difference between absorbance of the test and blank is equivalent to the decrease in uric acid concentration during the enzymatic reaction. Thus one unit of uricase activity was defined as the amount of uricase required to convert 1µmol of uric acid into allantoin per minute at 25°C and at pH

4th International Engineering Symposium - IES 2015

March 4-6, 2015, Kumamoto University, Japan

9.0, considering the milli-molar extinction co-efficient of uric acid (ϵ) at 293nm as $12.6\text{mM}^{-1}\text{cm}^{-1}$. Bradford's assay was used for determining the protein concentrations and hence the specific activities of native and PEGylated uricase.

SDS-PAGE (Sodium dodecyl sulphate polyacrylamide gel electrophoresis):

Sodium dodecyl sulphate-polyacrylamide gel electrophoresis (SDS-PAGE) was performed according to the method described by Laemmli U.K. (1970). 12% and 5% Acrylamide-bisacrylamide mixtures were used for the preparation of gels. Commercially obtained protein markers were in the molecular weight range of 14 kDa-110 kDa (Bangalore Genei). Staining and detection of protein bands was done using coomassie brilliant blue and de-stained with distilled water.

Polyacrylamide gel electrophoresis and iodine staining for mPEG-mal

Detection:

For the determination and visual quantification of free and bound PEG attached to the PEGylated proteins on the electrophoresis gel, a vertical polyacrylamide gel electrophoresis (PAGE) using iodine stain method was employed (method was adopted from Kurfurst M. (1992). Briefly, 15% and 6% acrylamide-bisacrylamide gel mixtures were prepared. PEGylated samples were prepared by dilution of the PEGylated reaction mixtures with an equal quantity of glycerol (to provide density to the sample for easy migration and to avoid sample spreading). After sample loading (12-15 μL), the electrophoresis procedure was carried out at 75 Volts and 20 mA for 2 hours in 1 litre of Tris-glycine buffer. The gels were recovered and subjected to iodine staining. For staining, the gel was washed in 20mL of perchloric acid solution for 10 minutes, 10 mL of 5% barium chloride solution for 5 minutes and 4mL of 0.1 M iodine aqueous solution for 2 min before washing in water to remove background staining. The complex formed by the reaction of the barium iodide with PEG is a brownish yellow complex, which can be detected and visualized after washing with water. The bands represent the presence and

position of free as well as uricase bound mPEG-mal.

Extent of modification:

For the determination of the extent of modification and the % of free thiols present after PEGylation, Ellman's assay was employed (adopted from Ellman G. L. (1959)). Briefly, to 970 μL of 0.1 M sodium phosphate buffer (pH 8.0, 1 mM EDTA), 50 μL of Ellman's reagent (4mg Ellman's Reagent in 1mL of Reaction Buffer) and 30 μL of the native and conjugated samples were added to make various test solutions. For the blank solution, 30 μL of buffer solution was added instead of Uricase solution. The reaction mixtures were incubated at room temperature for 15 minutes and their absorbencies was recorded at 412 nm.

The % free thiol groups was calculated using the **Eq 1:**

$$\% \text{ Free Thiol groups} =$$

$$\frac{(\text{Abs of PEGylated protein}) - (\text{Abs Blank})}{(\text{Abs of native protein}) - (\text{Abs Blank})}$$

The modification extent (ME) was determined using **Eq 2:**

$$ME = 100\% - \% \text{ Free Thiol groups.}$$

RESULTS AND DISCUSSION:

Degree of modification of uricase decides its overall quality like residual activity, immunogenicity and bio-compatibility. Binding of the mPEG-maleimide decides the degree of modification, residual uricolytic activity and molecular weight. Thiol PEGylation reactions carried out using mPEG-maleimide is as represented in **Fig 1**. Cysteine residues are valuable targets for achieving the site-specific modification of proteins. They are present in free form at a relatively low natural abundance level compared to the oxidized cysteine species. This advantage offers a very good scope of obtaining uniform and mono-PEGylated conjugates. Cysteine residues can be modified selectively, rapidly, quantitatively and in a reversible/irreversible fashion using maleimide terminated polymers [Colonna

C. et al. (2008)]. The aliquots of commercially purchased uricase were subjected to Thiol PEGylation reaction with mPEG-mal in the ratio of 1:5 as mentioned in the methods section. This ratio was selected based on the approximate number of cysteine molecules per subunit of uricase molecule.

After dialysis, it was observed from iodine staining and calorimetric methods that there was a significant reduction in the amount of free/ unbound mPEG-mal and other reaction by-products present in the PEGylation reaction mixture. The dialyzed mixture now contained only unmodified uricase and the site-specifically PEGylated Uricase conjugates, as the dialysis membrane used had a molecular weight cut off of 20 kDa. After gel filtration chromatography carried out at 25°C, size based separation of the reaction components was observed. The collected fractions were subjected to Uricase assay and residual uricolytic activities were determined. The uricolytic activities of the native and PEGylated Uricase were measured and were found to be 100% and 86.4% respectively. The result indicates that even after PEGylation the Uricase molecule possessed significant uricolytic activity, which is a very important criterion for a PEGylated molecule to be used for therapeutic purposes. Whereas, the previously reported randomly PEGylated Uricase conjugates possessed less than 70 % residual activity [Zhang C. et al. (2010); Bomalaski J. S. et al. (2002)].

The molecular weight of the site-specifically PEGylated Uricase conjugates possessing maximum residual activity was estimated by SDS-PAGE. **Fig 2a** and **b** represent the SDS-PAGE and iodine stained gel images of PEGylated and native Uricase. The apparent molecular weight of the site-specifically PEGylated conjugates was estimated to be approximately 40-45 kDa, significantly more in comparison to the native Uricase (35 kDa). It can be estimated that around 1-2 mPEG-mal molecules may be covalently bound per subunit of Uricase molecule, as observed by the iodine stained gel. Increase in molecular weight of the conjugates attributes to size enlargement and reduced

kidney ultrafiltration rate, hence its plasma half-life also increases.

The % of free thiols in gel filtration fractions containing the PEGylated Uricase was calculated to be 17.9% and the modification extent of thiol groups present on the enzyme surface was determined to be 82.1%. The results indicate the number of modified free thiols groups present on the surface accessible cysteine molecules. The modification extent is a very important criterion and is expected to be same for all the conjugate molecules formed. Uniformity of the conjugates eliminates any immunological ramifications caused due to conjugate heterogeneity. The results were also confirmed by calculating and comparing the molar sulphhydryl concentration of native and site-specifically PEGylated uricase molecules via Ellman's assay. It was observed that the sulphhydryl concentration of the PEGylated conjugates was lesser than the native uricase in comparison. Here, mono-PEGylated conjugates were obtained which eliminate the consequences of conjugate heterogeneity like immunological ramifications and varied immunological response. A high yield of mono-PEGylated conjugates can be obtained by reaction optimization and better chromatographic techniques. Future scope includes optimization of Thiol PEGylation reaction conditions and efficient purification of the conjugates, followed by detailed characterization of the site-specifically PEGylated conjugates by the present methodology.

CONCLUSIONS

The following conclusions are deduced from this study:

Even after PEGylation, the Uricase molecule possessed a very high uricolytic activity which is ideal for PEGylated enzyme to be employed for therapeutic purposes. High yields of monoPEGylated uricase conjugates can be obtained by using the described synthesis method, aided with efficient purification and characterization techniques.

4th International Engineering Symposium - IES 2015

March 4-6, Kumamoto University, Japan

REFERENCES

- [1] Bomalaski, J S et al (2002), Uricase formulated with polyethylene glycol (Uricase-PEG 20): biochemical rationale and preclinical studies, *J. RHEUMATOL.*, Vol. 29, pp. 1942–1948.
- [2] Colonna, C et al (2008), Site-directed PEGylation as successful approach to improve the enzyme replacement in the case of prolidase, *INT. J. PHARM.*, Vol. 358, pp. 230–237.
- [3] Ellman, GL (1959), Tissue sulfhydryl groups, *ARCH BIOCHEM BIOPHYS.*, Vol. 82, pp.70-77.
- [4] Foster, G R (2010), PEGylated interferons for the treatment of chronic hepatitis C: pharmacological and clinical differences between peginterferon-alpha-2a and peginterferon-alpha-2b, *DRUGS*, Vol.70, No.2, 147–165.
- [5] Friedman, T B et al (1985), On the loss of uricolytic activity during primate evolution-I, Silencing of urate oxidase in a hominoid ancestor, *COMP. BIOCHEM. PHYS. B*. Vol. 81, pp. 653–659.
- [6] Ganson, N J et al (2006), Control of hyperuricemia in subjects with refractory gout, and induction of antibody against poly(ethylene glycol) (PEG), in a phase I trial of subcutaneous PEGylated urate oxidase, *ARTHRITIS RES THER.*, Vol. 8, No. 1, pp 12.
- [7] Kurfurst, M M et al (1992), Detection and molecular weight determination of polyethyleneglycol-modified hirudin by staining after sodium dodecyl sulfate polyacrylamide gel electrophoresis, *ANAL BIOCHEM.*, Vol. 200, pp. 244–248.
- [8] Laemmli, U K (1970), Cleavage of structural proteins during the assembly of the head of bacteriophage T4, *NATURE*, Vol. 227, pp. 680–685.
- [9] Lotfy, W A (2008), Production of a thermostable uricase by a novel *Bacillus thermocatenulatus* strain, *BIORESOURCE. TECHNOL.*, Vol. 99, pp. 699–702.
- [10] Mahler, H et al (1955), Studies on Uricase. I. Preparation, Purification and Properties of a Cuproprotein, *J. BIOL. CHEM.*, Vol. 216, pp. 625.
- [11] Pui, C H et al (2001), Recombinant urate oxidase (rasburicase) in the prevention and treatment of malignancy-associated hyperuricemia in pediatric and adults patients: results of a compassionate-use trial, *LEUKEMIA*, Vol. 15, pp. 1505–1509.
- [12] Rodriguez, T M et al (2009), Peginterferon alfa-2a and ribavirin in Latino and non-Latino whites with hepatitis C, *N ENGL J MED*, Vol. 360, No 3, pp. 257–67.
- [13] Vogt, B (2005), Urate oxidase (rasburicase) for treatment of severe tophaceous gout, *NEPHROL DIAL TRANSPLANT*, Vol.20, pp. 431–433.
- [14] Wu, X et al (2004), Hyperuricemia and urate nephropathy in urate oxidase deficient mice, *PROC. NAT. ACAD. SCI.*, Vol. 91, pp. 742–746.
- [15] Yang, X et al (2013), Uricases as therapeutic agents to treat refractory gout: Current states and future directions, *DRUG DEV RES*, Vol. 73, No 2, pp. 66–72.
- [16] Yue, C S et al (2008), Population pharmacokinetic and pharmacodynamic analysis of Pegloticase in subjects with hyperuricemia and treatment-failure gout, *J CLIN PHARMACOL*, Vol. 48, No. 6, pp. 708–718.
- [17] Zhang, C et al (2010), Effects of modification of amino groups with Polyethylene Glycol on a recombinant Uricase from *Bacillus fastidiosus*. *BIOSCI. BIOTECHNOL. BIOCHEM.*, Vol. 74, No. 6, pp. 1298–1301.

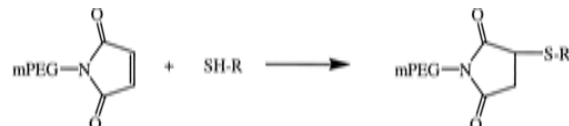


Fig 1: Reaction scheme for Thiol PEGylation at the free thiol group of a cysteine molecule

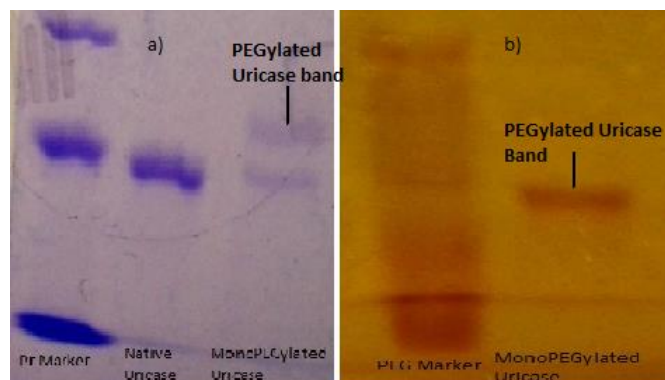


Fig 2: a) SDS-PAGE (Coomassie blue stained) gel for site-specifically PEGylated Uricase: b) Iodine stained gel for mPEG-mal detection for site-specifically PEGylated uricase

TREATMENT OF METHOXYANILINE CONTAINING SOLUTION USING ANAEROBIC- AEROBIC SEQUENTIAL BATCH REACTOR

Basavaraju Manu and Dangmei A P

*Department of Civil Engineering
National Institute of Technology Karnataka, Surathkal, India
email:bmanu8888@gmail.com*

ABSTRACT: In the present study, treatment of 2- Methoxyaniline (2MA) and 4-Methoxyaniline (4MA) containing solution has been carried out using anaerobic aerobic sequential batch reactor (AASBR). The Methoxyaniline compounds are reported to be possible human carcinogen. The major contributors of Methoxyaniline to the environment are effluents of pharmaceutical company, dyeing industry, oil refineries and chemical plants. Methoxyaniline also causes breathing problem, affect metabolism of body, skin irritation and allergy, kidney damage and death when exposed to higher concentration. Experiments were carried out for a period of more than 180 days at ambient liquid temperatures (26° - 28° C) for varying initial concentrations (0-40 mg/L) of Methoxyaniline at organic loading rate (OLR) of 2 kg COD/m³.d. The hydraulic retention time (HRT) of both the anaerobic and aerobic reactors was 24 hours. Six reactors were operated out of which three were under anaerobic conditions and three under aerobic conditions. Maximum overall removal efficiencies observed was 94% and 90% for 2MA and 4MA respectively at influent concentration of 20 mg/L. Degradation efficiencies were better for 2MA when compare to 4MA. At higher influent concentration of 40 mg/L of Methoxyanilines, anaerobic process was severely inhibited. Hence sequential Advanced Oxidation Processes followed by AASBR seems to be efficient and economical treatment for Methoxyaniline containing wastewater.

Keywords: 2-Methoxyaniline, 4-Methoxyaniline, Anaerobic, Aerobic, SBR

INTRODUCTION

The Methoxyaniline compounds are reported to be possible human carcinogen (Weast 1981). The major contributors of Methoxyaniline to the environment are effluents of pharmaceutical company, dyeing industry, oil refineries and chemical plants(<http://www.epa.gov/osw/hazard/wastetypes/wasteid/dyes/index.htm>).

Methoxyaniline also causes breathing problem, affect metabolism of body, skin irritation and allergy, kidney damage and death when exposed to higher concentration. Hence it is of utmost importance to treat wastewater containing methoxyaniline compounds in water and also meet the existing stringent

environmental regulations. Methoxyaniline (Anisidine) which is been identified as toxic and hazardous compound by various national and international regulatory bodies needs a treatment process which is clean and cost effective. The SBR technology which has already been used to treat other Aniline containing compounds as well as Benzene ring containing compound gives a very fair and encouraging sign for the biodegradation of this compound.

The biological treatment of complex chemical process contaminated wastewater is particularly challenging due to their low biodegradable nature and transient flow conditions. Efficiency of the biological process to treat wastewater

containing toxic and recalcitrant compounds depends on the presence of appropriate microorganisms, system acclimatization and specific operational conditions of the bioreactor.

SBR technology differs in various ways from conventional technologies used in biological treatment of wastewater. The most obvious difference is that in SBR technology, the reactor volume varies with time, whereas it remains constant in the traditional continuous flow system. The advantages of SBR technology include the flexibility of operation (change of phase), feasibility of operation at low retention time, control over microbial population and various reactor configurations. Hence in the present study degradation of 2-Methoxyaniline (2-MA) and 4-Methoxyaniline (4-MA) using Sequential Batch Reactor (SBR) technology has been carried out.

MATERIALS AND METHODS

The pollutant 2- Methoxyaniline and 4-Methoxyaniline purchased from Loba chemie Pvt. Ltd. (India) was used to prepare the synthetic pollutant wastewater. The chemical structures of 2-Methoxyaniline and 4- Methoxyaniline are given in Figure 1.

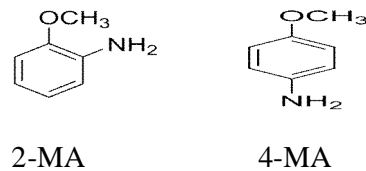


Fig.1 Chemical Structures of 2-MA and 4-MA

Microbial seeds obtained from NMPT Sewage treatment plant Mangalore are used as biomass for all the three anaerobic and three aerobic reactors. Effective volume for anaerobic reactors was 2L and for aerobic reactors volume was of 1L capacity. Organic loading rate of 1kg COD/m³.day was initially maintained to develop the biomass. Throughout the experiments, reactors were fed with synthetic wastewater containing Dextrose as the source of Carbon. Dextrose was used as a carbon source because it is capable of supporting biological system which is reflected in its frequent use as carbon source in waste water treatment

studies (Hickman and Novak, 1984). Sodium bicarbonate was used as buffer (for anaerobic reactors) and trace metal solution was used for providing the essential micronutrients. After some time OLR was increased to 2kg COD/m³.day and this was maintained throughout the study. Each anaerobic reactor was maintained with MLSS of 8-9 g/L and 4-5g/L in aerobic reactors.

After achieving the desired OLR of 2kg COD/m³.day, 2- MA was added to the 1st reactor and 4- MA was added in the 2nd reactor, the 3rd anaerobic reactor was maintained as control anaerobic reactor. After 24 hours, effluent of 1st, 2nd and 3rd reactor were fed to 4th, 5th and 6th aerobic reactor respectively. All the procedure like feeding, decanting and wasting were done manually. Aeration was provided using submerged diffusers placed at the bottom of the reactor. A single cycle consists of 24 hour anaerobic and 24 hour aerobic and hence it takes 48 hours to complete a full cycle. The procedure consists of fill, for both anaerobic phase and aerobic phase known as reaction phase, then it proceeds with settling and decanting (Idle phase was omitted in this study). So out of six reactors two are control reactors i.e. one aerobic and another anaerobic, therefore out of four remaining reactors one aerobic and one anaerobic are used for treating 2-MA and similarly the other two reactors are used for treating 4-MA. The influents as well as the effluents from each of the reactors were analyzed for pH, Alkalinity, COD, ORP test, DO and pollutant concentration. Three samples were collected for each cycle of SBR i.e. the influent, the end of anaerobic phase and the end of aerobic phase. All the samples were centrifuged at 10000 RPM and then filtered through Micro Filter paper (Whitman No. 2) before the analysis to prevent any possible occurrence of errors caused due to interference of suspended particles in the samples. The analysis was carried out according to the procedure outlined in Standard Methods (APHA, 2005). pH is measured by glass electrode pH meter. COD was determined using closed reflux titrimetric method. Alkalinity was determined by titrimetric method and mixed-liquor volatile suspended solids

(MLVSS) were determined by the gravimetric method. DO is also measured by DO meter and ORP by ORP meter. The pollutant concentrations were analyzed by using UV spectrophotometer. 283nm was used for analysis of 2MA. 4-MA was measured at 296nm. Experimental set up is shown in Figure 2.

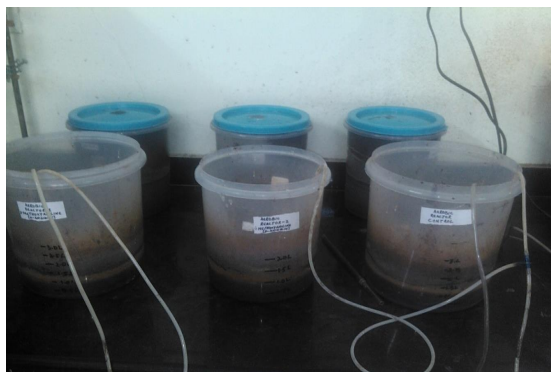


Fig.2 Photo of the experimental setup

RESULTS AND DISCUSSION

During the start-up phase, overall removal of COD started from 78% and it went up to 90% when quasi steady state was finally achieved. The other parameters like pH, DO, MLSS and MLVSS were routinely checked to determine the status and health of the reactor. After the stabilization of the reactor at OLR 2 Kg COD/m³.day, the feeding of the reactors with their respective pollutants was started. The feeding concentration of OLR of 2 Kg COD/m³.day was kept constant throughout the study period.

Sequential Anaerobic aerobic treatment of 2-MA containing solution

After adding the pollutant, the COD removal efficiency suddenly decreased for both aerobic reactor and anaerobic reactor. Later the efficiency was able to pick up slowly and at quasi steady state, an overall COD removal of 89% was observed. At the beginning of the treatment, for 20 mg/L 2MA, the pollutant degradation in anaerobic reactor was 20% but gradually it increased up to 41% when quasi steady state was achieved after 13th cycle. The overall COD removal efficiencies after aerobic treatment started from 71% and then gradually increased with number of cycles and reached 94% at the end of

quasi steady state. Figure 3 shows the UV-Visible spectrum for 2-MA during the study period when influent concentration of 2-MA was 20 mg/L. From the figure it can be observed that peak at 283 nm is slightly reduced for the anaerobic treated effluent but is has disappeared in the aerobic effluent suggesting the possible degradation of 2-MA after the aerobic treatment.

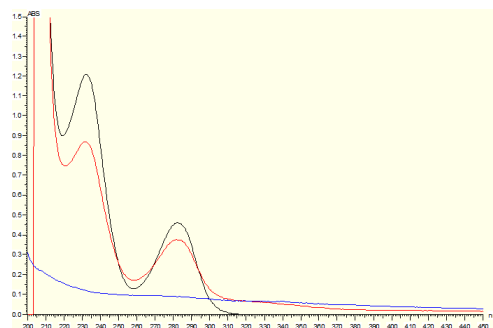


Fig: 3. UV-Visible spectrum of 2-MA containing solution during sequential anaerobic aerobic treatment.

(Influent ——)

Anaerobic Effluent ——

Aerobic Effluent ——)

After achieving quasi steady state at 20mg/L for 2MA and possible degradation of the pollutant, the influent dosage was increased to 30mg/L (0.24mM). This time 15 cycles were required to reach quasi steady state. The overall COD removal slightly decreased when the pollutant concentration was increased but with increase in number of cycle COD removal efficiencies of up to 85% at the end of quasi steady state was observed.

During the influent concentration of 30mg/L, 2-MA removal efficiencies was quite low at 29% in the beginning and no significant increase in the removal efficiencies was observed. It was 33% at quasi steady state which is lower than the 41% achieved during influent concentration of 20 mg/L. For sequential aerobic step, at the beginning removal efficiencies of pollutant was 65% but it gradually increased and reached up to 82% at the end of quasi steady state. The decrease in the removal efficiencies of pollutant might be associated with buildup of toxicity in both aerobic and anaerobic

the reactor. With some success in aerobic reactor removal efficiencies, the pollutant loading was further increased to 40mg/L (0.32mM). The overall COD removal efficiencies in the reactor decreased to 70% and this might be due to decrease in microbial activity.

At this 40mg/L dosage, pollutant removal efficiencies during the anaerobic phase kept on decreasing with time from 34% to 15% at the end of 13 cycles. In the same way the pollutant removal efficiencies after aerobic treatment also kept decreasing from 78% to 65% after 13 cycle of treatment. The degradation efficiencies kept on decreasing and hence further increase in influent dosage of 2MA was stopped. The reason behind the decrease in the degradation efficiencies of 2-MA during sequential anaerobic aerobic treatment might be due to the toxicity that was induced by 2-MA thus reducing the microbial activities. Thus the results suggest that optimum dosage should be between 20mg-30mg/L for sequential anaerobic aerobic treatment. Any higher dosages of 2-MA in the influent requires a prior Advanced Oxidative treatment to make it amenable for sequential biological treatment. The overall COD removal efficiencies and 2-MA removal efficiencies observed during the present study is given in Table 1.

Table 1. Overall COD efficiencies and 2-MA efficiencies observed sequential anaerobic removal removal during aerobic treatment

2 Methoxyani line (2MA) Concentrati on	20mg/L or 0.16 mM.	30mg/L or 0.24 mM.	40mg/L or 0.32 mM
Overall COD removal efficiencies	88 %	85%	70%
Maximum overall 2- MA removal during efficiencies	94%	82%	65%

Sequential Anaerobic aerobic treatment of 4-MA containing solution

After adding the initial 20mg/L of 4MA for the first time in the reactor, a sudden decrease in COD removal efficiencies during both aerobic and anaerobic reactor was observed. But with time, the efficiencies increased gradually and were able to reach up to 89% at the end of quasi steady state. When pollutant was added to the anaerobic reactor for the first time, at the beginning of the treatment for 20 mg/L 4MA, the pollutant degradation in anaerobic reactor was quite low at 21% but slowly it increased up to 42% when quasi steady state was achieved after 13 cycles. The overall degradation after aerobic treatment started from 72% and reached up to 90% when quasi steady state was achieved. Figure 4 shows the UV-Visible spectrum for 4-MA containing solution during sequential anaerobic-aerobic treatment. From the figure, it can be observed that peaks in both anaerobic and effluent have shifted to new wavelengths suggesting possible transformation of 4-MA during the studies but no degradation was observed.

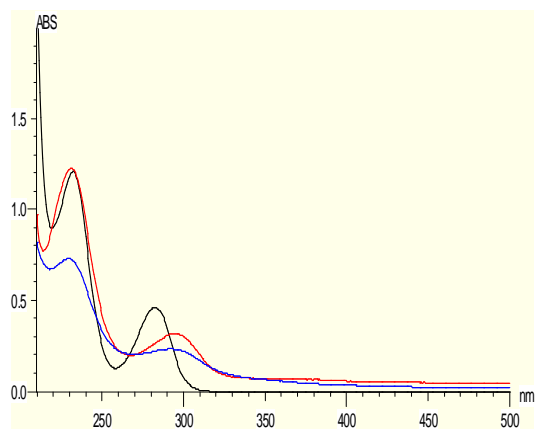


Fig: 4. UV-Visible spectrum of 2-MA containing solution during sequential anaerobic aerobic treatment.
(Influent _____
Anaerobic Effluent _____
Aerobic Effluent _____)

After achieving quasi steady state at 20mg/L for 4MA, the pollutant dosage was further increased to 30mg/L (0.24mM). This time 15 cycles were required to reach

4th International Engineering Symposium - IES 2015

March 4-6, Kumamoto University, Japan

quasi steady state. The overall COD removal efficiencies decreased gradually from 72% and came down till 62%. But with time it once again increased up to 75% at quasi steady state.

In the anaerobic reactor, the degradation efficiencies of 4-MA started slowly from 31% and decreased till 24%, and then with time it started increasing and finally reached 36% at the end of the quasi steady state. After aerobic treatment, 4-MA removal efficiencies could reach up to 76% at the end of quasi steady state.

The COD removal efficiencies and pollutant removal trend for 30mg/L dosage for 4MA, indicates that, in anaerobic reactor the degradation picks up slowly in the middle of the study but was not able to reach higher and thus stabilized at 36% which is low. In case of aerobic reactor, the degradation efficiencies were able to pick up in the middle and at the end of quasi steady state finally it was able to stabilise at 76%. With very little increase in removal efficiencies in 30mg/L in both the aerobic and anaerobic reactor, the loading of the pollutant was just increased by 5mg/L instead of 10mg/L in previous cases.

Thus 35mg/L of 4-MA was added to the reactor. The COD removal efficiencies was not significant at this dosage giving 71% overall removal efficiency.

The trend for 4-MA removal efficiencies was decreasing with more number of cycles. For anaerobic treatment, it decreased to 11% which is very less and so also with aerobic reactors which kept on decreasing till 55%. Study was stopped at this stage as the degradation efficiencies observed was quite low and still decreasing. In this study the degradation efficiencies observed during influent concentration of 20mg/L with 90% was quite successful even though with the subsequent increase in dosage of 30mg/L and 35mg/L which gives degradation of 75% and 55% might not be that significant. The decrease in the degradation efficiencies when the pollutant concentration was increased to higher dosage can be attributed to the buildup of toxicity inside the reactor thus decreasing the microbial activity. Hence sequential anaerobic aerobic treatment of 4-MA

containing effluent is possible with 4-MA influent concentration of 20 mg/L and with any further increase in influent concentration of 4-MA may require pretreatment with an Advanced oxidative treatment. COD removal efficiencies and pollutant removal efficacies observed during sequential anaerobic aerobic treatment of 4-MA containing solution is given in Table 2.

Table 2. Overall COD removal efficiencies and 4-MA removal efficiencies observed during sequential anaerobic and aerobic treatment

4-Methoxyaniline (4MA) Concentration	20mg/L or 0.16 mM.	30mg/L or 0.24 mM.	35mg/L or 0.28 mM.
Overall COD removal efficiencies	89 %	75%	70%
Maximum overall 4-MA removal efficiencies	90%	76%	55%

Zeyer J, Wasserfallen A and Timmis K N (1985) have reported that 4MA was not able to be utilized as sole source of carbon by *Moraxella sp.* Strain G.

CONCLUSIONS

The following conclusions are deduced from this study:

- A very good result of 94% overall removal was achieved for 2MA at 20mg/L dosage. But with increase in dosage the removal percentage came down to 82% and 65% for 30mg/L and 40mg/L respectively.
- The overall COD removal during 2MA treatment at lower dosage which is when the toxicity is lower gives a higher removal of 88% but at 40mg/L the COD removal was reduced to 70% suggesting that 2MA was inhibiting the microbial activity when compared with COD removal efficiencies of up to 85% observed in the control reactor.

4th International Engineering Symposium - IES 2015

March 4-6, Kumamoto University, Japan

- For 4MA also higher pollutant removal efficiencies was observed at 20mg/L when 90% overall removal efficiencies were observed. But with increase in influent concentration, removal percentage came down drastically to 76% and 55% for 30mg/L and 35mg/L respectively. The decrease in removal is more prominent for anaerobic reactor.
- The overall COD removal efficiencies observed during 4MA treatment at lower dosage when toxicity is lower was 89% but at 35mg/L the COD removal was reduce to 70% when compared with COD removal efficiencies of up to 85% observed in the control reactor suggesting that 4MA was inhibiting microbial activity.
- From the present study it can be observed that AASBR is able to degrade 2MA better than 4MA owing to its characteristic position of functional group where in methoxy group in the meta position was imparting more stability to the benzene ring thereby increasing its xenobioticity.

REFERENCES

- [1] APHA (2005) Standard Methods for Analysis of Water and Wastewater, New York, USA.
- [2]<http://www.epa.gov/osw/hazard/wastetypes/wast eid/dyes/index.htm>
- [3] Hickman G T and Novak J T (1984), Acclimation of Activated Sludge to Pentachlorophenol, Journal of Water Pollution Control Federation, Vol. 56, pp. 364-372.
- [4] Weast R C ed. (1981). *CRC Handbook of Chemistry and Physics* (62nd ed.). Boca Raton, FL: CRC Press. p. C-98.
- [5] Zeyer J, Wasserfallen, A and Timmis K N (1985), Microbial Mineralization of Ring-Substituted Anilines through an Ortho-Cleavage Pathway, Applied and Environmental Microbiology, Vol.50, No.2, pp 447-453.

Study of Microbial Fuel Cell operated on Sludge from Waste Water Treatment Plant - A Case Study

**Rahul Gautam, Arunabh Choudhury, S.K. Deepak,
Patel Jay Mahendra, Arun Kumar Thalla**

*Department of Civil Engineering, NITK Surathkal, India
Email: arunav.choudhury@gmail.com*

The present scenario of the world demands large energy resources to fulfil its increasing energy demands, which leads to more waste generation and depletion of resources. It is well recognized that alternative sources of energy is the need of the hour. Current reliance on fossil fuels is unsustainable due to finite resource of fuels and their associated pollution resulting in the degradation of the environment. With the depletion of the traditional energy resources and their contribution to serious environmental hazards, there needs to be a sustained effort to research and develop alternative sources to meet the needs of our communities. A lot of research is being conducted in the field of alternative energy sources. In past decades, high rate anaerobic processes are finding increased application in treatment of domestic and industrial wastes. The discovery that the electricity can be produced from bacterial activity from waste and biomass has gained much attention. This has led to increased interest towards the study of Microbial Fuel Cell (MFC).

MFCs are the devices which use microorganisms e.g. bacteria as a catalyst to oxidize organic matter, which results in the production of electrons and protons. In the present study the two chambered MFC was studied, connected with the PVC pipe containing solidified agar along with potassium chloride, which acts as both a proton exchange membrane as well as a salt bridge. The electrodes used were of graphite rod. The anode chamber was filled with the sludge collected from the Sewage treatment plant situated at NITK, Surathkal, while the cathode chamber was studied for tap water containing NaCl, tap water containing NaCl with aeration provided, the tap water and the tap water with aeration provided. The oxidation of the organic matter present in sludge takes place at anode and results into the production of electrons and protons. The protons travel to cathode chamber through proton exchange membrane i.e. PVC pipe containing agar saturated with KCl. Electrons produced by these bacteria are transferred to anode (negative terminal) and flow to cathode (positive terminal) linked by a conducting material containing a resistor or resistance.

As per the study, on the fifth day, it showed a potential of range 220 mV with tap water containing NaCl. But when aerator was applied to the cathodic chamber, the increase in voltage was reported, and reached to 250 mV. With the wasted activated sludge, it showed a potential in the range of 280- 290 mV with tap water containing NaCl but when tap water is used the voltage was recorded in range of 310- 320 mV and the voltage reached to 650 mV with tap water provided with aerator and current of 0.4 mA. The increase in the voltage and current is expected with the combination of different electron acceptors in the cathodic chamber e.g. Potassium ferricyanide, Potassium per magnate etc.

4th International Engineering Symposium - IES 2015

March 4-6, 2015, Kumamoto University, Japan

